

Motoichi Ohtsu
Editor

Handbook of Nano-Optics and Nanophotonics



SpringerReference

Handbook of Nano-Optics and Nanophotonics

Motoichi Ohtsu
Editor

Handbook of Nano-Optics and Nanophotonics

With 732 Figures and 24 Tables

 **Springer** Reference

Editor

Motoichi Ohtsu
Graduate School of Engineering
The University of Tokyo
Tokyo, Japan

ISBN 978-3-642-31065-2 ISBN 978-3-642-31066-9 (eBook)
ISBN 978-3-642-31067-6 (print and electronic bundle)
DOI 10.1007/978-3-642-31066-9
Springer Heidelberg New York Dordrecht London

Library of Congress Control Number: 2013936745

© Springer-Verlag Berlin Heidelberg 2013

This work is subject to copyright. All rights are reserved by the Publisher, whether the whole or part of the material is concerned, specifically the rights of translation, reprinting, reuse of illustrations, recitation, broadcasting, reproduction on microfilms or in any other physical way, and transmission or information storage and retrieval, electronic adaptation, computer software, or by similar or dissimilar methodology now known or hereafter developed. Exempted from this legal reservation are brief excerpts in connection with reviews or scholarly analysis or material supplied specifically for the purpose of being entered and executed on a computer system, for exclusive use by the purchaser of the work. Duplication of this publication or parts thereof is permitted only under the provisions of the Copyright Law of the Publisher's location, in its current version, and permission for use must always be obtained from Springer. Permissions for use may be obtained through RightsLink at the Copyright Clearance Center. Violations are liable to prosecution under the respective Copyright Law.

The use of general descriptive names, registered names, trademarks, service marks, etc. in this publication does not imply, even in the absence of a specific statement, that such names are exempt from the relevant protective laws and regulations and therefore free for general use.

While the advice and information in this book are believed to be true and accurate at the date of publication, neither the authors nor the editors nor the publisher can accept any legal responsibility for any errors or omissions that may be made. The publisher makes no warranty, express or implied, with respect to the material contained herein.

Printed on acid-free paper

Springer is part of Springer Science+Business Media (www.springer.com)

Preface

Recent advances in photonic systems demand drastic increases in the degree of integration of photonic devices for large-capacity, ultrahigh-speed signal transmission and information processing. Device size has to be scaled down to nanometric dimensions to meet this requirement, which will become even more strict in the future. Moreover, the equipment used for fabricating photonic devices must drastically decrease the size of the fabricated patterns in order to achieve ultralarge-scale integrated circuits. However, these requirements cannot be met even if the physical dimensions of material structures are decreased by advanced methods based on nanotechnology. It is also essential to decrease the spatial extent of the electromagnetic field used as a carrier for signal transmission, processing, and fabrication. Reducing the electromagnetic field to dimensions beyond the diffraction limit of propagating field is possible by using optical near fields. Nano-optics deals with the light generated in or on nanometer-sized particles. The concepts have been applied to open up an innovative field of technology “nanophotonics” allowing the development of novel photonic devices, fabrication techniques, and systems. Nanophotonics, proposed by the author in 1993, is a novel optical technology that exploits the unique properties of the optical near-field or dressed photon.

The interest in nanophotonics is due not only to its ability to meet the above requirements but also to its *qualitative innovations* in photonic devices, fabrication techniques, energy conversion, and information processing systems by utilizing the novel functions and phenomena made possible by optical near-field interactions, which are otherwise impossible with conventional propagating light. Based on interdisciplinary studies involving condensed-matter physics, optical science, and quantum field theory, nano-materials and optical energy transfer in the nanometric regime have been extensively studied in the last two decades. Through these studies, novel dressed photon theories have been developed, and a variety of novel phenomena have been found. The results of this basic research have been applied to develop nanometer-sized photonic devices, nanometer-resolution fabrication techniques, highly efficient energy conversion, and novel information processing, resulting in *qualitative innovations*. Further advancement in these areas is expected to create novel optical sciences in the nanometric domain, which will spur further progress in nanophotonics that will help to support the sustainable development of people’s lives all over the world.

This unique text “Handbook of Nano-optics and Nanophotonics” has been published to review the results of advanced studies in the field of nanophotonics and covers the most recent topics of theoretical and experimental interest in relevant fields. It is composed of six parts, and the chapters in these parts are written by leading scientists in the relevant field. Thus, this handbook will provide high-quality scientific and technical information to scientists, engineers, and students who are or will be engaged in nanophotonics research. Each chapter originally appeared in the monograph series “Progress in Nano-Electro-Optics I–VII” and “Progress in Nanophotonics I” (edited by M. Ohtsu, published in the Springer Series in Optical Science). The content of each original article has been revised, expanded, and updated for inclusion in this handbook.

I am grateful to Dr. C. Ascheron of Springer-Verlag for his guidance and suggestions throughout the preparation of this handbook. This handbook is published with the support of Prof. T. Yatsui of the University of Tokyo, an associate editor. I hope that this handbook will be a valuable resource for readers and future specialists in nanophotonics.

April 2013

Motoichi Ohtsu
Tokyo, Japan

About the Editor



Motoichi Ohtsu Graduate School of Engineering, The University of Tokyo, Tokyo, Japan

Motoichi Ohtsu received his Dr. Eng. degree in Electronics Engineering from the Tokyo Institute of Technology, Tokyo, in 1978. He was first appointed as research associate, then as associate professor, and finally as professor at the Tokyo Institute of Technology. From 1986 to 1987, while on leave from the Tokyo Institute of Technology, he joined the Crawford Hill Laboratory, AT&T Bell Laboratories, Holmdel, New Jersey, USA. In 2004, he moved to the University of Tokyo as a professor. He has been the leader of the “Photon Control” project (1993–1998: the Kanagawa Academy of Science and Technology, Kanagawa, Japan), the “Localized Photon” project (1998–2003: ERATO, JST, Japan), the “Terabyte Optical Storage Technology” project (2002–2006: NEDO, Japan), the “Near Field Optical Lithography System” project (2004–2006: Ministry of Education, Japan), the “Nanophotonics” team (2003–2009: SORST, JST, Japan), the “Innovative Nanophotonics Components Development” project (2006–2011: NEDO, Japan), and the “Nanophotonics Total Expansion: Industry-University Cooperation and Human Resource Development” project (2006–2011: NEDO, Japan).

Dr. Ohtsu has written over 470 papers and received 83 patents. He is the author, co-author, and editor of 62 books, including 27 in English. In 2000, he was appointed as President of the IEEE LEOS Japan Chapter. From 2000, he has been an executive director of the Japan Society of Applied Physics. His main field of interests are the nanophotonics and dressed photon technology. Dr. Ohtsu is a fellow of the Optical Society of America and a fellow of the Japan Society of Applied Physics. He is also a tandem member of the Science Council of Japan. He has been awarded 14 prizes from academic institutions, including the Issac Koga Gold Medal of URSI in 1984; the Japan IBM Science Award in 1988; two awards from the Japan Society of Applied Physics in 1982 and 1990; the Inoue Science Foundation Award in 1999; the Japan Royal Medal with a Purple Ribbon from the Japanese Government in 2004; the H. Inoue Award from JST in 2005; the Distinguished Achievement Award from the Institute of Electronics, Information and Communication Engineering of Japan in 2007; and the Julius Springer Prize for Applied Physics in 2009.

Contents

Volume 1

1 Introduction	1
Motoichi Ohtsu	
Part I Principle and Theoretical Background	9
2 Classical Theory of Optical Near Field	11
Itsuki Banno	
3 Optical Near-Field Interactions and Yukawa Potential	65
Kiyoshi Kobayashi, Suguru Sangu, and Motoichi Ohtsu	
4 A Phenomenological Description of Optical Near Fields and Optical Properties of N Two-Level Systems Interacting with Optical Near Fields	109
Akira Shojiguchi, Kiyoshi Kobayashi, Suguru Sangu, Kazuo Kitahara, and Motoichi Ohtsu	
5 Theory and Principles of Operation of Nanophotonic Functional Devices	187
Suguru Sangu, Kiyoshi Kobayashi, Akira Shojiguchi, Tadashi Kawazoe, and Motoichi Ohtsu	
6 Quantum Description of Optical Near Fields Including Vibrational Degrees of Freedom	251
Kiyoshi Kobayashi, Yuji Tanaka, Tadashi Kawazoe, and Motoichi Ohtsu	
Part II Basic Tools	279
7 Near-Field Optical Fiber Probes and the Applications I	281
Shuji Mononobe	

8	Near-Field Optical Fiber Probes and the Applications II	335
	Takashi Yatsui and Motoichi Ohtsu	
9	Near-Field Optical Head Technology for High-Density, Near-Field Optical Recording	367
	Takuya Matsumoto	
Part III	Sensing and Spectroscopy	401
10	Nano-optical Imaging and Spectroscopy of Single Semiconductor Quantum Constituents	403
	Toshiharu Saiki	
11	Optical Interaction of Light with Semiconductor Quantum-Confined States at the Nanoscale	443
	Toshiharu Saiki	
12	Recombination Dynamics in $\text{In}_x\text{Ga}_{1-x}\text{N}$-Based Nanostructures	483
	Yoichi Kawakami, Akio Kaneta, Kunimichi Omae, Yukio Narukawa, and Takashi Mukai	
13	Near-Field Optical Microscopy of Plasmonic Nanostructures	527
	Kohei Imura and Hiromi Okamoto	
14	Luminescent Nanomaterials for Molecular-Specific Cellular Imaging	563
	Andrei Vasilyevich Zvyagin, Zhen Song, Annemarie Nadort, Varun Kumaraswamy Annayya Sreenivasan, and Sergey Mikhailovich Deyev	

Volume 2

Part IV	Devices, Fabricated Structures, and Relevant Materials	597
15	Integration and Evaluation of Nanophotonic Devices Using Optical Near Field	599
	Takashi Yatsui, Wataru Nomura, Gyu-Chul Yi, and Motoichi Ohtsu	
16	Properties of Optical Near-Field Excitation Transfers in Randomly Distributed Spherical Quantum Dots	643
	Wataru Nomura, Takashi Yatsui, and Motoichi Ohtsu	
17	Ultrahigh-Density Storage Media for Near-Field Optical Recording	671
	Hiroyuki Hieda, Katsuyuki Naito, Takashi Ishino, Kuniyoshi Tanaka, Masatoshi Sakurai, Yoshiyuki Kamata, Seiji Morita, Akira Kikitsu, and Koji Asakawa	

18	Temperature-Induced and Photo-Induced Phase Transition in a Bistable Metal-Cyanide Polymer	693
	Hiroko Tokoro and Shin-ichi Ohkoshi	
19	Photoinduced Energy Transfer in Artificial Photosynthetic Systems	729
	Hiroshi Imahori and Tomokazu Umeyama	
20	Growth and Electro-Magneto-Optics of Oxide Quantum Structures Based on ZnO	767
	Hiroaki Matsui and Hitoshi Tabata	
21	Self-Formation of Semiconductor Quantum Dots	809
	Koichi Yamaguchi	
22	Simple Approaches for Constructing Metallic Nanoarrays on a Solid Surface	845
	Hidenobu Nakao	
Part V	Nanophotonic Systems	873
23	Nanophotonic Systems Based on Localized and Hierarchical Optical Near-Field Processes	875
	Makoto Naruse	
24	Probe-Free Nanophotonic Systems: Macroscale Applications Based on Nanophotonics	909
	Naoya Tate, Makoto Naruse, and Motoichi Ohtsu	
Part VI	Related Basic Sciences	943
25	Momentum Modulation of Electrons in Optical Near-Fields	945
	Jongsuck Bae, Ryo Ishikawa, and Koji Mizuno	
26	Deflecting and Detecting Atoms with Near-Field Lights	977
	Haruhiko Ito	
27	Laser Desorption and Ionization Mass Spectrometry Using Plasmonic Substrates	1017
	Lee Chuin Chen, Hirokazu Hori, and Kenzo Hiraoka	
	Index	1057

Contributors

Koji Asakawa Organic Materials Laboratory, Corporate Research & Development Center, Toshiba Corporation, Kawasaki, Japan

Jongsuck Bae Department of Engineering Physics, Electronics and Mechanics, Nagoya Institute of Technology, Nagoya, Japan

Itsuki Banno Department of Electrical and Electronic Engineering, University of Yamanashi, Yamanashi, Japan

Lee Chuin Chen Interdisciplinary Graduate School of Medicine and Engineering, University of Yamanashi, Yamanashi, Japan

Sergey Mikhailovich Deyev Laboratory of Molecular Immunology, Shemyakin & Ovchinnikov Institute of Bioorganic Chemistry of the Russian Academy of Sciences, Moscow, Russia

Hiroyuki Hieda Storage Materials & Devices Laboratory, Corporate Research & Development Center, Toshiba Corporation, Kawasaki, Japan

Kenzo Hiraoka Clean Energy Research Center, University of Yamanashi, Yamanashi, Japan

Hirokazu Hori Interdisciplinary Graduate School of Medicine and Engineering, University of Yamanashi, Yamanashi, Japan

Hiroshi Imahori Institute for Integrated Cell-Material Sciences (WPI-iCeMS), Kyoto University, Kyoto, Japan

Department of Molecular Engineering, Graduate School of Engineering, Kyoto University, Kyoto, Japan

Kohei Imura Department of Chemistry and Biochemistry, School of Advanced Science and Engineering, Waseda University, Tokyo, Japan

PRESTO, Japan Science and Technology Agency, Saitama, Tokyo, Japan

Ryo Ishikawa Department of Communication Engineering and Informatics, Graduate School of Informatics and Engineering, The University of Electro-Communications, Chofu, Japan

Takashi Ishino Storage Materials & Devices Laboratory, Corporate Research & Development Center, Toshiba Corporation, Kawasaki, Japan

Haruhiko Ito Department of Electronics and Applied Physics, Interdisciplinary Graduate School of Science and Engineering, Tokyo Institute of Technology, Kanagawa, Japan

Yoshiyuki Kamata Storage Materials & Devices Laboratory, Corporate Research & Development Center, Toshiba Corporation, Kawasaki, Japan

Akio Kaneta Department of Electronic Science and Engineering, Kyoto University, Kyoto, Japan

Yoichi Kawakami Department of Electronic Science and Engineering, Kyoto University, Kyoto, Japan

Tadashi Kawazoe School of Engineering, The University of Tokyo, Tokyo, Japan

Akira Kikitsu Storage Materials & Devices Laboratory, Corporate Research & Development Center, Toshiba Corporation, Kawasaki, Japan

Kazuo Kitahara Graduate School of Science Education, Tokyo University of Science, Shinjuku-ku, Tokyo, Japan

Kiyoshi Kobayashi Interdisciplinary Graduate School of Medicine and Engineering, University of Yamanashi, Kofu, Yamanashi, Japan

Hiroaki Matsui School of Engineering, The University of Tokyo, Tokyo, Japan

Takuya Matsumoto Central Research Laboratory, Hitachi Ltd., Tokyo, Japan

Koji Mizuno Research Institute of Electrical Communication, Tohoku University, Sendai, Japan

Seiji Morita Storage Materials & Devices Laboratory, Corporate Research & Development Center, Toshiba Corporation, Kawasaki, Japan

Shuji Mononobe Department of Mechanical Engineering, Toyo University, Saitama, Japan

Takashi Mukai Nichia Corporation, Tokushima, Japan

Annemarie Nadort Department of Biomedical Engineering and Physics, Academic Medical Center, University of Amsterdam, 1100 DE Amsterdam, The Netherlands

Katsuyuki Naito Storage Materials & Devices Laboratory, Corporate Research & Development Center, Toshiba Corporation, Kawasaki, Japan

Hideobu Nakao Ion Beam Group, National Institute for Materials Science, Ibaraki, Japan

Yukio Narukawa Nichia Corporation, Tokushima, Japan

Makoto Naruse Photonic Network Research Institute, National Institute of Information and Communications Technology, Tokyo, Japan

Nanophotonics Research Center, The University of Tokyo, Tokyo, Japan

Wataru Nomura School of Engineering, The University of Tokyo, Tokyo, Japan

Nanophotonics Research Center, The University of Tokyo, Tokyo, Japan

Shin-ichi Ohkoshi Department of Chemistry, School of Science, The University of Tokyo, Tokyo, Japan

Motoichi Ohtsu School of Engineering, The University of Tokyo, Tokyo, Japan

Nanophotonics Research Center, The University of Tokyo, Tokyo, Japan

Hiromi Okamoto Institute for Molecular Science, Aichi, Japan

The Graduate University for Advanced Studies, Aichi, Japan

Kunimichi Omae Nichia Corporation, Tokushima, Japan

Toshiharu Saiki Department of Electronics and Electrical Engineering, Keio University, Kanagawa, Japan

Masatoshi Sakurai Storage Materials & Devices Laboratory, Corporate Research & Development Center, Toshiba Corporation, Kawasaki, Japan

Suguru Sangu Device Technology Development Center, Ricoh Co., Ltd, Miyagi, Japan

Akira Shojiguchi Green Platform Research Laboratories, NEC Corp., Kawasaki, Kanagawa, Japan

Zhen Song MQ Biofocus Research Centre and MQ Photonics Research Centre, Macquarie University, Australia

Varun Kumaraswamy Annayya Sreenivasan MQ Biofocus Research Centre and MQ Photonics Research Centre, Macquarie University, Australia

Nanophotonics Research Center, The University of Tokyo, Tokyo, Japan

Hitoshi Tabata School of Engineering, Department of Electronic Engineering, The University of Tokyo, Tokyo, Japan

Kuniyoshi Tanaka Storage Materials & Devices Laboratory, Corporate Research & Development Center, Toshiba Corporation, Kawasaki, Japan

Yuji Tanaka Steel Research Laboratory, JFE Steel Corporation, Kawasaki-ku, Kawasaki, Japan

Naoya Tate School of Engineering, The University of Tokyo, Tokyo, Japan

Nanophotonics Research Center, The University of Tokyo, Tokyo, Japan

Hiroko Tokoro Department of Chemistry, School of Science, The University of Tokyo, Tokyo, Japan

Tomokazu Umeyama Department of Molecular Engineering, Graduate School of Engineering, Kyoto University, Kyoto, Japan

Koichi Yamaguchi Department of Engineering Science, The University of Electro-Communications, Tokyo, Japan

Takashi Yatsui School of Engineering, The University of Tokyo, Tokyo, Japan
Nanophotonics Research Center, The University of Tokyo, Tokyo, Japan

Gyu-Chul Yi Department of Physics and Astronomy, Seoul National University, Seoul, Korea

National Creative Research Institute, Center for Semiconductor Nanostructure, Seoul, Korea

Andrei Vasilyevich Zvyagin MQ Biofocus Research Centre and MQ Photonics Research Centre, Macquarie University, Australia

Motoichi Ohtsu

Contents

1.1 Background and Principles.....	2
1.2 Basic Tools, Sensing, and Spectroscopy.....	5
1.3 Devices, Fabricated Structures, and Relevant Materials.....	6
1.4 Nanophotonic Systems and Their Evolution to Related Sciences.....	7
1.5 Summary.....	7
References.....	8

Abstract

This chapter outlines the framework of this handbook, which is composed of six parts. It reviews the theoretical picture of the dressed photon by combining the concepts of quantum field theory, optical science, and condensed-matter physics. The possibility of coupling a dressed photon with a coherent phonon is also presented, revealing a novel phonon-assisted process in light–matter interactions in nanometric space. Examples of the qualitative innovations made possible by applying nanophotonic principles to optical devices, fabrication techniques, energy conversion, and systems are also given.

M. Ohtsu (✉)

School of Engineering, The University of Tokyo, Tokyo, Japan

Nanophotonics Research Center, The University of Tokyo, Tokyo, Japan

e-mail: ohtsu@ee.t.u-tokyo.ac.jp

1.1 Background and Principles

Nano-optics deals with the light generated in or on nanometer-sized particles. It has opened up an innovative field of technology, called “nanophotonics,” enabling the development of novel photonic devices, fabrication techniques, and systems [1].

Nanophotonics, proposed by the author in 1993, is a novel optical technology that utilizes the optical near-field. The optical near-field is the *dressed photons* that mediate the interaction between nanometric particles located in close proximity to each other. Nanophotonics allows the realization of *qualitative innovations* in photonic devices, fabrication techniques, and systems by exploiting the novel functions and phenomena enabled by optical near-field interactions that would otherwise be impossible with conventional propagating light. In this sense, the principles and concepts of nanophotonics are completely different from those of conventional wave-optical technology, encompassing photonic crystals, plasmonics, metamaterials, and silicon photonics. This handbook describes these differences and shows examples of such qualitative innovations.

The author’s primary motivation for proposing nanophotonics was to break the deadlock in optical technology that has existed due to the diffraction limit of light. In the case of information transmission systems, communications technology road maps had claimed that the size of photonic devices should be decreased to several hundred or tens of nanometers for future high-capacity optical transmission systems; however, this is impossible due to the diffraction limit. In the case of photolithography, although the road maps called for fabricated patterns to be decreased in size to several tens of nanometers for massproduction of future semiconductor electronic devices, such as highly integrated DRAMs, this task is difficult due to the diffraction limit. Short-wavelength light sources (excimer lasers, extreme UV light sources, and synchrotron radiation sources) have undergone intense development for use in photolithography systems in order to decrease the sizes of the fabricated patterns down to the diffraction limit or in other words, to increase the resolution up to that permitted by the diffraction limit. However, the resulting equipment is extremely large and expensive and consumes a great deal of power, which makes its practical use very difficult.

Focused spots of light are relatively large due to the diffraction limit. Therefore, photonic devices are correspondingly large and the resolution of photolithography is low. Even if the physical dimensions of these devices could be decreased by means of nanotechnology, photonic devices cannot be reduced in size beyond the diffraction limit as long as conventional propagating light is used for driving them. To decrease the device size and increase the resolution of photolithography, the size (spatial extent) of the light itself must be decreased.

One promising candidate technology to decrease the size of light is nanophotonics, which was proposed by the author in 1993: If a nanometer-sized particle is illuminated by propagating light, it generates scattered light, which propagates to the far field and exhibits diffraction. However, also generated at the surface of the particle is an *optical near-field*, which is non-propagating light whose energy is localized at the particle surface. The extent of localization is equivalent to the

particle size, which is independent of the incident light wavelength; in the case of a nanometric particle, it is much smaller than the wavelength. Therefore, if the optical near-field could be utilized for operating devices and fabricating structures, novel technologies that can break through the bounds imposed by the diffraction limit can be realized, thus enabling *quantitative innovations* in optical technology.

The optical near-field is a virtual cloud of photons that always exists around an illuminated nanometric particle. Its energy fluctuation, δE , and duration of the fluctuation, τ , are related by the Heisenberg uncertainty relation, $\tau\delta E \cong \hbar$, where \hbar is Planck's constant divided by 2π . From this relation, the linear dimension of the virtual cloud of photons (*virtual photons* for short) is given by $r \cong c\tau \cong \hbar c/\delta E$, where c is the speed of light. In the case of visible light illumination (photon energy $\sim 2\text{ eV}$), r is estimated to be about 100 nm. This means that the effect of the virtual photons at the surface of the illuminated particle is important if the particle is smaller than 100 nm. In other words, the optical properties of sub-micrometer matter are not free from the effects of virtual photons.

This feature of the optical near-field, i.e., the virtual photons, can be most appropriately described by using a Feynman diagram, popularly employed for elementary particle physics. In this diagram, a photon is emitted from an electron in the illuminated nanometric particle and can be reabsorbed within a short duration. This photon is nothing more than a virtual photon, and its energy is localized at the surface of the nanometric particle. Independently of this virtual photon, a real photon (also called a free photon) can also be emitted from the electron. This photon is conventional propagating scattered light. Since the virtual photon remains in the proximity of the electron, it can couple with the electron in a unique manner. This coupled state, called a *dressed photon*, is a quasiparticle from the standpoint of photon energy transfer and has applications to novel nanophotonic devices and fabrication technologies. It is the dressed photon, not the free photon, that carries the material excitation energy. Therefore, the energy of the dressed photon, $h\nu_{dp}$, is larger than that of the free photon, $h\nu$, due to contribution of the material excitation energy.

To detect the dressed photon, a second nanometric particle should be placed in close proximity to the first particle in order to disturb the dressed photon on the first particle. This disturbance generates a free photon, which is propagating scattered light that can be detected by a conventional photodetector installed in the far field. This detection scheme suggests that the dressed photon energy is exchanged between the two particles. That is, after a dressed photon is generated in the first particle, it is transferred to the other particle. It can be transferred back to the first particle again, which means that the dressed photon can be exchanged between the two particles. The detectable free photon is generated in the process of this exchange.

Part 1 of this handbook theoretically describes the dressed photon by assuming a multipolar quantum electrodynamic Hamiltonian in a Coulomb gauge and single-particle states in a finite nano-system. After a unitary transformation and some simple calculations, its annihilation and creation operators are derived. Based on this dressed photon picture, interactions between the nanometric particles can be

simply described by emission, absorption, and scattering of dressed photons, which provides a physically intuitive picture of the optical near-field interaction between the two particles.

The real system is more complicated because the nanometric subsystem (composed of the two nanometric particles and the dressed photons) is embedded in a macroscopic subsystem composed of the macroscopic substrate material and the macroscopic incident and scattered light fields. A novel theory was developed to avoid describing all of the complicated behaviors of these subsystems rigorously, since we are interested only in the behavior of the nanometric subsystem. In this theory, the macroscopic subsystem is expressed as an exciton–polariton, which is a mixed state of material excitation and electromagnetic fields. Since the nanometric subsystem is excited by an electromagnetic interaction with the macroscopic subsystem, the projection operator method is effective for describing the quantum mechanical states of these systems. As a result of this projection, the nanometric subsystem can be treated as being isolated from the macroscopic subsystem, where the magnitudes of effective interaction energy between the elements of the nanometric subsystem are influenced by the macroscopic subsystem. This local electromagnetic interaction can take place within a sufficiently short duration, during which the uncertainty relation allows the exchange of dressed photons nonresonantly as well as the exchange of a free photon resonantly. The interaction due to the nonresonant process is expressed by a screened potential using a Yukawa function, which represents the localization of the dressed photon around the nanometric particles. Its decay length is equivalent to the particle size, which means that the extent of localization of the dressed photon is equivalent to the particle size, as was described above. Because of this, the long-wavelength approximation, which has always been employed in conventional light–matter interaction theory, is not valid. This means that an electric dipole-forbidden state in the nanometric particle can be excited as a result of the dressed photon exchange between closely placed nanometric particles, which enables novel nanophotonic devices.

A real nanometric material is composed not only of electrons but also of a crystal lattice. In this case, after a dressed photon is generated on an illuminated nanometric particle, its energy can be exchanged with the crystal lattice. By this exchange, the crystal lattice can excite the vibration mode coherently, creating a coherent phonon state. As a result, the dressed photon and the coherent phonon can form a coupled state. The creation and annihilation operators of this novel form of elementary excitation have been derived. This coupled state (the dressed photon carrying the coherent phonon energy (DP–CP)) is a quasiparticle and is generated only when the particle size is small enough to excite the crystal lattice vibration coherently. If not, the vibration is incoherent, and thus, its energy is dissipated, heating the particle.

It is easily understood that the energy of the DP–CP, $h\nu_{DP-CP}$, is higher than that of the dressed photon, $h\nu_{DP}$. It is also higher than the free photon energy, $h\nu_{FP}$, incident on the nanometric particle. The relation between these energies is represented by $h\nu_{FP} < h\nu_{DP} < h\nu_{DP-CP}$. The first and second inequalities originate from the contribution of the electron and coherent phonon energies,

respectively. Novel fabrication techniques allowing qualitative innovations can be developed by utilizing the DP–CP.

1.2 Basic Tools, Sensing, and Spectroscopy

Fiber probes are basic tools in nanophotonics and are used for generating and/or detecting dressed photons efficiently and reproducibly. A new technology that has been established for fabricating high-quality fiber probes is selective chemical etching. Technical details will be described in Part 2 of this handbook. Chemical etching has been used to fabricate a high-resolution probe with an apex having a radius of curvature of 1 nm, a high-efficiency probe with 10 % dressed photon generation efficiency, and other related devices. Elsewhere in the world, methods involving heating and pulling fiber were most popular, although chemically etched fiber probes show superior performance. This chemical etching method was transferred to industry, resulting in high-quality commercial fiber probes. For example, a near-field optical microscope has been developed using these fiber probes, capable of producing ultrahigh-resolution images, such as an image of a single-strand DNA molecule with a resolution greater than 4 nm, which is a world record.

As will be described in the Part 3 of this handbook, a novel spectrometer has also been developed for analyzing single semiconductor quantum dots, semiconductor devices, single organic molecules, and biological specimens. Many experimental results on spatially resolved photoluminescence and Raman spectra with 10 nm resolution have been accumulated. Patents have been transferred to industry in order to produce commercial photoluminescence spectrometers that operate in the ultraviolet–infrared region, at liquid helium to room temperature, and in high magnetic fields. Since their introduction onto the market, they have been popularly used in a variety of fields in nanoscience and nanotechnology applications. Instead of using fiber probes, apertureless probes are sometimes used because of their ease of fabrication and the possibility of field enhancement. However, it has been demonstrated that apertureless probes cannot realize high resolution due to the scattering of residual propagating light.

Technology for fabricating a triple-tapered fiber probe has been developed to increase the optical near-field generation efficiency by up to 1,000 times through efficient excitation of the EH_{11} mode in a fiber. This was applied to develop a pyramidal silicon probe on a contact slider for writing and reading in a phase-change optical storage disk. The shortest mark length and the carrier-to-noise ratio were 110 nm and 10 dB, respectively, with a data transmission rate of 2.0 MHz. By using a two-dimensional probe array, the rate is expected to increase to 200 MHz. This and related work triggered the development of an ultrahigh-density magnetic storage system.

The upper limit of the storage density of conventional magnetic storage systems is about 0.3 Tb/in.², which is limited by the thermal instability of the magnetic domains on the disk. In order to break through this limit, dressed photons were

used to locally heat a magnetic domain in order to decrease the coercivity, followed by immediately applying a magnetic field to the domain to write a pit. With this technique, a storage density as high as 1 Tb/in.^2 is expected, which meets the requirements of the technology road maps for future magnetic storage systems.

To realize such a high-density magnetic storage system, a Japanese national project was organized with academia–industry collaboration, supervised by the author and involving eight Japanese companies. This project developed three main technologies: high-density storage media technology, recording technology, and nano-mastering technology. By assembling these technologies, isolated pits of 20 nm diameter at 30 nm pitch were successfully written on a storage disk, corresponding to a storage density of 1.5 Tb/in.^2 , which is higher than that dictated by the fundamental limits due to thermal fluctuations. Novel devices and storage media developed for this recording technology will be reviewed in Parts 3 and 4.

1.3 Devices, Fabricated Structures, and Relevant Materials

The size and energy consumption of electronic and optical devices must be reduced to improve the performance of information processing systems and energy conversion systems. It should be noted that conventional electronic devices can hardly meet these requirements because they need electrical wires for connection with external devices in order to fix the direction of the energy flow and the transmitted signal intensity. This means that they dissipate a large amount of energy in the external macroscopic wires. Furthermore, these electronic wires are susceptible to noninvasive attacks. Conventional optical devices also need connecting lines, such as optical fibers and dielectric optical waveguides, as long as propagating light is used as a signal carrier. (Even macroscopic light beams propagating through free space may play the role of the connecting lines here).

Nanophotonics is a promising candidate for meeting the above requirements for two reasons: (1) a signal can be transferred by the dressed photon exchange between nanometric particles without using any wires and (2) a noninvasive attack is impossible because the signal intensity is fixed by the energy dissipation inside the nanometric particles. A variety of basic devices, including an optical switch, logic gates, and input and output terminals, have been developed. Their unique features and application to information processing systems have been studied.

The unique phenomena originating from dressed photon exchange have been applied also to the development of novel high-resolution fabrication techniques. As described in [Sect. 1.2](#) above, the fabrication principle utilizes the DP–CP, which carries the coherent phonon energy. A variety of fabrication techniques, including photochemical vapor deposition, photolithography, and self-organized smoothing, have been developed. Details of novel devices and fabrication techniques described above and the relevant materials will be described in Part 4.

1.4 Nanophotonic Systems and Their Evolution to Related Sciences

Nanophotonics has resulted in both quantitative and qualitative innovations. For example, novel architectures have been proposed for optical signal transmission systems, and their performance has been confirmed experimentally. They include computing using nanophotonic switches and an optical nanofountain as well as data broadcasting using multiple nanophotonic switches. Quantitative innovations have been realized by decreasing the device size and power consumption beyond the diffraction limit. More importantly, qualitative innovations have been realized by exploiting the novel functions of nanophotonic devices, which are otherwise impossible using conventional photonic devices. Quantitative innovations have already been realized in optical/magnetic hybrid disk storage density by breaking through the diffraction limit (refer to [Sect. 1.2](#) above). Qualitative innovations have also been proposed by applying the hierarchy inherent in dressed photons to memory retrieval. These novel systems will be described in Part 5.

An example of evolution to a related science is atom photonics, in which the thermal motions of neutral atoms in a vacuum are controlled using dressed photons. Theoretical studies have examined single-atom manipulation based on the dressed photon model, and experimental studies have showed the first successful guidance of an atom through a hollow optical fiber. Recent studies have examined atom-detecting devices, atom deflectors, and atomic funnel. Atom photonics will open up a new field of science that examines the interactions between dressed photons and single atoms. Basic research in nanophotonics is being actively carried out. Evolution to these related basic sciences and atom photonics will be described in Part 6.

1.5 Summary

By combining the concepts of quantum field theory, optical science, and condensed-matter physics, nanometric materials and optical energy transfer in nanometric space have been studied. Through these studies, a theoretical picture of dressed photons has emerged. Based on this picture, the exchange of dressed photons has been investigated, revealing energy transfer to electric dipole-forbidden energy levels. Furthermore, the possibility of coupling a dressed photon with a coherent phonon has been shown, revealing a novel phonon-assisted process in light–matter interactions in nanometric space. These discoveries have been applied to develop novel technologies, such as devices, fabrication techniques, energy conversion, information systems, architectures, and algorithms.

Fundamental concepts, such as the behavior of photons in nanometric space, the excitation transfer and relaxation in nanometric space, and the primary mechanisms of the phonon-assisted process, should be delved into more deeply.

Such fundamental studies are expected to bring about further discoveries involving the coupling of dressed photons with various elementary excitations besides coherent phonons, leading to novel applications. This marriage of basic studies and technological applications is expected to establish a new field of dressed photon science and technology in the near future.

Dressed photons can be utilized to establish fundamental new technologies that can replace a wide range of conventional optical technologies. Even though users will not notice their existence, it is expected that technologies exploiting dressed photons will be widely used in everyday life in the near future. This is because dressed photons can be generated universally on the surface of illuminated nanometric materials.

The term “nanophotonics” is occasionally used for photonic crystals, plasmonics, metamaterials, silicon photonics, and quantum-dot lasers using conventional propagating light. Here, one should consider the stern warning given by C. Shannon on the casual use of the term “information theory,” which was a trend in the study of that field during the 1950s [2]. The term “nanophotonics” has been used in a similar way, although some purported work in “nanophotonics” is not based on optical near-field interactions. For the true development of nanophotonics, one needs deep physical insight into the behavior of dressed photons and the associated nanometric subsystem composed of electrons and photons.

References

1. M. Ohtsu, *Progress in Nanophotonics 1*, ed. by M. Ohtsu (Springer, Berlin, 2011), p. 1
2. C.E. Shannon, *IEEE Trans. Inform. Theory* **IT-2**, 3 (1956)

Part I

Principle and Theoretical Background

Itsuki Banno

Contents

2.1	Introduction.....	12
2.1.1	Purposes and Overview of This Chapter.....	13
2.1.2	Studies of Pioneers.....	14
2.2	Definition of Near Field and Far Field.....	16
2.2.1	A Naive Example of Super-Resolution.....	16
2.2.2	Retardation Effect as Wavenumber Dependence.....	16
2.2.3	Examination on Three Cases.....	18
2.2.4	Diffraction Limit in Terms of Retardation Effect.....	19
2.2.5	Definition of Near Field and Far Field.....	20
2.3	Quasi-static Picture: A Characteristic of Near Field Optics.....	20
2.3.1	A Sketch of the Quasi-static Picture.....	21
2.3.2	Polarization in a Finite-Sized Material.....	22
2.3.3	Boundary Effect of a Dielectric Material; Rayleigh Scattering Near Field.....	23
2.3.4	Boundary Effect of a Metallic Material.....	25
2.3.5	Boundary Magneto-Optical Effect.....	26
2.3.6	Boundary Electro-optical Effect.....	29
2.3.7	A Simple Interpretation of Near-Field Intensity.....	31
2.3.8	Summary: Boundary Effect of General Optical Responses.....	34
2.4	Boundary Scattering Formulation with Scalar Potential.....	34
2.4.1	Poisson's Equation with Boundary Charge Density.....	34
2.4.2	Notation Concerning Steep Interface.....	35
2.4.3	Boundary Scattering Problem Equivalent to Boundary Value Problem.....	36
2.4.4	Integral Equation for Source and Perturbative Treatment of MBC.....	37
2.4.5	An Application.....	38
2.4.6	Summary.....	39
2.5	Boundary Scattering Formulation with Dual EM Potential.....	40
2.5.1	Dual EM Potential as Minimum Degree of Freedom.....	41
2.5.2	Wave Equation for Dual Vector Potential.....	43
2.5.3	Boundary Scattering Problem Equivalent to the Boundary Value Problem.....	44
2.5.4	Integral Equation for Source and Perturbative Treatment of MBCs.....	46

I. Banno (✉)

Department of Electrical Electronic Engineering, University of Yamanashi, Yamanashi, Japan
e-mail: banno@yamanashi.ac.jp

2.5.5	Boundary Effect and Retardation Effect.....	48
2.5.6	Intuitive Picture Based on Dual Ampere Law under Near-Field Condition.....	50
2.5.7	Correction Due to Retardation Effect.....	52
2.5.8	Summary.....	55
2.6	Summary and Remaining Problems.....	56
2.7	Green's Function and Delta Function in Vector Field Analysis.....	57
2.7.1	Vector Helmholtz' Equation.....	58
2.7.2	Decomposition into Longitudinal and Transversal Components.....	59
	References.....	62

Abstract

The main purpose of this chapter is to present the quasi-static picture of an optical field in the vicinity of small-scale material. The quasi-static picture depends on the fact that the induced boundary charge density dominates the optical near field of a small-scale material *via* Coulomb's law; therefore, such an optical near field is of a non-radiative or longitudinal nature. This simple physics leads to an intuitive understanding, even in complicated systems with magneto- and electro-optical effects. As prerequisites, the definitions of elementary concepts are given: "retardation effect," "diffraction limit," "near field," and "far field." Furthermore, two numerical methods are presented using the minimum degree of freedom of an electromagnetic field; one is described by the scalar potential adequate for a quasi-static system and the other by a dual vector potential for general optical systems. This chapter is restricted to linear optical effects and is a revised version of the article titled by "Classical Theory on Electromagnetic Near Field" in *Progress in Nano-Electro-Optics II* (Springer-Verlag Berlin Heidelberg, 2004).

2.1 Introduction

The first milestone of near-field optics (NFO) is that a resolution far beyond the diffraction limit, namely super-resolution, had been attained in Scanning Near-field Optical Microscopy (SNOM). (In this chapter, the abbreviation "SNOM" represents for Scanning Near-Field *Microscopy*, not *Microscope*.) Now, NFO is a developing research area that treats material on a nanometer scale, and a treasure house filled with unknown phenomena including quantum phenomena; see [Sect. 2.1.2](#) for a brief history of NFO. In the frame of the classical theory, however, phenomena in the regime of NFO have not yet been exhausted. Actually, it is not clear what characteristics NFO has and what the difference is between NFO and conventional optics.

This chapter is focused on the classical theory of the optical near field. Here, classical theory means: the macroscopic theory based on Maxwell's equations and the constitutive equation with optical constants; a rather familiar framework in conventional optics. The present theory shows that the optical near field of a small-scale material is characterized by the quasi-static picture, which leads to an intuitive interpretation of the near field. The quasi-static picture depends on the fact that the

induced boundary charge density dominates the optical near field of a small-scale material *via* Coulomb's law.

Let us consider the boundary charge density, which is the master piece of the present theoretical approach. When a material is exposed to light, charge and current density are induced in the interface region to screen the electromagnetic (EM) field, so that most of the bulk region is maintained as it was. This behavior of negative feedback may be understood as Le Chatelier's principle, which is the strategy of a stable system to withstand an external fluctuation. The screening charge and current densities in the interface region can be idealized as boundary charge and current densities; those are localized inside the idealized interface region with an infinitesimal width. The key point to understand a characteristic of NFO is that the boundary effect predominates over the bulk effect in a small-scale structure, while the opposite is true for a large-scale structure. This is a general concept in physics, but it is not fully employed in optics.

In an ordinary treatment of conventional optics, the boundary effect is implicitly considered under the Maxwell boundary conditions (MBCs), which cause difficulty in understanding of physics and in numerical calculations. The idea using the boundary source overcomes the difficulty caused by MBCs, makes clear the physics of optical near field, and, furthermore, leads us to develop two novel formulations, namely the boundary scattering formulation with scalar potential and that with a dual EM potential.

2.1.1 Purposes and Overview of This Chapter

The purposes of this chapter are:

1. To give a clear definition of elementary concepts, i.e., "retardation effect," "diffraction limit," "near field," and "far field" ([Sect. 2.2](#)).
2. And mainly: to give an intuitive understanding of the optical near field of small-scale dielectric, metallic and ferro-materials based on a quasi-static picture. Such optical near fields are generated by the boundary charge density *via* Coulomb's law and are of a non-radiative (longitudinal) nature ([Sect. 2.3](#)).
3. We finally wish to formulate two novel numerical methods free from MBCs, namely the boundary scattering formulation with scalar potential and that with a dual EM potential ([Sects. 2.4](#) and [2.5](#)).

If one would like to take the shortest way, then read [Sects. 2.2](#) and [2.3](#), which are minimal and self-contained parts of this chapter. [Sections 2.4](#) and [2.5](#) with [2.7](#) are numerical methods compatible with a quasi-static picture. In particular, [Sect. 2.4](#) suggests a rather simple numerical method with a small amount of calculations. The following is an overview of this chapter.

[Section 2.1.2](#) gives a brief history of NFO.

[Section 2.2](#) makes clear the elementary concepts: retardation effect, diffraction limit, far field and near field. To understand them is a prerequisite to the following sections.

[Section 2.3](#) introduces the quasi-static picture in an intuitive manner. By imaging the boundary charge density, one may understand qualitative properties of the

optical near field around a small-scale material. This idea is extended to systems including a material with complicated shape and/or response, e.g., multidomain systems of magneto-optical and electro-optical materials.

It is crucial how one treats the boundary effect in the theory of NFO. In the ordinary theory of optics, MBCs are used instead of the boundary source and cause difficulty not only in a numerical calculation but also in our physical understanding. To overcome this difficulty, two formulations are given, based on the following principles:

1. A boundary value problem can be replaced by a scattering problem with an adequate boundary source; this boundary source is responsible for the MBCs.
2. The EM potential is the minimum degree of freedom of the EM field.

As described in Sect. 2.3, the electric near field of a small-scale material is generated by the boundary charge density *via* Coulomb's law. Therefore, a quasi-static picture holds and the scalar potential is the minimum degree of freedom of the electric field in such a system.

In Sect. 2.4, the ordinary boundary value formulation using MBCs is replaced by the boundary scattering formulation with scalar potential and boundary charge density.

In Sect. 2.5, it is shown that the minimum degree of freedom of an EM field in a general optical system is the *dual EM potential* (in the radiation gauge), which is derived from the ordinary EM potential by means of a dual transformation, i.e., the mutual exchange between the electric quantities and the magnetic ones. The source of the dual EM potential is the magnetic current density and an adequate boundary magnetic current density reproduces the MBCs. In this way, a boundary value problem is replaced by a scattering problem, namely *a boundary scattering problem*, which is applicable to a general optical system. We apply the boundary scattering formulation with the dual EM potential to the optical near field of a dielectric on a scale that permits coexistence of boundary and bulk effects. We numerically solve the boundary scattering problem using the dual EM potential and further give an intuitive understanding on the basis of "dual Ampère law" with a correction due to the retardation effect.

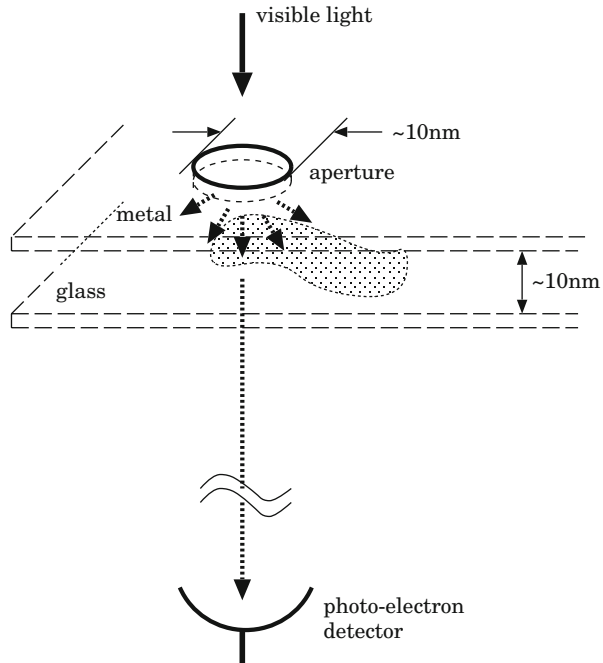
In Sect. 2.6, we give a summary of this chapter. Section 2.7 is an appendix dealing with the vectorial Green function.

All the numerical calculations in this chapter are restricted to the optical near field in the vicinity of a *dielectric*.

2.1.2 Studies of Pioneers

The first idea of SNOM with super-resolution appeared in a paper by E.H. Syngé in [37]. The same idea was seen in a letter by J.A. O'keefe in [30]. Syngé's proposal is sketched in Fig. 2.1. A sample is placed on a true plane of glass and exposed to penetrating visible light through a small aperture. The size of the aperture and the distance between the sample and the aperture are much smaller than the wavelength of the visible light. Part of the penetrating light is scattered by the sample and

Fig. 2.1 A sketch of Syngé's idea



reaches the photo-electric detector. Varying the position of the sample, one obtains the signal intensity profile, that is, the electric current intensity as a function of the position of the sample. Syngé pointed out a technical difficulty in his period and it has been overcome as time went by.

The first experiment of the microscope with super-resolution $\lambda/60$ was demonstrated in the microwave region in 1972 [1], then again, in the infra-red region in 1985 with the resolution $\lambda/4$ [25]; λ stands for the wavelength of the EM field. The super-resolution in the optical region had been attained by D.W. Pohl et al. in [31]; they implied that the resolution is $\lambda/20$. They formed a small aperture on the top of a metal-coated quartz tip; the radius of curvature of the sharpened tip was about 30 nm. Their result convinced us of microscopy with super-resolution in the visible light region. In 1987, E. Betzig et al. demonstrated the “collection mode” [10]. In the collection mode, the incident light exposes a wide region including the sample; the scattered light by the sample is picked up by an aperture on a metal-coated probe tip. They used visible light and an aperture with a diameter ~ 100 nm. The first experiment with high reproducibility and with nanometer resolution was done in 1992, using an aperture with diameter ~ 10 nm [18, 29].

Once the super-resolution had been attained, variations of the SNOM were developed, e.g., spatially resolved photoluminescence spectroscopy [32], apertureless SNOM [41, 42], local-plasmon SNOM [13], and so on. Currently, NFO provides the basis for various systems in a wide range of research areas using the optical

near fields of materials with small-scale structures. Such systems are fabricated as metallic structures for lithography [16, 23, 35], optical storage [15, 38] and biological and chemical sensing [39], and neighboring semiconductor dots for a nanometric optical switch [19–21].

For a long time, the classical theoretical approach for the optical near-field problem had been based on the diffraction theory of a highly symmetric system [9, 11]. After the collection mode operation had become popular since the 1990s, EM scattering theories have been applied and various numerical calculations have been carried out in low symmetry systems. Some authors solved the Dyson equation followed by the Green function [14, 24] and others calculated the time evolution of the EM field by the Finite Difference Time Domain (FDTD) method [40]. Both methods had been originally developed for calculations in conventional optics and it has been difficult to obtain a simple physical picture in NFO.

2.2 Definition of Near Field and Far Field

Although a certain simple property seems to exist in optical near field, a physical picture is smeared behind the complicated calculation procedures caused by the MBCs. There is no formalism for the optical near field compatible with a clear physical picture. So, before taking up a discussion of the optical near field, let us reconsider wave mechanics from a general point of view and make clear the following concepts: the retardation effect, the diffraction limit, the far field, and the near field [7].

2.2.1 A Naive Example of Super-Resolution

First of all, we introduce a simple example to explain why a super-resolution is attained in SNOM. Suppose a small stone is thrown into a pond. One finds that circular wave-lets spread on the surface of the water. We make sure that the shape of the wave-lets are circular and independent of the shape of the stone. This means that we cannot know the shape of the stone, if the observation points are far from the source point. Strictly speaking, there is a “diffraction limit” in the far-field observation, if the size of the stone is much smaller than the wavelength of the surface wave of the water. However, information concerning the shape of the stone is not lost, if an observation point is close enough to the source point. This type of observation is just the one in SNOM. In the next subsection, this idea will be refined using a pedagogical model.

2.2.2 Retardation Effect as Wavenumber Dependence

Suppose that there are two point-sources instead of a complicated-shaped source like a stone; see Fig. 2.2. These sources yield a scalar field and they are located at

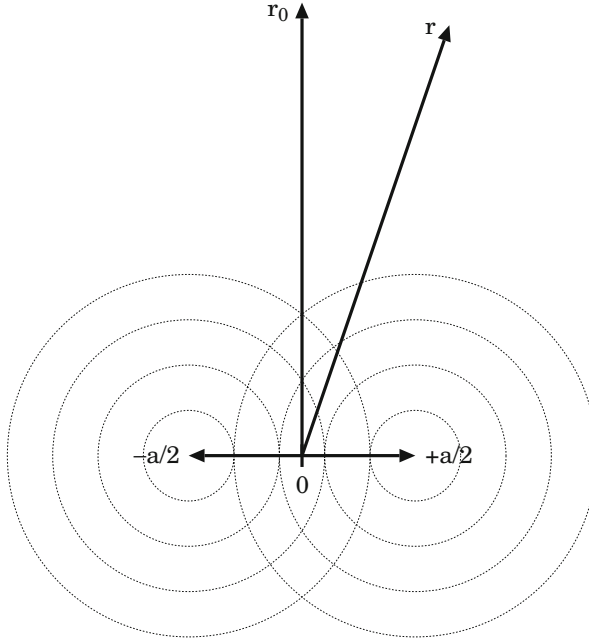


Fig. 2.2 A system with two point-sources. Only one parameter $a = |\mathbf{a}|$ characterize “the shape of the source” if $\hat{\mathbf{a}}$ is given

$\mathbf{r}' = +\mathbf{a}/2$ and $\mathbf{r}' = -\mathbf{a}/2$ in three-dimensional space. Furthermore, we assume that the two sources oscillate with the same phase and the same magnitude, i.e., $\delta^3(\mathbf{r}' \pm \mathbf{a}/2) \exp(i\omega t')$, where ω is the angular frequency. Our simplified problem is to know $a = |\mathbf{a}|$ by means of observations at some points \mathbf{r} . It is assumed that the directional vector $\hat{\mathbf{a}}$ is known. Let us consider the front of the wave that starts from each source point $\mathbf{r}' = \mp \mathbf{a}/2$ at time $t' = 0$. The front of each wave reaches the observation point \mathbf{r} at a certain time $\Delta t_{\mp \mathbf{a}/2}$. This time – “retardation” – is needed for the wave to propagate from $\mathbf{r}' = \mp \mathbf{a}/2$ to \mathbf{r} with the phase velocity ω/k . Therefore, the retardation is estimated as

$$\Delta t_{\mp \mathbf{a}/2} = k|\mathbf{r} \pm \mathbf{a}/2|/\omega . \quad (2.1)$$

After all, the amplitude of each partial wave at the observation point (\mathbf{r}, t) is as follows:

$$\frac{\exp(-i\omega(t - \Delta t_{\mp \mathbf{a}/2}))}{|\mathbf{r} \pm \mathbf{a}/2|} = \frac{\exp(-i\omega t + ik|\mathbf{r} \pm \mathbf{a}/2|)}{|\mathbf{r} \pm \mathbf{a}/2|} . \quad (2.2)$$

The magnitude of each partial wave is inverse proportional to the distance between the observation point and the source point because of the conservation of flux. The phase is just the one at the source point at the time $t - \Delta t_{\mp \mathbf{a}/2}$ because of the

retardation. Equation (2.2) is an expression for the Huygens principle or the Green function for the scalar Helmholtz' equation.

Equations (2.1) and (2.2) for the retardation tell us that *the retardation effect is the wavenumber dependence*, namely ka and/or kr dependence. In the following, the retardation effect will be used in this sense.

2.2.3 Examination on Three Cases

In order to explain the meaning of the diffraction limit and to give a clear definition of far field and near field, let us discuss the following three cases (Table 2.1):

- Case 1; $kr \gg ka \gg 1$, the observation of the far field generated by a large-sized source,
- Case 2; $kr \gg 1 \gg ka$, the observation of the far field generated by a small-sized source,
- Case 3; $ka \lesssim kr \ll 1$, the observation of the near field generated by a small-sized source.

In our simplified model introduced in the previous subsection, the observed amplitude at (\mathbf{r}, t) is the superposition of two partial waves,

$$A(\mathbf{r}, t) = \frac{\exp(-i\omega t + ik|\mathbf{r} + \mathbf{a}/2|)}{|\mathbf{r} + \mathbf{a}/2|} + \frac{\exp(-i\omega t + ik|\mathbf{r} - \mathbf{a}/2|)}{|\mathbf{r} - \mathbf{a}/2|}. \quad (2.3)$$

In the cases 1 and 2, Eq.(2.3) is reduced to the following expression, applying the condition $r \gg a$:

$$A(\mathbf{r}, t) = \frac{e^{-i\omega t + ikr}}{r} \left(2 \cos \left(\frac{1}{2}ka(\hat{\mathbf{r}} \cdot \hat{\mathbf{a}}) \right) + \mathcal{O} \left(\frac{a}{r} \right) \right). \quad (2.4)$$

In Eq.(2.4), “ a ” in question is coupled with “ k .” Therefore one must use the retardation effect (in the phase difference between the two partial waves) to know “ a ” by means of the far-field observation.

In case 1, “ a ” can be obtained in the following way. We restrict the observation points on a sphere $r = \text{const.}$ ($\gg a$) and select one point \mathbf{r}_0 on the sphere which satisfies $\hat{\mathbf{r}}_0 \cdot \hat{\mathbf{a}} = 0$. At this observation point, the phase difference of the two partial

Table 2.1 Definition and specification of near field and far field

Definition	Diffraction limit	Retardation effect	Examples
Far field $kr \gg 1, r \gg a$	Exists	Large	$ka \gg 1$ (case 1) ordinary optical microscopy $ka \ll 1$ (case 2) Rayleigh scattering system
Near field $1 \gtrsim kr \gtrsim ka$	Does not exist	small	$ka \ll 1$ (case 3) SNOM

waves is 0. Then, search another point \mathbf{r} on the sphere where the magnitude of the field A takes local minimum. If \mathbf{r} is one of the nearest points of \mathbf{r}_0 , the phase difference at \mathbf{r} of the two partial waves is $\pi/2$, i.e., $ka|\hat{\mathbf{r}} \cdot \hat{\mathbf{a}}|/2 = \pi/2$. As a result, we determine “ a ”; $a = \pi/(k|\hat{\mathbf{r}} \cdot \hat{\mathbf{a}}|)$.

In case 2, however, “ a ” cannot be obtained through the far-field observation. The phase difference among all the observation points on the sphere is zero because of the condition $ka \ll 1$. In other words, the two point-sources are so close that the observer far from the sources recognizes the two sources as a single source with double magnitude.

In case 3, Eq. (2.3) is reduced to the following expression, applying the condition $ka \lesssim kr \ll 1$,

$$A(\mathbf{r}, t) = \exp(-i\omega t) \left(\frac{1}{|\mathbf{r} + \mathbf{a}/2|} + \frac{1}{|\mathbf{r} - \mathbf{a}/2|} \right) (1 + \mathcal{O}(ka, kr)). \quad (2.5)$$

The leading order of Eq. (2.5) is independent of the wavenumber “ k .” This independence is because the size of the whole system – including all the sources and all the observation points – is much smaller than the wavelength, that is, the system cannot feel the wavenumber. “ a ” in question can be determined by means of the near-field observation. Search an observation point \mathbf{r}_0 where $\hat{\mathbf{r}}_0 \cdot \hat{\mathbf{a}} = 0$ is satisfied, then Eq. (2.5) results in $a = 2\sqrt{4 - r_0^2|A_0|^2/|A_0|}$. Note carefully that this expression for “ a ” is independent of “ k ,” i.e., independent of the retardation effect. As a result, we can know “ a ” through the near-field observation without using the retardation effect.

In short, information concerning the shape of the source is in the k -dependent phase of the far field or in the k -independent magnitude of the near field.

2.2.4 Diffraction Limit in Terms of Retardation Effect

In the above pedagogical model, the scalar field generated by the two point-sources has been discussed. Even in the case of a continuous source, the essential physics is the same if “ a ” is considered as the representative size of the source.

Now we can make clear the meaning of the diffraction limit. In the case of a far-field observation, information concerning the shape of the source is in the k -dependent phase of the far field; see Eq. (2.4). To recognize the anisotropy of the shape, the phase difference for some observation points on a certain sphere must be larger than $\pi/2$; this condition imposed on Eq. (2.4) leads to the following inequality:

$$ka|\hat{\mathbf{r}} \cdot \hat{\mathbf{a}}| \sim ka \gtrsim \pi, \quad (2.6)$$

where “ a ” is the representative size of the source. The inequality (2.6) is a rough expression for the diffraction limit and implies that the size of the source should be larger than the order of the wavelength to detect the anisotropy of the source. Note

that the concept “diffraction limit” is effective only in the far-field observation, i.e., the observation under the conditions $kr \gg 1$, $r \gg a$.

In the far-field observation like cases 1 and 2, we have to use the k -dependent phase to know the shape of the source and the resolution is bounded by the diffraction limit; see Eqs. (2.4) and (2.6). However, in a near-field observation like case 3, we know the shape of the source without diffraction limit, because information of the shape is in the k -independent magnitude of the near field; see Eq. (2.5).

2.2.5 Definition of Near Field and Far Field

The observation in SNOM corresponds to case 3, if the position of the probe tip is considered as the observation point. In fact, the signal in SNOM is independent of the wavenumber and free from the diffraction limit. On the contrary, the observation in the usual optical microscopy corresponds to case 1; therefore, the resolution for it is bounded by the diffraction limit. Case 2 is the condition for the Rayleigh scattering system. By means of a far-field observation, one can determine only the number (or density) of the sources as a whole but cannot obtain information regarding the shape or the distribution of the sources.

We define “far field” as the field observed under the condition $kr \gg 1$, $r \gg a$, i.e., cases 1 and 2, and “near field” as the field observed under the condition $ka \lesssim kr \lesssim 1$, i.e., case 3.

In particular, the limiting condition of the near field,

$$ka \lesssim kr \ll 1, \quad (2.7)$$

is simply referred to as “near-field condition (NFC)” in the following. Under the NFC, the k -independent picture, namely a quasi-static picture, holds owing to the negligible retardation effect; see Sect. 2.3.

In this section, only a scalar field has been treated. It is a characteristic of the optical near field (vector field) that the boundary effect is dominant; this will be apparent in the next section.

2.3 Quasi-static Picture: A Characteristic of Near Field Optics

This section addresses the main purpose of this chapter: the quasi-static picture is described in an intuitive manner. This entails the elementary nature of the optical near field under the NFC (2.7) and may be applied to NFO systems with dielectric, metal, and ferromaterials. The boundary and bulk effects are derived simultaneously and these two are qualitatively different. As mentioned in Sect. 2.1, the importance of the boundary effect in a small-scale system of NFO can be understood from the following fundamental concept of physics: the boundary effect predominates

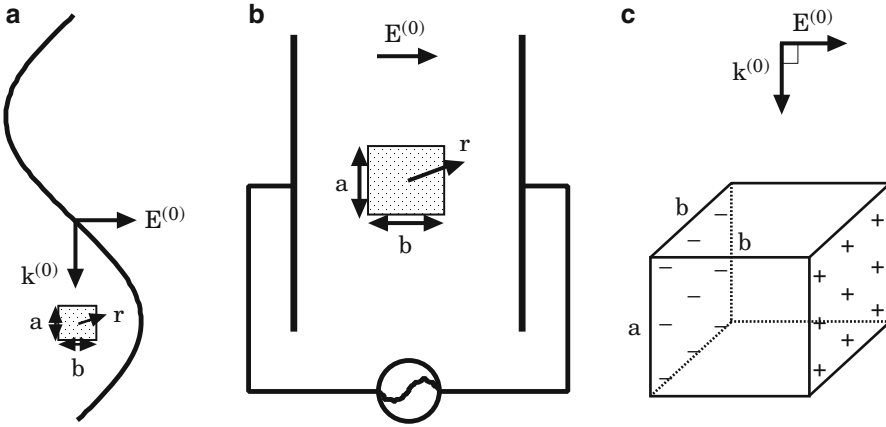


Fig. 2.3 A quasi-static picture of the near field of a sufficiently small structure. (a) A snapshot of the system at arbitrary time. Material with a structure on a scale much smaller than the wavelength is exposed to an incident field with wavenumber vector $\mathbf{k}^{(0)}$ ($|\mathbf{k}^{(0)}| = k$) and polarization vector $\mathbf{E}^{(0)}$. a and b are the characteristic lengths of the material and \mathbf{r} is the position vector of the observation point from the center of the material. (b) An equivalent quasi-static system under an alternating voltage. (c) The boundary charge density in a Rayleigh scattering system

over the bulk effect in a small-scale structure, while the opposite is true for a large-scale structure. This section is mainly based on Ref. [3] and the revision with some extension of Sects. 3.1–3.3 in the original book [2].

2.3.1 A Sketch of the Quasi-static Picture

Firstly, let us discuss the most simplest case: the Rayleigh scattering system with a small-scale dielectric material, as shown in Fig. 2.3a, is assumed to satisfy the NFC. The NFC means that the size of the system, including both the object of study and the observation point, is much smaller than a wavelength. Therefore, the system cannot “feel” the wavelength, and a quasi-static picture (wavenumber-independent picture) holds (Fig. 2.3b).

The electric field in a quasi-static system should be ruled by Coulomb’s law, and possesses a non-radiative or longitudinal nature. In such a system, like Fig. 2.3b, the source of electric field is the *boundary* charge density described in Fig. 2.3c, as we know empirically and will prove in Sect. 2.3.3. Actually, the Rayleigh scattering for near and far fields originate in a boundary effect, although it is not widely known.

The above sketch of a quasi-static picture will be refined in Sect. 2.3.3 and extended to other materials in Sects. 2.3.4–2.3.6, using the concept of polarization introduced in the next subsection.

2.3.2 Polarization in a Finite-Sized Material

To refine the sketch in the previous subsection, let us introduce the proper polarization for finite-sized materials with a general optical response; this polarization derives from the simultaneous boundary and bulk effects. Consider a finite-sized domain occupying a volume \mathcal{V} in a vacuum. We define the polarization \mathbf{P} in \mathcal{V} as that of an infinite-sized material \mathbf{P}_∞ times the step function $\theta(\mathbf{r} \in \mathcal{V})$:

$$\mathbf{P}(\mathbf{r}, t) = \theta(\mathbf{r} \in \mathcal{V})\mathbf{P}_\infty(\mathbf{r}, t), \quad (2.8)$$

$$\theta(\mathbf{r} \in \mathcal{V}) = \begin{cases} 1 & \text{for } \mathbf{r} \in \mathcal{V}, \\ 0 & \text{for } \mathbf{r} \notin \mathcal{V}. \end{cases} \quad (2.9)$$

The step function $\theta(\mathbf{r} \in \mathcal{V})$ represents the steep change in polarization at the material–vacuum interface and can properly represent the structure. Ignoring the dynamic magnetization, the induced charge density ρ and current density \mathbf{j} are derived *via*

$$\begin{aligned} \rho(\mathbf{r}, t) &= -\nabla \cdot \mathbf{P}(\mathbf{r}, t) \\ &= -\nabla\theta(\mathbf{r} \in \mathcal{V}) \cdot \mathbf{P}_\infty(\mathbf{r}, t) - \theta(\mathbf{r} \in \mathcal{V})\nabla \cdot \mathbf{P}_\infty(\mathbf{r}, t) \\ &= \int_{\partial\mathcal{V}} d^2s \delta^3(\mathbf{r} - \mathbf{s})\hat{\mathbf{n}}_s \cdot \mathbf{P}_\infty(\mathbf{s} - 0\hat{\mathbf{n}}_s, t) - \theta(\mathbf{r} \in \mathcal{V})\nabla \cdot \mathbf{P}_\infty(\mathbf{r}, t), \end{aligned} \quad (2.10)$$

$$\begin{aligned} \mathbf{j}(\mathbf{r}, t) &= \partial_t \mathbf{P}(\mathbf{r}, t) \\ &= \theta(\mathbf{r} \in \mathcal{V})\partial_t \mathbf{P}_\infty(\mathbf{r}, t), \end{aligned} \quad (2.11)$$

where $\partial\mathcal{V}$ is the boundary of \mathcal{V} , \mathbf{s} is the position vector on $\partial\mathcal{V}$, and $\hat{\mathbf{n}}_s$ is the outward normal unit vector from \mathcal{V} .

In Eqs. (2.10) and (2.11), the terms containing θ represent the bulk source. They are the same as those derived from \mathbf{P}_∞ at $\mathbf{r} \in \mathcal{V}$ and yield the familiar bulk effect in conventional optics. In contrast, the term containing the delta function is only nonzero at the boundary, that is, the boundary source (boundary charge density) guarantees MBCs; see Sect. 2.4.3 for the proof. To obtain a physical picture under the NFC, the present formulation using the boundary source is advantageous over the conventional formulation using the MBCs, as is described below. One can apply Eqs. (2.8)–(2.11) to any material, using adequate polarization of an infinite-sized material, \mathbf{P}_∞ . In the following, the boundary optical effects of dielectric, metallic, ferromagnetic (magneto-optical), and ferroelectric (electro-optical) materials are examined under the NFC.

2.3.3 Boundary Effect of a Dielectric Material; Rayleigh Scattering Near Field

The Rayleigh scattering system serves as a guide for a general discussion of the boundary effects in NFO; let us refine the sketch in Sect. 2.3.1. In Eq. (2.8), we use the following polarization for an infinite-sized dielectric:

$$\mathbf{P}_\infty(\mathbf{r}, t) = (\epsilon_1 - \epsilon_0)\mathbf{E}(\mathbf{r}, t), \quad (2.12)$$

where ϵ_1 and ϵ_0 are the dielectric constants of the material and the vacuum, respectively. To derive the boundary and bulk sources that appear under the NFC, we assume the incident field to be a linearly polarized plane wave for simplicity:

$$\mathbf{E}^{(0)} \exp(i\mathbf{k} \cdot \mathbf{r} - i\omega t), \quad (2.13)$$

$$\omega = c|\mathbf{k}|, \quad (2.14)$$

where \mathbf{k} is the wavenumber in vacuum, ω is the angular frequency, and c is the speed of light in vacuum. In the limit of weak scattering, we use the Born approximation [28], and replace the $\mathbf{E}(\mathbf{r}, t)$ appearing in Eqs. (2.10) and (2.11) with the incident electric field, Eq. (2.13). (The Born approximation in a low energy scattering system is effective under the condition that $|\epsilon_1/\epsilon_0 - 1| \ll 1$. Although limited systems can strictly satisfy this condition, the Born approximation is the first candidate method for exploring a scattering problem. We use it for the qualitative and semi-quantitative discussion. Subsequently, we use the long wavelength approximation. In electromagnetic scattering problems, the combination of these two approximations is called the Rayleigh–Gans approximation.) Then the sources are

$$\begin{aligned} \rho(\mathbf{r}, t) &\simeq \int_{\partial\mathcal{V}} d^2s \delta^3(\mathbf{r} - \mathbf{s})(\epsilon_1 - \epsilon_0)\hat{\mathbf{n}}_s \cdot \mathbf{E}^{(0)} \exp(i\mathbf{k} \cdot \mathbf{s} - i\omega t) \\ &\quad - i\theta(\mathbf{r} \in \mathcal{V})(\epsilon_1 - \epsilon_0)\mathbf{k} \cdot \mathbf{E}^{(0)} \exp(i\mathbf{k} \cdot \mathbf{r} - i\omega t), \end{aligned} \quad (2.15)$$

$$\mathbf{j}(\mathbf{r}, t) \simeq -ic\theta(\mathbf{r} \in \mathcal{V})|\mathbf{k}|(\epsilon_1 - \epsilon_0)\mathbf{E}^{(0)} \exp(i\mathbf{k} \cdot \mathbf{s} - i\omega t). \quad (2.16)$$

Under the NFC, the size of the material is sufficiently small relative to the incident light wavelength; therefore, we can also employ the long wavelength approximation; i.e., we can take the limit of $k \rightarrow 0$. Therefore, only the first term in Eq. (2.15) (the boundary charge density) survives and leads to a quasi-static picture as described in Sect. 2.3.1. In short, a *boundary* charge density is induced and is the dominant source of the near and far fields in the Rayleigh scattering system.

The boundary charge density at position \mathbf{s} on the surface is determined by the boundary charge factor (BCF) without the temporally oscillating factor $\exp(-i\omega t)$:

Table 2.2 The near- and far-field amplitude without phase factor in the Rayleigh scattering system; $ka, kb \ll 1$. All the quantities are in non-dimensional form

	Source	Near-field amplitude under $kr \ll 1$	Far-field amplitude under $kr \gg 1$
Boundary effect	k^3ab^2	ab^2/r^3	k^2ab^2/r
Bulk effect	k^4ab^3	kab^3/r^3	k^3ab^3/r

$$\hat{\mathbf{n}}_s \cdot \mathbf{P}_\infty \sim (\epsilon_1 - \epsilon_0) \hat{\mathbf{n}}_s \cdot \mathbf{E}^{(0)}, \quad (2.17)$$

which appears in Eq. (2.15) and is consistent with Fig. 2.3c, supporting our intuitive picture. The BCF is useful for an intuitive understanding of the optical near field of other materials discussed in the following subsections.

As the next step, let us estimate the order of boundary and bulk sources. At a certain time, the incident electric field $\mathbf{E}^{(0)}$ induces a dipole moment: a pair of boundary charge densities with strength $\sim k^3ab^2$ (in non-dimensional form). This expression is the product of the charge on a surface with area ab and length b for the charges in the pair shown in Fig. 2.3c. Furthermore, Eqs. (2.15) and (2.16) tell us that the bulk sources carry one more k (kb in non-dimensional form) relative to the boundary source, resulting in $\sim k^4ab^3$. We have multiplied by kb because b is the length that collapses due to the delta function of the boundary source. The length dependence of the sources is summarized in the second column of Table 2.2.

The near field should be a dipole field scaled by $1/r^3$, so that its amplitude (without a phase factor) results in $\sim ab^2/r^3$ and is k independent. In contrast, the bulk source generates a rather weak near-field amplitude $\sim kab^3/r^3$ and k dependence. The far field at $kr \gg 1$ is proportional to $1/r$ because of the conservation of flux in three dimensions. Therefore, the contributions to the near- and far-field amplitudes from the boundary and bulk sources are as shown in Table 2.2. The boundary source dominates the Rayleigh scattering in the near- and far-field amplitudes. Actually, in the case of an isotropic material ($a = b$), this causes the far-field intensity $\sim k^4a^6/r^2$. This coincides with the well-known expression in the Rayleigh scattering problem, supporting the validity of our scheme based on the boundary effect. In Table 2.6, the same result will be derived using the dual vector potential, which is introduced in Sect. 2.5.

From Table 2.2, one finds that the near field generated by the boundary source refers to the wavenumber-independent picture (quasi-static picture), while any field generated by the bulk source or the far field generated by any source are wavenumber dependent (the retardation effect). The key to understanding Rayleigh scattering as a boundary effect is that a pair of boundary charges on a scale smaller than the wavelength forms a dipole moment, causing a quasi-static or wavenumber-independent near field ruled by Coulomb's law. For a simple interpretation of the field intensity, see Sect. 2.3.7

We may apply the above procedure to other materials starting with an adequate \mathbf{P}_∞ .

2.3.4 Boundary Effect of a Metallic Material

For a metallic material, we start with the same expression as Eq. (2.12) but we include a complex-numbered term ϵ_1 ; the imaginary part of ϵ_1 is related to the conductivity σ *via*

$$\mathcal{I}m \epsilon_1 = \frac{\sigma}{\omega}. \quad (2.18)$$

The complex-numbered ϵ_1 leads to the complex-numbered refractive index, $(\epsilon_1/\epsilon_0)^{1/2}$, or wavenumber, $k_m = (\epsilon_1/\epsilon_0)^{1/2}k$. The imaginary part of k_m brings about one more scale of length, namely, the skin depth $d = \mathcal{I}m(1/k_m)$. The skin depth describes the decay length of the EM field amplitude or current density inside the metal surface (Note carefully that the penetration depth, d_p , means the decay length of the field *intensity*, i.e., $d_p = d/2$). In non-dimensional form, the skin depth is

$$kd = \mathcal{I}m \left(\frac{\epsilon_0}{\epsilon_1} \right)^{\frac{1}{2}}. \quad (2.19)$$

The skin depth represents the scale inside the material; however, the optical near field outside the material is influenced by the skin depth *via* reflection and/or absorption, if the representative size of material is larger than the skin depth. Considering the skin depth, the NFC for a metallic material (the condition under which the quasi-static picture holds) is

$$ka \lesssim kr \ll 1 \quad \text{and} \quad \frac{a}{d} \lesssim \frac{r}{d} \ll 1. \quad (2.20)$$

The skin depths of some metals at light wavelength are summarized in Table 2.3. One finds that the second inequality of the NFC for metal (2.20) is rather severe; it holds only in limited cases, e.g., $a \lesssim r \ll d \sim 10\text{--}40$ nm. Therefore, if one employs the procedure of Sect. 2.3.3 (using the Born approximation and long

Table 2.3 The skin depth of some metals at the light wavelength 551 nm (photon energy 2.25 eV). The complex-numbered dielectric constant is ϵ_1/ϵ_0 and refractive index is $(\epsilon_1/\epsilon_0)^{1/2}$. The data in this table are calculated by means of linear interpolation of the data at neighbouring photon energies in Ref. [22]

Material	Skin depth/nm	Dielectric constant	Refractive index
Al	13.08	$-44.02 + 13.01 i$	$0.97 + 6.71 i$
Fe	26.30	$-3.86 + 17.98 i$	$2.70 + 3.34 i$
Cu	33.80	$-5.86 + 4.85 i$	$0.94 + 2.60 i$
Ag	24.13	$-13.15 + 1.85 i$	$0.26 + 3.64 i$
Au	37.00	$-5.52 + 1.45 i$	$0.31 + 2.37 i$
Cr	19.83	$-10.12 + 27.18 i$	$3.07 + 4.42 i$
Mo	25.35	$2.22 + 26.07 i$	$3.77 + 3.46 i$
W	32.01	$4.67 + 19.13 i$	$3.49 + 2.74 i$

wavelength limit), it is limited to a qualitative level or may turn out to be nonsense in unfortunate cases.

A simplified treatment for the skin depth is effective under $\mathcal{I}m\epsilon_1 \gg \mathcal{R}e\epsilon_1$, that is, $\epsilon_1 \simeq i\sigma/\omega$. Equation (2.19) leads to

$$kd \simeq \sqrt{\frac{2\epsilon_0\omega}{\sigma}} \quad \text{or} \quad d \simeq \sqrt{\frac{2\epsilon_0}{\sigma\omega}}c. \quad (2.21)$$

For the derivation, we use $i^{1/2} = \pm(1+i)/\sqrt{2}$. We have to remind the reader that the conductivity of metal brings about a strong retardation effect (wavenumber dependence) of the EM field.

2.3.5 Boundary Magneto-Optical Effect

The magneto-optical effect (MOE) was discovered by Faraday in [12] and is used for optical sensing of magnetic fields. These MOE effects, the Faraday and Kerr effects (FK effects), cause rotation of the polarization vector and are assigned to a bulk optical effect that is dependent on wavenumber; see Fig. 2.4a. (The Faraday effect is the rotation of polarization vector of the transmitted light, while the Kerr effect is that of the reflected light. The difference is not important in this chapter; therefore, these two effects are not distinguished.)

A naive question is: “Does there exist a boundary MOE independent of wavenumber?” The answer is “yes,” as expected from the first term of Eq. (2.10). Considering that near field optics permits the observation of a small-scale system, the boundary MOE is situated at the crossroads of magneto-optics and near-field optics. We can derive the boundary MOE under the NFC and estimate its near-field amplitude as guided by Rayleigh scattering, discussed in Sect. 2.3.3. In this

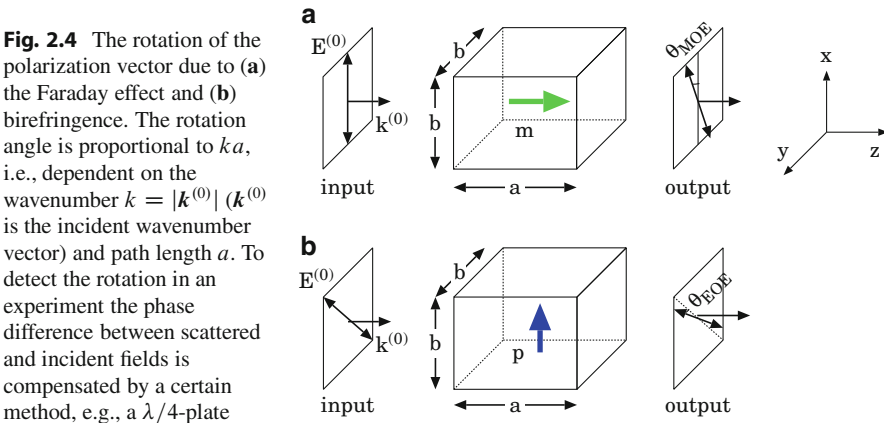


Fig. 2.4 The rotation of the polarization vector due to (a) the Faraday effect and (b) birefringence. The rotation angle is proportional to ka , i.e., dependent on the wavenumber $k = |\mathbf{k}^{(0)}|$ ($\mathbf{k}^{(0)}$ is the incident wavenumber vector) and path length a . To detect the rotation in an experiment the phase difference between scattered and incident fields is compensated by a certain method, e.g., a $\lambda/4$ -plate

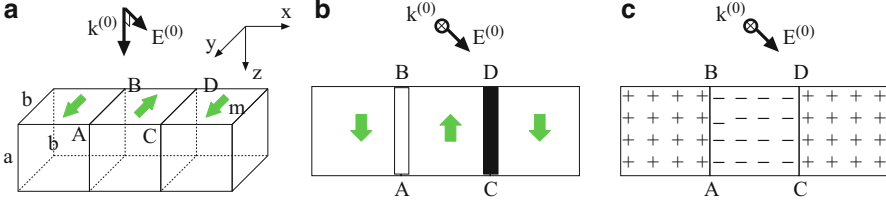


Fig. 2.5 An example system for examining the boundary MOE; $\mathbf{k}^{(0)}$ ($k = |\mathbf{k}^{(0)}|$) and $\mathbf{E}^{(0)}$ are the wavenumber and polarization vectors of the incident field. (a) The light is incident normal to the upper boundary of the ferromagnetic material and polarized linearly with the polarization vector pointing in an oblique direction to lines AB and CD . (b) The rotation of the polarization vector; the directions of rotation on the *black-and-white lines* are opposite to each other. (c) The sign of the MOE-related BCF in Eq. (2.23) on the upper boundary

subsection, we discuss the mechanism through which the boundary MOE dominates under the NFC.

We consider the MOE in an example system with three ferromagnetic domains that are exposed to normal incident and linearly polarized light, as in Fig. 2.5a. Such a system with multiple domains may be considered as a stack of isolated domains with hypothetical thin vacuum spaces between them. We assume that the width of the domain wall is sufficiently small for its optical response to be negligible. For simplicity, we set the light to be incident normal to the upper boundary surface.

Consider a single ferromagnetic domain under the NFC, starting with the following \mathbf{P}_∞ including a simple MOE:

$$\mathbf{P}_\infty(\mathbf{r}, t) = (\epsilon_1 - \epsilon_0)\mathbf{E}(\mathbf{r}, t) + i\epsilon_1 Q \hat{\mathbf{m}} \times \mathbf{E}(\mathbf{r}, t), \quad (2.22)$$

where \mathbf{m} is the magnetic dipole moment and $\hat{\mathbf{m}}$ is the unit vector of \mathbf{m} . Q is the parameter representing the MOE and includes the magnitude factor $|\mathbf{m}|$. Equation (2.22) leads to the familiar bulk MOE, i.e., magnetic circular birefringence (the FK effects; see Fig. 2.4a) and magnetic circular dichroism.

Following the manner of treating the Rayleigh scattering system in Sect. 2.3.3, the boundary charge density at position \mathbf{s} on the surface is dominant, and is determined by the following BCF without the temporally oscillating factor $\exp(-i\omega t)$ (see Eq. (2.15)):

$$\hat{\mathbf{n}}_s \cdot \mathbf{P}_\infty \sim (\epsilon_1 - \epsilon_0)\hat{\mathbf{n}}_s \cdot \mathbf{E}^{(0)} + i\epsilon_1 Q \hat{\mathbf{n}}_s \cdot \hat{\mathbf{m}} \times \mathbf{E}^{(0)}. \quad (2.23)$$

The first term in the BCF (2.23) is identical to Eq. (2.17), i.e., the BCF for the Rayleigh scattering system. The second term is the MOE-related BCF and we focus on this in the following discussion.

In the center domain, if we set the sign of the MOE-related BCF to be negative on the upper boundary at a certain time, it will be positive on the lower boundary and zero on the side boundary. Applying the same logic to the other domains, the

Table 2.4 The near- and far-field amplitudes (without phase factor) scattered by the multiple domains of ferromaterial in the model systems of Figs. 2.5 and 2.6 under the condition $ka, kb \ll 1$. All the quantities listed are in non-dimensional form and should be linearly scaled by Q and R for the cases of the MOE in Fig. 2.5 and the EOE in Fig. 2.6, respectively

	Source	Near-field amplitude under $kr \ll 1$	Far-field amplitude under $kr \gg 1$
Boundary effect ^a	$k^3 b^3$	b^3 / r^3	$k^2 b^3 / r$
Bulk effect ^b	$k^4 a b^3$	$k a b^3 / r^3$	$k^3 a b^3 / r$

^aThe boundary effect is the contribution from the upper boundary source

^bFor MOE, an oblique incident is assumed so that boundary and bulk effects coexist

sign of the MOE-related BCF on the upper boundary of each domain is filled in the corresponding area in Fig. 2.5c, which describes a snapshot of the MOE-related boundary charge density at a certain time.

Let us first focus on the upper boundary. We assume that the observation point is close to the upper boundary, so that the contribution from the lower boundary is relatively small. Within the scale of one wavelength, the dipole moment appears. It consists of a pair of boundary charges with opposite signs across lines AB and CD. We can derive a wavenumber-independent near field in the same manner as is demonstrated in Sect. 2.3.3 to evaluate the Rayleigh scattering near field. In fact, the strength of the dipole moment (the boundary source) across line AB is $k^3 b^3$, because the charge in the pair is distributed on the surface with area b^2 and the distance between the centers of the charge densities in the pair is b . An important feature of the MOE-related boundary source is the a independence. It means that the scattered field is caused by the upper boundary, without propagation into the bulk volume (and the same for the rotation of the polarization vector).

The bulk source that coexists with the boundary source is estimated as $\sim k^4 a b^3$, multiplying the boundary source by one more k term (or ka in non-dimensional form). Note carefully that a is the length that collapses due to the delta function at the upper boundary in the MOE-related boundary charge density (Eq. (2.10) with Eq. (2.22)).

The same procedure as for the Rayleigh scattering system is used to estimate the near- and far-field amplitudes (without a phase factor). This approach implies that the near-field amplitude is the dipole field scaled by $1/r^3$, while the far-field amplitude is scaled by $1/r$. The results are summarized in Table 2.4. The far-field amplitude originating from the boundary source in Table 2.4 is $\sim k^2 b^3 / r$ (without phase factor). In this formula, we consider only the contribution from the upper boundary source. However, the lower boundary source also contributes to the far-field amplitude. On the lower boundary, the sign of the MOE-related BCF and the direction of the dipole moment across the domain boundary are opposite to those on the upper boundary. The pair of dipole moments on the upper and lower boundaries under $ka \ll 1$ forms a quadrupole moment, which generates a rather weak far-field amplitude. In other words, the two partial-field amplitudes generated from the upper and lower boundaries interfere dispersively.

As a result, the boundary MOE generates a wavenumber-independent near field from the small-scale structure under the NFC and predominates over the bulk MOE. This near field causes exotic rotation of the polarization vector, which is completely different from the rotation due to the bulk effect (the FK effects). The boundary effect makes the near field independent of the wavenumber and the path length, while the bulk effect makes the near field dependent on them. We can understand how the scattered near field leads to rotation *via* the following argument. The scattered electric near field generated on top of line AB in Fig. 2.5 points in a direction different from that of transmitted or normally reflected light, so that the polarization vector of the total field rotates in a certain direction. Conversely, with respect to line CD, the polarization vector rotates in a direction opposite to the case of line AB. Note carefully that the rotational angle is proportional to the scattered-field amplitude under a sufficiently small Q , because the tangent of the rotational angle is the ratio between the component of the scattered-field amplitude perpendicular to the incident field and the incident or reflected field amplitude. Note that this rotation or, equivalently, the dipole field upon the domain wall may be detected in the near-field regime using SNOM, while in the far-field regime, the two partial-field amplitudes interfere dispersively as mentioned in the previous paragraph.

The BCF (2.23) tells us that the dielectric- and MOE-related boundary charge densities are out of phase in time because of the imaginary unit included in the latter. That is, no simultaneous Coulomb interaction exists between the two kinds of boundary charge density. This fact is advantageous for observation of the boundary MOE in NFO.

The existence of the above boundary MOE has been reported in a paper by the present author [4]. In the *far-field* of *large-scale* magnetic domains, Schäfer and Hubert [33, 34] first observed the MOE at the boundary wall under the Voigt configuration, in which the bulk effects (the FK effects) disappear. For a long time, their experimental results had not been supported by a clear physical picture. In [4], the Schäfer–Hubert effect was identified as the boundary MOE discussed above, but without use of the long wavelength approximation. In general, boundary and bulk effects coexist, but the bulk effect is dominant in such a large-scale system. However, the MOE in the Voigt configuration with adequate \mathbf{m} , $\mathbf{E}^{(0)}$ and \mathbf{k} is an exceptional case, because the bulk effect disappears and the boundary MOE becomes detectable even in the ordinary far-field observation.

2.3.6 Boundary Electro-optical Effect

We can predict the unknown boundary EOE under the NFC and estimate its near-field amplitude in the same manner as in the previous subsection. Let us consider an example system with three ferroelectric domains that are exposed to normal incident and linearly polarized light, as in Fig. 2.6a.

The procedure to derive and characterize boundary and bulk effects are parallel to that for the MOE in Sect. 2.3.5. We start with the following \mathbf{P}_∞ including a simple

EOE for each single ferroelectric domain under the NFC:

$$\mathbf{P}_\infty(\mathbf{r}, t) = (\epsilon_1 - \epsilon_0)\mathbf{E}(\mathbf{r}, t) + \epsilon_1 R \hat{\mathbf{p}}(\hat{\mathbf{p}} \cdot \mathbf{E}(\mathbf{r}, t)), \quad (2.24)$$

where \mathbf{p} is the electric dipole moment and $\hat{\mathbf{p}}$ is the unit vector of \mathbf{p} . R is the parameter representing the EOE, which includes a factor with magnitude $|\mathbf{p}|^2$. Then one finds the following BCF without the temporally oscillating factor $\exp(-i\omega t)$:

$$\hat{\mathbf{n}}_s \cdot \mathbf{P}_\infty \sim (\epsilon_1 - \epsilon_0)\hat{\mathbf{n}}_s \cdot \mathbf{E}^{(0)} + \epsilon_1 R(\hat{\mathbf{n}}_s \cdot \hat{\mathbf{p}})(\hat{\mathbf{p}} \cdot \mathbf{E}^{(0)}). \quad (2.25)$$

The first term in the BCF (2.25) is identical to Eq. (2.17), i.e., the BCF for the Rayleigh scattering system, and the second term is the EOE-related BCF. The signs of the EOE-related BCFs on the upper boundary are filled in the corresponding area in Fig. 2.6c, which describes a snapshot of the EOE-related boundary charge density at a certain time.

The same procedure as for MOE is applicable to an order estimation of the boundary and bulk sources, and near- and far-field amplitudes. The results are summarized in Table 2.4, again. As in the MOE case, the boundary EOE generates a wavenumber-independent near field from the small-scale structure under the NFC and predominates over the bulk EOE. This near field causes exotic rotation of the polarization vector, which is completely different from the rotation due to the bulk effect (the birefringence). The boundary effect makes the near field independent of the wavenumber and the path length, while the bulk effect makes the near field dependent on them. We can understand how the scattered near field leads to rotation by the same logic as in the MOE case. The scattered electric near field generated on top of line AB in Fig. 2.6 points in a direction different from that of the transmitted or normally reflected light, so that the polarization vector of the total field rotates in a certain direction. Conversely, with respect to line CD, the polarization vector rotates in the direction opposite to the case of line AB. Note carefully that the rotational angle is proportional to the scattered-field amplitude for sufficiently small R . As mentioned in the case of MOE, this rotation or, equivalently,

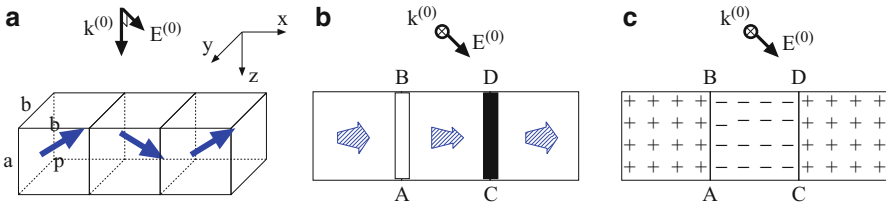


Fig. 2.6 The rotation of the polarization vector due to the boundary EOE; $\mathbf{k}^{(0)}$ ($k = |\mathbf{k}^{(0)}|$) and $\mathbf{E}^{(0)}$ are the wavenumber and polarization vectors of the incident field. (a) A simplified model system: $\mathbf{k} \parallel \hat{\mathbf{z}}$, $\mathbf{E}^{(0)} \parallel (\hat{\mathbf{x}} + \hat{\mathbf{y}})$ and $\mathbf{p} \parallel \hat{\mathbf{x}} \mp \hat{\mathbf{z}}$. (b) The top view of the direction of rotation; on the black-and-white lines, the polarization vector rotates in the opposite direction. (c) The sign of the EOE-related boundary charge density on the upper boundary

the dipole field upon the domain wall may be observed in the near-field regime using SNOM.

The BCF (2.25) tells us that the dielectric-related boundary charge density and the EOE-related one are temporally in phase. Hence, the simultaneous Coulomb interaction between the two kinds of boundary charge density affects the distribution of the EOE-related charge density. This is different from the boundary MOE case mentioned in Sect. 2.3.5, and is disadvantageous for observation of the boundary EOE in NFO. To check the influence of the Coulomb interaction, a numerical calculation and a careful experiment are required.

2.3.7 A Simple Interpretation of Near-Field Intensity

The field intensity is the most important quantity in the experiments of NFO and is often observed by SNOM in the time-averaged manner. Here we discuss the theoretical formulas for far-field intensity and near-field intensity. An additional consideration is given for a theoretical formula of the signal intensity in SNOM [6, 8].

In the linear scattering problem with the incident field (2.13), one may separate the temporal dependence of $\mathbf{E}^{(0)}(\mathbf{r}, t)$ and $\mathbf{E}(\mathbf{r}, t)$, respectively, as

$$\mathbf{E}^{(0)}(\mathbf{r}) \exp(-i\omega t) \quad \text{and} \quad \mathbf{E}(\mathbf{r}) \exp(-i\omega t). \quad (2.26)$$

The time-averaged field intensity at the position \mathbf{r} is defined by the equation

$$\begin{aligned} \Delta I(\mathbf{r}) &= \frac{|\mathbf{E}(\mathbf{r})|^2 - |\mathbf{E}^{(0)}(\mathbf{r})|^2}{|\mathbf{E}^{(0)}(\mathbf{r})|^2} \\ &= \frac{\mathbf{E}^{(0)*}(\mathbf{r}) \cdot \Delta \mathbf{E}(\mathbf{r}) + \text{c.c.} + |\Delta \mathbf{E}(\mathbf{r})|^2}{|\mathbf{E}^{(0)}(\mathbf{r})|^2}, \end{aligned} \quad (2.27)$$

where $|\mathbf{E}^{(0)}|^2$ in the denominator is introduced to make ΔI dimensionless and that in the numerator is done to eliminate the background intensity.

In the far-field observation ($kr \gg 1$), the observation point \mathbf{r} does not belong to the coherent region of the incident field, i.e., $\mathbf{E}^{(0)}(\mathbf{r}) = 0$. Therefore, Eq. (2.27) results in the far-field intensity

$$\Delta I_{\text{FF}}(\mathbf{r}) \simeq \frac{|\Delta \mathbf{E}(\mathbf{r})|^2}{|\mathbf{E}^{(0)}(\mathbf{r})|^2}. \quad (2.28)$$

We are familiar with this formula in ordinary scattering theory.

In the near-field observation ($kr \lesssim 1$), the observation point \mathbf{r} belongs to the coherent region of incident field. Therefore, Eq. (2.27) under the assumption $|\mathbf{E}^{(0)}| \gg |\Delta \mathbf{E}|$ results in the near-field intensity

$$\Delta I_{\text{NF}}(\mathbf{r}) \simeq \frac{\mathbf{E}^{(0)*}(\mathbf{r}) \cdot \Delta \mathbf{E}(\mathbf{r}) + \text{c.c.}}{|\mathbf{E}^{(0)}(\mathbf{r})|^2}. \quad (2.29)$$

Equation (2.29) implies that the interference term is dominant in the near-field regime. The interference effect enables negativeness of $\Delta I_{\text{NF}}(\mathbf{r})$ in the near-field region, that is, the field intensity can be smaller than the background intensity. This fact is considerably different from the far-field intensity, which is positive definite.

In the above discussion, the formulas are expressed without referring to the properties of the detector, e.g., the probe in SNOM. This means that the multiple scattering effect between the sample and the detector is negligible, so that the detected quantities are proportional to the intensity at the observation point in the system without the probe. In the case of the far-field observation, this assumption is reasonable, because the distance between the sample and the probe is so large that multiple scattering is negligible. In the near-field observation, this assumption is justified, if the size of the probe is small enough, i.e., $k \times (\text{size of probe}) \ll 1$. In the recent experiments in SNOM, this condition together with the near-field condition may be satisfied [29]; actually, the radius of curvature of the top of the probe tip is about 10 nm and is much smaller than the wavelength of the incident light, ~ 500 nm.

However, additional consideration is needed to interpret the signal intensity in SNOM. (This subsection treats ordinary SNOM, not apertureless SNOM. In the case of apertureless SNOM, the source may be the oscillating dipole moment composed of the charge density on the boundary of the material and that induced on the probe tip with opposite sign. So, the probe plays an essential role in the formation of the signal intensity. If one may image the above dipole moment, the signal intensity should be interpreted on the basis of dipole radiation.) The signal intensity in SNOM is considered as the field intensity of the transversal light; the light propagates in the optical fiber probe and possesses a polarization vector normal to the direction of the propagation. It is a rather simple assumption that the propagating field in the fiber is proportional to the near-field component normal to the direction of the fiber at the position of the probe tip. In this way, we may effectively take into account the filtering effect, which was pointed out by other authors to explain the polarization dependence in SNOM image [17, 27]. The filtered electric field is expressed by $-\mathbf{n}_p \times \mathbf{n}_p \times \mathbf{E}(\mathbf{r})$, where \mathbf{n}_p is the unit vector parallel to the direction of the fiber of SNOM probe at the observation point in the near-field region. (In general, for an arbitrary vector, \mathbf{E} , and an arbitrary unit vector, \mathbf{n}_p , the following identity holds: $\mathbf{E} = \mathbf{n}_p(\mathbf{n}_p \cdot \mathbf{E}) - \mathbf{n}_p \times \mathbf{n}_p \times \mathbf{E}$.) Then the signal intensity in SNOM is given by

$$\Delta I_{\text{NOM}}(\mathbf{r}) \equiv \frac{\{\mathbf{n}_p \times \mathbf{E}^{(0)*}(\mathbf{r})\} \cdot \{\mathbf{n}_p \times \Delta \mathbf{E}(\mathbf{r})\} + \text{c.c.} + |\mathbf{n}_p \times \Delta \mathbf{E}(\mathbf{r})|^2}{|\mathbf{E}^{(0)}(\mathbf{r})|^2}. \quad (2.30)$$

See Ref.[8] for qualitative comparison between theoretical calculation and experimental result in SNOM.

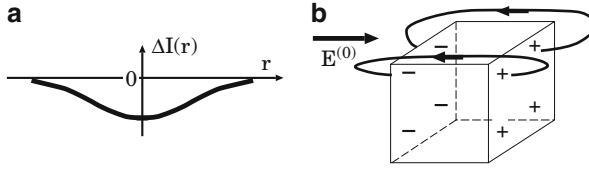


Fig. 2.7 An intuitive picture of the optical near field of a dielectric under the NFC. (a) The profile of electric field intensity along a scanning line parallel to $\mathbf{E}^{(0)}$ over the material. (b) The electric flux generated by the induced boundary charge density

Let us combine the above ideas concerning intensity and amplitude in the near-field regime. Firstly, suppose we have a dielectric material under the NFC, described in Fig. 2.3a. Under the NFC, the scattered electric field, $\Delta\mathbf{E} \equiv \mathbf{E} - \mathbf{E}^{(0)}$ or the equivalent electric flux is generated by the boundary charge density *via* Coulomb's law,

$$\nabla \cdot \Delta\mathbf{E}(\mathbf{r}) = \delta(\mathbf{r} \in \text{boundary}) \frac{\epsilon_1 - \epsilon_0}{\epsilon_0} \mathbf{n}_s \cdot \mathbf{E}^{(0)}, \quad (2.31)$$

where the r.h.s. represents $1/\epsilon_0$ times the boundary charge density, which should include the one-dimensional delta function along the boundary normal direction and BCF (2.17). (If the shape of the dielectric is enough isotropic, like a sphere, it may be recommended to replace ϵ_0 in the denominator of Eq. (2.31) by $1/3\epsilon_1 + 2/3\epsilon_0$; see Sect. 3.8 in the original book [2]; the present revised version omits this part.) Equation (2.31) reveals the situation that is described in Fig. 2.7b schematically; one may easily image the scattered electric field, $\Delta\mathbf{E}$ or the electric flux. Furthermore, under the NFC, the incident field is regarded as the constant vector $\mathbf{E}^{(0)}$ over the whole system; see Fig. 2.3a, b.

Once one can understand the profile of the field amplitude, one may guess the profile of the near-field intensity on the basis of Eq. (2.29). For example, in the system of Fig. 2.7, a negative intensity, $\Delta I_{\text{NF}}(\mathbf{r}) < 0$, appears at the observation points over the top of the material (Fig. 2.7a). This is because $\mathbf{E}^{(0)}$ and $\Delta\mathbf{E}(\mathbf{r})$ are anti-parallel at such observation points. Even if the shape of a dielectric is complicated, the above procedure to understand $\Delta\mathbf{E}(\mathbf{r})$ and $\Delta I(\mathbf{r})$ is available; see Sect. 2.4.5. In the present situation, the probe of SNOM may scan over the top of the material. The direction of electric field \mathbf{E} matches the polarization vector of the propagation mode in the probe fiber, so that the filtering effect is small. To the contrary, if the probe of SNOM is scanned along the direction parallel to the left- or right-side boundary, the electric field around the center position does not match the polarization vector of the propagation mode in the probe fiber, so that the signal intensity decreases in this scanning area.

In the magneto-optical and electro-optical systems as in Figs. 2.5 and 2.6, $\Delta\mathbf{E}$ (or the corresponding rotation) may be detected, if the probe of SNOM is scanned over and across the top of the domain wall.

In this way, one may understand or predict the near-field amplitude and the near-field intensity in a system under the NFC, even if the shape and/or response is complicated.

2.3.8 Summary: Boundary Effect of General Optical Responses

As demonstrated in this section, a characteristic of NFO is its quasi-static limit, in which the boundary effect dominates the physics even if the response and shape of the material are complicated. Indeed, setting the response *via* \mathbf{P}_∞ and setting the shape *via* \mathcal{V} , then using the BCF $\sim \hat{\mathbf{n}}_s \cdot \mathbf{P}_\infty$ on $\partial\mathcal{V}$, one could express various quasi-static phenomena, i.e., various boundary effects in NFO with a small-scale structure.

2.4 Boundary Scattering Formulation with Scalar Potential

In this section, a formulation to calculate the electric field under the NFC (2.7) is given. Under the NFC, a quasi-static picture holds and the scalar potential is the minimum degree of freedom of the EM field. Further, we replace the boundary value problem to a *boundary scattering problem*, i.e., a scattering problem with an adequate boundary source. The boundary scattering formulation with the scalar potential brings the logical basis of the simple picture in the NFO system under the NFC (Sect. 2.3) and a simple procedure of numerical calculation [7].

2.4.1 Poisson's Equation with Boundary Charge Density

Under the NFC, Maxwell's equations are reduced to Coulomb's law, which is described without temporal factor by

$$\nabla \cdot \mathbf{E}(\mathbf{r}) = -\frac{1}{\epsilon_0} \nabla \cdot \mathbf{P}(\mathbf{r}) , \quad (2.32)$$

$$\mathbf{P}(\mathbf{r}) = (\epsilon(\mathbf{r}) - \epsilon_0) \mathbf{E}(\mathbf{r}) , \quad (2.33)$$

where $\mathbf{P}(\mathbf{r})$ and $\mathbf{E}(\mathbf{r})$ are spatial part of the polarization and electric field in the manner of Eq. (2.26); $\epsilon(\mathbf{r})$ is the local and linear dielectric function and is assumed to be a smooth function of \mathbf{r} for a while.

In terms of the scalar potential which is defined as $\mathbf{E}(\mathbf{r}) = -\nabla\phi(\mathbf{r})$, Eqs. (2.32) and (2.33) become Poisson's equation,

$$-\Delta\phi(\mathbf{r}) = \nabla \cdot \left(\frac{\epsilon(\mathbf{r}) - \epsilon_0}{\epsilon_0} \nabla\phi(\mathbf{r}) \right) . \quad (2.34)$$

Now, using the equation $\nabla \cdot \{\epsilon(\mathbf{r})\nabla\phi(\mathbf{r})\} = \nabla\epsilon(\mathbf{r}) \cdot \nabla\phi(\mathbf{r}) + \epsilon(\mathbf{r})\Delta\phi(\mathbf{r})$, Eq. (2.34) results in another expression for the Poisson equation,

$$-\Delta\phi(\mathbf{r}) = \frac{\nabla\epsilon(\mathbf{r})}{\epsilon(\mathbf{r})} \cdot \nabla\phi(\mathbf{r}) . \quad (2.35)$$

The r.h.s. of Eq. (2.35) is the induced charge density divided by ϵ_0 ; this charge density is localized within the interface region where $\epsilon(\mathbf{r})$ varies steeply and $\nabla\epsilon(\mathbf{r})$ takes a large value. In the following, we simply refer to the quantity in the r.h.s. of Eq. (2.35) as “boundary charge density,” ignoring the constant factor $1/\epsilon_0$. Note carefully that “boundary charge density” means the charge per unit volume (not per unit area) in this chapter.

Equations (2.34) and (2.35) are equivalent, but we prefer Eq. (2.35), which is the starting point of our novel formulation, namely, the boundary scattering formulation. This for NFO brings about a simple procedure of a numerical method with a small amount of calculation, which, furthermore, is compatible with the clear physical picture described in Sect. 2.3.

2.4.2 Notation Concerning Steep Interface

In Sect. 2.3.7, we have discussed a system with a steep interface in an intuitive and qualitative manner. These systems should be ruled by Poisson’s equation (2.35). Strictly speaking, there is a difficulty to treat Eq. (2.35) in the limit of the steep interface, that is, the boundary charge density in the r.h.s. is a product of distributions and not well-defined in a general mathematical sense. Actually, in the limit of the steep interface, the quantities $\epsilon(\mathbf{r})$, $\nabla\phi$, and $\nabla\epsilon(\mathbf{r})$ in Eq. (2.35) become distributions, i.e., the step function and/or the delta function.

To treat this singularity in a proper manner, let us introduce some notation. A steep interface is characterized by a stepwise dielectric function,

$$\epsilon(\mathbf{r}) \equiv \epsilon_0 + \theta(\mathbf{r} \in \mathcal{V}_1)(\epsilon_1 - \epsilon_0), \quad (2.36)$$

$$\theta(\mathbf{r} \in \mathcal{V}_1) \equiv \begin{cases} 0 & \text{for } \mathbf{r} \in \mathcal{V}_0 \\ \text{not defined} & \text{for } \mathbf{r} \in \mathcal{V}_{01} \\ 1 & \text{for } \mathbf{r} \in \mathcal{V}_1 \end{cases}, \quad (2.37)$$

where \mathcal{V}_0 , \mathcal{V}_1 , and \mathcal{V}_{01} stand for the vacuum, the material, and the interface region, respectively, and ϵ_1 stands for the complex dielectric constant of the material. Note carefully that \mathcal{V}_{01} is volume, i.e., the three-dimensional space with infinitesimal width $\eta = +0$. A definition of $\epsilon(\mathbf{r})$ in the interface region is not given because it is not needed in the following discussion.

We define the notation (Fig. 2.8): \mathcal{V}_{01}/η is the whole surface of the material (two-dimensional space), $\mathbf{s} \in \mathcal{V}_{01}/\eta$ is a position vector on the surface located in the center of \mathcal{V}_{01} . \mathbf{n}_s is the outward normal vector at \mathbf{s} . $\sigma \subset \mathcal{V}_{01}/\eta$ is a small surface element containing \mathbf{s} . \mathbf{s}_0 and \mathbf{s}_1 are the position vectors just outside the interface region; those are defined as $\mathbf{s}_0 \equiv \mathbf{s} + \frac{\eta}{2}\mathbf{n}_s = \mathbf{s} + 0\mathbf{n}_s$ and $\mathbf{s}_1 \equiv \mathbf{s} - \frac{\eta}{2}\mathbf{n}_s = \mathbf{s} - 0\mathbf{n}_s$. Further, \mathbf{m}_1 and \mathbf{m}_2 are two independent unit vectors in the surface at \mathbf{s} , l_i ($i = 1, 2$) is a small length along \mathbf{m}_i ($i = 1, 2$) (so that $\sigma = l_1 \otimes l_2$), $\eta \otimes l_i$ ($i = 1, 2$) is an infinitesimal area and $\sigma \otimes \eta = l_1 \otimes l_2 \otimes \eta$ is an infinitesimal volume.

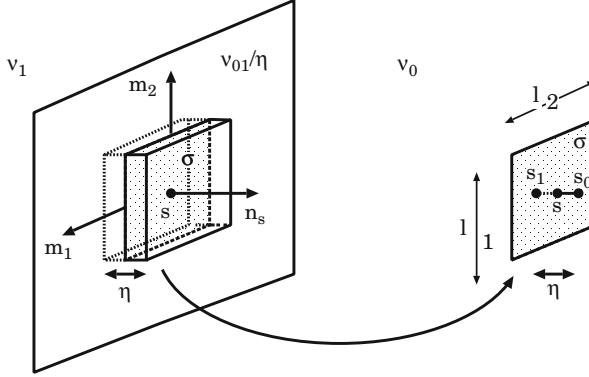


Fig. 2.8 Notation concerning a steep interface

2.4.3 Boundary Scattering Problem Equivalent to Boundary Value Problem

To overcome the difficulty to solve Eq.(2.35) with Eq.(2.36), i.e., in a system with a steep interface, there is a method without using MBCs, that is, the *boundary scattering formulation* with the scalar potential. The difficulty in the original problem is that the boundary charge density in Eq.(2.35) becomes a product of distributions, which does not seem to be well-defined in a general mathematical sense. However, in the following, it is proved that a certain expression of boundary charge density reproduces the MBCs properly and is the well-defined quantity.

With such a proper expressions for the boundary charge density, Eq.(2.35) becomes

$$-\Delta\phi(\mathbf{r}) = -\int_{\mathcal{V}_{01/\eta}} d^2s \delta^3(\mathbf{r} - \mathbf{s}) \frac{\epsilon_1 - \epsilon_0}{\epsilon(\mathbf{s})} \partial_n \phi(\mathbf{s}) \text{ for } \mathbf{r} \in \mathcal{V}_0 \cup \mathcal{V}_{01} \cup \mathcal{V}_1, \quad (2.38a)$$

$$\epsilon(\mathbf{s}) \equiv \alpha(\mathbf{s})\epsilon_1 + (1 - \alpha(\mathbf{s}))\epsilon_0, \quad (2.38b)$$

$$\partial_n \phi(\mathbf{s}) \equiv (1 - \alpha(\mathbf{s}))\partial_n \phi(\mathbf{s}_1) + \alpha(\mathbf{s})\partial_n \phi(\mathbf{s}_0). \quad (2.38c)$$

Equations (2.38b) and (2.38c) are merely the definitions of $\epsilon(\mathbf{s})$ and $\partial_n \phi(\mathbf{s})$, respectively; $\alpha(\mathbf{s})$ is an arbitrary smooth and complex-valued function on $\mathcal{V}_{01/\eta}$.

Here we show that Eqs.(2.38a)–(2.38c) of the boundary scattering problem leads to MBCs. Integrate Eq.(2.38a) over the infinitesimal volume element $\sigma \otimes \eta$ ($\eta = +0$) in Fig. 2.8, apply Gauss' theorem to the l.h.s. and carry out the volume integral of the delta function in the r.h.s. Then one obtains the following MBC:

$$\epsilon_0 \partial_n \phi(\mathbf{s}_0) = \epsilon_1 \partial_n \phi(\mathbf{s}_1) \quad \text{for } \mathbf{s} \in \mathcal{V}_{01/\eta}, \quad (2.39)$$

which means we have continuity of the surface-normal component of the electric flux field. The arbitrary function $\alpha(s)$ disappears automatically and does not affect the field in $\mathcal{V}_0 \cup \mathcal{V}_1$. You may know one more MBC concerning the electric field; it describes the continuity of the surface-parallel component of the electric field:

$$\mathbf{n}_s \times \nabla \phi(s_0) = \mathbf{n}_s \times \nabla \phi(s_1) . \quad (2.40)$$

Equation (2.40) is trivial because it is derived from the identity $\nabla \times \nabla \phi(\mathbf{r}) = 0$. Integrate this identity over the small area $l_i \otimes \eta$ for $i = 1, 2$, apply Stokes' theorem and take the limit $\eta \rightarrow +0$; then one obtains Eq. (2.40). Therefore, we do not need a boundary condition (2.40) in the calculation using the scalar potential.

As a result, it is confirmed that the MBCs concerning the electric field are reproduced from Eqs. (2.38a) to (2.38c). In principle, the solution of the boundary value problem with MBCs and that of Eqs. (2.38a)–(2.38c) of the boundary scattering problem are equivalent in the domain $\mathcal{V}_0 \cup \mathcal{V}_1$. This is so because the two solutions in the regions $\mathcal{V}_0 \cup \mathcal{V}_1$ satisfy the same boundary conditions. However, Eqs. (2.38a)–(2.38c) possesses considerable merits compared with the boundary value formulation. The first merit is that the boundary effect can be treated by a perturbative or an iterative method; see Sect. 2.4.4. The second is that the arbitrariness of the expression for the boundary source can be used to control the convergence in a numerical calculation.

The arbitrariness in Eqs. (2.38a)–(2.38c) comes from the degree of freedom of the charge density profile inside the interface region \mathcal{V}_{01} ; not any detail but the integration of the charge density over the width η ($= +0$) determines the field in $\mathcal{V}_0 \cup \mathcal{V}_1$. This integrated quantity is analogous to the well-known multipole moment; only the multipole moments of a source determine the EM field outside of finite source region [36]. Therefore, it is reasonable that a certain arbitrariness of the boundary source appears (For mathematical details, see Sect. 8.1 in the original book, Ref. [2]).

As a result, the MBCs can be built in the definition of the boundary charge density. The original problem (Eq. (2.35) with Eq. (2.36)) is replaced by the boundary scattering problem (Eqs. (2.38a)–(2.38c)). The boundary scattering formulation enables a perturbative treatment of the boundary effect.

2.4.4 Integral Equation for Source and Perturbative Treatment of MBC

Equations (2.38a)–(2.38c) are converted to the integral equation

$$\phi(\mathbf{r}) = \phi^{(0)}(\mathbf{r}) + \int_{\mathcal{V}_{01/\eta}} d^2s G(\mathbf{r}, \mathbf{s}) \frac{\epsilon_1 - \epsilon_0}{\epsilon(\mathbf{s})} \partial_n \phi(\mathbf{s}) , \quad (2.41)$$

$$G(\mathbf{r}, \mathbf{r}_1) = \frac{-1}{4\pi} \frac{1}{|\mathbf{r} - \mathbf{r}_1|} , \quad (2.42)$$

where $\phi^{(0)}(\mathbf{r}) = -\mathbf{E}^{(0)} \cdot \mathbf{r}$ is the incident scalar potential; $\phi^{(0)}$ leads to the incident electric field $\mathbf{E}^{(0)} = -\nabla\phi^{(0)}(\mathbf{r})$. $G(\mathbf{r}, \mathbf{r}_1)$ is Green's function for the Laplace equation; it is defined *via* $-\Delta G(\mathbf{r}, \mathbf{r}_1) = -\delta^3(\mathbf{r} - \mathbf{r}_1)$.

Equation (2.41) leads to an integral equation for the boundary source $\zeta(\mathbf{s}) \equiv -(\epsilon_1 - \epsilon_0)/\epsilon(\mathbf{s})\partial_n\phi(\mathbf{s})$, which is the charge per unit area. We have

$$\zeta(\mathbf{s}) = \zeta^{(0)}(\mathbf{s}) + \frac{\epsilon_1 - \epsilon_0}{\epsilon(\mathbf{s})} \int_{\mathcal{V}_{01}/\eta} d^2s' \left\{ (1 - \alpha(\mathbf{s})) \mathbf{n}_s \cdot \nabla_{s_1} G(\mathbf{s}_1, \mathbf{s}') \right. \quad (2.43a)$$

$$\left. + \alpha(\mathbf{s}) \mathbf{n}_s \cdot \nabla_{s_0} G(\mathbf{s}_0, \mathbf{s}') \right\} \zeta(\mathbf{s}') \quad \text{for } \mathbf{s} \in \mathcal{V}_{01}/\eta,$$

$$\zeta^{(0)}(\mathbf{s}) = -\frac{\epsilon_1 - \epsilon_0}{\epsilon(\mathbf{s})} \partial_n \phi^{(0)}(\mathbf{s}) = \frac{\epsilon_1 - \epsilon_0}{\epsilon(\mathbf{s})} \mathbf{n}_s \cdot \mathbf{E}^{(0)}. \quad (2.43b)$$

In a numerical calculation based on the boundary scattering formulation with the scalar potential, the essential work is to solve Eqs. (2.43a) and (2.43b). Once we obtain the source ζ , we can easily calculate the electric field using Eq. (2.41) together with $\mathbf{E} = -\nabla\phi$.

The usual perturbative method can be applied to Eqs. (2.43a) and (2.43b) and the solution satisfies the MBCs to a certain degree, according to the order of the approximation.

After all, our formulation to calculate the optical near field under the NFC is free from MBCs and one can treat the boundary effect using a perturbative or an iterative method.

2.4.5 An Application

As a numerical demonstration of the boundary scattering formulation with scalar potential, let us consider the system treated in Ref. [24]. The material is a dielectric ($\epsilon_1/\epsilon_0 = 2.25$) with the shape of the letter ‘‘F’’; the size of the longest side is 50 nm and it is placed in vacuum; see Fig. 2.9a. It is exposed to incident light with a wavelength of 633 nm and the observation point is assumed to be on the plane below the material by 5 nm. This system satisfies the NFC and our formulation with the scalar potential is applicable. Note that evidence for the quasi-static picture has already become apparent in Fig. 1c, d of Ref. [24]; we have \mathbf{k} independence, although it was not mentioned in that reference.

The procedure of the numerical calculation is as follows:

1. The surface of the dielectric material, \mathcal{V}_{01}/η , is considered as a set of surface elements which are the outside squares of the stacked cubes. The side of the small cube is set to 2.5 nm.
2. The source (the charge per unit area) in each surface element is assumed to be homogeneous and its value is estimated at the center of the surface element. The zeroth order source $\zeta^{(0)}(\mathbf{s})$ is given by Eq. (2.43b) at each surface element. The first order source $\zeta^{(1)}(\mathbf{s})$ at the center position of a selected surface element is calculated by Eq. (2.43a); we replace $\zeta(\mathbf{s}')$ in the integral to $\zeta^{(0)}(\mathbf{s}')$ and regard

the integral over $\mathcal{V}_{01/\eta}$ as the summation of each analytical integral over a single surface element. After scanning \mathbf{s} over all the center points of the surface elements, one obtains a set of $\zeta^{(1)}(\mathbf{s})$.

3. In the same way, the second and higher order source is obtained by solving Eq. (2.43a) iteratively. The convergence in every iteration is monitored by the standard deviation defined as

$$\text{s.d.} \equiv \left[\frac{\int_{\mathcal{V}_{01/\eta}} d^2s |\epsilon_0 \partial_n \phi^{(n)}(\mathbf{s}_0) - \epsilon_1 \partial_n \phi^{(n)}(\mathbf{s}_1)|^2}{|\epsilon_0 \mathbf{E}^{(0)}|^2 \int_{\mathcal{V}_{01/\eta}} d^2s} \right]^{1/2}. \quad (2.44)$$

This standard deviation approaches zero, if the MBC (2.39) is satisfied.

4. $\mathbf{E}(\mathbf{r})$ and $\Delta I(\mathbf{r})$ are calculated from the converged boundary source. The labor of coding program and the amount of calculations is much smaller than in the full-retarded formulation, because only the two-dimensional source appears in our non-retarded formulation, while a three-dimensional source is needed in a full-retarded one, e.g., the formulation developed in Sect. 2.5.

The standard deviation decreases monotonically as the order of the approximation increases and easily becomes of the order of 10^{-4} ; the convergence of the calculation is confirmed. The calculations with different α 's are converged to the same contour map of the intensity as Fig. 2.9c within the error of s.d. Comparing our result with Fig. 1a of Ref. [24], one will find good coincidence, although we ignore all the retardation effects.

Let us explain the contour map intuitively following the idea in Sect. 2.3.7. Take the zeroth order boundary source estimated by Eq. (2.43b) with $\alpha = 1/3$ (Fig. 2.9a), imagine the electric flux and $\Delta \mathbf{E}$ and consider the inner product between $\Delta \mathbf{E}$ and $\mathbf{E}^{(0)}$. Then, the (near-field) intensity profile in Fig. 2.9, including the change of the sign, is understood in the manner described in Fig. 2.7 of Sect. 2.3.7.

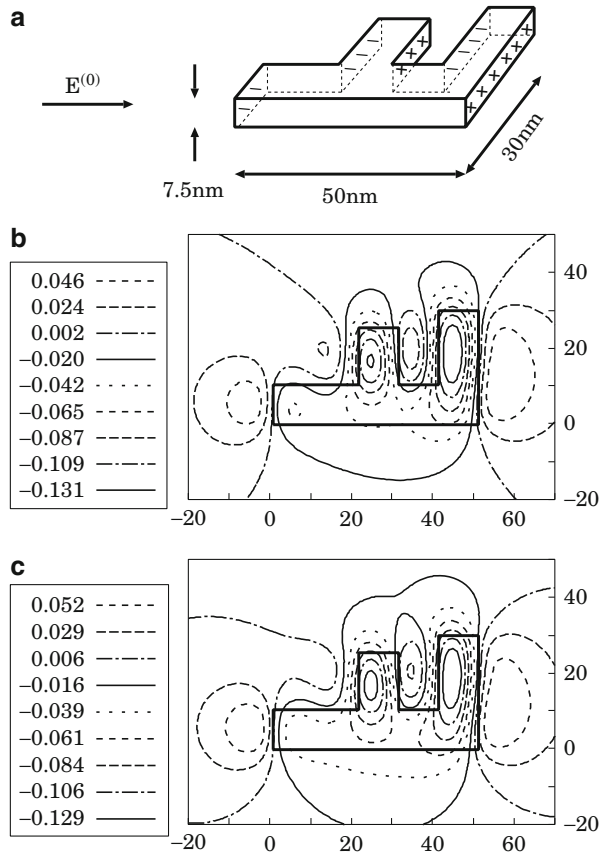
Among the intensity profile based on the zeroth order source with $\alpha = 0, 1/3, 1/2, \text{ and } 1$, that with $\alpha = 1/3$ (Fig. 2.9b) is most similar to the well-converged one, i.e., that with the seventh order source; see Fig. 2.9c. There is some advantage in using $\alpha = 1/3$ (This fact is compatible with the analytical calculation of dielectric sphere in Sect. 3.8 of the original book, Ref. [2]).

2.4.6 Summary

The essential points in this section are as follows:

- The scalar potential is the minimum degree of freedom in the EM field under the NFC.
- The boundary value problem in a system with a steep interface can be replaced to a boundary scattering problem.
- The boundary charge density in this formulation possesses arbitrariness originating from the source's profile in the interface region. This arbitrariness does not affect the electric field outside the interface region.

Fig. 2.9 The electric near field of a “F”-shaped dielectric under the NFC; the numerical calculations are performed based on our novel formulation; $E^{(0)}$ is the polarization vector of the incident field. (a) The shape of the material and the distribution of the zeroth order boundary source. (b) The contour map of the intensity produced by the zeroth boundary source with $\alpha = 1/3$; the intensity is observed on the plane below the material by 5 nm. (c) The contour map of the intensity produced by the seventh boundary source with $\alpha = 1/3$. The standard deviation is $\sim 1 \times 10^{-4}$



In short, the boundary scattering formulation with the scalar potential brings about a clear physical picture and a concise procedure to calculate the electric near field under NFC.

2.5 Boundary Scattering Formulation with Dual EM Potential

In order to discuss the optical near field with the retardation effect including the bulk effect, we would like to introduce a *boundary scattering formulation with dual EM potential*. The dual EM potential is the minimum degree of freedom of EM field under negligible magnetic response of the material [7]. In terms of the dual EM potential, one may describe a scattering problem with an adequate boundary source, by which the MBCs are reproduced. This formulation is analogous to that in the scalar potential version discussed in Sect. 2.4.3.

There is an additional merit to use the dual/ordinary EM potential for an EM problem with material. The wave equation for the ordinary/dual EM potential in

a stationary system is a vectorial Helmholtz equation; this wave equation for the EM field is analogous to that for the de Broglie field with spin = 1 in quantum mechanics. Therefore, in order to understand the behavior of a EM field, we can make use of well-established concepts in quantum mechanics, e.g., the tunneling effect, the bound state, the spin–orbit interaction, and so on. An example of this idea will appear in [Sect. 2.5.7](#). A further discussion based on this analogy is given in Ref. [5].

In this section, we treat the optical near field under the condition $ka \lesssim kr \lesssim 1$, which is looser than the NFC (2.7). Under this condition, the boundary and bulk effects are comparable and a balanced treatment of the two effects is needed. The boundary scattering formulation with the dual EM potential is appropriate not only to perform a numerical calculation but also to obtain an intuitive understanding of the optical near field.

2.5.1 Dual EM Potential as Minimum Degree of Freedom

In an ordinary EM problem with material, there is an induced electric charge density and current density, i.e., no external electric charge density, nor a current density. Maxwell’s equations for that case are

$$\begin{aligned}\nabla \cdot \mathbf{B}(\mathbf{r}, t) &= 0, \quad \nabla \times \mathbf{E}(\mathbf{r}, t) + \partial_t \mathbf{B}(\mathbf{r}, t) = \mathbf{0}, \\ \nabla \cdot \mathbf{D}(\mathbf{r}, t) &= 0, \quad \nabla \times \mathbf{H}(\mathbf{r}, t) - \partial_t \mathbf{D}(\mathbf{r}, t) = \mathbf{0},\end{aligned}\tag{2.45}$$

and the equations for the material are

$$\begin{aligned}\mathbf{B}(\mathbf{r}, t) &= \mu_0 \mathbf{H}(\mathbf{r}, t) + \mathbf{M}(\mathbf{r}, t), \\ \mathbf{D}(\mathbf{r}, t) &= \epsilon_0 \mathbf{E}(\mathbf{r}, t) + \mathbf{P}(\mathbf{r}, t),\end{aligned}\tag{2.46}$$

where the notation is as follows: \mathbf{E} is the electric field, \mathbf{B} is the magnetic flux density, \mathbf{H} is the magnetic field, \mathbf{D} is the electric flux density (or displacement vector field), \mathbf{P} is the polarization of the material, and \mathbf{M} is the magnetization of the material.

Now notice that there is a dual symmetry in Eqs.(2.45) and (2.46). Actually, Eqs.(2.45) and (2.46) are invariant under the dual transformation, i.e., the mutual exchange between the electric quantities and the magnetic ones as in [Table 2.5](#).

Table 2.5 Dual transformation in Maxwell’s equations and equations for material

Electric quantity	Magnetic quantity		Magnetic quantity	Electric quantity
\mathbf{D}	\mathbf{B}	\implies	\mathbf{B}	\mathbf{D}
\mathbf{E}	\mathbf{H}	\implies	$-\mathbf{H}$	$-\mathbf{E}$
\mathbf{P}	\mathbf{M}	\implies	\mathbf{M}	\mathbf{P}
ϵ_0	μ_0	\implies	$-\mu_0$	$-\epsilon_0$

On the other hand, it is well known that the minimum degree of freedom of the EM field is neither \mathbf{E} nor \mathbf{B} but the EM potential \mathbf{A} and ϕ . The ordinary EM potential is defined as $\mathbf{B} = \nabla \times \mathbf{A}$, $\mathbf{E} = -\partial_t \mathbf{A} - \nabla \phi$ and is especially convenient for electromagnetism with a material, which possesses a certain magnetic response and no electric response, i.e., $\mathbf{M} \neq \mathbf{0}$ and $\mathbf{P} = \mathbf{0}$. Although such a material is not realistic, we discuss the EM field generated by the source \mathbf{M} as a guide to introduce dual EM potential. Anyway, under the condition $\mathbf{M} \neq \mathbf{0}$ and $\mathbf{P} = \mathbf{0}$, the following wave equation for \mathbf{A} in the radiation gauge is derived from Eqs. (2.45) and (2.46):

$$\nabla \times \nabla \times \mathbf{A}(\mathbf{r}, t) + \epsilon_0 \mu_0 \partial_t^2 \mathbf{A}(\mathbf{r}, t) = \nabla \times \mathbf{M}(\mathbf{r}, t) , \quad (2.47a)$$

$$\nabla \cdot \mathbf{A}(\mathbf{r}, t) = 0 , \quad (2.47b)$$

$$\phi(\mathbf{r}, t) = 0 . \quad (2.47c)$$

In Eqs. (2.47a)–(2.47c), the source of the field \mathbf{A} is $\nabla \times \mathbf{M} = \mu_0 \times$ (magnetizing electric current density); this transversal vector source generates the transversal field, i.e., \mathbf{A} in the radiation gauge. Note carefully that the condition for the radiation gauge is satisfied in the whole space including the interface region.

The material of interest to us is just dual to that discussed in the above paragraph, because the material possesses a certain electric response and a negligible magnetic response, i.e., $\mathbf{P} \neq \mathbf{0}$ and $\mathbf{M} = \mathbf{0}$. Actually, this is a common case in the optical region. In connection with the duality, it is natural to introduce the *dual EM potential* defined as $\mathbf{D} = -\nabla \times \mathbf{C}$, $\mathbf{H} = -\partial_t \mathbf{C} - \nabla \chi$. Applying the dual transformation to Eqs. (2.47a)–(2.47c), i.e., $(\mathbf{A}, \phi, \mathbf{M}) \implies (-\mathbf{C}, -\chi, \mathbf{P})$, one obtains the wave equation followed by the dual EM potential,

$$\nabla \times \nabla \times \mathbf{C}(\mathbf{r}, t) + \epsilon_0 \mu_0 \partial_t^2 \mathbf{C}(\mathbf{r}, t) = -\nabla \times \mathbf{P}(\mathbf{r}, t) , \quad (2.48a)$$

$$\nabla \cdot \mathbf{C}(\mathbf{r}, t) = 0 , \quad (2.48b)$$

$$\chi(\mathbf{r}, t) = 0 . \quad (2.48c)$$

The minimum degree of freedom of the EM field in our problem is the dual EM potential in the radiation gauge and its source is $\nabla \times \mathbf{P} = -\epsilon_0 \times$ (polarizing magnetic current density). This source is dual to $\nabla \times \mathbf{M} = \mu_0 \times$ (magnetizing electric current density); see Eq. (2.47a). Equations (2.48a)–(2.48c) are equivalent to Maxwell's equations under $\mathbf{M} = \mathbf{0}$. In fact, one can know \mathbf{D} , \mathbf{E} , \mathbf{B} , and \mathbf{H} from \mathbf{C} using the following relations:

$$\mathbf{D}(\mathbf{r}, t) = -\nabla \times \mathbf{C}(\mathbf{r}, t) , \quad (2.49a)$$

$$\mathbf{E}(\mathbf{r}, t) = (-\nabla \times \mathbf{C}(\mathbf{r}, t) - \mathbf{P}(\mathbf{r}, t)) / \epsilon_0 , \quad (2.49b)$$

$$\mathbf{B}(\mathbf{r}, t) = \mu_0 \mathbf{H}(\mathbf{r}, t) = -\mu_0 \partial_t \mathbf{C}(\mathbf{r}, t) . \quad (2.49c)$$

2.5.2 Wave Equation for Dual Vector Potential

Suppose that the incident field oscillates with a constant angular frequency ω (or a constant wavenumber $k = \omega/c = \omega(\epsilon_0\mu_0)^{1/2}$) and that \mathbf{P} is defined through a local and linear dielectric function $\epsilon(\mathbf{r})$:

$$\mathbf{P}(\mathbf{r}, t) = (\epsilon(\mathbf{r}) - \epsilon_0)\mathbf{E}(\mathbf{r}, t) = -\left(1 - \frac{\epsilon_0}{\epsilon(\mathbf{r})}\right)\nabla \times \mathbf{C}(\mathbf{r}, t). \quad (2.50)$$

$\epsilon(\mathbf{r})$ is for a moment assumed to be a smooth function.

Omitting the common time dependence in $\mathbf{C}(\mathbf{r}, t) = \mathbf{C}(\mathbf{r})\exp(-i\omega t)$ and carrying out some calculation, Eqs. (2.48a) and (2.48b) together with Eq. (2.50) lead to the following vector Helmholtz' equation and the condition for the radiation gauge:

$$\nabla \times \nabla \times \mathbf{C}(\mathbf{r}) - k^2\mathbf{C}(\mathbf{r}) = -\hat{V}_s[\mathbf{C}](\mathbf{r}) - \hat{V}_v[\mathbf{C}](\mathbf{r}) \text{ for } \mathbf{r} \in \mathcal{V}_0 \cup \mathcal{V}_{01} \cup \mathcal{V}_1, \quad (2.51a)$$

$$\nabla \cdot \mathbf{C}(\mathbf{r}) = 0, \quad (2.51b)$$

$$\hat{V}_s[\mathbf{C}](\mathbf{r}) \equiv -\frac{\nabla \epsilon(\mathbf{r})}{\epsilon(\mathbf{r})} \times \nabla \times \mathbf{C}(\mathbf{r}), \quad (2.51c)$$

$$\hat{V}_v[\mathbf{C}](\mathbf{r}) \equiv -\left(\frac{\epsilon(\mathbf{r})}{\epsilon_0} - 1\right)k^2\mathbf{C}(\mathbf{r}). \quad (2.51d)$$

Equations (2.51a)–(2.51d) are the starting point of our novel formulation. The source is divided into two parts. One is (boundary magnetic current density) $\times(-\epsilon_0)$, i.e., $-\hat{V}_s[\mathbf{C}]$, which is responsible for the MBCs; see Sect. 2.5.3. The other is (bulk magnetic current density) $\times(-\epsilon_0)$, namely $-\hat{V}_v[\mathbf{C}]$. It produces the bulk effect, which is assigned to a retardation effect due to its k dependence. Note that there is one more contribution to the retardation effect from the second term in the l.h.s. of Eq. (2.51a). In the following, we simply refer to $-\hat{V}_s[\mathbf{C}]$ ($-\hat{V}_v[\mathbf{C}]$) as “boundary (bulk) magnetic current density,” ignoring the constant factor ϵ_0 .

Equations (2.51a)–(2.51d) are equivalent to Maxwell's equations under $\mathbf{M} = 0$ and are applicable both to the optical near and far fields. In particular, for an optical near-field problem under $ka \lesssim kr \lesssim 1$, we can consider both the boundary and bulk effects on an equal footing.

Physicists know from experience that a description in terms of the minimum degree of freedom often brings about a clear physical picture and/or convenience for calculation. In Sect. 2.4, we have already shown that the scalar potential is the minimum degree of freedom of the EM field under the NFC and that the description in terms of the scalar potential leads to a clear physical picture and a concise procedure of numerical calculation. However, in all the EM problem with material, the field \mathbf{E} , \mathbf{B} and the bulk source \mathbf{P} , \mathbf{M} have been extensively used and the minimum degrees of freedom, namely the ordinary/dual EM potential, have been

rarely used even in a simple problem like the reflection and/or the transmission phenomena at a plane interface. The present author guesses that this irrationality comes from a singularity that appears in the wave equation for EM potential; that singularity originates from the MBCs. Actually, if we introduce a steep interface through Eq. (2.36), $\hat{V}_s[\mathbf{C}]$ of Eq. (2.51c) becomes a product of distributions and a mathematical difficulty arises; we have already met with such a singularity, namely the boundary charge density in Sect. 2.4. In order to use Eqs. (2.51a)–(2.51d) instead of Maxwell's equations, we should control this singularity and this will be shown in the next subsection.

2.5.3 Boundary Scattering Problem Equivalent to the Boundary Value Problem

To overcome the difficulty to solve Eqs. (2.51a)–(2.51d) with Eq. (2.36), i.e., in a system with a steep interface, there is another way: the *boundary scattering formulation* with the dual EM potential. The difficulty in the original problem is that the boundary magnetic current density in Eq. (2.51c) is the product of distributions, which is not well-defined in a general mathematical sense. However, in the following, it is proved that a certain expression of boundary magnetic current density reproduces the MBCs properly and is a well-defined quantity.

With such a proper expressions for the boundary magnetic current density, Eqs. (2.51a)–(2.51d) become the following equations which are the elementary equations for the boundary scattering formulation with the dual EM potential:

$$\nabla \times \nabla \times \mathbf{C}(\mathbf{r}) - k^2 \mathbf{C}(\mathbf{r}) = -\hat{V}_s[\mathbf{C}](\mathbf{r}) - \hat{V}_v[\mathbf{C}](\mathbf{r}) \text{ for } \mathbf{r} \in \mathcal{V}_0 \cup \mathcal{V}_{01} \cup \mathcal{V}_1, \quad (2.52a)$$

$$\nabla \cdot \mathbf{C}(\mathbf{r}) = 0, \quad (2.52b)$$

$$\hat{V}_s[\mathbf{C}](\mathbf{r}) = \int_{\mathcal{V}_{01}/\eta} d^2s \delta^3(\mathbf{r} - \mathbf{s}) \frac{\epsilon_1 - \epsilon_0}{\epsilon(\mathbf{s})} \mathbf{n}_s \times \nabla \times \mathbf{C}(\mathbf{s}), \quad (2.52c)$$

$$\epsilon(\mathbf{s}) \equiv \alpha(\mathbf{s})\epsilon_1 + (1 - \alpha(\mathbf{s}))\epsilon_0 \quad \text{for } \mathbf{s} \in \mathcal{V}_{01}/\eta, \quad (2.52d)$$

$$\nabla \times \mathbf{C}(\mathbf{s}) \equiv \alpha(\mathbf{s})\nabla \times \mathbf{C}(\mathbf{s}_1) + (1 - \alpha(\mathbf{s}))\nabla \times \mathbf{C}(\mathbf{s}_0), \quad (2.52e)$$

$$\hat{V}_v[\mathbf{C}](\mathbf{r}) = -\theta(\mathbf{r} \in \mathcal{V}_1) \left(\frac{\epsilon_1}{\epsilon_0} - 1 \right) k^2 \mathbf{C}(\mathbf{r}), \quad (2.52f)$$

where $\mathbf{s}_0 = \mathbf{s} + 0\mathbf{n}_s$, $\mathbf{s}_1 = \mathbf{s} - 0\mathbf{n}_s$ (Fig. 2.8). Equations (2.52d) and (2.52e) are merely the definitions of $\epsilon(\mathbf{s})$ and $\nabla \times \mathbf{C}(\mathbf{s})$, respectively; $\alpha(\mathbf{s})$ is an arbitrary smooth and complex-valued function on \mathcal{V}_{01}/η .

Here we show that Eqs. (2.52a)–(2.52f) of the boundary scattering problem leads to the following MBCs:

$$\frac{1}{\epsilon_0} \mathbf{n}_s \times \nabla \times \mathbf{C}(s_0) = \frac{1}{\epsilon_1} \mathbf{n}_s \times \nabla \times \mathbf{C}(s_1) \quad \text{for } s \in \mathcal{V}_{01}/\eta, \quad (2.53a)$$

$$\mathbf{n}_s \cdot \mathbf{C}(s_0) = \mathbf{n}_s \cdot \mathbf{C}(s_1). \quad (2.53b)$$

Equations (2.53a) and (2.53b) have the meaning of the continuity of the surface-parallel component of the electric field and the continuity of the surface-normal component of the magnetic flux field, respectively. The derivation of Eq. (2.53a) is as follows: Take the inner product of Eq. (2.52a) with \mathbf{m}_i ($i = 1$ or 2), integrate over the infinitesimal volume $\sigma \otimes \eta$ ($\eta = +0$) in Fig. 2.8, apply Stokes' theorem to the l.h.s. over the infinitesimal area $l_i \otimes \eta$ and carry out the volume integral of the delta function in the r.h.s.; then one obtains

$$\mathbf{m}_i \cdot \mathbf{n}_s \times \nabla \times \mathbf{C}(s_0) - \mathbf{m}_i \cdot \mathbf{n}_s \times \nabla \times \mathbf{C}(s_1) = -\frac{\epsilon_1 - \epsilon_0}{\epsilon(s)} \mathbf{m}_i \cdot \mathbf{n}_s \times \nabla \times \mathbf{C}(s). \quad (2.54)$$

Equation (2.54) holds for $i = 1$ and 2 , and therefore, Eq. (2.54) without “ $\mathbf{m}_i \cdot$ ” is true. Substitute Eqs. (2.52d) and (2.52e) into Eq. (2.54) without “ $\mathbf{m}_i \cdot$ ”; then, one can obtain Eq. (2.53a). The arbitrary function $\alpha(s)$ disappears automatically and does not affect the field in $\mathcal{V}_0 \cup \mathcal{V}_1$. On the other hand, Eq. (2.53b) is obtained if one integrates the gauge condition (2.52b) over the small volume $\sigma \otimes \eta$, applies Gauss' theorem and takes the limit $\eta \rightarrow +0$. Note carefully that an explicit formula for $\epsilon(\mathbf{r})$ in the interface region is not needed in the above derivation of Eqs. (2.53a) and (2.53b). That is, the MBCs (2.53a) and (2.53b) are independent of the profile of dielectric function in the interface region.

You may know two more MBCs:

$$\mathbf{n}_s \cdot \nabla \times \mathbf{C}(s_0) = \mathbf{n}_s \cdot \nabla \times \mathbf{C}(s_1), \quad (2.55a)$$

$$\mathbf{n}_s \times \mathbf{C}(s_0) = \mathbf{n}_s \times \mathbf{C}(s_1). \quad (2.55b)$$

Equation (2.55a) describes the continuity of the surface-normal component of the electric flux field. Equation (2.55b) does the same for the continuity of the surface-parallel component of the magnetic field. Substituting Eqs. (2.49a)–(2.49c) into Eqs. (2.55a), (2.55b), (2.53a), and (2.53b), one obtains the familiar expressions for the MBCs in terms of \mathbf{D} , \mathbf{H} , \mathbf{E} and \mathbf{B} .

Equations (2.55a) and (2.55b) are trivial, because they are derived from an identity and an implicit assumption. The derivation is as follows: Let us keep η finite at first and afterward take the limit $\eta \rightarrow +0$. Equation (2.55a) is obtained by integrating the identity $\nabla \cdot \nabla \times \mathbf{C}(\mathbf{r}) = 0$ over the small volume $\sigma \otimes \eta$ in Fig. 2.8, applying Gauss' theorem and taking the limit $\eta \rightarrow +0$. Further, Eq. (2.55b) comes from the implicit assumption that the singularity of $\mathbf{P}(\mathbf{r})$ is, at most, that of the step function. Under this assumption, the singularity of $\nabla \times \mathbf{C}$ ($= -\mathbf{D}$) is that of the step function because of Eq. (2.50) with Eq. (2.36). Integrate $\nabla \times \mathbf{C}(\mathbf{r}) \sim$ (step function) over $\eta \otimes l_i$ ($i = 1, 2$), apply Stokes' theorem and take the limit $\eta \rightarrow +0$; then one

obtains Eq. (2.55b). Therefore, we do not need the MBCs (2.55a) and (2.55b) in the calculation in terms of the dual EM potential.

Now, it is confirmed that the MBCs are reproduced from Eqs. (2.52a) to (2.52f). In principle, the solution of boundary value problem with MBCs and that of Eqs. (2.52a)–(2.52f) of the boundary scattering problem are equivalent in the domain $\mathcal{V}_0 \cup \mathcal{V}_1$. This is so because the two solutions in the regions $\mathcal{V}_0 \cup \mathcal{V}_1$ satisfy the same boundary conditions. However, Eqs. (2.52a)–(2.52f) possess considerable merits compared with the boundary value formulation. The first merit is that boundary and bulk effects can be treated on an equal footing, while the two effects are treated in an unbalanced manner in the boundary value formulation. The second is that the arbitrariness of the expression for the boundary source can be used to improve the convergence in a numerical calculation.

The arbitrariness in Eqs. (2.52a)–(2.52f) comes from the degrees of freedom of the magnetic current density profile inside the interface region \mathcal{V}_{01} ; not the detailed profile but the integrated magnetic current density over the width η ($= +0$) determines the field in $\mathcal{V}_0 \cup \mathcal{V}_1$. This integrated quantity is analogous to the boundary charge density in the boundary scattering formulation with the scalar potential in Sect. 2.4.3. Another analogy is the multipole moment as is mentioned in Sect. 2.4.3. Therefore, it is reasonable that the arbitrariness of the boundary source appears (For mathematical details, see Sect. 8.2 in the original book, Ref. [2]).

As a result, the MBCs can be built in the definition of the boundary magnetic current density; the original problem (Eqs. (2.51a)–(2.51d) with Eq. (2.36)) is replaced by the boundary scattering problem (Eqs. (2.52a)–(2.52f)).

In the next section, we will treat both the boundary and bulk effects in a perturbative or an iterative method.

2.5.4 Integral Equation for Source and Perturbative Treatment of MBCs

Equations (2.52a)–(2.52f) are converted to the following integral equation:

$$\begin{aligned} \mathbf{C}(\mathbf{r}) = & \mathbf{C}^{(0)}(\mathbf{r}) \\ & + \int_{\mathcal{V}_{01/\eta}} d^2 s' \mathcal{G}^{(t)}(\mathbf{r}, \mathbf{s}') \cdot \frac{\epsilon_1 - \epsilon_0}{\epsilon(\mathbf{s}')} \mathbf{n}_s \times \nabla \times \mathbf{C}(\mathbf{s}') \\ & + \int_{\mathcal{V}_1} d^3 r' \mathcal{G}^{(t)}(\mathbf{r}, \mathbf{r}') \cdot \left(-\frac{\epsilon_1 - \epsilon_0}{\epsilon_0} k^2 \right) \mathbf{C}(\mathbf{r}') , \end{aligned} \quad (2.56)$$

where $\mathbf{C}^{(0)}(\mathbf{r})$ is the incident field and $\mathcal{G}_{ij}^{(t)}(\mathbf{r}, \mathbf{r}')$ is the transversal Green's function (tensor) for the vectorial Helmholtz equation; the explicit expression for this Green function is given in Sect. 2.7.2.

Equation (2.56) leads to coupled integral equations for the bulk source and the boundary source, i.e., $\mathbf{V}(\mathbf{r} \in \mathcal{V}_1) \equiv \mathbf{C}(\mathbf{r})$ and $\mathbf{S}(\mathbf{s} \in \mathcal{V}_{01/\eta}) \equiv \mathbf{n}_s \times \nabla \times \mathbf{C}(\mathbf{s})$;

V and S determine the bulk magnetic current density (Eq. (2.52f)), and the boundary magnetic current density (Eq. (2.52c)), respectively:

$$V(\mathbf{r}) = V^{(0)}(\mathbf{r}) \quad (2.57a)$$

$$\begin{aligned} & + \int_{\mathcal{V}_{01/\eta}} d^2 s' \mathcal{G}^{(t)}(\mathbf{r}, \mathbf{s}') \cdot \frac{\epsilon_1 - \epsilon_0}{\epsilon(\mathbf{s}')} \mathbf{S}(\mathbf{s}') \\ & + \int_{\mathcal{V}_1} d^3 r' \mathcal{G}^{(t)}(\mathbf{r}, \mathbf{r}') \cdot \left(-\frac{\epsilon_1 - \epsilon_0}{\epsilon_0} k^2 \right) V(\mathbf{r}') \quad \text{for } \mathbf{r} \in \mathcal{V}_1, \end{aligned}$$

$$V^{(0)}(\mathbf{r}) \equiv \mathbf{C}^{(0)}(\mathbf{r}), \quad (2.57b)$$

$$\mathbf{S}(\mathbf{s}) = \mathbf{S}^{(0)}(\mathbf{s}) \quad (2.57c)$$

$$\begin{aligned} & + \int_{\mathcal{V}_{01/\eta}} d^2 s' \{ \alpha(\mathbf{s}) \mathbf{n}_s \times \nabla_{s_1} \times \mathcal{G}^{(t)}(\mathbf{s}_1, \mathbf{s}') \\ & + (1 - \alpha(\mathbf{s})) \mathbf{n}_s \times \nabla_{s_0} \times \mathcal{G}^{(t)}(\mathbf{s}_0, \mathbf{s}') \} \cdot \frac{\epsilon_1 - \epsilon_0}{\epsilon(\mathbf{s}')} \mathbf{S}(\mathbf{s}') \\ & + \int_{\mathcal{V}_1} d^3 r' \{ \alpha(\mathbf{s}) \mathbf{n}_s \times \nabla_{s_1} \times \mathcal{G}^{(t)}(\mathbf{s}_1, \mathbf{r}') \\ & + (1 - \alpha(\mathbf{s})) \mathbf{n}_s \times \nabla_{s_0} \times \mathcal{G}^{(t)}(\mathbf{s}_0, \mathbf{r}') \} \cdot \left(-\frac{\epsilon_1 - \epsilon_0}{\epsilon_0} k^2 \right) V(\mathbf{r}') \\ & \quad \text{for } \mathbf{s} \in \mathcal{V}_{01/\eta}, \end{aligned}$$

$$\mathbf{S}^{(0)}(\mathbf{s}) \equiv -\mathbf{n}_s \times \mathbf{D}^{(0)}(\mathbf{s}), \quad (2.57d)$$

where $\epsilon(\mathbf{s}')$, and $\mathbf{S}(\mathbf{s}')$ appearing in above equations are estimated by Eqs. (2.52d) and (2.52e). In a numerical calculation based on the boundary scattering formulation with the dual EM potential, the essential work is to solve Eqs. (2.57a)–(2.57d). Once we obtain the sources V and S , we can easily calculate the EM field using Eq. (2.56) together with Eqs. (2.49a)–(2.49c).

The usual perturbative method can be applied to Eqs. (2.57a)–(2.57d) and the solution satisfies the MBCs to a certain degree according to the order of the approximation.

Note that the rigorous solution $\mathbf{C}(\mathbf{r})$ must satisfy the following condition, which is derived by taking the divergence of Eq. (2.52a):

$$\nabla \cdot \left(\hat{V}_s[\mathbf{C}](\mathbf{r}) + \hat{V}_v[\mathbf{C}](\mathbf{r}) \right) = 0. \quad (2.58)$$

Equation (2.58) implies transversality of the total magnetic current density. Equation (2.58) leads to the absence of the monopole moment of the magnetic current density, i.e.,

$$\begin{aligned}
& \int d^3r \left(\hat{V}_s[\mathbf{C}](\mathbf{r}) + \hat{V}_v[\mathbf{C}](\mathbf{r}) \right) \\
&= - \int d^3r \mathbf{r} \cdot \nabla \cdot \left(\hat{V}_s[\mathbf{C}](\mathbf{r}) + \hat{V}_v[\mathbf{C}](\mathbf{r}) \right) = \mathbf{0}. \quad (2.59)
\end{aligned}$$

The second h.s. is effective under the condition that the current is localized in a finite volume. We remark that the absence of a single magnetic pole – as we know from experience – is a sufficient condition for Eqs. (2.58) and (2.59). (Equation (2.58) together with the conservation law of a single magnetic pole only leads to *no motion* of the single magnetic pole.) Under a finite order approximation, Eq. (2.58) is not satisfied; in particular, in the interface region \mathcal{V}_{01} . Therefore, under the finite order approximation, the longitudinal component of the source possibly generates a longitudinal field so that the gauge condition Eq. (2.52b) and the MBC (2.53b) break down. However, in the procedure based on Eqs. (2.57a)–(2.57d), the gauge condition Eq. (2.52b) and the MBC (2.53b) are satisfied under every order of approximation owing to $\mathcal{G}^{(l)}$ in Eqs. (2.57a) and (2.57d); the error of the longitudinal component of the source is filtered out by means of the contraction between the transversal vector Green function $\mathcal{G}^{(l)}$ and the source. Therefore, in a practical numerical calculation, the condition of Eq. (2.58) under every order of approximation is not important. Equation (2.58) is satisfied automatically, as long as the calculation is convergent enough.

After all, the boundary scattering formulation with the dual EM potential is free from MBCs and applicable both to the near-field and the far-field problem. Further, one can treat both the boundary and bulk effects using a perturbative or an iterative method.

2.5.5 Boundary Effect and Retardation Effect

On the basis of the boundary scattering formulation with the dual EM potential, we can discuss boundary and bulk effects on an equal footing. Based on this balanced treatment, let us estimate the magnitude of the EM field generated by \hat{V}_s and \hat{V}_v in Eqs. (2.52a)–(2.52f) under the following two conditions: the NFC and Rayleigh’s far-field condition (cases 2 and 3 of Table 2.1 in Sect. 2.2.3).

The electric field in the vacuum region \mathcal{V}_0 is equivalent to the electric flux (displacement vector) field and estimated by means of Eq. (2.56) using the zeroth order source:

$$\begin{aligned}
\mathbf{D}(\mathbf{r}) &= -\nabla \times \mathbf{C}(\mathbf{r}) \\
&\simeq \mathbf{D}^{(0)}(\mathbf{r}) \\
&+ \int_{\mathcal{V}_{01/\eta}} d^2s' \nabla \times \mathcal{G}^{(l)}(\mathbf{r}, \mathbf{s}') \cdot \frac{\epsilon_1 - \epsilon_0}{\epsilon(\mathbf{s}')} \mathbf{n}_{s'} \times \mathbf{D}^{(0)}(\mathbf{s}')
\end{aligned}$$

$$- \int_{\mathcal{V}_1} d^3 r' \nabla \times \mathcal{G}^{(t)}(\mathbf{r}, \mathbf{r}') \cdot \left(-\frac{\epsilon_1 - \epsilon_0}{\epsilon_0} k^2 \right) \mathbf{C}^{(0)}(\mathbf{r}') . \quad (2.60)$$

In the last expression in Eq. (2.60), the first term is the incident field, and assumed to be $|\mathbf{D}^{(0)}| \sim \mathcal{O}(1)$, or equivalently $\mathbf{C}^{(0)} = \mathcal{O}(1/k)$; the second term and the third term are the fields generated by the boundary magnetic current density and the bulk magnetic current density, namely the boundary and bulk effects, respectively.

In the last expression in Eq. (2.60), the factor of the surface integral (without integrand) carries $\mathcal{O}(a^2)$ and that of the volume one carries $\mathcal{O}(a^3)$. We adopt $\epsilon(s') = \epsilon_0$ in the second term for a rough estimation. The estimation for the above factors are common both under the NFC and Rayleigh's far-field condition. The difference between the two cases comes from the factor of the Green function:

$$\begin{aligned} |\nabla \times \mathcal{G}^{(t)}(\mathbf{r} - \mathbf{r}'; k)| &= |\nabla \times \mathcal{G}(\mathbf{r} - \mathbf{r}'; k)| = |\nabla G(\mathbf{r} - \mathbf{r}'; k)| \\ &\simeq \left| \frac{1}{4\pi} \frac{\exp(ik|\mathbf{r} - \mathbf{r}'|)}{|\mathbf{r} - \mathbf{r}'|^2} (1 - ik|\mathbf{r} - \mathbf{r}'|) \right|. \end{aligned} \quad (2.61)$$

For details of Green's function in vector analysis, please see Sect. 2.7.

Under the NFC $ka \lesssim kr \ll 1$, the first term in the last expression in Eq. (2.61) is dominant and estimated as

$$|\nabla \times \mathcal{G}^{(t)}(\mathbf{r} - \mathbf{r}'; k)| \sim \mathcal{O}\left(\frac{1}{r^2}\right) + \mathcal{O}\left(\frac{a}{r^3}\right), \quad (2.62)$$

where we use a rough estimation of $|\mathbf{r} - \mathbf{r}'|$ under $r > r'$,

$$|\mathbf{r} - \mathbf{r}'| \simeq r - \hat{\mathbf{r}} \cdot \mathbf{r}' \sim \mathcal{O}(r) + \mathcal{O}(a).$$

The term carrying $\mathcal{O}(1/r^2)$ in Eq. (2.62) couples with the monopole moment of the magnetic current density; the monopole moment should vanish because of Eq. (2.58). Therefore this term does not contribute to the field. After all, under the NFC, the contribution to the electric field from the boundary effect and that from the bulk effect are estimated as

$$\text{the second term in Eq. (2.60)} \sim \mathcal{O}\left(\frac{a^3}{r^3} \frac{\epsilon_1 - \epsilon_0}{\epsilon_0}\right),$$

$$\text{the third term in Eq. (2.60)} \sim \mathcal{O}\left(ka \frac{a^3}{r^3} \frac{\epsilon_1 - \epsilon_0}{\epsilon_0}\right).$$

On the other hand, under Rayleigh's far-field condition, $ka \ll 1 \ll kr$, the second term in the last expression in Eq. (2.61) is dominant and estimated as

$$|\nabla \times \mathcal{G}^{(t)}(\mathbf{r} - \mathbf{r}'; k)| \sim \mathcal{O}\left(\frac{k}{r}\right) + \mathcal{O}\left(\frac{k}{r} ka\right). \quad (2.63)$$

Table 2.6 The order estimation of scattered-field amplitude under the near-field condition and Rayleigh's far-field condition. This table is equivalent to Table 2.2

	Incident term		Boundary term		Bulk term
Near-field condition	1	\gg	$\left(\frac{a}{r}\right)^3 \frac{\epsilon_1 - \epsilon_0}{\epsilon_0}$	\gg	$ka \left(\frac{a}{r}\right)^3 \frac{\epsilon_1 - \epsilon_0}{\epsilon_0}$
Rayleigh's far-field condition	1	\gg	$(ka)^2 \frac{a}{r} \frac{\epsilon_1 - \epsilon_0}{\epsilon_0}$	\gg	$(ka)^3 \frac{a}{r} \frac{\epsilon_1 - \epsilon_0}{\epsilon_0}$

Ignoring the first term due to the absence of the monopole moment in the magnetic current density (see Eqs. (2.58) and (2.59)), one obtains

$$\text{the second term in Eq. (2.60)} \sim \mathcal{O}\left((ka)^2 \frac{a}{r} \frac{\epsilon_1 - \epsilon_0}{\epsilon_0}\right),$$

$$\text{the third term in Eq. (2.60)} \sim \mathcal{O}\left((ka)^3 \frac{a}{r} \frac{\epsilon_1 - \epsilon_0}{\epsilon_0}\right).$$

The above results are summarized in Table 2.6, which are equivalent to Table 2.2. Under the NFC, the main contribution of the scattered field comes from the boundary effect and is independent of the wavenumber, i.e., the quasi-static picture holds as is discussed in Sect. 2.3. In fact, the electric field generated by the boundary effect carries $(a/r)^3$ that reveals the magnitude of the electric field generated by the electric dipole moment; the relation of the electric dipole moment and the boundary magnetic current density will be explained in the next subsection. Under Rayleigh's far-field condition, the boundary term carries the leading order and is dependent on "k," that is, there exists a retardation effect. The far-field intensity is the square of the scattered field and is $\mathcal{O}(k^4 a^6 / r^2)$. This corresponds to the well-known expression for far-field intensity in the Rayleigh scattering and the same result has been derived in Sect. 2.3.3.

Comparing the above two cases, one is convinced that the observation of Rayleigh's far field is k dependent and bounded by the diffraction limit, while that of the near field under the NFC is free from the diffraction limit; this fact is consistent with Table 2.1 in Sect. 2.2.3.

2.5.6 Intuitive Picture Based on Dual Ampere Law under Near-Field Condition

Under the NFC, the boundary effect is much larger than the bulk effect and a quasi-static picture holds, as discussed in Sects. 2.3 and 2.4. In such a system, Coulomb's law governs the electric field. Now we show that the quasi-static picture is described by the dual Ampère law based on the boundary scattering formulation with the dual EM potential.

Ignoring all of the retardation effect (wavenumber dependence) in Eq. (2.60), defining the scattered field by $\Delta \mathbf{D} \equiv \mathbf{D}(\mathbf{r}) - \mathbf{D}^{(0)}(\mathbf{r})$ and using $\nabla \cdot \mathbf{D}^{(0)}(\mathbf{r}) = 0$,

one obtains the “dual Ampère law” [6–8], that is,

$$\nabla \times \Delta \mathbf{D}(\mathbf{r}) = \hat{V}_s[\mathbf{C}^{(0)}](\mathbf{r}) = -\frac{\epsilon_1 - \epsilon_0}{\epsilon(\mathbf{r})} \delta(\mathbf{r} \in \text{boundary}) \mathbf{n}_s \times \mathbf{D}^{(0)}, \quad (2.64)$$

where $\delta(\mathbf{r} \in \text{boundary})$ stands for the one-dimensional delta function in the direction of \mathbf{n}_s and the value of $\epsilon(\mathbf{r})$ in the denominator is not well-defined but a value between ϵ_0 and ϵ_1 is physically acceptable in a naive sense. It is enough to set $\epsilon(\mathbf{r}) = \epsilon_0$ for a rough treatment here. Under the NFC, the incident field $\mathbf{D}^{(0)}$ is regarded constant over the whole system and the boundary source $\sim \mathbf{n}_s \times \mathbf{D}^{(0)}$ can be placed on each point of the boundary; see Fig. 2.10c.

Note carefully that the ordinary Ampère law is $\nabla \times \mathbf{B}(\mathbf{r}) = \mu_0 \times (\text{electric current density})$ and your right hand is useful to understand the relation between the field and the source; see Fig. 2.10a. Dual to the ordinary Ampère law, Eq. (2.64) reveals that $-\epsilon_0 \times$ (the boundary magnetic current density) in r.h.s. generates the scattered field $\Delta \mathbf{D}$ and your left hand is useful because of the negative sign in the r.h.s.; see Fig. 2.10b. Then we can easily understand the electric flux of the scattered field generated by the boundary magnetic current density.

Comparing Fig. 2.10c with Fig. 2.7b, it is found that the electric flux derived from the dual Ampère law is similar to that from the Coulomb law. The reason for this similarity is that the looped magnetic current is equivalent to a certain electric

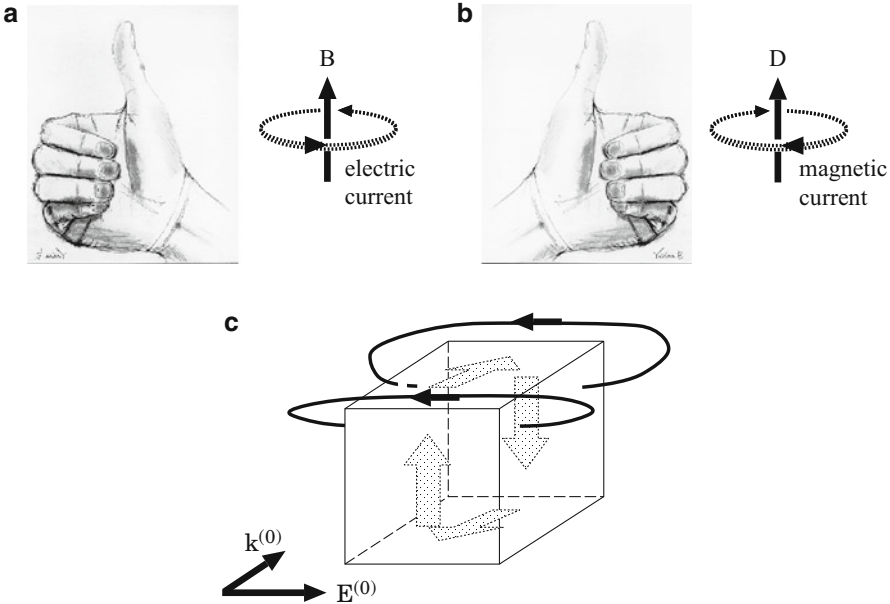


Fig. 2.10 The relation between the source and the field (a) in the ordinary Ampere law and (b) in the dual Ampere law. (c) The electric flux generated by the boundary magnetic current density under the NFC

dipole moment (Fig. 2.7b). This equivalence is dual to the well-known equivalence between a looped electric current and a magnetic dipole moment. Therefore, it is reasonable that the leading order of the scattered electric field under the NFC is estimated as $\mathcal{O}(a^3/r^3)$ in Sects. 2.3.3 and 2.5.5.

2.5.7 Correction Due to Retardation Effect

The difference between the numerical result under $ka \lesssim kr \lesssim 1$, and that under the NFC ($ka \lesssim kr \ll 1$), is attributed to the retardation effect. In order to learn how the retardation effect works, we examine the optical near field of a dielectric cube with $\epsilon_1/\epsilon_0 = 2.25$ in the three cases $ka = 0.01, 0.10$, and 1.00 , where “ a ” stands for the side length of the cube. The cubes are considered as a stack of small cubes, of which the side is set to $1/20$ of that of the whole cube. The numerical calculation is based on the boundary scattering formulation with the dual EM potential.

The procedure of the numerical calculation is as follows.

1. The body of the dielectric material \mathcal{V}_1 is considered as a set of volume elements which are small cubes, and the boundary of the sphere \mathcal{V}_{01}/η is considered as a set of surface elements which are the outside squares of the stacked cubes. The side of the small cube is set to $1/20$ of a side of the whole cube.
2. The bulk (boundary) source in each volume (surface) element is assumed to be homogeneous and its value is estimated at the center of the volume (surface) element. The zeroth order bulk (boundary) source is given by Eq.(2.57b) (Eq. (2.57d)).
3. The coupled equations (2.57a)–(2.57d) are solved iteratively. The convergence in every iteration is monitored by the standard deviation defined as

$$\text{s.d.} \equiv \left[\frac{\int_{\mathcal{V}_{01}/\eta} d^2s |\mathbf{n}_s \times \mathbf{D}^{(n)}(s_1)/\epsilon_1 - \mathbf{n}_s \times \mathbf{D}^{(n)}(s_0)/\epsilon_0|^2}{|\mathbf{D}^{(0)}/\epsilon_0|^2 \int_{\mathcal{V}_{01}/\eta} d^2s} \right]^{1/2}. \quad (2.65)$$

This standard deviation approaches zero, if the MBC (2.53a) is satisfied. We do not mind the other MBCs; the MBC (2.53b) is automatically satisfied because of $\mathcal{G}^{(l)}$ in Eqs. (2.57a)–(2.57d), and the MBCs (2.55a) and (2.55b) are trivial, as discussed in Sect. 2.5.3.

4. $\mathbf{E}(\mathbf{r})$ and $\Delta I(\mathbf{r})$ are calculated from the converged boundary and bulk sources. The results are shown in Fig. 2.11.

Let us reduce the difference of “ ka ” down to the difference of “ k ,” keeping “ a ” constant. In this point of view, Figs. 2.11a, b are regarded as the same profile, independent of “ k .” This k independence is understood as a characteristic of the quasi-static picture because the NFC is satisfied in the systems of Fig. 2.11a, b. In other words, the wavelength is so large that these systems cannot feel “ k ”; see Fig. 2.3.

Equivalently we can reduce the difference of “ ka ” down to that of “ a ,” keeping “ k ” constant. In this point of view, the commonness in Fig. 2.11a, b is considered as

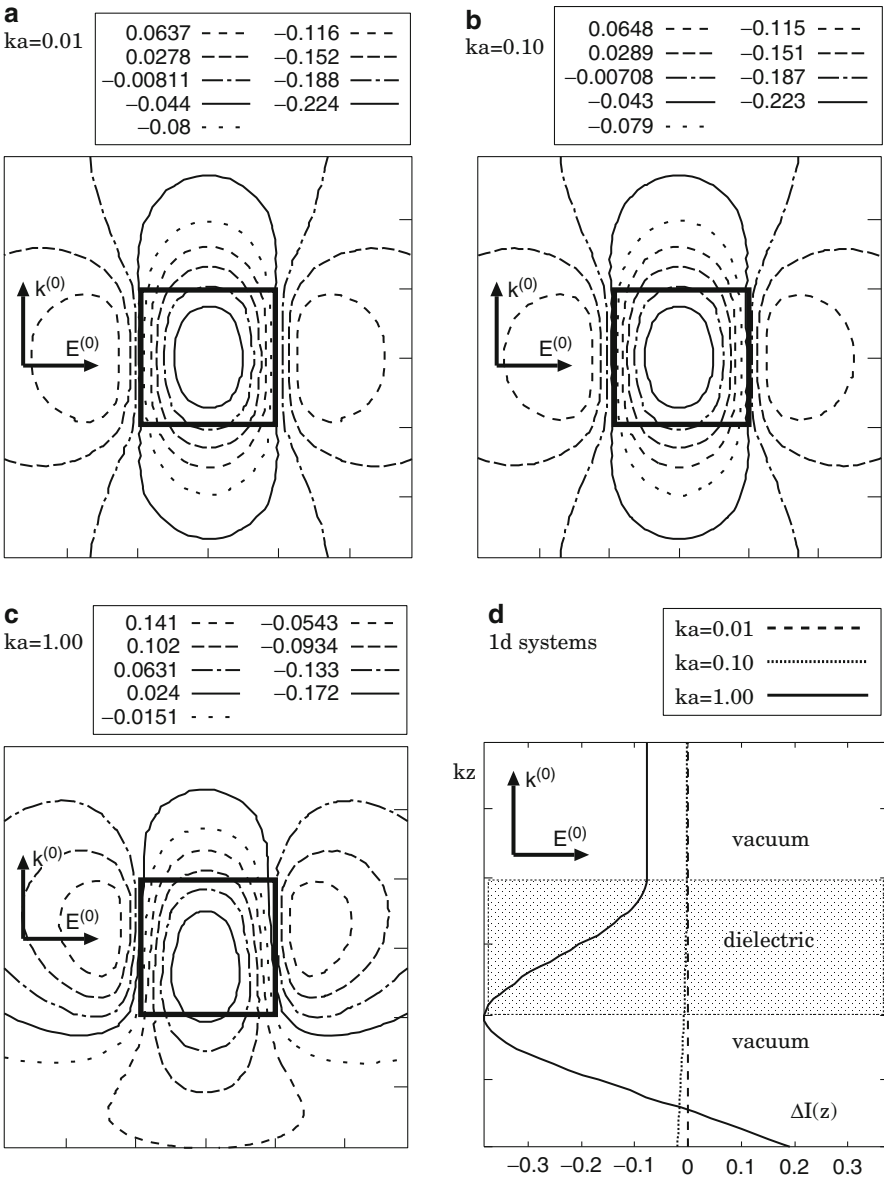


Fig. 2.11 The electric near field of a dielectric cube, of which the dielectric constant is $\epsilon_1/\epsilon_0 = 2.25$ and the side length is a ; the numerical calculations are performed based on our novel formulation with the dual EM potential; $\mathbf{k}^{(0)}$ ($k = |\mathbf{k}^{(0)}|$) and $\mathbf{E}^{(0)}$ are the wavenumber and polarization vectors of the incident field. The observation plane is located at a height of $0.7a$ from the center of the cube. (a), (b), and (c) The intensity profiles for $ka = 0.01$, $ka = 0.10$, and $ka = 1.00$, respectively. (d) The intensity profile in the one-dimensional problem with normal incidence, i.e., s-polarization incidence

an invariant profile under the scale transformation concerning the length. This comes from the fact that the wave equation, see Eqs. (2.51a)–(2.51d) or Eqs. (2.52a)–(2.52f), in the limit of $k \rightarrow 0$ is invariant under the scale transformation concerning the spatial coordinates. This invariance is a property of the quasi-static picture and, of course, the Poisson equation, i.e., Eq. (2.35) or Eqs. (2.38a)–(2.38c), is also invariant under the scale transformation.

If the retardation effect is not negligible, “ k ” in the wave equation survives and this equation is not invariant under the scale transformation keeping “ k ” constant. Therefore, Fig. 2.11c is different from Fig. 2.11a, b. In Fig. 2.11c, the intensity in the back side of the material is more negative than that in the front side.

In order to extract the retardation effect, let us consider a certain scattering problem with plane interfaces, namely a one-dimensional problem. Suppose that a dielectric occupies the region $-0.5 \leq kz \leq 0.5$ where the z direction is that of \mathbf{k} . Note carefully that \mathbf{k} of the incident field is normal to the interface, namely the s-polarized incident field. The whole field in this system possesses the same polarization vector as that of the incident field and can be expressed as

$$\mathbf{C}(\mathbf{r}) = -\frac{\epsilon_0}{k^2} \nabla \times \hat{y} E(z), \quad (2.66)$$

where $E(z) = \hat{y} \cdot \mathbf{E}(z)$ is the amplitude of the total electric field in question. Substituting Eq. (2.66) into Eqs. (2.51a)–(2.51d), one obtains the following one-dimensional wave equation:

$$(-\partial_z^2 - k^2)E(z) = -\theta\left(-\frac{1}{2} \leq kz \leq \frac{1}{2}\right) \left(-\left(\frac{\epsilon_1}{\epsilon_0} - 1\right)k^2\right) E(z). \quad (2.67)$$

In Eq. (2.67), there is no boundary source and the retardation effect (including bulk effect) exists. To solve Eq. (2.67) is equivalent to solving a quantum well problem and the solution is obtained easily in connection with quantum mechanics. We remark that the material is dielectric, i.e., $\epsilon_1/\epsilon_0 - 1 > 0$ and the potential well corresponds to an attractive one in quantum mechanics. The result is Fig. 2.11d and it is found that the intensity in just the back side of the material is more negative than that in the front side. This is because the wave, propagating from the vacuum to the dielectric, feels the boundary $z = -0.5$ like the fixed end and the interference between the incident wave and the reflected one suppresses the amplitude just in the back side of the material. In the front side of the material, however, there is no such destructive interference because of there being no incident field from $z = +\infty$.

Now in our three-dimensional problem both the boundary effect and the retardation effect (including the bulk effect) contribute to the electric field. Under the condition $ka \lesssim kr \lesssim 1$, the field feels the boundary of the back side to some degree, because the width of this boundary is given by $ka = 1$ and not negligible compared with the wavelength. Further, the polarization vector is parallel to the boundary and it is similar to the s-polarization vector in the one-dimensional problem. Therefore, the contribution from the retardation effect is expected to be

qualitatively the same as that of the one-dimensional problem. Now the (near-) field intensity formula Eq. (2.27) leads to

$$\begin{aligned} \Delta I(\mathbf{r}) &\simeq \frac{\mathbf{E}^{(0)*}(\mathbf{r}) \cdot \Delta \mathbf{E}(\mathbf{r}) + \text{c.c.}}{|\mathbf{E}^{(0)}(\mathbf{r})|^2} \\ &= \frac{\mathbf{E}^{(0)*}(\mathbf{r}) \cdot \Delta \mathbf{E}_{\text{surf}}(\mathbf{r}) + \text{c.c.} + \mathbf{E}^{(0)*}(\mathbf{r}) \cdot \Delta \mathbf{E}_{\text{vol}}(\mathbf{r}) + \text{c.c.}}{|\mathbf{E}^{(0)}(\mathbf{r})|^2}, \end{aligned} \quad (2.68)$$

where $\Delta \mathbf{E}_{\text{surf}}$ (\mathbf{E}_{vol}) is the scattered electric field coming from the surface (volume) integral in Eq. (2.56). $\Delta \mathbf{E}_{\text{surf}}$ contributes to the intensity in the same way both in the back side and in the front side, at least, under the lowest order approximation. However, $\Delta \mathbf{E}_{\text{vol}}$ contributes to the intensity in the back side more negatively than to that in the front side even in the lowest order approximation. In other words, $\Delta \mathbf{E}_{\text{vol}}$ in the back side is anti-parallel to $\mathbf{E}^{(0)}$ and causes destructive interference. Summing up both the contributions to Eq. (2.68), it is confirmed that the asymmetry in the intensity profile Fig. 2.11c comes from the retardation effect.

At least in some simple cases under $ka \lesssim kr \lesssim 1$, we expect that the optical near field is understood on the basis of the quasi-static picture with a certain correction due to the retardation effect, which is familiar in connection with quantum mechanics or wave mechanics.

2.5.8 Summary

The essential points in this section are as follows:

- The dual EM potential is the minimum degree of freedom in the EM field with a material of which the magnetic response is negligible.
- The boundary value problem in a system with a steep interface can be replaced by a boundary scattering problem. In this novel formulation, the boundary and bulk effects are treated on an equal footing.
- The boundary magnetic current density appearing in this formulation possesses arbitrariness originating from the source's profile in the interface region.
- The order of electric field under the NFC and that under the Rayleigh far-field condition are estimated on the basis of the boundary scattering formulation with the dual EM potential; the leading order in each case comes from the boundary effect and the field under NFC is “ k ” independent, while Rayleigh's far field is “ k ” dependent.
- Under the NFC, the quasi-static picture can be understood intuitively using the dual Ampère law; it is compatible with the picture in the context of the boundary scattering formulation with the scalar potential.
- Under the condition $ka \lesssim kr \lesssim 1$, a correction due to the retardation effect may be understood qualitatively in connection with quantum mechanics.
- It is confirmed that the arbitrariness in the boundary scattering formulation does not affect the field outside the interface region.

In short, the boundary scattering formulation with the dual EM potential is free from MBCs and is applicable to various EM problems, and is useful to understand and to calculate the optical near field under the coexistence of boundary and bulk effects.

2.6 Summary and Remaining Problems

In short, what we have done is the following.

- Simple explanations for the retardation effect and diffraction limit are given. Clear definitions of far field and near field are given.
- It is shown that a characteristic in NFO is its quasi-static limit in the system with a small-scale material. The electric field in such a system is of a non-radiative nature and is generated by the boundary charge density *via* Coulomb's law. One may predict the near-field amplitude and intensity intuitively, even if the material possesses a complicated shape and/or response. This idea is applied to multidomain systems with magneto-optical and electro-optical responses.
- The boundary scattering formulations with the scalar potential and with the dual EM potential are developed in order to treat the optical near field in a way compatible with the quasi-static picture. Both formulations are free from MBCs; a certain boundary source is responsible for the MBCs. In particular, the formulation using the dual vector potential enables a perturbative or an iterative treatment of the boundary and bulk effects on an equal footing.

The characteristics of the boundary scattering formulation with the scalar potential are as follows.

- It is available under the NFC and is grounded upon the quasi-static picture. Under the NFC, the minimum degree of freedom of the EM field is the scalar potential.
- The MBCs are built in the boundary charge density; it possesses a certain arbitrariness, which never affects physics. This formulation is free from the MBCs but equivalent to solving the corresponding boundary value problem.
- The boundary scattering problem can be solved by a perturbative or an iterative method. One can use the arbitrariness to improve the convergence in a numerical calculation.
- For the electric near field in the vicinity of a dielectric under the NFC, the lowest order approximation of the perturbative treatment brings about an intuitive picture based on Coulomb's law. This idea is effective even in a low symmetry system.
- It can be applied to a static-electric boundary value problem and a static-magnetic one; a certain scalar potential is the minimum degree of freedom in such systems.

The characteristics of the boundary scattering formulation with a dual vector potential are as follows.

- It is available, in principle, in the whole regime from near field to far field, because the wave equation for the dual vector potential (in radiation gauge) is equivalent to Maxwell's equations with a material of which the magnetic response is negligible.

- The MBCs are built in the boundary magnetic current density; it possesses a certain arbitrariness, which never affects the physics. This formulation is free from MBCs but equivalent to solving the corresponding boundary value problem.
- In this formulation, the boundary and the bulk effects are treated on an equal footing. This balanced treatment is especially appropriate to understand and to calculate the optical near field under $ka \lesssim kr \lesssim 1$; the two effects are comparable under this condition.

In the scheme of the boundary value problem, the two effects are treated in an unbalanced accuracy and it is difficult to obtain a simple physical picture.

- Under the NFC, an intuitive picture based on the dual Ampère law holds. It is consistent with the picture based on Coulomb's law in the boundary scattering formulation with the scalar potential.
- Under the condition $ka \lesssim kr \lesssim 1$, the correction due to the retardation effect may be understood qualitatively in connection with quantum mechanics.
- Under the condition $ka \lesssim kr \lesssim 1$, one can numerically calculate the optical near field by means of a perturbative or an iterative method. One can use the arbitrariness to improve the convergence.

Remaining problems are as follows.

- Extension of the numerical treatment of the system with material which possesses non-linear response. In particular, those boundary effects are dominant in the near-field regime and should be considerably different from the well-known bulk or volume optical effects.

2.7 Green's Function and Delta Function in Vector Field Analysis

Concerning Green's function in vector field analysis, we can refer to Ref. [26] or other books. However, there are many notational features and expressions; some of them possibly contain errors. Therefore, here we give a concise and self-contained derivation of Green's function, which is useful to solve inhomogeneous Helmholtz' equations including our master equations (2.38a)–(2.38c) (in the limit of $k \rightarrow 0$) and Eqs. (2.52a)–(2.52f). We treat the Helmholtz' equations in the scalar version,

$$(-\Delta - k^2)X(\mathbf{r}) = -V(\mathbf{r}) , \quad (2.69)$$

and the vector version,

$$(-\Delta - k^2)\mathbf{X}(\mathbf{r}) = -\mathbf{V}(\mathbf{r}) . \quad (2.70)$$

The corresponding Laplace equation can be regarded as the limit of $k \rightarrow 0$.

2.7.1 Vector Helmholtz' Equation

Let us start from solving Eq. (2.69); this solution is the basis to obtain a solution of Eq. (2.70). The Green function for Eq. (2.69) is defined as follows:

$$(-\Delta - k^2)G(\mathbf{r} - \mathbf{r}'; k) = -\delta^3(\mathbf{r} - \mathbf{r}') , \quad (2.71)$$

$$G(\mathbf{r} - \mathbf{r}'; k) = \frac{-1}{4\pi} \frac{\exp(\pm ik|\mathbf{r} - \mathbf{r}'|)}{|\mathbf{r} - \mathbf{r}'|} . \quad (2.72)$$

We may add elementary solution (solution of the homogeneous version of Eq. (2.71)) to Eq. (2.72) in order to adjust the boundary condition at $r \rightarrow \infty$ or elsewhere, if it is given. In many cases, we take the “+”-signed exponent in Eq. (2.72) because of causality. Using Eq. (2.72), Eq. (2.69) leads to the following integral form:

$$X(\mathbf{r}) = X^{(0)}(\mathbf{r}) + \int d^3r' G(\mathbf{r} - \mathbf{r}'; k) V(\mathbf{r}') , \quad (2.73)$$

where $X^{(0)}(\mathbf{r})$ is a solution of Eq. (2.69) without the source. If V is a functional of $X(\mathbf{r})$, Eq. (2.73) is an integral equation, e.g., Eq. (2.41).

Let us consider Eq. (2.70). The identity tensor (or delta tensor, delta dyadic) is defined as

$$\int d^3r' \mathcal{D}(\mathbf{r} - \mathbf{r}')_{ij} X(\mathbf{r}')_j = X(\mathbf{r})_i , \quad (2.74)$$

$$\mathcal{D}(\mathbf{r} - \mathbf{r}')_{ij} = \delta_{ij} \delta^3(\mathbf{r} - \mathbf{r}') , \quad (2.75)$$

where $X(\mathbf{r})$ is an arbitrary vector field and we use Einstein's rule for the contraction of tensor indices, e.g., $\mathcal{D}_{ij} X_j = \sum_{j=1}^3 \mathcal{D}_{ij} X_j$.

Then Green's tensor (or Green's dyadic) is defined as

$$(-\Delta - k^2)\mathcal{G}(\mathbf{r} - \mathbf{r}'; k)_{ij} = -\mathcal{D}(\mathbf{r} - \mathbf{r}')_{ij} , \quad (2.76)$$

$$\mathcal{G}(\mathbf{r} - \mathbf{r}'; k)_{ij} = \delta_{ij} G(\mathbf{r} - \mathbf{r}'; k) . \quad (2.77)$$

Equation (2.76) is merely Eq. (2.71) times δ_{ij} . Using Eq. (2.77), Eq. (2.70) leads to the following integral form:

$$X(\mathbf{r})_i = X^{(0)}(\mathbf{r})_i + \int d^3r' \mathcal{G}(\mathbf{r} - \mathbf{r}'; k)_{ij} V(\mathbf{r}')_j , \quad (2.78)$$

where $X^{(0)}(\mathbf{r})$ is a solution of Eq. (2.70) without the source. If V is a functional of $X(\mathbf{r})$, Eq. (2.78) is an integral equation, e.g., Eq. (2.56).

In the following, we call the delta tensor (Green's tensor) the delta function (Green's function) for simplicity.

2.7.2 Decomposition into Longitudinal and Transversal Components

It is well known, as the Helmholtz theorem, that a vector field $\mathbf{Y}(\mathbf{r})$ can always be decomposed into two orthogonal components, namely the longitudinal component $\mathbf{Y}^{(l)}$ and the transversal one $\mathbf{Y}^{(t)}$ (If necessary, one can prove the above fact, tracing the procedure from Eqs. (2.83) to (2.89d) with an adequate replacement.):

$$\mathbf{Y}(\mathbf{r}) = \mathbf{Y}^{(l)}(\mathbf{r}) + \mathbf{Y}^{(t)}(\mathbf{r}) , \quad (2.79a)$$

$$\nabla \times \mathbf{Y}^{(l)}(\mathbf{r}) = \mathbf{0} , \quad (2.79b)$$

$$\nabla \cdot \mathbf{Y}^{(t)}(\mathbf{r}) = 0 , \quad (2.79c)$$

$$\int d^3r \mathbf{Y}^{(l)}(\mathbf{r}) \cdot \mathbf{Y}^{(t)}(\mathbf{r}) = 0 . \quad (2.79d)$$

Applying Eqs. (2.79a)–(2.79c) to $\mathbf{X}(\mathbf{r})$ and $\mathbf{V}(\mathbf{r})$ in Eq. (2.70) and using the identity

$$-\Delta \mathbf{Y}(\mathbf{r} \cdots) = -\nabla \nabla \cdot \mathbf{Y}(\mathbf{r} \cdots) + \nabla \times \nabla \times \mathbf{Y}(\mathbf{r} \cdots) , \quad (2.80)$$

we obtain the longitudinal and the transversal vector Helmholtz equations,

$$(-\nabla \nabla \cdot -k^2) \mathbf{X}^{(l)}(\mathbf{r}) = -\mathbf{V}^{(l)}(\mathbf{r}) , \quad (2.81)$$

$$(\nabla \times \nabla \times -k^2) \mathbf{X}^{(t)}(\mathbf{r}) = -\mathbf{V}^{(t)}(\mathbf{r}) . \quad (2.82)$$

Each equation is natural because the longitudinal (transversal) source generates the longitudinal (transversal) field.

We remark that the decomposition of the equation is not effective in Eq. (2.70) under $k \rightarrow 0$, namely the vectorial Laplace equation. A solution of the vectorial Laplace equation does not propagate because of $k \rightarrow 0$ and the concept of longitudinal or transversal component of a solution is meaningless. In fact, the expressions for $\mathcal{G}^{(l)}$ and $\mathcal{G}^{(t)}$, i.e., Eqs. (2.95) and (2.96), possess a certain singularity in the limit of $k \rightarrow 0$, while Eqs. (2.72) and (2.77) do not.

Equations (2.81) and (2.82) lead to integral forms, if the corresponding longitudinal and transversal vector Green's functions are defined; we will define those in the following.

Suppose a diagonal tensor field is defined as the product of Kronecker's delta and a scalar field that depends only on the difference between the two spatial coordinates,

$$\mathcal{Y}(\mathbf{r} - \mathbf{r}')_{ij} \equiv \delta_{ij} Y(\mathbf{r} - \mathbf{r}') . \quad (2.83)$$

This diagonal tensor can always be decomposed into longitudinal and transversal tensor components. Note that \mathcal{D} and \mathcal{G} belong to such a class of tensor. We have

$$\mathcal{Y}(\mathbf{r} - \mathbf{r}')_{ij} = \delta_{ij} Y(\mathbf{r} - \mathbf{r}')$$

$$\begin{aligned}
&= \delta_{ij} \frac{1}{(2\pi)^3} \int d^3k \tilde{Y}(\mathbf{k}) \exp(+i\mathbf{k} \cdot (\mathbf{r} - \mathbf{r}')) \\
&= \frac{1}{(2\pi)^3} \int d^3k (\hat{\mathbf{k}}_i \hat{\mathbf{k}}_j + \hat{\mathbf{e}}_i^{(2)} \hat{\mathbf{e}}_j^{(2)} + \hat{\mathbf{e}}_i^{(3)} \hat{\mathbf{e}}_j^{(3)}) \\
&\quad \tilde{Y}(\mathbf{k}) \exp(+i\mathbf{k} \cdot (\mathbf{r} - \mathbf{r}')) , \quad (2.84)
\end{aligned}$$

where $\tilde{Y}(\mathbf{k})$ is the Fourier transformation of $Y(\mathbf{r})$; we implicitly assume that the Fourier integral is converging. To obtain the last expression in Eq. (2.84), we use the expansion of δ_{ij} by a normalized orthogonal complete set $\{\hat{\mathbf{e}}^{(\alpha)} | \alpha = 1, 2, 3\}$,

$$\delta_{ij} = \hat{\mathbf{e}}_i^{(1)} \hat{\mathbf{e}}_j^{(1)} + \hat{\mathbf{e}}_i^{(2)} \hat{\mathbf{e}}_j^{(2)} + \hat{\mathbf{e}}_i^{(3)} \hat{\mathbf{e}}_j^{(3)} . \quad (2.85)$$

Further we take one of the bases as the unit vector of the wavenumber vector $\hat{\mathbf{e}}^{(1)} = \hat{\mathbf{k}}$ in the integrand. Now let us define the first term (remaining terms) in the last expression in Eq. (2.84) as $\mathcal{Y}^{(l)}(\mathbf{r} - \mathbf{r}')_{ij}$ [$\mathcal{Y}^{(l)}(\mathbf{r} - \mathbf{r}')_{ij}$]. We recognize $\mathcal{Y}^{(l)}(\mathbf{r} - \mathbf{r}')$ as the longitudinal tensor because its integrand is composed of the direct product of the wavenumber vectors \mathbf{k} , while $\mathcal{Y}^{(l)}(\mathbf{r} - \mathbf{r}')_{ij}$ is the transversal tensor because $\hat{\mathbf{e}}^{(2)}$ and $\hat{\mathbf{e}}^{(3)}$ in the integrand are orthogonal to the wavenumber vector \mathbf{k} .

As a result, any diagonal tensor field \mathcal{Y} defined by Eq. (2.83) (including the cases of \mathcal{D} and \mathcal{G}) is decomposed into longitudinal and transversal components:

$$\mathcal{Y}(\mathbf{r} - \mathbf{r}')_{ij} = \mathcal{Y}^{(l)}(\mathbf{r} - \mathbf{r}')_{ij} + \mathcal{Y}^{(t)}(\mathbf{r} - \mathbf{r}')_{ij} , \quad (2.86a)$$

$$\nabla \times \mathcal{Y}^{(l)}(\mathbf{r} - \mathbf{r}') = -\nabla' \times \mathcal{Y}^{(l)}(\mathbf{r} - \mathbf{r}') = \mathcal{O} , \quad (2.86b)$$

$$\nabla \cdot \mathcal{Y}^{(t)}(\mathbf{r} - \mathbf{r}') = -\nabla' \cdot \mathcal{Y}^{(t)}(\mathbf{r} - \mathbf{r}') = \mathbf{0} . \quad (2.86c)$$

The detailed expression for Eq. (2.86b) using the antisymmetric tensor ϵ_{ijk} is

$$\epsilon_{ijk} \partial_j \mathcal{Y}^{(l)}(\mathbf{r} - \mathbf{r}')_{kl} = -\epsilon_{ijk} \partial'_j \mathcal{Y}^{(l)}(\mathbf{r} - \mathbf{r}')_{lk} = \mathcal{O} .$$

Now the vector delta function Eq. (2.75) and vector Green's function Eq. (2.77) are the same type of diagonal tensor and can be decomposed as $\mathcal{D} = \mathcal{D}^{(l)} + \mathcal{D}^{(t)}$ and $\mathcal{G} = \mathcal{G}^{(l)} + \mathcal{G}^{(t)}$, respectively.

Let us deduce explicit expressions for $\mathcal{D}^{(l)}$, $\mathcal{D}^{(t)}$, $\mathcal{G}^{(l)}$, and $\mathcal{G}^{(t)}$. The Fourier representation of the vector delta function Eq. (2.75) is Eq. (2.84) with $\tilde{Y}(\mathbf{k}) = 1$. Then $\mathcal{D}^{(l)}$ and $\mathcal{D}^{(t)}$ are calculated as follows:

$$\begin{aligned}
\mathcal{D}^{(l)}(\mathbf{r} - \mathbf{r}')_{ij} &\equiv \frac{1}{(2\pi)^3} \int d^3k \hat{\mathbf{k}}_i \hat{\mathbf{k}}_j \exp(+i\mathbf{k} \cdot (\mathbf{r} - \mathbf{r}')) \\
&= \partial_i \partial'_j \frac{1}{(2\pi)^3} \int d^3k \frac{1}{k^2} \exp(+i\mathbf{k} \cdot (\mathbf{r} - \mathbf{r}'))
\end{aligned}$$

$$\begin{aligned}
&= \partial_i \partial'_j \frac{1}{2\pi^2} \int_0^\infty dk \frac{\sin(k|\mathbf{r} - \mathbf{r}'|)}{k|\mathbf{r} - \mathbf{r}'|} \\
&= -\partial_i \partial'_j G(\mathbf{r} - \mathbf{r}'; 0) .
\end{aligned} \tag{2.87}$$

The third h.s. of Eq. (2.87) is deduced using the fact that “ $i\mathbf{k}$ ” is equivalent to the operator ∇ or $-\nabla'$ in the integrand and the fourth h.s. is the result of the integration over the angular variables in the spherical coordinates. The last expression is derived using $\int_0^\infty \sin x/x = \pi/2$. On the other hand,

$$\begin{aligned}
\mathcal{D}^{(t)}(\mathbf{r} - \mathbf{r}')_{ij} &\equiv \mathcal{D}(\mathbf{r} - \mathbf{r}')_{ij} - \mathcal{D}^{(l)}(\mathbf{r} - \mathbf{r}')_{ij} \\
&= \delta_{ij} \delta^3(\mathbf{r} - \mathbf{r}') + \partial_i \partial'_j G(\mathbf{r} - \mathbf{r}'; 0) .
\end{aligned} \tag{2.88}$$

We can check that $\mathcal{D}^{(l)}$ and $\mathcal{D}^{(t)}$ is the identity or the projection operator in the subspace of the longitudinal and the transversal vector field, respectively,

$$\int d^3 r' \mathcal{D}^{(l)}(\mathbf{r} - \mathbf{r}')_{ij} \mathbf{Y}^{(l)}(\mathbf{r}')_j = \mathbf{Y}^{(l)}(\mathbf{r})_i , \tag{2.89a}$$

$$\int d^3 r' \mathcal{D}^{(l)}(\mathbf{r} - \mathbf{r}')_{ij} \mathbf{Y}^{(t)}(\mathbf{r}')_j = \mathbf{0} , \tag{2.89b}$$

$$\int d^3 r' \mathcal{D}^{(t)}(\mathbf{r} - \mathbf{r}')_{ij} \mathbf{Y}^{(l)}(\mathbf{r}')_j = \mathbf{Y}^{(l)}(\mathbf{r})_i , \tag{2.89c}$$

$$\int d^3 r' \mathcal{D}^{(t)}(\mathbf{r} - \mathbf{r}')_{ij} \mathbf{Y}^{(t)}(\mathbf{r}')_j = \mathbf{0} . \tag{2.89d}$$

Now we can calculate $\mathcal{G}^{(l)}$ and $\mathcal{G}^{(t)}$. Applying Eqs. (2.86a)–(2.86c) to \mathcal{D} and \mathcal{G} in Eq. (2.70) and using Eq. (2.80), Eq. (2.70) is decomposed into the following two equations for longitudinal and transversal components:

$$(-\nabla \nabla \cdot - k^2) \mathcal{G}^{(l)}(\mathbf{r} - \mathbf{r}'; k) = -\mathcal{D}^{(l)}(\mathbf{r} - \mathbf{r}') , \tag{2.90}$$

$$(\nabla \times \nabla \times - k^2) \mathcal{G}^{(t)}(\mathbf{r} - \mathbf{r}'; k) = -\mathcal{D}^{(t)}(\mathbf{r} - \mathbf{r}') . \tag{2.91}$$

From Eq. (2.90), we obtain an explicit expression for $\mathcal{G}^{(l)}$ as follows:

$$\begin{aligned}
\mathcal{G}^{(l)}(\mathbf{r} - \mathbf{r}'; k)_{ij} &= \frac{1}{k^2} (-\nabla \nabla \cdot \mathcal{G}^{(l)}(\mathbf{r} - \mathbf{r}'; k) + \mathcal{D}^{(l)}(\mathbf{r} - \mathbf{r}'))_{ij} \\
&= \frac{1}{k^2} (-\nabla \nabla \cdot \mathcal{G}(\mathbf{r} - \mathbf{r}'; k) + \mathcal{D}^{(l)}(\mathbf{r} - \mathbf{r}'))_{ij} \\
&= \frac{1}{k^2} \left(-\partial_i \partial_k \delta_{kj} G(\mathbf{r} - \mathbf{r}'; k) - \partial_i \partial'_j G(\mathbf{r} - \mathbf{r}'; 0) \right) \\
&= \frac{1}{k^2} \partial_i \partial'_j (G(\mathbf{r} - \mathbf{r}'; k) - G(\mathbf{r} - \mathbf{r}'; 0)) .
\end{aligned} \tag{2.92}$$

Further, an expression for the transversal vector Green's function is

$$\begin{aligned} \mathcal{G}^{(l)}(\mathbf{r} - \mathbf{r}'; k)_{ij} &= \mathcal{G}(\mathbf{r} - \mathbf{r}'; k)_{ij} - \mathcal{G}^{(l)}(\mathbf{r} - \mathbf{r}'; k)_{ij} \\ &= \delta_{ij} G(\mathbf{r} - \mathbf{r}'; k) - \frac{1}{k^2} \partial_i \partial'_j (G(\mathbf{r} - \mathbf{r}'; k) - G(\mathbf{r} - \mathbf{r}'; 0)) . \end{aligned} \quad (2.93)$$

As a result, we can convert Eqs. (2.81) and (2.82) to the following two integral forms using Eqs. (2.89a)–(2.89d), (2.90), and (2.91):

$$X^{(l/l)}(\mathbf{r})_i = X^{(l/l)(0)}(\mathbf{r})_i + \int d^3r' \mathcal{G}^{(l/l)}(\mathbf{r} - \mathbf{r}'; k)_{ij} V^{(l/l)}(\mathbf{r}')_j . \quad (2.94)$$

For numerical calculation, the following expressions are convenient,

$$\begin{aligned} \mathcal{G}^{(l)}(\mathbf{R}; k)_{ij} &= -\frac{G(\mathbf{R}; 0)}{(ikR)^2} (-\delta_{ij} + 3\hat{R}_i \hat{R}_j) \\ &+ \frac{G(\mathbf{R}; k)}{(ikR)^2} \left(-\delta_{ij} (1 - ikR) + \hat{R}_i \hat{R}_j (3 - 3ikR + (ikR)^2) \right) , \end{aligned} \quad (2.95)$$

$$\begin{aligned} \mathcal{G}^{(l)}(\mathbf{R}; k)_{ij} &= +\frac{G(\mathbf{R}; 0)}{(ikR)^2} (-\delta_{ij} + 3\hat{R}_i \hat{R}_j) \\ &- \frac{G(\mathbf{R}; k)}{(ikR)^2} \left(-\delta_{ij} (1 - ikR + (ikR)^2) + \hat{R}_i \hat{R}_j (3 - 3ikR + (ikR)^2) \right) , \end{aligned} \quad (2.96)$$

where $\mathbf{R} \equiv \mathbf{r} - \mathbf{r}'$ and $\hat{R} = \mathbf{R}/|\mathbf{R}|$. The expressions in Sect. 13.1 of Ref. [26] corresponding to Eqs. (2.95) and (2.96) are not correct.

References

1. E.A. Ash, G.Nicholls, *Nature* **237**, 510 (1972)
2. I. Banno, Classical theory on electromagnetic near field, in *Progress in Nano-Electro-Optics II*, ed. by M. Ohtsu (Springer, Berlin, 2004), pp.1–57
3. I. Banno, *Phys. Rev. A* **78**, 033816 (2008)
4. I. Banno, *Phys. Rev. A* **77**, 033818 (2008); Erratum *Phys. Rev. A* **84**, 019906(E) (2011). The error was kindly pointed out by V. Kambersky, R. Schäfer, *Phys. Rev. A* **84**, 013815 (2011)
5. I. Banno, Surface phenomena caused by optical spin-orbit interaction: a pedagogical theory using quantum mechanical concepts, in *Plasmons: Theory and Applications*, ed. by K.N. Helsey (Nova Science Publishers, New York, 2011), pp. 437–466
6. I. Banno, H. Hori, Dual Ampere law and image of NOM (in Japanese), in *Handbook for Near-field Nano-photonics*, ed. by M. Ohtsu, S. Kawata (Optronics, Tokyo, 1996), pp. 240–244; *ibid*, in *Introduction to Near-field Nano-photonics*, ed. by M. Ohtsu, S. Kawata (Optronics, Tokyo, 2000), pp. 48–52
7. I. Banno, H. Hori, *Trans. IEE Jpn.* **119-C**, 1094 (1999) (in Japanese). In this review, the numerical results in Figure 4 and the related discussion are wrong; those concern the retardation

- effect in the vicinity of a dielectric. This error is corrected in [Sect. 2.5.7](#) in this chapter and [Sect. 5.4](#) in the original book [2]
8. I. Banno, H. Hori, T. Inoue, *Opt. Rev.* **3**, 454 (1996)
 9. H.A. Bethe, *Phys. Rev.* **66**, 163 (1944)
 10. E. Betzig, M. Issacson, A. Lewis, *Appl. Phys. Lett.* **51**, 2088 (1987)
 11. C.J. Bouwkamp, *Philips Res. Rep.* **5**, 401 (1950)
 12. M. Faraday, *Experimental Researches in Electricity*. Nineteenth Series (Dover, New York, 1965)
 13. U.Ch. Fischer, D.W. Pohl, *Phys. Rev. Lett.* **62**, 458 (1989)
 14. C. Girared, D. Coujon, *Phys. Rev. B* **42**, 9340 (1990)
 15. K. Goto, T. Ono, Y.-J. Kim, *IEEE Trans. Mag.* **41**, 1037 (2005)
 16. S.M. Huang, M.H. Hong, B.S. Luk'yanchuk, T.C. Chong, *Appl. Phys. Lett.* **82**, 4809 (2003)
 17. W. Jhe, K. Jang, *Ultramicroscopy* **61**, 81 (1995)
 18. S. Jiang, H. Ohsawa, K. Yamada, T. Pangaribuan, M. Ohtsu, K. Imai, A. Ikai, *Jpn. J. Appl. Phys.* **31**, 2282 (1992)
 19. T. Kawazoe, K. Kobayashi, J. Lim, Y. Narita, M. Ohtsu, *Phys. Rev. Lett.* **88**, 067404–1 (2002)
 20. T. Kawazoe, K. Kobayashi, S. Sangu, M. Ohtsu, *Appl. Phys. Lett.* **82**, 2957 (2003)
 21. T. Kawazoe, K. Kobayashi, M. Ohtsu, *Appl. Phys. Lett.* **86**, 103102–1 (2005)
 22. D.R. Lide, *CRC Handbook of Chemistry and Physics*, 87th edn. (CRC, Boca Raton, 2006). Chapter 10
 23. X. Luo, T. Ishihara, *Appl. Phys. Lett.* **84**, 4780 (2004)
 24. J.F. Martin, C. Girard, A. Dereux, *Phys. Rev. Lett.* **74**, 526 (1995). Note that their intensity is just the square of the electric field, while ours is non-dimensional and the background intensity is eliminated
 25. G.A. Massey, J.A. Davis, S.M. Katnik, E. Omon, *Appl. Opt.* **24**, 1498 (1985)
 26. P.M. Morse, H. Feshbach, *Methods of Theoretical Physics* (McGraw-Hill, New York/Toronto/London, 1953)
 27. M. Naya, S. Mononobe, R. Uma Maheswari, T. Saiki, M. Ohtsu, *Opt. Commun.* **124**, 9 (1996)
 28. R.G. Newton, *Scattering Theory of Waves and Particles*, 2nd edn. (Dover, Mineola, 2002). Section 3.2, In Newton's book, the Rayleigh–Gans approximation is identified as the Born approximation in the low energy limit
 29. M. Ohtsu (ed.), *Near-field Nano/Atom Optics and Technology* (Springer, Tokyo, 1998)
 30. J.A. O'keefe, *J. Opt. Soc. Am.* **46**, 359 (1956)
 31. D.W. Pohl, W. Denk, M. Lanz, *Appl. Phys. Lett.* **44**, 651 (1984)
 32. T. Saiki, S. Mononobe, M. Ohtsu, N. Saito, J. Kusano, *Appl. Phys. Lett.* **67**, 2191 (1995)
 33. R. Schäfer, A. Hubert, *Phys. Status Solidi a* **118**, 271 (1990)
 34. R. Schäfer, M. Rühlig, A. Hubert, *IEEE Trans. Mag.* **26**, 1355 (1990)
 35. D.B. Shao, S.C. Chen, *Appl. Phys. Lett.* **86**, 253107 (2005)
 36. J.A. Stratton, *Electromagnetic Theory* (McGraw-Hill, New York/London, 1941). Chapter 3 for multipolemoment and Chaps. 7 and 9 for the analytical solution in a spherical system
 37. E.H. Synge, *Philos. Mag.* **6**, 356 (1928)
 38. J. Tominaga, The super-resolution near-field structure and its applications, in *Optical Nanotechnologies*, ed. by J. Tominaga, D.P. Tsai (Springer, Berlin/Heidelberg/New York, 2003), pp. 1–22
 39. K.A. Willets, R.P. Van Duyne, *Annu. Rev. Phys. Chem.* **58**, 267 (2007)
 40. K.S. Yee, *IEEE Trans. Antennas Propag.* **AP14**, 302 (1966)
 41. F. Zenhauserm, M.P. O'Boyle, H.K. Wickramasinghe, *Appl. Phys. Lett.* **65**, 1623 (1994)
 42. F. Zenhauserm, Y. Martin, Y.K. Wickramasinghe, *Science* **269**, 1083 (1995)

Kiyoshi Kobayashi, Suguru Sangu, and Motoichi Ohtsu

Contents

3.1	Introduction.....	66
3.1.1	Basic Idea and Massive Virtual Photon Model.....	67
3.2	Projection Operator Method.....	68
3.2.1	Definition of the Projection Operator.....	69
3.2.2	Properties of the Projection Operator.....	69
3.3	Effective Operator and Effective Interaction.....	70
3.3.1	Equation for the Operator \hat{J} and Its Approximate Solution.....	72
3.3.2	Effective Interaction Operator in an Approximation.....	74
3.4	Electromagnetic Interaction with Matter: Minimal-Coupling and Multipole Hamiltonians.....	75
3.4.1	Minimal-Coupling Hamiltonian.....	75
3.4.2	Multipole Hamiltonian.....	77
3.5	Elementary Excitation Modes and Electronic Polarization.....	82
3.5.1	Polaritons and Electronic Polarization.....	83
3.6	Optical Near-Field Interaction: Yukawa Potential.....	86
3.6.1	Relevant Microscopic Subsystem and Irrelevant Macroscopic Subsystem.....	87
3.6.2	P Space and Q Space.....	87

K. Kobayashi (✉)

Interdisciplinary Graduate School of Medicine and Engineering, University of Yamanashi, Kofu, Yamanashi, Japan

e-mail: kkoba@yamanashi.ac.jp

S. Sangu

Device Technology Development Center, Ricoh Co., Ltd, Miyagi, Japan

e-mail: suguru.sangu@nts.ricoh.co.jp

M. Ohtsu

School of Engineering, The University of Tokyo, Tokyo, Japan

Nanophotonics Research Center, The University of Tokyo, Tokyo, Japan

e-mail: ohtsu@ee.t.u-tokyo

3.6.3	Effective Interaction in the Nanometric Subsystem.....	88
3.6.4	Effective Mass Approximation of Exciton–Polaritons and Yukawa Potential ...	91
3.7	Applications.....	93
3.7.1	Single-Atom Manipulation.....	93
3.7.2	Atom Deflection by Optical Near Fields.....	97
3.7.3	Fundamental Properties of Optical Near-Field Microscopy.....	99
3.8	Outlook.....	104
	References.....	105

Abstract

The interactions between the matter and electromagnetic fields on a sub-wavelength scale are discussed from a microscopic viewpoint. On the basis of the projection operator method, effective interactions between nanometric subsystems, that is, optical near-field interactions mediated by massive virtual photons, are derived from a microscopic multipolar Hamiltonian. It is shown that the major part of the effective interaction exerted is the Yukawa potential.

3.1 Introduction

Several theoretical approaches, different from their viewpoints to optical near-field problems, have been proposed for a decade. The essential points in difference are related to what the optical near-field interaction is, or how materials respond to light confined in a small area less than the wavelength. The so-called classical approach that is based on the macroscopic Maxwell equations extends the theory to describe electromagnetic phenomena taking place on a sub-wavelength or even on a nanometer scale, while matter response to the electromagnetic field is represented by a macroscopic refractive index or a dielectric constant. The main concern in this approach is to find field distributions around the material system after solving the macroscopic Maxwell equations. Note that the electromagnetic fields in or near the material, which are averaged over a large dimension, but still smaller than the wavelength, satisfy the macroscopic Maxwell equations and that the “bare” electromagnetic fields on a nanometer scale should be governed by the microscopic Maxwell equations [1]. A number of analytical and numerical methods have been reported in order to obtain the relevant electromagnetic fields [2, 3].

The semiclassical approach employs the Schrödinger equation to handle the material (electron) response by focusing on the internal energy structure of the material system, though electromagnetic fields are still not quantized. According to the electronic state of the material system, the susceptibility at an arbitrary point of the system is obtained, and thus, the local electromagnetic field combined with the susceptibility determines the polarization locally induced in the system. Macroscopic electromagnetic fields are then given by the macroscopic Maxwell equations with the induced polarization as a source term. We have a final solution of the problem after the induced polarization, and the macroscopic electromagnetic fields are made self-consistent by iteration. It should be noted that the induced

polarization at an arbitrary position is affected by the local electromagnetic fields at other positions, as well as the same position, because the susceptibility is nonlocal [4]. This nonlocality becomes important when the electron correlation length of the material system is comparable to the spatial averaging length of the microscopic electromagnetic fields [5, 6]. Recent advances in optical near-field experiments may reveal the nature of these phenomena.

The semiclassical approach implies the importance of the coupling between the matter and the electromagnetic fields on a sub-wavelength scale and of a microscopic formulation. If electromagnetic fields are quantized as well, we may also expect the analogous discussion provoked in the realm of quantum optics to open up a new field. However, it is difficult to develop a quantized nonlocal theory, and the difficulty forces us to adopt another standpoint. In this article, we avoid it and will develop a new formulation within a quantum-mechanical framework, putting matter excitations on an equal footing with photons.

3.1.1 Basic Idea and Massive Virtual Photon Model

There is no way to obtain all the energy states of all the microscopic constituents in a complicated system or to describe time evolution of the states. In most cases, one prefers to have any information about characteristic states or observables, instead of all the exact solutions. Projection operator methods and elementary excitation modes have been developed in this context and will be discussed in the following sections.

Let us consider an optical near-field system from this viewpoint. It consists of a macroscopic matter system larger than the wavelength of incident light (light source, fiber probe, prism substrate, optical detector, etc.) and a nanometric aperture or a protrusion of the probe tip as well as a nanometric matter system (sample material). Those systems are interacting with one another via optical near fields. Because of the huge number of degrees of freedom and complexity, it is impossible to obtain exact solutions of the system from the viewpoint of an atomic many-body system that consists of electrons and nuclei interacting with photons. We are not interested in exact solutions of such a many-body system. Instead, we are willing to know answers of fundamental optical near-field problems: What kind of interaction is exerted between the probe tip and sample? How is the interaction manifested? Why does the lateral resolution exceed the diffraction limit of the incident light? What kind of change should be made if we remove the assumption that the matter system is isolated from the other systems when we study the interaction between propagating light and matter.

The massive virtual photon model [7–9] has been proposed in order to examine such fundamental issues and promote specific advanced experiments. The model assumes that the effective optical near-field interaction between a probe and sample system is described by the Yukawa potential, as a result of mediation of a massive virtual photon, not the usual massless photon. It indicates that the interaction range is finite and that it is active only if the probe and the sample are closely located. According to the Heisenberg uncertainty relation, a process where the energy

conservation law is not satisfied can occur in a short period compared with the macroscopic time required for measurement. The massive virtual photon is the quantum associated with such a process and is a so-called dressed photon whose mass is attributed to the coupling with matter excitation, as will be discussed later.

It is well known that a scalar meson with effective mass m_{eff} satisfies the Klein-Gordon equation [10]

$$\left[\Delta - \left(\frac{m_{\text{eff}}c}{\hbar} \right)^2 \right] \phi(\mathbf{r}) = 0, \quad (3.1)$$

and that it has a solution

$$\phi(\mathbf{r}) = \frac{\exp\left(-\frac{m_{\text{eff}}c}{\hbar}r\right)}{r}. \quad (3.2)$$

Here \hbar and c are the Planck constant divided by 2π and the speed of light in vacuum, respectively. By way of comparison, we note that an electric field \mathbf{E} as a function of an angular frequency ω and position \mathbf{r} is described by the Helmholtz equation [1]:

$$\left[\Delta + \left(\frac{\omega}{c} \right)^2 \right] \mathbf{E}(\mathbf{r}, \omega) = -\frac{1}{\varepsilon_0} \left(\frac{\omega}{c} \right)^2 \mathbf{P}(\mathbf{r}, \omega). \quad (3.3)$$

One can infer that the electric field given by (3.3) is transformed into the Klein-Gordon field after the induced polarization $\mathbf{P}(\mathbf{r}, \omega)$ is renormalized into the effective mass as a result of many-body effects.

Using the projection operator method and elementary excitation modes, we formulate the idea of the virtual photon model and the optical near-field problems in the following sections. At the same time, some examples related to atom photonics and nanophotonics are discussed as an application of the formulation. Before getting into the detail of the formulation, the projection operator method is briefly outlined. Starting with the definition of the projection operator, some useful properties are discussed in the next section. Then the effective operator and effective interaction are derived in Sect. 3.3. In Sect. 3.4, the ‘‘bare interaction’’ is described in two ways in order to obtain more explicit expressions of the effective interaction. We introduce elementary excitation modes to describe electronic polarization in macroscopic matter systems in Sect. 3.5; in particular, the exciton–polariton concept is discussed in some detail. Section 3.6 is devoted to the main part of the formulation. As a related application of our approach, we address in Sect. 3.7 basic problems of single-atom manipulation with a near-field optical probe as well as conventional problems on optical near-field microscopy. Finally, we discuss prospects for this study.

3.2 Projection Operator Method

In this section, we discuss what the projection operator is and what kind of properties it has.

3.2.1 Definition of the Projection Operator

When one considers an interacting system such as a system consisting of an isolated quantum system and electromagnetic field, the Hamiltonian operator \hat{H} for the total system is represented as a sum of \hat{H}_0 and \hat{V} as

$$\hat{H} = \hat{H}_0 + \hat{V}, \quad (3.4)$$

where \hat{H}_0 describes the isolated system, while \hat{V} represents the interaction. If eigenstates and eigenvalues of the Hamiltonian \hat{H} are written as $|\psi_j\rangle$ and E_j , respectively, the following Schrödinger equation holds:

$$\hat{H} |\psi_j\rangle = E_j |\psi_j\rangle. \quad (3.5)$$

Here the suffix j is used to specify the quantum numbers that distinguish each eigenstate. In a similar way, we denote eigenstates of the Hamiltonian \hat{H}_0 as $|\phi_j\rangle$. Then we define the projection operator P as

$$P = \sum_{j=1}^N |\phi_j\rangle \langle \phi_j|, \quad (3.6)$$

where N is an arbitrary integer, but it is preferably a small number in practice. Operating with the projection operator on an arbitrary state $|\psi\rangle$, we obtain

$$P |\psi\rangle = \sum_{j=1}^N |\phi_j\rangle \langle \phi_j | \psi \rangle. \quad (3.7)$$

From this relation, it follows that the projection operator transforms an arbitrary state $|\psi\rangle$ into the P space spanned by the eigenstates $|\phi_j\rangle$. We have defined the projection operator based on stationary states of the Schrödinger equation. Readers who are interested in the time-dependent approach to the projection operator method are referred to [11–16].

3.2.2 Properties of the Projection Operator

Using the projection operator P , we can derive an effective operator \hat{O}_{eff} for an arbitrary operator \hat{O} that corresponds to a physical observable. In order to perform the calculation, we begin with some elementary and useful properties of the projection operator. Since the eigenstate $|\phi_j\rangle$ is orthonormalized, the projection operator P satisfies

$$P = P^\dagger, \quad P^2 = P. \quad (3.8)$$

The complementary operator Q given by

$$Q = 1 - P \quad (3.9)$$

satisfies

$$Q = Q^\dagger, \quad Q^2 = Q. \quad (3.10)$$

Any state in the P space is orthogonal to any state in the Q space, and thus, we have

$$PQ = QP = 0. \quad (3.11)$$

Note that $|\phi_j\rangle$ is an eigenstate of \hat{H}_0 , so the commutator of the projection operator and \hat{H}_0 vanishes:

$$[P, \hat{H}_0] = P\hat{H}_0 - \hat{H}_0P = 0, \quad (3.12a)$$

$$[Q, \hat{H}_0] = Q\hat{H}_0 - \hat{H}_0Q = 0. \quad (3.12b)$$

3.3 Effective Operator and Effective Interaction

Dividing the eigenstates $|\psi_j\rangle$ into two groups, we define $|\psi_j^{(1)}\rangle$ in the P space and $|\psi_j^{(2)}\rangle$ in the Q space as follows:

$$|\psi_j^{(1)}\rangle = P |\psi_j\rangle, \quad (3.13a)$$

$$|\psi_j^{(2)}\rangle = Q |\psi_j\rangle. \quad (3.13b)$$

Then we obtain a set of equations for $|\psi_j^{(1)}\rangle$ and $|\psi_j^{(2)}\rangle$. From (3.9), we have

$$|\psi_j\rangle = P |\psi_j^{(1)}\rangle + Q |\psi_j^{(2)}\rangle, \quad (3.14)$$

and from (3.4) and (3.5),

$$(E_j - \hat{H}_0) |\psi_j\rangle = \hat{V} |\psi_j\rangle \quad (3.15)$$

is derived. Inserting (3.14) into (3.15), we obtain

$$(E_j - \hat{H}_0) P |\psi_j^{(1)}\rangle + (E_j - \hat{H}_0) Q |\psi_j^{(2)}\rangle = \hat{V} P |\psi_j^{(1)}\rangle + \hat{V} Q |\psi_j^{(2)}\rangle. \quad (3.16)$$

Operating with P from the left on (3.16) and using (3.8), (3.11), (3.12a), and (3.12b), we obtain

$$\left(E_j - \hat{H}_0\right) P \left|\psi_j^{(1)}\right\rangle = P \hat{V} P \left|\psi_j^{(1)}\right\rangle + P \hat{V} Q \left|\psi_j^{(2)}\right\rangle. \quad (3.17)$$

Similarly, applying Q from the left on (3.16), we have

$$\left(E_j - \hat{H}_0\right) Q \left|\psi_j^{(2)}\right\rangle = Q \hat{V} P \left|\psi_j^{(1)}\right\rangle + Q \hat{V} Q \left|\psi_j^{(2)}\right\rangle. \quad (3.18)$$

From (3.18), it is possible to formally express $Q \left|\psi_j^{(2)}\right\rangle$ in terms of $P \left|\psi_j^{(1)}\right\rangle$ as

$$\begin{aligned} Q \left|\psi_j^{(2)}\right\rangle &= \left(E_j - \hat{H}_0 - Q \hat{V}\right)^{-1} Q \hat{V} P \left|\psi_j^{(1)}\right\rangle \\ &= \left\{ \left(E_j - \hat{H}_0\right) \left[1 - \left(E_j - \hat{H}_0\right)^{-1} Q \hat{V} \right] \right\}^{-1} Q \hat{V} P \left|\psi_j^{(1)}\right\rangle \\ &= \hat{J} \left(E_j - \hat{H}_0\right)^{-1} Q \hat{V} P \left|\psi_j^{(1)}\right\rangle, \end{aligned} \quad (3.19)$$

where the operator \hat{J} is defined as

$$\hat{J} = \left[1 - \left(E_j - \hat{H}_0\right)^{-1} Q \hat{V} \right]^{-1}. \quad (3.20)$$

Substituting (3.19) into the second term on the right-hand side of (3.17), one obtains the equation for $P \left|\psi_j^{(1)}\right\rangle$:

$$\begin{aligned} \left(E_j - \hat{H}_0\right) P \left|\psi_j^{(1)}\right\rangle &= P \hat{V} P \left|\psi_j^{(1)}\right\rangle + P \hat{V} \hat{J} \left(E_j - \hat{H}_0\right)^{-1} Q \hat{V} P \left|\psi_j^{(1)}\right\rangle \\ &= P \hat{V} \hat{J} \left\{ \hat{J}^{-1} + \left(E_j - \hat{H}_0\right)^{-1} Q \hat{V} \right\} P \left|\psi_j^{(1)}\right\rangle \\ &= P \hat{V} \hat{J} P \left|\psi_j^{(1)}\right\rangle. \end{aligned} \quad (3.21)$$

On the other hand, if (3.19) is inserted into (3.14), then we have

$$\begin{aligned}
 |\psi_j\rangle &= P \left| \psi_j^{(1)} \right\rangle + \hat{J} \left(E_j - \hat{H}_0 \right)^{-1} Q \hat{V} P \left| \psi_j^{(1)} \right\rangle \\
 &= \hat{J} \left\{ \hat{J}^{-1} + \left(E_j - \hat{H}_0 \right)^{-1} Q \hat{V} \right\} P \left| \psi_j^{(1)} \right\rangle \\
 &= \hat{J} P \left| \psi_j^{(1)} \right\rangle .
 \end{aligned} \tag{3.22}$$

Noticing the normalization condition for $|\psi_j\rangle$ and $|\psi_j^{(1)}\rangle$, it is possible to rewrite (3.22):

$$|\psi_j\rangle = \hat{J} P \left(P \hat{J}^\dagger \hat{J} P \right)^{-1/2} \left| \psi_j^{(1)} \right\rangle . \tag{3.23}$$

Since $|\psi_j\rangle$ has been expressed in terms of $|\psi_j^{(1)}\rangle$, one can obtain an effective operator \hat{O}_{eff} from the following relation:

$$\langle \psi_i | \hat{O} | \psi_j \rangle = \langle \psi_i^{(1)} | \hat{O}_{\text{eff}} | \psi_j^{(1)} \rangle . \tag{3.24}$$

Substituting (3.23) on the left-hand side of (3.24) and comparing it with the right-hand side, we obtain [17–19]

$$\hat{O}_{\text{eff}} = \left(P \hat{J}^\dagger \hat{J} P \right)^{-1/2} \left(P \hat{J}^\dagger \hat{O} \hat{J} P \right) \left(P \hat{J}^\dagger \hat{J} P \right)^{-1/2} . \tag{3.25}$$

If \hat{V} is taken as \hat{O} , then the effective interaction operator \hat{V}_{eff} is written as

$$\hat{V}_{\text{eff}} = \left(P \hat{J}^\dagger \hat{J} P \right)^{-1/2} \left(P \hat{J}^\dagger \hat{V} \hat{J} P \right) \left(P \hat{J}^\dagger \hat{J} P \right)^{-1/2} . \tag{3.26}$$

This is what we are searching for. As expected, \hat{V}_{eff} is defined so as to operate only on states in the P space. Once the bare interaction \hat{V} is given, it only remains to obtain the unknown operator \hat{J} .

3.3.1 Equation for the Operator \hat{J} and Its Approximate Solution

In order to obtain an explicit form of the operator \hat{J} , let us consider the operator $[\hat{J}, \hat{H}_0] P$ and apply it to the state $|\psi_j\rangle$. This yields

$$\begin{aligned}
 [\hat{J}, \hat{H}_0] P |\psi_j\rangle &= \left(\hat{J} \hat{H}_0 - \hat{H}_0 \hat{J} \right) P |\psi_j\rangle \\
 &= \left\{ \left(E_j - \hat{H}_0 \right) \hat{J} - \hat{J} \left(E_j - \hat{H}_0 \right) \right\} P |\psi_j\rangle .
 \end{aligned} \tag{3.27}$$

We replace the first term $(E_j - \hat{H}_0)$ in (3.27) by \hat{V} , which gives

$$\left[\hat{J}, \hat{H}_0 \right] P |\psi_j\rangle = \hat{V} \hat{J} P |\psi_j\rangle - \hat{J} (E_j - \hat{H}_0) P |\psi_j\rangle. \quad (3.28)$$

Using (3.17) and (3.19), the second term of (3.28) can be rewritten as

$$\begin{aligned} \hat{J} (E_j - \hat{H}_0) P |\psi_j\rangle &= \hat{J} (E_j - \hat{H}_0) P |\psi_j^{(1)}\rangle \\ &= \hat{J} \left\{ P \hat{V} P |\psi_j^{(1)}\rangle + P \hat{V} Q |\psi_j^{(2)}\rangle \right\} \\ &= \hat{J} P \hat{V} \left\{ P |\psi_j^{(1)}\rangle + \hat{J} (E_j - \hat{H}_0)^{-1} Q \hat{V} P |\psi_j^{(1)}\rangle \right\} \\ &= \hat{J} P \hat{V} \hat{J} \left\{ \hat{J}^{-1} + (E_j - \hat{H}_0)^{-1} Q \hat{V} \right\} P |\psi_j^{(1)}\rangle. \end{aligned} \quad (3.29)$$

Making use of (3.20) and noting that $P |\psi_j^{(1)}\rangle = P |\psi_j\rangle$, we can rewrite (3.28) as

$$\left[\hat{J}, \hat{H}_0 \right] P |\psi_j\rangle = \hat{V} \hat{J} P |\psi_j\rangle - \hat{J} P \hat{V} \hat{J} P |\psi_j\rangle. \quad (3.30)$$

Therefore, we have for the operator \hat{J}

$$\left[\hat{J}, \hat{H}_0 \right] P = \hat{V} \hat{J} P - \hat{J} P \hat{V} \hat{J} P, \quad (3.31)$$

where all operators involved are known except \hat{J} .

In order to solve (3.31) perturbatively, let us assume

$$\hat{J} = \sum_{n=0}^{\infty} g^n \hat{J}^{(n)}, \quad (3.32)$$

where the n th term $\hat{J}^{(n)}$ contains n \hat{V} 's and $\hat{J}^{(0)} = P$. Substituting (3.32) into (3.31) and equating terms of order g^n on the two sides, we successively obtain $\hat{J}^{(1)}$, $\hat{J}^{(2)}$, \dots , $\hat{J}^{(n)}$. For example, noting the identity

$$\begin{aligned} Q \left[\hat{J}^{(1)}, \hat{H}_0 \right] P &= Q \hat{V} \hat{J}^{(0)} P - Q \hat{J}^{(0)} P \hat{V} \hat{J}^{(0)} P \\ &= Q \hat{V} P, \end{aligned} \quad (3.33)$$

we take the matrix element of (3.33) with $|\psi_j\rangle$:

$$\begin{aligned} \langle \psi_i | Q \left[\hat{J}^{(1)}, \hat{H}_0 \right] P | \psi_j \rangle &= \langle \psi_i | Q \hat{J}^{(1)} \left(E_P^0 - E_Q^0 \right) P | \psi_j \rangle \\ &= \langle \psi_i | Q \hat{V} P | \psi_j \rangle, \end{aligned} \quad (3.34)$$

where we used the eigenvalues E_P^0 and E_Q^0 of the Hamiltonian \hat{H}_0 in the P space and Q space, respectively. From (3.34),

$$\hat{J}^{(1)} = Q \hat{V} \left(E_P^0 - E_Q^0 \right)^{-1} P. \quad (3.35)$$

Higher orders of $\hat{J}^{(n)}$ are successively given in a similar way.

3.3.2 Effective Interaction Operator in an Approximation

After inserting the perturbative solution discussed above into the operator \hat{J} , it is possible to approximately express \hat{V}_{eff} in (3.26), which operates only on states in the P space. Using $\hat{J}^{(0)}$, one can obtain \hat{V}_{eff} in lowest order as

$$\hat{V}_{\text{eff}} = P \hat{V} P, \quad (3.36)$$

which is equivalent to the so-called bare interaction because all effects from the Q space are neglected. The multipole Hamiltonian, which will be discussed as one of the bare interactions in the next section, cannot contribute to (3.36) if transverse photon states are not included in the P space. It is therefore necessary to employ $\hat{J}^{(1)}$ at least, in order to include Q -space effects. Then we have

$$\hat{V}_{\text{eff}} = 2P \hat{V} Q \left(E_P^0 - E_Q^0 \right)^{-1} Q \hat{V} P, \quad (3.37)$$

and in the following, we discuss the optical near-field interaction based on the formula (3.37). Whenever one improves the approximation of \hat{J} , one can examine the higher-order effects originating in the Q space. These procedures correspond to how to obtain many-body Green's functions for matter systems or Green's functions for photons "dressed with matter excitations" [20].

3.4 Electromagnetic Interaction with Matter: Minimal-Coupling and Multipole Hamiltonians

The “bare interaction” must be specified in order to obtain a more explicit expression of the effective interaction. There are two ways to describe the interaction between an electromagnetic field and a charged particle. One is to use the minimal-coupling Hamiltonian, and the other is to employ the multipole Hamiltonian. These two Hamiltonians are related to each other by a unitary transformation, and there are, in principle, no problems regardless of which is adopted [21–23]. However, it should be noted that the complexity of description depends on each problem: It may be easier for the minimal-coupling Hamiltonian formalism to describe one problem and more difficult to describe another.

3.4.1 Minimal-Coupling Hamiltonian

We can derive the minimal-coupling Hamiltonian for a charged particle, that is, the electromagnetic interaction with a charged particle, by imposing the local gauge invariance on the Hamiltonian describing free particle motion [24]. The minimal-coupling Hamiltonian is defined such that the Schrödinger equation is not changed if a wave function $\psi(\mathbf{r}, t)$ that satisfies the Schrödinger equation is transformed by the phase transformation $\chi(\mathbf{r}, t)$ to

$$\psi'(\mathbf{r}, t) = \exp[i\chi(\mathbf{r}, t)] \psi(\mathbf{r}, t) , \quad (3.38)$$

and if vector potential $\mathbf{A}(\mathbf{r}, t)$ and scalar potential $U(\mathbf{r}, t)$ are transformed by the following gauge transformation [10, 21, 25, 26]:

$$\mathbf{A}'(\mathbf{r}, t) = \mathbf{A}(\mathbf{r}, t) + \frac{\hbar}{e} \nabla \chi(\mathbf{r}, t) , \quad (3.39a)$$

$$U'(\mathbf{r}, t) = U(\mathbf{r}, t) - \frac{\hbar}{e} \frac{\partial}{\partial t} \chi(\mathbf{r}, t) . \quad (3.39b)$$

Here \hbar and e are the Planck constant divided by 2π and the electric charge of the particle. Let us simply assume the electromagnetic fields to be classical in this section. In order to satisfy the above requirement, it follows that the Hamiltonian must be

$$H' = \frac{1}{2m} [\mathbf{p} - e\mathbf{A}'(\mathbf{r}, t)]^2 + eU'(\mathbf{r}, t) , \quad (3.40)$$

where the mass and the momentum of the particle are denoted by m and \mathbf{p} , respectively. For confirmation, (3.38), (3.39a), (3.39b), and (3.40) are substituted into the Schrödinger equation:

$$i\hbar \frac{\partial}{\partial t} \psi'(\mathbf{r}, t) = H' \psi'(\mathbf{r}, t) . \quad (3.41)$$

Noting that the momentum \mathbf{p} must be an operator, $-i\hbar\nabla$, it follows that the left-hand side of (3.41) reads

$$-\hbar \exp[i\chi(\mathbf{r}, t)] \frac{\partial\chi(\mathbf{r}, t)}{\partial t} \psi(\mathbf{r}, t) + i\hbar \exp[i\chi(\mathbf{r}, t)] \frac{\partial\psi(\mathbf{r}, t)}{\partial t} . \quad (3.42)$$

On the other hand, the right-hand side of (3.41) can be rewritten as

$$\begin{aligned} & \frac{1}{2m} \left[-i\hbar\nabla - e \left\{ \mathbf{A}(\mathbf{r}, t) + \frac{\hbar}{e} \nabla\chi(\mathbf{r}, t) \right\} \right]^2 \exp[i\chi(\mathbf{r}, t)] \psi(\mathbf{r}, t) \\ & + e \left\{ U(\mathbf{r}, t) - \frac{\hbar}{e} \frac{\partial}{\partial t} \chi(\mathbf{r}, t) \right\} \exp[i\chi(\mathbf{r}, t)] \psi(\mathbf{r}, t) \\ & = \exp[i\chi(\mathbf{r}, t)] \left\{ \frac{1}{2m} [-i\hbar\nabla - e\mathbf{A}(\mathbf{r}, t)]^2 + eU(\mathbf{r}, t) \right\} \psi(\mathbf{r}, t) \\ & \quad - \hbar \exp[i\chi(\mathbf{r}, t)] \frac{\partial\chi(\mathbf{r}, t)}{\partial t} \psi(\mathbf{r}, t) . \end{aligned} \quad (3.43)$$

Therefore, we can leave the Schrödinger equation unchanged if

$$i\hbar \frac{\partial}{\partial t} \psi(\mathbf{r}, t) = H\psi(\mathbf{r}, t) , \quad (3.44a)$$

$$H = \frac{1}{2m} [-i\hbar\nabla - e\mathbf{A}(\mathbf{r}, t)]^2 + eU(\mathbf{r}, t) . \quad (3.44b)$$

In other words, the relevant Hamiltonian is obtained by formally adding $eU(\mathbf{r}, t)$ and replacing \mathbf{p} by $\mathbf{p} - e\mathbf{A}(\mathbf{r}, t)$ in the Hamiltonian for a free particle. From (3.44b), the interaction Hamiltonian for the electromagnetic field and the charged particle consists of two parts:

$$H_1 = -\frac{e}{m} \mathbf{p} \cdot \mathbf{A}(\mathbf{r}, t), \quad (3.45a)$$

$$H_2 = \frac{e^2}{2m} A^2(\mathbf{r}, t). \quad (3.45b)$$

Advantages of this form of the Hamiltonian are that it can easily describe relativistic covariance and is firmly rooted in gauge theory [25, 26]. However, it has the disadvantage that exact description including retardation is cumbersome in the Coulomb gauge ($\nabla \cdot \mathbf{A} = 0$), where the transversality of light is considered to be important in order to handle the interaction between light and matter as a many-body system.

3.4.2 Multipole Hamiltonian

In this subsection, we discuss another form of the light–matter interaction via a unitary transformation of the minimal-coupling Hamiltonian, which removes the disadvantages mentioned above. Such Hamiltonian has a simple form without the static Coulomb interaction and can exactly describe the retardation by exchanging only transverse photons [23].

Let us consider a charged-particle system confined in a microscopic area and hereinafter call it a molecule. Electric neutrality of the molecule is assumed, and thus, it may be an atom or a molecule as a physical entity. In the following, we choose a two-molecule system as an example and look for an appropriate Hamiltonian. When the wavelength of electromagnetic waves is much greater than the molecular dimension, the vector potential $\mathbf{A}(\mathbf{R})$ at the center position \mathbf{R} of a molecule is the same as $\mathbf{A}(\mathbf{q})$, independent of the position \mathbf{q} of an electric charge in the molecule:

$$\mathbf{A}(\mathbf{q}) = \mathbf{A}(\mathbf{R}) . \quad (3.46)$$

From (3.46), it follows that $\mathbf{B} = \nabla \times \mathbf{A} = 0$, and thus, we can neglect the interaction between the particle and the magnetic field. Moreover, the electric dipole interaction, for simplicity, is taken into account, that is, higher multipoles are neglected. We assume in addition that the electron exchange interaction is also negligible. Then the Lagrangian L for the system, consisting of three parts L_{mol} , L_{rad} , and L_{int} , can be written as

$$L = L_{\text{mol}} + L_{\text{rad}} + L_{\text{int}} , \quad (3.47a)$$

$$L_{\text{mol}} = \sum_{\zeta=1}^2 \left\{ \sum_{\alpha} \frac{m_{\alpha} \dot{\mathbf{q}}_{\alpha}^2(\zeta)}{2} - V(\zeta) \right\} , \quad (3.47b)$$

$$L_{\text{rad}} = \frac{\epsilon_0}{2} \int \left\{ \dot{\mathbf{A}}^2 - c^2 (\nabla \times \mathbf{A})^2 \right\} d^3r , \quad (3.47c)$$

$$L_{\text{int}} = \sum_{\zeta=1}^2 \sum_{\alpha} e \dot{\mathbf{q}}_{\alpha}(\zeta) \cdot \mathbf{A}(\mathbf{R}_{\zeta}) - V_{\text{inter}} , \quad (3.47d)$$

where the index ζ is used to distinguish the molecules 1 and 2 and α is used to specify a charged particle in a molecule. The energy of the charged particles with mass m_{α} and velocity $\dot{\mathbf{q}}_{\alpha}$ in the Coulomb potential $V(\zeta)$ is denoted by L_{mol} , while L_{rad} represents the energy of the electromagnetic field in free space. The third term in the Lagrangian represents the interaction between the charge and the electromagnetic field and the Coulomb interaction V_{inter} between molecules 1 and 2, which is given by

$$V_{\text{inter}} = \frac{1}{4\pi\epsilon_0 R^3} \{ \boldsymbol{\mu}(1) \cdot \boldsymbol{\mu}(2) - 3(\boldsymbol{\mu}(1) \cdot \mathbf{e}_R)(\boldsymbol{\mu}(2) \cdot \mathbf{e}_R) \} . \quad (3.48)$$

Here $R = |\mathbf{R}| = |\mathbf{R}_1 - \mathbf{R}_2|$ denotes the distance between the centers of molecules 1 and 2, and \mathbf{e}_R is \mathbf{R}/R , the unit vector in the direction of \mathbf{R} . The electric dipole moments of molecules 1 and 2 are $\boldsymbol{\mu}$ (1) and $\boldsymbol{\mu}$ (2), respectively.

In order to simplify the interaction Hamiltonian without changing the equations of motion, we carry out the Power–Zienau–Woolley transformation [21] on the original Lagrangian L :

$$L_{\text{mult}} = L - \frac{d}{dt} \int \mathbf{P}^\perp(\mathbf{r}) \cdot \mathbf{A}(\mathbf{r}) d^3r, \quad (3.49)$$

where $\mathbf{P}^\perp(\mathbf{r})$ is the transverse component of the polarization density $\mathbf{P}(\mathbf{r})$; this means that transverse photons can only contribute to the second term in (3.49). The polarization density $\mathbf{P}(\mathbf{r})$ is

$$\begin{aligned} \mathbf{P}(\mathbf{r}) &= \sum_{\zeta, \alpha} e(\mathbf{q}_\alpha - \mathbf{R}_\zeta) \int_0^1 \delta(\mathbf{r} - \mathbf{R}_\zeta - \lambda(\mathbf{q}_\alpha - \mathbf{R}_\zeta)) d\lambda \\ &= \sum_{\zeta, \alpha} e(\mathbf{q}_\alpha - \mathbf{R}_\zeta) \left[1 - \frac{1}{2!} \{(\mathbf{q}_\alpha - \mathbf{R}_\zeta) \cdot \nabla\} \right. \\ &\quad \left. + \frac{1}{3!} \{(\mathbf{q}_\alpha - \mathbf{R}_\zeta) \cdot \nabla\}^2 - \dots \right] \delta(\mathbf{r} - \mathbf{R}_\zeta), \end{aligned} \quad (3.50)$$

and only the electric dipole term is retained:

$$\begin{aligned} \mathbf{P}(\mathbf{r}) &= \sum_{\zeta, \alpha} e(\mathbf{q}_\alpha - \mathbf{R}_\zeta) \delta(\mathbf{r} - \mathbf{R}_\zeta) \\ &= \boldsymbol{\mu}(1) \delta(\mathbf{r} - \mathbf{R}_1) + \boldsymbol{\mu}(2) \delta(\mathbf{r} - \mathbf{R}_2). \end{aligned} \quad (3.51)$$

Note that the current density $\mathbf{j}(\mathbf{r})$ is

$$\mathbf{j}(\mathbf{r}) = \sum_{\zeta, \alpha} e \mathbf{q}_\alpha \delta(\mathbf{r} - \mathbf{R}_\zeta), \quad (3.52)$$

and the transverse component of the current density is related to the transverse component of the polarization density:

$$\mathbf{j}^\perp(\mathbf{r}) = \frac{d\mathbf{P}^\perp(\mathbf{r})}{dt}. \quad (3.53)$$

Using (3.52) and (3.53), we can rewrite the interaction Lagrangian L_{int} as

$$\begin{aligned} L_{\text{int}} &= \int \mathbf{j}^{\perp}(\mathbf{r}) \cdot \mathbf{A}(\mathbf{r}) \, d^3r - V_{\text{inter}} \\ &= \int \frac{d\mathbf{P}^{\perp}(\mathbf{r})}{dt} \cdot \mathbf{A}(\mathbf{r}) \, d^3r - V_{\text{inter}} , \end{aligned} \quad (3.54)$$

and thus, L_{mult} given by (3.49) becomes

$$\begin{aligned} L_{\text{mult}} &= L - \int \frac{d\mathbf{P}^{\perp}(\mathbf{r})}{dt} \cdot \mathbf{A}(\mathbf{r}) \, d^3r - \int \mathbf{P}^{\perp}(\mathbf{r}) \cdot \dot{\mathbf{A}}(\mathbf{r}) \, d^3r \\ &= L_{\text{mol}} + L_{\text{rad}} - \int \mathbf{P}^{\perp}(\mathbf{r}) \cdot \dot{\mathbf{A}}(\mathbf{r}) \, d^3r - V_{\text{inter}} . \end{aligned} \quad (3.55)$$

Here we recall the definition of the momentum \mathbf{p}_{α} conjugate to \mathbf{q}_{α} and $\mathbf{\Pi}(\mathbf{r})$ to $\mathbf{A}(\mathbf{r})$,

$$\mathbf{p}_{\alpha} = \frac{\partial L_{\text{mult}}}{\partial \dot{\mathbf{q}}_{\alpha}} = \frac{\partial L_{\text{mol}}}{\partial \dot{\mathbf{q}}_{\alpha}} = m_{\alpha} \dot{\mathbf{q}}_{\alpha} , \quad (3.56)$$

$$\begin{aligned} \mathbf{\Pi}(\mathbf{r}) &= \frac{\partial L_{\text{mult}}}{\partial \dot{\mathbf{A}}(\mathbf{r})} = \frac{\partial L_{\text{rad}}}{\partial \dot{\mathbf{A}}(\mathbf{r})} - \frac{\partial}{\partial \dot{\mathbf{A}}(\mathbf{r})} \int \mathbf{P}^{\perp}(\mathbf{r}) \cdot \dot{\mathbf{A}}(\mathbf{r}) \, d^3r \\ &= \varepsilon_0 \dot{\mathbf{A}}(\mathbf{r}) - \mathbf{P}^{\perp}(\mathbf{r}) = -\varepsilon_0 \mathbf{E}^{\perp}(\mathbf{r}) - \mathbf{P}^{\perp}(\mathbf{r}) . \end{aligned} \quad (3.57)$$

Since we have the relation between the electric field $\mathbf{E}(\mathbf{r})$ and the electric displacement $\mathbf{D}(\mathbf{r})$, those transverse components also satisfy

$$\mathbf{D}^{\perp}(\mathbf{r}) = \varepsilon_0 \mathbf{E}^{\perp}(\mathbf{r}) + \mathbf{P}^{\perp}(\mathbf{r}) , \quad (3.58)$$

and thus, the momentum $\mathbf{\Pi}(\mathbf{r})$ can be rewritten as

$$\mathbf{\Pi}(\mathbf{r}) = -\mathbf{D}^{\perp}(\mathbf{r}) . \quad (3.59)$$

By putting them together, canonical transformation of the Lagrangian L_{mult} gives a new Hamiltonian H_{mult} :

$$\begin{aligned}
 H_{\text{mult}} &= \sum_{\zeta, \alpha} \mathbf{p}_{\alpha}(\zeta) \cdot \dot{\mathbf{q}}_{\alpha}(\zeta) + \int \boldsymbol{\Pi}(\mathbf{r}) \cdot \dot{\mathbf{A}}(\mathbf{r}) d^3r - L_{\text{mult}} \\
 &= \sum_{\zeta} \left\{ \sum_{\alpha} \frac{\mathbf{p}_{\alpha}^2(\zeta)}{2m_{\alpha}} + V(\zeta) \right\} \\
 &\quad + \left\{ \frac{1}{2} \int \left[\frac{\boldsymbol{\Pi}^2(\mathbf{r})}{\varepsilon_0} + \varepsilon_0 c^2 (\nabla \times \mathbf{A}(\mathbf{r}))^2 \right] d^3r \right\} \\
 &\quad + \frac{1}{\varepsilon_0} \int \mathbf{P}^{\perp}(\mathbf{r}) \cdot \boldsymbol{\Pi}(\mathbf{r}) d^3r + \frac{1}{2\varepsilon_0} \int |\mathbf{P}^{\perp}(\mathbf{r})|^2 d^3r + V_{\text{inter}}. \quad (3.60)
 \end{aligned}$$

It is possible to simplify (3.60) by separating $(1/2\varepsilon_0) \int |\mathbf{P}^{\perp}(\mathbf{r})|^2 d^3r$ into two parts: inter- and intramolecular. Let us consider the intermolecular part:

$$\frac{1}{2\varepsilon_0} \int \mathbf{P}_1^{\perp}(\mathbf{r}) \cdot \mathbf{P}_2^{\perp}(\mathbf{r}) d^3r. \quad (3.61)$$

Noting that

$$\mathbf{P}_2(\mathbf{r}) = \mathbf{P}_2^{\parallel}(\mathbf{r}) + \mathbf{P}_2^{\perp}(\mathbf{r}), \quad (3.62a)$$

$$\mathbf{P}_1^{\perp}(\mathbf{r}) \cdot \mathbf{P}_2^{\parallel}(\mathbf{r}) = 0, \quad (3.62b)$$

and

$$\begin{aligned}
 \mathbf{P}_1^{\perp}(\mathbf{r}) \cdot \mathbf{P}_2^{\perp}(\mathbf{r}) &= \mathbf{P}_1^{\perp}(\mathbf{r}) \cdot \left\{ \mathbf{P}_2^{\parallel}(\mathbf{r}) + \mathbf{P}_2^{\perp}(\mathbf{r}) \right\} \\
 &= \mathbf{P}_1^{\perp}(\mathbf{r}) \cdot \mathbf{P}_2(\mathbf{r}), \quad (3.63)
 \end{aligned}$$

we rewrite (3.61) as follows:

$$\begin{aligned}
\frac{1}{\varepsilon_0} \int \mathbf{P}_1^\perp(\mathbf{r}) \cdot \mathbf{P}_2^\perp(\mathbf{r}) d^3r &= \frac{1}{\varepsilon_0} \int \mathbf{P}_1^\perp(\mathbf{r}) \cdot \mathbf{P}_2(\mathbf{r}) d^3r \\
&= \sum_{i,j} \frac{\mu_i(1) \mu_j(2)}{\varepsilon_0} \int \delta_{ij}^\perp(\mathbf{r} - \mathbf{R}_1) \delta(\mathbf{r} - \mathbf{R}_2) d^3r \\
&= \sum_{i,j} \frac{\mu_i(1) \mu_j(2)}{\varepsilon_0} \delta_{ij}^\perp(\mathbf{R}_1 - \mathbf{R}_2) \\
&= - \sum_{i,j} \frac{\mu_i(1) \mu_j(2)}{4\pi \varepsilon_0 R^3} (\delta_{ij} - 3\hat{e}_{Ri} \hat{e}_{Rj}) \\
&= - \frac{1}{4\pi \varepsilon_0 R^3} \{ \boldsymbol{\mu}(1) \cdot \boldsymbol{\mu}(2) - 3(\boldsymbol{\mu}(1) \cdot \mathbf{e}_R)(\boldsymbol{\mu}(2) \cdot \mathbf{e}_R) \} ,
\end{aligned} \tag{3.64}$$

where we used (3.51) in the first line, and the following identities for the Dirac δ function and the δ dyadics, $\delta_{ij}^\parallel(\mathbf{r})$ and $\delta_{ij}^\perp(\mathbf{r})$, in the third line:

$$\delta_{ij} \delta(\mathbf{r}) = \delta_{ij}^\parallel(\mathbf{r}) + \delta_{ij}^\perp(\mathbf{r}) , \tag{3.65a}$$

$$\begin{aligned}
\delta_{ij}^\perp(\mathbf{r}) &= -\delta_{ij}^\parallel(\mathbf{r}) \\
&= -\frac{1}{(2\pi)^3} \int \hat{e}_{ki} \hat{e}_{kj} \exp(i\mathbf{k} \cdot \mathbf{r}) d^3k \\
&= \nabla_i \nabla_j \left(\frac{1}{4\pi r} \right) = -\frac{1}{4\pi r^3} (\delta_{ij} - 3\hat{e}_{ri} \hat{e}_{rj}) .
\end{aligned} \tag{3.65b}$$

Here the subscripts i and j refer to Cartesian components, as usual. Since the exchange of the subscripts 1 and 2 gives the same result as (3.64), one can derive

$$\frac{1}{2\varepsilon_0} \int \mathbf{P}_1^\perp(\mathbf{r}) \cdot \mathbf{P}_2^\perp(\mathbf{r}) d^3r + V_{\text{inter}} = 0 . \tag{3.66}$$

Therefore, we can only take care of the intramolecular part of $(1/2\varepsilon_0) \times \int |\mathbf{P}^\perp(\mathbf{r})|^2 d^3r$ and have the simplified version of H_{mult} as

$$\begin{aligned}
H_{\text{mult}} = & \sum_{\zeta} \left\{ \sum_{\alpha} \frac{p_{\alpha}^2(\zeta)}{2m_{\alpha}} + V(\zeta) + \frac{1}{2\epsilon_0} \int |\mathbf{P}_{\zeta}^{\perp}(\mathbf{r})|^2 d^3r \right\} \\
& + \left\{ \frac{1}{2} \int \left[\frac{\mathbf{\Pi}^2(\mathbf{r})}{\epsilon_0} + \epsilon_0 c^2 (\nabla \times \mathbf{A}(\mathbf{r}))^2 \right] d^3r \right\} \\
& + \frac{1}{\epsilon_0} \int \mathbf{P}^{\perp}(\mathbf{r}) \cdot \mathbf{\Pi}(\mathbf{r}) d^3r, \tag{3.67}
\end{aligned}$$

where each line represents the charged particle motion in each molecule, free electromagnetic field, and the interaction, respectively. Since we can expand the polarization density in terms of 2^{ℓ} multipoles ($\ell = 1, 2, 3, \dots$), as shown in (3.50), we call H_{mult} the multipole Hamiltonian. The interaction part can be more explicitly written as

$$\begin{aligned}
\frac{1}{\epsilon_0} \int \mathbf{P}^{\perp}(\mathbf{r}) \cdot \mathbf{\Pi}(\mathbf{r}) d^3r &= -\frac{1}{\epsilon_0} \int \mathbf{P}^{\perp}(\mathbf{r}) \cdot \mathbf{D}^{\perp}(\mathbf{r}) d^3r \\
&= -\frac{1}{\epsilon_0} \int \mathbf{P}(\mathbf{r}) \cdot \mathbf{D}^{\perp}(\mathbf{r}) d^3r \\
&= -\frac{1}{\epsilon_0} \{ \boldsymbol{\mu}(1) \cdot \mathbf{D}^{\perp}(\mathbf{R}_1) + \boldsymbol{\mu}(2) \cdot \mathbf{D}^{\perp}(\mathbf{R}_2) \} \tag{3.68}
\end{aligned}$$

with the help of (3.51) and (3.59). When the considered system is quantized, quantities such as $\boldsymbol{\mu}(i)$ and $\mathbf{D}^{\perp}(\mathbf{R}_i)$ ($i = 1, 2$) should be replaced by the corresponding operators,

$$-\frac{1}{\epsilon_0} \{ \hat{\boldsymbol{\mu}}(1) \cdot \hat{\mathbf{D}}^{\perp}(\mathbf{R}_1) + \hat{\boldsymbol{\mu}}(2) \cdot \hat{\mathbf{D}}^{\perp}(\mathbf{R}_2) \}, \tag{3.69}$$

yielding the quantized multipole Hamiltonian.

3.5 Elementary Excitation Modes and Electronic Polarization

The concept of elementary excitations, or quasiparticles, has been discussed for a long time, and it is valuable for description of excited states, complex behavior, or dynamics of a many-body system [27–32]. Excited states of a many-body system are considered a collection of certain fundamental excited states that we call the elementary excitation. As a prerequisite, there must be a well-defined excitation energy whose value should be larger than the width of the relevant energy level. Then the relation between momentum \mathbf{p} and energy E of the elementary excitation, that is, $E = E(\mathbf{p})$, is referred to as the dispersion relation.

Phonons, as quanta of normal modes of crystal vibration, are well known as an example of the elementary excitation modes in a solid. The motion is collective, which means that the total number of phonons is independent of the number of crystal lattice. The momentum of the elementary excitation is $\mathbf{p} = \hbar \mathbf{k}$ in terms of

the wave vector \mathbf{k} of normal vibration, not the mechanical momentum of crystal lattice itself. The energy of the elementary excitation is also given by the angular frequency ω of the normal vibration as $E = \hbar\omega$.

As other examples of the elementary excitations, we have plasmons, which correspond to collective motion of electron density in interacting electron gas; polarons are quasiparticles originated from the coupling between conduction electrons and optical phonons; and magnons, corresponding to collective modes of spin-density waves. Excitons are also well known and describe the elementary excitation related to an electron–hole pair in a solid. As a limiting case, Frenkel excitons and Wannier excitons are frequently discussed. When the distance between the electron and hole in an exciton (Bohr radius of the exciton) is smaller than the atomic distance in the crystal, it is called a Frenkel exciton; Wannier excitons correspond to the opposite case, in which the Bohr radius of the exciton is larger than the lattice constant of the crystal.

3.5.1 Polaritons and Electronic Polarization

Let us consider the light–matter interaction on the basis of the exciton concept. Incident photons interact with matter and produce the successive creation and annihilation of excitons and photons in matter, that is, an electronic polarization field. This process indicates a new steady state with a new dispersion relation and energy due to the photon–exciton interaction. Normal modes, or elementary excitation modes for this coupled oscillation, are called polaritons. In particular, they are called exciton–polaritons due to the occurrence of the mixed states of photons and excitons. The situation is analogous to the case in which two coupled oscillations with angular frequencies ω_1 and ω_2 produce new normal oscillations with angular frequencies Ω_1 and Ω_2 . Dressed atom states in an atom–photon interacting system [33] are conceptually similar to the normal modes of the photon and electronic polarization field or exciton–polaritons as quasiparticles.

Rewriting the Hamiltonian for a photon–electron interacting system in terms of excitons, one can obtain the following Hamiltonian describing exciton–polaritons:

$$\hat{H} = \sum_{\mathbf{k}} \hbar\omega_{\mathbf{k}} \hat{a}_{\mathbf{k}}^{\dagger} \hat{a}_{\mathbf{k}} + \sum_{\mathbf{k}} \hbar\varepsilon_{\mathbf{k}} \hat{b}_{\mathbf{k}}^{\dagger} \hat{b}_{\mathbf{k}} + \sum_{\mathbf{k}} \hbar D \left(\hat{a}_{\mathbf{k}} + \hat{a}_{-\mathbf{k}}^{\dagger} \right) \left(\hat{b}_{\mathbf{k}}^{\dagger} + \hat{b}_{-\mathbf{k}} \right). \quad (3.70)$$

Here the first and second terms correspond to the Hamiltonians for free photons and free excitons, respectively, and the third term describes the photon–exciton interaction, whose coupling strength is $\hbar D$. The explicit expression for $\hbar D$ will be given in Sect. 3.6.3. Energies due to zero-point oscillation are suppressed in (3.70). Creation and annihilation operators for photons are denoted by $\hat{a}_{\mathbf{k}}^{\dagger}$ and $\hat{a}_{\mathbf{k}}$, while those for excitons are designated $\hat{b}_{\mathbf{k}}^{\dagger}$ and $\hat{b}_{\mathbf{k}}$. In the rewriting process, we define the creation and annihilation operators of excitons to be

$$\hat{b}_l^\dagger = \hat{c}_{l,c}^\dagger \hat{c}_{l,v}, \quad (3.71a)$$

$$\hat{b}_l = \hat{c}_{l,v}^\dagger \hat{c}_{l,c}, \quad (3.71b)$$

where we use the operator $\hat{c}_{l,v}$ that annihilates an electron in the valence band v within an atom at the lattice site l and its Hermitian conjugate operator $\hat{c}_{l,v}^\dagger$, as well as the operator $\hat{c}_{l,c}^\dagger$ that creates an electron in the conduction band c within an atom at the lattice site l , and its Hermitian conjugate operator $\hat{c}_{l,c}$. According to the conventional method, in addition, we introduce the operators

$$\hat{b}_k = \frac{1}{\sqrt{N}} \sum_l e^{-ik \cdot l} \hat{b}_l, \quad (3.72a)$$

$$\hat{b}_k^\dagger = \frac{1}{\sqrt{N}} \sum_l e^{ik \cdot l} \hat{b}_l^\dagger, \quad (3.72b)$$

in the momentum representation. Here the total number of lattice sites is assumed to be N in the crystal considered.

Once the Hamiltonian for exciton–polaritons is given by (3.70), one can obtain eigenstates and eigenenergies of exciton–polaritons, or the dispersion relation. For simplicity, we adopt the rotating wave approximation and neglect terms $\hat{a}_{-k}^\dagger \hat{b}_k^\dagger$ and $\hat{a}_k \hat{b}_{-k}$ which create or annihilate a photon and exciton at the same time and consider the Hamiltonian

$$\hat{H} = \sum_k \hat{H}_k, \quad (3.73a)$$

$$\hat{H}_k = \hbar \left(\omega_k \hat{a}_k^\dagger \hat{a}_k + \varepsilon_k \hat{b}_k^\dagger \hat{b}_k \right) + \hbar D \left(\hat{b}_k^\dagger \hat{a}_k + \hat{a}_k^\dagger \hat{b}_k \right). \quad (3.73b)$$

We next introduce the creation and annihilation operators of exciton–polaritons, $\hat{\xi}_1^\dagger$, $\hat{\xi}_2^\dagger$ and $\hat{\xi}_1$, $\hat{\xi}_2$, corresponding to new eigenfrequencies $\Omega_{k,1}$, $\Omega_{k,2}$, respectively. The Hamiltonian \hat{H}_k is assumed to be diagonalized in terms of $\hat{\xi}_1$, $\hat{\xi}_2$, and we rewrite (3.73b) as

$$\begin{aligned} \hat{H}_k &= \hbar \left(\Omega_{k,1} \hat{\xi}_1^\dagger \hat{\xi}_1 + \Omega_{k,2} \hat{\xi}_2^\dagger \hat{\xi}_2 \right) \\ &= \hbar \left(\hat{b}_k^\dagger, \hat{a}_k^\dagger \right) A \begin{pmatrix} \hat{b}_k \\ \hat{a}_k \end{pmatrix} \\ &= \hbar \left(a_{11} \hat{b}_k^\dagger \hat{b}_k + a_{12} \hat{b}_k^\dagger \hat{a}_k + a_{21} \hat{a}_k^\dagger \hat{b}_k + a_{22} \hat{a}_k^\dagger \hat{a}_k \right), \end{aligned} \quad (3.74)$$

where A is the 2 by 2 matrix whose elements are given by

$$A = \begin{bmatrix} a_{11} & a_{12} \\ a_{21} & a_{22} \end{bmatrix} = \begin{bmatrix} \varepsilon_k & D \\ D & \omega_k \end{bmatrix}. \quad (3.75)$$

Applying the unitary transformation U , (i.e., $U^\dagger = U^{-1}$)

$$\begin{pmatrix} \hat{b}_k \\ \hat{a}_k \end{pmatrix} = U \begin{pmatrix} \hat{\xi}_1 \\ \hat{\xi}_2 \end{pmatrix} \quad \text{with} \quad U = \begin{bmatrix} u_{11} & u_{12} \\ u_{21} & u_{22} \end{bmatrix} \quad (3.76)$$

to (3.74), we have

$$\hbar \begin{pmatrix} \hat{b}_k^\dagger \\ \hat{a}_k^\dagger \end{pmatrix} A \begin{pmatrix} \hat{b}_k \\ \hat{a}_k \end{pmatrix} = \hbar \begin{pmatrix} \hat{\xi}_1^\dagger \\ \hat{\xi}_2^\dagger \end{pmatrix} U^\dagger A U \begin{pmatrix} \hat{\xi}_1 \\ \hat{\xi}_2 \end{pmatrix}. \quad (3.77)$$

Since $U^\dagger A U = U^{-1} A U$ is diagonal, we put

$$U^{-1} A U = \begin{bmatrix} \Omega_{k,1} & 0 \\ 0 & \Omega_{k,2} \end{bmatrix} \equiv \Lambda \quad (3.78)$$

and obtain $A U = U \Lambda$, which reduces in terms of components ($j = 1, 2$) to

$$\begin{bmatrix} \varepsilon_k - \Omega_{k,j} & D \\ D & \omega_k - \Omega_{k,j} \end{bmatrix} \begin{pmatrix} u_{1j} \\ u_{2j} \end{pmatrix} = 0. \quad (3.79)$$

This immediately gives the eigenvalue equation

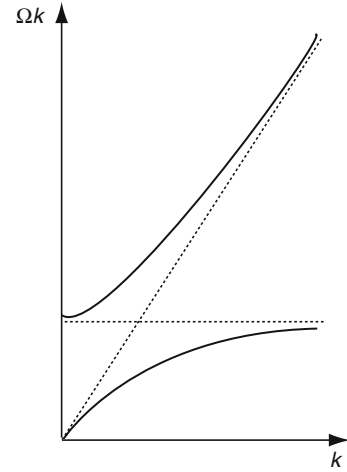
$$(\Omega - \varepsilon_k)(\Omega - \omega_k) - D^2 = 0, \quad (3.80)$$

and the eigenenergies of exciton–polaritons are

$$\hbar \Omega_{k,j} = \hbar \left[\frac{\varepsilon_k + \omega_k}{2} \pm \frac{\sqrt{(\varepsilon_k - \omega_k)^2 + 4D^2}}{2} \right]. \quad (3.81)$$

Equation (3.81) provides the new dispersion relation that we are looking for. Using the dispersion relation of photons $\omega_k = ck$ with $k = |\mathbf{k}|$, we can plot eigenenergies of exciton–polaritons as a function of k , as shown in Fig. 3.1. Here, for simplicity, we approximate the exciton dispersion as $\varepsilon_k = \hbar\Omega$, independent of k . Note that the exciton dispersion is proportional to k^2 when the center of motion is considered.

Fig. 3.1 Dispersion relation of exciton–polaritons. Energies of exciton–polaritons Ω_k shown as *solid curves* are schematically plotted as a function of k



From (3.79) and the unitarity of U , we have for the components of the eigenvectors

$$u_{2j} = -\frac{\varepsilon_k - \Omega_{k,j}}{D} u_{1j}, \quad (3.82a)$$

$$u_{1j}^2 + u_{2j}^2 = 1, \quad (3.82b)$$

and thus,

$$\left\{ 1 + \left(\frac{\varepsilon_k - \Omega_{k,j}}{D} \right)^2 \right\} u_{1j}^2 = 1. \quad (3.83)$$

Finally, the eigenvectors of exciton–polaritons are

$$u_{1j} = \left\{ 1 + \left(\frac{\varepsilon_k - \Omega_{k,j}}{D} \right)^2 \right\}^{-1/2}, \quad (3.84a)$$

$$u_{2j} = -\left(\frac{\varepsilon_k - \Omega_{k,j}}{D} \right) \left\{ 1 + \left(\frac{\varepsilon_k - \Omega_{k,j}}{D} \right)^2 \right\}^{-1/2}. \quad (3.84b)$$

New steady states for exciton–polaritons can be described by (3.81), (3.84a), and (3.84b).

3.6 Optical Near-Field Interaction: Yukawa Potential

Based on the concepts and methods introduced in the preceding sections, we investigate the formulation of an optical near-field system that was briefly mentioned in Sect. 3.1. Moreover, explicit functional forms of the optical near-field interaction

will be obtained by using either the effective interaction \hat{V}_{eff} in (3.26) or its approximation given in (3.37) [18, 19].

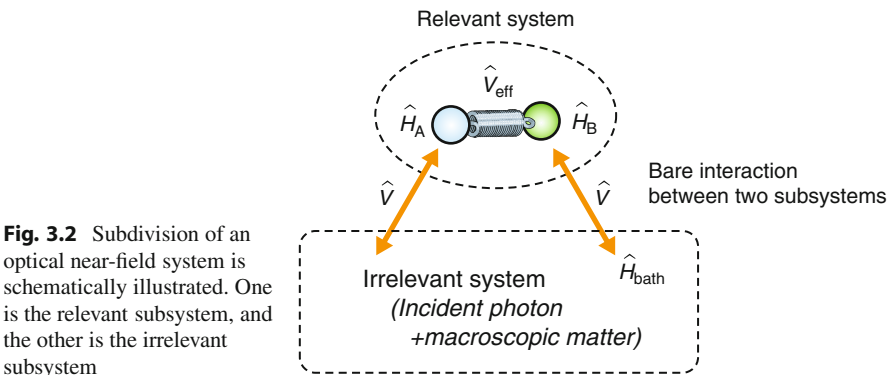
3.6.1 Relevant Microscopic Subsystem and Irrelevant Macroscopic Subsystem

As mentioned in Sect. 3.1, the optical near-field system consists of two subsystems: One is a macroscopic subsystem whose typical dimension is much larger than the wavelength of the incident light. The other is a nanometric subsystem whose constituents are a nanometric aperture or a protrusion at the apex of the near-field optical probe and a nanometric sample. We call such an aperture or protrusion a probe tip. As a nanometric sample, we mainly take a single atom/molecule or quantum dot (QD). Subdivision of the total system is schematically illustrated in Fig. 3.2. The two subsystems are interacting with each other, and it is very important to formulate the interactions consistently and systematically.

We call the nanometric subsystem the relevant subsystem n and the macroscopic subsystem the irrelevant subsystem M . We are interested in the subsystem n , in particular, the interaction induced in the subsystem n . Therefore, it is important to renormalize effects due to the subsystem M in a consistent and systematic way. We show a formulation based on the projection operator method described in Sects. 3.2 and 3.3.

3.6.2 P Space and Q Space

It is preferable to express exact states $|\psi\rangle$ for the total system in terms of a small number of bases or as a few degrees of freedom as possible that span P space. In the following, we assume two states as the P -space components: $|\phi_1\rangle = |s^*\rangle |p\rangle \otimes |0_{(M)}\rangle$ and $|\phi_2\rangle = |s\rangle |p^*\rangle \otimes |0_{(M)}\rangle$. Here $|s\rangle$ and $|s^*\rangle$ are eigenstates of the sample, which is isolated, while $|p\rangle$ and $|p^*\rangle$ are eigenstates of the probe tip, which is also isolated. Resonant excitation energies of the sample and the probe tip are assumed



to be $E_s = \hbar\Omega_0(s)$ and $E_p = \hbar\Omega_0(p)$, respectively. In addition, exciton–polariton states as bases discussed in Sect. 3.5 are used to describe the macroscopic subsystem M , and thus, $|0_{(M)}\rangle$ represents the vacuum for exciton–polaritons. Note that there exist photons and electronic matter excitations even in the vacuum state $|0_{(M)}\rangle$. The direct product is denoted by the symbol \otimes . The complementary space to the P space is called Q space, which is spanned by a huge number of bases of a large number of degrees of freedom not included in the P space.

3.6.3 Effective Interaction in the Nanometric Subsystem

When we evaluate the effective interaction given by (3.37) in the P space discussed above and trace out the other degrees of freedom, the result gives the effective interaction potential of the nanometric subsystem n after renormalizing the effects from the macroscopic subsystem M . Using the effective interaction potential, one can ignore the subsystem M , as if the subsystem n were isolated and separated from the subsystem M .

As the first step of the procedure, we employ the “bare interaction” between the two subsystems:

$$\hat{V} = -\frac{1}{\varepsilon_0} \left\{ \hat{\boldsymbol{\mu}}_s \cdot \hat{\mathbf{D}}^\perp(\mathbf{r}_s) + \hat{\boldsymbol{\mu}}_p \cdot \hat{\mathbf{D}}^\perp(\mathbf{r}_p) \right\} \quad (3.85)$$

(see (3.69)). It should be noted that there are no interactions without incident photons in the macroscopic subsystem M . The subscripts s and p represent physical quantities related to the sample and the probe tip, respectively. Representative positions of the sample and the probe tip are chosen for simplicity to be \mathbf{r}_s and \mathbf{r}_p , respectively, but those may be composed of several positions. In that case, the quantities in curly brackets in (3.85) should be summed over. The transverse component of the electric displacement operator, $\hat{\mathbf{D}}^\perp(\mathbf{r})$, can be expressed in terms of the vector potential $\hat{\mathbf{A}}(\mathbf{r})$ and its conjugate momentum $\hat{\boldsymbol{\Pi}}(\mathbf{r})$ from the multipole Lagrangian \hat{L}_{mult} :

$$\begin{aligned} \hat{\boldsymbol{\Pi}}(\mathbf{r}) &= \frac{\partial \hat{L}_{\text{mult}}}{\partial \dot{\hat{\mathbf{A}}}} = \varepsilon_0 \frac{\partial \hat{\mathbf{A}}}{\partial t} - \hat{\mathbf{P}}^\perp(\mathbf{r}) \\ &= -\varepsilon_0 \hat{\mathbf{E}}^\perp(\mathbf{r}) - \hat{\mathbf{P}}^\perp(\mathbf{r}) = -\hat{\mathbf{D}}^\perp(\mathbf{r}) . \end{aligned} \quad (3.86)$$

With the help of the mode expansion of $\hat{\mathbf{A}}(\mathbf{r})$

$$\hat{\mathbf{A}}(\mathbf{r}) = \sum_{\mathbf{k}} \sum_{\lambda=1}^2 \left(\frac{\hbar}{2\varepsilon_0 V \omega_{\mathbf{k}}} \right)^{1/2} \mathbf{e}_\lambda(\mathbf{k}) \left\{ \hat{a}_\lambda(\mathbf{k}) e^{i\mathbf{k}\cdot\mathbf{r}} + \hat{a}_\lambda^\dagger(\mathbf{k}) e^{-i\mathbf{k}\cdot\mathbf{r}} \right\} \quad (3.87)$$

and $\hat{\Pi}(\mathbf{r})$ from the minimal-coupling Lagrangian \hat{L}

$$\begin{aligned}\hat{\Pi}(\mathbf{r}) &= \frac{\partial \hat{L}}{\partial \dot{\hat{\mathbf{A}}}} = \varepsilon_0 \frac{\partial \hat{\mathbf{A}}}{\partial t} \\ &= -i \sum_{\mathbf{k}} \sum_{\lambda=1}^2 \left(\frac{\varepsilon_0 \hbar \omega_{\mathbf{k}}}{2V} \right)^{1/2} \mathbf{e}_{\lambda}(\mathbf{k}) \left\{ \hat{a}_{\lambda}(\mathbf{k}) e^{i\mathbf{k}\cdot\mathbf{r}} - \hat{a}_{\lambda}^{\dagger}(\mathbf{k}) e^{-i\mathbf{k}\cdot\mathbf{r}} \right\},\end{aligned}\quad (3.88)$$

we can rewrite (3.86) as

$$\hat{\mathbf{D}}^{\perp}(\mathbf{r}) = i \sum_{\mathbf{k}} \sum_{\lambda=1}^2 \left(\frac{\varepsilon_0 \hbar \omega_{\mathbf{k}}}{2V} \right)^{1/2} \mathbf{e}_{\lambda}(\mathbf{k}) \left\{ \hat{a}_{\lambda}(\mathbf{k}) e^{i\mathbf{k}\cdot\mathbf{r}} - \hat{a}_{\lambda}^{\dagger}(\mathbf{k}) e^{-i\mathbf{k}\cdot\mathbf{r}} \right\},\quad (3.89)$$

where the creation and annihilation operators of a photon with wave vector \mathbf{k} , angular frequency $\omega_{\mathbf{k}}$, and polarization component λ are designated as $\hat{a}_{\lambda}^{\dagger}(\mathbf{k})$ and $\hat{a}_{\lambda}(\mathbf{k})$, respectively. The quantization volume is V , and the unit vector related to the polarization direction is $\mathbf{e}_{\lambda}(\mathbf{k})$.

Since exciton–polariton states are employed as bases to describe the macroscopic subsystem M , the creation and annihilation operators of a photon in (3.89) can be rewritten in terms of the exciton–polariton operators $\hat{\xi}^{\dagger}(\mathbf{k})$ and $\hat{\xi}(\mathbf{k})$ and then substituted into (3.85). Using the electric dipole operator

$$\hat{\boldsymbol{\mu}}_{\alpha} = \left(\hat{\mathbf{B}}(\mathbf{r}_{\alpha}) + \hat{\mathbf{B}}^{\dagger}(\mathbf{r}_{\alpha}) \right) \boldsymbol{\mu}_{\alpha},\quad (3.90)$$

we obtain the “bare interaction” in the exciton–polariton picture:

$$\begin{aligned}\hat{V} &= -i \left(\frac{\hbar}{2\varepsilon_0 V} \right)^{1/2} \sum_{\alpha=s}^p \sum_{\mathbf{k}} \left(\hat{\mathbf{B}}(\mathbf{r}_{\alpha}) + \hat{\mathbf{B}}^{\dagger}(\mathbf{r}_{\alpha}) \right) \\ &\quad \times \left(K_{\alpha}(\mathbf{k}) \hat{\xi}(\mathbf{k}) - K_{\alpha}^*(\mathbf{k}) \hat{\xi}^{\dagger}(\mathbf{k}) \right).\end{aligned}\quad (3.91)$$

Here $K_{\alpha}(\mathbf{k})$ is the coupling coefficient between the exciton–polariton and the nanometric subsystem n and is given by

$$K_{\alpha}(\mathbf{k}) = \sum_{\lambda=1}^2 (\boldsymbol{\mu}_{\alpha} \cdot \mathbf{e}_{\lambda}(\mathbf{k})) f(k) e^{i\mathbf{k}\cdot\mathbf{r}_{\alpha}}\quad (3.92)$$

with

$$f(k) = \frac{ck}{\sqrt{\Omega(k)}} \sqrt{\frac{\Omega^2(k) - \Omega^2}{2\Omega^2(k) - \Omega^2 - (ck)^2}}.\quad (3.93)$$

The asterisk in (3.91) stands for the complex conjugate, while c , $\Omega(k)$, and Ω in (3.93) are the velocity of light in vacuum and the eigenfrequencies of the exciton–polariton and electronic polarization of the macroscopic subsystem M , respectively [34]. Note that the wave-number dependence of $f(k)$ characterizes a typical interaction range of exciton–polaritons coupled to the nanometric subsystem n .

The next step is to evaluate the amplitude of effective sample–probe tip interaction in the P space:

$$V_{\text{eff}}(2, 1) \equiv \langle \phi_2 | \hat{V}_{\text{eff}} | \phi_1 \rangle . \quad (3.94)$$

Using (3.37) as \hat{V}_{eff} , we can explicitly write (3.94) in the form

$$\begin{aligned} V_{\text{eff}}(2, 1) &= 2 \langle \phi_2 | P \hat{V} Q \left(E_P^0 - E_Q^0 \right)^{-1} Q \hat{V} P | \phi_1 \rangle \\ &= 2 \sum_m \langle \phi_2 | P \hat{V} Q | m \rangle \langle m | Q \left(E_P^0 - E_Q^0 \right)^{-1} Q \hat{V} P | \phi_1 \rangle , \end{aligned} \quad (3.95)$$

where the second line shows that a virtual transition from the initial state $|\phi_1\rangle$ in the P space to an intermediate state $|m\rangle$ in the Q space is followed by a subsequent virtual transition from the intermediate state $|m\rangle$ to the final state $|\phi_2\rangle$ in the P space. We can then proceed by substituting the explicit “bare interaction” \hat{V} in (3.91) with (3.92) and (3.93) into (3.95). Since one exciton–polariton state, as for the subsystem M within an arbitrary intermediate state $|m\rangle$, can only contribute to nonzero matrix elements, (3.95) can be transformed into

$$V_{\text{eff}}(2, 1) = -\frac{1}{(2\pi)^3 \varepsilon_0} \int d^3k \left[\frac{K_p(\mathbf{k})K_s^*(\mathbf{k})}{\Omega(k) - \Omega_0(s)} + \frac{K_s(\mathbf{k})K_p^*(\mathbf{k})}{\Omega(k) + \Omega_0(p)} \right], \quad (3.96)$$

where summation over \mathbf{k} is replaced by integration over \mathbf{k} in the usual manner.

Interchanging the arguments 1 and 2 (the role of the sample and probe tip), we can similarly calculate $V_{\text{eff}}(1, 2) \equiv \langle \phi_1 | \hat{V}_{\text{eff}} | \phi_2 \rangle$:

$$V_{\text{eff}}(1, 2) = -\frac{1}{(2\pi)^3 \varepsilon_0} \int d^3k \left[\frac{K_s(\mathbf{k})K_p^*(\mathbf{k})}{\Omega(k) - \Omega_0(p)} + \frac{K_p(\mathbf{k})K_s^*(\mathbf{k})}{\Omega(k) + \Omega_0(s)} \right]. \quad (3.97)$$

Therefore, the total amplitude of the effective sample–probe tip interaction is given by the sum of (3.96) and (3.97), which includes effects from the macroscopic subsystem M . We write this effective interaction potential for the nanometric subsystem n as $V_{\text{eff}}(r)$ because we have both $V_{\text{eff}}(2, 1)$ and $V_{\text{eff}}(1, 2)$ as a function of the distance between the sample and the probe tip after the \mathbf{k} -integration.

3.6.4 Effective Mass Approximation of Exciton–Polaritons and Yukawa Potential

The dispersion relation of exciton–polaritons, as schematically shown in Fig. 3.1, can be approximated by

$$\hbar\Omega(\mathbf{k}) = \hbar\Omega + \frac{(\hbar\mathbf{k})^2}{2m_{\text{pol}}} \quad (3.98)$$

in terms of the effective mass of exciton–polaritons m_{pol} . Note that it is valid for both upper and lower branches when the center of mass motion of excitons is included. From this and the discussion of (3.95), it follows that $V_{\text{eff}}(r)$ results from the exchange of virtual exciton–polaritons or massive virtual photons. Substituting (3.98) into (3.96) and (3.97), we can rewrite the effective potential $V_{\text{eff}}(r)$ as

$$\begin{aligned} V_{\text{eff}}(r) &= -\frac{4\mu_s\mu_p\hbar E_{\text{pol}}}{3i\pi r(\hbar c)^2} \int dk k f^2(k) e^{ikr} \\ &\quad \left\{ \frac{1}{k^2 + 2E_{\text{pol}}(E_m + E_s)(\hbar c)^{-2}} + \frac{1}{k^2 + 2E_{\text{pol}}(E_m - E_s)(\hbar c)^{-2}} \right. \\ &\quad \left. + \frac{1}{k^2 + 2E_{\text{pol}}(E_m + E_p)(\hbar c)^{-2}} + \frac{1}{k^2 + 2E_{\text{pol}}(E_m - E_p)(\hbar c)^{-2}} \right\} \\ &= \frac{2\mu_s\mu_p E_{\text{pol}}^2}{3i\pi r(\hbar c)^2} \int dk k F(k) e^{ikr}, \end{aligned} \quad (3.99)$$

where we use the notations $E_{\text{pol}} = m_{\text{pol}}c^2$ and $E_m = \hbar\Omega$ and average the summation over λ as $2/3$. In addition, we define $F(k)$ as

$$\begin{aligned} F(k) &\equiv \left(\frac{A_+}{k^2 + \Delta_{s+}^2} - \frac{A_-}{k^2 + \Delta_{s-}^2} \right) + \left(\frac{B_+}{k^2 + \Delta_{p+}^2} - \frac{B_-}{k^2 + \Delta_{p-}^2} \right) \\ &\quad + \left(\frac{C_+}{k^2 + \Delta_{m+}^2} - \frac{C_-}{k^2 + \Delta_{m-}^2} \right), \end{aligned} \quad (3.100)$$

with

$$\Delta_{s\pm} = \frac{\sqrt{2E_{\text{pol}}(E_m \pm E_s)}}{\hbar c}, \quad (3.101a)$$

$$\Delta_{p\pm} = \frac{\sqrt{2E_{\text{pol}}(E_m \pm E_p)}}{\hbar c}, \quad (3.101b)$$

which is related to the four kinds of effective masses of the Yukawa potential, as will soon be seen. The effective masses with the suffix + are larger than those with the suffix -, and thus, Δ_{s+} (Δ_{p+}) is heavier and has shorter interaction range than Δ_{s-} (Δ_{p-}). The two constants Δ_{m+} and Δ_{m-} mainly give the periodic functions related to the property of the macroscopic matter subsystem, not to the microscopic subsystem, and the third pair of terms in (100) will be omitted in the following. The weight factors in (100), that is, A_{\pm} and B_{\pm} , are functions of E_s , E_p , E_{pol} , and E_m and are given by

$$A_{\pm} = \pm \frac{2(E_m \mp E_s)(E_m \pm E_s)^2}{E_s(E_s \pm W_+ E_m)(E_s \pm W_- E_m)}, \quad (3.102a)$$

$$B_{\pm} = \pm \frac{2(E_m \mp E_p)(E_m \pm E_p)^2}{E_p(E_p \pm W_+ E_m)(E_p \pm W_- E_m)}, \quad (3.102b)$$

with

$$W_{\pm} = \frac{E_{\text{pol}}}{2E_m} \pm \sqrt{\left\{1 - \frac{E_{\text{pol}}}{2E_m}\right\}^2 - \frac{1}{2}}. \quad (3.103)$$

Finally, as the sum of the Yukawa functions with several kinds of masses, we obtain the following effective potential or near-field optical potential $V_{\text{eff}}(r)$:

$$V_{\text{eff}}(r) = \frac{2\mu_s\mu_p E_{\text{pol}}^2}{3(\hbar c)^2} \{A_+ Y(\Delta_{s+} r) - A_- Y(\Delta_{s-} r) \\ + B_+ Y(\Delta_{p+} r) - B_- Y(\Delta_{p-} r)\}, \quad (3.104a)$$

$$Y(\kappa r) \equiv \frac{\exp(-\kappa r)}{r}. \quad (3.104b)$$

To sum up, we find that the major part of the effective interaction exerted in the microscopic subsystem n is the Yukawa potential, after renormalizing the effects from the macroscopic subsystem. This interaction is mediated by massive virtual photons, or polaritons, where exciton-polaritons have been employed in the explicit formulation, but in principle other types of polaritons should be applicable.

In this section, we have mainly focused on the effective interaction of the microscopic subsystem n , after tracing out the other degrees of freedoms. It is certainly possible to have a formulation with the projection onto the P space that is spanned in terms of the degrees of freedoms of the massive virtual photons. This kind of formulation emphasizes a ‘‘dressed photon’’ picture, in which photons are not massless but massive due to the matter excitations.

3.7 Applications

Let us now turn to some applications of our formulation. Although there might be a variety of possibilities, we address basic problems related to atom deflection, trapping, and manipulation with optical near fields generated in a probe tip–atom system, which is expected to be developed towards nanophotonics and atom photonics. At the same time, we also apply our approach to some conventional optical near-field problems that have been discussed from classical electrodynamics viewpoints.

3.7.1 Single-Atom Manipulation

3.7.1.1 Previous Studies

In 1990 D. Eigler et al. manipulated both Xe atoms on a Ni substrate and CO molecules on a Pt substrate using a scanning tunneling microscope (STM) to demonstrate atom tweezers and nano-fabrication [35–37]. A single Cs atom was trapped in a cavity with a length of a few tens of micrometers by H. J. Kimble et al., who utilized propagating light and laser-cooling techniques that made rapid progress during these years [38]. Since the optical near field is independent of the diffraction limit that the propagating light suffers from, one can expect more precise control of an atom with the optical near field than that with propagating light. H. Hori and M. Ohtsu showed that a variety of atoms could be trapped near a nanometric near-field optical probe tip if the optical frequency of the incident light is negatively detuned from an atomic resonant frequency, that is, red detuned [8, 39, 40]. V. V. Klimov et al. estimated the spatial distribution of optical near fields required for an atom trap [41]. H. Ito et al. proposed a method to trap a single Rb atom with an optical near field, where they assumed a potential well due to the balance of attractive van der Waals forces and repulsive dipole forces exerted in a near-field optical probe tip and the atom system [42, 43]. They phenomenologically obtained the potential well, assuming the spatial distribution of the optical near field described by the Yukawa function. This assumption is now being verified by an experiment with two nanometric probe tips [43].

These studies are very important and intriguing from the following viewpoints: optical near-field observation with an atom probe nano-structure fabrication with single-atom manipulation, and local statecontrol of nano-structure, etc. We will thus devote ourselves to these themes in the rest of the section, on the basis of the formulation that we have developed.

3.7.1.2 Possibility of a Single-Atom Trap with Optical Near Fields

Let us first take an example with a typical alkali-metal atom ^{85}Rb , in order to qualitatively examine the features of the effective potential described by (3.104a). We take $E_s = 1.59\text{ eV}$ for the excitation energy between the $5S_{1/2}$ and $5P_{3/2}$ levels of ^{85}Rb . Assuming infrared and visible excitations of a macroscopic matter system

and a probe tip, we vary the values of E_m and E_p over the range $1.0 \leq E_m \leq 1.8$ eV and $1.0 \leq E_p \leq 1.2$ eV, respectively.

Then how does the near-field optical potential $V_{\text{eff}}(r)$ change? Figure 3.3a–c shows an example of such results. The curves shown as *A*, *B*, and *C* in Fig. 3.3a correspond to the term $A_+Y(\Delta_{s+r})$, the term $B_+Y(\Delta_{p+r})$, and the term $V_{\text{eff}}(r)$, respectively. These curves are obtained for $E_m = 1.0$ eV, $E_p = 1.2$ eV, and the detuning $\delta \equiv E_m - E_s < 0$, where both A_{\pm} and B_{\pm} are negative from (3.102a) and (3.102b), and thus, the total potential $V_{\text{eff}}(r)$ is negative, that is, an attractive potential is formed. On the other hand, the curves denoted *A*, *B*, and *C* in Fig. 3.3b and c correspond to the terms $A_+Y(\Delta_{s+r}) - A_-Y(\Delta_{s-r})$, $B_+Y(\Delta_{p+r}) - B_-Y(\Delta_{p-r})$, and $V_{\text{eff}}(r)$, respectively. We use $E_m = 1.8$ eV, $E_p = 1.0$ eV, and $\delta > 0$ in Fig. 3.3b, while in Fig. 3.3c $E_m = 1.8$ eV, $E_p = 1.2$ eV, and $\delta > 0$. It follows from the figures that the potential value depends on the sign and magnitude of each term. In both figures, (b) and (c), the term $A_+Y(\Delta_{s+r}) - A_-Y(\Delta_{s-r})$ represented by curve *A* is negative, and thus, an attractive potential is formed for the atom. The term $B_+Y(\Delta_{p+r}) - B_-Y(\Delta_{p-r})$ shown by curve *B* is positive and results in a repulsive potential for the atom. Moreover, we have $|A_+Y(\Delta_{s+r}) - A_-Y(\Delta_{s-r})| > |B_+Y(\Delta_{p+r}) - B_-Y(\Delta_{p-r})|$ for Fig. 3.3b, and as a result, the total potential $V_{\text{eff}}(r)$ becomes attractive. In contrast to Fig. 3.3b, the potential changes sign in Fig. 3.3c when r goes beyond some value. Since $|A_+Y(\Delta_{s+r}) - A_-Y(\Delta_{s-r})| > |B_+Y(\Delta_{p+r}) - B_-Y(\Delta_{p-r})|$ at large r , while $|A_+Y(\Delta_{s+r}) - A_-Y(\Delta_{s-r})| < |B_+Y(\Delta_{p+r}) - B_-Y(\Delta_{p-r})|$ at small r , the total potential $V_{\text{eff}}(r)$ has a minimum at some r and becomes a potential well. This example indicates that one can control the r -dependence of $V_{\text{eff}}(r)$, that is, the shape of the near-field optical potential, by choosing appropriate materials and probe structure. In addition, we can expect a trapping potential for a single Rb atom around a location with the dimensions of a probe tip.

One of the important factors in experiments with a near-field optical probe is how small a probe tip should be used. Therefore, one should examine the change in the near-field optical potential described by $V_{\text{eff}}(r)$ in (3.104a), taking account of the size of the probe tip. In the following, we assume for simplicity that an atom is the point-like object with discrete energy levels, while the probe tip is a sphere with radius a . The tip sphere at the position of \mathbf{r}_p , as shown in Fig. 3.4, produces a near-field optical potential at the atom position \mathbf{r}_A :

$$\begin{aligned}
 V(r) &= \frac{1}{4\pi a^3/3} \int V_{\text{eff}}(|\mathbf{r}_A - (\mathbf{r}' + \mathbf{r}_p)|) d^3r' \\
 &= \frac{\mu_s \mu_p E_{\text{pol}}^2}{(\hbar c)^2 a^3} \sum_{G=A}^B \sum_{g=s}^p \sum_{j=\pm} \frac{j G_j}{\Delta_{g j}^3} \\
 &\quad \times \left\{ (1 + a \Delta_{g j}) \exp(-\Delta_{g j} a) - (1 - a \Delta_{g j}) \exp(\Delta_{g j} a) \right\} Y(\Delta_{g j} r) \\
 &\equiv \sum_{G=A}^B \sum_{g=s}^p \sum_{j=\pm} j Z_{g j} G_j Y(\Delta_{g j} r) , \tag{3.105}
 \end{aligned}$$

Fig. 3.3 Examples of the near-field optical potential V_{eff} shown in the *solid curves*. The horizontal axis is normalized by the probe-tip size a (see the text for details of the parameters used)

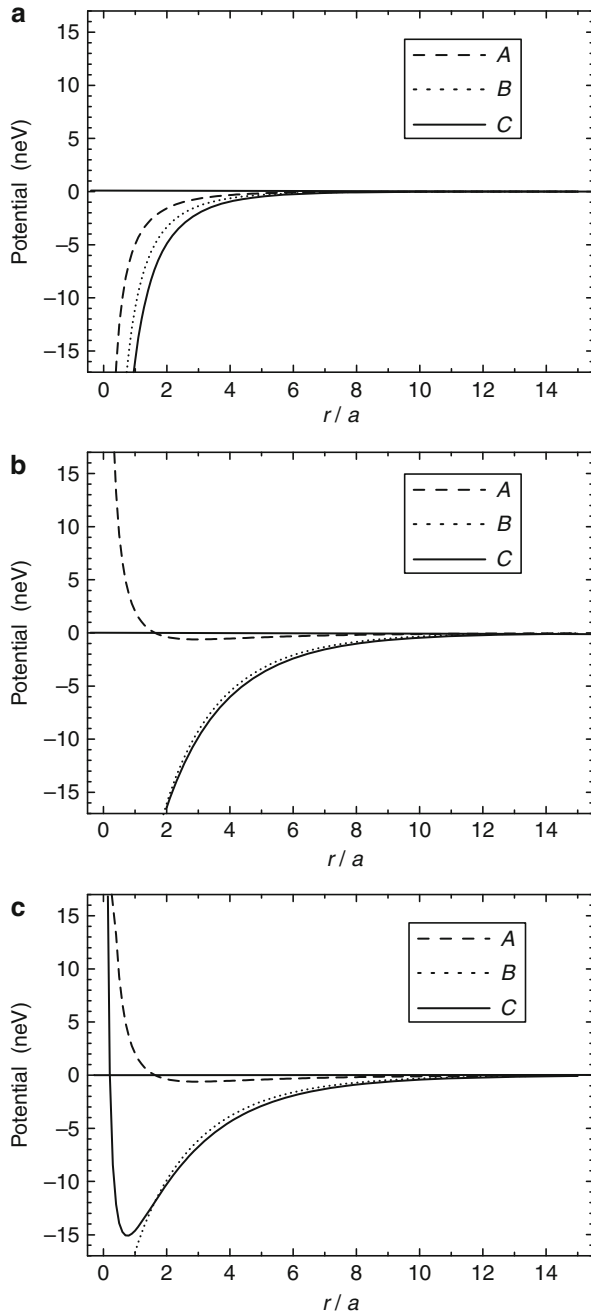
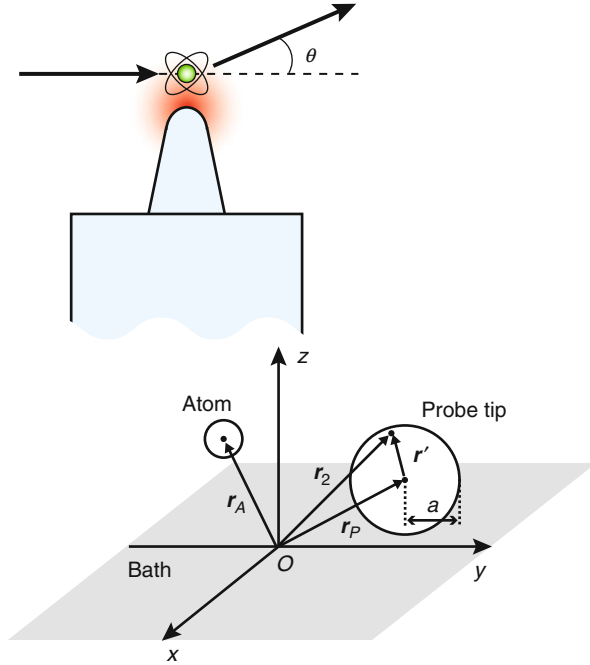


Fig. 3.4 Schematic drawing of an atom manipulation and the geometry of the model. The vectors r_A and r_p denote the center of the atom and the center of the tip sphere with radius a , respectively. An arbitrary position inside the tip sphere is represented by r_2 measured from the origin of the coordinate system and r' measured from the center of the tip sphere, respectively



where we assume the Yukawa sources are homogeneously distributed within the probe-tip sphere. Thus, the total potential $V(r)$ is expressed in terms of the Yukawa potential as a function of the distance between the center of the tip sphere and the atom position.

Now let us consider whether or not the total potential $V(r)$ can have a potential minimum suitable for atom trapping. As a test case, we again use a ^{85}Rb atom with $E_s = 1.59\text{ eV}$ and $\mu_s = 7.5$ debye. A probe tip with a radius of 10 nm is assumed, whose transition dipole moment $\mu_p = 1.5$ debye and excitation energy $E_p = 1.51\text{ eV}$ are assumed. They are coupled to macroscopic matter with $E_m = 2.0\text{ eV}$. For the effective mass of the exciton–polaritons, $E_{\text{pol}} = m_{\text{pol}}c^2 = E_m$ is employed. It follows from Fig. 3.5 that the potential has a minimum of -20 neV near a position $r = 2a$ from the probe-tip surface. Approximating it by a harmonic oscillator potential around the minimum point, we find that two or three vibrational levels can be supported; the lowest vibrational energy with the label $n = 0$ corresponds to 3.1 neV , or equivalently $35\text{ }\mu\text{K}$. This result suggests the possibility of single Rb-atom trapping at this level [19].

It may be interesting to compare the depth of the above potential well with the ones obtained for an atom and a microsphere system in which the radius of the sphere is much greater than ours. The potential depth for a Rb atom semiclassically calculated in [44] is of the same order of magnitude or possibly a little shallower than our results. However, their minimum position of the potential depends on the wavelength used and is different from ours. This is because they use a microsphere with a dielectric constant of 6 and a radius of about $1\text{ }\mu\text{m}$ for visible light.

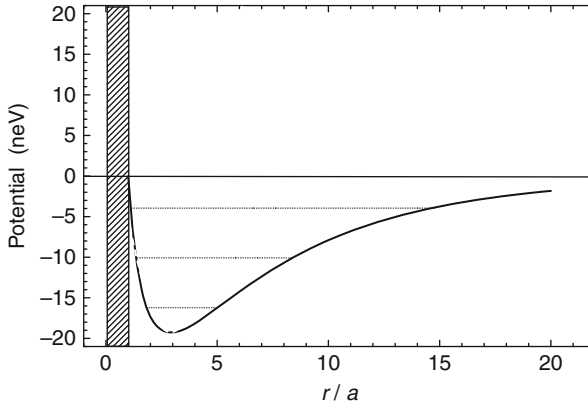


Fig. 3.5 Example of near-field optical potential for ^{85}Rb (resonance energy of 1.59 eV), represented by the *solid curve*. The probe tip is assumed to have a radius of 10 nm and an electronic excitation energy of 1.51 eV. Approximating it by a harmonic oscillator potential around the minimum point, three vibrational levels are shown. The *shaded area* shows the probe-tip size

The potential for a Cs atom quantummechanically calculated with a 50- μm sphere shows the similar tendency [45]. It follows that the nonresonant term neglected in [44], that is, the optical near field leading to size-dependent effects, becomes important as the tip sphere becomes smaller. The effect of an ideally conducting conical surface on an atom was also classically estimated [46], and the energy shift of the atom in the region of interest seems to be similar in order of magnitude, although the details of the parameters used are not known.

3.7.2 Atom Deflection by Optical Near Fields

The incident atomic beam for this kind of experiment is cooled by laser-cooling techniques [47], so that the atomic velocity is approximately 1 m/s in vacuum, or equivalently 10 mK. Such atoms with low velocity are deflected or scattered by the near-field optical potential given by (3.105). This thus can be formulated as a potential scattering problem within the Born approximation. As the velocity of the atom decreases, the first Born approximation becomes invalid. It is known, however, that the first Born approximation breaks down when the incident velocity is close to the submeter-per-second range or the kinetic energy is in the submillikelvin range [48].

The differential scattering cross-section $\sigma(\theta)$ is given in the first Born approximation by

$$\sigma(\theta) = \left| -\frac{1}{4\pi} \left(\frac{8\pi M}{K\hbar^2} \right) \int_a^\infty r dr V(r) \sin(Kr) \right|^2, \quad (3.106)$$

where the atomic mass is denoted by M , and the momentum transfer K is defined in terms of the velocity of the atom v , scattering angle θ , and M as

$$K = 2\frac{Mv}{\hbar} \sin\left(\frac{\theta}{2}\right). \quad (3.107)$$

Substituting the potential $V(r)$ described by (3.105) into (3.106), we have an explicit formula for the differential scattering cross section [19]:

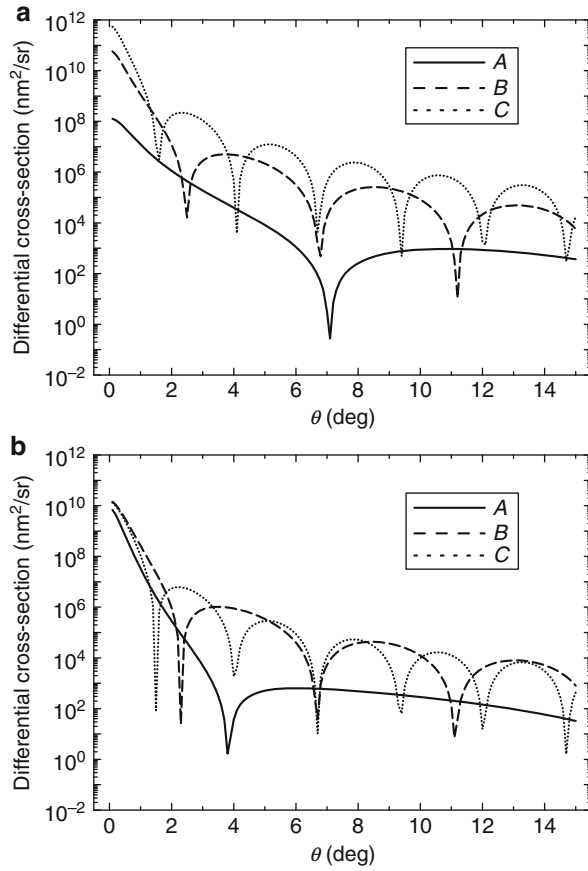
$$\begin{aligned} \sigma(\theta) &= \left| \left(\frac{2M}{K\hbar^2} \right) \sum_{G=A}^B \sum_{g=s}^p \sum_{j=\pm} j Z_{gj} G_j \int_a^{\infty} dr \exp(-\Delta_{gj} r) \sin(Kr) \right|^2 \\ &= \left| \left(\frac{2M}{K\hbar^2} \right) \sum_{G=A}^B \sum_{g=s}^p \sum_{j=\pm} j Z_{gj} G_j \frac{K \cos(Ka) + \Delta_{gj} \sin(Ka)}{K^2 + \Delta_{gj}^2} \right|^2, \quad (3.108) \end{aligned}$$

which provides us with the ratio of the atomic flux at scattering angle θ to the incident atomic flux.

Figure 3.6a and b shows the differential scattering cross section of ^{85}Rb with an incident velocity of 1 m/s when the effective potential $V_{\text{eff}}(r)$ is the attractive potential represented by curve C in Fig. 3.3a and b. The curves denoted A , B , and C are calculated with a tip sphere radius of 10, 30, and 50 nm, respectively. The periodic structure in both figures results from the finite size of the probe tip. From the analytic expression, it follows that the periodic length is inversely proportional to the tip size: The larger the tip size, the shorter the period. Comparing with the first minimum of the differential scattering cross section, we see that a smaller probe tip can deflect the atom more strongly in both figures, although the optimum size should be determined from a discussion of the de Broglie wavelength of the atom. The difference between Fig. 3.6a and b can be understood from the sign of each term in $V(r)$ given by (3.105). In Fig. 3.6a, each component in (3.108) has the same sign in terms of the sum of $Z_{gj}G_j$ and j and constructively contributes to the scattering amplitude. On the other hand, each component in (3.108) has the opposite sign for Fig. 3.6b and is destructively summed in the scattering amplitude. This reduces the first minimum of the deflection angle θ .

In order to estimate a typical displacement of the atomic beam from the incident direction, that is, a typical deflection angle, let us assume a case in which the incident atomic flux N is $10^{10}/(\text{cm}^2 \text{ s})$ and the atomic flux required for detection N_d is $10^3/\text{s}$. It is necessary for the measurement data to be meaningful that the inequality $N\sigma(\theta) \geq N_d$ holds. It follows from curve A in Fig. 3.6b that this condition is satisfied if $\theta \leq 1^\circ$ with a tip radius of 10 nm. This deflection angle is large enough to be detected in the current experimental situation.

Fig. 3.6 Differential scattering cross section of ^{85}Rb with an incident velocity of 1 m/s in the first Born approximation. The radius of the tip is 10 nm (A), 30 nm (B), or 50 nm (C). In (a) the near-field optical potential shown in Fig. 3.3a is assumed, while the potential corresponding to Fig. 3.3b is assumed in (b)



3.7.3 Fundamental Properties of Optical Near-Field Microscopy

In this section, we show that our formulation is also applicable to conventional problems in optical near fields in a unified way, as well as atom manipulation discussed above. The optical near-field intensity in an idealized probe-sample system is calculated in order to analyze fundamental properties of detected signals of optical near-field microscopy [49].

As shown in the preceding section, virtual exciton-polariton exchange is a source of the effective probe-sample interaction. From the dispersion relation of the exciton-polaritons, it follows that they are massive, with an effective mass which is usually determined from $\hbar k |d\Omega(k)/dk|_{k=0}^{-1}$. Here it should be noted that the electrons in a nanometric probe or sample are locally confined and that electron wave numbers are also localized around $k_0 = \pi/a_a$, depending on the size

a_α ($\alpha = s, p$) of the probe–sample system. Then the wave number or momentum of the exciton–polariton virtually exchanged between the probe and sample is expected to close to the wave number k_0 . Thus, we define the effective mass of the exciton–polaritons at $k = k_0$ instead of $k = 0$:

$$\frac{1}{m_{\text{pol}}} = \left[\frac{1}{\hbar k} \left| \frac{d\Omega(k)}{dk} \right| \right]_{k=k_0} \approx \frac{c}{\hbar k_0} = \frac{a_\alpha c}{\pi \hbar}, \quad (3.109)$$

because the eigenfrequency $\Omega(k)$ is close to the frequency of free photons around $k = k_0$. Using this approximation, we can rewrite the near-field optical potential described in (3.104a) as

$$V_{\text{eff}}(r) = \sum_{i,j=1}^3 \frac{8(\mu_s)_i(\mu_p)_j}{9} \left\{ \left(\frac{\pi^2}{a_s^2} \delta_{ij} - \nabla_i \nabla_j \right) Y \left(\frac{\pi}{a_s} r \right) + \left(\frac{\pi^2}{a_p^2} \delta_{ij} - \nabla_i \nabla_j \right) Y \left(\frac{\pi}{a_p} r \right) \right\}, \quad (3.110)$$

where the effective masses of the Yukawa function are approximated as $\Delta_{s\pm} = \pi/a_s$ and $\Delta_{p\pm} = \pi/a_p$ by assuming $\Omega_0(s), \Omega_0(p) \ll ck_0$ (cf. (3.101b)). This assumption is reasonable when the size of the dielectric probe–sample system is a few tens of nanometers. For future use, we sum exactly over λ , yielding the additional terms consisting of gradient operators in (3.110), instead of the previous averaging to 2/3.

Now let us discuss the fundamental signal intensity properties of the microscopy, using a typical nanometric probe–sample system. As shown in Fig. 3.7, we consider two cases: (a) A probe sphere with radius a_1 is scanned above a sample sphere with radius a_s on a plane of constant height, where the

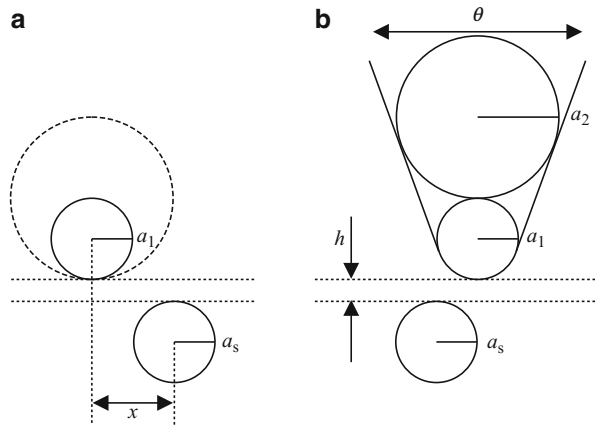


Fig. 3.7 Illustration of the models for an optical near-field probe and sample system: (a) a spherical probe with radius a_1 and (b) a tapered probe consisting of two spheres with radii of a_1 and a_2

height h is the shortest distance between the top of the sample sphere and the bottom of the probe sphere, and (b) tapered probe with angle θ , modeled by two spheres with radii of a_1 and a_2 , is scanned above the sample sphere as in the first case. From (3.110), the Yukawa potential as the effective interaction is generated between two arbitrary points ($\mathbf{r}_i, \mathbf{r}_s$) in the probe and sample spheres. Thus, the pickup signal I obtained from the entire probe sphere can be written as

$$\begin{aligned}
 I(r_{sp}) &\equiv \sum_{i=1}^2 \left| \iint \nabla_{r_i} V_{\text{eff}}(|\mathbf{r}_i - \mathbf{r}_s|) d^3 r_s d^3 r_i \right|^2 \\
 &\propto \sum_{i=1}^2 \left[a_i^3 \left\{ \frac{a_s}{a_i} \cosh\left(\frac{\pi a_s}{a_i}\right) - \frac{1}{\pi} \sinh\left(\frac{\pi a_s}{a_i}\right) \right\} \right. \\
 &\quad \left. \times \left(\frac{1}{r_{sp}} + \frac{a_i}{\pi r_{sp}^2} \right) \exp\left(-\frac{\pi r_{sp}}{a_i}\right) \right]^2, \quad (3.111)
 \end{aligned}$$

where r_{sp} denotes the distance between the center of the probe and the sample. The pickup signal decays in a similar way to the Yukawa function. The numerical results based on (3.111) are presented for the case (a) in Figs. 3.8 and 3.9 and for the case (b) in Figs. 3.10 and 3.11.

Figure 3.8 shows the signal intensity from the sample with $a_s = 10$ nm detected by the probe with $a_1 = 10$ or 20 nm, scanned in the lateral direction with constant height $h = 1$ nm. It follows that each full width at half maximum determining the lateral resolution of the system is nearly equal to the size of each probe tip. In Fig. 3.9, we present the signal intensity normalized by the volume of both probe and sample spheres when the probe radius is varied with the radius of the sample sphere fixed at $a_s = 10$ or 20 nm. It shows that the signal remains the highest when the probe size is comparable to the sample size. This is called the

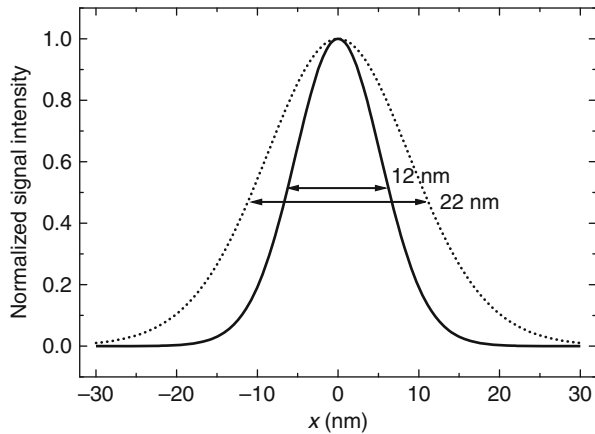
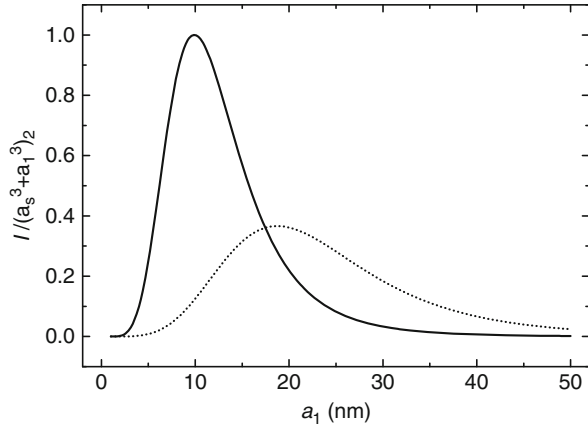


Fig. 3.8 Spatial distribution of signal intensity scanned with probe-tip sizes of $a_1 = 10$ nm (solid curve) and 20 nm (dotted curve), where the sample size $a_s = 10$ nm is assumed

Fig. 3.9 Dependence of signal intensity on probe-tip size. The *solid* and *dotted* curves represent results for sample sizes $a_s = 10$ and 20 nm, respectively



size-resonance effect. These results are consistent with numerical ones obtained with other methods [50, 51].

In Fig. 3.10, we plot the signal intensity as a function of the probe position, varying the taper angle θ . When the taper angle is as small as $\theta = 20^\circ$, as shown in Fig. 3.10a, the signal intensity due to the tapered part is negligibly small and the net signal is determined by the apex contribution. This means that the lateral resolution is dominated by the apex part. By contrast, as the taper angle becomes as large as $\theta = 80^\circ$, the taper contribution to the signal intensity becomes significant. This broadens the width of the net signal (see Fig. 3.10b), leading to the degradation of contrast, that is, the ratio of the signal intensity from the apex part to that from the tapered part. Figure 3.11 shows the dependence of this contrast on taper angle θ . It illustrates how the approach distance of the probe affects the contrast of the image. For an approach distance as small as $h = 1$ nm, the interaction between the apex and sample spheres is stronger than that between the taper and sample spheres. Thus, the apex sphere is the main factor determining the contrast, as well as the lateral resolution. As the approach distance becomes as large as $h = 10$ nm, the interaction between the apex and the sample is weakened in contrast with that between the taper and the sample. This can be understood by noting that the interaction range of a larger sphere is longer than that of a smaller sphere. Therefore, in such a case, the tapered part gradually determines the contrast with increasing taper angle. At taper angles as large as 60° , the contrast degrades again. It is worth noting here that we could improve the contrast, and accordingly the lateral resolution of the system, by screening the tapered part with some kind of metallic coating, which would reduce the interaction between the taper part and the sample.

At the end of this section, we comment on the polarization dependence of the signal intensity. It follows from (3.110) that the polarization effect manifests itself near the edge of a sample. As an example, we show the signal intensity from a circular aperture in Fig. 3.12, where the incident polarization relative to the aperture is fixed in the x -direction, while all polarization components of the probe are

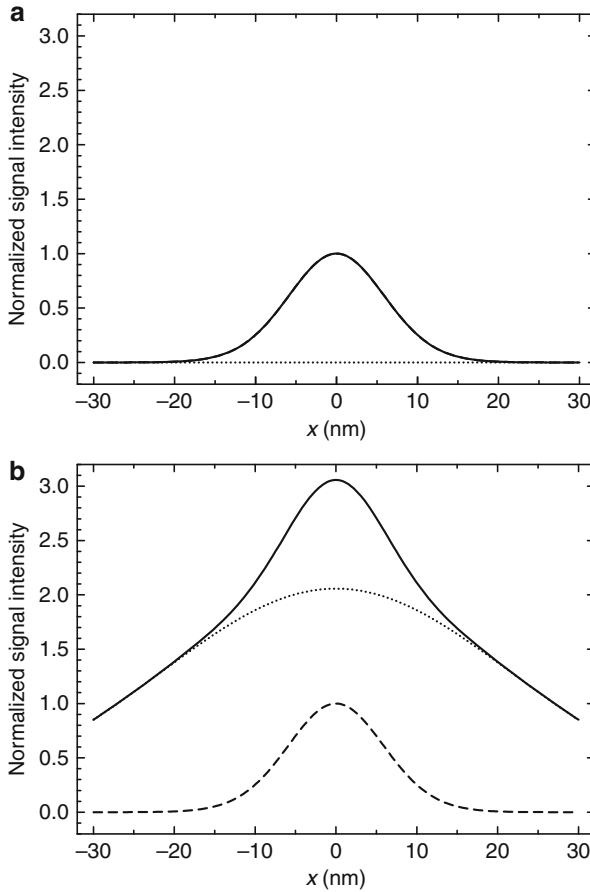


Fig. 3.10 Spatial distribution of signal intensity detected by a tapered probe with taper angles (a) 20° and (b) 80° . The *dashed*, *dotted*, and *solid* curves represent the contributions from the probe tip, the taper, and their sum, respectively

detected. The signal intensity is enhanced near both sides of the aperture that are perpendicular to the incident polarization direction. In Fig. 3.12b, the dependence of the signal intensity on approach distance of the probe is plotted. The enhancement of the signal at the aperture edges disappears, as the probe is located at a higher position. Such polarization dependence of the signal intensity has been explained theoretically and numerically by using macroscopic electromagnetic theory. Exact expressions of electromagnetic fields have been obtained for an infinitely thin conducting plane with a small aperture by Leviatan [52] and for a relatively thick one by Roberts [53]. Novotny et al. [54] have shown similar results numerically by means of the multiple multipole (MMP) method. The results presented here are qualitatively consistent with these previous studies.

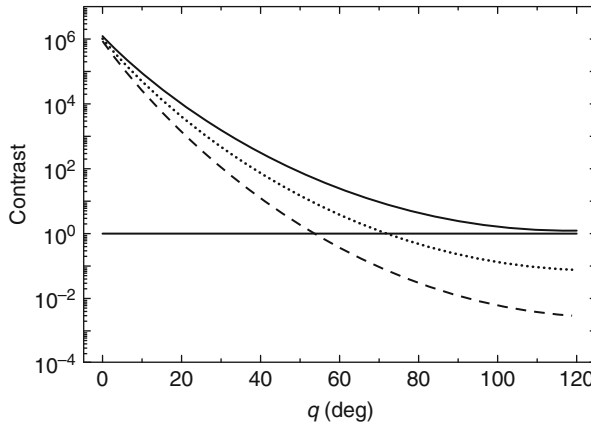


Fig. 3.11 Variation of the ratio of signal intensity from the apex part to that from the tapered part as a function of taper angle. The *solid*, *dotted*, and *dashed* curves represent results for heights, $h = 1, 5,$ and 10 nm, respectively. The region above the horizontal line, the ratio 1, indicates that the contrast can be determined from the probe tip, not the taper part. By contrast, the tapered part governs the contrast in the region below the ratio 1

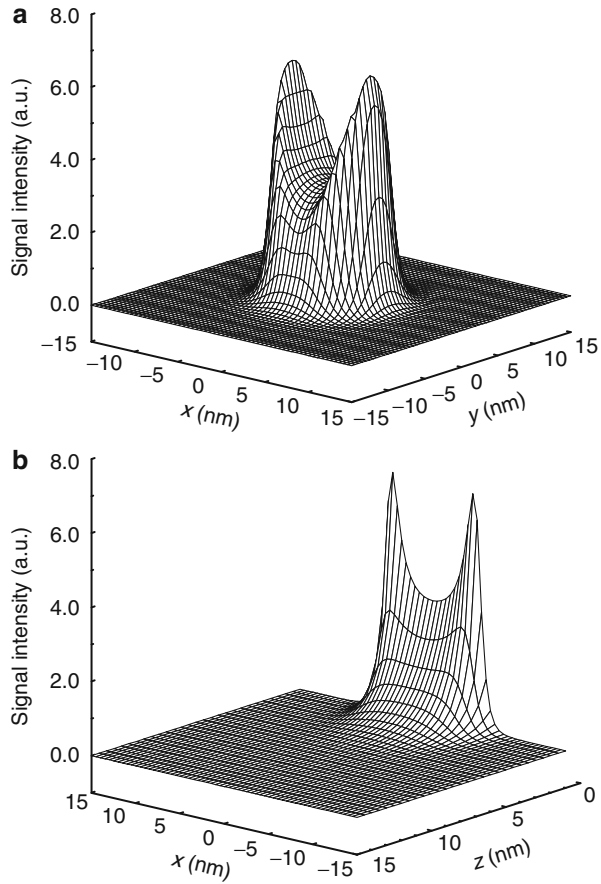
3.8 Outlook

From both basic and application viewpoints, there remain in this field a lot of intriguing issues that we could not discuss. The emphasis here lies in the coupling between a nanometric subsystem n and a macroscopic subsystem M , and the effective interaction induced in the nanometric subsystem. In such a system, cavity quantum electrodynamics (QED) effects are to be expected. One of them is the Casimir–Polder effect [55] due to vacuum fluctuation and retardation effects, both of which are easily included in our framework. In addition, cooperative or destructive effects inherent in the system might be found in dissociation and adsorption processes of atoms or molecules, which will help us to elucidate the nature of nanostructure and take advantage of it.

It will be possible to have another formulation emphasizing a “dressed photon” picture if the P space is spanned by including degrees of freedom of massive virtual photons mediating between constituents of a nanometric subsystem. Such a formulation will reveal more about the difference between propagating real photons and massive virtual photons, phases, and numbers of tunneling photons. Moreover, it can provide new understanding and insights related to observation problems and the reaction mechanism.

A low-dimensional system such as a nanometric quantum dot system is another candidate for a sample interacting with an optical near field as well as an atom or a molecule. The competition of several coupling sources may be of principle importance in such a system. There are fundamental and profound problems when we regard the optical near field as a mixed state of photons and matter excitations:

Fig. 3.12 Spatial distribution of signal intensity in the (a) xy -plane and (b) xz -plane. The circular aperture with a radius of 10 nm is chosen as a sample, and the polarization of incident light is parallel to the x -axis



What is the basic equation governing coherence and decoherence of the system? How are the coherence, population, and excitation energy transferred from one dot to another? The answers to such problems will open up new possibilities of applications using the optical near field such as nanometric photonic devices based on a new principle of operation.

References

1. J.D. Jackson, *Classical Electrodynamics*, 3rd edn. (Wiley, New York, 1999)
2. J.P. Fillard, *Near Field Optics and Nanoscopy* (World Scientific, Singapore, 1996)
3. M.A. Paesler, P.J. Moyer, *Near-Field Optics* (Wiley, New York, 1996)
4. K. Cho, *Prog. Theor. Phys. Suppl.* **106**, 225 (1991)
5. H. Ishihara, K. Cho, *Phys. Rev. B* **48**, 7960 (1993)
6. K. Cho, Y. Ohfuti, K. Arima, *Surf. Sci.* **363**, 378 (1996)

7. M. Ohtsu, H. Hori, *Near-Field Nano-Optics* (Kluwer Academic/Plenum Publishers, New York, 1999), pp. 281–296
8. H. Hori, in *Near Field Optics*, ed. by D.W. Pohl, D. Courjon (Kluwer Academic, Dordrecht, 1993), pp. 105–114
9. K. Kobayashi, M. Ohtsu, in *Near-Field Nano/Atom Optics and Technology*, ed. by M. Ohtsu (Springer, Tokyo/Berlin/Heidelberg, 1998), pp. 288–290
10. J.J. Sakurai, *Advanced Quantum Mechanics* (Addison-Wesley, Reading 1967)
11. U. Weiss, *Quantum Dissipative Systems*, 2nd edn. (World Scientific, Singapore 1999)
12. P. Fulde, *Electron Correlations in Molecules and Solids*, 2nd edn. (Springer, Berlin/Heidelberg/New York, 1993)
13. H. Grabert, *Projection Operator Techniques in Nonequilibrium Statistical Mechanics* (Springer, Berlin/Heidelberg/New York, 1982)
14. F. Haake, *Statistical Treatment of Open Systems by Generalized Master Equations* (Springer, Berlin/Heidelberg/New York, 1973)
15. C.R. Willis, R.H. Picard, *Phys. Rev. A* **9**, 1343 (1974)
16. J. Rau, B. Muller, *Phys. Rep.* **272**, 1 (1996)
17. H. Hyuga, H. Ohtsubo, *Nucl. Phys.* **A294**, 348 (1978)
18. K. Kobayashi, M. Ohtsu, *J. Microsc.* **194**, 249 (1999)
19. K. Kobayashi, S. Sangu, H. Ito, M. Ohtsu, *Phys. Rev. A* **63**, 013806 (2001)
20. A.L. Fetter, J.D. Walecka, *Quantum Theory of Many-Particle Systems* (McGraw-Hill, New York, 1971)
21. C. Cohen-Tannoudji, J. Dupont-Roc, G. Grynberg, *Photons and Atoms* (Wiley, New York, 1989)
22. C. Cohen-Tannoudji, J. Dupont-Roc, G. Grynberg, *Atom-Photon Interactions* (Wiley, New York, 1992)
23. D.P. Craig, T. Thirunamachandran, *Molecular Quantum Electrodynamics* (Dover, New York, 1998)
24. M. Scully, M.S. Zubairy, *Quantum Optics* (Cambridge University Press, Cambridge, 1997)
25. M. Kaku, *Quantum Field Theory* (Oxford University Press, Oxford, 1993), pp. 295–320
26. S. Weinberg, *The Quantum Theory of Fields I, II, and III* (Cambridge University Press, Cambridge, 1995)
27. H. Haken, *Quantum Field Theory of Solids* (North-Holland, Amsterdam, 1983)
28. J.J. Hopfield, *Phys. Rev.* **112**, 1555 (1958)
29. K. Cho, *J. Phys. Soc. Jpn.* **55**, 4113 (1986)
30. C. Kittel, *Quantum Theory of Solids* (Wiley, New York, 1972)
31. D. Pines, *Elementary Excitations in Solids* (Perseus Books, Reading, 1999)
32. P.W. Anderson, *Concepts in Solids* (World Scientific, Singapore, 1997)
33. C. Cohen-Tannoudji, *Atoms in Electromagnetic Fields* (World Scientific, Singapore, 1994)
34. M. Ohtsu, K. Kobayashi, H. Ito, G.-H. Lee, *Proc. IEEE* **88**, 1499 (2000)
35. D.M. Eigler, E.K. Schweizer, *Nature* **344**, 524 (1990)
36. P. Zeppenfeld et al., *Ultramicroscopy* **42–44**, 128 (1992)
37. U. Staufer, in *Scanning Tunneling Microscopy II* ed. by R. Wiesendanger, H.-J. Güntherodt (Springer, Berlin/Heidelberg/New York, 1992), pp. 273–302
38. J. Ye, D.W. Vernooy, H.J. Kimble, *Phys. Rev. Lett.* **83**, 4987 (1999)
39. M. Ohtsu, S. Jiang, T. Pangaribuan, M. Kozuma, in *Near Field Optics* ed. by D.W. Pohl, D. Courjon (Kluwer Academic, Dordrecht, 1993), pp. 131–139
40. J.P. Dowling, J. Gea-Banacloche, in *Advances in Atomic, Molecular, and Optical Physics 37*, ed. by B. Bederson, H. Walther (Academic, San Diego, 1996), pp. 1–94
41. V.V. Klimov, V.S. Letokhov, *Opt. Commun.* **121**, 130 (1995)
42. H. Ito, K. Otake, M. Ohtsu, *Proc. SPIE* **3467**, 250 (1998)
43. H. Ito, A. Takamizawa, H. Tanioka, M. Ohtsu, *Proc. SPIE* **3791**, 2 (1999)
44. V. Klimov, V.S. Letokhov, M. Ducloy, *Eur. Phys. J. D* **5**, 345 (1999)
45. D.W. Vernooy, H.J. Kimble, *Phys. Rev. A* **55**, 1239 (1997)
46. V.V. Klimov, Y.A. Perventsev, *Quantum Electron.* **29**, 847 (1999)

47. For example, *Laser Cooling and Trapping of Atoms* ed. by S. Chu, C. Wieman, J. Opt. Soc. Am. B **6**, 2020 (1989)
48. K. Kobayashi, S. Sangu, H. Ito, M. Ohtsu, in *Near-Field Optics: Principles and Applications*, ed. by X. Zhu, M. Ohtsu (World Scientific, Singapore, 2000), pp. 82–88
49. S. Sangu, K. Kobayashi, M. Ohtsu, J. Microsc. **202**, 279 (2001)
50. K. Jang, W. Jhe, Opt. Lett. **21**, 236 (1996)
51. T. Saiki, M. Ohtsu, in *Near-Field Nano/Atom Optics and Technology*, ed. by M. Ohtsu (Springer, Tokyo/Berlin/Heidelberg, 1998), pp. 15–29
52. Y. Leviatan, J. Appl. Phys. **60**, 1577 (1986)
53. A. Roberts, J. Appl. Phys. **70**, 4045 (1991)
54. L. Novotny, D.W. Pohl, P. Regli, J. Opt. Soc. Am. A **11**, 1768 (1994)
55. For example, *Cavity Quantum Electrodynamics*, ed. by P.R. Berman (Academic, San Diego, 1994)

A Phenomenological Description of Optical Near Fields and Optical Properties of N Two-Level Systems Interacting with Optical Near Fields

4

Akira Shojiguchi, Kiyoshi Kobayashi, Suguru Sangu, Kazuo Kitahara, and Motoichi Ohtsu

Contents

4.1	Introduction.....	110
4.1.1	What Are Optical Near Fields?.....	110
4.1.2	Theoretical Approaches.....	112
4.1.3	Difference Between Optical Near Fields and Propagating Fields: Local Versus Global Coupling.....	114
4.1.4	Radiation Properties of Two-Level System.....	115
4.1.5	Chapter Outline.....	116
4.2	Model Hamiltonian.....	117

A. Shojiguchi (✉)

Green Platform Research Laboratories, NEC Corp., Kawasaki, Kanagawa, Japan
e-mail: a-shoujiguchi@ap.jp.nec.com

K. Kobayashi

Interdisciplinary Graduate School of Medicine and Engineering, University of Yamanashi, Kofu, Yamanashi, Japan
e-mail: kkoba@yamanashi.ac.jp

S. Sangu

Device Technology Development Center, Ricoh Co., Ltd., Miyagi, Japan
e-mail: suguru.sangu@nts.ricoh.co.jp

K. Kitahara

Graduate School of Science Education, Tokyo University of Science, Shinjuku-ku, Tokyo, Japan
e-mail: kazuokit@tus.ac.jp

M. Ohtsu

School of Engineering, The University of Tokyo, Tokyo, Japan

Nanophotonics Research Center, The University of Tokyo, Tokyo, Japan
e-mail: ohtsu@ee.t.u-tokyo.ac.jp

4.3	Transportation of Dipole Moments in Weak Excited Systems.....	119
4.3.1	Boson Approximation in Dilute Limit.....	119
4.3.2	Dipole Dynamics Driven by Local Excitation.....	121
4.4	Controlling Dipole Dynamics.....	126
4.4.1	Perturbative Solution.....	126
4.4.2	Dynamic Properties.....	128
4.4.3	Controlling of Dipole Dynamics.....	131
4.4.4	Verification of Perturbation Solutions by Semiclassical Approximations.....	132
4.5	Classification of Quasi-steady States.....	135
4.5.1	Effective Hamiltonian.....	135
4.5.2	Classification of Quasi-steady States and Controlling of Dipole Distributions.....	136
4.5.3	Response to the Initial Input of a Localized Photon: The Robustness of Quasi-steady States.....	139
4.6	Dicke's Superradiance.....	142
4.6.1	Dicke States and Superradiance.....	144
4.6.2	Dicke Master Equation and Solutions for a Small System.....	146
4.6.3	Effect of the Dipole–Dipole Interaction.....	154
4.6.4	Large Sample Superradiance: Reabsorbion Effect.....	159
4.7	Dipole-Ordered States and Radiation Properties: Weak Couling Limit.....	162
4.8	Effect of Near-Field Couplings on Radiation Properties.....	164
4.8.1	Semiclassical Solution: Without Quantum Correlation.....	166
4.8.2	Effect of Quantum Correlation: Comparison with Dicke Model.....	167
4.9	Transport Phenomena of Localized Photons.....	171
4.9.1	Two Phases of Transportation: Switching Between Flow and Block Mode.....	171
4.9.2	Sensitive Switching of Flow and Block: Chaotic Behavior.....	175
4.9.3	Intermittent Chaotic Behavior in Two-Site Open System.....	178
4.10	Conclusions.....	180
	References.....	184

Abstract

In this chapter, we present a simple phenomenological model of an optical near fields interacting with two-level systems and discuss the dynamics of dipole excitation and radiation properties of the system. As a result, we find that the locally near-field coupling enables controlling the dipole distributions by manipulating the initial excitations and causes strong oscillating radiation pulses. Transport phenomena of the near-fields photons through material systems shows switching between flow and block depending on the coupling strength between material systems and near-field photons.

4.1 Introduction

4.1.1 What Are Optical Near Fields?

Since the insight of Synge [83], the localization of light near a material system has been recognized as one of the unique properties of an optical near field, and for more than two decades, a variety of theoretical and experimental studies have been intensively conducted [28, 62–66, 68, 70]. At the beginning of this chapter, we

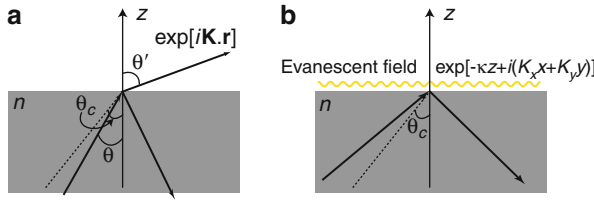


Fig. 4.1 (a) The infinite planar boundary between a dielectric surface and a vacuum. Incident light from the dielectric surface is generally reflected and refracted. (b) Evanescent light on the dielectric surface generated by total internal reflection of the incident light

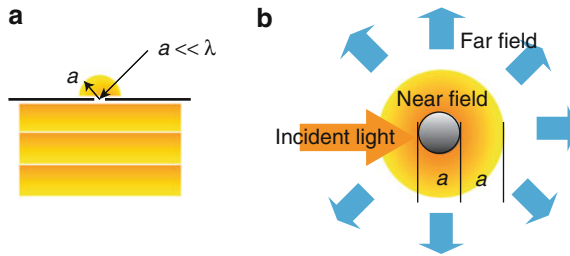


Fig. 4.2 Optical near fields in various boundary conditions. (a) An optical near field leaking from a hole that is much smaller than the wavelength of light. The leaking field attenuates as it leaves the aperture. The localization range of light is much smaller than the wavelength of light, depending on the size of the aperture. (b) An optical near field surrounding a small dielectric sphere and the scattered optical far field produced by an incident optical far field. The localization range of the optical near field is determined by the sphere radius and is independent of the wavelength of light

explain the spatial localization property of light, using two examples, in order to give a physical insight into the optical near-field phenomenon.

The first example is evanescent light, which is generated on a dielectric surface, as is well known, when the incident angle θ of a plane wave of light exceeds the critical angle θ_c and total internal reflection occurs as shown in Fig. 4.1 [65, 77]. The penetration or attenuation depth normal to the surface (along the z -axis) is of the order of the wavelength of light, which indicates the spatial localization of light along the z -axis. This differs from ordinary propagating light, and much attention has been paid to its characteristics [5, 8, 17, 23, 36, 37, 39, 43, 51, 61, 79, 86–90]. Note that the total internal reflection is a macroscopic phenomenon, and that it is valid only on a scale at which the refractive index n of bulk material has meaning.

Another example is illustrated in Fig. 4.2 [65, 66]. Figure 4.2a shows a plane wave of light incident to a plane with a small hole of radius a that is much smaller than the wave length λ of light. Little of the propagating far-field light passes through the hole, but light exists as an optical near field near the aperture on the other side. The localization range of the optical near field is much smaller than the wavelength of light and is determined by the aperture size a . This kind of field, which a scanning near-field optical microscope (SNOM) uses at the tip of an optical near-field probe,

has been investigated in detail [7, 13–15, 53]. A more general situation is depicted in Fig. 4.2b. By irradiating a dielectric that is much smaller than the wavelength of the incident light, optical near fields coiling around the object are generated together with scattering far fields. The localization range of the optical near fields is independent of the wavelength of the incident light and is determined by the size of the object: it depends on the radius a of the dielectric sphere as shown in Fig. 4.2b. Such spatial localization reflecting the structure of the source of the fields (i.e., the induced polarization in matter) gives SNOM and other nanophotonic devices based on optical near-field spatial resolution that is far greater than the diffraction limit [62, 65, 66, 70]. Readers interested in a variety of SNOM applications and the state of the art of nano- and atom photonics are recommended to refer to the literature [35, 40, 42, 62–67, 70, 82].

Theoretically, we need a reasonable explanation of why light waves or photons are localized, and present an example of an empirical method here. The evanescent field generated on a planar dielectric surface can be obtained by analytical continuation of the wave vector k_{\perp} normal to the surface as $\exp(i\mathbf{k}_{\parallel} \cdot \mathbf{r} - \gamma z)$ with $k_{\perp} = i\gamma$ (γ : real), whose localization range is about that of the wavelength of the incident light. Similarly, optical fields around a tiny dielectric sphere that is much smaller than the wavelength are described by the spherical Hankel function with analytic continuation of the radial component of the wave vector k_{\perp} to the pure imaginary $k_{\perp} = i\gamma$; the first kind of Hankel function of order 0 gives the typical form of an optical near field around a sphere as

$$\phi = \frac{e^{-\gamma r}}{\gamma r}. \quad (4.1)$$

The fields satisfying the spherical boundary condition can be expanded in terms of plane waves or can be expressed using angular spectrum representation. From a numerical analysis, it follows that the distribution of the angular spectrum has a peak at $\gamma = 1/a$ [65]. Applying the result to (Eq. 4.1), we see that the localization range of the optical near fields around a sphere is of the order of the radius a , that is, the size of the material system.

Here, it is obvious that an optical near field should be derived consistently from microscopic-induced polarization in matter because they are mutually related, and several approaches in this direction are outlined in the following Sect. 4.1.2.

4.1.2 Theoretical Approaches

Self-consistent descriptions of optical near fields are required, as mentioned above, and the recent advances in nanoscience and technology have promoted investigation of the dynamics of nanometric material systems interacting with optical near fields, which is a critical and fundamental base for nanophotonics. However, the situation is not simple; an optical near field involves both an optical field and the excitation of matter on a nanometer scale, which is considered as elementary excitation.

Moreover, the existence of a boundary or surface strongly affects the elementary excitation mode. It is mandatory to find a proper normal mode or a suitable basis function to satisfy such boundary conditions for a nanometric system. Such a basis function definitely differs from the plane-wave basis used in bulk theories [7, 17, 53], but it is very difficult to evaluate it in a rigorous manner except for the simple boundary condition. On a nanometric scale, a quantum nature appears in an optical field–material system, which requires a quantum description of the system creating additional fundamental difficulties.

One possible approach is the semiclassical, self-consistent theory proposed by Cho et al. [20] and Ishihara and Cho [38], which quantum-mechanically describes microscopic polarization in matter to include a nonlocal response, while the electromagnetic field is classically treated by Helmholtz' equation. They predicted the size dependence and allowance of a dipole-forbidden transition in a nanometric quantum dot system numerically [21]. Nevertheless, the principal difficulty of quantizing the electromagnetic field using a nonlocal approach remains, as does the difficulty in treating the dynamics of a nanometric material system coupled via optical near fields, because of the complexity involved in a self-consistent procedure.

An alternative approach is to use a normal mode or the Carniglia–Mandel mode as a complete and orthogonal set that satisfies the infinite planar boundary condition between the dielectric and a vacuum [8, 17, 37]. This formulation allows us to quantum-field-theoretically describe an evanescent field that is localized along the normal to the surface and possesses an anomalous dispersion relation different from free photons, both of which are important properties of an optical near field. This approach has revealed interesting phenomena that occur near the surface [17, 24, 36, 37, 39, 43, 56, 61, 86–90], but it unfortunately provides neither a self-consistent description of a material system nor a normal mode to satisfy more general or realistic boundary conditions, such as an optical near-field probe–sample system.

K. Kobayashi et al. proposed another approach for focusing on the relevant subsystem that we are interested in and to extract a characteristic feature of the subsystem after renormalizing the other irrelevant subsystem [46–48]. Using a quasiparticle representation for a macroscopic material–electromagnetic field system, which only considers the near-field configuration of the system without rigorously taking into account the boundary condition, they showed the localization of optical near fields around a nanometric material system. They have also discussed the dynamics of a single atom, molecule, or nanometric quantum dot system interacting with the optical near field [49, 74, 78].

In this chapter, we present a simple phenomenological model of an optical near field based on this last approach, in order to discuss the dynamic properties of a nanometric material system interacting with an optical near field. The model uses a concept of the “localized photon” to represent the localization property of the optical near field phenomenologically and two-level systems as representative of a nanometric material system. To clarify the difference between optical near fields and far fields, we compare the results obtained using our model with those of the

Dicke model, which consists of a two-level system interacting with radiation field and has been studied extensively since originally presented by Dicke [25].

4.1.3 Difference Between Optical Near Fields and Propagating Fields: Local Versus Global Coupling

The main difference between a material system coupled with optical near fields and that coupled with propagating far fields is that one is a locally coupled system and the other is a globally coupled one, as depicted schematically in Fig. 4.3.

Since the propagating field is usually expanded in terms of a plane-wave basis, photons emitted as plane waves propagate from one site to distant sites in the material system and can also excite the far sites (global excitation [72]), as shown in Fig. 4.3a. By contrast, as shown in Fig. 4.3b, “near-field photons” or “localized photons” can move only to nearby sites and excite them (individual excitation). Generally speaking, the dynamics of a locally coupled system differ from those of a globally coupled system with respect to its equilibrium state [41] or the relaxation speed toward equilibrium [71]. Therefore, we expect the dynamics and equilibrium states for a locally coupled system to differ from those of an ordinary globally coupled system, such as a propagating field-matter system. From this perspective, it is important to investigate the nanometric material system that is interacting with optical near fields via individual excitations [49, 74, 78, 80].

This chapter presents a model of a material system (a quantum dot system) interacting with optical near fields and discusses the dynamics of the electric dipole moment and the radiation properties of the system. The radiation properties of the system are compared with those of a material system interacting with optical far fields. The propagation dynamics of the excitations of quantum dots described in terms of excitons in N two-level systems locally prepared by an optical near field is investigated in detail. In a dilute limit of excitation, excitons are approximated as bosons [4, 45], and the dipole moments of the two-level system follow linear dynamics. In a nondilute case, excitons obey the fermion commutation relations

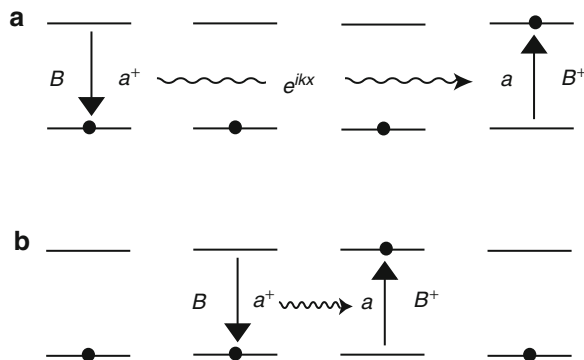


Fig. 4.3 Schematic drawing of (a) global and (b) a local coupling systems. Each element of the system in (a) can interact directly with arbitrary elements at a distant site, while the elements at the near site can interact only with each other in (b)

and are described in nonlinear equations of motion. We predict that with local manipulations of excitations (by using the optical near fields), as a result of the dynamics of the system, we obtain a coherent oscillation of all the dipoles in the system (dipole ordering) and strong radiation from some of the dipole-ordered states, which are comparable to Dicke's superradiance [25].

4.1.4 Radiation Properties of Two-Level System

In 1954, Dicke discussed the cooperative emission of radiation from a collection of excited two-level systems, the superradiance. He found that under certain conditions the radiation rate is proportional to the square of the number of two-level systems involved, and an intense pulse is emitted [25]. Superradiant phenomena attracted considerable attention from a large number of authors in the 1970s [2, 3, 9, 11, 12, 22, 29, 32, 52, 60, 73, 81]. For a small system that is much smaller than the wavelength of radiation, the equations of motion for the two-level system coupled to the radiation field (Dicke model) are given as follows:

$$\frac{\partial \rho_A}{\partial t} = -\gamma_0(R_+R_-\rho_A - 2R_-\rho_A R_+ + \rho_A R_+R_-) \quad (4.2)$$

where ρ_A is the density operator after eliminating the radiation field's degrees of freedom from the total density operator of the system, R_{\pm} is the collective raising and lowering operators of two-level systems [25], and $2\gamma_0$ is the inverse of the spontaneous emission lifetime of each two-level system (Einstein's A coefficient). From (Eq. 4.2), one obtains differential equations for the observables of the two-level system. By using a semiclassical approximation of neglecting quantum correlations in the two-level system, an analytical solution [3, 73] for the radiation intensity I can be written as

$$I \propto N^2 \text{sech}^2 [\gamma_0 N(t - t_0)] \quad (4.3)$$

which has a cowbell-shaped radiation profile, and shows a radiation pulse emitted under certain initial conditions whose height and width are proportional to N^2 and $1/N$, respectively. Note that the semiclassical approximation does not correctly predict the dynamics starting from completely inverted states [3, 60] with no dipole moments because the quantum fluctuations of the dipole moments are essential in the radiation process.

The above discussion holds for the case the two-level systems coherently interact with radiation fields. However, in the case that there exists inhomogeneity of the dynamics of the two-level systems and decoherence is generated, the superradiant states are modified. One of the origin of the decoherence is reabsorption of emitted photons [29] by the two-level systems; namely, some part of the coherence in the system is destroyed by the reabsorption. These effects occurred in large systems, in which the atomic system is large enough to reabsorb the emitted photons.

For two-level systems confined within a long cylindrical sample, Bonifacio et al. predicted multiple peaks in the radiation profile that stem from the stimulated absorptions and emissions in the long active region [9, 11]. Skribanowitz et al. [81] made experimental observations using a cylindrical sample, and their experimental results were analyzed by Bonifacio et al. [12].

Another origin of the decoherence is strong local couplings of the two-level systems. By introducing the dipole-dipole interactions among atoms it is shown that the interactions reduce the peak height and extend the tail of the radiation profile [22, 29]. To examine the dipole-dipole interactions in exciton systems, Tokihiro et al. examined a linear excitonic system, in which excitons can hop from one site to its nearest neighbors via the dipole-dipole interaction and showed that radiation from a totally inverted state as the initial condition has a reduced peak intensity with extension of the tail [84], as discussed by Coffey et al. [22]. They also claimed that the radiation profile from a partially excited state shows oscillatory behavior, as indicated by Bonifacio et al. [9]. In addition, T. Brades et al. discussed the oscillatory behavior of a superradiating system coupled to electron reservoirs [16]. It is clear that the peak intensity reduction of radiation in both cases comes from the dipole-dipole decoherence, but it is not obvious whether the multiple pulses so generated have the same origin.

For observation of radiation phenomena of quantum dot system, recently the emission spectra of CuCl quantum dots were measured, and Nakamura et al. [59] reported a single peak of pulse emission. Recently, Y. N. Chen et al. proposed a way to detect a current of superradiance in a double-dot system [19], while N. Piovella et al. discussed how to detect a photon echo in the superradiance from a Bose-Einstein condensate [69].

In this chapter we investigate the near-field interactions among material systems as a kind of local coupling of the system and discussed the effect of them on radiation properties.

4.1.5 Chapter Outline

The chapter is organized as follows. Section 4.2 presents a model of N two-level quantum dot systems interacting with optical near fields represented in terms of localized photons and describes the model Hamiltonian. In Sects. 4.3–4.5, we discuss dynamics of dipole moments of the system and examine effects of initial distributions of dipoles and excitations on their developing states. Section 4.3 gives dipole propagations in weak excited system (system with the “dilute limit” of excitons) within a boson approximation of excitons. In Sect. 4.4, for general cases without the dilute limit, we find the relation between quasi-steady states and initial distributions of excitations and show how to control the dipole distributions. Section 4.5 classifies series of the quasi-steady states of the dipole distribution by introducing an effective Hamiltonian by renormalizing the degrees of freedom of localized photons. In Sects. 4.6–4.8, the radiation properties of our system are investigated in comparison with those of the material systems coupling to far

fields. [Section 4.6](#) is devoted to a review of the radiation properties of N two-level systems (Dicke model) and of mathematical formalism to investigate radiation properties as a preparation for the following sections. In [Sect. 4.7](#), we examine the system in an artificial weak coupling limit, where the radiation field does not affect the dynamics of the system in order to briefly check the relation between radiation properties and dipole distributions. In [Sect. 4.8](#), we discuss the radiation properties of our system examining effects of quantum correlations due to the locally near-field couplings. [Section 4.9](#) deals with the transport phenomena of the near-field photon by investigating the dynamics of the localized photons in an open system and shows sensitive switching between flow and block depending on the coupling strength between material systems and near-field photons. We show that the sensitive switching of transportation of near-field photons comes from chaotic behaviors in the coupling constant dependence of the total number of localized photons. Finally, in [Sect. 4.10](#) concluding remarks are provided.

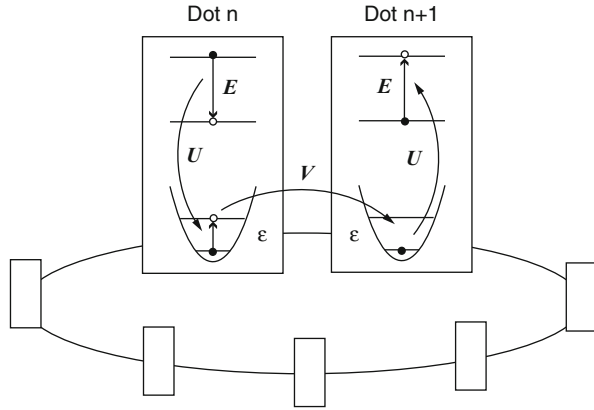
4.2 Model Hamiltonian

One of the most important features of optical near fields is the localization property, where it is not suitable to use a broad spreading wave as a basis function of quantization of the fields. Therefore, it is significant to find a good normal mode of the electromagnetic fields to satisfy a boundary condition specific to the problem, by which the optical near fields are produced and quantized [[17, 46, 47](#)]. It is difficult, however, to find a general and appropriate normal mode satisfying any arbitrary boundary conditions. As an alternative approach, it is possible to model optical near fields and their important characters phenomenologically. Such an approach is adopted here to formulate the problem and to discuss the dynamics of a nanoscale material system.

To describe the localizability of the optical near fields, it is very effective to use a localized basis function such as a Wannier function or a delta function instead of a plane wave. However, at the same time we need to describe the property of a short-range interaction among material sites via optical near fields or a steep gradient of optical near fields. Taking into account such circumstances, we model optical near fields phenomenologically in terms of localized photons which are described as a harmonic oscillator localized in each quantum dot site and are only allowed to hop from one site to the nearest neighbors [[75](#)]. [Fig. 4.4](#) schematically describes our model system.

We suppose a closely located quantum dot chain as a nanoscale material system that is expressed as a one-dimensional N two-level system, or an excitonic system with a periodic boundary condition. Since each exciton can only interact with localized photons in the same QD, each quantum dot indirectly interacts with one another via localized photons, as illustrated in [Fig. 4.4](#). This model is based on the unique property of localization or non-propagation of optical near fields mentioned above [[47](#)] and is preferable for an intuitive understanding of coherent excitation transfer between the QDs and its manipulation by the localized photons. The model

Fig. 4.4 Schematic diagram of a model system: N two-level QDs labelled by the site number are closely located in a ring, and are interacting with localized photons



Hamiltonian of the system can be written as

$$H = H_a + H_b + H_{\text{int}} \quad (4.4)$$

where H_a represents localized photons, H_b describes excitons, and H_{int} represents the localized photon–exciton interaction. Each Hamiltonian can be expressed as

$$H_a = \sum_{n=1}^N \left\{ \varepsilon a_n^\dagger a_n + V(a_{n+1}^\dagger a_n + a_n^\dagger a_{n+1}) \right\}, \quad (4.5a)$$

$$H_b = E \sum_{n=1}^N b_n^\dagger b_n, \quad (4.5b)$$

$$H_{\text{int}} = U \sum_{n=1}^N (a_n^\dagger b_n + b_n^\dagger a_n) \quad (4.5c)$$

where n indicates the site number and a_n (a_n^\dagger) and b_n (b_n^\dagger) represent annihilation (creation) operators of a localized photon and an exciton, respectively. The periodic boundary condition requires that the $(N + 1)$ -th site corresponds to the first site. The constant energies of the localized photons and excitons are represented by $\varepsilon = \hbar\omega$ and $E = \hbar\Omega$, respectively. The hopping energy of the localized photons is represented as $V = \hbar v$, and $U = \hbar g$ gives the strength of the conventional dipolar coupling between a localized photon and an exciton in the rotating wave approximation.

We apply the boson commutation relations to the localized photons as

$$[a_n, a_{n'}^\dagger] = \delta_{nn'}, \quad [a_n, a_{n'}] = [a_n^\dagger, a_{n'}^\dagger] = 0 \quad (4.6)$$

The creation operator of an exciton, b_n^\dagger , can be written in terms of the annihilation operator of a valence electron of n th site, c_{n0} , and the creation operator of a conducting electron of n th site, c_{nf}^\dagger , as $b_n^\dagger = c_{nf}^\dagger c_{n0}$. In the same way, the annihilation operator of an exciton, b_n , can be written as $b_n = c_{n0}^\dagger c_{nf}$. Assuming that only one exciton is generated in a quantum dot site, we obtain the relation as $N_f + N_0 = c_{nf}^\dagger c_{nf} + c_{n0}^\dagger c_{n0} = 1$. With the help of these expressions and the fermi commutation relations for electrons, the commutation relations for excitons are derived as [4,45]

$$[b_{n'}, b_n^\dagger] = \delta_{nn'}(1 - 2b_n^\dagger b_n) \quad (4.7)$$

which shows that excitons behave as fermions at intrasite and as bosons at intersite. It follows from (Eq. 4.7) that excitons are approximated as bosons in a dilute limit of the exciton density, $\langle b_n^\dagger b_n \rangle \equiv \langle N_n \rangle \ll 1$.

With the boson approximation, the Heisenberg equations of motion can be rigorously solved. First, we obtain a rigorous solution of the Heisenberg equations for bosonic excitons to investigate the dynamic properties. Then we investigate the dynamics of fermionic excitons, solving the Heisenberg equations both perturbatively and numerically.

4.3 Transportation of Dipole Moments in Weak Excited Systems

4.3.1 Boson Approximation in Dilute Limit

To solve the Heisenberg equation, we introduce the spatial Fourier transformation for a_n and b_n as

$$A_k = \frac{1}{\sqrt{N}} \sum_{n=1}^N e^{ikn} a_n, \quad (4.8a)$$

$$B_k = \frac{1}{\sqrt{N}} \sum_{n=1}^N e^{ikn} b_n, \quad (4.8b)$$

where we set $k = 2\pi l/N$ for $l = 1, \dots, N$ and the site distance as 1. Fourier transforms A_k satisfy the following commutation relations:

$$[A_k, A_{k'}^\dagger] = \delta_{kk'}, \quad [A_k, A_{k'}] = [A_k^\dagger, A_{k'}^\dagger] = 0, \quad (4.9)$$

and the commutation relations of Fourier transforms B_k are similarly obtained as

$$[B_k, B_{k'}^\dagger] = \frac{1}{N} \sum_{n,n'} e^{i(kn-k'n')} [b_n, b_{n'}^\dagger] = \frac{1}{N} \sum_n e^{i(k-k')n} (1 - 2b_n^\dagger b_n). \quad (4.10)$$

It follows from this expression that when the expectation value of the number of excitons is small as $\langle b_n^\dagger b_n \rangle \ll N$, the second term on the right-hand side of (Eq. 4.10) can be neglected, and excitons are approximated as bosons as

$$[B_k, B_{k'}^\dagger] = \delta_{kk'}, \quad [B_k, B_{k'}] = [B_k^\dagger, B_{k'}^\dagger] = 0, \quad (4.11)$$

where the following relation

$$\frac{1}{N} \sum_n e^{i(k-k')n} = \delta_{kk'} \quad (4.12)$$

is used. Fourier inverse transforms are also given as

$$a_n = \frac{1}{\sqrt{N}} \sum_{k \in 1BZ} e^{-ikn} A_k, \quad (4.13a)$$

$$b_n = \frac{1}{\sqrt{N}} \sum_{k \in 1BZ} e^{-ikn} B_k, \quad (4.13b)$$

where the summation of k runs over the first Brillouin zone (1BZ). Using (Eqs. 4.8a) and (4.8b) and the following relation

$$\frac{1}{N} \sum_{k \in 1BZ} e^{ik(n-n')} = \delta_{nn'}, \quad (4.14)$$

we can transform the Hamiltonian (Eq. 4.4) into a Fourier transform representation

$$\begin{aligned} H &= \sum_k \{(\varepsilon + 2V \cos k) A_k^\dagger A_k + E B_k^\dagger B_k + U(A_k B_k^\dagger + A_k^\dagger B_k)\} \\ &\equiv \sum_k H_k. \end{aligned} \quad (4.15)$$

Note that the dispersion relation of localized photons is changed from ε to $(\varepsilon + 2V \cos k)$. The transformed Hamiltonian H_k can be diagonalized into a simple quadratic form:

$$\begin{aligned} H_k &= (A_k^\dagger, B_k^\dagger) \begin{pmatrix} \varepsilon + 2V \cos k & U \\ U & E \end{pmatrix} \begin{pmatrix} A_k \\ B_k \end{pmatrix} \\ &\equiv (A_k^\dagger, B_k^\dagger) \begin{pmatrix} e & U \\ U & E \end{pmatrix} \begin{pmatrix} A_k \\ B_k \end{pmatrix} \equiv \sum_{i,j=1}^2 M_{ij} X^\dagger(k)_i X(k)_j, \end{aligned} \quad (4.16)$$

where the abbreviations $e = \varepsilon + 2V \cos k$ and $\mathbf{X}^\dagger(k) = (A_k^\dagger, B_k^\dagger)$ are used. The matrix kernel of the Hamiltonian, M , is diagonalized as

$$S^T M S = \begin{pmatrix} \lambda_+ & 0 \\ 0 & \lambda_- \end{pmatrix}, \quad (4.17)$$

by an orthogonal matrix S as

$$S = \begin{pmatrix} \sqrt{\frac{L+K}{2L}} & \sqrt{\frac{L-K}{2L}} \\ \sqrt{\frac{L-K}{2L}} & -\sqrt{\frac{L+K}{2L}} \end{pmatrix}. \quad (4.18)$$

Here eigenvalues λ_{\pm} are written as

$$\begin{aligned} \lambda_{\pm} &= \frac{e + E}{2} \pm \frac{1}{2} \sqrt{(e - E)^2 + 4U^2} \\ &\equiv K + E \pm L \end{aligned} \quad (4.19)$$

with $K = (e - E)/2$ and $L = \sqrt{K^2 + U^2}$. Using the polariton transformation as

$$\begin{pmatrix} \alpha_k \\ \beta_k \end{pmatrix} \equiv S^T \begin{pmatrix} A_k \\ B_k \end{pmatrix}, \quad (4.20)$$

we can finally diagonalize the Hamiltonian (Eq. 4.15) as follows:

$$H = \sum_k H_k = \sum_k (\lambda_+ \alpha_k^\dagger \alpha_k + \lambda_- \beta_k^\dagger \beta_k). \quad (4.21)$$

4.3.2 Dipole Dynamics Driven by Local Excitation

With the help of the diagonalized Hamiltonian (Eq. 4.21), we can immediately solve the Heisenberg equation and can express the time evolution of exciton–polariton operators $\alpha_k(t)$ and $\beta_k(t)$ as

$$\begin{pmatrix} \alpha_k(t) \\ \beta_k(t) \end{pmatrix} = \begin{pmatrix} e^{-i\lambda_+ t/\hbar} \alpha_k \\ e^{-i\lambda_- t/\hbar} \beta_k \end{pmatrix}, \quad (4.22)$$

where α_k and β_k denote the operators in the Schrödinger representation. It is assumed in this chapter that an operator with no indication of the time dependence is expressed in the Schrödinger picture as a time-independent operator. From the inverse transformation of (Eq. 4.20), we obtain a time-dependent solution of the Fourier transforms $A_k(t)$ and $B_k(t)$ as

$$\begin{pmatrix} A_k(t) \\ B_k(t) \end{pmatrix} = S \begin{pmatrix} \alpha_k(t) \\ \beta_k(t) \end{pmatrix} = S \begin{pmatrix} e^{-i\lambda_+ t/\hbar} \alpha_k \\ e^{-i\lambda_- t/\hbar} \beta_k \end{pmatrix}. \quad (4.23)$$

By transforming the exciton–polariton operators (α_k, β_k) into (A_k, B_k) again, explicit time-dependent solutions $A_k(t)$ and $B_k(t)$ of the Heisenberg equations are written as

$$A_k(t) = e^{-i(e+E)t/2\hbar} \left(\cos \frac{L}{\hbar} t - i \frac{K}{L} \sin \frac{L}{\hbar} t \right) A_k - i \frac{U}{L} e^{-i(e+E)t/2\hbar} \left(\sin \frac{L}{\hbar} t \right) B_k, \quad (4.24a)$$

$$B_k(t) = -i \frac{U}{L} e^{-i(e+E)t/2\hbar} \left(\sin \frac{L}{\hbar} t \right) A_k + e^{-i(e+E)t/2\hbar} \left(\cos \frac{L}{\hbar} t + i \frac{K}{L} \sin \frac{L}{\hbar} t \right) B_k. \quad (4.24b)$$

Using the Fourier inverse transformation, we obtain a final expression of the time evolution of the exciton operator $b_n(t)$ as follows:

$$b_n(t) = \frac{1}{N} \sum_{k,m} e^{ik(m-n)-i(e+E)t/2\hbar} \times \left\{ -i a_m \frac{U}{L} \sin \frac{Lt}{\hbar} + b_m \left(\cos \frac{Lt}{\hbar} + i \frac{K}{L} \sin \frac{Lt}{\hbar} \right) \right\}. \quad (4.25)$$

Here we introduce a physical quantity of the electric dipole moment for our two-level system defined as

$$\boldsymbol{\mu}_n(t) = \boldsymbol{\mu}(b_n(t) + b_n^\dagger(t)) = \boldsymbol{\mu} P_n(t), \quad (4.26)$$

where $P_n(t) = b_n(t) + b_n^\dagger(t)$ denotes the dipole operator that describes the electric dipole moment of each quantum dot. Moreover, two other independent operators are defined as

$$V_n(t) = i(b_n(t) - b_n^\dagger(t)), \quad W_n(t) = b_n^\dagger(t)b_n(t) - b_n(t)b_n^\dagger(t), \quad (4.27)$$

where the latter represents the population difference of the system. The unit operator and these three operators form a basis for any two-level system, and the set (P_n, V_n, W_n) corresponds to the Bloch vector in a collection of two-level atom system. However, it should be noted that the population difference W_n is always -1 for bosonic excitons, and the number operators of excitons $b_n^\dagger b_n$ are the independent operators in this case.

In order to investigate the coherent excitation dynamics of the system, we examine the time evolution of the expectation value of the dipole moment at an arbitrary QD n , $\langle P_n(t) \rangle$, under a variety of initial conditions. The expression given by (Eq. 4.25) and its Hermitian conjugate provide a useful result as

$$\begin{aligned} \langle P_n(t) \rangle = & \frac{1}{N} \sum_{k \in 1BZ} \sum_{m=1}^N \left\{ (\langle P_m \rangle \cos \xi_{mn} + \langle V_m \rangle \sin \xi_{mn}) \cos \frac{L}{\hbar} t \right. \\ & \left. + \frac{K}{L} (\langle V_m \rangle \cos \xi_{mn} - \langle P_m \rangle \sin \xi_{mn}) \sin \frac{L}{\hbar} t \right\}, \end{aligned} \quad (4.28)$$

where the operation $\langle \dots \rangle = \text{Tr} \rho \dots$ means the expectation value of an arbitrary operator. The notation $\xi_{mn} \equiv k(m-n) - t(e+E)/2\hbar$ is used. Localized photons are assumed to be initially in the vacuum state. In particular, it is intriguing to investigate the dynamics with the initial condition of a locally or individually excited state, that is, how the initial excitation prepared only at one site is transferred in the system. Setting $\langle P_n(0) \rangle = \delta_{n1} \langle P_1 \rangle$ and $\langle V_n(0) \rangle = 0$ for all n , we obtain from (Eq. 4.28) an explicit solution as

$$\langle P_n(t) \rangle = \frac{1}{N} \sum_k \left\{ \cos \xi_{1n} \cos \frac{L}{\hbar} t - \frac{K}{L} \sin \xi_{1n} \sin \frac{L}{\hbar} t \right\} \langle P_1 \rangle. \quad (4.29)$$

In Fig. 4.5, we present one of numerical results of the time evolution of the dipole moment distribution calculated from (Eq. 4.29), where the total number of sites is eight, and the parameter values $E = 2$, $\varepsilon = 1$, and $V = 1$ are used in a unit of a typical exciton energy in QD.

Although the dynamics seems complicated at first sight, we can find a characteristic behavior that the dipole of the first site moves to the fifth site (the opposite site) and returns to the first site again. To see the behavior more precisely, we show plots of the time evolution of the dipole moments of the first site and the fifth site in Fig. 4.6a, b, respectively.

The result clearly shows as a dominant behavior that when the dipole of the first site is active, that of the fifth site is inactive and vice versa, or the dipole moves like a seesaw between the first site and the fifth site. The recurrence behavior is reasonable from the fact that the Heisenberg equation of the system is linear in the boson approximation. Since the dipole moment P_n is quantum coherence between the ground and excited states of a two-level system, quantum coherence is transported to the farthest site of the chain and then comes back to the original site. When the total number of sites is odd, the seesaw motion arises between an initially excited site and its farthest pair of sites of the chain. An interesting point in this case is that we can obtain two copies of coherence at the farthest pair of sites as illustrated in Fig. 4.7b.

Moreover, it might be possible to use the system as a nanophotonic device of transporting or splitting quantum coherence.

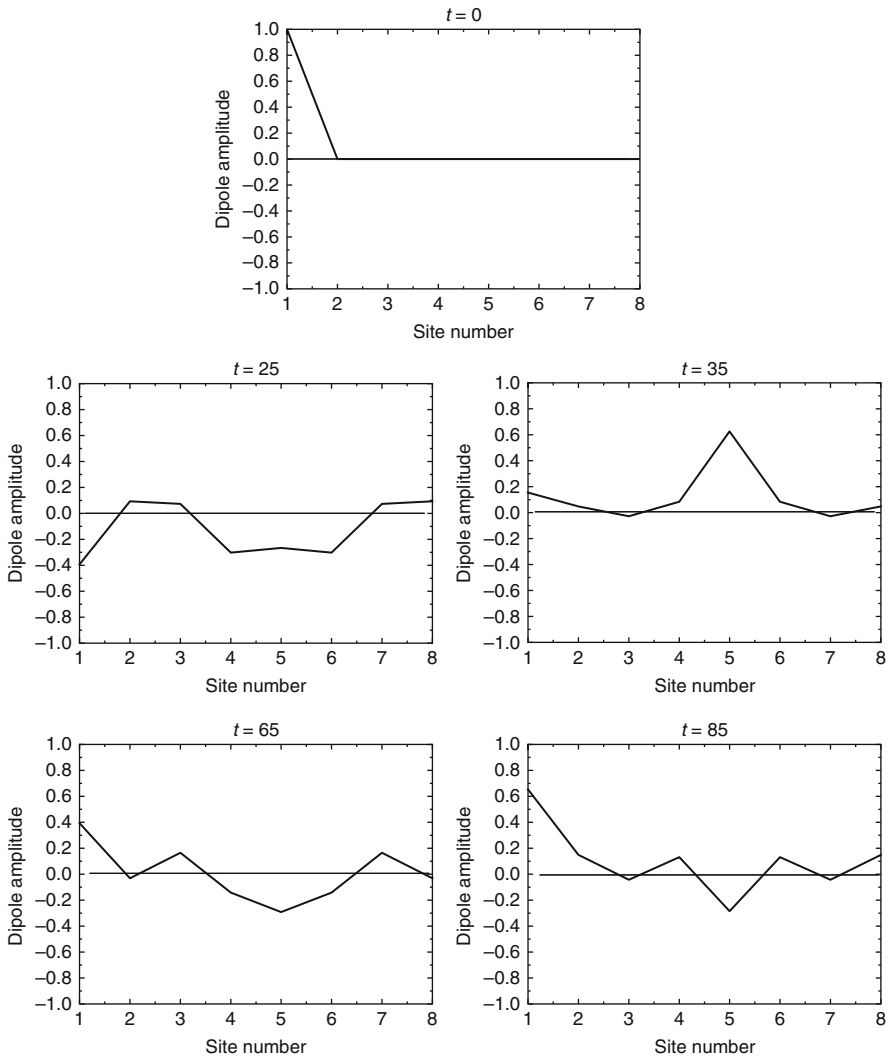


Fig. 4.5 Time evolution of the dipole-moment distribution when the total number of sites is eight. The parameters $E = 2$, $\varepsilon = 1$, and $V = 1$ are used in the calculation. The vertical and horizontal axes represent the dipole amplitude and the site number, respectively. The dipole moment is initially set only at the first site

Fig. 4.6 Time evolution of the dipole moment of (a) the first site and (b) the fifth site. When the dipoles are large in (a), corresponding dipoles in (b) are small and vice versa

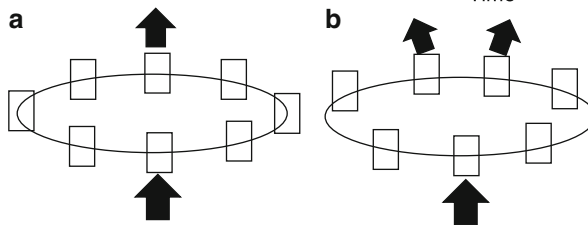
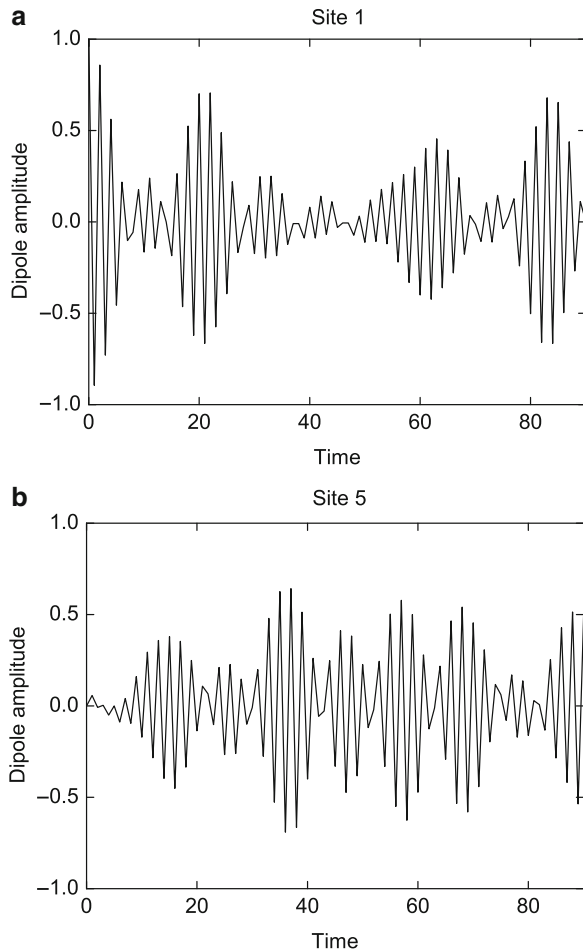


Fig. 4.7 Transportation of quantum coherence in (a) an even site number system and (b) an odd site number system. In the even site system (a), output signals are obtained from the opposite site to the input site. In the odd site system (b), output signals are split into the two-pair site opposite to the input site

4.4 Controlling Dipole Dynamics

If we rigorously adopt the commutation relation for excitons given by (Eq. 4.7), the Heisenberg equations for the system read

$$\frac{db_n(t)}{dt} = \frac{i}{\hbar}[H, b_n(t)] = -\frac{i}{\hbar}Eb_n(t) + \frac{i}{\hbar}Ua_n(t)W_n(t), \quad (4.30a)$$

$$\begin{aligned} \frac{da_n(t)}{dt} &= \frac{i}{\hbar}[H, a_n(t)] \\ &= -\frac{i}{\hbar}\varepsilon a_n(t) - \frac{i}{\hbar}V(a_{n+1}(t) + a_{n-1}(t)) - \frac{i}{\hbar}Ub_n(t). \end{aligned} \quad (4.30b)$$

Since the higher-order terms are produced by a mode–mode coupling such as $a_n W_n = a_n(b_n^\dagger b_n - b_n b_n^\dagger)$, the equations become nonlinear and are hardly solved analytically. Thus, we first solve the equations perturbatively in order to investigate the dynamics discussed in the preceding section.

4.4.1 Perturbative Solution

Noticing that the Hamiltonian for localized photons H_a given by (Eq. 4.5a) can be written in a quadratic form as

$$H_a = (a_1^\dagger, \dots, a_N^\dagger) \begin{pmatrix} \varepsilon & V & & & & V \\ V & \varepsilon & V & & & \\ & & \dots & \dots & & \\ & & & \dots & \dots & \\ & & & & V & \varepsilon & V \\ V & & & & V & \varepsilon \end{pmatrix} \begin{pmatrix} a_1 \\ \vdots \\ \vdots \\ \vdots \\ a_N \end{pmatrix} \quad (4.31)$$

$$\equiv \sum_{nm} a_n^\dagger R_{nm} a_m, \quad (4.32)$$

we obtain an orthogonal matrix P to diagonalize the matrix kernel R of the Hamiltonian as

$$(P^{-1}RP)_{ij} = \hbar\lambda_i\delta_{ij}. \quad (4.33)$$

Then new annihilation operators $v_j = \sum_n P_{nj}a_n$ and creation operator $v_j^\dagger = \sum_n P_{nj}a_n^\dagger$ of new modes of localized photons are introduced. Here note that the new modes are extended over a whole system since all the elements of the diagonalization matrix P are not zero. The commutation relation of the new operators can be given as $[v_i, v_j^\dagger] = \delta_{ij}$. With the help of (Eq. 4.33) and the modes v_i , the Hamiltonian in (Eqs. 4.32) or (4.5a) is diagonalized as

$$H_a = \sum_j \hbar \lambda_j v_j^\dagger v_j, \quad (4.34)$$

and the localized photon–exciton interaction H_{int} in (Eq. 4.5c) is written in terms of v_i as

$$H_{\text{int}} = \hbar g \sum_{nj} P_{nj} (v_j^\dagger b_n + v_j b_n^\dagger). \quad (4.35)$$

In order to derive a perturbative expansion of the time evolution of an arbitrary operator, we define the Liouvillians as

$$L \cdots = \frac{1}{\hbar} [H, \cdots], \quad L_0 \cdots = \frac{1}{\hbar} [H_0, \cdots], \quad L_{\text{int}} \cdots = \frac{1}{\hbar} [H_{\text{int}}, \cdots]. \quad (4.36)$$

Then the Heisenberg equation of an arbitrary operator O is written as

$$\dot{O} = \frac{i}{\hbar} [H, O] = iLO, \quad (4.37)$$

and we can obtain a formal solution as

$$O(t) = G(t)O(0), \quad (4.38)$$

with the time evolution operator $G(t) = e^{iLt}$ that satisfies the following equation:

$$\dot{G}(t) = iLG(t) = iL_0G(t) + iL_{\text{int}}G(t). \quad (4.39)$$

Treating the interaction term H_{int} as a perturbation, we solve (Eq. 4.39) perturbatively up to the second order of the perturbation as [45]

$$\begin{aligned} G^{(2)}(t) = & G_0(t) + i \int_0^t G_0(t-s) L_{\text{int}} G_0(s) ds \\ & - \int_0^t ds \int_0^s du G_0(t-s) L_{\text{int}} G_0(s-u) L_{\text{int}} G_0(u), \end{aligned} \quad (4.40)$$

where the notation $G_0(t) = e^{iL_0 t}$ is used. Substituting (Eq. 4.40) into (Eq. 4.38) and using (Eq. 4.36), we can obtain the time evolution of the exciton operator $b_n(t) = G^{(2)}(t)b_n$. Suppose that localized photons are initially in the vacuum and $\langle V_n \rangle = 0$, then the expectation value of $b_n(t)$ is expressed as

$$\begin{aligned} \langle b_n(t) \rangle = & e^{-i\Omega t} \langle b_n \rangle + g^2 \sum_{j=1}^N \Gamma_j(t) \\ & \times \left(\sum_{m=1}^N P_{nj} P_{mj} (1 - \delta_{nm}) \langle W_n \rangle \langle b_m \rangle - P_{nj}^2 \langle b_n \rangle \right), \end{aligned} \quad (4.41)$$

where the notation

$$\begin{aligned} \Gamma_j(t) = & e^{-i\Omega t} \int_0^t ds e^{is(\Omega - \lambda_j)} \int_0^s du e^{-iu(\Omega - \lambda_j)} \\ = & \frac{e^{-i\Omega t} - e^{-i\lambda_j t}}{(\Omega - \lambda_j)^2} + \frac{it e^{-i\Omega t}}{\Omega - \lambda_j} \equiv c_j(t) + i d_j(t) \end{aligned} \quad (4.42)$$

is used and $c_j(t)$ and $d_j(t)$ represent the real and imaginary parts of $\Gamma_j(t)$, respectively. The expression given by (Eq. 4.41) and its Hermitian conjugate provide a time evolution of the expectation value of the dipole at an arbitrary QD site n as

$$\begin{aligned} \langle P_n(t) \rangle = & \langle P_n \rangle \left(\cos \Omega t - g^2 \sum_j c_j(t) P_{nj}^2 \right) \\ & + g^2 \sum_j \sum_{m \neq n} c_j(t) P_{nj} P_{mj} \langle P_m \rangle \langle W_n \rangle. \end{aligned} \quad (4.43)$$

Corresponding to the discussion developed in Sect. 4.3.2, we set initially $\langle P_n \rangle = \delta_{n1}$ and obtain the perturbative solution that describes the dipole dynamics driven by a local excitation of QD site one as follows:

$$\begin{aligned} \langle P_n(t) \rangle = & \delta_{n1} \left(\cos \Omega t - g^2 \sum_j c_j(t) P_{nj}^2 \right) \langle P_1 \rangle \\ & + (1 - \delta_{n1}) g^2 \sum_j c_j(t) P_{nj} P_{1j} \langle P_1 \rangle \langle W_n \rangle. \end{aligned} \quad (4.44)$$

In the next section we discuss the dynamic properties of the system, on the basis of the solution given by (Eq. 4.44).

4.4.2 Dynamic Properties

As discussed in Sect. 4.3.2, we numerically examine the dynamics of the dipole of the system depending on the initial conditions. Suppose that localized photons are initially in the vacuum, $\langle V_n \rangle = 0$ for all n , the dipole is initially set only at the first

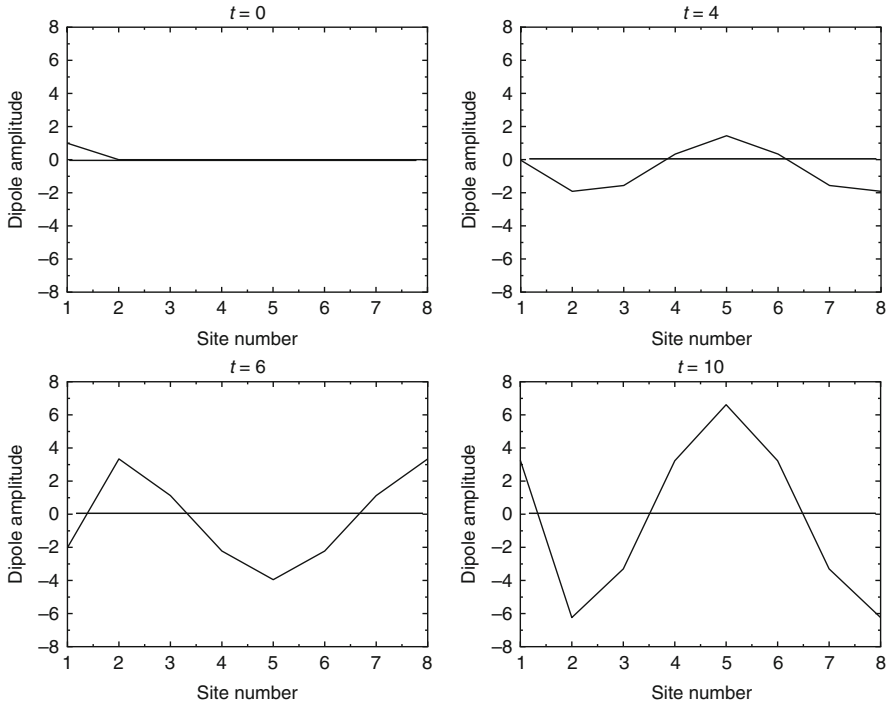


Fig. 4.8 Time evolution of the dipole distributions ($E = 2, \varepsilon = 1, V = 1$). Initially all of the sites without the first site are in the ground state, while the dipole moment is initially set only at the first site

site as $\langle P_n \rangle = \delta_{n1}$, and all the populations are in the ground states except for the first site as $\langle W_n \rangle = -(1 - \delta_{n1})$. As mentioned before, all the population differences are automatically -1 for bosonic excitons. In addition, we impose that the length of the Bloch vector (P_n, V_n, W_n) is normalized as

$$\langle P_n(t) \rangle^2 + \langle V_n(t) \rangle^2 + \langle W_n(t) \rangle^2 = 1. \quad (4.45)$$

In Fig. 4.8, the time evolution of the dipole distribution is plotted. The parameter values used are the same as in Sect. 4.3.2 ($E = 2, \varepsilon = 1$, and $V = 1$).

It follows from the figure that the dipole excitation of the first site moves to the opposite site as shown in the boson case (see Fig. 4.5). The reason is that the initial exciton density is so dilute as to validate the boson approximation. As time advances, the amplitude of each dipole increases because the perturbative solution violates the unitarity.

To find a new feature of fermionic excitons, we vary the initial conditions for the population differences from $\langle W_n \rangle = -(1 - \delta_{n1})$. Since the initial population

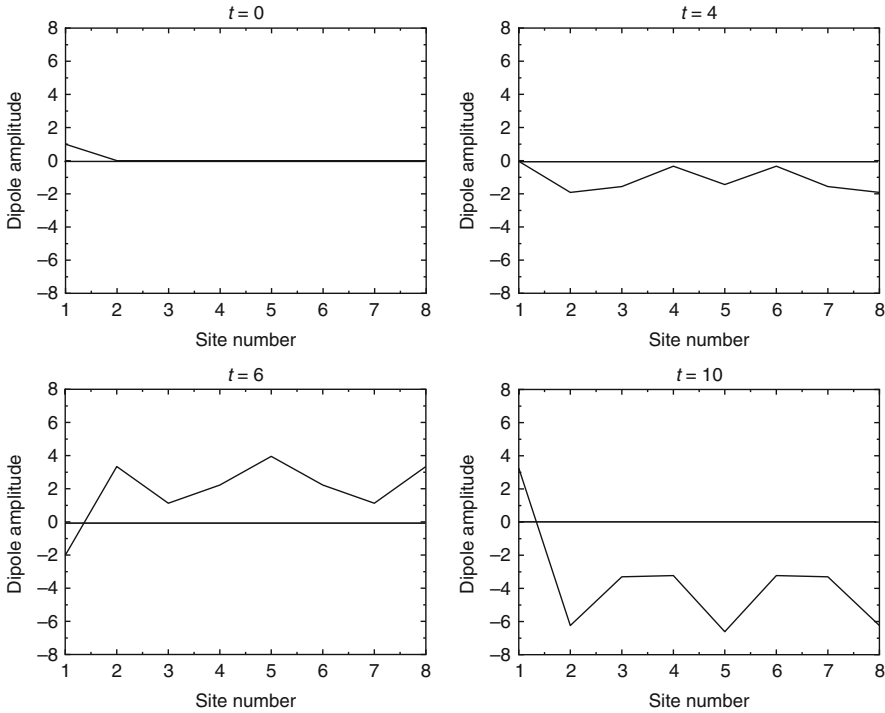


Fig. 4.9 Time evolution of the dipole distribution ($E = 2, \varepsilon = 1, V = 1$): the initial population differences of sites 4, 5, and 6 are inverted from $\langle W_n \rangle = -(1 - \delta_{n1})$

differences at site n contribute to the perturbative solution of the dipole at the same site, (Eq. 4.44), in a product of $\langle W_n \rangle \langle P_1 \rangle$, the following property is obtained.

Flip Property *If the sign of the initial population difference of the n th site, $\langle W_n(0) \rangle$, is inverted, then the direction of the dipole moment of the n th site at arbitrary time, $\langle P_n(t) \rangle$, is flipped.*

Since the dipoles at sites, 4, 5, and 6 in Fig. 4.8 are directed opposite to others, we invert the sign of $\langle W_n \rangle$ for $n = 4, 5, 6$.

Figure 4.9 shows the result that the direction of the dipoles at sites, 4, 5, and 6 are flipped and that all the dipoles oscillate with the same phase but with a different amplitude. Thus, we observe that the system is transferred from a locally excited state to a coherently oscillating state of the dipoles, in other words, to a dipole-ordered state. In the ordered state, the total dipole is N times larger than each single dipole. Moreover, since radiation from an oscillating dipole is proportional to the square of the dipole moment, we can expect a high intensity of radiation from the dipole-ordered state. The radiation property of the system will be discussed in Sect. 4.8.

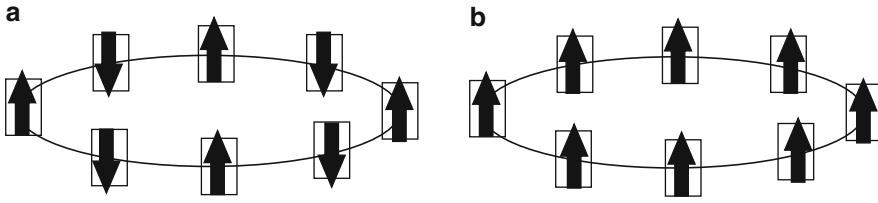


Fig. 4.10 Schematic illustration of (a) an alternating dipole distribution (a dipole-forbidden state) and (b) a dipole-ordered state. The state with alternating dipoles that result in the total dipole of zero cannot be coupled by the radiation field with the dipole interaction

4.4.3 Controlling of Dipole Dynamics

It is well known that the electric interaction between molecules with no dipole moments is weak when they are separated in a macroscopic distance and that the interaction becomes strong when they are very close to each other. Taking it into account, we investigate the dynamics of the system driven by localized photons, from an initial state that alternating dipoles are set, and thus, the total dipole of the system vanishes for an even number of sites (see Fig. 4.10a). Such a dipole-forbidden state can be manipulated by localized photons, not by propagating far fields.

As an initial condition, we set $\langle P_n \rangle = (-1)^n$, and for simplicity, localized photons are in the vacuum, $\langle V_n \rangle = 0$ and $\langle W_n \rangle = 0$. The system parameters $E = 2$, $\varepsilon = 1$, and $V = 1$ are used as before. Figure 4.11 shows the time evolution of such a dipole-forbidden state.

From Fig. 4.11, it follows that the system oscillates as schematically shown in Fig. 4.10a and that it remains in the initial dipole-forbidden state. This kind of dynamics is achieved in the system whose initial distribution of the population differences is uniform. For example, if we set $\langle P_n \rangle = (-1)^n/\sqrt{2}$ and $\langle W_n \rangle = 1/\sqrt{2}$ for all n , the result is the same as shown in Fig. 4.11 except for its amplitude of the oscillation.

Next, we manipulate the distribution of the population difference nonuniformly, so that the signs are set as opposite to those of the corresponding dipoles:

$$\begin{aligned}\langle P_n \rangle &= (-, +, -, +, -, +, -, +)/\sqrt{2}, \\ \langle W_n \rangle &= (+, -, +, -, +, -, +, -)/\sqrt{2}.\end{aligned}$$

Figure 4.12 presents the result that a dipole-forbidden state as shown in Fig. 4.10a is converted to a dipole-ordered state as illustrated in Fig. 4.10b.

Since the dipole ordering has occurred by manipulating the initial distribution of the population differences, the result can be interpreted by the “flip property” proposed in Sect. 4.4.2. As a collective oscillation of the dipoles occurred,

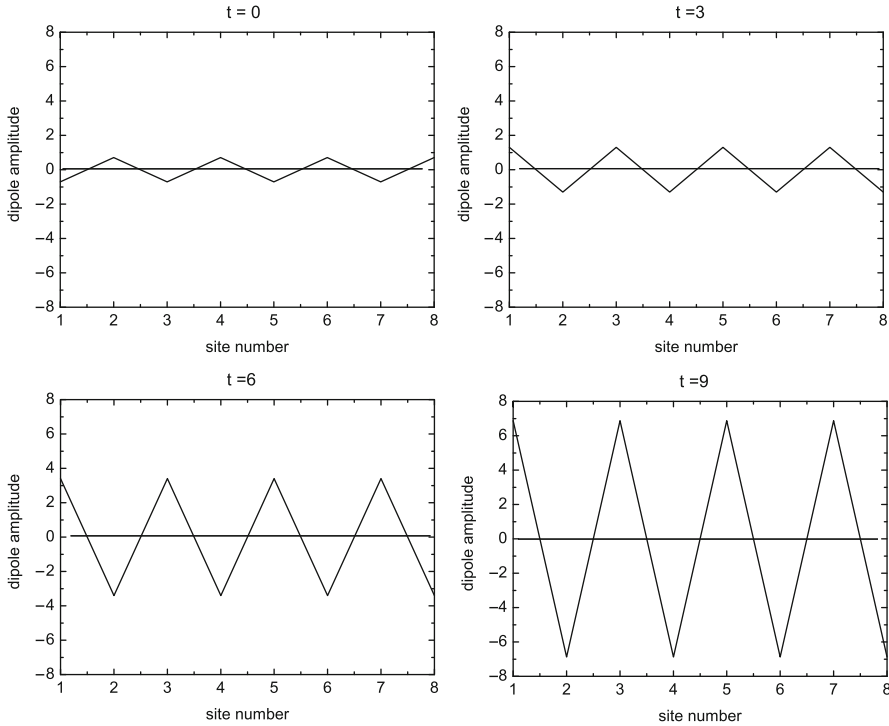


Fig. 4.11 Time evolution of a dipole-forbidden state (alternating dipole distribution). All the population differences are initially set as 0. We observe an oscillation of the alternating dipoles. The system remains in the dipole-forbidden state

the system evolved from a nonradiative state to a radiative state through the localized photon–exciton interaction.

4.4.4 Verification of Perturbation Solutions by Semiclassical Approximations

Here we should note that the second-order perturbative solutions break the unitarity and that the long-time behaviors of the dynamics given by the solutions are not necessarily same as the exact ones. Thus, we have to return to the Heisenberg equations, (Eq. 4.30a) and (Eq. 4.30b), to evaluate the time evolution of physical observables. The Heisenberg equations are first solved by neglecting the quantum correlations between excitons and localized photons such as $\langle W_n y_n \rangle = \langle W_n \rangle \langle y_n \rangle$, and later the quantum correlations are estimated in Sect. 4.8.2. In this semiclassical approximation, (Eqs. 4.30a) and (4.30b) can be converted to the following coupled differential equations

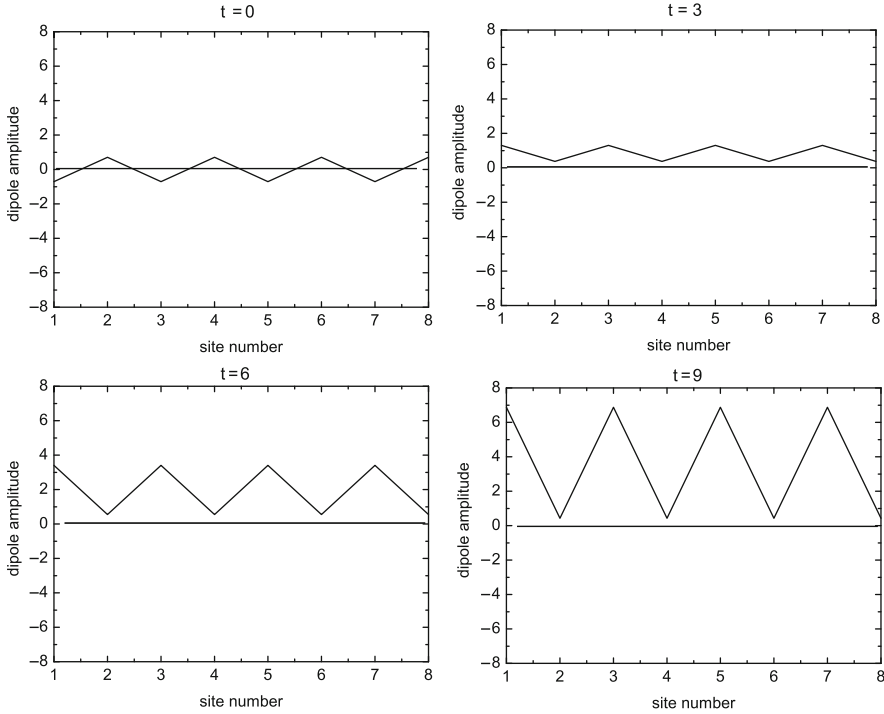


Fig. 4.12 Time evolution of a dipole-forbidden state ($E = 2, \varepsilon = 1, V = 1$). The population differences are initially set as $\langle W_n \rangle = -\langle P_n \rangle$. The system is converted from a dipole-forbidden state to a dipole-ordered state

$$\begin{cases} \partial_t \langle P_n \rangle = -\Omega \langle V_n \rangle + g \langle W_n \rangle \langle y_n \rangle, \\ \partial_t \langle V_n \rangle = \Omega \langle P_n \rangle - g \langle W_n \rangle \langle x_n \rangle, \\ \partial_t \langle W_n \rangle = g (\langle V_n \rangle \langle x_n \rangle - \langle P_n \rangle \langle y_n \rangle), \end{cases} \quad (4.46)$$

$$\begin{cases} \partial_t \langle x_n \rangle = -\omega \langle y_n \rangle - v (\langle y_{n-1} \rangle + \langle y_{n+1} \rangle) - g \langle V_n \rangle, \\ \partial_t \langle y_n \rangle = \omega \langle x_n \rangle + v (\langle x_{n-1} \rangle + \langle x_{n+1} \rangle) + g \langle P_n \rangle, \end{cases} \quad (4.47)$$

where the notations $x_n = a_n + a_n^\dagger$, $y_n = i(a_n - a_n^\dagger)$, and $v = V/\hbar$ are used.

To check the reliability of the semiclassical approximation, we again investigate the system examined in Sect. 4.4.2. Figure 4.13 shows the time evolution of the dipole distribution obtained from the semiclassical approach for the system corresponding to Fig. 4.8.

Comparing Fig. 4.13 with Fig. 4.8, we find that both profiles are the same and that the amplitude of each dipole obtained from the Heisenberg equations is less than 1, which means that the unitarity of the time evolution is conserved.

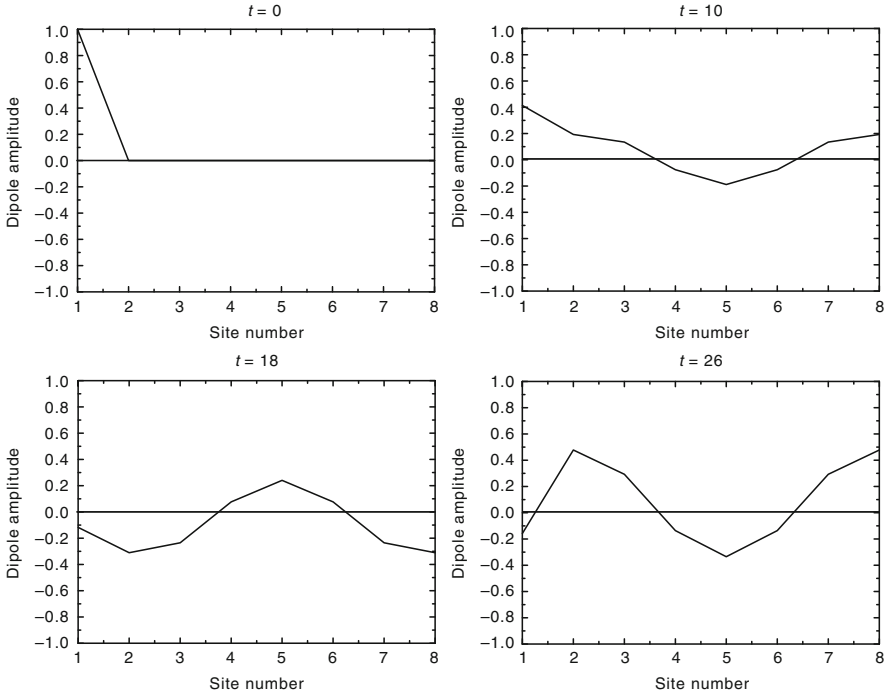


Fig. 4.13 Time evolution of the dipole distribution for the system ($E = 2, \varepsilon = 1, V = 1$) obtained from the Heisenberg equation with semiclassical approximation. Initially all of the sites without the first site are in the ground state

In Fig. 4.14, we show the time evolution of the dipole distribution obtained from the semiclassical approach when the initial population differences of sites, 4, 5, and 6 are inverted. It follows from the figure that each dipole is ordered as the flip property predicts and that the flip property is still valid in the numerical solution of the semiclassical Heisenberg equation.

Numerical results obtained from (Eqs. 4.46) and (4.47) with a semiclassical approximation predict the dipole dynamics with qualitative similarities as shown from the perturbative solution (Eq. 4.44). The flip property proposed in Sect. 4.4.2 is also verified by using the numerical solutions of (Eqs. 4.46) and (4.47) or those of the Heisenberg equations without quantum correlations. These results show that the approach discussed in this section, maintaining an advantage to conserve the unitarity, qualitatively describe the dipole dynamics of the system in a similar way as the other two approaches. The validity of the approximation employed here, which we will examine in Sect. 4.8.2, is reported in the Dicke model that superradiant phenomena can be described with a semiclassical approximation which neglects quantum correlations among the atoms [2] and that the contribution from the quantum correlations is of the order of $1/N$ for large N [3].

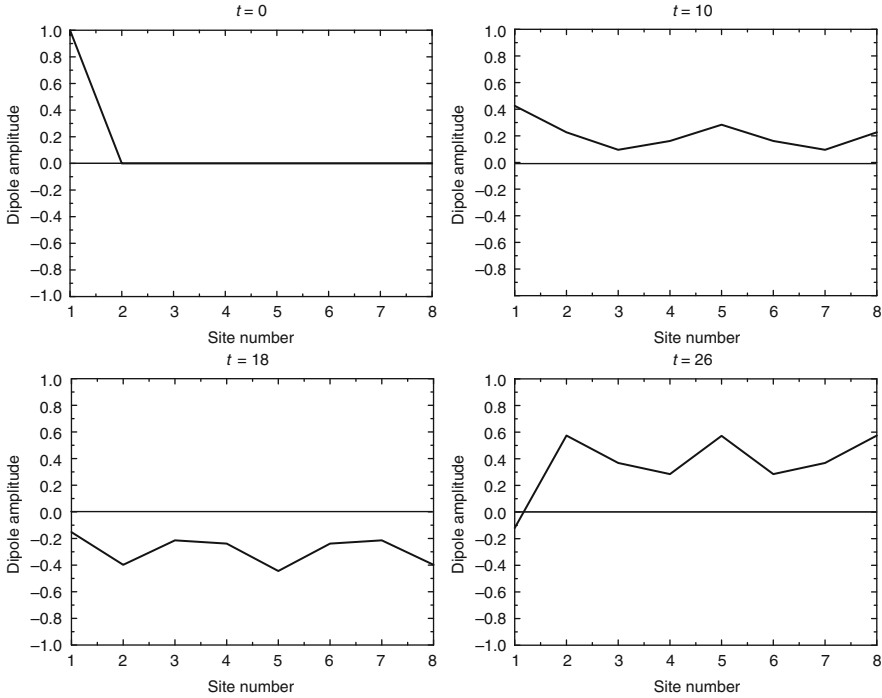


Fig. 4.14 Time evolution of the dipole distribution for the system ($E = 2, \varepsilon = 1, V = 1$) obtained from the Heisenberg equation with semiclassical approximation. The initial population differences of sites, 4, 5, and 6 are inverted

4.5 Classification of Quasi-steady States

In order to investigate the origin of the dipole ordering discussed above, we first introduce an effective Hamiltonian to renormalize the degrees of freedom of localized photons. Using the effective Hamiltonian, we then classify quasi-steady states with respect to the dipole distribution.

4.5.1 Effective Hamiltonian

A unitary transformation with an anti-Hermitian operator S is applied to the Hamiltonian (Eq. 4.4) as [6, 30, 44]

$$\tilde{H} = e^{-S} H e^S = H + [H, S] + \frac{1}{2} [[H, S], S] + \dots \quad (4.48)$$

If the Hamiltonian (Eq. 4.4) is divided into the unperturbed part $H_0 = H_a + H_b$ and perturbed part H_{int} and if S is chosen to satisfy

$$H_{\text{int}} + [H_0, S] = 0, \quad (4.49)$$

the terms linear in the coupling constant $g = U/\hbar$ vanish as

$$\tilde{H} = H_0 + \frac{1}{2}[H_{\text{int}}, S] + O(g^3). \quad (4.50)$$

The transformed Hamiltonian \tilde{H} contains the terms in the second order of the exciton-localized photon interaction that describe exciton–exciton interactions via localized photons. Taking the expectation value of \tilde{H} in terms of the vacuum of localized photons $|\text{vac}\rangle$, we obtain the effective Hamiltonian H_{eff} as

$$H_{\text{eff}} = \langle \text{vac} | \tilde{H} | \text{vac} \rangle = H_b + H_{b-b}, \quad (4.51a)$$

$$H_b = \sum_n \hbar \Omega b_n^\dagger b_n, \quad (4.51b)$$

$$H_{b-b} = \sum_{n,m} \left(\frac{\hbar g^2}{\Omega I - R/\hbar} \right)_{nm} b_n^\dagger b_m, \quad (4.51c)$$

where the exciton energy E is denoted as $\hbar\Omega$. With the help of the components of the Bloch vector (P_n, V_n, W_n) , the effective Hamiltonian (Eq. 4.51a) can be rewritten as

$$H_{\text{eff}} = \hbar \sum_n (\Omega + \Delta\Omega_n) \frac{1 + W_n}{2} + \frac{\hbar}{4} \sum_n \sum_{m \neq n} \Delta\Omega_{nm} (P_n P_m + V_n V_m), \quad (4.52)$$

where the interaction energy or coupling strength between excitons $\Delta\Omega_{nm}$ is given as

$$\Delta\Omega_{nm} = \left(\frac{g^2}{\Omega I - R/\hbar} \right)_{nm} = \sum_j \frac{g^2}{\Omega - \lambda_j} P_{nj} P_{mj}, \quad (4.53)$$

and the abbreviation $\Delta\Omega_n \equiv \Delta\Omega_{nn}$ is used for a special case.

4.5.2 Classification of Quasi-steady States and Controlling of Dipole Distributions

Using the effective Hamiltonian H_{eff} , we can obtain the time evolution of the dipole moment at site n in a similar way as discussed in Sect. 4.4.1:

$$\langle P_n(t) \rangle = \langle P_n \rangle \cos[(\Omega + \Delta\Omega_n)t] + \sum_{m \neq n} \Delta\Omega_{nm} t \langle W_n \rangle \langle P_m \rangle \sin(\Omega t). \quad (4.54)$$

If the dipole at site 1, in particular, is only excited at $t = 0$, (Eq. 4.54) reads

$$\begin{aligned} \langle P_n(t) \rangle &= \delta_{n1} \langle P_1 \rangle \cos[(\Omega + \Delta\Omega_n)t] \\ &+ (1 - \delta_{n1}) \Delta\Omega_{n1} t \langle W_n \rangle \langle P_1 \rangle \sin(\Omega t). \end{aligned} \quad (4.55)$$

It follows from this expression that the sign of the dipole at site n depends on the coefficient $\Delta\Omega_{n1}$ as well as the initial values of $\langle P_1(0) \rangle$ and $\langle W_n(0) \rangle$ and that the coefficient $\Delta\Omega_{n1}$ determines what kind of quasi-steady states of the dipole distribution the system reaches when the initial values are fixed. Therefore, we examine the matrix $\Delta\Omega$ to classify the quasi-steady states of the dipole distribution of the system. First, as an example, we show the matrix elements of $\Delta\Omega$ for the system examined in Sects. 4.3 and 4.4 whose material parameters are $E = 2$, $\varepsilon = 1$, and $V = 1$ as follows:

$$\Delta\Omega = \begin{pmatrix} \frac{1}{3} & \frac{2}{3} & \frac{1}{3} & -\frac{1}{3} & -\frac{2}{3} & -\frac{1}{3} & \frac{1}{3} & \frac{2}{3} \\ \frac{2}{3} & \frac{1}{3} & \frac{1}{3} & \frac{1}{3} & -\frac{1}{3} & -\frac{2}{3} & -\frac{1}{3} & \frac{1}{3} \\ \frac{1}{3} & \frac{1}{3} & \frac{2}{3} & \frac{1}{3} & \frac{1}{3} & -\frac{1}{3} & -\frac{1}{3} & -\frac{1}{3} \\ -\frac{1}{3} & \frac{1}{3} & \frac{1}{3} & \frac{2}{3} & \frac{1}{3} & \frac{1}{3} & -\frac{1}{3} & -\frac{1}{3} \\ -\frac{2}{3} & -\frac{1}{3} & \frac{1}{3} & \frac{1}{3} & \frac{2}{3} & \frac{1}{3} & \frac{1}{3} & -\frac{1}{3} \\ -\frac{1}{3} & \frac{1}{3} & -\frac{2}{3} & \frac{1}{3} & \frac{1}{3} & \frac{2}{3} & \frac{1}{3} & \frac{1}{3} \\ \frac{1}{3} & -\frac{1}{3} & -\frac{1}{3} & -\frac{2}{3} & \frac{1}{3} & \frac{1}{3} & \frac{2}{3} & \frac{1}{3} \\ \frac{2}{3} & \frac{1}{3} & -\frac{1}{3} & -\frac{1}{3} & -\frac{1}{3} & \frac{1}{3} & \frac{2}{3} & \frac{1}{3} \end{pmatrix}.$$

The matrix is symmetric and has a cyclic structure as

$$\Delta\Omega_{n+1,m+1} = \Delta\Omega_{n,m}.$$

This is due to the fact that the periodic boundary condition is imposed on the system and that the Hamiltonian given in (Eq. 4.4) has translational invariance. Owing to the symmetric structure as

$$(\Delta\Omega_{22}, \Delta\Omega_{23}, \Delta\Omega_{24}, \dots) = (\Delta\Omega_{11}, \Delta\Omega_{12}, \Delta\Omega_{13}, \dots),$$

the dipole distribution of the system initiated by the dipole excitation at site 2 can be discussed in terms of $\Delta\Omega_{1n}$ that governs the problem driven by the site-one excitation. In general the problem is reduced to examine the structure of the coefficients $\Delta\Omega_{1n}$ that depend on the material parameters Ω and λ_j or E , ε , and V . Since the parameter sets crossing the resonant points ($\Omega = \lambda_j$) change the pattern of the dipole distribution in the system, we can classify quasi-steady states of the dipole distribution into four groups in Table 4.1.

The system with $E = 2$, $\varepsilon = 1$, and $V = 1$, which has been investigated in Sect. 4.4, belongs to the first group. Since the coefficients $\Delta\Omega_{1n}$ in the first group have different signs at sites, 4, 5, and 6 from the others, the quasi-steady state of the dipole distribution that is predicted by the effective Hamiltonian is the one described

Table 4.1 Classification of quasi-steady states

Group	Signs of $\Delta\Omega_{1n}$ for $n = 1, 2, 3, \dots, 8$
First group	(-, -, -, +, +, +, -, -), (+, +, +, -, -, -, +, +)
Second group	(-, +, -, -, +, -, -, +), (+, -, +, +, -, +, +, -)
Third group	(-, -, -, -, -, -, -, -), (+, +, +, +, +, +, +, +)
Fourth group	(-, +, -, +, -, +, -, +), (+, -, +, -, +, -, +, -)

by the second-order perturbation solution (see (Eq. 4.44) and Fig. 4.8). The third and fourth groups are, in particular, interesting among the four groups of the quasi-steady states. The third group corresponds to a “ferromagnetic” system, in which all the electric dipole moments are aligned in the same direction, while the fourth group corresponds to an “antiferromagnetic” system, where the dipoles are aligned to have alternating signs.

Using numerical results of (Eqs. 4.46) and (4.47), we examine the dynamics of the third and fourth groups whether they behave as predicted by the effective Hamiltonian: “ferromagnetic” or “antiferromagnetic.” The parameter set of $E = 3.01$, $\varepsilon = 1$, and $V = 1$ gives

$$\Delta\Omega_{1n} = (-13.1, -12.7, -12.4, -12.2, -12.2, -12.2, -12.4, -12.7),$$

and thus, the system belongs to the third group. The results is shown in Fig. 4.15, which predicts the “ferromagnetic” behavior as expected.

When the parameter set of $E = 1$, $\varepsilon = 3.01$, and $V = 1$ is chosen, the system corresponds to the fourth group. Figure 4.16 presents the time evolution of the dipole distribution of the system that shows alternating changes in signs, as expected to be similar to antiferromagnetics.

In an even site number “antiferromagnetic” system, the dipole distribution from an initial state evolves to align the dipoles alternatingly up and down, as shown in Fig. 4.16. On the other hand, an odd site number system becomes frustrated because the dipole distribution cannot be perfectly aligned alternatingly. Thus, it is interesting to examine the time evolution of the dipole distribution in an odd site number system. The result for the $N = 9$ “antiferromagnetic” system is presented in Fig. 4.17. It follows from the figure that there are ordered dipoles near the one initially prepared at site 1 and alternating dipoles including a pair at opposite site to site 1. Since strong frustration, for example, occurred in spin glass, should produce a random distribution, the figure indicates that the odd site number system considered here is not frustrated so strongly.

With the help of the flip property proposed in Sect. 4.4.2, we infer that the distribution of the dipoles can be changed by individual manipulation of the initial population differences and that an “antiferromagnetic” state can be transformed into a dipole-ordered state. To verify it, the initial population differences are set in the zigzag form as $W_n = (0, -, +, -, +, -, +, -)$ for the “antiferromagnetic” system ($E = 1$, $\varepsilon = 3.01$, and $V = 1$), and the time evolution of the dipole distribution is examined. The result, as shown in Fig. 4.18, clearly indicates that a

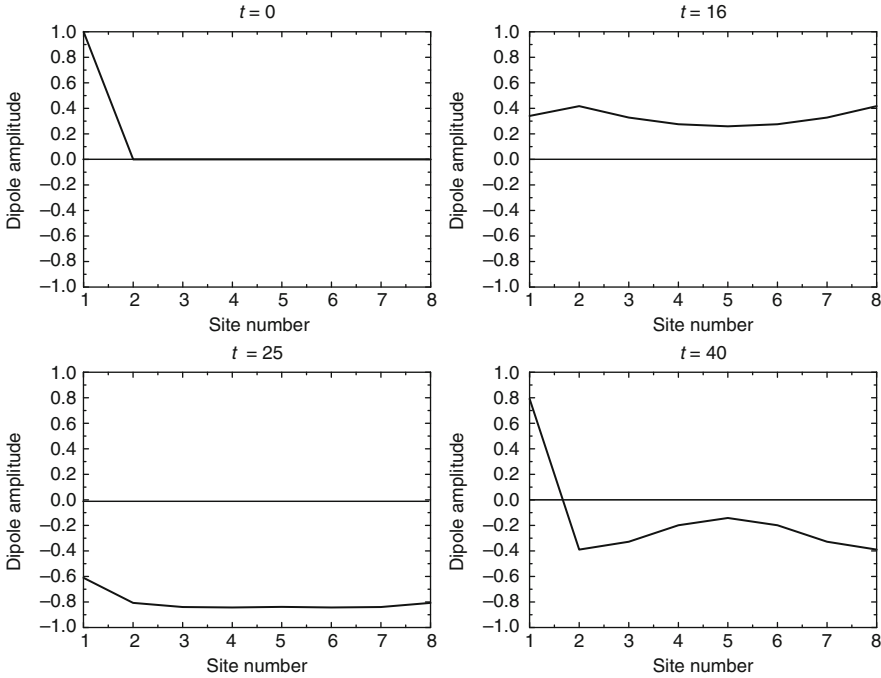


Fig. 4.15 Time evolution of the dipole distribution of the system belonging to the third group. The initial conditions are set as $\langle P_n \rangle = \delta_{n1}$ and $\langle W_n \rangle = 1 - \delta_{n1}$. All the electric dipole moments are aligned in the same direction, and a dipole-ordered state appears

dipole-ordered state manifests itself owing to the local manipulation of the initial population differences. It is noteworthy that the amplitude of each dipole is close to one and that the total dipole of the system is of the order of N , whose radiation property is investigated in the following sections.

4.5.3 Response to the Initial Input of a Localized Photon: The Robustness of Quasi-steady States

Until now, the state of localized photons at each site was initially taken to be a vacuum. Since localized photons in the Heisenberg equations have the different degrees of freedom, this section examines the temporal evolution given an initial distribution of localized photons. The initial conditions take the state given below, in which the distribution of localized photons is given for site 1 only:

$$\langle x_n \rangle = x_1 \delta_{n1}, \quad \langle y_n \rangle = 0, \quad \langle P_n \rangle = \langle V_n \rangle = 0, \quad \langle W_n \rangle = 1. \quad (4.56)$$

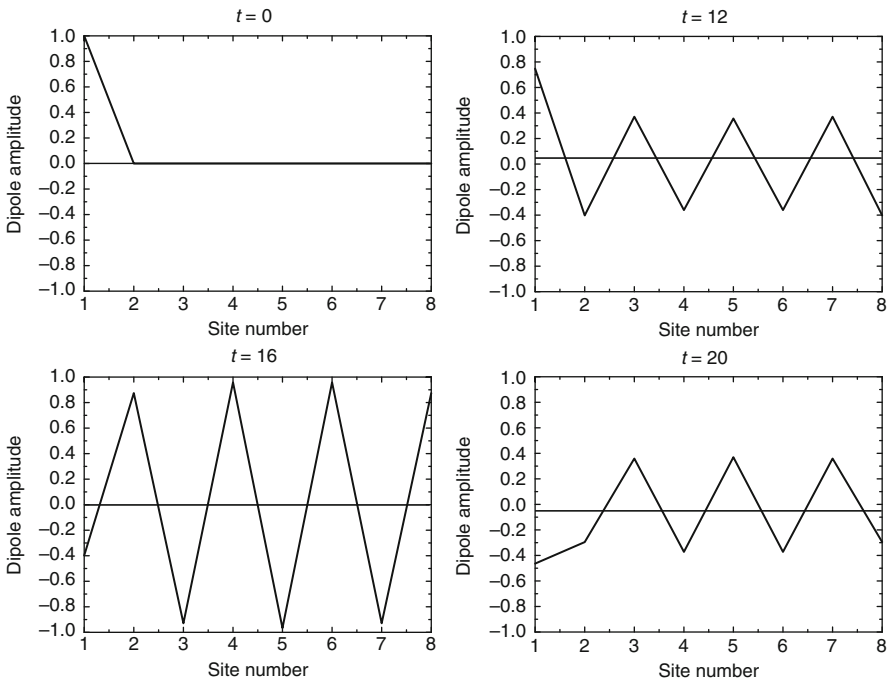


Fig. 4.16 Time evolution of the dipole distribution of the system belonging to the fourth group. The initial conditions are set as $\langle P_n \rangle = \delta_{n1}$ and $\langle W_n \rangle = 1 - \delta_{n1}$. The dipole distribution similar to the “antiferromagnetic” state is shown, where the dipoles alternatingly change the directions

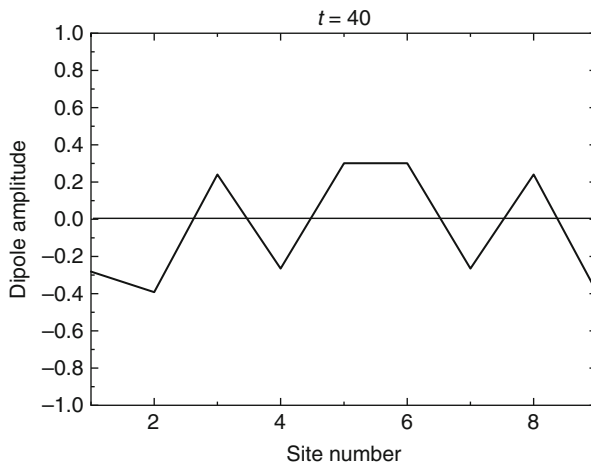


Fig. 4.17 Quasi-steady state of the dipole distribution in the “antiferromagnetic” system belonging to the fourth group. The total number of sites is assumed to be nine

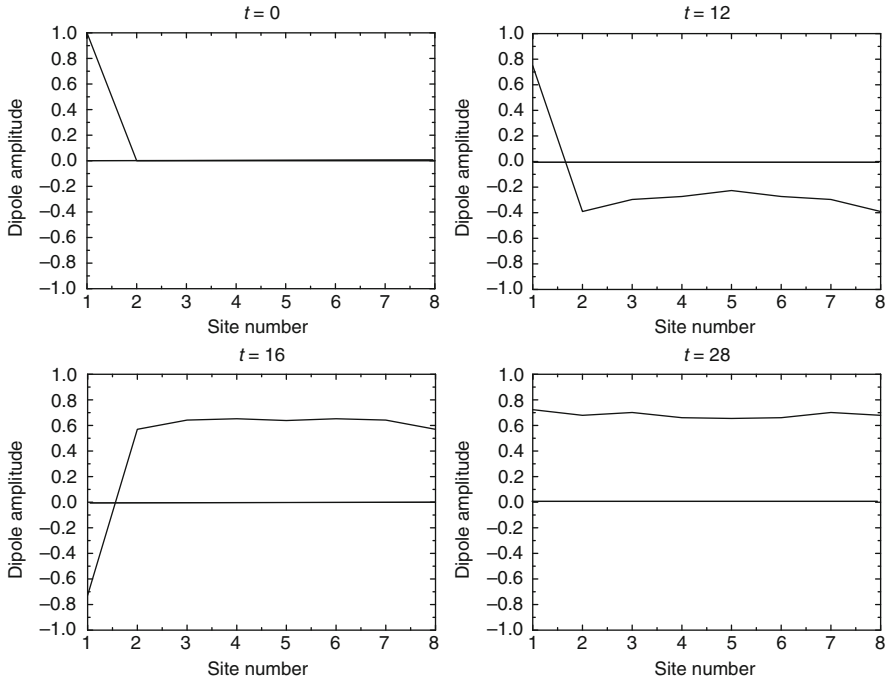


Fig. 4.18 Time evolution of the dipole distribution of the system belonging to the fourth group. The initial population differences are set as $W_n = (0, -, +, -, +, -, +, -)$. According to the flip property, the alternating dipoles change their directions and are aligned to form a dipole-ordered state

This state can be achieved by having the localized photons at site 1 take on a coherent state in which the eigenvalue is a real number. The coherent state is the eigenstate of the annihilation operator of a simple harmonic oscillator. Therefore, the initial state satisfying the following condition needs to be established at site 1:

$$a_1|x_1\rangle = x_1|x_1\rangle \quad x_1 \text{ is real.} \quad (4.57)$$

The temporal evolution of the dipole distribution is examined by solving the semiclassical Heisenberg equations (Eqs. 4.46) and (4.47) numerically with these initial conditions for each of the systems categorized in this section. Figure 4.19 shows the dynamics for group 1 systems.

A quasi-steady state emerges that is similar to the case in which dipoles were given as the initial condition (cf. Fig. 4.13). Figure 4.20 shows the quasi-steady states corresponding to each of the three systems considered in this section.

These results demonstrate that the states of each group behave exactly as predicted by the effective Hamiltonian. In other words, while the state derived for each group originally involved a dipole (instead of a localized photon), similar states

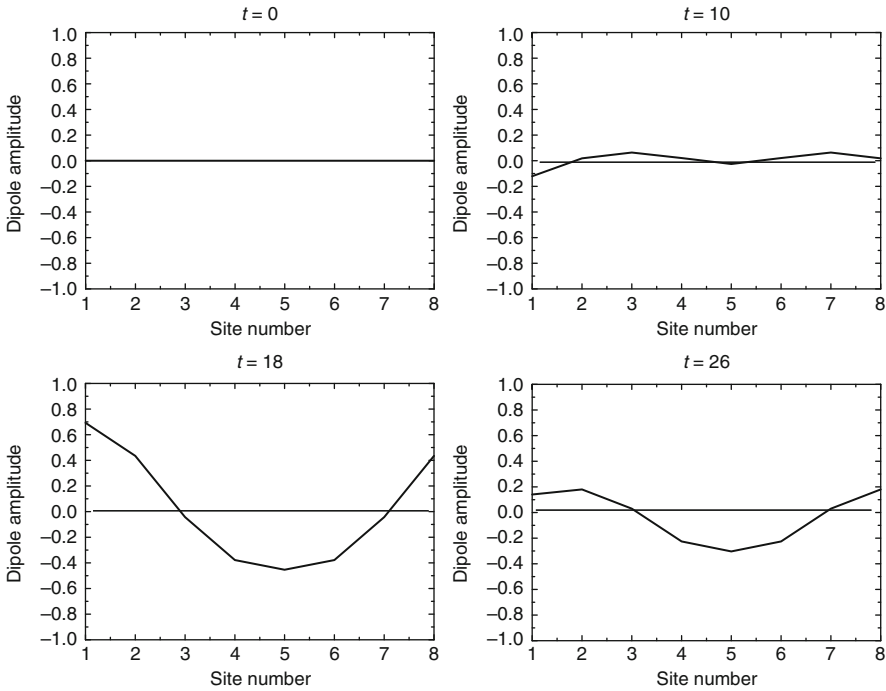


Fig. 4.19 The temporal evolution of the dipole distribution of the system for the first group in which the localized photonic states are initially in the coherent state at the first site and the other sites are in the vacuum state and all the excitonic states are in the totally inverted state

are also realized with the initial input of localized photons. On closer examination of Fig. 4.19, it can be seen that dipoles are first induced at the site during the initial time frame as a result of the input of localized photons. Therefore, these dipoles established the basis for realizing quasi-steady states via a mechanism that is similar to the case in which dipoles were the initial input. These results imply the robustness of each quasi-steady state predicted by the effective Hamiltonian against input.

4.6 Dicke's Superradiance

In the preceding section, we have shown that electric transition dipole moments of the system are aligned to have a large value, depending on material parameters of the system. It is then expected that strong radiation can be emitted due to a large total dipole moment, and it is intriguing to examine radiation properties of the dipole-ordered states obtained from our localized photon model. Before such investigation, we will outline superradiance [2, 9, 11, 25, 32, 52, 73] as a

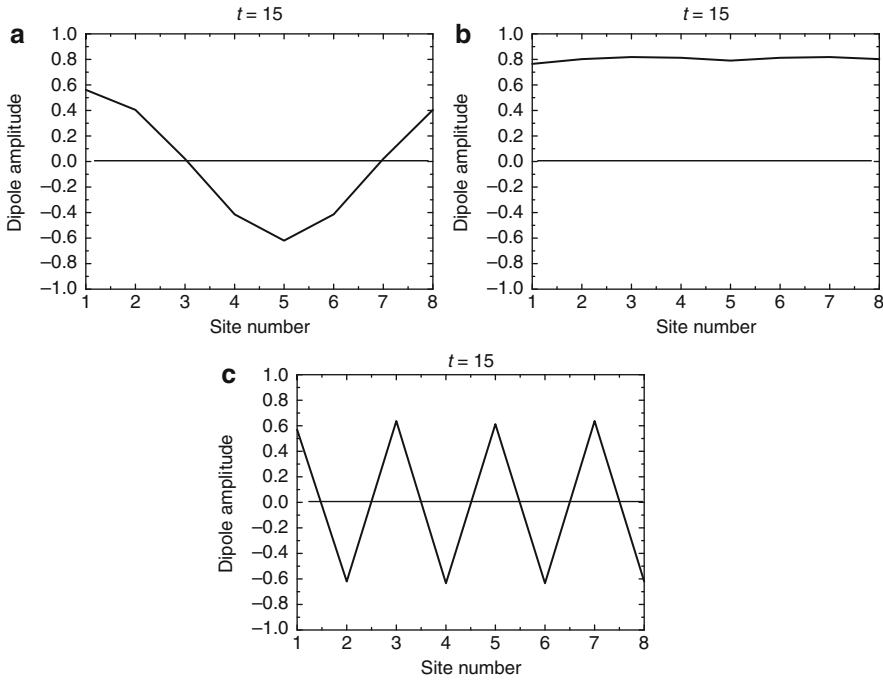


Fig. 4.20 Quasi-steady states arise from the initial condition in which there is localized photon excitation at a single site when the system parameters have various values (ϵ , V , E). The results in (a), (b), and (c) correspond to the first, third, and fourth groups, respectively

cooperative phenomenon, where radiation from N two-level systems interacting with propagating light exceeds the sum of the one individually emitted from the systems. More precisely speaking, a radiation pulse with a sharp width of $1/N$ and an intense intensity of N^2 is emitted [25]. This kind of system is called the Dicke model and has been extensively studied in the mid-1970s since the pioneering work of Dicke [25].

In this section, we first introduce the Dicke model and Dicke states and then discuss superradiant states, or superradiance, following Mandel and Wolf [57]. In order to examine how such states are dynamically obtained, master equation is derived with the help of the projection operator method, and time evolution of radiation is studied. Numerical solutions of Dicke master equation are presented for a small system whose size is much smaller than the wavelength of radiation field. At the same time, analytic solutions are obtained within a semiclassical approximation to discuss the importance of quantum correlation. Finally we examine the effects of the dipole–dipole interaction for an inhomogeneous system as well as the effects of reabsorption and reemission of photons for a large system, both of which violate the cooperative states and destroy some part of coherence in the system.

4.6.1 Dicke States and Superradiance

4.6.1.1 N Two-Level Systems and Dicke States

The Dicke model consists of N two-level systems, as a representative of atoms or quantum dots, coupled to radiation field. The free Hamiltonian for the two-level systems is written as

$$H_{\text{two-level}} = \hbar\Omega \sum_{n=1}^N b_n^\dagger b_n, \quad (4.58)$$

where $\hbar\Omega$, b_n^\dagger , and b_n denote the excitation energy, creation, and annihilation operators of excitation in n th site, respectively. Those operators can be also defined by spin operators $R_i^{(n)}$ ($i = 1, 2, 3$) and Bloch vectors (P_n, V_n, W_n) as follows:

$$R_1^{(n)} = \frac{1}{2}(b_n + b_n^\dagger) = \frac{1}{2}P_n, \quad (4.59a)$$

$$R_2^{(n)} = \frac{i}{2}(b_n - b_n^\dagger) = \frac{1}{2}V_n, \quad (4.59b)$$

$$R_3^{(n)} = \frac{1}{2}(b_n^\dagger b_n - b_n b_n^\dagger) = \frac{1}{2}W_n. \quad (4.59c)$$

The spin operators $R_i^{(n)}$ satisfy the commutation relations

$$[R_i^{(n)}, R_j^{(n')}] = i \delta_{nn'} \epsilon_{ijk} R_k^{(n)} \quad (4.60)$$

with Levi-Civita's symbol ϵ_{ijk} . Introducing total spin operators for the N two-level systems as

$$R_1 = \sum_{n=1}^N R_1^{(n)}, \quad R_2 = \sum_{n=1}^N R_2^{(n)}, \quad R_3 = \sum_{n=1}^N R_3^{(n)}, \quad (4.61)$$

we can rewrite the free Hamiltonian $H_{\text{two-level}}$ as

$$H_{\text{two-level}} = \hbar\Omega R_3, \quad (4.62)$$

where the total spin operators also obey the commutation relations

$$[R_i, R_j] = i \epsilon_{ijk} R_k, \quad (4.63)$$

similar to (Eq. 4.60).

Let us consider a state in which N_1 of the N two-level systems is in the lower state $|1\rangle$ and N_2 is in the excited state $|2\rangle$, where

$$N = N_1 + N_2, \quad m = \frac{1}{2}(N_2 - N_1). \quad (4.64)$$

Evidently m is a measure of the total population inversion, and it is an eigenvalue of the spin operator R_3 . Introducing the operator $R^2 = R_1^2 + R_2^2 + R_3^2$ and using (Eq. 4.63), we obtain the commutation relations

$$[R_i, R^2] = 0, \quad \text{for } i = 1, 2, 3, \quad (4.65)$$

so that the collective operators R_i obey the same algebra as the angular momentum. Thus, there exist the states $|l, m\rangle$ which are simultaneous eigenstates of both R_3 and R^2 as

$$R_3|l, m\rangle = m|l, m\rangle, \quad \text{for } \frac{1}{2}N \geq m \geq -\frac{1}{2}N, \quad (4.66a)$$

$$R^2|l, m\rangle = l(l+1)|l, m\rangle, \quad \text{for } \frac{1}{2}N \geq l \geq |m|. \quad (4.66b)$$

The quantum number l is called the cooperation number [25] and determines the collectivity of cooperative phenomena. For the raising and lowering operators as

$$R_+ = \sum_{n=1}^N b_n^\dagger = R_1 + iR_2, \quad R_- = \sum_{n=1}^N b_n = R_1 - iR_2, \quad (4.67)$$

it follows from the well-known properties of angular momentum operators that

$$R_\pm|l, m\rangle = \sqrt{(l \mp m)(l \pm m + 1)}|l, m \pm 1\rangle, \quad (4.68)$$

where the collective states $|l, m\rangle$ are called Dicke states.

4.6.1.2 Superradiant States

In the following, let us assume that the system size is much smaller than the wavelength of radiation and that the long wave approximation is valid. The interaction Hamiltonian between the two-level system and radiation in the dipole coupling is given by Dicke [25]

$$H_{\text{Fint}}(t) = -\boldsymbol{\mu}_{\text{tot}}(t) \cdot \mathbf{E}(\mathbf{r} = 0, t), \quad (4.69)$$

where the electric field is evaluated at the origin owing to the long wave approximation, and the total electric dipole of the system is written as

$$\boldsymbol{\mu}_{\text{tot}} = \boldsymbol{\mu} \sum_{n=1}^N (b_n + b_n^\dagger) = \boldsymbol{\mu}(R_+ + R_-). \quad (4.70)$$

Here we suppose a transition from an initial state $|l, m\rangle|\text{vac}\rangle$ to a final state $|\psi\rangle$, where $|l, m\rangle$ and $|\text{vac}\rangle$ represent a Dicke state and the vacuum of the radiation field, respectively. Then the transition probability can be written as

$$- \langle \psi | \boldsymbol{\mu} \cdot \mathbf{E}_-(t) R_-(t) | l, m \rangle | \text{vac} \rangle, \quad (4.71)$$

where $\mathbf{E}_-(t)$ is the $e^{-i\omega t}$ dependent part of the electric field $\mathbf{E}(t)$. By squaring the absolute value of the transition probability and summing over all possible final states, the probability of emission of radiation photons w_{emit} is given as [25, 57]

$$\begin{aligned} w_{\text{emit}} &= \sum_{\psi} |\langle \psi | \boldsymbol{\mu} \cdot \mathbf{E}(t) R_-(t) | l, m \rangle | \text{vac} \rangle|^2 \\ &= \langle l, m | R_+(t) R_-(t) | l, m \rangle \langle \text{vac} | \boldsymbol{\mu} \cdot \mathbf{E}_+(t) \boldsymbol{\mu} \cdot \mathbf{E}_-(t) | \text{vac} \rangle \\ &= \langle R_+(t) R_-(t) \rangle A = (l+m)(l-m+1)A, \end{aligned} \quad (4.72)$$

where (Eq. 4.68) is used for the final expression and $A = \langle \text{vac} | \boldsymbol{\mu} \cdot \mathbf{E}_+(t) \boldsymbol{\mu} \cdot \mathbf{E}_-(t) | \text{vac} \rangle$ is identified as the Einstein A coefficient for each two-level system like an atom or a quantum dot.

If all quantum dots are in the ground state $|1\rangle$, then $m = -N/2$, and from (Eq. 4.66b) we must have $l = N/2$. Hence, from (Eq. 4.72) the radiation rate w_{emit} is zero as expected. If all quantum dots are in the excited states $|2\rangle$, then $m = N/2$ and we again have $l = N/2$. Hence $w_{\text{emit}} = NA$, which is just what one would expect from a group of N independently radiating quantum dots. However, the situation is quite different if the initial state is not the completely excited state. Let us consider a state in which half of the quantum dots are excited and half are not, so that $m = 0$. Then we have

$$w_{\text{emit}} = l(l+1)A, \quad (4.73)$$

and l can have any value between 0 and $N/2$. The larger the value of l , the larger is collective rate of radiation of the system. In particular, if $l = N/2$, then

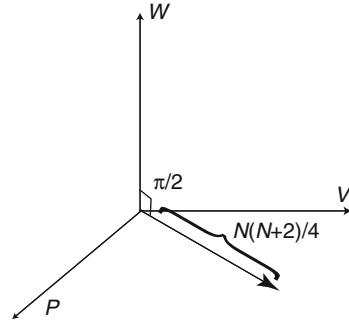
$$w_{\text{emit}} = \frac{1}{4}N(N+2)A, \quad (4.74)$$

which maximizes the value of cooperative spontaneous radiation. Since the maximum radiation probability is proportional to the square of the site number N , it becomes very large for large N . This phenomenon is called superradiance, and the state $|l = N/2, m = 0\rangle$ is called a superradiant Dicke state. From the definition of the total Bloch vector (P, V, W) as $P = \sum_n \langle P_n \rangle$, $V = \sum_n \langle V_n \rangle$, $W = \sum_n \langle W_n \rangle$, it follows that the Bloch vector for the superradiant state is on the P - V plane and its length reaches a maximum, as shown in Fig. 4.21.

4.6.2 Dicke Master Equation and Solutions for a Small System

In this section Dicke master equation is derived for a small system to discuss dynamic manifestation of superradiant states described in the preceding section.

Fig. 4.21 Total Bloch vector in a superradiant state. It is on the P - V plane, and its length has a maximal value



4.6.2.1 Nakajima–Zwanzig’s Method and Generalized Master Equation

According to Mandel and Wolf [57] and Agarwal [1], we outline the derivation of a generalized master equation by projection operators to project out of the density operator for a total system that part on which our interest is focused [50, 58, 91, 92]. The total system can be described in the interaction representation by the Liouville–von Neumann equation for the density operator $\rho(t)$ as

$$\frac{\partial \rho(t)}{\partial t} = \frac{1}{i\hbar} [H_I(t), \rho(t)] = -iL(t)\rho(t), \quad (4.75)$$

where $H_I(t)$ is the interaction Hamiltonian and $L \cdots = [H_I(t), \cdots]/\hbar$ is the Liouvillian operator, as before. We now introduce a time-independent projection operator P :

$$P^2 = P, \quad (4.76)$$

that is chosen so as to project out the most relevant part of $\rho(t)$. Using the complementary operator $(1 - P)$, we can express $\rho(t)$ as

$$\rho(t) = P\rho(t) + (1 - P)\rho(t). \quad (4.77)$$

On multiplying both sides of (Eq. 4.75) by P on the left and then using (Eq. 4.77) to substitute for $\rho(t)$ on the right, we have

$$P \frac{\partial \rho(t)}{\partial t} = -iPL(t)P\rho(t) - iPL(t)(1 - P)\rho(t). \quad (4.78)$$

Similarly, after multiplying (Eq. 4.75) by $(1 - P)$ on the left, we obtain

$$(1 - P) \frac{\partial \rho(t)}{\partial t} = -i(1 - P)L(t)P\rho(t) - i(1 - P)L(t)(1 - P)\rho(t). \quad (4.79)$$

Formally integrating the first-order differential equation (Eq. 4.79) and solving for $(1 - P)\rho(t)$, we find

$$(1 - P)\rho(t) = \exp\left(-i(1 - P) \int_0^t L(t') dt'\right) (1 - P)\rho(0) - i \int_0^t \exp\left(-i(1 - P) \int_\tau^t L(t') dt'\right) \times (1 - P)L(\tau)P\rho(\tau) d\tau. \quad (4.80)$$

Substitution of $(1 - P)\rho(t)$ into (Eq. 4.78) gives

$$P \frac{\partial \rho(t)}{\partial t} = -iPL(t)P\rho(t) - iPL(t) \exp\left(-i(1 - P) \int_0^t L(t') dt'\right) (1 - P)\rho(0) - PL(t) \int_0^t \exp\left(-i(1 - P) \int_\tau^t L(t') dt'\right) \times (1 - P)L(\tau)P\rho(\tau) d\tau. \quad (4.81)$$

If we set

$$U(t, \tau) \equiv \exp\left(-i(1 - P) \int_\tau^t L(t') dt'\right), \quad (4.82)$$

we finally obtain Nakajima–Zwanzig’s generalized master equation [50, 58, 91, 92] as follows:

$$P \frac{\partial \rho(t)}{\partial t} = -iPL(t)P\rho(t) - iPL(t)U(t, 0)(1 - P)\rho(0) - PL(t) \int_0^t U(t, \tau)(1 - P)L(\tau)P\rho(\tau) d\tau. \quad (4.83)$$

4.6.2.2 Application to the Dicke Problem

As an example, let us consider the application of (Eq. 4.83) to the Dicke problem, that is, to the interaction of a group of N closely spaced, identical two-level atoms (system) with electromagnetic field. For simplicity, we assume that two-level atoms are at the origin, and we make the rotating wave approximation. Then the Hamiltonian is given as [2]

$$H_D = \hbar\Omega R_3 + \hbar \sum_{\mathbf{k}\lambda} \omega a_{\mathbf{k}\lambda}^\dagger a_{\mathbf{k}\lambda} + \hbar \sum_{\mathbf{k}\lambda} (g_{\mathbf{k}\lambda} a_{\mathbf{k}\lambda}^\dagger R_- + h.c.), \quad (4.84)$$

where $a_{\mathbf{k}\lambda}^\dagger$ ($a_{\mathbf{k}\lambda}$) is the photon creation (annihilation) operator specified by wave vector \mathbf{k} , polarization λ , and frequency ω , and the coupling constant $g_{\mathbf{k}\lambda}$ is given by the formula

$$g_{\mathbf{k}\lambda} = \frac{i\Omega}{\sqrt{2\epsilon_0\hbar\omega V}}(\boldsymbol{\epsilon}_{\mathbf{k}\lambda} \cdot \boldsymbol{\mu}). \quad (4.85)$$

Here $\boldsymbol{\epsilon}_{\mathbf{k}\lambda}$ represents the polarization vector, and $\boldsymbol{\mu}$ denotes the matrix element of the dipole moment in the two-level (atomic) system.

In the following, we are mainly interested in the two-level (atomic) system as the relevant system and identify the “reservoir” with the radiation field, so that the projection operator P is given by

$$P \cdots = |\text{vac}\rangle\langle\text{vac}| \text{Tr}_F \cdots, \quad (4.86)$$

where Tr_F means that the trace is taken over the radiation field states. As the initial state of the coupled system, we also assume the direct product state with the radiation field in the vacuum state

$$\rho(0) = \rho_A(0) \otimes |\text{vac}\rangle\langle\text{vac}| \quad (4.87)$$

with the reduced density operator defined as $\rho_A(t) = \text{Tr}_F \rho(t)$. In order to work in the interaction picture, we transform the interaction Hamiltonian into

$$H_{\text{Fint}}(t) = \hbar \sum_{\mathbf{k}\lambda} (g_{\mathbf{k}\lambda} a_{\mathbf{k}\lambda}^\dagger R - e^{i(\omega-\Omega)t} + h.c.). \quad (4.88)$$

Under these conditions, the first term on the right-hand side of (Eq. 4.83), $PL(t)P\rho(t)$, can be written as

$$\begin{aligned} PL(t)P\rho(t) &= |\text{vac}\rangle\langle\text{vac}| \text{Tr}_F \frac{1}{\hbar} [H_{\text{Fint}}(t), |\text{vac}\rangle\langle\text{vac}| \rho_A(t)] \\ &= |\text{vac}\rangle\langle\text{vac}| \left(\sum_{\mathbf{k}\lambda} g_{\mathbf{k}\lambda} \langle\text{vac}| a_{\mathbf{k}\lambda}^\dagger |\text{vac}\rangle R - e^{i(\omega-\Omega)t} \rho_A(t) - h.c. \right) \\ &= 0, \end{aligned} \quad (4.89)$$

because

$$\langle\text{vac}| a_{\mathbf{k}\lambda}^\dagger |\text{vac}\rangle = 0 = \langle\text{vac}| a_{\mathbf{k}\lambda} |\text{vac}\rangle. \quad (4.90)$$

In addition, the second term on the right-hand side of (Eq. 4.83) can be rewritten as

$$(1 - P)\rho(0) = (1 - |\text{vac}\rangle\langle\text{vac}| \text{Tr}_F) \rho_A(0) |\text{vac}\rangle\langle\text{vac}| = 0. \quad (4.91)$$

Substituting (Eqs. 4.89) and (4.91) into (Eq. 4.83), we have

$$P \frac{\partial \rho}{\partial t} = -PL(t) \int_0^t L(\tau) P \rho(\tau) d\tau, \quad (4.92)$$

where we approximate $U(t, \tau) \sim 1$ (Born approximation). Explicit use of (Eq. 4.86) yields the equation

$$\frac{\partial \rho_A}{\partial t} = -\text{Tr}_F L(t) \int_0^t L(\tau) |\text{vac}\rangle \langle \text{vac}| \rho_A(\tau) d\tau. \quad (4.93)$$

After transforming the variable as $\tau = t - \tau'$ in the last integral, we can reduce (Eq. 4.93) to

$$\frac{\partial \rho_A}{\partial t} = -\text{Tr}_F L(t) \int_0^t L(t - \tau') |\text{vac}\rangle \langle \text{vac}| \rho_A(t - \tau') d\tau'. \quad (4.94)$$

Further approximation of replacing $\rho_A(t - \tau')$ by $\rho_A(t)$, which is known as the Markov approximation, provides the final relation

$$\begin{aligned} \frac{\partial \rho_A}{\partial t} &= -\text{Tr}_F L(t) \int_0^t L(t - \tau) |\text{vac}\rangle \langle \text{vac}| \rho_A(t) d\tau \\ &= -\frac{1}{\hbar^2} \text{Tr}_F \int_0^t [H_{\text{Fint}}(t), [H_{\text{Fint}}(t - \tau), |\text{vac}\rangle \langle \text{vac}| \rho_A(t)]] d\tau \\ &= -\frac{1}{\hbar^2} \text{Tr}_F \int_0^t \{H_{\text{Fint}}(t) H_{\text{Fint}}(t - \tau) |\text{vac}\rangle \langle \text{vac}| \rho_A(t) \\ &\quad - H_{\text{Fint}}(t) |\text{vac}\rangle \langle \text{vac}| \rho_A(t) H_{\text{Fint}}(t - \tau)\} d\tau + h.c. \end{aligned} \quad (4.95)$$

Noticing (Eq. 4.88) and the facts

$$\begin{aligned} \langle \text{vac} | a_{\mathbf{k}\lambda} a_{\mathbf{k}'\lambda'}^\dagger | \text{vac} \rangle &= \delta_{\mathbf{k}\mathbf{k}'} \delta_{\lambda\lambda'}, \\ \langle \text{vac} | a_{\mathbf{k}\lambda}^\dagger a_{\mathbf{k}'\lambda'}^\dagger | \text{vac} \rangle &= \langle \text{vac} | a_{\mathbf{k}\lambda} a_{\mathbf{k}'\lambda'} | \text{vac} \rangle = \langle \text{vac} | a_{\mathbf{k}\lambda}^\dagger a_{\mathbf{k}'\lambda'} | \text{vac} \rangle = 0, \end{aligned} \quad (4.96)$$

we have the following equation:

$$\begin{aligned} \frac{\partial \rho_A}{\partial t} &= - \int_0^t \sum_{\mathbf{k}\lambda} |g_{\mathbf{k}\lambda}|^2 \{ e^{i(\Omega - \omega)\tau} R_+ R_- \rho_A(t) + h.c. \\ &\quad - 2 \cos(\omega - \Omega)\tau R_- \rho_A(t) R_+ \} d\tau. \end{aligned} \quad (4.97)$$

In the limit $t \gg 1/\Omega$, we put

$$\int_0^t \sum_{\mathbf{k}\lambda} |g_{\mathbf{k}\lambda}|^2 e^{i(\Omega-\omega)\tau} d\tau \equiv \beta + i\gamma, \quad (4.98)$$

where β is half the Einstein A coefficient and γ is a frequency shift due to the interaction. Finally we obtain the appropriate master equation describing spontaneous emission from a collective two-level (atomic) system, which is called Dicke master equation [2, 52, 60]:

$$\frac{\partial \rho_A}{\partial t} = -\beta(R_+ R_- \rho_A - 2R_- \rho_A R_+ + \rho_A R_+ R_-) - i\gamma[R_+ R_-, \rho_A(t)], \quad (4.99)$$

or

$$\frac{\partial \rho_A}{\partial t} = -\beta([R_+, R_- \rho_A] + [\rho_A R_+, R_-]) - i\gamma[R_+ R_-, \rho_A(t)]. \quad (4.100)$$

4.6.2.3 Semiclassical Solutions of Dicke Master Equation

The rate of photon emission was obtained perturbatively in Sect. 4.6.1.2. In this section, we examine time evolution of this emission rate, using Dicke master Equation (Eq. 4.99). Since the rate of energy dissipation from the two-level (atomic) system is proportional to the emission rate, $-d\langle R_3 \rangle/dt$ should be evaluated. Multiplying (Eq. 4.99) by R_3 on the right and taking the trace, one finds

$$\begin{aligned} \frac{\partial}{\partial t} \langle R_3 \rangle &= \beta \{ -\langle R_3 R_+ R_- \rangle + 2\langle R_+ R_3 R_- \rangle - \langle R_+ R_- R_3 \rangle \} \\ &\quad - i\gamma \{ \langle R_3 R_+ R_- \rangle - \langle R_+ R_- R_3 \rangle \}. \end{aligned} \quad (4.101)$$

In order to simplify the above equation, we use the following relations:

$$[R_+, R_3] = -R_+, \quad (4.102)$$

$$R_+ R_- = R_3 + \frac{1}{2} N \sum_n \sum_{m \neq n} b_n^\dagger b_m, \quad (4.103)$$

which follow from the collective operators defined in (Eq. 4.67) and the commutation relations in (Eq. 4.63). In addition, using (Eq. 4.103), we can show

$$\begin{aligned} [R_+ R_-, R_3] &= \sum_n \sum_{m \neq n} [b_n^\dagger b_m, R_3] \\ &= \sum_n \sum_{m \neq n} [b_n^\dagger b_m - b_n^\dagger b_m] = 0 \end{aligned} \quad (4.104)$$

and rewrite (Eq. 4.101) as

$$\frac{\partial}{\partial t} \langle R_3 \rangle = 2\beta[\langle R_+ R_3 R_- \rangle - \langle R_3 R_+ R_- \rangle]. \quad (4.105)$$

With the help of (Eq. 4.102), this leads to the final equation

$$\begin{aligned} \frac{\partial}{\partial t} \langle R_3 \rangle &= 2\beta[\langle (R_3 R_+ - R_+) R_- \rangle - \langle R_3 R_+ R_- \rangle] \\ &= -2\beta \langle R_+ R_- \rangle. \end{aligned} \quad (4.106)$$

It follows from the above equation that time evolution of $\langle R_+ R_- \rangle$ is required to evaluate the rate of energy dissipation. Multiplying (Eq. 4.99) by $R_+ R_-$ on the right and taking the trace, we then find

$$\begin{aligned} \frac{\partial}{\partial t} \langle R_+ R_- \rangle &= -2\beta\{\langle R_+ R_- R_+ R_- \rangle - \langle R_+ R_+ R_- R_- \rangle\} \\ &\quad -i\gamma\langle [R_+ R_-, R_+ R_-] \rangle \\ &= -4\beta\{\langle R_+ R_- \rangle - \langle R_+ R_- R_3 \rangle\}, \end{aligned} \quad (4.107)$$

where we used the following relation to obtain the second line from the first line:

$$R_+ R_+ R_- R_- = R_+ R_- R_+ R_- - 2R_+ R_- + 2R_+ R_- R_3. \quad (4.108)$$

Neglecting the quantum correlation and putting

$$\langle R_+ R_- R_3 \rangle = \langle R_+ R_- \rangle \langle R_3 \rangle, \quad (4.109)$$

we then have

$$\frac{\partial}{\partial t} \langle R_+ R_- \rangle = -2\beta \langle R_+ R_- \rangle (1 - \langle R_3 \rangle). \quad (4.110)$$

Simultaneously solving (Eqs. 4.106) and (4.110), one can obtain the final result. Or putting $z = \langle R_3 \rangle$, this leads to the following nonlinear equation:

$$\ddot{z} = -4\beta\dot{z}(1 - z). \quad (4.111)$$

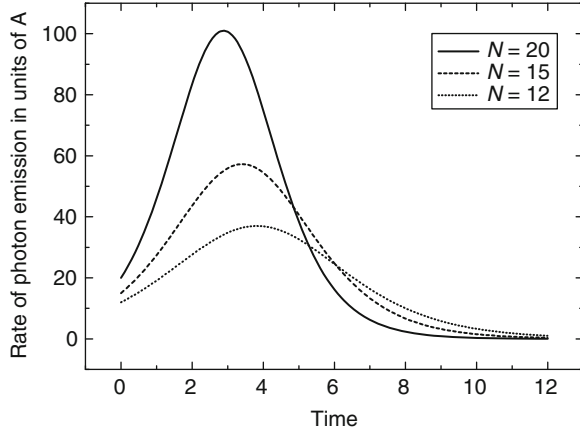
This allows us to evaluate the rate of energy dissipation, $-d \langle R_3 \rangle / dt = -\dot{z}$, and thus to obtain the rate of photon emission.

Under the following initial conditions

$$\langle R_3 \rangle(0) = N/2, \quad \langle R_+ R_- \rangle(0) = N, \quad (4.112)$$

which correspond to $l(0) = N/2$ and $m(0) = N/2$ in terms of Dicke states, we solve (Eq. 4.111) numerically. The result is shown in Fig. 4.22 for the case of $\beta = 0.05$ and the site number $N = 12, 15, 20$. It follows from Fig. 4.22 that the peak value of the rate of emission becomes higher and the width gets narrower, as

Fig. 4.22 Time evolution of the rate of photon emission that is numerically obtained from (Eq. 4.111) with the initial condition of a totally inverted state. The vertical axis is represented in units of the Einstein A coefficient $A = 2\beta$ for $\beta = 0.05$. The dotted, dashed, and solid curves show the results for the site numbers $N = 12$, 15, and 20, respectively



the site number becomes larger. As will be shown in the next subsection, a pulse of radiation whose height is proportional to N^2 and width is proportional to $1/N$ is emitted from the two-level system prepared in the initial condition.

4.6.2.4 Analytical Solutions of Dicke Master Equation in Semiclassical Approximation

In the preceding subsection, we have obtained simultaneously coupled equations after neglecting the quantum correlation more than third order, for example, approximating $\langle R_+ R_- R_3 \rangle$ as $\langle R_+ R_- \rangle \langle R_3 \rangle$, and numerically examined the emission rate of radiation to predict a characteristic feature. Here in this section, an analytical solution will be given for time evolution of the emission rate after making more approximations [3, 60, 73].

Using the polar angle θ of a Bloch vector (P, V, W) , we can express the expectation value of R_3 as

$$\langle R_3 \rangle = \frac{N}{2} \cos \theta \quad (4.113)$$

and that of $R_+ R_-$ as

$$\begin{aligned} \langle R_+ R_- \rangle &= \langle R_+ \rangle \langle R_- \rangle = \langle R_1 \rangle^2 + \langle R_2 \rangle^2 \\ &= \langle R \rangle^2 - \langle R_3 \rangle^2 = \frac{N^2}{4} \sin^2 \theta, \end{aligned} \quad (4.114)$$

where we neglected the quantum correlations more than second order as $\langle R_+ R_- \rangle = \langle R_+ \rangle \langle R_- \rangle$, which is called a semiclassical approximation [2]. Substitution of $z = \cos \theta$ into (Eq. 4.106) leads to

$$\dot{z} = -A \frac{N}{2} (1 - z^2), \quad (4.115)$$

where A is the Einstein A coefficient and is set to $A = 2\beta$. Similarly we can rewrite the left-hand side of (Eq. 4.110) as

$$\frac{\partial}{\partial t} \frac{N^2}{4} (1 - z^2) = -\frac{N^2}{2} z \dot{z}, \quad (4.116)$$

and the right-hand side as

$$-2A \frac{N^2}{4} (1 - z^2) \left(1 - \frac{N}{2} z\right) \simeq A \frac{N^3}{4} (1 - z^2) z, \quad (4.117)$$

where we assumed $N \gg 1$. Both results allow us to simplify (Eq. 4.110), and one finds

$$z \dot{z} = -A \frac{N}{2} z (1 - z^2), \quad (4.118)$$

which is the same equation as (Eq. 4.115). Thus, both (Eqs. 4.106) and (4.110) can be transformed to the same equation,

$$\frac{1}{\Gamma} \frac{dz}{1 - z^2} = -dt \quad (4.119)$$

with $\Gamma = AN/2$, and can be easily solved as

$$z = -\tanh \Gamma(t - t_0). \quad (4.120)$$

We can finally obtain the analytical solution of the emission probability as

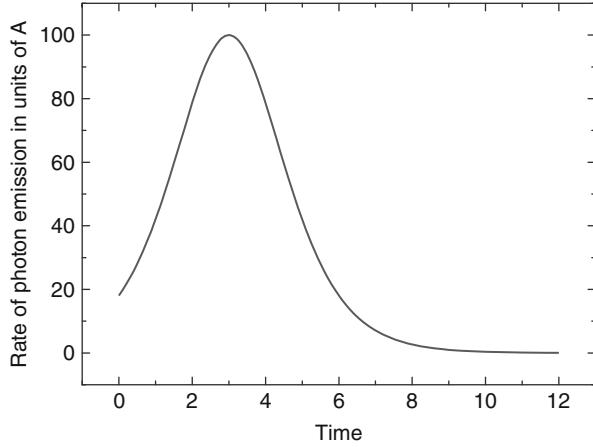
$$I \propto -\partial_t \langle R_3 \rangle = -\frac{N}{2} \dot{z} = \frac{\Gamma^2}{A} \operatorname{sech}^2 \Gamma(t - t_0), \quad (4.121)$$

which represents a cowbell shape function with a width of $2.6/N\beta$ and a peak position at $t = t_0$. This function is plotted in Fig. 4.23 for the case of $\beta = 0.05$, $t_0 = 3$, and $N = 20$. Comparing the result for $N = 20$ in Fig. 4.22 with the current result, one finds that a semiclassical treatment can describe radiation profile of the Dicke model very well. However, it should be noted that there must be nonzero total dipole moment in the initial condition in the semiclassical description because the semiclassical approximation is not valid for the totally inverted system [3, 60], where quantum correlation should be essentially included.

4.6.3 Effect of the Dipole–Dipole Interaction

The dipole–dipole interaction generally breaks the permutation symmetry of the atom (two-level system)–field coupling because various atoms in the sample have

Fig. 4.23 Time evolution of the rate of photon emission plotted according to the analytic solution obtained with the semiclassical approximation. The vertical axis is represented in units of the Einstein A coefficient $A = 2\beta$. The parameters are set to $\beta = 0.05$, $t_0 = 3$, and $N = 20$, corresponding to Fig. 4.22



different close-neighbor environments. This perturbation is analogous to an inhomogeneous dephasing of the dipoles, leading to a loss of dipole–dipole correlation. In order to discuss such an effect, we employ the following interaction Hamiltonian, instead of (Eq. 4.69):

$$H_{\text{Fint}} = - \sum_{n=1}^N \{ \mathbf{E}^+(\mathbf{r}_n) \cdot \mathbf{P}(\mathbf{r}_n) + \mathbf{E}^-(\mathbf{r}_n) \cdot \mathbf{P}^\dagger(\mathbf{r}_n) \}, \quad (4.122)$$

where the electric field operator \mathbf{E} is divided into the positive and negative frequency parts \mathbf{E}^+ and \mathbf{E}^- defined as

$$\mathbf{E}^+(\mathbf{r}_n) = i \sum_{\mathbf{k}\lambda} \sqrt{\frac{\hbar c k}{2\epsilon_0 V}} \mathbf{e}_\lambda a_{\mathbf{k}\lambda} e^{i\mathbf{k} \cdot \mathbf{r}_n}, \quad (4.123a)$$

$$\mathbf{E}^-(\mathbf{r}_n) = (\mathbf{E}^+(\mathbf{r}_n))^\dagger. \quad (4.123b)$$

The creation and annihilation operators $a_{\mathbf{k}\lambda}^\dagger$ and $a_{\mathbf{k}\lambda}$ act on the mode of the radiation field with wave vector \mathbf{k} and polarization \mathbf{e}_λ and obey the boson commutation relation. An arbitrary quantization volume is denoted as V . The dipole operator is similarly defined as

$$\mathbf{P}(\mathbf{r}_n) = \mu\epsilon(b_n^\dagger + b_n). \quad (4.124)$$

Using this interaction Hamiltonian, we can obtain the following master equation in Born–Markov approximation [22, 85]:

$$\frac{d\rho}{dt} = -i \sum_{n \neq m} \Omega_{nm} [b_n^\dagger b_m, \rho] - \sum_{nm} \gamma_{nm} [b_n^\dagger b_m \rho + \rho b_n^\dagger b_m - 2b_m \rho b_n^\dagger] \quad (4.125)$$

with

$$\gamma_{nm} = \frac{\mu^2 \Omega^3}{16\pi^2 c^3 \epsilon_0 \hbar} F(\Omega r_{nm}/c), \quad (4.126a)$$

$$\Omega_{nm} = -\frac{\mu^2}{16\pi^3 \epsilon_0} \int_0^\infty dk k^3 F(kr_{nm}) \frac{P}{k - \Omega/c}, \quad (4.126b)$$

$$F(kr_{nm}) = \int d\Omega_k (\mathbf{e} \cdot \boldsymbol{\epsilon})^2 e^{i\mathbf{k} \cdot \mathbf{r}_{nm}}, \quad (4.126c)$$

where Ω is the angular frequency corresponding to the excitation energy of the two-level system and r_{nm} is the absolute value of the vector $\mathbf{r}_{nm} = \mathbf{r}_n - \mathbf{r}_m$. The solid angle Ω_k is defined as $d\mathbf{k} = k^2 dk d\Omega_k$. Moreover, we have used the following formula:

$$\int_0^\infty c d\tau e^{\pm i(kc - \Omega)\tau} = \pi \delta(k - \Omega/c) \pm i \frac{P}{k - \Omega/c}, \quad (4.127)$$

whose real and imaginary parts produce site-dependent relaxation coefficient γ_{nm} and frequency shift Ω_{nm} , respectively. The integral in (Eq. 4.126c) can be explicitly calculated and gives [32]

$$F(kr_{nm}) = 4\pi \left(1 - \frac{(\boldsymbol{\epsilon} \cdot \mathbf{r}_{nm})^2}{r_{nm}^2} \right) \frac{\sin kr_{nm}}{kr_{nm}} + 4\pi \left(1 - 3 \frac{(\boldsymbol{\epsilon} \cdot \mathbf{r}_{nm})^2}{r_{nm}^2} \right) \left(\frac{\cos kr_{nm}}{(kr_{nm})^2} - \frac{\sin kr_{nm}}{(kr_{nm})^3} \right), \quad (4.128)$$

and one readily obtains, at the limit $kr_{nm} \rightarrow 0$,

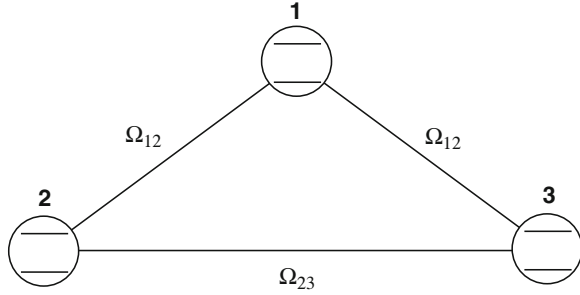
$$\hbar \Omega_{nm} = \frac{\mu^2}{4\pi \epsilon_0 r_{nm}^3} \left(1 - 3 \frac{(\boldsymbol{\epsilon} \cdot \mathbf{r}_{nm})^2}{r_{nm}^2} \right), \quad (4.129)$$

which is the static or Coulombic dipole–dipole interaction.

In order to examine the effects of the dipole–dipole interactions, we evaluate the magnitude of the total Bloch vector $\langle R^2 \rangle$, which is conserved in Dicke states. According to (Eq. 4.125), one finds [22]

$$\begin{aligned} \frac{d}{dt} \langle R^2 \rangle &= -i \left\langle [R^2, \sum_{n \neq m} \Omega_{nm} b_n^\dagger b_m] \right\rangle \\ &= -2i \sum_{n \neq m \neq l} \Omega_{nm} \langle R_z^{(m)} (b_n^\dagger b_l - b_l^\dagger b_n) \rangle, \end{aligned} \quad (4.130)$$

Fig. 4.24 Arrangement of three two-level systems. Each two-level system is configured at the apex of an isosceles triangle



from which it follows that $\langle R^2 \rangle$ is generally not conserved, but is a conserved quantity only if the site number N is equal to 2, or only if Ω_{nm} is constant for all suffixes [22, 84]. Therefore the state is not expressed by Dicke states, and quantum coherence of the two-level system is destroyed by the dipole–dipole interactions.

Now we consider how the dipole–dipole interactions affect superradiance. Let the site number be three and be arranged as shown in Fig. 4.24. For simplicity, we assume $\Omega_{12} = \Omega_{13} \neq \Omega_{23}$ and $\gamma_{mn} = \gamma$.

The following eight bases are employed to take matrix elements of (Eq. 4.125) and to solve the simultaneous differential equations:

$$|s_1, s_2, s_3\rangle \quad (s_i = \pm), \quad (4.131)$$

where the sign $+$ indicates that the upper level is occupied while the sign $-$ means that the lower level is occupied. Under the initial condition of $\langle + + + | \rho(0) | + + + \rangle = 1$, we obtain the matrix elements of the density operator $\rho(t)$ at time t to express radiation intensity

$$I(t) = \sum_{n,m} \langle b_n^\dagger b_m \rangle = \langle R_+ R_- \rangle. \quad (4.132)$$

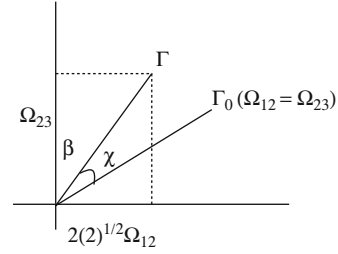
Using the Pauli matrices σ_μ ($\mu = 0, 1, 2, 3$), we can write nonzero components of the density matrices as $\sum_\mu x_\mu \sigma_\mu$. The vector $\mathbf{x} = (x_1, x_2, x_3)$ executes fast precession about a “torque” $\mathbf{\Gamma} = (2\sqrt{2}\Omega_{12}, 0, \Omega_{23})$ (see Fig. 4.25). When we introduce the rotation $R(\beta, \hat{2})$ which rotates about the 2 axis through an angle

$$\tan \beta = \frac{2\sqrt{2}\Omega_{12}}{\Omega_{23}}, \quad (4.133)$$

then the vector $\mathbf{\Gamma}$ is transformed as $R(\beta, \hat{2})\mathbf{\Gamma} = (0, 0, \Gamma)$ with

$$\Gamma = \sqrt{(2\sqrt{2}\Omega_{12})^2 + \Omega_{23}^2}.$$

Fig. 4.25 Relation between the angles β and χ . In the case of pure superradiance ($\Omega_{12} = \Omega_{23}$), the torque Γ is given by Γ_0



The solutions of the differential equations for the density matrices can be obtained from a similar rotation of \mathbf{x} with $\cos \chi$ defined as [22]

$$\cos(\chi + \beta) = \frac{1}{3}. \quad (4.134)$$

When $\cos \chi = 1$ or $\chi = 0$, $\Omega_{12} = \Omega_{23}$ is satisfied and the Dicke superradiant states become exact eigenstates while $\cos \chi = 0$ gives orthogonal states to the superradiant states. This means that the deviation of χ from zero shows the inhomogeneity of the system or a measure of the coherence properties.

According to Coffey et al. [22], we present the radiation intensity $I(t)$ in Fig. 4.26, which shows the peak and tail of $I(t)$ become reduced and longer, respectively, as $\cos \chi$ varies from one to zero corresponding to the sequence of (a), (c), (d), and (b) in Fig. 4.26.

Tokihiro et al. also examined the effects of the dipole–dipole interaction on superradiance, using a linear excitonic system, in which excitons can hop from one site to its nearest neighbors via the dipole–dipole interaction [84]. They used the following master equation in the interaction representation:

$$\begin{aligned} \frac{d\rho}{dt} = & -iJ \sum_n [b_n^\dagger b_{n+1} + b_{n+1}^\dagger b_n, \rho] \\ & -\gamma [R_+ R_- \rho + \rho R_+ R_- - 2R_- \rho R_+], \end{aligned} \quad (4.135)$$

where the hopping energy of an exciton and the radiation decay rate are denoted as

$$2\hbar J = \frac{\mu^2}{4\pi\epsilon_0 a^3} \left(1 - 3 \frac{(\boldsymbol{\epsilon} \cdot \mathbf{a})^2}{a^2} \right), \quad (4.136)$$

$$\gamma = \frac{\mu^2 \Omega^3}{3\pi c^3 \epsilon_0 \hbar}, \quad (4.137)$$

respectively. The first term in (Eq. 4.135) corresponds to the Hamiltonian of the XY model in a spin system whose exact solutions are well known [54]. Taking matrix elements of (Eq. 4.135) in terms of the solutions as basis functions, they numerically solved the master equation under the initial condition of a totally inverted system.

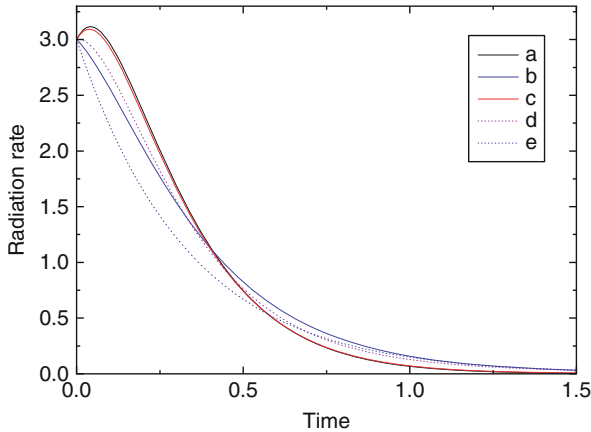


Fig. 4.26 Normalized radiation intensity for three two-level systems with different Ω_{12}/Ω_{23} : (a) $\Omega_{12} = \Omega_{23}$, $\cos \chi = 1$, corresponding to pure superradiance, (b) $\cos \chi = 0$, (c) $\Omega_{12} = 8\Omega_{23}$, $\cos \chi = 0.96$, (d) $\Omega_{12} = \Omega_{23}/8$, $\cos \chi = 0.63$, (e) $I = 3e^{-\gamma t}$, where three two-level systems radiate independently. The *vertical axis* is represented in units of the Einstein A coefficient while the *horizontal axis* is represented by γt

The result, similar to that of Coffey et al. [22], shows a reduced peak intensity with extension of the tail and a substantial deviation from Dicke's superradiance that is proportional to the system size N . In addition, they examined the initial condition dependence and showed the oscillation of the radiation profile obtained from a partially excited state [85]. This resembles the effects of reabsorption and reemission of photons which is discussed in the next subsection.

4.6.4 Large Sample Superradiance: Reabsorption Effect

In the preceding section, we have discussed superradiance in a small system whose size is much smaller than the wavelength of radiation field. Now we consider large sample superradiance, taking into consideration a finite system size. In such a system, inhomogeneous arrangement in the two-level system cannot be neglected, as well as the effects of reabsorption of emitted photons. Dipole-dipole interactions, in particular, become important for the inhomogeneous system and correlation of dipoles in the system are degraded to result in weakened radiation intensity [22, 84], as discussed in the preceding subsection. Reabsorption of emitted photons causes stimulated absorption and emission of photons in the system, which leads to oscillation of radiated pulses [9, 12]. We will analyze this effect semiclassically, according to Banifacio et al. [9–11], and comment on experimental observation.

As samples have a volume with linear dimensions much larger than the wavelength of radiation, some quantitative differences appear in the dynamics of

the system evolution due to the effects connected with the propagation of the electromagnetic field along the emitting sample. According to Bonifacio et al., we use laser model to describe equations of motion as

$$\dot{\rho}(t) = -i(L_{AF} + i\Lambda_F)\rho(t), \quad (4.138)$$

where L_{AF} denotes the Liouvillian operator and Λ_F is the dissipation term that represents photons coming away from the cavity. They are defined as follows:

$$L_{AF}\rho = \frac{1}{\hbar}[H_{AF}, \rho], \quad (4.139a)$$

$$H_{AF} = g(aR_+ + a^\dagger R_-), \quad (4.139b)$$

$$\Lambda_{FX} = \gamma\{[a\rho, a^\dagger] + [a, \rho a^\dagger]\}, \quad (4.139c)$$

where the constants (g and γ) and the operators have usual meanings, as before. If we multiply (Eq. 4.138) on the left by a , R_+ , and R_3 , respectively, and if we take the trace, we obtain equations for $\alpha(t) = i\langle a(t) \rangle$, $r_1(t) = \langle R_+(t) \rangle$, and $r_3(t) = \langle R_3(t) \rangle$ as

$$\dot{r}_1 = 2g\alpha r_3, \quad (4.140a)$$

$$\dot{r}_3 = -2g\alpha r_1, \quad (4.140b)$$

$$\dot{\alpha} = gr_1 - \gamma\alpha, \quad (4.140c)$$

where we have used the semiclassical approximation to neglect quantum correlations. Introducing the polar angle θ of a Bloch vector as

$$r_1(t) = \frac{N}{2} \sin \theta, \quad r_3(t) = \frac{N}{2} \cos \theta, \quad (4.141)$$

one finds the following differential equation that shows the damped harmonic oscillation [9, 11]:

$$\ddot{\theta}(t) + \gamma\dot{\theta}(t) = Ng^2 \sin \theta(t), \quad (4.142)$$

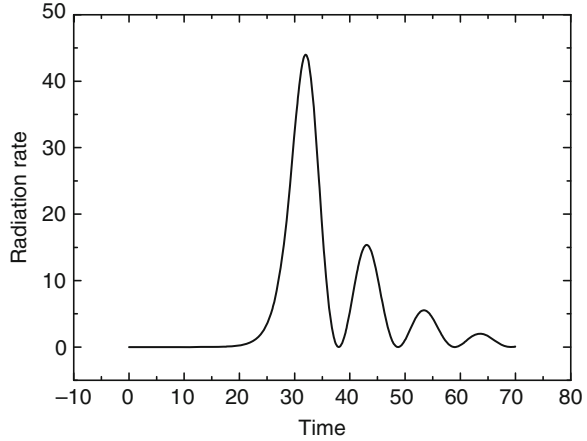
and the equations for conservation of the magnitude of the Bloch vector R^2 and energy of the system as

$$\partial_t(r_1^2 + r_3^2) = 0, \quad (4.143a)$$

$$\partial_t(\alpha^2 + r_3) = -2\gamma\alpha^2. \quad (4.143b)$$

It follows from (Eq. 4.143b) that dissipation energy from the system per unit time is $2\gamma\alpha^2$, and it corresponds to radiation energy from the system. Thus, we can write

Fig. 4.27 Time evolution of the rate of radiation from a large sample. The vertical axis is represented in units of the Einstein A coefficient as before. The parameters used are $\gamma = 0.1$, $g = 1/14$, and $N = 20$



radiation intensity $I(t)$ as

$$I(t) = 2\gamma\alpha^2 = \frac{\gamma}{2g^2}\dot{\theta}^2. \quad (4.144)$$

In Fig. 4.27, as an example, we show a numerical result obtained from (Eqs. 4.142) and (4.144), where the parameters $\gamma = 0.1$, $N = 20$, and $g = 1/14$ are used. This figure clearly illustrates an oscillation of large sample superradiance that was first predicted by Bonifacio et al. [9, 11].

If we assume that the reabsorption of photons emitted from the system can be negligibly small enough to drop the $\ddot{\theta}(t)$ term, (Eq. 4.142) can be reduced to

$$\dot{\theta}(t) = \frac{Ng^2}{\gamma} \sin \theta(t). \quad (4.145)$$

Multiplying $\sin \theta$ on the both side and setting $z = \cos \theta$, we can derive

$$\dot{z} = -\frac{Ng^2}{\gamma}(1 - z^2), \quad (4.146)$$

which is same as (Eq. 4.115), Dicke master equation for a small system obtained semiclassically.

At the end of this subsection, we briefly comment on experimental observation of superradiance. Skribanovitz et al. experimentally showed large sample superradiance similar to Fig. 4.27, using optically pumped HF atomic gas [81]. For a small system, radiation profile from CuCl quantum dots was shown to have a single pulse [59].

4.7 Dipole-Ordered States and Radiation Properties: Weak Coupling Limit

In this section we examine the radiation property of the dipole-ordered states discussed in Sects. 4.4.2 and 4.5.2. Our model has excluded radiation fields or free photons from the preceding discussions about the dynamics because the interaction energies of excitons with optical near fields are much larger in our system than those with radiation fields (weak coupling limit). This means that radiation fields are so weakly coupled with our system as not to disturb the dynamics of it. On the basis of such an understanding, we investigate radiation from a quantum dot system whose dynamics is driven by optical near fields.

According to the formulation developed in Sect. 4.6, we now investigate the radiation property of the dipole-ordered states discussed in Sects. 4.4.2 and 4.5.2. From the expression (Eq. 4.72) the radiation intensity at time t is determined by the radiation factor, $\langle R_+ R_- \rangle = (l + m)(l - m + 1)$, that is, the expectation value of the operator

$$R_+ R_- = R_1^2 + R_2^2 + R_3 = \left(\frac{P}{2}\right)^2 + \left(\frac{V}{2}\right)^2 + \frac{W}{2}, \quad (4.147)$$

which indicates that there are two elements mainly contributing to the radiation factor; one is the collectiveness of the system measured by the cooperation number l , and the other is the total energy of the quantum dot system given by $\langle R_3 \rangle = m$. Since the dynamics of the system is driven in our system by localized photons, the evolution of the radiation factor is also described in terms of $l(t)$ and $m(t)$ that are developed according to the localized photon–exciton interaction.

Numerical results of (Eqs. 4.46) and (4.47) are shown in Figs. 4.28 and 4.29. The upper parts in Fig. 4.28 show the time evolution of the radiation factors, while the lower parts illustrate the dipole distribution when each radiation factor has a maximal value. The total dipole in Fig. 4.28a is smaller than those in Fig. 4.28b, c, and the peak value of the radiation factor is also smaller. It follows from the figure that the radiation factor increases as the total dipole becomes larger. The peak values of the radiation factor in Fig. 4.28b, c, 15 and 14, correspond to the value for the Dicke’s superradiance, which is obtained as 20 for $N = 8$ from (Eq. 4.74). We thus expect that quasi-steady states shown in Fig. 4.28b, c are close to the superradiant states, and that the total Bloch vectors for such states are on the P – V plane.

In order to check whether the total Bloch vectors for the states belonging to the third group in Table 4.1 (see Fig. 4.28b) are on the P – V plane or not, we examine the time evolution of the polar angles of the Bloch vectors as well as the radiation factors. As shown in Fig. 4.29, the polar angle of the Bloch vector takes 90° , that is, on the P – V plane when the radiation factor has a maximal value. Therefore, we conclude that the system belonging to the third group in Table 4.1 are in transition to a quasi-steady state close to the superradiant Dicke state, judging from its large radiation factor and the polar angle of the total Bloch vector.

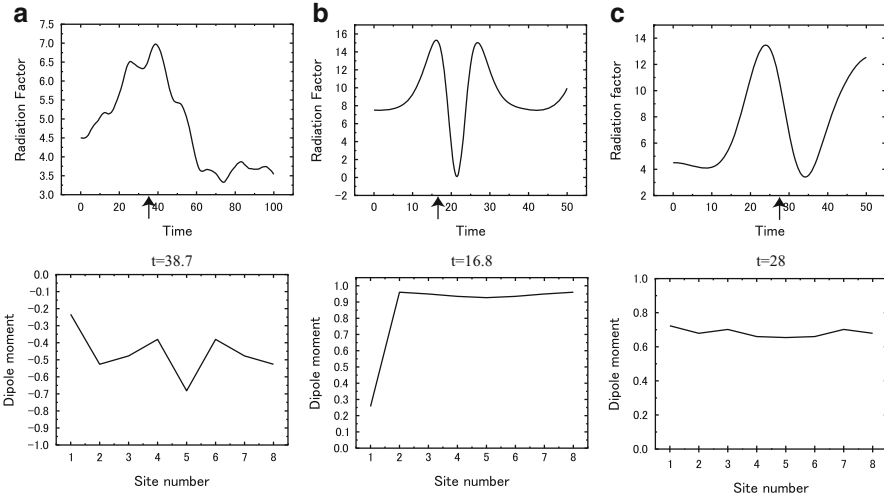


Fig. 4.28 Time evolution of the radiation factor $\langle R_+ R_- \rangle$ (upper) and the dipole distribution at time indicated by the *arrows* when the radiation factors take maximal values (lower) for (a) a system belonging to the first group with an initial population difference $W_n = (0 + + - - - + +)$, (b) a system belonging to the third group with an initial population difference $W_n = (0 + + + + + + +)$, and (c) a system belonging to the fourth group with an initial population difference $W_n = (0 - + - + - + -)$

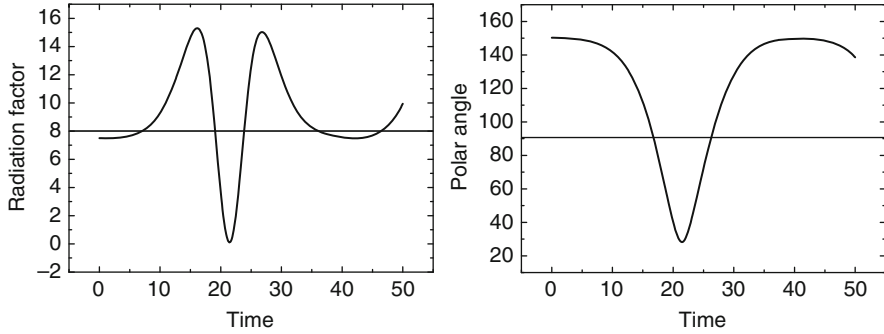


Fig. 4.29 Time evolution of the radiation factor (left) and the polar angle of the total Bloch vector (right) for a system belonging to the third group. The polar angle is measured from the $-W$ axis

In order to see the mechanism of the superradiance phenomena in our model, we shall investigate a dependence of the localized photon–exciton couplings g on the width of superradiant pulse. The result is shown in Fig. 4.30.

From this plot we find a relation as follows:

$$T \propto \frac{1}{g}. \tag{4.148}$$

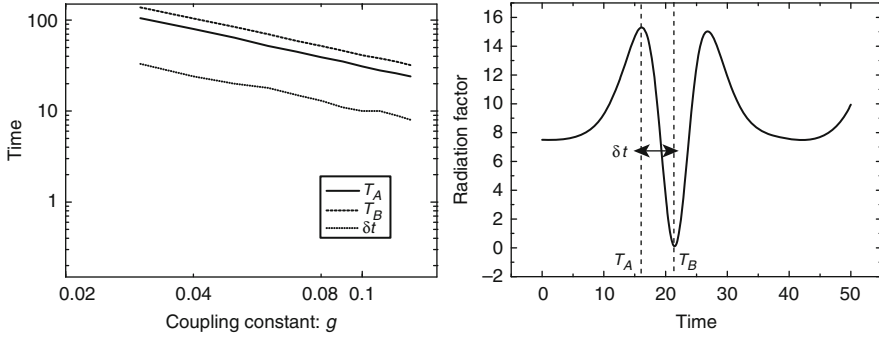


Fig. 4.30 The dependence of the width and the peak point of superradiant pulse on localized photon–exciton couplings g : double logarithmic plot (*left*) and the definitions of the pulse width δt , the pulse peak points T_A , and the bottom point of pulse valley T_B (*right*)

Recalling the mechanism of the oscillation of superradiant pulse in the Dicke model explained by Bonifasio (see (Eq. 4.142)), we know that this result means the oscillation of superradiant pulses in our model is caused by emission and absorption of localized photons.

Figure 4.28b, c indicates that multiple peaks appear in the radiation or that multiple pulses are emitted from the system. One may think, as a possible origin, that such a phenomenon stems from the recurrence inherent in an isolated system. However, such multiple pulses may survive even if the system becomes dissipative, which will be examined in detail in the next section.

4.8 Effect of Near-Field Couplings on Radiation Properties

We have assumed in the previous section that the radiation field is so weak as not to disturb the exciton dynamics of a quantum dot system. When radiation pulses are emitted from the system, however, energy has to be dissipated, and it is interesting but not clear whether multiple pulses shown in Fig. 4.28b, c are emitted from the system or not. In this section we thus study the radiation profile, adding a radiation field to the system as a reservoir that does not affect the dynamics but makes the system a dissipative one.

Suppose the Hamiltonian

$$H_2 = H_{\text{QDeff}} + H_{\text{F}} + H_{\text{Fint}}, \quad (4.149)$$

where H_{QDeff} is the effective Hamiltonian given by (Eq. 4.51a) that describes the N two-level quantum dot system interacting with localized photons. The Hamiltonians H_{F} and H_{Fint} describe the free radiation field and the exciton–free photon interaction, respectively. Explicit Hamiltonians are written as

$$H_F = \sum_{\mathbf{k}, \lambda} \hbar \omega_{\mathbf{k}} a_{\mathbf{k}, \lambda}^\dagger a_{\mathbf{k}, \lambda}, \quad (4.150)$$

$$H_{\text{Fint}}(t) = \sum_{\mathbf{k}, \lambda} \hbar g_{\mathbf{k}, \lambda} a_{\mathbf{k}, \lambda}^\dagger R e^{i(\omega_{\mathbf{k}} - \Omega)t} + h.c., \quad (4.151)$$

where creation and annihilation operators of a free photon with wave vector \mathbf{k} , polarization λ , and frequency $\omega_{\mathbf{k}}$ are denoted as $a_{\mathbf{k}, \lambda}^\dagger$ and $a_{\mathbf{k}, \lambda}$, respectively. The coupling constant between the free photon and exciton is given as

$$g_{\mathbf{k}, \lambda} = \frac{i\Omega}{\hbar \sqrt{V}} \sqrt{\frac{\hbar}{2\omega_{\mathbf{k}} \epsilon_0}} \boldsymbol{\mu} \cdot \boldsymbol{\epsilon}_{\mathbf{k}, \lambda}^*. \quad (4.152)$$

where V , $\boldsymbol{\epsilon}_{\mathbf{k}, \lambda}^*$, and ϵ_0 represent the quantization volume of the radiation field, the unit polarization vector, and the dielectric constant in vacuum, respectively. Using the Hamiltonian H_2 , we write the Liouville equation as

$$\frac{\partial \rho(t)}{\partial t} = \frac{1}{i\hbar} [H_2, \rho(t)] = -iL_2 \rho(t) \quad (4.153)$$

and eliminate the degrees of freedom of the radiation field with the help of a projection operator defined as [57]

$$\mathcal{P} \dots = |0\rangle \langle 0| \text{Tr}_F \dots \quad (4.154)$$

with the vacuum of the radiation field $|0\rangle$. Moving to the interaction representation, we obtain equations of motion for the density operator $\tilde{\rho}(t)$ as follows:

$$\begin{aligned} \mathcal{P} \frac{\partial \tilde{\rho}}{\partial t} &= -i\mathcal{P}L_2(t)\mathcal{P}\tilde{\rho}(t) - i\mathcal{P}L_2(t)U(t, 0)(1 - \mathcal{P})\tilde{\rho}(0) \\ &\quad - \mathcal{P}L_2(t) \int_0^t d\tau U(t, \tau)(1 - \mathcal{P})L_2(\tau)\mathcal{P}\tilde{\rho}(\tau), \end{aligned} \quad (4.155)$$

where $L_2(t)$ is the Liouville operator associated with $H_2(t)$ and the operator $U(t, \tau)$ is defined as

$$U(t, \tau) = \exp\left(-i(1 - \mathcal{P}) \int_\tau^t L_2(t') dt'\right). \quad (4.156)$$

With the Born–Markov approximation applied to the third term of (Eq. 4.155), we obtain the following equation for $\tilde{\rho}_A = \mathcal{P}\tilde{\rho}$ as

$$\begin{aligned} \frac{\partial \tilde{\rho}_A}{\partial t} &= -iL_{\text{QDeff}}(t)\tilde{\rho}_A(t) \\ &\quad -\text{Tr}_F L_{\text{Fint}}(t) \int_0^t d\tau U_{\text{QDeff}}(t-\tau)L_{\text{Fint}}(t-\tau)|0\rangle\langle 0|\tilde{\rho}_A(t) \end{aligned} \quad (4.157)$$

with

$$U_{\text{QDeff}}(t) = \exp(-iL_{\text{QDeff}}t), \quad (4.158)$$

where L_{QDeff} and L_{Fint} are the Liouville operators associated with the Hamiltonian H_{QDeff} and H_{Fint} , respectively. Moreover, using the Born approximation that neglects the exciton operators of higher than the second order [57], we approximate

$$U_{\text{QDeff}}(t) \sim 1 \quad (4.159)$$

to obtain a compact equation as

$$\begin{aligned} \frac{\partial \tilde{\rho}_A}{\partial t} &= -iL_{\text{QDeff}}(t)\tilde{\rho}_A(t) + \beta \{[R_-\tilde{\rho}_A(t), R_+] + [R_-, \tilde{\rho}_A(t)R_+]\} \\ &\quad -i\gamma[R_+R_-, \tilde{\rho}_A(t)] \end{aligned} \quad (4.160)$$

with

$$\beta + i\gamma \equiv \int_0^t \sum_{\mathbf{k}, \lambda} |g_{\mathbf{k}, \lambda}|^2 e^{i(\Omega - \omega_{\mathbf{k}})\tau} d\tau, \quad (4.161)$$

which is exactly the same form as the Lindblad's master equation [55] describing a general Markovian dynamics for a dissipative quantum system. Here the real and imaginary parts of the right-hand side of (Eq. 4.161) are designated as β and γ , respectively. In the following we neglect the energy shift as $\gamma = 0$, for simplicity. Note that the second and the third terms of the right hand-side of (Eq. 4.160) are known as the Dicke's master equation [2, 11, 22].

4.8.1 Semiclassical Solution: Without Quantum Correlation

Neglecting quantum correlation between excitons [3], we approximate the total density operator ρ_A as a direct product of the density operator ρ_n at each site n

$$\rho_A = \prod_n \rho_n, \quad (4.162)$$

and then solve (Eq. 4.160). Noticing that the dynamics governed by the original Hamiltonian (Eq. 4.4) is not rigorously identical to the one described by the effective Hamiltonian (Eq. 4.51a), we use an isolated system described by the effective Hamiltonian (Eq. 4.51a) in order to clarify the dynamics governed by (Eq. 4.160) for a dissipative system whose relevant system is described by the same

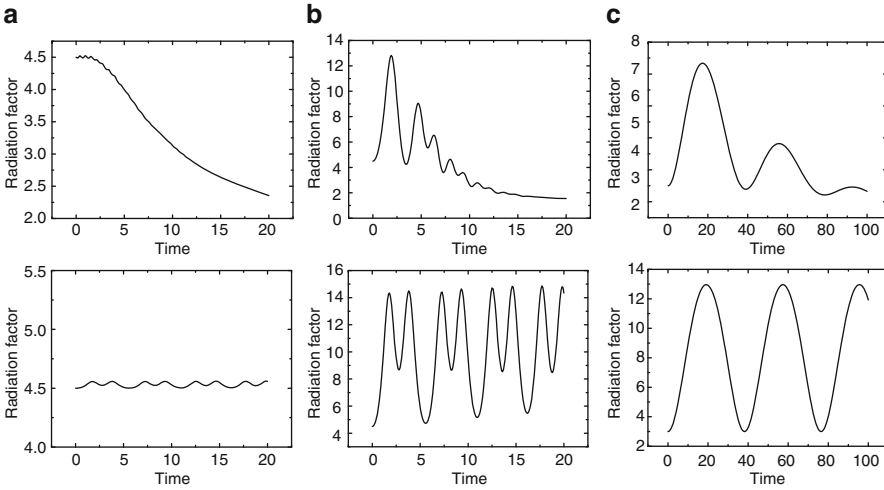


Fig. 4.31 Time evolution of the radiation factor for dissipative systems (*upper*) and isolated systems (*lower*). We consider the following three cases for both systems: (a) a “ferromagnetic” case, (b) an “antiferromagnetic” case which is turned to a dipole-ordered state after manipulating the initial population differences, and (c) a “dipole-forbidden” case discussed in Sect. 4.4.3. The parameters $\beta = 0.05$ and $\gamma = 0$ are used

Hamiltonian (Eq. 4.51a). By comparing the radiation factors for the isolated system and the dissipative system, the similarity and the difference are discussed.

Figure 4.31 shows the time evolution of the radiation factor for (a) a “ferromagnetic” system belonging to the third group of Table 4.1, (b) an “antiferromagnetic” system that belongs to the fourth group of Table 4.1 and is turned to a dipole-ordered state after manipulating the initial population differences, and (c) a “dipole-forbidden” system that is converted to a dipole-ordered state by the local manipulation discussed in Sect. 4.4.3 as $\langle W_n(0) \rangle = -\langle P_n(0) \rangle$. It follows from the lower part of Fig. 4.31a that superradiance is suppressed and does not manifest itself due to the difference between the original Hamiltonian (Eq. 4.4) and the effective Hamiltonian (Eq. 4.51a). On the other hand, superradiant multiple pulses are generated in the isolated system and survive in the dissipative system for both cases shown in Fig. 4.31b, c. Therefore, we find with a semiclassical approach that multiple pulses, as predicted for an isolated system, can be emitted superradiantly from dipole-ordered states even in a dissipative system coupled to a radiation reservoir.

4.8.2 Effect of Quantum Correlation: Comparison with Dicke Model

It is well known that superradiance in the Dicke model [25] occurs from a state where all excited states of all sites are occupied. On the other hand, the semiclassical

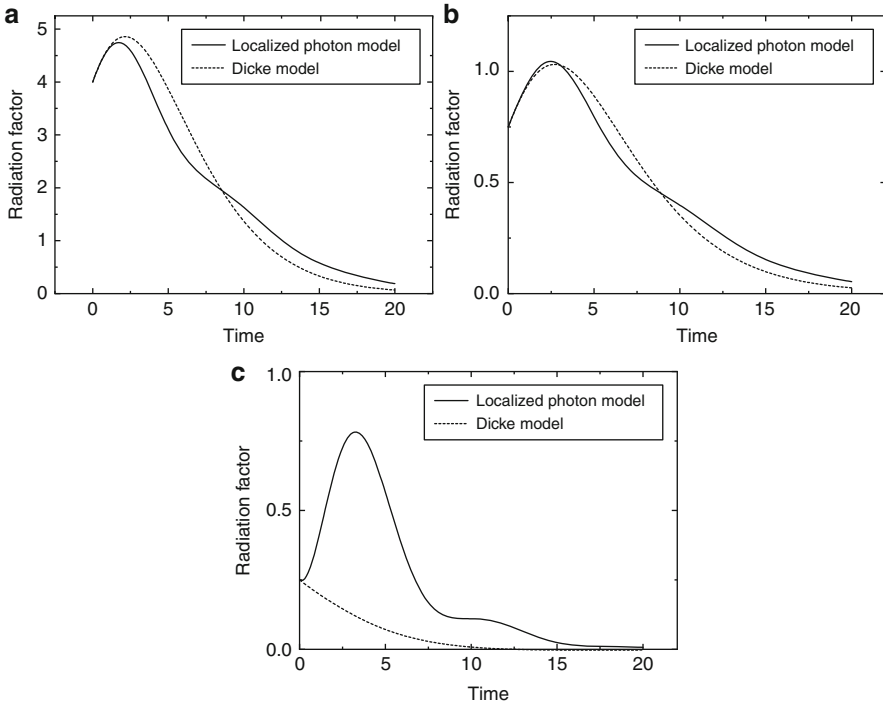


Fig. 4.32 Time evolution of the radiation factor obtained with quantum correlations. The *solid curves* are the results for our model, while the *dashed curves* represent the results for the Dicke model. The dissipative system is assumed, and the parameters $N = 4$, $\beta = 0.05$, and $\gamma = 0$ are used. In addition, the following initial conditions are used: (a) $\langle P_n \rangle = 1$ and $\langle W_n \rangle = 1$, (b) $\langle P_n \rangle = (-1)^n / \sqrt{2}$ and $\langle W_n \rangle = 1 / \sqrt{2}$ which correspond to a dipole-forbidden state as shown in Fig. 4.11, and (c) $\langle P_n \rangle = (-1)^n / \sqrt{2} = -\langle W_n \rangle$ which corresponds to a dipole-ordered state as shown in Fig. 4.12

approach discussed above cannot predict the occurrence of superradiance of the system when the total dipole of the system is zero as an initial condition [3]. This means that quantum fluctuations and correlations should be properly included so as to correctly describe the radiation properties of a system with no initial dipoles and that the semiclassical approximation is not appropriate in this case. Thus, we numerically solve the master equation (Eq. 4.160), taking quantum correlations into account, and we investigate the radiation properties of the dissipative system. In particular, we compare the results obtained from our model, that is, the localized photon model with those obtained from the Dicke model, for which the first term of the right-hand side is dropped from (Eq. 4.160). Some of such results are shown in Figs. 4.32 and 4.33.

Figure 4.32a shows the time evolution of the radiation factor for the case that all the populations are completely in the excited states and there are no dipoles as an initial condition. The solid curves are the results for our model, while the dashed

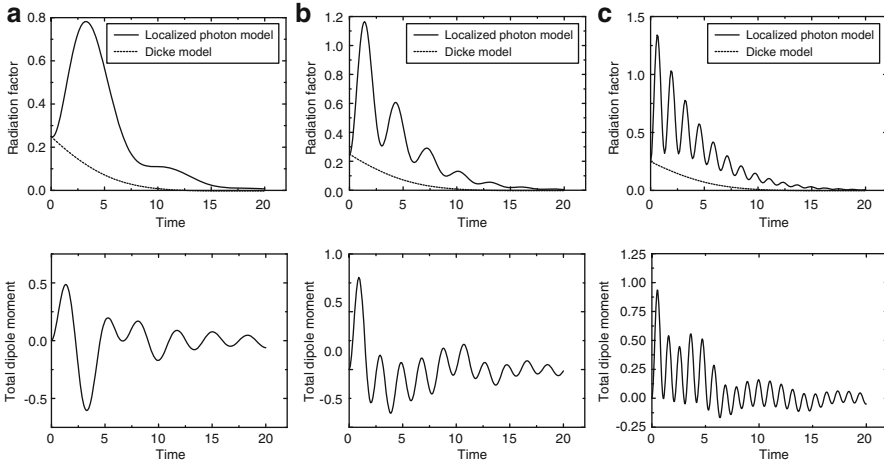


Fig. 4.33 Time evolution of the radiation factor (*upper*) and the total dipole moment (*lower*) obtained with quantum correlations. The *solid curves* are the results for our model, while the *dashed curves* represent the results for the Dicke model. The system is assumed to be dissipative and in a dipole-ordered state evolved from a dipole-forbidden state, that is, the same as in Fig. 4.32c. The initial conditions are also the same as in Fig. 4.32c, except for the exciton–localized photon coupling (a) $g = 0.5$, (b) $g = 0.8$, and (c) $g = 1.2$

curves represent the results for the Dicke model. It follows from the figure that a single superradiant pulse is emitted in both models but that the peak value of the superradiant pulse is reduced, while the tail is extended in our model. In Fig. 4.32b, we present the result obtained from the initial condition as a zigzag profile of the dipole distribution of $\langle P_n \rangle = (-1)^n / \sqrt{2}$ and flat population differences of $\langle W_n \rangle = 1 / \sqrt{2}$. The system corresponds to a dipole-forbidden state as shown in Fig. 4.11, where the total dipole is always zero. The radiation profiles obtained for both models are qualitatively same as found as in Fig. 4.32a. The time evolution of the radiation factor is illustrated in Fig. 4.32c for the case that initially the alternating dipole is set as $\langle P_n \rangle = (-1)^n / \sqrt{2}$ and the sign of the population difference in each QD is set opposite to that of the corresponding dipole as $\langle W_n \rangle = -\langle P_n \rangle$. Owing to the flip property, a dipole-ordered state emerges in this case, and a distinct difference between the two models is observed: our model (solid curve) shows superradiance, while the Dicke model (dashed curve) does not. Since we can infer that the difference stems from the dipole-ordering phenomenon, we further examine this case in order to clarify the relation between the radiation factor and the total dipole of the system.

Figure 4.33 presents the time evolution of the radiation factor (*upper*) and the total dipole (*lower*) by changing the exciton–localized photon coupling constant g as (a) $g = 0.5$, (b) $g = 0.8$, and (c) $g = 1.2$. It is found that the frequency of the total dipole increases as the coupling constant becomes strong. As a result, the oscillation frequency of the radiation factor increases, and thus, multiple pulses are emitted

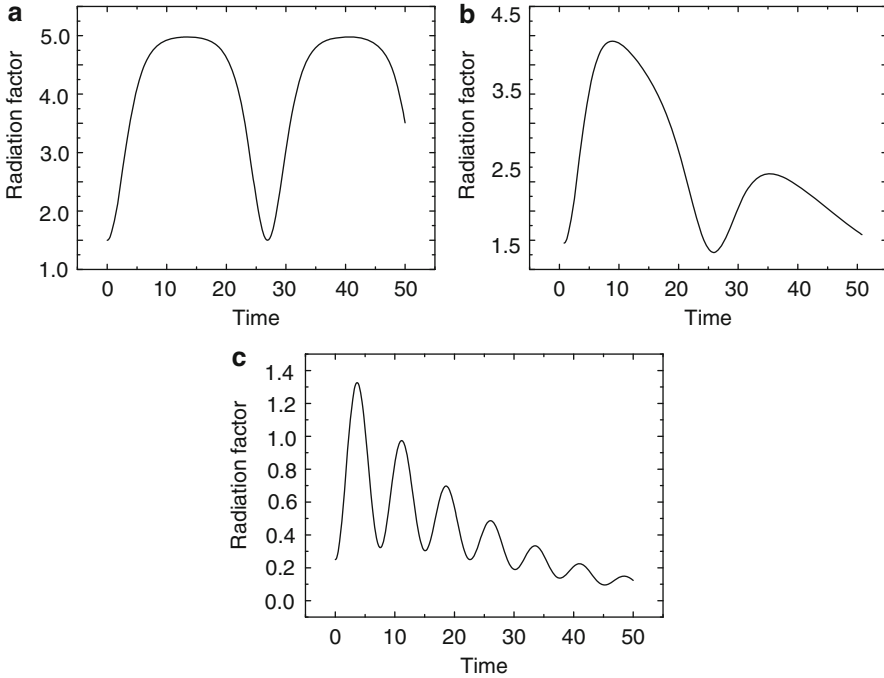


Fig. 4.34 Radiation profile obtained from three different methods. The system and the initial conditions to be considered are the same as in Fig. 4.33. The result is obtained (a) for the isolated system by the Liouvilian dynamics of the effective Hamiltonian with the semiclassical approximation, (b) for the dissipative system by the master equation (Eq. 4.160) with the semiclassical approximation, and (c) for the dissipative system by the master equation (Eq. 4.160) with quantum correlations. The parameters $N = 4$, $\beta = 0.05$, and $\gamma = 0$ are used

superradiantly from the dissipative system. Therefore, the difference between the two models, as we expected, originates from the occurrence of a dipole-ordered state or a collective dipole oscillation via localized photon–exciton interactions.

At the end of this section, we examine the applicability of the semi-classical approach which has an advantage over the quantum approach that one can easily handle a relatively large number N system. In Fig. 4.34, we show the radiation profile obtained from three different methods. The system and the initial conditions to be considered are the same as in Fig. 4.33. The result is obtained (a) for the isolated system by the Liouvilian dynamics of the effective Hamiltonian with the semiclassical approximation, (b) for the dissipative system by the master equation (Eq. 4.160) with the semiclassical approximation, and (c) for the dissipative system by the master equation (Eq. 4.160) with quantum correlations. We find from Fig. 4.34 that multiple pulses are generated for all the cases though each frequency of the oscillation is different. It indicates that the semiclassical approach can describe qualitatively the radiation properties of both isolated and dissipative systems when

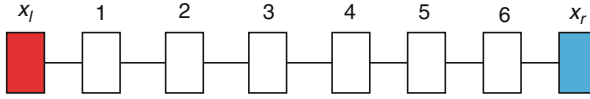


Fig. 4.35 The QDs interacting with localized photons are configured in a line. At each end of the line, we set different boundary conditions

the total dipole of the system is not zero. The strong radiation coming from the dipole-ordering phenomenon or the nonlinearity and the collective phenomena of the dynamics of the system considered in this chapter can be qualitatively predicted by the semiclassical approach.

4.9 Transport Phenomena of Localized Photons

Since the semiclassical Heisenberg equations (Eq. 4.46) are nonlinear, neglecting quantum correlations between quantum dots (QDs) and localized photons, we expect such a system to display nonlinear or possibly chaotic phenomena. Indeed, since a system with strong nonlinearity behaves chaotically and shows deterministic randomness, chaotic systems represent macroscopic transport phenomena. In this context, this section considers an open system for the localized photon model and investigates the transportation of localized photons.

As depicted in Fig. 4.35, we lined up QDs that interact with localized photons with a reservoir of localized photons at either end of the line.

In this setting, we investigated the transportation of localized photons through the system.

4.9.1 Two Phases of Transportation: Switching Between Flow and Block Mode

The numerical operator of the localized photons at site j is defined as $n_j = a_j^\dagger a_j$ and the equation of motion for the expectation value $\langle n_j \rangle$ using the semiclassical approximation is derived as follows:

$$\begin{aligned} \frac{d\langle n_j \rangle}{dt} &= \frac{v}{2}(\langle x_{j-1} \rangle + \langle x_{j+1} \rangle)\langle y_j \rangle \\ &\quad - \frac{v}{2}(\langle y_{j-1} \rangle + \langle y_{j+1} \rangle)\langle x_j \rangle - \frac{g}{2}(\langle V_j \rangle - \langle P_j \rangle)\langle y_j \rangle. \end{aligned} \quad (4.163)$$

Since the right-hand side of (Eq. 4.163) does not include the localized photon number $\langle n_j \rangle$, the dynamics of the localized photon number are decided by the other Heisenberg Equations (Eq. 4.46) and (Eq. 4.47). From the Heisenberg equations, it is clear that using the semiclassical approximation, the physical quantity that can be

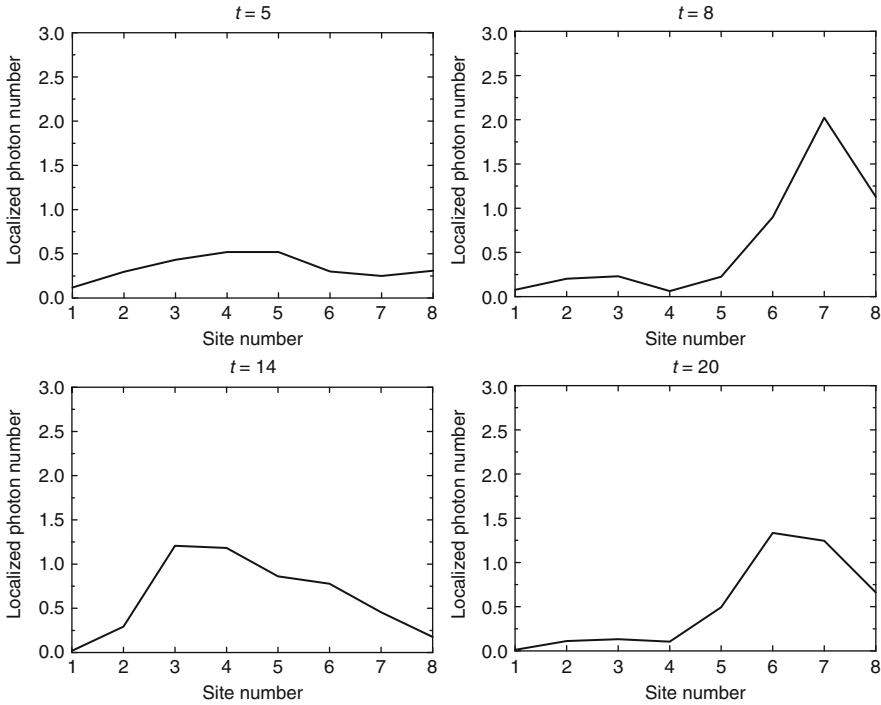


Fig. 4.36 The dynamics of the distribution of localized photons of an open system with reservoirs of localized photons in the coherent states at the zeroth and ninth sites in the first case. In this case we observe linear propagation and the reflection of excitation of localized photons

input from both ends as a boundary condition is the coherence of localized photons $x_j = a_j + a_j^\dagger$, $y_j = i(a_j - a_j^\dagger)$ (not the localized photon number $a_j^\dagger a_j$). Therefore, we define the boundary condition at both ends using (Eq. 4.57) to achieve a coherent state in which the eigenvalue is a real number. This boundary condition corresponds to the locally determined amplitude of the classical electric field oscillation (at the boundaries). The electric field is strengthened at the left boundary and weakened at the right boundary ($x_l > x_r$). The emerging dynamics are then examined with the focus on the distribution of localized photons. Consider the case where there are eight sites and the values at sites 0 and 9 are fixed at $\langle x_0 \rangle = 1$, $\langle x_9 \rangle = 0$, respectively, by assuming that a reservoir of localized photons has been attached, with all the excitons in the initial state of excitation, and the constituent expected values of the localized photon are set to 0 at all the other locations, except at the boundaries. In this configuration, the temporal evolution of localized photons shows that the resultant behavior can be broadly classified into the following two types: Behavior 1 is shown in Fig. 4.36, in which the excitation travels linearly from left to right. Behavior 2 is shown in Fig. 4.37, in which a structure similar to a standing wave forms and develops over time.

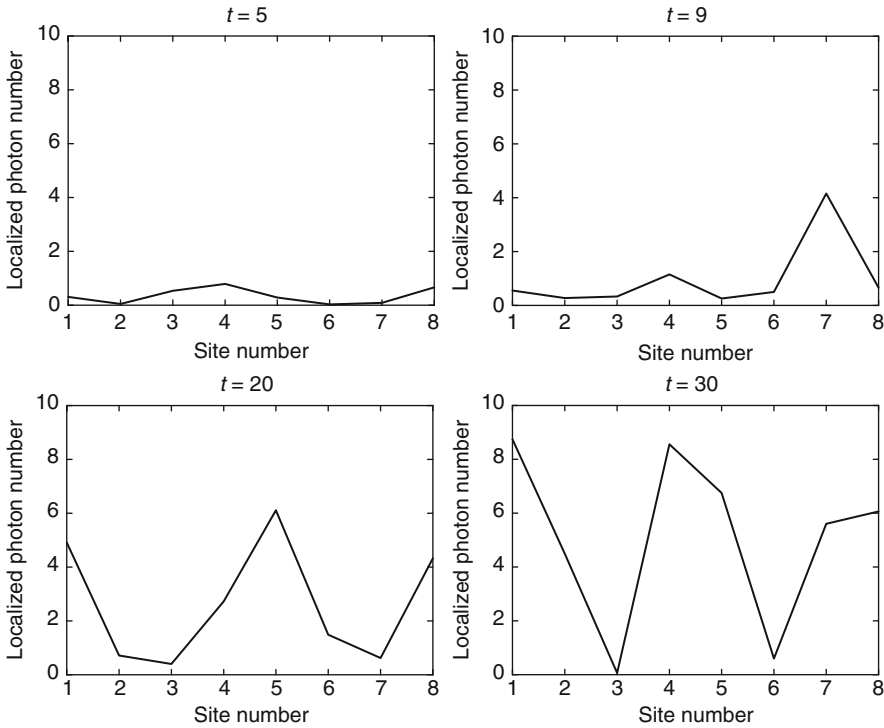


Fig. 4.37 The dynamics of the distribution of localized photons of an open system with reservoirs of localized photons in the coherent states at the zero-th and ninth sites in the second case. In this case, we observe the growth of a structure similar to a standing wave

In Fig. 4.36, a linear transmission wave can be observed in which excitation emerges from the input side, travels to the right, reflects off the right boundary, travels to the left, gets pushed back by the input on the left, and travels to the right again. Consequently, it travels back and forth. In other words, linear behavior can be observed in the temporal evolution of localized photons despite the nonlinear nature of the system dynamics.

In Fig. 4.37, there is a clear division between the sites where localized photons accumulate (peaks) and the sites where localized photons are rare (nodes). Localized photons continue to accumulate in the system and no stationary state emerges. This can be viewed as formation of a standing wave. Examination of the total number of localized photons $\sum_n \langle a_n(t)^\dagger a_n(t) \rangle$ in the system yields the results shown in Fig. 4.38.

Figure 4.38 clearly distinguishes between the two types of system when looking at the number of photons. In the system shown in Fig. 4.36, in which the transportation of localized photons follows a linear wave motion, the total number of photons is approximately constant. In the system shown in Fig. 4.37, the total number of localized photons increases monotonically, and localized photons continue to

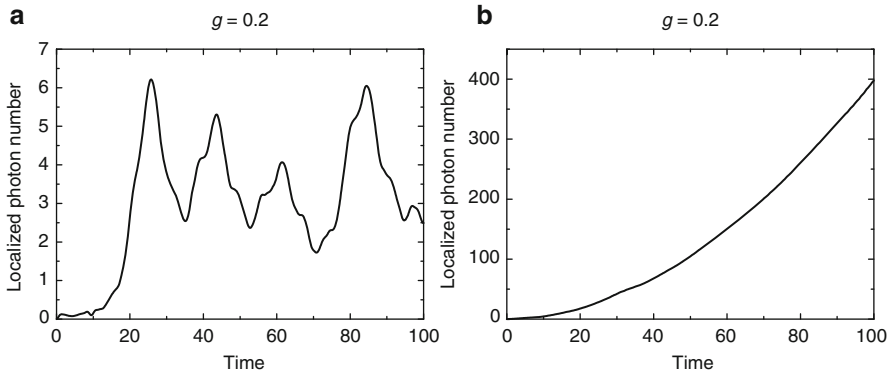


Fig. 4.38 Temporal evolution of the total localized photon number $\sum_n \langle a_n(t)^\dagger a_n(t) \rangle$. (a) and (b) correspond to the systems in Figs. 4.36 and 4.37, respectively

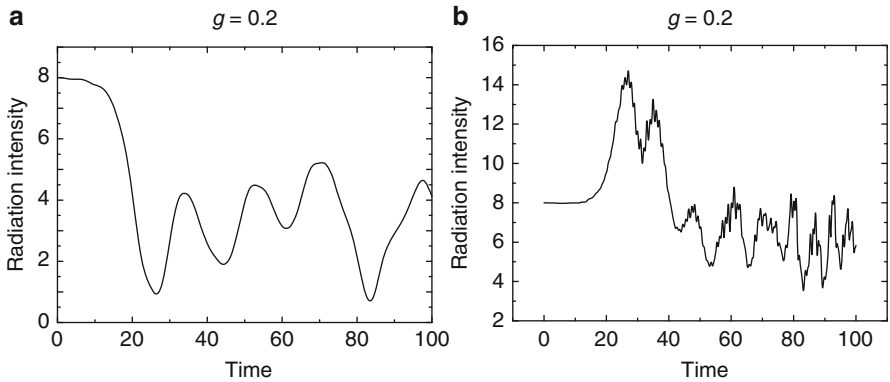


Fig. 4.39 Temporal evolution of the radiation intensity of the open systems. (a) and (b) correspond to the systems in Figs. 4.36 and 4.37, respectively. Strong radiation occurs in the system that is accumulating the localized photons and not in the system where there is no accumulation

accumulate in the system. The fact that the relaxation phenomenon does not occur implies that either photons can accumulate in the system or that the system relaxes very slowly and our calculations are insufficient for it to reach equilibrium.

Next, the radiation intensity was calculated for the two systems. Using the arguments given in Sect. 4.7, Fig. 4.39 shows the radiation intensity calculated using (Eq. 4.147).

In the system shown in Fig. 4.37, in which a standing wave develops, a cooperative effect close to superradiance is observed, whereas no cooperative effect exists in the system in Fig. 4.36 that shows linear behavior. In the system shown in Fig. 4.37, which corresponds to (b) in Fig. 4.28, if the system is opened in this manner, a time-irreversible phenomenon is observed, in which the repeating superradiant pulse observed in Fig. 4.28b does not emerge, and only a large single

peak forms. This is because the system has been opened by attaching reservoirs at both ends, which dissipate information. Moreover, because the coherence of the whole system is lost due to the forced input at both ends, which leads to loss of the cooperative effect caused by coherence, superradiance arises. Nevertheless, despite the nonlinearity of the equations, it becomes clear that a statistical mechanical transportation phenomenon does not occur as a nonequilibrium steady state, despite the nonlinear dynamics of system. One of the causes of this is that the system's nonlinearity is weak. Generally, the ergodicity or mixing property strengthens as nonlinearity increases, and relaxation is reached more quickly in the steady state [31]. Another cause may be that chaotic characteristics in the classical sense do not emerge because the system is currently dealt with in terms of semiclassical quantum mechanics. However, other phenomena characteristic of a nonlinear system should appear when nonlinearity exists in the system of equations, similar to quantum chaotic systems in which characteristic phenomena different from those of a regular system appear indirectly in the level statistics [33, 34]. The following subsection contains observations regarding this point.

4.9.2 Sensitive Switching of Flow and Block: Chaotic Behavior

4.9.2.1 Dependence of the Coupling Constant g

To study the appearance of nonlinearity in this system, the dependency of the temporal evolution of the localized photons on the coupling constant g is examined. The temporal evolution of the total number of localized photons that accumulate in the entire system for the case in Fig. 4.38b is plotted for various coupling constants, g , as shown in Fig. 4.40.

Looking at the plot, there is a characteristic sudden shift in behavior from monotonically increasing to oscillatory at $g = 0.67$, and this returns to monotonically increasing behavior at $g = 0.69$. Indeed, the number of localized photons decreases by one order of magnitude at the transition from monotonic behavior at $g = 0.65$ to oscillatory behavior at $g = 0.67$. This is nonlinear behavior. That is to say, we can expect nonlinear, random behavior in the dependency of the total number of localized photons on the exciton–photon coupling constant g . To examine this in detail, Fig. 4.41 plots the dependency of the total number of localized photons on the coupling constant g at time $t = 100$.

Figure 4.41 shows that the appearance of nonlinear, random behavior for the dependency of the total number of localized photons depends on the exciton–photon coupling constant g , for the systems in both Figs. 4.36 and 4.37. Particularly, for the system in Fig. 4.37, in which localized photons accumulate, the fluctuation in the dependency of the total number of photons on the coupling constant is extremely vigorous. Examination of the Heisenberg (Eqs. 4.46) and (4.47) shows that the coupling constant g is included in the nonlinear terms of the equations. Therefore, it is easy to see that it is one of the parameters that measure nonlinearity. Therefore, the dynamics of systems with boson-approximated excitons, in which nonlinear terms

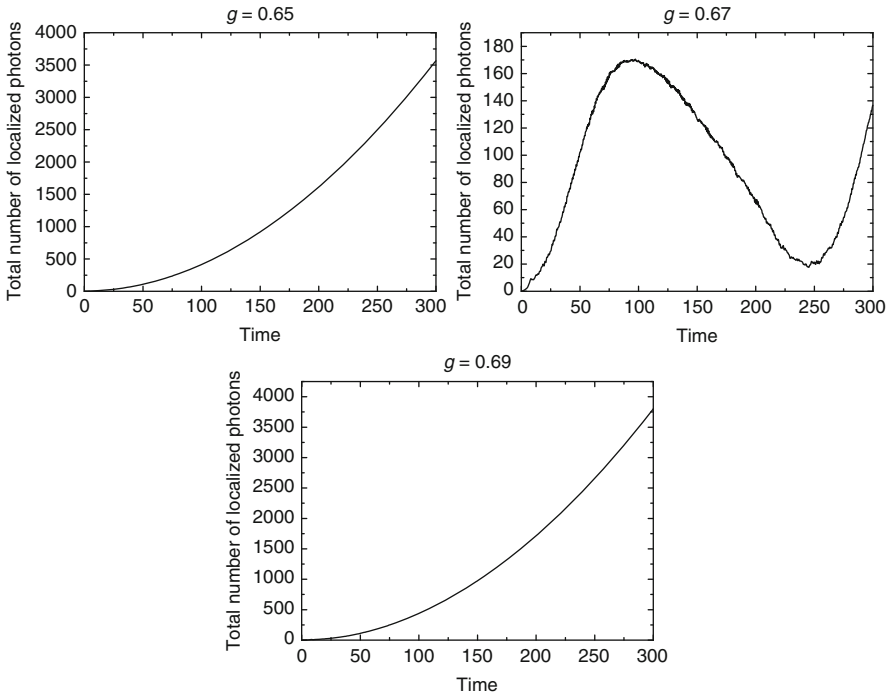


Fig. 4.40 Temporal evolution of the total number of localized photons in the system corresponding to Fig. 4.38b when the coupling constant g equals 0.65, 0.67, and 0.69. We observe a drastic change of the number of localized photons between $g = 0.65$ and $g = 0.67$. The difference amounts to a single digit

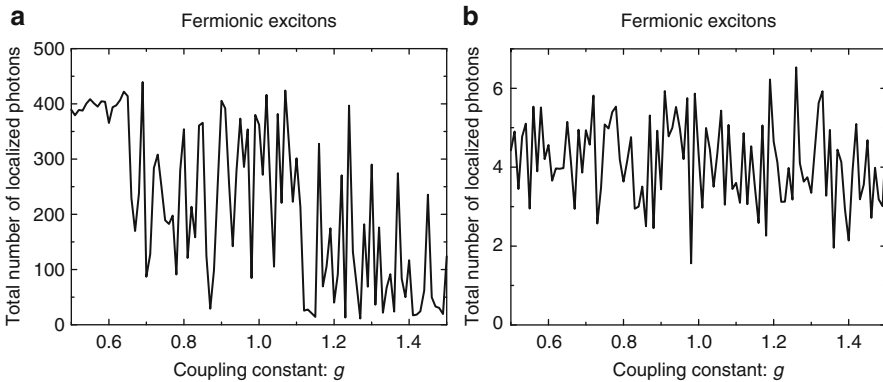


Fig. 4.41 Dependence of the total localized photon number on the coupling constant g at $t = 100$. (a) and (b) correspond to the systems in Figs. 4.36 and 4.37, respectively

do not emerge in the equations of motion, must be examined in order to confirm that this behavior originates from the nonlinearity of the equations.

4.9.2.2 Linear System: Effect of Nonlinearity

The Heisenberg equations of the system become the following when an exciton is approximated by a boson:

$$\begin{cases} \partial_t P_n = -\Omega V_n - g y_n, \\ \partial_t V_n = \Omega P_n + g x_n, \\ \partial_t x_n = -\omega y_n - v(y_{n-1} + y_{n+1}) - g V_n, \\ \partial_t y_n = \omega x_n + v(x_{n-1} + x_{n+1}) + g P_n. \end{cases} \quad (4.164)$$

These are clearly linear equations. Since the equation of motion of the number of localized photons $\langle a_n(t)^\dagger a_n(t) \rangle$ is the same as in the case of (Eq. 4.163) discussed above, which is obviously linear, in the boson-approximated system all the equations of motion are linear. Solving these equations, Fig. 4.42 shows the dependency of the total number of localized photons on the coupling constant g .

Although random behavior does not appear in this case, resonating coupling constant dependence is found. The meaning of the resonating coupling constants is not yet clear; however, at least there is no disorderly, unpredictable behavior. From these observations, we conclude that the disorderliness of Fig. 4.41 is a chaotic behavior originating from the nonlinearity of the dynamics.

Here, one must be cautious, because a system consisting of eight sites has many modes, and it is possible that an apparently disorderly dependence has emerged via the competition of different modes (e.g., the superposition of many types of quasiperiodic behavior). Quasiperiodic behavior (Since the nonlinear behavior that emerges here does not involve the dynamics (temporal evolution), but is the behavior concerned with the parameter g , it needs to be differentiated from the dynamics

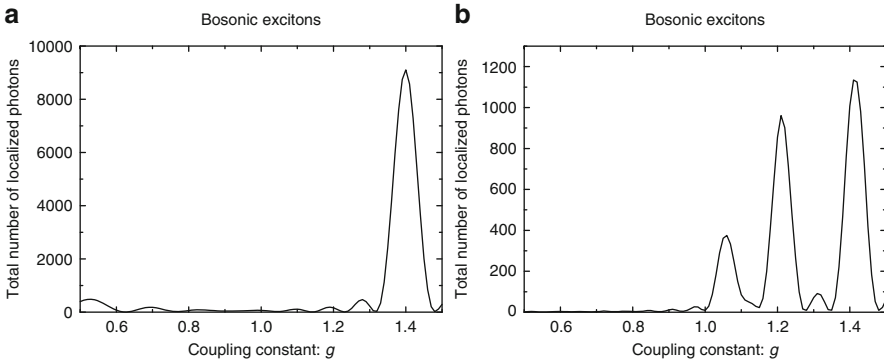


Fig. 4.42 The dependence of the coupling constant g of the total localized photon number at $t = 100$ for the system in which there is boson approximation of excitons. (a) and (b) take the same system parameters as the systems in Figs. 4.36 and 4.37, respectively

of time-dependent evolution in this situation. For this purpose, we referred to the phenomenon as “behavior.”) does not have a period either, so chaos does not exist simply because of a lack of periodicity. In the next section, the phenomenon is examined by simplifying the problem by reducing the degrees of freedom to the minimal value while considering the above.

4.9.3 Intermittent Chaotic Behavior in Two-Site Open System

This section considers the nonlinear dependency on the coupling constant g observed in the previous section in a system with two sites (four sites including the reservoirs at the two ends) in order to simplify the problem. This is done to reduce the degrees of freedom so as to differentiate between the disorderliness caused by the superposition of many quasiperiodic behaviors originating from the many modes and the nonlinearity of the dynamics of the system. Figure 4.43 shows the dependency of the total number of localized photons on the coupling constant g for the two-site system.

Examination of the magnified parts of the graph shows marked fluctuation in these regions, and the fluctuations are squeezed together so tightly that the area appears solid black. This shows that dependency on g behaves unpredictably. Since with two sites there are few participating modes, the vigorous fluctuations are a manifestation of chaotic behavior, reflecting the nonlinearity of the dynamic equations. Examination of Fig. 4.43A shows that there are vigorous fluctuations (chaotic regions) in some areas, and not in others (regular windows). In other words, this system displays “intermittent chaos,” using the terminology to describe the temporal evolution of chaos. Since chaotic systems display deterministic probabilistic behavior (e.g., diffusion) [31], the number of localized photons should obey a statistical distribution. Therefore, we examined histograms of the number of localized photons corresponding to Fig. 4.43a–d. Figure 4.44 shows the histograms of the numbers of localized photons in the chaotic regions of the system corresponding to Fig. 4.43a–d in a double logarithmic graph.

This figure shows that the histograms for each individual region share a common behavior. The double logarithmic plot of the histograms consists of two straight lines; the first line has a slope of approximately -1 . In other words, when the distribution of localized photons n is approximated as $P(n)$, the distribution in the regions of small n is given by $P(n) \propto 1/n$. The slope is very steep in the region where there are many photons, and the graph can be regarded as an exponential function. In conclusion, the emergence of a common statistical distribution of localized photons in regions (a) through (d) is the evident result of a universal statistical law caused by the chaotic dynamics of the system. This means that the apparent complexity does not arise merely by chance; there is a common principle working in the background. In other words, the nonlinear dynamics of the system indirectly cause such behavior to emerge.

As we shown above, many interesting phenomena emerge when we look at the behavior of localized photons, including the existence of a photon storage mode and

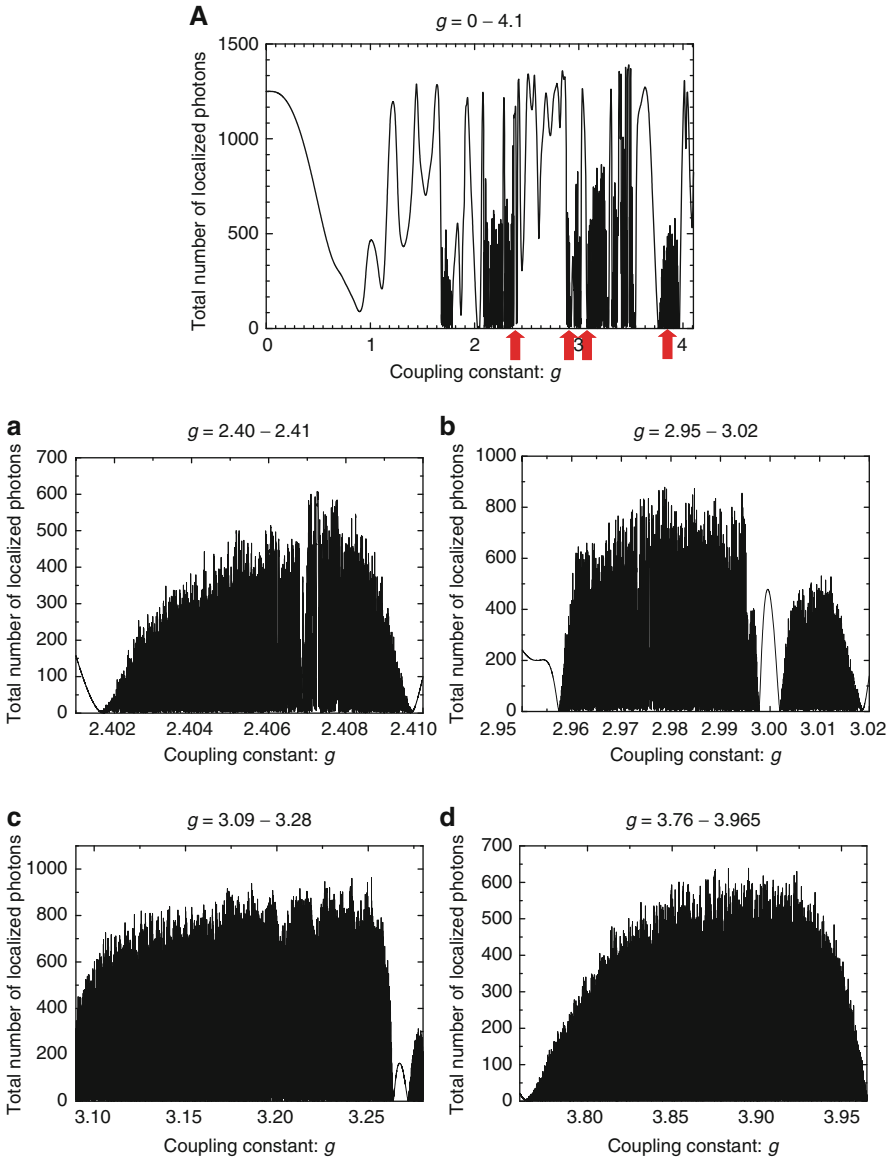


Fig. 4.43 The dependence of the coupling constant g on the total localized photon number of the two-site open system. (A) is the plot for the range from $g = 0$ to $g = 4.1$. (a)–(d) show the chaotic regions in (A). (a) Shows the range from $g = 2.40$ to $g = 2.41$, (b) is from $g = 2.95$ to $g = 3.02$, (c) is from $g = 3.09$ to $g = 3.28$, and (d) is from $g = 3.76$ to 3.965

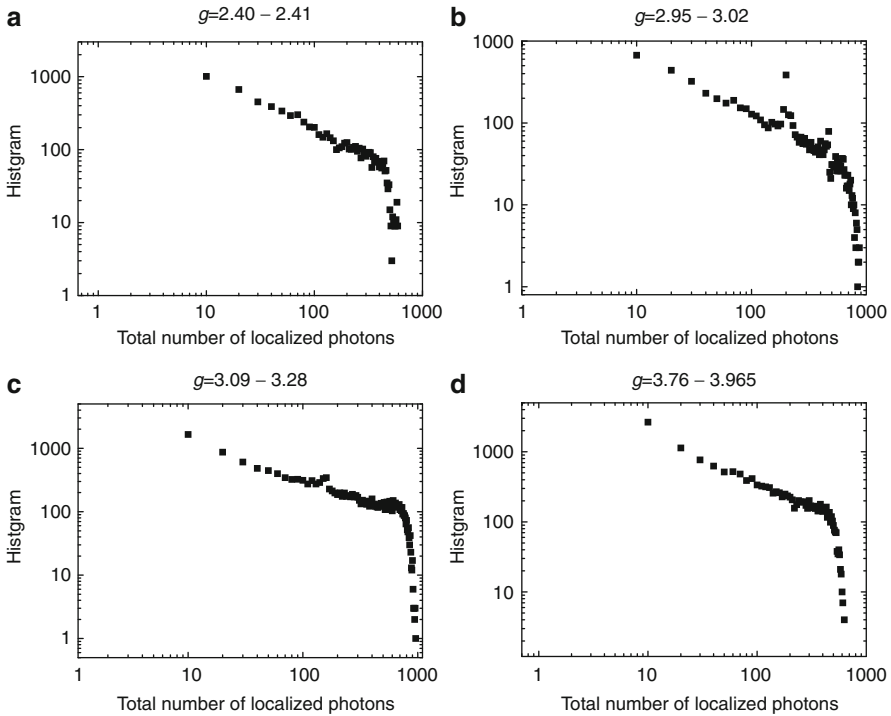


Fig. 4.44 A log–log plot of the histogram of the localized photon numbers for the regions depicted in Fig. 4.43. Figures (a)–(d) correspond to chaotic regions (a)–(d) in Fig. 4.43

the existence of chaotic dependency of the system’s mode on a system parameter. Nevertheless, our discussion is based on a semiclassical system of equations that ignores quantum correlations, and it remains to be determined whether these phenomena actually occur, that is, do these phenomena survive in the case using full quantum correlations? Therefore, we examined the behavior considering the quantum correlation of the next order. In this case, a storage mode for photons also exists. The fact that the behavior in the next order does not differ significantly suggests that the semiclassical approach is sufficient.

4.10 Conclusions

In order to investigate the dynamics of the system, we presented a model of N two-level quantum dot systems interacting with optical near fields that explicitly expressed in terms of the localized photonic degrees of freedom that characterize the unique property of the localization of optical near fields. At the low-density limit, excitons (N two-level systems) are approximated as bosons, and a rigorous solution of the Heisenberg equation is obtained. Using this solution, we examined

the dynamics of the excitonic system and showed that the dipole moments are transferred linearly within the system. Since the dipole moments in the system represent the quantum coherence between any two energy levels, this phenomenon might be applicable to a photonic device on a nanometer scale or to the transfer of quantum information.

For fermionic excitons, the Heisenberg equation becomes nonlinear, and the dynamics is more complicated. We obtained a perturbative solution given by (Eq. 4.43) within the second order with respect to the localized photon–exciton interaction, to investigate the dipole dynamics. The study revealed that several oscillating quasi-steady states exist, depending on the material parameters. Using the effective Hamiltonian obtained from renormalization of the localized photonic degrees of freedom, we classified such quasi-steady states into several groups: one is a “ferromagnetic” state with all the dipoles aligned in the same direction; the other is an “antiferromagnetic” state with the alternating dipoles, as shown in Table 4.1.

Note that if the sign of the population difference $\langle W_n(0) \rangle$ at arbitrary site n and time $t = 0$ is reversed, then the dipole of the same site at arbitrary time t , $\langle P_n(t) \rangle$, also changes sign (see (Eq. 4.44)). Using this flip property, we can transform an arbitrary dipole distribution of the system into a dipole-ordered state after manipulating the initial distribution of the population differences. This property is based on the perturbative solution (Eq. 4.44), which determines the sign of $\langle P_n(t) \rangle$ according to the sign of the product of $\langle P_1(0) \rangle \langle W_n(0) \rangle$. It also originates from the fermionic property of excitons, which gives the Heisenberg equations of motion for b_n ($\propto P_n$) as

$$[H_{b-b}, b_n] = \sum_{m \neq n} \Delta \Omega_{nm} W_n b_m. \quad (4.165)$$

The right-hand side of (Eq. 4.165) is proportional to $\langle P_m \rangle \langle W_n \rangle$ for fermions, while it is proportional to $\langle P_m \rangle$ for bosons. Therefore, the occurrence of this kind of nonlinearity for fermionic excitons is a possible origin of the flip property. Moreover, it is not trivial; this property can be applicable to results obtained from the semiclassical Heisenberg Equations (Eq. 4.46) and (Eq. 4.47).

We examined the radiation property of our system, solving the Heisenberg Equations (Eq. 4.46) and (Eq. 4.47) using the semiclassical approximation. In the investigation, we treated the system as isolated since the coupling between radiation fields and the system is very weak. The numerical analysis showed that dipole-ordered states, which have large total dipole moments, show a large radiation probability comparable to Dicke’s superradiance. In particular, it predicted that multiple pulses are emitted from the system superradiantly. In order to verify whether such a phenomenon is inherent in an isolated system, we solved the master equation (Eq. 4.160) for a dissipative system using the semiclassical approximation and found that such multiple pulses in the radiation profile can even survive in a dissipative system coupled to a radiation reservoir.

Multiple superradiant peaks have been observed experimentally in an atomic gas system [81] and are reported to originate from the dipole–dipole interaction between a two-level system within the framework of the Dicke model [12]. In our

model, excitons are coupled with one another indirectly through the interactions with localized photons; therefore, the pulse oscillation in the radiation profile occurs in a mechanism similar to that in the Dicke model.

We solved the master equation (Eq. 4.160), considering quantum correlations, and compared the results with those obtained from the Dicke model. When all the populations are initially in excited states, both models produce similar radiation profiles. They differ qualitatively in that the peak value of the radiation pulse in our model is reduced and the tail is extended. This tendency was examined by comparing atomic and Frenkel exciton systems, in which excitons can hop via the dipole–dipole interaction, and the same qualitative difference was reported [84]. Regarding the multiple-pulse generation that we obtained, the Frenkel exciton model also predicts the possibility of the superradiance profile oscillating if the system is initially prepared with a partial population inversion [85]. From our model, we concluded that the superradiant peaks of multiple pulses correspond to the occurrence of a collective dipole oscillation or a dipole-ordered state.

It is still not clear why the dipole distribution in our system has several quasi-steady states, which was predicted in our model using the perturbative expressions, numerical solutions of the Heisenberg equations, and the effective Hamiltonian. Since our system has several kinds of symmetry, we expect to clarify the stability of such quasi-steady states from the viewpoint of symmetry.

The size dependence of the radiation profile has been investigated in the Dicke model [32]. To clarify the differences between optical near fields and propagating fields, we should also examine such size dependence in our model. The semiclassical approach might be useful for such a qualitative study because it has an advantage over the quantum approach with respect to computation time.

One of our main goals was to clarify the inherent characteristics in optical near fields from the viewpoint of the coupling scheme, that is, a local coupling system versus a global coupling system. We have shown several differences between our model (local coupling system) and the Dicke model (global coupling system), but further effort is required to answer the question more directly. In spite of some common properties, we must emphasize that our model differs from the Frenkel exciton model of Tokihiro et al., which is an extended Dicke model that considers the dipole–dipole interaction between excitons. The similarities of the radiation properties in our model and the Tokihiro model arise from the similar master equations used (see (Eqs. 4.135) and (4.160)). However, our master equation (Eq. 4.160) was derived after neglecting the product of excitons with an order higher than two (see (Eq. 4.159)). This approximation is justified for a dilute excitonic system. Nevertheless, the precise conditions under which this approximation is applicable and its consistency should be investigated thoroughly.

Therefore, our localized photon model concurs with the model of Tokihiro et al. only in the simple case, and the true dynamics in our model is more complicated. Unfortunately, there is no straightforward way to derive a more correct equation beyond the approximation (Eq. 4.159). The difficulty comes from how to treat the dynamics of three different degrees of freedom: excitons, localized photons, and radiation photons. Rigorously speaking, the difficulty arises from the fact

that the unperturbed part $H = H_a + H_b + H_{\text{int}}$ (Eq. 4.4) is made up of a mixture of spin operators (excitons) and bosons (localized photons). However, it is possible to consider the next order of excitons in $U_{\text{QDef}}^{\text{eff}}$ in (Eq. 4.157) beyond the approximation (Eq. 4.159). To proceed to higher orders, we need to remove the time integration in (Eq. 4.157) and may use the time-convolution-less (TCL) formulation of the projection operator method [18, 76].

Finally, we focused on the nonlinearity of the Heisenberg equations in our system and investigated the transport phenomena of localized photons, adding a reservoir of localized photons to the system. Neither normal macroscopic transport phenomena nor equilibrium states were found, which indicates that the nonlinearity of this system is very weak, as a fully nonlinear system, such as a chaotic system, shows statistical transport phenomena (e.g., diffusion) [27, 31], and large-scale simulations are required to find the equilibrium states. Instead, as a transient behavior, we found a remarkable phenomenon in which the transfer of localized photons is jammed or through flowing, depending on the system parameters as ϵ , V , E , and U . We called the former case the storage mode of localized photons. Moreover, the number of localized photons stored varies drastically, depending on the localized photon–exciton coupling constant $U = \hbar g$. The dependence of the total number of localized photons on the coupling constant g is chaotic and unpredictable. Reduction of the system to the minimal size did not change this behavior; therefore, the complex behavior arose from the intrinsic nonlinearity of the system, not from the interference of many modes due to many degrees of freedom. Since the unpredictable coupling-constant dependence had both regular windows and chaotic regions (see Fig. 4.43), our system shows “intermittent chaos” in terms of usual dynamic chaos. We found that the chaotic regions have similar distributions, but the meanings of the distributions are not clear. We also checked the dynamics using the next order quantum correlation and observed the storage and through-flowing modes. The semiclassical treatment seems sufficient to produce these phenomena.

In summary, we found an interesting phenomenon arising from the nonlinearity in our system. The nonlinearity of the dynamics originates from the commutation relation of excitons which differs from that of bosons. This is true in the Dicke model. Therefore, the Dicke model has the same nonlinearity, which is essential for superradiance [3], and certain kinds of signatures of chaos. Indeed, it was recently reported that the Dicke model is a quantum chaotic system [26]. The term “quantum chaotic system” means that the distribution of the energy-level spacing of the Hamiltonian differs from that of a regular system [33]. Since there is no instability of orbits in a quantum system, due to the uncertainty principle, we need new signatures of chaos for a quantum system whose classical correspondence is also chaotic. One of the quantum signatures of chaos is the level statistics [34], and the analysis of these level statistics remains an intriguing open problem. Since our system has a richer structure than the Dicke model, we expect our model to produce more fruitful properties as a quantum chaotic system. Finally, we point out that the open system discussed using our localized photon model is one of the simplest nano-optical structures to use to examine the optical response of nanostructures and to discuss the susceptibilities of nanometric material systems.

Acknowledgments The authors are grateful to H. Hori, I. Banno, N. Ohnishi, and C. Uchiyama of Yamanashi University, T. Kawazoe of Japan Science and Technology Agency, and H. Nejo of National Institute for Materials Science for the fruitful discussions. They also gratefully acknowledge valuable suggestion from F. Shibata of Ochanomizu University on the topics in [Sect. 4.5.1](#).

References

1. G.S. Agarwal, Phys. Rev. **178**, 2025 (1969)
2. G.S. Agarwal, Phys. Rev. A **2**, 2038 (1970)
3. G.S. Agarwal, Phys. Rev. A **4**, 1791 (1971)
4. V.M. Agranovich, M.D. Galanin, *Electric Excitation Energy Transfer in Condensed Matter* (North-Holland, Amsterdam, 1982)
5. R. Asby, E. Wolf, J. Opt. Soc. Am. **61**, 52 (1971)
6. J. Bardeen, D. Pines, Phys. Rev. **99**, 1140 (1955)
7. H.A. Bethe, Phys. Rev. **66**, 163 (1944)
8. I. Bialynicki-Birula, J.B. Brojan, Phys. Rev. D **5**, 485 (1972)
9. R. Bonifacio, L.A. Lugiato, Phys. Rev. A **11**, 1507 (1975)
10. R. Bonifacio, L.A. Lugiato, Phys. Rev. A **12**, 587 (1975)
11. R. Bonifacio, P. Schwendimann, F. Haake, Phys. Rev. A **4**, 302 (1971)
12. R. Bonifacio, L.A. Lugiato, A.A. Crescentini, Phys. Rev. A **13**, 1507 (1976)
13. C.J. Bouwkamp, Philips Res. Rep. **5**, 321 (1950)
14. C.J. Bouwkamp, Philips Res. Rep. **5**, 401 (1950)
15. C.J. Bouwkamp, Rep. Prog. Phys. **17**, 35 (1954)
16. T. Brandes, J. Inoue, A. Shimizu, Phys. Rev. Lett. **80**, 3952 (1998)
17. C. Carniglia, L. Mandel, Phys. Rev. D **3**, 280 (1971)
18. S. Chaturvedi, F. Shibata, Z. Phys. B **35**, 297 (1979)
19. Y.N. Chen, D.S. Chuu, T. Brandes, Phys. Rev. Lett. **90**, 166801 (2003)
20. K. Cho, Suppl. Prog. Theor. Phys. **106**, 225 (1991)
21. K. Cho, Y. Ohfuti, K. Arima, Surf. Sci. **363**, 378 (1996)
22. B. Coffey, R. Friedberg, Phys. Rev. A **17**, 1033 (1978)
23. O. Costa de Beauregard, C. Imvert, J. Ricard, Int. J. Theor. Phys. **4**, 125 (1971)
24. R.T. Cox, Phys. Rev. **66**, 106 (1944)
25. R.H. Dicke, Phys. Rev. **93**, 99 (1954)
26. C. Emary, T. Brandes, Phys. Rev. Lett. **90**, 044101 (2003)
27. D.J. Evans, G.P. Morriss, *Statistical Mechanics of Nonequilibrium Liquids* (Academic, New York, 1997)
28. J.P. Fillard, *Near Field Optics and Nanoscopy* (World Scientific, Singapore, 1996)
29. R. Friedberg, S.R. Hartmann, Phys. Rev. A **10**, 1728 (1974)
30. H. Fröhlich, Phys. Rev. **79**, 845 (1950)
31. P. Gaspard, *Chaos, Scattering and Statistical Mechanics* (Cambridge University Press, Cambridge, 1998)
32. M. Gross, S. Haroche, Phys. Rep. **93**, 301 (1982)
33. M.C. Gutzwiller, *Chaos in Classical and Quantum Mechanics* (Springer, Berlin, 1995)
34. F. Haake, *Quantum Signatures of Chaos* (Springer, Berlin, 1991)
35. H. Htoon, T. Takagahara, D. Kulik, O. Baklenov, A.L. Holmes Jr., C.K. Shih, Phys. Rev. Lett. **88**, 087401 (2002)
36. S. Huard, Opt. Commun. **30**, 8 (1979)
37. T. Inoue, H. Hori, Phys. Rev. A **63**, 063805 (2001)
38. H. Ishihara, K. Cho, Phys. Rev. B **48**, 7960 (1993)
39. M. Janowicz, W. Zakowicz, Phys. Rev. A **50**, 4350 (1994)
40. H. Kamada, H. Gotoh, J. Temmyo, T. Takagahara, H. Ando, Phys. Rev. Lett. **87**, 246401 (2001)

41. K. Kaneko, Phys. Rev. Lett. **63**, 219 (1989)
42. T. Kawazoe, K. Kobayashi, J. Lim, Y. Narita, M. Ohtsu, Phys. Rev. Lett. **88**, 067404 (2002)
43. H. Khosravi, R. Loudon, Proc. R. Soc. Lond. A **433**, 337 (1991)
44. C. Kittel, *Quantum Theory of Solids*, 2nd revised printing (Wiley, New York, 1987)
45. J. Knoester, S. Mukamel, Phys. Rev. A **39**, 1899 (1989)
46. K. Kobayashi, M. Ohtsu, J. Microsc. **194**, 249 (1999)
47. K. Kobayashi, S. Sangu, H. Ito, M. Ohtsu, Phys. Rev. A **63**, 013806 (2001)
48. K. Kobayashi, S. Sangu, M. Ohtsu, Quantum theoretical approach to optical near-fields and some related applications, in *Progress in Nano-Electro-Optics I*, ed. by M. Ohtsu. Springer Series in Optical Sciences (Springer, Berlin, 2002) pp. 119–157
49. K. Kobayashi, S. Sangu, A. Shojiguchi, T. Kawazoe, K. Kitahara, M. Ohtsu, J. Microsc. **210**, 247 (2003)
50. R. Kubo, M. Toda, N. Hashitsume, *Statistical Physics II* (Springer, Berlin, 1985)
51. E. Lalor, E. Wolf, Phys. Rev. Lett. **26**, 1274 (1971)
52. R.H. Lehmburg, Phys. Rev. A **2**, 883 (1970)
53. H. Levine, J. Schwinger, Phys. Rev. **74**, 958 (1948)
54. E. Lieb, T. Schultz, D. Mattis, Ann. Phys. **16**, 407 (1961)
55. G. Lindblad, Commun. Math. Phys. **48**, 119 (1976)
56. J.G. Linhart, J. Appl. Phys. **26**, 527 (1955)
57. L. Mandel, E. Wolf, *Optical Coherence and Quantum Optics* (Cambridge University Press, Cambridge, 1995)
58. S. Nakajima, Prog. Theor. Phys. **20**, 948 (1958)
59. A. Nakamura, H. Yamada, T. Tokizaki, Phys. Rev. B **40**, 8585 (1989)
60. L.M. Narducci, C.A. Coulter, C.M. Bowden, Phys. Rev. A **9**, 829 (1974)
61. Y. Ohdaira, K. Kijima, K. Terasawa, M. Kawai, H. Hori, K. Kitahara, J. Microsc. **202**, 255 (2001)
62. M. Ohtsu (ed.), *Near-Field Nano/Atom Optics and Technology* (Springer, Tokyo, 1998)
63. M. Ohtsu (ed.), *Progress in Nano Electro-Optics I* (Springer, Berlin, 2002)
64. M. Ohtsu (ed.), *Progress in Nano Electro-Optics II* (Springer, Berlin, 2003)
65. M. Ohtsu, H. Hori, *Near-Field Nano-Optics* (Kluwer/Plenum publishers, New York, 1999)
66. M. Ohtsu, K. Kobayashi, *Optical Near Fields* (Springer, Heidelberg, 2003)
67. M. Ohtsu, K. Kobayashi, T. Kawazoe, S. Sangu, T. Yatsui, IEEE J. Sel. Top. Quantum Electron. **8**, 839 (2002)
68. M.A. Paesler, P.J. Moyer, *Near-Field Optics: Theory, Instrumentation, and Application* (Wiley, New York, 1996)
69. N. Piovela, V. Beretta, G.R.M. Robb, R. Bonifacio, Phys. Rev. A **68**, 021801 (2003)
70. D.W. Pohl, D. Courjon, *Near Field Optics* (Kluwer, Dordrecht, 1993)
71. H.A. Posch, W.G. Hoover, F.J. Vesely, Phys. Rev. A **33**, 4253 (1986)
72. L. Quiroga, N.F. Johnson, Phys. Rev. Lett. **83**, 2270 (1999)
73. N. Rehler, J.H. Eberly, Phys. Rev. A **3**, 1735 (1971)
74. S. Sangu, K. Kobayashi, A. Shojiguchi, T. Kawazoe, M. Ohtsu, J. Appl. Phys. **93**, 2937 (2003)
75. T. Saso, Y. Suzumura, H. Fukuyama, Suppl. Prog. Theor. Phys. **84**, 269 (1985)
76. F. Shibata, T. Arimitsu, J. Phys. Soc. Jpn. **49**, 891 (1980)
77. K. Shimoda, *Introduction to Laser Physics* (Springer, Berlin/Heidelberg, 1986)
78. A. Shojiguchi, K. Kobayashi, S. Sangu, K. Kitahara, M. Ohtsu, Nonlinear Opt. **29**, 563 (2002)
79. A. Shojiguchi, K. Kitahara, K. Kobayashi, M. Ohtsu, J. Microsc. **210**, 301 (2003)
80. A. Shojiguchi, K. Kobayashi, S. Sangu, K. Kitahara, M. Ohtsu, J. Phys. Soc. Jpn. **72**, 2984 (2003)
81. N. Skribanowitz, I.P. Herman, J.C. MacGillivray, M.S. Feld, Phys. Rev. Lett. **30**, 309 (1973)
82. T.H. Stievater, Xiaoqin Li, D.G. Steel, D. Gammon, D.S. Katzer, D. Park, C. Piermarocchi, L.J. Sham, Phys. Rev. Lett. **87**, 133603 (2001)
83. E.A. Sygne, Philos. Mag. **6**, 356 (1928)
84. T. Tokihiro, Y. Manabe, E. Hanamura, Phys. Rev. B **47**, 2019 (1993)
85. T. Tokihiro, Y. Manabe, E. Hanamura, Phys. Rev. B **51**, 7655 (1995)

-
86. J.M. Vigoureux, Emission and absorption of light by electrons or atoms in optical near fields, in *Near Field Optics*, ed. by D.W. Pohl, D. Courjon. NATO ASI Series, vol. 242 (Kluwer, Dordrecht, 1993), pp. 239–246
 87. J.M. Vigoureux, R. Payen, *J. Phys.* **35**, 617 (1974)
 88. J.M. Vigoureux, R. Payen, *J. Phys.* **36**, 631 (1975)
 89. J.M. Vigoureux, R. Payen, *J. Phys.* **36**, 1327 (1975)
 90. J.M. Vigoureux, L. D’Hooge, D. Van Labeke, *Phys. Rev. A* **21**, 347 (1980)
 91. R. Zwanzig, *J. Chem. Phys.* **33**, 1338 (1960)
 92. R. Zwanzig, *Phys. Rev.* **124**, 983 (1961)

Suguru Sangu, Kiyoshi Kobayashi, Akira Shojiguchi,
Tadashi Kawazoe, and Motoichi Ohtsu

Contents

5.1	Introduction.....	188
5.1.1	Nanophotonics for Functional Devices.....	188
5.1.2	Inherent Features to Nanophotonics.....	190
5.2	Optical Near-Field Coupling.....	194
5.2.1	Theoretical Descriptions of an Optical Near Field.....	194
5.2.2	Excitation and Transition in a Quantum-Dot.....	195
5.2.3	Optical Near-Field Coupling Between Quantum-Dot.....	199
5.2.4	Summary.....	202
5.3	Nanophotonic Switch Based on Dissipation Control.....	203
5.3.1	Dynamics in a Two-Quantum-Dot System with Dissipation.....	205
5.3.2	Nanophotonic Switch.....	213
5.3.3	Summary.....	216
5.4	Nanophotonic Functional Devices Using Coherently Coupled States.....	218

S. Sangu (✉)

Device Technology Development Center, Ricoh Co., Ltd, Miyagi, Japan
e-mail: suguru.sangu@nts.ricoh.co.jp

K. Kobayashi

Interdisciplinary Graduate School of Medicine and Engineering, University of Yamanashi, Kofu,
Yamanashi, Japan
e-mail: kkoba@yamanashi.ac.jp

A. Shojiguchi

Green Platform Research Laboratories, NEC Corp., Kawasaki, Kanagawa, Japan
e-mail: a-shojiguchi@ap.jp.nec.com

T. Kawazoe

School of Engineering, The University of Tokyo, Tokyo, Japan
e-mail: kawazoe@ee.t.u-tokyo.ac.jp

M. Ohtsu

School of Engineering, The University of Tokyo, Tokyo, Japan
Nanophotonics Research Center, The University of Tokyo, Tokyo, Japan
e-mail: ohtsu@ee.t.u-tokyo.ac.jp

5.4.1	Dynamics in a Coherently Coupled Quantum-Dot System.....	220
5.4.2	Nanophotonic Logic Gates.....	227
5.4.3	Nanophotonic Controlled Logic Gates.....	236
5.4.4	Nanophotonic Buffer Memory.....	240
5.4.5	Nanophotonic Signal Splitter for Quantum Entanglement.....	243
5.4.6	Summary.....	245
5.5	Conclusions.....	246
	References.....	248

Abstract

In a nanometric light-matter coupling system, characteristic features, such as local excitation, unidirectional energy transfer, and state-filling effect, can be used for signal transfer and control. In this chapter, optical near-field coupling is formulated in detail by using the second quantization, and then, switching, logic, and some typical operations are discussed theoretically and numerically as examples of nanophotonic functional devices the above features used. Especially, coherence and/or decoherence of matter excitation and spatial symmetry of a system play important roles in such device operations.

5.1 Introduction

5.1.1 Nanophotonics for Functional Devices

In recent years, explosive growth in data traffic becomes serious problem, which is caused by expanding of internet usage and spreading mobile terminals, such as smartphones and tablet computers [1]. Optical integrated circuits based on nanophotonics technologies are placed more expectations on large amount of data processing and switching, as well as green information technology (IT) with low energy consumption [2].

For nanophotonics technologies, the light localized in a nanometric space less than the diffraction limit of light plays important roles as signal carriers and agents to control the signal for unique device operations which never occur in conventional optics by using far-field light [3, 4]. The localized light, or optical near field, can make characteristic excited states, which are inactive for far-field light, with the help of electronic and/or phonon excitations. Such technologies using light-matter coupled excitation are referred to as the *dressed photon technologies* [5]. In this research field, some interesting progresses have been published: the NOT-gate operation [6] and excitation up-conversion [7] with phonon degrees of freedom in a quantum-dot system. System architectures appropriate to the nanophotonic energy transfer have been also proposed in the applications of data processing [8] and of certification technologies [9]. Furthermore, nanophotonics technologies have been extended to the outside field of information processing, that are nanoscale surface reforming with self-convergent chemical reactions such as etching and deposition

processes [10–12], and realization of light-emitting and detection devices using optical near-field assisted modification of material properties [13].

Fundamental physics supporting the above technological progresses would be explained theoretically in ►Chaps. 1 and ►4. This chapter is devoted to concentrate on signal propagation, control, and some functional operations in a nanophotonic device which is driven by optical near field, and to formulate the operations by means of quantum mechanical approach. The signal manipulation is considered in a simplified system consists of few energy-level systems like quantum dots. In such a system, detailed theory of light-matter interaction is necessary to describe the device operations. Especially, treating internal degree of freedom of each quantum system enables us to realized energy transfer via a dark state which is inactive for far-field light. The localization feature of signal carriers in nanophotonic devices seems to resemble electronic devices in which an electric charge always stays within the device. However, it is strikingly different in that the energy transfer occurs via excitation state, not electric charge. For mediating electric charge, unidirectional energy transfer is guaranteed by applying bias voltage, which necessarily involves thermal energy loss. While in the nanophotonic energy transfer, unidirectionality is determined in principle by only energy dissipation from high to low energy levels in intra-quantum system, which results in drastic low-energy device operations. There is a similar low-energy consumptive system of quantum-dot or molecular cellular automata [14]. Characteristic process inherent in a nanophotonic system is that the localized field is able to leave an object and release free photons in the far field via optical near-field interaction among several nanometric objects [15]. Important things for designing nanophotonic devices and nanophotonic device operations are to deal with light-matter interaction with a nanometric system and dissipation of matter excitation toward the outer field, simultaneously. Since the signal is eventually detected as far-field light, nanometric light-matter interaction also needs to control the dissipation process.

The advantages of nanophotonic devices are not only miniaturization but also possibilities for novel principles of functional operations that are inherent to nanophotonics. As I mentioned above, the physics of nanophotonic devices includes typical matter excited states due to optical near-field interaction, coupling between near- and far-field light, and coupling between matter excitation and phonons. Many of these characteristics have not been considered in conventional optics, and thus, system construction method for nanophotonic devices may differ from that for conventional devices. It is important to consider how these devices should be designed and how nanophotonic devices can coexist with other devices, such as conventional optical and electronic devices.

In the remainder of this section, our discussion focuses on how to use the features inherent to nanophotonics in functional device operations, what is possible, and how we can realize the possibilities. The next subsection will explain some characteristic features of nanophotonics, briefly, that becomes introductory concept for realizing the nanophotonic functional devices.

5.1.2 Inherent Features to Nanophotonics

In general, the following features are indispensable to a functional device: preparation of appropriate input states, propagation of a signal, and control of the signal. Nanophotonics has characteristic features for all of these, that are not observed for far-field light: a locally excited state that cannot be created using far-field light, unidirectional energy transfer, and a dependence on excitation number in which coupling between discrete energy levels and the optical near field plays an important role. These are all key features for nanophotonic device operations.

5.1.2.1 Locally Excited States

First, we will explain the difference between matter excitation of nanometric objects using far- and near-field light. [Figure 5.1a](#) illustrates nanometric objects being irradiated by far-field light. Since objects located in an area much smaller than the wavelength of the light are simultaneously excited by a uniform field, it is not possible to know the state of matter excitation in each object independently, and the detected far-field light has no information about the state of the excitation in each object. Optical near-field excitation can be accomplished by setting an optical near-field probe, such as a nanometric metallic aperture, an optical fiber probe, and a single molecule. This allows selective irradiation of individual object, and a locally excited state can be created because of the localized light around the probe. The excited object creates a secondary electromagnetic field that affects the state of the neighboring object via the optical near field, and consistently determines excited states in the two-object coupling system using optical near-field interaction. [Figure 5.1b](#) shows a schematic illustration of optical near-field excitation. This asymmetric excitation influences far-field light which will be detected as an information signal.

The following describes these excited states as algebraic expressions. For simplicity, the discussion is restricted to the coupling of two two-level systems of excitons (see [Fig. 5.2](#)). For far-field excitation, nanometric objects are uniformly

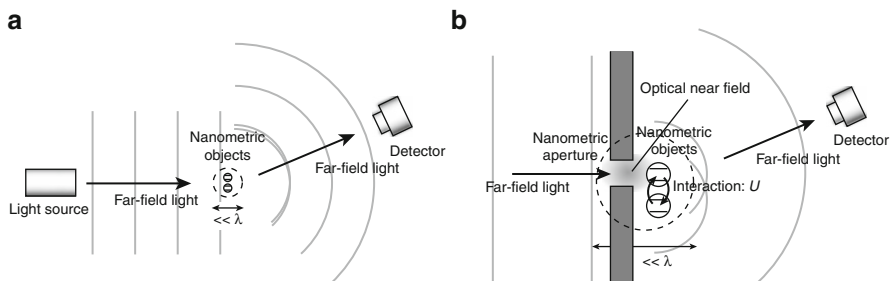


Fig. 5.1 Schematic illustration of nanometric matter excitation by using (a) far-field light and (b) near-field light

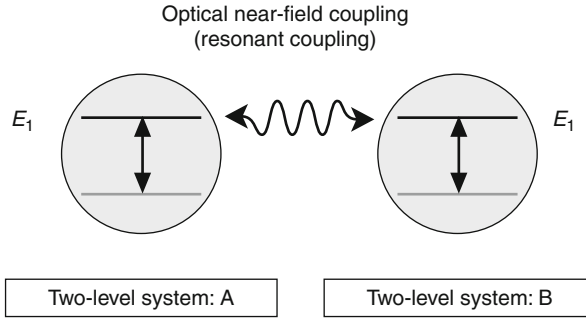


Fig. 5.2 Identical two two-level systems which are coupled via optical near-field interaction

excited; a one-exciton state, in which an exciton exists in the system, can thus be written as

$$|1\rangle_s = (|e\rangle_A|g\rangle_B + |g\rangle_A|e\rangle_B)/\sqrt{2}, \quad (5.1)$$

where $|e\rangle_i$ and $|g\rangle_i$ represent exciton state and crystal ground state, respectively. Subscripts $i = A$ and B label two nanometric objects, and the meaning of subscript s will be explained below. Equation (5.1) means that an exciton in an isolated system cannot be distinguished because the exciton exists in both object A and object B with equivalent probabilities.

On the other hand, as mentioned above, an optical near field allows an exciton to be created in an individual object. The exciton prepared in this system leaves and returns between two two-level systems for a period depending on the strength of optical near-field coupling, referred to as near-field optical nutation [16, 17]. However, if the pumping time is much shorter than the period of near-field optical nutation, locally excited states can be created in this system. Such locally excited states with an exciton in the system can be expressed by a linear combination of coupled states that extends between two objects, as follows:

$$|e\rangle_A|g\rangle_B = (|1\rangle_s + |1\rangle_a)/\sqrt{2}, \quad (5.2)$$

$$|g\rangle_A|e\rangle_B = (|1\rangle_s - |1\rangle_a)/\sqrt{2}. \quad (5.3)$$

The right-hand terms in (5.2) and (5.3) described states coupled via an optical near field, where the subscripts s and a refer to symmetric and antisymmetric states, respectively. It is clear that in the optical near-field excitation, there are two coupled states, while far-field light excites only the symmetric state. Note that we did not show the antisymmetric state in (5.1), since the state is optically inactive for far-field light. This can be verified using the following relation: ${}_a\langle 1|H_{\text{int}}|g\rangle = 0$, where $|g\rangle = |g\rangle_A|g\rangle_B$ and the interaction Hamiltonian refers to (5.7). Locally excited states are quite important for functional operations in our proposed nanophotonic devices, which are discussed in Sects. 5.3 and 5.4.

5.1.2.2 Unidirectional Energy Transfer

For functional device operations to manipulate information carriers, an excitation or carrier must transfer unidirectionally from the input to the output terminals. In conventional optical devices, a unidirectional energy transfer can be accomplished by using an optical isolator, which generally uses polarization to block reflected light. The size of such devices is obviously restricted by light wavelength. In electronic devices, a unidirectional signal transfer is easily attained since electrons flow along an electrical potential. However, as electronic devices become smaller, quantum mechanical effects arise, and electrical signals are affected by noise because of quantum fluctuations. In a nanophotonic device, signal isolation using light wave characteristics is impossible because of the light diffraction limit. Moreover, a signal carrier is composed of electrically neutral quasiparticles of electrons and holes, and thus, a static electrical potential cannot be used to drive them. However, unidirectional exciton energy transfer can be effectively realized using a relaxation process among quantum discrete energy levels [18]. Figure 5.3 is a schematic image of energy transfer via an optical near field in a system that consists of two nanometric objects with two- and three-energy levels. As I mentioned in the previous subsection, optical near-field interaction causes a coherently coupled excited state between the E_1 -level in the two-level system and the E_2 -level in the three-level system, which strengthens when both energies are equal. If excitation can be dropped into the lower E_1 -level in the three-level system before the radiative lifetime of E_1 -level in the two-level system (~ 1 ns), excitation is confined to the energy level due to off-resonance, and irreversibility in the nanometric system is guaranteed except for radiation from the energy level. Section 5.2 provides a detailed discussion about optical near-field coupling and energy transfer dynamics. In the three-level system, the E_2 -level is generally dipole inactive for far-field light, and thus, unidirectional energy transfer can be achieved by mediating the optical near field.

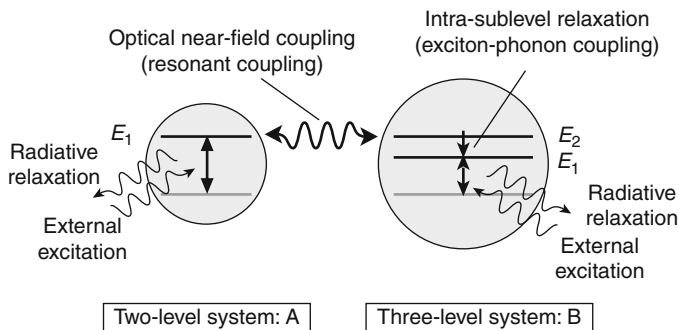


Fig. 5.3 Energy transfer between two-level and three-level systems. E_2 -level in the three-level system is dipole inactive, and thus, the unidirectional energy transfer is achieved only by mediating an optical near field

Since external far- or near-field light can cause excitations in dipole-active levels: the E_1 -level in the two-level system, and the E_2 -level in the three-level system energy transfer in this system is controllable. A simple switching operation can be constructed using the state-filling nature of excitons excited by the external field. In Sect. 5.3, a nanophotonic switch is proposed that uses energy transfer and state-filling, and the dynamics of excitation are evaluated both analytically and numerically.

5.1.2.3 Dependence of Excitation Number

Although symmetric and antisymmetric states in (5.1) and (5.2) describe one-exciton states, a quite interesting feature is evident in the two-exciton state in the system shown in Fig. 5.2. The two-exciton state, in which two excitons completely occupy both two-level systems, is algebraically written as

$$|2\rangle_p = |e\rangle_A |e\rangle_B, \quad (5.4)$$

where number 2 in the left-hand term refers to the two-exciton state. It is valuable to investigate energies for all base states, $|1\rangle_s$, $|1\rangle_a$, and $|2\rangle_p$. The Hamiltonian for the two-level systems coupled via an optical near-field interaction is given by

$$\hat{H} = \hat{H}_0 + \hat{H}_{\text{int}}, \quad (5.5)$$

$$\hat{H}_0 = \hbar\Omega \hat{A}^\dagger \hat{A} + \hbar\Omega \hat{B}^\dagger \hat{B}, \quad (5.6)$$

$$\hat{H}_{\text{int}} = \hbar U (\hat{A}^\dagger \hat{B} + \hat{A} \hat{B}^\dagger), \quad (5.7)$$

where \hat{H}_0 and \hat{H}_{int} represent the unperturbed and interaction Hamiltonian, respectively. (\hat{A}^\dagger , \hat{A}) and (\hat{B}^\dagger , \hat{B}) are the fermionic creation and annihilation operators in the two-level systems A and B, respectively. Since the excitations are assumed to be fermionic excitons and the optical near-field coupling U is considered a completely coherent process, this is explained in detail in Sect. 5.2. Energies for states are given as follows:

$${}_s\langle 1 | \hat{H} | 1 \rangle_s = \hbar(\Omega + U), \quad (5.8)$$

$${}_a\langle 1 | \hat{H} | 1 \rangle_a = \hbar(\Omega - U), \quad (5.9)$$

$${}_p\langle 2 | \hat{H} | 2 \rangle_p = 2\hbar\Omega. \quad (5.10)$$

Equations (5.8) and (5.9) indicate that the energies of the coupled states, $|1\rangle_s$ and $|1\rangle_a$, depend on the strength of optical near-field coupling, U , and differences in the energy from the two-level system have opposite contributions in each state. In the two-exciton states in (5.10), energy apparently degenerates because both systems are completely filled. These properties are useful for selective energy transfer in nanophotonic devices; sequential logic operations can be realized by using the excitation number dependence in this system.

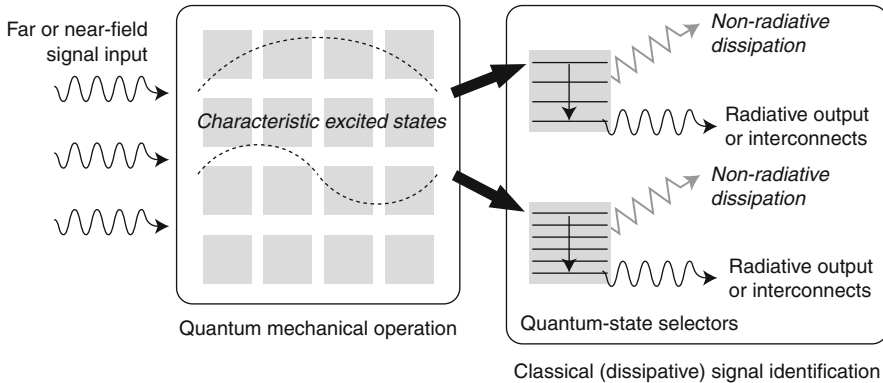


Fig. 5.4 Conceptual structure of nanophotonic devices, which consists of a quantum mechanical part and a classical dissipative part. Quantum mechanical part builds up characteristic excited states, and classical dissipative part identifies certain states and connects to outer detection systems

Figure 5.4 schematically illustrates how the above selectivity represents a concept that is fundamental to nanophotonic devices. In the device, quantum mechanical and classical parts coexist; some characteristic excited states are created in the quantum mechanical part, and in order to connect a signal to an outer detection system, these states must then be selectively extracted from quantum mechanical part to classical dissipative one. This process is key to driving the nanophotonic device. Functional operations based on such conceptual structures are discussed in Sect. 5.4.

5.2 Optical Near-Field Coupling

In this section, we give a full account of energy transfer between locally excited states via an optical near field. From our theoretical treatment of optical near-field coupling, the readers will understand why dipole-inactive energy transfer for far-field light changes allowed transition in the case of the optical near field. Concrete numerical results of coupling strength in a CuCl quantum-dot system are also provided, where the coupling strength determines operation speed of nanophotonic devices discussed in the following Sects. 5.3 and 5.4.

5.2.1 Theoretical Descriptions of an Optical Near Field

There are two ways to describe light-matter interaction theoretically: one is to use the minimal coupling Hamiltonian $\mathbf{p} \cdot \mathbf{A}$ [19], \mathbf{p} being the electronic momentum and \mathbf{A} the vector potential, and the other is to use the multipolar QED Hamiltonian [20, 21] in the dipole approximation, $\boldsymbol{\mu} \cdot \mathbf{D}$, where $\boldsymbol{\mu}$ and \mathbf{D} represent the electric dipole moment and electric displacement field, respectively. The two descriptions of light-matter interaction are connected by Power–Zienau–Woolley

transformation [22], which is a unitary transformation of the Coulomb-gauge Hamiltonian. Here, the multipolar QED Hamiltonian is used because there are several advantages in the multipolar QED: first of all, it does not contain any explicit intermolecular or inter-quantum-dot Coulomb interactions in the interaction Hamiltonian, and entire contribution to the fully retarded result is from exchange of transverse photons, while in the minimal coupling, the intermolecular interactions arise both from exchange of transverse photons, which include static components, and from instantaneous intermolecular electrostatic interactions [23]. Second, it clarifies physical interpretation of the dipole-inactive transition via the optical near field as we will discuss below.

Since our purpose of discussions is to propose and investigate nanophotonic solid devices, in the following, nanometric objects are assumed as quantum dots with discrete energy levels. In order to explain an extremely important feature in nanophotonics, internal electronic structures in a quantum dot are regarded as collection of local dipoles, which is convenient to express the interactions between nanometric objects and an optical near field spatially distributed in nanometric space. We can also depict a dipole in one-body problem by using an effective mass approximation. Such theoretical approach has been already published [24] where the enhancement of electric quadrupole coupling was pointed out by assuming steep variation of electric field due to the optical near field. This phenomenon is equivalent to our result of the dipole-inactive transition, but our theoretical formulation, in which field variation is caused by the coupling between the local dipoles in the neighboring quantum-dot pair, is easy to obtain a physical interpretation.

In the following subsections, interaction Hamiltonian is provided in the second-quantized form in terms of electron basis functions satisfying the quantum-dot boundary conditions, as well as transition dipole moments of excitons, and then, optical near-field coupling is derived on the basis of the projection operator method which is explained in Sect. 5.2.3.

5.2.2 Excitation and Transition in a Quantum-Dot

5.2.2.1 Interaction Hamiltonian

According to the dipole coupling in the multipolar QED Hamiltonian, the interaction between photons and nanometric materials can be written as [21]

$$\hat{H}_{\text{int}} = - \int \psi^\dagger(\mathbf{r}) \boldsymbol{\mu}(\mathbf{r}) \psi(\mathbf{r}) \cdot \hat{\mathbf{D}}(\mathbf{r}) d\mathbf{r} , \quad (5.11)$$

where $\psi^\dagger(\mathbf{r})$ and $\psi(\mathbf{r})$ denote field operators for electron creation and annihilation, respectively, and the dipole moment and the second-quantized electric displacement vector at position \mathbf{r} are expressed as $\boldsymbol{\mu}(\mathbf{r})$ and $\hat{\mathbf{D}}(\mathbf{r})$, respectively. In a quantum dot, the electron field operators should be expanded in terms of basis functions $\phi_{\nu n}(\mathbf{r})$ that satisfy the electron boundary conditions in a quantum dot that is analogy to those in bulk materials where the Bloch functions satisfying periodic boundary condition are used. The field operators are given by

$$\psi(\mathbf{r}) = \sum_{\nu=c,v} \sum_{\mathbf{n}} \hat{c}_{\nu\mathbf{n}} \phi_{\nu\mathbf{n}}(\mathbf{r}), \quad (5.12)$$

$$\psi^\dagger(\mathbf{r}) = \sum_{\nu=c,v} \sum_{\mathbf{n}} \hat{c}_{\nu\mathbf{n}}^\dagger \phi_{\nu\mathbf{n}}^*(\mathbf{r}), \quad (5.13)$$

where $\hat{c}_{\nu\mathbf{n}}^\dagger$ and $\hat{c}_{\nu\mathbf{n}}$ represent the creation and annihilation operators for the electrons specified by (ν, \mathbf{n}) , respectively, and the indices $\nu = c, v$ denote the conduction and valence bands. The discrete energy levels in the quantum dot are labeled \mathbf{n} . The basis functions satisfy the following completeness condition, as well as orthonormalization:

$$\sum_{\nu=c,v} \sum_{\mathbf{n}} \phi_{\nu\mathbf{n}}^*(\mathbf{r}) \phi_{\nu\mathbf{n}}(\mathbf{r}') = \delta(\mathbf{r} - \mathbf{r}'). \quad (5.14)$$

Simultaneously, we express the electric displacement vector $\hat{\mathbf{D}}(\mathbf{r})$ using exciton–polariton creation and annihilation operators $(\hat{\xi}_{\mathbf{k}}^\dagger, \hat{\xi}_{\mathbf{k}})$, where branch suffix of the exciton–polariton is suppressed by taking only an upper branch. We consider exciton–polaritons because a nanometric system in a near-field optical environment is always surrounded by macroscopic materials, such as the substrate, matrix, and fiber probe. Previously [25, 26], we proposed an effective interaction for such a nanometric system mediated by exciton–polaritons that exist in mixed states between photons and macroscopic material excitations instead of free photons. We showed that such a treatment provides a good description of the characteristics of an optical near field [27]. Using this, the electric displacement vector $\hat{\mathbf{D}}(\mathbf{r})$ in (5.11) can be written as [28]

$$\hat{\mathbf{D}}(\mathbf{r}) = i\sqrt{\frac{2\pi}{V}} \sum_{\mathbf{k}} \sum_{\lambda=1}^2 \mathbf{e}_\lambda(\mathbf{k}) f(k) (\hat{\xi}_{\mathbf{k}} e^{i\mathbf{k}\cdot\mathbf{r}} - \hat{\xi}_{\mathbf{k}}^\dagger e^{-i\mathbf{k}\cdot\mathbf{r}}) \quad (5.15)$$

with

$$f(k) = \frac{\hbar ck}{\sqrt{E(k)}} \sqrt{\frac{E^2(k) - E_m^2}{2E^2(k) - E_m^2 - \hbar^2 c^2 k^2}}, \quad (5.16)$$

where \hbar , V , $\mathbf{e}_\lambda(\mathbf{k})$, and \mathbf{k} are the Dirac constant, the quantization volume, the unit polarization vector, and the wavevector of the exciton–polaritons, respectively. Here we assume $\mathbf{e}_\lambda(\mathbf{k})$ as real. The speed of light in a vacuum is c , and the exciton–polariton energy with a wavevector \mathbf{k} and the macroscopic material excitation energy are $E(\mathbf{k})$ and E_m , respectively. Substituting (5.12) and (5.15) into (5.11) gives the interaction Hamiltonian in the second-quantized representation as

$$\hat{H}_{\text{int}} = \sum_{\nu n \nu' n' \mathbf{k} \lambda} \left(\hat{c}_{\nu n}^\dagger \hat{c}_{\nu' n'} \hat{\xi}_{\mathbf{k}} g_{\nu n \nu' n' \mathbf{k} \lambda} - \hat{c}_{\nu n} \hat{c}_{\nu' n'}^\dagger \hat{\xi}_{\mathbf{k}}^\dagger g_{\nu n \nu' n' -\mathbf{k} \lambda} \right) \quad (5.17)$$

with

$$g_{\nu n \nu' n' k \lambda} = -i \sqrt{\frac{2\pi}{V}} f(k) \int \phi_{\nu n}^*(\mathbf{r}) (\boldsymbol{\mu}(\mathbf{r}) \cdot \mathbf{e}_\lambda(\mathbf{k})) e^{i\mathbf{k} \cdot \mathbf{r}} \phi_{\nu' n'}(\mathbf{r}) d\mathbf{r} . \quad (5.18)$$

5.2.2.2 Transition Matrix Element for Exciton States

In order to describe the creation and annihilation of excitons in a quantum dot, it is convenient to use the Wannier representation in which electrons are localized in an atomic site \mathbf{R} . Then, the electron field operators can be expanded using the Wannier functions $w_{\nu \mathbf{R}}(\mathbf{r})$ instead of $\phi_{\nu n}(\mathbf{r})$,

$$\psi(\mathbf{r}) = \sum_{\nu=c,v} \sum_{\mathbf{R}} \hat{c}_{\nu \mathbf{R}} w_{\nu \mathbf{R}}(\mathbf{r}) , \quad \psi^\dagger(\mathbf{r}) = \sum_{\nu=c,v} \sum_{\mathbf{R}} \hat{c}_{\nu \mathbf{R}}^\dagger w_{\nu \mathbf{R}}^*(\mathbf{r}) , \quad (5.19)$$

where $c_{\nu \mathbf{R}}^\dagger$ and $c_{\nu \mathbf{R}}$ denote the creation and annihilation operators of electrons at site \mathbf{R} in the energy band ν . These operators in the Wannier representation are written in terms of $\hat{c}_{\nu n}$ and $\hat{c}_{\nu n}^\dagger$ in (5.12) as follows:

$$\hat{c}_{\nu \mathbf{R}} = \sum_{\nu'=c,v} \sum_n \hat{c}_{\nu' n} \int w_{\nu \mathbf{R}}^*(\mathbf{r}) \phi_{\nu' n}(\mathbf{r}) d\mathbf{r} , \quad (5.20)$$

$$\hat{c}_{\nu \mathbf{R}}^\dagger = \sum_{\nu'=c,v} \sum_n \hat{c}_{\nu' n}^\dagger \int w_{\nu \mathbf{R}}(\mathbf{r}) \phi_{\nu' n}^*(\mathbf{r}) d\mathbf{r} . \quad (5.21)$$

When we assume excitons in the weak-confinement regime, that is, an exciton Bohr radius to be smaller than the quantum-dot size, the exciton states in a quantum dot specified by the quantum number m and μ can be described by superposition of the excitons in the Wannier representation as [29]

$$\begin{aligned} |\Phi_{m\mu}\rangle &= \sum_{\mathbf{R}, \mathbf{R}'} F_m(\mathbf{R}_{\text{CM}}) \varphi_\mu(\boldsymbol{\beta}) \hat{c}_{c\mathbf{R}}^\dagger \hat{c}_{v\mathbf{R}} |\Phi_g\rangle \\ &= \sum_{\mathbf{R}, \mathbf{R}'} F_m(\mathbf{R}_{\text{CM}}) \varphi_\mu(\boldsymbol{\beta}) \sum_{n, n'} h_{\mathbf{R}n\mathbf{R}'n'} \hat{c}_{cn}^\dagger \hat{c}_{vn'} |\Phi_g\rangle , \end{aligned} \quad (5.22)$$

where $F_m(\mathbf{R}_{\text{CM}})$ and $\varphi_\mu(\boldsymbol{\beta})$ denote the envelope functions for the center of mass and relative motions of the excitons, respectively. These are $\mathbf{R}_{\text{CM}} = (m_e \mathbf{R}' + m_h \mathbf{R}) / (m_e + m_h)$ and $\boldsymbol{\beta} = \mathbf{R}' - \mathbf{R}$, where m_e and m_h are the effective masses of the electrons and holes. The overlap integrals $h_{\mathbf{R}n\mathbf{R}'n'}$ are defined as

$$h_{\mathbf{R}n\mathbf{R}'n'} = \iint w_{\nu \mathbf{R}}^*(\mathbf{r}_2) w_{c\mathbf{R}'}(\mathbf{r}_1) \phi_{cn}^*(\mathbf{r}_1) \phi_{vn'}(\mathbf{r}_2) d\mathbf{r}_1 d\mathbf{r}_2 . \quad (5.23)$$

The sum of ν' in (5.20) is determined automatically as $\hat{c}_{c\nu}^\dagger$ and $\hat{c}_{\nu n'}$ because the valence band is fully occupied in the initial ground state $|\Phi_g\rangle$. Using (5.17) and (5.22), the transition matrix element from the exciton state to the ground state is obtained as

$$\begin{aligned} \langle \Phi_g | \hat{H}_{\text{int}} | \Phi_{m\mu} \rangle &= \sum_{n_1, n_2} \sum_{\mathbf{R}, \mathbf{R}'} F_m(\mathbf{R}_{\text{CM}}) \varphi_\mu(\boldsymbol{\beta}) \\ &\times \sum_k \sum_{\lambda=1}^2 \left(\hat{\xi}_k g_{\nu n_1 c n_2 k \lambda} - \hat{\xi}_k^\dagger g_{\nu n_1 c n_2 -k \lambda} \right) h_{\mathbf{R} n_2 \mathbf{R}' n_1}, \end{aligned} \quad (5.24)$$

where we use the following relation:

$$\langle \Phi_g | \hat{c}_{\nu n_1}^\dagger \hat{c}_{c n_2} \hat{c}_{c n_3}^\dagger \hat{c}_{\nu n_4} | \Phi_g \rangle = \delta_{n_1, n_4} \delta_{n_2, n_3}. \quad (5.25)$$

In addition, with the help of the completeness and orthonormalization of $\phi_{\nu n}(\mathbf{r})$ [see (5.14)], we can simplify the product of g and h as

$$\begin{aligned} \sum_{n_1, n_2} g_{\nu n_1 c n_2 k \lambda} h_{\mathbf{R} n_2 \mathbf{R}' n_1} &= -i \sqrt{\frac{2\pi}{V}} f(k) \int w_{\nu \mathbf{R}}^*(\mathbf{r}) \boldsymbol{\mu}(\mathbf{r}) w_{c \mathbf{R}'}(\mathbf{r}) \cdot \mathbf{e}_\lambda(\mathbf{k}) e^{i\mathbf{k} \cdot \mathbf{r}} d\mathbf{r} \\ &\approx -i \sqrt{\frac{2\pi}{V}} f(k) (\boldsymbol{\mu}_{c\nu} \cdot \mathbf{e}_\lambda(\mathbf{k})) e^{i\mathbf{k} \cdot \mathbf{R}} \delta_{\mathbf{R}, \mathbf{R}'}, \end{aligned} \quad (5.26)$$

where the transformation of the spatial integral in the first line of (5.26) into the sum of the unit cells and the spatial localization of the Wannier functions provides $\delta_{\mathbf{R}, \mathbf{R}'}$ in the second line. The transition dipole moment for each unit cell is defined as

$$\boldsymbol{\mu}_{c\nu} = \int_{\text{UC}} w_{\nu \mathbf{R}}^*(\mathbf{r}) \boldsymbol{\mu}(\mathbf{r}) w_{c \mathbf{R}}(\mathbf{r}) d\mathbf{r}. \quad (5.27)$$

We assume that the transition dipole moment is the same as that of the bulk material, independent of the site \mathbf{R} , and that the electric displacement vector is uniform at each site. Finally, (5.24) is reduced to

$$\begin{aligned} \langle \Phi_g | \hat{H}_{\text{int}} | \Phi_{m\mu} \rangle &= -i \sqrt{\frac{2\pi}{V}} \sum_{\mathbf{R}} \sum_k \sum_{\lambda=1}^2 f(k) (\boldsymbol{\mu}_{c\nu} \cdot \mathbf{e}_\lambda(\mathbf{k})) F_m(\mathbf{R}) \varphi_\mu(0) \\ &\times (\hat{\xi}_k e^{i\mathbf{k} \cdot \mathbf{R}} - \hat{\xi}_k^\dagger e^{-i\mathbf{k} \cdot \mathbf{R}}). \end{aligned} \quad (5.28)$$

Here, we note that the exciton–polariton field expanded by the plane wave with the wavevector \mathbf{k} depends on the site \mathbf{R} in the quantum dot because we do not apply the long-wave approximation that is usually used for far-field light.

5.2.3 Optical Near-Field Coupling Between Quantum-Dot

5.2.3.1 Formulation

Until now, we have derived the transition matrix element from the exciton state to the ground state in a quantum dot. Considering operations of nanophotonic devices, signal carrier corresponds to the energy transfer between nanometric objects, or quantum dots, which are electronically separated, and the speed of the energy transfer is determined by the coupling strength of an optical near field. In this stage, we derive the coupling strength,

$$\hbar U = \langle \Psi_f | \hat{H}_{\text{int}} | \Psi_i \rangle, \quad (5.29)$$

where $|\Psi_i\rangle$ and $|\Psi_f\rangle$ represent exact initial and final states, respectively, in which the states consist of quantum-dot states, photon fields, and some external degrees of freedom, such as a substrate and a glass fiber probe. Since the exact states cannot be given rigorously, we deal with the problem for taking the minimum matter and photon states by using the projection operator method, where the theoretical treatment in such complex system comes down to two-body problem as we have reported in detail [26, 30].

We can rewrite the exact eigenstate as two substates which belong in a relevant P-space and an irrelevant Q-space, which are expressed by using projection operators P and Q as $|\Psi_\lambda^P\rangle = P|\Psi_\lambda\rangle$ and $|\Psi_\lambda^Q\rangle = Q|\Psi_\lambda\rangle$, respectively, where $\lambda = i, f$. Here, P and Q are specified by the following relations: $P = 1$, $P^2 = P$, $Q^2 = Q$, $P^\dagger = P$, and $Q^\dagger = Q$ [31]. In the case of two-quantum-dot system, P-space is constructed from the eigenstates of \hat{H}_0 , that is, a combination of the two energy levels for each quantum dot and the exciton–polariton vacuum state. In Q-space, which is complementary to P-space, the exciton–polariton states are not vacant. According to this notation, the exact state can be formally expressed by using the state in P-space only as

$$|\Psi_\lambda\rangle = \hat{J} P (P \hat{J}^\dagger \hat{J} P)^{-1/2} |\Psi_\lambda^P\rangle, \quad (5.30)$$

where

$$\hat{J} = \left[1 - (E_\lambda - \hat{H}_0)^{-1} Q \hat{H}_{\text{int}} \right]^{-1}, \quad (5.31)$$

and E_λ represents the eigenenergy of the total Hamiltonian \hat{H} . Using (5.30), we can obtain the effective interaction \hat{H}_{eff} as

$$\langle \Psi_f | \hat{H}_{\text{int}} | \Psi_i \rangle = \langle \Psi_f^P | \hat{H}_{\text{eff}} | \Psi_i^P \rangle, \quad (5.32)$$

where

$$\hat{H}_{\text{eff}} = (P \hat{J}^\dagger \hat{J} P)^{-1/2} (P \hat{J}^\dagger \hat{H}_{\text{int}} \hat{J} P) (P \hat{J}^\dagger \hat{J} P)^{-1/2}. \quad (5.33)$$

To evaluate further (5.32), we approximate operator \hat{J} and eigenvalue E_λ perturbatively with respect to \hat{H}_{int} ; that is, $\hat{J} = 1 + (E_0^P - E_0^Q)^{-1} \hat{H}_{\text{int}} + \dots$. Since the lowest

order is $\langle \Psi_f^P | P \hat{H}_{\text{int}} P | \Psi_i^P \rangle = 0$, (5.32) is rewritten within the second order as

$$\hbar U = \sum_m \langle \Psi_f^P | \hat{H}_{\text{int}} | m^Q \rangle \langle m^Q | \hat{H}_{\text{int}} | \Psi_i^P \rangle \left(\frac{1}{E_{0i}^P - E_{0m}^Q} + \frac{1}{E_{0f}^P - E_{0m}^Q} \right), \quad (5.34)$$

where E_{0i}^P , E_{0f}^P , and E_{0m}^Q represent the eigenenergies of the unperturbed Hamiltonian for the initial and final states in P-space and the intermediate state in Q-space, respectively. Since we focus on the interdot interaction of (5.34), we set the initial and final states in P-space to $|\Psi_i^P\rangle = |\Phi_{m\mu}^A\rangle |\Phi_g^B\rangle |0\rangle$ and $|\Psi_f^P\rangle = |\Phi_g^A\rangle |\Phi_{m'\mu'}^B\rangle |0\rangle$. Then, the intermediate states in Q-space that involve exciton–polaritons with the wavevector \mathbf{k} are utilized for the energy transfer from one quantum dot to the other, according to $|m^Q\rangle = |\Phi_g^A\rangle |\Phi_g^B\rangle |\mathbf{k}\rangle$ and $|\Phi_{m\mu}^A\rangle |\Phi_{m'\mu'}^B\rangle |\mathbf{k}\rangle$. The superscripts A and B are used to label two quantum dots. Substituting (5.28), one can rewrite (5.34) as

$$\begin{aligned} \hbar U &= \varphi_\mu^A(0) \varphi_{\mu'}^{B*}(0) \iint F_m^A(\mathbf{R}_A) F_{m'}^{B*}(\mathbf{R}_B) \\ &\quad \times (Y_A(\mathbf{R}_A - \mathbf{R}_B) + Y_B(\mathbf{R}_A - \mathbf{R}_B)) d\mathbf{R}_A d\mathbf{R}_B, \end{aligned} \quad (5.35)$$

where the sum of \mathbf{R}_α ($\alpha = A, B$) in (5.28) is transformed to the integral form. The functions $Y_\alpha(\mathbf{R}_{AB})$, which connect the two spatially isolated two envelope functions $F_m^A(\mathbf{R}_A)$ and $F_{m'}^B(\mathbf{R}_B)$, are defined as

$$\begin{aligned} Y_\alpha(\mathbf{R}_{AB}) &= -\frac{1}{4\pi^2} \sum_{\lambda=1}^2 \int (\boldsymbol{\mu}_{\text{cv}}^A \cdot \hat{\mathbf{e}}_\lambda(\mathbf{k})) (\boldsymbol{\mu}_{\text{cv}}^B \cdot \hat{\mathbf{e}}_\lambda(\mathbf{k})) f^2(k) \\ &\quad \times \left(\frac{e^{i\mathbf{k} \cdot \mathbf{R}_{AB}}}{E(k) + E_\alpha} + \frac{e^{-i\mathbf{k} \cdot \mathbf{R}_{AB}}}{E(k) - E_\alpha} \right) d\mathbf{k}, \end{aligned} \quad (5.36)$$

where $\mathbf{R}_{AB} = \mathbf{R}_A - \mathbf{R}_B$ is used.

In order to obtain an explicit functional form of $Y_\alpha(\mathbf{R}_{AB})$, we apply the effective mass approximation to the exciton–polaritons,

$$E(k) = \frac{\hbar^2 k^2}{2m_p} + E_m, \quad (5.37)$$

where m_p is the exciton–polariton effective mass. Using this approximation, (5.36) can be transformed into

$$\begin{aligned}
Y_\alpha(\mathbf{R}_{AB}) &= (\boldsymbol{\mu}_{cv}^A \cdot \boldsymbol{\mu}_{cv}^B) \\
&\left[W_{\alpha+} e^{-\Delta_{\alpha+} R_{AB}} \left(\frac{\Delta_{\alpha+}^2}{R_{AB}} + \frac{\Delta_{\alpha+}}{R_{AB}^2} + \frac{1}{R_{AB}^3} \right) \right. \\
&\quad \left. - W_{\alpha-} e^{-\Delta_{\alpha-} R_{AB}} \left(\frac{\Delta_{\alpha-}^2}{R_{AB}} + \frac{\Delta_{\alpha-}}{R_{AB}^2} + \frac{1}{R_{AB}^3} \right) \right] \\
&- (\boldsymbol{\mu}_{cv}^A \cdot \hat{\mathbf{R}}_{AB})(\boldsymbol{\mu}_{cv}^B \cdot \hat{\mathbf{R}}_{AB}) \left[W_{\alpha+} e^{-\Delta_{\alpha+} R_{AB}} \left(\frac{\Delta_{\alpha+}^2}{R_{AB}} + \frac{3\Delta_{\alpha+}}{R_{AB}^2} + \frac{3}{R_{AB}^3} \right) \right. \\
&\quad \left. - W_{\alpha-} e^{-\Delta_{\alpha-} R_{AB}} \left(\frac{\Delta_{\alpha-}^2}{R_{AB}} + \frac{3\Delta_{\alpha-}}{R_{AB}^2} + \frac{3}{R_{AB}^3} \right) \right], \tag{5.38}
\end{aligned}$$

where R_{AB} and $\hat{\mathbf{R}}_{AB}$ are the absolute value $|\mathbf{R}_{AB}|$ and the unit vector defined by \mathbf{R}_{AB}/R_{AB} , respectively. The weight coefficients $W_{\alpha\pm}$ and decay constants $\Delta_{\alpha\pm}$ are given by

$$W_{\alpha\pm} = \frac{E_p}{E_\alpha} \frac{(E_m - E_\alpha)(E_m + E_\alpha)}{(E_m - E_p \mp E_\alpha)(E_m \pm E_\alpha) - E_m^2/2}, \tag{5.39}$$

$$\Delta_{\alpha\pm} = \frac{1}{\hbar c} \sqrt{E_p(E_m \pm E_\alpha)}, \tag{5.40}$$

where the exciton–polariton effective mass is rewritten as $E_p = m_p c^2$. Since the dipole moments $\boldsymbol{\mu}_{cv}^A$ and $\boldsymbol{\mu}_{cv}^B$ are not determined as fixed values, we assume that they are parallel, and take a rotational average of (5.38). Therefore, $\langle (\boldsymbol{\mu}_{cv}^A \cdot \hat{\mathbf{R}}_{AB})(\boldsymbol{\mu}_{cv}^B \cdot \hat{\mathbf{R}}_{AB}) \rangle = \mu_{cv}^A \mu_{cv}^B / 3$ with $\mu_{cv}^\alpha = |\boldsymbol{\mu}_{cv}^\alpha|$, and we obtain the final form of the function $Y_\alpha(R_{AB})$ as

$$Y_\alpha(R_{AB}) = \frac{2\mu_{cv}^A \mu_{cv}^B}{3R_{AB}} (W_{\alpha+} \Delta_{\alpha+}^2 e^{-\Delta_{\alpha+} R_{AB}} - W_{\alpha-} \Delta_{\alpha-}^2 e^{-\Delta_{\alpha-} R_{AB}}). \tag{5.41}$$

Equation (5.41) is the sum of two Yukawa functions with a short and long interaction range (heavy and light effective mass) given in (5.40). We can estimate the coupling strength between two quantum dots from the analytic form of the interaction potential given by (5.35) and (5.41), and we can show the existence of dipole-forbidden energy transfer driven by the optical near-field coupling, as discussed in the following.

5.2.3.2 Numerical Results

In this subsection, we give typical values of the coupling strength of $\hbar U$ in (5.35) using an example of CuCl quantum cubes embedded in a NaCl matrix. Due to the effect of size confinement, the center of mass motion and relative motion for an exciton in a CuCl quantum cube are [29]

$$F_m^{\alpha}(\mathbf{R}_{\alpha}) = \left(\frac{2}{L_{\alpha}}\right)^{3/2} \sin\left(\frac{\pi m_x x_{\alpha}}{L_{\alpha}}\right) \sin\left(\frac{\pi m_y y_{\alpha}}{L_{\alpha}}\right) \sin\left(\frac{\pi m_z z_{\alpha}}{L_{\alpha}}\right), \quad (5.42)$$

$$\varphi_{1s}(r) = \frac{1}{\sqrt{\pi a^3}} e^{-r/a}, \quad (5.43)$$

respectively, where the atomic site and the quantum number are represented by $\mathbf{R}_{\alpha} = (x_{\alpha}, y_{\alpha}, z_{\alpha})$ with $\alpha = A, B$ and $\mathbf{m} = (m_x, m_y, m_z)$ with $m_x, m_y, m_z = 1, 2, 3, \dots$. The variables L_{α} and a denote a width of the quantum cube and the Bohr radius of the exciton, respectively. Here, we assume relative motion in the 1s state. The coupling strength is obtained numerically by substituting (5.41) and (5.42) into (5.35). In Fig. 5.5a, the calculation results are plotted as a function of the intercube distance. The curve with square dots represents the coupling between the dipole-active exciton levels, that is, $\mathbf{m} = \mathbf{m}' = (1, 1, 1)$, in two quantum cubes. When we set the intercube distance and a width of the quantum cubes as $d = 5$ nm and $L_A = L_B = 10$ nm, respectively, the coupling strength is about $89 \mu\text{eV}$ ($U^{-1} = 7.4$ ps). The curve with circular dots is the result for $\mathbf{m} = (1, 1, 1)$ and $\mathbf{m}' = (2, 1, 1)$. For conventional far-field light, $\mathbf{m}' = (2, 1, 1)$ is the dipole-inactive exciton level, and it follows that the optical near-field interaction inherently involves such a transition because of the finite interaction range. Figure 5.5b is a schematic illustration of the dipole-inactive transition, in which the optical near field enables to excite the local dipoles at the near side in a quantum dot with dipole-inactive level for far-field light. This coupling strength is estimated from Fig. 5.5a as $\hbar U = 37 \mu\text{eV}$ ($U^{-1} = 17.7$ ps) for $d = 5$ nm, and $\hbar U = 14 \mu\text{eV}$ ($U^{-1} = 46.9$ ps) for $d = 15$ nm, where the cube sizes are set as $L_A = 10$ nm and $L_B = 14.1$ nm to realize resonant energy transfer between the exciton state in QD-A and the first exciton excitation state in QD-B. The coupling strength ($\mathbf{m} \neq \mathbf{m}'$) is approximately half that of $\mathbf{m} = \mathbf{m}'$ at the same intercube distance, but it is strong enough for our proposed nanophotonic devices. For functional operations, the difference between the coupling strengths is important to divide the system into two parts, that is, a quantum mechanical part and a classical dissipative part, as already illustrated in Fig. 5.4.

5.2.4 Summary

In this section, we formulate an optical near-field coupling by using appropriate bases which are constructed from typical excitonic states in a quantum dot and exciton-polariton state in a surrounding system, and not using the long-wave approximation which often applies to a conventional optical interaction in an atomic system. Although we have derived the coupling in the lowest order as given in (5.34), our formulation would be exact if we take rigorous eigenstate of exciton-polaritons as the intermediate states, instead of the simple effective mass approximation which is applied in the above discussion. However, in the following sections, our interests are characteristic functional operations of nanophotonic devices on the basis of certain coupling strength of the optical near field, rather than

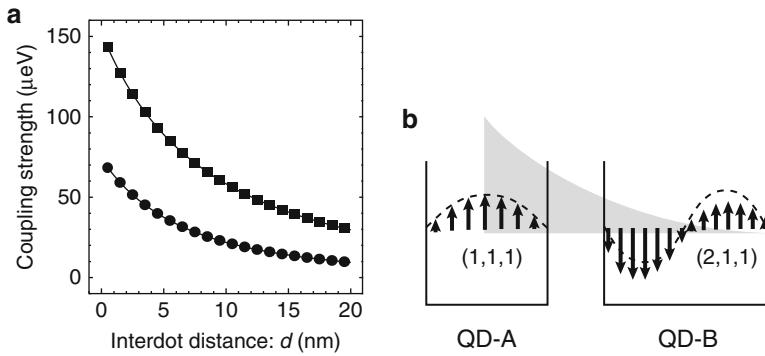


Fig. 5.5 (a) Coupling strength of the optical near field between pairs of CuCl quantum cubes embedded in a NaCl matrix. The curves shown with square and circular dots correspond to quantum numbers for the exciton center of mass motion $m = m' = (1, 1, 1)$, and $m = (1, 1, 1)$, and $m' = (2, 1, 1)$, respectively. The energy level $m' = (2, 1, 1)$ is a dipole-inactive state for conventional far-field light. The parameters are set as $E_A = E_B = 3.22$ eV, $E_m = 6.9$ eV, $\mu_{cv}^A = \mu_{cv}^B = 1.73 \times 10^{-2}$ eV, $L_A = 10$ nm, $L_B = 10$ and 14.1 nm ($m' = (1, 1, 1)$ and $(2, 1, 1)$), and $a = 0.67$ nm. (b) Schematic illustration of a transition between dipole-active and dipole-inactive states via the optical near-field coupling. Steeply gradient optical near field enables to excite near side local dipoles in a quantum dot with dipole-inactive $(2, 1, 1)$ -level

to understand fundamental properties of optical near-field coupling. More rigorous description of the optical near-field coupling will be discussed elsewhere.

From numerical results shown in Fig. 5.5, the coupling strength of optical near field depends on the interdot distance, which is one of key features for nanophotonic device operations. By using this, we can control the dynamics of energy flow in nanometric space and develop some functional operations inherent to nanophotonic devices. Furthermore, we showed that dipole-inactive energy transfer can occur when a distance between isolated quantum systems becomes enough small, which is related to the energy states in nanometric objects as well as steeply gradient spatial distribution of the optical near field. Especially, the dipole-inactive energy transfer between the states with different quantum numbers enables to realize unidirectional energy transfer in a nanometric system with the help of fast relaxation of exciton sublevels. This is a quite important feature for signal isolation in nanophotonic devices. In Sects. 5.3 and 5.4, we discuss operation principles of various functional devices by using such features of the optical near-field coupling skillfully.

5.3 Nanophotonic Switch Based on Dissipation Control

In the previous section, we had theoretically explained that an exciton in a dipole-inactive energy level can be excited by using an optical near field. A relaxation time of the exciton in the dipole-inactive level, the higher energy sublevel, is generally

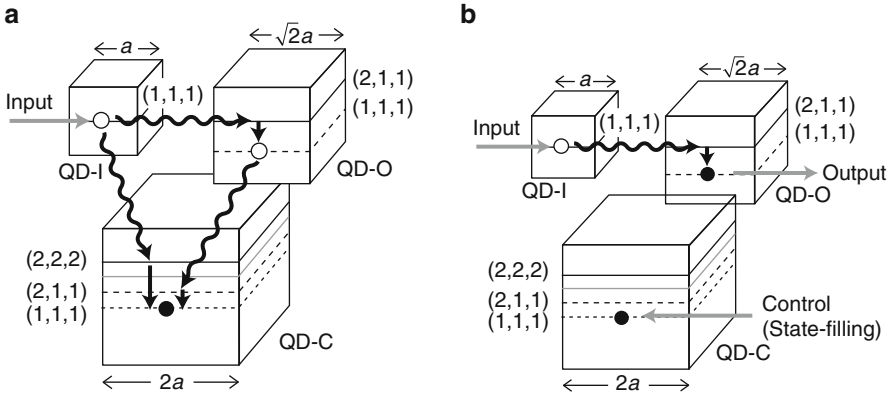


Fig. 5.6 A nanophotonic switch consisting of three quantum cubes with discrete energy levels showing the (a) off- and (b) on-states

in the order of a few ps because of the strong coupling between an exciton and a phonon reservoir in a surrounding system [32]. Since the coupling strength of the optical near field corresponds to about subhundred ps, which has been estimated in Sect. 5.2, the intra-sublevel relaxation is enough faster than energy transfer between two quantum dots. Therefore, unidirectional energy transfer can be realized in a two or more quantum-dot system by mediating the intra-sublevel relaxation. On the other hand, we can create and annihilate an exciton in an exciton ground state by using external pumping light. More than two excitons in a nanometric quantum-dot system induce exciton-exciton interaction, that is qualitatively regarded the exciton as fermionic particles, which is of course exact. When the lowest energy sublevel is occupied, the exciton population cannot drop into the lowest energy level, and thus, we can change the dissipation path selectively by arranging several quantum dots. This selectivity reads the origin of a nanophotonic switching operation.

In this section, we investigate our proposed nanophotonic switch, which is a basic element of nanophotonic devices [33]. Figure 5.6 illustrates a switch that consists of three quantum dots (cubes) with discrete exciton energy levels depending on the quantum-dot size. The one-side lengths of these cubes are chosen in the ratio $1:\sqrt{2}:2$, so that the adjacent quantum dots have resonant energy levels. The principle of operation of the switch is as follows: as shown in Fig. 5.6a, an exciton or population is created at the $(1, 1, 1)$ -level in QD-I as an initial condition. Then, the population is transferred to QD-O and QD-C as a result of an optical near-field coupling. Owing to the fast relaxation between sublevels in each dot via exciton-phonon coupling, the population is transferred to lower energy levels and finally collected at the lowest $(1, 1, 1)$ -level in QD-C. This corresponds to the off-state of the switch, and, consequently, we obtain no output signals from the output port, that is, the $(1, 1, 1)$ -level in QD-O. By contrast, in the on-state of the switch (Fig. 5.6b), the $(1, 1, 1)$ -level in QD-C is initially filled by the control light, isolating QD-C from the other two quantum dots. The input population only reaches the $(1, 1, 1)$ -level in

QD-O and can be detected as output signals, either by the optical near-field coupling to the detector or by far-field light emitted with electron-hole recombination.

From the above explanation, we understand that the key parameters determining the response time of the device are the coupling strength between two quantum dots via an optical near field, and that between excitons and a phonon reservoir. In Sect. 5.3.1, dynamics of exciton population is formulated on the basis of quantum mechanical density matrix formalism, where we consider the phonon field as well as the optical near field discussed in Sect. 5.2, and roles of some key parameters in such a quantum-dot system are numerically clarified. This allows us to discuss the temporal dynamics of our proposed nanophotonic. We evaluate the response time of the CuCl quantum-cube system as a numerical example, which has been extensively examined in experimental and theoretical studies of quantum dots [29, 32, 34, 35]. Section 5.3.2 devotes to evaluate switching operations in a three-quantum-dot system as shown in Fig. 5.6, where the effect of state-filling is introduced phenomenologically. Furthermore, faster iterative switching operations can be achieved in the order of 100 ps, when we apply appropriate control light pulse for utilizing stimulated absorption and emission effectively, which will be discussed by means of numerical analysis in Sect. 5.3.3.

5.3.1 Dynamics in a Two-Quantum-Dot System with Dissipation

As mentioned above, relaxation in the exciton sublevels guarantees the unidirectional energy transfer in a system with several quantum dots. The relaxation originates from coupling between exciton excited state and lattice vibrations in a quantum dot and surrounding matter which are regarded as a phonon reservoir. In order to understand energy transfer dynamics in such a quantum-dot system, which goes through a dissipative process, we first examine a two-quantum-dot system coupled to the phonon reservoir.

5.3.1.1 Formulation

In Fig. 5.7, we schematically illustrate a considered two-quantum-dot system and a phonon reservoir system, in which all energy transfer paths are depicted except for the coupling to far-field light because of different time scales. The Hamiltonian of the system is modeled as

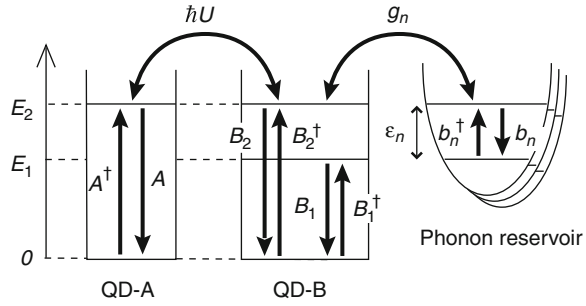
$$\hat{H} = \hat{H}_0 + \hat{H}_{\text{int}} + \hat{H}_{\text{SR}} , \quad (5.44)$$

and

$$\hat{H}_0 = \hbar\Omega_2 \hat{A}^\dagger \hat{A} + \hbar\Omega_1 \hat{B}_1^\dagger \hat{B}_1 + \hbar\Omega_2 \hat{B}_2^\dagger \hat{B}_2 + \hbar \sum_n \omega_n \hat{b}_n^\dagger \hat{b}_n , \quad (5.45)$$

$$\hat{H}_{\text{int}} = \hbar U (\hat{A}^\dagger \hat{B}_2 + \hat{B}_2^\dagger \hat{A}) , \quad (5.46)$$

Fig. 5.7 Two-quantum-dot system. QD-A and QD-B are resonantly coupled due to an optical near-field interaction, and the sublevels in QD-B are coupled with the phonon reservoir



$$\hat{H}_{\text{SR}} = \hbar \sum_n (g_n \hat{b}_n^\dagger \hat{B}_1^\dagger \hat{B}_2 + g_n^* \hat{b}_n \hat{B}_2^\dagger \hat{B}_1). \quad (5.47)$$

When we assume that initial and final states are constructed only in terms of one-exciton states, the creation (annihilation) operators of excitons can be written as follows: $\hat{A}^\dagger = [|e\rangle\langle g|]_A$ ($\hat{A} = [|g\rangle\langle e|]_A$), $\hat{B}_1^\dagger = [|e\rangle\langle g|]_{B_1}$, ($\hat{B}_1 = [|g\rangle\langle e|]_{B_1}$), and $\hat{B}_2^\dagger = [|e\rangle\langle g|]_{B_2}$, ($\hat{B}_2 = [|g\rangle\langle e|]_{B_2}$). We can readily understand the following commutation relations: $[\hat{B}_i^\dagger, \hat{B}_j] = \delta_{i,j} ([|e\rangle\langle e|]_{B_i} - [|g\rangle\langle g|]_{B_i})$ and $[\hat{B}_i, \hat{B}_j] = [\hat{B}_i^\dagger, \hat{B}_j^\dagger] = 0$ ($i, j = 1, 2$). Therefore, the operators are neither bosonic nor fermionic. Bosonic operators ($\hat{b}_n^\dagger, \hat{b}_n$) are for the phonons with eigenenergy $\hbar\omega_n$. For simplicity, the rotating wave approximation is used in the interaction Hamiltonian \hat{H}_{int} as $(\hat{A} + \hat{A}^\dagger)(\hat{B}_2 + \hat{B}_2^\dagger) \approx \hat{A}^\dagger \hat{B}_2 + \hat{A} \hat{B}_2^\dagger$. Phonon reservoir is assumed to be a collection of multiple harmonic oscillators labeled n . Note that the exciton-polariton degrees of freedom have already been traced out, and thus, the coupling strength of the optical near field, $\hbar U$, appears in (5.46). Dynamics of an exciton in this system is given by the following Liouville equation [36, 37]:

$$\dot{\hat{\rho}}(t) = -\frac{i}{\hbar} [\hat{H}, \hat{\rho}(t)], \quad (5.48)$$

where $\hat{\rho}(t)$ represents the density operator, which traced out the exciton-polariton degrees of freedom. In order to express the second-order temporal correlation clearly, the formal solution of (5.48) in the integral form is again substituted into the right-hand side of (5.48), and thus,

$$\begin{aligned} \hat{\rho}^I(t) &= -\frac{i}{\hbar} [\hat{H}_{\text{int}} + \hat{H}_{\text{SR}}^I(t), \hat{\rho}^I(0)] \\ &\quad - \frac{1}{\hbar^2} \int_0^t [\hat{H}_{\text{int}} + \hat{H}_{\text{SR}}^I(t), [\hat{H}_{\text{int}} + \hat{H}_{\text{SR}}^I(t'), \hat{\rho}^I(t')]] dt', \end{aligned} \quad (5.49)$$

where the superscript I means the interaction picture and the relation $\hat{H}_{\text{int}}^I(t) = \hat{H}_{\text{int}}$ is used [36]. Since we are interested in the exciton population in the

two-quantum-dot system, we take a trace with respect to the degrees of freedom of the phonon reservoir as $\hat{\rho}_S^I(t) = \text{Tr}_R[\hat{\rho}^I(t)]$. Here, the density operator is assumed to be a direct product of the quantum-dot system part $\hat{\rho}_S^I(t)$ and the reservoir system part $\hat{\rho}_R^I(t)$. If the reservoir has a very large volume, deviation from the initial value can be neglected, and the density operator is approximated as

$$\hat{\rho}^I(t) = \hat{\rho}_S^I(t)\hat{\rho}_R^I(t) \approx \hat{\rho}_S^I(t)\hat{\rho}_R(0), \quad (5.50)$$

which corresponds to the Born approximation [36]. Taking a trace on both sides of (5.49) about the reservoir operator, we obtain

$$\begin{aligned} \hat{\rho}_S^I(t) = & -iU(r)[\hat{A}^\dagger \hat{B}_2 + \hat{B}_2^\dagger \hat{A}] \\ & - \sum_n n(\omega_n, T)[\{\hat{C} \hat{C}^\dagger, \hat{\rho}_S^I(t)\} - 2\hat{C}^\dagger \hat{\rho}_S^I(t) \hat{C}] \otimes \gamma_n^i(t) \\ & - i[\hat{C} \hat{C}^\dagger, \hat{\rho}_S^I(t)] \otimes \gamma_n^i(t) \\ & - \sum_n [1 + n(\omega_n, T)][\{\hat{C}^\dagger \hat{C}, \hat{\rho}_S^I(t)\} - 2\hat{C} \hat{\rho}_S^I(t) \hat{C}^\dagger] \otimes \gamma_n^r(t) \\ & + i[\hat{C}^\dagger \hat{C}, \hat{\rho}_S^I(t)] \otimes \gamma_n^i(t), \end{aligned} \quad (5.51)$$

where the curly brackets $\{\cdot\}$ represent the anti-commutation relation and the notation \otimes designates the convolution integral. In order to avoid verbose expression, we make the following replacement: $\hat{C}^\dagger = \hat{B}_2^\dagger \hat{B}_1$ and $\hat{C} = \hat{B}_1^\dagger \hat{B}_2$. Since we assume that the reservoir system is at equilibrium, the terms including $\text{Tr}_R[\hat{b}_n^\dagger \hat{\rho}_R(0)]$ and $\text{Tr}_R[\hat{b}_n \hat{\rho}_R(0)]$ disappear in (5.51). The number of phonons in the equilibrium state is written as $n(\omega_n, T) = \text{Tr}_R[\hat{b}_n^\dagger \hat{b}_n \hat{\rho}_R(0)]$, and it follows Bose–Einstein statistics as

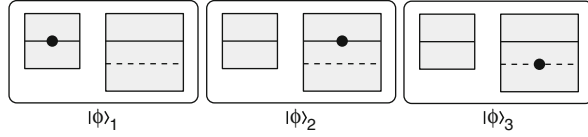
$$n(\omega_n, T) = \frac{1}{e^{\hbar\omega_n/k_B T} - 1}. \quad (5.52)$$

The real and imaginary parts of function

$$\gamma_n(t) = |g_n|^2 e^{i(\Delta\omega - \omega_n)t} \quad (5.53)$$

with $\hbar\omega = \hbar(\Omega_2 - \Omega_1)$ are represented as $\gamma_n^r(t)$ and $\gamma_n^i(t)$, respectively, and are related to the relaxation (real part) and energy shift (imaginary part) of the energy level in QD-B that is originated from the coupling to the phonon reservoir. The convolution integral in (5.51) expresses a memory effect due to time delay in the phonon reservoir. However, if the dynamics of the reservoir system are much faster than those of the two-quantum-dot system, one can approximate the density operator of the two-dot system as $\hat{\rho}_S^I(t - t') = \hat{\rho}_S^I(t)$ (a Markov approximation). Using this approximation and rewriting the summation as $\sum_n = \int_0^\infty D(\omega)d\omega$, with $D(\omega)$

Fig. 5.8 Three bases of the single-exciton state in a two-quantum-dot system



being the density of states for each phonon, we can express the convolution integral analytically as

$$\begin{aligned}
 & \sum_n n(\omega_n, T) \hat{\rho}_S^I(t) \otimes \gamma_n(t) \\
 &= \hat{\rho}_S^I(t) \int_0^\infty n(\omega, T) D(\omega) |g(\omega)|^2 \left(\int_0^t e^{i(\Delta\omega - \omega)t'} dt' \right) d\omega \\
 &\approx \hat{\rho}_S^I(t) \left[\pi n(\Delta\omega, T) D(\Delta\omega) |g(\Delta\omega)|^2 \right. \\
 &\quad \left. + iP \int_0^\infty \frac{n(\omega, T) D(\omega) |g(\omega)|^2}{\Delta\omega - \omega} d\omega \right]. \tag{5.54}
 \end{aligned}$$

Here, we extend the upper limit of the time integration to infinity. The equation of motion for the dot system is finally reduced to

$$\begin{aligned}
 \dot{\hat{\rho}}_S^I(t) &= iU(r) [\hat{A}^\dagger \hat{B}_2 + \hat{B}_2^\dagger \hat{A}, \hat{\rho}_S^I(t)] - n\gamma(\{\hat{C} \hat{C}^\dagger, \hat{\rho}_S^I(t)\} - 2\hat{C}^\dagger \hat{\rho}_S^I(t) \hat{C}) \\
 &\quad - (1+n)\gamma(\{\hat{C}^\dagger \hat{C}, \hat{\rho}_S^I(t)\} - 2\hat{C} \hat{\rho}_S^I(t) \hat{C}^\dagger), \tag{5.55}
 \end{aligned}$$

where $n \equiv n(\Delta\omega, T)$ and $\gamma \equiv \pi D(\Delta\omega) |g(\Delta\omega)|^2$. The terms indicating the energy shift are neglected in (5.55) because the shift is usually small in the case of weak coupling between the quantum-dot system and phonon reservoir.

Let us consider one-exciton dynamics in the system, using three bases, as illustrated in Fig. 5.8. The equations of motion for the matrix elements are then read in the Schrödinger picture as

$$\dot{\rho}_{11}(t) = iU(r) [\rho_{12}(t) - \rho_{21}(t)], \tag{5.56}$$

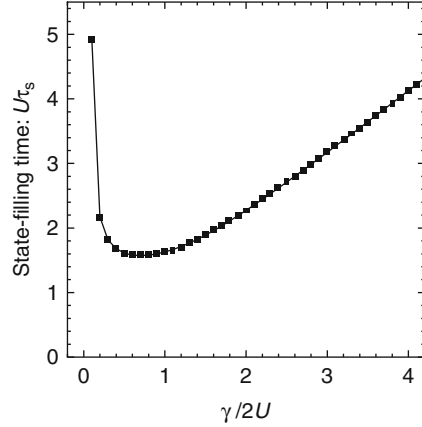
$$\dot{\rho}_{12}(t) - \dot{\rho}_{21}(t) = 2iU(r) [\rho_{11}(t) - \rho_{22}(t)] - (1+n)\gamma [\rho_{12}(t) - \rho_{21}(t)], \tag{5.57}$$

$$\dot{\rho}_{22}(t) = -iU(r) [\rho_{12}(t) - \rho_{21}(t)] - 2(1+n)\gamma \rho_{22}(t) + 2n\gamma \rho_{33}(t), \tag{5.58}$$

$$\dot{\rho}_{33}(t) = 2(1+n)\gamma \rho_{22}(t) - 2n\gamma \rho_{33}(t), \tag{5.59}$$

where $\rho_{mn}(t) \equiv \langle \Phi_m | \hat{\rho}_S(t) | \Phi_n \rangle$ is employed. When the temperature, T , equals zero ($n = 0$), (5.57) can be solved analytically. The diagonal parts representing the population probability for each energy level in QD-A and QD-B, as well as the off-diagonal parts representing quantum coherence, are given as

Fig. 5.9 The state-filling time τ_S plotted as a function of the ratio of the exciton–phonon coupling strength $\gamma/2$ to the interdot optical near-field coupling strength U



$$\rho_{11}(t) = \frac{1}{Z^2} e^{-\gamma t} \left[\frac{\gamma}{2} \sinh(Zt) + Z \cosh(Zt) \right]^2, \quad (5.60)$$

$$\rho_{22}(t) = \frac{U^2}{Z^2} e^{-\gamma t} \sinh^2(Zt), \quad (5.61)$$

$$\rho_{33}(t) = 1 - [\rho_{11}(t) + \rho_{22}(t)], \quad (5.62)$$

$$\rho_{12}(t) = -\rho_{21}(t) = i \frac{U}{Z^2} e^{-\gamma t} \sinh(Zt) \left[\frac{\gamma}{2} \sinh(Zt) + Z \cosh(Zt) \right], \quad (5.63)$$

where $Z \equiv \sqrt{(\gamma/2)^2 - U^2}$, and initial conditions $\rho_{11}(0) = 1$ and $\rho_{12}(0) = \rho_{21}(0) = \rho_{22}(0) = \rho_{33}(0) = 0$ are used. We define the state-filling time τ_S as $\rho_{33}(\tau_S) = 1 - e^{-1}$, which corresponds to the time for the excitation energy transfer from QD-A to the lower energy level in QD-B. From (5.60), it follows that the temporal evolution of the population is quite different at $U > \gamma/2$ and $U < \gamma/2$. Although (5.60) seems to be undefined at $U = \gamma/2$ ($Z = 0$), taking a limit value, there is a definite solution regardless of whether $Z \rightarrow$ or -0 is taken. In Fig. 5.9, the state-filling time τ_S is plotted as a function of the ratio of $\gamma/2$ to U . For $U > \gamma/2$, population shows damped oscillation with envelope function $e^{-\gamma t}$; thus, τ_S is determined by the relaxation constant γ , that is, $\tau_S \sim \gamma^{-1}$. By contrast, for $U < \gamma/2$, $\rho_{22}(t)$ decays monotonically. At first glance, as $\gamma/2$ increases, we expect τ_S to decrease monotonically, because the population flows into the lower energy level more quickly; nevertheless, τ_S increases again, as shown in Fig. 5.9. This occurs because the upper energy level in QD-B becomes effectively broad with increasing γ , which results in a decrease in the resonant energy transfer between the quantum dots. When the ratio $\gamma/2U$ is sufficiently large, τ_S increases linearly, as seen in Fig. 5.9. Therefore, the state-filling time is determined not only by the coupling strength between two quantum dots via the optical near field but also by the coupling strength to the phonon reservoir system. From Fig. 5.9, it follows that the fastest energy transfer is obtained when $\gamma/2 \sim U$ is satisfied.

The term $2\gamma n\rho_{33}(t)$ on the right-hand side of (5.58) indicates that the finite temperature effect due to the finite number of phonons ($n \neq 0$) induces back transfer of the excitation energy from the reservoir to the two-quantum-dot system. Within the Born approximation adopted in (5.50), this term incoherently increases population $\rho_{22}(t)$. As population $\rho_{33}(t)$ increases, the back transfer becomes large and gives residual populations $\rho_{11}(t)$ and $\rho_{22}(t)$ in the upper levels in both quantum dots.

5.3.1.2 Numerical Results

Using (5.57) and (5.60), we present numerical results for the dynamics of exciton population for zero and finite temperatures in order to verify the theoretical consideration just presented and to estimate the state-filling time for some practical cases. Suppose that the system consists of two CuCl quantum cubes embedded in a NaCl matrix. The quantum cube size is set as $a:\sqrt{2}a$, so that the (1, 1, 1)-level of QD-A is resonant with the (2, 1, 1)-level of QD-B. The variable parameters are the coupling strength $\hbar U$ or the intercube distance, the relaxation constant γ , and the temperature T of the phonon reservoir system.

In Fig. 5.10a and b, the E_2 - and E_1 -level populations $\rho_{22}(t)$ and $\rho_{33}(t)$ in QD-B are plotted for the coupling strengths of the optical near field, $\hbar U = 100, 60, \text{ and } 40 \mu\text{eV}$ ($U = 1.51 \times 10^{-1}, 0.90 \times 10^{-1}, \text{ and } 0.60 \times 10^{-1} \text{ ps}^{-1}$). In order to investigate a behavior of the dynamics around the critical condition $U = \gamma/2$, appropriate coupling strengths are chosen, though these are a little strong compared with the estimated values in Sect. 5.2. The relaxation constant γ is assumed to be $(1 \text{ ps})^{-1}$ from the experimental study [32], and the temperature is $T = 0 \text{ K}$. The exciton populations for all three cases in Fig. 5.10a show monotonic decays, because $U < \gamma/2$ is satisfied. From Fig. 5.10b, the state-filling time τ_S is estimated for the coupling strength $\hbar U = 100, 60, \text{ and } 40 \mu\text{eV}$ as 22, 60, and 140 ps, respectively. This indicates that an energy transfer time of less than 100 ps can be realized when the coupling strength is larger than about $50 \mu\text{eV}$.

Figure 5.11 shows the result for $\gamma^{-1} = 10 \text{ ps}$, which corresponds to weaker coupling between an exciton and the phonon reservoir. Damped oscillation due to nutation between two resonant levels is clearly seen for $\hbar U = 100 \mu\text{eV}$ in Fig. 5.11a, where $U > \gamma/2$ is satisfied. Although $U > \gamma/2$ is also satisfied for $\hbar U = 60$ and $40 \mu\text{eV}$, we cannot observe the oscillation because of the small amplitudes. From Fig. 5.11b, the state-filling time τ_S for the three cases is estimated as 12, 18, and 25 ps, respectively. Compared with Fig. 5.10b, the state-filling speed becomes faster in Fig. 5.11b in spite of the decrease in γ because U is nearly equal to $\gamma/2$. Figures 5.10 and 5.11 indicate that the intercube distance should be adjusted so that the optical near-field coupling is of the same order as the exciton–phonon coupling in order to obtain the fastest energy transfer in the system.

Figure 5.12a and b show the temperature dependence of populations $\rho_{22}(t)$ and $\rho_{33}(t)$, respectively. The temperature is set as either $T = 50$ or 100 K . These results are obtained by using a Laplace transform of (5.57), where singular points are derived numerically for the given numerical parameters. As mentioned in the beginning in Sect. 5.3, a finite temperature induces the incoherent back transfer

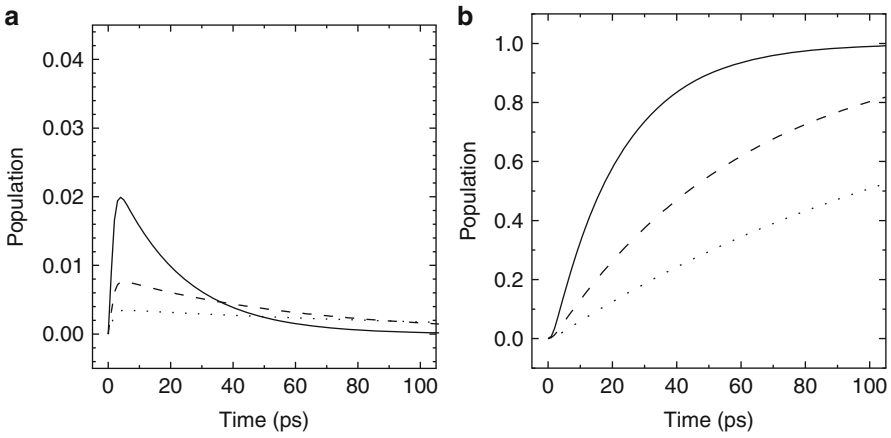


Fig. 5.10 Temporal evolution of (a) E_1 -level population $\rho_{22}(t)$ and (b) E_2 -level population $\rho_{33}(t)$, where the relaxation constant γ and temperature T are set as $(1 \text{ ps})^{-1}$ and 0 K , respectively. The *solid*, *dashed*, and *dotted* curves represent the cases for coupling strengths, $\hbar U = 100, 60,$ and $40 \mu\text{eV}$, respectively

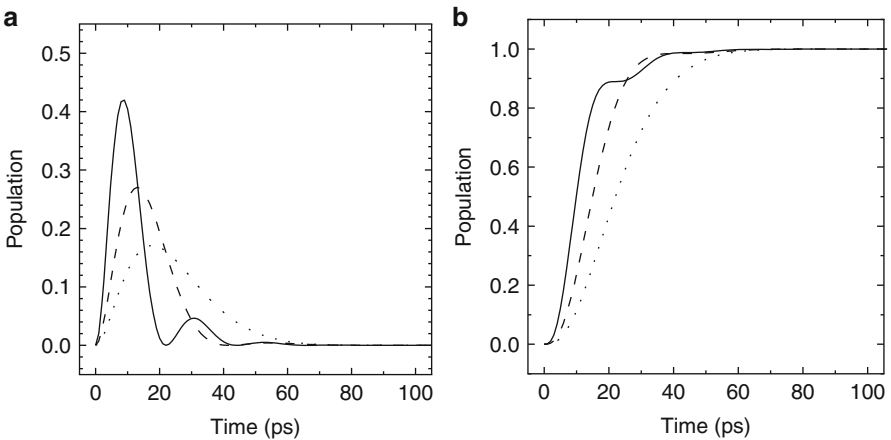


Fig. 5.11 Temporal evolution of (a) E_1 -level population $\rho_{22}(t)$ and (b) E_2 -level population $\rho_{33}(t)$, where the relaxation time γ and temperature are set as $(10 \text{ ps})^{-1}$ and 0 K , respectively. The *solid*, *dashed*, and *dotted* curves represent the cases for coupling strengths, $\hbar U = 100, 60,$ and $40 \mu\text{eV}$, respectively

of energy, and this results in residual populations at the upper energy levels in both quantum cubes. Figure 5.12a shows that the E_2 -level population in QD-B converges on a finite temperature-dependent value that can be derived numerically and is denoted by the horizontal dotted lines in Fig. 5.12a. As shown in Fig. 5.12b,

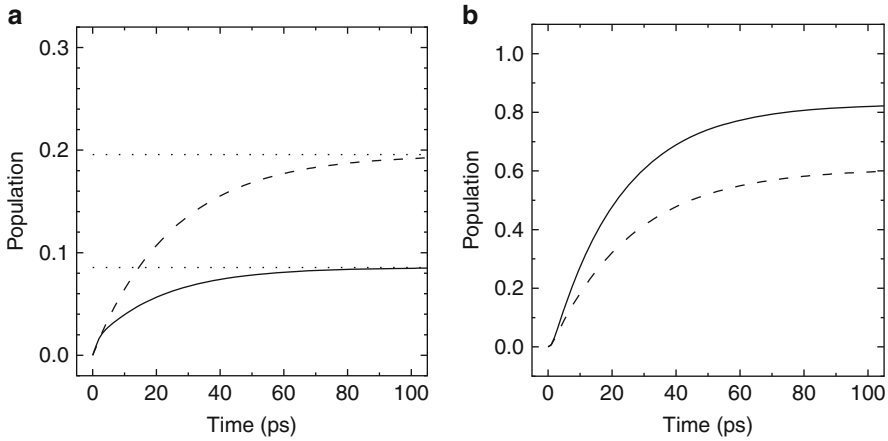


Fig. 5.12 Temperature dependence of (a) E_1 -level population $\rho_{22}(t)$ and (b) E_2 -level population $\rho_{33}(t)$, when $\hbar U = 100 \mu\text{eV}$ and $\gamma = (1 \text{ ps})^{-1}$. The *solid* and *dashed* curves represent the cases for temperature $T = 50$ and 100 K , respectively. The two dotted lines denote the limit values of E_1 -level population for both temperature at infinite time

however, the time evolution of the E_1 -level population is almost independent of the temperature, except for a decrease in the amplitude because of the residual populations at upper energy levels.

5.3.1.3 System Tolerance and Further Discussion

So far, the theoretical modeling of the population dynamics in a two-quantum-dot system has assumed an ideally perfect resonance condition, which may be too tight to fabricate such a system with definite size ratios. In order to release the resonance condition, we estimate allowable tolerance, or size deviation of quantum dots from designed values. When the deviation from the resonant energy $\hbar\Delta\Omega$ in QD-B is introduced, the factor on the right-hand side in (5.61) is modified, and the ratio of that in off-resonance to on-resonance is approximately proportional to $\gamma^2/(\gamma^2 + \Delta\Omega^2)$ ($\gamma/2 \gg U$). Therefore, we can achieve efficiency more than 50 % even if the deviation $\Delta\Omega < \gamma$ is introduced. When the dot size and relaxation constant are set as 7.1 nm ($= 5\sqrt{2} \text{ nm}$) and $\hbar\gamma = 3 \text{ meV}$, respectively, approximately 10 % deviation of the dot size can be allowed. As the size of quantum dots is larger, the tolerable deviation is more relaxed. It is feasible to make such quantum dots by the recent advancement of nanofabrication techniques [38, 39]. In fact, experimental results in our research group [40] show the consistent population dynamics as we discussed above.

Our results and discussion might be valid within the Born–Markov approximation. Even if the Born approximation is admitted because of the large volume of the phonon reservoir, the Markov approximation may not be guaranteed at low temperature, as assumed in the transformation in (5.54). Therefore, we might need to deal with it more carefully, since it has been pointed out that non-Markov behavior

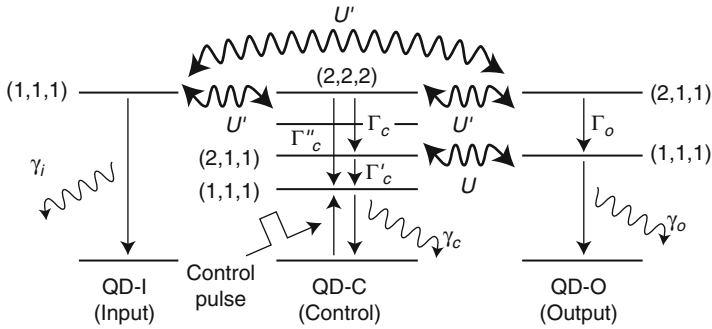


Fig. 5.13 Theoretical model of a nanophotonic switch

manifests itself at low temperature [36,41]. The effects of non-Markov behavior on the dynamics are now under investigation.

We focused our attention on the energy transfer process in the nanometric regime, but it is quite important to investigate signal control and to manipulate the electronic states of the components in a nanophotonic device, where we must deal with a two-exciton state, as shown in Fig. 5.6b. In the following, we show numerical results of exciton population dynamics with signal manipulation in a three-quantum-dot system, which is formulated by the same manner except for phenomenological insertion of control light pulse.

5.3.2 Nanophotonic Switch

5.3.2.1 Switching Operations

In Fig. 5.13, we show a theoretical model of the nanophotonic switch, in which each neighboring pair of quantum dots has a resonant energy level that is determined by setting the size as 1(I):2(C): $\sqrt{2}$ (O), and thus, the system consists of two-level, three-level, and five-level quantum dots depending on the size ratios. In Sect. 5.3.1, we ignore radiative relaxation in the exciton ground levels because the radiative relaxation time is the order of 1 ns which is enough longer than the non-radiative one. However, for an iterative switching operation discussed here, exciton population has to be swept out to the external field and return into the initial state. This radiative relaxation, that is, spontaneous emission of photons, is described in the same manner in (5.55) based on the Born–Markov approximation for a surrounding photon reservoir, where the radiative relaxation constants are much smaller than the non-radiative ones. In Fig. 5.13, the notations of radiative and non-radiative relaxation constants are distinguished by the Greek characters γ and Γ , respectively, where the subscripts of the relaxation constants represent the terminal quantum dots for the input, output, and control. For simplicity, we assume that photon and phonon reservoirs are both empty ($T = 0$), where the effect of temperature is just lowering the signal contrast and does not affect the dynamics

in the nanophotonic switch. In a switching device, we require another important element, that is, injection of external control signal to change the on- and off-states. Rigorous modeling of the external exciton excitation is quite difficult since matter coherence presents. Here, we assume weak excitation in which optical nutation or Rabi oscillation due to the control pulse does not appear and approximately regards the excitation as an incoherent process. Thus, the external excitation can be also written by using the Born–Markov approximation with the very large number of photons. Adding the external excitation in (5.55), a phenomenological equation of motion for the density operator reads

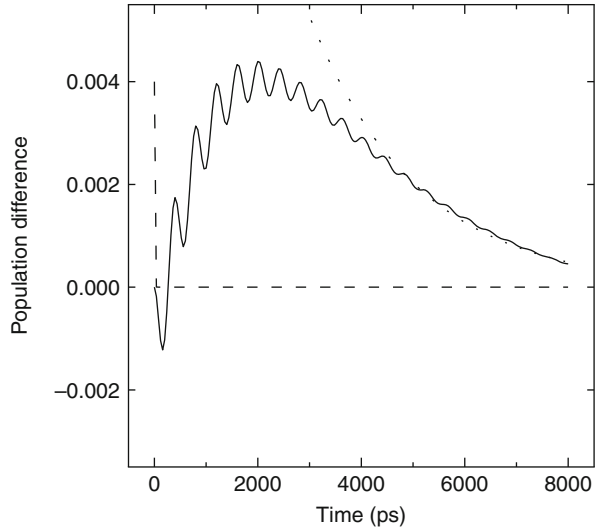
$$\begin{aligned} \hat{\rho}(t) = & -\frac{i}{\hbar} [\hat{H}_0 + \hat{H}_{\text{int}}, \hat{\rho}(t)] \\ & + (\text{non-radiative relaxation part}) + (\text{radiative relaxation part}) \\ & + A_{\text{pump}}(t)(\hat{C}_1 \hat{\rho}(t) \hat{C}_1^\dagger + \hat{C}_1^\dagger \hat{\rho}(t) \hat{C}_1), \end{aligned} \quad (5.64)$$

where \hat{C}_1^\dagger and \hat{C}_1 represent the creation and annihilation operators of an exciton at the energy sublevel in QD-C, and the other verbose descriptions for the radiative and non-radiative relaxations are omitted. $A_{\text{pump}}(t) \propto n_{\text{ph}}$ (n_{ph} : photon number) is a time-dependent pumping rate of the control light pulse.

The operation of this switch is as follows: an input signal creates an exciton at the (1, 1, 1)-level in QD-I, and this transfers to the resonant energy levels of the adjacent two quantum dots via an optical near-field coupling [25]. While some energy levels with even total quantum numbers are optically (dipole) forbidden and are not directly excited by far-field light, the optical near field allows such transition because their spatial localization resolves the wave function of adjacent nanometric quantum dots far beyond light diffraction limits. The on- or off-state of the switch corresponds whether the lowest (1, 1, 1)-level in QD-C is unoccupied or occupied, respectively. When this energy level is occupied (state-filling), the initial excitation in QD-A ultimately reaches the (2, 1, 1)-level in QD-C or the (1, 1, 1)-level in QD-O, leading to an output signal. The lowest energy level in each quantum dot is coupled to a free photon reservoir to sweep out the excitation energy radiatively and to a laser photon reservoir to control this device by using a light pulse. Intra-sublevel transitions in QD-C and D guarantee unidirectional energy transfer in the three-quantum-dot system.

By using this model, we derived equations of motion for density matrix elements for possible one- and two-exciton states similar to (5.57) and calculated the exciton dynamics numerically. As an initial exciton population, a steady state is prepared, where the (1, 1, 1)-level in QD-I is excited weakly and continuously. The output signal (luminescence intensity) is proportional to the (1, 1, 1)-level population in QD-O. Figure 5.14 shows the temporal evolution of the exciton population in QD-O after an incoherent short pulse (10 ps) is applied to QD-C. This situation corresponds to transition from the off-state to the on-state. When state-filling is achieved instantaneously, the exciton population in QD-O increases and fast vibration appears as shown in Fig. 5.14. The vibration manifests itself only for the state-filling

Fig. 5.14 Temporal evolution of the (1, 1, 1)-level population in QD-O from the initial steady state. The adjustable parameters are set as follows: optical near-field coupling $U = U' = (130 \text{ ps})^{-1}$, radiative relaxation constants $\gamma_i = (16.8 \text{ ns})^{-1}$, $\gamma_c = (2.1 \text{ ns})^{-1}$, and $\gamma_o = (5.9 \text{ ns})^{-1}$, and non-radiative relaxation time $\Gamma_c = (20 \text{ ps})^{-1}$, $\Gamma'_c = (10 \text{ ps})^{-1}$, $\Gamma''_c = (30 \text{ ps})^{-1}$, and $\Gamma_o = (20 \text{ ps})^{-1}$



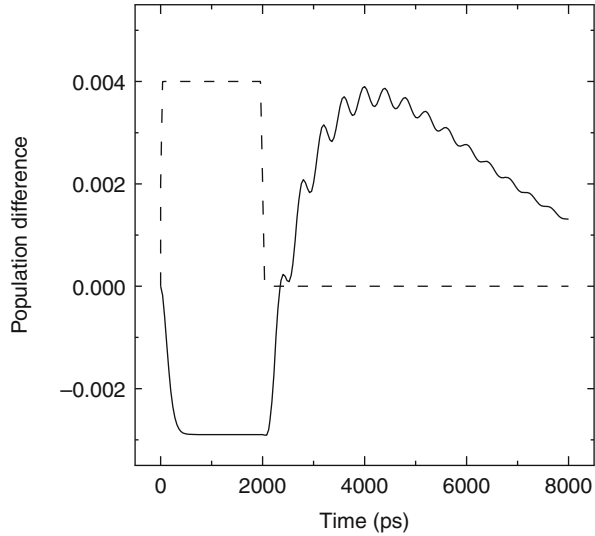
condition. This is apparently caused by nutation between the (2, 1, 1) - and (1, 1, 1) levels in QD-C and QD-O, since the intra-sublevel transition in QD-C is prevented due to the state-filling. In this case, the switching speed from the off to on-states is about 2 ns, which is not so fast. However, as discussed in Sect. 5.3.1, we expect that the fastest switching time about sub-100 ps can be obtained, when the coupling strength of the optical near field is designed as the same order of non-radiative relaxation constant.

The readers may notice that the relaxation time in the later stage over 2 ns is very slow, which is approximately twice of an isolated quantum dot, and the switch seems to spend much time for recovery to the initial state. This long relaxation time is caused by the coherence between QD-C and QD-O during the state-filling in QD-C. Thus, the phenomenon cannot be reproduced using incoherent rate equation approach and is a negative property in the nanophotonic switch. One way to realize fast recovery time is that another larger quantum dot which has fast relaxation time is located near QD-C to break the state-filling condition. We also have another interesting idea to use stimulated absorption and emission process for the recovery of the system, which is discussed in the following subsection.

5.3.2.2 Operation Using Stimulated Absorption and Emission

For switching and recovery operations in this system, we have found an important feature related to spontaneous absorption and emission process. At first glance, it seems that the switching device does not return the initial off-state unless it spends very long time depending on the radiative lifetime as demonstrated in Fig. 5.14. However, the exciton population in the system actually decays less than that of the initial steady state during control light injection and reaches another stable state, where the transition time from the initial state to the second steady state is much

Fig. 5.15 Temporal evolution of the $(1, 1, 1)$ -level population in QD-O from the initial steady state. The applied control pulse width is set as 2 ns. The same adjustable parameters in Fig. 5.6 are adopted



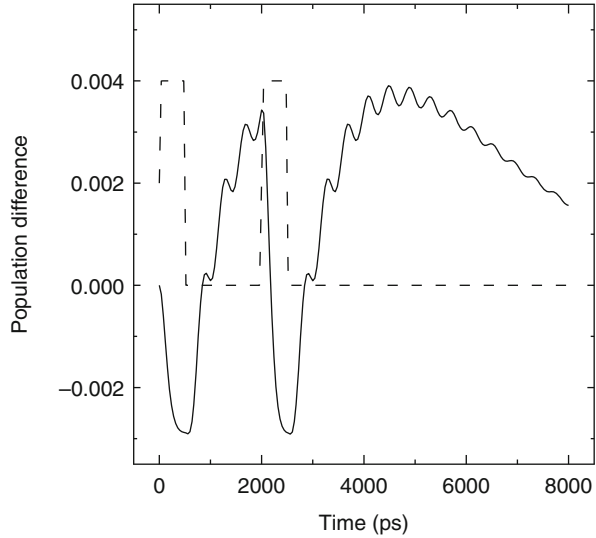
faster than the spontaneous emission lifetime as shown in Fig. 5.15. The effect can be explained by the stimulated absorption and emission in QD-C. For the control light injected, the exciton population in the lower energy sublevel in QD-C approaches by force a half of a unit value due to the stimulated absorption and emission. In the initial steady state, the exciton population in the level is beyond a half value, and thus, the stimulated emission dominantly operates to decrease the population less than the initial steady state, leading to the stable state with lower population. When we stop the control light injection, the exciton population increases beyond that of the beginning steady state with the fast transition time depending on the coupling strength via the optical near field. Using this stimulated absorption and emission process, the fast and iterative switching operations can be achieved.

Figure 5.16 is one of the calculated results, where two control light pulses with 500 ps pulse width are applied. We observe that the transition from on- to off-states takes only a few 100 ps. With further optimization of the intercube distance, quantum-dot size, and surrounding materials of photon reservoir, we can obtain a switching time (off to on, and on to off) less than 100 ps, which is in the order of the inverse of optical near-field coupling strength and is fast enough for our proposed highly integrated nanophotonic devices.

5.3.3 Summary

In this section, at first, we have formulated exciton dynamics in a two-quantum-dot system coupled to phonon reservoir, that is, two-level and three-level quantum-dot systems, where energy transfer occurs between energy sublevels with different quantum numbers. Such energy transfer is inactive for far-field light and is not

Fig. 5.16 Demonstration of the switching operation using two control light pulses with 500 ps pulse width. The *solid* and *dashed* curves represent the population at the (1, 1, 1)-level in QD-O and the temporal profile of the control light pulses, respectively. The same adjustable parameters in Fig. 5.6 are adopted



realized unless using the optical near-field interaction. Moreover, owing to the fast relaxation via exciton–phonon coupling, unidirectional energy transfer can be realized in nanometric space, which is difficult in conventional optical devices when miniaturization of the device progresses. With the help of density operator formalism, temporal evolution can be solved analytically for zero temperature. As a result, we have found that an optimal condition exists for the fast switching operation; the coupling strength of an optical near field is comparable to the intra-sublevel relaxation constant. On the other hand, for finite temperature, the excitation from lower sublevels to upper sublevels occurs, and the signal contrast in this switch becomes lower. In order to improve the signal contrast, a mechanism to sweep out the population compulsorily from the output energy level is required. Although we have not mentioned in Sect. 5.3.1, stimulated absorption and emission process may be one of useful phenomena for an improvement of the signal contrast, which has been described as another viewpoint in Sect. 5.3.2.

A fundamental switch is generally a three-terminal device for input, output, and control signals. We have investigated a three-quantum-dot system numerically as a nanophotonic switch. The energy transfer dynamics is almost the same as a two-quantum-dot system, except for control excitation. When the control light pulse is applied, there are two excitons in the switch, and energy transfer path of an exciton changes due to a state-filling effect. For iterative operation of the nanophotonic switch, a mechanism to sweep out the exciton population is again required. We can use spontaneous emission for this, but the spontaneous lifetime is not so fast as in the order of 1 ns. Here, we have found that the stimulated absorption and emission process is valuable for the fast iterative operations, because the time for sweeping out the exciton population is free from the spontaneous emission lifetime and is determined by the coupling strength of the optical near field. By using

these process and optimizing the coupling strength of the optical near field, we have roughly estimated the switching time of sub-100 ps. Such a nanophotonic switch has been already demonstrated experimentally in our research group by using CuCl quantum cubes embedded in a NaCl matrix [40], where they searched out appropriate quantum-dot trio with the ratios of $1:\sqrt{2}:2$ by means of a spectroscopic method.

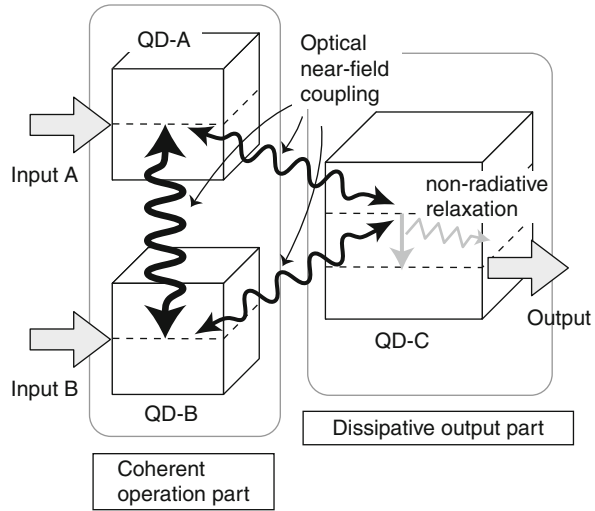
With further progress in nanofabrication techniques, any quantum dots will be aligned at desired positions, and thus, a highly integrated optical information processing device which consists of the nanophotonic switch can be realized. Furthermore, novel type of devices, which does not operate in a conventional way, should be proposed in the next stage. Our imagined form of such nanophotonic functional devices is composed by a quantum mechanical information processing part as well as a classical dissipative information processing part. In the next section, such type of nanophotonic devices, in which coherently coupled states due to several quantum dots are positively utilized, will be explained analytically. We expect that the reader will feel a large possibility in nanophotonics and future nanophotonic device technologies.

5.4 Nanophotonic Functional Devices Using Coherently Coupled States

As we mentioned in Sect. 5.1, characteristic coupled states via an optical near-field interaction can be generated in a system without dissipation, such as symmetric and antisymmetric states. These states extend two or more quantum systems with matter coherence as explained in Sect. 5.1.2 and have different energies in relation with the coupling strength of the optical near field. When we prepare another quantum system which interacts with these states, the energy difference affects resonant conditions of energy transfer via the optical near field. Therefore, the coherently coupled states can be utilized to pick up some information signal selectively.

In this section, we propose some nanophotonic functional devices, which consist of several quantum dots coupled via an optical near field. Such devices have two key operation parts: one is a *coherent operation part* or a quantum mechanical operation part and the other is a *dissipative output part* (see Fig. 5.4 in Sect. 5.1). As we mentioned in the previous sections, unidirectional energy transfer is indispensable in any functional devices for identification of a final state or an output signal, which can be guaranteed by using intra-sublevel relaxation due to exciton–phonon coupling. The dissipative output part includes such unidirectional irreversibility with the help of the energy sublevels in quantum dots. On the other hand, in the coherent operation part, an exciton excitation exists at the resonant energy levels in several quantum dots mediating the optical near field, where the coherently coupled states survive for a short period of time, before the excitation decays in the dissipative output part [42]. This section focuses on taking full advantage of these coherent operation parts and dissipative output parts to realize functional operations based on nanophotonic inherent features [43]. In the former part of this section, as a typical

Fig. 5.17 Illustration of a three-quantum-dot system that consists of two identical two-level dots (QD-A and QD-B) and a three-level dot (QD-C). Since the coupling between QD-A and QD-B is stronger than that between QD-A and QD-C (QD-B and QD-C), the system is divided into two parts: a coherent operation part with optical nutation, and a dissipative output part with non-radiative relaxation



example, we consider a three-quantum-dot system illustrated in Fig. 5.17. In this system, two identical quantum dots (QD-A and QD-B) are resonantly coupled with each other via an optical near field that consists of the coherent operation part, and a third quantum dot with larger size than the other two corresponds to the dissipative output part.

Various authors have investigated the coupling properties and dynamics in a pair of quantum dots. For example, the energy shift due to exciton–exciton or Coulomb interactions between electrons and holes has been evaluated theoretically to process quantum information [44, 45], and a controlled-NOT-logic gate has been proposed using the energy shift [46]. In these studies, excitons or qubits were controlled by two-color laser pulses of far-field light. As a similar subject to this section, Quiroga and Johnson [47] theoretically discussed the dynamics in two- and three-quantum-dot systems and presented a way to prepare both quantum Bell and Greenberger–Horne–Zeilinger entangled states, by using far-field light, which allows only global excitation of two and three quantum dots with spatially symmetric arrangement. By contrast, we deal with coupled quantum-dot systems arranged symmetrically and asymmetrically, which are individually excited by the optical near field, and the intra-sublevel relaxation is also considered for the unidirectional energy transfer. Note that the excitation in each quantum dot can be prepared individually owing to the spatial localization of the optical near field. The exciton dynamics driven by the optical near field has been investigated in the case of a coupled two-quantum-dot system with a relaxation process in Sect. 5.3.1. The energy transfer between two quantum dots is expressed as a Förster-like process [16], and the nutation of excitation occurs in the strongly coupled or resonant energy levels, corresponding to the coherent operation part in our system. For the short period before relaxation, certain coherently coupled states appear in the coherent operation part, depending on the initial excitation. In order to prepare

the initial excitation, the shorter excitation time in the individual quantum dot than the energy transfer time between two identical quantum dots is necessary, where the excitation time is inversely proportional to the optical near-field intensity. The energy transfer time or coupling strength via an optical near field can be controlled by adjusting interdot distance. The population in the coherently coupled states can be transferred to the third quantum dot (QD-C) if the energy level of QD-C is adjusted to couple resonantly with the entangled states in the coherent operation part. If this happens, QD-C operates as the dissipative output part, which involves an intra-sublevel relaxation process due to the exciton–phonon interaction. In this manner, unidirectional energy or signal transfer is satisfied.

This section is organized as follows. First of all, we formulate the simplest case of three-quantum-dot system by using the density matrix formalism in [Sect. 5.4.1](#). Here, to choose appropriate bases, which reflect symmetry of excited states, helps us to catch the physical meanings of the selective energy transfer, and also shows that the selective energy transfer can be controlled by adjusting spatial symmetry of quantum-dot arrangement. In [Sect. 5.4.2](#), we provide concrete AND- and XOR-logic operations in symmetrically arranged quantum-dot systems. Moreover, when the number of quantum dots, which form the coherent operation part, increases, the degrees of freedom for selective energy transfer are extended. As an example, we numerically demonstrate controlled-type logic operations in [Sect. 5.4.3](#), in which three identical quantum dots are utilized in the coherent operation part. Spatial symmetry is a key parameter in such a nanophotonic device using coherently coupled quantum dots because we can realize some strange operations mediating via so-called “dark state” [48]. [Section 5.4.4](#) devotes to propose a nanophotonic buffer memory by using a spatially asymmetric system, which is an extremely interesting device because the device controls dissipation into a far-field photon reservoir. Furthermore, we show a device for identification of quantum-entangled state in [Sect. 5.4.5](#). Note that these logic and functional operations are in the irreversible process, although quantum-entangled states are partially mediated to sort out information about initial excitations. This resembles quantum information processing; however, we do not require long coherence time as a quantum computation. In regard to quantum information processing with dissipation or decoherence, there are several reports that discussed tolerance and decoherence-free operations [49, 50].

5.4.1 Dynamics in a Coherently Coupled Quantum-Dot System

In order to examine, conditions of selective energy transfer from the coherent operation part to the dissipative output part, we derive analytic form of equations of motion in a simplest three-quantum-dot system, where two quantum dots are coherently coupled and a larger third quantum dot is assigned as the dissipative output part.

5.4.1.1 Symmetric and Antisymmetric States

Before a discussion about exciton population dynamics in a nanophotonic functional device using coherently coupled states, we explain several appropriate bases in a three-quantum-dot system, which reflect spatial symmetry among the three quantum dots. In such a system, we obtain a clear perspective of exciton dynamics by choosing the bases of the coupled states rather than those of isolated quantum-dot states which have been used in Sect. 5.3. From the symmetry of the system, the following bases are suitable for describing the dynamics of the one-exciton states using the smallest number of density matrix elements [51]:

$$|1\rangle_s = \frac{1}{\sqrt{2}}(|e\rangle_A|g\rangle_B|g, g\rangle_C + |g\rangle_A|e\rangle_B|g, g\rangle_C), \quad (5.65)$$

$$|1\rangle_a = \frac{1}{\sqrt{2}}(|e\rangle_A|g\rangle_B|g, g\rangle_C - |g\rangle_A|e\rangle_B|g, g\rangle_C), \quad (5.66)$$

$$|1\rangle_{ph} = |g\rangle_A|g\rangle_B|e, g\rangle_C, \quad (5.67)$$

$$|1\rangle_{pl} = |g\rangle_A|g\rangle_B|g, e\rangle_C, \quad (5.68)$$

where $|i, j\rangle_C$ ($i, j = g, e$) represents the isolated quantum-dot states in QD-C with upper energy level i and lower energy level j . One-exciton state describes the condition whereby an exciton exists in either one of the three quantum dots. The crystal ground state and exciton state in each quantum dot, which is written as $|\Phi_g^\alpha\rangle$ and $|\Phi_{m(1s)}^\alpha\rangle$ in Sect. 5.2, are given by simplified form, such as $|g\rangle_A$ and $|e\rangle_A$, respectively. Similarly, a *two-exciton state* indicates that two excitons stay in the system. The suitable bases for the two-exciton states without occupation of the lower energy level in QD-C are expressed as

$$|2\rangle_{sh} = \frac{1}{\sqrt{2}}(|e\rangle_A|g\rangle_B|e, g\rangle_C + |g\rangle_A|e\rangle_B|e, g\rangle_C), \quad (5.69)$$

$$|2\rangle_{ah} = \frac{1}{\sqrt{2}}(|e\rangle_A|g\rangle_B|e, g\rangle_C - |g\rangle_A|e\rangle_B|e, g\rangle_C), \quad (5.70)$$

$$|2\rangle_{ph} = |e\rangle_A|e\rangle_B|g, g\rangle, \quad (5.71)$$

and those with occupation of the lower energy level are expressed as

$$|2\rangle_{sl} = \frac{1}{\sqrt{2}}(|e\rangle_A|g\rangle_B|g, e\rangle_C + |g\rangle_A|e\rangle_B|g, e\rangle_C), \quad (5.72)$$

$$|2\rangle_{al} = \frac{1}{\sqrt{2}}(|e\rangle_A|g\rangle_B|g, e\rangle_C - |g\rangle_A|e\rangle_B|g, e\rangle_C), \quad (5.73)$$

$$|2\rangle_{pl} = |g\rangle_A|g\rangle_B|e, e\rangle, \quad (5.74)$$

where $|n\rangle_s$ and $|n\rangle_a$ ($n = 1, 2$) represent symmetric and antisymmetric states in the coherent operation part, respectively, and the numbers 1 and 2 on the left-hand sides in (5.65), (5.69), and (5.72) denote the one- and two-exciton states, respectively. In the following, first, we use these bases to investigate the exciton dynamics in a symmetrically arranged three-quantum-dot system. Then, we describe how to realize logic operation devices by using the symmetrically arranged quantum dots. Our discussion can expand into some interesting functional devices using spatial asymmetry of the system, which can be caught by the above characteristic bases.

5.4.1.2 Master Equation

By tracing out the photon degrees of freedom in the optical near-field coupling, which is formulated in Sect. 5.2, a model Hamiltonian for the three-quantum-dot system \hat{H} is given by

$$\hat{H} = \hat{H}_0 + \hat{H}_{\text{int}}, \quad (5.75)$$

where

$$\hat{H}_0 = \hbar\Omega_A \hat{A}^\dagger \hat{A} + \hbar\Omega_B \hat{B}^\dagger \hat{B} + \hbar \sum_{i=1}^2 \Omega_{C_i} \hat{C}_i^\dagger \hat{C}_i, \quad (5.76)$$

$$\begin{aligned} \hat{H}_{\text{int}} = & \hbar U_{AB} (\hat{A}^\dagger \hat{B} + \hat{B}^\dagger \hat{A}) \\ & + \hbar U_{BC} (\hat{B}^\dagger \hat{C}_2 + \hat{C}_2^\dagger \hat{B}) + \hbar U_{CA} (\hat{C}_2^\dagger \hat{A} + \hat{A}^\dagger \hat{C}_2), \end{aligned} \quad (5.77)$$

where the definitions of the creation and annihilation operators, $(\hat{A}^\dagger, \hat{A})$, $(\hat{B}^\dagger, \hat{B})$, and $(\hat{C}_i^\dagger, \hat{C}_i)$, are shown schematically in Fig. 5.18. We assume that these are fermionic operators to give the effect of exciton–exciton interaction phenomenologically in the same energy level, but we neglect the exciton–exciton interaction between sublevels in QD-C. The eigenfrequencies for QD-A and QD-B are represented by Ω_A and Ω_B , and the optical near-field couplings among three quantum dots are denoted as U_{AB} , U_{BC} , and U_{CA} . The equation of motion for the density operator of the quantum-dot system, $\hat{\rho}(t)$, is expressed by using the Born–Markov approximation [36] as

$$\begin{aligned} \dot{\hat{\rho}}(t) = & -\frac{i}{\hbar} [\hat{H}_0 + \hat{H}_{\text{int}}, \hat{\rho}(t)] \\ & + \frac{\Gamma}{2} \left\{ 2\hat{C}_1^\dagger \hat{C}_2 \hat{\rho}(t) \hat{C}_2^\dagger \hat{C}_1 - \hat{C}_2^\dagger \hat{C}_1 \hat{C}_1^\dagger \hat{C}_2 \hat{\rho}(t) - \hat{\rho}(t) \hat{C}_2^\dagger \hat{C}_1 \hat{C}_1^\dagger \hat{C}_2 \right\}, \end{aligned} \quad (5.78)$$

where the non-radiative relaxation constant due to exciton–phonon coupling is denoted as Γ . The radiative relaxation due to exciton–photon coupling is omitted because the time scale of the optical near-field coupling and the exciton–phonon coupling is much faster than the radiative lifetime, which is in the order of a few nanoseconds. Taking matrix elements of (5.78) in terms of (5.65) after substituting (5.75) and (5.76) into (5.78), we obtain the following simultaneous

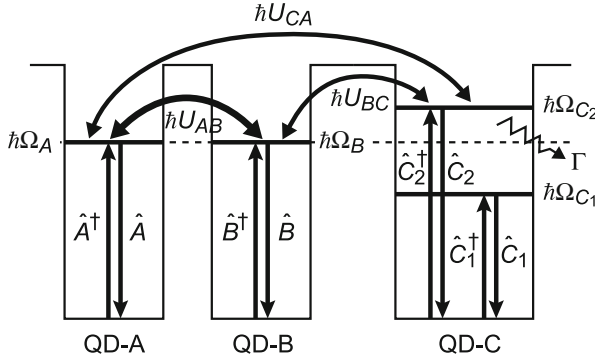


Fig. 5.18 Schematic drawing of exciton creation and annihilation operators and the energy transfer process in a three-quantum-dot system. The optical near-field coupling for the quantum-dot pairs are represented by U_{AB} for QD-A and B, U_{BC} for QD-B and C, and U_{CA} for QD-C and A. The non-radiative relaxation constant due to exciton-phonon coupling is denoted by Γ

differential equations for the one-exciton states:

$$\begin{aligned} \dot{\rho}_{s_1, s_1}(t) &= i\sqrt{2}\bar{U}'(\rho_{s_1, \text{ph}_1}(t) - \rho_{\text{ph}_1, s_1}(t)) \\ &\quad + i\Delta\Omega_{AB}(\rho_{s_1, a_1}(t) - \rho_{a_1, s_1}(t)), \end{aligned} \quad (5.79)$$

$$\begin{aligned} \dot{\rho}_{s_1, \text{ph}_1}(t) &= \left\{ i(\Delta\Omega - U) - \frac{\Gamma}{2} \right\} \rho_{s_1, \text{ph}_1}(t) \\ &\quad + i\sqrt{2}\bar{U}'(\rho_{s_1, s_1}(t) - \rho_{\text{ph}_1, \text{ph}_1}(t)) \\ &\quad - i\sqrt{2}\Delta U' \rho_{s_1, a_1}(t) - i\Delta\Omega_{AB} \rho_{a_1, p'_1}(t), \end{aligned} \quad (5.80)$$

$$\begin{aligned} \dot{\rho}_{\text{ph}_1, s_1}(t) &= \left\{ -i(\Delta\Omega - U) - \frac{\Gamma}{2} \right\} \rho_{\text{ph}_1, s_1}(t) \\ &\quad - i\sqrt{2}\bar{U}'(\rho_{s_1, s_1}(t) - \rho_{\text{ph}_1, \text{ph}_1}(t)) \\ &\quad + i\sqrt{2}\Delta U' \rho_{a_1, s_1}(t) + i\Delta\Omega_{AB} \rho_{p'_1, a_1}(t), \end{aligned} \quad (5.81)$$

$$\begin{aligned} \dot{\rho}_{\text{ph}_1, \text{ph}_1}(t) &= -\Gamma \rho_{\text{ph}_1, \text{ph}_1}(t) - i\sqrt{2}\bar{U}'(\rho_{s_1, \text{ph}_1}(t) - \rho_{\text{ph}_1, s_1}(t)) \\ &\quad - i\Delta U'(\rho_{\text{ph}_1, a_1}(t) - \rho_{a_1, \text{ph}_1}(t)), \end{aligned} \quad (5.82)$$

$$\begin{aligned} \dot{\rho}_{a_1, \text{ph}_1}(t) &= \left\{ i(\Delta\Omega + U) - \frac{\Gamma}{2} \right\} \rho_{a_1, \text{ph}_1}(t) \\ &\quad - i\sqrt{2}\Delta U'(\rho_{a_1, a_1}(t) - \rho_{\text{ph}_1, \text{ph}_1}(t)) \end{aligned}$$

$$+i\sqrt{2}\bar{U}'\rho_{a_1,s_1}(t) - i\Delta\Omega_{AB}\rho_{s_1,p'_1}(t), \quad (5.83)$$

$$\begin{aligned} \dot{\rho}_{ph_1,a_1}(t) &= \left\{ -i(\Delta\Omega + U) - \frac{\Gamma}{2} \right\} \rho_{ph_1,a_1}(t) \\ &+ i\sqrt{2}\Delta U'(\rho_{a_1,a_1}(t) - \rho_{ph_1,ph_1}(t)) \\ &- i\sqrt{2}\bar{U}'\rho_{s_1,a_1}(t) + i\Delta\Omega_{AB}\rho_{ph_1,s_1}(t), \end{aligned} \quad (5.84)$$

$$\begin{aligned} \dot{\rho}_{s_1,a_1}(t) &= -i2U\rho_{s_1,a_1}(t) - i\sqrt{2}\bar{U}'\rho_{p'_1,a_1}(t) - i\sqrt{2}\Delta U'\rho_{s_1,ph_1}(t) \\ &+ i\Delta\Omega_{AB}(\rho_{s_1,s_1}(t) - \rho_{a_1,a_1}(t)), \end{aligned} \quad (5.85)$$

$$\begin{aligned} \dot{\rho}_{a_1,s_1}(t) &= i2U\rho_{a_1,s_1}(t) + i\sqrt{2}\bar{U}'\rho_{a_1,ph_1}(t) + i\sqrt{2}\Delta U'\rho_{ph_1,s_1}(t) \\ &- i\Delta\Omega_{AB}(\rho_{s_1,s_1}(t) - \rho_{a_1,a_1}(t)), \end{aligned} \quad (5.86)$$

$$\begin{aligned} \dot{\rho}_{a_1,a_1}(t) &= i\sqrt{2}\Delta U'(\rho_{ph_1,a_1}(t) - \rho_{a_1,ph_1}(t)) \\ &- i\Delta\Omega_{AB}(\rho_{s_1,a_1}(t) - \rho_{a_1,s_1}(t)), \end{aligned} \quad (5.87)$$

where the density matrix element ${}_{\alpha}\langle n|\hat{\rho}(t)|n\rangle_{\beta}$ is abbreviated $\rho_{\alpha n, \beta n}(t)$ and the parameters, which have a dimension of frequency and characterize the dynamics in this system, are defined as $\Delta\Omega = \Omega_{C_2} - (\Omega_A + \Omega_B)/2$, $\Delta\Omega_{AB} = \Omega_A - \Omega_B$, $\bar{U}' = (U_{BC} + U_{CA})/2$, and $\Delta U' = (U_{BC} - U_{CA})/2$. The optical near-field coupling between QD-A and QD-B, which is in a coherent operation part, is rewritten as $U = U_{AB}$. Similarly, in the case of two-exciton states described in (5.69), we obtain

$$\begin{aligned} \dot{\rho}_{sh_2,sh_2}(t) &= -\Gamma\rho_{sh_2,sh_2}(t) + i\sqrt{2}\bar{U}'(\rho_{sh_2,ph_2}(t) - \rho_{ph_2,sh_2}(t)) \\ &+ i\Delta\Omega_{AB}(\rho_{sh_2,ah_2}(t) - \rho_{ah_2,sh_2}(t)), \end{aligned} \quad (5.88)$$

$$\begin{aligned} \dot{\rho}_{sh_2,ph_2}(t) &= \left\{ -i(\Delta\Omega + U) - \frac{\Gamma}{2} \right\} \rho_{sh_2,ph_2}(t) \\ &+ i\sqrt{2}\bar{U}'(\rho_{sh_2,sh_2}(t) - \rho_{ph_2,ph_2}(t)) \\ &+ i\sqrt{2}\Delta U'\rho_{sh_2,ah_2}(t) - i\Delta\Omega_{AB}\rho_{ah_2,ph_2}(t), \end{aligned} \quad (5.89)$$

$$\begin{aligned} \dot{\rho}_{ph_2,sh_2}(t) &= \left\{ i(\Delta\Omega + U) - \frac{\Gamma}{2} \right\} \rho_{ph_2,sh_2}(t) \\ &- i\sqrt{2}\bar{U}'(\rho_{sh_2,sh_2}(t) - \rho_{ph_2,ph_2}(t)) \\ &- i\sqrt{2}\Delta U'\rho_{ah_2,sh_2}(t) + i\Delta\Omega_{AB}\rho_{ph_2,ah_2}(t), \end{aligned} \quad (5.90)$$

$$\begin{aligned} \dot{\rho}_{ph_2,ph_2}(t) &= -i\sqrt{2}\bar{U}'(\rho_{sh_2,ph_2}(t) - \rho_{ph_2,sh_2}(t)) \\ &+ i\sqrt{2}\Delta U'(\rho_{ph_2,ah_2}(t) - \rho_{ah_2,ph_2}(t)), \end{aligned} \quad (5.91)$$

$$\begin{aligned} \dot{\rho}_{\text{ah}_2, \text{ph}_2}(t) = & \left\{ -i(\Delta\Omega - U) - \frac{\Gamma}{2} \right\} \rho_{\text{ah}_2, \text{ph}_2}(t) \\ & + i\sqrt{2}\Delta U'(\rho_{\text{ah}_2, \text{ah}_2}(t) - \rho_{\text{ph}_2, \text{ph}_2}(t)) \\ & + i\sqrt{2}\bar{U}'\rho_{\text{ah}_2, \text{sh}_2}(t) - i\Delta\Omega_{\text{AB}}\rho_{\text{sh}_2, \text{ph}_2}(t) , \end{aligned} \quad (5.92)$$

$$\begin{aligned} \dot{\rho}_{\text{ph}_2, \text{ah}_2}(t) = & \left\{ i(\Delta\Omega - U) - \frac{\Gamma}{2} \right\} \rho_{\text{ph}_2, \text{ah}_2}(t) \\ & - i\sqrt{2}\Delta U'(\rho_{\text{ah}_2, \text{ah}_2}(t) - \rho_{\text{ph}_2, \text{ph}_2}(t)) \\ & - i\sqrt{2}\bar{U}'\rho_{\text{sh}_2, \text{ah}_2}(t) + i\Delta\Omega_{\text{AB}}\rho_{\text{ph}_2, \text{sh}_2}(t) , \end{aligned} \quad (5.93)$$

$$\begin{aligned} \dot{\rho}_{\text{sh}_2, \text{ah}_2}(t) = & (-i2U - \Gamma)\rho_{\text{sh}_2, \text{ah}_2}(t) \\ & - i\sqrt{2}\bar{U}'\rho_{\text{ph}_2, \text{ah}_2}(t) + i\sqrt{2}\Delta U'\rho_{\text{sh}_2, \text{ph}_2}(t) \\ & + i\Delta\Omega_{\text{AB}}(\rho_{\text{sh}_2, \text{sh}_2}(t) - \rho_{\text{ah}_2, \text{ah}_2}(t)) , \end{aligned} \quad (5.94)$$

$$\begin{aligned} \dot{\rho}_{\text{ah}_2, \text{sh}_2}(t) = & (i2U - \Gamma)\rho_{\text{ah}_2, \text{sh}_2}(t) \\ & + i\sqrt{2}\bar{U}'\rho_{\text{ah}_2, \text{ph}_2}(t) - i\sqrt{2}\Delta U'\rho_{\text{ph}_2, \text{sh}_2}(t) \\ & - i\Delta\Omega_{\text{AB}}(\rho_{\text{sh}_2, \text{sh}_2}(t) - \rho_{\text{ah}_2, \text{ah}_2}(t)) , \end{aligned} \quad (5.95)$$

$$\begin{aligned} \dot{\rho}_{\text{ah}_2, \text{ah}_2}(t) = & -\Gamma\rho_{\text{ah}_2, \text{ah}_2}(t) - i\sqrt{2}\Delta U'(\rho_{\text{ph}_2, \text{ah}_2}(t) - \rho_{\text{ah}_2, \text{ph}_2}(t)) \\ & - i\Delta\Omega_{\text{AB}}(\rho_{\text{sh}_2, \text{ah}_2}(t) - \rho_{\text{ah}_2, \text{sh}_2}(t)) . \end{aligned} \quad (5.96)$$

From (5.79) and (5.88), we can attract three important features with regard to energy transfer from the coherent operation part to the dissipative output part. Comparing (5.80) with (5.83), where the diagonal elements represent the transition probability, opposite contributions appear in the first terms, that is, $\Delta\Omega - U$ and $\Delta\Omega + U$. These correspond to the difference of resonance conditions for symmetric and antisymmetric states, respectively. The resonance conditions are easily interpreted by considering the energies for the symmetric and antisymmetric states, which can be derived from (5.75) and (5.76) as

$$\langle s_1 | \hat{H} | s_1 \rangle = \hbar(\bar{\Omega}_{\text{AB}} + U) , \quad (5.97)$$

$$\langle a_1 | \hat{H} | a_1 \rangle = \hbar(\bar{\Omega}_{\text{AB}} - U) , \quad (5.98)$$

where $\bar{\Omega}_{\text{AB}} = (\Omega_{\text{A}} + \Omega_{\text{B}})/2$. Figure 5.19a is the schematic illustration that explains relation between isolated quantum-dot states and coherently coupled states. A filled circle indicates that an exciton occupies the corresponding energy level, while a semicircle indicates that an exciton exists in the energy level in either QD-A or QD-B with a certain probability. The first feature is that we can select the symmetric and antisymmetric states by adjusting the energy level in QD-C, where the energy shift $\Delta\Omega$ is determined by the strength of the optical near-field coupling U .

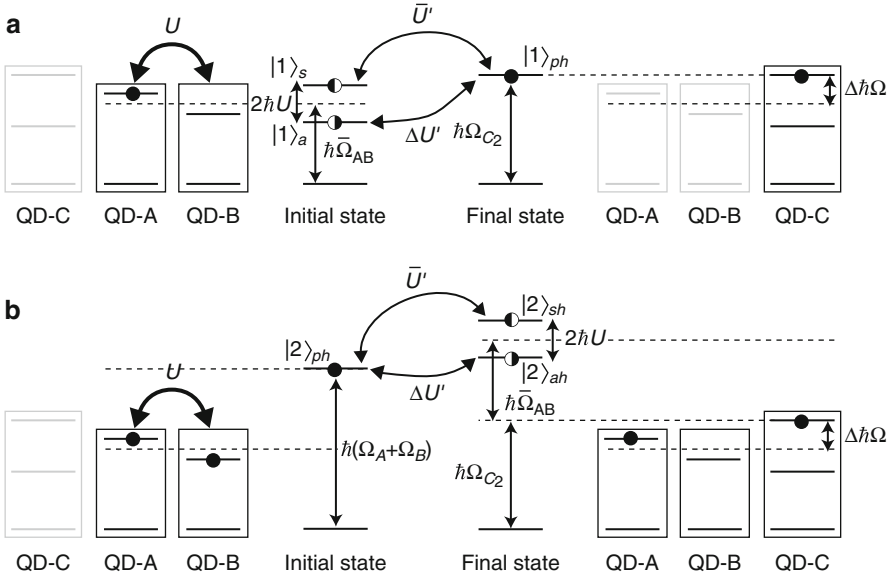


Fig. 5.19 Schematic explanation of a relation between isolated quantum-dot states and coupled states for (a) one- and (b) two-exciton states. The *left* and *right* illustrations represent the initial and final states, respectively, and the center figures denote the coupled states for input and output. The energy transfer between symmetric states $|n\rangle_s$ and output states $|n\rangle_{ph}$, where $n = 1, 2$, occurs via coupling strength $\hbar U'$ and that between asymmetric states $|n\rangle_a$ and output states $|n\rangle_{ph}$ does via $\hbar \Delta U'$

The second feature is also observed from the second terms in (5.80) and (5.83). These terms determine the strength or the speed of resonant energy transfer between the coherent operation part and dissipative output part. The difference is as follows: the symmetric state resonantly couples to the upper energy level in QD-C, that is, $|1\rangle_{ph}$ -state, by mediating the averaged coupling strength \bar{U}' , while the antisymmetric state does by mediating the difference between two coupling paths, $\Delta U'$. When the three quantum dots are arranged symmetrically in nanometric space, the energy transfer between $|1\rangle_a$ -state and $|1\rangle_{ph}$ -state is forbidden because of $\Delta U' = 0$, in other words, ${}_{ph}\langle 1|\hat{H}_{int}|1\rangle_a = 0$. Therefore, we can control the energy transfer or signal flow by using spatial symmetry in the system.

The third feature is related to the exciton numbers in the system, which is interpreted by comparing (5.80) and (5.89), or (5.83) and (5.92). Similar to the first feature, the resonance conditions for the energy transfer from the coherent operation part to the dissipative output part indicate opposite contribution, that is, $\Delta\Omega - U$ and $\Delta\Omega U$ for one- and two-exciton states, respectively. In Fig. 5.19b, the correspondence of isolated quantum-dot states and coupled states are schematically drawn, where we can see the inversion of the resonance conditions. The difference of the resonance conditions is applicable to two input logic operations discussed below.

Note that the first two features, which are discussed for only one-exciton state, are reversed in the case of two-exciton state as you observed in (5.88).

5.4.2 Nanophotonic Logic Gates

In order to realize well-known AND- and XOR-logic operations, we assume spatially symmetric quantum-dot system, and thus, the related differential equations in (5.79) and (5.88) are restricted, which decouples the antisymmetric $|1\rangle_a$ - and $|2\rangle_a$ -states from the above. In this case, the dynamics can be solved analytically with the help of Laplace transforms for typical initial conditions. The output population for the one-exciton state can be written as

$$\begin{aligned}\rho_{p1,p1}(t) &= \Gamma \int_0^t \rho_{ph_1,ph_1}(t') dt' \\ &= \frac{1}{2} + \frac{4U'^2}{\omega_+^2 - \omega_-^2} e^{-(\Gamma/2)t} \\ &\quad \times \{\cos \phi_+ \cos(\omega_+ t + \phi_+) - \cos \phi_- \cos(\omega_- t + \phi_-)\} \quad (5.99)\end{aligned}$$

with

$$\begin{aligned}\omega_{\pm} &= \frac{1}{\sqrt{2}} \left[(\Delta\Omega - U)^2 + W_+ W_- \right. \\ &\quad \left. \pm \sqrt{\{(\Delta\Omega - U)^2 + W_+^2\} \{(\Delta\Omega - U)^2 + W_-^2\}} \right]^{1/2}, \\ \phi_{\pm} &= \tan^{-1} \left(\frac{2\omega_{\pm}}{\Gamma} \right), \\ W_{\pm} &= 2\sqrt{2}U' \pm \frac{\Gamma}{2}, \quad (5.100)\end{aligned}$$

for the initial condition $\rho_{s_1,s_1}(0) = \rho_{a_1,a_1}(0) = \rho_{s_1,a_1}(0) = \rho_{a_1,s_1}(0) = 1/2$, which corresponds to the condition ${}_A\langle e|_B\langle g|_C\langle g, g|\hat{\rho}(t)|e\rangle_A|g\rangle_B|g, g\rangle_C = 1$ and otherwise zero. The notation of optical near-field coupling is rewritten as $U' = \bar{U}'$ because the coupling strengths between QD-B and QD-C, and QD-C and QD-A are equivalent for symmetrically arranged system, that is, $U' = U_{BC} = U_{CA}$. The first line in (5.99) denotes the irreversible process of non-radiative relaxation, which is easily interpreted from the temporal sequence of the one-exciton state illustrated in Fig. 5.20a.

Analytic solutions for two-exciton states can be obtained from an equation similar to (5.99), except for the sign of U , that is, with the resonance conditions inverted. The probability of an exciton occupying the lower energy level in QD-C is

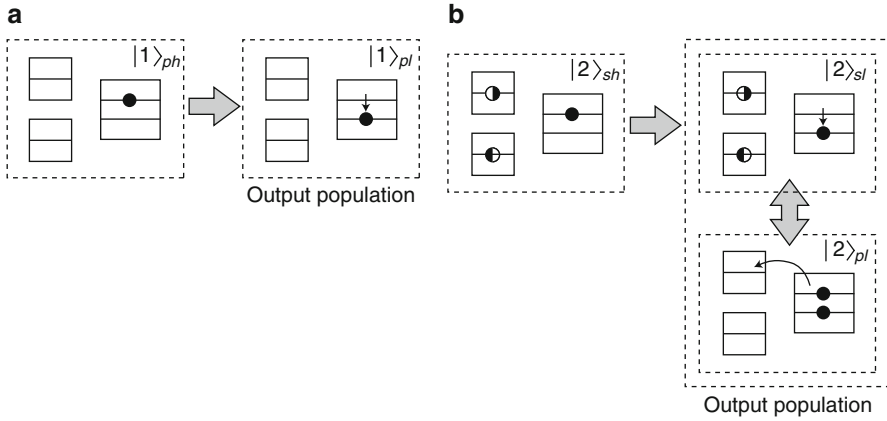


Fig. 5.20 Schematic illustration of temporal sequences at the final output stages in the cases of (a) one-exciton state and (b) two-exciton state

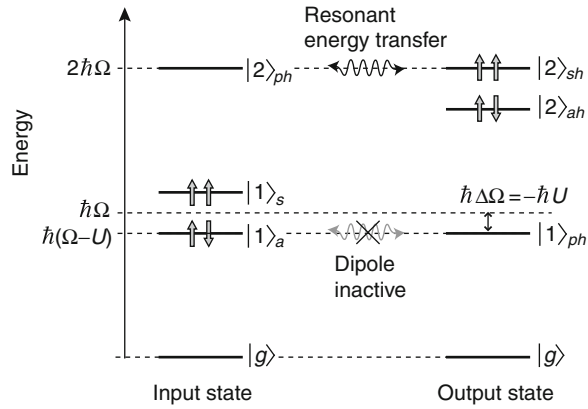
$$\begin{aligned}
 & \rho_{sl_2,sl_2}(t) + \rho_{pl_2,pl_2}(t)\Gamma \int_0^t \rho_{sh_2,sh_2}(t')dt' \\
 &= 2 \left[\frac{1}{2} + \frac{4U'^2}{\omega'_+{}^2 - \omega'_-{}^2} e^{-(\Gamma/2)t} \right. \\
 & \quad \left. \times \{ \cos \phi'_+ \cos(\omega'_+ t + \phi'_+) - \cos \phi'_- \cos(\omega'_- t + \phi'_-) \} \right] \quad (5.101)
 \end{aligned}$$

with

$$\begin{aligned}
 \omega'_\pm &= \frac{1}{\sqrt{2}} \left[(\Delta\Omega + U)^2 + W_+ W_- \right. \\
 & \quad \left. \pm \sqrt{\{(\Delta\Omega + U)^2 + W_+^2\} \{(\Delta\Omega + U)^2 + W_-^2\}} \right]^{1/2}, \\
 \phi'_\pm &= \tan^{-1} \left(\frac{2\omega'_\pm}{\Gamma} \right), \quad (5.102)
 \end{aligned}$$

where the factor 2 in (5.101) comes from the initial conditions for the two-exciton state, that is, $\rho_{ph_2,ph_2}(0) = 1$ and otherwise zero. As you can see from the right-hand side in the first line in (5.101), there are two final output states: $|2\rangle_{sl}$ and $|2\rangle_{pl}$. However, the previous excited state, $|2\rangle_{sh}$, only contributes to the output population, because the state $|2\rangle_{pl}$ is made from $|2\rangle_{sl}$, and thus, the total population does not change, which is illustrated in Fig. 5.20b. In both of (5.99) and (5.101), the second terms with the denominators $\omega_+^2 - \omega_-^2$ and $\omega'_+{}^2 - \omega'_-{}^2$, respectively, contribute to the increase of population in the output energy levels. When we set

Fig. 5.21 Energy diagram in a coupled three-quantum-dot system with negative energy detuning in QD-C



$\Delta\Omega = U$, efficiency of energy transfer is dominant for the one-exciton state because $\omega_+^2 - \omega_-^2$ becomes minimum, while that is dominant for the two-exciton state in the case of $\Delta\Omega = -U$. These are analytical descriptions of resonant energy transfer depending on the number of input excitons and a basic idea for logic operation. In the following, we explain AND- and XOR-logic operations schematically and show concrete calculated results of them.

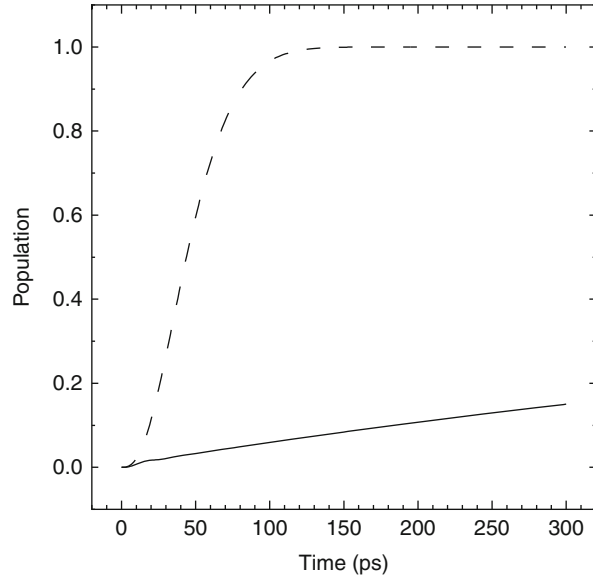
5.4.2.1 AND-Logic Operation

When the upper energy level in QD-C is negatively shifted, which corresponds to $\hbar(\Omega - U)$, we can realize an AND-logic gate. Figure 5.21 represents energy diagram in the system with negative detuning in QD-C. As you can see from Fig. 5.21a, the resonant energy transfer occurs only for the two-exciton state via the symmetric state in QD-A and QD-B, while the energy transfer for the one-exciton state does not because the energy level in QD-C is resonant to the antisymmetric state which is dipole-inactive state for the symmetrically arranged quantum-dot system. This characteristic selective energy transfer assures an AND-logic operation.

The temporal evolution of the exciton population on the lower energy level in QD-C, which is analytically derived in (5.99) and (5.101), is plotted in Fig. 5.22, where the strengths of optical near-field coupling, $\hbar U = 89 \mu\text{eV}$ and $\hbar U' = 14 \mu\text{eV}$, referred to the estimated values in Sect. 5.2 for CuCl quantum cubes embedded in NaCl matrix. As we discussed above, the coupling to far-field light is neglected because our interests are fast population dynamics due to the optical near-field coupling, which is in the order of sub-100 ps. In Fig. 5.22, the exciton population is almost occupied at about 100 ps for the two-exciton state, which is determined by the coupling strength $\hbar U'$ between QD-A and QD-C (QD-B and QD-C). The negative energy shift is also set as $89 \mu\text{eV}$, and the non-radiative relaxation is 10 ps.

From Fig. 5.22, the output population can be observed only for the two-exciton state as we expected, because the coupling occurs via the symmetric state. On the other hand, in the case of the one-exciton state, the population increases very slowly. This is caused by the weak coupling between the symmetric state in the input side

Fig. 5.22 Temporal evolution of exciton population on the lower energy level (output level) in QD-C. The *solid* and *dashed* curves represent the cases for one- and two-exciton states, respectively. The coupling strength between QD-A and QD-B is set as $\hbar U = 89 \mu\text{eV}$, and that between QD-B and QD-C (QD-A and QD-C) is $U' = 14 \mu\text{eV}$



and the output state. The state-filling time is much longer than spontaneous emission lifetime, and thus, the exciton population for the one-exciton state does not affect the output signal, that is, off-level. In this manner, these operations for the one- and two-exciton states surely correspond to the AND-logic gate whose size is much smaller than light diffraction limits.

5.4.2.2 XOR-Logic Operation

Opposite to the AND-logic gate, suppose a system in which the upper energy level in QD-C is positively shifted, that is, $\hbar(\Omega + U)$. Energy diagram in this system is illustrated in Fig. 5.23. In this case, the symmetric and antisymmetric states for one and two excitons satisfy the conditions for an XOR-logic gate. The energy transfer from the input system to the output system allows when an exciton is excited in either QD-A or QD-B, while, for the two-exciton state, the antisymmetric state in the output system is dipole inactive against the input state in the symmetrically arranged quantum-dot system.

Figure 5.24 shows analytic curves of the temporal evolution for the one- and two-exciton states. The given parameters, such as the coupling strength via the optical near-field, non-radiative relaxation time, are completely the same as those in Fig. 5.22. In Fig. 5.24, the output population appears for the one-exciton state, and the state-filling time is determined by the coupling strength U' between QD-A and QD-C (QD-B and QD-C), which is the same as the AND-logic gate. The readers immediately put the question why the exciton population reaches a half of the maximum for the one-exciton state in the XOR-logic gate. This is because a one-side quantum dot is locally excited as an initial condition, in which both the symmetric and antisymmetric states are simultaneously excited with the same

Fig. 5.23 Energy diagram in a coupled three-quantum-dot system with positive energy detuning in QD-C

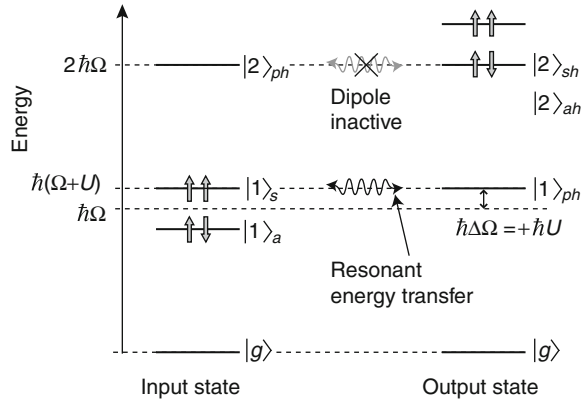
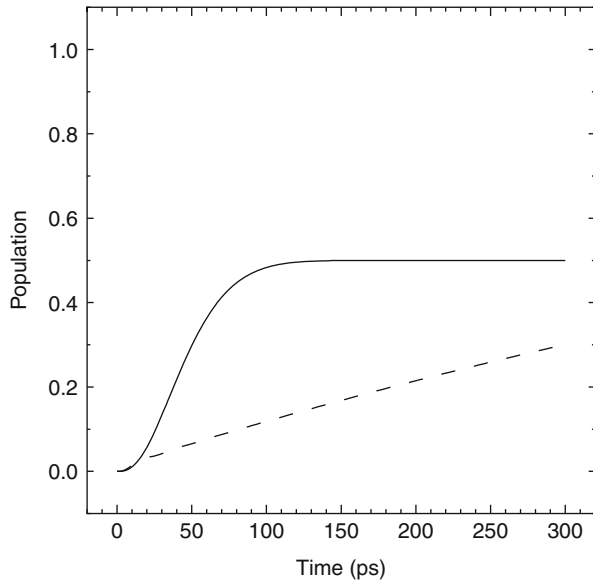


Fig. 5.24 Temporal evolution of exciton population on the lower energy level (output level) in QD-C. The *solid* and *dashed* curves represent the cases for one- and two-exciton states, respectively. The coupling strength between QD-A and QD-B is set as $U = 89 \mu\text{eV}$, and that between QD-B and QD-C (QD-A and QD-C) is $U' = 14 \mu\text{eV}$



occupation probability as described in (5.65) and (5.66). On the other hand, we can observe slow increase of exciton population for the two-exciton state (off-level) in Fig. 5.22, which is as twice fast as that for the AND-logic gate. This also originates from the initial excited state; the symmetric state in the input system is occupied a half of the maximum at the initial time because of local excitation, while a full of the initial population for the two-exciton state can couple to QD-C in the case of positive energy shift.

The above behavior that the output population is detected when a one-side quantum dot in the input system is initially excited corresponds to an XOR-logic gate as a stochastic meaning. This means that the fully occupied output state cannot achieve for a single-exciton process.

Table 5.1 Relationship between the input and output populations for the energy difference $\Delta\Omega = \pm U$

Input		Output: C	
A	B	$\Delta\Omega = -U$	$\Delta\Omega = U$
0	0	0	0
1	0	0	0.5
0	1	0	0.5
1	1	1	0

Here, we summarize the operation of our proposed AND- and XOR-logic gates in [Table 5.1](#), which are inherent operations in nanophotonic devices using typical coherent and dissipative process. The system behaves as an AND-logic gate when the energy difference is set to $\Delta\Omega = -U$, and the system provides an XOR-like-logic operation when $\Delta\Omega = U$. It is noteworthy that these operations are different from the quantum logic operation, because long quantum coherence time is unnecessary. The critical limit of these logic gates is determined by the following condition; the energy transfer time from the coherent operation part to the dissipative output part, which is estimated about 50 ps for the CuCl quantum-cube system, is enough shorter than the radiative lifetime (~ 1 ns) of excitons in each quantum dot.

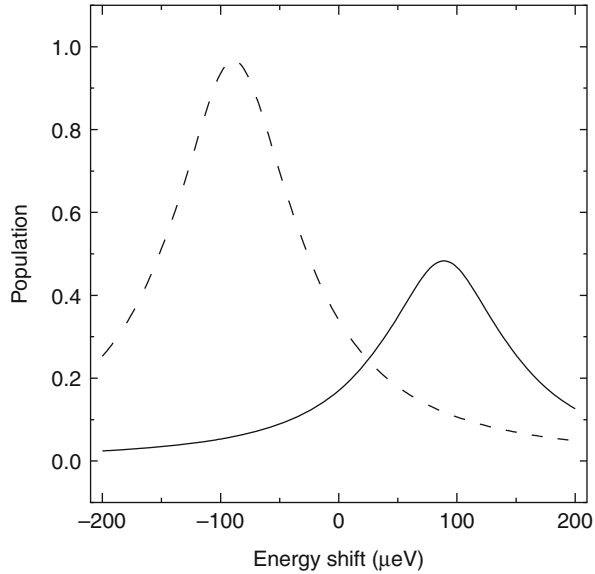
5.4.2.3 Signal Contrast

The steepness of the resonance determines the contrast of the output signal. In order to discuss how to obtain high contrast signal, dependence of the exciton population on the energy shift $\Delta\Omega$ in the above symmetrically arranged quantum-dot system is plotted in [Fig. 5.25](#). The longitudinal axis is the population at $t = 100$ ps, which is the time until energy transfer almost finishes under resonance conditions $\Delta\Omega = \pm U$ and is analytically derived from [\(5.99\)](#) and [\(5.101\)](#). We clearly find that two types of switching operations, that is, AND- and XOR-logic operations, can be realized by choosing the energy shift as $\Delta\Omega = \pm U$. Here, the peak width of both curves in [Fig. 5.25](#) is given by the product $W_+ W_-$ in [\(5.100\)](#) or [\(5.102\)](#), which corresponds to a balance between the coupling strength U' between the coherent operation part and the dissipative output part and the non-radiative relaxation constant Γ . Therefore, narrow peaks are obtained when the conditions $W \ll 1$ and $W_- = 0$, that is, $2\sqrt{2}U' \sim \Gamma/2 \ll 1$, are satisfied. In this case, the highest contrast of the logic operations can be achieved.

5.4.2.4 Effects of Asymmetry

It is valuable to examine the exciton dynamics in an asymmetrically arranged quantum-dot system to estimate the fabrication tolerance for the system described above and to propose further functional operations inherent to nanophotonic devices which we will be discussed in [Sects. 5.4.4](#) and [5.4.5](#). Here, we investigate the effects of asymmetry numerically. In addition, we comment on a positive use of these effects. When the three quantum dots are arranged asymmetrically, we must consider the dynamics of all density matrix elements given in [\(5.79\)](#) and [\(5.88\)](#), because the exciton population leaks to the antisymmetric states, which decouples

Fig. 5.25 Variation in the output populations at a fixed time of $t = 100$ ps as a function of the energy shift $\Delta\Omega$. The *solid* and *dashed* curves represent the one- and two-exciton states, respectively. The optical near-field coupling strengths $\hbar U$ and $\hbar U'$, and the non-radiative relaxation constant Γ have the same values as in Fig. 5.22



in the case of symmetrically arranged system. In the asymmetrically arranged system, the exciton dynamics between states $|n\rangle_s$ and $|n\rangle_{ph}$ do not change from the symmetrically arranged system, where the coupling strength is replaced by the average value \bar{U}' . The main difference is that the matrix elements for states $|n\rangle_a$ can couple with states $|n\rangle_s$ and $|n\rangle_{ph}$ in the asymmetrically arranged system, while these are decoupled in the symmetrically arranged system. Two types of coupling emerge in the asymmetric system: one originates from the energy difference $\Delta\Omega_{AB}$ between QD-A and QD-B, and the other comes from the arrangement of the three quantum dots, which is expressed using the parameter $\Delta U'$. Previously [17], we discussed the influence of the energy difference on the exciton dynamics in a two-quantum-dot system that mainly degrades the signal contrast. Here, we focus on the effects of asymmetry due to the spatial arrangement of each quantum dot, by assuming $\Delta\Omega_{AB} = 0$.

In order to examine the effects of the quantum-dot arrangement, the average coupling strength \bar{U}' is fixed so that states $|n\rangle_s$ and $|n\rangle_{ph}$ maintain the same temporal evolution that was found in the symmetrically arranged system. Then, the difference between the coupling strengths $\Delta U'$ varies from 0 to $\pm U$, where the exciton dynamics are independent of the sign of $\Delta U'$. Therefore, an asymmetry factor is defined by the ratio of $|\Delta U'|$ to \bar{U}' , varying from 0 (symmetry) to 1 (maximum amount of asymmetry).

Figure 5.26 presents the temporal evolution of the output population for the energy shift $\Delta\Omega = -U$ (an AND-logic gate case) with and without an asymmetric arrangement. For the one-exciton state (Fig. 5.26a), the asymmetric arrangement strongly affects the exciton dynamics, and the off-state in the AND-logic gate operation is no longer valid because the off-resonance condition for the energy

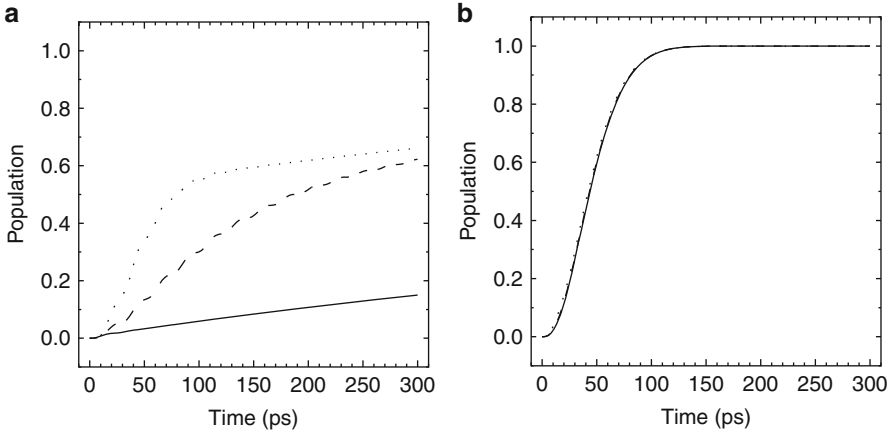


Fig. 5.26 Temporal evolution of the output populations where the energy difference is set to $\Delta\Omega = -U$ ($\hbar U = 89 \mu\text{eV}$). Parts (a) and (b) show the populations for one- and two-exciton states, respectively. The *solid*, *dashed*, and *dotted* curves represent the results for asymmetry factors $\Delta U'/\bar{U}' = 0, 0.5$, and 1.0 , respectively, where the average coupling strength is set to $\hbar\bar{U}' = 14 \mu\text{eV}$. In part (b), the three curves are almost identical

transfer between states $|1\rangle_s$ and $|1\rangle_{\text{ph}}$ acts oppositely to the resonance condition between states $|1\rangle_a$ and $|1\rangle_{\text{ph}}$. This is evident in (5.79), for example, by comparing the matrix elements $\rho_{s_1, \text{ph}_1}(t)$ with $\rho_{a_1, \text{ph}_1}(t)$. Therefore, in the one-exciton state, the exciton population is very sensitive to the asymmetric arrangement. By contrast, the two-exciton state is not influenced by the quantum-dot arrangement (see Fig. 5.26b). We also observe small- and high-frequency oscillations for the dashed and dotted curves ($|\Delta U'|/\bar{U}' = 0.5$ and 1.0) in Fig. 5.26a. These come from the coherence between states $|1\rangle_s$ and $|1\rangle_a$ which can be seen in the equations of motion of $\rho_{s_1, a_1}(t)$ and $\rho_{a_1, s_1}(t)$. Since the coherence is always excited by mediating state $|1\rangle_{\text{ph}}$ and the state $|1\rangle_{\text{ph}}$ has a short lifetime dominated by the relaxation constant Γ , the oscillations have no relation to the population dynamics. Figure 5.27 shows the variation in the output population at $t = 100$ ps as a function of the asymmetry factor $|\Delta U'|/\bar{U}'$. From this figure, it follows that the asymmetry only affects the one-exciton state, where it breaks the off-state in the logic gate, as shown by the curve with squares, and the signal contrast decreases with increasing asymmetry.

Conversely, for the XOR-logic gate ($\Delta\Omega = U$), the two-exciton states correspond to the off-resonant states in the symmetric system. Therefore, the excitation is transferred to the output energy level in QD-C as the asymmetry factor increases, as shown in Fig. 5.28b. Similarly, the variation in the output population with the asymmetry factor is plotted in Fig. 5.29, where the time is fixed at $t = 100$ ps. The figure shows that the XOR-logic operation in the symmetric system is reversed when the asymmetry factor exceeds 0.5 because a one-exciton state can occupy the initial state of $|1\rangle_s$ with a probability of $1/2$, as shown above. Consequently, the output population also reaches a probability of $1/2$. This is also valid in the

Fig. 5.27 Variation in the output populations at a fixed time of $t = 100$ ps as a function of the asymmetry factor, where the energy difference is set to $\Delta\Omega = -U$ ($\hbar U = 89 \mu\text{eV}$) and an average coupling strength of $\hbar\bar{U} = 14 \mu\text{eV}$ is used. The curves shown with *square* and *circular dots* represent the one- and two-exciton states, respectively. Only the exciton population in the one-exciton state is modified by increasing the asymmetry factor

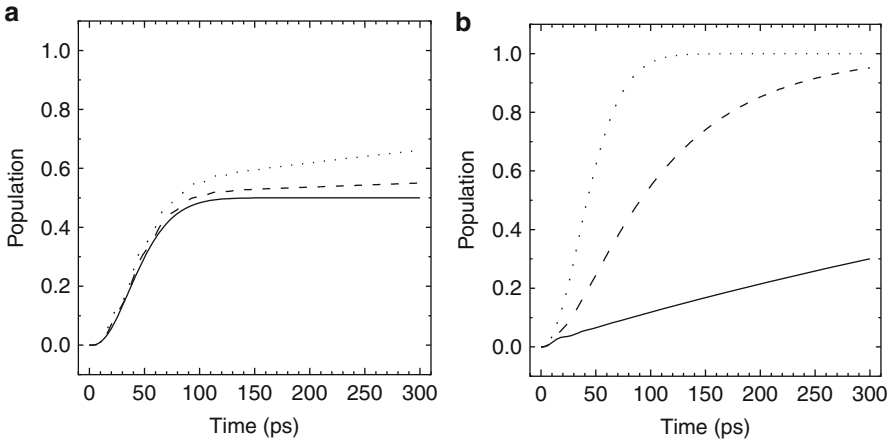
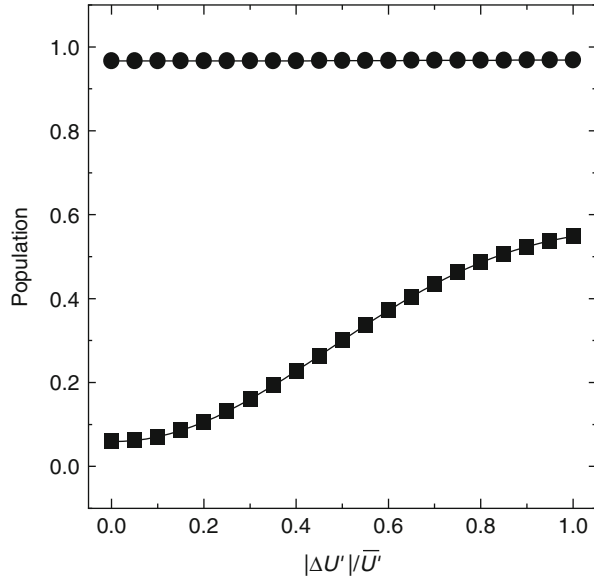
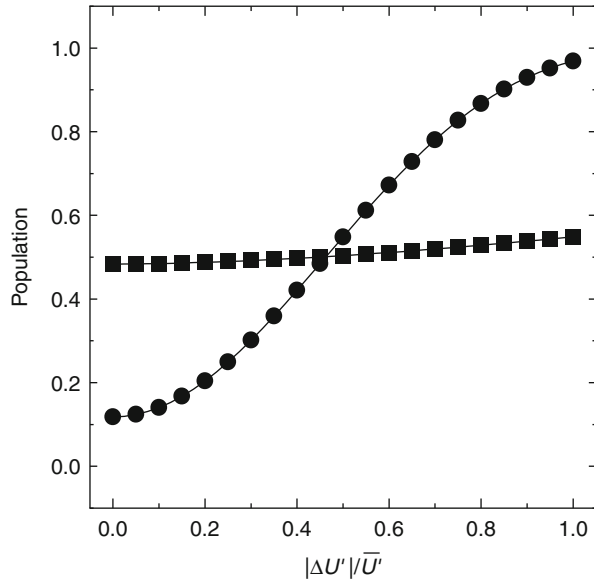


Fig. 5.28 Temporal evolution of the output populations for an the energy difference of $\Delta\Omega = U$ ($\hbar U = 89 \mu\text{eV}$). Parts (a) and (b) show the populations for the one- and two-exciton states, respectively. The *solid*, *dashed*, and *dotted* curves represent the results for asymmetry factors $\Delta U'/\bar{U}' = 0, 0.5,$ and $1.0,$ respectively, where the average coupling strength is set to $\hbar\bar{U}' = 14 \mu\text{eV}$

asymmetric system. However, the asymmetric arrangement enables coupling of the two-exciton states, $|2\rangle_{\text{ph}}$ and $|1\rangle_{\text{ah}}$. State $|2\rangle_{\text{ph}}$ can be fully excited in the initial stage, so the output population reaches a unit value via states $|2\rangle_{\text{ah}}$. This exceeds the output population 0.5 for a one-exciton state with a larger amount of asymmetry.

Fig. 5.29 Variation in the output populations at the fixed time of $t = 100$ ps as a function of the asymmetry factor, where the energy difference is set to $\Delta\Omega = U$ ($\hbar U = 89 \mu\text{eV}$) and an average coupling strength of $\hbar\bar{U} = 14 \mu\text{eV}$ is used. The curves shown with *square* and *circular dots* represent the one- and two-exciton states, respectively. The exciton population in the two-exciton state exceeds that of the one-exciton state when the asymmetry factor $\Delta U'/\bar{U}'$ exceeds 0.5, so the XOR-logic operation is reversed



Although spatial asymmetry decreases the signal contrast for the above logic operations by using a symmetrically arranged system, while this has hidden potential toward nanophotonic inherent functions. As mentioned above, the effect of asymmetry is based on coupling to states $|n\rangle_a$ in an asymmetrically arranged system, which are so-called “dark states” [48]. If we create such dark states by using optical near-field interaction just as we intended, which cannot be excited by far-field light, confinement of photons in a nanophotonic device can be realized, which is discussed in the following. Furthermore, in such an asymmetrically arranged system with via coherent excitations, the symmetric and antisymmetric states can be excited partially, where both states are expressed by the superposition of eigenstates in isolated (noninteracting) quantum dots. Therefore, a system composed of three quantum dots cannot only select information that depends on the initially prepared excitations but also information that reflects the initial quantum-entangled states in the coherent operation part. From this perspective, such nanophotonic devices are useful in connecting quantum devices as a detector and interface devices which identify occupation probability of the quantum-entangled states in an input signal.

5.4.3 Nanophotonic Controlled Logic Gates

Up to this point, we have instructively discussed the simplest system with three quantum dots. Focused on a coherent operation part, the readers easily understand that more coupled states can be prepared when the number of quantum dots increases; for example, the coherent operation part which consists of three identical quantum dots, that is, a four-quantum-dot system illustrated in Fig. 5.30a, has three

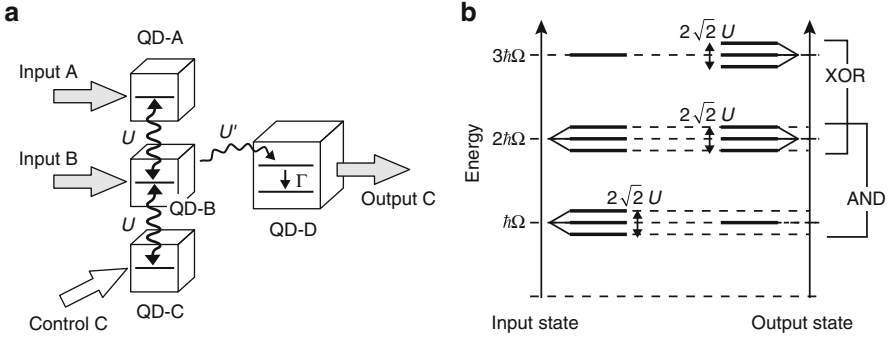


Fig. 5.30 (a) Schematic illustration of four-quantum-dot system, which consists of three identical quantum dots as the coherent operation part and a quantum dot with energy sublevels as the dissipative output part. (b) Energy diagram in the four-quantum-dot system. The *left* and *right* diagrams correspond to the input and output states, respectively, and the energy are splitted into three levels with the energy shift of $\sqrt{2}U$ for the one- and two-exciton states in the input state and for the two- and three-exciton states in the output state

coupled states:

$$|1\rangle_{su} = \frac{1}{2}(|e\rangle_A|g\rangle_B|g\rangle_C + \sqrt{2}|g\rangle_A|e\rangle_B|g\rangle_C + |g\rangle_A|g\rangle_B|e\rangle_C), \quad (5.103)$$

$$|1\rangle_a = \frac{1}{\sqrt{2}}(|e\rangle_A|g\rangle_B|g\rangle_C - |g\rangle_A|g\rangle_B|e\rangle_C), \quad (5.104)$$

$$|1\rangle_{sl} = \frac{1}{2}(|e\rangle_A|g\rangle_B|g\rangle_C - \sqrt{2}|g\rangle_A|e\rangle_B|g\rangle_C + |g\rangle_A|g\rangle_B|e\rangle_C) \quad (5.105)$$

for the one-exciton states, and

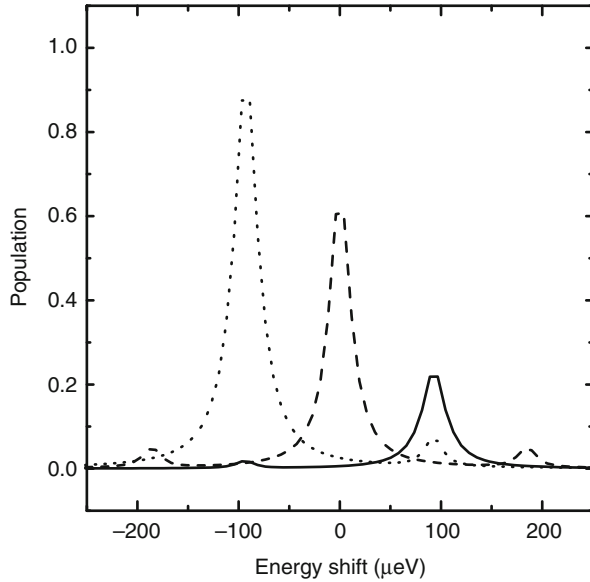
$$|2\rangle_{su} = \frac{1}{2}(|e\rangle_A|e\rangle_B|g\rangle_C + \sqrt{2}|e\rangle_A|g\rangle_B|e\rangle_C + |g\rangle_A|e\rangle_B|e\rangle_C), \quad (5.106)$$

$$|2\rangle_a = \frac{1}{\sqrt{2}}(|e\rangle_A|e\rangle_B|g\rangle_C - |g\rangle_A|e\rangle_B|e\rangle_C), \quad (5.107)$$

$$|2\rangle_{sl} = \frac{1}{2}(|e\rangle_A|e\rangle_B|g\rangle_C - \sqrt{2}|e\rangle_A|g\rangle_B|e\rangle_C + |g\rangle_A|e\rangle_B|e\rangle_C) \quad (5.108)$$

for the two-exciton states. A three-exciton state is degenerated since the energy levels in all three quantum dots are occupied. By using these coupled states, we can propose a characteristic functional device, which is named controlled AND- and XOR-logic gates. Although equations of motion for density matrix elements build up in a similar manner to (5.79) and (5.88), it is tedious to describe differential equations for all density matrix elements. Here we explain energy transfer property by using schematic illustration. The energy diagram is illustrated in Fig. 5.30b,

Fig. 5.31 Variation in the output populations at a fixed time of $t = 300$ ps as a function of the energy difference $\Delta\Omega$. The *solid*, *dashed*, and *dotted* curves represent the one-, two-, and three-exciton states, respectively. The optical near-field coupling strengths $\hbar U$ and $\hbar U'$ and the non-radiative relaxation constant Γ are set as $66 \mu\text{eV}$, $3.3 \mu\text{eV}$, and $(50 \text{ps})^{-1}$, respectively

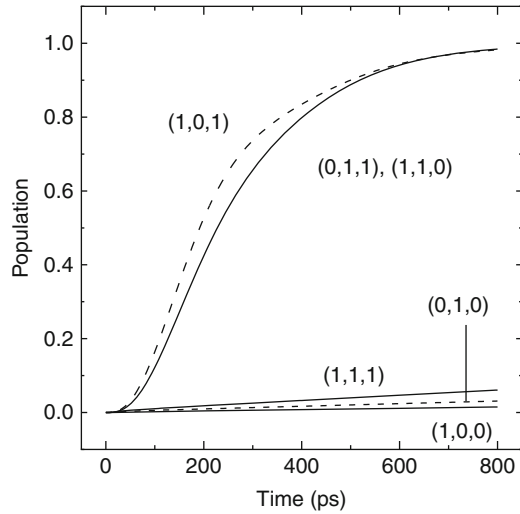


where the energies for one- and two-exciton states are divided into three levels with eigenenergies, $\hbar\Omega + \sqrt{2}$, $\hbar\Omega$, and $\hbar\Omega - \sqrt{2}$ due to the optical near-field coupling. Note that the coupled state with middle energy is dipole-inactive state in a symmetric arranged system (Fig. 5.30a). The left side in the diagram corresponds to the input (initial) state, where only the three-exciton state is degenerated, while the right denotes the output state in which the three-exciton state becomes nondegenerated since an exciton stays in QD-D without going back to the coherent operation part because of fast intra-sublevel relaxation.

In Fig. 5.31, we show the result of output population at 300 ps as a function of the energy shift $\Delta\Omega$, where initial states are set as $(1, 0, 0)$, $(1, 1, 0)$, and $(1, 1, 1)$, the notation corresponding to the quantum-dot label of (A, B, C) . In order to obtain clear energy splitting (sharp resonance) for the one-, two-, and three-exciton states, the strength of optical near-field coupling is set as a suitably optimized value of $\hbar U = 66 \mu\text{eV}$ (10 ps). This seems somewhat strong as compared with the previously estimated value for CuCl quantum cubes embedded in a NaCl matrix. Therefore, we require some optimization in materials and size of quantum dots to realize this controlled logic devices. From Fig. 5.31, we understand that only two-exciton states can be coupled to the output state, when we choose the upper energy level in QD-D equivalent to the middle energy level in the coupled states, no energy shift being applied. Regarding to the input terminals as QD-A and QD-B, the exciton population transfers to the output terminal of QD-D differently, whether the control terminal of QD-D is excited or not. In other words, QD-C plays a role to exchange the AND- and XOR-logic operations.

In the following, we discussed temporal evolution of exciton population on the output energy level in QD-D, which is numerically derived by using bases of isolated

Fig. 5.32 Temporal evolution of the output populations for possible initial states, $(A, B, C) = (1, 0, 0)$, $(0, 1, 0)$, $(1, 1, 0)$ (without control signal), and $(1, 0, 1)$, $(0, 1, 1)$, $(1, 1, 1)$ (with control signal). The upper energy level in QD-D is adjusted equal to the energy of the other three quantum dots, and the optical near-field coupling strengths $\hbar U$ and $\hbar U'$, and the non-radiative relaxation constant Γ are set as $U = 66 \mu\text{eV}$, $\hbar U' = 3.3 \mu\text{eV}$, and $(50 \text{ ps})^{-1}$, respectively



quantum dots. Figure 5.32 shows the results of calculation for all possible initial excitations in the symmetrically arranged four-quantum-dot system. The parameters are set as the same values in Fig. 5.31. At first, we focus on the exciton dynamics when the population in QD-C (control dot) is empty at the initial time. In this case, an exciton which is prepared in QD-A or QD-B cannot move to the output energy level in QD-D. The reason is as follows: a locally excited state in QD-A is expressed as a superposition of the coupled states, $|e\rangle_A|g\rangle_B|g\rangle_C = (|1\rangle_{su} + \sqrt{2}|1\rangle_a + |1\rangle_{sl})/2$, where the output energy level is resonant for the state $|1\rangle_a$ and off-resonant for the states $|1\rangle_{su}$ and $|1\rangle_{sl}$ as you can see in Fig. 5.30. However, the state $|1\rangle_a$ is dipole inactive for the symmetrically arranged system, and thus, the energy transfer does not occur for the one-exciton state as we can observe the curves labeled as $(1, 0, 0)$ and $(0, 1, 0)$ in Fig. 5.30. On the other hand, when both of QD-A and QD-B are initially excited, that is, $(1, 1, 0)$, the output signal appears because three pairs of energy levels in the input and output states are completely resonant. Here we emphasize that the states $|2\rangle_a|g\rangle_D$ and $|1\rangle_a|e\rangle_D$ can also couple with each other because they have same symmetries.

Second, we pay attention to the case that an exciton is initially prepared in QD-C. In this case, the output population only appears when either QD-A or QD-B is initially excited, which shows similar dynamics to the initial condition of $(1, 1, 0)$. The readers notice that the curves for the initial $(0, 1, 1)$ - and $(1, 0, 1)$ -states are slightly different. This is caused by the symmetry of the $(1, 0, 1)$ -state, while the $(1, 1, 0)$ -state is asymmetric. When both of QD-A and QD-B are excited, that is, the three-exciton state labeled as $(1, 1, 1)$, the signal becomes enough small, which is the off-level in this logic gate. The above operations are summarized in Table 5.2. We clearly understand that the four-quantum-dot system operates as AND- and XOR-logic gates in the cases without and with the control signal, respectively.

Table 5.2 Relationship between the input and output populations for the four-quantum-dot system

Input		Control	Output
A	B	C	D
0	0	0	0
1	0	0	0
0	1	0	0
1	1	0	1
0	0	1	0
1	0	1	1
0	1	1	1
1	1	1	0

Such a nanophotonic device is quite interesting because two types of operations are carried out in a same quantum-dot system, which has large advantages to avoid complex nanofabrication process, and lowering the number of device elements in an integrated nanophotonic circuit.

5.4.4 Nanophotonic Buffer Memory

As mentioned in Sect. 5.4.2.4, we discuss realization of characteristic nanophotonic devices in the remaining sections, in which the coupling features of antisymmetric states. Since the antisymmetric states have no total dipole, it cannot be excited by far-field light and also cannot radiate far-field light. Using this dipole-inactive feature, we can realize an interesting operation, in which exciton–polariton or incident photon energy is retained in the system for a long time. We refer to this type of device as photon storage or photon buffer memory.

The three-quantum-dot system is the simplest configuration to obtain a completely antisymmetric state for the photon buffer memory, which is illustrated in Fig. 5.33. The upper energy level in QD-C is positively shifted by $\Delta\Omega = U$, which is the resonance condition between the input and output parts in the asymmetrically arranged quantum-dot system. For this system, the antisymmetric state for the one-exciton state is not directly excited, because both of the symmetric and antisymmetric states are simultaneously excited. However, if the two-exciton state is initially excited in the input part, we can create completely antisymmetric state. This is explained by using temporal sequence of the energy states as illustrated in Fig. 5.34. According to (5.88), the energy transfer from the two-exciton states $|2\rangle_{\text{ph}}$ to $|2\rangle_{\text{Ah}}$ is active when QD-C is asymmetrically located and the upper energy level in QD-C is positively shifted by $\Delta\Omega = U$. An exciton transfers into the upper energy level in QD-C, resonantly, where the rest exciton in the coherent operation part completely stays in the antisymmetric state. Then, the exciton on the upper energy level in QD-C drops into the lower energy level via intra-sublevel relaxation with leaving the antisymmetric state in QD-A and QD-B. The lower energy level in QD-C is dipole-active state for far-field light; therefore, the exciton annihilates due to spontaneous emission, which spends several ns, while the antisymmetric state

Fig. 5.33 Schematic illustration of maximally asymmetric arranged quantum-dot system. Two identical quantum dots, QD-A and QD-B, make dipole-inactive state for far-field light, which corresponds to the antisymmetric

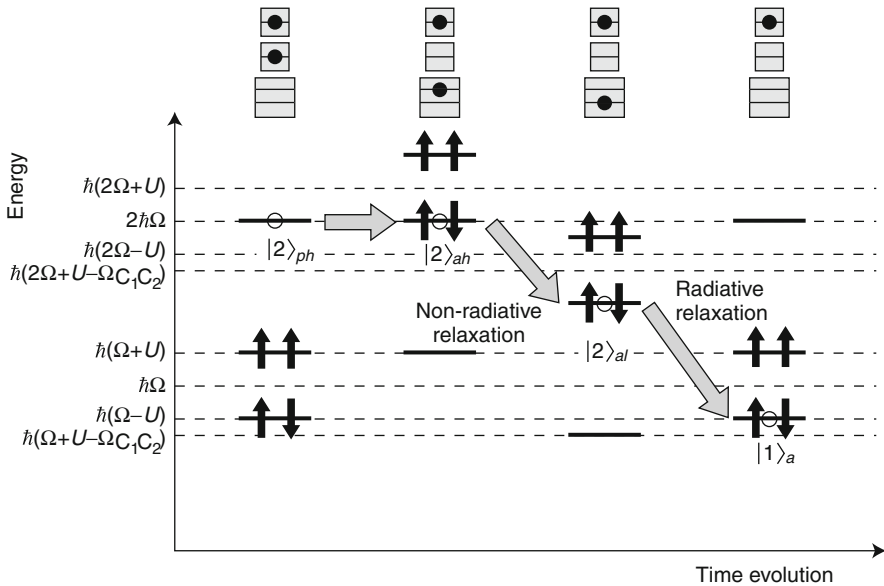
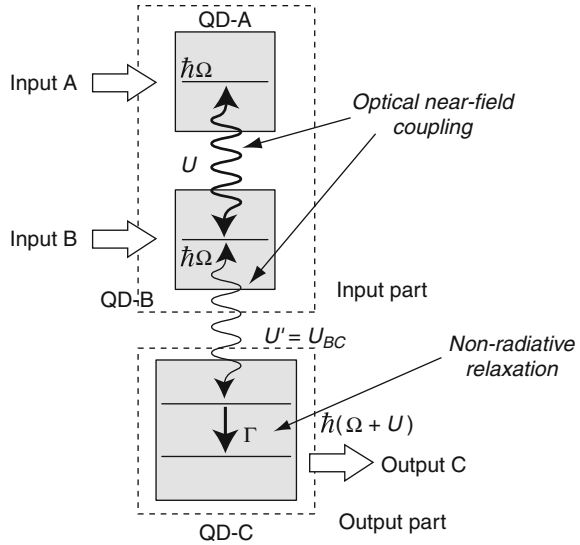
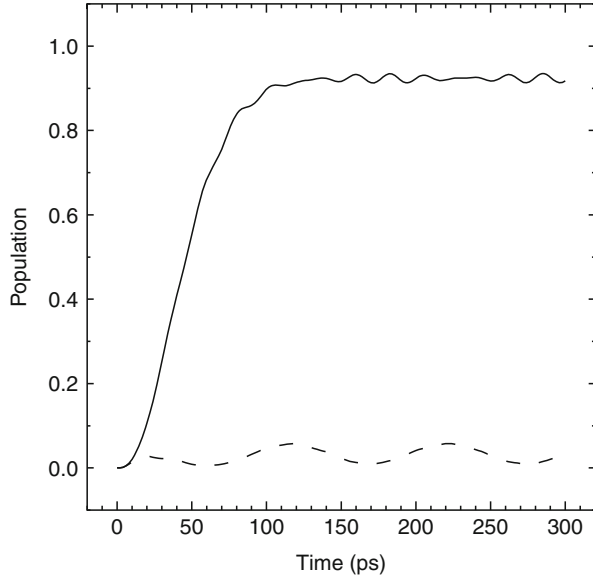


Fig. 5.34 Temporal sequence of energy states in a three-quantum-dot system, which starts from two-exciton state. $\hbar\Omega_{C_1, C_2}$ denotes the energy difference between upper and lower energy levels in QD-C

Fig. 5.35 Temporal evolution of exciton population for the two-exciton state. The *solid* and *dashed* curves represent for the antisymmetric and symmetric states, respectively. The coupling strength between QD-A and QD-B is set as $\hbar U = 89 \mu\text{eV}$, and that between QD-B and QD-C is $\hbar U' = \hbar U_{BC} = 14 \mu\text{eV}$. The coupling between QD-A and QD-C is assumed to be zero, $\hbar U_{CA} = 0$



does not couple to far-field light because the total dipole moment in a coherent operation part is zero. Moreover, the antisymmetric one-exciton state is off-resonant to the upper energy level in QD-C, and thus, very long lifetime is expected. In this manner, a complete antisymmetric state for one-exciton state can be obtained in such a maximally asymmetric system.

Figure 5.35 represents a numerical result of the time evolution derived by using (5.79) and (5.88). The solid curve in Fig. 5.35 corresponds to the sum of exciton population for the states $|1\rangle_a$, $|2\rangle_{ah}$, and $|2\rangle_{al}$, which holds zero total dipole moment for far-field light. On the other hand, the sum of exciton population in the states, $|1\rangle_s$, $|2\rangle_{sh}$, and $|2\rangle_{sl}$ is plotted by the dashed curve in Fig. 5.35, which is almost zero value since the initial stage. Actually, the far-field radiation cannot be restrained completely in this system because the weak coupling from the antisymmetric state to the symmetric state exists, where the energy transfer depends on the average coupling strength \bar{U}' and the difference of the couplings $\Delta U'$ as shown in (5.79). The oscillating behavior is observed for both curves in Fig. 5.35, which is also caused by the coupling between the antisymmetric and symmetric states. Although we have neglected the coupling to far-field light in this calculation, the slow exponential decay could be observed in the antisymmetric state when we take into account the far-field coupling.

The above discussion is devoted to a writing process in the photon buffer memory, or how to prepare an antisymmetric state in a coupled quantum-dot system. However, in a general system, we need to consider a mechanism for reading information in addition to the writing process, which will be discussed elsewhere.

5.4.5 Nanophotonic Signal Splitter for Quantum Entanglement

In the above section, we have focused on realization of conventional functional devices in nanometer space. Note that our proposed functional devices consist of two parts: coherent operation part with matter coherence and dissipative output part as illustrated in Figs. 5.17 or Fig. 5.4. The matter coherence in the coherent operation part is maintained for the period that exciton population moves to the dissipative output part. In other words, the output quantum dot acts as a selector to identify a certain quantum state by using resonant energy transfer and spatial symmetry in a quantum-dot system. Therefore, such a system is useful for detecting some information about quantum entanglement. In this section, we propose a special signal splitting device regarding to quantum-entangled states. To use quantum mechanical and classical dissipative process, simultaneously, is a novel concept inherently originating from nanophotonics.

Figure 5.36 shows schematic illustration of the device, in which two output terminal quantum dots, QD-C and QD-D, exist. The QD-C is located symmetrically regarding to two identical quantum dots, and the upper energy level is set with a positive shift by U . The QD-D is configured maximally asymmetrically with a negative energy shift $\Delta\Omega = -U$. From the resonance conditions, QD-C can extract exciton population from the coherent operation part via the symmetric state, while QD-D resonantly selects the antisymmetric state, where resonant energy transfer is allowed because symmetry breaking (see Fig. 5.35). Therefore, this system can distinguish an initial quantum-entangled state, $|\phi\rangle = c_1|1\rangle_s + c_2|1\rangle_a$, and information of weight coefficients c_1 and c_2 is converted to optical frequency or wavelength of far-field light, which is released after the spontaneous lifetime (several ns) of excitons.

Numerical results of the exciton population dynamics in the above system are given in Fig. 5.37, which is calculated by using the density matrix formalism. Figure 5.37a is the time evolution in the case of $|c_1|^2 = 2/3$ and $|c_2|^2 = 1/3$ as an initial condition, and Fig. 5.37b is that of $|c_1|^2 = 1/3$ and $|c_2|^2 = 2/3$. Such initial quantum-entangled states can be established by using asymmetrically located optical near-field source against QD-A and QD-B, or by connecting to some quantum computing devices. Both cases in Fig. 5.37 show that the exciton population on the energy levels in QD-C and QD-D well reflects the initial weight coefficients, where the horizontal gray lines in Fig. 5.37 indicate the expected values. Note that the deviation from the expected values becomes large, as the weight coefficient of symmetric state c_1 increases. This is caused that the off-resonant energy transfer from symmetric state to the output state slightly occurs in the asymmetrically arranged quantum-dot system. In contrast, the off-resonant energy transfer from antisymmetric state to the output state is completely forbidden, since QD-C is located symmetrically. Therefore, a part of the exciton population that should flow into symmetrically arranged system, moves into asymmetrically arranged QD-D. This results in the difference depending on these weight coefficients.

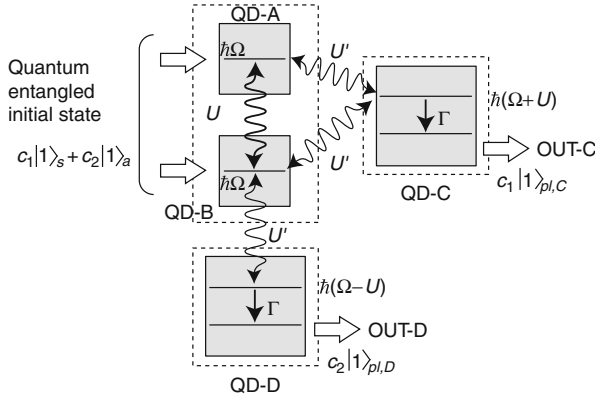


Fig. 5.36 Schematic illustration of signal splitter reflected quantum-entangled states, which constructs from symmetrically arranged system with positive energy shift and maximally asymmetrically arranged system with negative energy shift. Two identical quantum dots, QD-A and QD-B, hold quantum mechanical motion, which is the coherent operation part, and QD-C and QD-D correspond to the dissipative output part

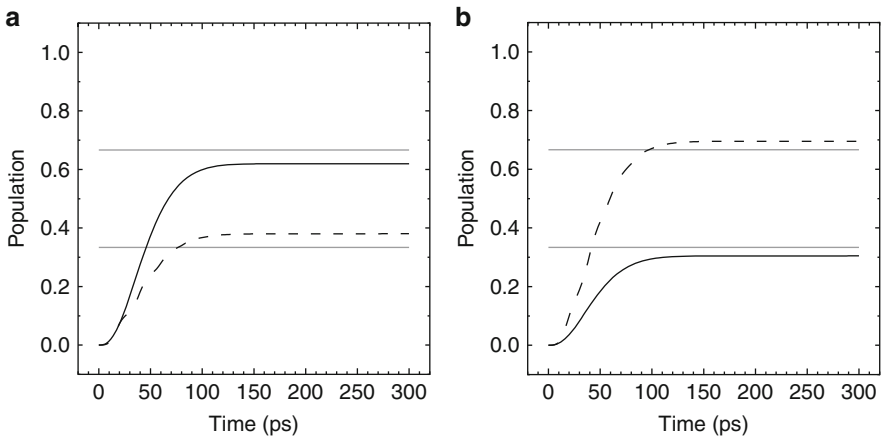


Fig. 5.37 Temporal evolution of exciton population on the lower energy level in QD-C (*solid curve*) and that in QD-D (*dashed curve*). (a) *Left* and (b) *right* figures represent the weight coefficients $|c_1|^2 = 2/3, |c_2|^2 = 1/3$, and $|c_1|^2 = 1/3, |c_2|^2 = 2/3$, respectively. The coupling strength between QD-A and QD-B is set as $\hbar U = 89 \mu\text{eV}$, and that between QD-B and QD-C (QD-A and QD-C, QD-A and QD-D, QD-B and QD-D) is $\hbar U' = 14 \mu\text{eV}$

To use quantum mechanical and classical process is one of characteristic device operations inherent to nanophotonic devices. We suppose there are further useful applications to be realized. Progressive investigation will be expected from the system architecture viewpoint.

5.4.6 Summary

In this section, we have discussed nanophotonic functional devices in which a coherently coupled state between optical near field and nanometric quantum dots are utilized. For a theoretical aspect, we have derived equations of motion for excitons by using the bases of appropriate coupled states, that is, symmetric and antisymmetric states, while we had solved them by using those of isolated quantum-dot states in Sect. 5.3. As a result, a principle and conditions for selective energy transfer from the coherently coupled states to the output state have been analytically shown. The selective energy transfer originates from two important factors: one is whether the coherently coupled state is symmetric or antisymmetric, where the two states have different eigenenergies. In addition, it is a characteristic feature that optical near field can access the antisymmetric state, which is impossible for far-field light to excite because the antisymmetric state has dipole-inactive nature. The other is that we can control exciton energy transfer by designing spatial arrangement of several quantum dots; in the case of symmetrically arranged system antisymmetric state is dipole inactive, while in asymmetrically arranged system, the exciton population in the antisymmetric state can be attracted intently by adjusting the system asymmetry. By using these factors and preparing a larger quantum dot for an output terminal, some functional operations can be realized. As an analytical demonstration, we have proposed AND- and XOR-logic gates and investigated their dynamics and system tolerance due to spatial asymmetry. Consequently, the AND-logic gate can be achieved by shifting the output energy level negatively, while the XOR-gate can be achieved by shifting that positively, where the energy shifts are determined by the optical near-field coupling strength, that is, $\pm U$. When the number of quantum dots increases, we can realize higher-degree functional devices, although the selectivity or resonance conditions become more critical. As an example, we have proposed a controlled-type logic gate by using four quantum dots, in which the AND- and XOR-logic operations are exchanged in the same device depending on the number of incident excitons.

The above logic operations have been achieved by designing the system completely symmetrically and adjusting the output energy level to the resonance conditions. A system with spatial asymmetry is very interesting from the following viewpoints: we can create a characteristic state which decouples from far-field light. Such a state expects to have longer population lifetime than usual exciton lifetime (spontaneous emission time), and thus, we can store photon energy or exciton-polariton energy in the system. It is useful for a buffer memory which directly stores photon energy. We have shown the operation to create a pure antisymmetric state by using a maximally asymmetrically arranged three-quantum-dot system. For another viewpoint, we can realize an information processing device in which mixed states between symmetric and antisymmetric states are utilized. We have proposed a device which identifies quantum-entangled states by using the spatial symmetry and resonance conditions. This kind of device is different from simple

quantum information processing devices. Both of quantum mechanical and classical information processing can be applied in suitable situations, which is one of inherent operations in nanophotonic devices.

In [Sect. 5.3](#), although we had discussed a nanophotonic switch (equivalent to an AND-logic gate), where only energy states or resonance conditions have been considered, nanophotonic functional operations discussed in this section are realized by intentionally using the spatial degree of freedom, which is one of key features in nanophotonics. With future progress of nanofabrication techniques, where we can control materials, size, and position arbitrarily in nanometric space, nanophotonics and its device architecture have a large possibility for expanding optical and electronic device technologies. We expect that the readers notice a part of such possibility in nanophotonics from discussions in this section.

5.5 Conclusions

In this chapter, we have theoretically investigated operation principles of typical nanophotonic devices and their dynamics as well as formulated characteristic interaction between nanometric objects and nanometric light. The nanophotonic devices discussed here are based on several nanophotonic inherent features, such as local excited states, unidirectional energy transfer, and exciton number dependence. In [Sect. 5.2](#), we have formulated energy transfer between two quantum dots by using exciton–polariton picture and estimated strength of optical near-field coupling and energy transfer time. Moreover, we theoretically proved that the optical near-field interaction enables to excite a dipole-inactive energy level for far-field light. The energy transfer rate or optical near-field coupling strength can be expressed by the overlap integral of envelope functions for two quantum dots and spatial spreading of the optical near field which is described by a Yukawa function in the lowest perturbation. Therefore, we find that the dipole-inactive state can excite easier as inter-quantum-dot distance becomes smaller.

Using the results in [Sect. 5.2](#), characteristic nanophotonic devices, which consist of several quantum dots, have been proposed in [Sects. 5.3](#) and [Sect. 5.4](#), and we have formulated and analyzed exciton dynamics by using quantum mechanical density matrix formalism. In [Sect. 5.3](#), a nanophotonic switch has been numerically demonstrated. In the switch, we use resonant and unidirectional energy transfer, and the unidirectional energy transfer path changes due to a fermionic interaction of excitons in the lowest energy level, that is, a state-filling. Our numerical estimation shows that the state-filling time is sub-100 ps for a CuCl quantum-cube system. Furthermore, recovery time to the initial conditions can be improved in the same order of the inverse of the optical near-field coupling by using stimulated absorption and emission process for coupling to the far-field reservoir. In other words, fast recovery time is achieved by adjusting illumination power and pulse width of control light, which is independent of spontaneous emission lifetime.

In addition to the operation principles in [Sect. 5.3](#), we have proposed other kinds of nanophotonic devices which adopt symmetry of exciton excited states as well

as spatial arrangement of quantum dots as a novel degree of freedom. In such devices, the signal can be selectively extracted by adjusting the energy level in the output quantum dot, as the output energy level is resonant to the coherently coupled states in the input system with several quantum dots. These are useful for a multi-input computation. We have shown realization of AND- and XOR-logic gates by using a symmetrically arranged three-quantum-dot system. In these device operations, it is a key feature that the resonance conditions are different depending on the exciton number. Based on the similar principle, we show possibility for a higher-degree functional device, such as a controlled-type AND- and XOR-logic gates, by using more number of quantum dots. On the other hand, resonant energy transfer via an antisymmetric state becomes possible in an asymmetrically arranged system. Although the antisymmetric state cannot be excited by far-field light, simultaneously, this is also the state which cannot radiate the far-field photons. We have shown that the antisymmetric state is intentionally created by using the optical near-field coupling and its spatial asymmetry. This indicates that the photon energy can be stored in the system as the form of an exciton–polariton. In principle, a photon buffer memory can be realized by this mechanism. To extract the symmetric and antisymmetric states selectively is equivalent to identify some quantum-entangled states, since the bases are superposition of several quantum-dot excitations. Therefore, the asymmetry of the system is useful for an interface device which manipulates quantum-entangled states. As an example, we have numerically demonstrated that quantum-entangled states with the symmetric and antisymmetric states can be separately detected in the symmetrically and asymmetrically arranged quantum dots, which means that the quantum-entangled states are distinguished by the output photons with different energies. Although in the field of quantum information processing only parallel information processing is attracted, a device, which intentionally lowers the coherence or partially uses it, has large possibility to extend a viewpoint in conventional device technologies.

In the above, our discussions have been focused in the theoretical aspects. Experimental studies for nanophotonic devices have been intensively advanced. A nanophotonic switch discussed in Sect. 5.3 has already verified experimentally [40]. Our theoretical study has been used for fitting into the experimental data and for evaluation of physical constant, such as the strength of optical near-field coupling. Furthermore, some interesting devices have been also proposed and investigated, for example, the so-called nanofountain [52], which a nanophotonic summation device has been successfully demonstrated, and in such device, the unidirectional energy transfer is utilized. Moreover, the other types of nanophotonic devices, NOT-gate [6] and energy up-converter [7, 53], that we have not discussed here have been reported. Operation principles for these devices are based on energy shift due to exciton state-filling and phonon-assisting process. On the other hand, a device, in which coherently coupled states are used, has not been reported as far as we know. However, there are some fundamental studies related to the coherently coupled state; for example, presence of anomalous long lifetime, which originates from an antisymmetric state, has been discussed theoretically and experimentally [54, 55]. For realization of such a device using a spatial degree of freedom

in nanometric space, further progress of nanofabrication technology is required. However, nanofabrication technology has been developed recently [56, 57].

Finally, we spare the remaining for the future perspective. All of our investigations about nanophotonic devices are based on the quantum mechanical density matrix formalism, which is the manner to describe averaged dynamics with respect to the photon degree of freedom. We anticipate that an ultimate operation of nanophotonic devices should be done by the energy consumption with single or a few photon level. In order to realize such a device, theory for nanophotonic device operations must be rewritten in the form including a photon statistics rigorously, which is an interesting problem to be solved in the near future.

Acknowledgements The most part of this work was carried out at the project of ERATO, Japan Science and Technology Agency, from 1998 to 2003. The authors are grateful to H. Hori, I. Banno (Yamanashi University), T. Yatsui (The University of Tokyo), and M. Naruse (National Institute of Information and Communications Technology) for fruitful discussions.

Cross-References

- ▶ [A Phenomenological Description of Optical Near Fields and Optical Properties of N Two-Level Systems Interacting with Optical Near Fields](#)
- ▶ [Integration and Evaluation of Nanophotonic Devices Using Optical Near Field](#)
- ▶ [Nanophotonic Systems based on Localized and Hierarchical Optical Near-Field Processes](#)
- ▶ [Optical Near-Field Interactions and Yukawa Potential](#)
- ▶ [Quantum Description of Optical Near Fields Including Vibrational Degrees of Freedom](#)

References

1. Cisco Visual Networking Index: Forecast and Methodology, 2010–2015 (2011), http://www.cisco.com/en/US/solutions/collateral/ns341/ns525/ns537/ns705/ns827/white_paper_c11-481360.pdf
2. M. Ohtsu, K. Kobayashi, T. Kawazoe, S. Sangu, T. Yatsui, *IEEE J. Sel. Top. Q. Electron.* **8**, 839 (2002)
3. A. Yariv, *Introduction to Optical Electronics* (Holt, Rinehart and Winston, New York, 1971)
4. J.W. Goodman, *Introduction to Fourier Optics*, 2nd edn. (McGraw-Hill, Tokyo, 1996)
5. M. Ohtsu (ed.), *Progress in Nanophotonics 1* (Springer, Berlin/Heidelberg, 2011), pp. 1–58
6. T. Kawazoe, K. Kobayashi, K. Akahane, M. Naruse, N. Yamamoto, M. Ohtsu, *Appl. Phys. B* **84**, 243 (2006)
7. T. Yatsui, S. Sangu, K. Kobayashi, T. Kawazoe, M. Ohtsu, J. Yoo, G.-C. Yi, *Appl. Phys. Lett.* **94**, 083113 (2009)
8. M. Naruse, T. Kawazoe, T. Yatsui, S. Sangu, K. Kobayashi, M. Ohtsu, Architectural approach to nanophotonics for information and communication systems, in *Progress in Nano-Electro-Optics V*, ed. by M. Ohtsu (Springer, Berlin/Heidelberg, 2006), pp. 163–182
9. N. Tate, M. Naruse, T. Yatsui, T. Kawazoe, M. Hoga, Y. Ohyagi, T. Fukuyama, M. Kitamura, M. Ohtsu, *Opt. Expr.* **18**, 7497 (2010)

10. W. Nomura, T. Yatsui, Y. Yanase, K. Suzuki, M. Fujita, A. Kamata, M. Naruse, M. Ohtsu, *Appl. Phys. B* **99**, 75 (2010)
11. T. Yatsui, K. Hirata, Y. Tabata, W. Nomura, T. Kawazoe, M. Naruse, M. Ohtsu, *Nanotechnology* **21**, 355303 (2010)
12. T. Yatsui, K. Hirata, Y. Tabata, Y. Miyake, Y. Akita, M. Yoshimoto, W. Nomura, T. Kawazoe, M. Naruse, M. Ohtsu, *Appl. Phys. B* **103**, 527 (2011)
13. T. Kawazoe, M.A. Mueed, M. Ohtsu, *Appl. Phys. B* **104**, 747 (2011)
14. I. Amlani, A.O. Orlov, G. Toth, G.H. Bernstein, C.S. Lent, G.L. Snider, *Science* **284**, 289 (1999)
15. M. Ohtsu, H. Hori, *Near-Field Nano-Optics* (Kluwer Academic/Plenum, New York, 1999)
16. Th. Förster, Delocalized excitation and excitation transfer, in *Modern Quantum Chemistry*, ed. by O. Sinanoğlu (Academic, London, 1965), pp. 93–137
17. S. Sangu, K. Kobayashi, T. Kawazoe, A. Shojiguchi, M. Ohtsu, *J. Appl. Phys.* **93**, 2937 (2003)
18. T. Kawazoe, K. Kobayashi, J. Lim, Y. Narita, M. Ohtsu, *Phys. Rev. Lett.* **88**, 067404 (2002)
19. K. Cho, *Optical Responses of Nanostructures: Microscopic Nonlocal Theory* (Springer, Tokyo, 2003)
20. C. Cohen-Tannoudji, J. Depont-Roc, G. Grynberg, *Photons and Atoms: Introduction to Quantum Electrodynamics* (Wiley, New York, 1989)
21. D.P. Craig, T. Thirunamachandran, *Molecular Quantum Electrodynamics* (Academic, London, 1984)
22. R. Guy Woolley, *Handbook of Molecular Physics and Quantum Chemistry, Vol.1* (Wiley, Chichester, 2003)
23. J. Knoester, S. Mukamel, *Phys. Rev. A* **39**, 1899 (1989)
24. J.R. Zurita-Sanchez, L. Novotny, *J. Opt. Soc. Am. B* **19**, 1355 (2002)
25. K. Kobayashi, M. Ohtsu, *J. Microsc.* **194**, 249 (1999)
26. K. Kobayashi, S. Sangu, H. Ito, M. Ohtsu, *Phys. Rev. A* **63**, 013806 (2001)
27. S. Sangu, K. Kobayashi, M. Ohtsu, *J. Microsc.* **202**, 279 (2001)
28. M. Ohtsu, K. Kobayashi, *Optical Near Fields: Electromagnetic Phenomena in Nanometric Space* (Springer, Tokyo, 2003)
29. E. Hanamura, *Phys. Rev. B* **37**, 1273 (1988)
30. K. Kobayashi, S. Sangu, M. Ohtsu, Quantum theoretical approach to optical near-fields and some related applications, in *Progress in Nano-Electro-Optics I*, ed. by M. Ohtsu (Springer, Tokyo, 2003), pp. 119–158
31. P. Fulde, *Electron Correlations in Molecules and Solids* (Springer, Berlin, 1995)
32. Y. Masumoto, M. Ikezawa, B.-R. Hyun, K. Takemoto, M. Furuya, *Phys. Status Solidi b* **224**, 613 (2001)
33. K. Kobayashi, T. Kawazoe, S. Sangu, M. Ohtsu, Technical Digest of the 4th Pacific Rim Conference on Laser and Electro-Optics (Makuhari Messe, Japan, 2001), pp. I192–I193
34. N. Sakakura, Y. Masumoto, *Phys. Rev. B* **56**, 4051 (1997)
35. T. Kataoka, T. Tokizaki, A. Nakamura, *Phys. Rev. B* **48**, 2815 (1993)
36. H.J. Carmichael, *Statistical Methods in Quantum Optics I* (Springer, Berlin, 1999)
37. L. Mandel, E. Wolf, *Optical Coherence and Quantum Optics* (Cambridge University, Cambridge, 1995)
38. K. Akahane, N. Ohtani, Y. Okada, M. Kawabe, *J. Cryst. Growth* **245**, 31 (2002)
39. W.I. Park, G.-C. Yi, M. Kim, S.J. Pennycook, *Adv. Mater.* **15**, 526 (2003)
40. T. Kawazoe, K. Kobayashi, S. Sangu, M. Ohtsu, *Appl. Phys. Lett.* **82**, 2957 (2003)
41. K. Lindenberg, B. West, *Phys. Rev. A* **30**, 568 (1984)
42. H. Hori, Electronic and electromagnetic properties in nanometer scales, in *Optical and Electronic Process of Nano-Matters*, ed. by M. Ohtsu (KTK Scientific/Kluwer Academic, Tokyo/Dordrecht, 2001), pp. 1–55
43. S. Sangu, K. Kobayashi, A. Shojiguchi, M. Ohtsu, *Phys. Rev. B* **69**, 115334 (2004)
44. S. De Rinaldis, I. D'Amico, F. Rossi, *Appl. Phys. Lett.* **81**, 4236 (2002)
45. F. Troiani, U. Hohenester, E. Molinari, *Phys. Rev. B* **65**, 161301 (2002)
46. E. Biolatti, R.C. Iotti, P. Zanardi, F. Rossi, *Phys. Rev. Lett.* **85**, 5647 (2000)

47. L. Quiroga, N.F. Johnson, *Phys. Rev. Lett.* **83**, 2270 (1999)
48. M.O. Scully, M.S. Zubairy, *Quantum Optics* (Cambridge University Press, Cambridge, 1997), pp. 222–225
49. P. Zanardi, F. Rossi, *Phys. Rev. Lett.* **81**, 4752 (1998)
50. M. Thorwart, P. Hänggi, *Phys. Rev. A* **65**, 012309 (2001)
51. B. Coffey, *Phys. Rev. A* **17**, 1033 (1978)
52. M. Naruse, T. Miyazaki, F. Kubota, T. Kawazoe, K. Kobayashi, S. Sangu, M. Ohtsu, *Opt. Lett.* **30**, 201 (2005)
53. H. Fujiwara, T. Kawazoe, M. Ohtsu, *Appl. Phys. B* **98** 283 (2010)
54. G. Parascandolo, V. Savona, *Phys. Rev. B* **71**, 045335 (2005)
55. T. Kawazoe, K. Kobayashi, M. Ohtsu, *IEICE Trans. Electron.* **E88-C** (2005)
56. T. Yatsui, T. Kawazoe, M. Ueda, Y. Yamamoto, M. Kurogi, M. Ohtsu, *Appl. Phys. Lett.* **81**, 3651 (2002)
57. W. Nomura, T. Yatsui, M. Ohtsu, *Appl. Phys. Lett.* **86**, 181108 (2005)

Quantum Description of Optical Near Fields Including Vibrational Degrees of Freedom

6

Kiyoshi Kobayashi, Yuji Tanaka, Tadashi Kawazoe,
and Motoichi Ohtsu

Contents

6.1	Introduction.....	252
6.2	Quantum Theoretical Approach to Optical Near Fields.....	253
6.2.1	Localized Photon Model.....	253
6.2.2	Photodissociation of Molecules and EPP Model.....	255
6.3	Localized Phonons.....	259
6.3.1	Lattice Vibration in Pseudo One-Dimensional System.....	259
6.3.2	Quantization of Vibration.....	261
6.3.3	Vibration Modes: Localized Versus Delocalized.....	262
6.4	Model.....	264
6.4.1	Optically Excited Probe System.....	264
6.4.2	Davydov Transformation.....	265
6.4.3	Quasiparticle and Coherent State.....	268
6.4.4	Localization Mechanism.....	269
6.5	Conclusions.....	275
	References.....	276

K. Kobayashi (✉)

Interdisciplinary Graduate School of Medicine and Engineering, University of Yamanashi, Kofu,
Yamanashi, Japan

e-mail: kkoba@yamanashi.ac.jp

Y. Tanaka

Steel Research Laboratory, JFE Steel Corporation, Kawasaki-ku, Kawasaki, Japan

e-mail: yuji-tanaka@jfe-steel.co.jp

T. Kawazoe

School of Engineering, The University of Tokyo, Tokyo, Japan

e-mail: kawazoe@ee.t.u-tokyo.ac.jp

M. Ohtsu

School of Engineering, The University of Tokyo, Tokyo, Japan

Nanophotonics Research Center, The University of Tokyo, Tokyo, Japan

e-mail: ohtsu@ee.t.u-tokyo.ac.jp

M. Ohtsu (ed.), *Handbook of Nano-Optics and Nanophotonics*,

DOI 10.1007/978-3-642-31066-9_7, © Springer-Verlag Berlin Heidelberg 2013

Abstract

Quantum theoretical description of optical near fields is discussed from the viewpoint of effective photon–matter interactions and localized photons. On the basis of experimental data of photodissociation of molecules, a phonon's role is emphasized in light-matter interacting system at the nanoscale. After the brief introduction of localized and delocalized phonon modes, a simple extended model for a pseudo one-dimensional optical near-field probe system is presented in order to discuss the mechanism of photon localization in space as well as the role of phonons at the nanoscale.

6.1 Introduction

Optical near fields have been used in high-resolution microscopy/spectroscopy for a variety of samples [1], especially for a single molecules [2] and a single quantum dots [3], as well as nanofabrication [4–6]. These applications are based on the fact that optical near-field probes, whose tips are sharpened to a few nanometers, can generate a light field localized around the apex of the same order. The spatial localization is, of course, independent of the wavelength of incident light, and the size of the localization is much smaller than the wavelength. It means that optical near-field probes are one of the essential elements in the applications.

In fabricating nanophotonic devices [7–10] with such probes, for example, it is critical to control the size and position of the nanostructures, which requires efficient control and manipulation of the localization of light fields. If one could control and manipulate the localization of light field at will, one would necessarily obtain more efficient and functional probes with higher precision, which will be applicable to predict quantum phenomena. It is true not only in a probe system but also in an optical near-field problem, in general. In these respects it is very important to clarify the mechanism of spatial localization of optical near fields on a nanometer scale.

From a theoretical viewpoint, self-consistency between light field and induced electronic polarization fields is crucial on the nanometer scale, and the importance of quantum coherence between photon and matter fields is pointed out [11–14]. On the basis of such a viewpoint, superradiance, as a cooperative phenomenon, of a quantum-dot chain system excited by an optical near field [15, 16], and excitation transfer to a dipole-forbidden level in a quantum-dot pair system [17, 18] have been investigated.

Recently experimental results on superradiance using a collection of quantum dots have been reported [19]. Moreover, experiments on photodissociation of diethylzinc (DeZn) and zinc-bis (acetylacetonate) or $\text{Zn}(\text{acac})_2$ molecules and deposition of Zn atoms using an optical near field have been conducted for nanostructure fabrication, as will be discussed in the next section. The experimental results show that the molecules illuminated by the optical near field are dissociated even if the energy of incident light is lower than the dissociation energy, which is impossible when a far field with the same energy and intensity is used. A simple analysis indicates that data cannot be explained by conventional theories based on

the Franck–Condon principle or the adiabatic approximation for nuclear motions in a molecule and suggests that phonons in an optically excited probe system might assist the molecular dissociation process in a nonadiabatic way [20–22].

In this situation, it is necessary to study the photon–phonon interaction as well as the photon–electronic excitation interaction in a nanometer space and to clarify the phonon’s role in the nanometric optical near-field probe system, or more generally in light–matter interacting system on a nanometer scale. Then a quantum theoretical approach is appropriate to describe an interacting system of photon and matter (electronic excitation and phonon) fields. It will allow us not only to understand an elementary process of photochemical reactions with optical near fields but also to explore phonon’s role in nanostructures interacting with localized photon fields.

6.2 Quantum Theoretical Approach to Optical Near Fields

A “photon,” as is well known, corresponds to a discrete excitation of electromagnetic modes in a virtual cavity, whose concept has been established as a result of quantization of a free electromagnetic field [23]. Different from an electron, a photon is massless, and it is hard to construct a wave function in the coordinate representation that gives a photon picture as a spatially localized point particle as an electron [24]. However, if there is a detector such as an atom to absorb a photon in an area whose linear dimension is much smaller than the wave length of light, it would be possible to detect a photon with the same precision as the detector size [25, 26]. In optical near-field problems, it is required to consider the interactions between light and nanomaterials and detection of light by another nanomaterials on a nanometer scale. Then it is more serious for quantization of the field how to define a virtual cavity, or which normal modes to be used, since there exists a system composed of an arbitrary shape, size, and material on the nanometer region.

In this section, we describe a theoretical approach to address the issue. Then photodissociation of molecules is discussed, as an example of applications using optical near fields, which is an essential part of nanofabrication to construct nanophotonic devices.

6.2.1 Localized Photon Model

Effective Interaction and Localized Photons. Let us consider a nanomaterial system surrounded by an incident light and a macroscopic material system, which are electromagnetically interacting one another in a complicated way, as schematically shown in Fig. 6.1. Using the projection operator method, we can derive an effective interaction between the relevant nanomaterials in which we are interested, after renormalizing the other effects [9, 13, 27, 28]. It corresponds to an approach to describe “photons localized around nanomaterials” as if each nanomaterial would work as a detector and light source in a self-consistent way. The effective interaction related to optical near fields is hereafter called a near-field optical interaction.

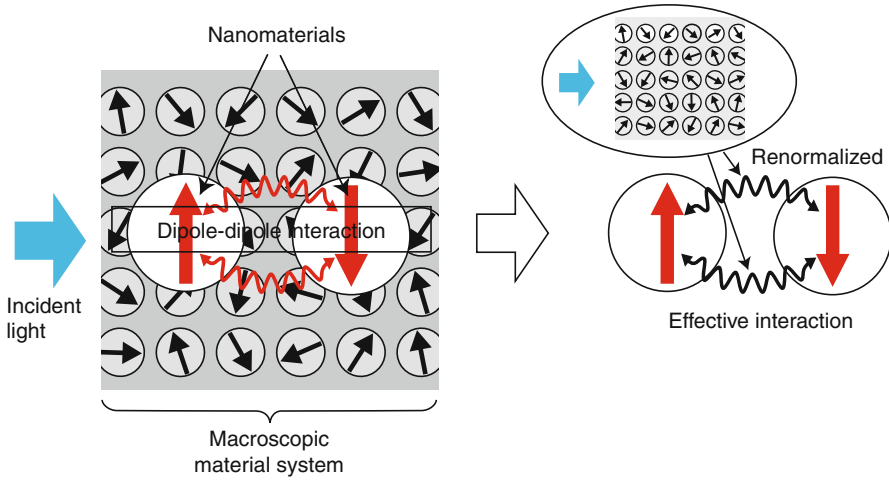


Fig. 6.1 Schematic drawing of near-field optical interactions. The effects from the irrelevant system in which we are not interested are renormalized as the effective interaction between nanomaterials

As discussed in Refs. [9, 13, 27, 28] in detail, the near-field optical interaction potential between nanomaterials separated by R is given as follows:

$$V_{\text{eff}} = \frac{\exp(-aR)}{R}, \quad (6.1)$$

where a^{-1} is the interaction range that represents the characteristic size of nanomaterials and does not depend on the wavelength of light. It indicates that photons are localized around the nanomaterials as a result of the interaction with matter fields, from which a photon, in turn, can acquire a finite mass. Therefore, we might consider as if the near-field optical interaction would be produced via the localized photon hopping [15, 29, 30] between nanomaterials.

In an example, let us look at an optically excited probe system whose apex is sharpened on a nanometer scale, where the radius of curvature of the probe tip, r_0 , is regarded as a characteristic size of the light-matter interacting system. The probe system is coarse-grained in terms of r_0 , and then photons are localized at each coarse-grained point with interaction range r_0 , which causes the localized photons to hop to the nearest neighbor points.

In experiments, the above explanation can be applied to usual near-field imaging and spectroscopy. In addition, the near-field optical interactions between semiconductor quantum dots [17, 31, 32], between semiconductor nanorods [33], as well as light-harvesting antenna complex of photosynthetic purple bacteria [34, 35], have been observed by using the optically forbidden excitation energy transfer. Moreover, the near-field optical interactions are used in nanofabrication, which will be discussed in the following subsection.

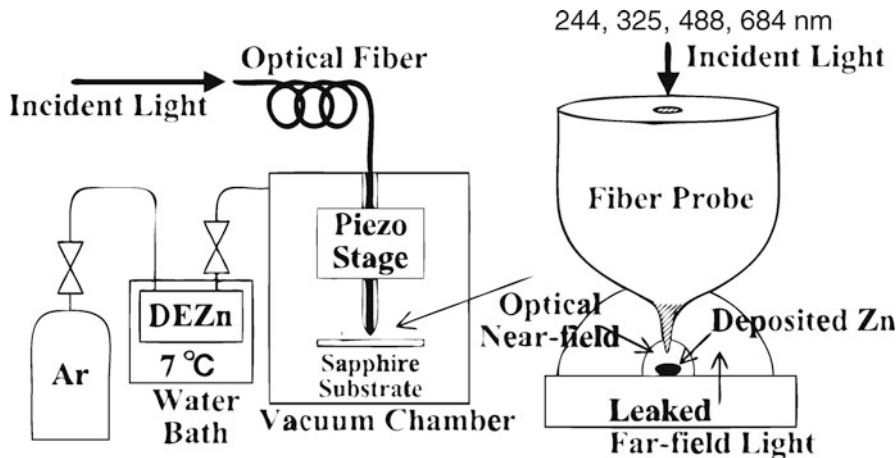


Fig. 6.2 Experimental setup for chemical vapor deposition using an optical near field. The DEZn bottle and CVD chamber were kept at 7 and 25 °C, respectively, to prevent the condensation of DEZn on the sapphire substrate. During deposition, the partial pressure of DEZn was 100 mTorr and the total pressure in the chamber was 8 Torr

6.2.2 Photodissociation of Molecules and EPP Model

We review the nanofabrication technique using the optical near field, and discuss the unique feature found in the results of photodissociation experiments, using a simple model (exciton–phonon polariton (EPP) model).

Experimental. As schematically illustrated in Fig. 6.2, optical near-field chemical vapor deposition (NFO-CVD) is used to fabricate a nanometer-scale structure while controlling position and size [4, 5]. Incident laser light is introduced into an optical near-field probe, that is, a glass fiber that is chemically etched to have a nanometric sized apex without metal coating usually employed. The propagating far field is generated by light leaking through the circumference of the fiber, while the optical near field is mainly generated at the apex. This allows us to investigate the deposition by an optical near field and far field simultaneously. The separation between the fiber probe and the sapphire (0001) substrate is kept within a few nanometers by shear-force feedback control. By appropriately selecting reactant molecules to be dissociated, NFO-CVD is applicable to various materials such as metals, semiconductors, and insulators. In the following, however, we concentrate on diethylzinc (DEZn) and zinc-bis (acetylacetonate) ($\text{Zn}(\text{acac})_2$) as reactant molecules, at 70–100 mTorr at room temperature.

In order to investigate the mechanism of the photochemical process, deposition rates depending on photon energy and intensity have been measured with several laser sources: for DEZn molecules,

1. The second harmonic of an Ar^+ laser ($\hbar\omega = 5.08$ eV, corresponding wavelength $\lambda = 244$ nm), whose energy is close to the electronic excitation energy (5 eV) of a DEZn molecule

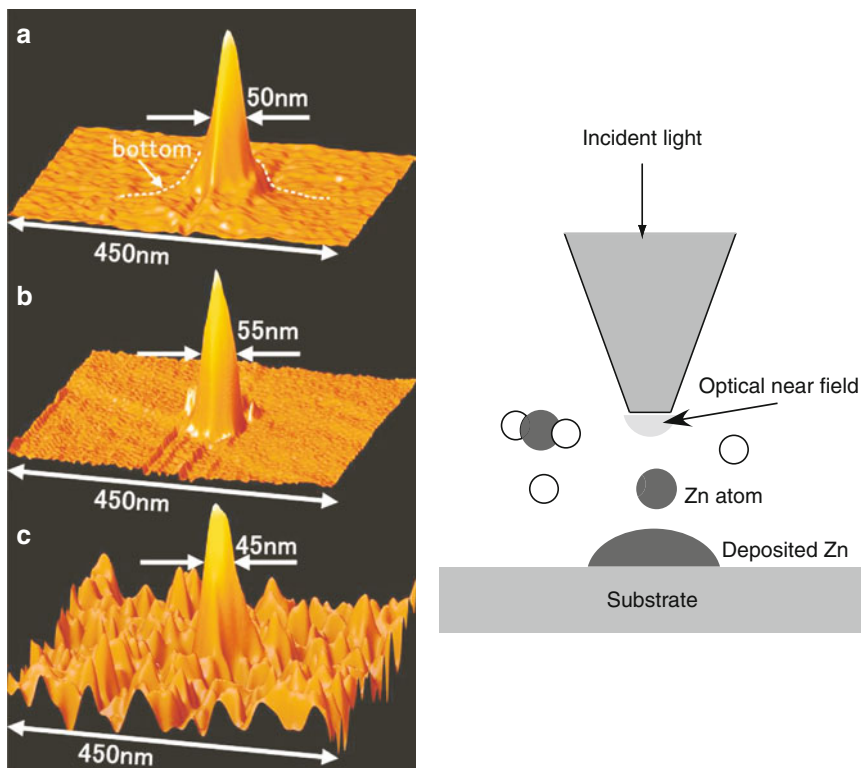


Fig. 6.3 Schematic drawing of NFO-CVD and experimental results. Incident photon energies used are (a) 3.81 eV, (b) 2.54 eV, and (c) 1.81 eV

2. An He-Cd laser ($\hbar\omega = 3.81$ eV, corresponding wavelength $\lambda = 325$ nm), whose energy is close to $E_{\text{abs}} \sim 4.13$ eV [36, 37] corresponding to the energy of the absorption band edge
3. An Ar^+ laser ($\hbar\omega = 2.54$ eV, corresponding wavelength $\lambda = 488$ nm), whose energy is larger than the dissociation energy of the molecule (2.26 eV), but much smaller than the electronic excitation energy and E_{abs}
4. A diode laser ($\hbar\omega = 1.81$ eV, corresponding wavelength $\lambda = 684$ nm), whose energy is smaller than both the dissociation and electronic excitation energies, as well as E_{abs} .

And for $\text{Zn}(\text{acac})_2$:

1. An Ar^+ laser ($\hbar\omega = 2.71$ eV, corresponding wavelength $\lambda = 457$ nm), whose energy is much smaller than the electronic excitation energy and $E_{\text{abs}} \sim 5.17$ eV. Shear-force topographical images are shown in Fig. 6.3 after NFO-CVD at photon energies listed above. In conventional CVD using a propagating light, photon energy must be higher than E_{abs} because dissociative molecules should be excited from the ground state to an excited electronic state, according to the adiabatic

approximation [38,39]. In contrast, even if photon energy less than E_{abs} is employed in NFO-CVD, the deposition of Zn dots are observed on the substrate just below the apex of the probe used. Much more interested, photons with less energy than the dissociation energy can resolve both DEZn and Zn(acac)₂ molecules into a composite atoms and deposit them as a nanometric dots [20,40].

One possibility inferred from the results is a multiple photon absorption process, which is negligibly small because the optical power density used in the experiment was less than 10 kW/cm² that is too low for the process. The other possibility is a multiple step transition via an excited molecular vibrational level that is forbidden by the Franck–Condon principle, but allowed in a nonadiabatic process. In order to clarify the unique feature of NFO-CVD, we will give a simple model to discuss the process below.

EPP Model. We propose a quasiparticl (exciton–phonon polariton) model as a simple model of an optically excited probe system, in order to investigate the physical mechanisms of the chemical vapor deposition using an optical near field (NFO-CVD) [21]. We assume that exciton–phonon polaritons, the quanta of which are transferred from the optical near-field probe tip to both gas and adsorbed molecules, are created at the apex of the optical near-field probe. Here it should be noted that the quasiparticle transfer is valid only if the molecules are very close to the probe tip because the optical near field is highly localized near the probe tip, which will be discussed in Sect. 6.4.4. The optical near field generated on the nanometric probe tip, which is a highly mixed state with material excitation rather than the propagating light field [13,28], is described in terms of the following model Hamiltonian:

$$\begin{aligned}
 H &= \sum_p \hbar \left\{ \omega_p a_p^\dagger a_p + \omega_p^{\text{ex}} b_p^\dagger b_p + \frac{i\Omega_c}{2} (a_p^\dagger b_p - b_p^\dagger a_p) \right\} \\
 &\quad + \sum_p \hbar \Omega_p c_p^\dagger c_p + \sum_{p,q} \left[i\hbar M (p-q) b_p^\dagger b_q \{c_{p-q} + c_{q-p}^\dagger\} + h.c. \right] \\
 &= \sum_p \hbar \omega_p^{\text{pol}} B_p^\dagger B_p + \sum_p \hbar \Omega_p c_p^\dagger c_p \\
 &\quad + \sum_{p,q} \left[i\hbar M' (p-q) B_p^\dagger B_q \{c_{p-q} + c_{q-p}^\dagger\} + h.c. \right], \tag{6.2}
 \end{aligned}$$

where the creation (annihilation) operators for a photon, an exciton (a quasiparticle for an electronic polarization field), a renormalized phonon (whose physical meanings will be discussed in Sect. 6.4.3), and an exciton polariton are, respectively, denoted by a_p^\dagger (a_p), b_p^\dagger (b_p), c_p^\dagger (c_p), and B_p^\dagger (B_p), and their frequencies are ω_p , ω_p^{ex} , Ω_p , and ω_p^{pol} , respectively. The subscripts p and q indicate the momenta of the relevant particle in the momentum representation such as a photon, an exciton, a renormalized phonon, an exciton polariton, or an exciton–phonon polariton.

Each coupling between a photon and an exciton, a phonon and an exciton, and an exciton polariton and a phonon is designated as Ω_c , $M(p - q)$, and $M'(p - q)$, respectively. The first line of this description expresses the Hamiltonian for a photon-exciton interacting system and is transformed into the exciton-polariton representation as shown in the third line [41], while the second line represents the Hamiltonian for a phonon-exciton interacting system. Note that electronic excitations near the probe tip, driven by photons incident into the fiber probe, cause mode-mode couplings or anharmonic couplings of phonons and that they are taken into account as a renormalized phonon; therefore, multiple phonons as coherently squeezed phonons in the original representation can interact with an exciton or an exciton polariton simultaneously. In the model, quasiparticles (exciton-phonon polaritons) in bulk material (glass fiber) are approximately used, and thus their states are specified by the momentum. Strictly speaking, momentum is not a good quantum number to specify the quasiparticle states at the apex of the probe, from the symmetry consideration, and they should be a superposition of such momentum-specified states with different weights. Instead of this kind of treatment, we simply assume that the quasiparticles specified by the momentum are transferred to a vapor or adsorbed molecule that is located near the probe tip, utilizing highly spatial localization of the optical near field to be discussed in Sect. 6.4.4 in detail.

Now we assume that exciton polaritons near the probe tip are expressed in the mean field approximation as

$$\langle B_{k_0}^\dagger \rangle = \langle B_{k_0} \rangle = \sqrt{\frac{I_0(\omega_0) V}{\hbar \omega_0 d}}. \quad (6.3)$$

Here $I_0(\omega_0)$ is the photon intensity inside the probe tip with frequency ω_0 and momentum $\hbar k_0$ and V represents the volume to be considered while the probe tip size is denoted by d . Using the unitary transformation as

$$\begin{pmatrix} B_p \\ c_{p-k_0} \end{pmatrix} = \begin{pmatrix} i v'_p & u'_p \\ u'_p & i v'_p \end{pmatrix} \begin{pmatrix} \xi_{(-)p} \\ \xi_{(+)p} \end{pmatrix}, \quad (6.4)$$

we can diagonalize the Hamiltonian in the exciton-phonon polariton representation [42] as

$$\begin{aligned} H &= \sum_p \hbar \omega_p^{\text{pol}} B_p^\dagger B_p + \sum_p \hbar \Omega_p c_p^\dagger c_p \\ &+ \sum_p \left\{ i \hbar \sqrt{\frac{I_0(\omega_0) V}{\hbar \omega_0 d}} M'(p - k_0) (B_p^\dagger c_{p-k_0} + B_p c_{p-k_0}^\dagger) \right\} \\ &= \sum_p \sum_{j=\pm} \hbar \omega(p) \xi_{jp}^\dagger \xi_{jp}, \end{aligned} \quad (6.5)$$

where the creation (annihilation) operator for an exciton–phonon polariton and the frequency are denoted by ξ_{jp}^\dagger (ξ_{jp}) and $\omega(p)$, respectively. The suffix (–) or (+) indicates the lower or upper branch of the exciton–phonon polariton. The transformation coefficients u'_p and v'_p are given by

$$u'_p = \frac{1}{2} \left(1 + \frac{\Delta}{\sqrt{\Delta^2 + (2Q)^2}} \right), \quad v'_p = \frac{1}{2} \left(1 - \frac{\Delta}{\sqrt{\Delta^2 + (2Q)^2}} \right), \quad (6.6)$$

where the detuning between an exciton polariton and a phonon is denoted by $\Delta = \omega_p^{\text{pol}} - \Omega_{p-k_0}$, and the effective coupling constant is expressed as $Q = \sqrt{I_0(\omega_0) V / (\hbar\omega_0 d) M' (p - k_0)}$. Therefore, in this model, a molecule located near the probe tip does absorb not simple photons but exciton–phonon polaritons whose energies are transferred to the molecule, which excite molecular vibrations as well as electronic transitions. In the following sections, we will discuss how phonons work in the optically excited probe system in detail.

6.3 Localized Phonons

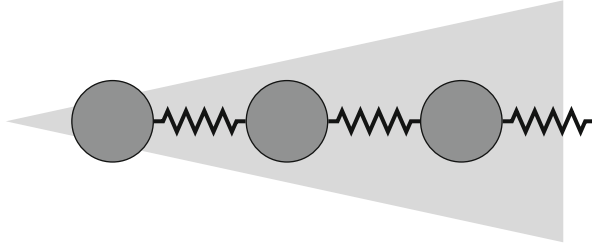
In this section, lattice vibrations in a pseudo one-dimensional system are briefly described and then quantized. We examine the effects of impurities or defects in such a system to show that the localized vibration modes exist as eigenmodes, and those energies are higher than those of delocalized ones.

6.3.1 Lattice Vibration in Pseudo One-Dimensional System

Owing to the progress in nanofabrication, the apexes of optical near-field probes are sharpened on the order of a few nanometers. In this region, the guiding modes of light field are cut off and visible light cannot propagate in a conventional way. Therefore, it is necessary to clarify the interactions among light, induced electronic, and vibrational fields on the nanometer space such as the optically excited probe tip, and the mechanism of localization (delocalization) of light field as a result of self-consistency of those interacting fields. As the first step, we examine the lattice vibrations themselves in this section.

Let us assume a pseudo one-dimensional system for the probe tip, as schematically illustrated in Fig. 6.4. The system consists of a finite number (N) of atoms or molecules, which will be representatively called molecules. Each molecule is located at a discrete site and is connected with the nearest-neighbor molecules by springs. The size of each molecule and the spacing between the molecules depend on how the system is coarse-grained. In any case, the total site number N is finite, and the wave number is not a good quantum number because the system breaks the translational invariance [43]. That is why we begin with the Hamiltonian of

Fig. 6.4 A pseudo one-dimensional system for a NFO probe tip



the system to analyze vibrational (phonon) modes, instead of the conventional method using the dynamical matrix [44]. By denoting a displacement from an equilibrium point of a molecule by \mathbf{x}_i and its conjugate momentum by \mathbf{p}_i , the model Hamiltonian is given by

$$H = \sum_{i=1}^N \frac{\mathbf{p}_i^2}{2m_i} + \sum_{i=1}^{N-1} \frac{1}{2}k(\mathbf{x}_{i+1} - \mathbf{x}_i)^2 + \frac{1}{2}k\mathbf{x}_1^2 + \frac{1}{2}k\mathbf{x}_N^2, \quad (6.7)$$

where m_i is the mass of a molecule at site i , and k represents the spring constant. Both edges ($i = 1$ and $i = N$) are assumed to be fixed, and longitudinal motions in one-dimension are considered in the following.

The equations of motion are determined by the Hamilton equation as

$$\frac{d}{dt}\mathbf{x}_i = \frac{\partial H}{\partial \mathbf{p}_i}, \quad \frac{d}{dt}\mathbf{p}_i = -\frac{\partial H}{\partial \mathbf{x}_i}. \quad (6.8)$$

If one uses a matrix form defined by

$$\mathbf{M} = \begin{pmatrix} m_1 & & & \\ & m_2 & & \\ & & \ddots & \\ & & & m_N \end{pmatrix}, \quad \mathbf{\Gamma} = \begin{pmatrix} 2 & -1 & & \\ -1 & 2 & \ddots & \\ & \ddots & \ddots & -1 \\ & & -1 & 2 \end{pmatrix}, \quad (6.9)$$

one can obtain the following compact equations of motion:

$$\mathbf{M} \frac{d^2}{dt^2} \mathbf{x} = -k\mathbf{\Gamma} \mathbf{x}, \quad (6.10)$$

with transpose of the column vector \mathbf{x} as

$$\mathbf{x}^T \equiv (\mathbf{x}_1, \mathbf{x}_2, \dots, \mathbf{x}_N). \quad (6.11)$$

Multiplying the both hand sides of (6.10) by $\sqrt{\mathbf{M}}^{-1}$ with $(\sqrt{\mathbf{M}})_{ij} = \delta_{ij} \sqrt{m_i}$, we have

$$\frac{d^2}{dt^2} \mathbf{x}' = -k \mathbf{A} \mathbf{x}', \quad (6.12)$$

where the notation $\mathbf{x}' = \sqrt{M} \mathbf{x}$ and $\mathbf{A} = \sqrt{M}^{-1} \Gamma \sqrt{M}^{-1}$ are used. Since it is symmetric, the matrix \mathbf{A} can be diagonalized by an orthonormal matrix \mathbf{P} as follows:

$$\Lambda = \mathbf{P}^{-1} \mathbf{A} \mathbf{P}, \quad \text{or} \quad (\Lambda)_{pq} = \delta_{pq} \frac{\Omega_p^2}{k}. \quad (6.13)$$

Substitution of (6.13) into (6.12) leads us to equations of motion for a set of harmonic oscillators as

$$\frac{d^2}{dt^2} \mathbf{y} = -k \Lambda \mathbf{y}, \quad \text{or} \quad \frac{d^2}{dt^2} \mathbf{y}_p = -\Omega_p^2 \mathbf{y}_p, \quad (6.14)$$

where \mathbf{y} is set as $\mathbf{y} = \mathbf{P}^{-1} \mathbf{x}'$. There are N normal coordinates to describe the harmonic oscillators, each of which is specified by the mode number p . The original spatial coordinates \mathbf{x} are transformed to the normal coordinates \mathbf{y} as

$$\mathbf{x} = \sqrt{M}^{-1} \mathbf{P} \mathbf{y}, \quad \text{or} \quad x_i = \frac{1}{\sqrt{m_i}} \sum_{p=1}^N P_{ip} \mathbf{y}_p. \quad (6.15)$$

6.3.2 Quantization of Vibration

In order to quantize the vibration field described by (6.14), we first rewrite the Hamiltonian (6.7) in terms of normal coordinates \mathbf{y}_p and conjugate momenta $\boldsymbol{\pi}_p$ as

$$H(\mathbf{y}, \boldsymbol{\pi}) = \sum_{p=1}^N \frac{1}{2} \boldsymbol{\pi}_p^2 + \sum_{p=1}^N \frac{1}{2} \Omega_p^2 \mathbf{y}_p^2. \quad (6.16)$$

Then the commutation relation between $\hat{\mathbf{y}}_p$ and $\hat{\boldsymbol{\pi}}_q$ as

$$[\hat{\mathbf{y}}_p, \hat{\boldsymbol{\pi}}_q] = i \hbar \delta_{pq}, \quad (6.17)$$

is imposed for quantization. When we define operators \hat{b}_p and \hat{b}_p^\dagger as

$$\hat{b}_p = \frac{1}{\sqrt{2\hbar\Omega_p}} (\hat{\boldsymbol{\pi}}_p - i\Omega_p \hat{\mathbf{y}}_p), \quad (6.18a)$$

$$\hat{b}_p^\dagger = \frac{1}{\sqrt{2\hbar\Omega_p}} (\hat{\boldsymbol{\pi}}_p + i\Omega_p \hat{\mathbf{y}}_p), \quad (6.18b)$$

they satisfy the boson commutation relation

$$[\hat{b}_p, \hat{b}_q^\dagger] = \delta_{pq} . \quad (6.19)$$

The Hamiltonian describing the lattice vibration of the system, (6.16), can then be rewritten as

$$\hat{H}_{\text{phonon}} = \sum_{p=1}^N \hbar \Omega_p \left(\hat{b}_p^\dagger \hat{b}_p + \frac{1}{2} \right) , \quad (6.20)$$

and it follows that \hat{b}_p (\hat{b}_p^\dagger) is the annihilation (creation) operator of a phonon with energy of $\hbar \Omega_p$ specified by the mode number p .

6.3.3 Vibration Modes: Localized Versus Delocalized

In this subsection, we examine the effects of impurities or defects in the system. When all the molecules are identical, that is, $m_i = m$, the Hamiltonian (6.7), or the matrix A can be diagonalized in terms of the orthonormal matrix P whose elements are given by

$$P_{ip} = \sqrt{\frac{2}{N+1}} \sin \left(\frac{ip}{N+1} \pi \right) , \quad (1 \leq i, p \leq N) , \quad (6.21)$$

and the eigenfrequencies squared are obtained as follows:

$$\Omega_p^2 = 4 \frac{k}{m} \sin^2 \left(\frac{p}{2(N+1)} \pi \right) . \quad (6.22)$$

In this case, all the vibration modes are delocalized, that is, they are spread over the whole system. On the other hand, if there are some doped impurities or defects with different mass, the vibration modes highly depend on geometrical configuration and mass ratio of the impurities to the others. In particular, localized vibration modes manifest themselves when the mass of the impurities is lighter than that of the others, where vibrations with higher frequencies are localized around the impurity sites [45–48].

Figure 6.5a, b illustrate that the localized vibration modes exist as eigenmodes in the one-dimensional system due to the doped molecules with different mass in the chain, and eigenenergies of localized modes are higher than those of delocalized ones. In Fig. 6.5a, phonon energies are plotted as a function of the mode number when the total number of sites is 30. The squares represent the eigenenergies of phonons in the case of no impurities, and the circles show those in the case of six impurities, where the doped molecules are located at site 5, 9, 18, 25, 26, and 27.

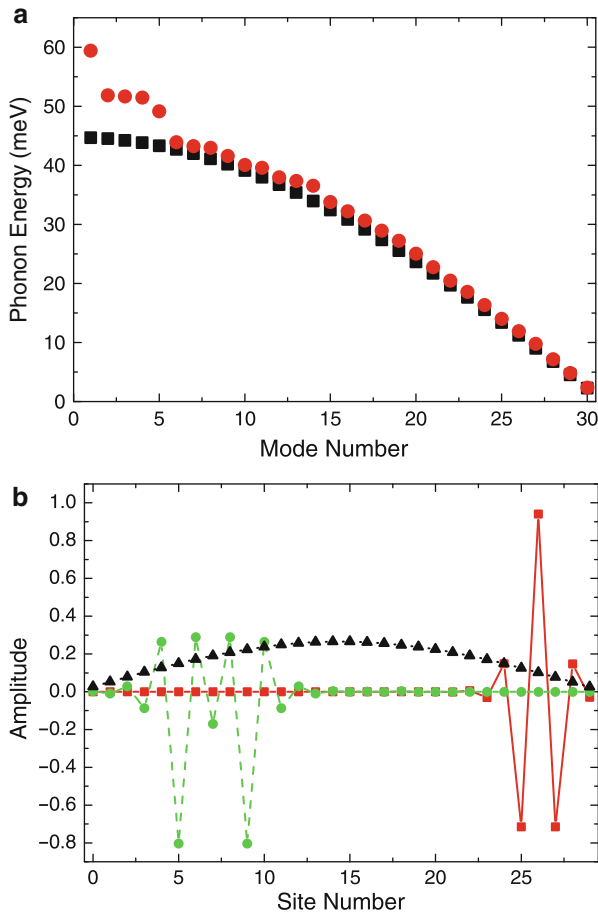


Fig. 6.5 (a) Eigenfrequencies of all phonon modes with/without impurities (depicted with the *circles/squares*), in the case of $N = 30$, and (b) the first and second localized phonon modes and the lowest delocalized phonon mode (represented by the *solid, dashed, and dotted curves*). Impurities are doped at site 5, 9, 18, 25, 26, and 27. The mass ratio of the host molecules to the impurities is set as 1 to 0.5, and $\hbar\sqrt{k/m} = 22.4$ meV is used for both (a) and (b)

It follows from the figure that phonon energies of the localized modes are higher than those of the delocalized modes, where the mass ratio of the doped molecules to the others is 1/2, and the parameter $\hbar\sqrt{k/m} = 22.4$ meV is used. Figure 6.5b shows the vibration amplitude as a function of the site number. The solid curve with squares and the dashed curve with circles represent two localized modes with the highest and the next highest energies of phonons, respectively, while the dotted curve with triangles illustrates the delocalized mode with the lowest energy. In the localized modes, the vibration amplitudes are localized around the impurity sites.

In the next section, we will discuss the interactions between photons and inhomogeneous phonon fields on the nanometer scale, since we have found inhomogeneous phonon fields in the one-dimensional system with impurities.

6.4 Model

In this section, we propose a simple model for a pseudo one-dimensional optical near-field probe system to discuss the mechanism of photon localization in space as well as phonon's role. In order to focus on the photon-phonon interaction, the interacting part between photon and electronic excitation is first expressed in terms of a polariton and is called a photon in the model. Then the model Hamiltonian, which describes the photon and phonon interacting system, is presented. Using the Davydov transformation [43, 49, 50], we rewrite the Hamiltonian in terms of quasiparticles. On the basis of the Hamiltonian, we present numerical results on spatial distribution of photons and discuss the mechanism of photon localization due to phonons.

6.4.1 Optically Excited Probe System

We consider an optical near-field probe, schematically shown in Fig. 6.4, as a system where light interacts with both phonons and electrons in the probe on a nanometer scale. Here the interaction of a photon and an electronic excitation is assumed to be expressed in terms of a polariton basis [28] as discussed in Sect. 6.2.2 and is hereafter called a photon so that a special attention is paid on the photon-phonon interaction. The system is simply modeled as a one-dimensional atomic or molecular chain coupled with photon and phonon fields. The chain consists of a finite N molecules (representatively called) each of which is located at a discrete point (called a molecular site) whose separation represents a characteristic scale of the near-field system. Photons are expressed in the site representation and can hop to the nearest neighbor sites [15] due to the short-range interaction nature of the optical near fields (see (6.1)).

The Hamiltonian for the above model is given by

$$\begin{aligned} \hat{H} = & \sum_{i=1}^N \hbar\omega \hat{a}_i^\dagger \hat{a}_i + \left\{ \sum_{i=1}^N \frac{\hat{p}_i^2}{2m_i} + \sum_{i=1}^{N-1} \frac{k}{2} (\hat{x}_{i+1} - \hat{x}_i)^2 + \sum_{i=1, N} \frac{k}{2} \hat{x}_i^2 \right\} \\ & + \sum_{i=1}^N \hbar\chi \hat{a}_i^\dagger \hat{a}_i \hat{x}_i + \sum_{i=1}^{N-1} \hbar J (\hat{a}_i^\dagger \hat{a}_{i+1} + \hat{a}_{i+1}^\dagger \hat{a}_i), \end{aligned} \quad (6.23)$$

where \hat{a}_i^\dagger and \hat{a}_i correspondingly denote the creation and annihilation operators of a photon with energy of $\hbar\omega$ at site i in the chain, \hat{x}_i and \hat{p}_i represent the displacement

and conjugate momentum operators of the vibration, respectively. The mass of a molecule at site i is designated by m_i , and each molecule is assumed to be connected by springs with spring constant k . The third and the fourth terms in (6.23) stand for the photon–vibration interaction with coupling constant χ and the photon hopping with hopping constant J , respectively.

After the vibration field is quantized in terms of phonon operators of mode p and frequency Ω_p , \hat{b}_p^\dagger and \hat{b}_p , the Hamiltonian (6.23) can be rewritten as

$$\begin{aligned} \hat{H} = & \sum_{i=1}^N \hbar\omega \hat{a}_i^\dagger \hat{a}_i + \sum_{p=1}^N \hbar\Omega_p \hat{b}_p^\dagger \hat{b}_p + \sum_{i=1}^N \sum_{p=1}^N \hbar\chi_{i,p} \hat{a}_i^\dagger \hat{a}_i (\hat{b}_p^\dagger + \hat{b}_p) \\ & + \sum_{i=1}^{N-1} \hbar J (\hat{a}_i^\dagger \hat{a}_{i+1} + \hat{a}_{i+1}^\dagger \hat{a}_i), \end{aligned} \quad (6.24)$$

with the coupling constant $\chi_{i,p}$ of a photon at site i and a phonon of mode p . This site-dependent coupling constant $\chi_{i,p}$ is related to the original coupling constant χ as

$$\chi_{i,p} = \chi P_{ip} \sqrt{\frac{\hbar}{2m_i\Omega_p}}, \quad (6.25)$$

and the creation and annihilation operators of a photon and a phonon satisfy the boson commutation relation as follow:

$$\begin{aligned} [\hat{a}_i, \hat{a}_j^\dagger] &= \delta_{ij}, & [\hat{b}_p, \hat{b}_q^\dagger] &= \delta_{pq}, \\ [\hat{a}_i, \hat{a}_j] &= [\hat{a}_i^\dagger, \hat{a}_j^\dagger] = 0 = [\hat{b}_p, \hat{b}_q] = [\hat{b}_p^\dagger, \hat{b}_q^\dagger], \\ [\hat{a}_i, \hat{b}_p] &= [\hat{a}_i, \hat{b}_p^\dagger] = [\hat{a}_i^\dagger, \hat{b}_p] = [\hat{a}_i^\dagger, \hat{b}_p^\dagger] = 0. \end{aligned} \quad (6.26)$$

The Hamiltonian (6.24), which describes the model system, is not easily handled because of the third order of the operators in the interaction term. To avoid the difficulty, this direct photon-phonon interaction term in (6.24) will be eliminated by the Davydov transformation in the following section.

6.4.2 Davydov Transformation

Before going into the explicit expression, we discuss a unitary transformation \hat{U} generated by an anti-Hermitian operator \hat{S} defined as

$$\hat{U} \equiv e^{\hat{S}}, \quad \text{with } \hat{S}^\dagger = -\hat{S}, \quad (6.27a)$$

$$\hat{U}^\dagger = \hat{U}^{-1}. \quad (6.27b)$$

Suppose a Hamiltonian \hat{H} that consists of a diagonalized part \hat{H}_0 and a non-diagonal interaction part \hat{V} as

$$\hat{H} = \hat{H}_0 + \hat{V}. \quad (6.28)$$

Transforming the Hamiltonian in (6.28) as

$$\tilde{H} \equiv \hat{U} \hat{H} \hat{U}^\dagger = \hat{U} \hat{H} \hat{U}^{-1}, \quad (6.29)$$

we have

$$\begin{aligned} \tilde{H} &= \hat{H} + [\hat{S}, \hat{H}] + \frac{1}{2} [\hat{S}, [\hat{S}, \hat{H}]] + \dots \\ &= \hat{H}_0 + \hat{V} + [\hat{S}, \hat{H}_0] + [\hat{S}, \hat{V}] + \frac{1}{2} [\hat{S}, [\hat{S}, \hat{H}_0]] + \dots \end{aligned} \quad (6.30)$$

If the interaction \hat{V} can be perturbative, and if the operator \hat{S} is chosen so that the second and the third terms in (6.30) are canceled out as

$$\hat{V} = -[\hat{S}, \hat{H}_0], \quad (6.31)$$

the Hamiltonian (6.30) is rewritten as

$$\tilde{H} = \hat{H}_0 - \frac{1}{2} [\hat{S}, [\hat{S}, \hat{H}_0]] + \dots, \quad (6.32)$$

and can be diagonalized within the first order of \hat{V} .

Now we apply the above discussion to the model Hamiltonian (6.24),

$$\hat{H}_0 = \sum_{i=1}^N \hbar \omega \hat{a}_i^\dagger \hat{a}_i + \sum_{p=1}^N \hbar \Omega_p \hat{b}_p^\dagger \hat{b}_p, \quad (6.33a)$$

$$\hat{V} = \sum_{i=1}^N \sum_{p=1}^N \hbar \chi_{i,p} \hat{a}_i^\dagger \hat{a}_i (\hat{b}_p^\dagger + \hat{b}_p), \quad (6.33b)$$

tentatively neglecting the hopping term. Assuming the anti-Hermitian operator \hat{S} as

$$\hat{S} = \sum_i \sum_p f_{ip} \hat{a}_i^\dagger \hat{a}_i (\hat{b}_p^\dagger - \hat{b}_p), \quad (6.34)$$

we can determine f_{ip} from (6.31) as follows:

$$f_{ip} = \frac{\chi_{ip}}{\Omega_p}. \quad (6.35)$$

This operator form of \hat{S} leads us to not the perturbative but the exact transformation of the photon and phonon operators as

$$\hat{\alpha}_i^\dagger \equiv \hat{U}^\dagger \hat{a}_i^\dagger \hat{U} = \hat{a}_i^\dagger \exp \left\{ - \sum_{p=1}^N \frac{\chi_{ip}}{\Omega_p} (\hat{b}_p^\dagger - \hat{b}_p) \right\}, \quad (6.36a)$$

$$\hat{\alpha}_i \equiv \hat{U}^\dagger \hat{a}_i \hat{U} = \hat{a}_i \exp \left\{ \sum_{p=1}^N \frac{\chi_{ip}}{\Omega_p} (\hat{b}_p^\dagger - \hat{b}_p) \right\}, \quad (6.36b)$$

$$\hat{\beta}_p^\dagger \equiv \hat{U}^\dagger \hat{b}_p^\dagger \hat{U} = \hat{b}_p^\dagger + \sum_{i=1}^N \frac{\chi_{ip}}{\Omega_p} \hat{a}_i^\dagger \hat{a}_i, \quad (6.36c)$$

$$\hat{\beta}_p \equiv \hat{U}^\dagger \hat{b}_p \hat{U} = \hat{b}_p + \sum_{i=1}^N \frac{\chi_{ip}}{\Omega_p} \hat{a}_i^\dagger \hat{a}_i. \quad (6.36d)$$

These transformed operators can be regarded as the creation and annihilation operators of quasiparticles – dressed photons and phonons – that satisfy the same boson commutation relations as those of photons and phonons before the transformation:

$$[\hat{\alpha}_i, \hat{\alpha}_j^\dagger] = \hat{U}^\dagger [\hat{a}_i, \hat{a}_j^\dagger] \hat{U} = \delta_{ij}, \quad (6.37a)$$

$$[\hat{\beta}_p, \hat{\beta}_q^\dagger] = \hat{U}^\dagger [\hat{b}_p, \hat{b}_q^\dagger] \hat{U} = \delta_{pq}. \quad (6.37b)$$

Using the quasiparticle operators, we can rewrite the Hamiltonian (6.24) as

$$\begin{aligned} \hat{H} = & \sum_{i=1}^N \hbar \omega \hat{\alpha}_i^\dagger \hat{\alpha}_i + \sum_{p=1}^N \hbar \Omega_p \hat{\beta}_p^\dagger \hat{\beta}_p - \sum_{i=1}^N \sum_{j=1}^N \sum_{p=1}^N \hbar \frac{\chi_{ip} \chi_{jp}}{\Omega_p} \hat{\alpha}_i^\dagger \hat{\alpha}_i \hat{\alpha}_j^\dagger \hat{\alpha}_j \\ & + \sum_{i=1}^{N-1} \hbar \left(\hat{J}_i \hat{\alpha}_i^\dagger \hat{\alpha}_{i+1} + \hat{J}_i^\dagger \hat{\alpha}_{i+1}^\dagger \hat{\alpha}_i \right), \end{aligned} \quad (6.38)$$

with

$$\hat{J}_i = J \exp \left\{ \sum_{p=1}^N \frac{(\chi_{i,p} - \chi_{i+1,p})}{\Omega_p} (\hat{\beta}_p^\dagger - \hat{\beta}_p) \right\}, \quad (6.39)$$

where it is noted that the direct photon-phonon coupling term has been eliminated while the quadratic form $\hat{N}_i \hat{N}_j$ with the number operator of $\hat{N}_i = \hat{\alpha}_i^\dagger \alpha_i$ has emerged as well as the site-dependent hopping operator (6.39). The number states of quasiparticles are thus eigenstates of each terms of the Hamiltonian (6.38), except the last term that represents the higher order effect of photon-phonon coupling through the dressed photon hopping. Therefore, it is a more appropriate form to discuss the phonon's effect on photon's behavior as localization.

6.4.3 Quasiparticle and Coherent State

In the previous section, we have transformed the original Hamiltonian by the Davydov transformation. In order to grasp the physical meanings of the quasiparticles introduced above, the creation operator $\hat{\alpha}_i^\dagger$ is applied to the vacuum state $|0\rangle$. Then it follows from (6.36a)

$$\begin{aligned} \hat{\alpha}_i^\dagger |0\rangle &= \hat{a}_i^\dagger \exp \left\{ - \sum_{p=1}^N \frac{\chi_{ip}}{\Omega_p} (\hat{b}_p^\dagger - \hat{b}_p) \right\} |0\rangle, \\ &= \hat{a}_i^\dagger \exp \left\{ - \sum_{p=1}^N \frac{1}{2} \left(\frac{\chi_{ip}}{\Omega_p} \right)^2 \right\} \exp \left\{ - \sum_{p=1}^N \frac{\chi_{ip}}{\Omega_p} \hat{b}_p^\dagger \right\} |0\rangle, \end{aligned} \quad (6.40)$$

where a photon at site i is associated with phonons in coherent state, that is, a photon is dressed by an infinite number of phonons. This corresponds to the fact that an optical near field is generated from a result of interactions between the photon and matter fields.

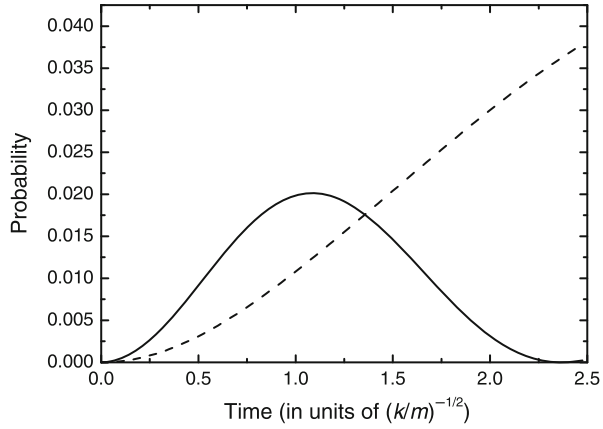
When β_p^\dagger is applied to the vacuum state $|0\rangle$, we have

$$\beta_p^\dagger |0\rangle = b_p^\dagger |0\rangle, \quad (6.41)$$

and it is expressed by only the bare phonon operator (before the transformation) in the same p mode. Therefore, we mainly focus on the quasiparticle expressed by $(\hat{\alpha}_i^\dagger, \hat{\alpha}_i)$ in the following section. Note that it is valid only if the bare photon number (the expectation value of $\hat{a}_i^\dagger a_i$) is not so large that the fluctuation is more important than the bare photon number. In other words, the model we are considering is suitable for discussing the quantum nature of a few photons in an optically excited probe system.

The coherent state of phonons is not an eigenstate of the Hamiltonian, and thus the number of phonons as well as energy is fluctuating. This fluctuation allows incident photons into the probe system to excite phonon fields. When all the phonon fields are in the vacuum at time $t = 0$, the excitation probability $P(t)$ that a photon incident on site i in the model system excites the phonon mode p at time t is given by

Fig. 6.6 Temporal evolution of the excitation probability of a localized (delocalized) phonon mode that is represented by the *solid* (*dashed*) curve. The system is initially excited by a photon at the impurity site 26. The coupling constant $\chi = 10.0$ (fsec $^{-1}$ nm $^{-1}$) and the parameter $\hbar\sqrt{k/m} = 22.4$ meV are used, while other parameters are the same as those in Fig. 6.5



$$P(t) = 1 - \exp \left\{ 2 \left(\frac{\chi_{ip}}{\Omega_p} \right)^2 (\cos \Omega_p t - 1) \right\}, \quad (6.42)$$

where the photon-hopping term is neglected for simplicity. The excitation probability oscillates at frequency of $2\pi/\Omega_p$, and has the maximum value at $t = \pi/\Omega_p$. The frequencies of the localized phonon modes are higher than those of the delocalized ones, and the localized modes at the earlier time are excited by the incident photons.

Figure 6.6 shows the temporal evolution of the excitation probability $P_{p_0}(t)$ calculated from

$$P_{p_0}(t) = \left[1 - \exp \left\{ 2 \left(\frac{\chi_{ip_0}}{\Omega_{p_0}} \right)^2 (\cos \Omega_{p_0} t - 1) \right\} \right] \times \exp \left\{ \sum_{p \neq p_0} 2 \left(\frac{\chi_{ip}}{\Omega_p} \right)^2 (\cos \Omega_p t - 1) \right\}, \quad (6.43)$$

where a specific phonon mode p_0 is excited while other modes are in the vacuum state. In Fig. 6.6, the solid curve represents the probability that a localized phonon mode is excited as the p_0 mode, while the dashed curve illustrates how the lowest phonon mode is excited as the p_0 mode. It follows from the figure that the localized phonon mode is dominantly excited at the earlier time.

6.4.4 Localization Mechanism

In this section, we discuss how phonons contribute to the spatial distribution of photons in the pseudo one-dimensional system under consideration. When there are

no interactions between photons and phonons, the frequency and hopping constant are equal at all sites, and thus the spatial distribution of photons are symmetric. It means that no photon localization occurs at any specific site. However, if there are any photon-phonon interactions, spatial inhomogeneity or localization of phonons affects the spatial distribution of photons. On the basis of the Hamiltonian (6.38), we analyze the contribution from the diagonal and off-diagonal parts in order to investigate the localization mechanism of photons.

Contribution from the Diagonal Part. Let us rewrite the third term of the Hamiltonian (6.38) with the mean field approximation as

$$-\sum_{i=1}^N \sum_{j=1}^N \sum_{p=1}^N \hbar \frac{\chi_{ip} \chi_{jp}}{\Omega_p} \hat{\alpha}_i^\dagger \hat{\alpha}_i \langle \hat{N}_j \rangle \equiv -\sum_{i=1}^N \hbar \omega_i \hat{\alpha}_i^\dagger \hat{\alpha}_i, \quad (6.44)$$

with

$$\omega_i \equiv \sum_{j=1}^N \sum_{p=1}^N \frac{\chi_{ip} \chi_{jp}}{\Omega_p} \langle \hat{N}_j \rangle = \sum_{j=1}^N \sum_{p=1}^N \frac{\hbar \chi^2 \mathbf{P}_{ip} \mathbf{P}_{jp}}{2N \Omega_p^2 (m_i m_j)^{1/2}}, \quad (6.45)$$

where (6.25) is used to obtain the expression in the last line of (6.45). In addition, we neglect the site dependence of the hopping operator \hat{J}_i to approximate J , for the moment. Then the Hamiltonian regarding the quasiparticles ($\hat{\alpha}$ and $\hat{\alpha}^\dagger$) can be expressed as

$$\hat{H} = \sum_{i=1}^N \hbar (\omega - \omega_i) \hat{\alpha}_i^\dagger \hat{\alpha}_i + \sum_{i=1}^{N-1} \hbar J \left(\hat{\alpha}_i^\dagger \hat{\alpha}_{i+1} + \hat{\alpha}_{i+1}^\dagger \hat{\alpha}_i \right), \quad (6.46)$$

or in the matrix form as

$$\hat{H} = \hbar \hat{\alpha}^\dagger \begin{pmatrix} \omega - \omega_1 & J & & \\ J & \omega - \omega_2 & \ddots & \\ & \ddots & \ddots & J \\ & & J & \omega - \omega_N \end{pmatrix} \hat{\alpha}, \quad (6.47a)$$

$$\hat{\alpha}^\dagger \equiv \left(\hat{\alpha}_1^\dagger, \hat{\alpha}_2^\dagger, \dots, \hat{\alpha}_N^\dagger \right), \quad (6.47b)$$

where the effect from the phonon fields is involved in the diagonal elements ω_i . Denoting an orthonormal matrix to diagonalize the Hamiltonian (6.47a) as Q and the r -th eigenvalue as E_r , we have

$$\hat{H} = \sum_{r=1}^N \hbar E_r \hat{A}_r^\dagger \hat{A}_r, \quad (6.48a)$$

$$\hat{A}_r = \sum_{i=1}^N (\mathbf{Q}^{-1})_{ri} \hat{\alpha}_i = \sum_{i=1}^N Q_{ir} \hat{\alpha}_i, \quad (6.48b)$$

$$[\hat{A}_r, \hat{A}_s^\dagger] = \delta_{rs}. \quad (6.48c)$$

Using the above relations (6.48a)–(6.48c), we can write down the time evolution of the photon number operator at site i as follows:

$$\begin{aligned} \hat{N}_i(t) &= \exp\left(i\frac{\hat{H}t}{\hbar}\right) \hat{N}_i \exp\left(-i\frac{\hat{H}t}{\hbar}\right), \\ &= \sum_{r=1}^N \sum_{s=1}^N Q_{ir} Q_{is} \exp\{i(E_r - E_s)t\} \hat{A}_r^\dagger \hat{A}_s. \end{aligned} \quad (6.49)$$

The expectation value of the photon number operator $\hat{N}_i(t)$ is then given by

$$\begin{aligned} \langle N_i(t) \rangle_j &= \langle \psi_j | \hat{N}_i(t) | \psi_j \rangle, \\ &= \sum_{r=1}^N \sum_{s=1}^N Q_{ir} Q_{jr} Q_{is} Q_{js} \cos\{(E_r - E_s)t\}, \end{aligned} \quad (6.50)$$

in terms of one photon state at site j defined by

$$|\psi_j\rangle = \hat{\alpha}_j^\dagger |0\rangle = \sum_{r=1}^N Q_{jr} \hat{A}_r^\dagger |0\rangle. \quad (6.51)$$

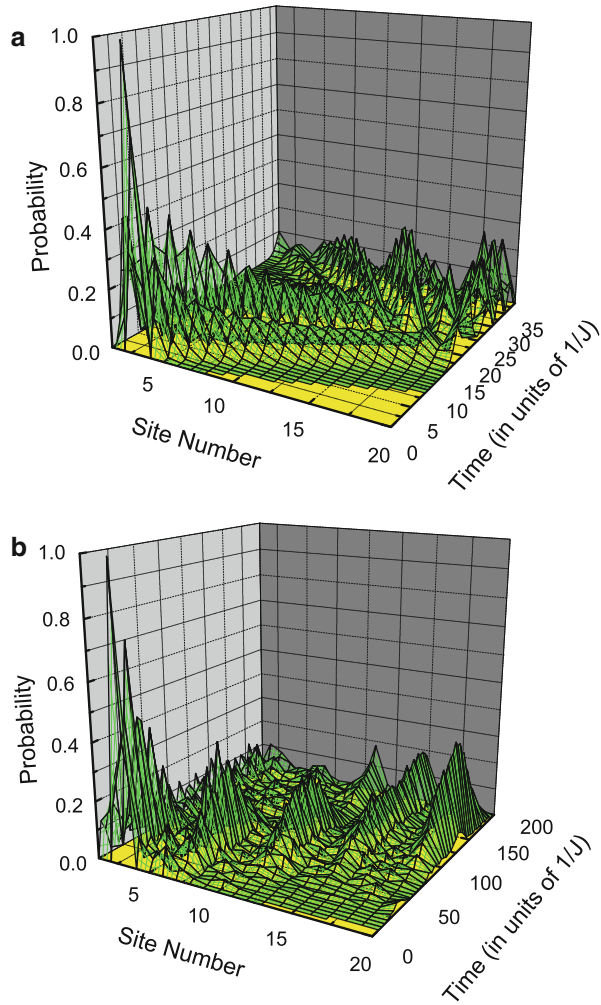
Since the photon number operator \hat{N}_i commutes with the Hamiltonian (6.46), the total photon number is conserved, which means that a polariton called as a photon in this chapter conserves the total particle number within the lifetime. Moreover, $\langle N_i(t) \rangle_j$ can be regarded as the observation probability of a photon at an arbitrary site i and time t , initially populated at site j . This function is analytically expressed in terms of the Bessel function as

$$\langle N_i(t) \rangle_j = \{J_{j-i}(2Jt) - (-1)^j J_{j+i}(2Jt)\}^2, \quad (6.52)$$

when there are no photon-phonon interactions ($\omega_i = 0$) and the total site number N becomes infinite. Here the argument J is the photon hopping constant, and (6.52) shows that a photon initially populated at site j delocalizes to a whole system.

Focusing on the localized phonon modes, we take the summation in (6.45) over the localized modes only, which means that an earlier stage is considered after the incident photon excites the phonon modes, or that the duration of the localized phonon modes dominant over the delocalized modes is focused (see Fig. 6.6).

Fig. 6.7 (a) The probability that a photon is found at each site as a function of time in the case of $\chi = 0$ and $\hbar J = 1$ eV. The time scale is in units of $1/J$. Other parameters are the same as those in Fig. 6.5. (b) The probability that a photon is found at each site as a function of time, in the case of $J \sim (\hbar/k)(\chi/N)^2$. The time scale is in units of $1/J$. Other parameters are the same as those in Fig. 6.5



This kind of analysis provides us with an interesting insight to the photon-phonon coupling constant and the photon hopping constant, which is necessary for the understanding of the mechanism of photon's localization.

The temporal evolution of the observation probability of a photon at each site is shown in Fig. 6.7. Without the photon-phonon coupling ($\chi = 0$), a photon spreads over the whole system as a result of the photon hopping, as shown in Fig. 6.7a. Here the photon energy $\hbar\omega = 1.81$ eV and the hopping constant $\hbar J = 0.5$ eV are used in the calculation. The impurities are assumed to be doped at site 3, 7, 11, 15, and 19 while the total site number N is 20, and the mass ratio of the host molecules to the impurities is 5. Figure 6.7b shows a result with $\chi = 1.4 \times 10^3$ fsec $^{-1}$ nm $^{-1}$ while other parameters used are the same as those in Fig. 6.7a. It follows from the figure that a photon moves from one impurity to other impurity sites instead of delocalizing to a whole system. As the photon-phonon coupling constant becomes much larger

than $\chi = 1.4 \times 10^3 \text{ fsec}^{-1} \text{ nm}^{-1}$, a photon cannot move from the initial impurity site to others and stay there.

The effect due to the photon-phonon coupling χ is expressed by the diagonal component in the Hamiltonian, while the off-diagonal component involves the photon-hopping effect due to the hopping constant J . The above results indicate that photon's spatial distribution depends on the competition between the diagonal and off-diagonal components in the Hamiltonian, that is, χ and J , and that a photon can move among impurity sites and localize at those sites when both components are comparable under the condition

$$\chi \sim N \sqrt{\frac{k}{\hbar}} J, \quad (6.53)$$

where the localization width seems very narrow.

Contribution from the Off-Diagonal Part. In the previous section, we have approximated J as a constant independent of the sites, in order to examine the photon's spatial distribution as well as the mechanism of the photon localization. Now let us treat the photon-hopping operator \hat{J}_i more rigorously, and investigate the site dependence of the off-diagonal contribution, which includes the inhomogeneity of the phonon fields. Noticing that a quasiparticle transformed from a photon operator by the Davydov transformation is associated with phonons in the coherent state (see (6.40)), we take expectation values of \hat{J}_i in terms of the coherent state of phonons $|\gamma\rangle$ as

$$J_i \equiv \langle \gamma | \hat{J}_i | \gamma \rangle. \quad (6.54)$$

Here the coherent state $|\gamma\rangle$ is an eigenstate of the annihilation operator \hat{b}_p with eigenvalue γ_p and satisfies the following equations

$$\hat{b}_p |\gamma\rangle = \gamma_p |\gamma\rangle, \quad (6.55a)$$

$$\exp\left(-\sum_p c_p \hat{b}_p\right) |\gamma\rangle = \exp\left(-\sum_p c_p \gamma_p\right) |\gamma\rangle, \quad (6.55b)$$

where c_p is a real number. Since the difference between the creation and annihilation operators of a phonon is invariant under the Davydov transformation, the following relation holds:

$$\hat{\beta}_p^\dagger - \hat{\beta}_p = \hat{b}_p^\dagger - \hat{b}_p. \quad (6.56)$$

Using (6.55a), (6.55b), and (6.56), we can rewrite the site-dependent hopping constant J_i in (6.54) as

$$\begin{aligned}
J_i &= J \langle \gamma | \exp \left\{ \sum_{p=1}^N C_{ip} (\hat{b}_p^\dagger - \hat{b}_p) \right\} | \gamma \rangle \\
&= J \exp \left(-\frac{1}{2} \sum_{p=1}^N C_{ip}^2 \right) \langle \gamma | \exp \left(\sum_{p'=1}^N C_{ip'} \hat{b}_{p'}^\dagger \right) \exp \left(-\sum_{p''=1}^N C_{ip''} \hat{b}_{p''} \right) | \gamma \rangle \\
&= J \exp \left(-\frac{1}{2} \sum_{p=1}^N C_{ip}^2 \right) \langle \gamma | \exp \left(\sum_{p'=1}^N C_{ip'} \gamma_{p'} \right) \exp \left(-\sum_{p''=1}^N C_{ip''} \gamma_{p''} \right) | \gamma \rangle \\
&= J \exp \left(-\frac{1}{2} \sum_{p=1}^N C_{ip}^2 \right), \tag{6.57}
\end{aligned}$$

where C_{ip} is denoted by

$$C_{ip} \equiv \frac{\chi_{i,p} - \chi_{i+1,p}}{\Omega_p}. \tag{6.58}$$

Figure 6.8 shows the site dependence of J_i in the case of $N = 20$. Impurities are doped at site 4, 6, 13, and 19. The mass ratio of the host molecules to the impurities is 5, while $\hbar J = 0.5$ eV and $\chi = 14.0$ fsec⁻¹ nm⁻¹ are used. It follows from the figure that the hopping constants are highly modified around the impurity sites and the edge sites. The result implies that photons are strongly affected by localized localized phonons and hop to the impurity sites to localize. Here we have not considered the temperature dependence of J_i , which is important for phenomena dominated by incoherent phonons [51]. This is because coherent phonons weakly depend on the temperature of the system. However, there remains

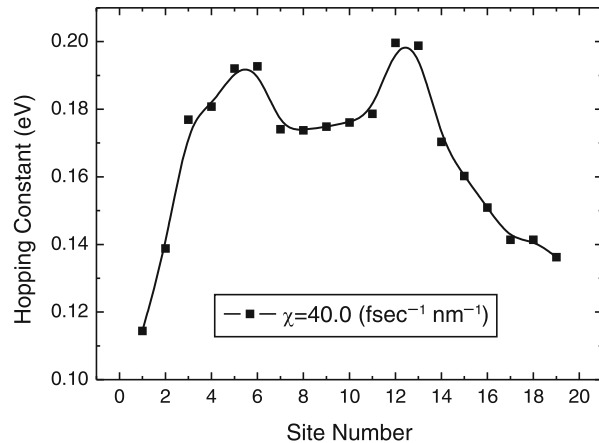
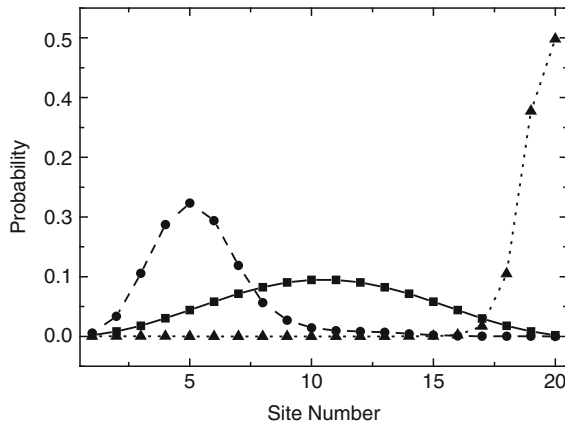


Fig. 6.8 The site dependence of the hopping constants J_i in the case of $N = 20$. Impurities are doped at site 4, 6, 13, and 19. The mass ratio of the host molecules to the impurities is 1 to 0.2, while $\hbar J = 0.5$ eV and $\chi = 40.0$ fsec⁻¹ nm⁻¹ are used

Fig. 6.9 Probability of photons observed at each site. The filled squares, circles, and triangles represent the results for $\chi = 0, 40.0$ and $54.0 \text{ fsec}^{-1} \text{ nm}^{-1}$, respectively. Other parameters are the same as those in Fig. 6.8



room to discuss more fundamental issue, that is, whether the probe system is in a thermal equilibrium state or not.

In Fig. 6.9, we present a typical result that photons localize around the impurity sites in the system as the photon-phonon coupling constants χ vary from zero to $40.0 \text{ fsec}^{-1} \text{ nm}^{-1}$ or $54.0 \text{ fsec}^{-1} \text{ nm}^{-1}$ with $\hbar J = 0.5 \text{ eV}$ kept. As depicted with the filled squares in the figure, photons delocalize and spread over the system without the photon-phonon couplings. When the photon-phonon couplings are comparable to the hopping constants, $\chi = 40.0 \text{ fsec}^{-1} \text{ nm}^{-1}$, photons can localize around the impurity site with a finite width, two sites at HWHM, as shown with the filled circles. This finite width of photon localization comes from the site-dependent hopping constants. As the photon-phonon couplings are larger than $\chi = 40.0 \text{ fsec}^{-1} \text{ nm}^{-1}$, photons can localize at the edge sites with a finite width, as well as the impurity sites. In Fig. 6.9, the photon localization at the edge site is shown with the filled triangles, which originates from the finite size effect of the molecular chain [43, 52]. This kind of localization of photons dressed by the coherent state of phonons leads us to a simple understanding of phonon-assisted photodissociation using an optical near field; molecules in the electronic ground state approach to the probe tip within the localization range of the dressed photons and can be vibrationally excited by the dressed photon transfer to the molecules, via multi-phonon component of the dressed photons, which might be followed by the electronic excitation. Thus, it leads to the dissociation of the molecules even if the incident photon energy less than the dissociation energy is used.

6.5 Conclusions

As a natural extension of the localized photon model, we have discussed the inclusion of phonon's effects into the model. The study was initially motivated by the experiments of photodissociation of molecules by optical near fields, whose results show unique feature different from the conventional one with far fields. After

clarifying delocalized or localized vibration modes in a pseudo one-dimensional system, we have focused on the interaction between dressed photons and phonons by using the Davydov transformation. We have theoretically shown that photons are dressed by the coherent state of phonons and found that the competition between the photon-phonon coupling constant and the photon-hopping constant governs the photon localization or delocalization in space. The obtained results lead us to a simple understanding of an optical near field itself as an interacting system of photon, electronic excitation (induced polarization), and phonon fields in a nanometer space, which are surrounded by macroscopic environments, as well as phonon-assisted photodissociation using an optical near field.

Acknowledgements The authors are grateful to H. Hori (Yamanashi Univ.), S. Sangu (Ricoh Co., Ltd.), A. Shojiguchi (NEC Co.), K. Kitahara (International Christian Univ.), T. Yatsui (Japan Science and Technology Agency), M. Tsukada (Waseda Univ.), H. Nejo (National Institute for Materials Science), M. Naruse (National Institute of Information and Communications Technology), M. Ikezawa (Univ. of Tsukuba), A. Sato (Tokyo Institute of Technology), and I. Banno (Yamanashi Univ.) for stimulating discussions. This work was supported in part by the twenty-first Century COE program at Tokyo Institute of Technology "Nanometer-Scale Quantum Physics" and by a Grant-in-Aid for Scientific Research from the Ministry of Education, Culture, Sports, Science and Technology, Japan, and by CREST, Japan Science and Technology Agency.

References

1. M. Ohtsu, K. Kobayashi, *Optical Near Fields* (Springer, Berlin/Heidelberg, 2004)
2. N. Hosaka, T. Saiki, *J. Microsc.* **202**, 362 (2001)
3. K. Matsuda, T. Saiki, S. Nomura, M. Mihara, Y. Aoyagi, S. Nair, T. Takagahara, *Phys. Rev. Lett.* **91**, 177401 (2003)
4. Y. Yamamoto, M. Kourogi, M. Ohtsu, V. Polonski, G.H. Lee, *Appl. Phys. Lett.* **76**, 2173 (2000)
5. T. Kawazoe, Y. Yamamoto, M. Ohtsu, *Appl. Phys. Lett.* **79**, 1184 (2001)
6. T. Yatsui, M. Ueda, Y. Yamamoto, T. Kawazoe, M. Kourogi, M. Ohtsu, *Appl. Phys. Lett.* **81**, 3651 (2002)
7. T. Kawazoe, K. Kobayashi, S. Sangu, M. Ohtsu, *Appl. Phys. Lett.* **82**, 2957 (2003)
8. K. Kobayashi, S. Sangu, A. Shojiguchi, T. Kawazoe, K. Kitahara, M. Ohtsu, *J. Microsc. B* **210**, 247 (2003)
9. S. Sangu, K. Kobayashi, A. Shojiguchi, M. Ohtsu, *Phys. Rev. B* **69**, 115334 (2004)
10. T. Kawazoe, K. Kobayashi, M. Ohtsu, *Appl. Phys. Lett.* **86**, 103102 (2005)
11. I. Bialynicki-Birula, Photon wave function, in *Progress in Optics*, vol. 36, ed. by E. Wolf (North-Holland, Amsterdam, 1996), pp. 248–294
12. K. Cho, *Optical Response of Nanostructures: Microscopic Nonlocal Theory* (Springer, Berlin, 2003)
13. K. Kobayashi, S. Sangu, M. Ohtsu, Quantum theoretical approach to optical near-fields and some related application, in *Progress in Nano-Electro-Optics I*, ed. by M. Ohtsu (Springer, Berlin/Heidelberg, 2003), pp. 119–157
14. O. Keller, *Phys. Rep.* **411**, 1 (2005)
15. A. Shojiguchi, K. Kobayashi, S. Sangu, K. Kitahara, M. Ohtsu, *J. Phys. Soc. Jpn.* **72**, 2984 (2003)
16. A. Shojiguchi, K. Kobayashi, S. Sangu, K. Kitahara, M. Ohtsu, A phenomenological description of optical near fields and optical properties of N two-level systems interacting with optical near fields, in *Progress in Nano-Electro-Optics III*, ed. by M. Ohtsu (Springer, Berlin/Heidelberg, 2005), pp. 145–220

17. T. Kawazoe, K. Kobayashi, J. Lim, Y. Narita, M. Ohtsu, *Phys. Rev. Lett.* **88**, 067404 (2002)
18. K. Kobayashi, S. Sangu, T. Kawazoe, M. Ohtsu, *J. Lumin.* **112**, 117 (2005); **114**, 315 (2005)
19. M. Scheibner, T. Schmidt, L. Worschech, A. Forchel, G. Bacher, T. Passow, D. Hommel, *Nat. Phys.* **3**, 106 (2007)
20. T. Kawazoe, K. Kobayashi, S. Takubo, M. Ohtsu, *J. Chem. Phys.* **122**, 024715 (2005)
21. K. Kobayashi, T. Kawazoe, M. Ohtsu, *IEEE Trans. Nanotechnol.* **4**, 517 (2005)
22. T. Kawazoe, K. Kobayashi, M. Ohtsu, *Appl. Phys. B* **84**, 247 (2006)
23. See, for example, J.J. Sakurai, *Advanced Quantum Mechanics* (Addison-Wesley, Reading, 1967)
24. T.D. Newton, E.P. Wigner, *Rev. Mod. Phys.* **21**, 400 (1949)
25. J.E. Sipe, *Phys. Rev. A* **52**, 1875 (1995)
26. M.O. Scully, M.S. Zubairy, *Quantum Optics* (Cambridge University Press, Cambridge, 1997)
27. K. Kobayashi, M. Ohtsu, *J. Microsc.* **194**, 249 (1999)
28. K. Kobayashi, S. Sangu, H. Ito, M. Ohtsu, *Phys. Rev. A.* **63**, 013806 (2001)
29. S. John, T. Quang, *Phys. Rev. A* **52**, 4083 (1995)
30. H. Suzuura, T. Tsujikawa, T. Tokihiro, *Phys. Rev. B* **53**, 1294 (1996)
31. C.R. Kagan, C.B. Murray, M. Nirmal, M.G. Bawendi, *Phys. Rev. Lett.* **76**, 1517 (1996)
32. S.A. Crooker, J.A. Hollingsworth, S. Tretiak, V.I. Klimov, *Phys. Rev. Lett.* **89**, 186802 (2002)
33. T. Yatsui, M. Ohtsu, S.J. An, J. Yoo, G.-C. Yi, *Appl. Phys. Lett.* **87**, 033101 (2005)
34. G. McDermott, S.M. Prince, A.A. Freer, A.M. Hawthornthwaite-Lawless, M.Z. Papiz, R.J. Cogdell, N.W. Isaacs, *Nature* **374**, 517 (1995)
35. K. Mukai, S. Abe, H. Sumi, *J. Phys. Chem. B* **103**, 6096 (1999)
36. R.L. Jackson, *Chem. Phys. Lett.* **163**, 315 (1989)
37. R.L. Jackson, *J. Chem. Phys.* **96**, 5938 (1992)
38. R. Schinke, *Photodissociation Dynamics* (Cambridge University Press, Cambridge, 1993)
39. H. Haken, H.C. Wolf, *Molecular Physics and Elements of Quantum Chemistry* (Springer, Berlin/Heidelberg, 1995)
40. T. Kawazoe, K. Kobayashi, M. Ohtsu, *Appl. Phys. B* **84**, 247 (2006)
41. J.J. Hopfield, *Phys. Rev.* **112**, 1555 (1958)
42. A.L. Ivanov, H. Haug, L.V. Keldysh, *Phys. Rep.* **296**, 237 (1998)
43. C. Falvo, V. Pouthier, *J. Chem. Phys.* **122**, 014701 (2005)
44. M.E. Striefler, G.R. Barsch, *Phys. Rev. B* **12**, 4553 (1975)
45. D. Paton, W.M. Visscher, *Phys. Rev.* **154**, 802 (1967)
46. A.J. Sievers, A.A. Maradudin, S.S. Jaswal, *Phys. Rev.* **138**, A272 (1965)
47. S. Mizuno, *Phys. Rev. B* **65**, 193302 (2002)
48. T. Yamamoto, K. Watanabe, *Phys. Rev. Lett.* **96**, 255503 (2006)
49. A.S. Davydov, G.M. Pstryakov, *Phys. Status Solidi (b)* **49**, 505 (1972)
50. L. Jacak, P. Machnikowski, J. Krasnyj, P. Zoller, *Eur. Phys. J. D* **22**, 319 (2003)
51. K. Mizoguchi, T. Furuihi, O. Kojima, M. Nakayama, S. Saito, A. Syouji, K. Sakai, *Appl. Phys. Lett.* **87**, 093102 (2005)
52. V. Pouthier, C. Girardet, *J. Chem. Phys.* **112**, 5100 (2000)

Part II

Basic Tools

Near-Field Optical Fiber Probes and the Applications I

7

Shuji Mononobe

Contents

7.1	Introduction.....	282
7.2	Basic Techniques for Tapering and Metallizing Optical Fibers.....	284
7.2.1	Heating-and-Pulling and Metallization Techniques.....	284
7.2.2	Meniscus Etching.....	286
7.2.3	Selective Etching.....	287
7.3	Protrusion-Type Probe and Its Imaging Applications.....	292
7.3.1	Protrusion-Type Probe.....	292
7.3.2	Fabricating Protrusion-Type Probes by Selective Resin-Coating Method.....	292
7.3.3	c-mode NSOM Imaging of Salmonella Flagellar Filaments in Air and Water.....	294
7.3.4	c-mode NSOM Images of Microtubules.....	298
7.3.5	Near-Field Spectroscopic Investigation of Semiconductor Quantum Dots Under Extremely Low Temperature.....	300
7.3.6	Transmission Efficiencies of the Protrusion-Type Probes.....	302
7.4	Metal–Dielectric–Metal-Coated Fiber Probe and Near-Field Imaging of DNA Molecules.....	302
7.4.1	Ag–MgF ₂ –Al-Coated Fiber Probe.....	303
7.4.2	Sample Preparation.....	304
7.4.3	DNA Images.....	304
7.5	Apertured Probes for Near-Field Imaging of Dye-Doped Samples.....	305
7.6	Double-Tapered Fiber Probe and Spectroscopic Applications.....	308
7.6.1	Double-Tapered Probe.....	308
7.6.2	Near-Field Photoluminescence Image of Lateral p–n Junctions Obtained with the i-c mode NSOM.....	311
7.6.3	Near-Field Raman Spectroscopy of Polydiacetylene.....	312

S. Mononobe (✉)

Department of Mechanical Engineering, Toyo University, Saitama, Japan

e-mail: mononobe@toyo.jp

7.7 Pure Silica Core Fiber Probes and Ultraviolet Applications.....	313
7.7.1 UV Triple-Tapered Probe.....	316
7.7.2 UV Near-Field Photoluminescence Images of Polysilane.....	318
7.7.3 Fabrication of a Pure Silica Fiber Probe by Pulling and Etching.....	322
7.8 Outlook.....	326
References.....	331

Abstract

A double-tapered type of fiber probe with a typical aperture diameter of 100 nm and the GeO₂-doped silica core has been widely used for near-field optical microscopy in infrared and visible wavelength regions. However, it is difficult to employ such commercial probes for near-ultraviolet applications because the GeO₂-doped silica fiber probe has the strong guiding loss based on the Rayleigh scattering. Furthermore, the GeO₂-doped core, under the excitation of a visible light, generates photoluminescence and scattered lights which seriously decreases the ratio of near-field signal to background noise in some near-field applications such as fluorescence imaging and Raman scattering spectroscopy. This chapter describes various types of probe, fabrication methods, and imaging applications.

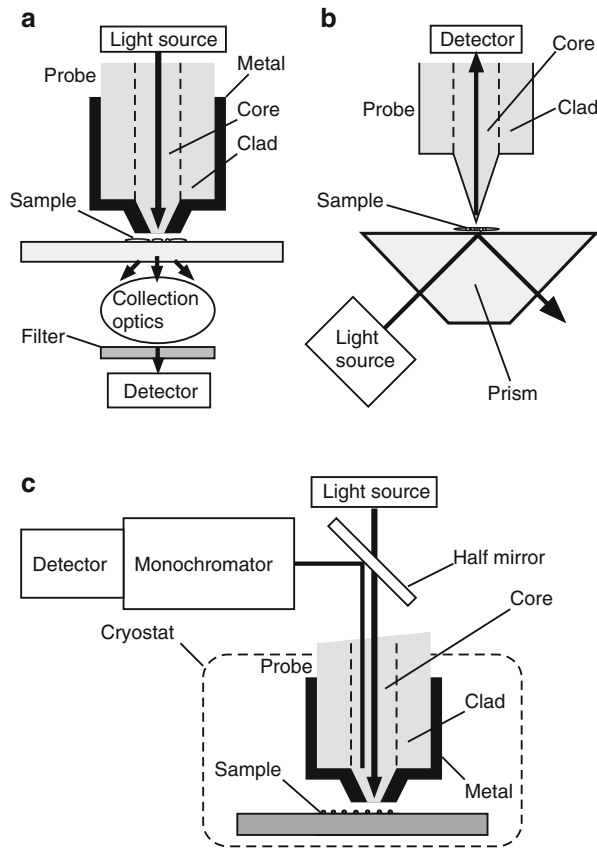
7.1 Introduction

Recently, near-field scanning optical microscopy (NSOM or SNOM) employing an apertured probe has been expected as a powerful tool for nano-optical applications due to its high-spatial-resolution capability down to a few tens nanometers or less. The resolution is mainly determined by the aperture size of the probe and the sample–probe distance because the NSOM is a scanning probe microscope based on short-range electromagnetic interaction between the probe and sample, which are much smaller than the optical wavelength. It is apparent that fabricating such probes and controlling the sample–probe distance have been the most important factors in the development of high-resolution NSOM (►Chap. 1).

Near-field optical interaction system can be operated in two complementary ways called illumination mode and collection mode, where the probe acts as a selective generator of a localized optical near-field and a sensitive scatterer of an optical near-field generated over the sample, respectively. Figure 7.1a, b shows schematic illustrations of i-mode NSOM and c-mode NSOM, respectively. In the c-mode NSOM where the light is incident to the total internal reflection, the sample–probe distance can be controlled by using near-field optical (NFO) variation as a feedback control signal. For i-mode NSOM, a shear-force feedback technique [7, 47] has been widely used to regulate the sample–probe distance.

In order to realize such a scattering probe and a generating probe, forming a dielectric taper and metallizing the taper has been used as an effective method. Tapered probes have been fabricated by the following methods:

Fig. 7.1 Schematic illustrations of (a) the i-mode, (b) the c-mode, and (c) the i-c mode. In the c-mode NSOM, the light is incident to the total internal reflection. The three-dimensional optical near field generated and localized on the sample surface is scattered by the probe, and part of the scattered field is collected and detected through the probe. The principle of operation of i-mode is similar except that the probe works as a generator of the optical near field to illuminate the sample surface. The scattered field by the sample is collected by conventional optics. In i-c mode, a sample is excited by an optical near field on the probe. The light generated on the sample is scattered and collected by the probe



- Etching a quartz crystal rod [33]
- Heating and pulling a glass pipette by micropipette puller [5]
- Meniscus etching of an optical fiber [8, 10, 11, 15, 22, 27, 35, 45, 49]
- Heating and pulling an optical fiber [3, 4, 9, 32, 53, 54]
- Selective etching of an optical fiber [14, 20, 24, 48, 50]
- Heating-and-pulling and etching of an optical fiber [16, 44]
- Meniscus etching and selective etching of an optical fiber [18, 19]

For metallizing the tapered probes, a vacuum evaporation method [6] has been applied, where the dielectric taper is coated with an aluminum or gold film by a vacuum evaporation unit except for its apex region. Among the metallized tapered probes, fiber-type probes have high transmission efficiencies due to their waveguide structure and, moreover, have been demonstrated to have the molecular sensitivity, the nanometric spatial resolution, and the locally spectroscopic capability in i-mode NSOM, c-mode NSOM, and hybrid NSOM called illumination–collection mode (i-c mode). Figure 7.1c shows schematic illustrations of i-c mode NSOM where the apertured probe functions as both an optical generator exciting the sample and a scatterer of the excited optical near fields.

i-mode NSOM and i-c mode NSOM are often employed for near-field imaging of dye-doped samples and spectroscopic investigation of semiconductor devices. In such spectroscopic applications where one must cope with extremely low detected power, the probe should have high throughput in i-mode NSOM and be highly sensitive in c-mode NSOM. Further, in the i-mode fashion, to avoid thermal damage to the sample and the probe, the probe should be used with an input power as low as possible. Therefore, the resolution capability and throughput of the tapered probe have to be optimized depending on NSOM applications. This optimization should be done by varying the probe shape, i.e., the cone angle. Furthermore, to obtain a highly resolved image, one must fabricate a metallized probe with an apex region emerging from a metal film.

We have developed several application-oriented fiber probes called protrusion-type probe, double-tapered probe, and pure silica fiber probe and performed near-field imaging of biomolecules and dye-doped samples, spectroscopic study of semiconductor, and ultraviolet applications. In this chapter, the near-field optical fiber probes and near-field microscopy applications are described. [Section 7.2](#) discusses the basic techniques for tapering and metallizing fibers. The protrusion-type probe and the biological imaging are described in [Sect. 7.3](#). [Section 7.4](#) describes apertured probes and their application to near-field imaging of dye-doped samples. The double-tapered probe and pure silica fiber probe are described in [Sects. 7.5](#) and [7.6](#), respectively. [Table 7.1](#) summarizes the NSOM images appeared in this chapter.

7.2 Basic Techniques for Tapering and Metallizing Optical Fibers

For tapering an optical fiber, three basic techniques, i.e., heating and pulling, meniscus etching, and selective etching have been used. The characteristics of these techniques are summarized in [Table 7.2](#).

7.2.1 Heating-and-Pulling and Metallization Techniques

In the heating-and-pulling technique [3], a silica-based optical fiber is heated and pulled by a micropipette puller combined with a CO₂ gas laser as shown in [Fig. 7.2](#). One can fabricate a tapered fiber with an apex diameter of 50 nm and a cone angle of 20–40° by a commercial micropipette puller. This tapering can be applied to any optical fibers with a diameter more than 125 μm by adjusting the laser power, the strength of pull, and the delay time between the end of the heating and the beginning of the pulling. However, it is difficult to control the cone angle while maintaining an apex diameter as small as 50 nm. In the tapered portion, strong optical leaky modes are generated due to the varied core diameter.

For i-mode NSOM, the pulled fiber with apex diameter of about 50 nm must be metallized except for its apex region. To metallize the fiber, the pulled fiber is rotated while evaporating aluminum in vacuum as shown in [Fig. 7.3a](#) so that the

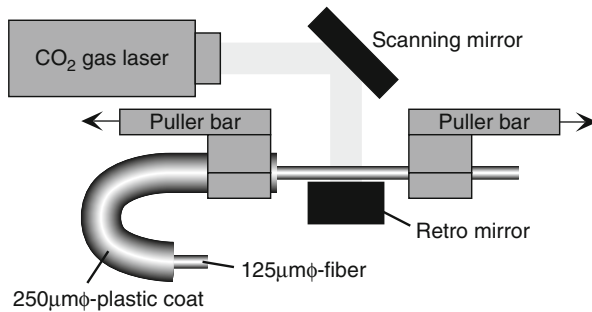
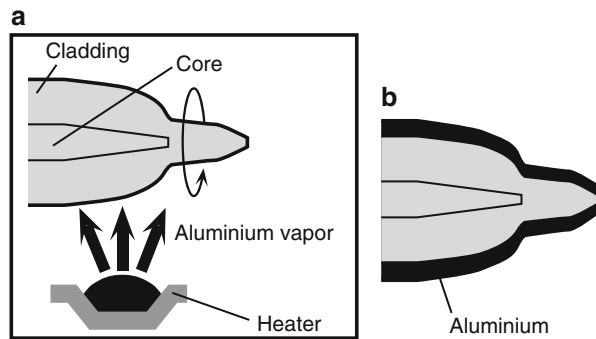
Table 7.1 List of the NSOM images appeared in ►Chap. 1

Fig.	Image	Probe type	Mode	Feedback	Ref.
Fig. 7.15c	Near-field image of salmonella flagellar filaments in air	Protrusion-type probe	c-mode	NFO intensity	[30]
Fig. 7.15d	Near-field image of salmonella flagellar filaments in water	Protrusion-type probe	c-mode	NFO intensity	[31]
Fig. 7.18c	Near-field image of microtubules of a pig brain	Protrusion-type probe	c-mode	Shear force	[56]
Fig. 7.20d–f	Photoluminescence images of GaAs quantum dots	Protrusion-type probe	i-mode	Shear force	[46]
Fig. 7.24b	Near-field image of deoxyribonucleic acid	Ag–MgF ₂ –Al-coated probe	c-mode	NFO intensity	[52]
Fig. 7.31b, c	Near-field images of neurons and microtubules labeled with toluidine blue	Apertured-type probe	i-mode	Shear force	[51]
Fig. 7.32b	Fluorescence image of Rhodamine 6G molecules	Double-tapered probe	i-c mode	Shear force	[12]
Fig. 7.29b	Photoluminescence imaging lateral p–n junction based on GaAs	Double-tapered probe	i-c mode	Shear force	[38]
Fig. 7.30b	Raman spectroscopic mapping of tabular polydiacetylene single crystal	Double-tapered probe	i-mode	Shear force	[29]
Fig. 7.40b	UV photoluminescence image of polydihexyl-silane	Triple-tapered probe with a pure silica core	i-mode	Shear force	[24]
Fig. 7.41b	UV photoluminescence image of n-decyl-(s)-2-methylbutyl silane	Triple-tapered probe with a pure silica core	i-mode	Shear force	[2]
Fig. 7.45	UV photoluminescence image of polydihexyl-silane	Pulled and etched probe with a pure silica core	i-mode	Shear force	[36]

metallized probe has a thickness profile as shown in Fig. 7.3b. Here, the typical radial thickness is around 150 nm. The apex region is aluminized with a thickness smaller than the half radial thickness due to the throwing of evaporated vapor. The metal thickness covering the apex region can be reduced to a quarter of the radial thickness by inclining the rotating fiber in vacuum.

Table 7.2 Characteristics of the three basic techniques for tapering an optical fiber

Technique	Cone angle θ	Apex diameter d	Reproducibility
Meniscus etching	9–40°	60 nm or more	80 % or less
Selective etching	14–180°	10 nm	Almost 100 %
Pulling	20–40°	50 nm	Around 80 %

Fig. 7.2 Schematic illustration of the micropipette puller used for tapering an optical fiber with a diameter of 125 μm **Fig. 7.3** Schematic illustrations of (a) the vacuum evaporation unit for metallizing the pulled fiber and (b) the metallized fiber

7.2.2 Meniscus Etching

In the meniscus etching, (The meniscus-etching technique was originally developed to fabricate a fiber-optic microlens.) a single-mode fiber is immersed in HF acid with a surface layer of an organic solution such as silicone oil as shown in Fig. 7.4a. It is tapered with a cone angle since the height of meniscus formed around the fiber is reduced depending on the fiber diameter (Fig. 7.4b). When the fiber completely tapered, the etching stops automatically (Fig. 7.4c). The cone angle can be increased up to 35–40°. However, the obtained tapered fiber has a geometrically eccentric apex with an elliptical cross section. The longer and shorter principal diameters of this elliptical apex take values of 200 and 10–20 nm, respectively.

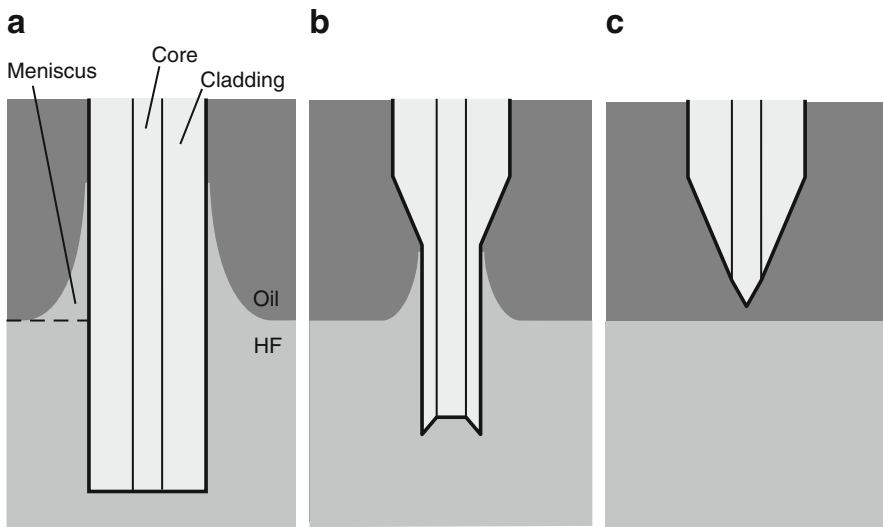


Fig. 7.4 Schematic illustrations of meniscus etching of a fiber at (a) the start, (b) tapering, and (c) stop

The vacuum evaporation method as shown in Fig. 7.3a can be applied to metallize the meniscus-etched fibers. Before metallizing, the etched fibers have to remove organic dirt on the surface by cleaning techniques, i.e., immersing a H_2SO_4 solution.

7.2.3 Selective Etching

By applying the selective etching method to a high- GeO_2 -doped fiber, one can obtain probe tips with a small apex diameter less than 10 nm. By varying the concentration of etching solutions based on hydrogen fluoride (HF) and ammonium fluoride (NH_4F), the cone angle can be controlled in a wide region from 20° to 180° for an apex diameter less than 10 nm. Further, selective etching is the most highly reproducible technique among the three tapering techniques. This method can be applied to any single-mode fibers produced by vapor-phase axial deposition (VAD) [13].

Figure 7.5a shows a cross-sectional profile of the refractive index of a silica fiber with a GeO_2 -doped core and a pure silica clad. Here, n_1 and n_2 are the refractive indexes of the core and clad, respectively. r_1 and r_2 are the radii of the core and clad, respectively. At immersing the fiber in a buffered HF solution (BHF) with a volume ratio of [40% NH_4F aqueous sol.]:[50% HF acid]:[H_2O] = X :1:1 at 25°C , the core is hollowed at $X = 0$ and is tapered at $X = 10$. Figure 7.5b shows schematic explanation of the geometrical model for the tapering process based on selective etching. Bright shading and dark shading in the upper part represent the

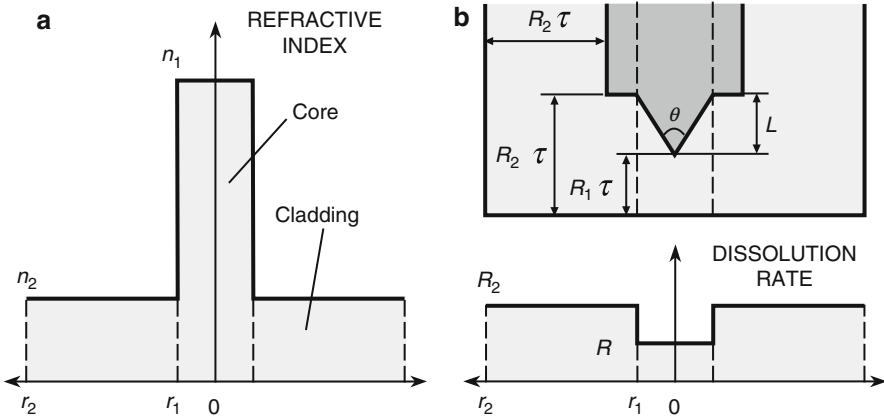


Fig. 7.5 (a) Cross-sectional profile of a refractive index of a silica fiber. Here, n_1 and n_2 are the refractive indices of the core and clad, respectively; r_1 and r_2 are the radii of the core and clad, respectively. (b) *Top*, a geometrical model for the tapering process. Here, τ is the etching time required for making the apex diameter zero. θ is the cone angle of the tapered core. L is the length of the tapered core. *Bottom*, cross-sectional profiles of the dissolution rates R_1 and R_2 of the core and clad

cross-sectional profiles of the fiber before and after the etching with an etching time τ , respectively. τ is the etching time required for making the apex diameter zero; θ and d are the cone angle and apex diameter of the probe, respectively. The lower part shows the dissolution rates R_1 and R_2 of the core and clad, respectively. Here, $R_1 < R_2$. Assuming that the dissolution rates R_1 and R_2 are constant within the core and clad regions, respectively, relations between the cone angle θ , the length L of the tapered core and the apex diameter d are represented by

$$\sin \frac{\theta}{2} = \frac{R_1}{R_2}, \tag{7.1}$$

$$L = \frac{r_1 - d/2}{\tan(\theta/2)}, \tag{7.2}$$

and

$$d(T) = \begin{cases} 2r_1(1 - T/\tau) & (T < \tau), \\ 0 & (T \geq \tau). \end{cases} \tag{7.3}$$

Here, the etching time τ that is required for making the apex diameter zero is expressed as

$$\tau = \frac{r_1}{R_1} \sqrt{\frac{R_1 + R_2}{R_2 - R_1}}. \tag{7.4}$$

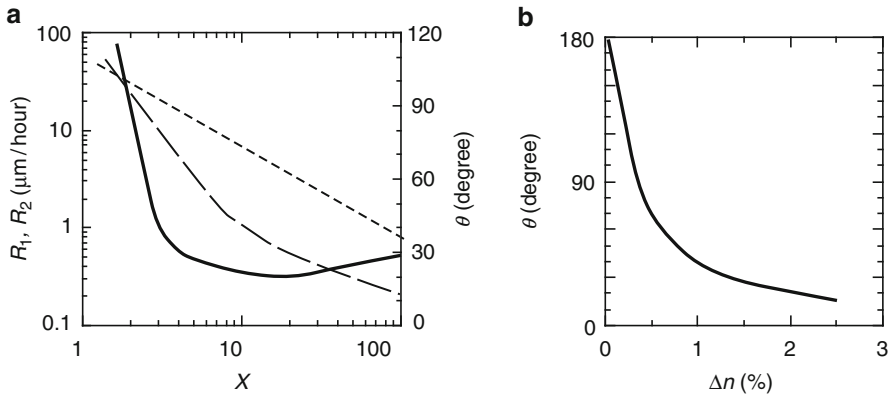


Fig. 7.6 (a) Dependencies of the dissolution rate R_1 (broken curve) of the GeO_2 -doped core, R_2 (dotted line) of the pure silica clad, and the cone angle θ (solid curve) on X . Here, the value of Δn defined as $(n_1^2 - n_2^2)/2n_1^2$ is 2.5%. (b) Dependency of θ on Δn at $X = 10$

7.2.3.1 GeO_2 -Doped Fiber

When a fiber with a GeO_2 -doped core and a pure silica clad is immersed in BHF with volume ratios of $X:1:1$, the core region is hollowed in $X < 1.7$ and is tapered in $X > 1.7$ as shown in Fig. 7.5. Based on Eq. 7.1, the cone angle is determined by the dissolution rate ratio of the core and clad. Figure 7.6a shows variations of the dissolution rates R_1 and R_2 and the cone angle θ as a function of X . Here, the used fiber was produced by vapor-phase axial deposition (VAD) so as to have an index difference of 2.5%. The dissolution rate ratio R_1/R_2 decreases with increasing the NH_4F volume ratio of X and approaches a constant value at $X = 10$ –30. The cone angle that is determined by the ratio R_1/R_2 takes a minimum value of 20° at $X = 10$. In the case that X is fixed, the cone angle is determined by the index difference. Figure 7.6b shows the dependence of the cone angle on the index difference at $X = 10$. The index difference is increased by increasing the GeO_2 -doping ratio.

The VAD is an effective method to produce a GeO_2 -doped fiber with an index difference as large as 2.5–3.0%. A dispersion-compensating fiber (DCF) with an index difference of $\Delta n = 2.5\%$ and core diameter of $2\ \mu\text{m}$ can be applied to various selective etching methods of fabricating a protrusion-type probe, a double-tapered probe, etc. This DCF was originally produced as a device for controlling the optical dispersion of a 1,500-nm optical transmission system by VAD and has a cutoff wavelength of around $0.8\ \mu\text{m}$.

By immersing the DCF in BHF with a volume ratio of 10:1:1 at 25°C , a tapered fiber probe with a small cone angle of 20° and an apex diameter less than $10\ \text{nm}$ is fabricated with almost 100% reproducibility. Further, the cone angle can be controlled as $20^\circ \leq \theta < 180^\circ$ by varying the volume ratio X of BHF, as shown in Fig. 7.6a. Such high controllability of the cone angle is indispensable for tailoring a high-throughput probe and a high-resolution probe.

7.2.3.2 Pure Silica Core Fiber with a Fluorine-Doped Clad

Pure silica core fiber has the high transmittance in a wide region from near ultraviolet to near infrared (see Fig. 7.33). To make an index difference between the pure silica core and the clad, the clad is often made of fluorine-doped silica. We produced a pure silica core fiber with the fluorine-doped clad and an index difference -0.7% . (For the following discussion, we define the relative refractive index difference Δn of doped glass to pure silica, which is expressed as $(n_2^2 - n_1^2)/2n_2^2$ and $(n_1^2 - n_2^2)/2n_1^2$ for a pure silica core fiber and a pure silica clad fiber, respectively). By immersing the fiber in BHF with volume ratios 1.7:1:1 and 10:1:1, the obtained probe has cone angles of 62° and 77° , respectively. The fiber could not be hollowed at any volume ratios of BHF. In selective etching of a pure silica fiber, varying the index difference or the fluorine-doping ratio controls the cone angle. Among single-mode fibers, only 1,500-nm pure silica fiber (PSF) with an index difference of -0.3% and core diameter of $10\ \mu\text{m}$ is commercially available.

7.2.3.3 Controlling the Clad Diameter

For shear-force feedback technique, the clad diameter of the probe is one of the main parameters governing the resonance frequency of dithering a probe. In our experience, tapered probes with a clad diameter of $20\text{--}30\ \mu\text{m}$ is usually needed to obtain a proper resonance frequency, i.e., $20\text{--}40\ \text{kHz}$. Figure 7.7 schematically shows an etching method to fabricate tapered probes with the reduced clad diameter. Here, r_2 is the clad radius before etching, D is the clad diameter of the probe, θ is

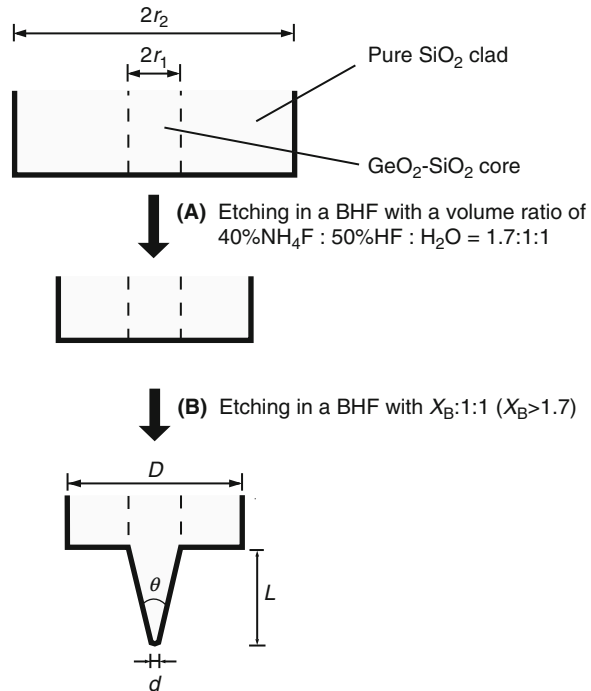


Fig. 7.7 Etching method to fabricate a shoulder-shaped probe. r_1 and r_2 , radii of the core and clad, respectively. D , reduced clad diameter. θ , cone angle of the tapered core. L , length of the tapered core

hhhhthe cone angle of the tapered core, d is the apex diameter, and L is the length of the tapered core. This method involves two steps: (A) reducing the clad thickness and (B) tapering the core.

In step A, the fiber is immersed in BHF with volume ratio of $[\text{NH}_4\text{F}$ aqueous solution (40 %)] : $[\text{HF}$ acid (50 %)] : $[\text{H}_2\text{O}] = 1.7:1:1$ for an etching time T_A . Then, the clad diameter is reduced to $[2r_2 - 2R_{2A}T_A]$. The core end is kept flat since the dissolution rates R_{1A} and R_{2A} of the core and clad are equal.

In step B, the fiber is selectively etched in $X_B:1:1$ (where $X_B > 1.7$) for etching time T_B . The core is tapered with the cone angle θ represented by

$$\sin \frac{\theta}{2} = \frac{R_{1B}}{R_{2B}} . \quad (7.5)$$

To make the apex diameter zero, the etching time T_B must be longer than the time τ which is given by

$$\tau = \frac{r_1}{R_{1B}} \sqrt{\frac{R_{1B} + R_{2B}}{R_{2B} - R_{1B}}} . \quad (7.6)$$

The clad diameter D is represented by

$$D = 2r_2 - 2(R_{2A}T_A + R_{2B}T_B) , \quad (7.7)$$

which is proportional to the etching time T_B .

Using a DCF with core diameter of $2 \mu\text{m}$, clad diameter of $125 \mu\text{m}$, and an index difference of 2.5 %, we obtained a tapered probe with a cone angle of $\theta = 20^\circ$ and a clad diameter of $D = 25 \mu\text{m}$. Figure 7.8a, b shows SEM micrographs of the probe and the magnified top region, respectively. The conditions of the etching process are summarized in Table 7.3. By substituting $r_1 = 1 \mu\text{m}$, $R_{1B} = 1.1 \mu\text{m h}^{-1}$, and $R_{2B} = 6.5 \mu\text{m h}^{-1}$ into Eq. 7.6, an estimated value of $\tau = 64 \text{ min}$ is obtained.

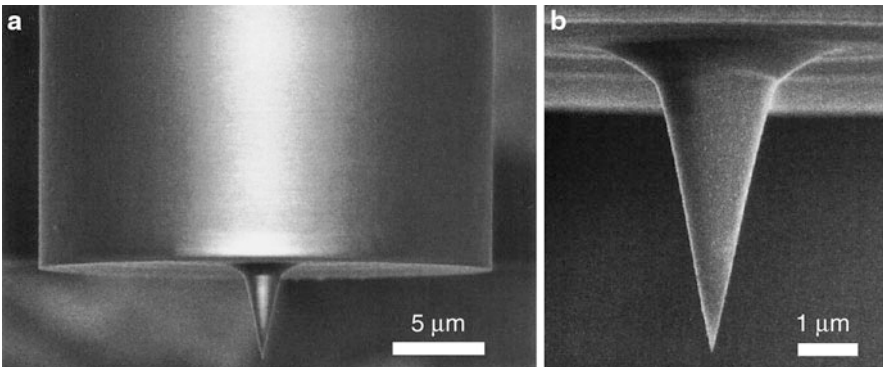


Fig. 7.8 SEM micrographs of (a) a shoulder-shaped probe and (b) the magnified apex region. $D = 25 \mu\text{m}$; $\theta = 20^\circ$; $d < 10 \text{ nm}$

Table 7.3 Conditions for fabricating the probe as shown in Fig. 7.8a

Step	Volume ratio of BHF	Etching time (min)	Dissolution rates ($\mu\text{m h}^{-1}$)
A	1.7:1:1	86	$R_1 = R_2 = 30$
B	10:1:1	75	$R_1 = 1.1, R_2 = 6.5$

For $T_B = 75 \text{ min } (>\tau)$, the clad diameter D is represented by $D = -60T_A + 106$ (μm). The cone angle is controlled by varying the NH_4F volume ratio in step B. For the dependence of the cone angle on the volume ratio, refer to Fig. 7.6a.

7.3 Protrusion-Type Probe and Its Imaging Applications

7.3.1 Protrusion-Type Probe

The uncoated fiber probe with a nanometric apex can be employed for the c-mode NSOM as shown in Fig. 7.1b. Although the principal factor governing the resolution is the small apex size, the resolution is affected by propagating components and the scattering of low-spatial-frequency components of the optical near field. To obtain highly resolved c-mode images, such unwanted scattered light must be suppressed. To perform high-resolution near field imaging, we developed a fiber probe with a protruding tip from metal film, which is called protrusion-type probe [23]. Figure 7.9a shows the cross-sectional schematic illustration of the protrusion-type probe. Here, θ , d , d_f , and t_M represent the cone angle, the apex diameter, the foot diameter, and the thickness of the metal film, respectively. This probe scatters frequency components between $(1/d_f)$ and $(1/d)$ and suppresses the generation of components of less than $(1/d_f)$. To realize such a probe, a selective resin-coating (SRC) method [23] was developed, which can be applied to tapered probes fabricated by the etching method as shown in Fig. 7.7. Apertured probes are also effective for suppressing the unwanted light. However, it is difficult to produce apertured probes with an apex diameter of a few tens nanometers by vacuum evaporation unit. If applying the vacuum evaporation method to a fiber tip with a cone angle of 20° , an entirely coated fiber probe as shown in Fig. 7.9b is obtained. The thickness t_A of metal covering the apex could not be made less than 40 nm for $t_M = 150 \text{ nm}$.

7.3.2 Fabricating Protrusion-Type Probes by Selective Resin-Coating Method

Figure 7.10 shows a schematic diagram of the SRC involving four steps: (A) metal coating, (B) resin coating, (C) preferential etching of metal covering the apex region, and (D) removing the resin. Figure 7.11 shows a scanning electron micrograph of the top region of the fabricated protrusion-type probe. The probe has a protrusion from a gold film and a foot diameter d_f of less than 30 nm.

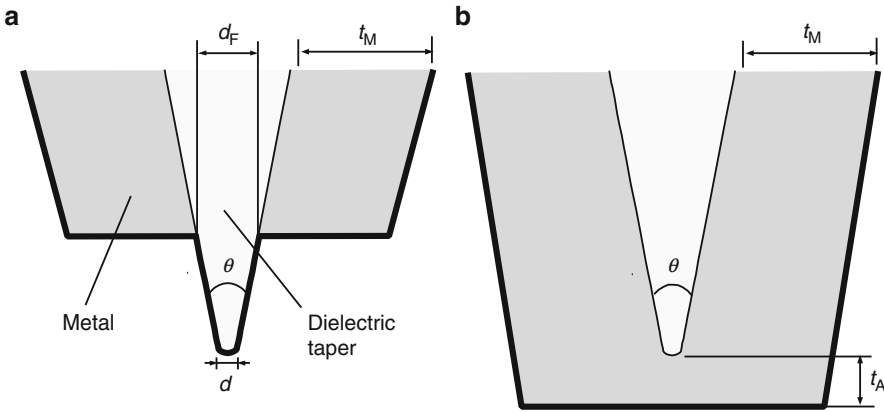


Fig. 7.9 (a) Schematic cross-sectional profiles of a protrusion-type probe and (b) entirely coated probe. θ , cone angle of the taper; d and d_f , apex and foot diameters of the protruding tip, respectively; t_M , thickness of the metallic film

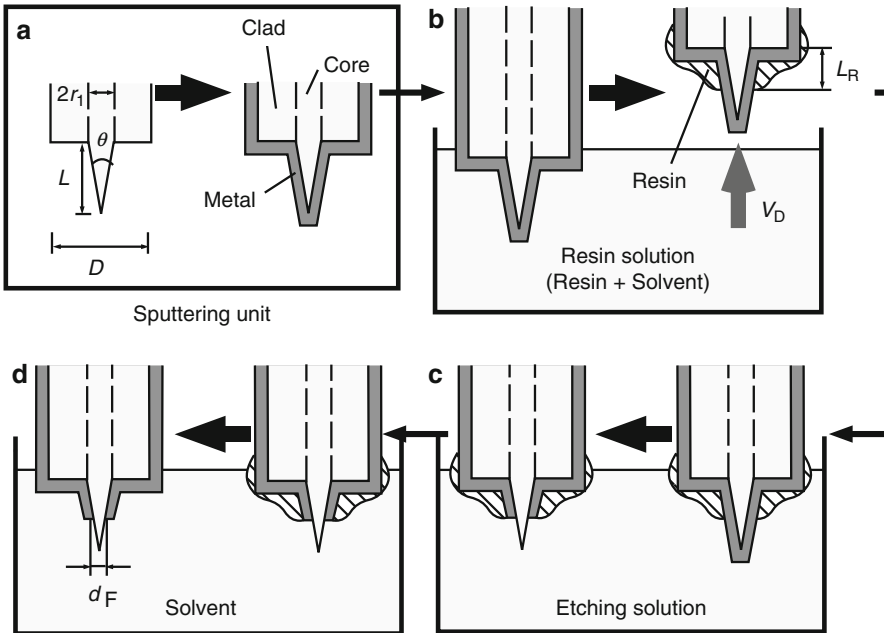


Fig. 7.10 Schematic diagram of the selective resin-coating method for fabricating a protrusion-type probe; D , clad diameter of the probe; r_1 , core radius; θ and L , cone angle and length of the tapered core, respectively; V_D , withdrawing speed of the fiber from the resin solution; L_R , length of the tapered core where the resin is coated; d_f , foot diameter of the protrusion; t_A , thickness of metal covering the apex

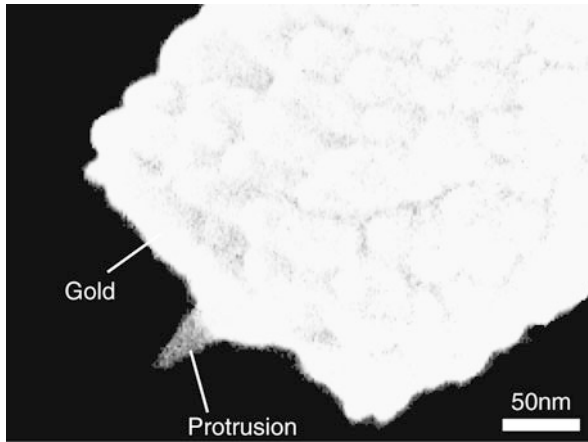


Fig. 7.11 Scanning electron micrograph of a protrusion-type probe fabricated by the SRC method as shown in Fig. 7.10; $\theta = 20^\circ$; $d < 10$ nm; $d_f = 30$ nm

Before applying the SRC method, a tapered probe was fabricated with a clad diameter $D = 45 \mu\text{m}$ and a cone angle $\theta = 20^\circ$ based on selective etching. In step A, the probe was coated with 120-nm-thick gold by a magnetron sputtering unit. In step B, the probe was dipped in an acrylic resin solution and then was removed from the acrylic solution with a withdrawal speed of $V_D = 5 \text{ cm s}^{-1}$. The acrylic resin solution with a low viscosity coefficient of 11 cP was chosen for this process not to coat with the fiber tip resin film. The density of the acrylic solution is 0.85 g cm^{-3} at 25°C . In step C, the probe was etched for 2 min in a solution $\text{KI-I}_2\text{-H}_2\text{O}$, mixed with a weight ratio of 20:1:400, and diluted 50 times with deionized water. In step D, the acrylic film was removed away by immersing the probe in acetone.

Figure 7.12a, b shows the dependencies of the foot diameter on the clad diameter and the withdrawal speed, respectively. The foot diameter can be controlled by varying the viscosity of the resin solution, withdrawing speed, and the clad diameter.

7.3.3 c-mode NSOM Imaging of Salmonella Flagellar Filaments in Air and Water

Using a protrusion-type probe fabricated by selective etching and selective resin coating, Naya et al. [30, 31] succeeded in obtaining high-resolved c-mode NSOM images of Salmonella flagellar filaments in both air and water.

7.3.3.1 Instrument of the c-mode NSOM

Figure 7.13 shows the schematic illustration of the optical system of c-mode NSOM under near-field optical intensity feedback control. The sample substrate is mounted

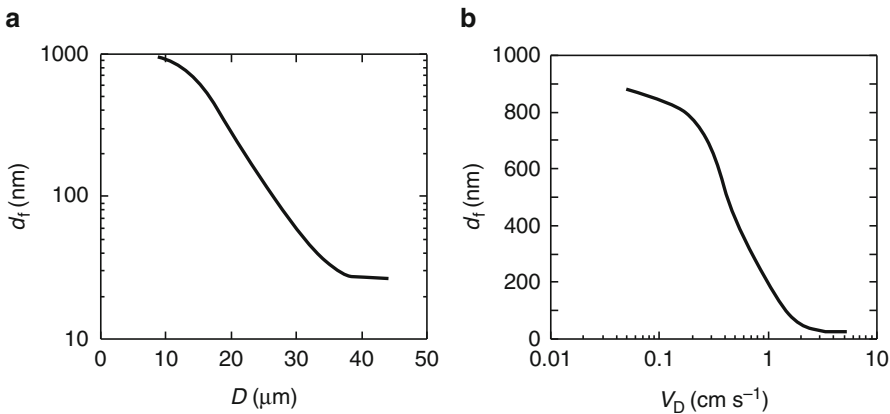


Fig. 7.12 Dependencies of the foot diameter d_f on (a) the clad diameter D for a withdrawing speed of 5 cm s^{-1} and (b) the withdrawal speed V_D for a clad diameter of $45 \mu\text{m}$

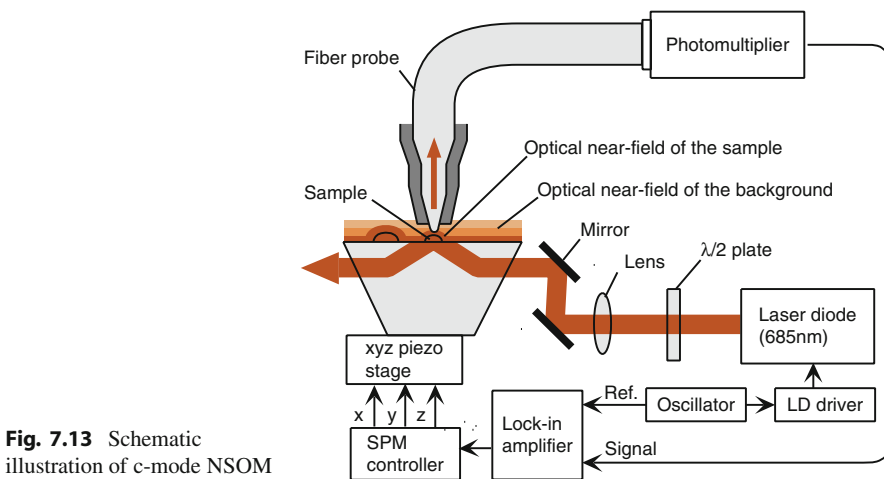
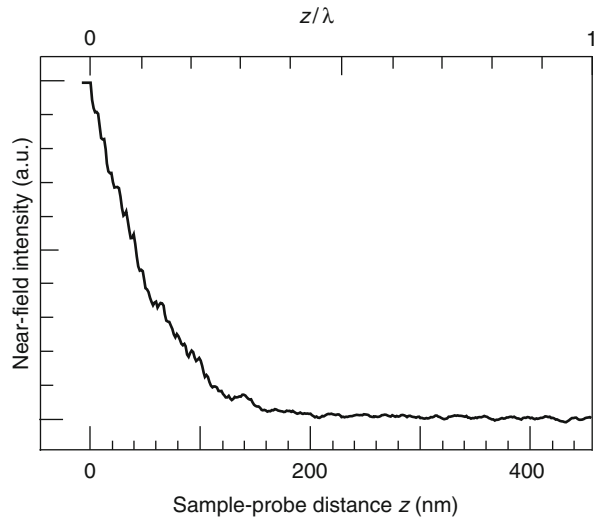


Fig. 7.13 Schematic illustration of c-mode NSOM

on the xyz piezo stage. The piezo parameters are decided depending on features such as the lateral and longitudinal variations of the sample. Here, the piezo stage has a total lateral span of $100 \times 100 \mu\text{m}$. The z stage has a span of $5 \mu\text{m}$. A right angle prism or dove prism is used for generating the optical near field on the sample surface. Here, care should be taken to avoid unwanted scattering light generated from the prism surface due to the dust and scratches. The probe is mounted on an xyz stage.

The light from a laser diode of the 680-nm wavelength was used as the light source. The light is incident on the prism and is totally internally reflected. Then, optical near field is generated on the sample surface. As shown by shaded region in Fig. 7.13, the optical near field is localized three dimensionally and follows the

Fig. 7.14 Variation of the optical near-field intensity as a function of the sample–probe distance, obtained with c-mode NSOM employing a protrusion-type probe



spatial variations of the sample. When the probe approaches closer to the sample surface, the optical near field is detected through the probe by highly sensitive detector such as a photomultiplier tube. By scanning the sample, information about the sample feature can be extracted. Typical value of the detected power is of the order of 1 nW–100 pW. In this system, the signal over the background can be effectively extracted by modulating the light and by amplifying the modulated signal with a lock-in amplifier.

Figure 7.14 shows the variation of the optical near-field intensity as a function of the sample–probe distance, which is obtained with c-mode NSOM employing a protrusion-type probe with a foot diameter of 30 nm as shown in Fig. 7.15a. The optical near-field intensity sharply increases by decreasing the sample–probe distance. This sharp variation of the near-field intensity can be used as a feedback control signal to regulate the sample–probe distance.

7.3.3.2 Sample

The samples were fabricated by fixing the separated filaments from the body on a hydrophilic glass substrate. A single filament has a typical length of a few micrometers and a diameter of around 25 nm as shown in Fig. 7.15b. The sample substrate was mounted on the prism of the optical system as Fig. 7.13.

7.3.3.3 Near-Field Optical Images of Salmonella Flagellar Filaments

Figure 7.15c shows a near-field image of Salmonella flagellar filaments, obtained by the c-mode NSOM under near-field optical (NFO) intensity feedback control. Here, the incident light was s-polarized. The pixel size is 25×25 nm. The sample–probe distance was kept to be less than 15 nm. The full width at half maximum (FWHM) of the region as indicated by arrows is 50 nm. This value is comparable

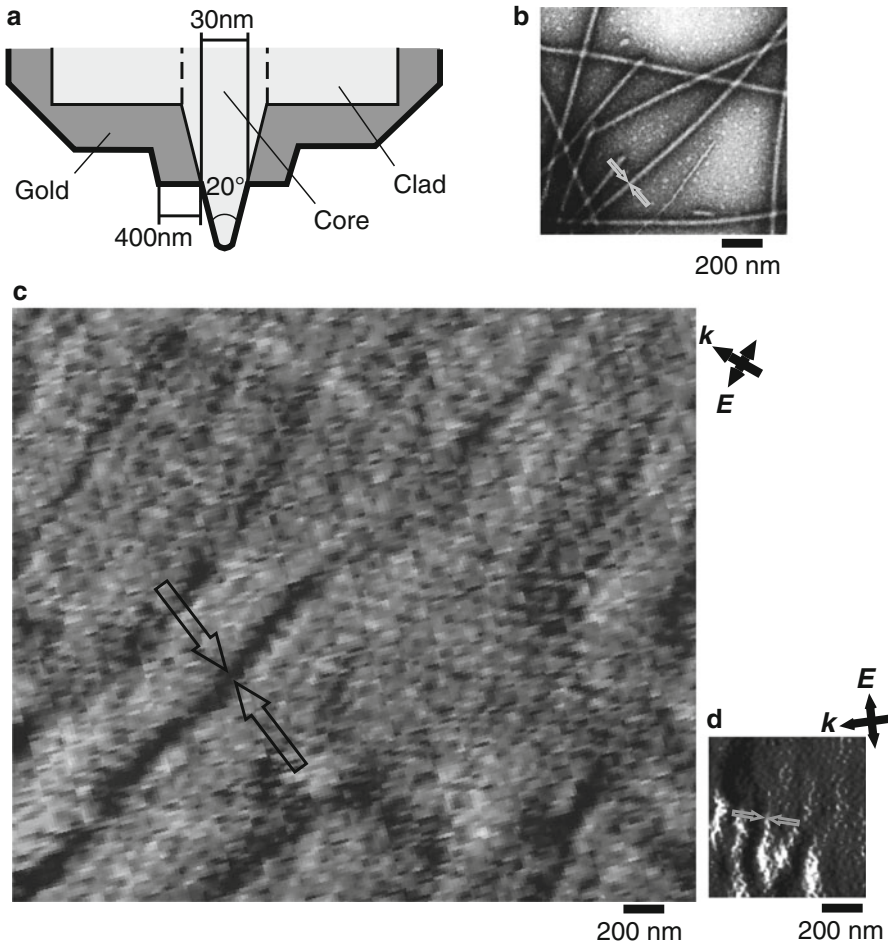


Fig. 7.15 (a) Schematic illustration of the fabricated protrusion-type fiber probe with cone angle of 20° , a foot diameter of 30 nm, and apex diameter less than 10 nm. (b) A transmission electron micrograph of the Salmonella flagellar filaments. The diameter of a flagellar filament, as indicated by arrows, is 25 nm. (c) A c-mode NSOM image of Salmonella flagellar filaments. The arrows at the top right hand represent the directions of wave-vector \mathbf{k} and electric field vector \mathbf{E} . (d) Perspective view of the near-field image of Salmonella flagellar filaments in water. The bright region, as indicated by arrows, is 50 nm. The arrows at the top right hand are defined as the directions of wave-vector \mathbf{k} and electric field vector \mathbf{E} .

to the diameter obtained from the TEM image (Fig. 7.15a) and indicates the high-resolution capability of NSOM employing the protrusion-type probe.

Figure 7.15d shows the near-field optical image of Salmonella flagellar filaments obtained in water. The pixel size is 10×10 nm. This near-field optical imaging in water was also done by c-mode NSOM under NFO intensity feedback control as in air. The filament sample was fixed on a glass substrate and was fitted with an acrylic

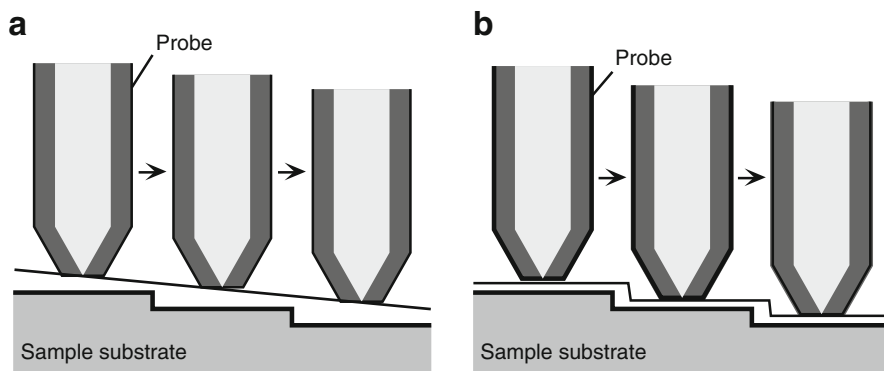


Fig. 7.16 (a) Constant height mode and (b) constant distance mode

ring. The columnar bath with an inner diameter of 10 mm and a height of 2 mm was filled with water during the observation. The sample–probe distance was estimated to be less than 30 nm. The bright segments correspond to the filaments. The FWHM of the bright region as indicated by arrows is 50 nm. The c-mode NSOM employing the probe with a protruding tip is effective in the near-field imaging of biological sample in water.

Figure 7.15c, d was obtained with c-mode NSOM operated under constant height mode as schematically shown in Fig. 7.16a. The monotonous variation as shown in Fig. 7.14 was used to decide the initial distance. To compensate the tilt effects of the substrate, the time constant of the feedback loop was carefully adjusted so that the probe followed only sample features larger than $1\ \mu\text{m}$. When the c-mode NSOM was operated under constant distance mode (Fig. 7.16b), such highly resolved images could not be obtained.

7.3.4 c-mode NSOM Images of Microtubules

Zvyagin et al. [56] isolated microtubules from the brain of a pig and observed with c-mode NSOM using a protrusion-type probe with a foot diameter of 30 nm. For this observation, a c-mode NSOM with the s-polarized incident light was used. To regulate the sample–probe distance, a shear-force feedback system [7, 47] was added to c-mode NSOM. In the shear-force feedback system, the differential force and frictional force are detected by dithering the probe at its resonance frequency at some amplitude, and the amplitude of dithering is measured by an optical interference technique. Figure 7.17 shows a variation of the amplitude of dithering the protrusion-type probe as a function of the sample–probe distance. The inset is the resonance frequency spectrum.

Figure 7.18a shows the transmission electron micrograph of microtubules. The dark region seen in the middle of a strand corresponds to microtubules. The width

Fig. 7.17 Variation of the dithering amplitude of the probe as a function of the sample-probe distance. The inset is the resonance frequency spectrum of the dithering probe

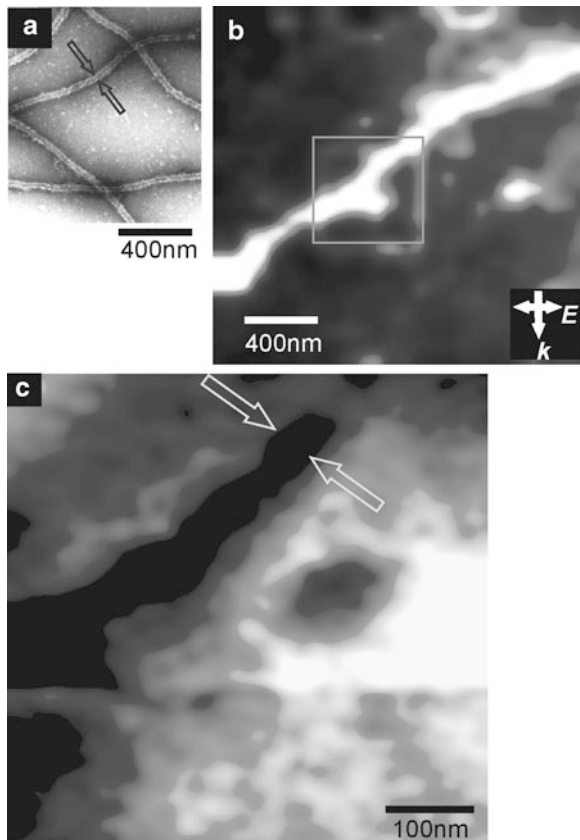
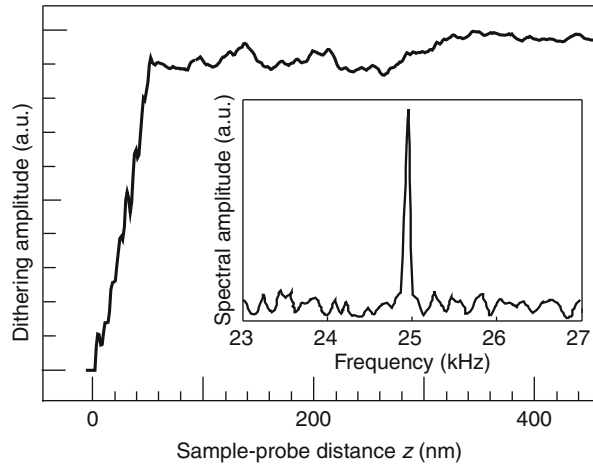


Fig. 7.18 (a) Transmission electron micrograph of a microtubule sample; (b) shear-force topographic image of the microtubule sample; (c) c-mode NSOM image in the rectangular region in (b). The FWHM of the dark line structure is approximately 40 nm

of microtubules, as indicated by arrows, is 25 nm. [Figure 7.18b](#) shows a shear-force topographic image of microtubules. The sample–probe distance was kept to be less than 5 nm during the scanning. Here, the long bright structure and the round ones correspond to a microtubule and protein aggregates, respectively. From this high-resolution imaging result, the protrusion-type probe is very effective for high-resolution shear-force microscopy. [Figure 7.18c](#) shows the near-field optical image of the rectangular region in [Fig. 7.18b](#), which is obtained under constant height mode without using shear-force feedback. The sample–probe distance was about 30 nm.

7.3.5 Near-Field Spectroscopic Investigation of Semiconductor Quantum Dots Under Extremely Low Temperature

Toda et al. [46] carried out spectroscopic study of GaAs quantum dots ([►Chap. 9](#)) by low-temperature NSOM employing a protrusion-type probe. [Figure 7.19a](#) shows schematic illustration of the microscope, the probe, and the GaAs quantum dots grown on SiO₂-patterned GaAs substrates with metalorganic chemical vapor deposition. Here, the probe has a foot diameter of 100 nm and a cone angle of 40°. The length of the protruding tip is about 130 nm. The quantum dots pattern has a size of 190 × 160 × 12 nm and a separation of 2 μm. The excitation light is delivered via the fiber probe with a length longer than 2 m from the outside of the cryostat to the sample. The photoluminescence spectrum as shown in [Fig. 7.20a](#) was obtained by positioning the protruding tip 200 nm above the top of the quantum dots at a low

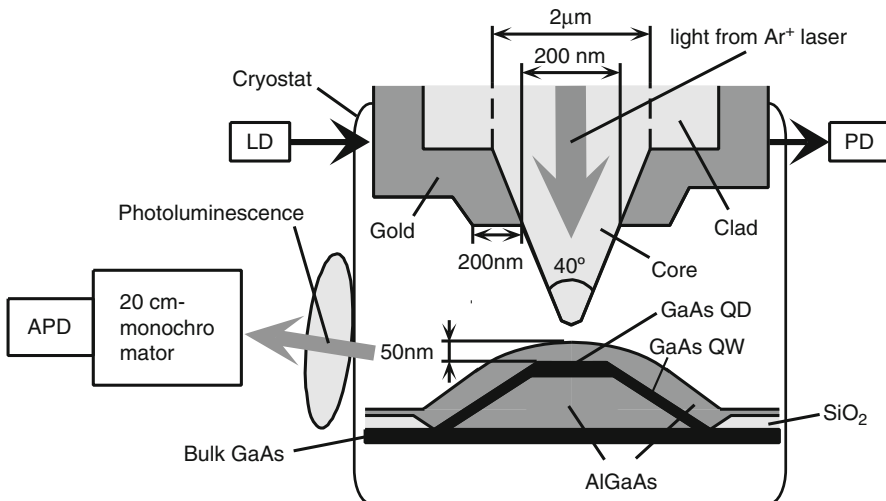


Fig. 7.19 Schematic illustration of i-mode NSOM developed for photoluminescence spectroscopy of GaAs quantum dots at a low temperature of 18 K

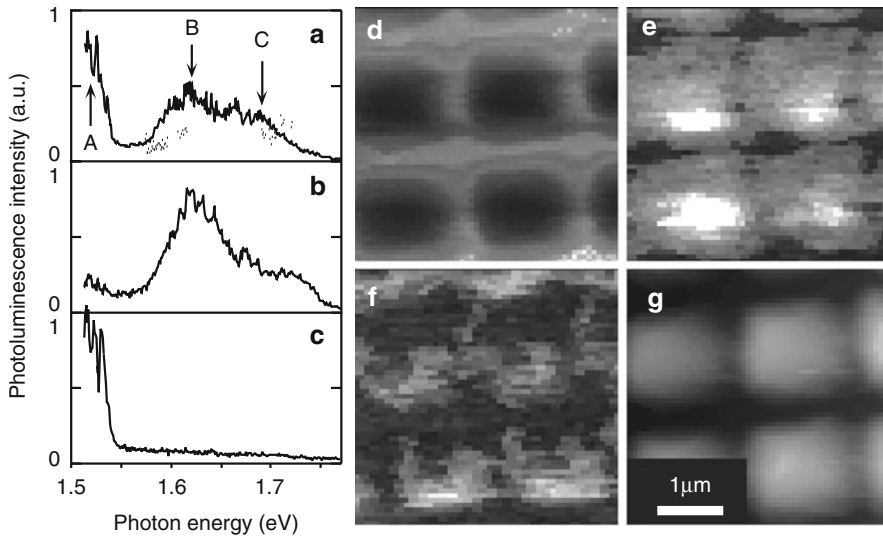


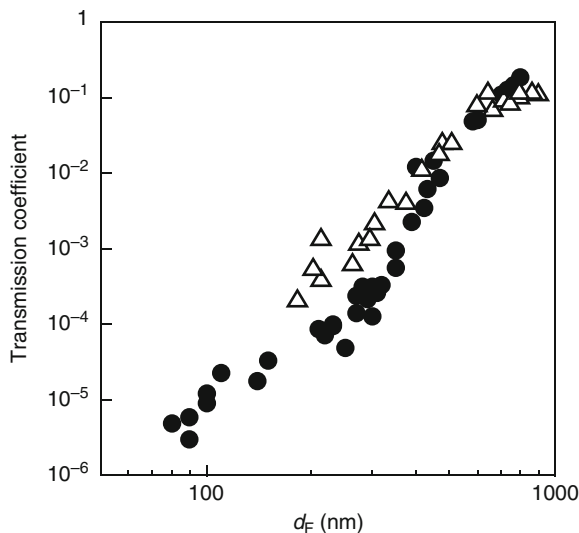
Fig. 7.20 Photoluminescence spectrums at maintaining the protruding tip (a) 200 nm above the quantum dots, (b) less than 10 nm above the quantum dots, and (d) less than 10 nm above the SiO_2 mask. Figures (c)–(f) are monochromatic photoluminescence images at the energy regions labeled A–C, respectively and simultaneously obtained topographic image

temperature of 18 K. This corresponds to the spectrum from the carriers excited in the whole quantum dots structure including the regions A–C. Figure 7.20b, c shows photoluminescence spectrums with tip position less than 10 nm above the region of the quantum dots and that of SiO_2 mask, respectively.

Figure 7.20d–f shows monochromatic photoluminescence images obtained under constant distance mode at 18 K with the energy regions indicated by the arrows labeled A–C, which originated from the three regions of the GaAs bulk, GaAs quantum dots, and GaAs quantum well, respectively. Figure 7.20g is a shear-force topographic image obtained simultaneously. The protrusion-type fiber probe with the long protruding length is convenient for scanning such bumpy sample surface.

For this near-field imaging, other type probes were also used, which we fabricated by pulling and etching the high- GeO_2 -doped fiber. In the heating-and-pulling process, the fiber was tapered with the highest pulling strength by a commercial puller (Sutter, P-2000) so as to have a dip structure at the taper end. By the etching in a BHF with a volume ratio of 10:1:1, the dip was flattened, and then, the core is protruded from the pure silica clad. The tapered fibers were aluminized by vacuum evaporation method. Some of the probes had throughputs higher than the protrusion-type probes. However, we could not fabricate high-throughput probes with reproducibility because it is difficult to control the sizes of the dip generated at the pulling. Figure 7.20a, b shows scanning electron micrographs of a pulled and etched probe and its magnified view. The broken lines represent to cross-section the GeO_2 -doped core.

Fig. 7.21 Dependences of the transmission efficiencies of two protrusion-type probes with (a) a cone angle of $\theta = 20^\circ$ (closed circles) and (b) $\theta = 50^\circ$ (open triangles) on the foot diameter



7.3.6 Transmission Efficiencies of the Protrusion-Type Probes

In near-field spectroscopic applications, one has to cope with too small near-field signal. In i-mode NSOM, the transmission efficiency of the probe is defined as the ratio of the output power to input power coupled into fiber probe. The low efficiency is caused by a large guiding loss, which is generated along tapered core due to optical interaction with the metal clad. Therefore, the throughput is affected by the length of the metallized tapered core or the cone angle. Figure 7.21 shows variations of the measured throughput values of protrusion-type probes for the different cone angles of 20° and 50° as a function of the foot diameter of the protrusion. Here, the closed circles and open triangles correspond to the variations for the cone angles of 20° and 50° , respectively. To collect the scattered light from the apex of the probe, an objective lens with a numerical aperture of 0.4 was inserted in front of the photodetector. At $d_F = 200$ nm, the throughput of the probe with a large cone angle of 50° is 10 times larger than that with $\theta = 20^\circ$. Increasing the cone angle enhances the throughput. For a near-field spectroscopic application requiring the high throughput, tapered probe with a large cone angle, i.e., $50\text{--}90^\circ$, should be fabricated by selective etching method.

7.4 Metal–Dielectric–Metal-Coated Fiber Probe and Near-Field Imaging of DNA Molecules

For imaging application of single biomolecules, i.e., a single DNA string with a lateral width of 4 nm and a height of 2 nm, one should fabricate near-field probe

with high-resolution capability beyond 10 nm. Recently, we fabricated a specially designed probe with metal–dielectric–metal coat for nanometer level resolving NSOM and succeeded in obtaining c-mode NSOM image of deoxyribonucleic acid (DNA) molecules [52].

7.4.1 Ag–MgF₂–Al-Coated Fiber Probe

Figure 7.22a shows schematic image of fabricated probe with metal–dielectric–metal coat. The probe consists of two tapered structures with the initial taper with a cone angle of 62° and a tapered apex region of with a cone angle of 30°. We call this tapered fiber a pencil-shaped probe. The method for fabricating the pencil-shaped probe with metal–dielectric–metal coat involves two steps: first, sharpening of an optical fiber into pencil-shaped structure method and, second, coating in a vacuum evaporation unit.

7.4.1.1 Fabrication of a Pencil-Shaped Probe

The pencil-shaped probe with a cone angle of 30° and an apex diameter less than 10 nm was fabricated with almost 100% based on selective etching of a multistep index fiber with the GeO₂-doped silica core, pure silica clad, and a F-doped silica support. This fiber is specially designed and fabricated by VAD method to produce pencil-shaped probes and triple-tapered probe. For details of the etching process, refer to Appendix.

7.4.1.2 Ag–MgF₂–Al Coating

The pencil-shaped probe is coated in a vacuum evaporation unit. The coating consists of three layers with an inner thin coating of silver (Ag), middle layer of

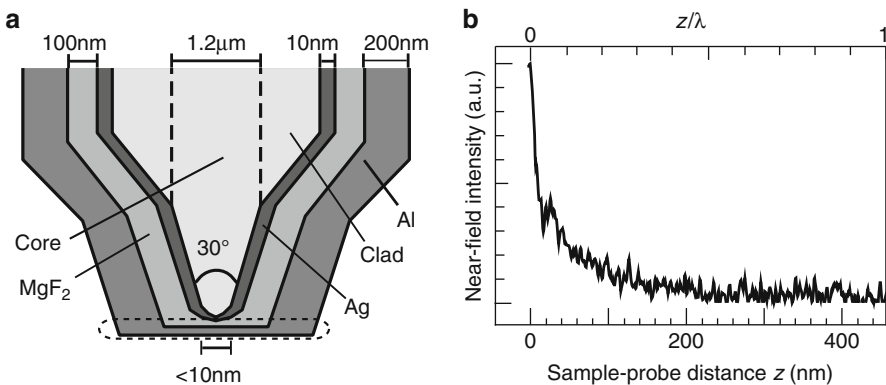


Fig. 7.22 (a) Ag–MgF₂–Al-coated fiber probe. (b) Variation of the optical near-field intensity as a function of the sample–probe distance

magnesium fluoride (MgF_2), and an outer aluminum coat. These materials were chosen due to the following facts:

- The inner thin layer of Ag is mainly for enhancing the scattering efficiency of the three-dimensionally localized near-field around the sample. Ag has a high reflectivity at the region of the wavelength used and has a higher dielectric constant than silica. Further, based on calculated results of Novotny et al. [46], the field confinement for a tapered probe with a thin silver coating is highly concentrated in both the lateral and vertical or z-directions. The field confinement of the Ag– MgF_2 –Al-coated probe in the z-direction could be inferred directly from Fig. 7.22b, which indicates strong near-field intensity enhancement very close to the sample surface.
- The middle layer of MgF_2 has a lower refractive index of 1.3 compared with 1.5 of the sharpened core and forms an efficient clad. It not only protects the deterioration of the inner layer of silver on exposure to air but also plays some role in suppressing the propagating light. Based on experimental experience, adding of MgF_2 improves the scattering efficiency of the probe and also robustness of the probe due to its soft nature.
- The outer Al coating with a fairly thick thickness of 200 nm in comparison with the skin depth which is a few tens of nanometers is coated in order to suppress background unwanted scattered light.

7.4.2 Sample Preparation

The double-stranded plasmid DNA with a ring structure (puc 18 and 2868 base pairs) has been used as the sample. It was diluted with distilled water to a final concentration of $5 \text{ ng}/\mu\text{L}$. A quantity of $2 \mu\text{L}$ of this was dropped onto the center of a wet-treated sapphire substrate with an ultrasmooth surface. Next the wet-treated surface was blow-dried with compressed air on it.

The sapphire substrate was produced with an epitaxial growth method [55], which is stable both in air and in water for a considerable duration. The surface has a staircase-like step structure whose step height and terrace width can be carefully controlled. As the sapphire surface itself is hydrophobic, it is necessary to make it hydrophilic for a stronger adsorption of organic DNA to the surface. For this purpose, the sapphire surface was treated with a sodium diphosphate solution with a concentration of 0.5 mol/L for a few minutes and then was rinsed with distilled water. After dried in air, the DNA solution was dropped.

7.4.3 DNA Images

Figure 7.21a shows a atomic force topographic image of the DNA sample [55]. The bright ring structures correspond to DNA molecules. The observed width of a single strand, as indicated by open arrows, is estimated to be around 10 nm.

The experimental system of c-mode as appeared in Fig. 7.13 was used for near-field optical imaging of single DNA molecules. The DNA sample is mounted on the prism, and optical near field is sensitively picked up by the Ag–MgF₂–Al-coated probe. Figure 7.21b shows the c-mode NSOM image, obtained under near-field optical intensity feedback control. The pixel size is 5×5 nm. The arrows at the top left hand of the figure indicate the propagation k and electric field E vectors of the incident light with the 680-nm wavelength. The coiled loop and single-strand of DNA are observed in this figure. The FWHM of the intensity variation at the portion, as indicated by the line, is around 20 nm. Figure 7.21c shows the magnified view of the single strands DNA. The pixel size is 2×2 nm. The FWHM, as indicated by the arrows, is about 4 nm. This nanometric spatial resolution attributes to the special care taken during preparation of the sample and of the probe to avoid unwanted scattered light.

We tried to obtain near-field optical images of DNA molecules by employing the protrusion-type probe with a foot diameter of 30 nm. However, successful results could not be obtained. The metal–dielectric–metal-coated probe tip with a layer of thin silver coating acts as a scattering probe much more sensitive than a dielectric tip protruding from metal.

7.5 Apertured Probes for Near-Field Imaging of Dye-Doped Samples

In investigating biological samples with i-mode NSOM, it is an effective method of enhancing the optical contrast to attach the sample with absorbing and fluorescing dye labels. For high-resolution imaging of a dye-labeled sample, one has to fabricate the apertured probe with aperture diameter of a few tens nanometers. Uma Maheswari et al. produced a fiber probe with an aperture diameter of around 15 nm and obtained near-field image of dye-labeled neurons of rats with an i-mode system under the shear-force feedback control. Figure 7.23 shows the schematic illustration of the used i-mode system. Here, the light from an argon ion laser with the 488-nm wavelength is coupled into the fiber probe to generate a localized optical near field around the apex region of the probe. The sample is mounted on the xyz piezo stage. As approaching the sample surface very close to the apex of the probe, the optical near field generated around the probe is scattered and detected by the sample fine structures. The scattered light is detected by a photomultiplier tube through collection optics such as the objective lens with a high numerical aperture. To regulate the sample–probe distance, shear-force feedback system is added, consisting of the 685-nm laser diode, dithering probe, and photodiode.

Figure 7.24a shows the schematic illustration of the fabricated probe. The cone angle is 20° . To fabricate the probe, a dispersion-compensating fiber was consecutively etched in three BHF with volume ratios of 1.7:1:1, 10:1:1, and 10:1:120, for 60, 75, and 2 min, respectively, and then was metallized with 5-nm-thick chromium and gold with a thickness of 120 nm by a vacuum evaporation unit.

Fig. 7.23 Schematic illustration of an i-mode NSOM

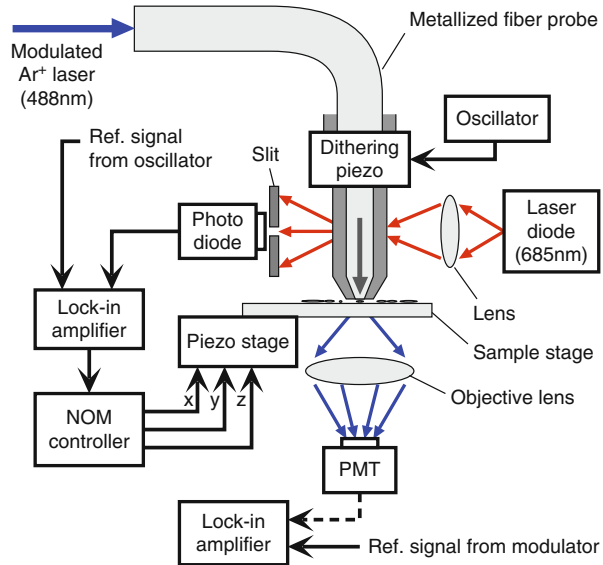


Figure 7.24b shows the i-mode near-field image of neuron labeled with toluidine blue. Here, the sample–probe distance is less than 50 nm. The wide dark arrows and the bright arrow correspond to the neural process and the cell body, respectively. Before this imaging, the metal covering the top region of the probe, enclosed by the dotted rectangular in Fig. 7.21a, was removed away by rubbing with the sample substrate under shear-force feedback control. As shown in Fig. 7.24c, the shear-force topographic variation is monotonous. Figure 7.24d shows i-mode near-field image of the magnified region, as shown indicated by the long dark arrow, in the neural process in Fig. 7.24b. The fringe-like structures are seen in the near-field image of Fig. 7.24d, however not appeared in topographic image. This shows that the fringe-like structure labeled with toluidine blue lies just underneath the cell membrane on the surface. The structures are identified as microtubules, which are the main constituent elements of the neural process. The FWHM of near-field intensity variation at the portion, as indicated by the line in Fig. 7.24d, is estimated to be 26 nm, which agrees with the typical diameter of 25 nm of a single microtubule.

Recently, another apertured probe with a large cone angle, i.e., 50–90°, has been chosen for performing i-mode and i-c mode imaging applications including single dye molecules detection because the probe has a much higher throughput than the tapered probe as shown in Fig. 7.21a. Hosaka et al. [12] fabricated a double-tapered probe [39] with a cone angle of 90° and an aperture diameter of a few tens nanometers and succeeded in obtaining near-field fluorescence imaging of dye molecules with a high resolution of around 10 nm. Figure 7.23 shows the near-field

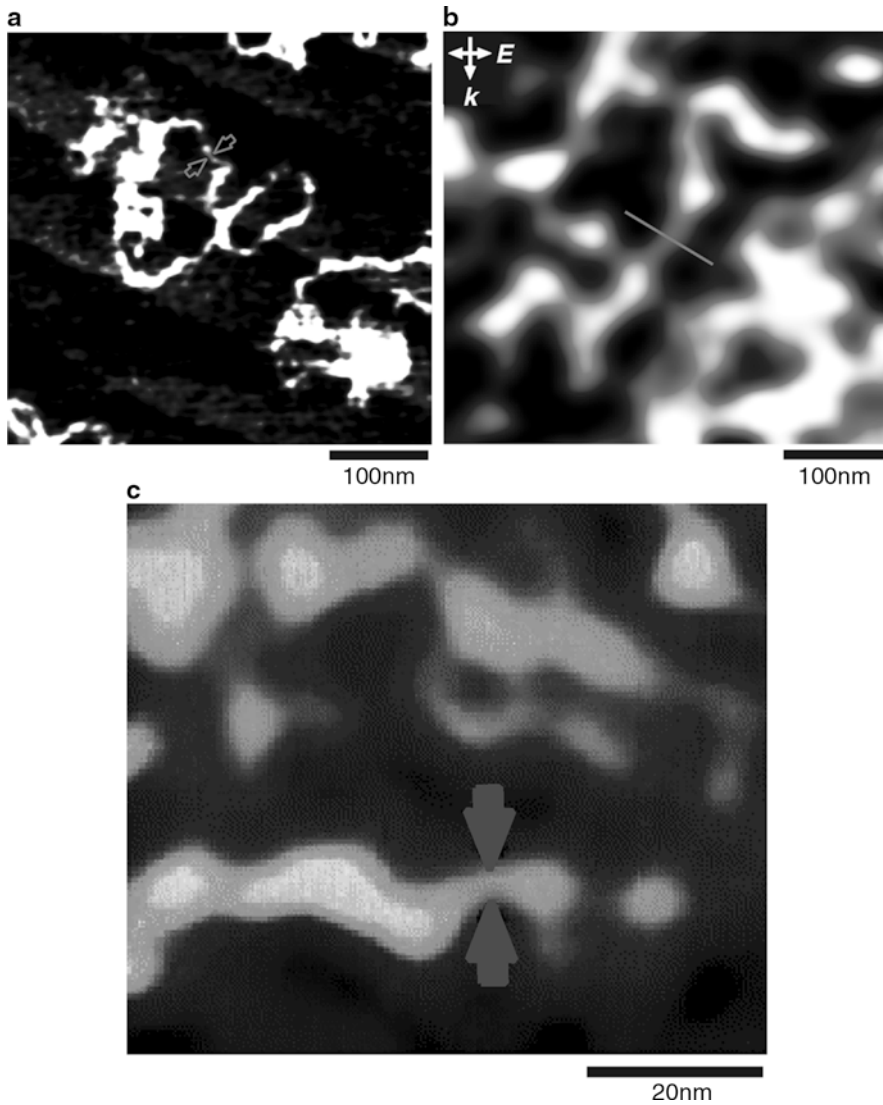
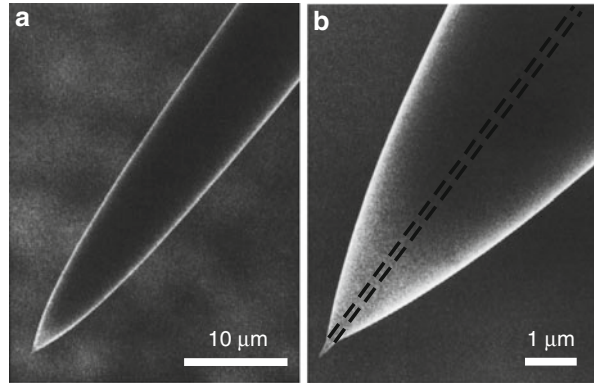


Fig. 7.24 (a) AFM image and (b) and (c) near-field optical images of a DNA sample, obtained with c-mode NSOM employing the fiber probe in Fig. 7.25a

fluorescence image of single Rhodamine 6G molecules dispersed on the quartz glass at 700 ± 20 nm. In this experiment, the dye was excited by a He–Ne laser with the 633-nm wavelength. The bright spots correspond to emitting single dye molecules. The estimated resolution is around 10 nm. Details of the double-tapered probe are discussed in Sect. 7.5.

Fig. 7.25 Scanning electron micrographs of (a) a pulled and etched probe and (b) its magnified view



7.6 Double-Tapered Fiber Probe and Spectroscopic Applications

NSOM is a powerful tool for studying semiconductor devices with submicron- and nanometer-sized structures by the imaging and spectroscopy. For photoluminescence investigation of a semiconductor device, i-c mode NSOM whose resolution is not affected by carrier diffusion effect should be chosen. In i-c mode NSOM (Fig. 7.1c), the sample is effectively excited by optical near field generated around the probe in the i-mode fashion, and the near-field photoluminescence of the sample is scattered by the probe in the c-mode fashion. To perform imaging and spectroscopic applications by illumination-collection hybrid mode NSOM, high-throughput probes must be fabricated. Saiki et al. [39] have developed a double-tapered probe with the high throughput and have performed spectroscopic study of semiconductor devices by i-mode NSOM and i-c mode NSOM employing the probes. In this section, double-tapered probe and spectroscopic applications are described.

7.6.1 Double-Tapered Probe

Figure 7.26a, b shows the cross-sectional profiles of the protrusion-type double-tapered probe and apertured-type double-tapered probe. Here, θ_1 and θ_2 ($< \theta_1$) are the cone angles of the first and second taper, respectively. λ is the cross-sectional diameter which agrees with the optical wavelength in the core. d_B is the base diameter of the first taper, which is larger than the wavelength size λ , and d and d_f are the apex and foot diameters of the protrusion, respectively.

As discussed in Sect. 7.3.6, the first cone angle of the double-tapered probe has to be increased to enhance the throughput of the probe. Since the light entering the tapered core is strongly attenuated by metal film in the subwavelength cross-sectional portion, by making the base diameter the value of λ or more, the double-tapered probe with the first cone angle of 90° has transmission coefficient

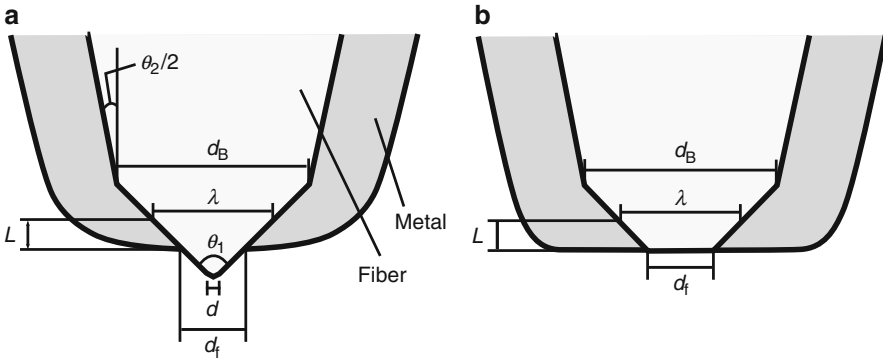


Fig. 7.26 Schematic cross-sectional profiles of double-tapered probes with a protruding tip from metal and with (b) an aperture. θ_1 and θ_2 , cone angles of the first and second tapers, respectively; d , apex diameter; d_f , foot diameter in (a) and aperture diameter in (b); d_B , base diameter of the first taper; λ , optical wavelength in the core; L , length of the lossy part between the cross-sectional diameters of λ and d_f

as high as the single-tapered probe with a cone angle of 90° . Based on FDTD simulation [28], the double-tapered probe can have collection efficiency higher than the single-tapered probe. The double-tapered structure is suitable for coupling the scattered light into the core.

7.6.1.1 Forming a Double-Tapered Tip

The method for fabricating the probe involves two steps: (A) controlling the clad diameter and forming the first taper and (B) forming the second taper, which are based on selective etching as described in Sect. 7.2.3. Figure 7.27a shows the method schematically. In step A, by immersing the fiber in BHF with X_A :1:1 (where $X_A > 1.7$), the core is protruded from the clad with the cone angle θ_1 represented by

$$\sin \frac{\theta_1}{2} = \frac{R_{1A}}{R_{2A}}. \quad (7.8)$$

In step B, immersing the fiber in BHF with 10:1:1, the core is tapered with cone angles of θ_1 and θ_2 , where

$$\sin \frac{\theta_2}{2} = \frac{R_{1B}}{R_{2B}}. \quad (7.9)$$

The base diameter d_B is represented by

$$d_B = 2r_1 \left(1 - \frac{T_B}{\tau}\right) \quad (T_B < \tau), \quad (7.10)$$

which is controlled by varying the etching time T_C . Here, τ is defined by Eq. 7.4. The clad diameter D is given by Eq. 7.7.

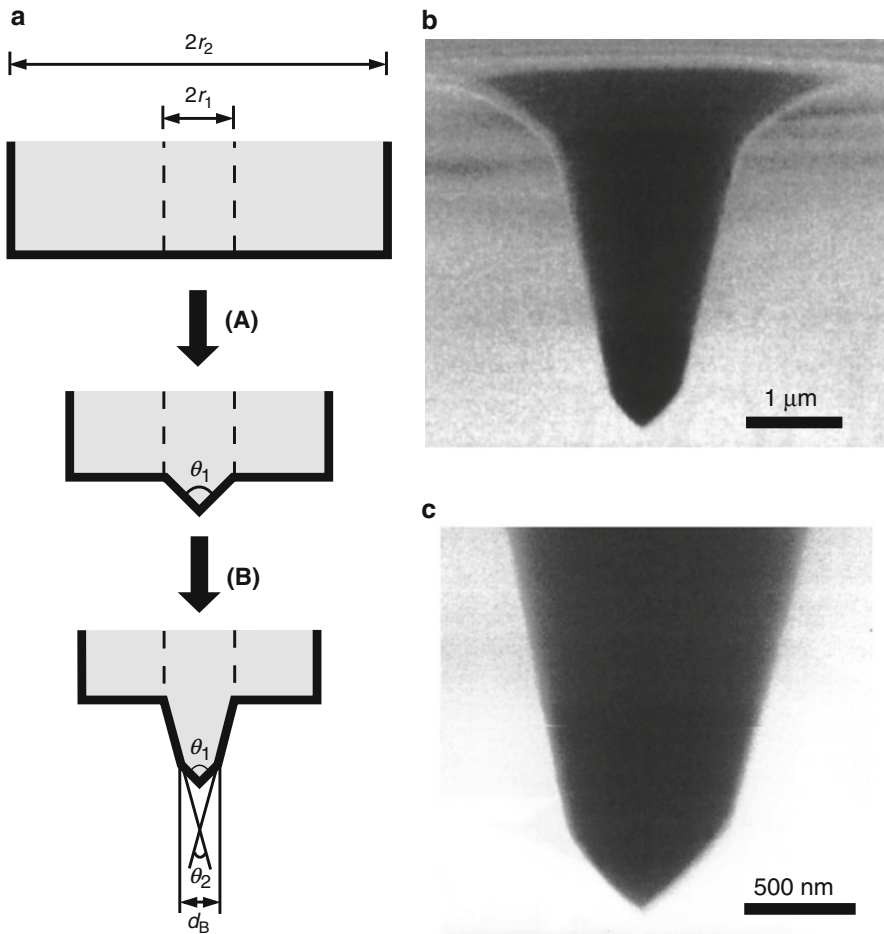


Fig. 7.27 (a) Etching method for fabricating a double-tapered probe. The fiber is consecutively etched in buffered HF with volume ratios of $X_A:1:1$ ($1.7 < X_A < 10$) and 10:1:1 in steps A and B, respectively. Here, $2r_1$ and $2r_2$ are the core and cladding diameters, respectively. θ_1 and θ_2 are the first and second cone angles of the double-tapered probe. SEM micrographs of (b) a double-tapered core and (c) the magnified top region. $\theta_1 = 90^\circ$; $\theta_2 = 20^\circ$; $d_B = 500$ nm

Table 7.4 Conditions for fabricating a probe as in Fig. 7.27

Step	Volume ratio of BHF	Etching time (min)
A	1.8:1:1	70
B	10:1:1	40

In actual conditions as shown in Table 7.4, a probe with a double-tapered core with cone angles of $\theta_1 = 90^\circ$ and $\theta_2 = 20^\circ$ and a base diameter of $d_B = 500$ nm was obtained. Figure 7.27b, c shows SEM micrographs of the tapered core region of a double-tapered probe and its magnified top region.

7.6.2 Near-Field Photoluminescence Image of Lateral p–n Junctions Obtained with the i-c mode NSOM

With NSOM employing double-tapered probe, Saiki et al. [38] investigated a GaAs-based lateral p–n junction and obtained its near-field photoluminescence image with i-c mode NSOM. Figure 7.28a, b shows the schematic illustrations of the double-tapered probe and experimental setup of the i-c mode NSOM, respectively. Here, the probe was produced based on selective resin coating. The foot diameter and cone angle of the double-tapered probe are 200 nm and 50°, respectively. The GaAs sample is fixed on the inclined substrate to avoid the bumpy sample surface with the edge of the metallized clad at scanning. The sample is excited by laser light with 633 nm through the double-tapered probe. The laser power coupled into the fiber is 0.5 mW. The sample–probe distance was controlled by the shear-force feedback technique to scan the sample. The sample is fabricated by growing a silicon-doped GaAs layer on a semi-insulating GaAs (111)A substrate with (311)A slopes [40]. The thickness of the silicon-doped layer is around 1 μm.

Figure 7.29a, b shows the shear-force topographic image and near-field photoluminescence image, which were simultaneously obtained. Because photoexcited electrons and holes are separated and drifted by the internal electric field in the upper and lower junctions, the emission intensity is lower than those of the other regions as seen in Fig. 7.29b. Further, in the lower junction region, some bright portions where the photoluminescence intensity increased locally are observed. From the intensity variation in this region, the spatial resolution is estimated to be 200 nm or less. Recently, near-field photoluminescence images of single GaAs dots and a GaNAs layer have been obtained with i-c mode NSOM employing double-tapered

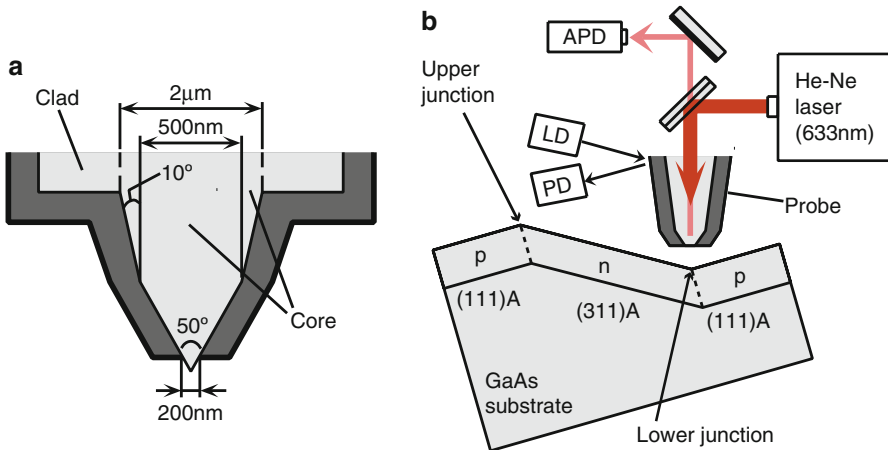
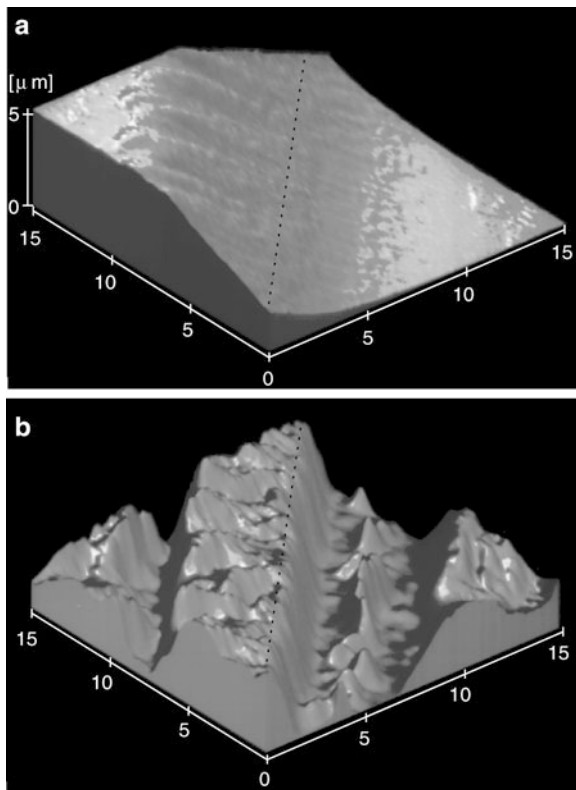


Fig. 7.28 Schematic illustrations of (a) a double-tapered probe and (b) a i-c mode NSOM for investigating the lateral p–n junction

Fig. 7.29 (a) Shear-force topographic and (b) i-c mode NSOM images of the GaAs lateral p-n junction



probe with an aperture diameter of 20–30 nm, and the resolution of 20–30 nm has been achieved. For details of these works, refer to Saiki [37].

7.6.3 Near-Field Raman Spectroscopy of Polydiacetylene

With i-mode NSOM employing the double-tapered probe with an aperture diameter of 100 nm, Narita et al. [29] succeeded in obtaining two-dimensional mapping of Raman signal features of a tabular polydiacetylene single crystal. The sample was excited by 532-nm Nd:YAG laser with a power of 10 nW. The near-field Raman spectrum was measured at 10×10 points in a portion with an area of $1 \times 1 \mu\text{m}$. Figure 7.30a shows a near-field Raman spectrum of polydiacetylene. Here, two Raman peaks L and S are observed at $1,457$ and $1,520 \text{ cm}^{-1}$, which relate the C=C bond and reflect the difference in the number of successive *cis*-bond. Peaks L and S are originated from longer successive bond and shorter ones, respectively. Figure 7.30b shows two-dimensional mapping of the relative Raman intensity of peak S at $1,520 \text{ nm}$ to peak L at $1,457 \text{ nm}$.

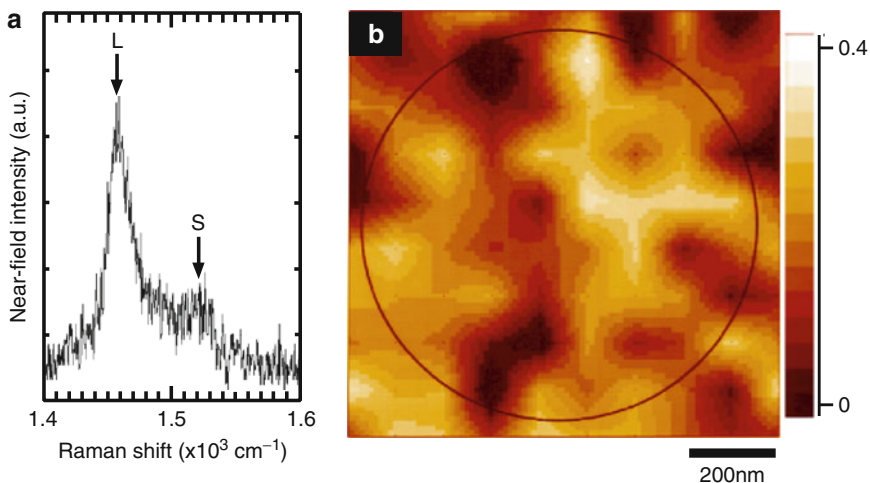


Fig. 7.30 (a) Near-field Raman spectrum of a tabular polydiacetylene single crystal. (b) Two-dimensional mapping the relative near-field intensity at peak S to peak L

7.7 Pure Silica Core Fiber Probes and Ultraviolet Applications

Using GeO₂-doped fibers such as the dispersion-compensating fiber and the double-clad fiber, one can fabricate the near-field probes as appeared in Figs. 7.15a, 7.19a, 7.22a, 7.25a, 7.28a, 7.31a, and 7.32a and carry out NSOM applications in the visible and infrared regions. However, it is difficult to employ such probes for ultraviolet (UV) near-field optical microscopy applications because the GeO₂-doped silica fiber has the strong guiding loss based on the Rayleigh scattering and moreover has UV absorption, luminescence, and Raman scattering which are originated from defects of GeO₂. In order to overcome this difficulty and to realize UV-NSOM, we have proposed fiber probes with the pure silica core. Figure 7.33 shows optical transmission spectrums of a GeO₂-doped fiber with an index difference of 1% and a fiber with the pure silica core and the fluorine-doped clad. It is found that the pure silica fiber probe has high transmittance in a wide region from near UV to near infrared. To realize pure silica fiber probes, we have developed methods to fabricate the following pure silica core probes:

- Single-tapered probe with a large cone angle of 120°
- Pulled and etched probe with the tapered core and clad [16]
- UV triple-tapered fiber probe [25]

as schematically shown in Fig. 7.34a–c, respectively. The single-tapered fiber is fabricated by immersing a 1,300-nm pure silica fiber (PSF) (Sumitomo, PS1) with a core diameter of 10 μm in a BHF as described in Sect. 7.2.3. Figure 7.35 shows a scanning electron micrograph of the single-tapered fiber with the pure silica core and

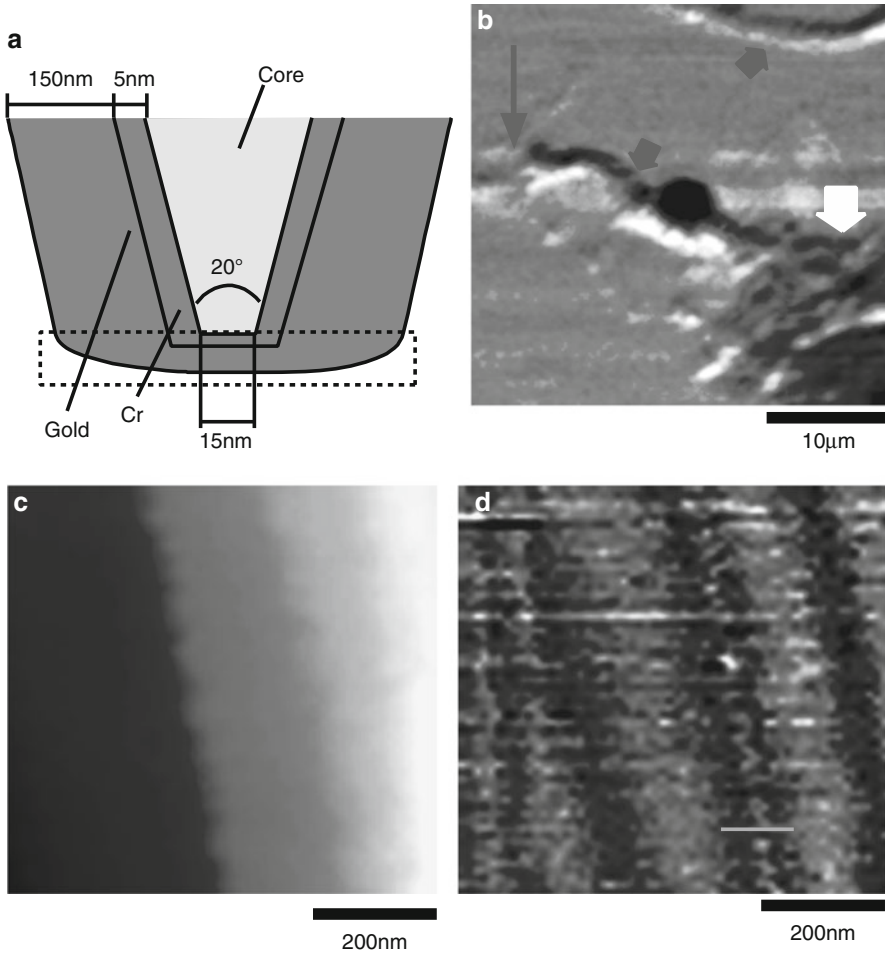


Fig. 7.31 (a) Cross-sectional illustration of the fabricated metallized fiber by the vacuum evaporation method. Its *top region* enclosed by the *dotted rectangular* was removed away by rubbing with the substrate under shear-force feedback control before the near-field imaging. (b) Shear-force topographic image of neurons of rats. The magnified view of (c) shear-force image and (d) i-mode NSOM images of the same area

a cone angle of 120° . We have tried to develop UV single-mode fibers with a cutoff wavelength less than 400 nm in order to fabricate UV single-tapered fiber. Details of these fibers will be discussed elsewhere. Using the pulled and etched probe and triple-tapered probe, we have obtained UV near-field photoluminescence images of polysilane and near-field Raman spectrum of silicon crystal. In the following, triple-tapered probe and pulled and etched probe are described.

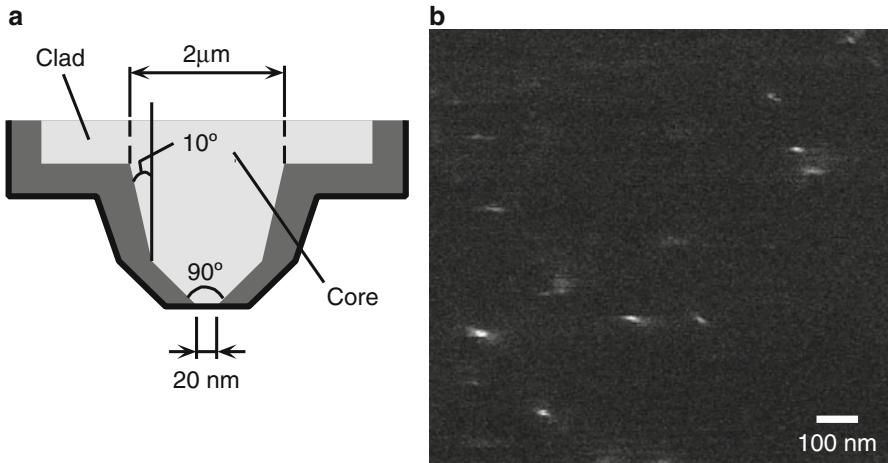


Fig. 7.32 (a) Schematic illustration of the double-tapered probe with a cone angle of 90° . (b) i-c mode near-field fluorescence image of single Rhodamine 6G molecules dispersed on a quartz substrate at 700 ± 20 nm

Fig. 7.33 Optical transmission spectra of a GeO_2 -doped core fiber with a refractive index difference of 1% (dotted line) and a pure silica core fiber (solid line)

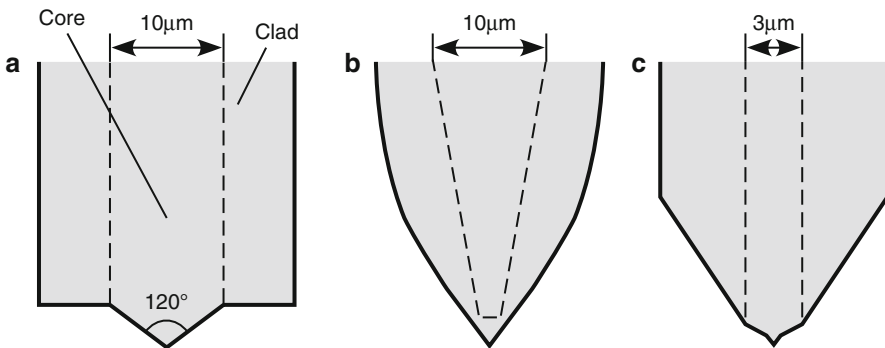
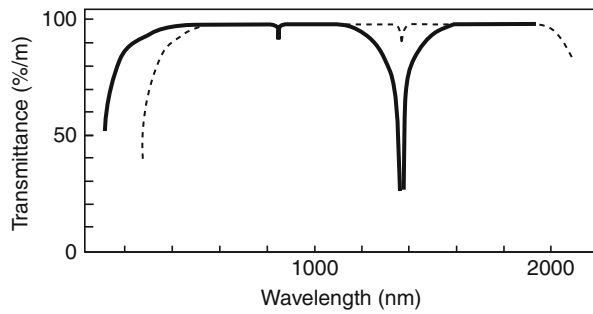
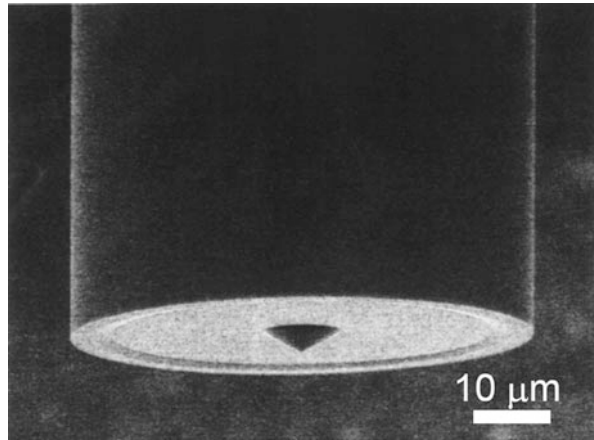


Fig. 7.34 Pure silica core probes with (a) the conical core protruded from the flat clad end, (b) tapered clad and core, and (c) triple-taper structure

Fig. 7.35 Scanning electron micrograph of a tapered fiber with the pure silica core, obtained by immersing a 1,300-nm fiber with a core diameter of $10\ \mu\text{m}$ for 240 min in a BHF with a volume ratio of 10:1:1. The cone angle is 120°



7.7.1 UV Triple-Tapered Probe

To fabricate a UV triple-tapered fiber probe, we newly developed a UV multistep index fiber [25] with the double core involving a subwavelength core and a pure silica core. In the following text, this fiber is called a double-core fiber. For triple-tapered probes with the GeO_2 -doped core, refer to Appendix.

7.7.1.1 Fabrication of UV Triple-Tapered Probe Based on Selective Etching of a Double-Core Fiber

The inset in Fig. 7.36 shows the index difference profile of the double-core fiber. The diameters of Sects. 7.1–7.5 are 100 nm, 2.9, 40, 42, and $125\ \mu\text{m}$, respectively. Sections 7.3–7.5 correspond to the clad region. Sections 7.3 and 7.5 are made of low fluorine-doped silica with an index difference of -0.35% . Section 7.4 is made of the high fluorine-doped silica with an index difference of -0.94% . The core region consists of Sects. 7.1 and 7.2, which are made of GeO_2 -doped silica and pure silica, respectively. The index difference of Sects. 7.1 and 7.2 is estimated to be around 0.7% . The diameter of Sect. 7.1 is only 100 nm. Since 99.9% cross-sectional area of the core region is occupied by the pure silica, the double-core fiber has transmittance as high as that of the pure silica fiber as shown in Fig. 7.33.

To fabricate this double-core fiber, we fabricated a preform glass rod by a combination of vapor-phase axial deposition and plasma-activated chemical vapor deposition and then drew the $125\text{-}\mu\text{m}$ -diameter fiber by heating the preform. Table 7.5 summarizes parameters for drawing the fiber.

As shown in Fig. 7.36, the double-core fiber is tapered by a selective etching method, which involves three steps: (A) hollowing of Sects. 7.1 and 7.4, (B) tapering of Sects. 7.2 and 7.3, and (C) sharpening of Sect. 7.1. Here, a BHF with a volume ratio of NH_4F solution (40%): HF acid (50%): H_2O is denoted as $X:1:1$. The values of X in steps A–C are $X_A = 0.6$, $X_B = 1.7$, and $X_C = 10$, respectively.

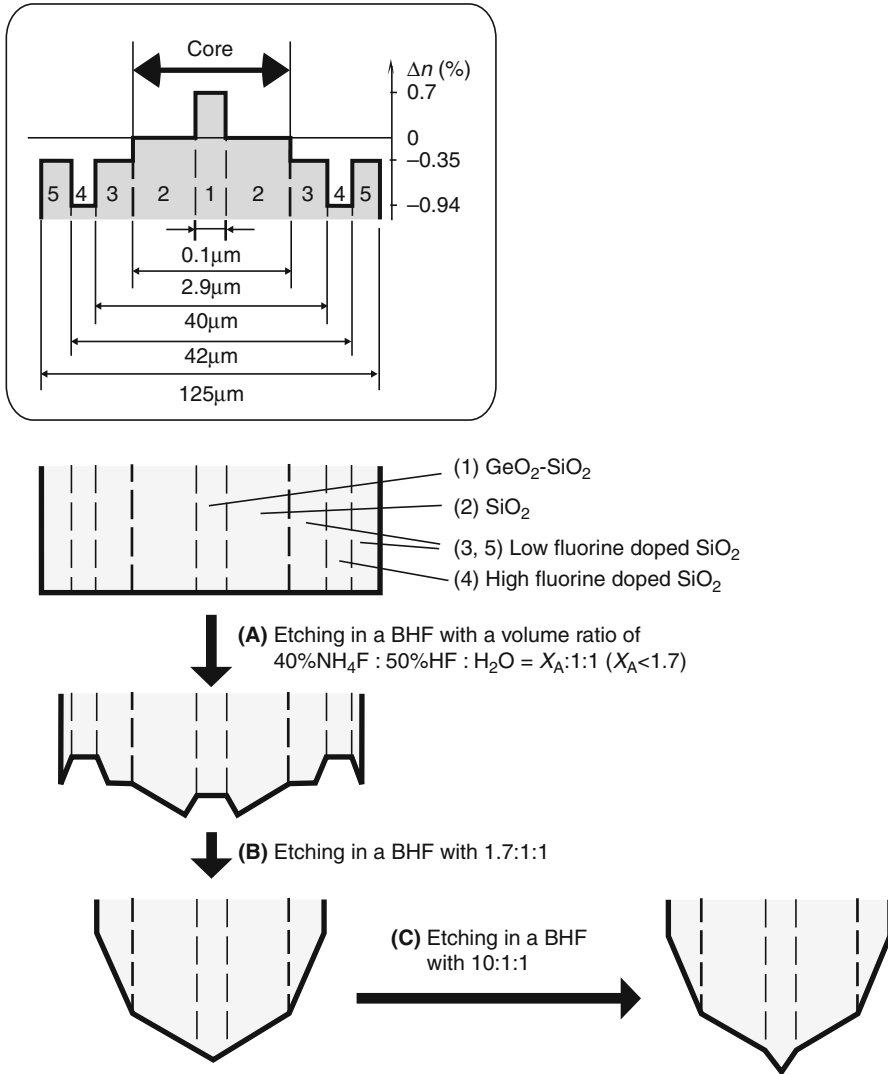


Fig. 7.36 Etching process to fabricate a triple-tapered probe. The inset shows the cross-sectional profile of the relative refractive index difference Δn of a multistep index fiber produced to fabricate the probe

Figure 7.37a, b show, scanning electron micrographs of the fabricated triple-tapered probe and its top region, respectively. The probe has an apex diameter of less than $10\ \text{nm}$. The values of the base diameters of d_{B1} and d_{B2} are $100\ \text{nm}$ and $2\ \mu\text{m}$, respectively. The first cone angle θ_1 , the second cone angle θ_2 , and the third cone angle θ_3 are $60^\circ (\pm 1^\circ)$, $120^\circ (\pm 1^\circ)$, and $60^\circ (\pm 1^\circ)$, respectively. Table 7.6 summarizes parameters of the etching process for fabricating the

Table 7.5 Parameters for drawing process to produce the double-core fiber

Drawing speed	150 m/s
Temperature	2,106 °C
Drawing tension	75 g
Clad diameter of the preform glass rod	25.5 mm
Clad diameter of the drawn fiber	125 μm

Fig. 7.37 Cross-sectional profile of the index difference Δn of a multistep index fiber produced to fabricate the probe. SEM micrographs of (a) a triple-tapered probe and (b) its magnified apex region. $\theta_1 = 60^\circ$; $\theta_2 = 120^\circ$; $\theta_3 = 60^\circ$; $d < 10$ nm

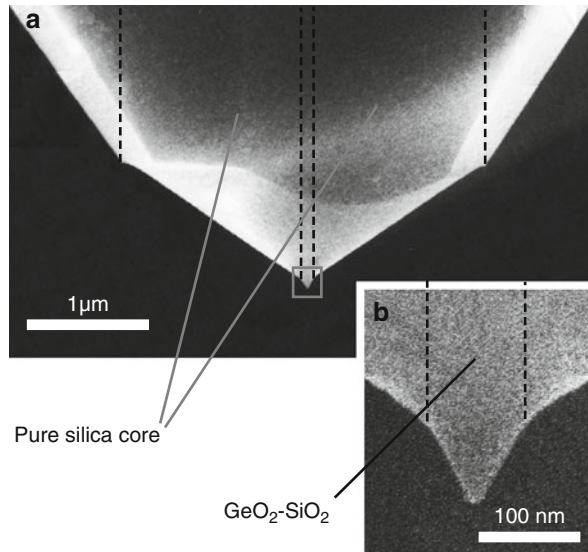


Table 7.6 Parameters of etching process for fabricating the triple-tapered probe

Step	Volume ratio of BHF	Etching time (min)	Temperature (°C)
A	0.6:1:1	40	25
B	1.7:1:1	20	25
C	10:1:1	10	25

probe of Fig. 7.37a. After the etching, the triple-tapered probe was coated with the 200-nm-thick aluminum film by vacuum evaporation method.

7.7.2 UV Near-Field Photoluminescence Images of Polysilane

To demonstrate the UV triple-tapered probe, we performed UV near-field photoluminescence imaging of polysilanes, which can be regarded as quantum wires based on silicon and are expected to be applied to the UV-light-emitting device. By changing the conformation of the silicon backbones, the optical properties can be controlled. Figure 7.38a, b shows absorption (dotted curves) and photoluminescence

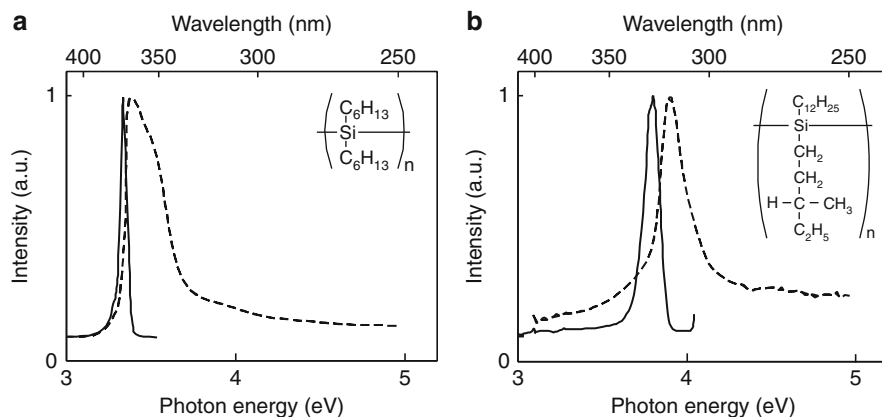


Fig. 7.38 Absorption (*dotted curves*) and photoluminescence (*solid curves*) spectra of polydihexylsilane (PDHS) and n-decyl-(s)-2-methylbutyl silane (chiral-PS), respectively. These polysilanes have different backbone structures called transplanar and 7/3 helical, respectively

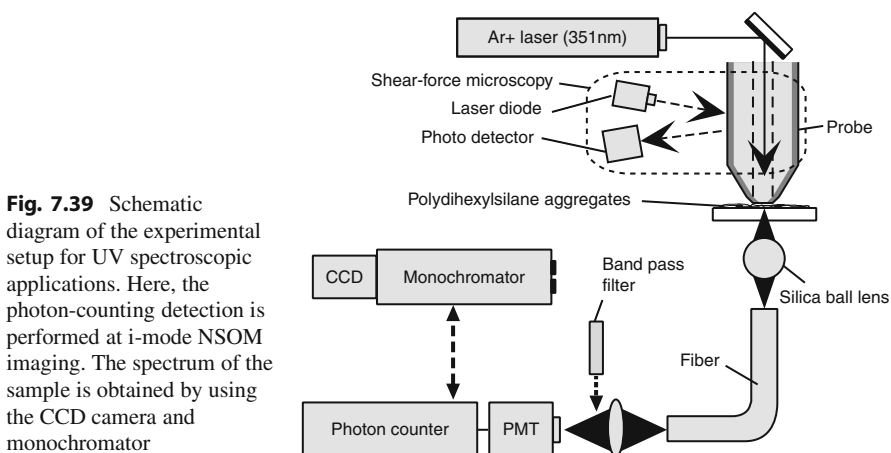


Fig. 7.39 Schematic diagram of the experimental setup for UV spectroscopic applications. Here, the photon-counting detection is performed at i-mode NSOM imaging. The spectrum of the sample is obtained by using the CCD camera and monochromator

(solid curves) spectra of two polysilanes named polydihexylsilane (PDHS) and n-decyl-(s)-2-methylbutyl silane (chiral-PS), respectively. They have different backbone structures called trans-planar and 7/3 helical, respectively. For the first UV photoluminescence imaging, PDHS was chosen, which has absorption and photoluminescence peaks at 370 and 380 nm, respectively. The quantum efficiency is evaluated to be 5%. PDHS was fixed on a glass substrate. Figure 7.39 shows schematic diagram of the i-mode UV-NSOM employing the triple-tapered probe. Here, an argon ion laser with the 351-nm wavelength is coupled into the fiber probe, and the UV optical near field generated around the probe excites the sample. Photoluminescence of PDHS is collected by an objective lens or silica ball lens.

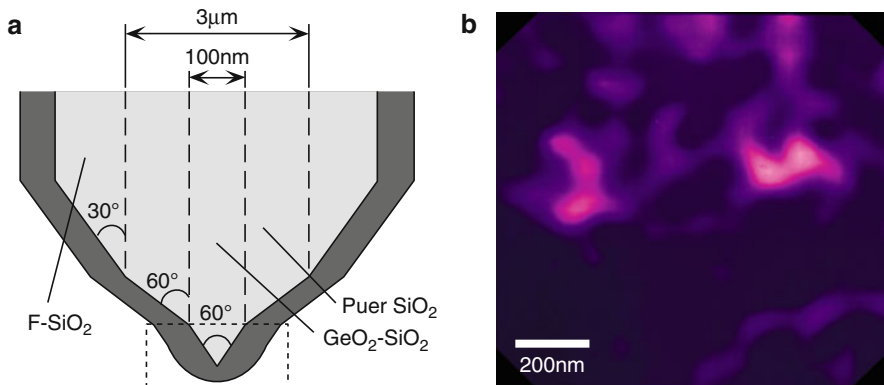


Fig. 7.40 (a) Triple-tapered fiber probe with a pure silica core and (b) UV near-field photoluminescence image of transplanar-type polydihexylsilane obtained with *i*-mode NSOM and probe as shown in (a) and (b), respectively. The *top region* of the probe, surrounded by the *dotted rectangular* in (b), was removed away before the imaging

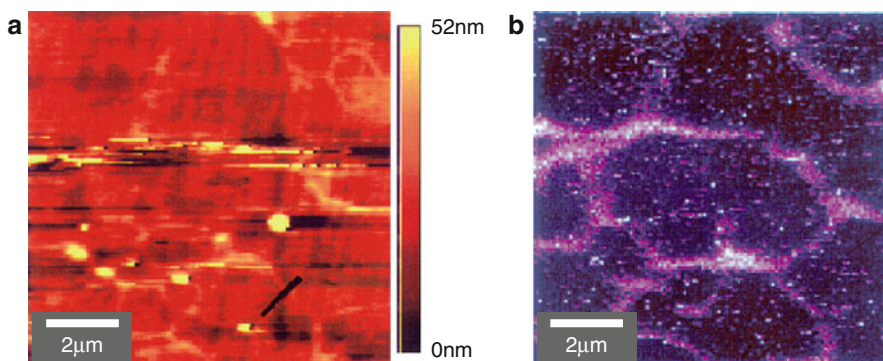


Fig. 7.41 (a) Topographic image and (b) *i*-mode near-field photoluminescence image of chiral-PS molecules at 325 nm

The triple-tapered probe has three cone angles of 60° , 120° , and 60° as shown in Fig. 7.40a. Figure 7.40b shows a UV near-field photoluminescence image of PDHS at 380 nm. The FWHM of the bright portion is estimated to be around 100 nm. Such near-field signal could not be detected through double-tapered probes with the GeO_2 -doped core due to background originated from the luminescence of the core.

Next, by applying the above-described UV-NSOM technique to chiral-PS, we succeeded in obtaining *i*-mode near-field photoluminescence image of chiral-PS molecules dispersed on ultra-flat sapphire substrate. Figure 7.41a shows topographic image of chiral-PS. The height of the observed fibril-like structure is 7–50 nm. Since the diameter of chiral-PS molecules has been estimated to be around 1 nm,

we guess the fibril-like structures are constructed by several molecules. Figure 7.41b shows UV near-field photoluminescence image of chiral-PS molecules at 325 nm in the same area as Fig. 7.41a. For the excitation of the sample, UV light with a wavelength of 300 nm is used. The achieved spatial resolution is around 60 nm. The used probe was UV triple-tapered probe with a small core diameter of around 2 μm . It was fabricated based on selective etching of a new double-core fiber, which was produced by only vapor-phase axial deposition. Details of this fiber will be discussed elsewhere.

7.7.2.1 Near-Field Raman Spectroscopy of Silicon Crystal

Near-field Raman spectroscopy of silicon is expected to analyze silicon-based electronic devices. The Raman signal of silicon has a rather weaker scattering efficiency and a smaller wavenumber than that of polydiacetylene and competes with the background signal of Raman scattering from the GeO_2 -doped silica core. To suppress the background, a fiber probe with a pure silica core should be used. The background of the probe is suppressed to less than 10 % compared with that of a double-tapered probe.

Figure 7.42 shows a near-field Raman spectrum of a silicon crystal, obtained by i-mode NSOM employing the triple-tapered probe with an aperture diameter of 100 nm. A sharp peak from silicon is clearly seen at 520 cm^{-1} . The broad signal around 400 cm^{-1} corresponds to the Raman scattering from the SiO_2 core. It is found that the fiber probe is very effective in suppressing the background originated from GeO_2 .

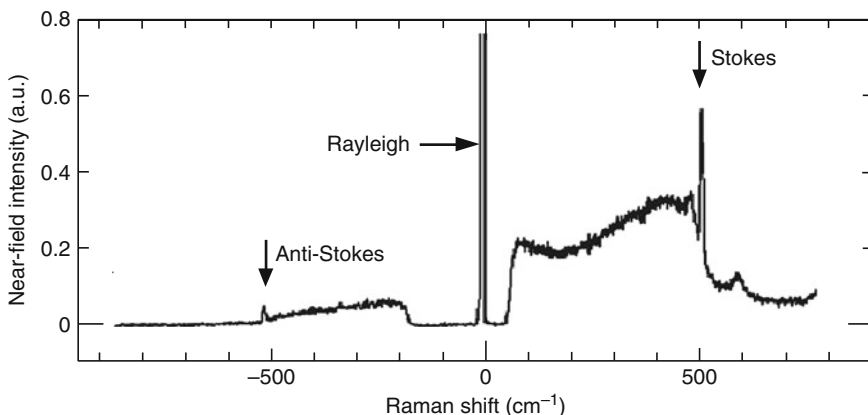


Fig. 7.42 Near-field Raman spectrum of a silicon crystal obtained by an aluminized fiber probe with a pure silica core and an aperture diameter of 100 nm

7.7.3 Fabrication of a Pure Silica Fiber Probe by Pulling and Etching

Among commercial single-mode fibers, only 1.3- μm fiber (PSF) with a pure silica core has a high transmittance at near UV. We developed a new method of tapering a 1.3- μm PSF based on combination of pulling and etching. The method involves two steps: (A) heating and pulling the fiber by a micropipette puller and (B) etching the fiber in buffered hydrogen fluoride solution as shown schematically in Fig. 7.43a. Figure 7.43b shows the magnified top region of the tapered shape formed by step B. Here, θ and $2r_{1E}$ are the cone angle in the apex region of the fiber and the reduced core diameter at the end of the tapered core, respectively. Figure 7.43c shows the cross-sectional profile of the tapered probe obtained by increasing the etching time in step B. Details of this profile are discussed later. The fabricated tapered fiber has the tapered shape and the magnified top region as seen in scanning electron micrographs of Fig. 7.44a, b, respectively. Figure 7.44c, d corresponds to

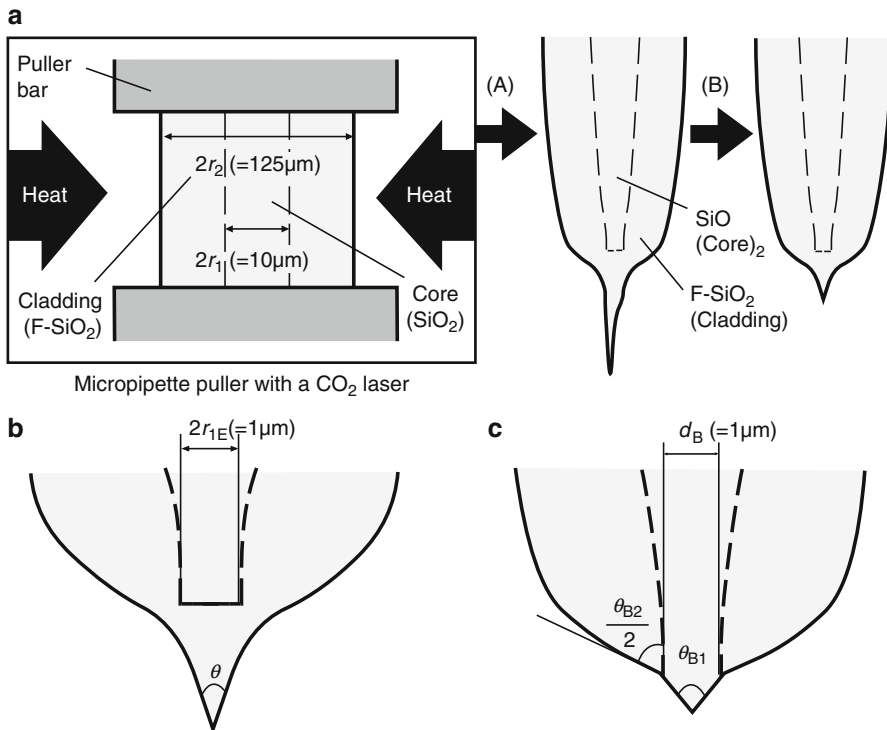


Fig. 7.43 (a) Method for fabricating a tapered fiber with the pure silica core. (b) Cross-sectional profile of the top of the fiber formed by step A in (a). r_{1E} , reduced core diameter at the end of the tapered core; θ_{B1} and θ_{B2} , cone angles of the core and clad, respectively. (c) Cross-sectional profile obtained by increasing the etching time in step B

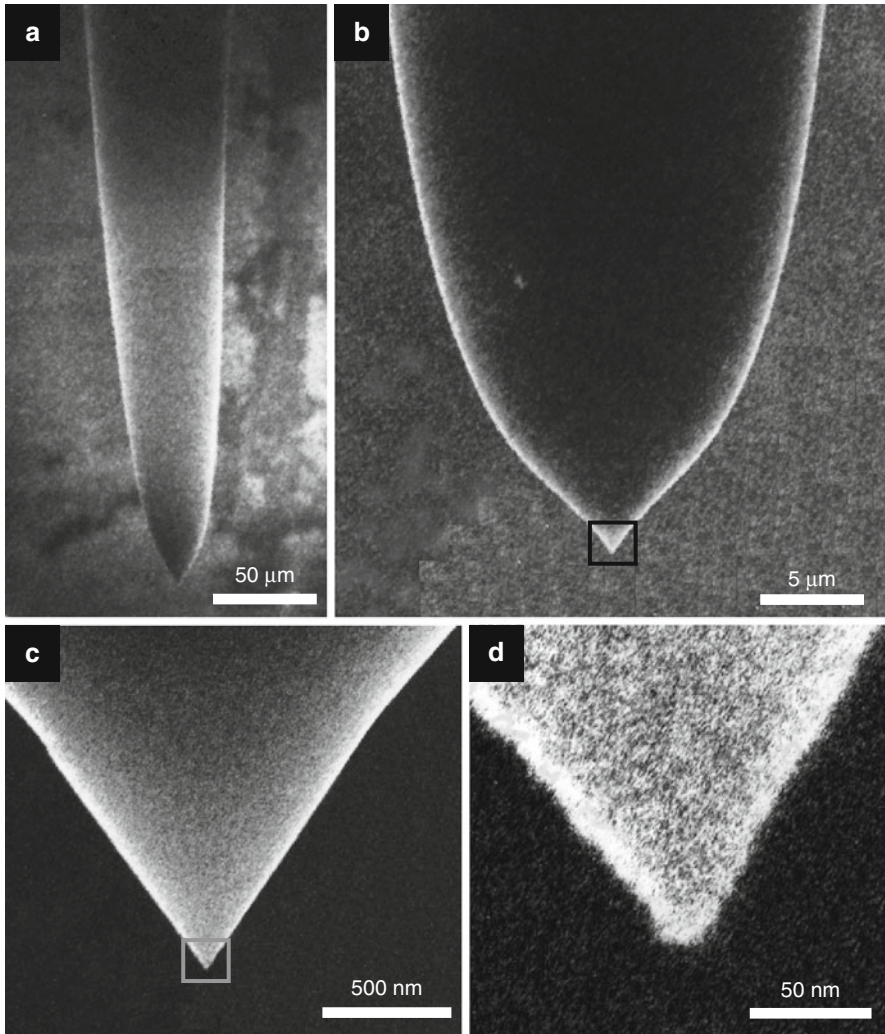


Fig. 7.44 Scanning electron micrographs of (a) the pulled and etched probe with the pure silica core and (b) its magnified *top region*. (c) and (d) The magnified apex regions as indicated by the squares in the figure (b) and (c), respectively. The cone angle and apex diameter are 65° and 20 nm, respectively

the magnified view of regions indicated by squares in b and c, respectively. The cone angle and the apex diameter are $\theta = 65^\circ$ and 10–20 nm, respectively. By investigating 20 fiber samples, we obtained 80 % reproducibility for a cone angle $\theta = 60^\circ (\pm 5^\circ)$ and an apex diameter of 10–20 nm. We now describe the method for producing this pure silica core fiber.

In step A, a PSF with core diameter of $10 \mu\text{m}$, a clad diameter of $125 \mu\text{m}$, and an index difference of -0.3% was heated and pulled by a micropipette puller (Sutter

Table 7.7 Parameters of the puller for a pure silica core fiber

Heat \mathcal{H} , CO ₂ laser power	350
Filament \mathcal{F} , length of the fiber scanned with the laser beam	0
Velocity \mathcal{V} , velocity of the puller bar at the end of the heating time	1
Delay \mathcal{D} , delay time between the heating and pulling	130
Pull \mathcal{P} , strength of pull	150

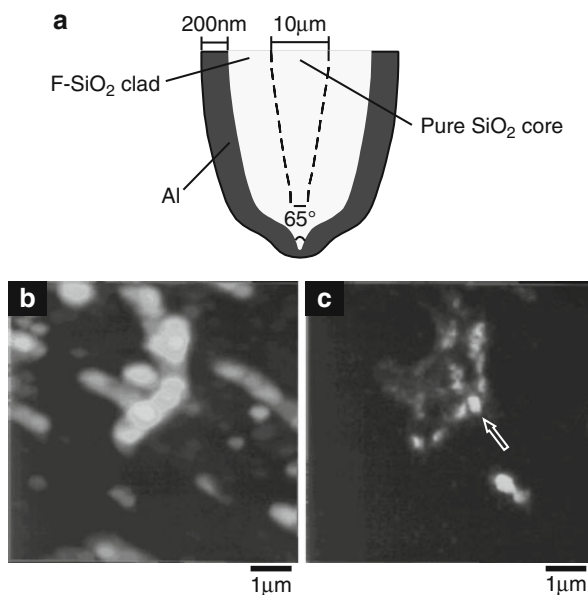
Instrument, P-2000) combined with a CO₂ laser. This puller has been mechanically adjusted to fabricate a micropipette with a diameter of 1 mm. To pull the fiber, the two puller bars were exchanged to optional ones on which a 125- μm bare fiber can be attached. In our case, to produce a probe with a bare-portion length as small as 1 cm, a plastic-coated portion of the fiber sample was carefully attached on one bar, and a bare portion was fixed to on another bar. The puller is adjusted with its parameters shown in Table 7.7. Here, the heat parameter \mathcal{H} ($0 \leq \mathcal{H} \leq 999$) decides the CO₂ laser power. The filament parameter \mathcal{F} is the length of the fiber which is scanned with the CO₂ laser beam. The velocity parameter \mathcal{V} ($1 \leq \mathcal{V} \leq 255$) shows the velocity of the puller bar at the end of the heating time. The delay parameter \mathcal{D} ($0 \leq \mathcal{D} \leq 255$) represents the delay time between the end of the heating and the beginning of the pulling (in millisecond units). The puller is mechanically adjusted to make the delay zero at $\mathcal{D} = 125$. The pull parameter \mathcal{P} decides the pull strength and is controlled in a region of $0 \leq \mathcal{P} \leq 255$. If step A is repeated using the same puller and the same fiber, some of the parameters, such as \mathcal{H} and \mathcal{D} , may be changed to fabricate a pulled fiber as seen in Fig. 7.44a.

In step B, the fiber was etched by immersing for 10 min in a buffered hydrogen fluoride solution (BHF) with a volume ratio of 40% NH₄F aqueous solution:50% HF acid:deionized water=1.7:1:1. The temperature of the BHF was 25 °C (± 0.1 °C). The fluorine-doped clad and the pure silica core have dissolution rates of $R_1 = 6.6 \mu\text{m h}^{-1}$ and $R_2 = 7.6 \mu\text{m h}^{-1}$, respectively. The pulled and etched probe with a few tens nanometers was obtained by stopping the etching before the core was protruded from the fluoride-doped clad. The cone angle θ is increased by increasing the etching time T . In our experiments, the cone angles were 35° and 65° for etching times of 5 and 10 min, respectively. However, we could not realize the pulled and etched probe with a reproducibility more than 80% due to the mechanical misalignment of the puller.

On the other hand, once the core is exposed from fluorine-doped silica, the core is selectively etched due to the difference of the dissolution rate R_1 of the core and the dissolution rate R_2 of the clad ($> R_1$). Then, the fiber has two cone angles of θ_{B1} and θ_{B2} , as shown in Fig. 7.43c, where d_B is the base diameter of the conical core, with the angle θ_{B1} given by

$$\sin \frac{\theta_{B1}}{2} = \frac{R_1}{R_2} \sin \frac{\theta_{B2}}{2}. \quad (7.11)$$

Fig. 7.45 (a) Schematic illustration of the probe fabricated by pulling and etching a commercial fiber with the pure silica core, (b) shear-force topographic image, and (c) i-mode near-field photoluminescence images of polydihexylsilane aggregates at 380 nm



The pulled and etched probe as shown in Fig. 7.25a was fabricated by selective etching and has a GeO_2 tip protruding from silica clad. In the case of using a PSF, the cross section of the apex region was elliptical, with a longer principal diameter of around 200 nm. Therefore, we could not employ the selectively etched PSF as a probe. The value of d_B is equal to the reduced core diameter $2r_{IE}$ of the fiber as shown in Fig. 7.43a. The reduced core diameter is estimated to be $2\ \mu\text{m}$ from an SEM image of selectively etched fibers which were immersed in BHF with 1.7:1:1 for times longer than 10 min. It is straightforward to obtain a minimum ratio of $r_{IE}/r_1 = 1/5$.

Employing the fabricated probe with a design of Fig. 7.45a, i-mode near-field photoluminescence imaging of polydihexylsilane were performed. The shear-force topographic and 380 nm-photoluminescence images are shown in the Fig. 7.45b and c, respectively.

7.7.3.1 UV Application Performed with i-mode NSOM Employing a Pulled and Etched Probe

The pure silica-tapered probes were aluminized by vacuum evaporation method and applied to UV near-field photoluminescence image of polydihexylsilane. Figure 7.46a, b shows shear-force topographic image and near-field photoluminescence image at 380 nm. In Figure 7.46b, the value of FWHM of the bright portion as indicated by the arrow is estimated to be around 100 nm. The background signal in the dark region is almost zero in contrast to the maximum counting rate of the photoluminescence signal. Since the pulled and etched fiber can be fabricated

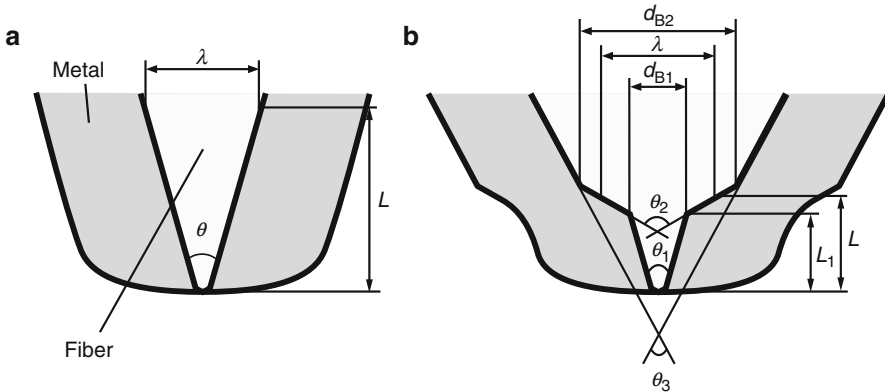


Fig. 7.46 (a) Cross-sectional profiles of the single-tapered probe and (b) the triple-tapered probe; θ , cone angle of the tapered core; λ , optical wavelength; L , length of the tapered core with the foot diameter equal to λ ; t_s , skin depth of the metal; θ_1 , θ_2 , and θ_3 , cone angles of the first, second, and third tapers, respectively; d_{B1} and d_{B2} , base diameters of the first and second tapers, respectively; L_1 , length of the first taper

by pulling and etching commercial fiber, the probe has been widely used as a low-noise probe for near-field fluorescent imaging in a visible region [1] and UV nanofabrication [34] based on photoenhanced chemical vapor deposition.

7.8 Outlook

The resolution capability and throughput of NSOM have been greatly improved by employing application-oriented probes such as a double-tapered probe with an aperture diameter of a few tens nanometers and a pure silica fiber probe, and various imaging and spectroscopic applications have been successfully carried out. However, the techniques for mass-producing these probes are not yet established due to the low reproducibility of the metallizing process for forming a nanometric aperture. Further, single-mode fiber probes should be newly developed for some imaging applications such as polarization measurements in ultraviolet and visible regions. If these techniques are established, NSOM and related techniques will be further used widely by many researchers and engineers. To realize the mass production of near-field optical probes, the author has concentrated on the development of a novel metallization technique based on size-dependent electroless plating [17, 21, 26, 41] and on the fabrication of new single-mode fibers [42, 43].

Acknowledgements The author wish to thank Prof. M. Ohtsu, Prof. H. Ito, Dr. R. Uma Maheswari, Prof. T. Saiki, Dr. M. Naya, Prof. Y. Toda, Dr. N. Hosaka, and Dr. M. Sakai for their assistance and fruitful discussions.

Appendix

Fabrication of Tapered Fibers Based on Hybrid Selective Etching of a Double-Clad Fiber

The double-clad fiber [20] was developed for fabricating pencil-shaped probes and triple-tapered probes. These probes can be fabricated with almost 100% reproducibility based on selective etching. In this section, we describe the structure of a triple-tapered probe and design/fabrication of the fiber.

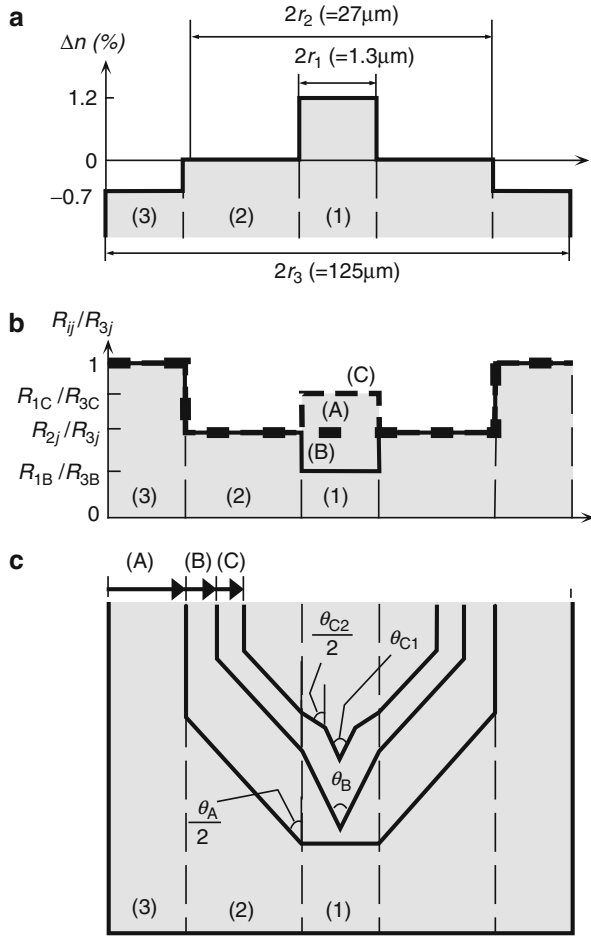
Triple-Tapered Probe

Figure 7.46a, b shows cross-sectional profiles of the single-tapered probe and triple-tapered probe. In a, θ is the cone angle and λ is the optical wavelength in the fiber. In b, L is defined as the length of the portion with a cross-sectional diameter of λ to the apex. L_1 is the length of the first taper; θ_1 , θ_2 , and θ_3 are the cone angles of the first, second, and third tapers, respectively; and d_{B1} and d_{B2} are the base diameters of the first and second tapers, respectively. As described in Sect. 7.3.6, the light entering in the single-tapered probe is strongly attenuated by metal from the portion with diameter λ to the apex. To reduce the attenuation, the length L must be decreased by increasing the cone angle. In the case of fabricating the tapered probe with a large cone angle, i.e., 120° , one must accept the limited resolution affected by optical leaking out of the metal around the apex region of the probe. In the triple-tapered probe, we can decrease the length L by increasing θ_2 in order to enhance the throughput. Thus, the resolution capability is increased by simultaneously decreasing the cone angle and decreasing the first taper length L_1 to a few hundreds nanometers, which corresponds to several times the skin depth of metal.

Selective Etching of a Double-Clad Fiber

Figure 7.47a shows the cross-sectional profile of the index difference of the double-clad fiber. Here, the fiber involves three sections: (1) a GeO₂-doped silica core, (2) a pure silica clad, and (3) a fluorine-doped silica support. The index difference of Sects. 7.1 and 7.3 with respect to Sect. 7.2 are 1.2 and -0.7% , respectively. The radii of Sects. 7.1–7.3 are $r_1 = 0.65 \mu\text{m}$, $r_2 = 13.5 \mu\text{m}$, and $r_3 = 62.5 \mu\text{m}$, respectively. Figure 7.47b shows a schematic diagram of the etching process consisting of three steps: A–C. By defining the dissolution rate of section i in step j as R_{ij} (where $i = 1, 2, 3$; $j = \text{A, B, C}$), the relative dissolution rates R_{ij}/R_{3j} are represented by Fig. 7.47c. As described in Sect. 7.2.3, the relative dissolution rate of GeO₂-doped glass to pure silica glass depends on the concentration of buffered HF mixed with a volume ratio of 40% NH₄F sol.:50% HF acid:H₂O = $X:1:Y$. We now use 1.7:1:1, 10:1:1, and 1.7:1:5, in which the dissolution rates of Sects. 7.1 and 7.2 are experimentally found to satisfy the relation

Fig. 7.47 (a) Cross-sectional profile of the index difference Δn . r_1 , radius of the GeO₂-doped silica core; r_2 , radius of the pure silica clad; r_3 , radius of a fluorine-doped silica support. (b) Etching method for fabricating application-oriented probes. (c) Cross-sectional profile of the relative dissolution rate



$$\frac{R_{1B}}{R_{2B}} = 0.29 < \frac{R_{1A}}{R_{2A}} = 1.0 < \frac{R_{1C}}{R_{2C}} = 1.48 . \quad (7.12)$$

On the other hand, the relative dissolution rate of the fluorine-doped section to the pure silica section is approximately fixed for the concentration of BHF. So,

$$R_{2j}/R_{3j} = 0.51 \quad (j = A, B, C) . \quad (7.13)$$

We now discuss the etching process using 1.7:1:1, 10:1:1, and 1.7:1:5 in steps A–C, respectively.

In step A, the fiber is tapered to an angle of θ_A represented by

$$\sin(\theta_A/2) = R_{2j}/R_{3j} \quad (\text{where } j = A, B, C) . \quad (7.14)$$

If the fiber diameter is equal to $[2r_2]$ after step A, the etching time T_A is represented by

$$T_A = (r_3 - r_2)/R_{3A} . \quad (7.15)$$

The tapered fiber will have an apex diameter smaller than $2r_1$ if $T_A \geq \tau_A$, where τ_A is the time required to make an apex diameter of $2r_1$ and is

$$\tau_A = \frac{r_2 - r_1}{R_{3A}} \sqrt{\frac{R_{2A} + R_{3A}}{R_{3A} - R_{2A}}} . \quad (7.16)$$

Thus, it is straightforward to find that the radius r_2 of Sect. 7.2 must be smaller than the critical radius r_{2P} expressed as

$$r_{2P} = \frac{r_3 + \xi \cdot r_1}{1 + \xi} , \quad \text{where} \quad \xi = \sqrt{\frac{R_{2A}/R_{3A} + 1}{1 - R_{2A}/R_{3A}}} . \quad (7.17)$$

In step B, Sect. 7.1 is sharpened with a different angle θ_B , given by

$$\sin(\theta_B/2) = R_{1B}/R_{3B} . \quad (7.18)$$

We obtain pencil-shaped probes with zero apex diameter and cone angles θ_A and θ_B when the etching time T_B is larger than τ_B , expressed as

$$\tau_B = \frac{r_1}{R_{1B}} \sqrt{\frac{R_{1B} + R_{3B}}{R_{3B} - R_{1B}}} . \quad (7.19)$$

Further, to obtain a triple-tapered probe, we perform step C, when the largest cone angle θ_{C2} is given by

$$\sin \frac{\theta_{C2}}{2} = \frac{R_{1C}}{R_{3C}} \quad (\text{where } R_{1C} > R_{2C}) . \quad (7.20)$$

The cone angle θ_{C1} is increased from θ_B by increasing the etching time T_C and is equal to θ_{C2} at $T_C > \tau_C$, where τ_C is given by

$$\tau_C = \frac{r_1}{R_{1C}} \sqrt{\frac{R_{1C} + R_{3C}}{R_{3C} - R_{1C}}} . \quad (7.21)$$

Therefore, we can obtain a triple-tapered probe and a pencil-shaped probe with a cone angle $\theta_B = \theta_{C2}$ at $0 < T_C < \tau_C$ and $T_C > \tau_C$, respectively.

To obtain a cone angle θ_A as small as 62° , the index difference of Sect. 7.3 is estimated from Eqs. 7.15 and 7.19 to be as high as 0.7%. To obtain a cutoff wavelength of around 400 nm, Sect. 7.1 is tailored with an index difference of 1.2%

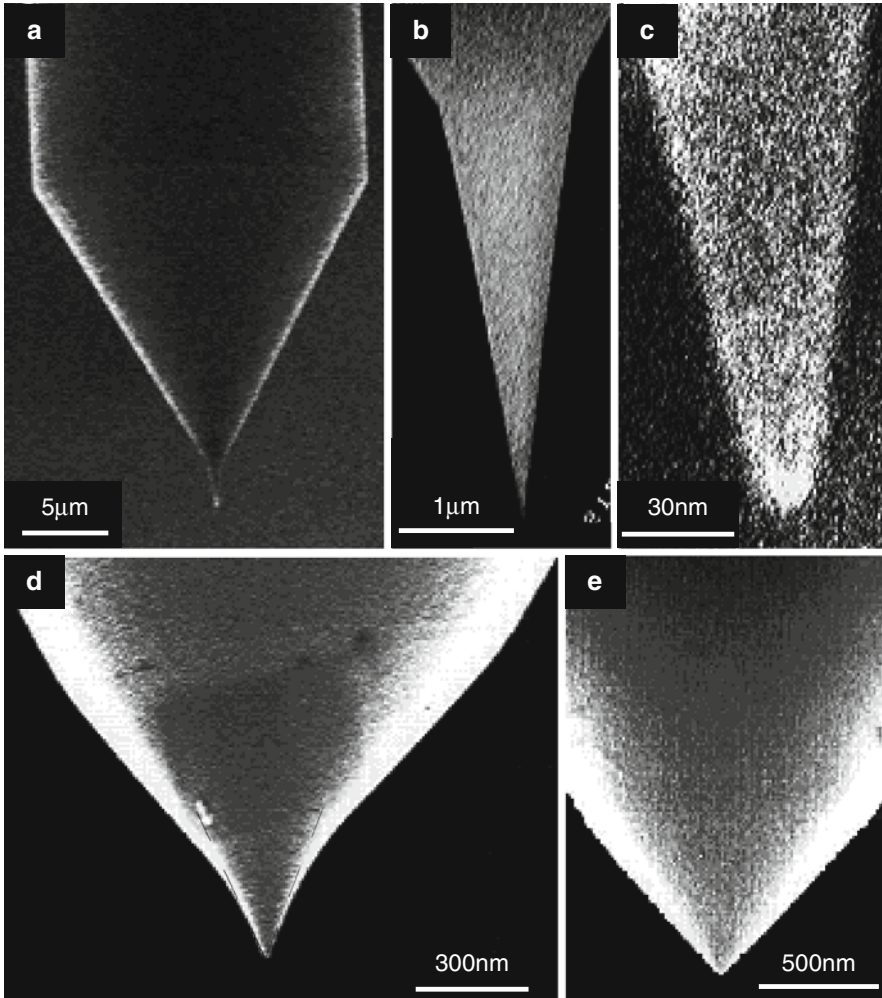
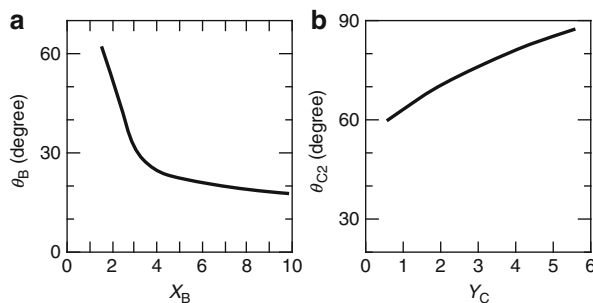


Fig. 7.48 (a)–(c) SEM micrographs of a pencil-shaped probe, its magnified tapered core, and its magnified apex region. $\theta_A = 62^\circ$; $\theta_B = 17^\circ$; $d < 10$ nm. (d) SEM micrograph of a triple-tapered probe. $\theta_A = 62^\circ$; $\theta_{C1} = 50^\circ$; $\theta_{C2} = 85^\circ$. (e) SEM micrograph of a pencil-shaped probe. $\theta_A = 62^\circ$; $\theta_B = 85^\circ$

and a core radius of $r_1 = 0.65 \mu\text{m}$. Then we obtain an estimated value of $\theta_A = 17^\circ$ from Eqs. 7.13 and 7.19. Further, when the clad radius r_3 is a standard value of $62.5 \mu\text{m}$, we obtain a critical radius of $r_{2P} = 23 \mu\text{m}$ from Eqs. 7.14 and 7.18. We make the radius r_2 have a value of $13.5 \mu\text{m}$, which is smaller than the critical radius.

To realize the fiber as shown in Fig. 7.47a, we fabricated a perform glass rod by vapor-phase axial deposition and drew the fiber. To suppress the diffusion of GeO_2 and fluorine, the drawing tension should be as high as possible. However, in the case

Fig. 7.49 (a) Dependencies of the taper angle θ_B on the volume ratio X_B of NH_4F aqueous solution in the etching solution. (b) Dependency of the taper angle θ_{C2} on the volume ratio of H_2O in the etching solution



of drawing the fiber with a high tension of 60 g, we could not reproducibly cleave the fiber to obtain a flat facet with a commercial fiber cleaver. We consider that the low reproducibility can be attributed to the remaining stress between Sects. 7.2 and 7.3. To suppress this remained stress, we kept a low tension of less than 28 g during the drawing.

To demonstrate the tailoring capability of the different types of probes, we actually performed the etching process using the fabricated fiber. We prepared 30 fiber samples with flat ends. The fibers were etched consecutively for $T_A = 40$ min in a 1.7:1:1 solution and for $T_B = 20$ min in a 10:1:1 solution. We obtained a pencil-shaped probe with a small cone angle for high resolution. Figure 7.48a–c shows SEM micrographs of the probe, the magnified tapered core, and the magnified apex region, respectively. Here, the apex diameter is less than 10 nm. The cone angles are $\theta_A = 62^\circ$ and $\theta_B = 17^\circ$, which agree with the estimated values from Eqs. 7.15 and 7.19.

Further, by etching the pencil-shaped probe in a 1.7:1:5 solution for $T_C = 2$ min, we obtained a triple-tapered probe with high-resolution capability and high throughput. Figure 7.48d shows an SEM micrograph of the triple-tapered probe. The probe has three cone angles of $\theta_{C1} = 50^\circ$, $\theta_{C2} = 85^\circ$, and $\theta_A = 62^\circ$ and an apex diameter of less than 10 nm. The two base diameters of tapers with $\theta_{C1} = 50^\circ$ and $\theta_{C2} = 85^\circ$ are $d_{B1} = 250$ nm and $d_{B2} = 1.28$ μm , respectively. At $T_C = 2.75$ min, we obtained another type of pencil-shaped probe with a large angle of 85° near the apex region as shown in Fig. 7.48e. Figure 7.49a, b shows the dependencies of θ_B and θ_{C2} , respectively, on the volume ratios of BHF. Here, 1.7:1:1, X_B :1:1, and 1.7:1: Y_C are used in steps A–C. The cone angles θ_B and θ_{C2} are controlled by varying X_B and Y_C , respectively.

References

1. H. Aoki, Y. Sakurai, S. Ito, T. Nakagawa, J. Phys. Chem. B **103**, 10553 (1999)
2. M. Arai, S. Koshihara, M. Ueda, M. Yoshimoto, T. Saiki, S. Mononobe, M. Ohtsu, T. Miyazawa, M. Kira, J. Lumin. **87–89**, 951 (2000)
3. E. Betzig, Principles and application of near-field scanning optical microscopy (NSOM), in *Near Field Optics*. NATO ASI Series E, vol. 242 (Kluwer, Dordrecht, 1993), p. 7

4. E. Betzig, J.K. Trautman, *Science* **257**, 189 (1992)
5. E. Betzig, M. Isaacson, A. Lewis, *Appl. Phys. Lett.* **51**, 2088 (1987)
6. E. Betzig, J.K. Trautman, T.D. Harris, J.S. Weiner, R.L. Kostelak, *Science* **251**, 1468 (1991)
7. E. Betzig, P.L. Finn, J. S. Weiner, *Appl. Phys. Lett.* **60**, 2484 (1992)
8. D. Courjon, K. Sarayeddine, M. Spajer, *Opt. Commun.* **71** 23 (1989)
9. M. Garcia-Parajo, T. Tate, Y. Chen, *Ultramicroscopy* **61**, 155 (1995)
10. T. Hartmann, R. Gatz, W. Wiegäbe, A. Kramer, A. Hillebrand, K. Lieberman, W. Baumeister, R. Guckenberger, A scanning near-field optical microscope (SNOM) for biological applications, in *Near Field Optics*. NATO ASI Series E, vol. 242 (Kluwer, Dordrecht, 1993), p. 35
11. P. Hoffmann, B. Dutoit, R.-P. Salathé, *Ultramicroscopy* **61**, 165 (1995)
12. N. Hosaka, T. Saiki, *J. Microsc.* **202**(Part 2) 362 (2001)
13. T. Izawa, S. Sudo, *Optical Fibers: Materials and Fabrication* (KTK Scientific, Tokyo, 1987)
14. S. Jiang, H. Ohsawa, K. Yamada, T. Pangaribuan, M. Ohtsu, K. Imai, A. Ikai, *Jpn. J. Appl. Phys.* **31**, 2282 (1992)
15. P. Lambelet, A. Sayah, M. Pfeffer, C. Philipona, F. Marquis-Weible, *Appl. Opt.* **37**, 7289 (1998)
16. S. Mononobe, Probe fabrication, in *Near-Field Nano/Atom Optics and Technology* (Springer, Berlin, 1998), p. 31
17. S. Mononobe, *Jpn. J. Appl. Phys.* **47**, 4317 (2008)
18. S. Mononobe, M. Ohtsu, *J. Lightwave Technol.* **14**, 2231 (1996); Erratum *J. Lightwave Technol.* **15**, 162 (1997)
19. S. Mononobe, M. Ohtsu, *J. Lightwave Technol.* **15**, 1051 (1997)
20. S. Mononobe, M. Ohtsu, *IEEE Photonics Technol. Lett.* **10**, 99 (1998)
21. S. Mononobe, M. Ohtsu, *Jpn. J. Appl. Phys.* **46**, 6258 (2007)
22. S. Mononobe, R. Uma Maheswari, M. Ohtsu, *Opt. Express* **1**, 229 (1997), <http://epubs.osa.org/opticsexpress/>
23. S. Mononobe, M. Naya, T. Saiki, M. Ohtsu, *Appl. Opt.* **36**, 1496 (1997)
24. S. Mononobe, T. Saiki, T. Suzuki, S. Koshihara, M. Ohtsu, *Opt. Commun.* **146**, 45 (1998)
25. S. Mononobe, T. Saiki, T. Suzuki, S. Koshihara, M. Ohtsu, *Opt. Commun.* **126**, 45 (1998)
26. S. Mononobe, Y. Saito, M. Ohtsu, H. Honma, *Jpn. J. Appl. Phys.* **43**, 2862 (2006)
27. H. Muramatsu, N. Chiba, N. Yamamoto, K. Honma, T. Ataka, M. Shigeno, H. Monobe, M. Fujihira, *Ultramicroscopy* **71**, 73 (1998)
28. H. Nakamura, T. Sato, H. Kanbe, K. Sawada, T. Saiki, *J. Microsc.* **202**, 50 (2001)
29. Y. Narita, T. Tadokoro, T. Ikeda, T. Saiki, S. Mononobe, M. Ohtsu, *Appl. Spectrosc.* **52**, 1141 (1998)
30. M. Naya, S. Mononobe, R. Uma Maheswari, T. Saiki, M. Ohtsu, *Opt. Commun.* **124**, 9 (1996)
31. M. Naya, R. Micheletto, S. Mononobe, R. Uma Maheswari, M. Ohtsu, *Appl. Opt.* **36**, 1681 (1997)
32. L. Novotony, D.W. Pohl, B. Hecht, *Ultramicroscopy* **61**, 1 (1995)
33. D.W. Pohl, W. Denk, M. Lanz, *Appl. Phys. Lett.* **44**, 651 (1984)
34. V.V. Polonski, Y. Yamamoto, M. Kourogi, H. Fukuda, M. Ohtsu, *J. Microsc.* **194**, 545 (1999)
35. R.C. Reddick, R.J. Warmack, T L. Ferrel, *Phys. Rev. B* **39** 767 (1989)
36. T. Saiki, Diagnosing semiconductor nano-materials and devices, in *Near-Field Nano/Atom Optics and Technology* (Springer, Berlin, 1998), p. 153
37. T. Saiki, Nano-optical imaging and spectroscopy of single quantum constituents, in *Progress in Nano-Electro-Optics II*, ed. by M. Ohtsu (Springer, Berlin, 2003), p. 111
38. T. Saiki, S. Mononobe, M. Ohtsu, N. Saito, J. Kusano, *Appl. Phys. Lett.* **67**, 2191 (1995)
39. T. Saiki, S. Mononobe, M. Ohtsu, N. Saito, J. Kusano, *Appl. Phys. Lett.* **68**, 2612 (1996)
40. N. Saito, M. Yamaga, F. Sato, I. Fujimoto, M. Inai, T. Yamamoto, T. Watanabe, *Inst. Phys. Conf. Ser.* **136**, 601 (1993)
41. Y. Saito, S. Mononobe, M. Ohtsu, H. Honma, *Jpn. J. Appl. Phys.* **46**, 6258 (2007)
42. M. Sakai, S. Mononobe, K. Yusu, T. Tadokoro, T. Saiki, *Jpn. J. Appl. Phys.* **44**, 6855 (2005)
43. M. Sakai, S. Mononobe, S. Akiba, A. Matsuda, W. Hara, M. Yoshimoto, T. Saiki, *Opt. Rev.* **13**, 266 (2006)

44. M. Spajor, A. Jalocha, The reflection near field optical microscope: an alternative to STOM, in *Near Field Optics*. NATO ASI Series E, vol. 242 (Kluwer, Dordrecht, 1993), p. 87
45. K.M. Takahashi, *J. Colloid Interface Sci.* **134**, 181 (1990)
46. Y. Toda, M. Kourogi, M. Ohtsu, Y. Nagamune, Y. Arakawa, *Appl. Phys. Lett.* **69**, 827 (1996)
47. R. Toledo-Crow, P.C. Yang, Y. Chen, M. Vaez-Iravani, *Appl. Phys. Lett.* **60**, 2957 (1992)
48. P. Tomanek, Fiber tips for reflection scanning near-field optical microscopy, in *Near Field Optics*. NATO ASI Series E, vol. 242 (Kluwer, Dordrecht, 1993), p. 295
49. D.R. Turner, US Patent, 4,469,554 (1983)
50. R. Uma Maheswari, S. Mononobe, M. Ohtsu, *J. Lightwave Technol.* **13**, 2308 (1995)
51. R. Uma Maheswari, H. Tatsumi, Y. Katayama, M. Ohtsu, *Opt. Commun.* **120**, 325 (1995)
52. R. Uma Maheswari, S. Mononobe, K. Yoshida, M. Yoshimoto, M. Ohtsu, *Jpn. J. Appl. Phys.* **38**, 6713 (1999)
53. G.A. Valaskovic, M. Holton, G.H. Morrison, *Appl. Opt.* **34**, 1215 (1995)
54. B.I. Yakobson, A. LaRosa, H.D. Hallen, M.A. Paesler, *Ultramicroscopy* **61**, 179 (1995)
55. K. Yoshida, M. Yoshimoto, K. Sasaki, T. Ohnishi, T. Ushiki, J. Hitomi, S. Yamamoto, M. Sigeno, *Biophys. J.* **74**, 1654 (1998)
56. A.V. Zvyagin, J.D. White, M. Ohtsu, *Opt. Lett.* **22**, 955 (1997)

Near-Field Optical Fiber Probes and the Applications II

8

Takashi Yatsui and Motoichi Ohtsu

Contents

8.1 High-Throughput Probes.....	336
8.1.1 Mode Analysis in a Metallized Tapered Probe.....	336
8.1.2 Light Propagation in a Tapered Probe with Ideal Metal Cladding.....	337
8.1.3 Measurement of the Spatial Distribution of Optical Near-Field Intensity in the Tapered Probe.....	341
8.1.4 Further Increase in Throughput.....	344
8.2 Application to High-Density and High-Speed Optical Memory.....	356
8.2.1 Using an Apertured Fiber Probe.....	356
8.2.2 High-Density and High-Speed Recording Using a Pyramidal Silicon Probe on a Contact Slider.....	359
8.3 Outlook.....	363
References.....	364

Abstract

Recent developments in near-field optical microscopy have made it possible to obtain optical images with nanometer-scale spatial resolution by scanning a fiber probe with a subwavelength aperture [1]. In attempts to improve performance in spatially resolved spectroscopy, a serious problem of the fiber probe is its low throughput (in the case of illumination-mode operation, the throughput is defined

T. Yatsui (✉) · M. Ohtsu

School of Engineering, The University of Tokyo, Tokyo, Japan

Nanophotonics Research Center, The University of Tokyo, Tokyo, Japan

e-mail: yatsui@ee.t.u-tokyo.ac.jp; ohtsu@ee.t.u-tokyo.ac.jp

as the ratio of the output light power at the apex to the incident light power coupled into the fiber). The essential cause of the low throughput is the guiding loss along the metallized tapered core. Based on a mode analysis of the tapered core, we review our work to realize high-throughput probes and the applications.

8.1 High-Throughput Probes

8.1.1 Mode Analysis in a Metallized Tapered Probe

Mode analysis has been carried out by approximating a tapered core as a concatenated cylindrical core with a metal cladding (see Fig. 8.1) [2].

Figure 8.2 shows the equivalent refractive indices of relevant modes as a function of a core diameter D (at $\lambda = 830$ nm), which is derived by a mode analysis for an infinitely thick gold-coated core. Refractive indices of the glass and the gold used for this derivation are 1.53 and $0.17 + i5.2$ [3], respectively. Definitions of the EH_{11} and HE_{11} modes in this figure are based on those in [2]. This figure shows that the cutoff core diameter (D_c) of HE_{11} mode is as small as 30 nm while that of the EH_{11} is 450 nm. It means that only the HE_{11} mode can excite the optical near field efficiently in $D < 100$ nm. This figure also shows that, as D increases, the equivalent refractive indices of the EH_{11} and HE_{11} modes approach the refractive index of the core and that of a surface plasmon at the boundary between the plane surface of semi-infinite gold and the air, respectively. It also means that the origin of the EH_{11} and HE_{11} modes in a tapered core with metal cladding is the lowest mode in the single-mode fiber and the surface plasmon, respectively. Thus, we call the HE_{11} the HE-plasmon modes from now on.

Figure 8.3a–c shows the spatial distributions of the electric field intensities of EH_{11} , EH_{12} , and HE-plasmon modes, respectively, for $D = 3 \mu\text{m}$. Note the localization of the electric field of the HE-plasmon mode at the boundary of the core and metal cladding (Fig. 8.3c). Thus, the HE-plasmon mode should not be easily excited in the conventional core because of its low coupling efficiency with the lowest-order mode (HE_{11}) guided through the optical fiber, owing to the mode mismatch between the HE_{11} and HE-plasmon modes at the foot of the tapered core. As a consequence, the throughput of the conventional fiber probe is very low.

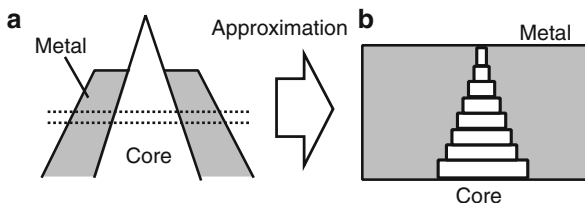
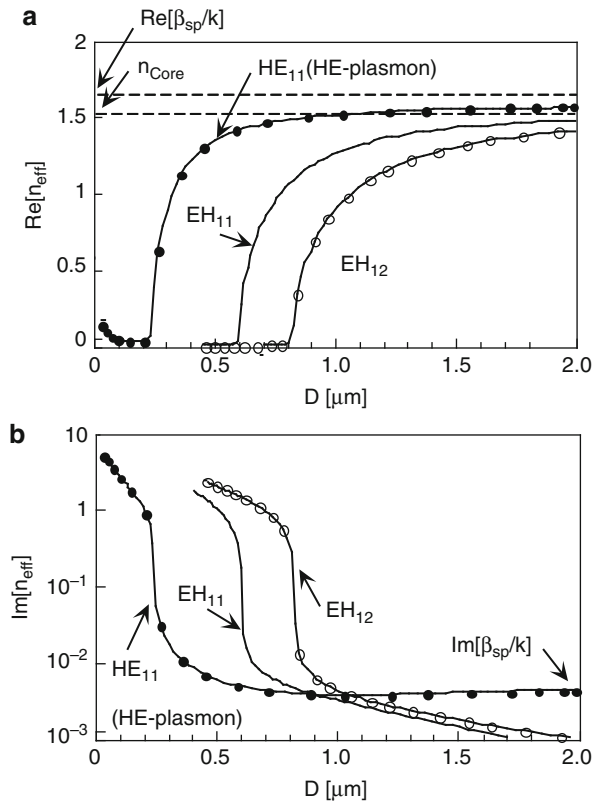


Fig. 8.1 (a) Metal-coated tapered core. (b) Concatenated cylindrical core

Fig. 8.2 (a) and (b) Real and imaginary part of equivalent refractive indices of the relevant modes guided through a glass core with a gold metallic film, respectively. D core diameter, β_{sp} propagation constant of the surface plasmon at a planar boundary between gold and air



The skin depth in the metal cladding has been estimated by considering the EH_{11} mode as a guided mode. Figure 8.4 shows the skin depth in the metal cladding as a function of D . Note that the light hardly leaks into the cladding. Furthermore, since the imaginary part of the equivalent refractive index of the EH_{11} mode is smaller than that of the HE-plasmon mode when $D > 800$ nm (see Fig. 8.2b), the EH_{11} mode should be excited when $D > 800$ nm for increasing throughput. Based on this calculation, we analyzed the characteristics of light propagation in a tapered probe surrounded by an ideal metal in the next section.

8.1.2 Light Propagation in a Tapered Probe with Ideal Metal Cladding

Light propagation analysis has been carried out by a staircase concatenation method. This is based on the following assumptions: first, since the light hardly penetrates the metal cladding in the large D region (see Fig. 8.4), the cladding is assumed to be an ideal metal, i.e., the imaginary part of the refractive index is zero. Second,

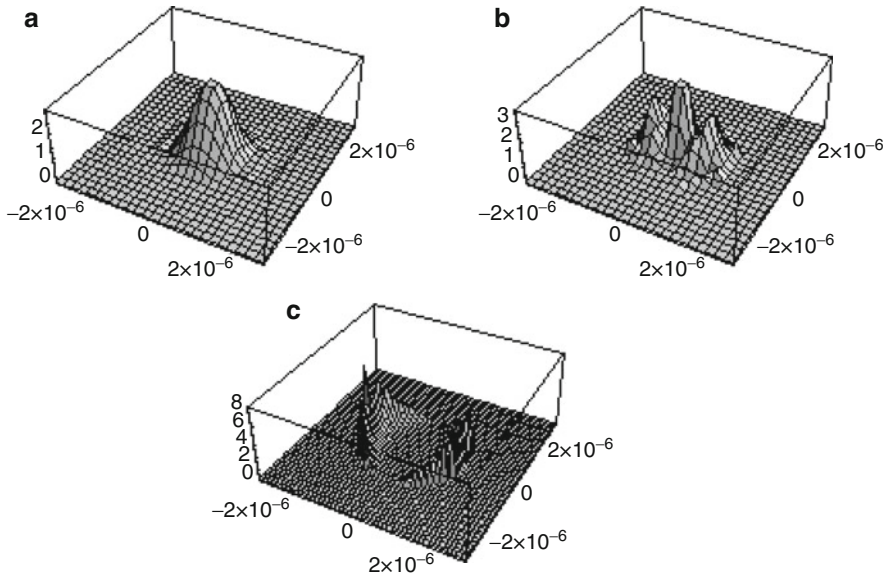


Fig. 8.3 Spatial distributions of electric field intensity for $D = 3 \mu\text{m}$. (a) EH_{11} mode, (b) EH_{12} mode, and (c) HE-plasmon mode

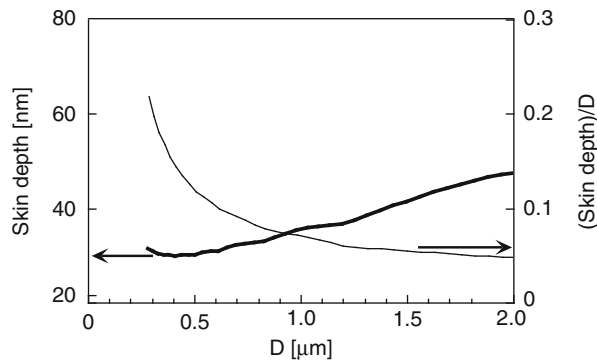


Fig. 8.4 Skin depth of EH_{11} mode in the metal cladding as a function of a core diameter (D)

since the propagation mode is symmetrical in the single-mode optical fiber, only symmetrical modes can exist inside this probe. By these assumptions, only TE_{1m} and TM_{1m} modes can exist inside the probe, where m represents the order of mode with respect to radial direction. For this analysis, the relevant modes are derived for a dielectric core ($n = 1.53$) coated with an infinitely thick ideal metal. [Figure 8.5a–c](#) shows the spatial distribution of electric field intensities of TE_{11} , TE_{12} , and TM_{11} modes, respectively. [Figure 8.5d](#) shows the equivalent refractive indices of these modes.

Using these modes, the spatial distribution of the electric field intensity was calculated by a staircase concatenation method for a tapered probe with a cone

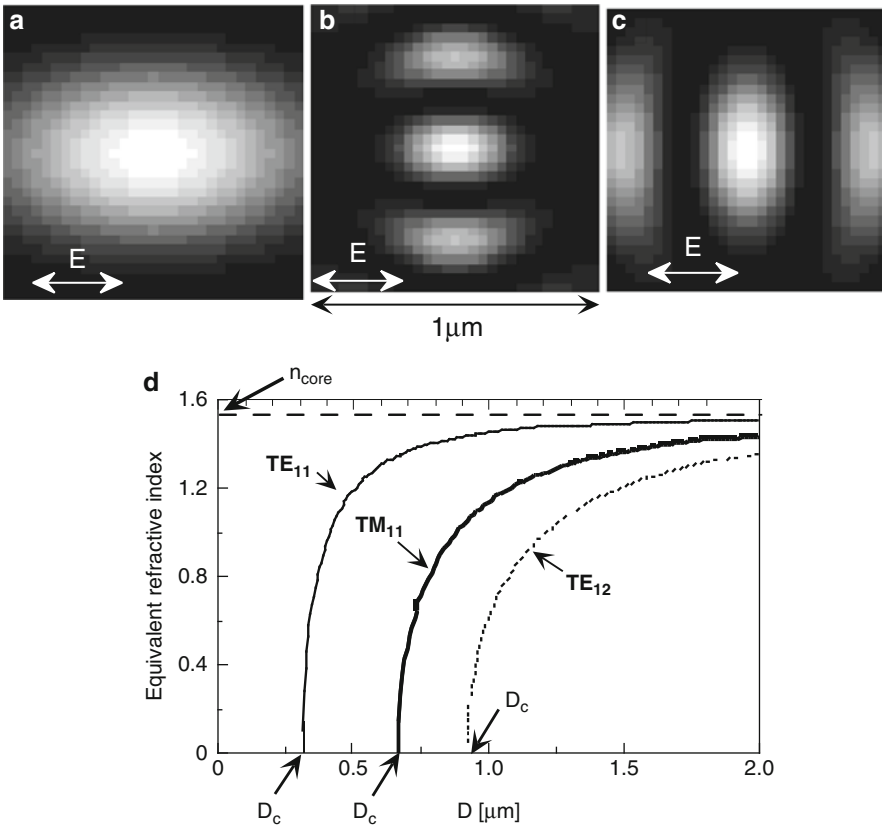


Fig. 8.5 (a)–(c) Spatial distribution of the intensities of TE_{11} , TE_{12} , and TM_{11} modes, respectively, in a dielectric core ($n = 1.53$) with an ideal metal cladding ($\lambda = 830$ nm). The vector E in these figures represents the direction of incident light polarization. (d) Equivalent refractive indices of the three modes. D_c is the cutoff diameter

angle (α) of 25° . For this calculation, a Gaussian incident light beam with full width at half maximum (FWHM) of $3\mu\text{m}$ is assumed, where the foot core diameter is $3\mu\text{m}$. Figure 8.6 represents the calculated result, which shows that the spatial distribution of the electric field intensity goes through the progression “single peak \rightarrow double peak \rightarrow triple peak \rightarrow single peak.”

Figure 8.7 shows the intensity at the center of the core and the FWHM of the central part as a function of D . It shows that the locally maximum electric field intensities are realized at $D = 1.47\mu\text{m}$, 920 nm, and 315 nm and that the smallest spots are realized at $D = 1.47\mu\text{m}$ and 920 nm. Note that the minimum of FWHM is as small as 175 nm ($\sim\lambda/5$) at $D = 920$ nm.

Figure 8.8 shows the calculated electric field intensity for relevant modes at the center of the core. Note that all electric field intensities peak at each D_c due to the resonance. Furthermore, as has been shown by Fig. 8.7, the FWHM takes its

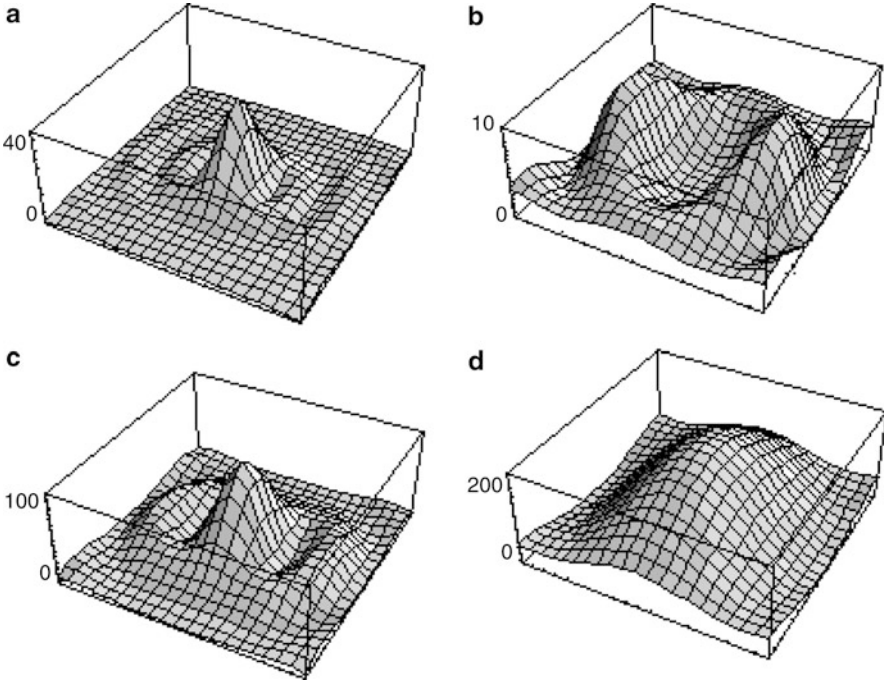


Fig. 8.6 Spatial distribution of electric-field intensity in a tapered probe with $\alpha = 25^\circ$ calculated by a staircase concatenation method. (a) $D = 1.47 \mu\text{m}$, (b) $D = 1.06 \mu\text{m}$, (c) $D = 920 \text{ nm}$, and (d) $D = 315 \text{ nm}$

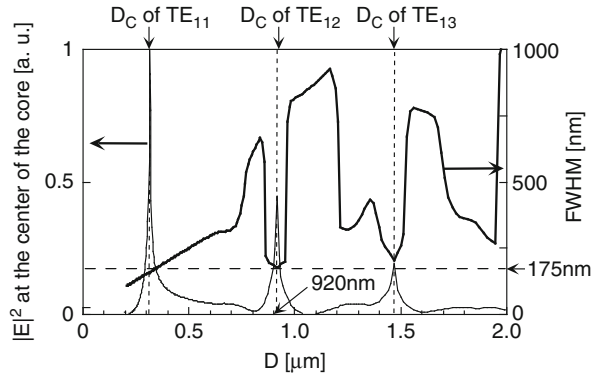


Fig. 8.7 Calculated electric field intensity at the center of the core and the FWHM of the profiles given in Fig. 8.6. D_c is the cutoff diameter

minimum at each D_c except at $D = D_c$ of the TE_{11} mode, where only the TE_{11} mode can exist. The decrease in the FWHM is due to the interference of the guided modes inside the metallized tapered probe. Thus, we call these dependencies of electric field intensity and FWHM on the core diameter D as the “interference characteristics of the guided modes” from now on.

Fig. 8.8 Calculated electric field intensity at the center of the core. $S = |\sum E_i|^2$, D_c is the cutoff diameter

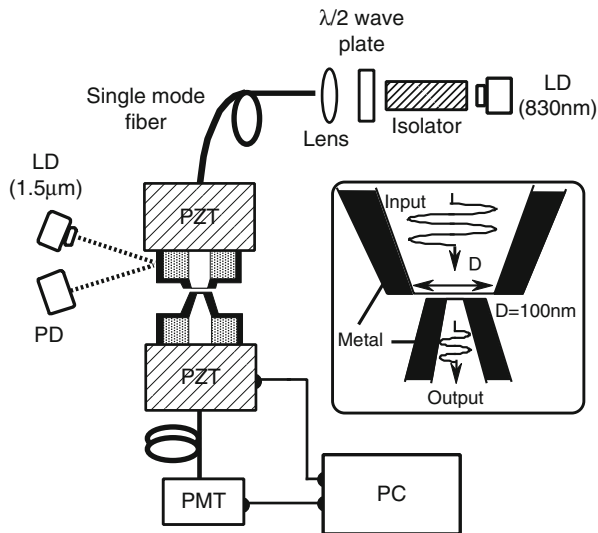
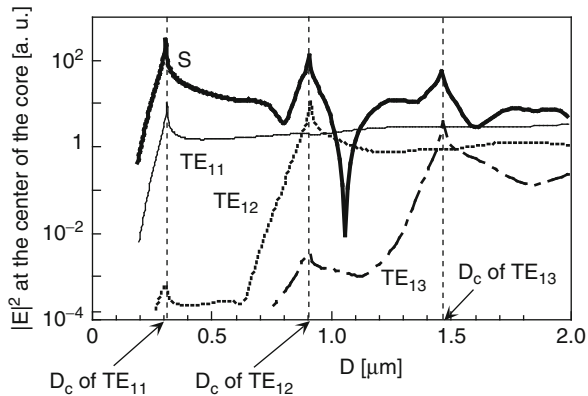


Fig. 8.9 Probe-to-probe method. LD laser diode, PD photo diode, PMT photomultiplier tube

8.1.3 Measurement of the Spatial Distribution of Optical Near-Field Intensity in the Tapered Probe

High throughput and a small spot can be expected by optimizing the above-mentioned interference characteristics of the guided modes. In this section, we describe experimental results which show the validity to this expectation.

For this purpose, the optical near field generated on the apertured fiber probe was observed by scanning another probe with $D = 100 \text{ nm}$ over the aperture to scatter and detect the optical near field [4]. The experimental setup, i.e., probe-to-probe method, is shown in Fig. 8.9, where the separation between the probes was kept within several nanometers by shear-force techniques.

Linearly polarized light from a laser diode (830 nm) was coupled into the single-tapered apertured probe, which was fabricated in the following three steps:

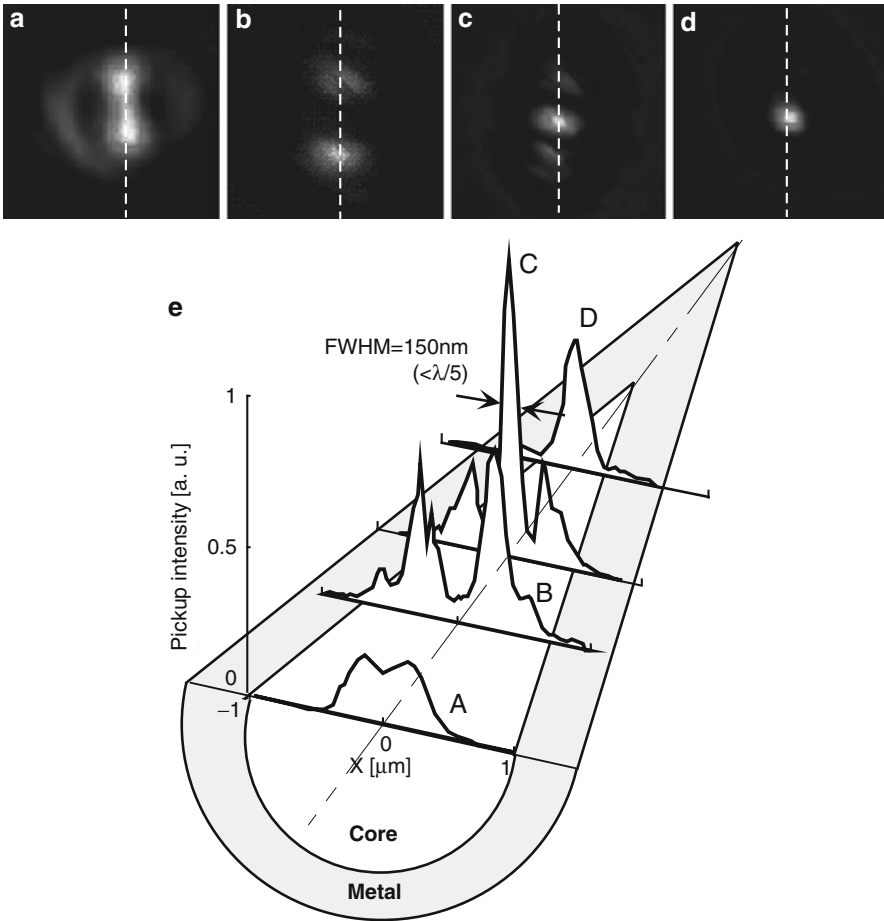


Fig. 8.10 Spatial distribution of the optical near-field intensity in a conventional single-tapered probe. (a)–(d) Are for a single-tapered probe with $D = 2 \mu\text{m}$, $1.4 \mu\text{m}$, 900 nm , and 550 nm , respectively. Image sizes are $1.5 \times 1.5 \mu\text{m}$. Curves A, B, C, and D in (e) are cross-sectional profiles along the dashed white line in (a), (b), (c), and (d), respectively

1. The GeO₂-doped core with a diameter of $3 \mu\text{m}$ was tapered with $\alpha = 25^\circ$ by the selective chemical etching technique [5].
2. The core was coated with 500-nm-thick gold film.
3. Since the core diameter D cannot be defined accurately by the angled evaporation [6], the apex of the core was removed by a focused ion beam (FIB) to form a definite aperture. The value of D was then determined from scanning electron micrographic images.

Figure 8.10a–d shows the observed spatial distribution of the optical near-field intensity with D of $2 \mu\text{m}$, $1.4 \mu\text{m}$, 900 nm , and 550 nm , respectively. Curves A,

Fig. 8.11 Spatial distribution at $D = 900$ nm. Curve A: calculated result; curve B: experimental result

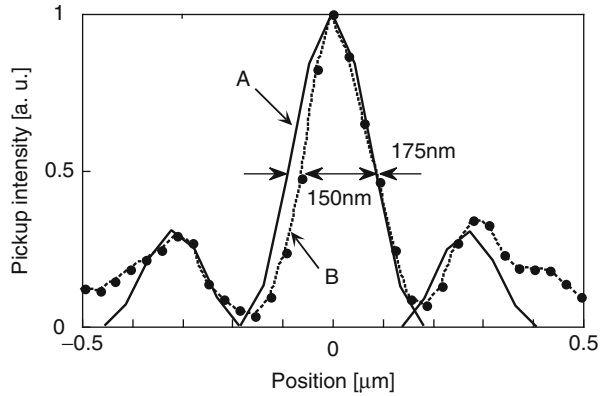
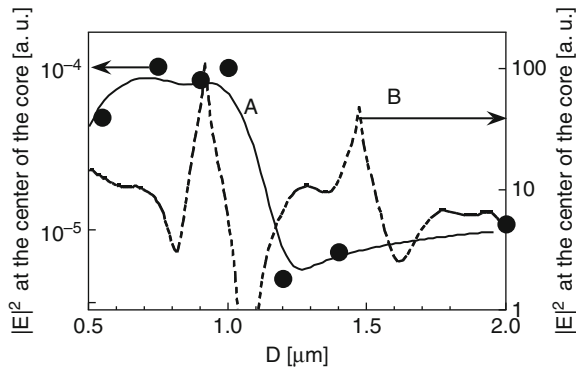


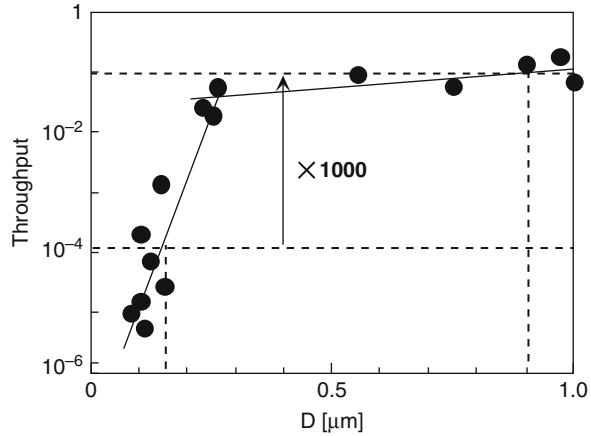
Fig. 8.12 Closed circles and curve A represent the measured relations between the electric field intensity at the center of the core and D . Curve B is the calculated result



B, C, and D in Fig. 8.10e show the cross-sectional profiles along the dashed white line in Fig. 8.10a–d, respectively. Note that the decrease in FWHM of the cross-sectional profile is not monotonic with decreasing D and that the optical near-field intensity at the center of the core peaks at $D = 900$ nm (curve C). Furthermore, the spatial distribution of the electric field goes through the progression “double peak \rightarrow triple peak \rightarrow single peak.” Note that the FWHM of curve C is as narrow as 150 nm ($< \lambda/5$). Curves A and B in Fig. 8.11 show the cross-sectional profiles of the experimental and calculated results, respectively. Note that curve B is in good agreement with curve A with respect to the FWHM of the main lobe, the position of the side peak, and the ratio of side peak intensity to the central peak intensity. In Fig. 8.12, the measured intensity at the center of the core is plotted as a function of D . This is in good agreement with calculated results with respect to the maximum intensity around $D = D_c$ (of TE_{12} mode).

In Fig. 8.13, the throughput is plotted as a function of D , where the throughput is defined as (output power)/(input power coupled into the fiber). This figure shows that the probe with $D = 900$ nm has throughput of 10%, 1,000 times that of the probe with $D = 150$ nm. Using a fiber probe with $D = D_c$ (of TE_{12} mode), we obtained both high throughput (10%) and a small spot (150 nm). Because of the

Fig. 8.13 Measured relation between D and the throughput for conventional single-tapered apertured probe



guiding loss along the metallized tapered core, the throughput decreases drastically when $D < D_c$ (of the TE_{11} mode).

8.1.4 Further Increase in Throughput

We review our work on decreasing the minimum spot size by optimizing the interference characteristics of the guided modes.

8.1.4.1 Triple-Tapered Probe with $D = D_c$ (of TE_{11} Mode)

As described in the last part of Sect. 8.1.3, the intensity of the optical near field does not peak at $D = D_c$ (of TE_{11} mode) due to the guiding loss in the metallized tapered probe with $\alpha = 25^\circ$. We describe here a new probe with short probe length and with $D = D_c$ (of TE_{11} mode), introducing a triple-tapered structure [7].

The triple-tapered probe was fabricated in five steps:

1. The GeO_2 -doped core was tapered with $\alpha = 25^\circ$ by the selective chemical etching technique [5].
2. To reduce the core diameter, the FIB was irradiated over the sharpened core (Fig. 8.14a).
3. The first and second tapers of the core were formed by the chemical etching technique. The foot diameter of second taper D_f was $1.6 \mu\text{m}$ (Fig. 8.14b). The length and apex diameter of the third tapers were 315 and 25 nm, respectively (Fig. 8.14c). The cone angles of the second and third tapers were 30° and 150° , respectively.
4. The core was coated with 300-nm-thick gold film.
5. The top of the third taper was removed by FIB to form an aperture.

Figure 8.14d shows an SEM image of a fabricated triple-tapered probe with $D = 60 \text{ nm}$. Since the length of the third taper (350 nm) is much less than that of the single-tapered probe ($5 \mu\text{m}$), a decrease in the propagation loss is expected.

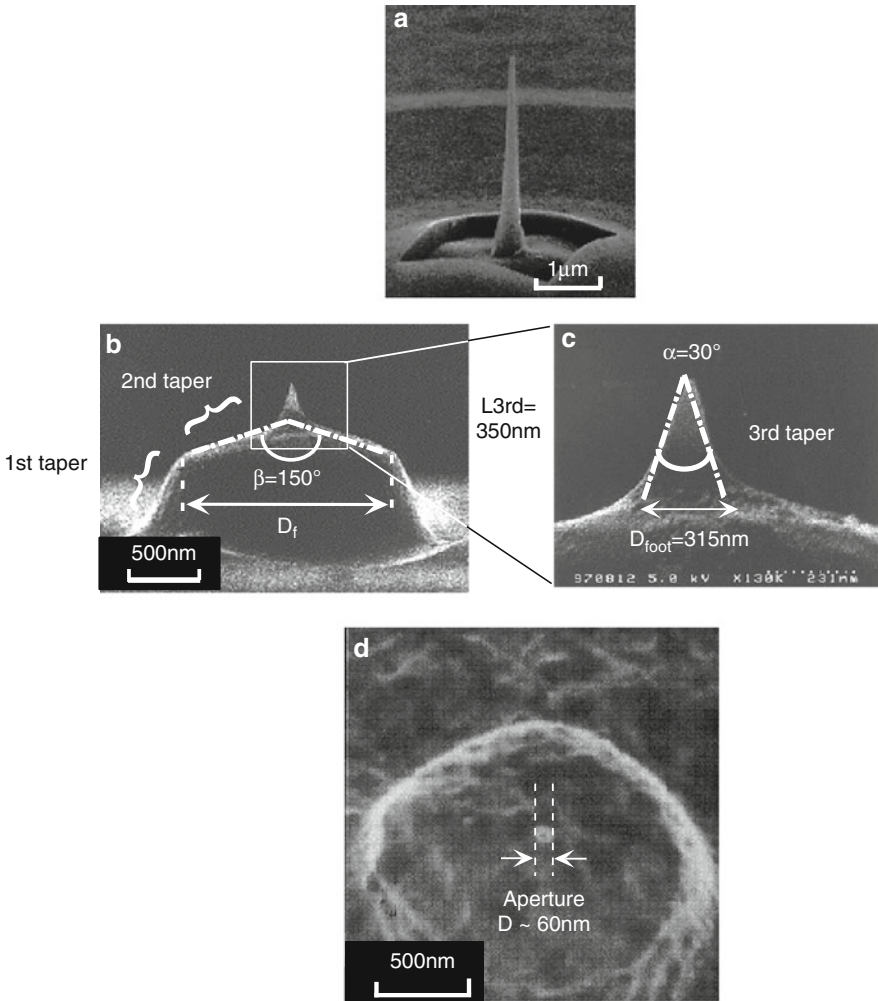


Fig. 8.14 SEM images of triple-tapered probe. (a) Results of step 2. (b) and (c) Profile of a triple-tapered core formed by step 3 and a magnified image of the third taper, respectively. (d) Bird's-eye view of the probe after steps 5

In Fig. 8.15, the throughput is plotted as a function of D for a triple-tapered probe and a conventional single-tapered probe. It shows that triple-tapered apertured probes have 1,000 times the throughput of a single-tapered probe with $D < 100$ nm. Such a drastic increase in throughput of a triple-tapered probe is a consequence of the efficient excitation of an HE-plasmon mode. The efficient excitation of the HE-plasmon mode is attributed to the drastic change in the shape of the probe at $D = D_c$ (of the TE_{11} mode).

Fig. 8.15 Measured relations between D and the throughput of a conventional single-tapered probe (*open circles*) and triple-tapered probe (*closed circles*)

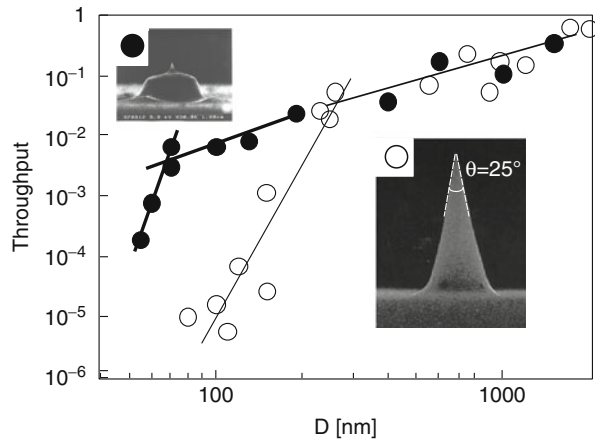
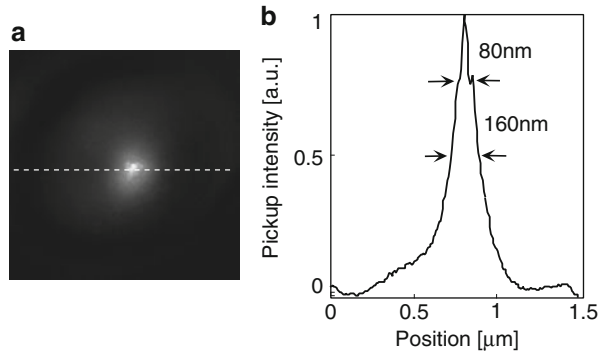


Fig. 8.16 Measured spatial distribution of the optical near field of a triple-tapered probe with $D = 60$ nm.

(a) A two-dimensional profile of the distribution. The image is $1.5 \times 1.5 \mu\text{m}$. (b) Cross-sectional profile along the dashed white line in (a)

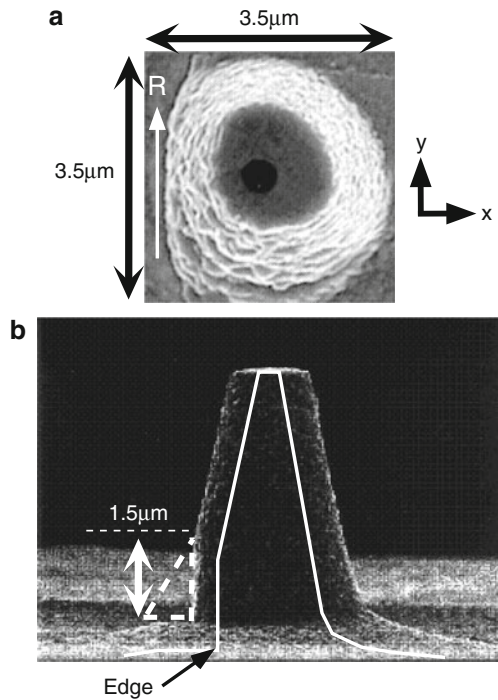


We checked whether the triple-tapered structure led to high spatial resolution. For this purpose, the spatial distribution of the optical near-field intensity in a triple-tapered probe with $D = 60$ nm was observed using the probe-to-probe method (see Fig. 8.9). To enhance the efficiency of light scattering, a sharpened probe with 50-nm-thick gold was used as a scanning probe [8]. Figure 8.16a, b shows the observed spatial distribution of the optical near-field intensity on the aperture and its cross-sectional profile, respectively. Due to the thin coating of the metallized probe used for the measurement, the 160-nm FWHM is a consequence of leakage of the propagating far field. However, a very sharp and narrow (80 nm) part at the center of the curve can be attributed to localization of the optical near field due to small α of the third taper. This part leads to high spatial resolution in imaging, spectroscopy, fabrication, and so on.

8.1.4.2 Edged Probe for Efficient Excitation of HE-Plasmon Mode

An efficient way of exciting the HE-plasmon mode is to utilize coupling of the plasmon by scattering at the edge of the metal [9]. If the tapered core has a sharp edge at its foot, a part of the guided light inside the single-mode fiber can be

Fig. 8.17 Scanning electron micrographs of an edged probe. (a) Top view, (b) side view. The arrow R in (a) indicates the direction parallel to the surface from which the core was removed. The x and y axes are normal and parallel to the arrow R , respectively



scattered at this edge and converted to the HE-plasmon mode [10]. We call a probe with such a core an edged probe [4].

Figure 8.17 shows scanning electron micrographs of a fabricated edged probe. The arrow R in Fig. 8.17a indicates the direction parallel to the surface from which the core has been removed. The x and y axes are normal and parallel to the arrow R , respectively. The white folded lines in Fig. 8.17b represent the profile of the tapered core buried in a gold metallic film. A part of the foot of the core was removed to form a sharp edge, where the height of the removed part was $1.5 \mu\text{m}$. This probe was fabricated by the following four steps:

1. By the elective chemical etching technique, the GeO_2 -doped core was tapered to $\alpha = 25^\circ$ [5].
2. The foot of the core was removed by FIB.
3. The core was coated with a 500-nm-thick gold film.
4. The top of the core was removed to form an aperture with FIB.

Note that apertured probes with D as small as 30 nm has been realized with this fabrication process.

We compared the near-field optical intensity of a conventional single-tapered probe and that of two edged probes with $D = 500 \text{ nm}$ ($\sim D_c$ of EH_{11} mode) and $D = 100 \text{ nm}$ ($\sim \lambda/8$). Though both EH_{11} and HE-plasmon modes can propagate in a probe with $D = 500 \text{ nm}$, note that the EH_{11} mode cannot exist in a probe with $D = 100 \text{ nm}$.

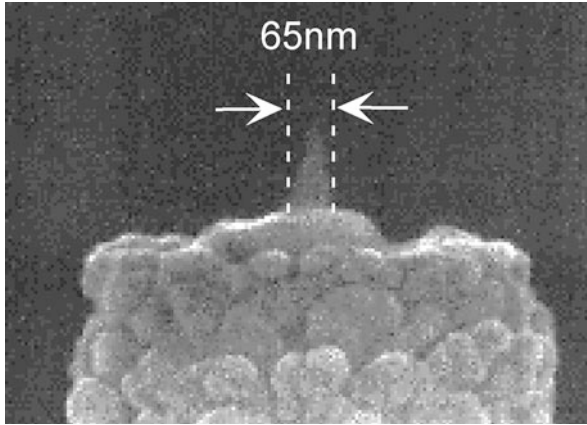
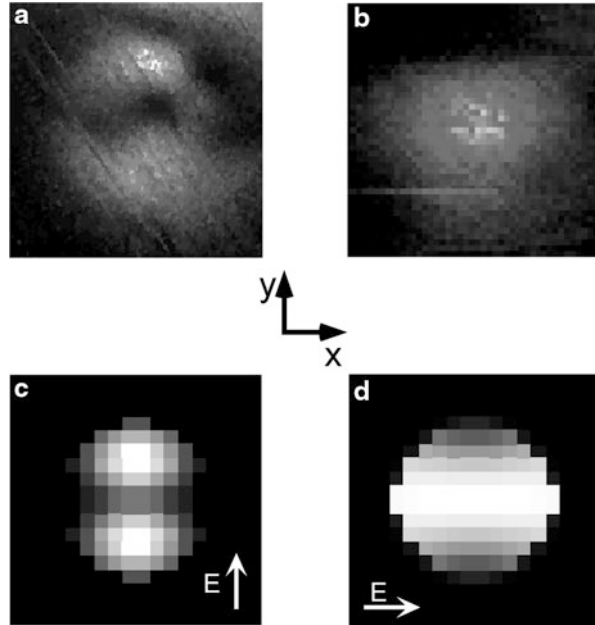


Fig. 8.18 SEM image of a protruding probe with $D_{\text{apex}} = 10$ nm and foot diameter 65 nm

First, we checked whether the edged structure of the probe led to efficient excitation of the HE-plasmon mode. We observed the spatial distribution of the optical near-field intensity in an edged probe with $D = 500$ nm. A protruding probe with an apex diameter (D_{apex}) of 10 nm and a foot diameter of 65 nm was used as a scanning probe (see Fig. 8.18) in the probe-to-probe method [11]. Figure 8.19a, b shows the observed distributions, where the directions of incident light polarization were orthogonal to each other. Figure 8.19c, d shows calculated distributions, corresponding to the EH_{11} and HE-plasmon modes for $D = 500$ nm, respectively. Note that the distributions in Fig. 8.19a, b are in good agreement with those in Fig. 8.19c, d, respectively, with respect to the number of lobes. Because the direction of light polarization changes in the fiber, we could not experimentally determine the direction of polarization at the foot of the probe. However, it seems most reasonable to consider the polarization directions of Fig. 8.19a, b to be those of Fig. 8.19c, d, respectively. We also observed the spatial distribution in a conventional probe (fabricated without step 2) with $D = 500$ nm. In this case, only a double-peaked distribution, which corresponds to the EH_{11} mode, was observed, where the lobes rotated as the direction of the incident light polarization changed. This indicates that an edged structure supports excitation of the HE-plasmon mode, where its excitation efficiency depends on the direction of incident light polarization.

Second, in order to check whether the optical near-field intensity in the apertured probe is enhanced due to the edged structure, we compared the spatial distributions of conventional and edged probes with $D = 100$ nm. To increase the efficiency of light scattering in the probe-to-probe method, we used a sharpened probe coated with 30-nm-thick gold as the scanning probe [8]. Figure 8.20 shows the observed cross-sectional distributions. Curves A and B are for the edged apertured probe, where the directions of incident light polarization were orthogonal to each other.

Fig. 8.19 Spatial distributions of the optical near field on top of an edged probe with $D = 500$ nm. The images are 750×750 nm. (a) and (b) Measured results. The directions of incident light polarization for these figures are orthogonal to each other. (c) and (d) Calculated results for the EH_{11} and the HE-plasmon mode, respectively. The vectors E in these figures represent the directions of polarization of the incident light



A single-peaked distribution, which corresponds to the HE-plasmon mode, was observed. Curve C is for a conventional apertured probe. Note that the intensity for the curve A is ten times that of curves B and C. The FWHM of the intensity distribution of the HE-plasmon mode for $D = 100$ nm is analytically estimated to be 120 nm, which is comparable to that of curve A (~ 150 nm). This indicates that the increase in the intensity of the optical near field is a consequence of efficient excitation of the HE-plasmon mode at the sharp edge.

Finally, we compared the throughput of an edged probe, triple-tapered probe, and conventional probe. In Fig. 8.21, the throughput is plotted as a function of D . It shows that the throughput of the triple-tapered probe is 1,000 times that of the conventional probe for $D < 100$ nm. Such a drastic increase in the throughput of the triple-tapered probe can be attributed to efficient excitation of an HE-plasmon mode. Since the dependence of the throughput on D for the triple-tapered probe is similar to that of an edged probe with $70 \text{ nm} < D < 200 \text{ nm}$ (see Fig. 8.21), the HE-plasmon mode should be excited in the triple-tapered probe. As a consequence of the scattering coupling at the foot of the third taper [9], the HE-plasmon mode is excited efficiently. Furthermore, note that the triple-tapered probe has throughput ten times that of the edged probe with $D < D_c$ (of the HE-plasmon mode). This is because mode conversion from EH_{11} to HE-plasmon in the edged probe takes place at the foot of the core, where the guiding loss of the HE-plasmon mode is greater than that of EH_{11} mode. Thus, the edged probe has a greater guiding loss than a triple-tapered probe in which the mode is converted at the foot of the third-tapered core.

Fig. 8.20 Measured cross-sectional profiles of the optical near field. Curves *A* and *B* are for an edged probe, where the directions of polarization of the incident light are orthogonal to each other. Curve *C* is for a probe without an edge

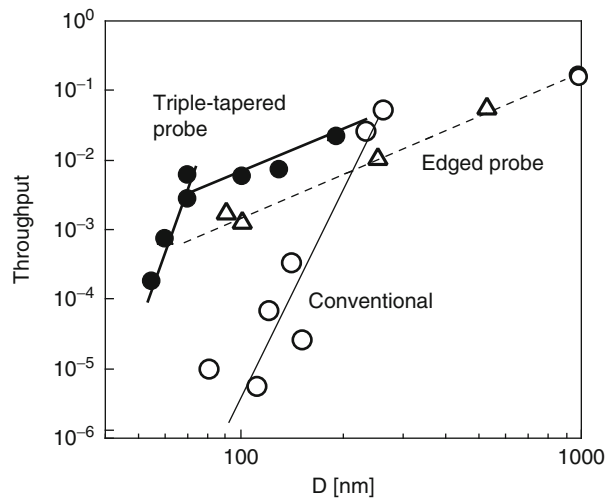
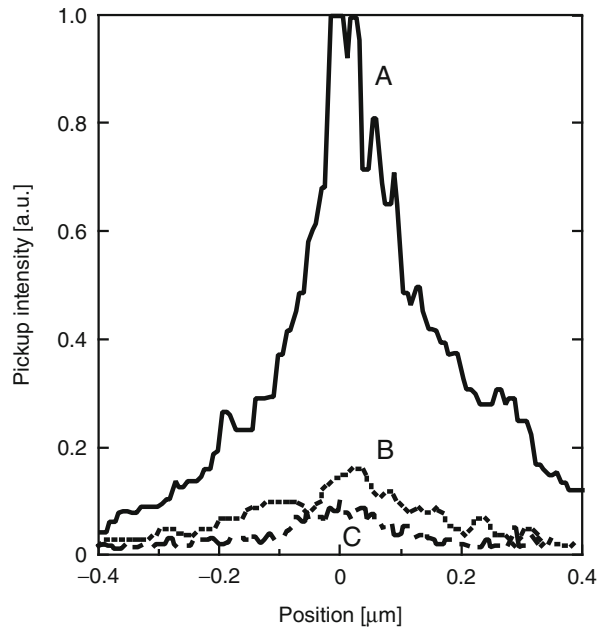


Fig. 8.21 Measured reactions between *D* and the throughput

8.1.4.3 Pyramidal Silicon Probe

For further improvements in the performance of a near-field optical probe, we describe here the extremely high throughput and resolution capability of a pyramidal silicon probe. Since the high refractive index of the silicon ($n = 3.67$ at $\lambda = 830$ nm) leads to a short effective wavelength inside the probe, higher

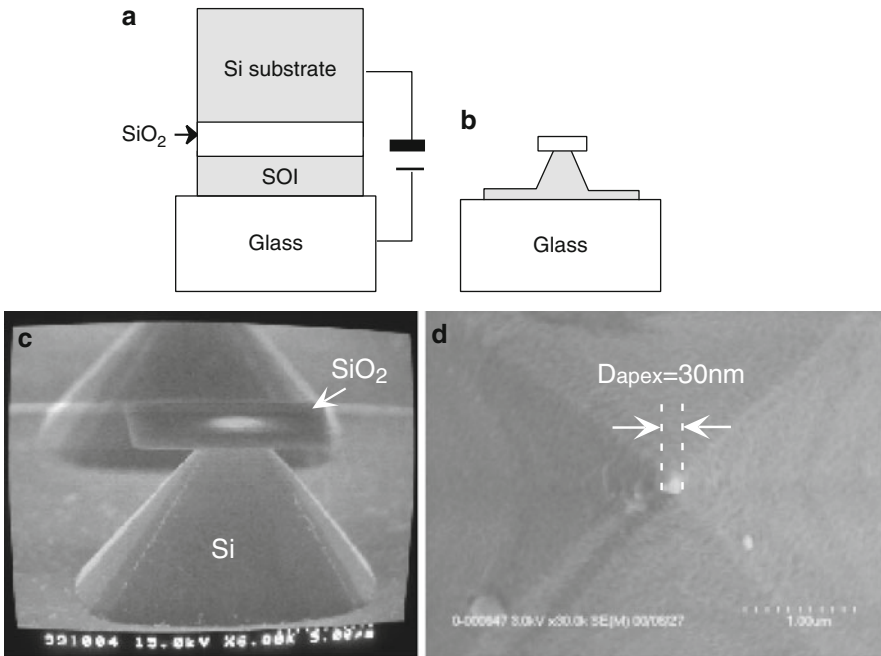


Fig. 8.22 (a) and (b) Schematic of the fabrication process of a pyramidal silicon probe. D_{apex} : apex diameter. SEM images of a pyramidal silicon probe: (c) bird's-eye view of the probe by step 3, (d) top view of the probe by step 4, respectively

throughput and a smaller spot size are expected in comparison with conventional fiber probes [12].

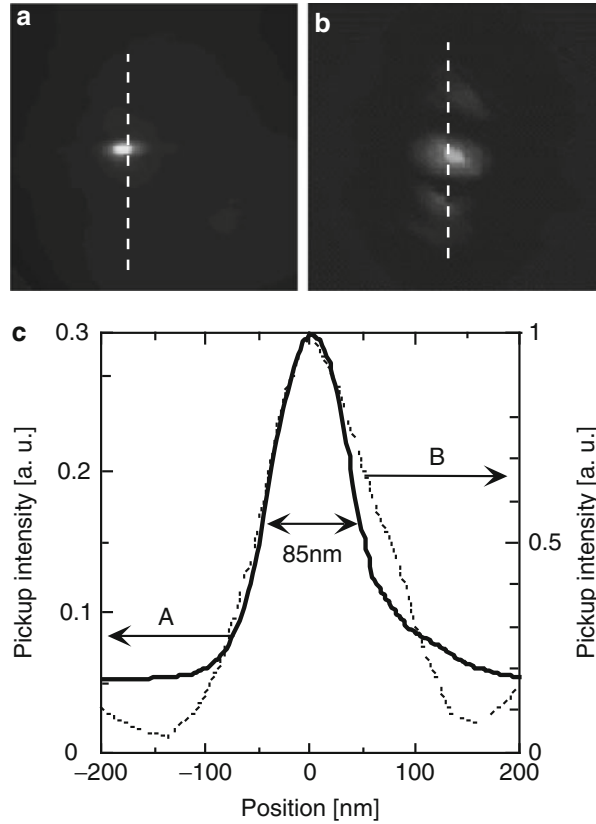
A pyramidal silicon probe was fabricated from a (100)-oriented silicon on insulator (SOI) wafer by following four steps:

1. The SOI was bonded to the glass substrate by anodic bonding (300 V, 350 °C, 10 min, Fig. 8.22a) [13].
2. After removing the silicon substrate, the SiO_2 layer was patterned by photolithography.
3. The single-tapered pyramidal probe was fabricated by anisotropic etching (40 g:KOH+60 g:H₂O+40 g:isopropyl alcohol at 80 °C, Fig. 8.22b, c).
4. The probe was coated with 20-nm-thick aluminum (Fig. 8.22d).

Note that the pyramidal silicon probe with D_{apex} as short as 30 nm was realized by this process.

We evaluated the throughput and spot size of a pyramidal silicon probe with $D_{\text{apex}} = 30 \text{ nm}$. For comparison, we also evaluated a fiber probe with $D = 920 \text{ nm}$ ($= D_c$ of TE_{11} mode). As described in detail in Sect. 8.1.3, an apertured probe with $D = D_c$ (of TE_{11} mode) has a very small spot (FWHM = 150 nm) due to the interference characteristics of the guided modes. The throughput has been calibrated

Fig. 8.23 Spatial distribution of the optical near-field intensity. (a) and (b) are for a pyramidal silicon probe with $D_{\text{apex}} = 30$ nm and a fiber probe with $D = 920$ nm, respectively. The images are $1.5 \times 1.5 \mu\text{m}$. Curves A (solid line) and B (dashed line) in (c) are the cross-sectional profiles along the dashed white line in (a) and (b), respectively



to be 10%. As a scanning probe for the probe-to-probe method, we used a fiber probe with D of 50 nm.

Figure 8.23a, b shows the observed spatial distribution of the optical near-field intensity for a pyramidal silicon probe with $D_{\text{apex}} = 30$ nm and an apertured fiber probe with $D = 920$ nm, respectively. Curves A and B in Fig. 8.23c show the cross-sectional profiles along the dashed white line in (a) and (b), respectively. Note that the FWHM of curve A is as narrow as 85 nm ($\sim \lambda/10$). Furthermore, the peak intensity of curve A is 25% that of B. This indicates that a pyramidal silicon structure can yield high throughput and small spot size simultaneously [14].

8.1.4.4 A Metallized Slit-Shaped Pyramidal Si Probe

To achieve higher throughput and a smaller spot size, we optimized the mode interference in a Si probe with a slit-shaped tip [15]. Our probe is illustrated schematically in Fig. 8.24a. Since this probe has a slit-type aperture, the lowest mode does not have a cutoff when the illuminating light is polarized perpendicular to the slit (y -polarization). Therefore, a throughput higher than that of a conventional

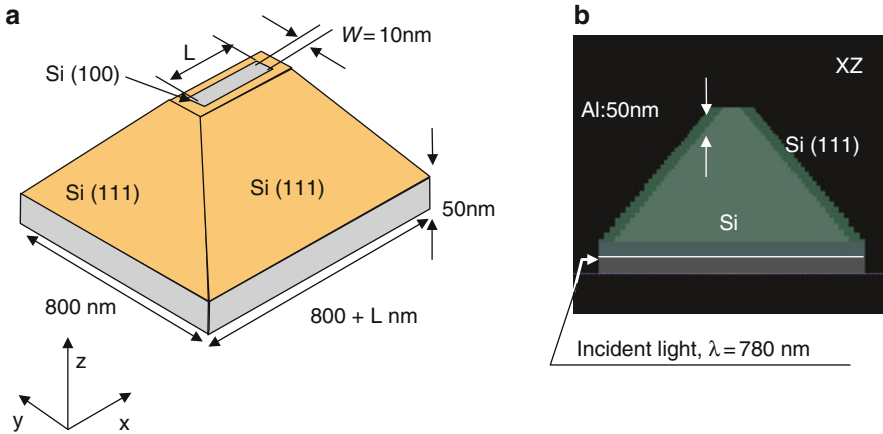


Fig. 8.24 Schematic of the pyramidal Si probe with a slit-type aperture. (a) Bird's-eye view. (b) Cross-sectional view in the XZ plane of (a)

cylindrical tapered fiber probe is expected. Furthermore, such a slit-shaped aperture structure results in the strong polarization dependence of the electric field intensity through the probe.

To find the tip parameters required to increase the optical near-field intensity at the probe tip, numerical calculations were performed using the finite-difference time-domain (FDTD) method. The minimum cell around the aperture was $2.5 \times 2.5 \times 2.5$ nm. As shown in Fig. 8.24b, the pyramidal Si probe (refractive index $n = 3.7$ at $\lambda = 785$ nm) was coated with 50-nm-thick aluminum (Al) film ($n = 2.8 + i8.45$) [3], and the four sidewalls resulted from the (111) Si crystal planes. The pyramidal Si probe was illuminated from the bottom (see Fig. 8.24b) with linearly polarized light ($\lambda = 785$ nm). The bottom surface of the probe was $(800 + L) \times 800$ nm. The slit width W was fixed at 10 nm.

Figure 8.25a shows the relationship between L and the cross-sectional profile of the electric field intensity along the x -axis with y -polarization at the 5 nm from the aperture. The electric field intensity distribution varies from a triple peak ($L = 510$ nm) to a single peak ($L = 50$ nm) via a double peak ($L = 330$ nm) on decreasing the value of L . This variation concurs with that of the mode interference observed with a tapered fiber probe [7]. In Fig. 8.25b, curves A and B show the electric field intensities, I_C , at the center of the aperture with y - and x -polarization, respectively, plotted as a function of L . Note that I_C does not decrease monotonically on decreasing L and takes local maxima at $L = 50$ (P_{A1}) and 510 (P_{A2}) nm, for which the values of L correspond to the cutoff diameter of the modes. For comparison, I_C is also plotted for a pyramidal probe with a square aperture in Fig. 8.25a (curve C). This curve takes local maxima at $L = 50$ (P_{C1}) and $L = 250$ nm (P_{C2}), which originate from the mode interferences, as has been found for the slit-shaped aperture probe. Comparing the curves, we

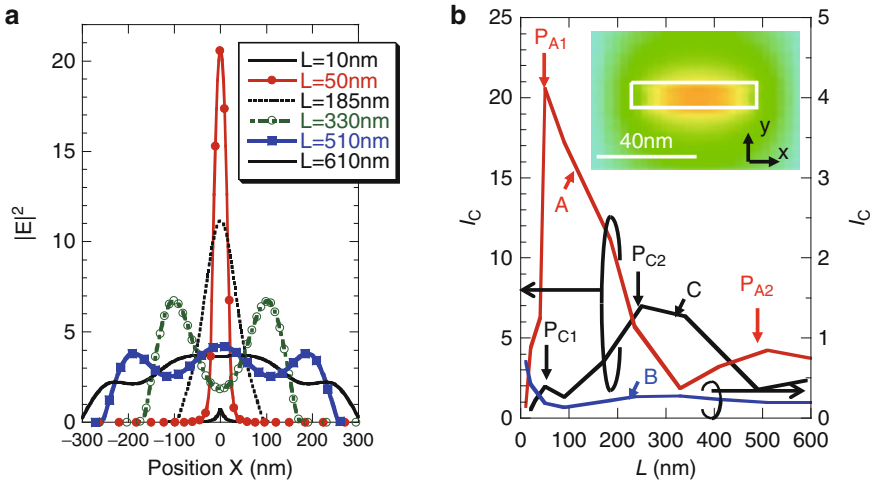


Fig. 8.25 (a) Calculated electric field intensity distributions along the x -axis for $W = 10$ nm with y -polarization. (b) L dependence of the electric field intensity at the center of the aperture, I_C . Curves A and B: y - and x -polarization of the slit-type probe. Curve C: y -polarization of a square aperture probe. *Inset*: Electric field intensity distribution of the slit-type probe with $L = 50$ nm and y -polarization

confirmed that the slit-shaped aperture probe with $L = 50$ nm has an I_C ten times larger than that of the square aperture probe at $L = 50$ nm. That is, the slit-shaped Si probe can realize a smaller spot size with high throughput due to the smaller cutoff diameter (P_{A1} of the slit-shaped aperture). From the electric field intensity distribution 5 nm from the aperture with y -polarization (see the inset of Fig. 8.25b), we obtained a small spot size of 13×30 nm with a maximum peak intensity at $L = 50$ nm, which corresponds to a recording density of 1.6 Tbit/in². Furthermore, on comparing the I_C at $L = 50$ nm between the y - (curve A in Fig. 8.25b) and x -polarization (curve B in Fig. 8.25b), the slit-type Si probe with y -polarization has a 100 times larger I_C than that with x -polarization. This means that the slit-shaped Si probe has a large extinction coefficient depending on the polarization.

Based on the above calculation, we fabricated a pyramidal Si probe with a slit-shaped aperture [16]. A (100)-oriented Si-on-insulator (SOI) wafer was bonded to a glass substrate using anodic bonding [13]. After removing the Si substrate from the SOI wafer using wet etching, the SiO₂ layer was patterned using photolithography. The pyramidal Si structure was fabricated using anisotropic etching. Maintaining the Si probe height at less than 10 μ m, its propagation loss was kept sufficiently low. The mesa length was controlled accurately using the etching time. Finally, after removing the SiO₂ layer, the probe was coated with a 50-nm-thick aluminum layer. Figure 8.26a, b show scanning electron microscopic images of our pyramidal Si probe. The Al-coated mesa at the probe tip measured 50×35 nm ($L' \times W'$) (see Fig. 8.26c). Since the fabricated structure was totally coated with aluminum, we could not determine the value of L .

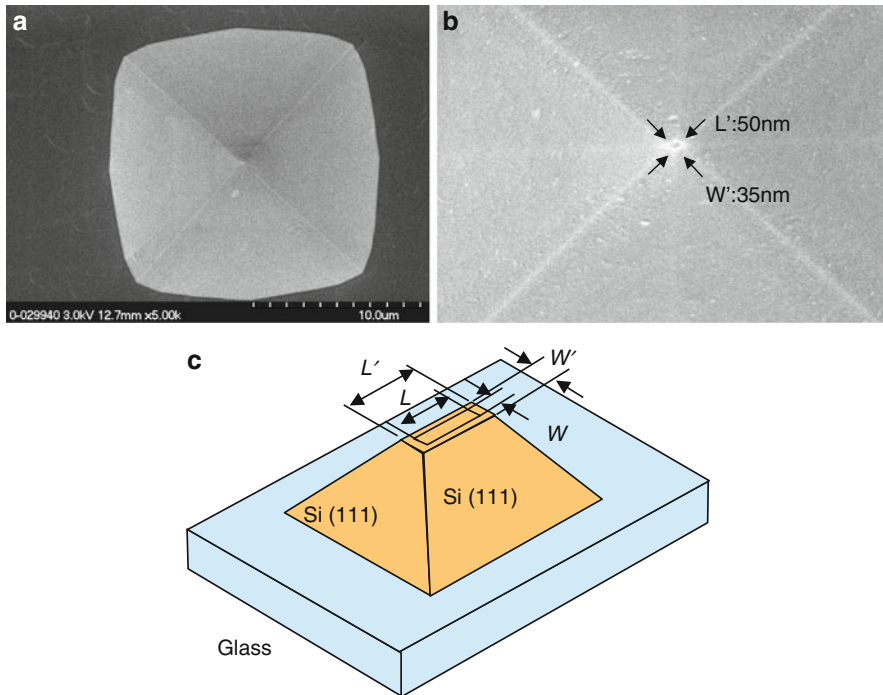


Fig. 8.26 Scanning electron microscopy images of the fabricated Si probe with a slit-type aperture. (a) Overview of the probe. (b) Magnified image of (a). (c) Schematic of the Si probe

The spatial distribution of the optical near-field intensity on the pyramidal Si probe was evaluated by measuring the fluorescence intensity from a single dye molecule (Cy7) [17]. For this measurement, the molecules were dispersed on the flat tip of another apertured fiber probe with an aperture diameter D of 50 nm (see Fig. 8.27) [7]. To fabricate this fiber probe, a fiber was sharpened using the selective chemical etching technique [5]. Then, the sharpened core was coated with a 500-nm-thick gold film. Finally, the probe tip was removed using a focused ion beam to form an aperture [4, 7]. To excite the dye molecules, we used a laser diode with a wavelength of 785 nm. The fluorescence signals were collected through the apertured probe and detected using the photon-counting method. The separation between the pyramidal Si probe and the fiber probe was kept within 5 nm using the shear-force feedback technique.

Figure 8.28a, b show the observed spatial distributions of the optical near-field intensity with y - (perpendicular to the slit) and x -polarization (parallel to the slit), respectively. The bright spot in Fig. 8.28a (y -polarization) represents the fluorescence signals from a single molecule. Figure 8.28c, d show the cross-sectional profiles along A-A' and B-B' in Fig. 8.28a, respectively. Note that the full widths at half maximum of the signal profile are 16×26 nm, which correspond to an areal data density of 1.5 Tbit/in². However, since the obtained spot size along

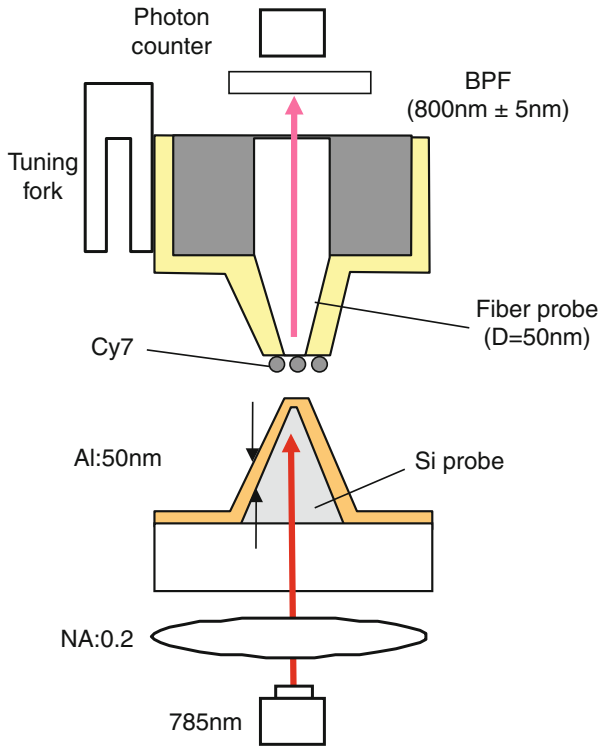


Fig. 8.27 Schematic of the experimental configuration. *BPF* band pass filter

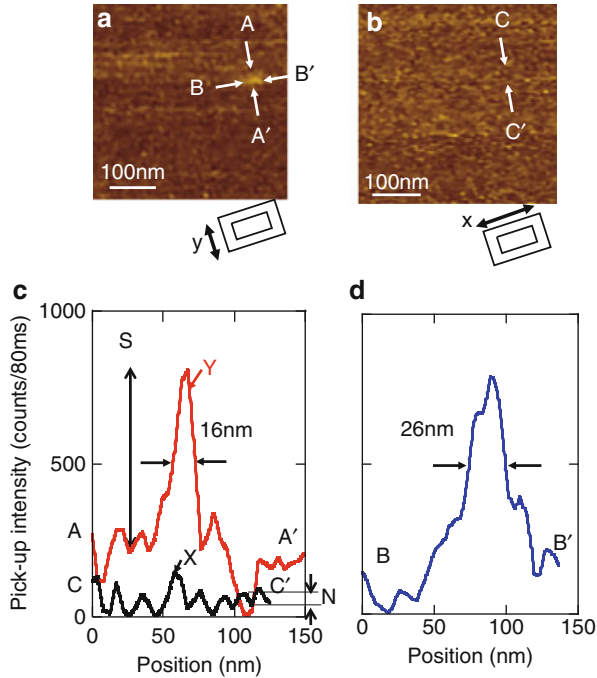
$B-B'$ (26 nm) was smaller than that of calculated results for $L = 50$ nm and $W = 10$ nm without coating over the aperture (30 nm), we believe that the fabricated aperture size was smaller than $L' = 50$ nm and $W' = 35$ nm. From the signal profile of the y -polarization (curve Y in Fig. 8.28c), the typical fluorescence signal intensity was as high as 7.5×10^3 counts per second. Since the signal intensity of the x -polarization (curve X in Fig. 8.28c) was as low as the noise intensity (6.2×10^2 counts per second), the extinction coefficient of the pyramidal Si probe is estimated to exceed 12.

8.2 Application to High-Density and High-Speed Optical Memory

8.2.1 Using an Apertured Fiber Probe

We applied a high-throughput fiber probe for optical recording and reading. An as-deposited phase-change material in an amorphous phase was used as the recording medium. The phase-change film on a glass substrate consisted of a 20-nm-thick

Fig. 8.28 Schematic of the experimental configuration. BPF band pass filter



SiO₂ film, a 25-nm-thick AgInTe₂, and a 20-nm-thick SiO₂ film. These films were deposited by RF sputtering. We carried out the phase-change recording and reading with the high-throughput fiber probe. The experimental setup is shown in Fig. 8.29. Linearly polarized light from a laser diode ($\lambda = 830$ nm) was coupled into the single-mode fiber to generate the optical near field on the aperture. The irradiation time was fixed to 2 μ s. The separation between the probe and the recording medium was kept within several nanometers by shear-force techniques. The light transmitted through the aperture and the sample was detected with a photodetector under the medium (illumination mode; I mode). The reflected light was also detected with a photomultiplier tube (illumination–collection mode; I-C mode).

Figure 8.30 shows the spatial distribution of the optical near-field intensity on the fiber probe, with $D = 920$ nm used for phase-change recording and reading. As described in Sect. 8.1.3, since D is equal to D_c of the TE₁₂ mode, it has high throughput (10%) and small spot size (FWHM = 180 nm) at the center of the cross-sectional profile in Fig. 8.30b, which is a consequence of the interference characteristics of the guided modes.

After optical near-field recording was carried out over a range of optical recording power, the spatial distribution of transmitted light was measured at an optical reading power of 0.2 mW. Figure 8.31a, b shows the spatial distribution obtained by I mode operation for a writing power of 7.0 and 8.6 mW, respectively. A small bright spot in Fig. 8.31b (indicated by an arrow) represents the recorded

Fig. 8.29 Schematic of the system used for near-field phase-change recording and reading. *PD* photodetector for I mode signal, *PMT* photomultiplier tube for I-C mode signal

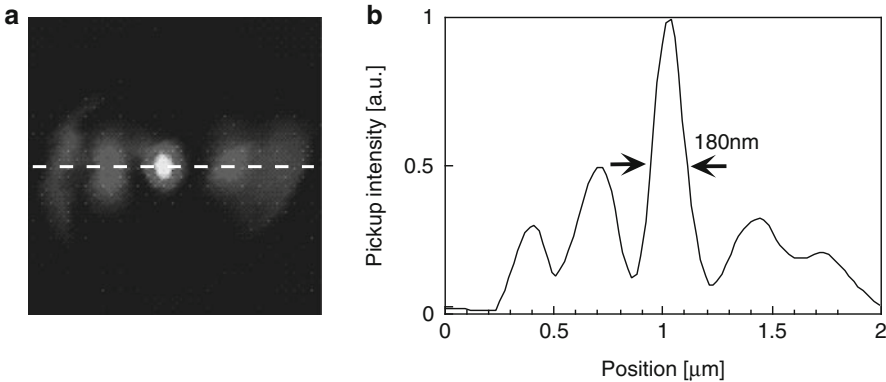
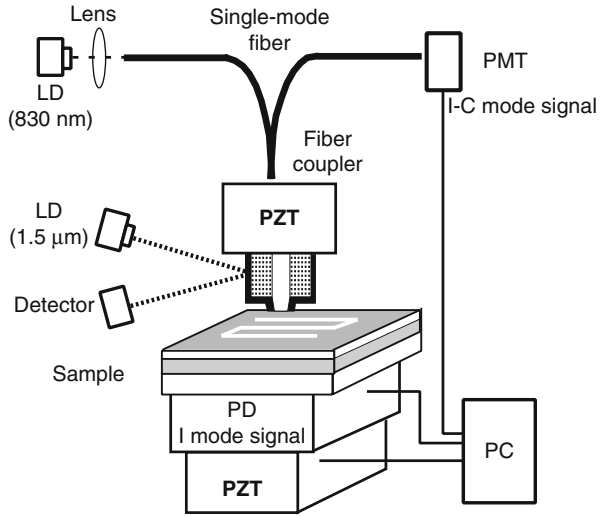


Fig. 8.30 Spatial distribution of the optical near-field intensity on the aperture, with $D = 920$ nm used for phase-change recording. (a) Two-dimensional image. (b) Cross-sectional image along the dashed white line in (a)

mark. The dark ellipse around the spot as well as that in Fig. 8.31a is due to the photodarkening in thin films of amorphous chalcogenides [18, 19]. Since Te, being a twofold coordinated atom, has chain-molecule fragments [20], structural changes are induced by exposure light. This results in an increase in the absorption coefficient, which is called photodarkening [20]. The photodarkening might be caused by the side lobes of the curve in Fig. 8.30b.

Figure 8.31c shows the spatial distributions obtained by I-C mode operation for a writing power of 8.6 mW. Note the dark small spot at the center and a ring, which are due to photodarkening. In Fig. 8.31d, curves A and B are the cross-sectional profiles

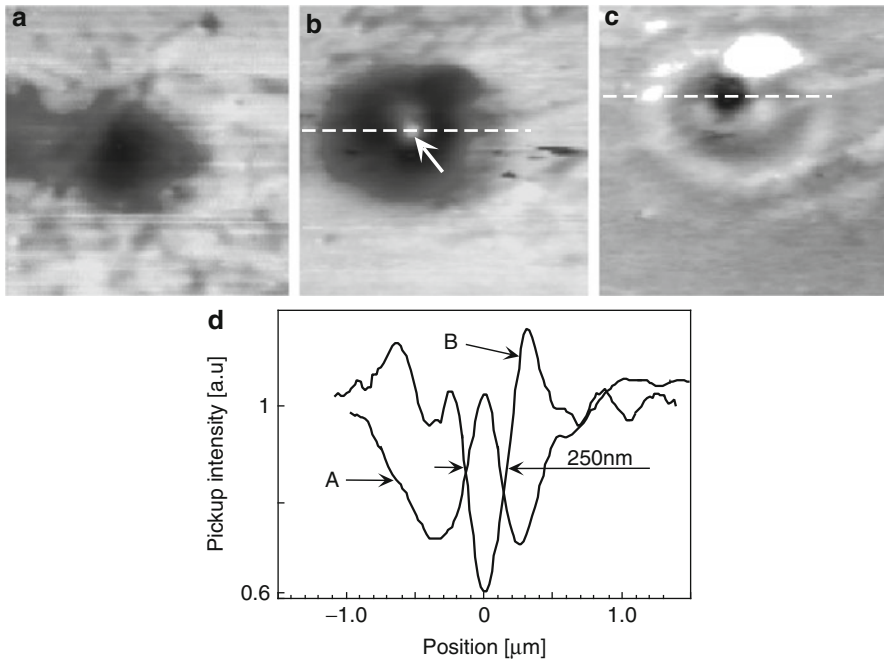


Fig. 8.31 Spatial distribution of the optical near-field intensity images of phase-change recordings. (a) and (b) Obtained by I mode operation for writing power of 7 and 8.6 mW, respectively. (c) Obtained by I-C mode operation for writing power of 8.6 mW. (d) Curves A and B show the cross-sectional profiles along the *dashed white lines* in (b) and (c), respectively

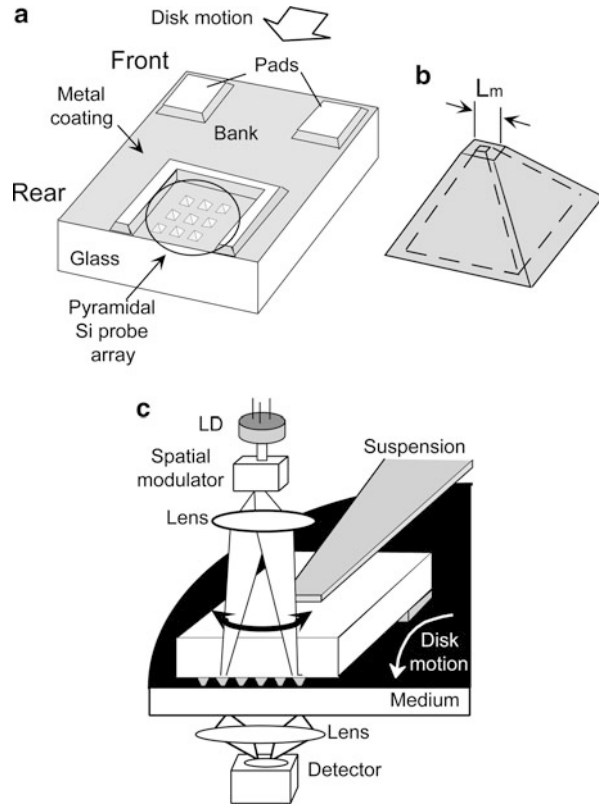
along the dashed white lines in (b) and (c), respectively. Note that the FWHM of these curves is as narrow as 250 nm.

8.2.2 High-Density and High-Speed Recording Using a Pyramidal Silicon Probe on a Contact Slider

To realize a high data transmission rate, a superresolution near-field structure [21] and a planar probe mounted on an optical slider [22] have been proposed recently. Since these methods do not require shear-force feedback, reading speed is increased without technical difficulties. However, since the incident light has to be focused by a lens in these systems, the efficiency of the optical near-field generation on a subwavelength aperture is low.

In this section, we describe a new contact slider with a high throughput of optical near-field intensity to realize a high recording density on the phase-change medium and fast readout [16]. Schematics of the slider structure and the data storage system

Fig. 8.32 (a) Contact slider with a pyramidal silicon probe array. (b) Pyramidal silicon probe with a mesa. L_m is the mesa length. (c) Schematic of the storage system with the slider: LD laser diode



are illustrated in Fig. 8.32. A pyramidal silicon probe array is arranged at the rear end of the slider. The advantages of such a slider are:

1. As described in Sect. 8.1.4, the high refractive index of silicon ($n = 3.67$ at $\lambda = 830$ nm) leads to a short effective wavelength inside the probe, which results in higher throughput and smaller spot size than for conventional fiber probes made of silica glass.
2. The height of the pyramidal silicon probe array is controlled to be less than $10\ \mu\text{m}$ so that sufficiently low propagation loss in the silicon is maintained. Furthermore, the probe array has high durability because it is bonded to a thick glass substrate.
3. Compared with those of previously reported pyramidal probes fabricated by use of a focused ion beam [23] or by the transfer mold technique in a pyramidal silicon groove [24], ultrahigh homogeneity in the heights of the probes and pads can be realized. This is because the flatness of the mesa at the probe tip and of the upper surface of the pads are determined by the uniformity of the thickness of silicon wafer.
4. Use of a probe array with many elements increases the total data transmission rate by parallel readout [24–26]. In this system the incident light is spatially

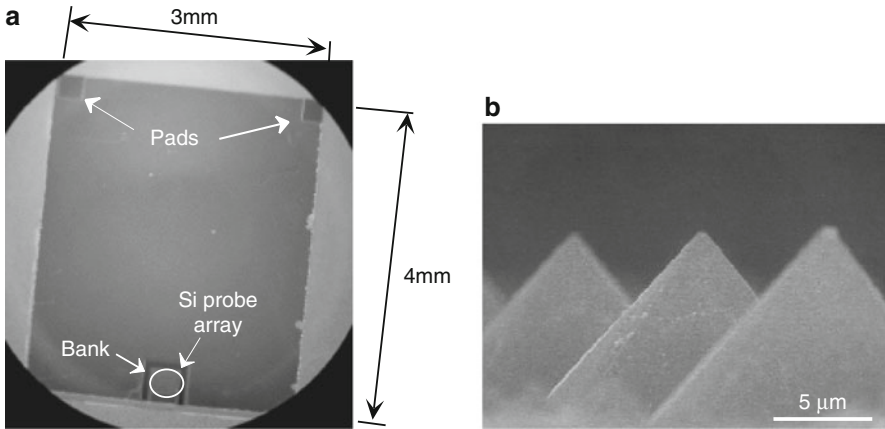


Fig. 8.33 (a) Photographic image of the contact slider with a pyramidal silicon probe array and pads. (b) Magnified scanning electron microscope image of the fabricated pyramidal silicon probe array

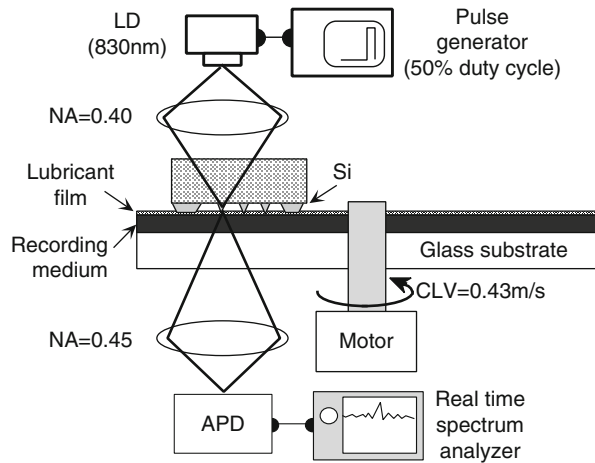
modulated by an electro-optical modulator, and the scattered light from a different probe can be read out as a time-sequential signal.

Since the key issue in realizing a pyramidal silicon probe array is high homogeneity in the heights of the probes, the probe array is fabricated from a (100)-oriented SOI wafer in four steps:

1. The SOI wafer was bonded to the glass substrate by anodic bonding (300 V, 350 °C, 10 min) [13].
2. After removing the silicon substrate from the SOI wafer by mean of wet etching, the SiO₂ layer was patterned by photolithography.
3. The probe array, the bank, and the pads were fabricated by means of anisotropic etching (40 g:KOH+60 g:H₂O+40 g:isopropyl alcohol, 80 °C). Note that height homogeneity was maintained by the remaining SiO₂ layer.
4. The slider was quarried with a dicing saw.
5. After removing the SiO₂ layer, the slider was coated with 30-nm-thick aluminum to increase the efficiency of light scattering [8].

Figure 8.33a, b shows an optical image of the contact slider and a scanning electron microscopic image of the pyramidal silicon probe array fabricated on the slider, respectively. As shown in Fig. 8.33b, the height dispersion of the probes and pads has been reduced to less than 10 nm, because this dispersion is determined by the thickness uniformity of the SOI wafer. Here the slider is designed by use of the design criteria [27] for a contact-type hard-disk head so that its jumping height over the phase-change medium is maintained to less than 10 nm. Furthermore, since the phase-change medium is fragile, we designed the bank so that the contact stress becomes 0.01 times the yield stress of the magnetic disk at a constant linear velocity (CLV) of 0.3 m/s, which corresponds to a data transmission rate of 10 MHz for a data storage density of 1 Tbit/in². To increase the readout speed 100-fold, i.e., to realize

Fig. 8.34 Schematic of the experimental setup for phase-change recording and reading by the contact slider. APD avalanche photodiode, LD laser diode, NA numerical aperture



a 1 Gbit/s data transmission rate for data storage density of 1 Tbit/in², we fabricated 100 probe elements on the inner part of the bank for parallel readout.

In recording and readout experiments with the fabricated contact slider, we compared the signal transmitted through phase-change marks recorded with a single element of the probe array and that recorded with focused propagating light. Figure 8.34 shows the experimental setup. The contact slider was glued to a carrier. The slider was in contact with a phase-change medium coated with a thin lubricant film (Fomblin Z-DOL). A laser beam ($\lambda = 830$ nm) was focused on one element of the probe array on the slider. The frequency of the rectangularly modulated signal with 50% duty cycle was varied from 0.16 to 2.0 MHz at a $CLV = 0.43$ m/s. The light transmitted through the recording medium was detected with an avalanche photodiode. We used an as-deposited AgInSbTe film as a recording medium. The optical recording powers for a pyramidal silicon probe with a mesa length L_m of 150 nm (see Fig. 8.35a) and propagating light focused by a microscope objective ($N.A. = 0.40$) were 200 and 15 mW, respectively, which are, to the authors' knowledge, the lowest recording powers. The throughput of optical near-field generation of the metallized pyramidal silicon probe is 7.5×10^{-2} , which is estimated from the ratio of the optical powers for near- and far-field recording. Readout was carried out at a $CLV = 0.43$ m/s. The reading optical powers for the pyramidal silicon probe and the focused propagating light were 20 and 3.6 mW, respectively. The resolution bandwidth was fixed at 30 kHz.

The dependence of the carrier-to-noise ratio (CNR) on the mark length is shown in Fig. 8.35b. Note that shorter crystalline phase-change marks beyond the diffraction limit were recorded and read out by an optical near field generated on the pyramidal silicon probe. The shortest mark length was 110 nm at a CLV of 0.43 m/s, which corresponds to a data transmission rate of 2.0 MHz. Since this slider has 100 elements in the probe array, a 100-fold increase in the data transmission rate is expected by parallel readout using all the elements. Furthermore, a higher CLV is

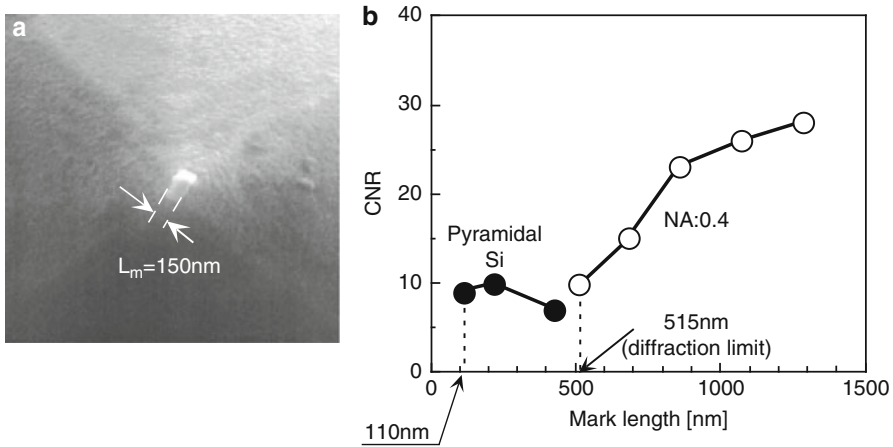


Fig. 8.35 Magnified scanning electron microscope image of the pyramidal silicon probe tip used for optical near-field recording and reading. L_m mesa length. **(b)** *CNR* dependence on the mark length for (closed circles) the optical near field with the pyramidal silicon probe and (open circles) propagating light focused by an objective

expected since we did not observe any damage on the probe tip or the recording medium after a series of experiments. The *CNR* of the pyramidal silicon probe seen in Fig. 8.35b was independent of mark length, due to the small spot of the optical near field and the narrow recorded mark width, which are as small as L_m of the pyramidal silicon probe. These results indicate that an increased *CNR* and shorter mark length can be achieved by employing servo control for tracking during readout. Furthermore, it is expected that the recording density can be increased to as high as 1 Tbit/in² by optimization of the interference characteristics of the guided modes in the pyramidal silicon probe.

8.3 Outlook

Higher throughput is expected by improving the techniques reviewed in this chapter. In addition to these techniques, use of the plasmon effect is advantageous for further increases in throughput [28, 29]. For extension to the ultraviolet, a pure silica core fiber of low transmission loss has been developed and used to fabricate a high-throughput fiber probe [30]. For improvements in mechanical stability, micromachining technology is advantageous for fabricating a silicon probe. A silicon probe with throughput as high as 2.5 % (see Sect. 8.1.4.3) and a hollow silicon probe with 20-nm aperture diameter for the ultraviolet [31] have been fabricated using this technique. Furthermore, functional probes, e.g., probes on which light-emitting dye molecules [32] and ZnO films [33] are deposited, are attractive for their optical frequency conversion capabilities which can be used in biological applications.

Section 8.2 was devoted to describing the application of high-throughput probes to optical memory. However, one can find further applications. These are spatially resolved spectroscopy in the ultraviolet, visible, and infrared by detecting photoluminescence, electroluminescence, photocurrent, and Raman signals of semiconductor quantum dots [34], semiconductor devices [35], and organic materials [36]. Application to nano-fabrication, e.g., photochemical vapor deposition of nanostructures of metals (Zn and Al), oxides (ZnO), and composite semiconductors, has also been demonstrated in order to realize high-density nano-photonic integrated circuits for future optical transmission systems [37–39]. These techniques can open a new field of nano-photonics. Further, high-throughput fiber probes can be also used to manipulate neutral atoms in vacuum by controlling their thermal motion, which can open a new field of atom-photonics [39].

Acknowledgements Valuable discussions with Drs. M. Kourogi, K. Tsutsui (Tokyo Institute of Technology), J. Tominaga (National Institute of Advanced Industrial Science and Technology), and J. Takahashi (Ricoh Company, Ltd.) are deeply appreciated.

References

1. M. Ohtsu (ed.), *Near-Field Nano/Atom Optics and Technology* (Springer, Tokyo, 1998)
2. L. Novotny, C. Hafner, *Phys. Rev. E* **50**, 4094 (1994)
3. E.D. Palik (ed.), *Handbook of Optical Constants of Solids* (Academic, San Diego, 1985)
4. T. Yatsui, M. Kourogi, M. Ohtsu, *Appl. Phys. Lett.* **71**, 1756 (1997)
5. T. Pangaribun, K. Yamada, S. Jiang, H. Ohsawa, M. Ohtsu, *Jpn. J. Appl. Phys.* **31**, L1302 (1992)
6. G.A. Valaskovic, M. Holton, G.H. Morrison, *Appl. Opt.* **34**, 1215 (1995)
7. T. Yatsui, M. Kourogi, M. Ohtsu, *Appl. Phys. Lett.* **73**, 2090 (1998)
8. Y. Inoue, S. Kawata, *Opt. Lett.* **19**, 159 (1994)
9. D. Marcuse, *Light Transmission Optics*, 2nd edn. Chap. 10 (Krieger, Malabar, 1982)
10. A. Sommerfeld, *Optics*, Chap. VI, 39 (Academic, New York, 1954)
11. S. Mononobe, M. Naya, T. Saiki, M. Ohtsu, *Appl. Opt.* **36**, 1496 (1997)
12. H.U. Danzebrink, T. Dziomba, T. Sulzbach, O. Ohlsson, C. Lehrer, L. Frey, *J. Microsc.* **194**, 335 (1999)
13. T.R. Anthony, *J. Appl. Phys.* **58**, 1240 (1998)
14. T. Yatsui, K. Itsumi, M. Kourogi, M. Ohtsu, *Appl. Phys. Lett.* **80**, 2257 (2002)
15. T. Yatsui, W. Nomura, M. Ohtsu, *J. Nanophotonics* **1**, 011550 (2007)
16. T. Yatsui, M. Kourogi, K. Tsutsui, J. Takahashi, M. Ohtsu, *Opt. Lett.* **25**, 1279 (2000)
17. H. Hosaka, T. Saiki, *J. Microsc.* **202**, 362 (2001)
18. F. Yonezawa (ed.), *Fundamental Physics of Amorphous Semiconductors*, vol. 104 (Springer, Berlin/Heidelberg/New York, 1981)
19. K. Tanaka, *J. Non-Crys. Solids* **59/60**, 925 (1993)
20. B.W. Corb, W.D. Wei, B.L. Averbach, *J. Non-Crys. Solids* **53**, 29 (1994)
21. J. Tominaga, T. Nakano, N. Atoda, *Appl. Phys. Lett.* **73**, 2078 (1998)
22. H. Yoshikawa, Y. Andoh, M. Yamamoto, K. Fukuzawa, T. Tamamura, T. Ohkubo, *Opt. Lett.* **25**, 67 (2000)
23. F. Isshiki, K. Ito, S. Hosaka, *Appl. Phys. Lett.* **76**, 804 (2000)
24. Y.J. Kim, K. Kurihara, K. Suzuki, M. Nomura, S. Mitsugi, M. Chiba, K. Goto, *Jpn. J. Appl. Phys.* **39**, 1538 (2000)

25. T. Yatsui, M. Kourogi, K. Tsutsui, J. Takahashi, M. Ohtsu, *Proc. SPIE 3791* (Denver, Co, USA, 1999) p. 76
26. D.W. Pohl, *IBM J. Res. Dev.* **39**, 701 (1995)
27. M. Yanagisawa, A. Sato, K. Ajiki, F. Watanabe, In: *Tribology of Contact/Near-Contact Recording for Ultra High Density Magnetic Storage*, ed. by C.S. Bhatia, A.K. Menon. TRIB-6 (American Society of Mechanical Engineers, New York, 1996), p. 25
28. M. Ashino, M. Ohtsu, *Appl. Phys. Lett.* **72**, 1299 (1998)
29. T. Matsumoto, T. Ichimura, T. Yatsui, M. Kourogi, T. Saiki, M. Ohtsu, *Opt. Rev.* **5**, 369 (1998)
30. S. Mononobe, T. Saiki, T. Suzuki, S. Koshihara, M. Ohtsu, *Opt. Commun.* **146**, 45 (1998)
31. T. Yatsui, M. Kourogi, M. Ohtsu, *Technical Digest of Quantum Electronics and Laser Science Conference*, Baltimore, 2001, p. 79
32. K. Kurihara, M. Ohtsu, T. Yoshida, T. Abe, H. Hisamoto, K. Suzuki, *Anal. Chem.* **71**, 3558 (1999)
33. Y. Yamamoto, G.-H. Lee, K. Matsuda, T. Shimizu, M. Kourogi, M. Ohtsu, *Opt. Rev.* **7**, 486 (2000)
34. T. Saiki, K. Nishi, M. Ohtsu, *Jpn. J. Appl. Phys.* **37**, 1638 (1998)
35. H. Fukuda, Y. Kadota, M. Ohtsu, *Jpn. J. Appl. Phys.* **38**, L571 (1999)
36. Y. Narita, T. Tadokoro, T. Ikeda, T. Saiki, S. Mononobe, M. Ohtsu, *Appl. Spectrosc.* **52**, 1141 (1998)
37. V.V. Polonski, Y. Yamamoto, M. Kourogi, H. Fukuda, M. Ohtsu, *J. Microsc.* **194**, 545 (1999)
38. Y. Yamamoto, M. Kourogi, M. Ohtsu, V. Polonski, G.-H. Lee, *Appl. Phys. Lett.* **76**, 2173 (2000)
39. M. Ohtsu, K. Kobayashi, H. Ito, G.-H. Lee, *Proc. IEEE* **88**, 1499 (2000)

Takuya Matsumoto

Contents

9.1	Introduction.....	368
9.2	Review of Near-Field Optical Recording.....	368
9.2.1	The Limit of Conventional Optical Recording.....	368
9.2.2	Near-Field Optical Recording Method.....	370
9.2.3	Thermally Assisted Magnetic Recording.....	370
9.2.4	Planer Near-Field Optical Heads.....	371
9.2.5	Highly Efficient Near-Field Optical Head.....	372
9.3	Near-Field Optical Head with a Wedge-Shaped Antenna.....	377
9.3.1	Principle.....	377
9.3.2	Simulation Method.....	378
9.3.3	An Aperture and a Metallic Disk.....	378
9.3.4	Wedge-Shaped Antenna Placed in Air.....	380
9.3.5	Wedge-Shaped Antenna Placed Near the Recording Medium.....	386
9.3.6	Near-Field Optical Head Using a Double Antenna.....	390
9.4	Nanobeak Head.....	392
9.4.1	Principle.....	392
9.4.2	Optical Simulation.....	393
9.4.3	Head Fabrication.....	393
9.4.4	Writing Experiments.....	394
9.5	Summary.....	397
	References.....	398

Abstract

Near-field optical recording is a promising way to realize a recording density of over 1 Tb/in². In this chapter, we focus on anear-field optical head, which is a key device for the near-field opticalrecording. After reviewing the near-field optical

T. Matsumoto (✉)
Central Research Laboratory, Hitachi Ltd., Tokyo, Japan
e-mail: Takuya.Matsumoto@hgst.com

recording technology, we describe highly efficient near-field optical heads with a wedge-shaped antenna and a beaked antenna. Their optical properties and writing experiment results are described.

9.1 Introduction

Increased recording density is required in the storage devices used in personal computers, network servers, home servers, and other multimedia devices as users increasingly want to save large amount of images, movies, music files, and so on. To meet this demand, the recording density of storage devices has been steadily increased. For example, the recording density of optical recording devices reached 19.5 Gb/in^2 in the case of the Blu-ray disk drive introduced to the market in 2003, while that of hard disk drives (HDDs) on the market reached about 700 Gb/in^2 in 2011.

However, the rise in recording densities seems to be encountering barriers in both optical and magnetic recording. In the case of optical recording, the recording density depends on the spot size of the focused laser. However, the minimum spot size is limited by the diffraction of light, and the recording density cannot be increased beyond this limit. In the case of magnetic recording, the recorded information is expected to decay spontaneously because of thermal fluctuation in the magnetic domains when the recording density approaches 1 Tb/in^2 . A solution is to increase the coercivity of magnetic recording medium. However, conventional writing heads cannot generate a magnetic field large enough to write data on such recording medium because of a fundamental limit on the saturation moment of the writing head material.

As a method to overcome these limits, near-field optical recording is now drawing much attention. In this recording, the data bits are written and read by using an optical near-field generated near a nanometer-scale object. Because the size of the optical spot is not limited by the diffraction of light and can be reduced to less than a few tens of nanometers [1], this method is expected to enable a recording density of over 1 Tb/in^2 .

In a near-field optical recording device, the key component is a near-field optical head that generates the optical near-field. In this chapter, after briefly reviewing near-field optical recording, we describe a highly efficient near-field optical head that uses a plasmonic antenna; the intensity of the optical near-field is enhanced by a plasmon generated in the antenna.

9.2 Review of Near-Field Optical Recording

9.2.1 The Limit of Conventional Optical Recording

The recording density of conventional optical recording drives has been increased by reducing the spot size of the focused laser. However, the minimum spot size, D , is governed by the law of diffraction and is approximately

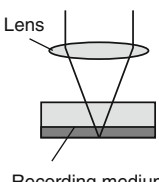
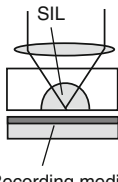
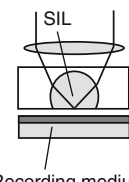
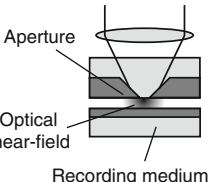
	Conventional lens	Solid immersion lens		Near-field optical head (Aperture)
		Hemisphere	Weierstrass sphere	
Head				
Spot size	λ/NA	$\lambda/(n \cdot NA)$	$\lambda/(n^2 \cdot NA)$	Aperture diameter (<100 nm)
Head-media separation	$> 1 \mu\text{m}$	$< 100 \text{ nm}$	$< 100 \text{ nm}$	$< 10\text{-}20 \text{ nm}$

Fig. 9.1 Light focusing methods in optical recording devices

$$D = \lambda/N.A. \quad (9.1)$$

where λ is the light wavelength and N.A. is the numerical aperture of the focusing lens. As an example, in the most advanced optical recording device, the Blu-ray disk drive, the laser wavelength is 405 nm, and the N.A. is 0.85; thus, the spot size is approximately 480 nm. To reduce the spot size further, we must decrease the laser wavelength or increase the N.A. of the focusing lens. However, a wavelength of less than 405 nm cannot be obtained from currently available semiconductor laser diodes, and it is difficult to make the N.A. larger than 0.85 because a larger N.A. reduces the tolerance for recording disk fluctuation. Therefore, it will be difficult to further reduce the spot size.

One way to reduce the spot size is to place a hemispherical or a Weierstrass-sphere-shaped lens, called a solid immersion lens (SIL), near the recording medium (Fig. 9.1) [2, 3]. When an SIL is placed near the recording medium, the wavelength inside the sphere is reduced by a factor of n , where n is the refractive index of the lens; thus, the spot size is reduced to

$$D = \lambda/n N.A. \quad (9.2)$$

In addition, in the case of the Weierstrass-sphere lens, the incident rays are refracted at the sphere's surface. This corresponds to an increased N.A., and the spot size is further reduced to

$$D = \lambda/n^2 N.A. \quad (9.3)$$

This small optical spot enables increased recording density. For example, a recording density of about 70 Gb/in² has been realized using an SIL made of Bi4Ge3O12 with a refractive index of 2.23 [4]. This type of recording method is

sometimes classified as near-field optical recording because it uses an evanescent wave generated by a ray whose incident angle is larger than the critical angle. However, the spot size is still limited by the diffraction limit of light, and no dramatic increase of recording density is expected.

9.2.2 Near-Field Optical Recording Method

In near-field optical recording, the data bits are written and read by using the optical near-field. When light is introduced into a nanometer-scale object, such as a subwavelength aperture or scatterer, a localized electromagnetic field – the optical near-field – is generated near the object. The distribution of the optical near-field is determined by the object's shape and size and does not depend on the light wavelength. For example, when the optical near-field is generated by the subwavelength aperture, the width of the near-field distribution is as small as the aperture diameter [1]. Therefore, a high recording density beyond the diffraction limit can be achieved by writing and reading data bits using the optical near-field.

Betzig et al. have demonstrated near-field optical recording using a magneto-optical recording medium [5]. They generated the optical near-field using a fiber probe, which is widely used in scanning near-field optical microscopy (SNOM). In the writing process, a Pt/Co multilayer recording medium was heated to the Curie temperature by the optical near-field to reverse the magnetization of the recording medium. In the reading process, transmitted light from the recording medium was collected by the fiber probe and the rotation of the light polarization caused by the Faraday effect was detected. They have written and read recording marks with a diameter of 60 nm, which corresponds to a recording density of 170 Gb/in².

Near-field optical recording using a phase-change recording medium or a photochromic recording medium has been reported by, respectively, Hosaka et al. [6] and Jiang et al. [7]. In the phase-change recording, the recording medium is heated by light to change its phase from amorphous to crystal. Hosaka et al. used GeSbTe recording medium and wrote and read recording marks with a diameter of 60 nm using a fiber probe. In the photochromic recording, the recording marks are written through a photochemical reaction. Jiang et al. wrote and read recording marks with a diameter of 130 nm on a Langmuir-Blodgett film of photochromic material.

9.2.3 Thermally Assisted Magnetic Recording

A hybrid recording method, known as thermally assisted magnetic recording or heat-assisted magnetic recording, has also been proposed [8–10]. In this method, data bits are written on a magnetic recording medium by applying a magnetic field, while the medium is heated by the optical near-field and read out with a reading

head used for hard disk drives, such as a giant magneto-resistive (GMR) head or a tunneling magnetoresistive (TMR) head. Because GMR and TMR heads are highly sensitive to magnetic fields, a high signal-to-noise ratio in the reading signal can be achieved. Note that the problem of thermal fluctuation in the magnetic domains can be solved when data bits are written using the optical near-field. During the writing process, the recording medium is heated by light; hence, its coercivity is decreased. Therefore, a recording medium with high coercivity can be used to make the magnetic domains stable.

9.2.4 Planer Near-Field Optical Heads

The optical near-field is localized near the aperture or the scatterer and its intensity decreases exponentially as the distance from the surface of the head increases. Because the decay length is less than 10 nm, the spacing between the head and the recording medium must be maintained within a range of 5–10 nm.

With the fiber probe, the spacing is controlled by using the shear force acting between the fiber probe and the recording medium [11, 12]. In this method, the fiber probe is dithered parallel to the surface of the recording medium. Because the dithering amplitude is changed by the shear force, a feedback loop can be constructed by detecting the change in the dithering amplitude. However, in a practical recording device, the recording disk rotates at a very high speed. For example, when the recording density is 1 Tb/in² and the data transmission rate is 1 Gbps, the linear velocity of the recording medium is about 30 m/s. If the fiber probe is placed near recording medium rotating at such speed, the fiber probe soon crashes because the response based on shear-force feedback is too slow.

This problem can be solved by using mounting the near-field optical head on the slider used for the hard disk drive. In the hard disk drive, the spacing between the head and the recording medium is maintained at a constant value by air pressure acting between the slider and the recording medium (The air pressure is determined by the design of pads formed on the slider surface). The head-medium spacing of hard disk drives is less than 10 nm, and by applying this technology to the near-field optical head, we can precisely control and maintain the spacing between the near-field optical head and the recording medium.

To mount the near-field optical head on the slider, several planar near-field optical heads have been proposed.

Lee et al. have proposed a silicon planar near-field optical head that has an array of square apertures (Fig. 9.2a) [13]. The 60 × 60 nm apertures were fabricated by an isotropic etching process and a line pattern with a line width of 250 nm was read out with this near-field optical head.

Isshiki et al. have proposed a planar near-field optical head with an aperture formed on a pyramidal protrusion (Fig. 9.2b) [14]. They fabricated the pyramidal protrusion by cutting the glass substrate with a focused ion beam and fabricated the aperture by coating the protrusion with metal and slicing the apex with a focused ion beam. They read out a 250-nm line pattern on a disk rotating at a linear velocity

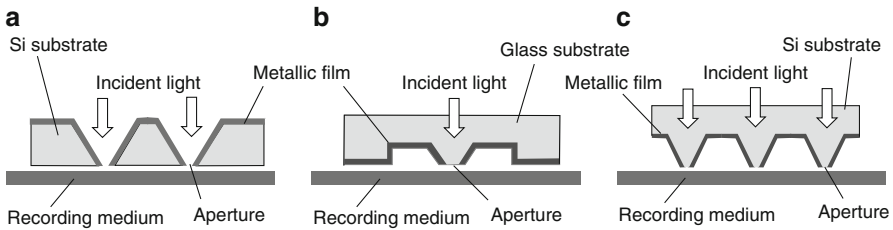


Fig. 9.2 Examples of planar near-field optical heads: (a) Head with an array of apertures formed in a Si substrate, (b) head with an aperture formed on a glass protrusion, and (c) head with an array of apertures formed on Si protrusions

of 0.38 m/s. The data transmission rate and carrier-to-noise ratio were, respectively, 1.5 Mbps and 37 dB (bandwidth: 10 kHz).

Yatsui et al. have also proposed a planar near-field optical head with an array of apertures formed on silicon pyramidal protrusions (Fig. 9.2c) [15]. They fabricated the array of silicon pyramidal protrusions through an isotropic etching process and formed the apertures at the apices of the protrusions. They used phase-change recording medium and succeeded in writing and reading data bits using the apertures. The recording medium was rotated at a linear velocity of 0.43 m/s, and the minimum mark length and the data transmission rate were, respectively, 110 nm and 2.0 MHz. Note that parallel writing and reading using the aperture array is expected to enable a high data transmission rate.

9.2.5 Highly Efficient Near-Field Optical Head

When a subwavelength aperture is used to generate the optical near-field, efficiency (defined as the ratio between the power of the optical near-field and that of the incident light) is quite low. For example, the efficiency is 10^{-4} – 10^{-5} when the aperture diameter is 60 nm [5], and it decreases further as the aperture diameter becomes smaller. This is because a cutoff diameter exists for mode propagation in the waveguide. When the diameter of the tapered waveguide becomes smaller than the cutoff diameter, the propagating light suffers a huge loss and its intensity decays exponentially.

This low efficiency is a serious hindrance to realizing practical near-field optical recording devices. For example, in the case of thermally assisted recording, the required temperature rise in the medium is more than 300°C, and the rise time has to be less than a few ns. For this requirement, the efficiency of the head has to be more than 10%.

To raise efficiency, several methods have been proposed, such as:

1. Optimization of the waveguide shape
2. Use of a metallic waveguide
3. Use of a surface plasmon

Low efficiency has also been a problem for SNOM when observing a weak optical signal, such as photoluminescence or a nonlinear signal. Although most of these methods have been developed for SNOM applications, they may also be applied to near-field optical recording. Here, we explain these methods briefly.

Optimization of the Waveguide Shape. A double- and triple-tapered fiber probe (Fig. 9.3) have been proposed to increase the efficiency by, respectively, Saiki et al. [16] and Yatsui et al. [17]. In this type of fiber probe, efficiency is increased by optimizing the waveguide shape. As mentioned, when light is introduced into the tapered waveguide, the light power decreases in the loss region where the waveguide diameter is smaller than the cutoff diameter. In double- and triple-tapered fiber probes, high efficiency is realized by shortening the length of the loss region. In the case of the triple-tapered probe, efficiency is also increased because the edge between the second and third tapers excites the HE-plasmon mode, which has a smaller cutoff diameter. The efficiency of the double-tapered probe is 10 times higher than that of a conventional probe, and the efficiency of the triple-tapered probe is 1,000 times higher than that of a conventional probe.

Use of a Metallic Waveguide. A coaxial probe and a metallic pin probe have been proposed by, respectively, Fischer et al. [18] and Takahara et al. [19]. These probes have metallic cores, and high efficiency is expected because there exists a mode propagating at the surface of the metallic core, and this mode does not have a cutoff diameter.

Use of a Surface Plasmon. Fischer et al. have proposed a tetrahedral probe that uses a surface plasmon generated on a surface of a metallic film [20, 21]. The surface plasmon is a collective oscillation of electrons generated on a surface of a thin metallic film by irradiating the film with light [22]. When the surface plasmon is excited, the electric field near the metallic field is enhanced. In the tetrahedral probe, the surface plasmon is excited on the metallic film on the tetrahedral glass chip and propagates toward the apex. Thus, the electric field at the apex is enhanced.

Thio et al. have proposed a structure that consists of a subwavelength aperture created in a metallic film and a set of concentric circular grooves surrounding the aperture [23]. When light is introduced into this structure, the surface plasmon is excited on the metallic film by the circular grooves, and the optical near-field intensity at the aperture is enhanced because the surface plasmon assists the light transmitting through the aperture. In their experiment, the transmission of the aperture with the grooves was 50 times that of an aperture without grooves.

Fischer et al. have also proposed a probe that uses a surface plasmon generated at a subwavelength metallic sphere [24].

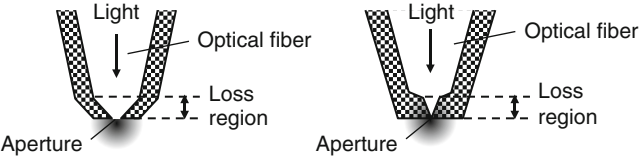
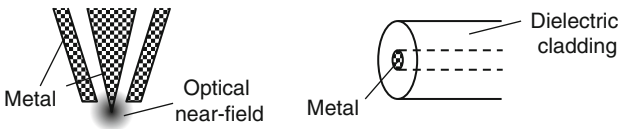
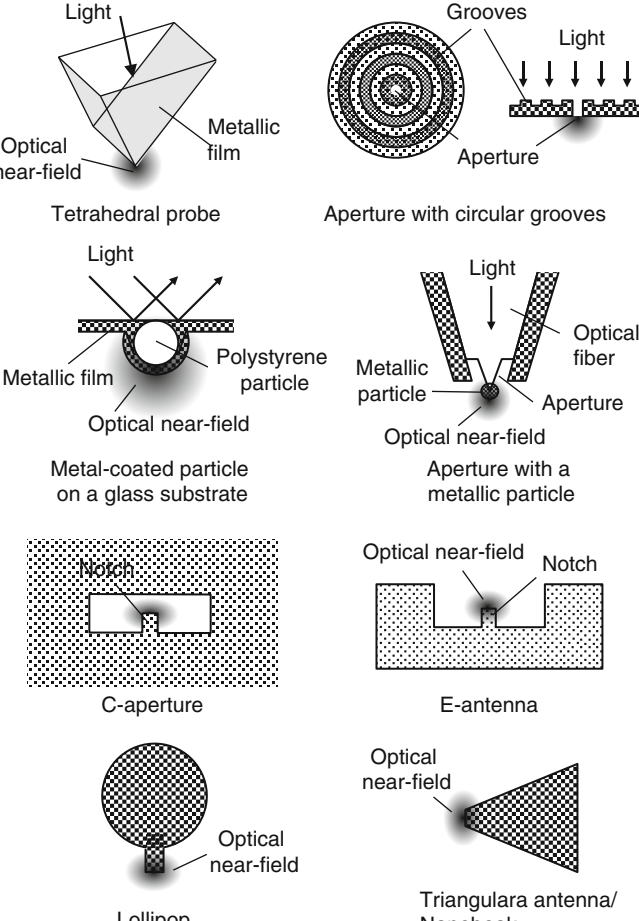
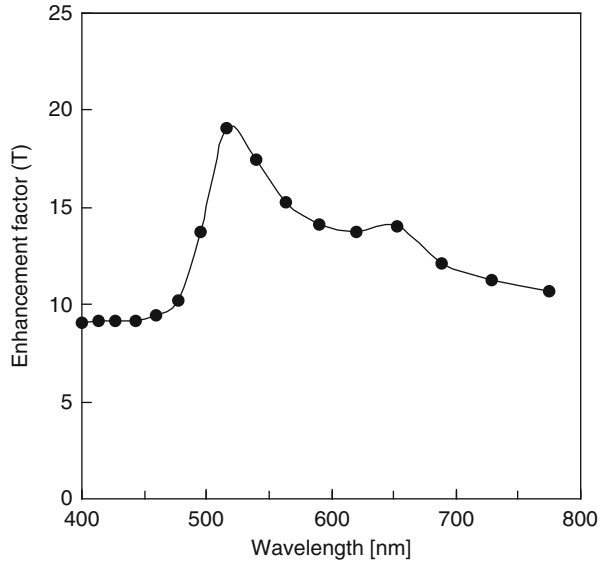
<p>Optimize the waveguide shape</p>	 <p>Light</p> <p>Optical fiber</p> <p>Aperture</p> <p>Loss region</p> <p>Double-tapered probe</p> <p>Triple-tapered probe</p>
<p>Use of a metallic waveguide</p>	 <p>Metal</p> <p>Optical near-field</p> <p>Metal</p> <p>Dielectric cladding</p>
<p>Use of a surface plasmon</p>	 <p>Light</p> <p>Optical near-field</p> <p>Metallic film</p> <p>Tetrahedral probe</p> <p>Grooves</p> <p>Light</p> <p>Aperture</p> <p>Aperture with circular grooves</p> <p>Light</p> <p>Metallic film</p> <p>Polystyrene particle</p> <p>Optical near-field</p> <p>Metal-coated particle on a glass substrate</p> <p>Light</p> <p>Metallic particle</p> <p>Optical fiber</p> <p>Aperture</p> <p>Optical near-field</p> <p>Aperture with a metallic particle</p> <p>Optical near-field</p> <p>Notch</p> <p>C-aperture</p> <p>Optical near-field</p> <p>Notch</p> <p>E-antenna</p> <p>Optical near-field</p> <p>Lollipop</p> <p>Optical near-field</p> <p>Triangular antenna/Nanobeak</p>

Fig. 9.3 Examples of methods to increase efficiency

Fig. 9.4 Relation between the enhancement factor and the wavelength for a gold sphere calculated by a dipole model



When light is introduced into the subwavelength metallic sphere, the dipole moment p inside the sphere is given by

$$p = 4\pi\epsilon_0 a^3 (\epsilon(\omega) - 1) / (\epsilon(\omega) + 2) E_0, \quad (9.4)$$

where $\epsilon(\omega)$ is the dielectric constant of the sphere, ω is the angular frequency of the light, a is the radius of the sphere, ϵ_0 is the dielectric constant of vacuum, and E_0 is the magnitude of the applied electric field [22]. The field E_s at the surface of the sphere is the superposition of the field generated by the dipole and the applied field E_0 and is given by

$$E_s = 3\epsilon(\omega) / (\epsilon(\omega) + 2) E_0. \quad (9.5)$$

As shown in this equation, E_s is enhanced when the light frequency satisfies the equation

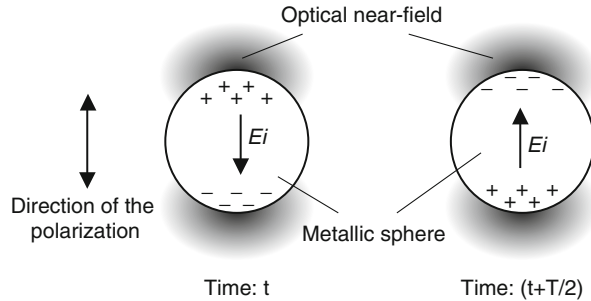
$$\text{Re}(\epsilon(\omega)) = -2. \quad (9.6)$$

As an example, Fig. 9.4 shows the relation between the wavelength and an enhancement factor T given by

$$T = |E_s/E_0|^2 \quad (9.7)$$

for a gold sphere. In this calculation, the experimental value given in [25] was used as the dielectric constant of the gold. As shown in this figure, the field at the surface became greater when the wavelength was near 500 nm.

Fig. 9.5 Schematic of a localized plasmon excited in a metallic particle



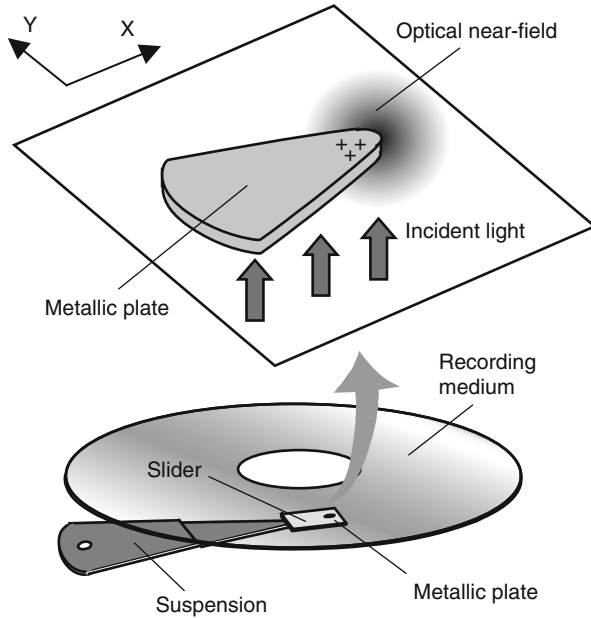
The peak corresponds to a resonance condition of the collective oscillation of the electrons in the metallic sphere. When the sphere is illuminated by light, charges in the sphere move to the surface (Fig. 9.5). These charges give rise to an internal field (depolarization field) E_i ; hence, a restoring force acts on the charges. This force causes a charge oscillation that has a resonance frequency satisfying Eq. (9.6). If the light frequency corresponds to the resonance frequency of the charge oscillation, light energy is strongly absorbed by the sphere and the optical near-field at the surface is enhanced. The quantum of the collective oscillation of the charges in the small metallic particle is called a localized surface plasmon or a localized plasmon.

In the experiment by Fischer et al., a small polystyrene sphere coated with gold film was formed on a prism surface, and it was illuminated by light under a total internal reflection condition to excite the localized plasmon. The field enhancement effect by the localized plasmon was observed by placing a substrate near the particle and detecting the scattered light caused by the interaction with the substrate.

A fiber probe having a metallic particle at its apex has also been proposed by Matsumoto et al. [26]. An aperture was formed at the apex of a tapered optical fiber, and the particle was created at the center of the aperture. Because the light was introduced and collected through the aperture, the amount of background light in the detected light was reduced.

Shi et al. has proposed a C-aperture that consists of a subwavelength aperture and a notch created in a metallic film [27]. When it is illuminated by light polarized parallel to the notch, charges in the metallic film concentrate at the notch and an optical near-field is generated in the vicinity of the notch. By optimizing the dimensions of the aperture and the notch, a surface plasmon is excited in the metallic film, and the optical near-field intensity is enhanced. Stipe et al. has proposed an E-antenna which works with the same operating principles and integrated it into a magnetic head [28]. Using a bit-patterned magnetic medium, thermally assisted magnetic recording at an areal density of about 1 Tb/in^2 was demonstrated.

Fig. 9.6 Schematic of the near-field optical head with a wedge-shaped antenna



Challener et al. has proposed a lollipop transducer that consists of a subwavelength gold disk and a peg for thermally assisted magnetic recording [29]. When the gold disk is illuminated by light, a surface plasmon is excited at the disk, and a strong optical near-field is generated in the vicinity of the peg. This transducer was integrated into a magnetic head and used to record data at an areal density of 240 G/in².

9.3 Near-Field Optical Head with a Wedge-Shaped Antenna

As an highly efficient near-field optical head, a near-field optical head using a plasmon generated by a wedge-shaped antenna has been proposed [30, 31]. In this section, we describe its principle and simulation results.

9.3.1 Principle

This head consists of a transparent substrate and a wedge-shaped metallic antenna, a metallic antenna in the shape of a sector or a triangle, formed at the bottom of the substrate (Fig. 9.6). When the antenna is illuminated by light polarized in the x direction, charges oscillate in the x direction and concentrate at the apex. These concentrated charges generate a localized electromagnetic field, i.e., an optical near-field close to the apex of the antenna.

The optical near-field is enhanced when the plasmon is excited in the antenna. That is, the displacement of charges creates a depolarization field inside the antenna. Because of this field, the charges act like an oscillator system as is the case with a metallic sphere. When the light frequency corresponds to the resonance frequency of this oscillation, light energy is strongly absorbed and the intensity at the apex is enhanced.

9.3.2 Simulation Method

To check the feasibility of the proposed head, the distribution of the optical near-field was calculated through a finite-difference time-domain (FDTD) calculation.

In this calculation, the incident light was assumed to be a plane wave. Experimental values given in reference [25] were used as the dielectric constants of the metal. The cell size was made large near the boundary and small near the object to be calculated to minimize the computer memory required. When the object was the wedge-shaped antenna, the cell size was designed to have the smallest value near the apex, and the minimum cell size was 1/10 of the radius of the apex. As the boundary condition, Mur's absorption boundary condition was used. A parallel computer with 24 processors was used for the calculation.

9.3.3 An Aperture and a Metallic Disk

To begin with, for reference we will show the optical near-field distribution generated near a subwavelength aperture and a metallic disk.

9.3.3.1 Aperture

Figure 9.8 shows the intensity distribution of an optical near-field generated near an aperture created in a metallic film as shown in Fig. 9.7. For this calculation, we assumed that the metallic film was a gold film with a thickness (t) of 100 nm, the diameter (a) of the aperture was 30 nm, and the wavelength of the incident light was 650 nm. The polarization of the incident light was in the direction of the arrows in Fig. 9.8. The distance (d) between the observation plane and the aperture was 5 nm. The unit of intensity was the ratio between the intensity of the optical near-field and that of the incident light. As shown in this figure, intensity at the aperture became lower than the incident light intensity. The intensity at the peak was about 0.04 times that of the incident light.

9.3.3.2 Metallic Disk

Figure 9.10 shows the intensity distribution of the optical near-field near a metallic disk as shown in Fig. 9.9. For this calculation, we assumed that both the diameter (a') and the thickness (t) were 30 nm, the metal was gold, and the wavelength of the incident light was 650 nm. The polarization of the incident light was in the direction of the arrows shown in Fig. 9.10. The distance (d) between the observation plane and

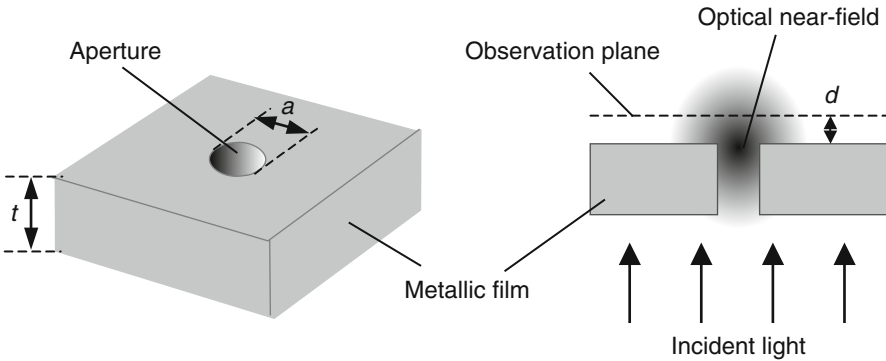


Fig. 9.7 Simulation model for an aperture

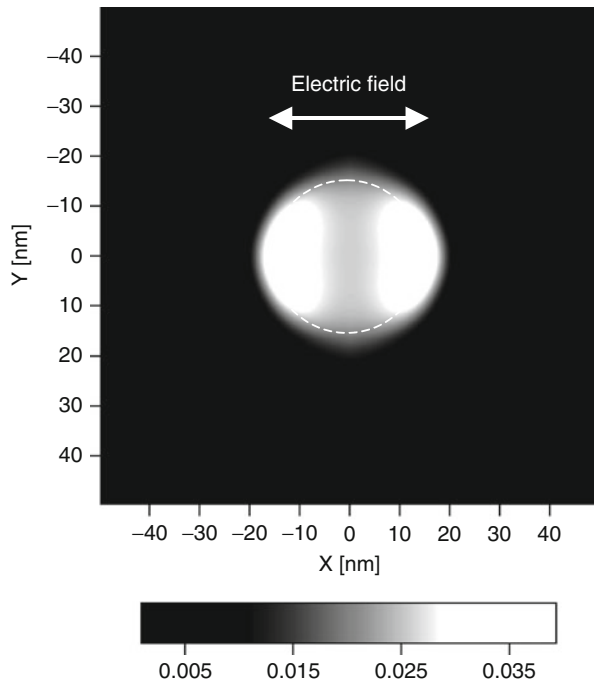


Fig. 9.8 Intensity distribution of the optical near-field generated near an aperture created in a metallic film. It was assumed that the metal was gold, the aperture diameter was 30 nm, and the thickness of the metallic film was 100 nm. The distribution was measured on a plane 5 nm from the antenna

the aperture was 5 nm. As shown in this figure, the near-field intensity became high at the edges A and A' of the metallic disk. This is because the charges in the metallic disk accumulated at these edges. The intensity at the peak was 3.5 times that of the incident light. Figure 9.11 shows the dependence of the optical near-field intensity (intensity at the peak) on the wavelength of the incident light. In this calculation, the near-field intensity was measured on a plane 2 nm from the metallic disk. As shown in this figure, the curve was almost the same as that of the metallic sphere calculated

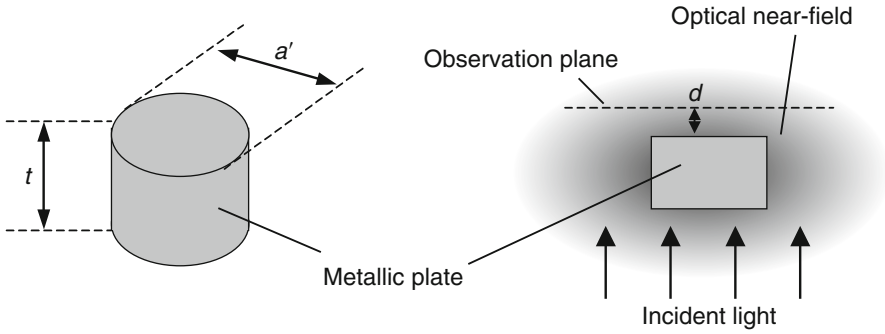


Fig. 9.9 Simulation model for a metallic disk

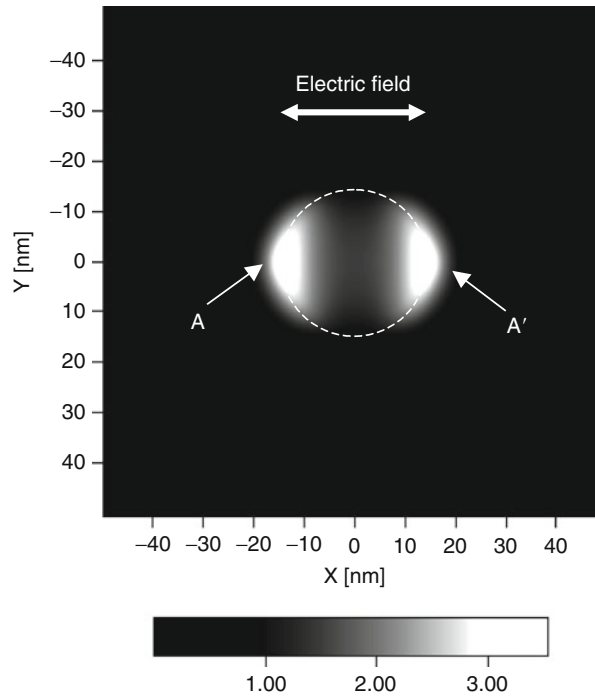


Fig. 9.10 Intensity distribution of the optical near-field generated near a metallic disk. It was assumed that the metal was gold, and the circle diameter and the metallic film thickness were both 30 nm. The distribution was measured on a plane 5 nm from the antenna

by Eq. (9.6), and the optical near-field intensity became high near a wavelength of 550 nm, which corresponds to the resonance wavelength of the localized plasmon.

9.3.4 Wedge-Shaped Antenna Placed in Air

In this subsection, we will present simulation results for the wedge-shaped antenna placed in air and describe the fundamental properties of the optical near-field

Fig. 9.11 Intensity of the optical near-field generated near the metallic disk as a function of the incident light wavelength. The intensity was measured on a plane 2 nm from the antenna

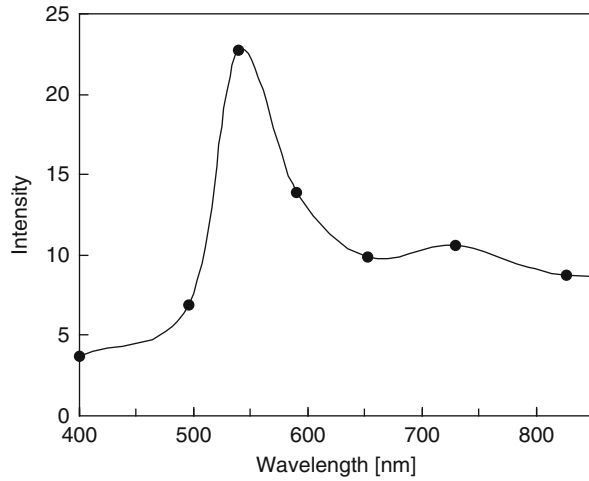
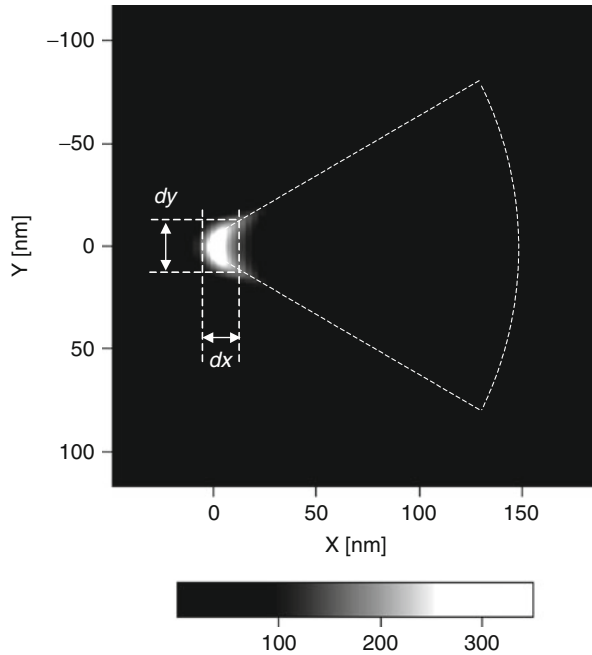


Fig. 9.12 Intensity distribution of the optical near-field generated near an antenna in the shape of a sector. It was assumed that the radius (r) of the apex was 10 nm, the length (L) was 150 nm, the thickness (t) was 30 nm, the apex angle (θ) was 60° , and the incident light wavelength was 690 nm. The distribution was measured on a plane 5 nm from the antenna. The unit of intensity was the ratio between the intensity of the optical near-field and that of the incident light



generated near the antenna, such as the intensity distribution, efficiency, and resonance property of the plasmon.

9.3.4.1 Near-Field Distribution

Figure 9.12 shows the optical near-field distribution near the antenna in the shape of a sector as shown in Fig. 9.13a. For this simulation, we assumed that the metal

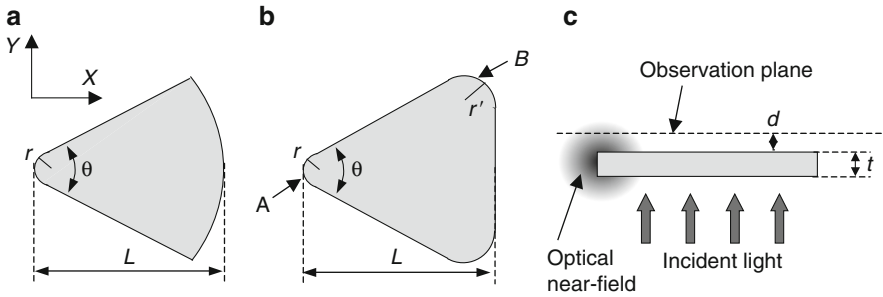


Fig. 9.13 Simulation model for the wedge-shaped antenna: (a) antenna in the shape of a sector, (b) antenna in the shape of a triangle, and (c) side view

was gold, the radius (r) of the apex was 10 nm, the length (L) was 150 nm, the thickness (t) was 30 nm, the apex angle (θ) was 60° , and the wavelength of the incident light was 690 nm. The distribution was measured on a plane 5 nm from the antenna. The unit of intensity was the ratio between the intensity (power density) of the optical near-field and that of incident light. As shown in these figures, a strong optical near-field was generated at the apex, and the peak intensity was 350 times that of the incident light. This intensity was 8,750 times that of the 30-nm aperture created in the metallic film and 85 times that of the metallic disk. The distribution measured at half maximum was 15 nm wide in the x direction and 25 nm wide in the y direction.

For this type of near-field optical head, the polarization must be in the x direction as shown in Fig. 9.13. Figure 9.14 shows a near-field distribution when the polarization of the incident light was in the y direction. As shown in this figure, the optical near-field became strong along the side edges of the antenna but weak at the apex. This is because the charges oscillate in the direction parallel to the y -axis; hence, the charges accumulate along the side edges instead of accumulating at the apex.

Figure 9.15 shows the near-field distribution when the shape of the antenna was a triangle. For this calculation, we assumed that the metal was gold, the radius (r) of apex A was 10 nm, the radius (r') of apices B was 30 nm, the apex angle (θ) was 60° , the thickness (t) was 30 nm, and the wavelength of the incident light was 690 nm. The distribution was measured on a plane 5 nm from the antenna. As shown in this figure, a strong optical near-field was also generated at apex A as with the antenna in the shape of the sector. The distribution at the apex was the same as that of the antenna in the shape of the sector. Note that the radius (r') of apices B should be larger than the radius (r) of the apex A; otherwise charges also concentrate at apices B, and a high optical near-field intensity is also generated there.

9.3.4.2 Dependence of the Spot Size on the Radius of the Apex

The size of the optical spot also depends on the radius (r) of the apex. Figure 9.16 shows the size of the optical spot as a function of the radius of the apex simulated

Fig. 9.14 Intensity distribution of the optical near-field when the polarization was in the y direction

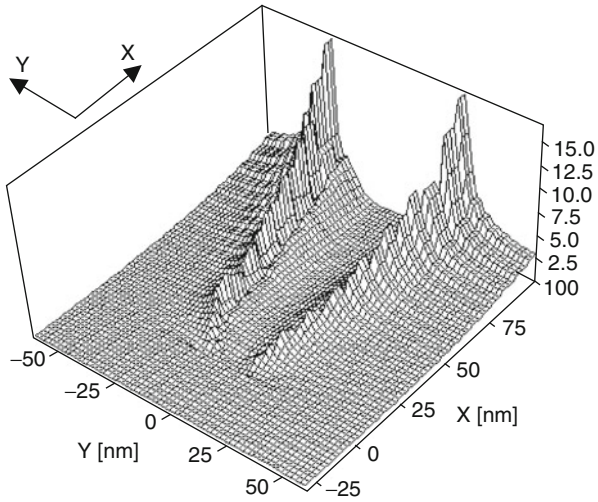
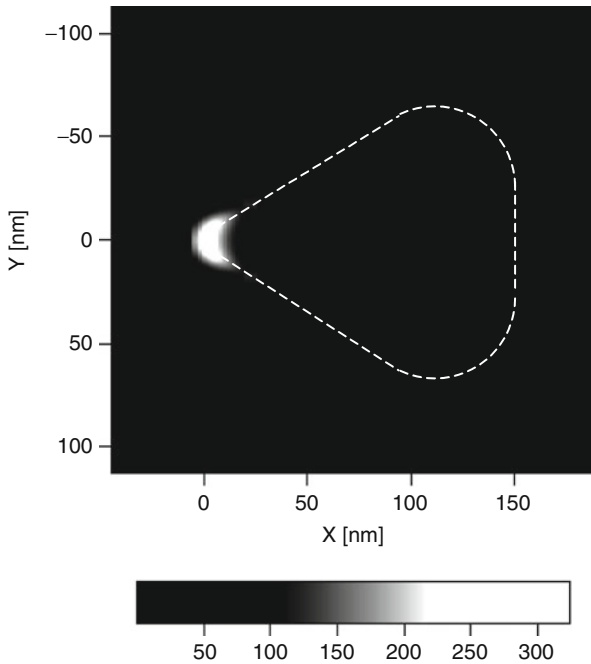
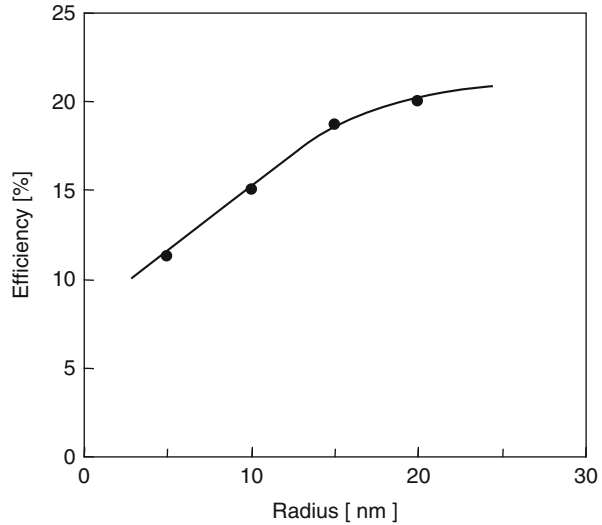


Fig. 9.15 Intensity distribution of the optical near-field generated near an antenna in the shape of a triangle. It was assumed that the metal was gold, the radius (r) of apex A was 10 nm, the radius (r') of apices B was 30 nm, the apex angle (θ) was 60° , the thickness (t) was 30 nm, and the incident light wavelength was 690 nm. The distribution was measured on a plane 5 nm from the antenna



for the antenna in the shape of the sector. The solid line shows the width measured at half maximum in the x direction (dx), and the broken line shows the width measured at half maximum in the y direction (dy). The distribution was measured on a plane 5 nm from the antenna. As shown, the spot size decreased linearly as the radius of the apex became smaller. Note that the peak intensity rose as the apex radius

Fig. 9.16 Dependence of the spot size and the intensity on the radius of the apex. The distance between the observation plane and the antenna was 5 nm



was reduced (dash-dot line in Fig. 9.18). This is because oscillating charges are concentrated in a smaller area, and the charge density at the apex increases.

9.3.4.3 Efficiency

Here, we estimate the efficiency (η) by defining it as

$$\eta = \frac{\int_S p_{\text{near}} dS}{\int_{S'} p_{\text{in}} dS'} \quad (9.8)$$

where p_{near} is the power density (intensity) of the optical near-field, p_{in} is that of the incident light, and S and S' are the areas where the power density is higher than half maximum. The efficiency calculated for the near-field distribution in Fig. 9.12 was about 15% if we assume that the incident beam was a Gaussian beam with a full width at half maximum of $1 \mu\text{m}$ (corresponding to an optical spot focused by a lens with an N.A. of 0.35). When we calculated the near-field distribution, we assumed the incident light was a plane wave. Therefore, in this estimation, the diameter of the incident beam was assumed to be $1 \mu\text{m}$ so that the incident light intensity would be nearly constant at the antenna. However, under such a condition, the energy loss is large because much of the light is not incident on the antenna. Higher efficiency should be attainable by reducing the diameter of the incident light.

9.3.4.4 Tuning of the Resonance Wavelength of the Plasmon

The wavelength of the incident light must correspond to the resonance wavelength of the plasmon to generate a strong optical near-field. However, the available wavelength is limited if we use a semiconductor laser as the light source. Therefore, we need to tune the resonance wavelength of the plasmon to the wavelength of

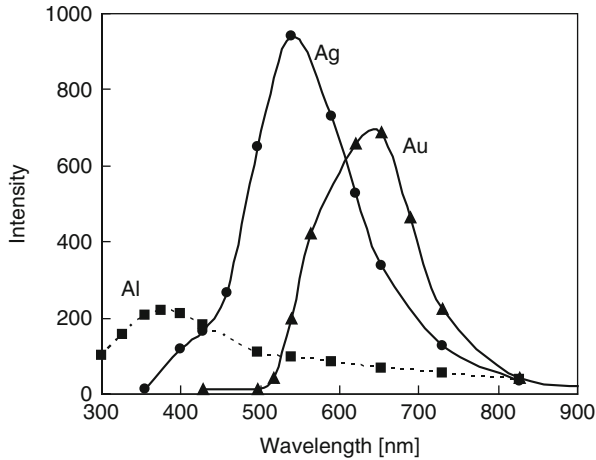


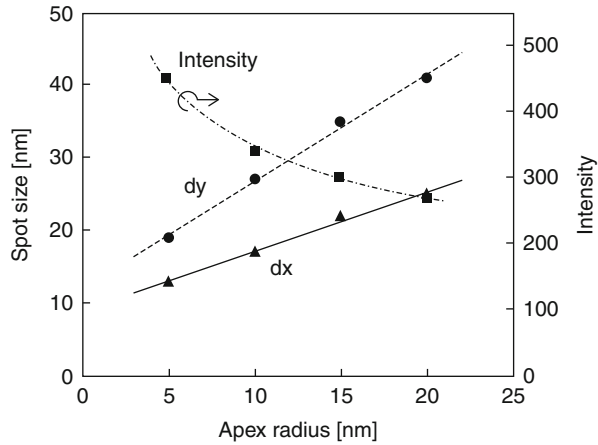
Fig. 9.17 Relation between the near-field intensity and the wavelength for antennas made of silver, gold, and aluminum. The shape of the antenna was assumed to be a sector with an apex radius (r) of 20 nm, a length (L) of 150 nm, a thickness (t) of 30 nm, and an apex angle (θ) of 60° . The closed triangles, closed circles, and closed squares represent the values for gold, silver, and aluminum, respectively. The intensity represents the peak intensity in the distribution measured on a plane 2 nm from the antenna

the semiconductor laser. For the wedge-shaped antenna, the resonance wavelength of the plasmon can be adjusted by changing the material or the length (L) of the antenna. In this subsection, we will describe how the resonance wavelength depends on these parameters.

Figure 9.17 shows the relation between the optical near-field intensity and the incident light wavelength for antennas made of gold, silver, and aluminum. For this calculation, we assumed the shape of the antenna was a sector with an apex radius (r) of 20 nm, a length (L) of 150 nm, a thickness (t) of 30 nm, and an apex angle (θ) of 60° . The intensity represents the peak intensity in a distribution measured on a plane 2 nm from the antenna. The closed triangles, closed circles, and closed squares represent the values for gold, silver, and aluminum, respectively. The resonance wavelength of gold was about 650 nm, which is near the wavelengths of a red semiconductor laser (635, 650, and 670 nm). The resonance wavelength of aluminum was 370 nm, which is near the wavelength of a blue semiconductor laser (405 nm). In the case of silver, the resonance wavelength was 550 nm. Although, there is no semiconductor laser of such wavelength, the resonance wavelength can be shifted toward the red or near-infrared regions by changing the length (L) as we explain next.

The near-field intensity at the resonance wavelength became larger in the order of $\text{Al} < \text{Au} < \text{Ag}$. This indicates that the near-field intensity becomes large when the imaginary part of the dielectric constant becomes small. This is because the damping of the charge oscillation, which causes energy loss, becomes small when

Fig. 9.18 Relation between the near-field intensity and the wavelength for antennas of various lengths. It was assumed that the shape of the antenna was a sector with an apex radius (r) of 20 nm, a thickness (t) of 30 nm, and an apex angle (θ) of 60° , and that the metal was silver. The intensity represents the peak intensity in the distribution measured on a plane 2 nm from the antenna



the imaginary part of the dielectric constant is small. To realize high efficiency, we therefore need to use a metal whose dielectric constant has a small imaginary part.

The resonance wavelength depends on the depolarization field inside the antenna. Because the depolarization field depends on the length (L) of the antenna, the resonance wavelength can be adjusted by changing the length. Figure 9.18 shows the resonance curves when the length (L) was varied from 100 to 600 nm. For this calculation, we assumed that the shape of the antenna was a sector with an apex radius (r) of 20 nm, a thickness (t) of 30 nm, and an apex angle (θ) of 60° , and that the metal was silver. The intensity represents the peak intensity in the distribution measured on a plane 2 nm from the antenna. As shown, the resonance wavelength of the plasmon shifted toward a longer wavelength when the antenna became longer. When the length became greater than 400 nm, a second peak appeared at a short wavelength. This is because another resonance mode was excited at this peak. The broadening of the resonance curve when the length increases was probably due to the radiation damping [32].

9.3.5 Wedge-Shaped Antenna Placed Near the Recording Medium

In the previous calculation, the antenna was placed in air. However, in recording devices, the antenna is formed on the slider (a transparent substrate), and placed near the recording medium. In this subsection, we will describe the resonance property of the plasmon and the near-field distribution in such a situation.

Simulation Model. To realize high durability, the antenna should be embedded in the slider surface as shown in Fig. 9.19. Thus, we assumed that the antenna was embedded in a glass substrate with a refractive index of 1.45. The recording medium was assumed to be a thin film of TbFeCo or GeSbTe with a thickness of 20 nm, and the separation between the recording medium and the antenna was assumed to be

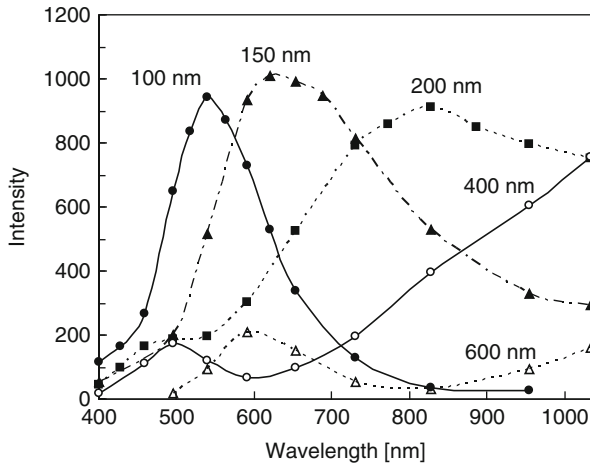


Fig. 9.19 Simulation model when the recording medium and slider were placed near the antenna: (a) when there was no recording medium and (b) when there was a recording medium

10 nm. For the antenna, we assumed that the metal was gold, the apex radius (r) was 10 nm, the length (L) was 150 nm, the thickness (t) was 30 nm, and the apex angle (θ) was 60° .

Resonance Property of the Plasmon. First, we show the influence of the glass substrate on the resonance property of the plasmon. Figure 9.20 shows the resonance curve when there was no recording medium. The solid line represents the resonance curve for the antenna embedded in the glass substrate, and the broken line represents the resonance curve when the antenna was placed in air. The intensity represents the peak intensity in the distribution measured on a plane 2 nm from the antenna. As shown, the resonance wavelength shifted by about 50 nm toward a longer wavelength when the antenna was embedded in the glass substrate. We believe this was because the dipoles in the dielectric substrate interact with the charges in the antenna and weaken the restoring force working on the charges.

Figure 9.21 shows the resonance curves when the recording medium was placed near the antenna embedded in the glass substrate. The solid line represents the resonance curve when the TbFeCo recording medium was used, the broken line represents the resonance curve when the GeSbTe medium was used, and the dash-dot line represents the resonance curve when there was no recording medium. The intensity represents the peak intensity in the distribution measured on a plane 2 nm from the antenna. As shown, the resonance wavelength was shifted toward a longer wavelength by interaction with the recording medium. The shift was about 50 nm for both TbFeCo and GeSbTe.

Near-Field Distribution. Fig. 9.22a shows the intensity distribution of the optical near-field when there was no recording medium, and Fig. 9.22b shows

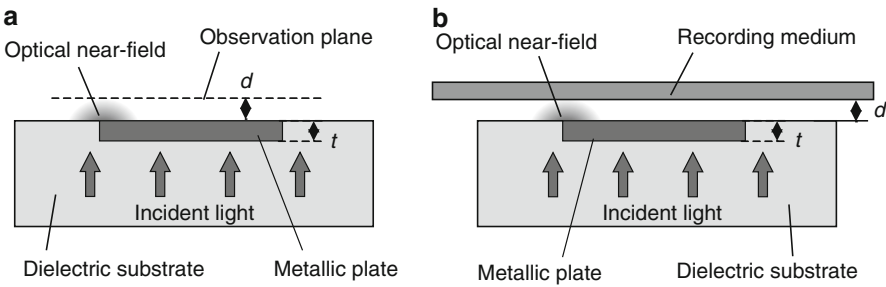


Fig. 9.20 Relation between the near-field intensity and the wavelength for the antennas embedded in a glass substrate. The *solid line* represents the resonance curve for the antenna embedded in the glass substrate, and the *broken line* represents the resonance curve when the antenna was placed in air. The intensity represents the peak intensity in the distribution measured on a plane 2 nm from the antenna

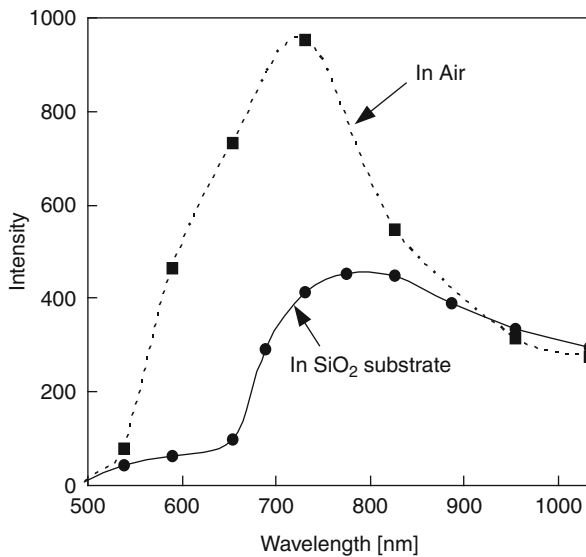


Fig. 9.21 Relation between the near-field intensity and the wavelength when a recording medium was placed near the antenna. The *solid line* represents the resonance curve for a TbFeCo recording medium, the *broken line* represents the resonance curve for a GeSbTe recording medium, and the *dash-dot-line* represents the resonance curve when there was no recording medium. The spacing between the recording medium and the antenna was assumed to be 10 nm. The intensity represents the peak intensity in the distribution measured on a plane 2 nm from the antenna

the intensity distribution when the TbFeCo recording medium was placed near the antenna. The wavelength of the incident light was assumed to be at the resonance wavelength of the plasmon – 780 nm when there was no recording medium and 830 nm when there was a recording medium. Both distributions were measured on a plane 10 nm from the antenna (on the surface of the recording

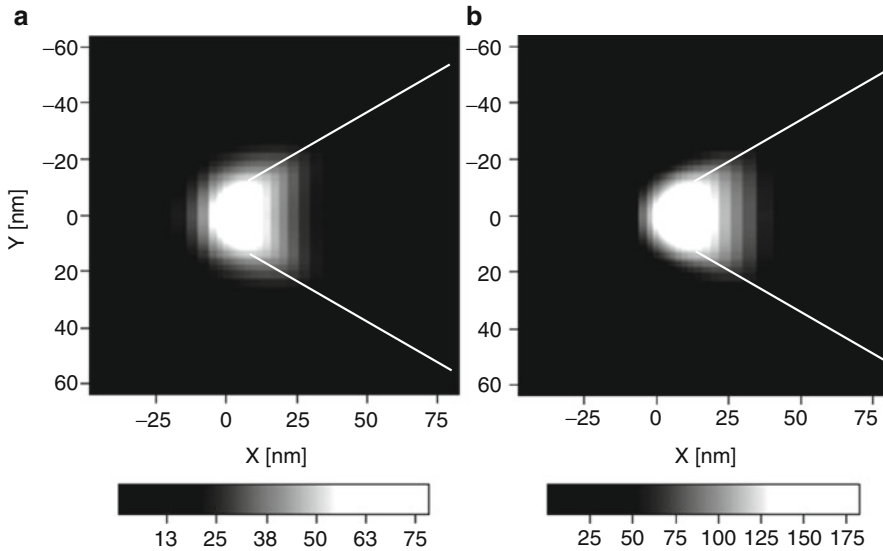
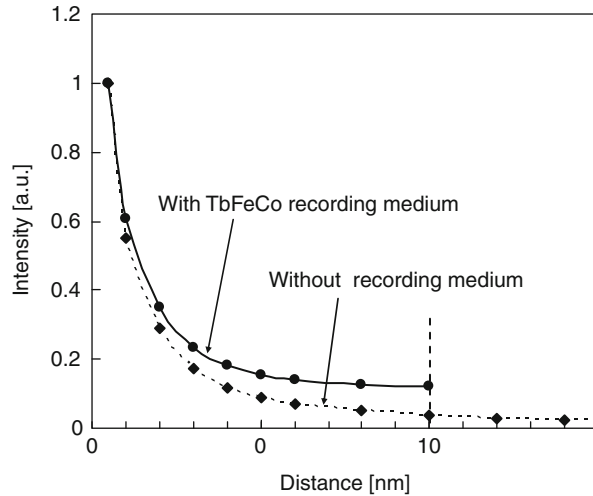


Fig. 9.22 Intensity distributions of the optical near-field generated near the antenna: (a) when there was no recording medium and (b) when there was a TbFeCo medium. The distribution was measured on a plane 10 nm from the antenna

medium when a recording medium was used). As shown in these figures, the optical spot was crescent shaped when there was no recording medium but was semicircular when the recording medium was used. With the recording medium, the distribution measured at half maximum was about 30 nm wide in both the x and y directions. If we compare this spot size with that of a 4.7-Gb, DVD-RAM (full width at half maximum of the optical spot = 580 nm, recording density = 3.7 Gb/in²), this spot size corresponds to a recording density of approximately 1 Tb/in². The calculated efficiency for this distribution was 20% when we assumed that the incident beam was a Gaussian beam with a full width at half maximum of 1 μm .

When we placed the recording medium near the antenna, the intensity of the optical near-field increased by a factor of about 2.5. This was because the decay length of the optical near-field changes when the recording medium is placed near the antenna. Figure 9.23 shows the dependence of the near-field intensity on the distance from the surface of the antenna. The solid line represents the curve when a recording medium was used, and the broken line represents the curve when there was no recording medium. The near-field intensity decreased exponentially as the distance increased, and its decay length increased when the recording medium was placed near the antenna. We believe this was because image charges were induced in the recording medium, and the intensity of the optical near-field between the head and the recording medium became greater because of the

Fig. 9.23 Intensity of the optical near-field as a function of the distance from the antenna. The *solid line* represents the curve when a recording medium was used, and the *broken line* represents the curve when there was no recording medium



interaction of the charges induced at both the apex of the antenna and the recording medium.

9.3.6 Near-Field Optical Head Using a Double Antenna

When a wedge-shaped antenna is used, the recording density can be further increased by reducing the apex radius or the spacing between the head and the recording medium. An alternative way to increase the recording density is to use a double antenna (Fig. 9.24). When the double antenna is illuminated by light, an optical near-field is generated between the two apices because of the interaction of charges concentrated at these apices. This mechanism is similar to that of the bow-tie antenna used at microwave frequencies. However, at optical frequencies, the intensity of the optical near-field can be enhanced when the plasmon is excited in the antennas by optimizing the material and the size of the antenna.

Figure 9.25 shows the intensity distribution of the optical near-field generated near the double antenna. For this calculation, we assumed that the shape of the antennas was a sector, the metal was silver, the gap width (g) was 5 nm, the radius (r) of each apex was 20 nm, the length (L) was 200 nm, the thickness (t) was 30 nm, and the apex angle (θ) was 60° , and the wavelength was 830 nm. The distribution was measured on a plane 2 nm from the antennas. As shown, a strong optical near-field was generated at the gap. The peak intensity was about 2,000 times that of the incident light. The distribution measured at half maximum was 5 by 5 nm, which was the same as the gap width. When using such a small optical spot, a recording density of over 10 Tb/in² should be attainable.

Fig. 9.24 Schematic of the double antenna

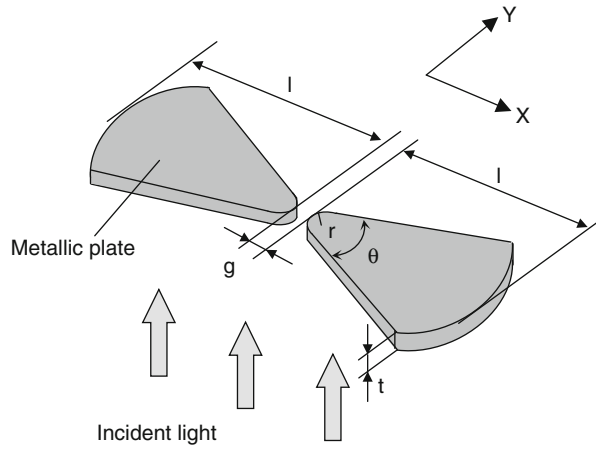


Fig. 9.25 Intensity distribution of the optical near-field generated near the double antenna. It was assumed that the antenna had a sector shape, the metal was silver, the gap width (g) was 5 nm, the apex radius (r) was 20 nm, the length (L) was 200 nm, the thickness (t) was 30 nm, the apex angle (θ) was 60° , and the wavelength was 830 nm. The distribution was measured on a plane 2 nm from the antenna

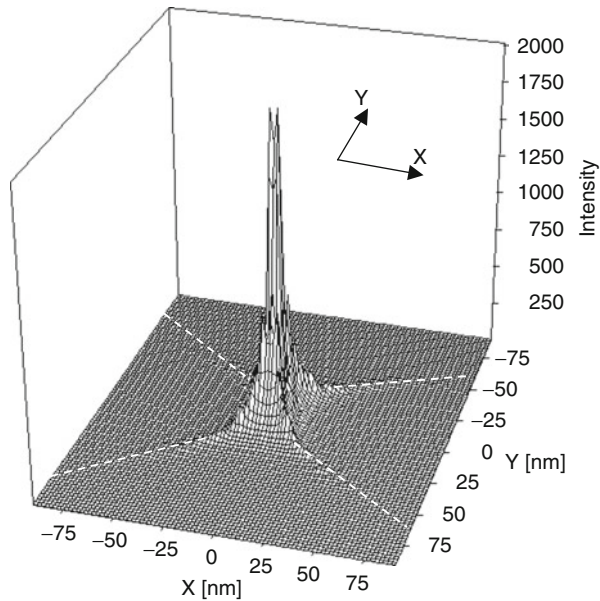
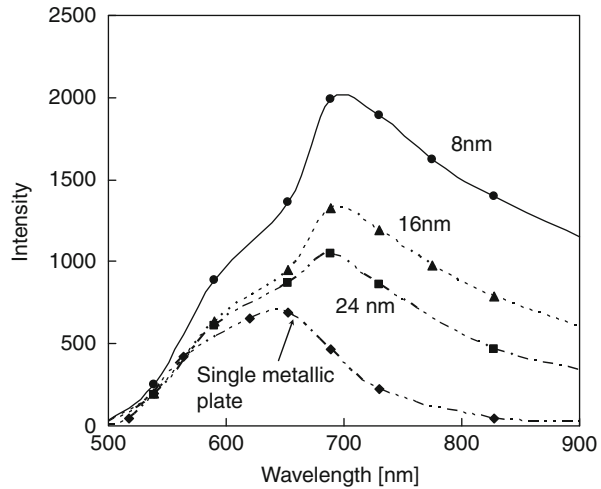


Figure 9.26 shows the intensity of the optical near-field as a function of the incident light wavelength when the gap width of the double antenna was varied from 24 to 8 nm. For this calculation, we assumed that the metal was silver, the length (L) was 100 nm, the radius (r) of each apex was 20 nm, the thickness (t) was 30 nm, the apex angle (θ) was 60° . As shown, the intensity of the optical near-field increased when the plasmon was excited in the antennas, as was the case with a single antenna. The resonance wavelength shifted toward a longer wavelength, and the intensity rose as the gap width became smaller because of the interaction of plasmons generated on both sides of the antennas.

Fig. 9.26 Relation between the near-field intensity and the wavelength for the double antenna with a gap width of 24, 16, and 8 nm



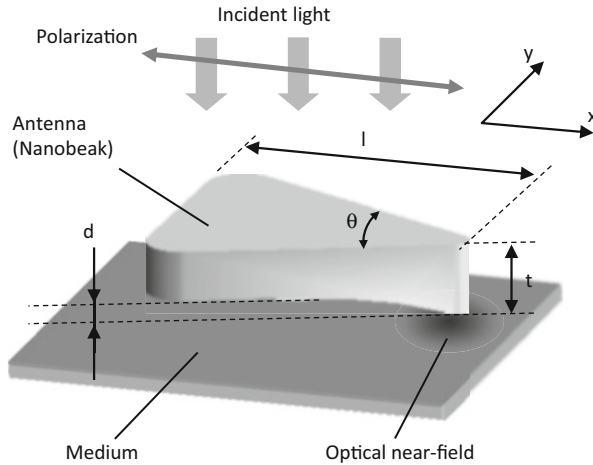
9.4 Nanobeak Head

To generate smaller optical spot by using the wedge-shaped antenna, an optical near-field head with a beaked apex has been proposed. In this section, we describe its principle, simulation results, and writing experiments using this head.

9.4.1 Principle

Figure 9.27 shows a schematic of the head. It consists of a triangular antenna with a three dimensionally tapered apex. When the antenna is illuminated with light polarized in the x direction, a plasmon is excited in the antenna, a strong optical near-field is generated around the apex as the wedge-shaped antenna. The antenna has a recess near the edge that is opposite the apex, and it has a beaked apex. When the medium is placed near the probe, charges that have accumulated at the apex are drawn toward the medium because of their interaction with the image charges induced inside the medium. The beaked apex causes the charges at the apex to be confined to a smaller area. Thus, the spot size is small compared to that of a probe without a beaked apex. The recess is also useful to suppress background light generated near the edge opposite the apex. The background light is generated by the charges accumulated at the edge, and it localizes near the edge. This background light becomes large especially when the radius of corners of the edge is small. Forming the recess moves the edge further from the medium, and the influence of the background on the medium thus becomes weaker. We call this head a “nanobeak” [33, 34].

Fig. 9.27 Schematic of the nanobeak head



9.4.2 Optical Simulation

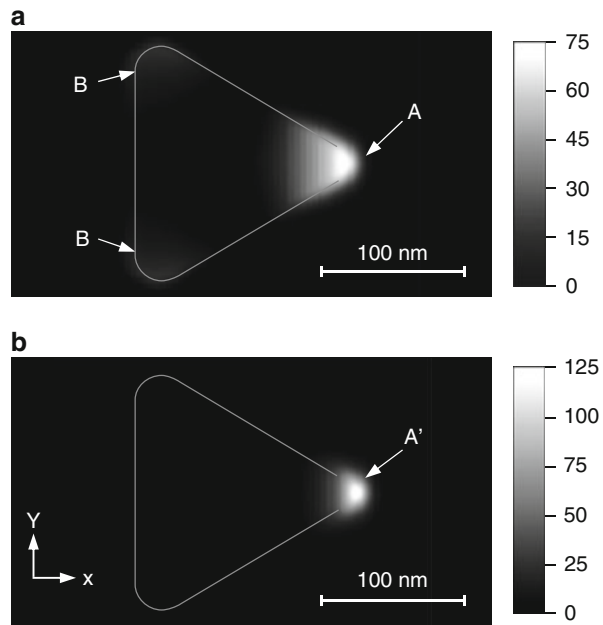
Here we describe calculation results for the nanobeak head. For the calculation, we assumed that a triangular gold antenna was embedded in a glass substrate, and a phase-change medium was placed near the head. The thickness (t), depth of the recess (d), length (l), apex angle (θ), and apex radius of the plate were 50 nm, 15 nm, 150 nm, 60° , and 12 nm, respectively. The medium consisted of a 30-nm-thick $\text{Ge}_2\text{Sb}_2\text{Te}_5$ layer and a 5-nm-thick SiO_2 protective layer, and the spacing between the medium and the probe apex was 3 nm. The incident light was a plane wave with a wavelength of 780 nm.

Figure 9.28 shows the intensity distribution of the optical near-field calculated on the surface of the $\text{Ge}_2\text{Sb}_2\text{Te}_5$ layer. Figure 9.28a is the head without the recess (flat head), and Fig. 9.28b is the head with the recess (nanobeak). As shown, a strong optical near-field was generated at the apices indicated by arrows A and A'. The optical spot size for the nanobeak was smaller than that for the flat probe. The width of the optical spot for the nanobeak measured at half of the maximum was 15 nm in the x direction and 20 nm in the y direction, whereas that for the flat head was 25 nm in both the x and the y directions. In the distribution for the flat probe, we can see background light around the edge, as indicated by arrow B. However, in the case of the nanobeak, the background light could be removed. The peak intensity (power density) for the nanobeak was 125 times that of the incident light, whereas for the flat probe it was 75 times that of the incident light.

9.4.3 Head Fabrication

The antenna must be embedded in the surface of the slider to prevent the apex from being damaged while the slider is scanned on the medium. In the fabrication process,

Fig. 9.28 Intensity distribution of the optical near-field generated near the nanobeak head: (a) head without the recess and (b) head with the recess



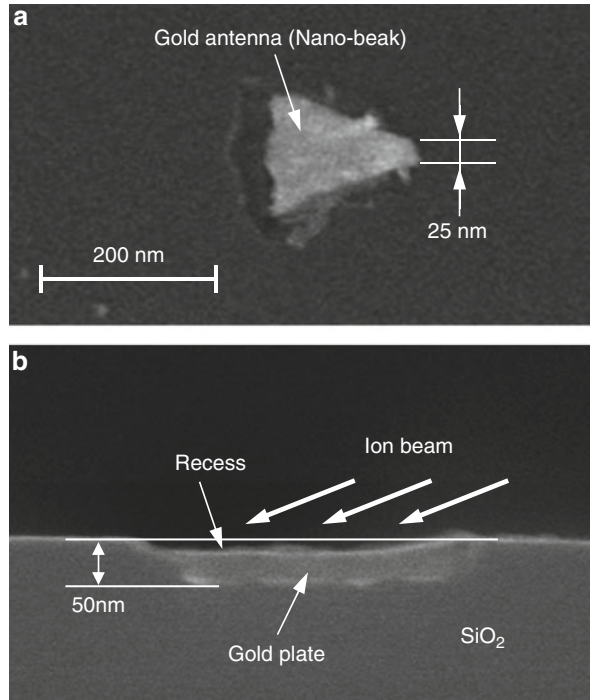
a depression in the shape of a triangle was first formed on the surface of a quartz substrate by using electron beam lithography and reactive-ion etching. Next, gold film was deposited in the depression by vacuum evaporation, and after that a recess was formed on the surface of the gold film with an ion milling machine. In the ion milling process, the ion beam was incident on the substrate at an angle to fabricate the beaked apex, as shown in Fig. 9.29b. Figure 9.29a shows a scanning electron microscope (SEM) image of the fabricated gold antenna, and Fig. 9.29b shows a cross-sectional view of a line pattern fabricated through the same fabrication process as the nanobeak. As shown in these figures, a nanobeak embedded in a quartz slider was successfully fabricated. The thickness (t), length (l), and depth (d) of the recess were 50, 150, and 15 nm, respectively. The apex diameter of the fabricated nanobeak was approximately 25 nm.

9.4.4 Writing Experiments

Here we describe recording experiments in which we used the nanobeak head to write marks on phase change media and bit patterned magnetic media.

Writing on Phase-Change Media. In the experiment, the quartz slider with the nanobeak was placed on the recording medium, and the medium was scanned with a piezo stage. The nanobeak was illuminated with light from a laser diode with a wavelength of 785 nm, and the incident beam was focused with an objective lens

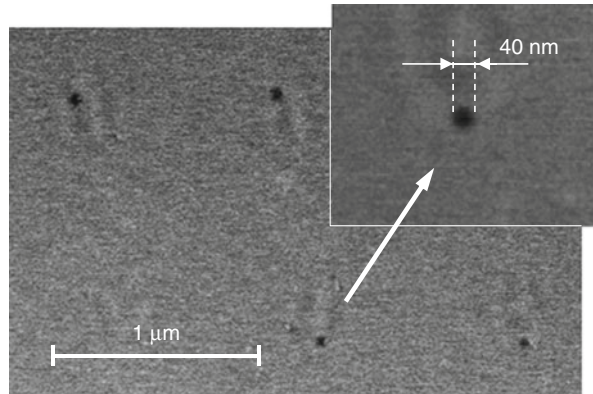
Fig. 9.29 SEM images of the fabricated nanobeak: (a) top view of the fabricated nanobeak and (b) cross-sectional view of the line pattern fabricated by using the same process as for the nanobeak



with an NA of 0.8. The medium consisted of a 5-nm-thick SiO₂ protective layer and a 30-nm-thick Ge₂Sb₂Te₅ recording layer deposited on a glass substrate. The recording layer was amorphous before writing and changed to a crystalline state after writing. The written marks were observed with a scanning electron microscope (SEM) [35]. That is, after the writing, the medium is dipped into an alkali solution. Because etching speeds for crystalline and amorphous states are different, the written marks change into pits. The marks are then observed with a SEM.

Figure 9.30 shows SEM images of the medium after etching. The dark spots (depressed regions) correspond to the crystalline regions formed by writing. As shown, marks with a diameter of 40 nm were successfully written. For this writing process, the power and the pulse width of the incident light were 13 mW and 60 ns, respectively. When the heating time is 60 ns, the crystallization temperature for the Ge₂Sb₂Te₅ film is approximately 400°C [36]. Therefore, the written marks correspond to regions where the temperature rose to more than 400°C. In this experiment, the medium without a heat sink layer was used to increase the sensitivity of the medium. In this case, thermal diffusion in the lateral direction causes broadening of the temperature distribution. To confirm this, the temperature distribution in the medium was calculated assuming that the medium was heated by a Gaussian heat source with a full width at half maximum (FWHM) of 20 nm. When the heating time was 60 ns, the FWHM of the temperature distribution was 60 nm (the width was 40 nm at 65 % of the peak). It should be possible to write

Fig. 9.30 SEM images of the medium after writing and etching. The *inset* shows a magnified view of one of the marks



smaller marks by using a medium with a heat sink layer. Note that the heat sink layer necessitates an increase in the input power. Therefore, thermal design of the medium, i.e., optimization of the material and thickness of the heat sink layer, is necessary to fabricate actual devices.

Writing on Bit-Patterned Magnetic Media. Co/Pd bit-patterned magnetic media were used for writing recording bits. The same optical setup was used for writing and a magnetic field was applied to the medium by a bar magnet placed on the opposite side of the slider to reverse the magnetization. The patterned medium was fabricated by cutting a Co/Pd multilayer thin film into dots by using self-assembled block copolymers [37, 38]. First Co(0.3 nm)/Pd(0.7 nm) multilayer was deposited by sputtering. A solution of polystyrene polymethyl methacrylate (PMMA) block copolymers was then coated on it and annealed to generate a self-assembled dot array of PMMA. The Co/Pd film was etched by an ion milling using the PMMA dots as an etching mask. After the etching, carbon was sputter deposited to fill the space between the dots and make the surface flat. Figure 9.31a shows an atomic force microscope (AFM) image of the Co/Pd dots observed before depositing carbon between the dots. The diameter and pitch of a dot were 20–25 and 30 nm, respectively, corresponding to a recording density of 830 Gbits/in².

Figure 9.31b, c shows magnetic-force-microscope (MFM) images of marks written on the medium with a mark pitch of 120 nm in the horizontal direction and 1 μm in the vertical direction. For this writing, the power and pulse width of the laser were 8.5 mW and 25 ns, respectively, and the applied magnetic field was 1.8 kOe. As shown in the figure, the magnetizations of the dots are selectively reversed, and the minimum size of the reversed regions in the MFM image is 30 nm (arrow A). These magnetically reversed areas correspond to single dots, because the size of the regions that are magnetically reversed becomes larger than 60 nm if two dots are magnetically reversed. The size of a magnetic domain in the MFM image appeared bigger than its actual size because of the resolution limit of the MFM. In the MFM image, larger marks are also observed (arrows labeled B). In the used media, the dots

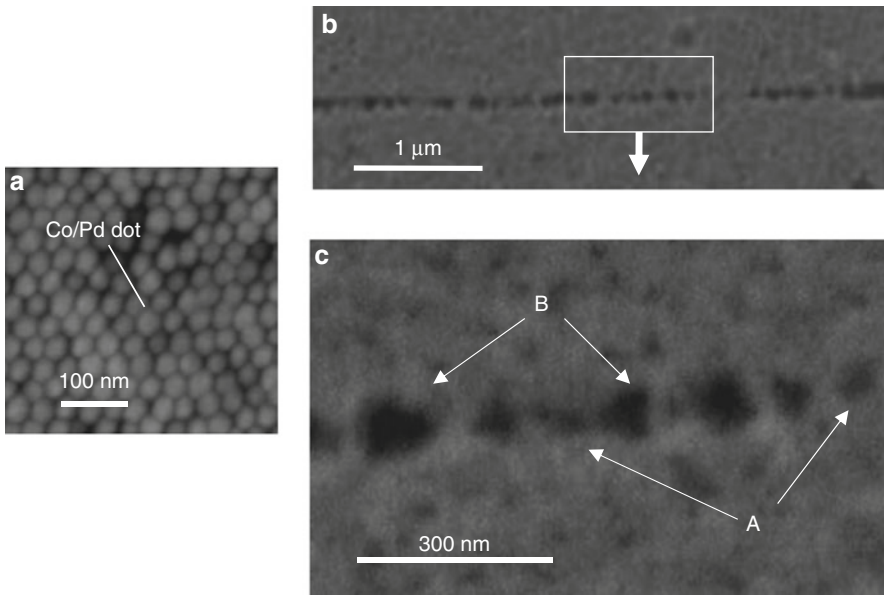


Fig. 9.31 (a) AFM image of the bit-patterned medium, (b) MFM images of medium after writing marks, and (c) magnified view of the region surrounded by the *dotted line* in (b)

were not perfectly aligned in the direction of the sample scanning. It is expected that in these regions, the optical spot was not at the center of the dot, and several dots were heated simultaneously, resulting in magnetization reversal of several dots.

9.5 Summary

Near-field optical recording is a promising way to realize a recording density of over 1 Tb/in^2 . In this chapter, we focused on the near-field optical head, which is a key device for near-field optical recording. After reviewing the near-field optical recording technology, we focused on a highly efficient near-field optical head that uses a wedge-shaped antenna and described its optical properties based on a simulation using a finite-difference time-domain method. The simulation results confirmed that a strong optical near-field is generated at the apex of the antenna when a plasmon is excited in the antenna. When a TbFeCo recording medium was placed 10 nm from the near-field optical head, the size of the optical spot was 30 nm, which corresponds to an areal recording density of approximately 1 Tb/in^2 . The efficiency was 20% if we assume that the incident beam was a Gaussian beam with a full width at half maximum of $1 \mu\text{m}$. Furthermore, we discussed a triangular antenna with a beaked apex called a “nanobeak.” Numerical analysis shows we can reduce the spot size further by using the nanobeak head. The nanobeak head was fabricated on the surface of a quartz slider and used for writing marks

on a phase-change recording medium. The marks were observed with a scanning electron microscope, and it was confirmed that marks with a diameter of 40 nm were successfully written on the medium. The nanobeak head was also used for writing marks on a Co/Pd bit-patterned medium with a diameter of 20–25 nm and a pitch of 30 nm, corresponding to an areal density of 830 Gbits/in². Magnetic-force-microscope images of the medium show that the magnetizations of single dots were selectively reversed by the head.

Acknowledgements This work was supported by the “Terabyte optical storage technology” project of the Optoelectronic Industry and Technology Development Association (OITDA). OITDA contracted with the Ministry of Economy Trade and Industry of Japan (METI) to undertake the project in 2002 and recontracted with the New Energy and Industrial Technology Development Organization (NEDO) to undertake it in 2003 (Funds were provided by METI).

References

1. M. Ohtsu (ed.), *Near-Field Nano/Atom Optics and Technology* (Springer, Tokyo, 1998)
2. S.M. Mansfield, G.S. Kino, *Appl. Phys. Lett.* **57**, 2615 (1990)
3. B.D. Terris, H.J. Mamin, D. Rugar, W.R. Studenmund, G.S. Kino, *Appl. Phys. Lett.* **65**, 388 (1994)
4. M. Shinoda, K. Saito, T. Ishimoto, T. Kondo, A. Nakaoki, M. Furuki, M. Takeda, M. Yamamoto, *Technical Digest of Optical Data Storage 2003*, Canada, 120 (2003)
5. E. Betzig, J.K. Trautman, R. Wolfe, E.M. Gyorgy, P.L. Finn, M.H. Kryder, C.-H. Chang, *Appl. Phys. Lett.* **61**, 142 (1992)
6. S. Hosaka, T. Shintani, M. Miyamoto, A. Kikukawa, A. Hirtsune, M. Terao, M. Yoshida, K. Fujita, S. Krammer, *J. Appl. Phys.* **79**, 8082 (1996)
7. S. Jiang, J. Ichihashi, H. Monobe, M. Fujihira, M. Ohtsu, *Opt. Commun.* **106**, 173 (1994)
8. H. Saga, H. Nemoto, H. Sukeda, M. Takahashi, *Jpn. J. Appl. Phys.* **38**(Part 1), 1839 (1999)
9. H. Sukeda, H. Saga, H. Nemoto, Y. Ito, C. Haginoya, *IEEE Trans. Magn.* **37**, 8082 (2001)
10. T.W. McDaniel, *J. Phys. Condens. Matter* **17**, R315–R332 (2005)
11. M. Vasz-Iravani, R. Toledo-Crow, Y. Chen, *J. Vac. Sci. Technol. A* **11**, 742 (1993)
12. E. Betzig, P. L. Finn, J. S. Weiner, *Appl. Phys. Lett.* **60**, 2484 (1995)
13. M.B. Lee, M. Kourogi, T. Yatsui, K. Tsutsui, N. Atoda, M. Ohtsu, *Appl. Opt.* **38**, 3566 (1999)
14. F. Isshiki, K. Ito, K. Etoh, S. Hosaka, *Appl. Phys. Lett.* **76**, 804 (2000)
15. T. Yatsui, M. Kourogi, K. Tsutsui, J. Takahashi, M. Ohtsu, *Opt. Lett.* **25**, 1279 (2000)
16. T. Saiki, S. Mononobe, M. Ohtsu, N. Saito, J. Kusano, *Appl. Phys. Lett.* **68**, 2612 (1996)
17. T. Yatsui, M. Kourogi, M. Ohtsu, *Appl. Phys. Lett.* **73**, 2090 (1998)
18. U.C. Fischer, *Ultramicroscopy* **42**, 393 (1992)
19. J. Takahara, S. Yamagishi, H. Taki, A. Morimoto, T. Kobayashi, *Opt. Lett.* **22**, 475 (1997)
20. U.C. Fischer et al., in *Near-Field Optics*, ed. by D.W. Pohl, D. Courjon (Kluwer Academic, Dordrecht, 1993), p. 255
21. J. Koglin, U.C. Fischer, H. Fuchs, *Phys. Rev. B* **55**, 7977 (1997)
22. H. Raether, *Surface Plasmon on Smooth and Rough Surface and on Grating* (Springer, Berlin, 1988)
23. T. Thio, K.M. Pellerin, R.A. Linke, H.J. Lezec, T.W. Ebbesen, *Opt. Lett.* **26**, 1972 (2001)
24. U.C. Fischer, D.W. Pohl, *Phys. Rev. Lett.* **62**, 458 (1989)
25. E.D. Palik (ed.), *Handbook of Optical Constants of Solids* (Academic, San Diego, 1985)
26. T. Matsumoto, T. Ichimura, T. Yatsui, M. Kourogi, T. Saiki, M. Ohtsu, *Opt. Rev.* **5**, 369 (1998)

27. X. Shi, L. Hesselink, R. L. Thornton, N. Robertson, T. Albrecht, B.D. Terris, *Opt. Lett.* **2**, 1320 (2003)
28. B.C. Stipe, T. Strand, C. Poon, H. Balamane, T. Boone, J. Katine, J. Li, V. Rawat, H. Nemoto, A. Hirotsune, O. Hellwig, R. Ruiz, E. Dobisz, D.S. Kercher, N. Robertson, T. Albrecht, B.D. Terris, *Nature Photo.* **4**, 484 (2010)
29. W.A. Challener, C. Peng, A.V. Itagi, D. Karns, W. Peng, Y. Peng, X. Yang, X. Zhu, N.J. Gokemeijer, Y.-T. Hsia, G. Ju, R.E. Rottmayer, M.A. Seigler, E.C. Gage, *Nature Photo.* **3**, 220 (2009)
30. T. Matsumoto, T. Shimano, S. Hosaka, *Technical Digest of 6th International Conference on Near Field Optics and Related Techniques*, Netherlands, 55 (2000)
31. T. Matsumoto, T. Shimano, H. Saga, H. Sukeda, M. Kiguchi, *J. Appl. Phys.* **95**, 3901 (2004)
32. A. Wokaun, J.P. Gordon, P.F. Liao, *Phys. Rev. Lett.* **48**, 957 (1982)
33. T. Matsumoto, Y. Anzai, T. Shintani, K. Nakamura, T. Nishida, *Opt. Lett.* **31**, 259 (2006)
34. T. Matsumoto, K. Nakamura, T. Nishida, H. Hieda, A. Kikitsu, K. Naito, T. Koda, *Appl. Phys. Lett.* **93**, 031108 (2008)
35. T. Shintani, Y. Anzai, H. Minemura, H. Miyamoto, J. Ushiyama, *Appl. Phys. Lett.* **85**, 639 (2004)
36. M. Terao, Y. Miyauchi, K. Andoo, H. Yasuoka, R. Tamura, *Proc. SPIE* **1078**, 2 (1989)
37. K. Naito, H. Hieda, M. Sakurai, Y. Kamata, K. Asakawa, *IEEE Trans. Magn.* **38**, 1949 (2002)
38. H. Hieda, Y. Yanagit, A. Kikitsu, T. Maeda, and K. Naito, *J. Photopolym. Sci. Technol.* **19**, 425 (2006)

Part III

Sensing and Spectroscopy

Nano-optical Imaging and Spectroscopy of Single Semiconductor Quantum Constituents

10

Toshiharu Saiki

Contents

10.1	Introduction.....	404
10.2	General Description of NSOM.....	405
10.3	Design, Fabrication, and Evaluation of NSOM Aperture Probes.....	406
10.3.1	Basic Process of Aperture Probe Fabrication.....	406
10.3.2	Tapered Structure and Optical Throughput.....	407
10.3.3	Simulation-Based Design of a Tapered Structure.....	408
10.3.4	Fabrication of a Double-Tapered Aperture Probe.....	412
10.3.5	Evaluation of Transmission Efficiency and Collection Efficiency.....	413
10.3.6	Evaluation of Spatial Resolution with Single Quantum Dots.....	415
10.4	Super-resolution in Single Molecule Detection.....	416
10.5	Single Quantum-Dot Spectroscopy.....	420
10.5.1	Homogeneous Linewidth and Carrier–Phonon Interaction.....	421
10.5.2	Homogeneous Linewidth and Carrier–Carrier Interaction.....	426
10.6	Real-Space Mapping of Exciton Wave Function Confined in a QD.....	431
10.7	Carrier Localization in Cluster States in GaNAs.....	433
10.8	Perspectives.....	438
	References.....	439

Abstract

In this chapter, current progress in the instrumentation and measurements of aperture-based near-field scanning optical microscopy and its application to spectroscopic study of semiconductor nanostructures are described. The design and fabrication of the probe with regard to aperture quality and the efficiency of light propagation are carefully examined. The recent dramatic improvements in spatial resolution and optical throughput are demonstrated by single quantum dot spectroscopy.

T. Saiki (✉)

Department of Electronics and Electrical Engineering, Keio University, Kanagawa, Japan
e-mail: saiki@elec.keio.ac.jp

10.1 Introduction

The optical control of single electronic quantum states is the most fundamental and critical technique needed for the functioning of nano-optical devices and for the implementation of quantum-information processing. Semiconductor quantum dots (QDs), where electrons are confined in a nanoscale volume, are one of the promising candidates for a prototype of such quantum systems due to their atom-like density of states, long duration of coherence [1, 2] (narrow transition linewidth [3–5]), and strong interaction between confined carriers. So far, as a result of these specific properties in QDs, optical manipulations of single quantum states such as qubit rotations [6, 7], optically induced entanglement [8], and single-photon turnstile [9] are realized in well-characterized QD systems including interface QDs formed in a narrow quantum well and self-assembled QDs grown in Stranski–Krastanov mode.

Conventional far-field optical techniques are unsatisfactory for exploring and addressing these individual nanoscale systems in terms of spatial resolution, which is limited to half the wavelength of used light due to the diffraction limit. Probing systems with fixed apertures or with mesa structures is a useful solution for isolating single quantum constituents, but the imaging ability is sacrificed. Near-field scanning optical microscopy (NSOM), where single systems are observed through a small aperture at the end of a scanning probe, is a more powerful tool for locally accessing individual QDs and obtaining spatial information [10–12]. By achieving spatial resolution higher than 50 nm with reasonable sensitivity for spectroscopic measurements, we are able to explore internal structures of QDs; real-space mapping out of wave functions of electrons and holes (excitons) confined in the QDs.

The combination of femtosecond spectroscopy with NSOM offers new perspectives for the direct investigation of carrier dynamics [13, 14] and the local manipulation of electronic quantum states [15, 16] on the nanometer length scale. Time-resolved optical spectroscopy also provides a wealth of information on dynamic processes like the phase and energy relaxation of carriers. Real-space diffusion, trapping, and relaxation processes of photogenerated carriers in low-dimensional semiconductors are of interest from the viewpoint of fundamental physics as well as with regard to potential device applications. Moreover, coherent control of electronic excitation of the quantum-confined system is of great importance because of its possible application in quantum-information processing such as quantum computation, as described above.

In this chapter, current progress in the instrumentation and measurements of NSOM and its application to imaging spectroscopy of single quantum constituents are described. The most critical element in NSOM is an aperture probe, which is a tapered and metal-coated optical fiber. We examine the design and fabrication of the probe with regard to aperture quality and the efficiency of light propagation. The recent dramatic improvements in spatial resolution and optical throughput are illustrated by single quantum dot spectroscopy, which reveals the intrinsic nature of quantum-confined systems. Beyond such an application, real-space mapping of exciton wave functions confined in a quantum dot is also demonstrated.

10.2 General Description of NSOM

When a small object is illuminated, its fine structures with high spatial frequency generate a localized field that decays exponentially normal to the object. This evanescent field on the tiny substructure can be used as a local source of light illuminating and scanning a sample surface so close that the light interacts with the sample without diffracting. There are two methods by which a localized optical field suitable for NSOM can be generated. As illustrated in Fig. 10.1a, one method uses a small aperture at the apex of a tapered optical fiber coated with metal. Light sent down the fiber probe and through the aperture illuminates a small area on the sample surface. The fundamental spatial resolution of so-called aperture NSOM is determined by the diameter of the aperture, which ranges from 10 to 100 nm [10].

In the other method, called apertureless (or scattering) NSOM and illustrated in Fig. 10.1b, a strongly confined optical field is created by external illumination at

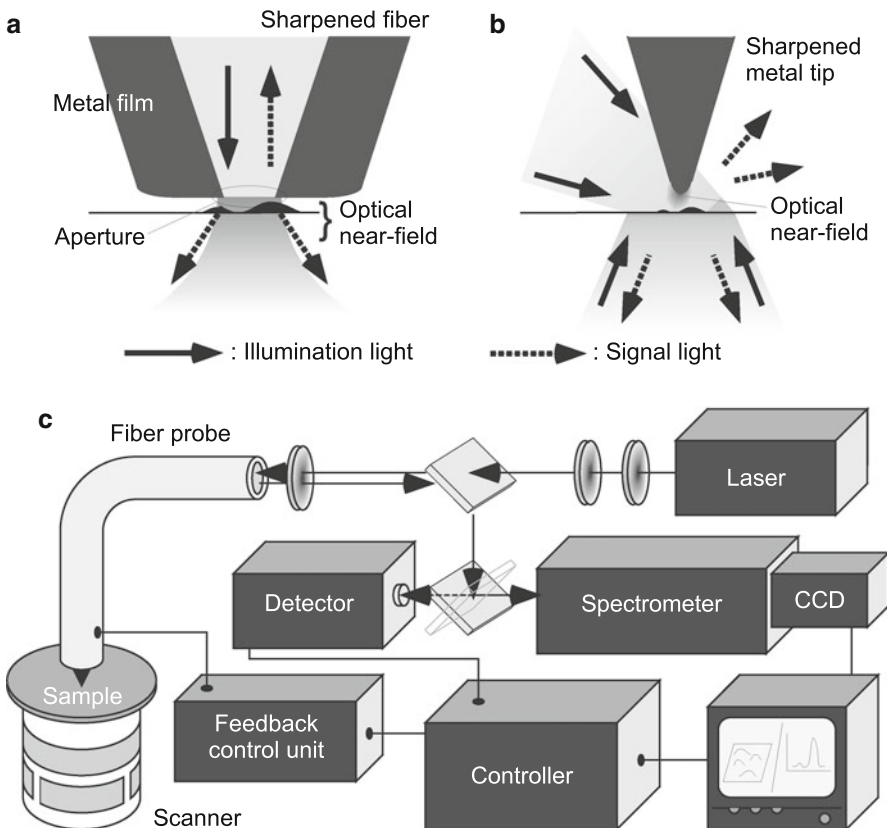


Fig. 10.1 Schematic illustration of (a) aperture NSOM and (b) apertureless (scattering) NSOM. (c) Schematic of standard NSOM setup with a local illumination and local collection configuration

the apex of a sharpened metal or dielectric tip [12]. Spatial resolution approaching the atomic scale is expected, and laboratory experiments have yielded resolutions ranging from 1 to 20 nm. A rather large (diffraction limited) laser spot focused on a tip apex frequently causes an intense background that reduces the signal-to-noise ratio. This contrasts with what is done in aperture NSOM, where the aperture serves as a localized light source without any background. The general applicability of the apertureless method to a wide range of samples is currently being investigated.

The simplest setup for aperture NSOM, a configuration with local illumination and local collection of light through an aperture, is illustrated in Fig. 10.1c. The probe quality and the regulation system for tip-sample feedback are critical to NSOM performance, and most NSOMs use a method similar to that used in an atomic force microscope (AFM), called shear-force feedback, the regulation range of which is 0–20 nm. The light emitted by the aperture interacts with the sample locally. It can be absorbed, scattered, or phase-shifted, or it can excite fluorescence. Which of these occurs depends on the sample and produces contrast in the optical images. In any case, light emerging from the interaction volume must be collected as efficiently as possible. When the sample is prepared on a transparent substrate, signal light is frequently collected with an objective lens arranged in a transmission configuration.

10.3 Design, Fabrication, and Evaluation of NSOM Aperture Probes

10.3.1 Basic Process of Aperture Probe Fabrication

Great efforts have been devoted to the fabrication of the aperture probe, which is the heart of NSOM. Since the quality of the probe determines the spatial resolution and sensitivity of the measurements, tip fabrication remains of major interest in the development of NSOM. The fabrication of fiber-based optical probes can be divided into the three main steps illustrated in Fig. 10.2: (a) the creation of a tapered structure with a sharp apex, (b) the coating with a metal (Al, Au, Ag) to obtain an entirely opaque film on the probe, and (c) the formation of a small aperture at the apex.

There are two methods used to make tapered optical fibers with a sharp tip and reasonable cone angle. One is the heating-and-pulling method, where the fiber is locally heated using a CO₂ laser and is subsequently pulled apart [17]. The other method, based on chemical etching in a hydrofluoric acid (HF) solution, is a more easily reproducible production and can be used to make many probes at the same time [18, 19]. To realize the ideal taper structures of the sort that will be discussed below, the chemical-etching method is advantageous because the taper angle can be adjusted by changing the composition of a buffered HF solution. Another important advantage of the chemical-etching method is the excellent stability of the polarization state of the probe. When the heating-and-pulling method is used, in contrast, temporal fluctuation of polarization occurs due to the relaxation of strain induced by the production process.

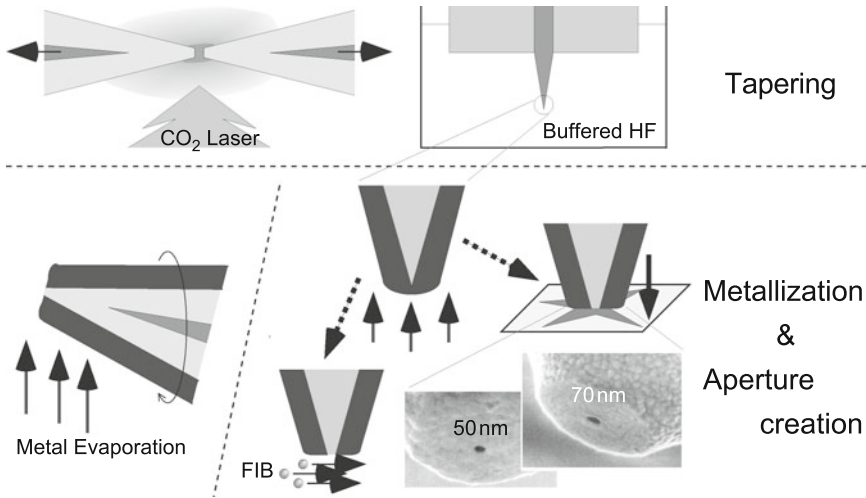


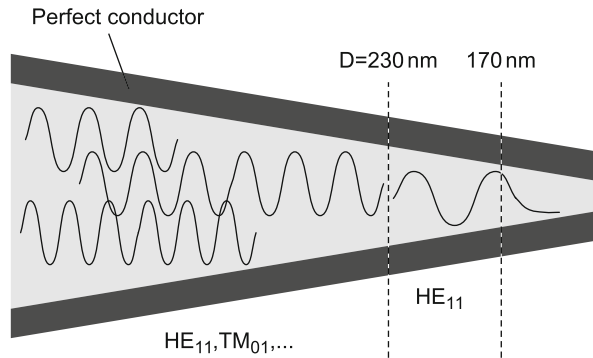
Fig. 10.2 Fabrication of an aperture NSOM probe: creation of the taper structure, metallization of an exterior surface, and formation of the aperture at the apex. The inset shows scanning electron micrographs of 50- and 70-nm apertures made by the impact method

The technique most often used to form a small aperture is based on the geometrical shadowing method used in the evaporation of metal. Since the metal is evaporated at an angle from behind, the coating rate at the apex is much slower than that on the sides. The evaporated metal film generally has a grainy texture, resulting in an irregularly shaped aperture with asymmetric polarization behavior. The grains also increase the distance between the aperture and the sample, not only degrading resolution, but also reducing the intensity of the local excitation. A method for making a high-definition aperture probe by milling and polishing using a focused ion beam has been developed [20], as has a simple method based on the mechanical impact of the tip on a suitable surface [21]. In both methods, the resulting probe has a flat end and a well-defined circular aperture. Furthermore, the impact method assures that the aperture plane is strictly parallel to the sample surface, which is important in minimizing the distance between the aperture and the sample surface.

10.3.2 Tapered Structure and Optical Throughput

Improvement of the optical transmission efficiency (throughput) and collection efficiency of aperture probes is the most important issue to be addressed for the application of NSOM in the spectroscopic studies of nanostructures. In addition to contributing to the high sensitivity of NSOM measurements, optical probes with high throughput will open up attractive new areas of research, such as nonlinear processes and optical manufacturing on the nanometer scale. It is therefore of great

Fig. 10.3 Mode propagation in a tapered optical fiber probe coated with a perfect conductor at a wavelength of 633 nm



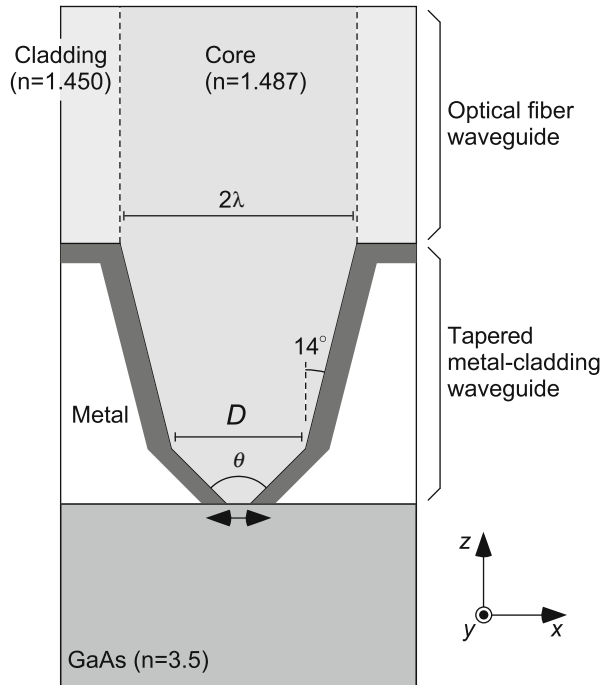
importance to understand the limitations and possibilities of aperture probes with respect to light transmission.

The tapered region of the aperture probe operates as a metal-clad optical waveguide. The mode structure in a metallic waveguide is completely different from that in an unperturbed fiber and is characterized by the cutoff diameter and absorption coefficient of the cladding metal. Theoretical and systematic experimental studies have confirmed that the transmission efficiency of the propagating mode decreases in the region where the core diameter is smaller than half the wavelength of the light in the core (Fig. 10.3) [22]. The power that is actually delivered to the aperture depends on the distance between the aperture plane and the plane in which the probe diameter is equal to the cutoff diameter, which distance is determined by the cone angle of the taper. We therefore proposed a double-tapered structure with a large cone angle [22]. This structure is easily realized using a multistep chemical-etching technique, as will be described below. With this technique, the transmission efficiency is much improved by two orders of magnitude as compared to the single-tapered probe with a small cone angle [21, 22].

10.3.3 Simulation-Based Design of a Tapered Structure

Further optimization of the tapered structure is needed to achieve much higher probe efficiency. However, it is very time-consuming to assess many structure parameters, such as the cone angle and taper length, by trial and error. Numerical analysis is a more reasonable way to attain an optimized structure efficiently and to understand the electromagnetic field distribution in a tapered waveguide including the vicinity of the aperture. Computational calculation by the finite-difference time-domain (FDTD) method is the most popular and promising method available for this purpose, because it can be easily applied to actual three-dimensional problems [23]. Although there have been many simulations focusing on the electric field distribution in the vicinity of the aperture to examine the spatial resolution of NSOM, no calculations have been reported that deal with the light propagation in the tapered region in terms of the sensitivity of the probe. Here, using the

Fig. 10.4 Cross-sectional view of the FDTD geometry of the three-dimensional NSOM model

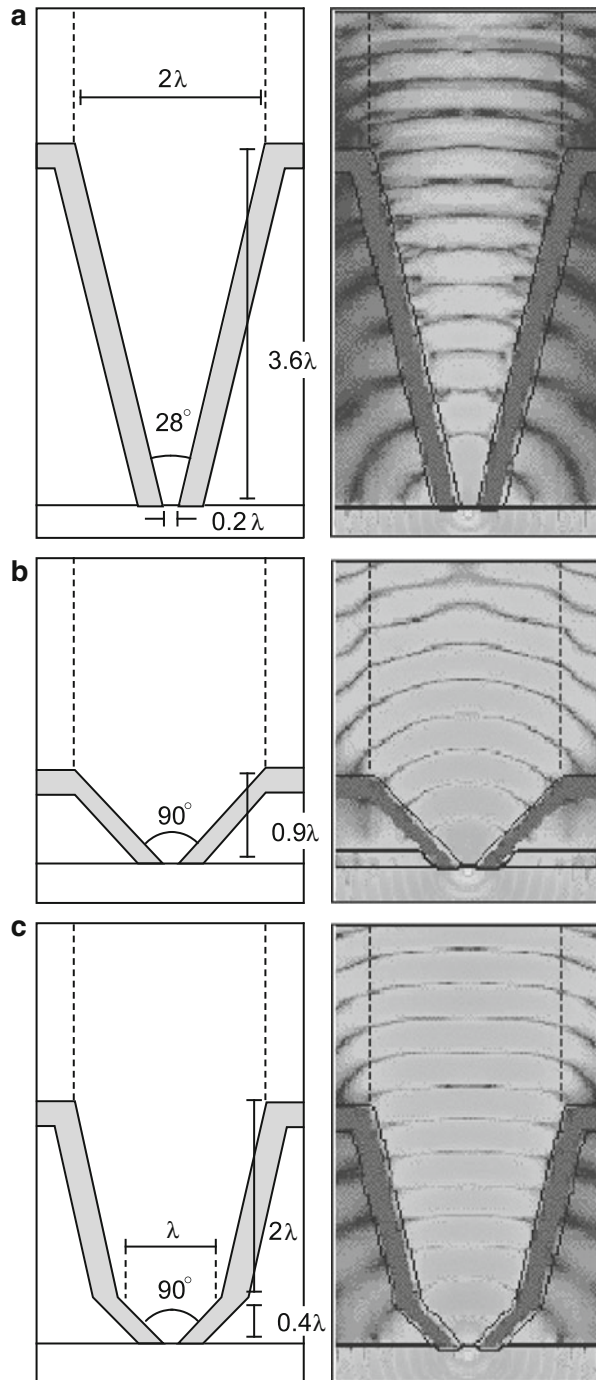


three-dimensional FDTD method, we demonstrate the high collection efficiency of double-tapered probes including guiding optical fibers, as compared with single-tapered probes [24]. We also describe in detail the dependence of the collection efficiency on the cone angle and taper length.

Figure 10.4 illustrates the cross-sectional view of the FDTD geometry of the three-dimensional problem, which reproduces the experimental situation of single quantum-dot imaging. A fiber probe with a double- or single-tapered structure collects luminescence ($\lambda = 1 \mu\text{m}$) from a quantum dot buried $3\lambda/40$ beneath the semiconductor (GaAs; $n = 3.5$) surface. We assume that the source of luminescence is a point-like dipole current linearly polarized along the x direction. The radiation caught by the aperture with a diameter of $\lambda/5$ propagates in the tapered region clad with a perfectly conducting metal and then is guided to the optical fiber waveguide. The refractive indices of the core and cladding of the fiber are 1.487 and 1.450, respectively. The intensity of the collected signal, I_{coll} , is evaluated by two-dimensionally integrating the electric field intensity in the core area of the optical fiber. The simulation box consists of a $120 \times 120 \times 360$ grid in the x , y , and z directions; the space increment is $\lambda/40$. We run the simulation employing Mur's boundary condition.

To demonstrate the performance of the double-tapered probe, we performed calculations for three types of probes, as shown in Fig. 10.5, where the spatial distribution of the electric field intensity is shown on a logarithmic scale.

Fig. 10.5 Calculated distribution of the electric field intensity for three types of probes. (a) Single-tapered probe with a cone angle $\theta = 28^\circ$, (b) single-tapered probe with $\theta = 90^\circ$, and (c) double-tapered probe with $\theta = 90^\circ$ and neck diameter $D = \lambda$



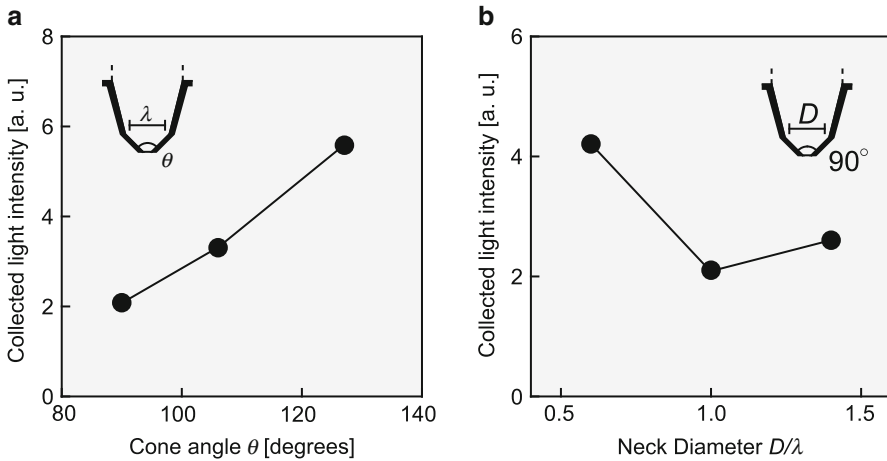


Fig. 10.6 Plots of the intensity of collected light as a function of (a) cone angle θ and (b) neck diameter D

In Fig. 10.5a, b, I_{coll} is compared for probes with $\theta = 28^\circ$ and $\theta = 90^\circ$. The I_{coll} ratio is estimated to be 1:32. Such a distinct improvement in I_{coll} can be attributed to the difference in the length of the cutoff region. By making the cone angle large and shortening the cutoff region, we can direct much of the radiation power towards the tapered region. Figure 10.5c shows the calculation result in the case of a double-tapered probe whose cone angle is the same as in Fig. 10.5b. The neck diameter D is assumed to be λ , which is threefold the cutoff diameter of the cylindrical waveguide clad with a perfectly conducting metal. I_{coll} of Fig. 10.5c is found to be three times greater than I_{coll} in Fig. 10.5b. The radiation pattern in Fig. 10.5c clearly illustrates that the second tapered region modifies the wave front of the propagating light to match the guiding mode of the optical fiber, while the spherical-wave-like propagation in Fig. 10.5b cannot be coupled to the guiding mode so efficiently. To summarize, the collection efficiency of the double-tapered probe in Fig. 10.5c is greater by two orders than that of the conventional single-tapered probe in Fig. 10.5a.

Although we have demonstrated the advantage of a double-tapered probe, its performance is also dependent on various structure parameters. In Fig. 10.6a, b, the values of I_{coll} as a function of cone angle θ and neck diameter D , respectively, are plotted. The enhancement of I_{coll} with the increase in θ is easy to understand. I_{coll} will increase monotonously as θ approaches 180° . In the case of a realistic metal aperture, however, a large θ will cause diminished spatial resolution due to the finite skin depth of the metal. The optimum value of θ should be chosen by balancing the collection efficiency with the spatial resolution. As depicted in Fig. 10.6b, the dependence of I_{coll} on D is found to be more complicated and seems to be less essential. One significant result is that a neck diameter D as small as $3d_c/2$ is preferable compared with a diameter of $3d_c$ to attain high efficiency in coupling to the guiding mode of the optical fiber.

10.3.4 Fabrication of a Double-Tapered Aperture Probe

We used a chemical-etching process with buffered HF solution to fabricate the double-tapered probe. Since the details of probe fabrication with selective etching are described in Ref. [18], we describe the process only briefly here. The cone angle θ can be controlled by the buffering condition of the etching solution, which is adjusted by the volume ratio X of NH_4F maintaining the proportion of HF to H_2O at 1:1. Here, the composition of the solution is expressed as $X:1:1$. A two-step etching process is employed to make a double-tapered probe, as shown in Fig. 10.7a. In the first step, using a solution with a composition of $X = 1.8$, a short tip with a large cone angle of 150° is fabricated. Second, the guiding region is obtained with a solution of $X = 10$. As shown in the scanning electron micrograph of Fig. 10.7b, the resultant cone angle is approximately 90° . The neck diameter D can be controlled by the etching time in the second step.

The next step for metal coating and aperture formation is summarized in Fig. 10.8a. The entire exterior surface of the etched probe was metal-coated with an Au film 200 nm in thickness using a sputtering coating method. A small aperture was created by pounding the metal-coated probe on a sapphire substrate or on the sample itself and squeezing the Au off to the side. Figure 10.8b shows a scanning electron micrograph of the 70-nm aperture, taken after conducting photoluminescence (PL)

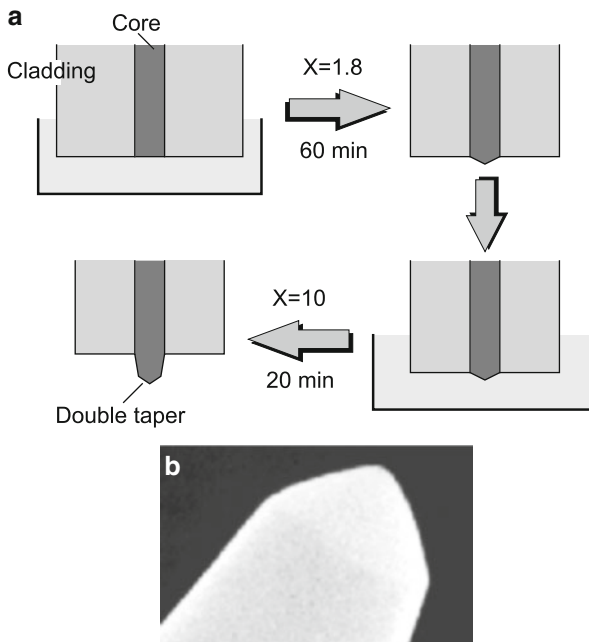
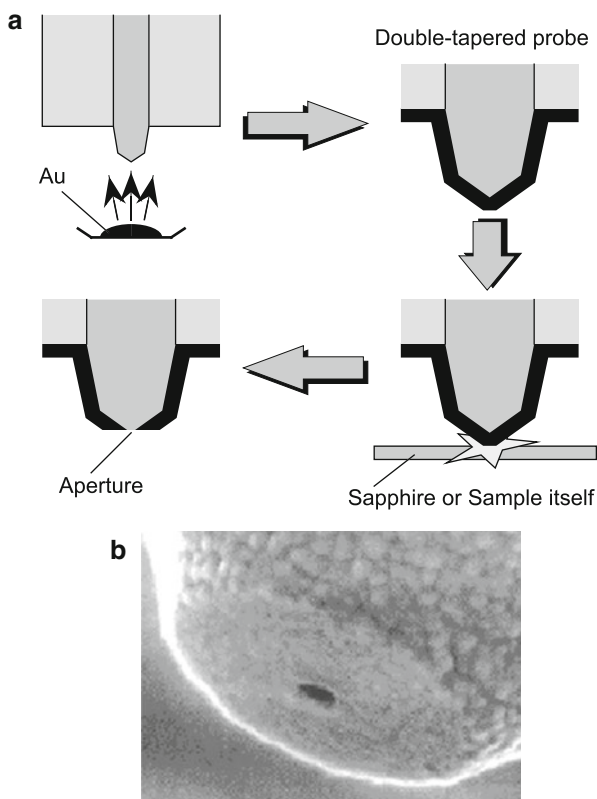


Fig. 10.7 (a) Two-step chemical etching for the fabrication of a double-tapered fiber probe. (b) Scanning electron micrograph of a double-tapered probe

Fig. 10.8 (a) Process for coating the tapered probe with metal and formation of an aperture. (b) Scanning electron micrograph of the aperture with a diameter of 70 nm



imaging several times. Not only a smooth and flat end face but also a round and well-defined aperture was obtained in this fabrication process. As mentioned above, the aperture plane is parallel to the sample surface to minimize the distance between the aperture and the sample surface. The size of the aperture can be selected by carefully monitoring the intensity of light transmitting from the apex, since the throughput of the probe is strictly dependent on the aperture diameter. Such controllability in aperture formation is demonstrated in the scanning electron micrographs of ultrasmall apertures in Fig. 10.9.

10.3.5 Evaluation of Transmission Efficiency and Collection Efficiency

To evaluate the transmission efficiency of aperture probes, researchers often measure the light power emitted by the aperture in the far-field region. However, in many experimental situations, the instantaneous electric fields are dominant in the interaction between light and matter. Thus, the far-field transmission coefficient (the ratio of the far-field light power emitted by the aperture to the power coupled

Fig. 10.9 Scanning electron micrographs of (a) an entirely metal-coated probe and an apertured probe with aperture diameters of (b) 15 nm, (c) 30 nm, and (d) 50 nm

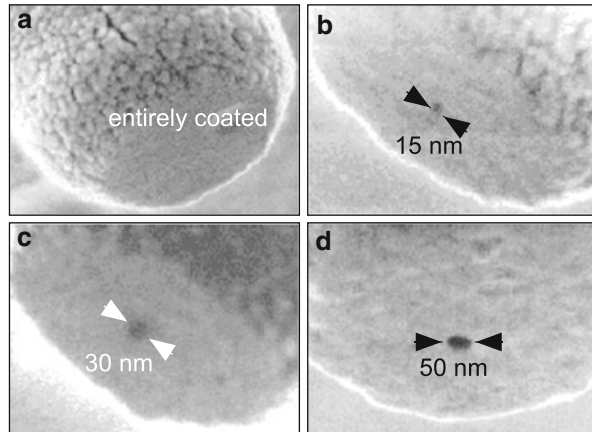
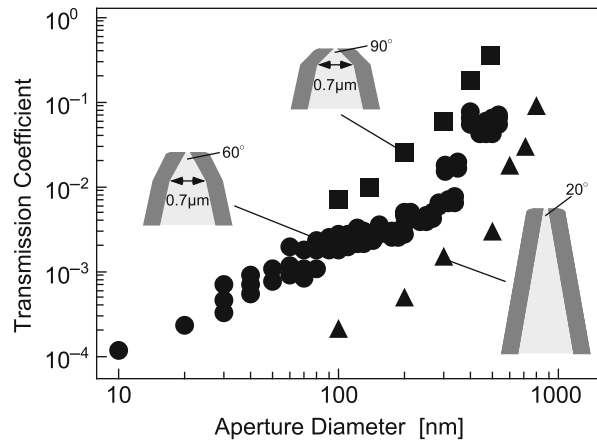


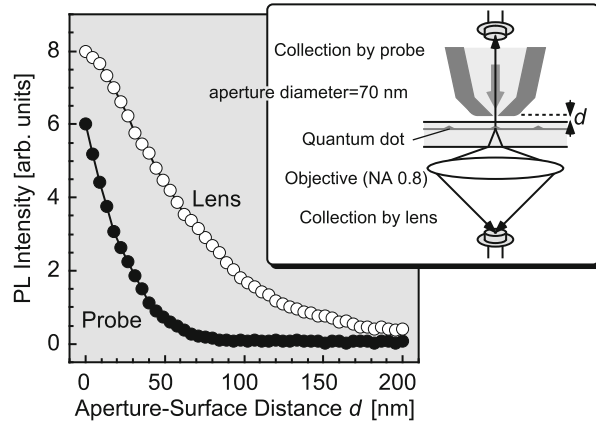
Fig. 10.10 Plots of the transmission coefficient of an aperture probe as a function of aperture diameter for single-tapered and double-tapered probes with cone angles of 60° and 90° . A He–Ne laser with a wavelength of 633 nm was used for this measurement



into the fiber) does not reflect the field enhancement in the near-field region. However, in comparing probes with the same aperture diameter in terms of the transmission efficiency in tapered regions, the far-field transmission coefficient can be valuable information.

In Fig. 10.10 the transmission coefficient is plotted against the aperture diameter for conventional single-tapered probes and for double-tapered probes with cone angles of 60° and 90° . As a light source for the measurement, we used a He–Ne laser ($\lambda = 633$ nm). It is clear that the transmission efficiency of the double-tapered structure with a large cone angle is improved by two orders of magnitude greater than that of the single-tapered probe with a small cone angle. In the case of a 100-nm aperture, the transmission coefficient is as large as 10^{-2} . The reduction of the throughput with a decrease of aperture diameter is not so severe as predicted by Bethe's theory, where the throughput must be proportional to d^{-6} (d : aperture diameter) [25]. Thus, we obtain reasonable illumination intensity even in the case of a 10- to 30-nm aperture.

Fig. 10.11 Comparison of collection efficiency of an objective (*open circles*) and a probe with a 70-nm aperture (*closed circles*). Photoluminescence intensities collected from a single quantum dot are plotted as a function of distance between the aperture and the surface



In addition to a high throughput for efficient illumination of light, superior collection of the locally emitted signal is critical for the observation of opaque materials such as semiconductors. We checked the collection efficiency of a 70-nm aperture probe quantitatively by collecting PL from an InGaAs QD buried 70 nm beneath the surface. We compared the PL intensity collected by the aperture probe with that collected simultaneously by an objective with a numerical aperture of 0.8 (Fig. 10.11 inset). In Fig. 10.11, the PL signal intensities are plotted as a function of distance between the aperture and the sample surface. Within 15 nm of the surface, the amount of light collected by the aperture probe increases rapidly and reaches a value as great as the amount collected by an objective with a numerical aperture of 0.8. This suggests that fabrication of the flat-ended probe makes a considerable contribution to the efficient interaction of the aperture and evanescent field in the vicinity of the sample.

The overall throughput (or collection efficiency) of light is determined by various factors such as the wavelength of propagating light and the corresponding dielectric constant of the cladding metal, as well as by the structure of unperturbed fiber. The FDTD simulation of light propagation is a useful and efficient way to obtain the information needed to make an optimized structure.

10.3.6 Evaluation of Spatial Resolution with Single Quantum Dots

Fluorescence imaging of point-like emission sources is the most straightforward and reliable method for evaluating the spatial resolution of a probe. In particular, semiconductor quantum dots are most suitable in terms of their sizes, quantum efficiency, and optical stability. We evaluated the spatial resolution for various aperture diameters by PL imaging of single InAs self-assembled QDs [26]. The typical lateral size and height of the dots were 22 and 3 nm, respectively. The thickness of the GaAs cap layer, which determines the achievable spatial resolution,

is of critical importance. While a thinner cap layer contributes to the higher resolution, it also causes the degradation of the optical quality of the QDs [4, 27]. We used the QD sample with a cap layer of 20-nm thickness, taking into account the balance between the achievable spatial resolution and the optical quality.

By illuminating the sample with diode laser light ($\lambda = 685$ nm) through the aperture, we generated most of the carriers in a barrier layer surrounding the QDs. After diffusing in the barrier layer, the carriers were captured in the confined states of QDs. The PL signal from a single QD was collected by the same aperture. All of the measurements were performed at 9 K in a cryostat. The tapered structure, defined by a cone angle ($\theta = 90^\circ$) and a neck diameter ($D = 1$ μm), was optimized from the viewpoint of both the optical throughput and the spatial resolution, based on the results of FDTD simulation.

Figure 10.12a–c show the low-temperature PL images of InAs QDs obtained (center photon energy $E = 1.33$ eV, $\Delta E = 60$ meV) by the apertures with diameters of 135, 75, and 30 nm, respectively. The individual bright spots correspond to the PL signal from single QDs. The size of each spot becomes smaller with a decrease of the aperture diameter employed. To evaluate the spatial resolution in Fig. 10.12c, we plotted the cross-sectional profiles of PL signal intensity for the spots indicated by arrows in Fig. 10.12d. Full width at half maximum (FWHM) of the PL signal profile was 37 ± 2 nm. Taking into account the size of QD (22 nm), we estimated the spatial resolution of this measurement to be about 30 nm, which corresponds to $\lambda/30$. In the illumination–collection mode operation of NSOM, the small aperture plays roles in both excitation and collection of the PL signal. In the case of carrier generation in the barrier layer, however, the excitation process does not contribute to such a high spatial resolution due to the carrier diffusion in several hundreds nanometers. We conclude that high resolution could be achieved solely by the collection process of the PL signal.

We carried out the same measurements as described above for other probes and evaluated PL spot size as a function of aperture diameter, as shown in Fig. 10.13. The aperture size of 0 nm means that there is no physical aperture at the apex, which was obtained by stopping the pounding procedure just before opening the aperture. In spite of the lack of physical aperture, we could detect reasonable intensity of the PL signal and image with a resolution of 75 nm. Except for the 0-nm aperture, the spatial resolution is monotonously enhanced with a decrease of the aperture diameter. The spatial resolution is almost equal to the aperture diameter, whose behavior is also reproduced well by the FDTD simulation.

10.4 Super-resolution in Single Molecule Detection

NSOM fluorescence measurements are the simplest and most informative method because they provide high-contrast imaging of nanostructures, revealing the chemical composition and molecular structure as well as the defects and dopants in semiconductors. High-resolution optical imaging of biological samples with fluorescence labels is also a promising field of application. NSOM has the potential to create images of the distribution of such labels down to the level of single

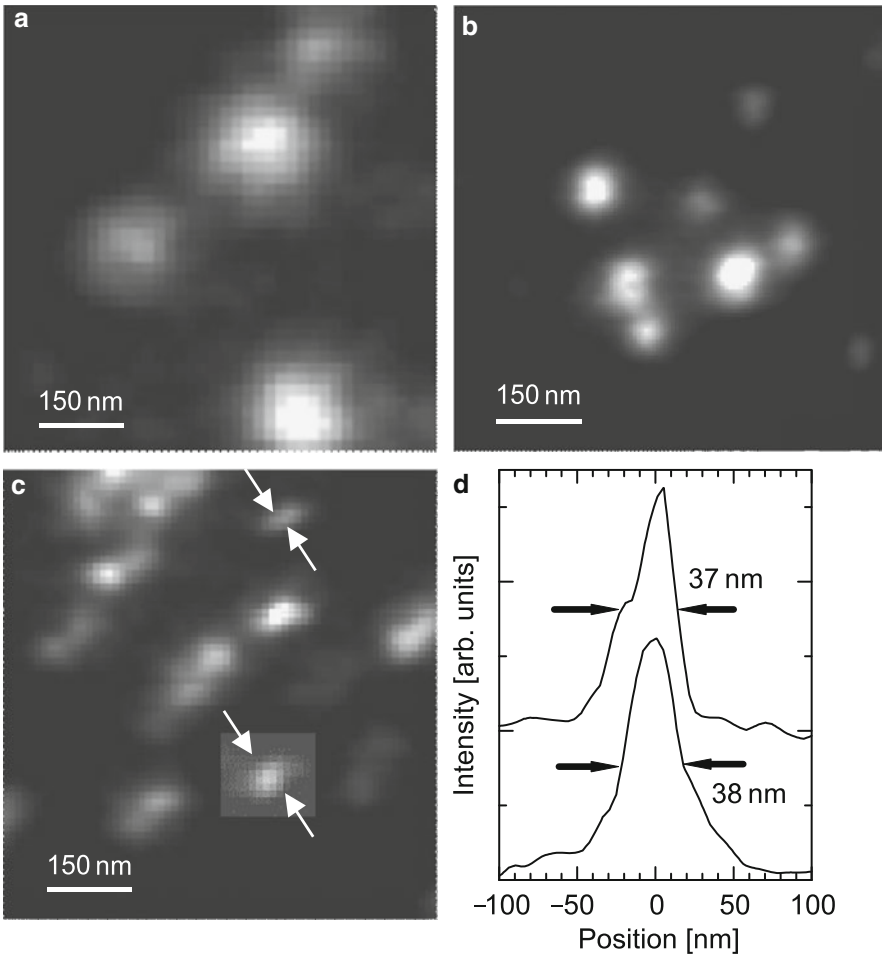
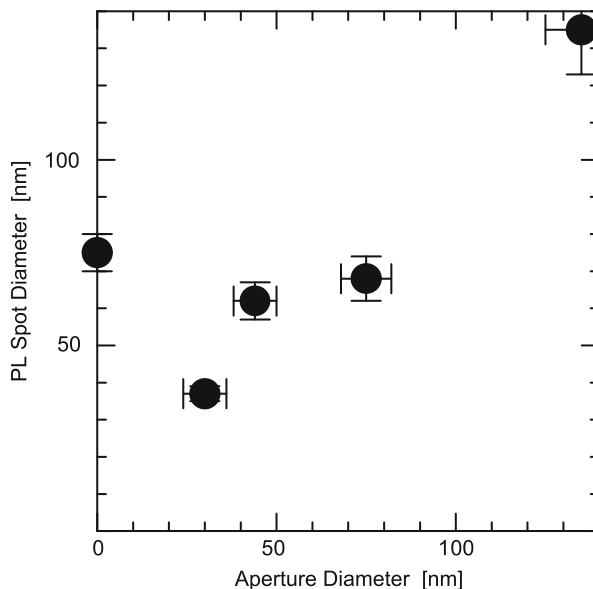


Fig. 10.12 Low-temperature near-field PL images of InAs QDs, obtained by using the probes with aperture diameters of (a) 135 nm, (b) 75 nm, and (c) 30 nm, respectively. (d) Cross-sectional PL intensity profiles of the spots indicated by the *arrows*

fluorophores. Furthermore, the presence of the probe (metal aperture) alters the fluorescence lifetime and emission pattern, making it possible to control radiation in the immediate vicinity of the probe (i.e., locally within the nanoenvironment).

Although NSOM offers attractive possibilities with regard to the detection of single molecules, the current spatial resolution of 100 nm is not sufficient for application to actual biological samples. Imaging with a very small aperture (<30 nm) has often been impossible because the transmission efficiency decreases drastically with aperture diameter. Moreover, even a small grain on the aperture plane is problematic because the consequent increase of the aperture–sample distance reduces the spatial resolution. As mentioned in the previous section,

Fig. 10.13 PL spot diameter as a function of aperture size. The aperture size of 0 nm means that the probe does not have a physical aperture (entirely metal-coated probe)



however, the development of tailored probes with a high-quality aperture has solved this problem.

We have made fluorescence images of single dye molecules by using an aperture significantly smaller than that usually employed [28]. Cy5.5 dye molecules were dispersed on a quartz substrate and illuminated by He–Ne laser light through an aperture made of gold. The fluorescence from a single molecule was collected by the same aperture or by an objective in transmission configuration. Figure 10.14a shows a typical fluorescence image of individual molecules, and Fig. 10.14b is magnified views of some of the bright spots in Fig. 10.14a. The diameter of each spot was estimated to be 30 nm, which corresponds to the aperture diameter produced by using the impact method. Steplike digital bleaching, which occurred at the moment indicated by the arrow, confirms that we actually observed single molecules. The highest resolution we achieved by using an aperture with a diameter of approximately 10 nm is shown in Fig. 10.15. The diameter of the fluorescence spot was as small as 10 nm.

The spatial resolution of 10 nm achieved in the experiment is inconsistent with conventional NSOM resolution; the optical spot generated at the aperture should be larger than the physical aperture diameter because of the finite penetration of light into the coated metal. When we use a gold-coated probe with a cone angle of 90° , the spatial resolution (spot size) should be limited to 30 nm at $\lambda = 633$ nm even in the case of a 10-nm aperture. To examine this discrepancy, we used FDTD calculation to take into account a realistic situation, including the complex dielectric function of the gold film. Figure 10.16a shows the model for calculation. The radiation ($\lambda = 633$ nm) from a point dipole current, oscillating in the x direction, propagates in the tapered region, and then a small light spot is created by the aperture. The

Fig. 10.14 (a) Typical near-field fluorescence image of single dye molecules. (b) Magnified view of one of the bright spots in part (a). Irreversible photobleaching occurred at the moment indicated by the *arrow*

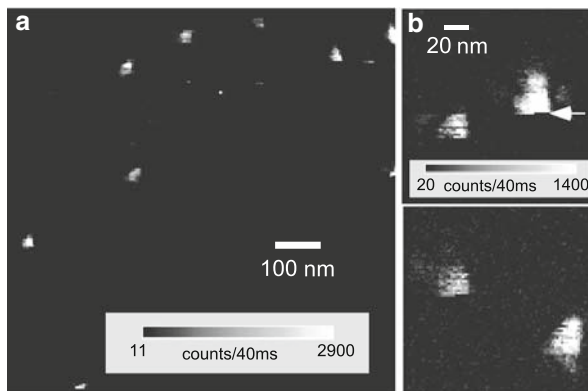
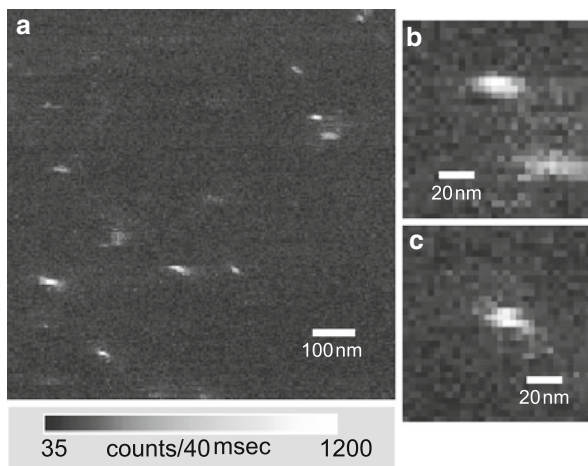


Fig. 10.15 (a) One of the highest-resolution images obtained by using a 10-nm aperture. (b) and (c) Magnified view of two of the bright spots in part (a)



cone angle is 90° , and the aperture diameter is 10 nm. The simulation box is $500 \text{ nm} \times 500 \text{ nm} \times 425 \text{ nm}$ in the x , y , and z directions, respectively, and the space increment is 2.5 nm. [Figure 10.16b](#) shows the cross-sectional profile of the electric field intensity along the x direction 5 nm below the aperture. The twin-peak structure comes from the enhancement of the electric field at the edge of the aperture. The spot size, which is defined as a full width at half maximum of the profile, is estimated to be 16 nm. In [Fig. 10.17](#), calculated spot sizes are plotted as a function of the aperture diameter. While we could expect to achieve 10-nm resolution from this simulation, a contribution of another mechanism, such as energy transfer from an excited molecule to the metal aperture, is also possible [29]. When the molecule is beneath the metal coating, the energy transfer shortens the fluorescence decay time and thus reduces emission intensity dramatically. On the other hand, no energy is transferred when the molecule is below the aperture hollow. Because the interaction distance in the process of energy transfer is only a few nanometers, we expect to reach a spatial resolution of less than 10 nm.

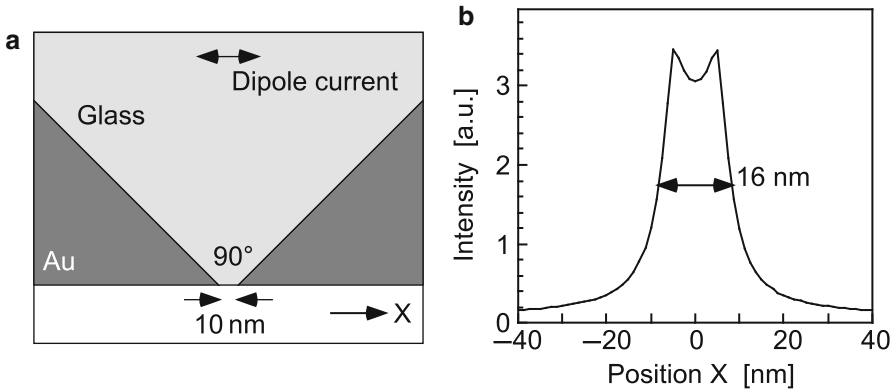


Fig. 10.16 (a) Simulation model for a gold-coated probe with a 10-nm aperture. (b) Cross-sectional profile of the electric field intensity along the x direction 5 nm below the aperture

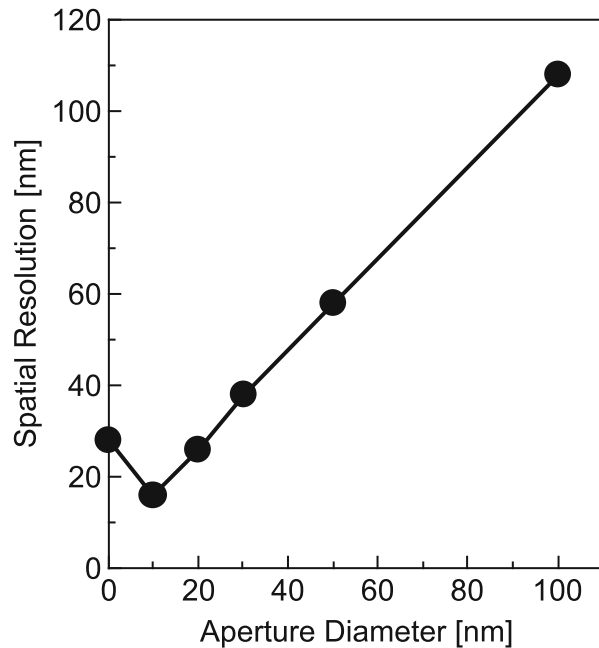


Fig. 10.17 Plot of calculated spot sizes (spatial resolution) as a function of the aperture diameter

10.5 Single Quantum-Dot Spectroscopy

With the recent progress in the nanostructuring of semiconductor materials and in the applications of these nanostructured materials in optoelectronics, near-field optical microscopy and spectroscopy have become important tools for determining the local optical properties of these structures. In single quantum-dot spectroscopy, NSOM provides access to individual QDs, an ensemble of which

exhibits inhomogeneous broadening due to the wide intra-ensemble distribution of sizes and strains [4,5,30–35]. NSOM can thus elucidate the nature of QDs, including the narrow optical transition arising from the atom-like discrete density of states and the line broadening due to the interaction with phonons and/or carriers.

10.5.1 Homogeneous Linewidth and Carrier–Phonon Interaction

The electronic and optical quality of semiconductor QDs has been improved remarkably by using the Stranski–Krastanov growth mode. Owing to the atom-like density of states caused by the three-dimensional nanoscale confinement, the improvement of laser device performance such as ultralow threshold current and ultrahigh gain characteristics is theoretically predicted. Not only in terms of the device applications but also because of its fundamental physics, the QD is an interesting system due to its novel electronic and optical properties. The linewidth of PL or the absorption spectrum is one of the most fundamental and important parameters of these properties. There are intrinsic and extrinsic mechanisms responsible for the spectral broadening in semiconductor QDs. The former is homogeneous linewidth broadening, which is determined by the dephasing processes in electronic systems. The electron–phonon interactions, lifetime broadening, and carrier–carrier interactions are considered to cause the homogeneous broadening. The latter is inhomogeneous linewidth broadening due to the fluctuation in size, shape, and strain distribution of QD ensembles. Such inhomogeneity leads to variation in the optical transition energy from dot to dot and prevents us from understanding its intrinsic properties.

From the viewpoint of device applications, the homogeneous linewidth at room temperature is of great interest. The several mechanisms for linewidth broadening at high temperature such as carrier–carrier interaction [36] and carrier–phonon interaction [37] have been investigated by theoretical consideration. Compared with cryogenic measurement, however, single-QD PL spectroscopy at room temperature is technically more difficult, since the PL intensity decreases by a few orders due to the escape of carriers to the nonradiative recombination paths and/or thermal excitation to the barrier layer. For that reason, researchers have not yet reported the detailed experimental results of homogeneous linewidth broadening or the comparison between the experimental and the theoretical calculation results at high temperature.

In our single-QD PL spectroscopy study performed over a wide temperature range from 10 to 300 K, we observed that the spectral homogeneous linewidth increases with temperature, and it finally reaches a level greater than 10 meV at 300 K. We also found a correlation between the homogeneous linewidth and the inter-level spacing energy. These measured properties can be explained by theoretical calculations considering the electron–longitudinal optical (LO) phonon and electron–longitudinal acoustic (LA) phonon interactions [38].

The samples investigated in this study were $\text{In}_{0.5}\text{Ga}_{0.5}\text{As}$ self-assembled QDs grown on GaAs (100) substrate fabricated by gas source molecular beam epitaxy [39].

The substrate was not rotated during growth of the QDs to create a gradient in the QD density. There were 70-nm thick cap layers covering the QDs. In order to achieve isolation of a single QD, we measured the region over the wafer where the density of the QDs was from 10^8 to 10^9 cm^{-2} . The typical lateral size and height of the dots were 32 ± 6 and 8 ± 2 nm, respectively, as measured by means of an atomic force microscope.

The QD sample on the scanning stage was illuminated with a laser diode ($\lambda = 687$ nm) through an aperture of the fiber probe under shear-force feedback control. The PL measurements were performed in the illumination and collection hybrid mode to prevent a decrease in spatial resolution due to carrier diffusion. The collected PL signal was sent into a monochromator equipped with a cooled charge-coupled device (CCD). The spectral resolution of this measurement was about 1.5 meV. The NSOM head was mounted in a temperature-controlled cryostat.

Figure 10.18a shows the ground-state emission of single QDs under weak excitation conditions at various temperatures. The excitation power density was kept at a sufficiently low level, where the average number of photoexcited electron–hole pairs (excitons) is less than one in the dot. Under these excitation conditions, the additional PL linewidth broadening due to carrier–carrier interaction does not occur [40, 41]. As shown in Fig. 10.18a, the PL spectrum is sharp at 8 K and the full width of half maximum (FWHM) of the spectrum is 1.5 meV, which is restricted by the spectral resolution in our instrumental response. The real PL linewidth is thought to be much narrower than 1.5 meV, as reported by other groups. The PL spectrum slightly broadens at 96 K, and the line shape can be reproduced by the Lorentzian function indicated by the fitting line. The FWHM of the PL spectrum, which corresponds to the homogeneous linewidth, is about 4 meV. With a further increase in temperature up to 250 K, the PL linewidth reaches approximately 10 meV. To demonstrate the linewidth variation from dot to dot, we measured the PL spectra of three different QDs at 250 K, as shown in Fig. 10.18b. The FWHM varies from 8.5 to 11 meV, and this type of variation of the spectral linewidths has also been reported [42].

Figure 10.19 shows the temperature dependence of the PL linewidths of single QDs from 8 to 300 K. We measured the PL spectra of several different QDs at various temperatures and plotted the experimental PL linewidths as open circles. Below 60 K, the PL linewidths are less than 1.5 meV. With an increase in temperature, the PL linewidth gradually broadens and finally becomes larger than 10 meV at 300 K. We compared this experimental finding with the results obtained by theoretical calculation. Our theoretical approach is fundamentally based upon the Kadanoff–Baym–Keldysh nonequilibrium Green’s function technique [43]. The carriers interacting with phonons have a finite lifetime and violate a unique relation between the carrier energy and its wave vector. The spectral function is used to describe the relationship between them. To simplify the discussion, we consider only the lowest energy levels of the confined electron and the hole inside the quantum box. The LO phonon and LA phonon are assumed to be confined in the QD as well as the electron and the hole. We have plotted the calculation results in Fig. 10.21 as the solid squares and solid triangles, which correspond to the results considering

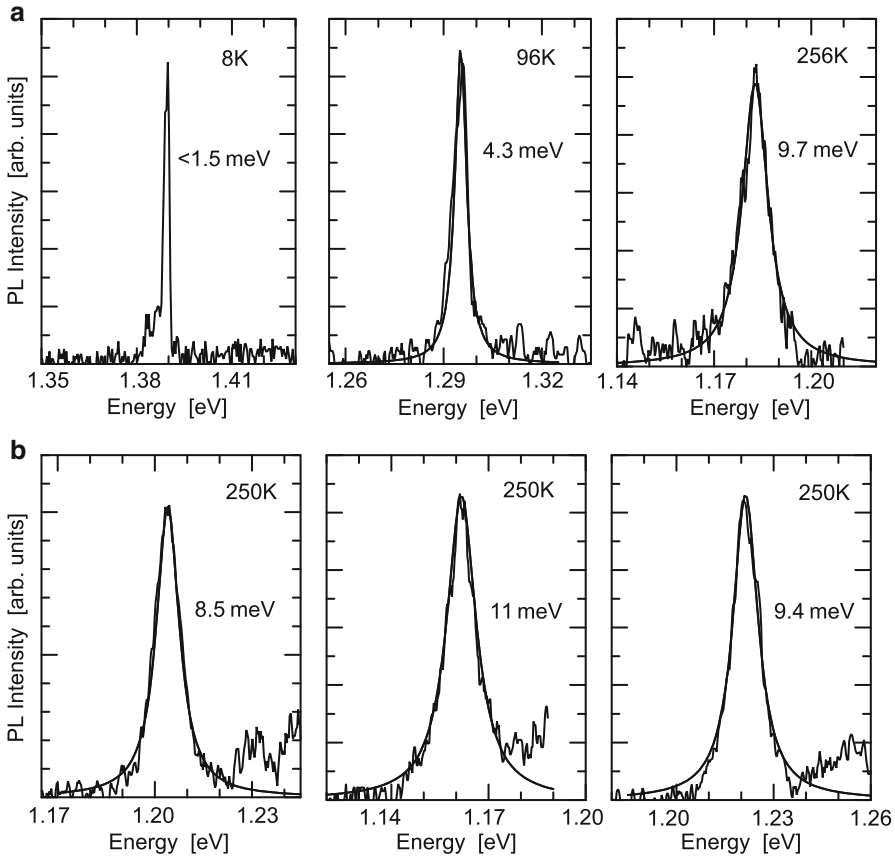
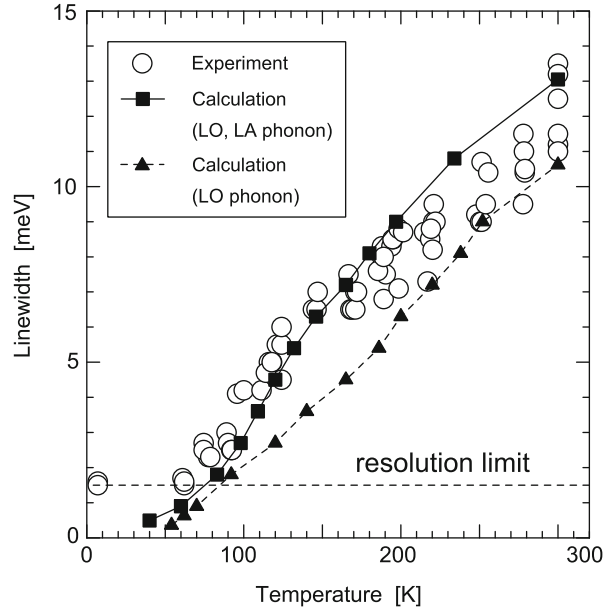


Fig. 10.18 (a) PL spectra of InGaAs single QDs under low excitation conditions at various temperatures. *Smooth lines* correspond to the Lorentzian function. (b) PL spectra of three different QDs at 250 K

both electron–LO and electron–LA phonon interactions and only the electron–LO phonon interaction, respectively. As a matter of course, the increase in the theoretical curves with temperature is coming from the temperature dependence of the phonon numbers. In view of the fairly good agreement between the experimental findings and the results obtained by theoretical calculation, we believe that the homogeneous linewidths measured in this study are governed by the interactions between carriers and phonons. In addition, we found that the interaction with LO phonons dominated the homogeneous linewidth in the high-temperature region.

Next, to understand why the homogeneous linewidths vary from dot to dot, we performed careful measurement of the homogeneous linewidths of many QDs at room temperature. To address the individual QD, we introduce the inter-level spacing energy (ΔE), which reflects the size of the QD. [Figure 10.20a](#) shows the excitation power dependence of the PL spectra of a single QD. The peak intensity

Fig. 10.19 Experimental and theoretical results for homogeneous linewidths as a function of temperature. *Solid squares* and *solid triangles* correspond to the calculated results considering both electron–LO phonon and electron–LA phonon interactions and only the electron–LO phonon interaction, respectively. The *dotted line* represents the spectral resolution in our measurement



of each spectrum is normalized by the excitation power. Under weak excitation conditions, a single peak is observed at 1.158 eV (E_1), which originates from the recombination of the ground state. When the excitation power is higher than 10 μ W, another PL peak appears at the higher energy of 1.205 eV (E_2). From the threshold-like PL behavior as a function of excitation power, it is evident that this emission line of E_2 is associated with the first excited state. Figure 10.20b shows a plot of the PL spectrum at intermediate excitation power. Here, we define the inter-level spacing energy (ΔE) as the energy difference between the ground state and the first excited state ($= E_2 - E_1$).

Figure 10.21 shows the homogeneous linewidths as a function of ΔE , where the experimental data are plotted with open circles. The linewidths tend to increase with ΔE . Here, the absolute values and large variation (25–45 meV) of ΔE are considered to be reasonable as determined by comparing these findings with the results obtained by theoretical calculation taking into account the averaged QD size and its distribution, respectively. Based upon Green’s function theory mentioned above, the homogeneous linewidths are computed for QDs of different size. The closed squares in Fig. 10.21 denote the calculated results considering the interactions with LO and LA phonons. The theoretical calculation results quantitatively reproduce the experimental results, indicating that the magnitude of electron–phonon interaction depends on the ΔE (size of QDs). That is, in the case of a smaller quantum dot, the overlap integral of the carrier and phonon eigenfunctions becomes larger, which leads to a more strongly coupled electron–phonon system. In Fig. 10.21, the contributions from LO– and LA–phonon interactions are also plotted separately. We can see that the ΔE dependence of the LA phonon contribution is

Fig. 10.20 (a) PL spectra of a single QD at various excitation powers ranging between 3 and 20 μW at 300 K. The vertical axis is normalized by the excitation intensity. (b) PL spectra of a single QD under intermediate excitation conditions, where several electron-hole pairs are excited in a QD. Inter-level spacing energy (ΔE) is defined as the energy difference between the ground-state emission energy (E_1) and the first excited state energy (E_2)

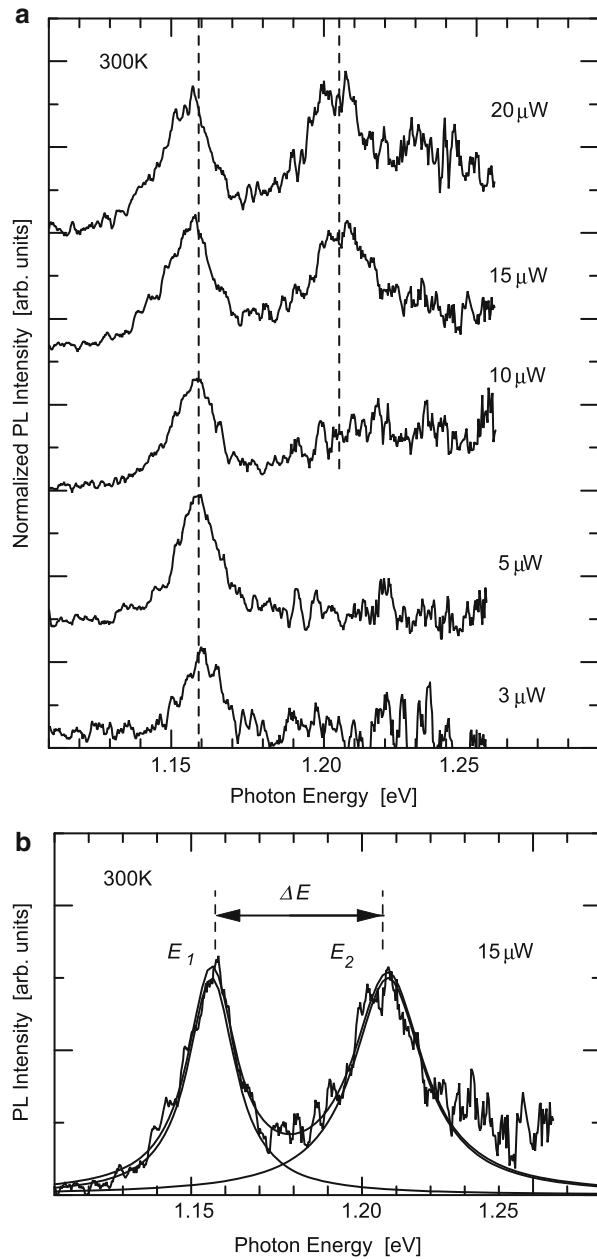
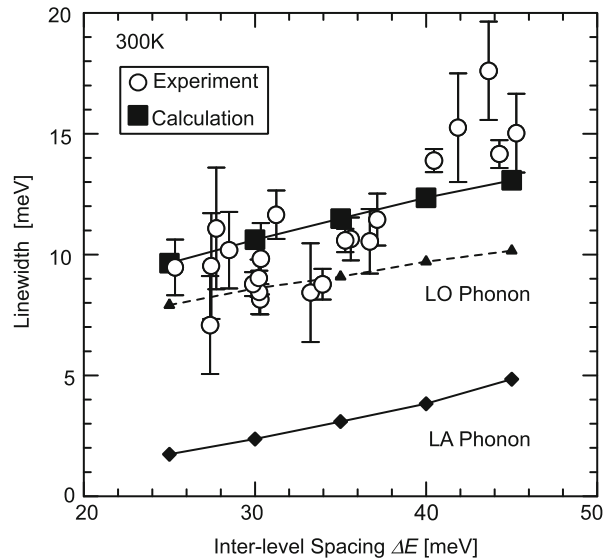


Fig. 10.21 Experimental (open circles) and theoretical (closed squares) results for homogeneous linewidth as a function of inter-level spacing energy (ΔE) at 300 K. Contributions from electron–LO phonon and electron–LA phonon interactions are also plotted separately



slightly larger than that of the LO phonon contribution, which is due to the fact that the deformation potential includes the spatial derivative of the lattice displacement.

As for GaAs/Al_{0.3}Ga_{0.7}As quantum well structures, Gammon et al. have reported the well-width dependence of the homogeneous linewidth [44]. According to their experimental and theoretical results, the linewidth has a weak dependence on the quantum well width. On the contrary, our experimental and theoretical results demonstrate that the strength of the electron–phonon interaction largely varies depending on the spatial confinement in a given QD. Such a size-dependent electron–phonon interaction implies that the QD would have a novel character with a strongly coupled electron–phonon mode.

10.5.2 Homogeneous Linewidth and Carrier–Carrier Interaction

Phenomena occurring under highly excited conditions have been one of the most significant topics that have been frequently studied in bulk, quantum well (QW), and quantum wire (QWR) systems [45–48]. In semiconductors occupied by many carriers, the carrier–carrier interaction appears as a consequence of a change of self-energy. Changes of the real and the imaginary part of a self-energy induce the shrinkage of a fundamental bandgap (band-gap renormalization) and an increase of the damping rate, respectively [45]. The experimental results show that the band-gap renormalization is reduced in accordance with the reduction of a dimensionality from bulk to QWR [48].

As mentioned in the previous subsection, the most essential problem in preventing the realization of ideal QD devices is the several kinds of inhomogeneity

of QD such as size, shape, and strain. However, the homogeneity of QD size is drastically improved when growth conditions are optimized. In this case, the narrow inhomogeneous broadening of 20 meV in the optical spectrum has been realized [49], and the performance of the QD lasers has been much improved. If the inhomogeneous broadening can be suppressed enough, the intrinsic homogeneous linewidth becomes one of the restrictive parameters with respect to attaining the maximum gain. In the operation of a QD laser at room temperature, many carriers are injected in and around the QDs, and the carrier–carrier interaction affects the homogeneous linewidth. Several scattering mechanisms via carrier–carrier interaction have been discussed, and the dephasing rate (linewidth) has been estimated by several theoretical calculations [37]. So far, however, the detailed experimental results involving carrier–carrier interaction in QDs at room temperature have not been reported.

In this subsection, we described a single-QD PL spectroscopy in high excitation conditions at room temperature. We concentrated on the characteristic excitation power-dependent shift and broadening of ground-state emission. These behaviors have been discussed while taking into consideration the carrier–carrier interaction in QDs.

Figure 10.22a shows the excitation power dependence of PL spectra in a single QD and WL at 300 K. In the weak excitation condition, a single PL line originating from the recombination of an electron and hole pair in the lowest energy level (ground state: E_1) is observed at 1.222 eV. With an increase of the excitation power density, additional lines associated with excited states (E_2 , E_3) appear and grow up at 1.252 and 1.280 eV. The shape of each spectrum is well reproduced by a sum of Lorentzian functions. The precise values of the transition energy and the linewidth are determined from the fitting results. The additional broadening and spectral redshift of the ground-state emission are observed at several kW/cm². Such behaviors have been commonly observed in 20 QDs, which we have investigated.

Figure 10.22b shows the integrated PL intensities of both the ground state and the first excited state as a function of excitation power densities. The PL intensity of the ground state (I_g : closed circles) grows linearly as a function of excitation power density and reaches saturation at approximately 1.5 kW/cm². The nonlinear power dependence of the PL intensity indicates that the nonradiative recombination process is dominant at room temperature [50]. The PL intensity of the first excited state (I_{exc} : open squares) increases more rapidly than I_g above 0.5 kW/cm². The inset of Fig. 10.22b shows the excitation power dependence of the ratio of the emission intensity from the first excited state to that from the ground state ($= I_{exc}/I_g$), which reflects the degree of a carrier population in the first excited state. The PL intensity ratio is constant below 0.5 kW/cm². The finite population in the first excited state at the lowest excitation condition is well understood by the thermal carrier excitation at 300 K. The ratio exhibits critical increases above 0.5 kW/cm² because additional carriers occupy the first excited state due to the strong excitation. Hereafter, we define the power density where the PL intensity ratio critically changes as I_0 .

Fig. 10.22 (a) PL spectra of a single QD at various excitation densities ranging from 0.3 to 7.1 kW/cm². (b) Excitation power dependence of integrated PL intensity at ground-state emission (I_g : closed circles) and at the first excited state (I_{exc} : open circles). Inset shows the PL intensity ratio (I_g/I_{exc}) as a function of excitation density. The excitation power density at which the PL intensity ratio exhibits a critical increase is defined as I_0

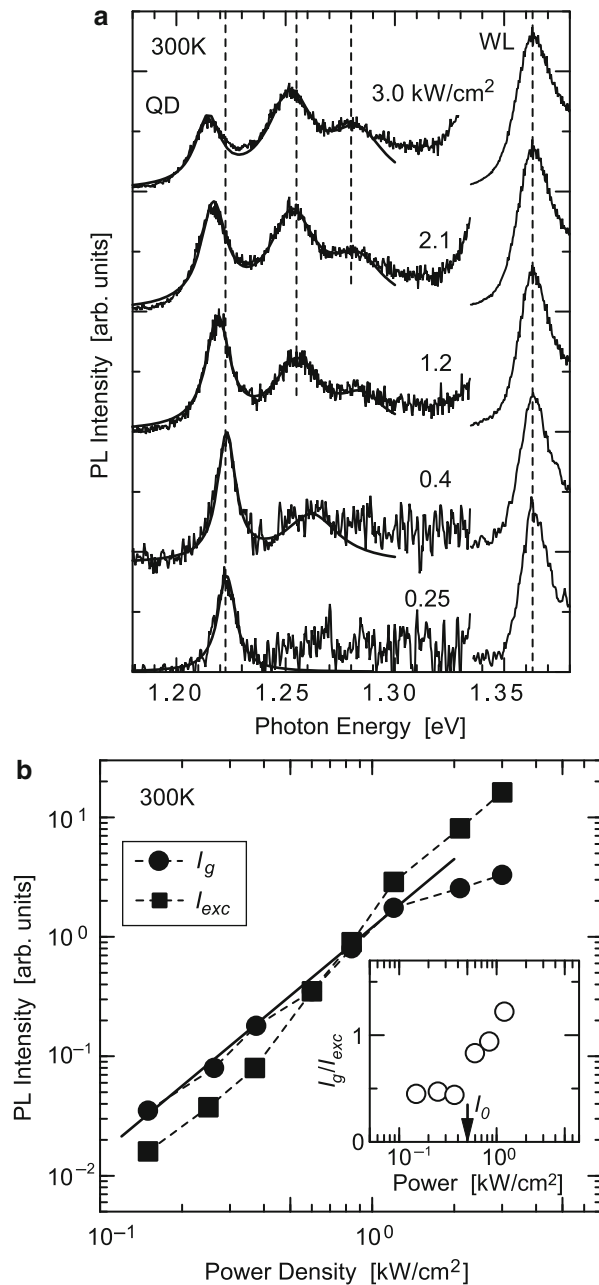
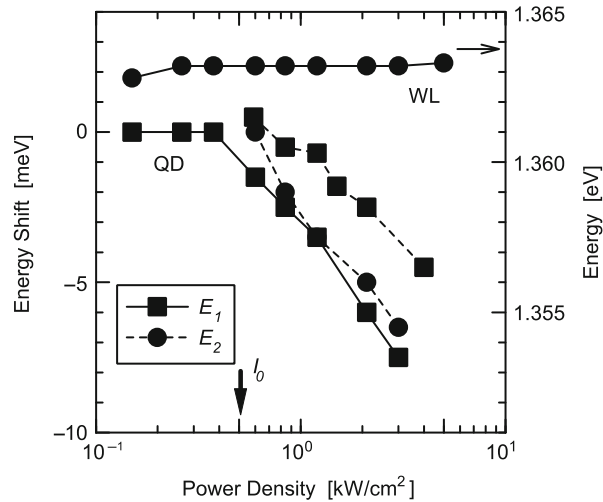


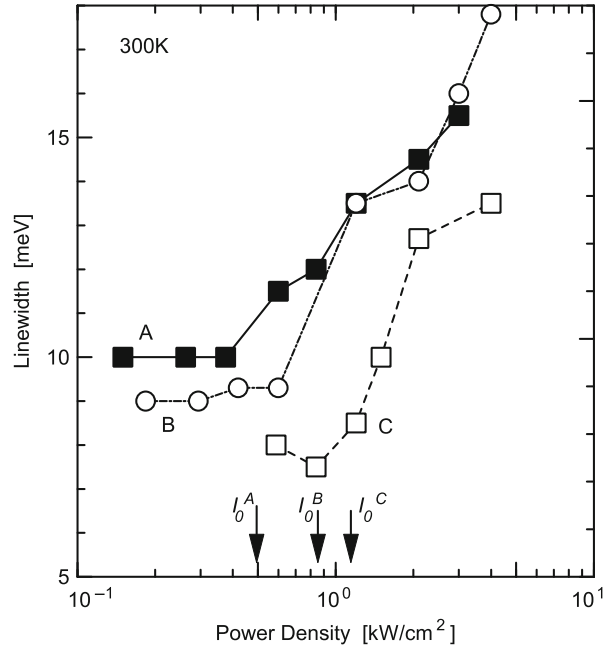
Fig. 10.23 Energy shifts of the ground-state emission (E_1) and the first excited state (E_2) of QD as a function of excitation power density. The PL peak energy of WL as a function of power density is also plotted



To study the many-body effect in the QD, we have plotted the spectral energy shift of the ground state (E_1) and the first excited state emission (E_2) of the QD and WL as a function excitation power in Fig. 10.23. Both E_1 and E_2 shift to the lower energy side with an increase in excitation density [51]. As the PL peak energy of the WL and GaAs barrier layer (not shown) does not change, the redshift of E_1 and E_2 cannot be explained by simple band-gap shrinkage of the barrier layer; rather, it is caused by the band-gap renormalization of the QD itself due to the Coulomb interaction between carriers. When the excited carrier density is $2 \times 10^{17} \text{ cm}^{-3}$, the value of band-gap renormalization is evaluated to be 8 meV, which is in good agreement with the theoretical predictions [52, 53].

Next, we examined additional broadening by evaluating the linewidth of the ground-state emission. Figure 10.24 shows a dependence of the emission linewidth (A: closed squares) on the excitation power density. Results of two different QDs (B: open circles, C: open squares) are also plotted. The linewidth remains constant below I_0 . In this regime, the broadening is well explained by the dephasing process due to the interaction between electron (carrier) and phonon, which has already been discussed in detail [38]. At higher excitation, the linewidth increases with the excitation power. Through the investigation of many QDs, we found that the values of I_0 were scattered from QD to QD, and we also found that additional broadening always starts to occur at I_0 , that is, when the carriers are populated in the excited state of QD. The strong dependence of this broadening on the excitation power implies that the interaction between carriers, such as the Auger scattering process, would lead to an increased dephasing rate. We should consider two types of Auger scattering process in the QD system grown in the S-K mode. One is the scattering process that takes place between confined carriers in the QD and free carriers in two-dimensional (2D) WL. The other is the intra-QD process, in which carriers in the QD interact each other.

Fig. 10.24 Linewidth of the ground-state emission (E_1) as a function of excitation power density for three different QDs



We will discuss which processes are dominant in terms of causing the excitation power-dependent broadening in the QD system. First, we consider the scattering process between confined carriers in a QD and free carriers in a 2D WL. A theoretical calculation predicts that the exchange process between a carrier in the QD and a free carrier in the WL causes a broadening of several meV at high carrier density and that the value of broadening is determined by the carrier density in the WL. However, this mechanism should be ruled out because the broadening behavior in the experiment differs from QD to QD (Through the 2D mapping of PL intensity, we confirmed that the carrier density in WL was uniform in the observation area).

Next, we consider the intra-QD scattering process, where the broadening depends on the carrier population in the QD [54, 55]. The correlation between the additional broadening and the carrier population in the excited states of the QD, as shown in Fig. 10.24, indicates that the intra-QD process is a dominant mechanism for the broadening. From the experimental results, we conclude that an Auger scattering process with the following scenario is most probable. First, there is a relaxation of the hole into the QD from the WL and the excitation of an electron into a higher level via Coulomb interaction. As a next step, the electron relaxes to the lowest level and the hole is emitted into the WL. Theoretically, the additional broadening of several meV is possible if the capture and emission processes are efficient. Further theoretical studies that take the realistic electronic structure into consideration will be needed for the quantitative explanation of the experimental results.

10.6 Real-Space Mapping of Exciton Wave Function Confined in a QD

As described in the previous section, the near-field optical characterization of semiconductor quantum structures, with a resolution of approximately $0.2\ \mu\text{m}$, reveals sharp PL spectra from individual quantum constituents and provides a significant contribution to the investigation of their intrinsic electronic structure and dynamics. Beyond such single-constituent spectroscopy, the next challenge of near-field optical measurement is to illustrate directly the internal features of quantum-confined systems [56]. If the spatial resolution of NSOM reaches the length scale of the quantum structure, theoretical studies predict that the NSOM will allow mapping of the real-space distribution of eigenstates (wave functions) within quantum-confined systems [57]. Moreover, in combination with ultrafast pulsed excitation, the local access to single QD systems enables control of individual eigenstates in a coherent manner, which provides a fundamental technique in quantum-information technology.

In this section, the near-field optical mapping of exciton and biexciton center-of-mass wave functions confined in 100-nm GaAs interface QDs is demonstrated. The QDs investigated in this study are much smaller than those investigated in a previous report [56]. The successful imaging of such a small quantum electronic structure is attributed to improvement in the design and fabrication of the near-field fiber probe.

The sample investigated in this study was a 5-nm (18–19ML) GaAs QW sandwiched between layers of AlAs and $\text{Al}_{0.3}\text{Ga}_{0.7}\text{As}$ grown by molecular beam epitaxy. Growth interruptions for 2 min at both interfaces led to the formation of naturally occurring QDs, as shown in Fig. 10.25. The GaAs QW was capped with a 15-nm $\text{Al}_{0.3}\text{Ga}_{0.7}\text{As}$ layer and a 5-nm GaAs layer. As we see in the above section, a spatial resolution as high as 30 nm can be achieved even when QDs are covered with 20-nm cap layers. As depicted in Fig. 10.25, the sample was non-resonantly

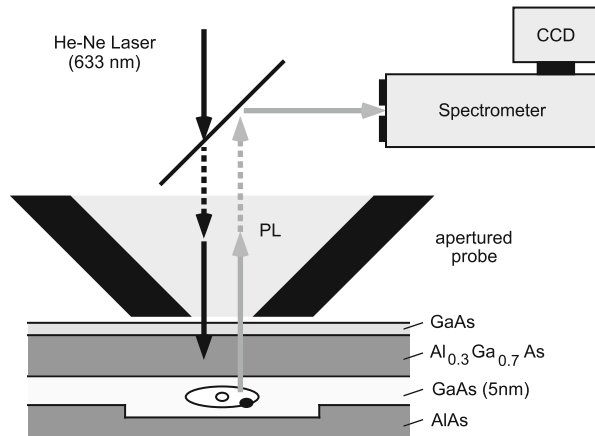


Fig. 10.25 Schematic of the sample structure and the configuration of the near-field optical measurement

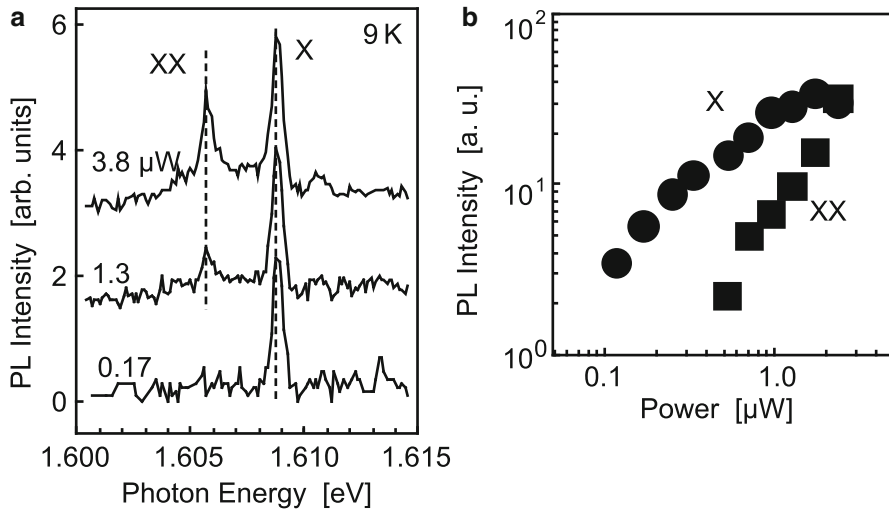


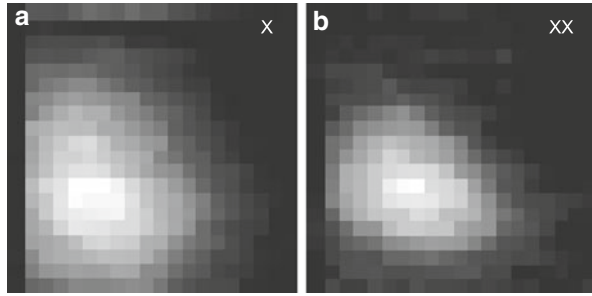
Fig. 10.26 (a) Near-field PL spectra of a single QD at 9K under various excitation power densities. (b) Excitation power dependence of PL intensities of the X and the XX emission line

excited with He–Ne laser light ($\lambda = 633$ nm) through the aperture, and the resultant PL signal was collected via the same aperture to prevent a reduction of the spatial resolution due to carrier diffusion. The near-field PL spectra were measured at every 10-nm step in a 210-nm \times 210-nm area, and the near-field images were constructed from a series of PL spectra.

Figure 10.26a shows near-field PL spectra of a single QD at 9K at excitation power densities ranging from 0.17 to 3.8 W/cm². A single sharp emission line (denoted by X) at 1.6088 eV is observed below 0.4 W/cm². With an increase in excitation power density, another emission lines appear at 1.6057 eV (denoted by XX). In order to clarify the origin of these emissions, we show the excitation power dependence of PL intensities in Fig. 10.26b. Based on the linear increase of the intensity of the X emission line and the saturation behavior, the X line is identified as an emission from a single-exciton state. The quadratic dependence of the XX emission with excitation power density indicates that XX is attributed to an emission from a biexciton state [47, 58]. The identification of the XX line is also supported by the correlation energy of 3.1 meV (the energy difference between the XX line and the X line), which agrees well with the value reported previously [47, 58].

High-resolution PL images in Fig. 10.27a, b were obtained by mapping the PL intensity with respect to the X and the XX lines under the excitation density of 1.3 W/cm². In this excitation regime, both the emissions from single-exciton (X) and biexciton (XX) states appear in a PL spectrum. The two images were obtained by selecting the detection peak in a series of PL spectra. The exciton PL image in Fig. 10.27a manifests an elongation along the $[-110]$ crystal axis. The image sizes along the $[110]$ and $[-110]$ axes are 80 nm and 130 nm, respectively, which

Fig. 10.27 High-resolution PL mapping for the emissions from (a) the exciton state (X) and (b) the biexciton state (XX). The excitation power density and scanning area are 1.3 W/cm^2 and $210 \text{ nm} \times 210 \text{ nm}$, respectively



are larger than the PL collection spot diameter, that is, the spatial resolution of the NSOM. The size and the elongation along the $[-110]$ axis are consistent with a previous observation made with a scanning tunneling microscope [5]. These findings lead to a conclusion that the local optical probing of the NSOM directly maps out the center-of-mass wave function of an exciton confined in a monolayer-high island elongated along the $[110]$ crystal axis.

We also obtained the elongated biexciton PL image along the $[-110]$ crystal axis and found a clear difference in the spatial distribution between the exciton and the biexciton emissions. This tendency was reproduced for other QDs in using the same measurement. The different properties between exciton and biexciton wave functions may explain this. Since the relative-motion wave function of the biexciton state extends more widely than does that of the exciton state, the center-of-mass motion of the biexciton is more strongly confined in the monolayer-high island.

10.7 Carrier Localization in Cluster States in GaNAs

In contrast to the well-defined quantum-confined systems such as QDs grown in a self-assembled mode, the more common disordered systems with local potential fluctuations leave unanswered questions. For example, a large reduction of the fundamental band gap in GaAs with small amounts of nitrogen is relevant to the clustering behavior of nitrogen atoms and resultant potential fluctuations. NSOM characterization with high spatial resolution can give us a lot of important information that is useful in our quest to fully understand such complicated systems, such as details about the localization and delocalization of carriers, which determine the optical properties in the vicinity of the band gap.

The GaNAs and GaInNAs semiconductor alloy system has attracted a great deal of attention due to its interesting physical properties, such as its extremely large band-gap bowing [59], and its wide range of potential applications in solar cells and optoelectronic devices. In particular, for long-wavelength semiconductor laser application, high-temperature stability of the threshold current is realized in the GaInNAs/GaAs quantum well as compared to the conventional InGaAsP/InP quantum well due to strong electron confinement [60]. However, GaNAs and

GaInNAs with a high nitrogen concentration of more than 1% have been successfully grown only under nonequilibrium conditions by molecular beam epitaxy [61, 62] and metal-organic vapor phase epitaxy [63].

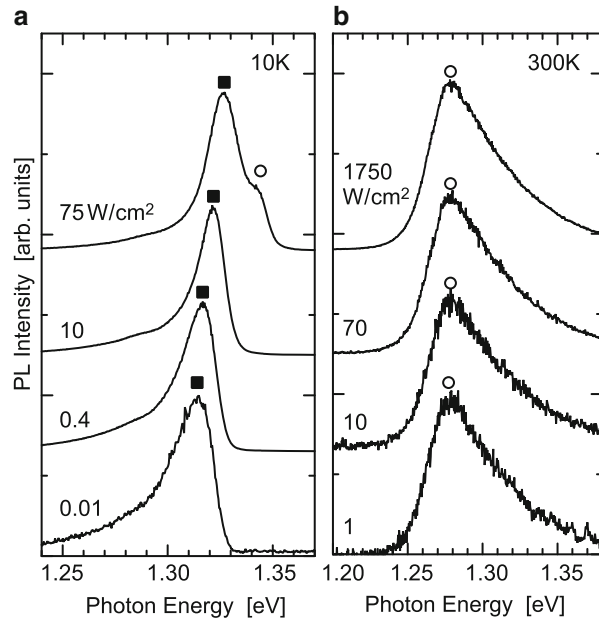
The incorporation of nitrogen generally induces degradation of optical properties [64–69]. To date, several groups of researchers have reported characteristic PL properties of GaNAs and GaInNAs, for example, the broad asymmetric PL spectra [64, 67, 69] and the anomalous temperature dependence of the PL peak energy [65, 68]. With respect to this characteristic PL behavior, it has been pointed out in the realm of macroscopic optical characterization that carrier localization plays an important role. By contrast, microscopic optical characterization techniques with high spatial resolution can give us a lot of important information that allows us to understand the optical properties, especially the localization or delocalization of carriers.

In this section, we show the results of spatially resolved PL spectroscopy at both 7.5 and 300 K obtained using NSOM with a high spatial resolution of 150 nm. At low temperature, we observed sharp-structured PL spectra and the spatial distribution of the PL intensity of the GaNAs alloy. This spatial inhomogeneity is direct evidence of carrier localization in the potential minimum case caused by the compositional fluctuation [70].

The samples investigated in this study were GaNAs epilayers grown on (001) GaAs substrates by low-pressure metal-organic vapor phase epitaxy. The details of the growth conditions are described in Ref. [71]. The GaNAs layer was sandwiched by a 100-nm thick GaAs buffer layer and a 50-nm thick GaAs cap layer. The GaNAs layer was 500 nm thick, and the N concentration was estimated to be 0.8% by high-resolution X-ray diffraction and secondary ion mass spectroscopy. After growth, thermal annealing was performed for 10 minutes in H₂ ambient at 700 K to improve the optical properties [71]. The macro-PL spectra were measured at both 10 and 300 K with excitation by means of a laser diode ($\lambda = 687$ nm). In the NSOM measurement, the sample was also illuminated by the laser diode through the aperture of the fiber probe, and the PL signal from the GaNAs epilayer was collected by the same aperture.

Figure 10.28a shows the excitation power dependence of the macro-PL spectrum from a GaNAs epilayer at 10 K. Broad and asymmetric PL spectra with a low-energy tail as shown in Fig. 10.28a were observed under low excitation conditions. With an increase in excitation power density, the PL intensity of the low energy-tail gradually reaches saturation, and the peak energy of the PL spectra (solid square) is shifted to the higher energy side. In the PL spectrum under the highest excitation conditions, we can see the appearance of a shoulder (open circles) corresponding to the transition energy of the band edge (1.343 eV) determined by the photoreflectance spectrum [72]. Figure 10.28b shows the excitation power dependence of the macro-PL spectra at room temperature. In contrast to what occurs at low temperature, the peak energy indicated by the open circles and the shape of the PL spectra do not change with an increase in excitation power. Here, it should be noted that we observed no broad emission due to recombination of the carriers at a deep trap in GaAs, and the quality of this sample was high. From the PL behavior as a

Fig. 10.28 Power dependence of the macro-photoluminescence (PL) spectra of a GaNAs epilayer at (a) 10 and (b) 300 K. The vertical axis of the PL spectrum was normalized by the maximum value of each peak



function of excitation power dependence, it is evident that the carrier recombination mechanism drastically changes from 10 to 300 K.

In order to investigate the spatial distribution of the optical properties, we performed spatially resolved PL spectroscopy with NSOM at room temperature. Figure 10.29a shows a typical topographic image of the sample surface. The flatness of the sample surface is within a few nanometers, which does not affect the artificial effect for near-field optical images. Figure 10.29b shows the monochromatic PL image obtained at a detection energy of 1.268 eV with a spatial resolution of 150 nm at 300 K. Weak contrast on a large scale of a few micrometers is observed. Figure 10.29c shows the near-field and macro-PL spectra at 300 K. The near-field PL spectrum is almost the same as the macro-PL spectrum, indicating that the carriers do not localize spatially. The PL spectrum with a higher energy tail is well reproduced by the fitted curves (open circles), assuming that the carriers are found in a bulk system with Boltzmann distribution. Therefore, we can conclude that the dominant emission of the GaNAs epilayer at room temperature comes from the recombination of the delocalized carriers at the band edge.

To examine the difference in the mechanism of recombination of carriers between room temperature and cryogenic temperature, we conducted a near-field PL measurement at 7.5 K. Figure 10.30a, b show the low-temperature monochromatic PL images obtained at a detection energy of 1.316 and 1.328 eV, respectively. We observed high-contrast images with structures on a scale of within 1 μm , as shown in both Figs. 10.30a, b. By comparing Figs. 10.30a, b, we can see that the contrast pattern of the monochromatic image changes in accordance with the detected photon

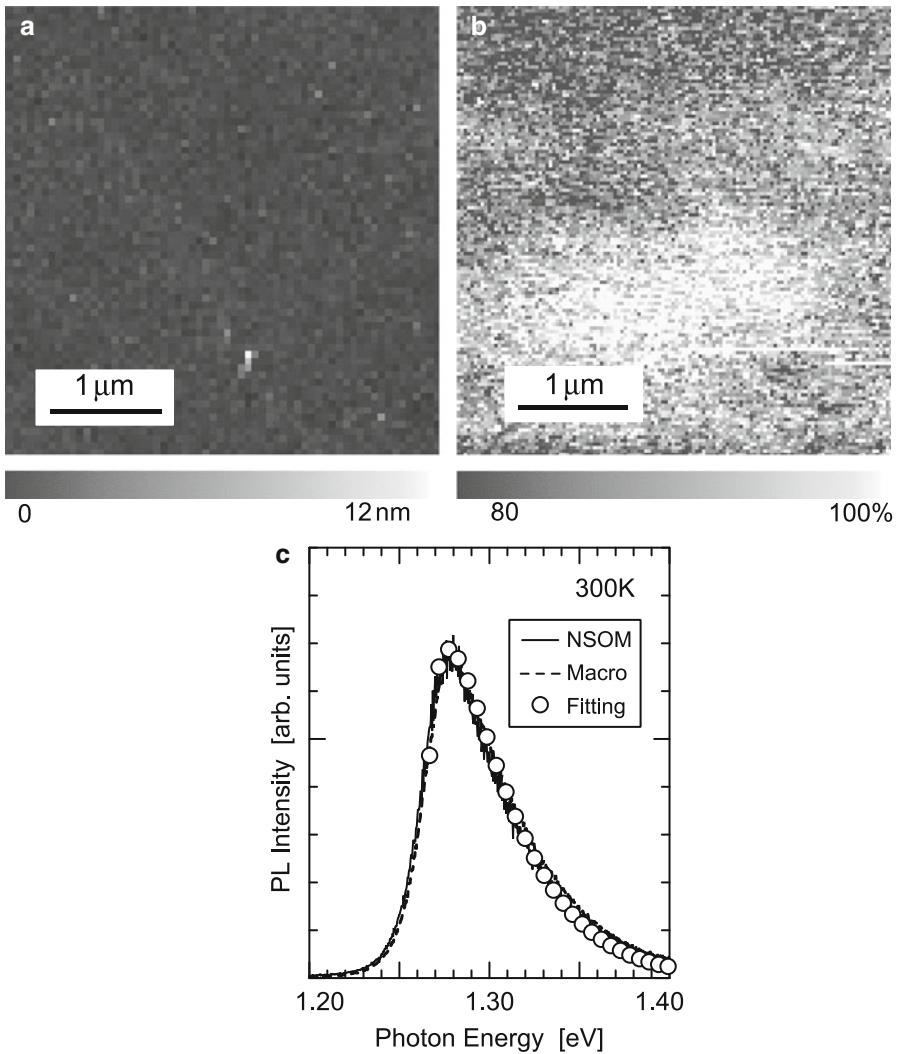


Fig. 10.29 (a) Topographic image of the sample surface. The scanning area and power density is $4.0\ \mu\text{m} \times 4.0\ \mu\text{m}$. (b) Monochromatic PL images obtained at a detection energy of 1.268 eV with a spectral window of 6 meV at 300 K. (c) PL spectra obtained with the macro (*dotted line*) and near-field (*solid line*) configuration. The power density of near-field PL measurement is $200\ \text{W}/\text{cm}^2$. The *open circles* represent the fitted curves assuming the free-carrier recombination at the band edge

energy. These high-contrast and energy-dependent images suggest the existence of energy fluctuation on a scale of within $1\ \mu\text{m}$. [Figure 10.30c](#) shows the integrated PL intensity image obtained at a photon energy of 1.325 eV with a spectral window of 30 meV to detect the whole PL signal at 7.5 K. Spatial inhomogeneity of the

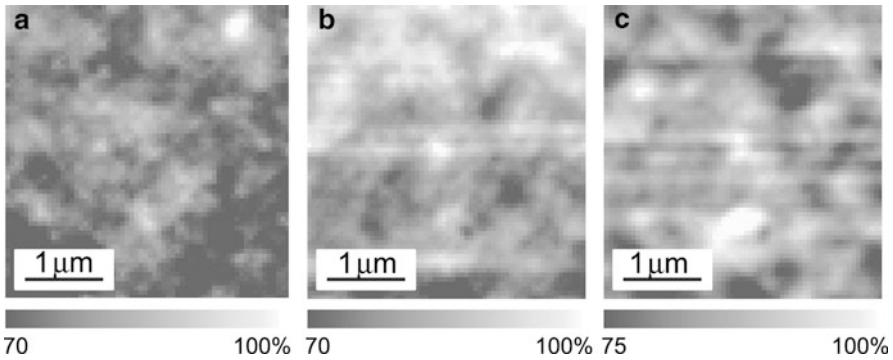


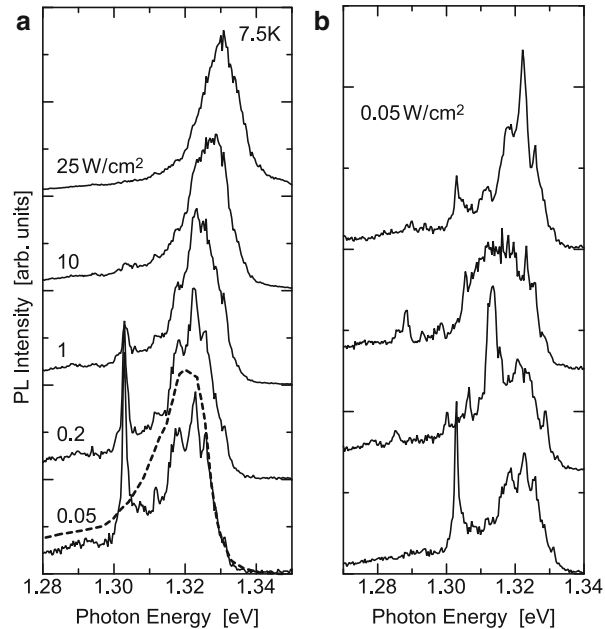
Fig. 10.30 (a), (b) Monochromatic PL images obtained at a photon energy of 1.316 and 1.328 eV, respectively, with a spectral resolution of 4 meV, measured at 7.5 K. (c) Integrated PL intensity image obtained at a photon energy of 1.325 eV with a spectral window of 30 meV. The scanning area and excitation power density are $4.0 \mu\text{m} \times 4.0 \mu\text{m}$ and about 5 W/cm^2 , respectively

integrated PL intensity with a scale of several hundred nanometers was observed, indicating that the density of the defect and the nonradiative recombination center are distributed spatially [73].

Figure 10.31a shows the near-field PL spectrum and its power dependence as determined by fixing the fiber probe at a certain position. Under the lowest excitation conditions (the lowest spectrum in Fig. 10.31a), several sharp peaks at around 1.32 eV, not seen in the macro-PL spectrum (dotted line), are clearly observed. With an increase in excitation density, the sharp PL peaks gradually show saturation, and the center of gravity in the PL spectrum shifts to the higher energy side. Finally, we observed structureless PL spectra similar to the macro-PL spectra. Judging from the sharp spectral features and the rapid saturation behavior, it seems that the sharp PL peaks observed under low excitation conditions come from the recombination of localized carriers (excitons).

To confirm whether these sharp PL peaks originate from the recombination of localized carriers (excitons), we measured the position dependence of the near-field PL spectra shown in Fig. 10.31b. These four PL spectra were obtained at different positions under low excitation conditions. The number of sharp peaks and these energy positions in each spectrum is drastically different from position to position. These sharp emissions occur in a small area on a scale of within 150 nm, that is, in the local potential minimum, and the scale of the local potential fluctuation is estimated to be at least within 150 nm. Therefore, we conclude that the dominant emission mechanism at low temperature is recombination of the trapped and localized carriers (excitons) due to energy fluctuation. This energy fluctuation could come from the compositional variation of nitrogen, since the spatial distribution of the optical properties strongly depends on the nitrogen concentration and the scale of the inhomogeneity decreases with an increase in nitrogen concentration.

Fig. 10.31 (a) Near-field PL spectra at various excitation power densities at 7.5 K. The dotted line represents the macro-PL spectrum. (b) Near-field PL spectra obtained in different positions under low excitation conditions



10.8 Perspectives

The quality and reproducibility of aperture NSOM measurements have been greatly improved in the last decade by the introduction of high-definition fiber probes made by combining chemical etching with ion-beam milling or by using a simpler impact method. The flat end of the probe provides high spatial resolution determined solely by the aperture size, down to 10 nm. The probes, however, should be improved with respect to optical transmission, tip stability, and damage threshold for routine applications in material characterization, device diagnostics, and industrial testing. Micromachined, cantilever-based probes offer a promising solution to these difficulties. Recently, these kinds of high-performance probes are available as commercial products and contribute to expanding NSOM users and its application field. Nano-imaging spectroscopy of semiconductor nanostructures will continue to attract much attention by extending the operation wavelength into infrared region. At such wavelength we can determine the free-carrier density and hence the dopant concentration nondestructively. Also near-field imaging of thermal radiation will reveal the possibility of enhanced heat transfer. NSOM working in THz regime will allow spatiotemporal visualization of phonon dynamics and phase transition process. In combination with polarization control and measurement, NSOM makes it possible to generate, manipulate, and read out the electron spin state at the nanoscale. This will open new perspectives towards nano-spin photonics with semiconductor nanostructures.

Acknowledgements We are grateful to M. Ohtsu, S. Mononobe, K. Matsuda, N. Hosaka, H. Kambe, K. Sawada, H. Nakamura, T. Inoue, F. Sato, K. Nishi, H. Saito, Y. Aoyagi, M. Mihara, S. Nomura, M. Takahashi, A. Moto, and S. Takagishi for their assistance and fruitful discussions.

References

1. P. Borri, W. Langbein, S. Schneider, U. Woggon, R.L. Sellin, D. Ouyang, D. Bimberg, Phys. Rev. Lett. **87**, 157401 (2001)
2. D. Birkedal, K. Leosson, J.M. Hvam, Phys. Rev. Lett. **87**, 227401 (2001)
3. K. Brunner, G. Abstreiter, G. Bohm, G. Trankel, G. Weimann, Phys. Rev. Lett. **73**, 1138 (1994)
4. H.F. Hess, E. Betzig, T.D. Harris, L.N. Pfeiffer, K.W. West, Science **264**, 1740 (1994)
5. D. Gammon, E.S. Snow, B.V. Shanabrook, D.S. Katzer, Phys. Rev. Lett. **76**, 3005 (1996)
6. T.H. Stievater, X. Li, D.G. Steel, D. Gammon, D.S. Katzer, D. Park, C. Piermarocchi, L.J. Sham, Phys. Rev. Lett. **87**, 133603 (2001)
7. H. Kamada, H. Gotoh, J. Temmyo, T. Takagahara, H. Ando, Phys. Rev. Lett. **87**, 246401 (2001)
8. G. Chen, N.H. Bonadeo, D.G. Steel, D. Gammon, D.S. Katzer, D. Park, L.J. Sham, Science **289**, 1906 (2000)
9. P. Michler, A. Kiraz, C. Becher, W.V. Schoenfeld, P.M. Petroff, L. Zhang, E. Hu, A. Imamoglu, Science **290**, 2282 (2000)
10. M. Ohtsu, *Near-Field Nano/Atom Optics and Spectroscopy* (Springer, Tokyo, 1998)
11. M. Ohtsu, *Optical and Electronic Process of Nano-Matters* (Kluwer Academic, Dordrecht, 2001)
12. S. Kawata, *Near-Field Optics and Surface Plasmon Polaritons* (Springer, Telos, 2001)
13. V. Emiliani, T. Guenther, C. Lienau, R. Nötzel, K.H. Ploog, Phys. Rev. B **61**, R10583 (2000)
14. M. Achermann, B.A. Nechay, F. Morie-Genoud, A. Schertel, U. Siegner, U. Keller, Phys. Rev. B **60**, 2101 (1999)
15. N.H. Bonadeo, J. Erland, D. Gammon, D. Park, D.S. Katzer, D.G. Steel, Science **282**, 1473 (1998)
16. Y. Toda, T. Sugimoto, M. Nishioka, Y. Arakawa, Appl. Phys. Lett. **76**, 3887 (2000)
17. G.A. Valaskovic, M. Holton, G.H. Morrison, Appl. Opt. **34**, 1215 (1995)
18. T. Pangaribuan, K. Yamada, S. Jiang, H. Ohsawa, M. Ohtsu, Jpn. J. Appl. Phys. **31**, L1302 (1992)
19. S. Mononobe, M. Ohtsu, IEEE Photon. Technol. Lett. **10**, 99 (1998)
20. M. Muranishi, K. Sato, S. Hosaka, A. Kikukawa, T. Shintani, K. Ito, Jpn. J. Appl. Phys. **36**, L942 (1997)
21. T. Saiki, K. Matsuda, Appl. Phys. Lett. **74**, 2773 (1999)
22. T. Saiki, S. Mononobe, M. Ohtsu, N. Saito, J. Kusano, Appl. Phys. Lett. **68**, 2612 (1996)
23. H. Furukawa, S. Kawata, Opt. Commun. **132**, 170 (1996)
24. H. Nakamura, T. Sato, H. Kambe, K. Sawada, T. Saiki, J. Microsc. **202**, 50 (2001)
25. H.A. Bethe, Phys. Rev. **66**, 163 (1944)
26. K. Matsuda, T. Saiki, S. Nomura, M. Mihara, Y. Aoyagi, Appl. Phys. Lett. **81**, 2291 (2002)
27. D. Gammon, E.S. Snow, D.S. Katzer, Appl. Phys. Lett. **67**, 2391 (1995)
28. N. Hosaka, T. Saiki, J. Microsc. **202**, 362 (2001)
29. X.S. Xie, R.C. Dunn, Science **265**, 361 (1994)
30. T. Saiki, K. Nishi, M. Ohtsu, Jpn. J. Appl. Phys. **37**, 1639 (1998)
31. E. Dekel, D. Gershoni, E. Ehrenfreund, D. Spektor, J.M. Garcia, P.M. Petroff, Phys. Rev. Lett. **80**, 4991 (1998)
32. Y. Toda, O. Moriwaki, M. Nishioka, Y. Arakawa, Phys. Rev. Lett. **82**, 4114 (1999)
33. M. Notomi, T. Furuta, H. Kamada, J. Temmyo, T. Tamamura, Phys. Rev. B **53**, 15743 (1996)

34. K. Ota, N. Usami, Y. Shiraki, *Phys. E* **2**, 573 (1998)
35. D. Gammon, E.S. Snow, B.V. Shanabrook, D.S. Katzer, D. Park, *Science* **273**, 87 (1996)
36. A.V. Uskov, K. Nishi, R. Lang, *Appl. Phys. Lett.* **74**, 3081 (1999)
37. H. Tsuchiya, T. Miyoshi, *Solid-State Electron.* **42**, 1443 (1998)
38. K. Matsuda, K. Ikeda, T. Saiki, H. Tsuchiya, H. Saito, K. Nishi, *Phys. Rev. B* **63**, 121304 (2001)
39. K. Nishi, R. Mirin, D. Leonard, G. Medeiros-Ribeiro, P.M. Petroff, A.C. Gossard, *J. Appl. Phys.* **80**, 3466 (1996)
40. H. Kamada, J. Temmyo, M. Notomi, T. Furuta, T. Tamamura, *Jpn. J. Appl. Phys.* **36**, 4194 (1998)
41. P. Borri, W. Langbein, J.M. Hvam, F. Heinrichsdorff, M.-H. Mao, D. Bimberg, *Appl. Phys. Lett.* **76**, 1380 (2000)
42. K. Matsuda, T. Saiki, H. Saito, K. Nishi, *Appl. Phys. Lett.* **76**, 73 (2000)
43. H. Tsuchiya, T. Miyoshi, *Microelectron. Eng.* **47**, 139 (1999)
44. D. Gammon, S. Rudin, T.L. Reinecke, D.S. Katzer, C.S. Kyono, *Phys. Rev. B* **51**, 16785 (1995)
45. H. Haug, S.W. Koch, *Quantum Theory of the Optical and Electronic Properties of Semiconductors* (World Scientific, Singapore, 1993)
46. G. Trankel, E. Lach, A. Forchel, F. Scholz, C. Ell, H. Haug, G. Wimann, *Phys. Rev. B* **36**, 3712 (1987)
47. Q. Wu, R.D. Grober, D. Gammon, D.S. Katzer, *Phys. Rev. B* **62**, 13022 (2000)
48. R. Rinaldi, G. Coli, A. Passaseo, R. Cingolani, *Phys. Rev. B* **59**, 2230 (1999)
49. K. Nishi, H. Saito, S. Sugou, J.-S. Lee, *Appl. Phys. Lett.* **74**, 1111 (1999)
50. M. Sugawara, K. Mukai, Y. Nakata, *Appl. Phys. Lett.* **75**, 656 (1999)
51. R. Heitz, F. Guffarth, I. Mukhametzhanov, M. Grundmann, A. Madhukar, D. Bimberg, *Phys. Rev. B* **62**, 16881 (2000)
52. S.V. Nair, Y. Masumoto, *Phys. Status Solidi A* **178**, 303 (2000)
53. S.V. Nair, Y. Masumoto, *J. Lumin.* **87–89**, 438 (2000)
54. A.V. Uskov, I. Magnusdottir, B. Tomborg, J. Mork, R. Lang, *Appl. Phys. Lett.* **79**, 1679 (2001)
55. R. Ferreira, G. Bastard, *Appl. Phys. Lett.* **74**, 2818 (1999)
56. J.R. Guest, T.H. Stievater, G. Chen, E.A. Tabak, B.G. Orr, D.G. Steel, D. Gammon, D.S. Katzer, *Science* **293**, 2224 (2001)
57. G.W. Bryant, *Appl. Phys. Lett.* **72**, 768 (1998)
58. G. Chen, T.H. Stievater, E.T. Batteh, X. Li, D.G. Steel, D. Gammon, D.S. Katzer, D. Park, L.J. Sham, *Phys. Rev. Lett.* **88**, 117901 (2002)
59. M. Weyers, M. Sato, H. Ando, *Jpn. J. Appl. Phys.* **31**, 853 (1992)
60. X. Yang, J.B. Heroux, M.J. Jurkovic, W.I. Wang, *Appl. Phys. Lett.* **76**, 795 (2000)
61. M. Kondow, S. Nakatsuka, T. Kitatani, Y. Yazawa, M. Okai, *Jpn. J. Appl. Phys.* **35**, 5711 (1996)
62. M. Kondow, K. Uomi, K. Hosomi, T. Mozume, *Jpn. J. Appl. Phys.* **33**, L1056 (1994)
63. M. Sato, *J. Cryst. Growth* **145**, 99 (1994)
64. I.A. Buyanova, W.M. Chen, G. Pozina, J.P. Bergman, B. Monemar, H.P. Xin, C.W. Tu, *Appl. Phys. Lett.* **75**, 501 (1999)
65. L. Grenouillet, C. Bru-Chevallier, G. Guillot, P. Gilet, P. Duvaut, C. Vannuffel, A. Million, A. Chenevas-Paule, *Appl. Phys. Lett.* **76**, 2241 (2000)
66. K. Uesugi, I. Suemune, T. Hasegawa, T. Akutagawa, T. Nakamura, *Appl. Phys. Lett.* **76**, 1285 (2000)
67. I.A. Buyanova, W.M. Chen, B. Monemar, H.P. Xin, C.W. Tu, *Appl. Phys. Lett.* **75**, 3781 (1999)
68. B.Q. Sun, D.S. Jiang, X.D. Luo, Z.Y. Xu, Z. Pan, L.H. Li, R.H. Wu, *Appl. Phys. Lett.* **76**, 2862 (2000)
69. R.A. Mair, J.Y. Lin, H.X. Jiang, E.D. Jones, A.A. Allerman, S.R. Kurtz, *Appl. Phys. Lett.* **76**, 188 (2000)

-
70. K. Matsuda, T. Saiki, M. Takahashi, A. Moto, S. Takagishi, *Appl. Phys. Lett.* **78**, 1508 (2001)
 71. A. Moto, S. Tanaka, N. Ikoma, T. Tanabe, S. Takagishi, M. Takahashi, T. Katsuyama, *Jpn. J. Appl. Phys.* **38**, 1015 (1999)
 72. M. Takahashi, A. Moto, S. Tanaka, T. Tanabe, S. Takagishi, K. Karatani, M. Nakayama, K. Matsuda, T. Saiki, *J. Cryst. Growth* **221**, 461 (2000)
 73. T. Someya, Y. Arakawa, *Jpn. J. Appl. Phys.* **38**, L1216 (1999)

Optical Interaction of Light with Semiconductor Quantum-Confined States at the Nanoscale

11

Toshiharu Saiki

Contents

11.1	Introduction.....	444
11.2	Near-Field Scanning Optical Microscope.....	445
11.2.1	General Description.....	445
11.2.2	Aperture-NSOM Probe.....	446
11.3	Spatial Resolution of NSOM Studied by Single-Molecule Imaging.....	447
11.3.1	Single-Molecule Imaging with Aperture Probes.....	448
11.3.2	Numerical Simulation of NSOM Resolution.....	449
11.4	Single Quantum Dot Spectroscopy and Imaging.....	454
11.5	NSOM Spectroscopy of Single Quantum Dots.....	455
11.5.1	Type II Quantum Dot.....	455
11.5.2	NSOM Spectroscopy of Single GaSb QDs.....	456
11.6	Real-Space Mapping of Electron Wavefunction.....	461
11.6.1	Light–Matter Interaction at the Nanoscale.....	461
11.6.2	Interface Fluctuation QD.....	463
11.6.3	Real-Space Mapping of Exciton Wavefunction Confined in a QD.....	465
11.7	Real-Space Mapping of Local Density of States.....	469
11.7.1	Field-Induced Quantum Dot.....	470
11.7.2	Mapping of Local Density of States in a Field Induces QD.....	472
11.8	Carrier Localization in Cluster States in GaNAs.....	474
11.8.1	Dilute Nitride Semiconductors.....	474
11.8.2	Imaging Spectroscopy of Localized and Delocalized States.....	475
11.9	Perspectives.....	480
	References.....	480

Abstract

In this chapter, near-field imaging spectroscopy of quantum-confined systems with a spatial resolution as high as 10–30 nm is described. Spatial profiles of

T. Saiki (✉)

Department of Electronics and Electrical Engineering, Keio University, Kanagawa, Japan
e-mail: saiki@elec.keio.ac.jp

local density of states and exciton wavefunctions confined in quantum dots are visualized. The fundamental aspects of localized and delocalized electrons in interface and alloy disorder systems are also discussed.

11.1 Introduction

Optical probing and manipulation of electron quantum states in semiconductors at the nanoscale are key to the development of future nanophotonic devices which are capable of ultrafast and low-power operation [1]. To optimize device performance and to go far beyond conventional devices based on the far-field optics, the degree of confinement of the electron and light must be properly designed and engineered. This is because while stronger confinement of the electron is favorable to utilize its quantum nature, its interaction with light becomes weaker with reduction of the confinement volume. To maximize their interaction, the overlap in scale between confinement volume of electron and that of light is required. More generally, the spatial profile of the light field should be designed to match that of electron wavefunction in terms of phase as well as amplitude.

Semiconductor quantum dots (QDs) provide ideal electron systems because electrons are three-dimensionally confined, resulting in a discrete density of states, in which level energy spacing exceeds the thermal energy. Due to such nature of QDs, they exhibit ultranarrow optical transition spectrum and long duration of coherence [2]. Moreover, they can be engineered to have desired properties by controlling the size, shape, and strains, as well as appropriate selection of material. Regarding the size of QDs, with the maturation of crystal growth along with the nanofabrication of semiconductors, we have obtained QDs with a wide range of sizes from a few nm to larger than 100 nm. For example, interface fluctuation QDs, which confine excitons by imperfect GaAs quantum well, are extensively studied [3]. By adopting a growth interruption technique, monolayer high islands larger than 100 nm develop at the well-barrier interface. Large QDs are advantageous to maximize the magnitude of the light–electron (exciton) interaction due to the enhancement of oscillator strength, which is proportional to the size of QDs [4].

The progress in confinement of light, on the other hand, has been also remarkable [5, 6]. Basically efforts to focus light more tightly than half the wavelength (diffraction limit) have been motivated by ultimate spatial resolution of optical microscopy. For example, a near-field scanning optical microscope (NSOM) [5, 6] uses a sharpened optical fiber probe with a small metal hole at its apex to squeeze light in an area determined by the size of the hole. Recent advances in fabrication of NSOM probe enable us to generate a light spot smaller than 10 nm [7]. An optical antenna is also attracting attentions due to higher efficiency in the delivery of energy to a nano–focused spot [8]. Metal nanorods and more sophisticated metal structures

provide an opportunity to engineer the light field at the nanoscale with high degree of freedom.

Broad-range overlap in scale between the confinement volume of electrons and light, as described above, leads to the change of their interaction from the far-field counterpart [9]. More specifically in case that the spatial resolution of NSOM falls below the size of QD, it becomes possible to directly map out the distribution of the wavefunction [10]. More interestingly the optical selection rule can be broken; one can excite the dark states whose optical transition is forbidden by the far field and can open new radiative decay channels. The light–matter coupling at the nanoscale offers guiding principles for future nanophotonic devices.

In this article, we describe development of a high-resolution NSOM with a carefully designed aperture probe and near-field imaging spectroscopy of quantum-confined systems. Thanks to a spatial resolution as high as 1–30 nm, we visualize spatial profiles of local density of states and wavefunctions of electrons confined in QDs and clarify the fundamental aspects of localized and delocalized electrons in interface and alloy disorder systems.

11.2 Near-Field Scanning Optical Microscope

11.2.1 General Description

When a small object is illuminated, its fine structures with high spatial frequency generate a localized field that decays exponentially normal to the object [5, 6]. This evanescent field on the tiny substructure can be used as a local source of light illuminating and scanning a sample surface so close that the light interacts with the sample without diffraction. A metal opening (aperture) is a popular method by which a localized optical field suitable for NSOMs can be generated. As illustrated in Fig. 11.1, aperture NSOM uses a small opening at the apex of a tapered optical fiber coated with metal. Light sent down the fiber probe and through the aperture illuminates a small area on the sample surface. The fundamental spatial resolution is determined by the diameter of the aperture, which ranges from 10 to 100 nm.

The simplest setup for imaging spectroscopy based on aperture NSOM, a configuration with local illumination and local collection of light through an aperture, is illustrated in Fig. 11.1. The light emitted by the aperture interacts with the sample locally. Resultant signals from the interaction volume must be collected as efficiently as possible. In photoluminescence (PL) or Raman spectroscopy, collected signal is dispersed by a spectrometer and is detected by a CCD recording device. The regulation system for tip–sample feedback is essential for NSOM performance, and most NSOMs employ a method similar to that used in an atomic force microscope (AFM), called shear-force feedback, the regulation range of which is 0–10 nm [11]. For the measurement at low temperature to reduce phonon-induced broadening, the sample, probe tip, and scanner are placed into a cryostat [12].

Fig. 11.1 A schematic illustration of standard NSOM setup with a local illumination and local collection configuration

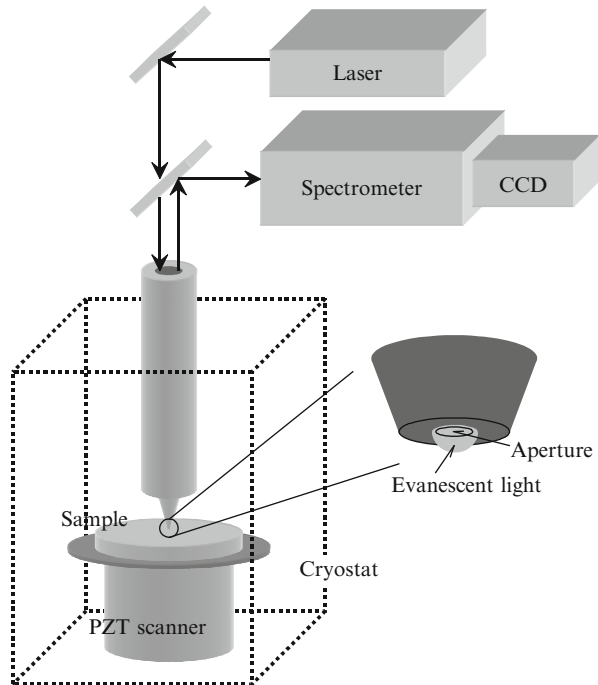
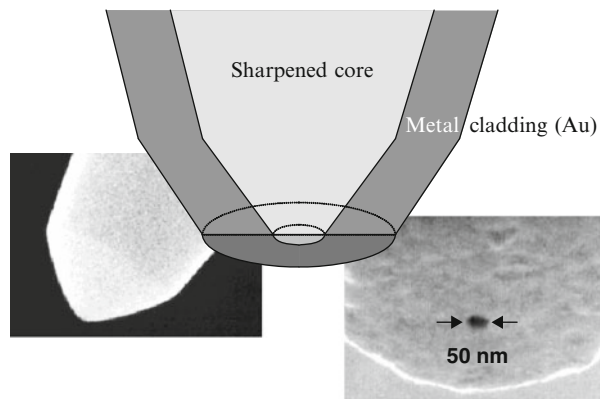


Fig. 11.2 A schematic illustration of aperture-NSOM probe. Scanning electron micrographs of a double-tapered probe (taken prior to metal coating) and a well-defined aperture are also shown



11.2.2 Aperture-NSOM Probe

Great efforts have been devoted to the fabrication of the aperture probe, which is the heart of NSOM. Since the quality of the probe determines the spatial resolution and sensitivity of the measurements, tip fabrication remains of major interest in the development of NSOM. To enhance the performance of aperture NSOM, we focus on two important features of the probe: the light propagation efficiency of the tapered waveguide and the quality of aperture as illustrated in Fig. 11.2.

Improvement of the optical transmission efficiency (throughput) and collection efficiency of aperture probes is the most important issue to be addressed for the application of NSOM in the spectroscopic studies of nanostructures. The tapered region of the aperture probe operates as a metal-clad optical waveguide. The mode structure in a metallic waveguide is completely different from that in an unperturbed fiber and is characterized by the cutoff diameter and absorption coefficient of the cladding metal. Theoretical and systematic experimental studies have confirmed that the transmission efficiency of the propagating mode decreases in the region where the core diameter is smaller than half the wavelength of the light in the core. The power that is actually delivered to the aperture depends on the distance between the aperture plane and the plane in which the probe diameter is equal to the cutoff diameter, which distance is determined by the taper angle. We therefore proposed a double-tapered structure with a large taper angle [13, 14]. This structure is easily realized using a multistep chemical-etching technique, as will be described below. With this technique, the transmission efficiency is much improved by one and two orders of magnitude as compared to the single-tapered probe with a small taper angle.

We used a chemical-etching process with buffered HF solution to fabricate the probe. The etching method is easily reproducible and can be used to make many probes at the same time. The details of probe fabrication with selective etching are described in Ref. [14]. The taper angle can be adjusted by changing the composition of a buffered HF solution. A two-step etching process is employed to make a double-tapered probe. Another important advantage of the chemical-etching method is the excellent stability of the polarization state of the probe.

The next step is metal coating and aperture formation. In general, the evaporated metal film generally has a grainy texture, resulting in an irregularly shaped aperture with nonisotropic polarization behavior. The grains also increase the distance between the aperture and the sample, not only degrading resolution but also reducing the intensity of the local excitation. As a method for making a high-definition aperture probe, we use a simple method based on the mechanical impact of the metal (Au)-coated tip on a suitable surface [15, 16]. The resulting probe has a flat end and a well-defined circular aperture. Furthermore, the impact method assures that the aperture plane is strictly parallel to the sample surface, which is important in minimizing the distance between the aperture and the sample surface. The size of the aperture can be selected by carefully monitoring the intensity of light transmitting from the apex, since the throughput of the probe is strictly dependent on the aperture diameter.

11.3 Spatial Resolution of NSOM Studied by Single-Molecule Imaging

Ultimate spatial resolution of NSOM is of great interest from the viewpoint of revealing the nature of light–matter interaction at the nanoscale. As a standard method for the evaluation of spatial resolution of NSOM, fluorescence imaging of

a single molecule is most reliable because it behaves as an ideal point-like light source. Many groups have made efforts to improve the resolution in the single-molecule imaging using a variety of methods, such as apertureless NSOM [17] and a single-molecule light source [18]. A spatial resolution as high as 32 nm has been reported in fluorescence imaging by using a microfabricated cantilevered probe [19]. By using an aperture probe, a spatial resolution as high as 25 nm has been reported recently in single-molecule fluorescence imaging by scanning near-field optical/atomic force microscopy [20].

In this section, single-molecule imaging with a high resolution approximately 10 nm achieved by an aperture NSOM is described [21]. To discuss the dependence of the resolution on the wavelength of excitation light, measurements with two different excitation lasers for the same probes are carried out. These results are compared with a computational calculation employing the finite-difference time-domain (FDTD) method, which is appropriate for simulation of electromagnetic field distributions applied to actual three-dimensional problems [22]. Thus, we discuss the achievable spatial resolution of the aperture NSOM.

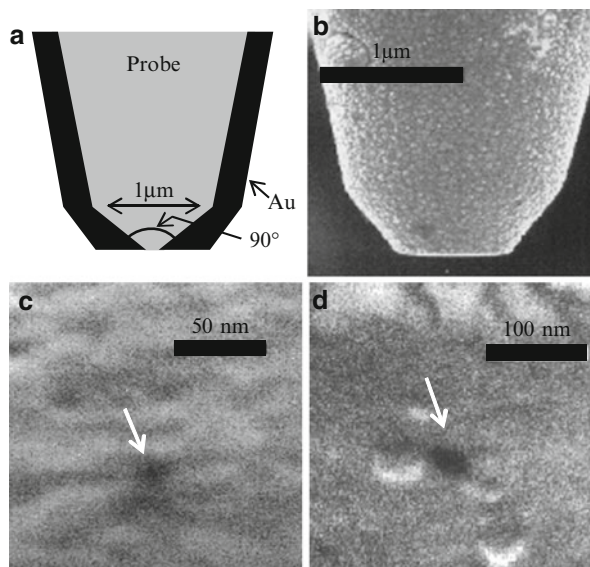
11.3.1 Single-Molecule Imaging with Aperture Probes

An NSOM fiber probe with the double-tapered structure and well-defined aperture created by the mechanical impact method, as described in Sect. 11.2, was employed. Samples examined were single dye molecules of Cy5.5 and Rhodamine dispersed on quartz substrates. Single-molecule dispersion on the substrate was confirmed by observing one-step photobleaching of almost all of the molecules. The fluorescence NSOM was operated in the illumination mode. As excitation light sources, a He–Ne laser ($\lambda = 633$ nm) and a SHG YVO₄ laser ($\lambda = 532$ nm) were employed. The emission from a single dye molecule was collected by an objective lens and transported to an avalanche photodiode (APD) through a band-pass filter (center wavelength $\lambda = 700$ nm, bandwidth $\Delta\lambda = 40$ nm for the Cy5.5 dye, $\lambda = 600$ nm, $\Delta\lambda = 40$ nm for the Rhodamine dye). The sample–probe distance was controlled by a shear-force feedback mechanism.

Figure 11.3a shows a cross-sectional illustration of the Au-coated probe. Scanning electron micrographs of aperture probes are shown in Fig. 11.3b–d: a side view of a probe with the double-tapered structure and overhead views of apertures. From the scanning electron micrographs, which were taken after several scanning measurements, it is found the probes have flat endfaces with small round apertures. The diameters of the apertures in Fig. 11.3c, d are estimated to be 10 and 30 nm, respectively.

Figure 11.4a shows a fluorescence image of single Cy5.5 dye molecules irradiated by the He–Ne laser light. Each bright spot is attributed to the fluorescence from a single molecule. The bright spot circled in the image is magnified in Fig. 11.4b. Figure 11.4c shows a cross-sectional profile of the fluorescence signal intensity evaluated along a line indicated by a pair of arrows in Fig. 11.4b. From the full

Fig. 11.3 (a) A cross-sectional illustration of the Au-coated probe. (b)–(d) Scanning electron micrographs of aperture probes: (b) a side view of a probe with the double-tapered structure and (c) and (d) apertures created by the impact method. Aperture diameters are 10 and 30 nm, respectively



width at half maximum (FWHM) of the profile, the spatial resolution is estimated to be 20 nm.

Figure 11.5a shows a fluorescence image obtained using the same probe and the same sample of single Cy5.5 dye molecules, but not measured in the same area as in Fig. 11.4a, by the SHG YVO₄ laser excitation. The bright spot circled in Fig. 11.5a is magnified in Fig. 11.5b, and Fig. 11.5c shows its cross-sectional profile. The spatial resolution estimated from the FWHM of the profiles is 21 nm.

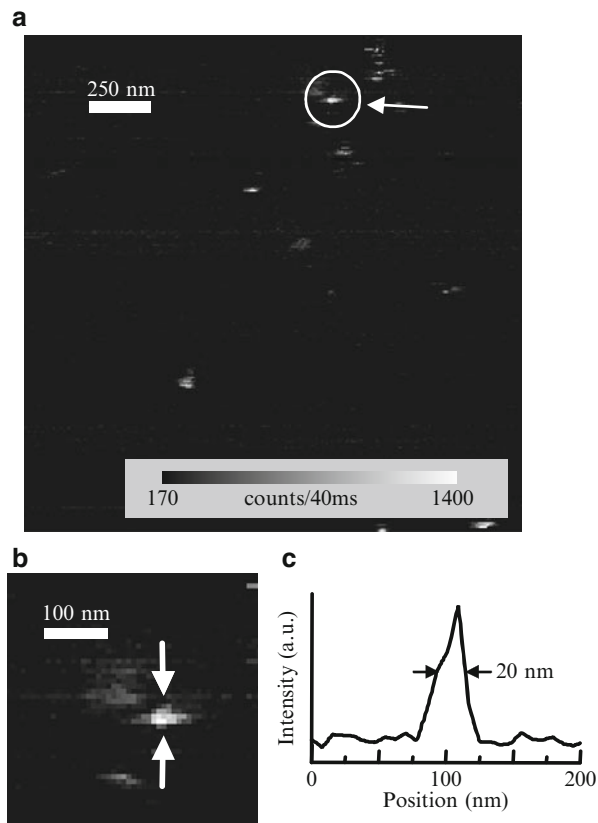
The highest resolution images obtained with Rhodamine at 532 nm excitation and Cy5.5 at 633 nm excitation are shown in Fig. 11.6a, b, respectively. The resolution is estimated to be 11 nm at 532 nm excitation and 8 nm at 633 nm excitation.

11.3.2 Numerical Simulation of NSOM Resolution

To evaluate the achievable resolution of the aperture NSOM in visible range in the illumination mode of operation, a computer simulation by the FDTD method was employed for various aperture sizes and wavelengths. Electric fields (E) were calculated for the probe tip with an aperture diameter $D = 20$ nm at various wavelengths ($\lambda = 405, 442, 488, 514.5, 532,$ and 633 nm) of irradiation lights and for the probe tips with various aperture sizes ranging from $D = 0$ to 50 nm at the wavelength $\lambda = 633$ nm.

Figure 11.7a illustrates a cross-sectional view of the FDTD geometry of the three-dimensional problem, which reproduces the tip of the double-tapered probe with an aperture employed in the experiments. A three-dimensional illustration of

Fig. 11.4 (a) A fluorescence image of single Cy5.5 molecules at 633 nm excitation. (b) A magnified image of the *bright spot* circled in (a). (c) A cross-sectional profile of the signal intensity evaluated along a line indicated by the pair of arrows in (b). The spatial resolution determined from the FWHM of the profile is 20 nm



the probe is shown in Fig. 11.7b. The origin of the Cartesian coordinate was located at the center of the aperture. We assumed the light source, which was placed at 10 nm below the upper end of the tapered probe with a cone angle $\theta = 90^\circ$, was a plane wave with a Gaussian distribution polarized along the x direction. The refractive index of the core of the fiber was 1.5, and the refractive indices of the real Au metal were extracted from Ref. [23]. The simulation box had a size of $1.6 \times 1.6 \times 0.8 \mu\text{m}^3$ in the x , y , and z directions. The space increment of the z directions around the aperture was 2 nm, and the increments of the x and y directions were 1 nm for aperture diameters less than $D = 10$ nm and were 2 nm for the other aperture diameters.

Figure 11.8a and 11.6b show the intensity distribution of electronic field $|\mathbf{E}|^2$ along the x - and y -axis, respectively, on $z = -4$ nm plane for the probe with the aperture of $D = 20$ nm at $\lambda = 633$ nm excitation. Here we define the spatial resolution of Δx and Δy as the FWHM of the intensity distribution, indicated by arrows in Fig. 11.8a, b.

Fig. 11.5 (a) A fluorescence image of single Cy5.5 molecules at 532 nm excitation obtained using the same probe and the same sample as those in Fig. 11.4, but not measured in the same area as in Fig. 11.4. (b) A magnified image of the *bright spot circled* in (a). (c) A cross-sectional profile along a line indicated by the pair of *arrows* in (b). The spatial resolution is estimated to be 21 nm

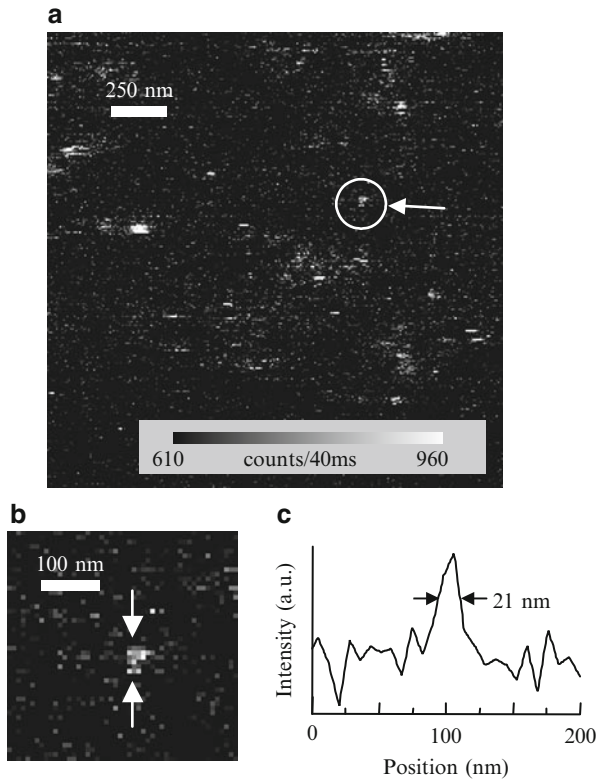
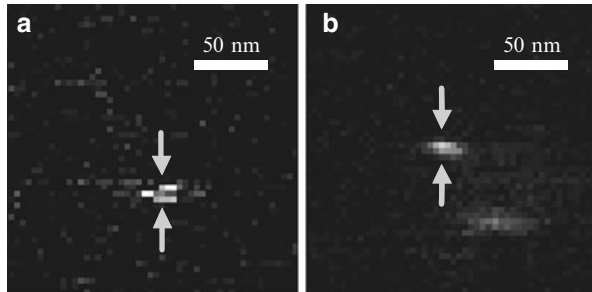


Fig. 11.6 The highest resolution images obtained with Rhodamine at 532 nm excitation (a) and Cy5.5 at 633 nm excitation (b). Estimated resolutions are 11 and 8 nm, respectively



Spatial resolutions for the aperture of $D = 20$ nm at various wavelengths are plotted in Fig. 11.9. The skin depth of Au calculated from its optical constants is indicated by a dashed line. It is found that the dependence of the resolution on the excitation wavelength has similar tendency as the skin depth of Au. Figure 11.10 shows the resolutions for various aperture diameters: $D = 0, 10, 20, 30,$ and 50 nm at $\lambda = 633$ nm. The result indicates that the discrepancy between the predicted

Fig. 11.7 (a) An illustration of the cross-sectional view of the FDTD geometry of three-dimensional problem, which reproduces the experimental situation. (b) A three-dimensional illustration of the tapered probe

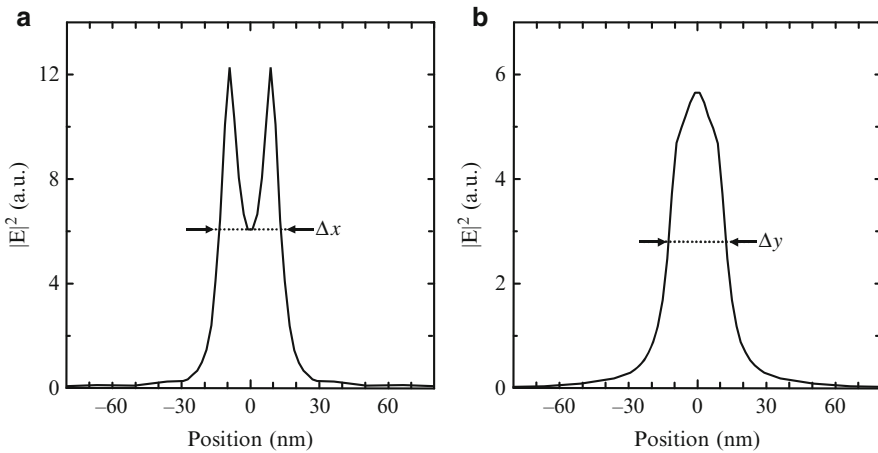
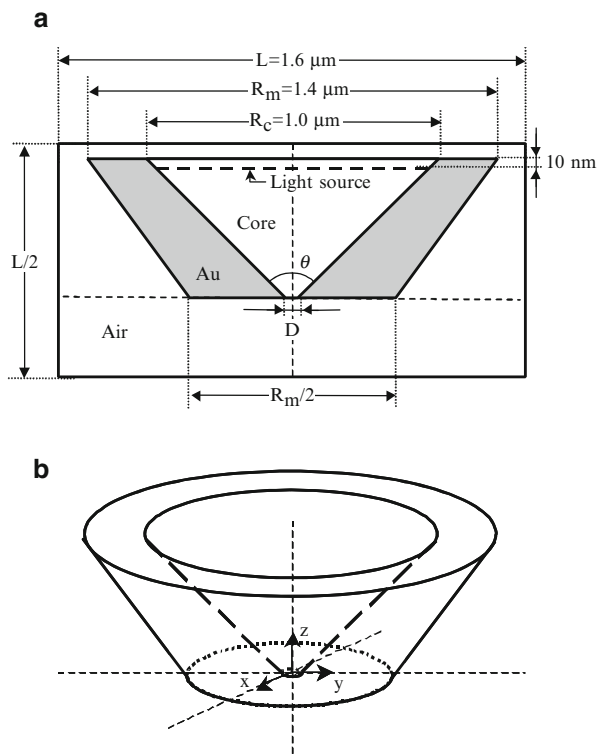


Fig. 11.8 The intensity distributions of electronic field along the x -axis (a) and y -axis (b), calculated on $z = -4$ nm plane for the probe with an aperture of $D = 20$ nm at $\lambda = 633$ nm excitation. The spatial resolutions of Δx and Δy are defined as the FWHM of the intensity distributions indicated by the pairs of arrows

Fig. 11.9 Calculated spatial resolutions for the aperture with $D = 20$ nm at various wavelengths

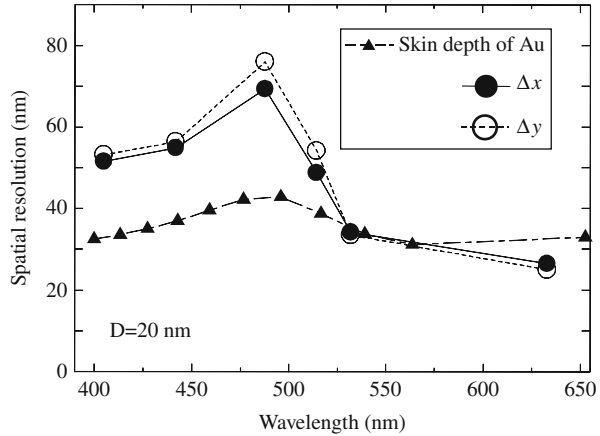
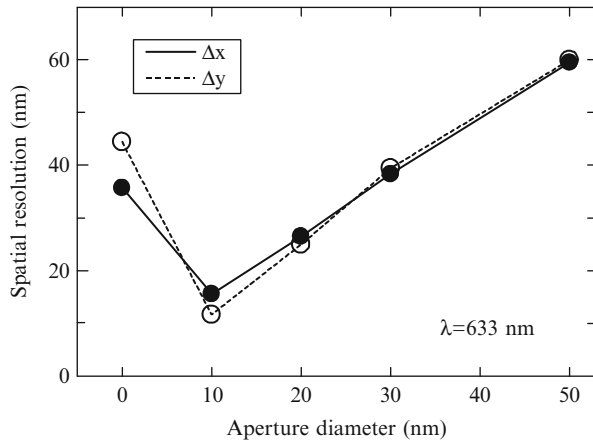


Fig. 11.10 Calculated spatial resolutions for various aperture diameters at $\lambda = 633$ nm



resolution and the physical aperture size is less than 10 nm for $D > 10$ nm. The highest resolution is obtained at $D = 10$ nm and is evaluated to be $\Delta x = 16$ nm and $\Delta y = 12$ nm.

To discuss the resolution attainable using the NSOM with a tiny aperture, we compare the results of the computational calculation by the FDTD method with the experimental results obtained by the fluorescence imaging of single molecules. The same spatial resolutions as small as 20 nm were obtained experimentally at the different excitation wavelengths ($\lambda = 532$ and 633 nm) using the same aperture probe. The result does not agree with the results of the computational calculation for various excitation wavelengths in which about 10 nm of difference is predicted between the resolutions for the wavelengths of 532 and 633 nm. The dependence of the calculation results on the aperture sizes indicates that our computational simulation also does not reproduce the best resolutions in our measurements as high as 10 nm realized at excitations of both $\lambda = 532$ and 633 nm. The profile of

intensity distribution of fluorescence signal obtained in the experimental operations is also greatly different from that evaluated along the x -axis in the computational calculation as characterized by the well-defined double peaks in Fig. 11.8. The disappearance of the double peaks can be explained by some distortion of the aperture shape. A slight inclination of the aperture face also results in contribution of a single peak because the intensity of the other peak decreases rapidly with the distance from aperture face. Taking account of the value of the FWHM of the intensity profile for one of the double peaks in Fig. 11.8, the experimental resolution as high as 10 nm is attributed to the efficient use of the localized near-field light with a single peak profile at the rim of the aperture.

11.4 Single Quantum Dot Spectroscopy and Imaging

In order to evaluate optical properties of QDs, such as an extremely sharp PL line, a macroscopic measurement, where an ensemble of QDs is observed at a time, is insufficient. This is because inhomogeneous broadening is inherent to QDs due to the distribution of their sizes and shapes. Thus, the intrinsic natures are hidden in an inhomogeneously broadened signal, and spectroscopy on a single QD is strongly required. An NSOM offers a high spatial resolution, typically 100–200 nm, which is comparable to a typical dot-to-dot separation, and allows to optically address individual quantum dots as illustrated in Fig. 11.11a.

As described above, usually the size of light spot created by the NSOM probe is larger than the size of QD. Recent progress in the fabrication of aperture near-field fiber probe has pushed the spatial resolution to less than 30 nm [21, 24], which is comparable to or below the sizes of QDs. In such a case, NSOM allows to investigate the inside of the QD. Roughly speaking, if the size of QD is smaller than 100 nm, the energy separation of discrete quantum levels is greater than thermal energy at a cryogenic temperature, NSOM can visualize the spatial profile of a single quantum state: real-space mapping of an electron wavefunction [25–27]. The situation is illustrated in Fig. 11.11b. Moreover, illumination of QD with extremely narrow light source makes it possible to excite optically “dark” states whose excitation is forbidden by symmetry in the far field (breakdown of the usual optical selection rules) [9, 28]. These interesting observation and manipulation of electronic states in quantum confinement systems are unique to light–matter interaction at the nanoscale and the essential motivation to utilize near-field optical method.

In another case we deal with a QD created by means of a nanofabrication technique. In contrast to naturally grown QDs, the size of artificially fabricated QDs can be as large as several hundreds of nm. In such a weakly localized electron systems, where energy separation of quantized states is smaller than thermal energy, NSOM maps out the local density of states as shown in Fig. 11.11c. Spatially and energetically resolved spectroscopy is a powerful tool to reveal the localized and delocalized electron systems and, more importantly, their crossover region (weakly localized system).

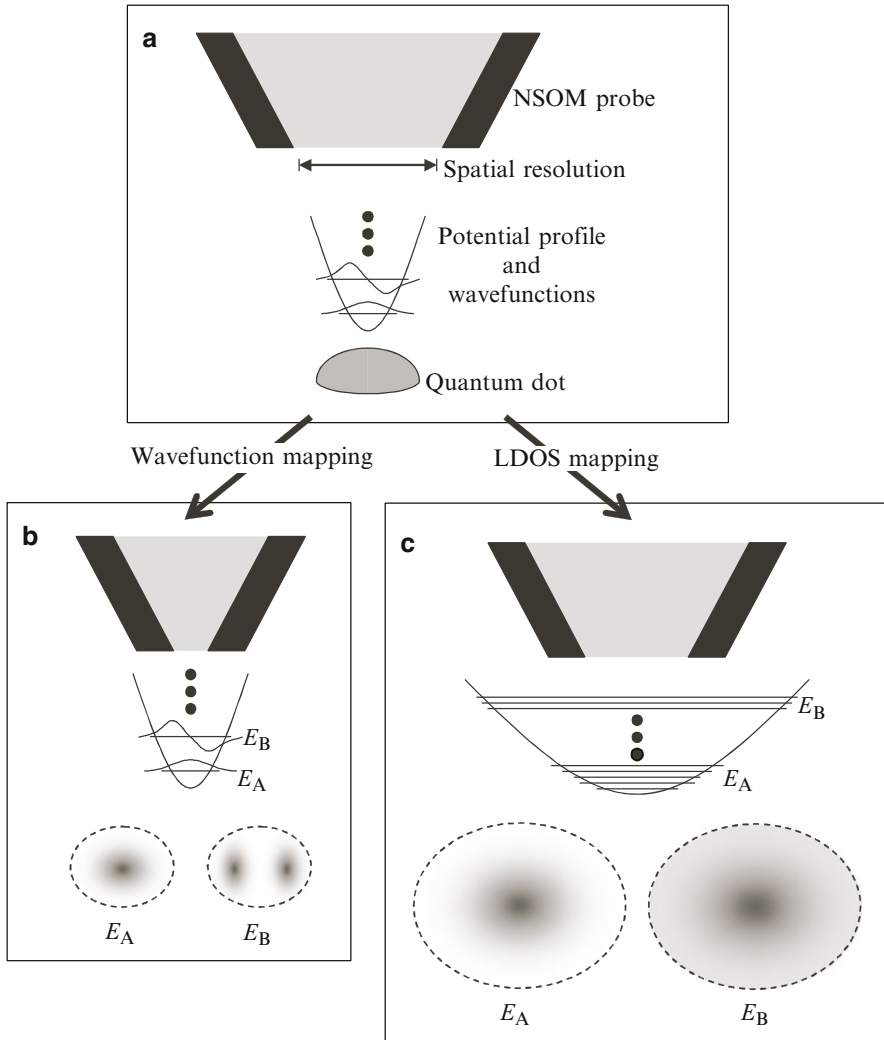


Fig. 11.11 Conceptual illustration of wavefunction mapping and LDOS mapping in single QD spectroscopy

11.5 NSOM Spectroscopy of Single Quantum Dots

11.5.1 Type II Quantum Dot

A self-assembled quantum dot is an ideal system for studying zero-dimensional quantum effects and has the potential for realizing future quantum devices. In self-assembled In(Ga)As/GaAs QDs with a band alignment classified as type I, both

electrons and holes are confined in the QD. In a staggered type II band structure, the lowest energy states for an electron and a hole are concentrated on different layers [29–33]. Spatial separation occurs between the electron wavefunction in the GaAs layer and the hole wavefunction in a type II GaSb QD, and the optical properties differ from those of a type I QD [29, 31].

Single QD PL spectroscopy allows us to study multiexciton states by creating many excitons in a QD under high excitation conditions [34]. The two-exciton state is an especially interesting system, because it easily forms a bound biexciton state due to the attractive Coulomb interaction in a type I In(Ga)As QD [35, 36]. The energy level of a bound biexciton state is lowered by the binding energy from the two excitons, where the binding energy is defined as the downward shift in energy of the biexciton relative to that of two uncorrelated excitons. As the stability of the biexciton state is sensitive to the structural and electronic parameters [37], the interaction between excitons in a type II GaSb QD should be different from that in a type I In(Ga)As QD. Here we describe an experimental study of the exciton and two-exciton states in a single type II GaSb QD using the NSOM.

11.5.2 NSOM Spectroscopy of Single GaSb QDs

The sample in this study was self-assembled GaSb QDs grown on a GaAs (100) substrate using molecular beam epitaxy [38]. The lateral size, height, and density of the GaSb QDs of an uncovered sample were 16–26 nm, 5–8 nm, and $2 \times 10^{10} \text{ cm}^{-2}$, respectively, as measured by an atomic force microscope. Cross-sectional transmission electron microscopy showed that a GaSb QD has a lens shape after capping with a GaAs cover layer of 100 nm. The sample was illuminated through the aperture with a diode laser ($\lambda = 685 \text{ nm}$), and the PL from a GaSb QD was collected via the same aperture. The PL signal was detected using a 32 cm monochromator equipped with a cooled charge-coupled device with a spectral resolution of $250 \mu\text{eV}$. All measurements were conducted at cryogenic temperature.

Figure 11.12a, b shows typical near-field PL images, monitored at photon energies of 1.266 and 1.259 eV, respectively, under relatively low excitation conditions. Several bright spots of the PL signals from single GaSb QDs are observed in both images. We can confirm the spectroscopic observation of a single GaSb QD from the PL images. The average size of the bright spots, defined by the full width at half maximum (FWHM) of the PL intensity profile, is estimated to be about 120 nm, a value that corresponds to the spatial resolution of the measurement. The spatial resolution is somewhat larger than the aperture diameter of the probe tip (80 nm), because the GaSb QDs are embedded at a depth of 100 nm from the sample surface.

Figure 11.13 shows, typical near-field PL spectra of the exciton emission from three different single GaSb QDs on an expanded energy scale. The linewidths of the three emission peaks are estimated to be $250 \mu\text{eV}$, where the value is limited by the spectral resolution of the measurements. Consequently, the homogeneous linewidth of an exciton state in a type II GaSb QD is evaluated to be less than $250 \mu\text{eV}$, which is narrower than the $280 \mu\text{eV}$ theoretically predicted in an ideal quantum well (QW)

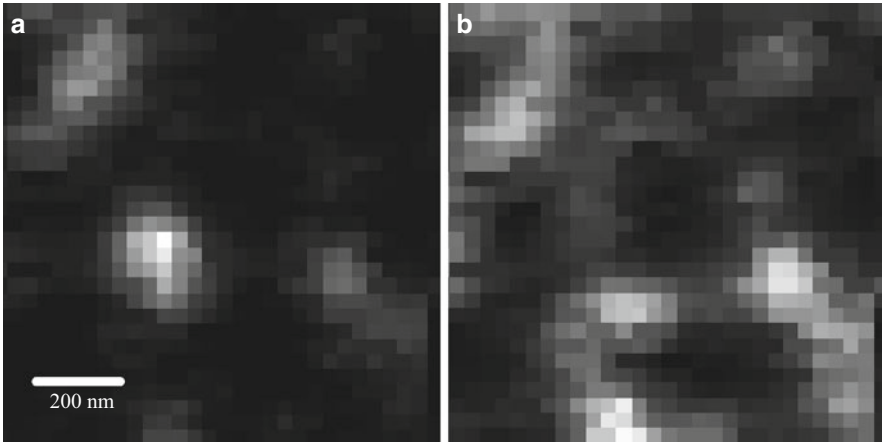


Fig. 11.12 Near-field PL images of single GaSb QDs monitored at photon energies of (a) 1.266 and (b) 1.259 eV, respectively

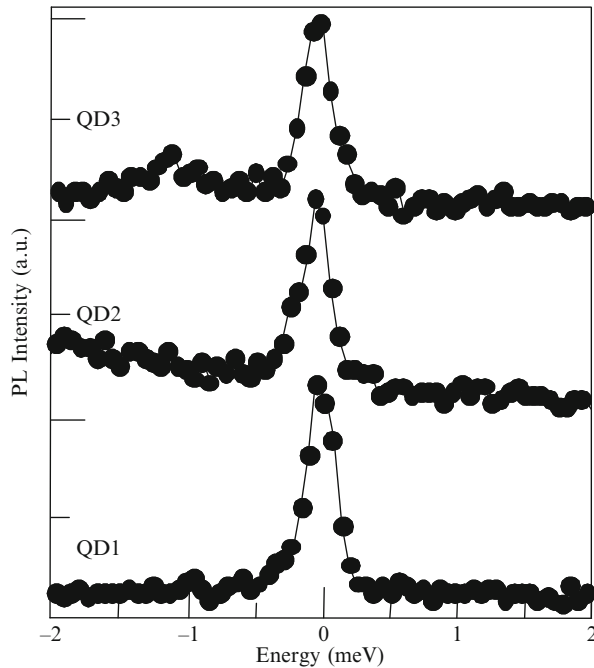
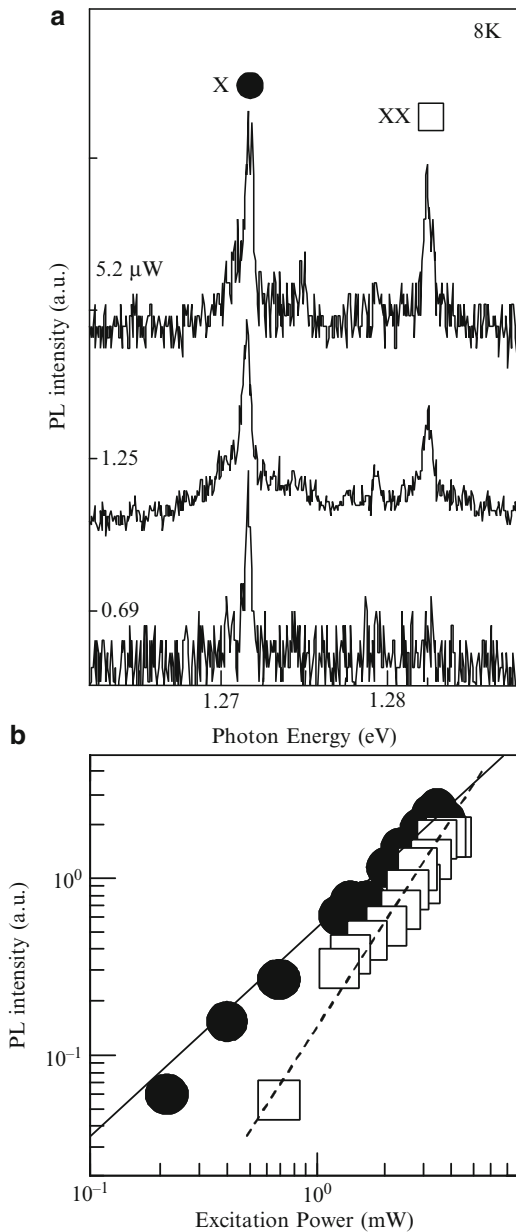


Fig. 11.13 PL spectra of three different single GaSb QDs at 8 K

at 8 K. The narrow PL linewidth means that the exciton state in a type II GaSb QD has a longer coherence time than that in the QW.

Figure 11.14a shows near-field PL spectra of a single GaSb QD at various excitation power densities. A single emission peak in the PL spectrum, denoted as X, is observed at 1.2716 eV under lower excitation conditions (less than $1 \mu\text{W}$).

Fig. 11.14 (a) Near-field PL spectra of a single GaSb QD at 8 K under various excitation power densities. The PL peaks at 1.2716 and 1.2824 eV are denoted as X and XX, respectively. (b) Excitation power dependence of PL intensities of the X and XX lines. The *solid (dotted) line* corresponds to the gradient associated with linear (quadratic) power dependence



As shown in Fig. 11.14b, the PL intensities of the X line, as a function of excitation power densities, show an almost linear power dependence under lower excitation conditions. The sharp, less than 1 meV FWHM linewidth, X emission line is assigned to the radiative recombination of the exciton consisting of a hole confined

in a GaSb QD and an electron in the surrounding GaAs barrier layer, which are weakly bound together by an attractive Coulomb interaction.

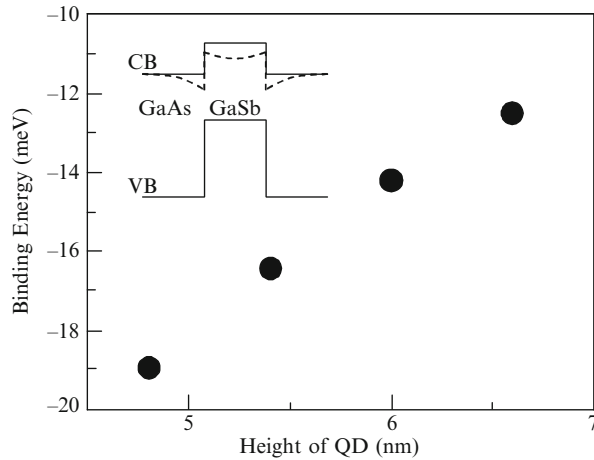
Next, in Fig. 11.14a, we focus on the PL spectra at higher excitation conditions (greater than $1 \mu\text{W}$). An additional peak appears at 1.2824 eV in the PL spectra, and the peak denoted as XX is observed at about 11 meV higher energy than the exciton emission (X). Figure 11.14b shows a nearly quadratic power dependence of the XX line as a function of the excitation power. The power dependence of the PL intensity suggests that the XX emission results from the radiative transition from a two-exciton state to the exciton ground state. In type I self-assembled In(Ga)As QDs [35] and naturally occurring GaAs QDs [36], the PL line is usually observed at $3\text{--}5 \text{ meV}$ to the lower-energy side of the exciton emission with the quadratic power dependence generally assigned to the bound biexciton emission. This experimental result, with the two-exciton emission occurring on the higher-energy side of the exciton emission, contrasts the results in type I QDs. This is consistent with the results of the macroscopic PL spectra from GaSb QD ensembles showing a blueshift of the PL peak with increasing excitation power [29, 32].

The energy difference between the two-exciton emission (XX) and the exciton emission (X) corresponds to the binding energy ($E_{\text{bin}} = 2E_X - E_{\text{XX}}$), where E_{XX} and E_X are the energy of the two-exciton state and the exciton ground state, respectively. After measuring many GaSb QDs in the same sample, we found that E_{bin} always has negative values, ranging from -11 to -21 meV . A negative E_{bin} implies that the sign of the exciton–exciton interaction is repulsive in these QDs. In type II GaSb QDs, only the holes are confined inside the QD, while the electron wavefunction is relatively delocalized in the GaAs barrier layer around the QDs. Consequently, it is reasonable to expect the Coulomb energy of the two-exciton ground state to be mainly dominated by the hole–hole repulsive Coulomb interaction, and to have a negative value, because the strengths of the electron–hole and electron–electron interactions are smaller than that of the hole–hole interaction.

For a quantitatively accurate understanding, we performed theoretical calculations of two-exciton states in these QDs. We used the empirical pseudopotential model (EPM) that has been applied to various III–V type I QDs [39]. The single-particle states are obtained by solving the one-electron Schrödinger equation in a potential, which is obtained from the superposition of atomic pseudopotentials centered at the location of each atom in a supercell containing the QD and the surrounding matrix. Spin–orbit coupling is included as a similar sum of nonlocal potentials [39]. The EPM parameters fitted to the bulk band structure parameters of GaSb and GaAs were taken from Ref. [40].

As described earlier, the exciton and two-exciton states involve electrons weakly bound to the QD solely by the Coulomb attraction of the confined holes. This situation makes it practically impossible to calculate the exciton and two-exciton states using the conventional configuration interaction approach typically used in type I QD calculations. To handle this situation, we developed a self-consistent mean field (SCF) calculation method for multiple electron-hole pair excitations within the EPM framework. In this approach, each single-particle state of a multiexciton complex is calculated by including the Coulomb potential due to all the other

Fig. 11.15 Calculated biexciton binding energy as a function of the height of the lens-shaped GaSb QDs. The height-to-diameter ratio was fixed as 0.3. The *inset* shows a schematic of the conduction band (CB) and valence band (VB) lineup of the GaSb/GaAs QDs. The *dashed lines* schematically illustrate the potential sensed by an electron when a hole is present



particles occupying the lowest possible single-particle orbitals. We use Resta's model [41] for the nonlocal dielectric constant. Our approach treats the electron–electron and electron–hole interactions at the Hartree–Fock level for one-exciton and two-exciton ground states and is identical to Hartree with a self-interaction correction for three or more exciton complexes.

First, we calculated the single-particle energies and orbitals for a few lowest conduction and highest valence band states with zero, one, and two electron–hole pairs using a linear combination of bulk Bloch functions as the basis [42]. The single- and two-exciton calculations are iterated to self-consistency. The exciton and two-exciton (biexciton) energies are calculated as the sum of single-particle energies corrected for double counting of the Coulomb interaction. A negative E_{bin} indicates that the two-exciton emission in PL spectra appears on the higher-energy side of the exciton emission.

Although the structure is grown as nominally pure GaSb QDs in GaAs, independent studies have shown that relatively strong admixing of Sb and As atoms is expected [42]. Calculations were done for the lens-shaped $\text{GaSb}_{1-x}\text{As}_x$ QDs in a GaAs matrix. The absolute exciton energies depend strongly on the alloying, as well as the size and shape of the QDs. In addition, PL studies of GaSb/GaAs type II heterostructures tell us that the observed emission energies can be explained only by using a much smaller valence offset than is theoretically accepted [43]. Therefore, it is difficult to correlate the absolute exciton energies with the experiment. The calculated E_{bin} as a function of QD size is shown in Fig. 11.15. The calculated data correspond to QDs of heights ranging from 4.8 to 6.6 nm with the height-to-diameter ratio fixed at 0.3. We found E_{bin} from -12 to -19 meV, that is, negative values for the entire range of QD sizes considered. The range of experimentally observed binding energies is well consistent with the calculated results. A detailed analysis of the results shows that although the two-exciton energy shift relative to the exciton could be understood qualitatively as due to the repulsion between the

two confined holes, the contributions from electron–hole attraction and electron–electron repulsion are not negligible. For example, for a 4.8 nm high QD, the E_{bin} of -19 meV includes -27 meV of hole–hole repulsion, -5 meV of electron–electron repulsion, and $+12$ meV of electron–hole attraction.

11.6 Real-Space Mapping of Electron Wavefunction

With the recent progress in the nanostructuring of semiconductor materials and in the applications of these nanostructured materials in optoelectronics, NSOM microscopy and spectroscopy have become important tools for determining the local optical properties of these structures. In single quantum constituent spectroscopy, NSOM provides access to individual quantum constituent, such as QD, an ensemble of which exhibits inhomogeneous broadening due to the distribution of sizes, shapes, and strains. NSOM can thus elucidate the nature of QD, including the narrow optical transition arising from the atom-like discrete density of states.

Single QD spectroscopy has revealed their long coherence times at low temperature and large oscillator strengths of optical transition. However, to improve these parameters for implementation of quantum computers, accurate information on the wavefunction for individual QDs is of great importance. In addition, in the study of coupled-QD systems as interacting qubits, in which it is difficult to predict the exact wavefunction within theoretical frameworks, an optical spectroscopic technique for probing the wavefunction itself should be developed. By enhancing the spatial resolution of NSOM up to 10–30 nm, which is smaller than the typical size of QDs, local probing allows direct mapping of the real-space distribution of the quantum eigenstate (wavefunction) within a QD, as predicted by theoretical studies [25–27].

In contrast to the well-defined quantum-confined systems like QDs, the more common disordered systems with local potential fluctuations still leave open questions. To fully understand such complicated systems, exciton wavefunctions should be visualized with an extremely high resolution less than the spatial extension of wavefunction. NSOM with a spatial resolution of 10 nm level is the only tool to obtain such information.

11.6.1 Light–Matter Interaction at the Nanoscale

In this section we summarize a theoretical approach to understand the light–matter interaction at the nanoscale [44]. When the nanoscale-confined electron system, such as a semiconductor QD, is excited by light with a frequency ω , the absorbed power $\alpha(\omega)$ is

$$\alpha(\omega) \propto \int E(\mathbf{r})P(\mathbf{r}, \omega) d\mathbf{r} \quad (11.1)$$

where $E(\mathbf{r})$ is the spatial distribution of electromagnetic field and $P(\mathbf{r}, \omega)$ is the induced interband polarization. In the general form the relationship between $P(\mathbf{r}, \omega)$

and $E(\mathbf{r})$ should be expressed by the nonlocal electrical susceptibility $\chi(\mathbf{r}, \mathbf{r}'; \omega)$ as

$$P(\mathbf{r}, \omega) = \int \chi(\mathbf{r}, \mathbf{r}'; \omega) E(\mathbf{r}') d\mathbf{r}' \quad (11.2)$$

$\chi(\mathbf{r}, \mathbf{r}'; \omega)$ can be obtained by eigenfunction ψ_{ex} and eigenenergy E_{ex} of exciton state confined in a QD:

$$\chi(\mathbf{r}, \mathbf{r}'; \omega) \propto \frac{\psi_{\text{ex}}(\mathbf{r}) \psi_{\text{ex}}^*(\mathbf{r}')}{E - \hbar\omega - i\gamma} \quad (11.3)$$

Here we assume that quasi-resonant excitation at E_{ex} , and therefore, the contribution of other quantized exciton states are negligible. γ is a damping constant due to phonon scattering and radiative decay of exciton. By using (Eq. 11.2) and (Eq. 11.3), $\alpha(\omega)$ can be written in the form

$$\alpha(\omega) \propto \frac{\left| \int \psi_{\text{ex}}(\mathbf{r}) E(\mathbf{r}) d\mathbf{r} \right|^2}{E - \hbar\omega - i\gamma} \quad (11.4)$$

To illustrate the physical meaning in (Eq. 11.4), we discuss two limiting cases. For far-field excitation, where QD is illuminated by a spatially homogeneous electromagnetic field, $\alpha(\omega)$ is given by the spatial integration of the exciton wavefunction,

$$\alpha(\omega) \propto \left| \int \psi_{\text{ex}}(\mathbf{r}) d\mathbf{r} \right|^2 \quad (11.5)$$

From the value of this integral, so-called optical selection rules are derived. If the integral is zero, the corresponding transition is “forbidden” and the exciton state is optically “dark.” In the opposite limit of extremely confined light, $E(\mathbf{r})$ is assumed to be $\delta(\mathbf{r} - \mathbf{R})$, where \mathbf{R} is the position of nanoscale light source, say a near-field tip. As a result one can probe the local value of the exciton wavefunction,

$$\alpha(\omega) \propto |\psi_{\text{ex}}(\mathbf{R})|^2 \quad (11.6)$$

By measuring $\alpha(\omega)$ as a function of the tip position, we can map out the exciton wavefunction. More interestingly, dark-state exciton becomes visible by breaking the selection rule of optical transition. In the intermediate regime in terms of the confinement of light, ψ_{ex} are averaged over an illumination region.

Now we try to give an intuitive explanation on the local optical excitation using a classical coupled oscillator model as shown in Fig. 11.16. Each pendulum represents a localized dipole, such as a constituent molecule that makes up a molecular crystal. The dipole–dipole interaction, which forms exciton as a collective excitation of constituent molecules, is taken into account by introducing springs to couple neighboring pendulums. Here we assume the size of the system (the size of

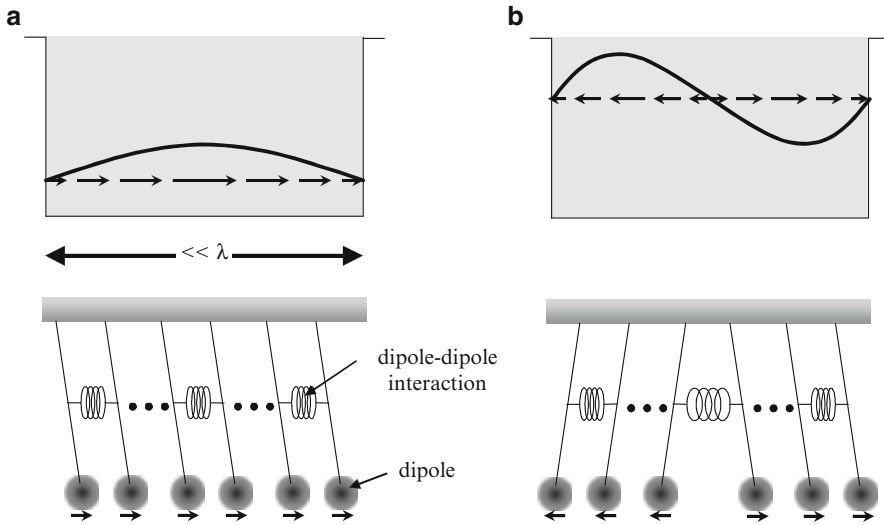


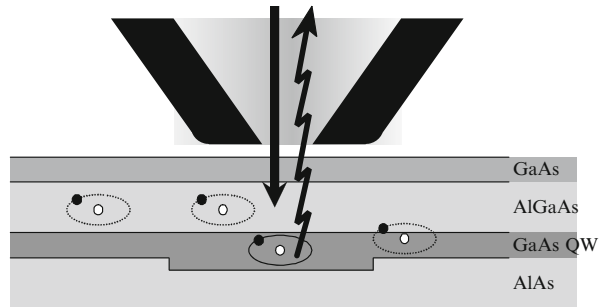
Fig. 11.16 Coupled pendulum model to intuitively explain the light–matter interaction at the nanoscale. (a) The lowest mode and (b) the second lowest mode of the coupled oscillator

molecular crystal) is much smaller than the wavelength of light. Figure 11.16a, b illustrates the lowest and the second lowest normal modes of the coupled oscillator, respectively. For the far-field illumination, all the pendulums are swung together at the frequency of irradiated light with the same phases. Therefore, the second lowest mode, where two halves of pendulums move opposite, cannot be excited by the far-field light, whereas the lowest mode can be. This corresponds to the optical selection rule for far-field excitation of confined exciton systems. For the near-field regime, on the other hand, the situation drastically changes. The trick that the nanoscale-confined light plays is to grasp solely a single pendulum and swing it. In this case, if the light frequency matches eigenfrequency of the individual oscillation mode, any normal mode can be excited regardless of the symmetry of oscillation, which means that the optical selection rule is broken by the near-field excitation. The efficiency of mode excitation is dependent on which pendulum is swung, that is, the position of nanoscale light source. By swinging a pendulum in order from the end and observing the magnitude of mode oscillation for each, we can map out the distribution of oscillation amplitude of individual pendulums. This illustrates the principle of the wavefunction mapping of exciton states.

11.6.2 Interface Fluctuation QD

Here we describe PL imaging spectroscopy of a GaAs QD by NSOM with a spatial resolution of 30 nm. This unprecedented high spatial resolution relative to the size of

Fig. 11.17 A schematic of a GaAs quantum dot naturally formed in a quantum well due to the fluctuation of well thickness



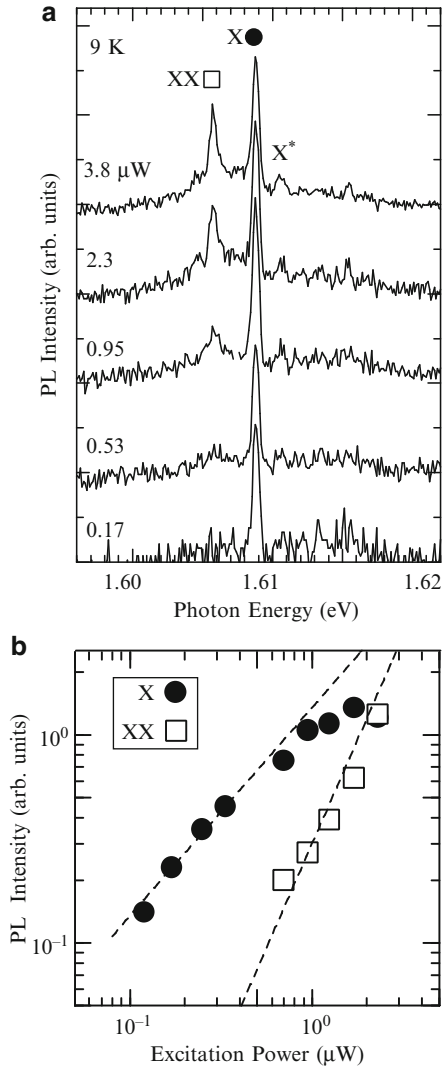
the QD (100 nm) permits a real-space mapping of the center-of-mass wavefunction of an exciton confined in the QD based on the principle discussed above [10, 45].

A schematic of QD sample structure is shown in Fig. 11.17. We prepared a 5-nm-thick GaAs QW, sandwiched between layers of Al(Ga)As grown by molecular-beam epitaxy. Two-minute interruptions of the growth process at both interfaces lead to the formation of large monolayer-high islands which localize excitons in QD-like potential with lateral dimensions on the order of 40–100 nm [3]. The GaAs QW layer was covered with a thin barrier, and a cap layer of totally 20 nm allows the near-field tip to be close enough to the emission source (QD).

The GaAs QD was excited with He–Ne laser light ($\lambda = 633$ nm) through the aperture, and carriers (excitons) were created in the barrier layers as well as the QW layer. Excitons diffused over several hundreds of nm and relaxed into the QDs. The PL signal from the QD was collected via the same aperture to prevent a reduction of the spatial resolution due to carrier diffusion. Near-field PL spectra were measured, for example, at 11 nm steps across a 210×210 nm² area and two-dimensional images were constructed from a series of PL spectra.

Figure 11.18a shows near-field PL spectra of a single QD at 9 K at excitation densities ranging from 0.17 to 3.8 μ W. At low excitation densities, a single emission line (denoted by X) at 1.6088 eV is observed. With an increase in excitation density, the other emission lines appear at 1.6057 eV (XX) and at 1.6104 eV (X^*). In order to clarify the origin of these emissions, excitation power dependence of PL intensities is examined as shown in Fig. 11.18b. The X line can be identified as an emission from a single-exciton state by its linear increase in emission intensity and its saturation behavior. The quadratic dependence of the XX emission with excitation power indicates that XX is an emission from a biexciton state. This identification of the XX line is also supported by the difference in the emission energy of 3.1 meV, which corresponds to the binding energy of biexciton and agrees well with the values reported previously [46]. The X^* emission line can be attributed to the radiative recombination of the exciton excited state by considering its energy position (higher-energy side of the single-exciton emission by about 1.6 meV) [47]. Figure 11.19 shows low-magnification PL maps for the intensity of X emissions with three different energies in the same scanning area. These emission profiles were found to differ from QD to QD.

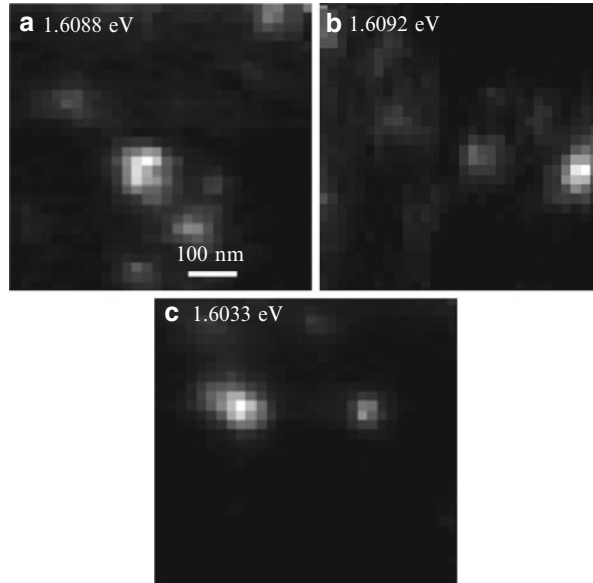
Fig. 11.18 (a) Near-field PL spectra of a single QD at 9 K for various excitation densities. The PL peaks at 1.6088, 1.6057, and 1.6104 eV are denoted by X, XX, and X*. (b) Excitation power dependence of PL intensities of the X and the XX lines. The two dotted lines correspond to the gradient associated with linear and quadratic power dependence



11.6.3 Real-Space Mapping of Exciton Wavefunction Confined in a QD

High-magnification PL images in Fig. 11.20 were obtained by mapping the PL intensity with respect to the X ((a), (c), and (e)) and the XX ((b), (d), and (f)) lines of three different QDs. The exciton PL images in Fig. 11.20 ((a), (c), and (e)) show an elongation along the $[-110]$ crystal axis. The image sizes are larger than the PL collection spot diameter, that is, the spatial resolution of the NSOM. The elongation along the $[-110]$ axis due to the anisotropy of the monolayer-high island

Fig. 11.19 Two-dimensional mapping of the PL intensity for three different X lines

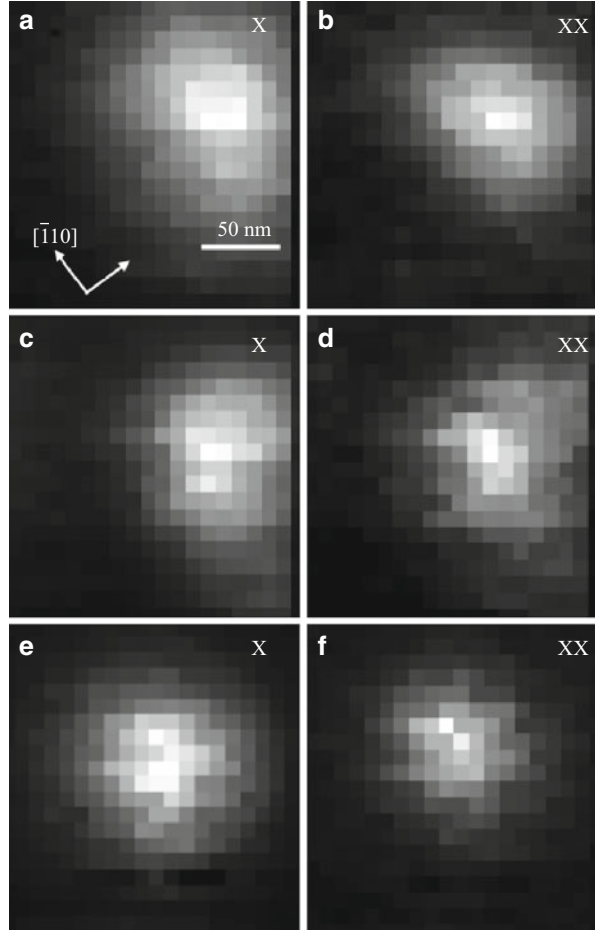


is consistent with previous observations with a scanning tunneling microscope (STM) [3]. We also obtained elongated biexciton PL images along the $[-110]$ crystal axis in Fig. 11.20 ((b), (d), and (f)) and found a clear difference in the spatial distribution between the exciton and biexciton emission. Here the significant point is that the PL image sizes of biexcitons are always smaller than those of excitons.

Figure 11.21a, b shows the normalized cross-sectional PL intensity profiles of exciton (thick lines) and biexciton (thin lines) along the $[110]$ and $[-110]$ crystal axes. The spreads in the exciton (biexciton) images, defined as the full width at half maximum (FWHM) of each profiles are 80 (60) nm and 115 (80) nm along the $[110]$ and $[-110]$ crystal axes, respectively.

Theoretical considerations can clarify what we see in the exciton and biexciton PL images. The relevant quantity is the optical near field around a single QD associated with an optical transition. This field can be calculated with Maxwell's equations using the polarization field of the exciton or biexciton as the source term. The observed luminescence intensity is proportional to the square of the near field detected by the probe. In the following, however, we have calculated the emission patterns simply by the squared polarization fields without taking account of the instrumental details. The polarization fields at the position of the probe (r_s) are derived from the transition matrix element from the exciton state (X) to the ground state (0) and that from the biexciton state (XX) to the exciton state (X) as follows [48]:

Fig. 11.20 Series of high-resolution PL images of exciton (X) state ((a), (c), and (e)) and biexciton (XX) state ((b), (d), and (f)) for three different QDs. Crystal axes along $[110]$ and $[\bar{1}10]$ directions are indicated

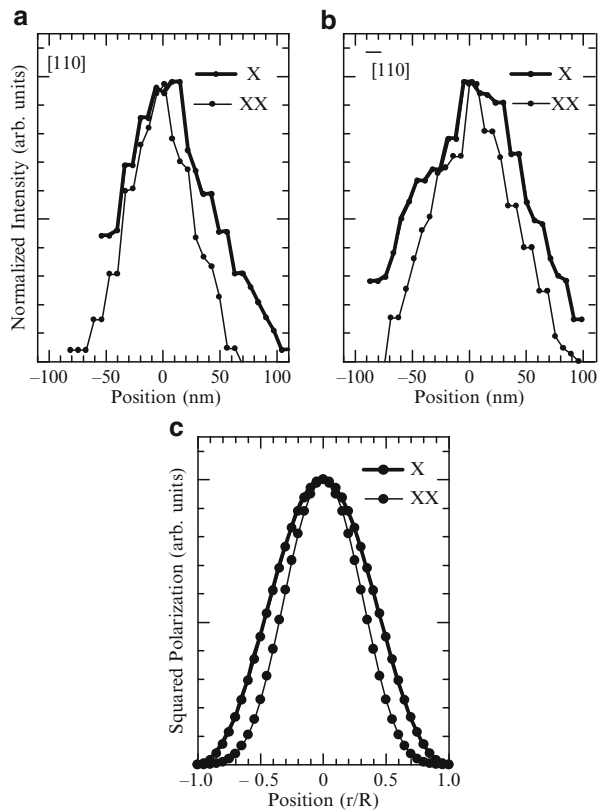


$$\langle 0 | p\delta(\mathbf{r} - \mathbf{r}_s) | X \rangle = -\sqrt{2}p_{cv}\phi(\mathbf{r}_s, \mathbf{r}_s) \quad (11.7)$$

$$\begin{aligned} \langle X | p\delta(\mathbf{r} - \mathbf{r}_s) | XX \rangle &= -\sqrt{\frac{3}{2}}p_{cv} \sum_{\mathbf{r}_1, \mathbf{r}_a} \phi(\mathbf{r}_1, \mathbf{r}_a) \Phi^{++}(\mathbf{r}_1, \mathbf{r}_s, \mathbf{r}_a, \mathbf{r}_s) \\ &\quad - \sqrt{\frac{1}{6}}p_{cv} \sum_{\mathbf{r}_1, \mathbf{r}_a} \phi(\mathbf{r}_1, \mathbf{r}_a) \Phi^{--}(\mathbf{r}_1, \mathbf{r}_s, \mathbf{r}_a, \mathbf{r}_s) \end{aligned} \quad (11.8)$$

where $\phi(\mathbf{r}_e, \mathbf{r}_h)$ stands for the exciton envelope function with the electron and hole coordinates denoted by \mathbf{r}_e and \mathbf{r}_h , $\Phi^{++}(\Phi^{--})(\mathbf{r}_1, \mathbf{r}_2, \mathbf{r}_a, \mathbf{r}_b)$ represents the biexciton envelope function with electron coordinates $(\mathbf{r}_1, \mathbf{r}_2)$ and hole coordinates $(\mathbf{r}_a, \mathbf{r}_b)$ that are symmetrized (antisymmetrized) with respect to the interchange between two electrons and between two holes, and p_{cv} is the transition dipole moment between the conduction band and the valence band. The spatial distribution

Fig. 11.21 High-resolution PL images and corresponding cross-sectional intensity profiles of the exciton ((a) and (b)) and the exciton excited ((c) and (d)) state. The intensity profiles are taken along *solid* and *dotted* lines in the images

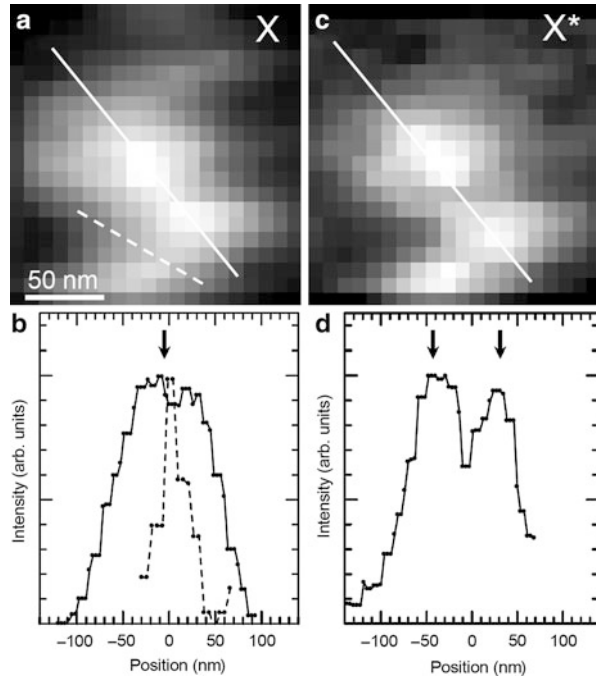


of the exciton polarization field corresponds to the center-of-mass envelope function of a confined exciton. For the biexciton emission, the polarization field is determined by the overlap integral, which represents the spatial correlation between two excitons forming the biexciton and is expected to be more localized than the single-exciton wavefunction.

Figure 11.21c shows the squared polarization amplitudes of the exciton (thick line) and biexciton (thin line) emission, which have been calculated for a GaAs QD with size parameters relevant to our experiments. The calculated profile of the squared polarization amplitude of the biexciton emission is narrower than that of the exciton emission. The spread of the biexciton emission normalized by that of the exciton emission is estimated to be 0.76, which is in good agreement with the experimental result (0.75 ± 0.08). This theoretical support and the experimental facts lead to the conclusion that the local optical probing by the near-field scanning optical microscope directly maps out the center-of-mass wavefunction of an exciton confined in a monolayer-high island.

Furthermore, we can demonstrate a novel powerful feature of the wavefunction mapping spectroscopy. Figure 11.22 shows the PL image and corresponding cross-

Fig. 11.22 (a) and (b) Normalized cross-sectional intensity profiles of exciton (*thick lines*) and biexciton (*thin lines*) PL images corresponding to Fig. 11.20a, b. (c) Spatial distributions of squared polarization fields of the exciton (*thick line*) and biexciton (*thin line*) emission, which are theoretically calculated for a GaAs quantum dot (radius of 114 nm, thickness of 5 nm). The horizontal axis is normalized by the disk radius R

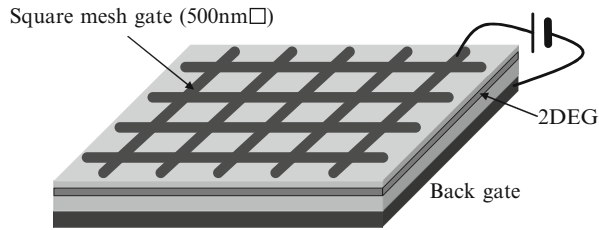


sectional intensity profiles of the exciton ground state X ((a) and (b)) and the exciton excited state X^* ((c) and (d)) from a single QD, which is different from that observed in Fig. 11.21. The exciton PL image exhibits a complicated shape in this QD, unlike the simple elliptical shape shown in Fig. 11.21. This is because the exciton is confined in a monolayer-high island with an extremely anisotropic shape. The significant point is that the exciton ground state image exhibits a single maximum peak in the intensity profile, while a double-peaked intensity profile is obtained from the exciton excited state. This is attributable to the difference in spatial distribution of the center-of-mass wavefunction, which has no node in the ground state, but does have a node in the excited state.

11.7 Real-Space Mapping of Local Density of States

Since the local electronic structure defined as the local density of states (LDOS) in metal corrals was first demonstrated using scanning probe microscopy and spectroscopy [49, 50], the LDOS mapping technique has been applied to many interesting quantum systems, such as two-dimensional (2D) electron gas [51], one-dimensional quantum wires [52], and zero-dimensional (0D) quantum dots (QDs) [53]. Although NSOM is useful for studying the elementary excitation of these quantum structures with less than subwavelength spatial resolution, there are

Fig. 11.23 A schematic of AlGaAs/GaAs two-dimensional electron gas with a mesh gate structure



only a few results of LDOS mapping using NSOM: for example, observation of the optical LDOS of an optical corral structure with a forbidden light [54].

Here we probed the local electronic states of a Be-doped GaAs/Al_{1-x}Ga_xAs single heterojunction with a surface gate using an NSOM. The spatial distribution of LDOS in a field-induced quantum structure can be mapped using near-field PL microscopy, as the quantum structure investigated here is larger than the spatial resolution of NSOM and the PL spectrum reflects the DOS of electrons.

11.7.1 Field-Induced Quantum Dot

The QDs formed by an electrostatic field effect have been extensively studied [55–58]. In a field-induced QD, the strength and lateral profile of the confinement potential can be tuned using the design of the surface gate and the strength of the bias voltage applied to the surface gate. As the degradation and imperfections at interfaces are minimized owing to electrostatic confinement, the electrons are confined by the well-defined lateral potential in this system. The properties of confined electrons have been investigated using macroscopic PL spectroscopy in a field-induced quantum structure based on a Be-doped single heterojunction [58, 59]. In this characteristic structure, the PL spectrum arising from the recombination of holes bound to Be acceptors with electrons in an electron gas provides us with a probe to investigate the DOS of electrons owing to relaxation of the *k*-selection rule in the optical process [58, 60, 61].

The sample investigated in this study was a Be-doped single heterojunction of a GaAs/Al_{1-x}Ga_xAs (*x* = 0.7) structure fabricated using molecular beam epitaxy [58, 61]. Figure 11.23 illustrates a rough schematic of sample structure. The heterostructure was grown on an n-type GaAs substrate used as the back contact and was fabricated under 75 nm from the surface. The nominal concentration of Be dopant was $2.0 \times 10^{10} \text{ cm}^{-2}$, and the Be-doped layer was inserted 25 nm below the heterojunction interface. The estimated sheet electron density without modulation using an external bias voltage (V_B) was $3.6 \times 10^{11} \text{ cm}^{-2}$ at 1.8 K, using an optical Shubnikov-de Hass measurement. A semitransparent Ti/Au Schottky gate structure on the surface was fabricated with a square mesh of a 500 nm period using electron beam lithography. The bias voltage was applied between the surface Schottky gate and the Ohmic back electrode.

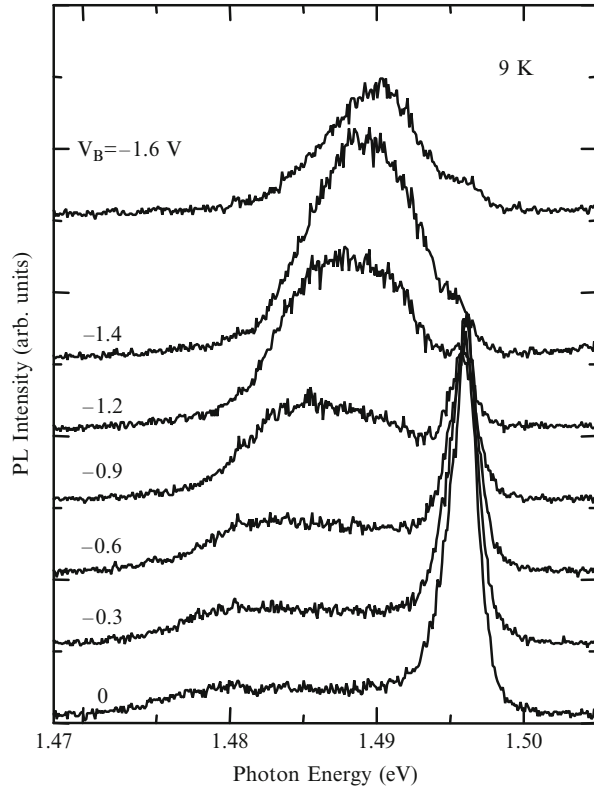
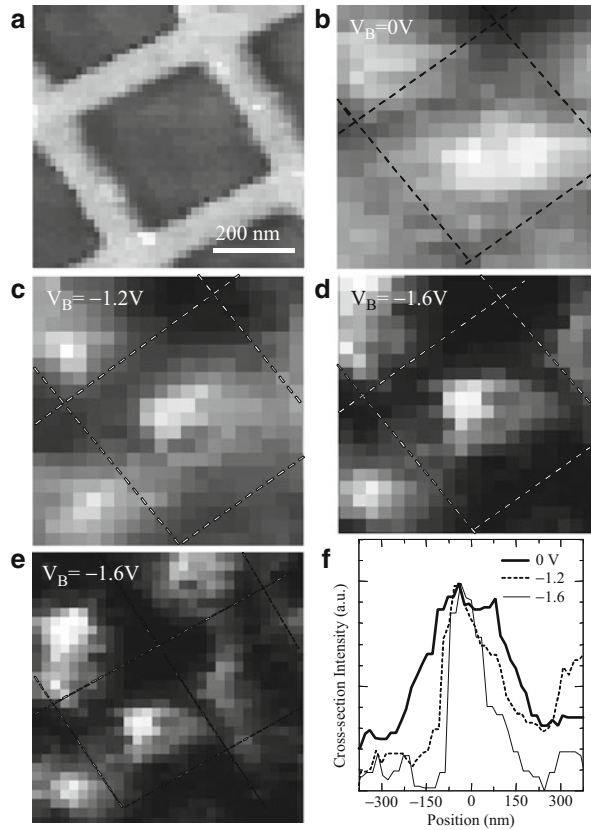


Fig. 11.24 Bias-voltage (V_B) dependence of macroscopic PL spectra of a Be-doped single heterojunction

An aperture about 120 nm in diameter was fabricated by milling of the probe apex using a focused ion beam (FIB) apparatus. The sample on the scanning stage was illuminated with a cw diode laser light ($\lambda = 685$ nm) through the aperture, and a time-integrated PL signal from the sample was collected via the same aperture. The PL signal was sent to a 32 cm monochromator with a cooled charge-coupled device with a spectral resolution of $220 \mu\text{eV}$. The spatial resolution of NSOM in this study was about 140 nm.

Figure 11.24 shows far-field PL spectra, measured at the V_B ranging from 0 to -1.6 V. The PL signal from the 1.475 to 1.491 eV region is attributed to the recombination between the localized holes bound to Be acceptors with electrons in the electron gas. The holes bound to Be acceptors can recombine with any electrons with wave vectors up to the inverse of the hole Bohr radius with nearly equal optical transition probabilities [58–61]. Owing to the small effective Bohr radius of the hole bound to the Be acceptor, the PL spectrum of the 1.475–1.491 eV region reflecting the DOS of electrons [58] is used as a probe to investigate the electronic structure. Under low negative bias conditions ($V_B < -0.35$ V), the signals from 1.480 to 1.489 eV show flat shape PL spectra reflecting the 2D DOS. The strong peaks at 1.496 eV come from the recombination between 2D electrons in the second subband

Fig. 11.25 (a) Shear-force microscopy (topographic) image of the gated sample surface (height contrast, 50 nm). (b)–(d) Near-field PL images at different bias voltages $V_B = 0$, -1.2 , and -1.6 V, respectively. These images were monitored at a detection energy of around 1.483 eV at 9 K. The dotted lines in the images correspond to the position of the surface gate. (e) Near-field PL image at $V_B = -1.6$ V, measured for a wide area. (f) Cross-sectional PL intensity profiles taken along a diagonal of the mesh gate



with holes bound to the acceptors [59]. When the V_B is increased to -1.6 V, the PL spectra show a linear increase in intensity toward higher photon energies from 1.480 to 1.489 eV. This behavior is expected from the 0D DOS of electrons because the linear dependence is in accordance with the generally accepted picture, in which the degeneracy of states increases with the quantum number.

11.7.2 Mapping of Local Density of States in a Field Induces QD

We investigated the local electronic states of the field-induced quantum structure while tuning the external bias voltage. As the PL intensity owing to the recombination of holes with electrons in an electron gas is proportional to the amplitude of the DOS and the spatial resolution of NSOM is higher than the size of the quantum structure, we can map the LDOS experimentally by monitoring the spatial distribution of the PL intensity from 1.475 to 1.491 eV. The atomic force microscopy image of a gated sample surface in Fig. 11.25a shows a square mesh gate with a 500 nm period. Figure 11.25b–e shows near-field optical images obtained by

detecting the PL intensity at around 1.483 eV while changing the external bias voltage ($V_B = 0, -1.2, \text{ and } -1.6$ V). In a series of images, we can observe the change in the PL images from 2D (plane) to 0D (dot) features with the application of V_B to the surface gate. For $V_B = -1.6$ V, a bright spot is observed in the center of the square mesh gate in the PL image in Fig. 11.25d. Looking at a wide spatial area, we see an array of PL spots corresponding to the period of the square mesh, as shown in Fig. 11.25e. The change induced by applying a bias voltage is also supported by the cross-sectional intensity profiles shown in Fig. 11.25f, taken along a diagonal of the mesh gate at the same positions. The size of the full width at half maximum (FWHM) of the profiles decreases from 400 nm at $V_B = 0$ V to 160 nm at $V_B = -1.6$ V. The narrow distribution of the PL intensity is caused by depletion of the electron density in the electron gas around the mesh gate under the external bias voltage. As a result, there is a dense electron population at positions far from the mesh gate, and the potential for electrons is minimal at the center of the mesh gate. Therefore, the change in the PL image directly connects to the change in electronic structure from a 2D electron gas to the confined 0D electronic state (QD) and an artificially formed QD array, induced by the electrostatic confinement potential.

Figure 11.26a–c shows PL images in the QD state under $V_B = -1.6$ V, detected at 1.4827, 1.4863, and 1.4882 eV, respectively. The spatial distribution of the PL intensity changes with the monitored photon energy and gradually spreads, going from an image at a lower photon energy to one at a higher photon energy (from Fig. 11.26a–c). We evaluated the spread of the PL image defined as the FWHM of the intensity profile as a function of photon energy and plotted the values for various bias voltages in Fig. 11.26d. At low bias voltage (-0.7 V), the values of the spread in the PL images are essentially constant for the entire energy range from 1.477 to 1.490 eV, which is easily understood from the 2D DOS characteristics. By contrast, under higher bias voltage, the spread of the PL image strongly depends on the monitored energy and the value increases gradually toward the higher-energy side, which indicates that the distribution of the LDOS gradually spreads from lower to higher-energy states in a field-induced QD.

To confirm the feasibility of the LDOS mapping, we refer the numerical calculation results of the electron density distribution derived from solving Schrödinger and Poisson's equations [61–64]. The calculated potential for electrons in this quantum structure is minimal at the center of the mesh gate with an application of the bias voltage [61, 62]. The electrons with lower energy near the bottom of the electrostatic potential are confined strictly and the spatial distribution of the wavefunction extends with increasing energy. The experimental results obtained from the near-field PL images are consistent with the calculated electron density distributions and its energy dependence. Thus, the optical near-field microscopy maps the LDOS in a field-induced quantum structure.

Finally, we will mention the near-field PL spectrum of a field-induced single QD (not shown here). We did not observe the sharp spectral features, as frequently observed for 0D systems (QDs) [65, 66]. A peak in the PL spectrum arising from each confined level should be broadened by at least 0.5 meV with taking into consideration of the estimated energy separation between confined levels [62].

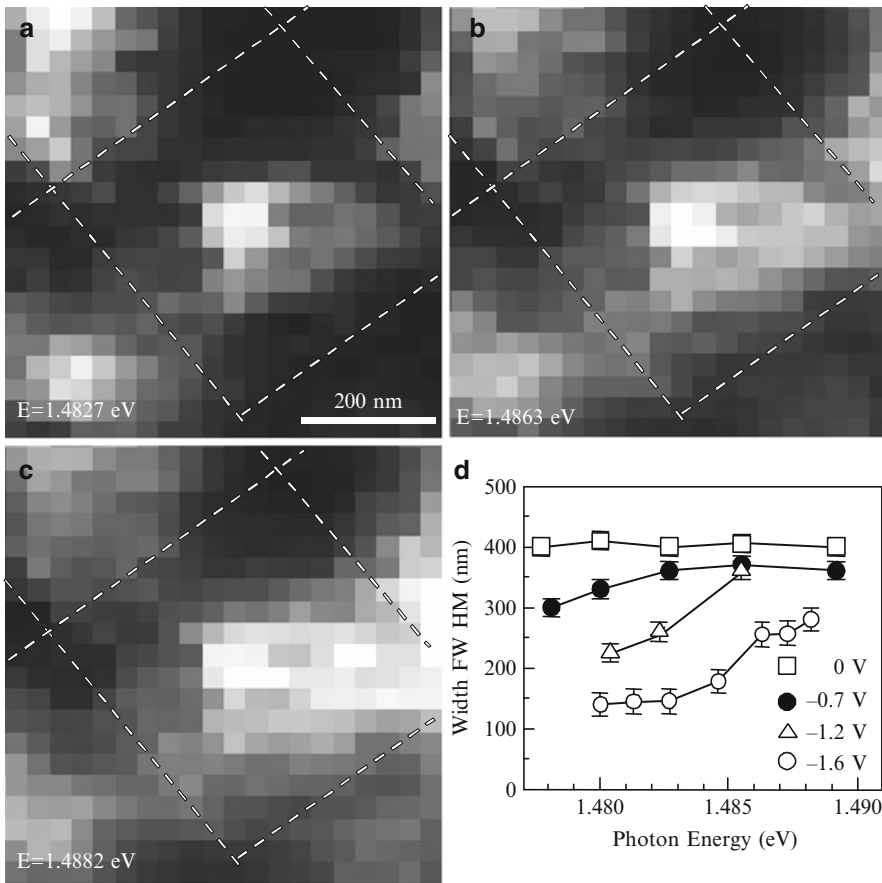


Fig. 11.26 (a)–(c) Near-field PL images obtained at different detection energies under a bias voltage of 1.6 V. (d) PL intensity distribution defined as the FWHM of the profiles as a function of the detection photon energy under various bias-voltage conditions

This broadening might be because it takes 0.1–1 μs for the nonequilibrium electrons to cool after excitation [60]. Therefore, the combination of near-field PL microscopy with the time-gated PL detection technique will enable us to observe fine spectral structures of a field-induced QD.

11.8 Carrier Localization in Cluster States in GaNAs

11.8.1 Dilute Nitride Semiconductors

In contrast to the well-defined quantum-confined systems such as QDs grown in a self-assembled mode, the more common disordered systems with local potential fluctuations leave unanswered questions. For example, a large reduction of the

fundamental band gap in GaAs with small amounts of nitrogen is relevant to the clustering behavior of nitrogen atoms and resultant potential fluctuations [67]. NSOM characterization with high spatial resolution can give us a lot of important information that is useful in our quest to fully understand such complicated systems, such as details about the localization and delocalization of carriers, which determine the optical properties in the vicinity of the band gap.

Dilute GaNAs and GaInNAs alloys are promising materials for optical communication devices [68–70] because they exhibit large band gap bowing parameters. In particular, for long-wavelength semiconductor laser application, high-temperature stability of the threshold current is realized in the GaInNAs/GaAs quantum well as compared to the conventional InGaAsP/InP quantum well due to strong electron confinement. However, GaNAs and GaInNAs with a high nitrogen concentration of more than 1% have been successfully grown only under nonequilibrium conditions by molecular beam epitaxy and metal organic vapor phase epitaxy.

The incorporation of nitrogen generally induces degradation of optical properties. To date, several groups of researchers have reported characteristic PL properties of GaNAs and GaInNAs, for example, the broad asymmetric PL spectra and the anomalous temperature dependence of the PL peak energy. More seriously emission yield drastically degraded with an increase of nitrogen concentration.

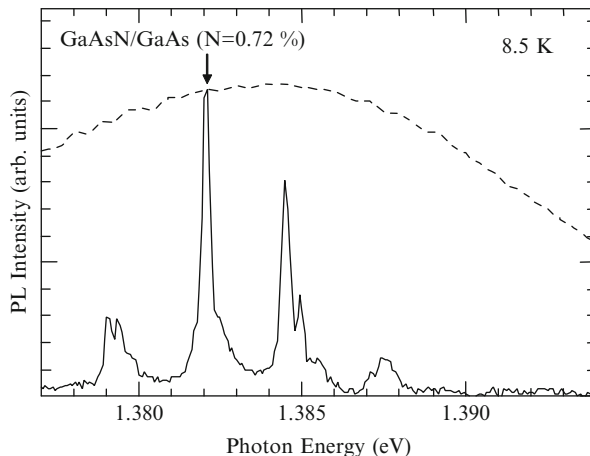
For improvement of their fundamental optical properties, it is strongly required to clarify electronic states due to single N impurities [71, 72] or N clusters, which interact with each other and with the host states. The interaction gives rise to the formation of weakly localized and delocalized electronic states at the band edge. Hence, the shape of optical spectra is extremely sensitive to the N composition. In conventional spatially resolved PL spectroscopy, it is easy to detect single impurity emissions in ultradilute compositional region. However, in order to resolve complicated spectral structures and to clarify the interaction of localized states and the onset of alloy formation, a spatial resolution far beyond the diffraction limit is needed.

Here we show the results of spatially resolved PL spectroscopy with a high spatial resolution of 30 nm. Spatial inhomogeneity of PL is direct evidence of carrier localization in the potential minimum case caused by the compositional fluctuation. PL microscopy with such a high spatial precision enables the direct optical observation of compositional fluctuations, that is, spontaneous N clusters and N random alloy regions, which are spatially separated in $\text{GaN}_x\text{As}_{1-x}/\text{GaAs}$ QWs.

11.8.2 Imaging Spectroscopy of Localized and Delocalized States

The samples investigated in this study were 5 nm thick $\text{GaN}_x\text{As}_{1-x}/\text{GaAs}$ single QWs with different N compositions ($x = 0.7$ and 1.2%) grown on (001) GaAs substrates using low-pressure metalorganic vapor phase epitaxy [73]. The growth temperature was 510 °C, and the details of the growth conditions have been described elsewhere [73]. The GaNAs layer was sandwiched between a 200 nm thick GaAs buffer layer and a 20 nm thick GaAs barrier layer. The thin 20 nm thick

Fig. 11.27 Far-field (*dotted line*) and near-field (*solid line*) PL spectra of a $\text{GaN}_x\text{As}_{1-x}/\text{GaAs}$ ($x = 0.72\%$) single QW at 8.5 K



barrier layer allowed a near-field probe tip to come close enough to the emission sources to achieve a spatial resolution as high as 35 nm. The N composition (x) of the QW layer was estimated using secondary ion mass spectroscopy and cross checked using the energy position in the PL spectra [74]. After growth, thermal annealing was performed for 10 min in a mixture of H_2 and TBAs at 670°C to improve the PL intensity [73].

We used NSOM probe tips with apertures of different diameters (30 and 150 nm), depending on the measurements. Optical measurements were performed at 8 K with a similar setup as described above. Near-field PL spectra were obtained at every 12 nm steps for a 300×300 nm area, and two-dimensional PL maps were constructed from a series of these spectra.

The dotted line in Fig. 11.27 shows a far-field PL spectrum of a single $\text{GaN}_x\text{As}_{1-x}/\text{GaAs}$ ($x = 0.7\%$) QW at low temperature. The far-field spectrum has a broad linewidth of 30 meV and a lower-energy tail. To resolve the inhomogeneously broadened PL spectrum, we carried out near-field PL measurements with a high spatial resolution of 35 nm. The near-field PL spectrum in Fig. 11.27 has fine structures that are not observed in the far-field spectrum [75–77]. After analyzing several thousands of near-field PL spectra, we found that the fine structures in the near-field PL spectra were divided into two groups: sharp luminescence peaks with narrow linewidths below 1 meV and broad peaks with linewidths of several meV. We discuss the origin of these spectral features using both spectral and spatial information.

Figure 11.28a shows a typical near-field PL spectrum with sharp emission lines. To evaluate the linewidth, we show one of the sharp emission lines (1.382 eV) at an expanded energy scale in the inset; the spectral linewidth, defined as the full width at half maximum (FWHM), was determined to be less than $220 \mu\text{eV}$, which is limited by the spectral resolution. The narrow PL linewidth means that the exciton state has a long coherence time, that is, there is a reduction of the scattering rate

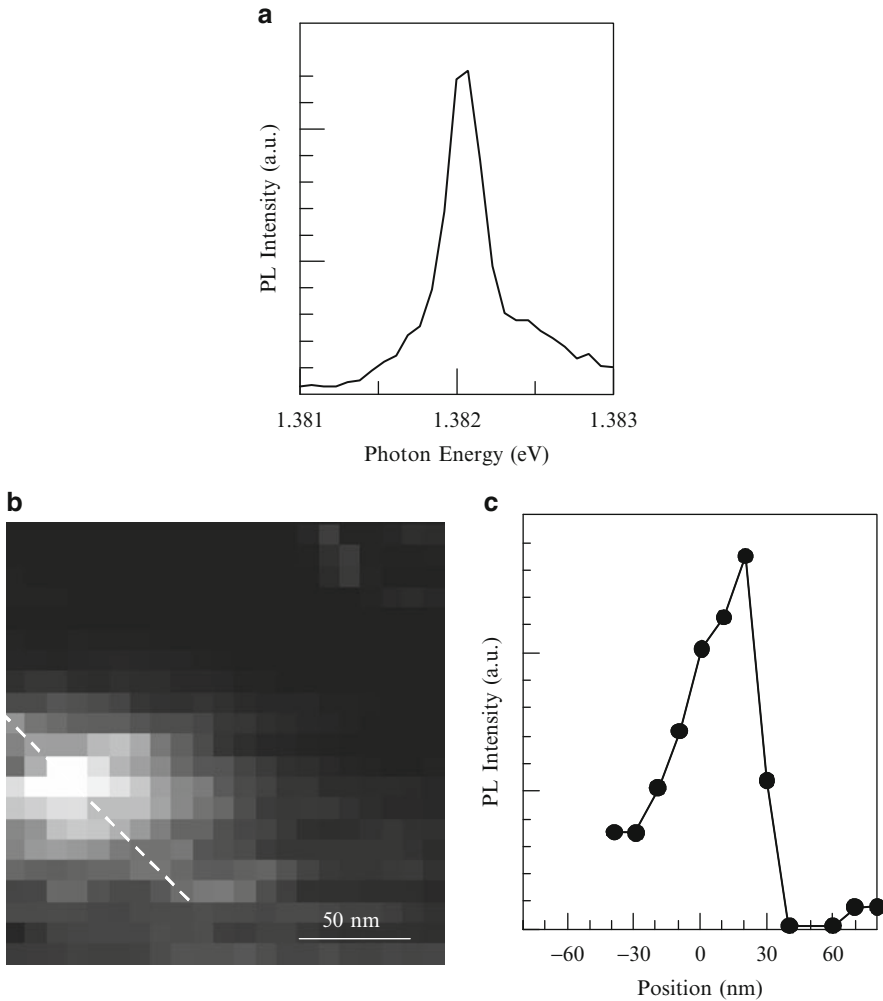
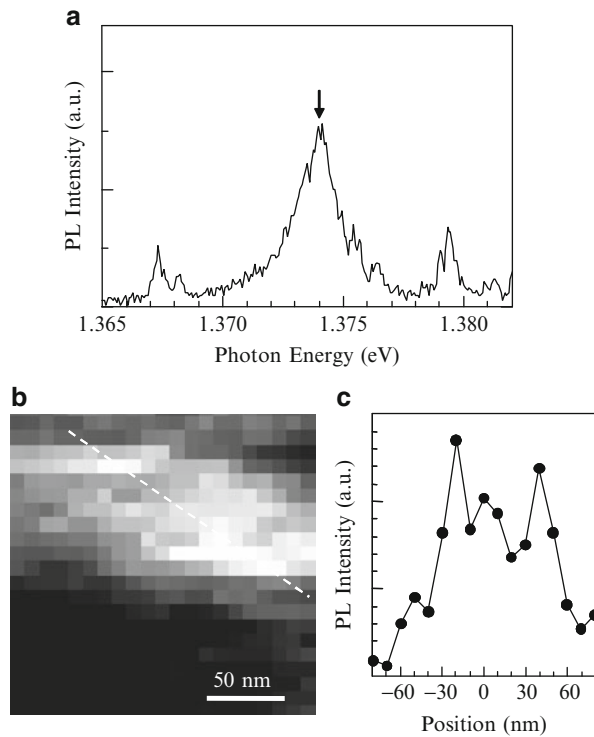


Fig. 11.28 (a) Near-field PL spectrum with a sharp emission peak. (b) Two-dimensional PL intensity mapping of the sharp emission line at 1.382 eV. (c) Cross-sectional PL intensity profile taken along the *dotted line* in (b). The size of the emission profile, defined as the FWHM, is 35 nm (restricted by the spatial resolution of NSOM)

between an exciton and phonons due to the change in the electronic structures from a continuum to discrete density of states. Such discrete density of states might be explained by the formation of naturally occurring quantum dot (QD) structures in a narrow $\text{GaN}_x\text{As}_{1-x}/\text{GaAs}$ QW ($x = 0.7\%$).

The spatial characteristics of the naturally occurring QD structures in a narrow QW showing the sharp emissions should be investigated. Figure 11.28b shows a high-resolution optical image of the sharp PL line, obtained by mapping the

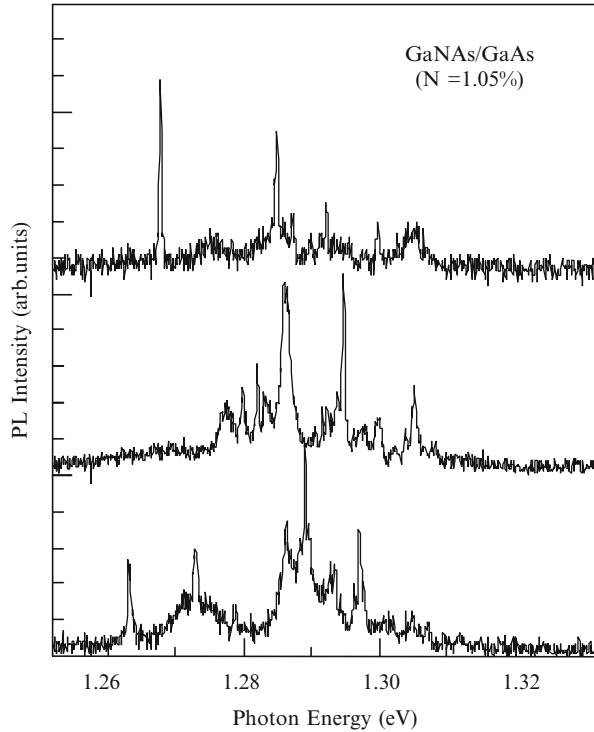
Fig. 11.29 (a) Near-field PL spectrum with a broad emission peak. (b) PL intensity map of the broad emission line at 1.374 eV. The scanning area is same as that of Fig. 11.28b. (c) Cross-sectional PL intensity profile of the broad emission along the dotted line in (b). The FWHM of the profile is 80 nm



intensity (denoted by the arrow in Fig. 11.27). The surface topography did not influence the optical images, because the sample had a flat surface with a roughness of less than several nm, as estimated from a shear-force topographic image. The PL image clearly shows a point emission feature, and the spot size defined as the FWHM of the cross-sectional profile shown in Fig. 11.28c is estimated to be 35 nm, which is limited by the spatial resolution of NSOM. The experimental spatial and spectral results suggest that the exciton strongly localizes in a potential minimum of naturally occurring QD structure in a narrow QW. The local N-rich regions (spontaneous N clusters) in a GaNAsN layer are the origin of the naturally occurring QD structures, as indicated by transmission electron microscopy [78].

Consider the broad peaks in the near-field PL spectrum. Figure 11.29a shows a typical PL spectrum of a broad peak with a 3 meV linewidth, which is much broader than below $220 \mu\text{eV}$ for the sharp emission line. The two-dimensional PL intensity map of the broad emission line in Fig. 11.29b shows spatially extended behavior that extends approximately 80 nm, as estimated from the cross-sectional profile in Fig. 11.29c (taken along the dotted line in the PL image). These characteristics of the broad PL line indicate that the exciton has a delocalized nature due to the random alloy state, which is frequently observed in isovalent semiconductor alloys. In addition, the energy positions and linewidths in the PL spectra are unchanged throughout the bright regions in Fig. 11.29b, which supports the delocalized nature

Fig. 11.30 Near-field PL spectra of $\text{GaN}_x\text{As}_{1-x}/\text{GaAs}$ ($x = 1.2\%$). The PL spectra measured at different positions were normalized by the maximum peak intensity



of excitons. Note that the PL images in [Figs. 11.28b](#) and [11.29b](#) were obtained in the same scanning area. Therefore, the regions with randomly distributed N and the spontaneous N-rich clusters are separated spatially in $\text{GaN}_x\text{As}_{1-x}$ ($x = 0.7\%$), as observed directly using NSOM with a high spatial resolution of 35 nm.

We investigated the compositional fluctuations in $\text{GaN}_x\text{As}_{1-x}$ for different concentrations of N. [Figure 11.30](#) shows near-field PL spectra for $x = 1.2\%$ at different spatial positions. These PL spectra were obtained using a probe tip with a 150 nm aperture, because the PL intensity strongly depends on x [[76](#)] and the intensity at higher x ($=1.2\%$) decreases by about one order of magnitude compared with that for $x = 0.7\%$. The near-field PL spectra in [Fig. 11.30](#) consist of many sharp lines from localized exciton recombinations in N-rich clusters and broad emissions, similar to the near-field PL spectra for $x = 0.7\%$. Note that sharp emission peaks are observed in the PL spectra for $x > 1\%$. Recent macroscopic PL [[79](#)] and magneto-PL [[80](#)] measurements of $\text{GaN}_x\text{As}_{1-x}$ for $x = 1.0\%$ showed broad, smooth spectra, which were assigned to emissions from delocalized excitons. However, our near-field PL spectroscopy reveals that the inhomogeneous broadened PL spectrum consists of the sharp emission lines owing to the recombinations of excitons localized in N-rich clusters superimposed on the broad emissions from the delocalized exciton state in $\text{GaN}_x\text{As}_{1-x}$ ($x = 1.2\%$). The regions of randomly distributed N and spontaneous N-rich clusters coexist at N compositions over 1%.

11.9 Perspectives

The dramatic progress in the spatial resolution of near-field optical microscope down to 10 nm offers an exciting opportunity for the study of light–matter interaction at the nanoscale. Real-space imaging of spatial distributions of quantized states can answer fundamental questions about the localized and delocalized nature of electrons in complicated potential systems and will lead to wavefunction engineering. Ultimately small light spot affect the light–matter interaction through the modification of quantum interference. For example, the near-field optical coupling of nano-electronic systems can enhance far-field forbidden transitions. Such alternation of the selection rule of optical transition will enable spatiotemporal coherent control of electronic excitation, which can be utilized as the principal function of nanometric devices. Light-harvesting devices like a mimic of photosynthesis antenna systems are also anticipated. A nanoscale light source also provides new techniques for wave packet engineering: creation, detection, transport, tailoring, and coherent control of electron wave packet. Pronounced quantum features of wave packet dynamics in nanoscale length will open new possibilities to control the capture processes from delocalized states to localized states, which will improve the quantum efficiency of light-emitting devices.

Acknowledgements We are grateful to M. Ohtsu, S. Mononobe, K. Matsuda, N. Hosaka, M. Sakai, K. Sawada, H. Nakamura, Y. Aoyagi, M. Mihara, S. Nomura, S. Nair, T. Tagahara, M. Takahashi, A. Moto, and S. Takagishi for their assistance and fruitful discussions.

References

1. M. Ohtsu, K. Kobayashi, T. Kawazoe, S. Sangu, T. Yatsui, *IEEE J. Sel. Top. Quantum Electron.* **8**, 839 (2002)
2. P. Micheler, *Single Quantum Dots* (Springer, Berlin/Heidelberg, 2003)
3. D. Gammon, E.S. Snow, B.V. Shanabrook, D.S. Katzer, D. Park, *Phys. Rev. Lett.* **76**, 3005 (1996)
4. J. Hours, P. Senellart, E. Peter, A. Cavanna, J. Bloch, *Phys. Rev. B* **71**, R161306 (2005)
5. M. Ohtsu, *Near-Field Nano/Atom Optics and Spectroscopy* (Springer, Tokyo, 1998)
6. L. Novotny, B. Hecht, *Principle of Nano-optics* (Cambridge University Press, New York, 2006)
7. N. Hosaka, T. Saiki, *Opt. Rev.* **13**, 262 (2006)
8. J.N. Farahani, D.W. Pohl, H.-J. Eisler, B. Hecht, *Phys. Rev. Lett.* **95**, 17402 (2005)
9. K. Cho, *Optical Response of Nanostructures* (Springer, Berlin/Heidelberg, 2003)
10. K. Matsuda, T. Saiki, S. Nomura, M. Mihara, Y. Aoyagi, S. Nair, T. Takagahara, *Phys. Rev. Lett.* **91**, 177401 (2003)
11. K. Karrai, R.D. Grober, *Appl. Phys. Lett.* **66**, 1842 (1995)
12. T. Saiki, K. Nishi, M. Ohtsu, *Jpn. J. Appl. Phys.* **37**, 1638 (1998)
13. H. Nakamura, T. Sato, H. Kambe, K. Sawada, T. Saiki, *J. Microsc.* **202**, 50 (2001)
14. T. Saiki, S. Mononobe, M. Ohtsu, N. Saito, J. Kusano, *Appl. Phys. Lett.* **68**, 2612 (1996)
15. D.W. Pohl, W. Denk, M. Lanz, *Appl. Phys. Lett.* **44**, 651 (1984)
16. T. Saiki, K. Matsuda, *Appl. Phys. Lett.* **74**, 2773 (1999)
17. P. Anger, P. Bharadwaj, L. Novotny, *Phys. Rev. Lett.* **96**, 113002 (2006)
18. J. Michaelis, C. Hettich, J. Mlynek, V. Sandoghdar, *Nature* **405**, 325 (2000)

19. R. Eckert, J.M. Freyland, H. Gersen, H. Heinzelmann, G. Schurmann, W. Noell, U. Staufer, N.F. de Rooij, *Appl. Phys. Lett.* **77**, 3695 (2000)
20. J.M. Kim, T. Ohtani, H. Muramatsu, *Surf. Sci.* **549**, 273 (2004)
21. N. Hosaka, T. Saiki, *J. Microsc.* **202**, 362 (2001)
22. H. Furukawa, S. Kawata, *Opt. Commun.* **132**, 170 (1996)
23. E.D. Palik, *Handbook of Optical Constants of Solids* (Academic, New York, 1985)
24. K. Matsuda, T. Saiki, S. Nomura, M. Mihara, Y. Aoyagi, *Appl. Phys. Lett.* **81**, 2291 (2002)
25. G.W. Bryant, *Appl. Phys. Lett.* **72**, 768 (1998)
26. Di Stefano, S. Savasta, G. Pistone, G. Martino, R. Girlanda, *Phys. Rev. B* **68**, 165329 (2003)
27. E. Runge, C. Lienau, *Appl. Phys. B* **84**, 103 (2006)
28. U. Hohenester, G. Goldone, E. Molinari, *Phys. Rev. Lett.* **95**, 216802 (2005)
29. F. Hatami, M. Grundmann, N.N. Ledentsov, F. Heinrichsdorff, R. Heitz, J. Bohrer, D. Bimberg, S.S. Ruvimov, P. Werner, V.M. Ustinov, P.S. Kop'ev, Zh.I. Alferov, *Phys. Rev. B* **57**, 4635 (1998)
30. K. Suzuki, R.A. Hogg, Y. Arakawa, *J. Appl. Phys.* **85**, 8349 (1999)
31. Ph. Lelong, K. Suzuki, G. Bastard, H. Sakaki, Y. Arakawa, *Physica E* **7**, 393 (2000)
32. L. M-Kirsch, R. Heitz, A. Schliwa, O. Stier, D. Bimberg, H. Kirmse, W. Neumann, *Appl. Phys. Lett.* **78**, 1418 (2001)
33. E. Ribeiro, A.O. Govorov, W. Carvalho, G. Medeiros-Ribeiro, *Phys. Rev. Lett.* **92**, 126402 (2004)
34. E. Dekel, D. Gershoni, E. Ehrenfreund, D. Spektor, J.M. Garcia, P.M. Petroff, *Phys. Rev. Lett.* **80**, 4991 (1998)
35. D.V. Regelman, U. Mizrahi, D. Gershoni, E. Ehrenfreund, W.V. Schoenfeld, P.M. Petroff, *Phys. Rev. Lett.* **87**, 257401 (2001)
36. K. Brunner, G. Abstreiter, G. Bohm, G. Trankle, G. Weimann, *Phys. Rev. Lett.* **73**, 1138 (1994)
37. S. Rodt, R. Heitz, A. Schliwa, R.L. Sellin, F. Guffarth, D. Bimberg, *Phys. Rev. B* **68**, 035331 (2003)
38. T. Nakai, S. Iwasaki, K. Yamaguchi, *Jpn. J. Appl. Phys.* **43**, 2122 (2004)
39. A.J. Williamson, L.W. Wang, A. Zunger, *Phys. Rev. B* **62**, 12963 (2000)
40. R. Resta, *Phys. Rev. B* **16**, 2717 (1977)
41. L.-W. Wang, J. Kim, A. Zunger, *Phys. Rev. B* **59**, 5678 (1999)
42. T. Nakai, K. Yamaguchi, *Jpn. J. Appl. Phys.* **44**, 3803 (2005)
43. N.N. Ledentsov, J. Bohrer, M. Beer, F. Heinrichsdorff, M. Grundmann, D. Bimberg, S.V. Ivanov, B.Ya. Meltser, S.V. Shaposhnikov, I.N. Yassievich, N.N. Faleev, P.S. Kop'ev, Zh.I. Alferov, *Phys. Rev. B* **52**, 14058 (1995)
44. C.D. Simserides, U. Hohenester, G. Goldone, E. Molinari, *Phys. Rev. B* **62**, 13657 (2000)
45. T. Saiki, K. Matsuda, S. Nomura, M. Mihara, Y. Aoyagi, S. Nair, T. Takagahara, *J. Electron Microsc.* **53**, 193 (2004)
46. Q. Wu, R.D. Grober, D. Gammon, D.S. Katzer, *Phys. Rev. B* **62**, 13022 (2000)
47. D. Gammon, E.S. Snow, D.S. Katzer, *Appl. Phys. Lett.* **67**, 2391 (1995)
48. S.V. Nair, T. Takagahara, *Phys. Rev. B* **55**, 5153 (1997)
49. M.F. Crommie, C.P. Lutz, D.M. Eigler, *Nature* **363**, 524 (1993)
50. M.F. Crommie, C.P. Lutz, D.M. Eigler, *Science* **262**, 218 (1993)
51. M. Morgenstern, J. Klijn, C. Meyer, M. Getzlaff, R. Adelung, R.A. Romer, K. Rossnagel, L. Kipp, M. Skibowski, R. Wiesendanger, *Phys. Rev. Lett.* **89**, 136806 (2002)
52. C. Meyer, J. Klijn, M. Morgenstern, R. Wiesendanger, *Phys. Rev. Lett.* **91**, 076803 (2003)
53. K. Kanisawa, M.J. Butcher, Y. Tokura, H. Yamaguchi, Y. Hirayama, *Phys. Rev. Lett.* **87**, 196804 (2001)
54. C. Chicanne, T. David, R. Quidant, J.C. Weeber, Y. Lacroute, E. Bourillot, A. Dereux, G. Colas des Francs, C. Girard, *Phys. Rev. Lett.* **88**, 097402 (2002)
55. D. Heitmann, J.P. Kotthaus, *Phys. Today* **46**, 56 (1993)
56. A. Lorke, J.P. Kotthaus, K. Ploog, *Phys. Rev. Lett.* **64**, 2559 (1990)
57. W. Hansen, T.P. Smith III, K.Y. Lee, J.A. Brum, C.M. Knoedler, J.M. Hong, D.P. Kern, *Phys. Rev. Lett.* **62**, 2168 (1989)

58. S. Nomura, Y. Aoyagi, *Phys. Rev. Lett.* **93**, 096803 (2004)
59. V. Kukushkin, K. von Klitzing, K. Ploog, V.B. Timofeev, *Phys. Rev. B* **40**, 7788 (1989)
60. V. Kukushkin, R.J. Haug, K. von Klitzing, K. Ploog, *Phys. Rev. Lett.* **72**, 736 (1994)
61. S. Nomura, Y. Aoyagi, *Surf. Sci.* **529**, 171 (2003)
62. S. Nomura, T. Nakanishi, Y. Aoyagi, *Phys. Rev. B* **63**, 165330 (2001)
63. A. Kumar, S.E. Laux, F. Stern, *Phys. Rev. B* **42**, 5166 (1990)
64. M.P. Stopa, *Phys. Rev. B* **54**, 13767 (1996).
65. D. Gammon, E.S. Snow, B.V. Shanabrook, D.S. Katzer, D. Park, *Science* **273**, 87 (1996)
66. M. Grundmann, J. Christen, N.N. Ledentsov, J. Bohrer, D. Bimberg, S.S. Ruvimov, P. Werner, U. Richter, U. Gosele, J. Heydenreich, V.M. Ustinov, A.Yu. Egorov, A.E. Zhukov, P.S. Kop'ev, Zh.I. Alferov, *Phys. Rev. Lett.* **74**, 4043 (1995)
67. A. Buyanova, W.M. Chen, G. Pozina, J.P. Bergman, B. Monemar, H.P. Xin, C.W. Tu, *Appl. Phys. Lett.* **75**, 501 (1999)
68. M. Kondow, K. Uomi, A. Niwa, T. Kitatani, S. Watahiki, Y. Yazawa, *Jpn. J. Appl. Phys.* **35**, 1273 (1996)
69. D. Gollub, M. Fischer, M. Kamp, A. Forchel, *Appl. Phys. Lett.* **81**, 4330 (2002)
70. M. Kawaguchi, T. Miyamoto, E. Gouardes, D. Schlenker, T. Kondo, F. Koyama, K. Iga, *Jpn. J. Appl. Phys.* **40**, L744 (2001)
71. F. Masia, A. Polimeni, G.B.H. von Hogersthal, M. Bissiri, M. Capizzi, P.J. Klar, W. Stolz, *Appl. Phys. Lett.* **82**, 4474 (2003)
72. S. Francoeur, S.A. Nikishin, C. Jin, Y. Qiu, H. Temkin, *Appl. Phys. Lett.* **75**, 1538 (1999)
73. A. Moto, S. Tanaka, N. Ikoma, T. Tanabe, S. Takagishi, M. Takahashi, T. Katsuyama, *Jpn. J. Appl. Phys.* **38**, 1015 (1999)
74. J. Sik, M. Schubert, G. Leibiger, V. Gottschalch, G. Wagner, *J. Appl. Phys.* **89**, 294 (2001)
75. K. Matsuda, T. Saiki, S. Takahashi, A. Moto, M. Takagishi, *Appl. Phys. Lett.* **78**, 1508 (2001)
76. M. Takahashi, A. Moto, S. Tanaka, T. Tanabe, S. Takagishi, K. Karatani, M. Nakayama, K. Matsuda, T. Saiki, *J. Cryst. Growth* **221**, 461 (2001)
77. M. Mintairov, T.H. Kosel, J.L. Merz, P.A. Blagnov, A.S. Vlasov, V.M. Ustinov, R.E. Cook, *Phys. Rev. Lett.* **87**, 277401 (2001)
78. L. Grenouillet, C. Bru-Chevallier, G. Guillot, P. Gilet, P. Duvaut, C. Vannuffel, A. Million, A. Chenevas-Paule, *Appl. Phys. Lett.* **76**, 2241 (2000)
79. X.D. Luo, J.S. Huang, Z.Y. Xu, C.L. Yang, J. Liu, W.K. Ge, Y. Zhang, A. Mascarenhas, H.P. Xin, C.W. Tu, *Appl. Phys. Lett.* **82**, 1697 (2003)
80. Y.J. Wang, X. Wei, Y. Zhang, A. Mascarenhas, H.P. Xin, Y.G. Hong, C.W. Tu, *Appl. Phys. Lett.* **82**, 4453 (2003)

Yoichi Kawakami, Akio Kaneta, Kunimichi Omae, Yukio Narukawa,
and Takashi Mukai

Contents

12.1	Introduction.....	484
12.2	Material Parameters of In _x Ga _{1-x} N.....	485
12.2.1	Bandgap Energies in In _x Ga _{1-x} N Alloys.....	485
12.2.2	Alloy Broadening Factor in In _x Ga _{1-x} N Alloys.....	487
12.2.3	Piezoelectric Fields in Strained In _x Ga _{1-x} N Layers.....	488
12.3	General Transition Models.....	489
12.3.1	Localization Versus Screening of Piezoelectric Field.....	489
12.3.2	Photo-Induced Change of Optical Density Induced by Two Major Effects....	493
12.4	Pump and Probe Spectroscopy on In _x Ga _{1-x} N Thin Layers and Quantum Wells.....	495
12.5	SNOM-Luminescence Mapping Results.....	500
12.5.1	Instrumentation.....	500
12.5.2	SNOM-PL Mapping at Low Temperature under Illumination- Collection Mode.....	504
12.5.3	Multimode SNOM at RT.....	512
12.6	Conclusion.....	522
	References.....	523

Abstract

Recombination dynamics in InGaN-based semiconductors has been assessed taking into account the effect of potential modulations which are induced not only by potential fluctuations in InGaN plane but also by quantum-confined Stark effects perpendicular to the plane. Local diffusion, radiative, and nonradiative

Y. Kawakami (✉) · A. Kaneta

Department of Electronic Science and Engineering, Kyoto University, Kyoto, Japan
e-mail: kawakami@kuee.kyoto-u.ac.jp; akio.kaneta@optomater.kuee.kyoto-u.ac.jp

K. Omae · Y. Narukawa · T. Mukai

Nichia Corporation, Tokushima, Japan

e-mail: kunimichi.omaie@nichia.co.jp; yukio.narukawa@nichia.co.jp;
takashi.mukai@nichia.co.jp

processes have been identified, by employing multimode scanning near-field optical microscopy where time-resolved photoluminescence data are taken by both illumination-collection mode and illumination mode.

12.1 Introduction

Recent progress of epitaxial growth techniques has achieved the successful introduction of indium into gallium nitride, leading to the realization of light-emitting devices based on $\text{In}_x\text{Ga}_{1-x}\text{N}/\text{GaN}/\text{Al}_y\text{Ga}_{1-y}\text{N}$ heterostructures in wurtzite crystal phase, such as dazzling violet, blue, green, and amber light-emitting diodes (LEDs) [1–3], as well as laser diodes (LDs) operated from ultraviolet (350 nm) to blue (480 nm) spectral region [4–6]. However, further improvement of emission efficiency, reduction of lasing threshold, and extension of operable wavelength range are required to expand the application field of such devices. Therefore, it is very important to assess the carrier/exciton recombination processes, through which positive feedback can be made not only to the growth conditions but also to the appropriate design of device structures.

There has been controversy concerning a major role on the modulation of optical transitions in $\text{In}_x\text{Ga}_{1-x}\text{N}$ -based semiconductors [7]. One important effect, as schematically depicted in Fig. 12.1a, is exciton localization induced by potential fluctuation because of compositional modulation of In [8–12]. This can be understood as a nature of $\text{In}_x\text{Ga}_{1-x}\text{N}$ ternary alloys, where insoluble tendency of InN is energetically favored in GaN at the growth temperatures [13–16]. Actually, spontaneous formation of In-rich region on the nanoscopic scale has been reported by a lot of groups [9, 17–21]. In this case, large Stokes-like shifts between absorption and emission have been attributed to the exciton/carrier distribution to localized tail states acting as quantum disks or quantum dots (QDs) depending on the lateral spatial confinement [22–26]. It has been claimed that the high quantum efficiency of $\text{In}_x\text{Ga}_{1-x}\text{N}$ -based emitters in spite of high threading-dislocation density is mostly due to the large localization of excitons/carriers because the pathway to the nonradiative recombination centers is prohibited once they are captured in a small

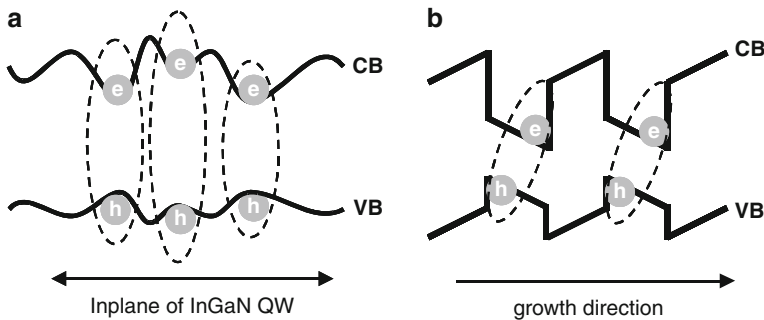


Fig. 12.1 (a) Potential fluctuation induced by inhomogeneity of indium distribution within $\text{In}_x\text{Ga}_{1-x}\text{N}$ QW. (b) Piezoelectric field induced in $\text{In}_x\text{Ga}_{1-x}\text{N}/\text{GaN}$ QW grown toward (0001) orientation (C-axis)

volume [9]. Another important effect is large piezoelectric fields in $\text{In}_x\text{Ga}_{1-x}\text{N}/\text{GaN}$ quantum wells (QWs) perpendicular to (0001)-oriented growth direction as shown in Fig. 12.1b that induces the quantum-confined Stark effect (QCSE) [27–31] and the Franz-Keldysh effect (FKE) [32]. As described in the forthcoming section, both effects contribute to the Stokes-like shifts, and to the localization-like behavior, so that conventional macroscopic optical data do not provide adequate information on the mechanism [33]. Therefore, photo-induced change of optical absorption spectra was assessed [34–37] to determine which effect plays a major role, by employing white-light pump and probe spectroscopy [38].

A number of reports have recently been appeared on the spatial mapping of luminescence in $\text{In}_x\text{Ga}_{1-x}\text{N}/\text{GaN}$ QWs by optical microscope [39–41], by cathodoluminescence (CL) [42, 43], or by scanning near-field optical microscopy (SNOM) [44–53]. It is worth noting that such SNOM technique is not only useful for the photoluminescence (PL) mapping but also applicable to the electroluminescence (EL) mapping under the current driving condition of LEDs [54, 55]. Although spatial resolution of optical microscope is typically a few to several hundred nm that is restricted by diffraction limit, CL has a much smaller diameter in exciting electron beam (e-beam). However, the spatial resolution is generally much larger than the e-beam diameter not only because incident electrons spread during the penetration to the sample but also because generated carriers/excitons diffuse spatially in lateral direction before recombining radiatively or nonradiatively. Another drawback of CL is that both active and cladding layers are photoexcited, while selective photoexcitation to active layers is achieved in optical excitation by tuning incident laser wavelength. SNOM technique has a potential to attain spatial resolution with nm scale. Moreover, spatial and temporal dynamics can be detected by combining with time-resolved (TR) spectroscopy [50–52].

In this chapter, material parameters are summarized such as bandgap energy and alloy broadening of $\text{In}_x\text{Ga}_{1-x}\text{N}$, and piezoelectric field in $\text{In}_x\text{Ga}_{1-x}\text{N}/\text{GaN}$ QWs, and then general transition models are discussed based on screening of piezoelectric field, as well as on localization behavior of excitons/carriers. Finally, detailed results are shown on SNOM-luminescence mapping in an $\text{In}_x\text{Ga}_{1-x}\text{N}/\text{GaN}$ single quantum well (SQW) structure, by which the physical interpretation was made for the recombination mechanism in $\text{In}_x\text{Ga}_{1-x}\text{N}$ -based nanostructures.

12.2 Material Parameters of $\text{In}_x\text{Ga}_{1-x}\text{N}$

12.2.1 Bandgap Energies in $\text{In}_x\text{Ga}_{1-x}\text{N}$ Alloys

In order to assess the optical transitions in $\text{In}_x\text{Ga}_{1-x}\text{N}$ -based nanostructures, it is essential to estimate the bandgap energies (E_g) of $\text{In}_x\text{Ga}_{1-x}\text{N}$ ternary alloys and then take into account the effects of quantum confinement under an electric field, as well as those of localization induced by fluctuation of composition or of well width. However, there have been a lot of papers discussing the exact bandgap energies of $\text{In}_x\text{Ga}_{1-x}\text{N}$. This is due to the difficulty in obtaining high-quality InN crystals caused by the low dissociation temperature and high vapor pressure of nitrogen.

Although $\text{In}_x\text{Ga}_{1-x}\text{N}$ -based light-emitting devices are in practical use, only small amount of In up to a few tens of % was successfully incorporated to gallium nitride with sufficient quality in current fabrication technology. Moreover, fabricated $\text{In}_x\text{Ga}_{1-x}\text{N}$ active layers are highly strained, and their layer thicknesses are as small as a few nm. Therefore, the fundamental bandgap of InN has been thought to be about 1.89 eV at room temperature (RT) for a long period, where the value had been obtained by the optical absorption measurement on polycrystalline InN grown by sputtering technique [56]. The bandgap energies of $\text{In}_x\text{Ga}_{1-x}\text{N}$ have also been estimated by the similar way, and the most commonly cited equation was

$$E_g = 3.42 \text{ eV}(1 - x) + 1.89 \text{ eV}x - bx(1 - x), \quad (12.1)$$

where b denotes the bowing parameters, reported values of which scattered in the range between 1.0 and 3.8 eV [57–59].

However, PL and absorption measurements of high-quality InN epitaxial layers grown by metallorganic vapor phase epitaxy (MOVPE) and RF-molecular beam epitaxy (RF-MBE) have demonstrated that the fundamental bandgap of InN is about 0.78 eV [60–63], revealing that appropriate equation should be

$$E_g = 3.42 \text{ eV}(1 - x) + 0.78 \text{ eV}x - bx(1 - x). \quad (12.2)$$

$\text{In}_x\text{Ga}_{1-x}\text{N}$ alloy films with an entire alloy composition have been grown by RF-MBE at about 550 °C without noticeable phase separation, and $b = 2.3 \text{ eV}$ [64] was reported by fitting PL and CL peak positions as a function of x -value, while $b = 1.43 \text{ eV}$ [65] was claimed by fitting absorption data as shown in Fig. 12.2. Although there still exists to some extent the scattering of the value of b , the

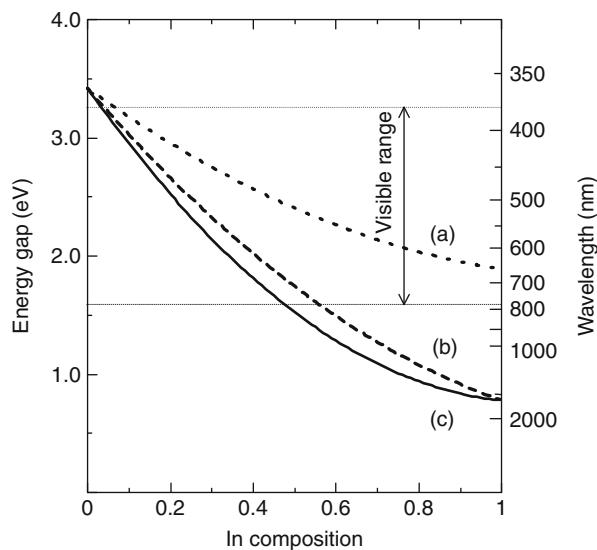


Fig. 12.2 Bandgap energies of $\text{In}_x\text{Ga}_{1-x}\text{N}$ alloys as a function of In-contents x , calculated assuming various parameters, (a) E_g of InN = 1.8 eV, $b = 1.0 \text{ eV}$ [57]; (b) E_g of InN = 0.78 eV, $b = 2.3 \text{ eV}$ [64]; and (c) $E_g = 0.77 \text{ eV}$, $b = 1.43 \text{ eV}$ [65]

difference in this case may be contributed from the localization effects, where the luminescence peaks are located on the low-energy side on absorption edge. Consequently, it has been clarified that $\text{In}_x\text{Ga}_{1-x}\text{N}$ alloy semiconductors cover not only in ultraviolet and full-visible range but also in infrared reaching to the wavelength used for optical communications [66].

12.2.2 Alloy Broadening Factor in $\text{In}_x\text{Ga}_{1-x}\text{N}$ Alloys

The effect of disorder in alloy semiconductors can be classified into two categories, where inhomogeneous broadening is induced by inevitable nature inherent to alloys as well as by compositional modulation. The former takes place in random distribution of alloy composition because of standard deviation of alloy composition within exciton Bohr radius. This effect is significant in widegap semiconductors owing to their small exciton Bohr radius. The full width at half maximum (FWHM) of an excitonic transition $[\Delta(x)]$ in A_{1-x}B_x alloy due to this effect is given by the following equation [67]:

$$\Delta(x) = 2\sqrt{2\ln 2} [dE_{\text{ex}}(x)/dx] \sqrt{x(1-x)V_0(x)/V_{\text{ex}}(x)} \quad (12.3)$$

if a Gaussian line shape is assumed, where $E_{\text{ex}}(x)$ is the exciton transition energy, $V_0(x)$ is the volume of elementary cell, and $V_{\text{ex}}(x)$ is that of exciton. Zimmermann [68] has derived the relevant exciton volume using a statistical theory expressed by

$$V_{\text{ex}}(x) = 8\pi r_{\text{B}}^3(x), \quad (12.4)$$

where $r_{\text{B}}(x)$ denotes the Bohr radius of exciton. The $\Delta(x)$ values have been calculated for $\text{In}_x\text{Ga}_{1-x}\text{N}$ using r_{B} values of GaN and InN as 2.9 and 7.3 nm, respectively. It should be noted here that no experimental data have been reported for excitonic properties of InN because of the screening of Coulomb force between electron and hole induced by high density of residual donor concentration (approximately in the range of 10^{18} – 10^{20} cm^{-3}) in current InN layers. Therefore, the r_{B} value of InN has been calculated by

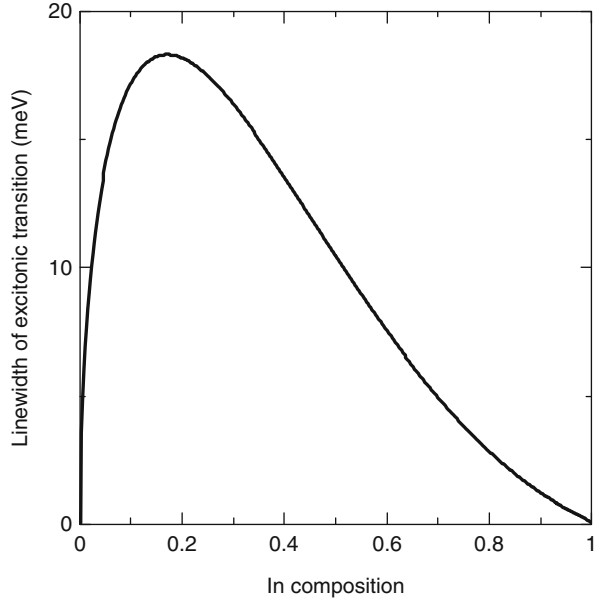
$$r_{\text{B}} = a_0\epsilon_r \left(\frac{m_0}{m_e} + \frac{m_0}{m_h} \right), \quad (12.5)$$

where a_0 and ϵ_r are Bohr radius of hydrogen (0.0529 nm) and relative dielectric constant ($\epsilon_r = 15.3$ [69]) and m_0 , m_e , and m_h are free electron mass, effective mass of electron ($m_e = 0.12m_0$ [70]) and effective mass of hole ($m_h = 1.56m_0$ [71]), respectively. For x dependence of r_{B} , a linear variation with x has been assumed.

As shown in Fig. 12.3, it was found that the FWHM due to this effect is at most 20 meV.

However, observed PL linewidths are much larger than this value, typically from several ten meV to a few hundred meV depending on samples. This suggests that the compositional modulation and alloy clustering are induced in samples grown by current growth techniques.

Fig. 12.3 Theoretical FWHM values of excitonic transition in $\text{In}_x\text{Ga}_{1-x}\text{N}$ ternary alloys induced by the effect of alloy broadening



12.2.3 Piezoelectric Fields in Strained $\text{In}_x\text{Ga}_{1-x}\text{N}$ Layers

Unlike other semiconductors with zinc blende crystal structures grown toward (001) orientation, large piezoelectric field is induced in wurtzite-structured $\text{In}_x\text{Ga}_{1-x}\text{N}$ with c -axis [(0001) orientation] [27]. This is not only because of large piezoelectric constants with this direction but also due to high biaxial-compressive strain in $\text{In}_x\text{Ga}_{1-x}\text{N}$ layers coherently grown on almost unstrained GaN-based layers. The piezoelectric polarization to the c -axis defined as P_z is given by

$$P_z = e_{31}\epsilon_{xx} + e_{31}\epsilon_{yy} + e_{33}\epsilon_{zz}, \quad (12.6)$$

where e_{31} and e_{33} are piezoelectric constants and ϵ_{xx} , ϵ_{yy} , and ϵ_{zz} are strain elements defined by the following equation using a -axis lattice constant of GaN ($a_{\text{GaN}} = 0.3189 \text{ nm}$) and $\text{In}_x\text{Ga}_{1-x}\text{N}$ ($a_{\text{InGaN}} = 0.3189(1-x) + 0.3548x \text{ nm}$), as well as elastic stiffness constants of c_{13} and c_{33}

$$\epsilon_{xx} = \epsilon_{yy} = \frac{a_{\text{GaN}} - a_{\text{InGaN}}}{a_{\text{GaN}}}, \quad (12.7)$$

$$\epsilon_{zz} = -\frac{2c_{13}}{c_{33}}\epsilon_{xx}. \quad (12.8)$$

The internal electric field along the c -axis (E_z) is then given by

$$E_z = -\frac{P_z}{\epsilon_r\epsilon_0}, \quad (12.9)$$

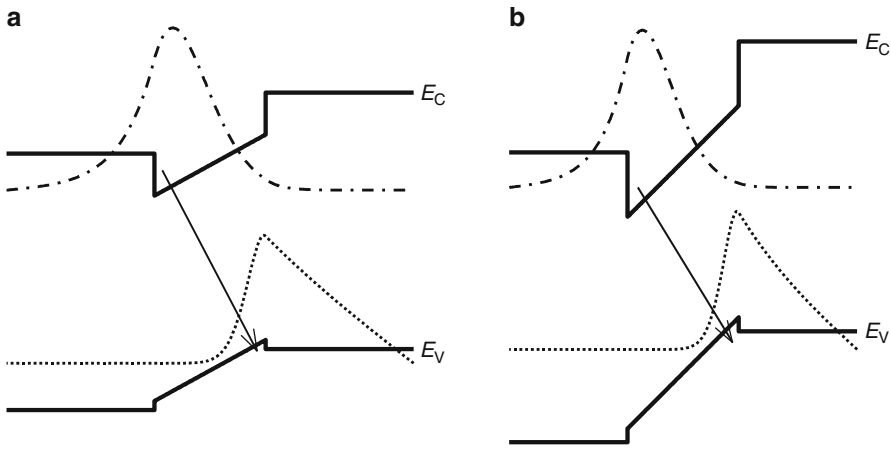


Fig. 12.4 Band structures as well as wavefunctions of both electrons and holes in $\text{GaN}/\text{In}_x\text{Ga}_{1-x}\text{N}/\text{GaN}$ having 3-nm QW thickness, for (a) $x = 25\%$, $E_z = 2.7 \text{ MV/cm}$, and for (b) $x = 50\%$, $E_z = 4.5 \text{ MV/cm}$

where ϵ_r and ϵ_0 are relative dielectric constants of $\text{In}_x\text{Ga}_{1-x}\text{N}$ and the permittivity of free space, respectively. Although there still exists wide scattering of reported values of e_{31} , e_{33} , c_{13} , and c_{33} of both GaN and InN [72], E_z value is estimated to be in the order of MV/cm for $\text{In}_x\text{Ga}_{1-x}\text{N}$ layers with $x = 0.1 \sim 0.2$ used for active layers of blue-green emitters [73–75].

In Fig. 12.4, band structures of $\text{GaN}/\text{In}_x\text{Ga}_{1-x}\text{N}/\text{GaN}$ are depicted assuming that only $\text{In}_x\text{Ga}_{1-x}\text{N}$ QWs are under compressive strain. Due to the internal field, the effective bandgaps as well as oscillator strengths of excitons become much lower than those in the case of flat bands.

12.3 General Transition Models

12.3.1 Localization Versus Screening of Piezoelectric Field

Potential fluctuation induces localization of excitons and/or carriers to potential minima in real space. Besides the effect of inevitable alloy broadening, thermodynamical theory shows that the fluctuation of In composition leading to local clustering or phase separation is energetically favored considering the free energy of mixing in $\text{In}_x\text{Ga}_{1-x}\text{N}$ alloys [13–15]. If an In clustering takes place with a size less than several nanometers, localization centers act as QDs [9, 17–21]. Such localization is conspicuous even with small amount of disorder because of both small exciton Bohr radius and large bandgap variation with x -value in $\text{In}_x\text{Ga}_{1-x}\text{N}$. The model of exciton localization due to potential fluctuation, as well as density of states (DOS) of exciton energy distribution induced by localization, is schematically shown in Figs. 12.5 and 12.6, respectively. The observation of large Stokes shift

Fig. 12.5 Potential fluctuation induced by the alloy disorder or by the randomness of well width

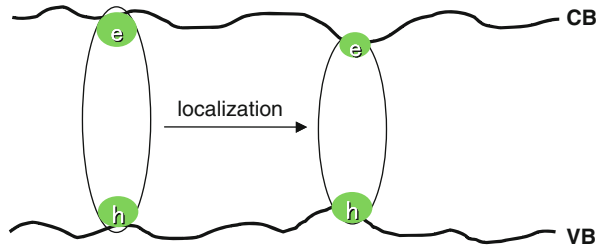
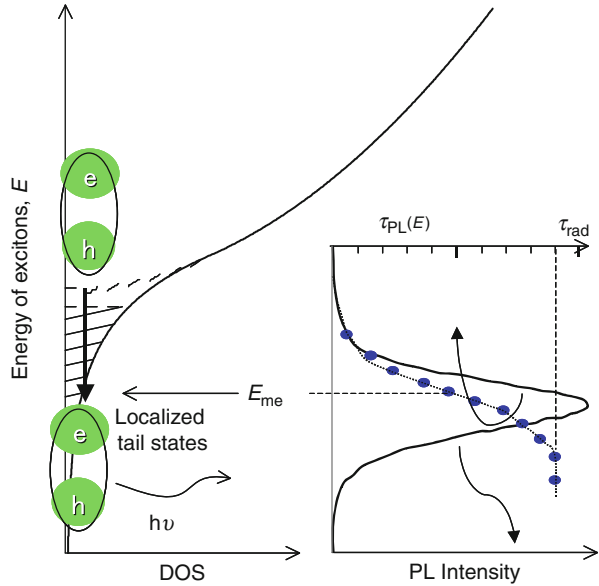
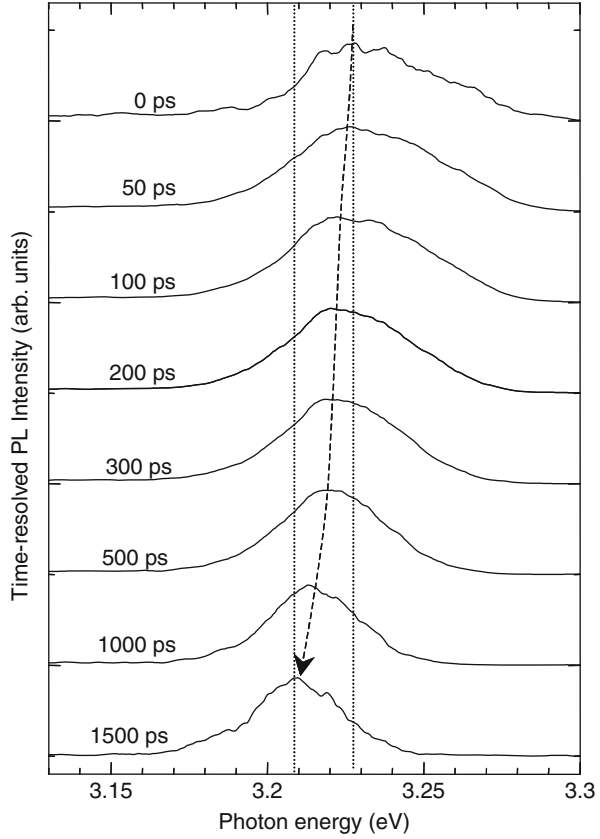


Fig. 12.6 DOS in localized band structure. PL spectrum, as well as observed PL lifetimes $[\tau_{PL}(E)]$, is plotted schematically



between absorption edge and PL peak energy may be interpreted as a result of this effect because radiative recombination takes place at localized tail states, DOS of which is very small. The recombination dynamics of localized exciton can be assessed by TRPL spectroscopy. If the pulsed photoexcitation is made at continuum energy levels, TRPL peak energies make red shift with increasing monitored time after excitation, so that PL decay time depends on monitored photon energy with a function of $\tau(E)$. This is because exciton transition is due not only to radiative and/or nonradiative recombination processes but also to transfer process to the localized levels distributed to lower energy side [76]. If the density of localized states is approximated as single exponential tail with $g_E = \exp(-E/E_0)$ using parameters for the localization depth as E_0 , and if radiative recombination lifetime (τ_{rad}) is constant within the emission band neglecting nonradiative recombination processes, it is possible to estimate $\tau(E)$ by fitting the experimental data with the theoretical equation [76], so that the density of excitons is expressed as functions of energy (E) and time (t) after pulsed excitation with $n(E, t)$

Fig. 12.7 TRPL spectra of a 0.1- μm -thick $\text{In}_{0.08}\text{Ga}_{0.92}\text{N}$ single epilayer taken at various time delays (0–1,500 ps) after pulsed photoexcitation at 24 K



$$\tau(E) = \frac{\tau_{\text{rad}}}{1 + \exp\{(E - E_{\text{me}})/E_0\}}, \quad (12.10)$$

$$n(E, t) = n_0 \exp\{-t/\tau(E)\}, \quad (12.11)$$

where E_{me} shows characteristic energy analogous to mobility edge. Typical examples of TRPL spectra taken at a 0.1- μm -thick $\text{In}_{0.08}\text{Ga}_{0.92}\text{N}$ single epilayer at 24 K are shown in Figs. 12.7 and 12.8, where localization dynamics induced by compositional fluctuation have been revealed [77]. Such characteristics have been observed in wide-bandgap ternary alloys, for example, in $\text{CdS}_x\text{Se}_{1-x}$ [78] and $\text{Zn}_x\text{Cd}_{1-x}\text{S}$ [79]. However, one has to be careful in interpreting the recombination mechanism in $\text{In}_x\text{Ga}_{1-x}\text{N}/\text{GaN}$ QW structures by means of TRPL because such localization-like behavior can also be contributed from the QCSE.

As shown in Fig. 12.9, electron and hole wavefunctions in $\text{In}_x\text{Ga}_{1-x}\text{N}$ wells are spatially separated to opposite direction due to piezoelectric field as described in the previous section [27, 27–30]. This leads not only to the reduction of recombination probability of electrons and holes but also to the QCSE, where transition energy

Fig. 12.8 Time-integrated PL (TIPL) spectrum and the PL decay times [$\tau(E)$] plotted as a function of monitored photon energies taken at a 0.1- μm -thick $\text{In}_{0.08}\text{Ga}_{0.92}\text{N}$ single epilayer at 24 K. The best fitting of $\tau(E)$ was made using values of $\tau_{\text{rad}} = 440$ ps, $E_0 = 21$ meV, and $E_{\text{me}} = 3.242$ eV

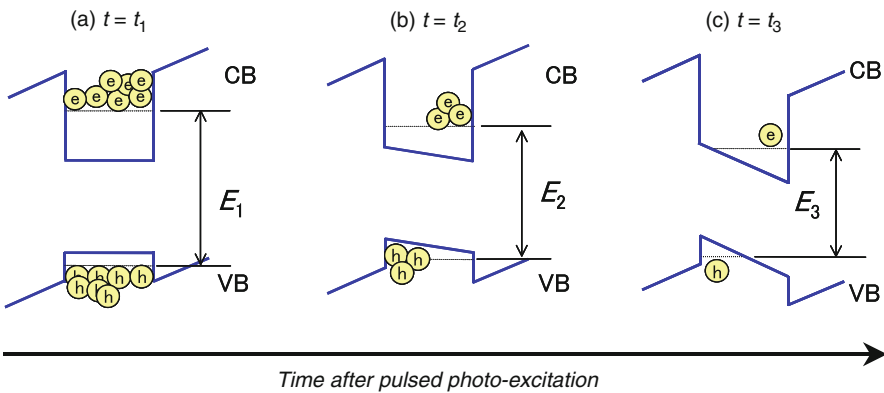
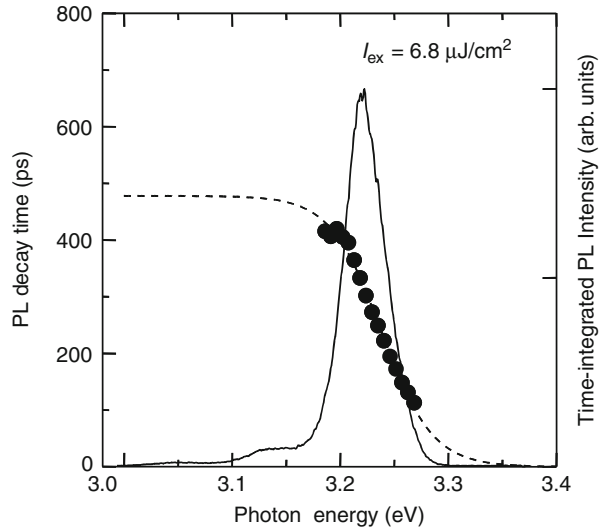


Fig. 12.9 Radiative recombination in a quantum well under piezoelectric field. Just after pulsed excitation [(a) $t = t_1$], screening of the field is significant due to large amount of photogenerated carriers. With increasing time, the effect of screening becomes less dominant in accordance with the reduction of carrier density, so that transition energy as well as recombination probability is decreased

is red-shifted compared to the case of flat band with zero internal electric field. Since the electric field is screened by carriers either by photoexcitation or by electrical injection, $\text{In}_x\text{Ga}_{1-x}\text{N}$ -based LEDs show blue shift of emission energy with increasing injection current density. This effect becomes significant for wider well thicknesses and for higher In mole fractions (x -value). PL lifetime also shows large well dependence where it varies from sub-ns to more than μs if the well width is increased from 2 to 7 nm. Consequently, PL peak makes red shift and PL lifetime increases with increasing time after excitation in accordance with the reduction of

carriers contributing to the screening. It should be noted that the typical well width of $\text{In}_x\text{Ga}_{1-x}\text{N}$ -based LEDs and LDs is as small as 2–3 nm in order to avoid such QCSE as small as possible.

12.3.2 Photo-Induced Change of Optical Density Induced by Two Major Effects

Two effects, internal electric fields versus potential fluctuation, can be separated if the photo-induced change of absorption spectra is characterized by means of pump and probe spectroscopy, by which the transmission spectrum of the probe beam detected in the presence of the pump beam ($T + \Delta T$) is compared with the spectrum without pump beam (T) [34–37]. Photo-induced change of the transmission [$\Delta T(\omega, I_{\text{ex}}, t_d)$] depends not only on the frequency of incident photon (ω) but also on both the photo-pumping energy densities (I_{ex}) and time delay between pump and probe beams (t_d) as shown in Fig. 12.10. The photo-induced change of optical density [$\Delta OD(\omega, I_{\text{ex}}, t_d)$] is given by the following equation:

$$\Delta OD = \log \left(\frac{T}{T + \Delta T} \right) = \Delta \alpha d \times 0.434, \quad (12.12)$$

where $\Delta \alpha(\omega, I_{\text{ex}}, t_d)$ is the photo-induced change of absorption coefficient and d is the total thickness of absorbing layer. Schematic of band structures in $\text{In}_x\text{Ga}_{1-x}\text{N}$ QW under (a) FKE and QCSE and (b) localization effect is shown in Fig. 12.11. Since both effects contribute to the broadening of absorption edge, it is difficult to separate two effects by linear absorption spectra. However, the modification of such optical density due to injected carriers is different between two cases. If the time domain of about 1 ps to ns order is concerned, internal electric field is reduced by the screening effect in case of (a), so the optical density (OD) spectra corresponding to absorption spectra (as well as to DOS) become sharp, so the feature of ΔOD is as shown in the figure, where the positive signal is sandwiched between two negative

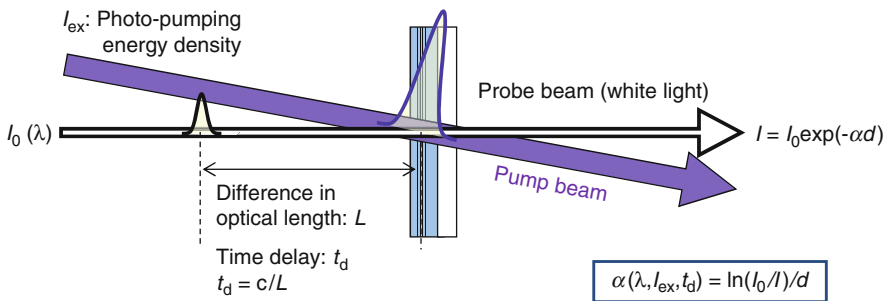
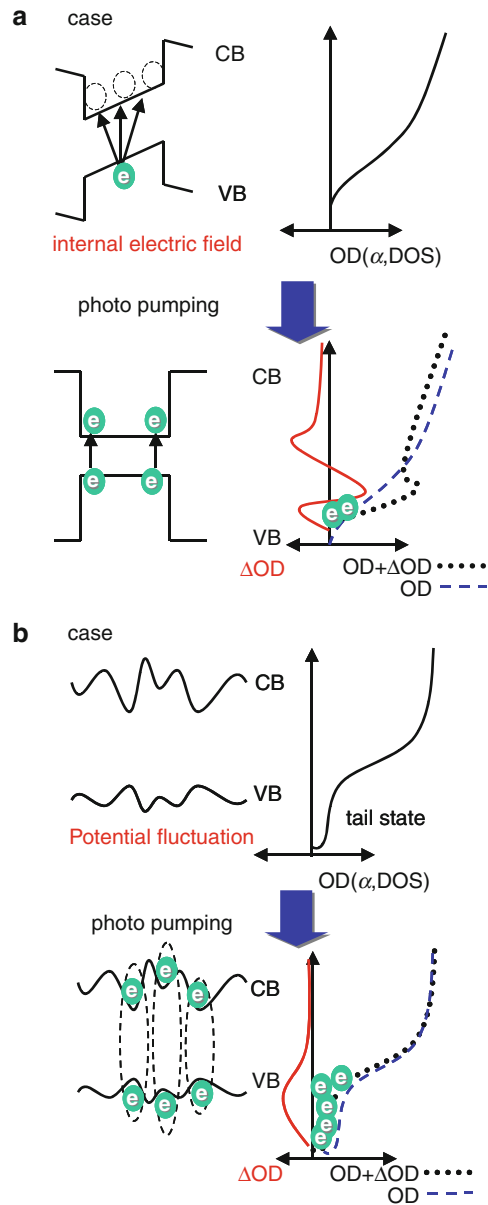


Fig. 12.10 Optical configuration in pump and probe spectroscopy. Time difference between two pulses can be controlled by changing the optical length difference

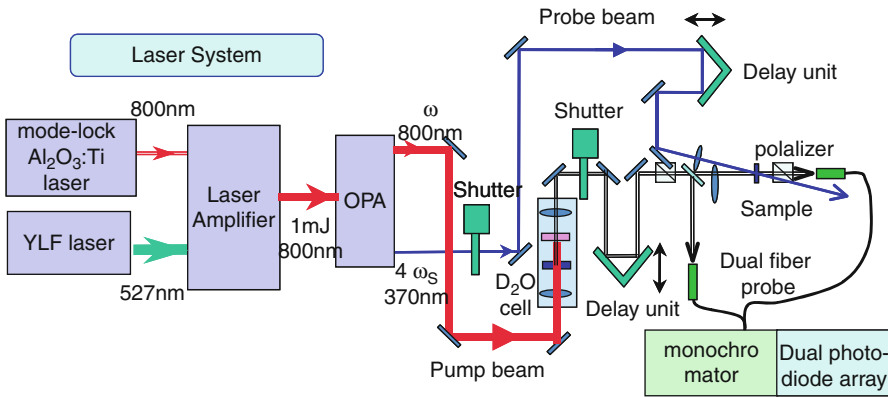
Fig. 12.11 Schematic band structure and corresponding OD and ΔOD spectra in $\text{In}_x\text{Ga}_{1-x}\text{N}$ QW under (a) FKE and QCSE effects and (b) localization effect



signals. However, in case of (b), only the negative signal is observed in ΔOD due to the band filling of localized tail states. Motivated by this idea, the dynamics of ΔOD was estimated by employing white-light pump and probe spectroscopy to $\text{In}_x\text{Ga}_{1-x}\text{N}/\text{GaN}$ multiple quantum well (MQW) structures. The effects of (a) the screening and (b) the band filling are the major origins of nonlinear optical

Table 12.1 Various types of optical nonlinearities dependent on time domains by classifying positive or negative polarity in ΔOD

Time domain	Origin of nonlinearity	Positive or negative polarity of ΔOD
0–2 ps	Optical Stark effect	$\Delta OD > 0$
	Nonthermal distribution of carriers	$\Delta OD < 0$
	Energy relaxation	$\Delta OD < 0$
1–10 ps	Optical gain	$\Delta OD < 0$ $OD + \Delta OD < 0$
1 ps–ns order	Band filling of localized states	$\Delta OD < 0$
	Screening of internal electric fields	$\Delta OD > 0$
ns order– μs order	Screening by trapped carriers	$\Delta OD > 0$
	Thermal effect	$\Delta OD > 0$

**Fig. 12.12** Optical apparatus used for the pump and probe spectroscopy

density in this time domain, the applicable duration period of which is determined by the carrier recombination times. Optical Stark effect, nonthermal distribution of carriers, energy relaxation, and optical gain are the possible origins of optical nonlinearity in the faster time domain, while the persistent trapped carriers or thermal effects in the slower one can contribute to ΔOD as shown in Table 12.1.

12.4 Pump and Probe Spectroscopy on $\text{In}_x\text{Ga}_{1-x}\text{N}$ Thin Layers and Quantum Wells

The pump and probe spectroscopy depicted in Figs. 12.12 and 12.13 was performed for the measurement of temporal behavior of differential absorption spectra. The pump beam with wavelength 370 nm, pulse width 150 fs, and repetition rate; 1 kHz was formed by passing the output beam from regenerative amplifier (RGA) to optical parametric amplifier (OPA). The white light used for the probe beam was

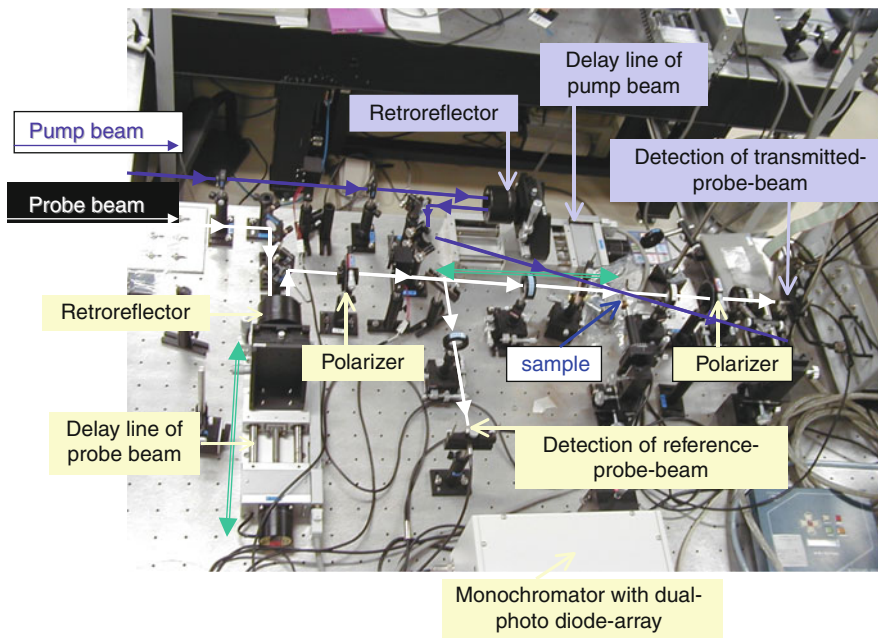
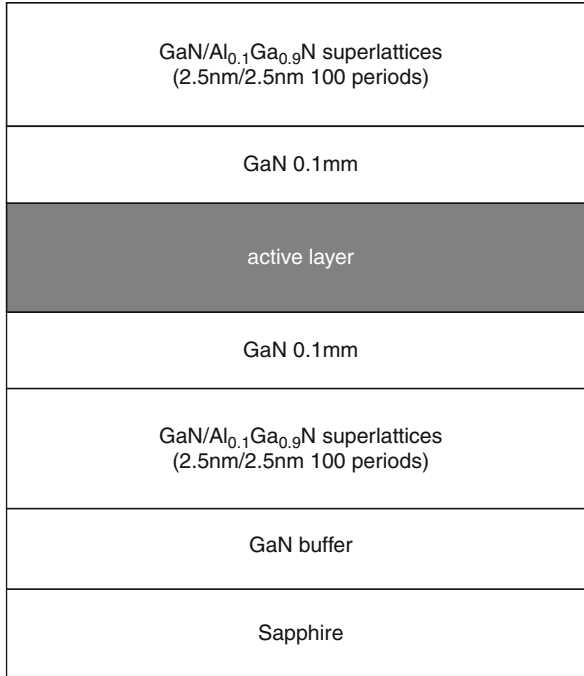


Fig. 12.13 Picture of beam path and optical component for the pump and probe spectroscopy

generated by focusing the part of output beam from the RGA on a D_2O cell. The pulse width of both pump and probe beam, was 150 fs. Delay time of the probe beam with respect to the pump beam was tuned by changing the position of retroreflector which could be controlled by the pulse stage. Since the minimum difference in optical path was $2\ \mu\text{m}$, the time resolution down to 6.7 fs was achieved. In order to detect the probe beam with spatially uniform carrier distribution in the sample, the focus size of the pump beam ($500\ \mu\text{m}$ in diameter) was set so as to be much larger than that of the probe beam ($200\ \mu\text{m}$ in diameter). Furthermore, the probe beam was perpendicularly polarized with respect to the pump beam, and the transmitted probe beam polarized in this direction was detected to avoid the scattered component of the pump beam. Both pump and probe beams were detected by a dual photodiode array in conjunction with a 25-cm monochromator. The four types of samples of $\text{In}_x\text{Ga}_{1-x}\text{N}$ -based quantum structures used in this study are shown in Fig. 12.14. They are composed of, respectively, (a) an $\text{In}_{0.1}\text{Ga}_{0.9}\text{N}$ single layer (30 nm), (b) $\text{In}_{0.1}\text{Ga}_{0.9}\text{N}/\text{GaN}$ (10/10 nm) MQWs with three periods, (c) $\text{In}_{0.1}\text{Ga}_{0.9}\text{N}/\text{GaN}$ (5/10 nm) MQWs with six periods, and (d) $\text{In}_{0.1}\text{Ga}_{0.9}\text{N}/\text{GaN}$ (3/10 nm) MQWs with ten periods. Although the active layers in each sample differ, the total thickness of the InGaN active layers in each sample is 30 nm. All the active layers are sandwiched between GaN layers ($0.1\ \mu\text{m}$) and $\text{Al}_{0.1}\text{Ga}_{0.9}\text{N}/\text{GaN}$ (2.5/2.5 nm) superlattices with 100 periods. All layers are grown on GaN buffer layers on sapphire substrates under an undoped condition. Since the PL lifetime of

active layer

- a. $\text{In}_{0.1}\text{Ga}_{0.9}\text{N}$ (30nm)
- b. $\text{In}_{0.1}\text{Ga}_{0.9}\text{N}/\text{GaN}$ (10nm/10nm x 3)
- c. $\text{In}_{0.1}\text{Ga}_{0.9}\text{N}/\text{GaN}$ (5nm/10nm x 6)
- d. $\text{In}_{0.1}\text{Ga}_{0.9}\text{N}/\text{GaN}$ (3nm/10nm x 10)

Fig. 12.14 Sample structures for pump and probe spectroscopy consisting of four types of samples having different well widths: 30, 10, 5, and 3 nm. The total thickness of all $\text{In}_x\text{Ga}_{1-x}\text{N}$ active layers was set to 30 nm in order to make the OD of each sample to comparable value

stimulated emission is much shorter than that of spontaneous one, it was confirmed by means of TRPL that the appearance of stimulated emission at about 3.1 eV if photoexcitation energy density (I_{ex}) is above about $10 \mu\text{J}/\text{cm}^2$ for all samples at 10 K. Therefore, the threshold carrier density can be estimated to be on the order of 10^{18}cm^{-3} .

Figure 12.15 shows the ΔOD spectra taken at the sample of (a) 30-nm-thick $\text{In}_{0.1}\text{Ga}_{0.9}\text{N}$ single layer at 10 K as a function of time after pumping at 370 nm (3.350 eV) under (a) $I_{\text{ex}} = 800 \mu\text{J}/\text{cm}^2$ and under (b) $I_{\text{ex}} = 8 \mu\text{J}/\text{cm}^2$. The photo-pumping energy is located below the absorption edge of GaN barrier layers, so that the selective photoexcitation to the active layer was made. OD spectrum taken under weak photoexcitation, as well as PL spectra under both the same of ΔOD spectra ($I_{\text{ex}} = 800 \mu\text{J}/\text{cm}^2$; stimulated emission, $I_{\text{ex}} = 8 \mu\text{J}/\text{cm}^2$; spontaneous emission) and

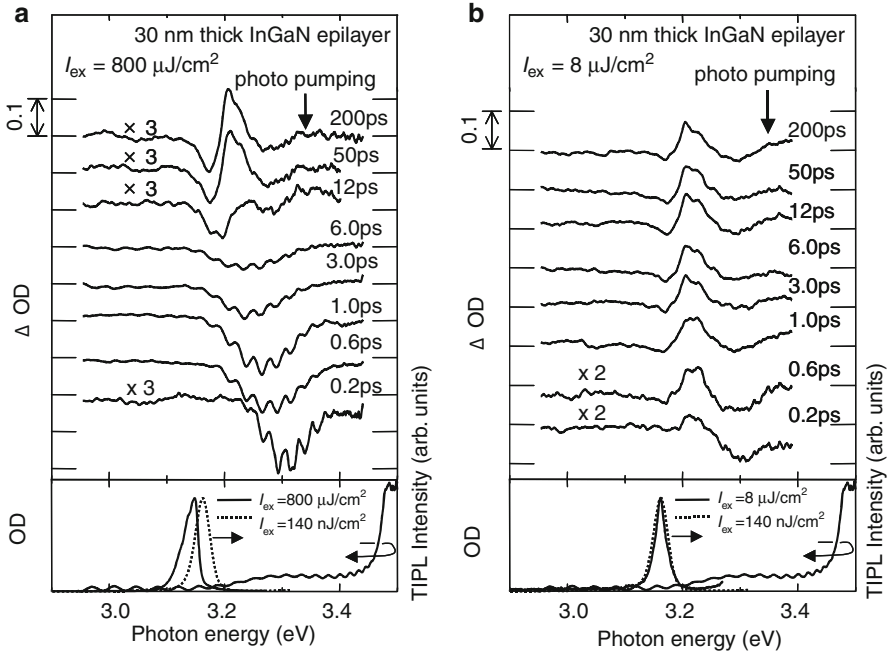


Fig. 12.15 Variation of ΔOD spectra taken at 30-nm-thick $\text{In}_{0.1}\text{Ga}_{0.9}\text{N}$ epilayer as a function of time after pumping at 3.350 eV (370 nm) under (a) $I_{\text{ex}} = 800 \mu\text{J}/\text{cm}^2$ and under (b) $I_{\text{ex}} = 8 \mu\text{J}/\text{cm}^2$. The OD spectrum under weak photo-excitation, as well as the TIPL spectra under the same and weak excitation conditions, is shown at the bottom of each plot

weak ($I_{\text{ex}} = 140 \text{ nJ}/\text{cm}^2$, spontaneous emission) excitation conditions, is shown for references. In case of (a) $I_{\text{ex}} = 800 \mu\text{J}/\text{cm}^2$, the carrier density just after the excitation is estimated to be about $1 \times 10^{20} \text{ cm}^{-3}$; negative signal appears at the initiation of time in the whole observed energies. However, positive signal appears at about 3.2 eV after about 12 ps. These phenomena indicate that the bleaching due to high-density carriers dominates the spectra initially, but the carrier density is rapidly decreased due to the process of stimulated emission and photo-induced screening of internal electric field plays major role on the photo-induced enhancement of OD . In fact, only this positive spectral feature is observed in the whole time range if the pumping energy density is as low as (b) $I_{\text{ex}} = 8 \mu\text{J}/\text{cm}^2$ where no stimulated emission was observed. It is noted that the same mechanism is also observed in a GaN epilayer, where photo-induced enhancement was observed clearly in excitonic absorption [34].

ΔOD spectra taken at samples of (b) $\text{In}_{0.1}\text{Ga}_{0.9}\text{N}/\text{GaN}$ (10/10 nm) MQWs and of (c) $\text{In}_{0.1}\text{Ga}_{0.9}\text{N}/\text{GaN}$ (5/10 nm) MQWs at 10 K under $I_{\text{ex}} = 800 \mu\text{J}/\text{cm}^2$ are shown in Fig. 12.16. Similar results with the sample (a) were observed for the sample (b) of 10-nm-thick $\text{In}_{0.1}\text{Ga}_{0.9}\text{N}$ QW. However, the positive feature became less dominant for the sample (c) of 5-nm-thick $\text{In}_{0.1}\text{Ga}_{0.9}\text{N}$ QW.

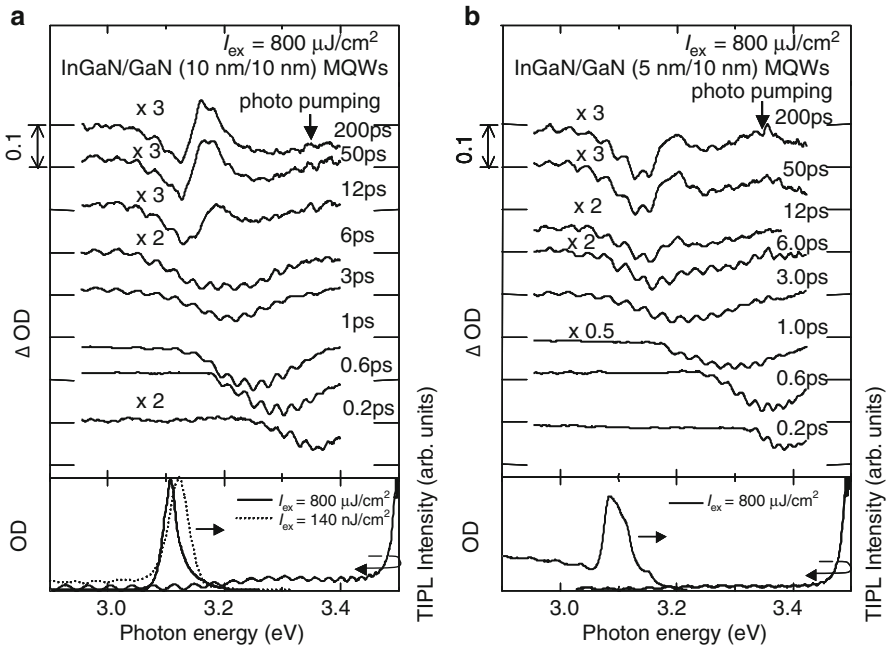


Fig. 12.16 Variation of ΔOD spectra taken at (a) $\text{In}_{0.1}\text{Ga}_{0.9}\text{N/GaN}$ (10/10 nm) MQWs [sample (b)] and (b) $\text{In}_{0.1}\text{Ga}_{0.9}\text{N/GaN}$ (5/10 nm) MQWs [sample (c)] as a function of time after pumping at 3.350 eV (370 nm) under $I_{ex} = 800 \mu\text{J}/\text{cm}^2$. The OD spectra under weak photo-excitation, as well as the TIPL spectra under the same and weak excitation conditions, are shown at the bottom of each plot. For the sample (c), the PL spectrum under the weak excitation condition was located at about 2.7 eV that is out of plotted energy range

ΔOD spectra was taken for the sample (d) $\text{In}_{0.1}\text{Ga}_{0.9}\text{N/GaN}$ (3/10 nm) MQWs (Fig. 12.17). It was found that carriers photogenerated at 3.350 eV rapidly reach to the bottom of density states within the time scale of several ps. And the important finding is that only negative signal is observed in the whole spectra indicating the importance of band-filling effect compared to the effect of piezoelectric field.

The following things were clarified, summarizing the results of the pump and probe spectroscopy. In samples (a) and (b), the screening of the internal electric field has a dominant effect on optical transitions after carrier generation. The internal electric field reduces the oscillator strength of optical transition due to QCSE and FKE. When the photogenerated carriers screen the internal electric field, excitonic absorption is restored. As a result, photo-induced enhancement of the absorption coefficient is observed. The internal electric field strength due to piezoelectric polarization was calculated to be 0.45–1.6 MV/cm using the scattered value of the piezoelectric constants [73, 75] as discussed in the previous section. In sample (d), exciton localization has a dominant effect on optical transitions. The density of localized levels is so small that the DOS is easily occupied by the photo-generated carriers. As a result, the broad negative signals of ΔOD are observed. Piezoelectric

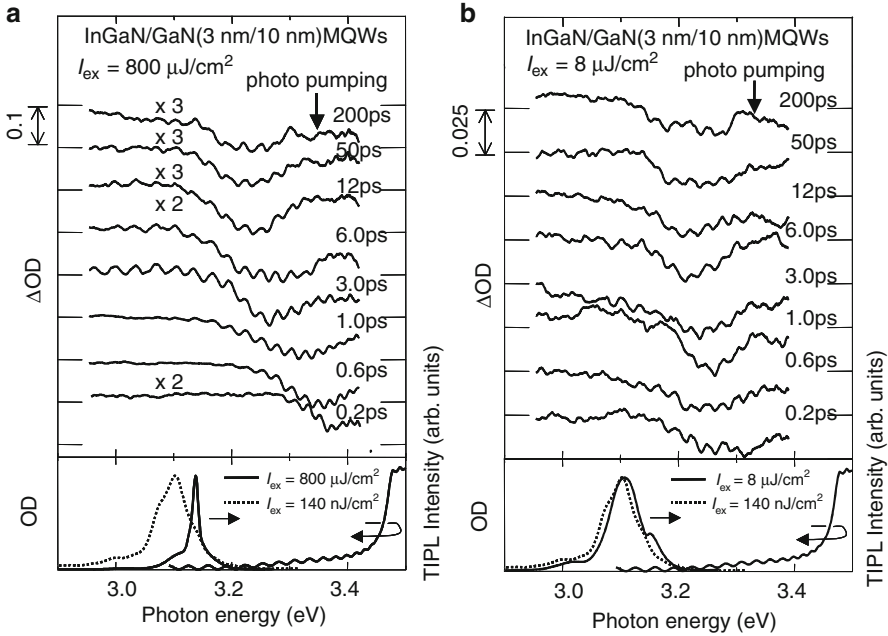


Fig. 12.17 Variation of ΔOD spectra taken at $\text{In}_{0.1}\text{Ga}_{0.9}\text{N}/\text{GaN}$ (3/10 nm) MQWs [sample (d)] as a function of time after pumping at 3.350 eV (370 nm) under (a) $I_{ex} = 800 \mu\text{J}/\text{cm}^2$ and under (b) $I_{ex} = 8 \mu\text{J}/\text{cm}^2$. The OD spectrum under weak photoexcitation, as well as the TIPL spectra under the same and weak excitation conditions, is shown at the bottom of each plot

field dominates over inhomogeneity in samples with layer thickness more than the exciton Bohr radius (3.4 nm) [80, 81]. Similar results have been observed at RT though carrier density to observe the screening of piezoelectric fields in ΔOD is reduced compared to that at low temperature, suggesting that intrinsic carriers activated by thermal energy also contribute persistently to the partial screening of piezoelectric fields.

12.5 SNOM-Luminescence Mapping Results

12.5.1 Instrumentation

The SNOM-PL detection has recently been developed as the PL mapping technique, where the optical access in near-field regime is made through the tip of optical fibers having very small aperture. Optical configurations in SNOM-PL technique are schematically illustrated in Fig. 12.18, where photo-excitation is made in near-field through optical fiber and the PL signal is detected from far-field with an objective lens in (a) illumination mode (*I* mode); the optical accesses for excitation and detection are opposite to (a) in (b) collection mode (*C* mode), while both

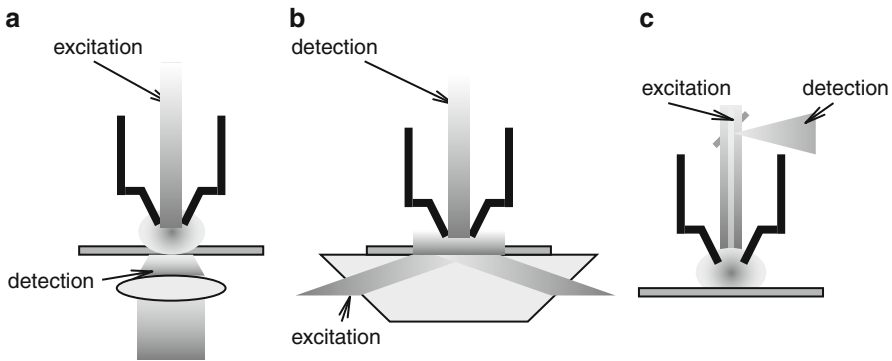


Fig. 12.18 Three types of optical configuration used for SNOM-PL measurements: (a) *I* mode, (b) *C* mode, and (c) *I-C* mode

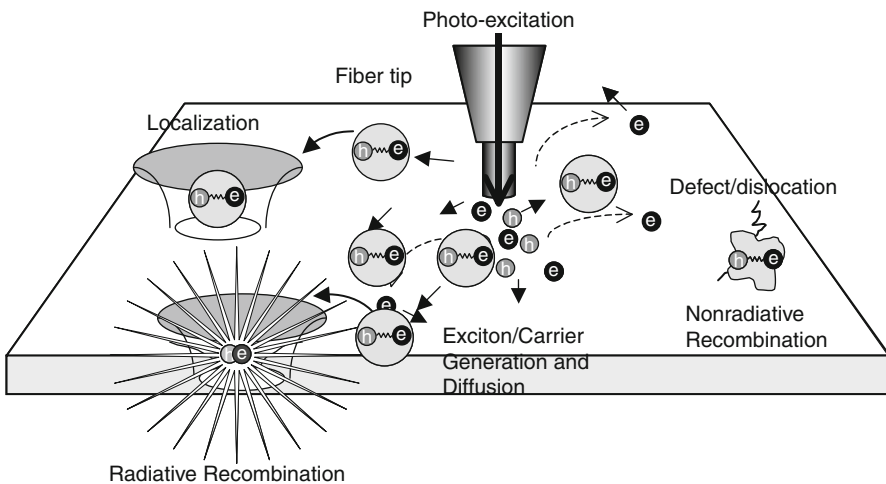


Fig. 12.19 Schematic of exciton/carrier generation induced by local photoexcitation by fiber tip and their recombination dynamics based on diffusion, localization, radiative, and nonradiative processes

excitation and detection are in near-field in (c) illumination-collection mode (*I-C* mode). In Fig. 12.19, the dynamics of carriers/excitons are schematically shown in $\text{In}_x\text{Ga}_{1-x}\text{N}$ -based layers. Even if they are photogenerated at very small area by the tip of optical fiber, some of them diffuse out of the area and captured by radiative centers or by nonradiative recombination centers. The most of SNOM results for the assessment of $\text{In}_x\text{Ga}_{1-x}\text{N}$ have initially been performed in the *I* mode with an aperture diameter of optical fiber of 100 nm to a few hundred nm [44–48, 51]. However, it is not possible by this mode to determine the true size of localization centers because the spatial resolution is affected by the diffusion process before radiative recombination. This problem can be overcome by means of *I-C* mode,

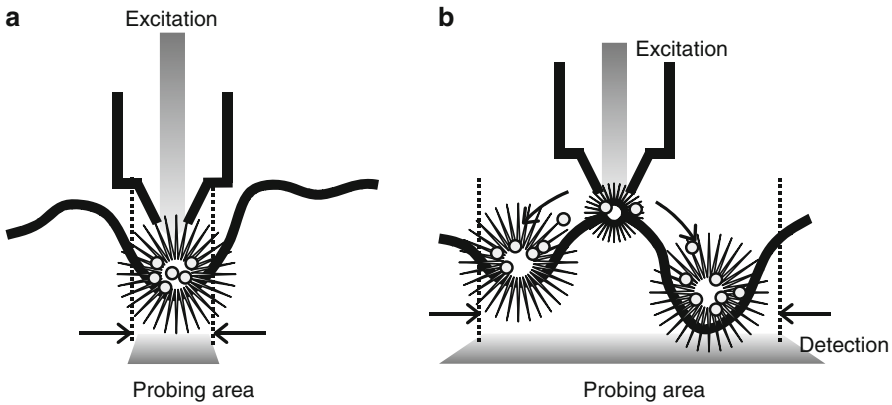


Fig. 12.20 SNOM-PL detection with (a) *I-C* mode and (b) *I* mode under potential fluctuation. Spatial resolution is not affected by the carrier/exciton diffusion for (a) *I-C* mode

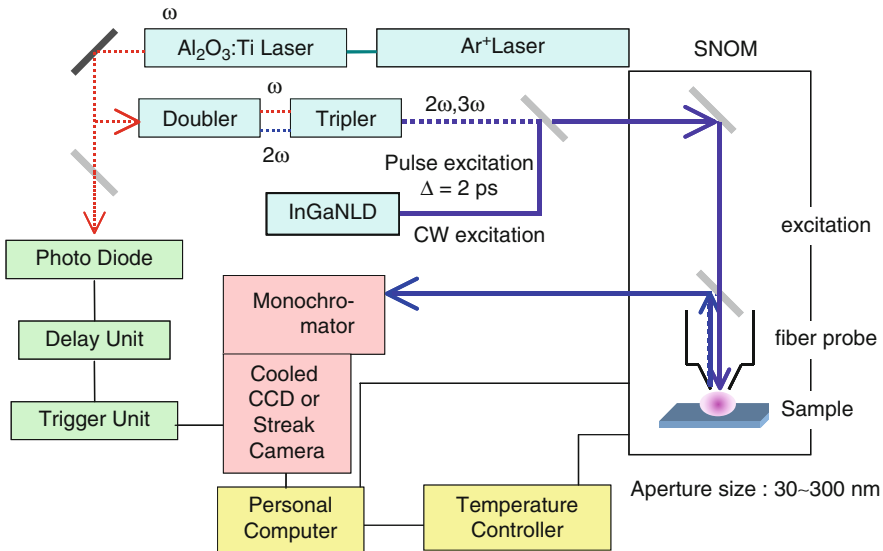


Fig. 12.21 Schematic of the SNOM system composed of SNOM head, excitation laser, and detection parts, where PL mapping can be performed in both CW and time-resolved modes

where the resolution is solely limited by the diameter of aperture formed at the fiber tip. The difference between *I* mode and *I-C* mode in detecting PL can be understood by taking a look at probing areas described in Fig. 12.20.

The SNOM measurements were performed with NFS-300 near-field spectrometer developed at JASCO Corp. (Figs. 12.21 and 12.22) that is capable of PL mapping with scanning near-field optical microscopy under *I-C* mode. Two types of fibers

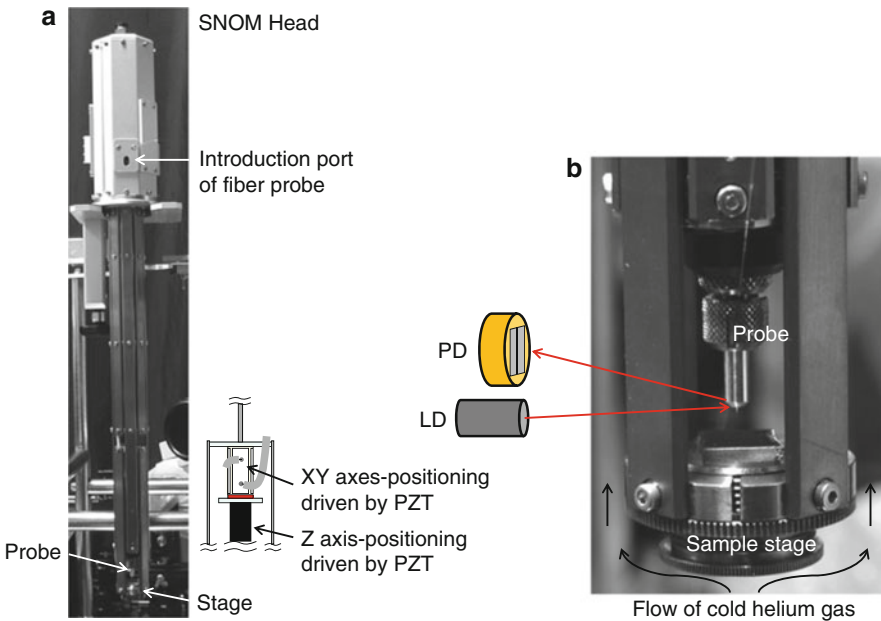
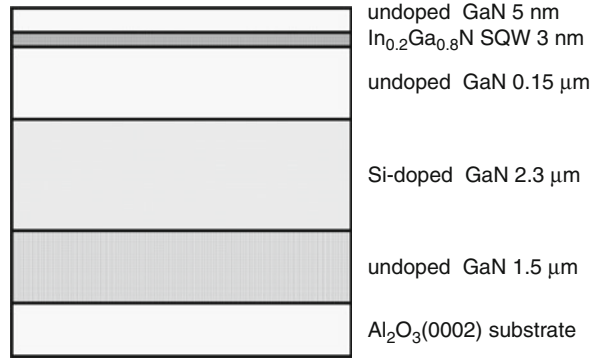


Fig. 12.22 (a) SNOM head (whole view). The position of sample stage is controlled by PZT in xyz directions. (b) The closed view of the sample stage and the probe. The separation between the sample and the fiber tip is controlled by monitoring the friction force using the optical configuration in the figure

were used in this study: double-tapered Ge-doped- SiO_2 cores with aperture diameter in the range from 30 to 150 nm and single-tapered pure- SiO_2 cores with aperture diameter of 300 nm. A double-tapered structure is fabricated by a multistep etching technique using hydrofluoric-buffered solution, by which high efficiency of light transmission is achieved compared to that in conventional single-tapered probes. However, one drawback of this structure is the fluorescence of Ge-doped- SiO_2 core that sometimes buries the PL from the sample in the background level if the signal intensity of PL is not strong enough. Therefore, single-tapered pure- SiO_2 fibers fabricated were used for detecting TRPL, where long exposure time was enabled by the elimination of fluorescence background. Apertures of fiber probes were obtained by applying the mechanical impact on a suitable surface after evaporating Au at the apex. The sample-probe separation was controlled by detecting the amplitude of dithered probe. The amplitude of this oscillation was less than 1 nm at the first-order resonance frequency of the probe. This amplitude was fed back to control the height of the sample PZT [$\text{Pb}(\text{Zr},\text{Ti})\text{O}_3$] stage. As a result, the sample-probe separation was regulated to be 10 nm. The cooling of the samples was performed by flowing cool He gas. The stable measurement was achieved by flowing an appropriated flux of He gas from the bottom to the top parts of the cryostat. An $\text{In}_x\text{Ga}_{1-x}\text{N}$ -based laser

Fig. 12.23

$\text{In}_{0.2}\text{Ga}_{0.8}\text{N}$ -SQW structure used for the SNOM measurement



diode emitting at 400 nm (developed at Nichia Corp.) was used as the excitation source with continuous wave (CW) condition. An optical power of 1 mW was coupled to the probe, and about 2 μW was used to illuminate the samples through the probes of both Ge-doped- SiO_2 fibers with aperture diameter of 100 nm and pure- SiO_2 cores with aperture diameter of 300 nm, while about 0.1 μW was used through Ge-doped- SiO_2 fibers with aperture diameter of 30 nm. PL signal was collected by the probe and was introduced into a monochromator in conjunction with a cooled charge-coupled device (CCD) detector (Roper Scientific, Spec-10:400B/LN). For TRPL measurement, the frequency-doubled mode-locked $\text{Al}_2\text{O}_3:\text{Ti}$ laser emitting at 400 nm with the pulse width of 2 ps was used as an excitation source. A streak camera (Hamamatsu Photonics, C5680) was used as a detector. It is noted that the selective photoexcitation to the $\text{In}_x\text{Ga}_{1-x}\text{N}$ active layer was achieved for both measurements. Since the cutoff wavelength of pure- SiO_2 fiber is about 1.3 μm , the beam propagation properties were assessed by measuring pulse width and spectra before and after passing the fiber of 1 m length. It was found that the broadening of the pulse width after transmission is as small as about 10 ps keeping the same wavelength. Therefore, the pure- SiO_2 fiber used in this study is capable enough for employing TR-SNOM-PL measurement with time-resolution of about 10 ps.

12.5.2 SNOM-PL Mapping at Low Temperature under Illumination-Collection Mode

The sample (shown in Fig. 12.23) is grown on sapphire (0002) substrate by metalorganic chemical vapor deposition (MOCVD) and is composed of a 1.5- μm -thick undoped-GaN, a 2.3- μm -thick n-type GaN:Si, a 3-nm-thick $\text{In}_x\text{Ga}_{1-x}\text{N}$ -SQW active layer ($x =$ about 0.2), and a 5-nm-thick undoped GaN layer. Macroscopic PL peak is located at about 480 nm at 18 K as shown in Fig. 12.24a. LO-phonon side bands are associated on the low-energy side of the main peak. Temperature dependence of integrated PL intensity plotted in Fig. 12.24b shows that the internal

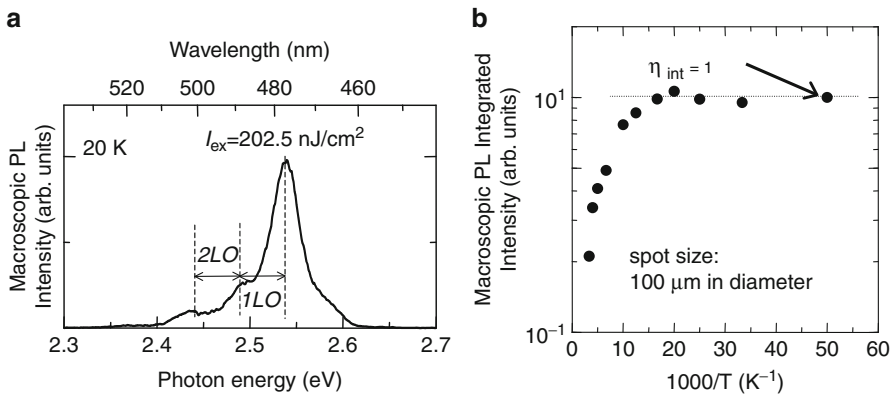


Fig. 12.24 (a) Macroscopic PL of the sample at 18 K taken with the spot diameter of 100 μm . (b) Macroscopic integrated PL intensity plotted as a function of inverse of temperature

quantum efficiency (η_{int}) is nearly unity below 50 K because of the suppression of nonradiative recombination process and that it is decreased to about 20% at RT.

Figure 12.25 shows the PL mapping plotted with PL peak intensity (a) as well as with PL peak wavelength (b) at 18 K under photoexcitation power density of 100 W/cm^2 . The scanning was made in the area of $4 \times 4 \mu\text{m}^2$ square with an interval of 100 nm using a 150-nm aperture fiber probe in I - C mode. It was found that the relative PL intensity fluctuates from 1 to 6 and that the PL peak wavelength is distributed from 470 to 490 nm, both of which consist of island-like structures within the range approximately 0.1–1 μm .

Clear correlation was observed between PL intensity and wavelength as shown in Fig. 12.26, where the areas of strong PL intensity correspond to those of long PL wavelength (low PL peak energy). Temperature dependence of macroscopic PL measurements reveals that the η_{int} is nearly unity (0.9–1.0) below 100 K. Moreover, atomic force microscopy (AFM) assessed in-situ during the SNOM measurements shows that the root mean square of surface unevenness is as small as 5.1 nm within the scanning area of $4 \mu\text{m}$ square. The PL peak intensity map (Fig. 12.25a) shows a relative intensity variation of approximately 1–6, corresponding to the η_{int} variation of 0.17–1.00 if the maximum is 1.00. If nonradiative recombination alone explained the spatial variation, then the spatially averaged quantum efficiency is estimated to be 0.41 taking into account the area of each PL intensity. This value is much smaller than unity that is the macroscopic η_{int} as mention above. Therefore, nonradiative recombination alone cannot explain the results; diffusion of carriers from the low-intensity to the high-intensity regions must occur.

In order to confirm such mechanism, TRPL was employed under SNOM configuration using a pure- SiO_2 fiber probe with a 300-nm aperture. Figure 12.27a shows the PL image mapped with the PL intensity taken under 100 W/cm^2 with CW condition. TRPL was detected across the white bar drawn in the figure with

Fig. 12.25 SNOM-PL image of an $\text{In}_{0.2}\text{Ga}_{0.8}\text{N}$ -SQW structure mapped with (a) PL peak intensity and with (b) peak wavelength at 18 K under photoexcitation power density of 100 W/cm^2 using a 150-nm aperture fiber probe

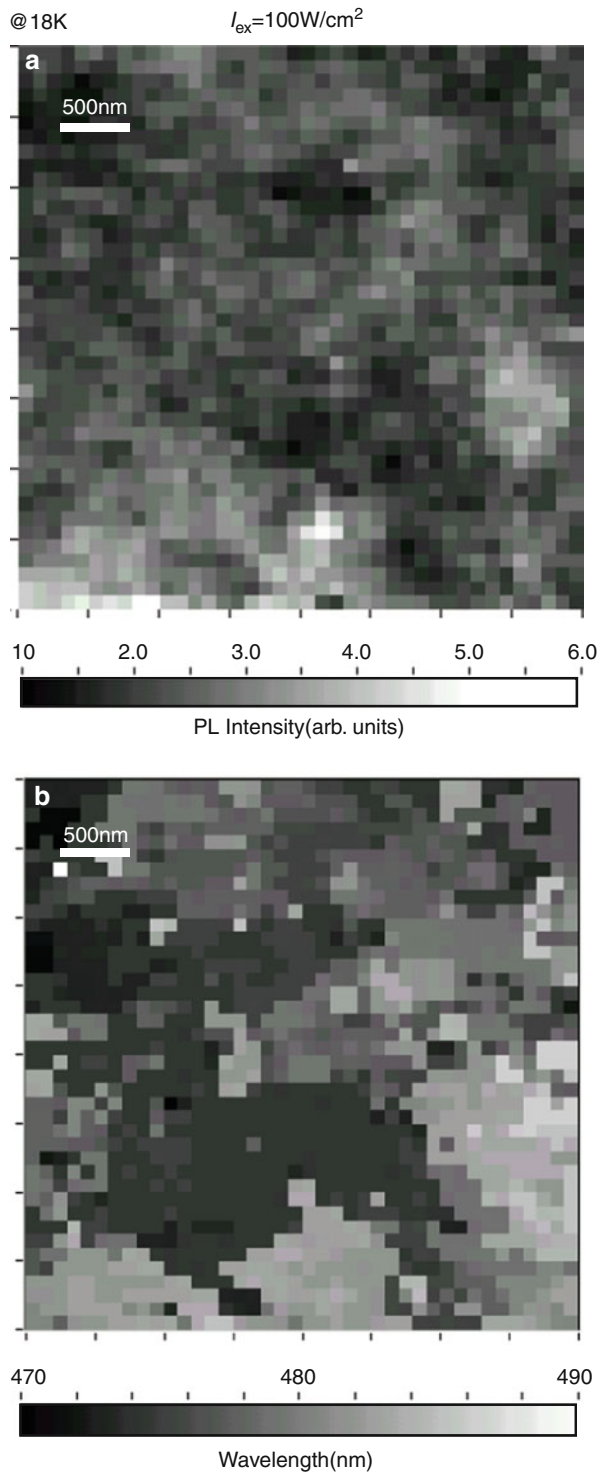
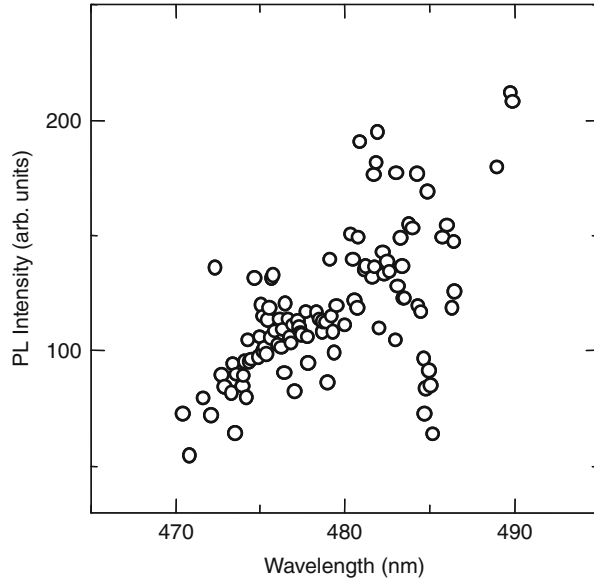


Fig. 12.26 PL peak intensity plotted as a function of PL peak wavelength from the data of SNOM-PL mapping in Fig. 12.25

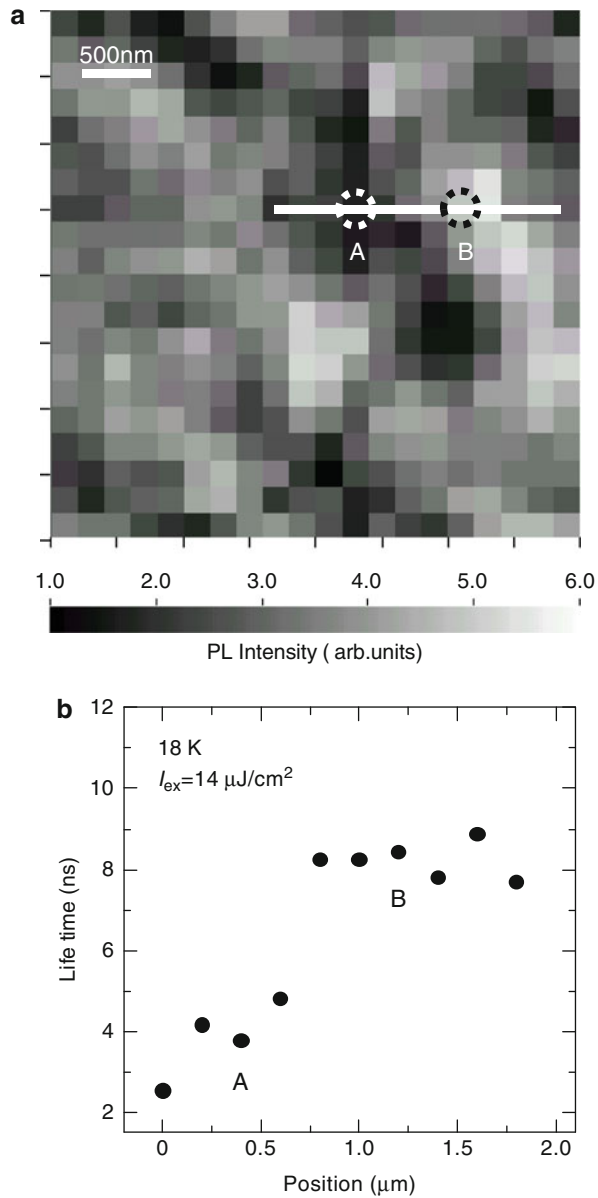


an interval of 180 nm. The photoexcitation energy density is $14 \mu\text{J}/\text{cm}^2$ in this case. PL lifetimes of the emission peak are plotted as a function of position as shown in Fig. 12.27b. It was found that the short lifetimes (2.5–4.8 ns) rapidly jump to the longer ones (7.6–9.0 ns) at about $0.75 \mu\text{m}$. This position corresponds to the boundary where PL intensity changes from approximately 2.5 to 5.0. The PL lifetime (τ_{PL}) is expressed by the equation by

$$\frac{1}{\tau_{\text{PL}}} = \frac{1}{\tau_{\text{rad}}} + \frac{1}{\tau_{\text{nonrad}}} + \frac{1}{\tau_{\text{trans}}}, \quad (12.13)$$

where τ_{rad} and τ_{nonrad} are radiative and nonradiative lifetimes, respectively, and τ_{trans} represents the transfer lifetime to lower lying energy levels arising from the localization phenomena. As mentioned above, the term of $1/\tau_{\text{nonrad}}$ can be neglected at this temperature. Therefore, the shorter lifetimes at weak PL regions are contributed from the transfer lifetimes. This can be interpreted because PL peak energies of such regions are higher than other surrounding regions. Figure 12.28a, b shows the Time-integrated PL (TIPL) as well as TRPL spectra as a function of time after pulsed excitation monitored at positions A and B, respectively. TIPL spectrum in Fig. 12.28a is composed of two emission bands peaking at 458 and 464 nm. The main PL peak at 458 nm decays with the lifetime of 3.8 ns, while the longer peak at 464 nm does with 6.4 ns. However, for Fig. 12.28b, the PL band is composed of single emission peak associated with one LO-phonon replica and decays with 8.4 ns. Two emission bands with different PL lifetimes in Fig. 12.28a are probably because the two regions having different energy levels are included

Fig. 12.27 (a) SNOM-PL peak intensity mapping taken with a pure-SiO₂ fiber with a 300-nm aperture at 18 K. (b) PL lifetimes plotted as a function of the position along the bar shown in (a)



within the probing aperture, and the excitons and/or carriers generated at the shorter wavelength region transfer to the longer wavelength regions distributed within or out of the aperture. This model is schematically illustrated in Fig. 12.29.

SNOM-PL spectra were taken at various excitation power density [(a) 100 W/cm², (b) 1 kW/cm², and (c) 10 kW/cm²] under CW excitation condition

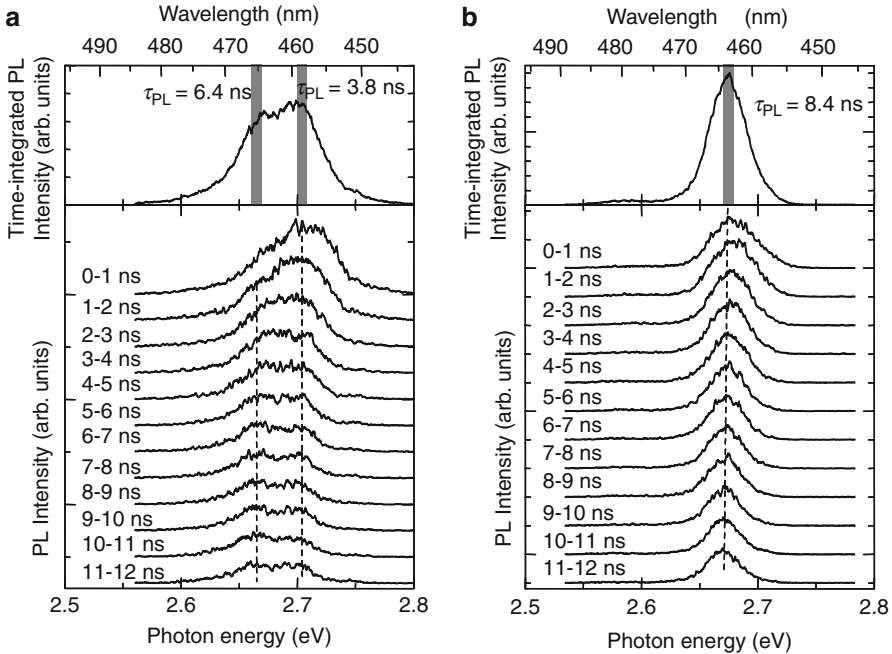
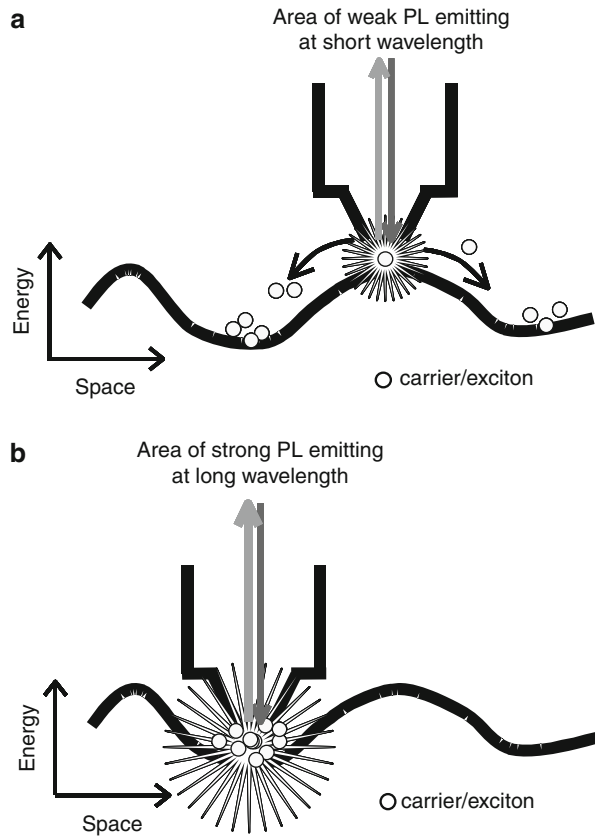


Fig. 12.28 TIPL and TRPL spectra as a function of time after pulsed excitation measured at position A (a) and position B (b) at 18 K

as shown in Fig. 12.30. Each monitored position made the shift toward shorter wavelength with increasing excitation power density. However, such shift is not uniformly distributed as revealed from the mapping of wavelength shifts between $I_{\text{ex}} = 100 \text{ W/cm}^2$ and 1 kW/cm^2 (Fig. 12.30d), as well as between $I_{\text{ex}} = 1.0 \text{ kW/cm}^2$ and 10 kW/cm^2 (Fig. 12.30e). Figure 12.31 shows the PL peak energies plotted as a function of excitation power for two data points, namely, for the weak intensity region [averaged 100 data point for smaller value than 25% of PL maximum intensity (I_{max})] and for the strong intensity regions (averaged 100 data point for larger value than 75% of I_{max}). The PL peak energy increases with increasing excitation power in both the strong intensity region and the weak intensity region. However, the blue shift is larger in the strong intensity region than in the weak intensity region for the same excitation intensity. These results can be explained by assuming that the density of states of localized levels decreases with increasing localization depth. Hence, more filling of the exciton and/or carrier band occurs in the strong intensity region than in the weak intensity region for the same excitation intensity. An additional factor that probably contributes to the blue shift in both regions is screening of piezoelectric field induced by the photogenerated excitons and/or carriers.

In order to assess the spatial distribution of localization centers, CW-PL was performed using a 30-nm aperture probe taken at different positions as shown

Fig. 12.29 Model of exciton/carrier localization induced by potential fluctuation, and the correlation with the PL intensity monitored by fiber probe



in Fig. 12.32. Several peaks are clearly observed by using small aperture size fiber probe, and the spectral shape is different from each other. The minimum PL linewidth is about 11.6 meV. This value is one-fifth of macroscopic PL linewidth (about 60 meV), indicating that the macroscopic linewidth is not mainly contributed from the homogeneous broadening due to the interaction with phonon, but from the inhomogeneous one due to potential fluctuation. It is likely that inhomogeneous broadening due to potential fluctuations is still a significant effect on a 30-nm-length scale. Therefore, even smaller PL linewidth might be observed with smaller aperture size. SNOM-PL intensity mapping was performed with a 30-nm aperture under *I-C* mode as shown in Fig. 12.33. The images are taken with four different emission energies, ranging from low-energy emission component to high-energy one [(a) 2.560 eV, (b) 2.597 eV, (c) 2.615 eV, and (d) 2.636 eV]. The size of island-like area is in the range from 20 to 70 nm for (a) to (c), showing close distribution. However, islands tend to be connected if the monitored photon energy is the highest (Fig. 12.33d). It should be noted that such fine structures disappear if monitored under *I* mode and that exciton/carrier localization from high-energy region to

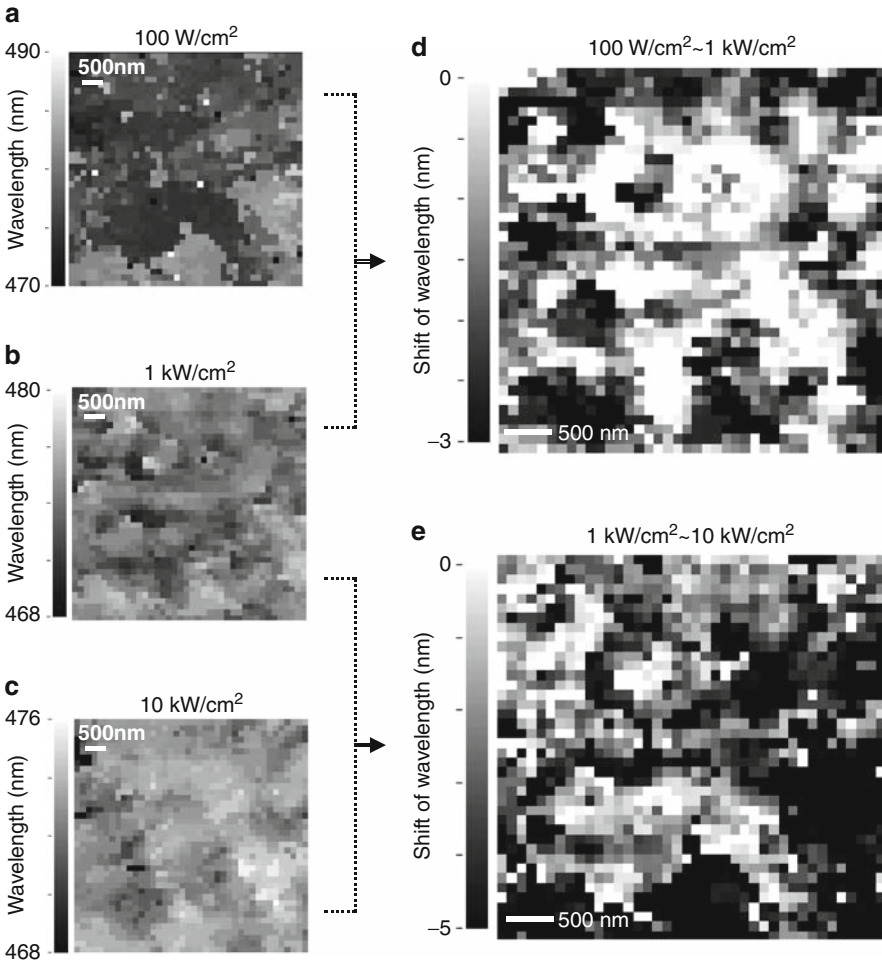
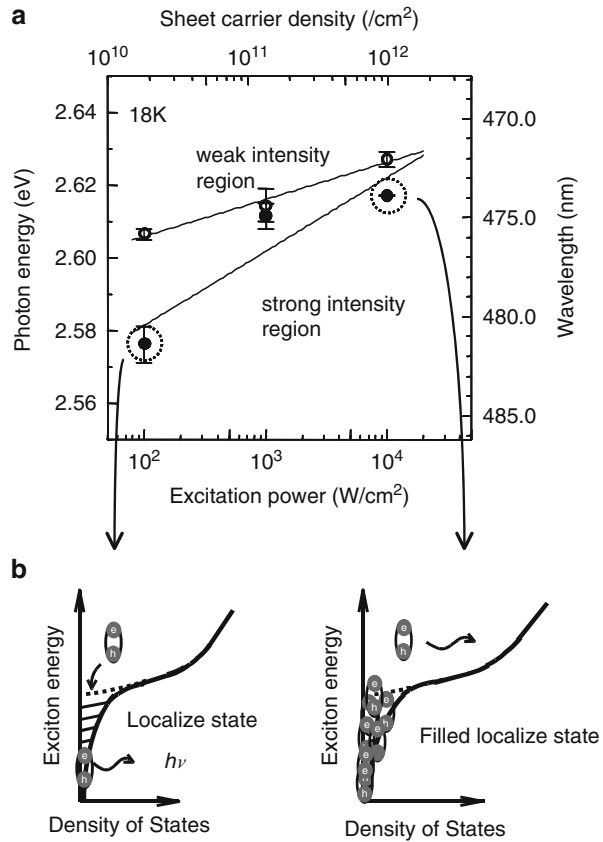


Fig. 12.30 SNOM-PL mapped with PL peak wavelength under (a) $I_{\text{ex}} = 100 \text{ W/cm}^2$, (b) 1 kW/cm^2 and (c) 10 kW/cm^2 . Shift of PL peak wavelength between (d) $I_{\text{ex}} = 100 \text{ W/cm}^2$ and 1 kW/cm^2 , and between (e) $I_{\text{ex}} = 1 \text{ kW/cm}^2$ and 10 kW/cm^2

low-energy one was observed by TR-SNOM-PL measurement. Therefore, it is probable that excitons and/or carriers are deeply localized, but each localization center is so closely distributed that they are mobile within the layer as illustrated by the schematic model in Fig. 12.34. AFM assessed in-situ during the SNOM measurements shows that the root mean square of surface unevenness is about 3 nm and that the no correlation was found between the unevenness and PL intensity within the scanning area of 250 nm squares. The origin of localization centers thus may be mainly due to the fluctuation of In composition rather than the interface

Fig. 12.31 (a) PL peak wavelength and corresponding peak energy plotted as a function of excitation power density at 18 K, averaged at strong and weak PL intensity regions. The error bar shows the distribution of the data. (b) The model of band filling in strong PL intensity region where the degree of localization is higher than that in weak PL intensity region

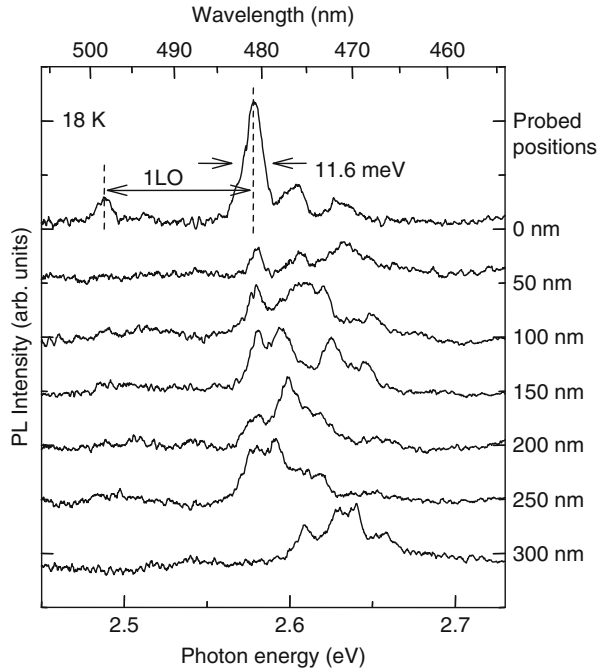


roughness. Cross-sectional TEM observation shows the formation of In-rich QD-like region having about 3 nm in diameter [9]. In compositions in QW and in QDs are estimated to be 20 and 30%, respectively, by energy-dispersive X-ray (EDX) microanalysis. Transition energy was thus calculated as a function of the in-plane quantum box size assuming that $L_x = L_y$. The result shows that the variation of $L_x (= L_y)$ in the range 2.2–3 nm leads to the distribution of localization depth from 70 to 170 meV.

12.5.3 Multimode SNOM at RT

As described in the previous section, high spatial resolution limited only by the size of aperture is achieved in SNOM-PL mapping under *I-C* mode. However, a disadvantage of *I-C* mode is that it is impossible to detect the signal of radiative recombinations in regions not directly under the probe while it is possible by a

Fig. 12.32 SNOM-PL spectra taken at each position with a 30-nm aperture under $I_{\text{ex}} = 100 \text{ W/cm}^2$ at 18 K



far-field detector of an I mode configuration. Therefore, it is difficult for the I - C mode to attribute the weak PL intensity to nonradiative recombination processes or to diffusion of photogenerated carriers outside the detection area of the fiber probe. This is critical for the assessment at RT because the former processes cannot be neglected, unlike at cryogenic temperature.

Focusing on these optical configuration problems, and understanding the importance to collect different signal simultaneously, we set up an SNOM apparatus able to operate simultaneously in multiple modes, I and I - C modes, and designed to probe TRPL spectra in both modes. The multiple measurements taken in this way allowed us to map at high resolution the PL signal, and we could clearly discriminate radiative and nonradiative processes in $\text{In}_x\text{Ga}_{1-x}\text{N}$ -based semiconductors. A schematic experimental setup of this multimode-SNOM is shown in Fig. 12.35, where optical access in an I mode was made from the backside of the sample through a cube-type half mirror because the sapphire substrate is transparent within the whole spectral range of the detection.

Figure 12.36 shows spatial distribution of PL peak intensity under I - C mode (a) and I mode (b) taken in the same scanning area. Excitation power density is 2.5 kW/cm^2 under CW condition. The mean carriers/excitons density for this excitation condition is estimated to be about $5 \times 10^{17} \text{ cm}^{-3}$, considering the absorption coefficient and the light source energy if uniform distribution of carriers is assumed. The scanning area is $4 \mu\text{m} \times 4 \mu\text{m}$ with an interval of 100 nm using

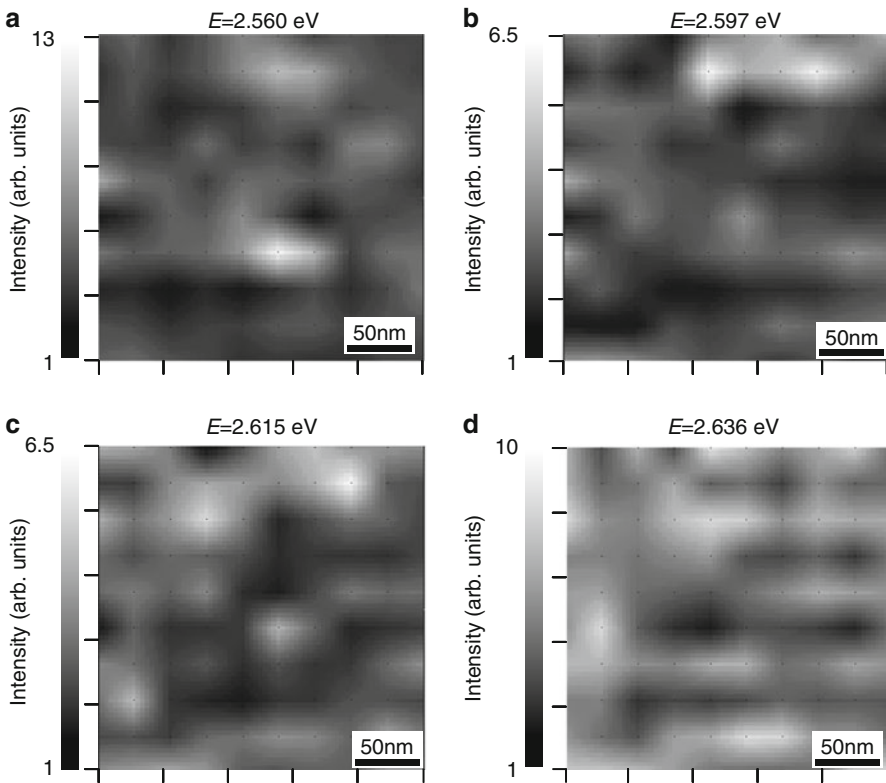


Fig. 12.33 SNOM-PL intensity images monitored at each emission energy with a 30-nm aperture at 18 K

a 200-nm aperture fiber probe. Concerning the *I-C* mode measurement, it was found that relative PL intensity fluctuates from 0.2 to 2.8, consisting of island-like structures within the range of approximately 0.3–1 μm . On the other hand, in *I* mode measurement, relative PL intensity fluctuates from 0.1 to 2.7, a value larger than that of *I-C* mode. Also at RT, there is no correlation with PL intensity signal and surface roughness of 3.1 nm within the scanning area of $4 \times 4 \mu\text{m}^2$. It is very interesting to find that the differences between two images, where the presence of weak PL intensity domains (indicated by the arrows) that appear as high PL intensity in *I* mode. Other regions appear to remain unchanged if observed in the two modes. This behavior can be explained as follows. In the case of domains that appear of weak PL intensity in *I-C* mode and turn out as high PL intensity in *I* mode, we believe that the carrier and/or exciton that is photogenerated directly under the optical aperture of the probe is diffused and localized to out of the *I-C* mode probing area, but they remain in the range of the far-field *I* mode detector. In the other case, the photogenerated carriers and/or excitons do not migrate further than the *I-C* mode probing region; they are presumably captured at nonradiative

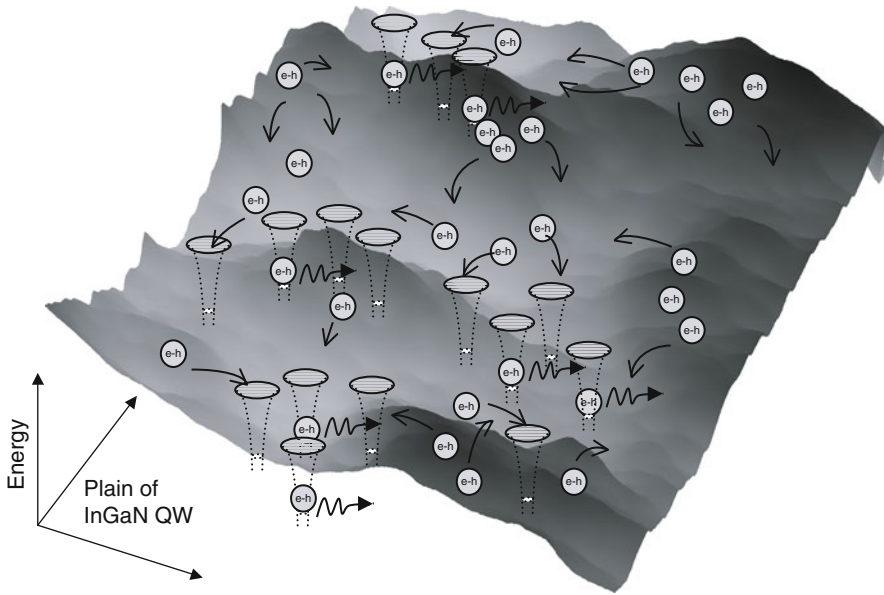


Fig. 12.34 Recombination model of localized excitons for interpreting SNOM data

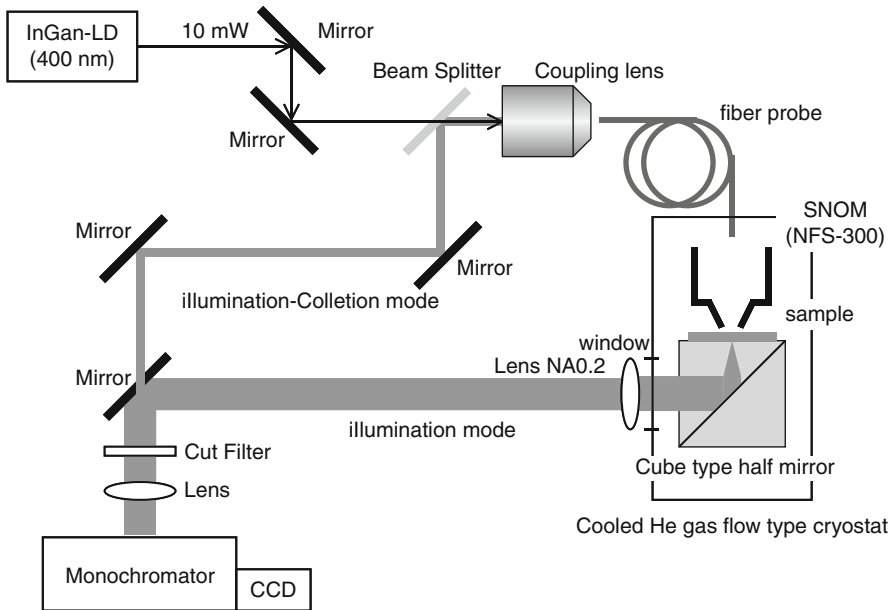


Fig. 12.35 Schematic of the experimental setup of multimode SNOM system capable of working simultaneously in I mode and I - C mode to perform CW-PL and TRPL

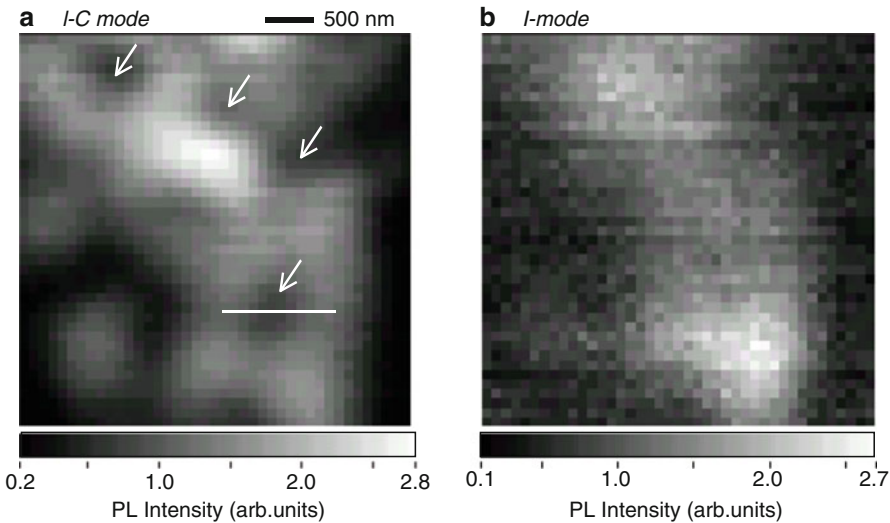


Fig. 12.36 Near-field PL intensity images taken under (a) *I-C* mode and (b) *I*-mode probed with double tapered fiber (aperture size is 200 nm in diameter) at RT. The excitation power density is 2.5 kW/cm^2 under CW condition. The scanning area is $4 \mu\text{m} \times 4 \mu\text{m}$ with probing step of 100 nm

recombination centers, origin of which is related to microscopic dislocations and/or to nanoscopic point defects. Cross-sectional profile of PL intensity along the white line in Fig. 12.36a is plotted in Fig. 12.37. The FWHM of a Gaussian fitting result of this profile is 550 nm; therefore, the diffusion length to radiative recombination center is at least 275 nm in this area. It is noted that the similar value is reported by Cherns et al. [82] as the diffusion length in $\text{In}_x\text{Ga}_{1-x}\text{N}$ -based quantum structures using CL spectroscopy technique though this method is for the characterization of the diffusion to nonradiative recombination centers originating from threading dislocations.

Figure 12.38a, b shows the PL intensity mapped in *I-C* mode and *I* mode, respectively. TRPL was detected at four different positions that are indicated with the letters (a)–(d). These positions were selected as representative of four different behaviors: (a) relatively weak PL intensity in *I-C* mode while stronger PL intensity in *I*-mode, (b) opposite situation to the case of (a), (c) relatively strong PL intensity in both modes, and (d) relatively weak PL intensity in both modes. The photoexcitation energy density is $5.5 \mu\text{J/cm}^2$ corresponding to an estimated carrier/exciton density just after photoexcitation to be about $1 \times 10^{18} \text{ cm}^{-3}$. It was found that the PL lifetime under *I-C* mode are always shorter than those in *I* mode. The difference is significant for the data at (a), where τ_{PL} values of spectrally integrated PL intensity are 0.541 and 1.553 ns, for *I-C* mode and *I* mode, respectively, as shown in Fig. 12.39, both of which are fast components in double exponential fitting. This assumption is valid because the faster components are

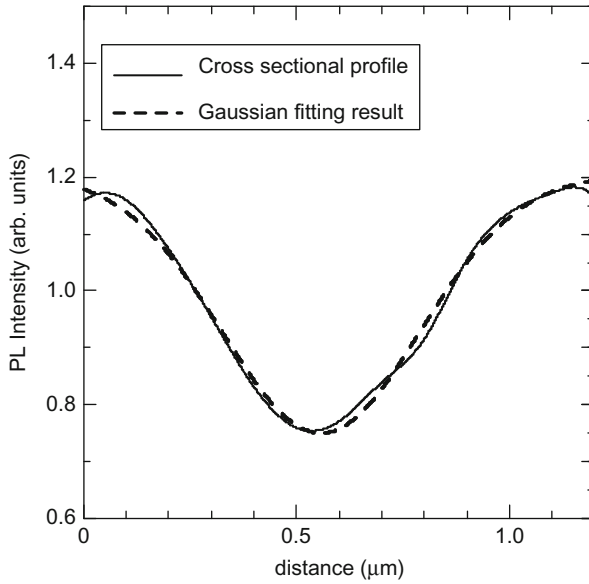


Fig. 12.37 Cross-sectional profile of PL intensity along the white bar in (a) Fig. 12.36. The dashed line represents the best-fit result using a Gaussian shape

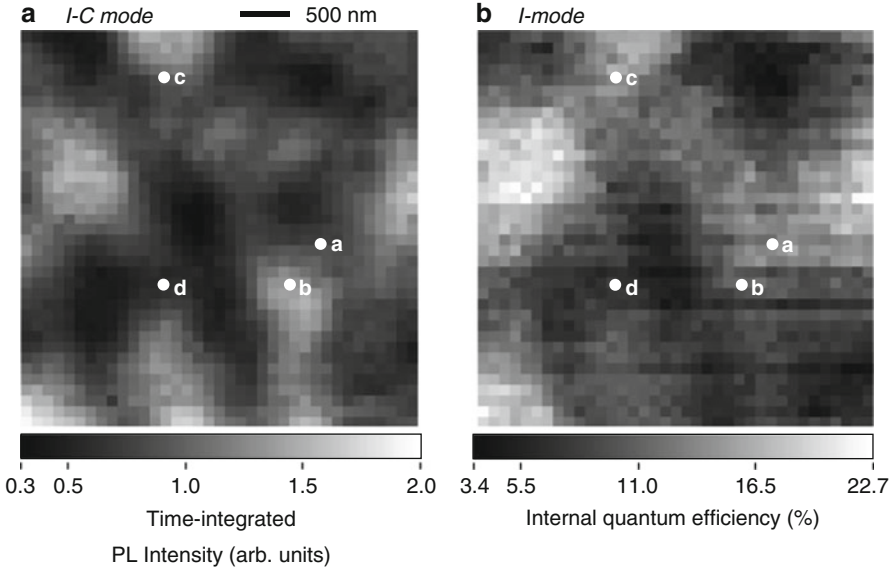


Fig. 12.38 Near-field PL intensity images taken under *I-C* mode (a) and (b) *I* mode probed with single tapered fiber (pure SiO_2 , aperture size is 200 nm in diameter) at RT. The excitation energy density is $5.5 \mu\text{J}/\text{cm}^2$ under pulsed condition. The scanning area is $3.7 \mu\text{m} \times 3.7 \mu\text{m}$ with probing step of 100 nm

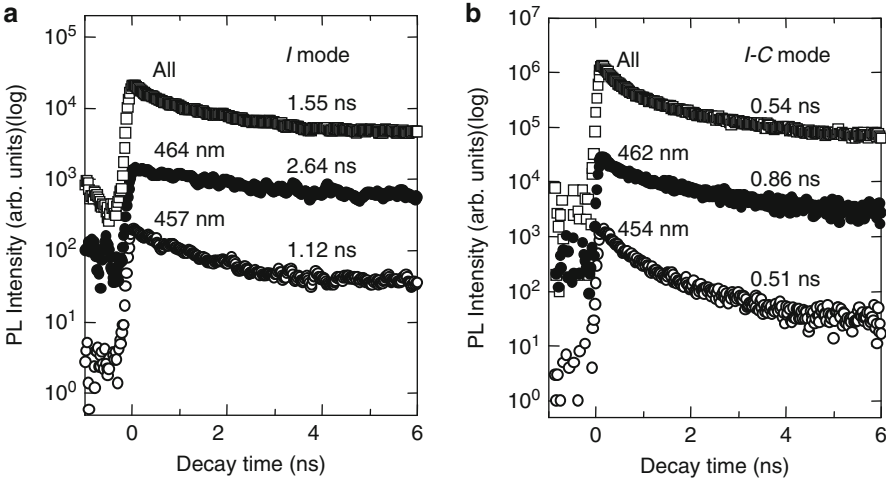


Fig. 12.39 Decay spectra under (a) *I* mode, and (b) *I-C* mode monitored at spectrally integrated PL intensity (all) and at each PL-energy components. Decay curves are fitted with double exponential curves, but the fast components of lifetimes are shown in the figure

dominant comparing to the slower ones and is necessary to make a simple discussion as described below. The PL lifetime in *I-C* mode ($\tau_{\text{PL-I-C}}$) is

$$\frac{1}{\tau_{\text{PL-I-C}}} = \frac{1}{\tau_{\text{rad}}} + \frac{1}{\tau_{\text{nonrad}}} + \frac{1}{\tau_{\text{tr-out}}}, \quad (12.14)$$

where τ_{rad} and τ_{nonrad} are radiative and nonradiative lifetimes, respectively, and $\tau_{\text{tr-out}}$ represents the lifetime of carrier transfer from the area directly under the tip aperture (within the *I-C* mode probing range, *I* mode and *I-C* mode detection are both possible) to the external region (in this case only *I* mode detection is possible). Since PL signal is detected in far-field configuration under *I* mode, the term of $1/\tau_{\text{tr-out}}$ can be neglected; the PL lifetime under *I* mode ($\tau_{\text{PL-I}}$) is expressed by

$$\frac{1}{\tau_{\text{PL-I}}} = \frac{1}{\tau_{\text{rad}}} + \frac{1}{\tau_{\text{nonrad}}}. \quad (12.15)$$

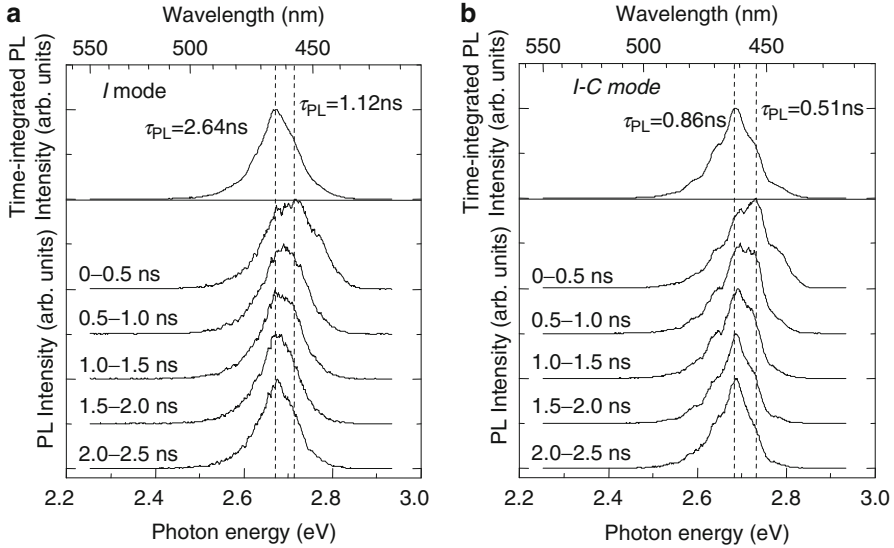
It should be noted that this treatment is based on the first-order assumption, where radiative lifetimes as well as nonradiative recombination times in *I* mode are averaged to be same as those in *I-C* mode. More detailed analysis taking into account the difference in radiative/nonradiative lifetimes is in progress. TIPL intensity mapped under *I* mode (Fig. 12.38b) represents the spatial distribution of η_{int} . According to the temperature dependence of macroscopic PL measurements, it was found that the internal quantum efficiency of this sample is nearly unity (more than 90%) at temperatures less than 50 K. Consequently, the distribution of

Table 12.2 Internal quantum efficiency and PL lifetime in each mode monitored at four different positions

Position	$I_{I-C\text{mode}}$	$I_{I\text{mode}}$	η_{int}	$\tau_{\text{PL-I-C}}$ (ns)	$\tau_{\text{PL-I}}$ (ns)
a	Weak	Strong	21.1	0.541	1.55
b	Strong	Weak	15.0	0.673	0.67
c	Strong	Strong	22.6	0.564	0.568
d	Weak	Weak	9.0	0.552	0.677

Table 12.3 Recombination lifetimes at each position obtained by the calculation of experimental data

Position	$\tau_{\text{tr-out}}$ (ns)	τ_{rad} (ns)	$\tau_{\text{non-rad}}$ (ns)
a	0.83	7.35	1.97
b	4.18	4.49	0.79
c	87.1	2.50	0.73
d	3.00	7.44	0.74

**Fig. 12.40** TIPL and TRPL spectra monitored under (a) I mode and under (b) $I-C$ mode. Lifetimes in the figure are experimental decay times monitored at each emission energy shown by dotted lines

PL intensities from 0.1 to 2.7 at RT corresponds to η_{int} values ranging from 3.4 to 22.7%. Since the η_{int} value is expressed by

$$\eta_{\text{int}} = \frac{\tau_{\text{nonrad}}}{\tau_{\text{rad}} + \tau_{\text{nonrad}}}, \quad (12.16)$$

all recombination lifetimes can be calculated using the experimental data as shown in Table 12.3.

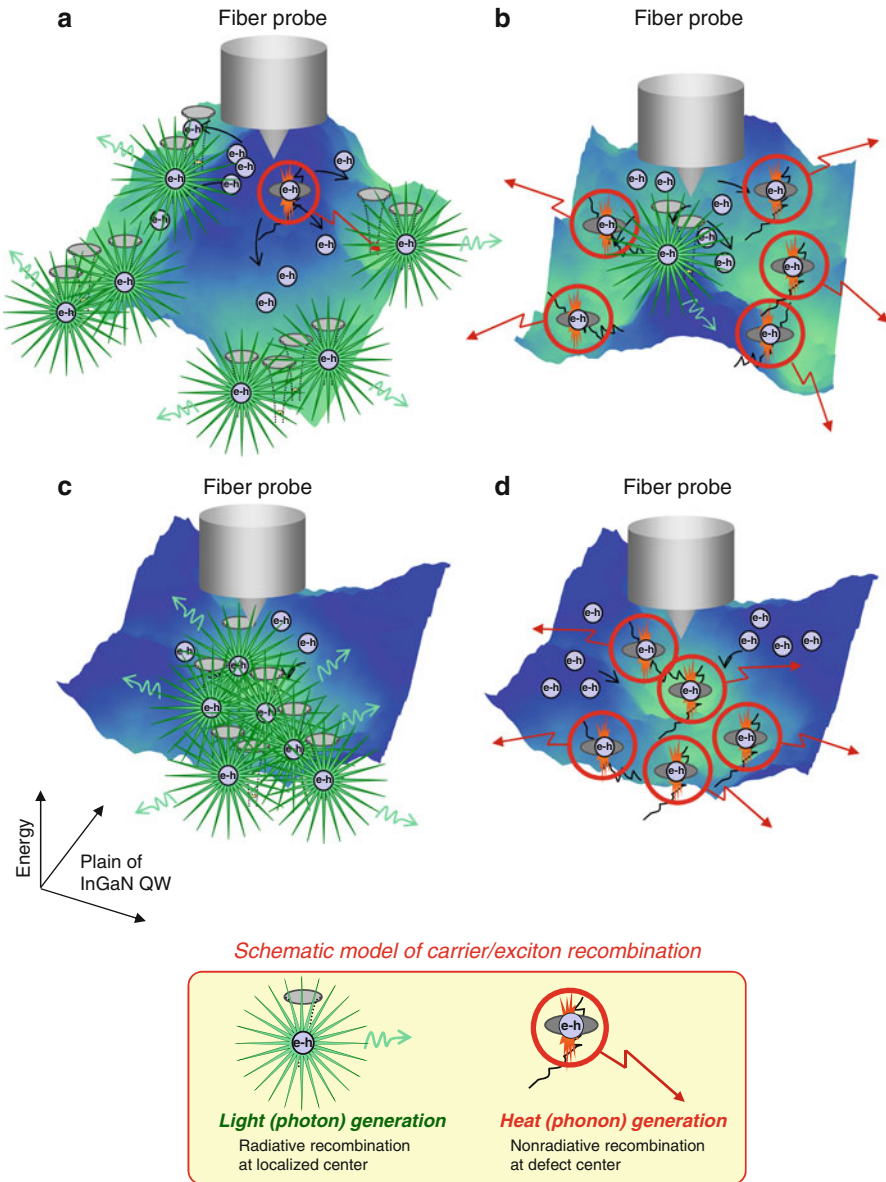


Fig. 12.41 Schematics of recombination model probed at positions of (a), (b), (c), and (d)

It is evident that the shorter lifetime of $\tau_{\text{PL-I-C}}$ probed at position (a) is due to a small $\tau_{\text{tr-out}} = 0.83 \text{ ns}$ term. This transfer process is probably caused by exciton/carrier localization centers that are local potential minima distributed in the proximity of the tip but external of the *I-C* mode probing range. This idea is

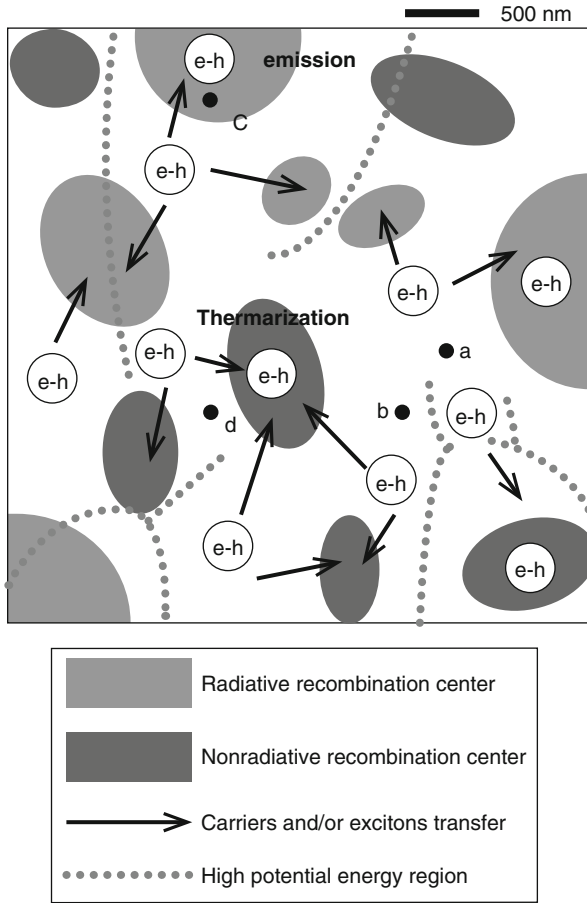


Fig. 12.42 Schematics of the different carrier dynamics as observed in Fig. 12.38 with its four studied positions of (a), (b), (c), and (d)

confirmed by examining the time integration of the PL peaks; in the case of position (a), the time integrated peak is located at 461.9 nm (2.683 eV) under I - C mode, while it is at 464.2 nm (2.670 eV) under I mode, as shown in Fig. 12.40.

In the point indicated with (b), relatively weak PL intensity in I mode is caused by a transfer process to nonradiative recombination centers distributed in the region external to the I - C probing, as it is indicated by the small $\tau_{\text{nonrad}} = 0.79$ ns. Concerning the point in (c), the strong PL intensities in both modes are due to radiative recombinations that mainly take place within the aperture, as shown by a large value of $\tau_{\text{tr-out}} = 87.1$ ns. Moreover, in the position (d), a weak PL intensity in both modes is due by large density of nonradiative recombination centers distributed within and outside of the aperture range. Direct mapping of such nonradiative carrier

dynamics has been achieved by employing a transient lens spectroscopy in the SNOM configuration [83].

Recombination processes probed at (a)–(d) within in-plane potential fluctuation are schematically illustrated in Fig. 12.41a–d. Based on the dynamics described above, the transfer, radiative, and nonradiative processes taking place are represented in the scheme of Fig. 12.42. Radiative and nonradiative recombination centers are present all over the sample. Since their densities are inhomogeneously distributed, dense areas act as attractive domains for photogenerated excitons/carriers. Potential energy was estimated by PL peak mapping that we performed separately; in Fig. 12.42 the dotted lines represent regions where the potential energy is higher. These high-energy lines form a potential ridge that presumably would suppress the carrier/exciton diffusion, creating the carrier dynamics we observed. Such inhomogeneous potential distributions depend strongly on the mean In compositions in InGaN QWs, and the detailed correlation has been assessed between PL mapping and the location of threading dislocations for violet- blue-, and green-emitting InGaN SQWs [84].

12.6 Conclusion

Material parameters, such as bandgap energies, piezoelectric constants and alloy broadening, have been summarized for $\text{In}_x\text{Ga}_{1-x}\text{N}$ alloys; the general model of optical transitions have been described in $\text{In}_x\text{Ga}_{1-x}\text{N}/\text{GaN}$ QW structures taking in to account two major effects of localization and screening of piezoelectric fields.

The $\text{In}_{0.1}\text{Ga}_{0.9}\text{N}$ well-width dependence on transient absorption revealed that the screening of internal electric fields plays an important role on photo-induced change of absorption spectra in wider wells of 30 and 10 nm. However, this effect was less dominant for the well width of 5 nm and was not detectable for the well width of 3 nm, resulting in the observation of the photobleaching of localized tail states.

PL mapping with SNOM has revealed the dense distribution of island-like localized structures, the size of which ranges from 20 to 70 nm in a 3-nm-thick $\text{In}_{0.2}\text{Ga}_{0.8}\text{N}$ SQW structure emitting at blue spectral region. Moreover, local diffusion, radiative, and nonradiative processes have been identified at RT in this structure, by employing multimode SNOM where TRPL data are taken by both *I-C* mode and *I* mode. It was found that the probed area could be classified into four different regions whose dominating processes are (1) radiative recombination within a probing aperture, (2) nonradiative recombination within an aperture, (3) diffusion of photogenerated excitons/carriers out of an aperture resulting in localized luminescence, and (4) the same diffusion process as (3) but resulting in nonradiative recombination. It should be noted that such a finding has led to the development of a dual-probe SNOM technique, where the probe for photoexcitation is fixed at a specific position and then another probe is scanned in the vicinity of it for the detection of local PL to visualize anisotropic carrier motions [85].

We believe our experimental technique can be a powerful tool for any nano-photonic materials because of an applicability to study on carrier/exciton dynamics where spatial and temporal dynamics have to be taken into account.

Acknowledgements The authors would like to express their deep gratitude to Prof. Shigeo Fujita for providing the opportunity to this work, for his continuous guidance and encouragement, and also for his sincere attitude to education and research devoted just before his death. Special thanks are also due to Dr. Mitsuru Funato, Dr. Koichi Okamoto, and Dr. Ruggero Micheletto for their valuable discussion and comments.

References

1. T. Mukai, H. Narimatsu, S. Nakamura, *Jpn. J. Appl. Phys.* **37**, L479 (1998)
2. T. Mukai, K. Takekawa, S. Nakamura, *Jpn. J. Appl. Phys.* **37**, L839 (1998)
3. M. Yamada, Y. Narukawa, T. Mukai, *Jpn. J. Appl. Phys.* **41**, L246 (2002)
4. S. Nagahama, N. Iwasa, M. Senoh, T. Matsushita, Y. Sugimoto, H. Kiyoku, T. Kozaki, M. Sano, H. Matsumura, H. Umemoto, K. Chocho, T. Mukai, *Jpn. J. Appl. Phys.* **39**, L647 (2000)
5. S. Nagahama, T. Yanamoto, M. Sano, T. Mukai, *Jpn. J. Appl. Phys.* **40**, L785 (2001)
6. K. Iida, T. Kawashima, A. Miyazaki, H. Kasugai, S. Mishima, A. Honshio, Y. Miyatake, M. Iwaya, S. Kamiyama, H. Amano, I. Akasaki, *Jpn. J. Appl. Phys.* **43**, L499 (2003)
7. B. Gil, *Low-Dimensional Nitride Semiconductors* (Oxford University Press, Oxford, 2002)
8. S. Chichibu, T. Azuhata, T. Sota, S. Nakamura, *Appl. Phys. Lett.* **69**, 4188 (1996)
9. Y. Narukawa, Y. Kawakami, M. Funato, Sg. Fujita, S. Nakamura, *Appl. Phys. Lett.* **70**, 981 (1997)
10. Y. Narukawa, Y. Kawakami, Sz. Fujita, Sg. Fujita, S. Nakamura, *Phys. Rev. B* **56**, R10024 (1997)
11. A. Satake, Y. Masumoto, T. Miyajima, T. Asatsuma, F. Nakamura, M. Ikeda, *Phys. Rev. B* **57**, R2041 (1998)
12. Y.H. Cho, T.J. Schmidt, S. Bidnyk, G.H. Gainer, J.J. Song, S. Keller, U.K. Mishra, S.P. Den-Baars, *Phys. Rev. B* **61**, 7571 (2000)
13. I. Ho, G.B. Stringfellow, *Appl. Phys. Lett.* **69**, 2701 (1996)
14. T. Matsuoka, *Appl. Phys. Lett.* **71**, 105 (1997)
15. A. Koukitu, N. Takahashi, T. Taki, H. Seki, *Jpn. J. Appl. Phys.* **35**, L673 (1996)
16. T. Okumura, M. Ishida, T. Kamikawa, *Jpn. J. Appl. Phys.* **39**, 1044 (2000)
17. C. Kisielowski, Z.L. Weber, S. Nakamura, *Jpn. J. Appl. Phys.* **36**, 6932 (1997)
18. N.A. El-Masry, E.L. Piner, S.X. Liu, S.M. Bedair, *Appl. Phys. Lett.* **72**, 40 (1998)
19. L. Nistor, H. Bender, A. Vantomme, M.F. Wu, J. Van Landuyt, K.P. O'Donnell, R. Martin, K. Jacobs, I. Moerman, *Appl. Phys. Lett.* **7**, 507 (2000)
20. M. Strassburg, A. Hoffman, I.L. Krestnikov, N.N. Ledentsov, *Phys. Status Solidi a* **183**, 99 (2001)
21. Y.T. Moon, D.J. Kim, J.S. Park, J.T. Oh, J.M. Lee, Y.W. Ok, H. Kim, S.J. Park, *Appl. Phys. Lett.* **79**, 599 (2001)
22. H. Gotoh, H. Ando, T. Takagahara, H. Kamada, A. Chavez-Pirson, J. Temmyo, *Jpn. J. Appl. Phys.* **36**, 4204 (1997)
23. Y. Narukawa, Y. Kawakami, Sg. Fujita, S. Nakamura, *Phys. Rev. B* **59**, 10283 (1999)
24. Y. Kawakami, Y. Narukawa, K. Omae, Sg. Fujita, S. Nakamura, *Phys. Status Solidi a* **178**, 331 (2000)
25. P. Lefebvre, J. Allegre, B. Gil, A. Kavokine, H. Mathieu, W. Kim, A. Salvador, A. Botchkarev, H. Morkoc, *Phys. Rev. B* **57**, R9447 (1998)
26. P. Lefebvre, T. Taliercio, A. Morel, J. Allegre, M. Gallart, B. Gil, *Appl. Phys. Lett.* **78**, 1538 (2001)

27. T. Takeuchi, S. Sota, M. Katsuragawa, M. Komori, H. Takeuchi, H. Amano, I. Akasaki, *Jpn. J. Appl. Phys.* **36**, L382 (1997)
28. J.S. Im, H. Kolmer, J. Off, A. Sohmer, F. Scolz, A. Hangleiter, *Phys. Rev. B* **55**, R9435 (1998)
29. P. Riblet, H. Hirayama, A. Kinoshita, A. Hirata, T. Sugano, Y. Aoyagi, *Appl. Phys. Lett.* **75**, 2241 (1999)
30. C. Wetzel, T. Takeuchi, H. Amano, I. Akasaki, *Phys. Rev. B* **62**, R13302 (2000)
31. T. Kuroda, A. Takeuchi, T. Sota, *Appl. Phys. Lett.* **76**, 3753 (2000)
32. C. Wetzel, T. Takeuchi, H. Amano, I. Akasaki, *J. Appl. Phys.* **85**, 3786 (1999)
33. Y. Kawakami, A. Kaneta, K. Omae, A. Shikanai, K. Okamoto, G. Marutsuki, Y. Narukawa, T. Mukai, *Sg. Fujita, Phys. Status Solidi b* **240**, 337 (2003)
34. K. Omae, Y. Kawakami, Sg. Fujita, M. Yamada, Y. Narukawa, T. Mukai, *Phys. Rev. B* **65**, 073308 (2002)
35. K. Omae, Y. Kawakami, Sg. Fujita, Y. Narukawa, Y. Watanabe, T. Mukai, *Phys. Status Solidi a* **190**, 93 (2002)
36. K. Omae, Y. Kawakami, Sg. Fujita, Y. Narukawa, T. Mukai, *Phys. Rev. B* **68**, 085303 (2003)
37. M. Nomura, M. Arita, Y. Arakawa, S. Ashihara, S. Kako, M. Nishioka, T. Shimura, K. Kuroda, *J. Appl. Phys.* **94**, 6468 (2003)
38. Y. Kawakami, Y. Narukawa, K. Omae, S. Nakamura, Sg. Fujita, *Mater. Sci. Eng. B* **82**, 188 (2001)
39. T. Izumi, Y. Narukawa, K. Okamoto, Sg. Fujita, S. Nakamura, *J. Lumim.* **87–89**, 1196 (2000)
40. A. Kaneta, K. Okamoto, Y. Kawakami, G. Marutsuki, Y. Nakagawa, G. Shinomiya, T. Mukai, Sg. Fujita, *Phys. Status Solidi b* **228**, 93 (2001)
41. K. Okamoto, J. Coi, Y. Kawakami, M. Terazima, T. Mukai, Sg. Fujita, *Jpn. J. Appl. Phys.* **43**, 839 (2004)
42. S. Chichibu, K. Wada, S. Nakamura, *Appl. Phys. Lett.* **71**, 2346 (1997)
43. X. Zhang, D.H. Rich, J.T. Kobayashi, N.T. Kobayashi, P.D. Dapkus, *Appl. Phys. Lett.* **73**, 1430 (1998)
44. P.A. Crowell, D.K. Young, S. Keller, E.L. Hu, D.D. Awschalom, *Appl. Phys. Lett.* **72**, 927 (1998)
45. A. Vertikov, M. Kuball, A.V. Nurmikko, Y. Chen, S.-Y. Wang, *Appl. Phys. Lett.* **72**, 2645 (1998)
46. A. Vertikov, A.V. Nurmikko, K. Doverspike, G. Bulman, J. Edmond, *Appl. Phys. Lett.* **73**, 493 (1998)
47. A. Vertikov, I. Ozden, A.V. Nurmikko, *Appl. Phys. Lett.* **74**, 850 (1999)
48. D.K. Young, M.P. Mack, A.C. Abare, M. Hansen, L.A. Coldren, S.P. Denbaars, E.L. Hu, D.D. Awschalom, *Appl. Phys. Lett.* **74**, 2349 (1999)
49. A. Kaneta, T. Izumi, K. Okamoto, Y. Kawakami, Sg. Fujita, Y. Narita, T. Inoue, T. Mukai, *Jpn. J. Appl. Phys.* **40**, 110 (2001)
50. A. Kaneta, K. Okamoto, Y. Kawakami, Sg. Fujita, G. Marutsuki, Y. Narukawa, T. Mukai, *Appl. Phys. Lett.* **81**, 4353 (2002)
51. J. Kudrna, P.G. Gucciardi, A. Vinattieri, M. Colocci, B. Damilano, F. Semond, N. Grandjean, J. Massies, *Phys. Status Solidi a* **190**, 155 (2002)
52. A. Kaneta, T. Mutoh, Y. Kawakami, Sg. Fujita, G. Marutsuki, Y. Narukawa, T. Mukai, *Appl. Phys. Lett.* **83**, 3462 (2003)
53. R. Micheletto, N. Yoshimatsu, A. Kaneta, Y. Kawakami, Sg. Fujita, *Appl. Surf. Sci.* **229**, 338 (2004)
54. G. Marutsuki, Y. Narukawa, T. Mitani, T. Mukai, Gi. Shinomiya, A. Kaneta, Y. Kawakami, Sg. Fujita, *Phys. Status Solidi a* **192**, 110 (2002)
55. H. Itoh, S. Watanabe, M. Goto, N. Yamada, M. Misra, A.Y. Kim, S.A. Stockman, *Jpn. J. Appl. Phys.* **42**, L1244 (2003)
56. K. Osamura, K. Nakajima, Y. Murakami, *Solid State Commun.* **11**, 617 (1972)
57. K. Osamura, S. Naka, Y. Murakami, *J. Appl. Phys.* **46**, 3432 (1975)
58. C. Wetzel, T. Takeuchi, S. Yamaguchi, H. Katoh, H. Amano, I. Akasaki, *Appl. Phys. Lett.* **73**, 1994 (1998)

59. L. Bellaiche, T. Mattila, L.W. Wang, S.H. Wei, A. Zunger, *Appl. Phys. Lett.* **74**, 1842 (1999)
60. T. Inushima, V.V. Mamutin, V.A. Vekshin, S.V. Ivanov, T. Sakon, S. Motokawa, *J. Cryst. Growth* **227**, 481 (2001)
61. V.Y. Davydov, A.A. Klochikin, R.P. Sesyan, V.V. Emstev, S.V. Ivanov, F. Bechstedt, J. Furthmüller, H. Harima, A.V. Murdryi, J. Adrhold, O. Semchinova, J. Graul, *Phys. Status Solidi b* **229**, R1 (2002)
62. T. Matsuoka, H. Okamoto, M. Nakao, H. Harima, E. Kurimoto, *Appl. Phys. Lett.* **81**, 1246 (2002)
63. Y. Saito, H. Harima, E. Kueimoto, T. Yamaguchi, N. Teraguchi, A. Suzuki, T. Araki, Y. Nanishi, *Phys. Status Solidi b* **234**, 796 (2001)
64. M. Hori, K. Kano, T. Yamaguchi, Y. Saito, T. Araki, Y. Nanishi, N. Teraguchi, A. Suzuki, *Phys. Status Solidi b* **234**, 750 (2002)
65. J. Wu, W. Walukiewicz, K.M. Yu, J.W. Arger III, E.E. Haller, H. Lu, W.J. Schaff, Y. Saito, Y. Nanishi, *Appl. Phys. Lett.* **80**, 3967 (2002)
66. Y. Nanishi, Y. Saito, T. Yamaguchi, *Jpn. J. Appl. Phys.* **42**, 2549 (2003)
67. I.M. Lifshitz, *Advert. Phys.* **13**, 483 (1965)
68. R. Zimmermann, *J. Cryst. Growth* **101**, 346 (1990)
69. V.W.L. Chin, T.L. Tansley, T. Osotchan, *J. Appl. Phys.* **75**, 7365 (1994)
70. R.B. Zetterstrom, *J. Mater. Sci.* **5**, 1102 (1970)
71. Y.C. Yeo, T.C. Chong, M.F. Li, *J. Appl. Phys.* **83**, 1429 (1998)
72. I. Vurgaftman, J.R. Meyer, *J. Appl. Phys.* **94**, 3675 (2003)
73. F. Bernardini, V. Fiorentini, D. Vanderbilt, *Phys. Rev. B* **56**, R10024 (1997)
74. A.D. Bykhovski, V.V. Kaminski, M.S. Shur, Q.C. Chen, M.A. Khan, *Appl. Phys. Lett.* **68**, 818 (1996)
75. S. Chichibu, T. Sota, K. Wada, O. Brandt, K.H. Ploog, S.P. DenBaars, S. Nakamura, *Phys. Status Solidi a* **183**, 91 (2001)
76. C. Gourdon, P. Lavallard, *Phys. Status Solidi b* **153**, 641 (1989)
77. Y. Kawakami, The optical properties of InGaN-based quantum wells and quantum dots, in *Low-Dimensional Nitride Semiconductors*, ed. by B. Gill (Oxford University Press, Oxford 2002), pp. 233–255
78. S. Permogorov, A. Reznitskii, S. Verbin, G.O. Müller, P. Flögel, M. Nikiforov, *Phys. Status Solidi b* **113**, 589 (1982)
79. Y. Kawakami, M. Funato, Sz. Fujita, Sg. Fujita, Y. Yamada, Y. Masumoto, *Phys. Rev. B* **50**, 14655 (1994)
80. S.F. Chichibu, A.C. Abare, M.S. Minsky, S. Keller, S.B. Fleischer, J.E. Bowers, E. Hu, U.K. Mishra, L.A. Coldren, S.P. DenBaars, T. Sota, *Appl. Phys. Lett.* **73**, 2006 (1998)
81. E. Berkowicz, D. Gershoni, G. Bahir, E. Lakin, D. Shilo, E. Zolotoyabko, A.C. Abare, S.P. DenBaars, L.A. Coldren, *Phys. Rev. B* **61**, 10994 (2000)
82. D. Cherns, S.J. Heniey, F.A. Ponce, *Appl. Phys. Lett.* **78**, 2691 (2001)
83. K. Okamoto, A. Sherer, Y. Kawakami, *Appl. Phys. Lett.* **87**, 161104 (2005)
84. A. Kaneta, M. Funato, Y. Kawakami, *Phys. Rev. B* **78**, 125317 (2008)
85. A. Kaneta, T. Hashimoto, K. Nishimura, M. Funato, Y. Kawakami, *Appl. Phys. Exp.* **3**, 102102 (2010)

Kohei Imura and Hiromi Okamoto

Contents

13.1	Introduction.....	528
13.2	Optical Properties of Nanoparticles.....	529
13.3	Plasmon Wave Functions.....	533
13.4	Principle of Wave Function Visualization.....	534
13.5	Near-Field Optical Microscope.....	535
	13.5.1 Instrumentation of Near-Field Optical Microscope.....	536
	13.5.2 Time-Resolved and Nonlinear Measurements.....	537
13.6	Photonic Local Density-of-States (LDOS) Calculation.....	538
13.7	Near-Field Transmission Measurements.....	540
	13.7.1 Near-Field Transmission Measurement of Spherical Gold Nanoparticles [73].....	540
	13.7.2 Near-Field Transmission Measurement of Gold Nanorods [68, 71, 75].....	541
	13.7.3 Near-Field Transmission Measurement of Gold Nanodisks [53].....	545
13.8	Time-Resolved Measurements.....	546
13.9	Nonlinear Measurements.....	550
	13.9.1 Gold Nanorods [97, 106].....	552
	13.9.2 Gold Nanoplates [107].....	553
	13.9.3 Dimeric Nanoparticles [108, 109].....	554
	13.9.4 Larger Assemblies of Nanoparticles [110, 111].....	556
13.10	Summary.....	558
	References.....	559

K. Imura (✉)

Department of Chemistry and Biochemistry, School of Advanced Science and Engineering,
Waseda University, Tokyo, Japan

PRESTO, Japan Science and Technology Agency, Saitama, Tokyo, Japan

e-mail: imura@waseda.jp

H. Okamoto

Institute for Molecular Science, Aichi, Japan

The Graduate University for Advanced Studies, Aichi, Japan

e-mail: aho@ims.ac.jp

Abstract

Plasmonic metal nanostructures exhibit unique optical properties, and fundamental studies of them are relevant to wide range of research areas. Unique characteristics of the plasmonic nanostructures originate from the localized optical fields and are closely related to spatiotemporal properties of plasmon waves. In this chapter, visualization of plasmon wave functions and localized optical fields by scanning near-field optical microscopy is described.

13.1 Introduction

The unique colors of noble metal nanoparticles have been used as dyes for various items since ancient times. Red and yellow colors in stained glasses arise from the scattering and absorption of light by gold and silver nanoparticles, respectively. These optical properties of noble metal nanoparticles originate from the collective oscillations of free electrons (plasma) known as plasmons [1–3]. Whereas plasma in bulk material cannot be optically excited because of the momentum mismatch between photons and electrons [4], plasmons in nanoparticles, the sizes of which are smaller than those of the wavelengths of light, are optically excited because the momentum mismatch is compensated by the spatial frequency of the nanoparticle and also by the highly distorted optical field in the vicinity of the nanoparticle. Optically excited plasmons are hybrid modes of optical fields and the electronic oscillations and thus are called as plasmon-polaritons [5]. Herein, the plasmon-polariton is simply called a plasmon for convenience.

Plasmons induce a large polarization in the nanoparticle and confine the optical field on a nanometer scale. The confinement results in the enhancement of the field. The enhanced optical field has been used to amplify Raman scattering from molecules adsorbed on the nanoparticle [6]. Since the discovery of surface enhanced Raman scattering (SERS) [7–9], much research has been devoted to developing chemical- and biosensors based on SERS because the vibrational bands in Raman spectra are useful for the identification of molecules. In 1997, single-molecule sensitivity SERS was reported [10, 11]. Since then, the research area has been further pursued in order to attain ultimate sensitivity for sensing applications and also to elucidate the enhancement mechanism of the SERS. Currently, applications of the enhanced field are expanding from sensing [12] to nano-optical devices [13–15], imaging [16, 17], novel photochemical reactions [18, 19], and optical trapping [20–23]. Plasmon-based materials also have a large impact on basic science [24–31]. The negative refractive index of meta-materials and super resolution using plasmons have been reported [32, 33], for example.

As described above, plasmons have attracted much attention not only in applied science but also in basic science. For understanding and controlling the functions of plasmons, it is essential to reveal the spatial features of plasmon wave functions and optical fields. To study the spatial characters of a certain object, an

optical microscope is useful in many occasions. The spatial resolution of optical microscopes is limited to about $<1\ \mu\text{m}$ in the visible range, however [34, 35]. Spatial features of plasmon wave functions are smaller than that achieved by optical microscopy, and thus optical microscopy cannot be useful for the visualization of plasmon wave functions and optical fields. Visualization of the smaller features beyond the resolution of optical microscopy is feasible by means of the recently developed near-field optical methods [36–38]. The optical contrast mechanism in near-field optical microscopy provides very different images from those observed in the conventional microscopy [39]. The conventional microscope uses an objective lens with a high numerical aperture (NA) to achieve high resolution. However, because a lens is used, the diffraction of light is always involved [34], and thus the spatial resolution is limited by the diffraction limit of light. Near-field optical microscopes, on the other hand, do not use lenses, and thus their spatial resolution is not limited by the diffraction limit. Near-field optical microscopes can achieve much higher spatial resolutions down to the 10 nm level [40, 41] and possess the potential to visualize wave functions of elemental excitation [42–44]. In this review, visualization of plasmon wave functions and optical fields using various near-field optical methods will be described.

13.2 Optical Properties of Nanoparticles

Optical properties of nanoparticles can be elucidated by solving the electromagnetic wave equations, considering the boundary conditions near the nanoparticles. In 1908, G. Mie formulated vector wave equations for spherical nanoparticles and obtained rigorous solutions for them [45]. This is known as Mie theory. Mie theory predicts the scattering and absorption properties of spherical nanoparticles regardless of the particles' size and the material. For example, Mie theory predicts that a spherical gold nanoparticle of a diameter of 20 nm shows a plasmon resonance near 520 nm and that the resonance shifts to the longer wavelength side with the increase of the diameter. The theory also predicts that the scattering and absorption cross-sections scale linearly and quadratically with the particle volume, respectively. These predictions are confirmed to be correct experimentally.

As long as small spherical nanoparticles ($<\lambda/20$) are concerned, dipolar approximation is applicable to obtain optical properties, instead of solving the complex vector wave equations. As a typical example, here we consider a spherical nanoparticle of diameter a illuminated by a plane wave. Upon illumination, polarization is induced in the nanoparticle and is proportional to the incident field (E_0), the dielectric constant ϵ_m of the surrounding material, and the polarizability P of the nanoparticle as follows:

$$P = \epsilon_m \alpha E_0 \quad (13.1)$$

The polarizability can be obtained by considering the boundary conditions of the scalar potential near the particle:

$$\alpha = 4\pi a^3 \frac{\epsilon - \epsilon_m}{\epsilon + 2\epsilon_m} \quad (13.2)$$

The induced polarization reradiates the electromagnetic energy into the far-field. Extinction and scattering cross-sections are given by the following relations, respectively:

$$C_{\text{ext}} = k\text{Im}(\alpha) \quad (13.3)$$

$$C_{\text{sca}} = \frac{k^4}{6\pi} |\alpha|^2 \quad (13.4)$$

Because the extinction cross-section is a sum of the absorption and the scattering cross-sections, the absorption cross-section is obtained by subtracting the scattering from the extinction:

$$C_{\text{abs}} = C_{\text{ext}} - C_{\text{sca}} \quad (13.5)$$

For a smaller nanoparticle, the scattering cross-section is much smaller than the absorption cross-section, and thus $C_{\text{abs}} \sim C_{\text{ext}}$. From Eqs. 13.2–13.4, it is revealed analytically that the absorption and scattering cross-sections are proportional to the particle volume and its square, respectively.

Mie theory gives the rigorous solutions of wave equations only for spherical nanoparticles. For particles with other shapes like ellipsoids, Mie theory cannot be applied, and treatment with the dipolar approximation is useful to discuss the optical properties of the particle qualitatively. By taking the shape-dependent depolarization factor into account, the polarizability of the ellipsoid can be obtained as a form similar to that of the sphere [46]:

$$\alpha = V \frac{\epsilon - \epsilon_m}{\epsilon_m + L_i(\epsilon - \epsilon_m)} \quad (13.6)$$

where V is the volume of the ellipsoid and L_i is the geometrical factor for one of the semi-principle axes of the spheroid:

$$L_1 + L_2 + L_3 = 1 \quad (13.7)$$

The geometrical factors satisfy the above relation, and thus for a sphere in which three principal axes are identical, L_i is equal to $1/3$. Substitution of $L_1 = 1/3$ in Eq. 13.6 yields the same formula as that of Eq. 13.2.

The spheroid is a special kind of ellipsoid in which two principal axes are identical to each other, and therefore only one of the geometrical factors is independent. For a prolate spheroid ($L_1 < L_2 = L_3$), the geometrical factor is obtained by the following equations [47]:

$$L_1 = \frac{1 - e^2}{e^2} \left(-1 + \frac{1}{2e} \ln \frac{1 + e}{1 - e} \right) \quad (13.8)$$

$$e^2 = 1 - \frac{b^2}{a^2}$$

where a and b denote half-lengths of the major and minor axes of the spheroid, respectively. As is understood from Eq. 13.8, the geometrical factor changes with the aspect ratio (alb) of the prolate spheroid. For an oblate spheroid ($L_1 = L_2 < L_3$), similarly, the geometrical factor is dependent on the aspect ratio (a/c where c is half-length of the minor axis):

$$L_1 = \frac{g(e)}{2e^2} \left(\frac{\pi}{2} - \tan^{-1} g(e) \right) - \frac{g^2(e)}{2} \quad (13.9)$$

$$g(e) = \left(\frac{1 - e^2}{e^2} \right)^{1/2}, e^2 = 1 - \frac{c^2}{a^2}$$

When the particle size becomes comparable to the wavelength of light, a retardation effect occurs and has to be taken into account in analysis [48]. Radiation damping becomes significant as the particle volume increases. These factors can be taken into account in the following equation:

$$\alpha = V \frac{1}{\frac{\epsilon_m + L_i(\epsilon - \epsilon_m)}{\epsilon - \epsilon_m} - \frac{k^2 V}{b 4\pi} - \frac{2}{3} i k^3 \frac{V}{4\pi}} \quad (13.10)$$

On the right-hand side of the equation, the second and third terms in the denominator denote the retardation and radiation damping effects, respectively.

For particles with other shapes, the optical properties are numerically calculated by solving the Maxwell equations. For this purpose, the finite-difference time-domain (FDTD) method [49], discrete dipole approximation (DDA) method [50], Green dyadic methods [51, 52], etc. have been developed. FDTD calculation is based on the time-evolution of the electromagnetic wave in the scattering system, and dynamical information of the electromagnetic wave can be obtained in addition to static properties. However, the discretization of the scatterer sometimes induces artifacts due to a finite size of the mesh, and thus careful operation is required to extract the genuine optical properties of the particle.

Figure 13.1 shows extinction spectra for spherical gold nanoparticles, with diameters of 20 and 100 nm, suspended in water. Gold nanoparticles with diameters of 20 and 100 nm exhibit broad extinction bands near 520 and 580 nm, respectively. Spectral features of the particles are well reproduced by Mie theory (Fig. 13.1b), and the bands are assigned to plasmon resonances. As mentioned, Mie theory gives rigorous solutions for spherical nanoparticles, and thus discrepancy between

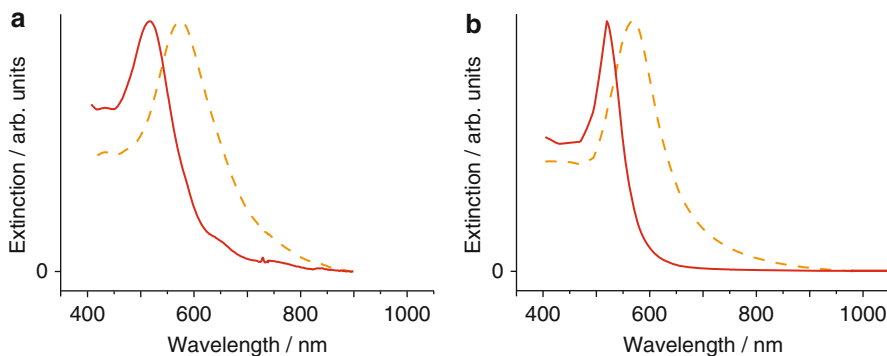


Fig. 13.1 Far-field extinction spectra of spherical gold nanoparticles in water solution. *Solid line:* 20 nm. *Dotted line:* 100 nm. (a) Observation and (b) calculation by Mie theory

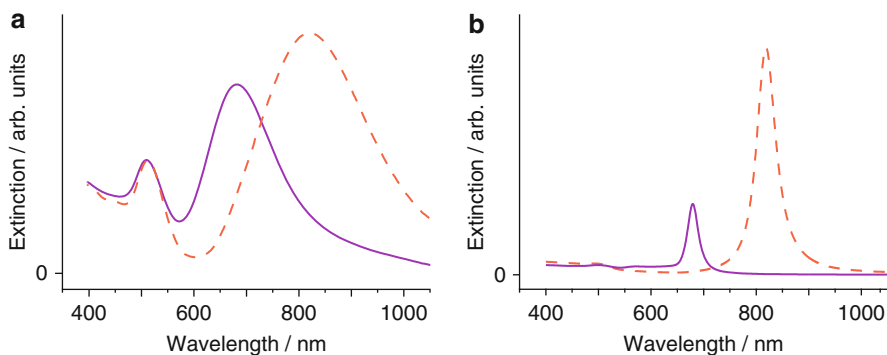


Fig. 13.2 Far-field extinction spectra of gold nanorods in water solution. *Solid line:* aspect ratio ~ 3 . *Dotted line:* aspect ratio ~ 4 . (a) Observation and (b) calculation by Eqs. 13.6–13.8

the observation and calculation is attributable to inhomogeneity (distribution of the size and shape) of the sample.

Figure 13.2 shows extinction spectra of gold nanorods in water. The spectrum shows two bands in the visible to near-infrared region. The peak position of the intense band appearing in the near-infrared region depends on the aspect ratio of the nanorod and shifts toward the longer wavelength side with the increase of the aspect ratio, while the other band appearing near 520 nm depends little on the aspect ratio. The extinction band observed in the long-wavelength region is assigned to the plasmon resonance polarized along the long axis of the nanorod. The other band near 520 nm is assigned to the plasmon resonance polarized across the long axis of the nanorod. These are called longitudinal and transverse plasmon modes, respectively. The dependence of the aspect ratio on the longitudinal plasmon resonance is qualitatively reproduced by simulations using Eqs. 13.6–13.8, as shown in Fig. 13.2b. The observed bandwidths are broader than the calculated ones because of the inhomogeneity of the sample.

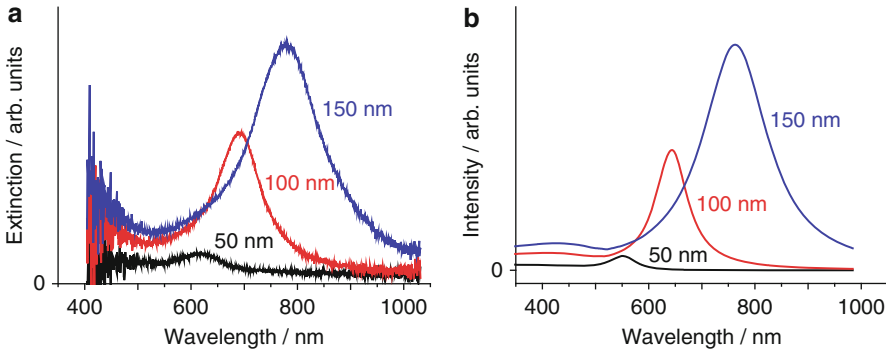


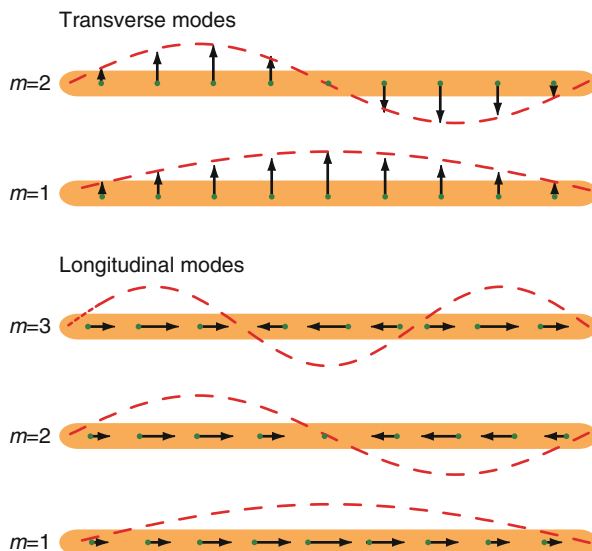
Fig. 13.3 Far-field extinction spectra of gold nanodisks (thickness 35 nm, diameters: 50, 100, and 150 nm) on glass substrate. (a) Observation and (b) calculation by Eq. 13.10

Figure 13.3 shows extinction spectra of gold nanodisks prepared on the cover slip by the electron beam lithography and liftoff technique [53]. The spectrum shows an extinction band in the visible to near-infrared region, depending on the size of the disk. The band shifts toward the longer wavelength with the increment of the aspect ratio defined as (diameter)/(thickness), as is similar to the nanorod. Spectral bandwidth gets broader with the increase of the disk size. Since the sample is monodispersed, the broad bandwidth is attributed to the volume damping effect, which is more significant for the larger disks. The observed spectral features are well reproduced by the simulations using Eq. 13.10, as shown in Fig. 13.3b. From the simulation, the extinction band is assigned to the dipolar plasmon mode excited in the surface of the disk.

13.3 Plasmon Wave Functions

Spectral features of spherical nanoparticles, nanorods, and disks have been discussed in relation to plasmon resonances. The plasmon resonances considered so far are the lowest dipolar mode, where free electrons in the particles oscillate collectively in a single direction concerted with the optical field. The amplitude of the electronic oscillation as a function of the position represents the wave function of the plasmon. The plasmon wave function of the dipolar mode extends over the nanoparticles and does not show any nodal planes. In addition to the dipolar mode, higher plasmon modes can be excited in nanoparticles. Plasmon wave functions of the higher modes, where the direction of the collective oscillation is reversed, show nodal planes in nanoparticles. Longitudinal plasmon wave functions for gold nanorods are schematically shown in Fig. 13.4. Arrows in the nanorod indicate the directions of the oscillations of free electrons. Similar to the wave functions of a “particle in a box,” there are higher modes in addition to the dipolar mode. The mode with one node at the center is the second-lowest mode to the dipolar mode.

Fig. 13.4 Schematic drawing of plasmon modes. Arrows indicate the amplitude of free electron oscillation. Dotted lines indicate plasmon wave functions



Wave functions of the transverse plasmons show periodic oscillations across the long axis of the nanorod. Plasmon resonance frequency of the mode is only little dependent on the order of the mode, and many modes are spectrally overlapped. On the other hand, for longitudinal plasmons, the plasmon resonances are spectrally well separated, and thus selective excitation of the individual mode is feasible. Since the spatial features of the plasmon wave functions are finer than the diffraction limit of light, only near-field optical methods have the ability to visualize them optically.

13.4 Principle of Wave Function Visualization

In physics and chemistry, phenomena are always linked to the wave functions of elementary excitations, and thus understanding the wave functions is of prime importance. Molecular wave functions are indispensable for understanding molecular properties. Photoexcitation processes of molecules and chemical reaction routes are also elucidated from the view of the wave functions. Spatial scales of wave functions are generally very small, and direct visualization of wave functions requires very high spatial resolution. The first visualization of electronic wave functions was demonstrated with a scanning tunneling microscope (STM). Scanning tunneling microscopy visualizes electronic wave functions of an object with atomic-scale spatial resolution. In optics, to realize the ultimate resolution like that of STM, several breakthroughs may still be needed. However, wave functions of elementary excitations such as excitons and plasmons can be visualized if a sufficiently high spatial resolution is achieved. Near-field optical microscopy is promising for this purpose. Wide spectral range and compatibility with dynamic measurements are

the great advantages of optical methods and allow one to study materials properties from broad points of view. Here the principles of visualization of wave functions using a near-field optical microscope will be briefly described in comparison with that of STM.

STM detects electric currents due to tunnel electrons between the sample and the probe tip. Tunneling probability at the tip position is dependent on the overlap of electronic wave functions between the sample and the tip. Because the wave function of the electron at the tip is localized on a single atom, STM visualizes the electronic local density-of-states (LDOS) of the sample at tip position \vec{r} and energy E with atomic resolution [54,55]. Operation principles of a near-field optical microscope is similar to that of an STM [56,57]. Instead of using tunnel electrons as in an STM, a near-field optical microscope uses tunnel photons between the sample and the near-field probe tip and visualizes photonic LDOS at position \vec{r} and frequency ω . In general, LDOS is defined by the following equation [58]:

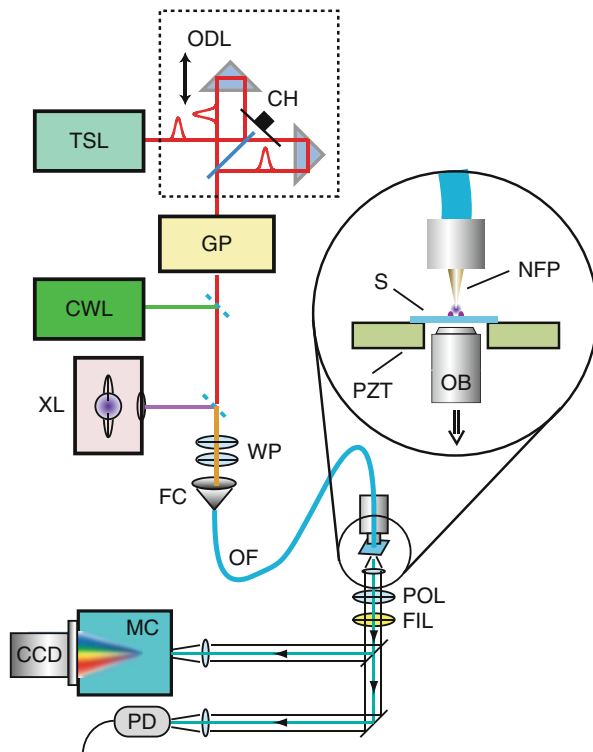
$$\rho(\vec{r}, \omega) = \sum_n \delta(\omega - \omega_n) \phi_n(\vec{r}) \phi_n^*(\vec{r}) \quad (13.11)$$

where ϕ_n is a set of orthogonal wave functions of electromagnetic modes and ω_n denotes the resonance frequency of an eigenstate n . From Eq. 13.11, it is acceptable that, under resonance $\omega \approx \omega_n$, LDOS is approximately equal to the square amplitude of the wave function $|\phi_n|^2$. Because near-field optical microscopy observes the photonic LDOS, it enables visualization of the wave functions of elementary excitations resonant with the incident photons. The near-field methods have been utilized to visualize wave functions of exciton and biexcitons photoexcited in a quantum dot [59] and wavy patterns arising from photonic modes in optical corrals [60]. In the following, visualization of wave functions of plasmons using similar operational principles will be described.

13.5 Near-Field Optical Microscope

Since the first demonstration of near-field optical imaging in the early 1990s [38], the near-field optical microscope has expanded its application area from basic to applied science and become an indispensable tool in imaging the optical properties of objects with high spatial resolution. The operational principles of the near-field optical microscope were first proposed by Syngé in 1928 [61]. Syngé suggested the use of a tiny aperture created in an opaque screen. When the screen is illuminated from its backside, a localized optical field is created in the close vicinity of the aperture. High spatial resolution can be achieved if the localized photons interact with the object, and then the resulting scattered photons are detected. Near-field optical microscopes using a tiny aperture are called aperture-type near-field microscopes. A localized optical field can also be created at the tip of a metal needle with external illumination. Near-field optical microscopes using this type of the optical field are called scattered-type near-field microscopes. Both types of

Fig. 13.5 Schematic diagram of an aperture-type scanning near-field optical microscope. *TSL* Ti:Sapphire laser, *GP* grating pair, *ODL* optical delay line, *CH* mechanical chopper wheel, *CWL* CW laser, *XL* Xe lamp, *WP* wave plates, *FC* fiber coupler, *OF* optical fiber, *S* sample substrate, *NFP* near-field probe, *PZT* piezo-driven stage, *OB* objective lens, *POL* polarizer, *FIL* optical filter, *MC* monochromator, *CCD* charge-coupled device, *PD* photodiode

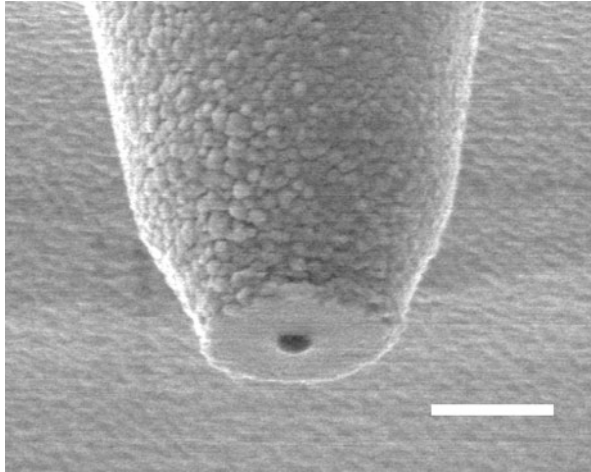


near-field microscope have advantages and disadvantages, and we need to select one of them, considering the sample condition and the information to be obtained. Detailed operational principles have been well described in the references [39, 62]. In this review, we deal only with the experimental results taken by the aperture-type near-field optical microscope.

13.5.1 Instrumentation of Near-Field Optical Microscope

Figure 13.5 shows schematic diagrams of an aperture-type near-field optical microscope. The apparatus consists of a light source, a sample scanner, a near-field probe, a control unit, and a detection system. A light source is chosen from various lasers and discharge lamps depending on the spectroscopic purposes. For example, a Xe lamp (XL) is used for transmission measurements, and continuous wave lasers (CWL) are used for Raman and fluorescence measurements. Aperture-type near-field optical probe (NFP) is used for local illumination and is prepared by chemical etching followed by metal coating and aperture fabrication. The aperture size of the probe tip is several tens of nm confirmed by scanning electron microscope (SEM) observation of the tip and/or near-field fluorescence images of single molecules

Fig. 13.6 Scanning electron micrograph of an aperture near-field probe. Scale bar: 400 nm



using the tip. [Figure 13.6](#) shows a SEM image of an aperture near-field probe tip. The aperture, where the glass part is exposed outside of the metal film, appears as a dark spot at the tip of the probe. An optical near-field is created at the aperture by coupling the photons from a light source to the other end of an optical fiber of the near-field probe. A sample is dispersed on a transparent glass or silica substrate by spin-coating a colloidal solution. The sample substrate (S) is installed on the piezo-driven stage (PZT) for lateral scanning. The piezo stage, with a closed-loop feedback system for position regulation, is advantageous in improving the stability and reproducibility of the sample positioning. Because the optical near-field is localized in the vicinity of the near-field aperture, the near-field aperture should be kept in close vicinity to the sample surface while scanning the sample. A shear-force feedback mechanism was utilized for this purpose and enables the regulation of the tip-sample distance within several nm [39]. The regulation signal can be used for extracting topographic information of the sample. This enables simultaneous observation of topography and the optical image of the sample. To take the optical image, the sample is illuminated locally through the aperture of the near-field probe, and the transmitted light and/or luminescence from the sample is detected. To collect the light from the sample effectively, an objective lens (OB) with a high NA is used. The detection system adopts either a multichannel or single channel detector taking the required sensitivity and the purposes into consideration.

13.5.2 Time-Resolved and Nonlinear Measurements

By combining near-field optical microscopy with pulsed laser sources, time-resolved and nonlinear measurements become possible. Several research groups have succeeded in attaining ps time resolution and subwavelength spatial resolution at the same time [63–67]. To excite nonlinear processes, short pulse duration is

essential. Although higher time resolution in the fs regime is sometimes desired for time-resolved near-field observation, the simple combination of a near-field optical microscope with an ultrashort pulsed laser source does not allow us to achieve very high time resolution. This is because the pulses delivered from the laser source are seriously broadened as the pulses propagate in optical media due to the group velocity dispersion (GVD) of the material. In an aperture near-field optical microscope, the pulses travel through an optical fiber tens of cm in length, and the pulse duration is broadened to several ps at the aperture of the near-field probe even if the initial pulse duration is about 100 fs. By compensating for the GVD with a grating pair (GP) before the pulses couple to the fiber, the GVD effect can be cancelled out, and the original pulse width can be recovered at the aperture of the near-field probe. This way, high time resolution can be achieved while retaining the high spatial resolution of a near-field optical microscope. For time-resolved and nonlinear near-field measurements, a mode-locked Ti:Sapphire laser (TSL) oscillator is useful as a light source. Amplified lasers, which are frequently used for far-field time-resolved measurements, are not compatible with the aperture near-field probe because pulses with high power break the near-field tip easily by thermal effects. Moderate peak power is desirable for combination with aperture near-field probes.

Time-resolved near-field pump-probe measurements are feasible by the apparatus shown in Fig. 13.5. The optical beam from the laser is split into pump and probe beams by a beam splitter. One of the two beams is introduced to a reflector mounted on a motor-driven stage and the other to a reflector mounted on a fixed stage. The two beams are coupled again collinearly by the beam splitter and introduced to the downstream. The delay time between the pump and the probe pulses is adjusted by the optical path difference of the beams, which is controlled by the movable stage. Transient optical response induced by the pump pulse is observed by the probe pulse using the one-color equal pulse correlation (EPC) method. To detect the transient signal effectively, a phase-sensitive detection scheme is useful, where the pump and the probe beams are modulated at different frequencies and the signal is detected as the difference of the modulation frequencies. Dynamic information at the tip position can be obtained by monitoring the transient signal as a function of the delay time, and time-resolved image can be obtained by scanning the sample while monitoring the transient signal [68].

13.6 Photonic Local Density-of-States (LDOS) Calculation

In near-field observation, the contrasts of the optical and topographic images often do not match well. This originates from the fact that the optical contrast reflects photonic LDOS at the tip position on the sample, which does not necessarily coincide with the topography. However, artifacts sometimes contribute to the image as well. The artifacts mostly arise from up-and-down motions of the near-field probe tip as the tip follows the topography of the sample surface (topographic artifact) [69]. The artifact interferes seriously with the genuine optical signal and makes

correct interpretation of the image difficult. To interpret the observed optical contrast appropriately, special care must be taken. In this respect, comparison of the observed optical image with calculated photonic LDOS maps is beneficial in many cases. Here the method of photonic LDOS calculations based on the Green dyadic method is briefly described.

Analysis of the photonic LDOS relies on electromagnetic wave equations derived from Maxwell's equations. Electromagnetic properties of the scatterer can be evaluated by solving the vector wave equations, where the boundary condition near the scatterer is appropriately taken into account. The vector wave equation at position \vec{r} and angular frequency ω is given as

$$-\nabla \times \nabla \times \vec{E}(\vec{r}, \omega) + \frac{\omega^2}{c^2} \epsilon_{\text{ref}} \vec{E}(\vec{r}, \omega) + \frac{\omega^2}{c^2} \epsilon_s(\vec{r}, \omega) \vec{E}(\vec{r}, \omega) = 0 \quad (13.12)$$

where ϵ_s and ϵ_{ref} are the dielectric constants of the scatterer and reference medium, respectively. The equation can be rewritten with the Green dyadic of the scatterer:

$$\begin{aligned} -\nabla \times \nabla \times \overleftrightarrow{G}(\vec{r}, \vec{r}', \omega) + \frac{\omega^2}{c^2} \epsilon_{\text{ref}} \overleftrightarrow{G}(\vec{r}, \vec{r}', \omega) + \frac{\omega^2}{c^2} \epsilon_s \overleftrightarrow{G}(\vec{r}, \vec{r}', \omega) \\ = \delta(\vec{r} - \vec{r}') \end{aligned} \quad (13.13)$$

where $\delta(\vec{r} - \vec{r}')$ is the delta function. The Green dyadic in the scattering system can be obtained with the aid of the discretized Dyson equation by referencing the Green dyadic of the homogeneous medium \overleftrightarrow{G}_0 [70]:

$$\overleftrightarrow{G}(\vec{r}, \vec{r}', \omega) = \overleftrightarrow{G}_0(\vec{r}, \vec{r}', \omega) + \overleftrightarrow{G}_0(\vec{r}, \vec{r}', \omega) \frac{\omega^2}{c^2} (\epsilon_{\text{ref}} - \epsilon_s) \overleftrightarrow{G}(\vec{r}, \vec{r}', \omega) \quad (13.14)$$

The Green dyadic is correlated with the photonic LDOS as follows:

$$\rho(\vec{r}, \omega) = -\frac{1}{\pi} \text{Im}[\text{Tr} \overleftrightarrow{G}(\vec{r}, \vec{r}, \omega)] \quad (13.15)$$

Once the Green dyadic of the scattering system is obtained, the scattered field can be calculated using the Lippmann-Schwinger equation:

$$\vec{E}(\vec{r}, \omega) = \vec{E}_0(\vec{r}, \omega) + k^2 \int_{\Omega} d\vec{r}' \overleftrightarrow{G}(\vec{r}, \vec{r}', \omega) (\epsilon_{\text{ref}} - \epsilon_s) \cdot \vec{E}_0(\vec{r}', \omega) \quad (13.16)$$

where the integration should be taken over the volume of the scatterer.

13.7 Near-Field Transmission Measurements

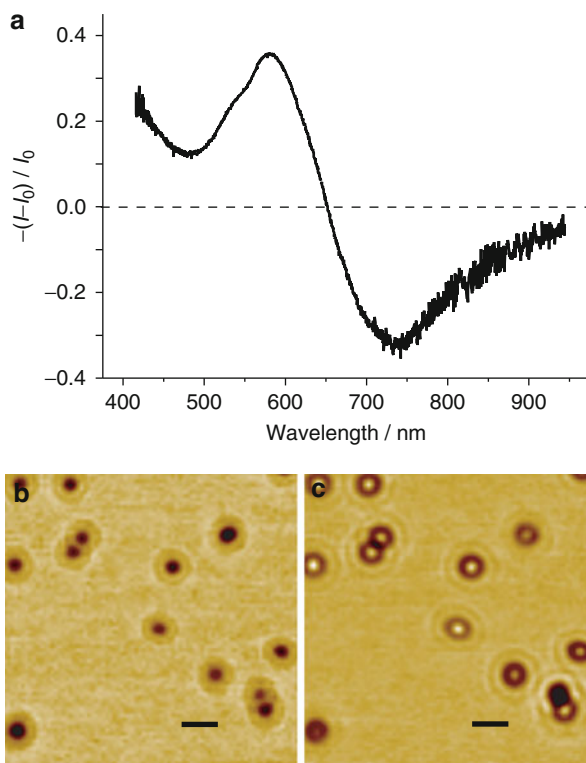
Transmission measurement enables us to gain spectroscopic information with a wide spectral range and thus is generally useful for understanding the basic properties of some materials. However, the near-field version of transmission spectroscopy has not been well utilized partly because of the low light throughput of the near-field probe as well as interference from topographic artifacts as mentioned in the last section. The chemical etching method for near-field probe tip fabrication improves the throughput of the probe greatly [62] and facilitates the transmission spectral measurement practicable level. As for topographic artifacts, pseudo-constant-height mode operation, where the tip travels in a horizontal plane above the substrate, reduces the artifacts to a considerable extent [71, 72], which partially removes this problem. These techniques enable us to obtain reliable spectroscopic information from the near-field transmission measurements.

In far-field measurements, the transmission spectrum is defined as the intensity spectrum for the sample $I(\lambda)$ divided by the intensity spectrum of the reference $I_0(\lambda)$. Instead, the near-field transmission spectrum is obtained by $(I - I_0)/I_0$, where I and I_0 represent the intensity spectrum taken at the sample location and that at the bare substrate, respectively.

13.7.1 Near-Field Transmission Measurement of Spherical Gold Nanoparticles [73]

Figure 13.7a shows a typical near-field transmission spectrum of a single spherical gold nanoparticle (diameter 100 nm). Positive and negative signs in the vertical axis correspond to the reduction and enhancement of transmitted light intensity with respect to that taken at the bare substrate. The spectrum shows a minimum and a maximum at 580 and 730 nm, respectively. Near-field transmission images taken at these wavelengths show reversed optical contrast to each other as shown in Fig. 13.7b, c. The reduction peak observed at 580 nm is very close to the plasmon resonance of the spherical nanoparticle. On the other hand, the transmission enhancement peak appears rather far from the resonance. The enhancement cannot be ascribed to luminescence from the particle because the quantum efficiency of gold is extremely low. The enhanced transmission is attributed to an “antenna effect” of the particle, where the nanoparticle extracts photons from the aperture of the near-field probe and scatters them into the far-field. In the aperture-type near-field microscope, near-field photons are localized at the aperture and can interact with the object only when the object enters the near-field region. During the interaction, the photons are first coupled to the object, and then they are either damped in the object or reradiated toward far-field. The wavelength-dependent coupling between the near-field and the far-field is described by the “near-field scattering” spectrum [74], which can be calculated based on Mie theory. On the other hand, there is a propagating (far-field) radiation component emanating from the aperture, which

Fig. 13.7 (a) Near-field transmission spectrum of a spherical gold nanoparticle (diameter 100 nm). (b) and (c) Near-field transmission images taken at 580 and 720 nm, respectively. Scale bars: 1 μm

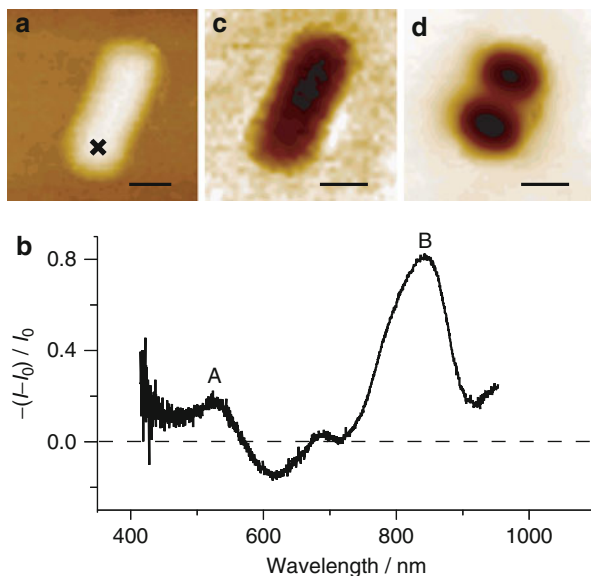


is also scattered and absorbed by the particle. The spectral behavior of this far-field component is also given by Mie theory. The observed transmission spectrum is considered to be composed of these near-field and far-field scattering components. The spectrum simulated using this idea reproduces the enhancement and reduction of transmission and shows good qualitative agreement with the observation. The peak observed near 580 nm can thus be assigned to the dipolar plasmon resonance of the spherical particle.

13.7.2 Near-Field Transmission Measurement of Gold Nanorods [68, 71, 75]

Near-field optical microscopy provides simultaneous observation of topography and optical images, and a direct comparison between the morphology of the sample and optical properties is feasible. Figure 13.8a shows the topography of a short nanorod obtained using a near-field microscope. The topography of the sample is broadened because of the finite size of the tip curvature. The dimensions of the nanorod were estimated from the topography image by taking the tip-broadening effect into account and were determined to be 30 nm in diameter and 180 nm in

Fig. 13.8 (a) Topography of a short gold nanorod (diameter 30 nm, length 180 nm). (b) Near-field transmission spectrum taken at the cross point in (a). (c) and (d) Near-field transmission images taken at 532 and 780 nm, respectively. Scale bars: 100 nm



length. Figure 13.8b shows a near-field transmission spectrum of the nanorod taken at its edge (cross point in Fig. 13.8a). The spectrum shows two major peaks at 530 and 850 nm (denoted as bands A and B, respectively) and a minor peak at 690 nm. The polarization dependence of band A shows the maximum extinction as the incident field is parallel to the short axis of the nanorod. In contrast, the polarization dependence of band B shows the maximum extinction as the field is parallel to the long axis of the nanorod. Based on the polarization dependencies, bands A and B are assigned to transverse and longitudinal plasmon resonances, respectively.

Figure 13.8c, d show near-field transmission images of the nanorod taken at 532 and 780 nm, respectively. The dark parts correspond to reduction of the transmission due to the absorption and scattering of light. The image reflects the transition probability at the tip position. The images observed at 532 and 780 nm are markedly different from each other. The image obtained at 532 nm shows a spatial feature similar to that of the topography image. On the other hand, the image obtained at 780 nm shows an oscillating feature along the long axis of the nanorod. The oscillating feature is well reproduced by the photonic LDOS calculation and is attributed to the square of the amplitude of the wave function associated with a longitudinal plasmon mode resonant with the incident wavelength. The wave function shows a node at the center of the nanorod and is assigned to $m = 2$ mode in Fig. 13.4, which is the second-lowest dipolar mode. The dipolar mode appears at a wavelength longer than $1 \mu\text{m}$. The observed minor peak at 690 nm can be assigned to $m = 3$ mode based on the LDOS calculation as well as the spatial feature of the observed transmission image. As the resonant frequency of the transverse plasmon mode is weakly dependent on mode number (m in Fig. 13.4), the band

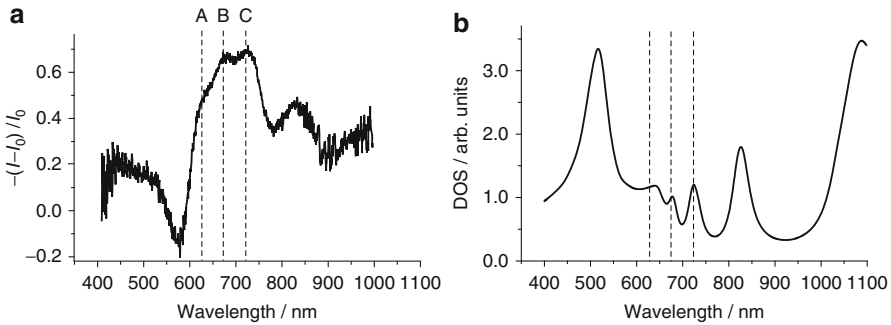


Fig. 13.9 (a) Near-field transmission spectrum of a long gold nanorod (diameter 20 nm, length 510 nm). Dotted lines indicate plasmon resonances. (b) Calculated density-of-states (DOS) spectrum of the gold nanorod

A may originate from various transverse modes. Consequently, the spatial feature in Fig. 13.8c may be attributable to the overlap of many transverse plasmon-mode wave functions.

Plasmon modes with odd parity characters are dipolar forbidden because no polarization is created upon photoexcitation. Observation of the odd plasmon mode in Fig. 13.8d indicates that the optically forbidden mode becomes optically allowed by the local illumination of the near-field. It is also noted that observation of the wave function image indicates that the coherence of the polarization wave extends from the tip position to the whole area of the nanorod.

Figure 13.9a shows the near-field transmission spectrum of a longer nanorod (diameter 20 nm, length 510 nm). Compared with the transmission spectrum of the short nanorod, many plasmon resonances are observable in the spectral region longer than 600 nm. Peak positions of the plasmon resonances are well reproduced by the calculated photonic DOS spectrum in Fig. 13.9b, which was obtained by spatially integrating the LDOS along the nanorod. The peaks are only visible when the incident field is polarized along the long axis of the nanorod and are assigned to longitudinal plasmon resonances. Transmission images at the plasmon resonances are shown in Fig. 13.10a–c along with the corresponding calculated LDOS maps in Fig. 13.10d–f. Periodic oscillating features along the long axis of the nanorod are again observed and are assigned to plasmon wave functions with the mode numbers $m = 5, 6,$ and 7 . It should be noted that the period of spatial oscillation becomes longer as the wavelength of observation increases.

The resonance energy and the wave vector of the plasmon can be obtained from the extinction peak wavelength of the transmission spectrum and the spatial oscillation period of the image of the nanorod, respectively. By plotting the wave vector of the plasmon versus the resonance photon energy, the dispersion relation of the plasmon in the nanorod can be determined. Figure 13.11 shows the dispersion relation determined from near-field transmission measurements of various nanorods with different lengths and the same diameter. The results show that the dispersion

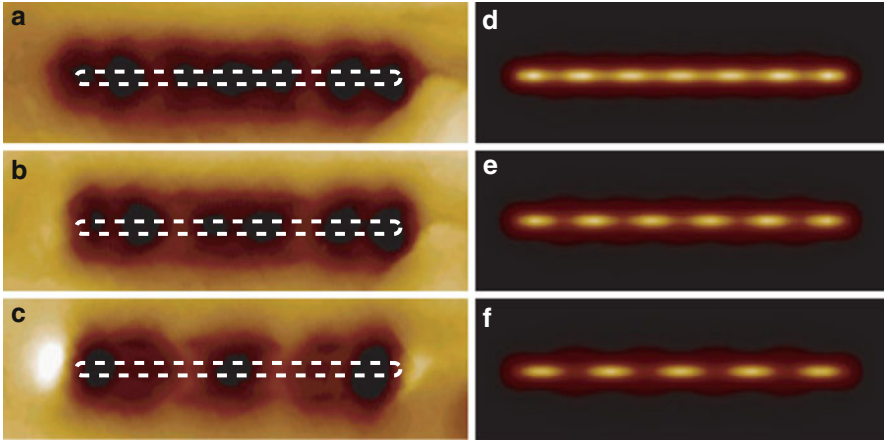
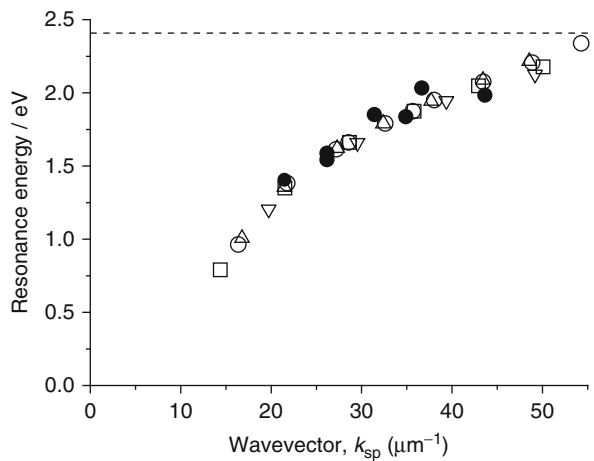


Fig. 13.10 (a)–(c) Near-field transmission images of the gold nanorod (diameter 20 nm, length 510 nm, the same rod as Fig. 13.9) obtained near the plasmon resonances shown in Fig. 13.9a: (a) 647–666 nm, (b) 666–686 nm, (c) 705–725 nm. (d)–(f) Calculated local density-of-states images of the nanorod at (d) 636 nm, (e) 679 nm, and (f) 722 nm, respectively

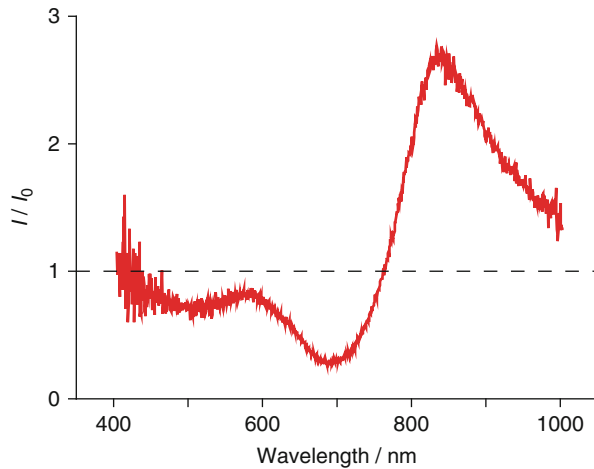
Fig. 13.11 Dispersion relation of single gold nanorods (diameter 20 nm). Closed circles: observations. Open symbols: calculations. Dotted horizontal line indicates the transverse plasmon resonance



relation follows a single dispersion curve regardless of the length of the nanorod if the diameter is the same. The dispersion relation obtained by the DOS calculation also follows the same curve and converges to a value close to the resonance energy of the transverse plasmon.

A similar result was also reported by far-field measurements for gold nanowires fabricated by electron beam lithography [76]. The dispersion relation of the plasmons excited in silver nanorods was also determined in the same manner [77]. The dispersion relation of silver nanorods follows a single curve regardless of the length of the rod, but the dispersion curve depends on the diameter of the rod.

Fig. 13.12 Near-field transmission spectrum of a gold nanodisk (diameter 150 nm, height 35 nm) taken at the center of the disk



The dispersion curve shifts toward the higher-energy side as the diameter increases. The shift has the same origin in the aspect-ratio dependence as that of the resonance wavelength found in the far-field measurement of the nanorods [78] and is attributed to the depolarization effect in the nanorod.

13.7.3 Near-Field Transmission Measurement of Gold Nanodisks [53]

Figure 13.12 shows a typical near-field transmission spectrum of a single gold nanodisk (diameter 150 nm) taken at the center of the disk. The disk diameter is larger than that of the aperture of the near-field probe, and thus the disk geometrically blocked the light path emanated from an aperture of the near-field probe. As is expected from the configuration, in the visible region transmitted light intensity is reduced, compared to that observed at the bare substrate. In the near-infrared region, however, as is opposed to the expectation, transmitted light intensity is enhanced. The spectrum shows a minimum and a maximum in the visible and near-infrared region, respectively. Similar transmission spectral characteristics are also observed for larger disks. The maximum peak shifts to longer wavelength region with an increase of the disk diameter, and the enhancement becomes larger at the same time. These diameter dependencies of the spectral characteristics are consistent with those observed for far-field transmission spectrum of the disks in Fig. 13.3. The enhancement is attributed to the antenna effect of the dipolar plasmon resonance excited, as is also the case for the near-field transmission in the spherical nanoparticles. The spectral features can be reproduced by theoretical simulations taking the near-field and far-field scattering components into account, as described in the near-field transmission measurement of gold spherical nanoparticles in Sect. 13.7.1.

13.8 Time-Resolved Measurements

Photoexcited plasmons decay quickly within a few fs to a few tens of fs, and various energy dissipation processes occur after that [79, 80]. In the case of noble metals, hot electrons are created by electron-electron (e-e) collisions within a few hundreds fs, and the electron distribution is cooled down within several ps by the e-e and electron-phonon (e-ph) scattering processes [47, 81]. The photoexcitation energy is finally released to the heat bath through the phonon-phonon scattering process. Since plasmons are the collective oscillation of free electrons, plasmonic properties are correlated with the electronic distribution and thus the energy dissipation processes. In the case of nanoparticles, as the particle size becomes comparable to the mean-free path of free electrons, the electron-surface scattering may also have some influence on the e-e and e-ph processes. To understand electronic and nonlinear properties of plasmonic materials, dynamics of free electrons after photoexcitation is of special importance. Time-resolved measurements give direct information for that. Far-field studies on colloidal solutions of gold nanoparticles have elucidated decay dynamics of the e-e and e-ph processes [82–84]. The information obtained suffers from the inhomogeneity of the sample, however, and is ensemble averaged over many particles with various sizes and shapes. Time-resolved microscopy enables us to give direct access to the dynamics of single particles. By using a confocal microscope, a single particle study becomes feasible and gives valuable information about dynamics and nonlinearity [85, 86]. Though confocal microscopy can achieve very high time resolution (15 fs) [87], the spatial resolution of the conventional microscope is limited to submicrons, and thus position-dependent dynamics on the nanostructures cannot be directly investigated. The combination of near-field microscopy with time-resolved methods achieves high time resolution of less than 100 fs with a higher spatial resolution in a wide spectral range for various samples under ambient conditions. A typical example for the study of gold nanoparticles is described below. Time-resolved photoemission electron microscope (PEEM) also enables ultrafast measurements with a high spatial resolution under high vacuum. By using the two-photon excitation scheme of the PEEM process, propagation of the excited plasmon in metal films was visualized [88, 89].

We describe here the result of ultrafast near-field measurements on a gold nanorod (diameter 30 nm, length 300 nm) [68]. In the polarized near-field transmission spectrum, the nanorod (Fig. 13.13a, b) shows a longitudinal plasmon resonance at 750 nm. A near-field transmission image taken at 750 nm shows two dark spots on both sides and a node at the center of the nanorod (Fig. 13.13c). The spatial feature is in excellent agreement with the calculated photonic LDOS at the excitation wavelength. The spatial feature of the image is assigned to the plasmon wave function of $m = 2$ mode. Similarly, a near-field transmission image taken at 900 nm (Fig. 13.13d) is assigned the plasmon wave function of $m = 1$ mode. To examine the ultrafast dynamics in the nanorod, the single-color EPC method was adopted, with near-infrared pulses as the excitation sources. At the excitation wavelength, both the $m = 1$ and $m = 2$ modes were excited at the same time. In EPC,

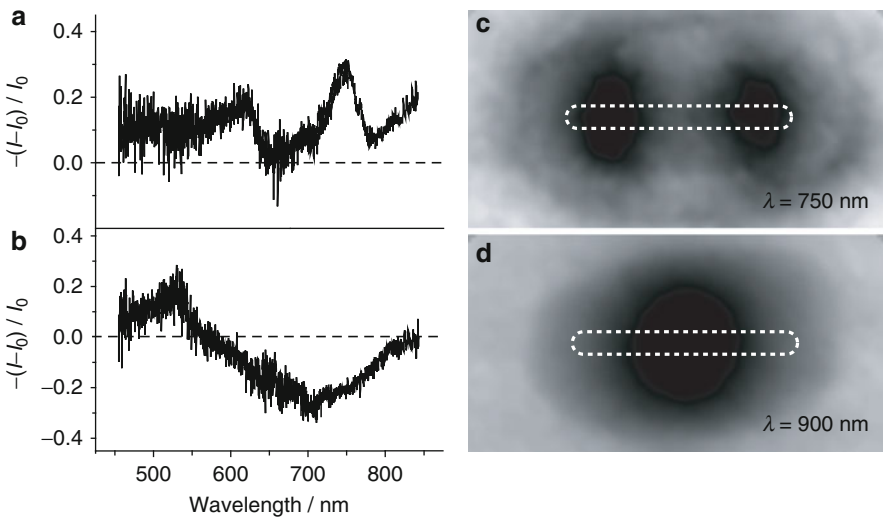


Fig. 13.13 (a) and (b) Polarized near-field transmission spectrum of a gold nanorod (diameter 30 nm, length 300 nm); polarization parallel (a) and across (b) to the long axis of the nanorod. (c) and (d) Polarized near-field transmission images obtained at 750 and 900 nm, respectively. Polarization is parallel to the long axis of the nanorod

the pump pulse induces the transient absorption in the nanorod, and the probe pulse is used to detect the transient transmission change. Ultrafast dynamics in the nanorod can be investigated by detecting the transmission change as a function of pump-probe delay time. Figure 13.14 shows the pump-probe time-resolved traces taken at various positions in the nanorod. Depending on the position on the nanorod, the time-resolved signal shows the induced and bleached absorption. Because the e-e and e-ph processes in noble metals occur at different time scales in the fs to ps regime, the observed pump-probe trace was analyzed by double exponential functions. The results of the analysis are summarized in Table 13.1. The fast component with a time constant of 600 fs was observed in the entire nanorod and is attributed to the e-e scattering. The slow component with a ps time constant was observed everywhere except at the center and is attributed to the e-ph scattering. The ps component varies from 2.8 to 1.5 ps depending on the position on the nanorod and becomes faster toward the end of the nanorod. The short lifetime at the end and the position dependence may indicate that the electron-surface scattering has some influence on the dynamics of the e-ph scattering. However, the far-field studies using ensembles of colloidal solutions concluded that the electron-surface scattering is of great significance only for nanoparticles smaller than 10 nm, which is contradictory to the interpretation above [90–92]. Further investigation is underway to clarify the position-dependent energy dissipation processes observed in the near-field measurements.

Fig. 13.14 Transient transmission signal traces obtained in the gold nanorod (diameter 30 nm, length 300 nm). *Solid curves* indicate double (for *a, c–e*) and single (for *b*) exponential fits. Inset: observed positions in the nanorod

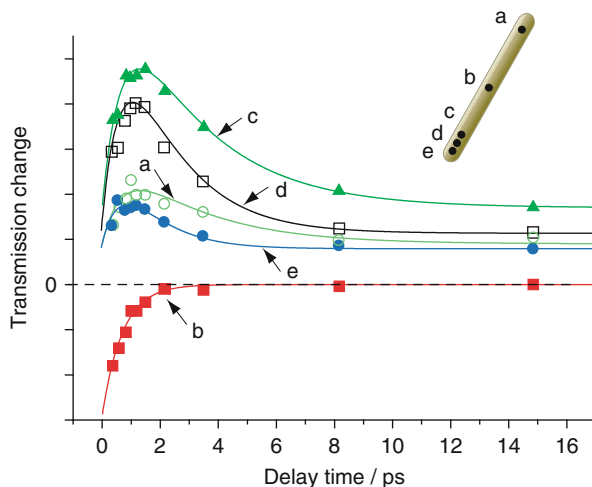


Table 13.1 Time constants of relaxation after photoexcitation in the nanorod obtained from double exponential fits

Position	$t_{\text{fast}}/\text{ps}$	$t_{\text{slow}}/\text{ps}$
a	0.6	2.8
b	0.6	–
c	0.6	2.8
d	0.6	1.8
e	0.6	1.5

The spatiotemporal behavior of the nanorod can be visualized by detecting the transmission change at a fixed delay time while scanning the nanorod position to obtain a near-field transmission image. Figure 13.15a shows the transient transmission image of the nanorod at a 600 fs delay. Dark and bright parts in the image correspond to the reduction (bleached absorption) and enhancement (induced absorption) of the transmission induced by the pump pulse. Interestingly, both bleached and induced absorptions are observed in the single nanorod. To reveal the origin of the spatial feature, an electromagnetic simulation was performed [93]. In the simulation, the electronic temperature in the nanorod was assumed to be homogeneously elevated upon photoexcitation. An ultrafast study of gold films reported that the heat transport in a 300 nm thick gold film occurs within 300 fs [81, 94]. If the heat transport mechanism in the nanorod is similar to that in the metal film, it is reasonable to consider that the electronic temperature in the nanorod is homogeneously increased and equilibrated within 600 fs. It may also be reasonable to consider that the transient transmission change at each position arises from the LDOS change due to the elevation of the electronic temperature, since the static near-field transmission images are well reproduced by the LDOS maps

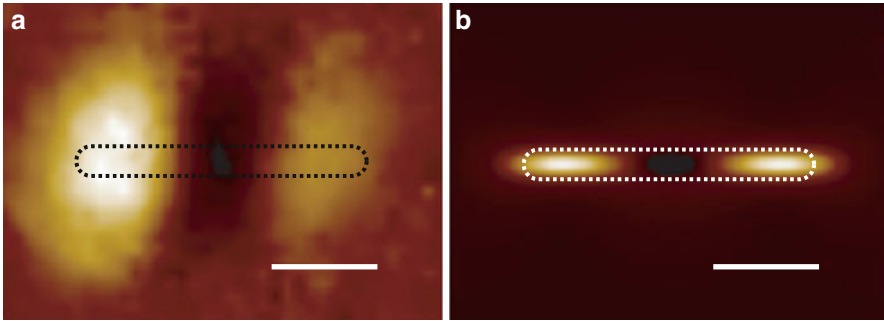


Fig. 13.15 (a) Near-field transient transmission image of the nanorod taken at delay time of 600 fs. (b) Simulated transient transmission image of the nanorod. *Dotted lines*: approximate shape of the nanorod. Scale bars: 100 nm

as shown in the previous section. Thus, we assume that the transient transmission change ΔI is proportional to the difference between LDOS at room temperature and that at elevated temperature:

$$\Delta I(\vec{r}, \omega) = \rho(\vec{r}, \omega, T + \Delta T) - \rho(\vec{r}, \omega, T) \quad (13.17)$$

where ΔT denotes the electronic temperature change induced by the pump pulse. The temperature dependence of the LDOS originates from the variation of the dielectric function of the material and induces variation of the spatial feature of the LDOS. Figure 13.15b shows the simulated image based on Eq. 13.17. Bright and dark parts in the image correspond to the increase and decrease of the LDOS, respectively. The spatial feature calculated is well correlated to the observed image. Upon elevation of the electronic temperature, plasmon resonance energies of both $m = 1$ and $m = 2$ modes are shifted to the red, which makes the contributions of these modes to the image at the probe wavelength different from those at room temperature. The increased LDOS in both sides and the decreased LDOS at the center arise from this effect. Transient images of other nanorods with different diameters and/or lengths sometimes show reversed optical contrasts. Also, in such cases, the images are well reproduced in terms of variation of the LDOS under elevated electronic temperature. These results indicate that the transient image of the nanorod arises from the deformation of plasmon wave functions induced by a rise in electronic temperature in the nanorod.

Ultrafast dynamics investigated here are the phenomena that occur after the plasmons are completely dephased. Spatiotemporal dephasing dynamics of plasmon waves is of prime importance in attaining a deeper understanding of plasmons. For this purpose, ultimately high time resolution (several fs), which is shorter than the lifetime of the plasmon, is required and is still a challenge for near-field optical microscopy to achieve.

13.9 Nonlinear Measurements

Nonlinear optical methods have various advantages over linear methods [95]. Spatial resolution, optical contrast, and occasionally, signal-to-noise ratio can be improved in the nonlinear measurements with respect to those of the linear measurements. In addition, the nonlinear methods often enable us to obtain information that is not accessible by linear methods. Since high peak power is essential to excite the nonlinear processes, a pulse laser with a short pulse width is frequently used. For excitation of the nonlinear processes, spatial confinement and focusing of light is helpful. Combination of the near-field method and the short pulse laser source enables effective excitation of nonlinear processes, such as two-photon-induced photoluminescence (PL), second harmonic generation (SHG), and so forth in nanomaterials.

The quantum yield of PL from gold is extremely low [96]. This is because the excited energy decays very rapidly through non-radiative processes before the excited energy decays by radiating photons to the far-field. Recently, many research groups reported that the PL from gold is significantly enhanced when the PL is excited by two-photon absorption [97–101]. The two-photon absorption process in materials occurs via either simultaneous or sequential photon absorptions. The two-photon signal intensity scales with the square of the incident power, in contrast to the one-photon signal where the intensity scales linearly with the incident power. Thus, two-photon-induced PL (TPI-PL) is more sensitive to the optical field than one-photon PL. Near-field TPI-PL of gold holds great potential in visualizing the enhanced optical field in the vicinity of gold nanostructures. TPI-PL of gold has been applied in, for example, white-light continuum generation [102] and bioimaging [103–105]. In this section, visualization of the optical fields for single gold nanoparticles [97, 106, 107], and their assembly [108–111], using near-field TPI-PL is described.

The PL process of gold begins with the excitation of an electron in the d band to the sp band above the Fermi level and the creation of a hole in the d band [112, 113]. Photoluminescence is radiated after a manifold of collision processes occur when the electron-hole pair recombines. With near-field irradiation of infrared light pulses (800 nm), some gold nanoparticles emit strong PL in the visible spectral range. From the incident power dependence of the PL intensity, it was confirmed that the PL was excited by two-photon absorption. Spherical gold nanoparticles show no TPI-PL, but the gold nanorod exhibits strong TPI-PL. [Figure 13.16a](#) shows a typical spectrum of TPI-PL from a single gold nanorod. TPI-PL shows two bands near 550 and 620 nm. The relative intensity of the two bands varies depending on the size and shape of the particle. However, the peak positions of the two bands show little dependence. Based on the band structure calculation of gold [114], the photon energies of these two bands are in good agreement with the band gap energies between the d band and the Fermi energy levels near the L and X symmetric points, respectively. The two bands are thus assigned to radiative recombination of an electron in the sp band near the Fermi energy level and a hole in the d band

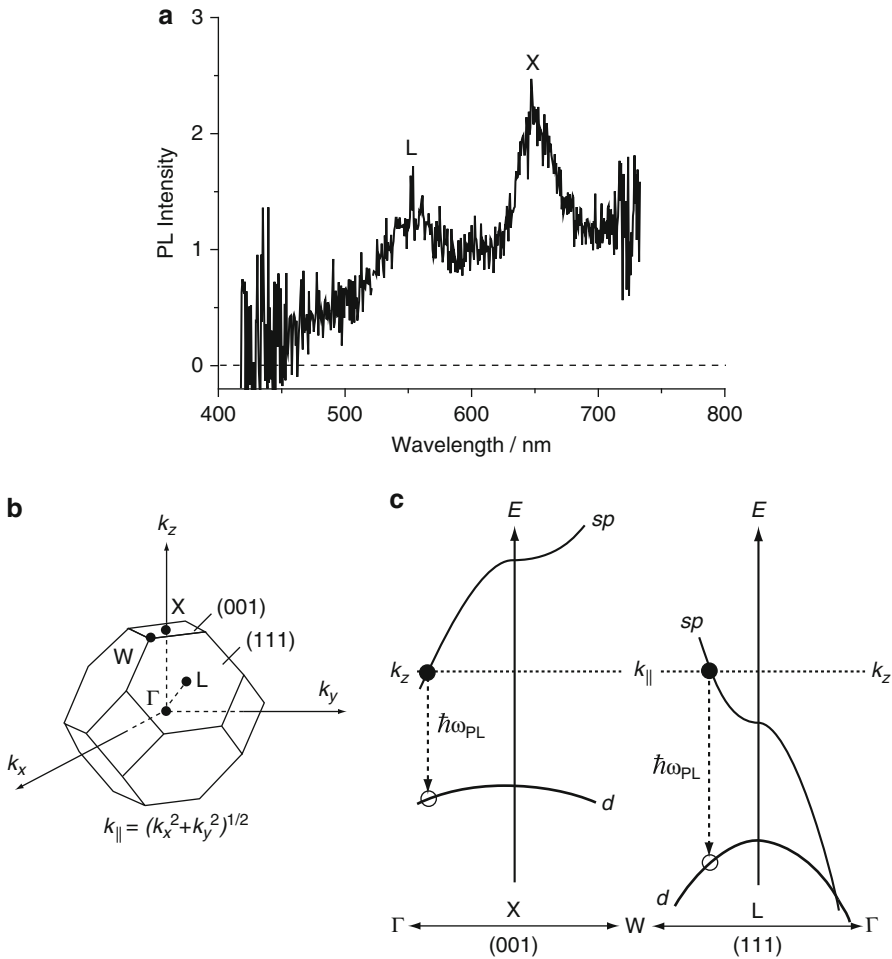


Fig. 13.16 (a) Two-photon induced photoluminescence from a single gold nanorod. (b) Symmetry points and axes in the first Brillouin zone of gold. (c) Band structures of gold near the X and L symmetric points. The notations sp and d denote, respectively, the sp conduction band and the d valence band. The *dashed line*: Fermi energy level. $\hbar\omega_{\text{PL}}$: photon energy of photoluminescence radiated through recombination of an electron-hole pair

near these symmetric points (Fig. 13.16b, c). Polarization characteristics of PL for these bands are also consistent with the emission mechanism described above and the crystalline structure of the gold. Incident polarization dependence of the TPI-PL intensity indicates that the two-photon process occurs through the sequential absorption of photons via the intermediate state. Time-resolved measurements for the TPI-PL revealed that the lifetime of the intermediate state is shorter than several tens of fs.

13.9.1 Gold Nanorods [97, 106]

Visualization of the optical field is feasible by detecting the PL intensity while scanning the sample surface laterally. Optical images obtained in this way reflect the excitation probability at the tip position (we should note that the observed image is not the map of PL intensity itself). [Figure 13.17](#) shows the two-photon excitation images of single gold nanorods. Similar to the transmission image ([Fig. 13.10](#)), periodic spatial oscillation along the long axis of the nanorod is found in [Fig. 13.17a](#). The period of the oscillation depends on the incident wavelength and becomes longer with increasing wavelength. By comparing with the calculated photonic LDOS map, the observed oscillating feature is attributable to the plasmon wave function resonant with the incident photons. As mentioned before, the two-photon process is very sensitive to the optical field strength, and the image reflects the enhanced optical fields in the vicinity of the nanorods. In the present case, the PL signal was enhanced because of the resonance between the incident field and the plasmon mode of the nanorod, which was confirmed by the excitation wavelength dependence. Some gold nanorods show different spatial features in which the optical fields are enhanced only at the end parts of the nanorod, as shown in [Fig. 13.17b](#). It is known that the optical field enhancement occurs at sharp corners or edges of metal nanostructures. This is known as the “lightning rod effect” [115–117]. The effect is mainly determined by the geometry of the sample and shows little dependence on the incident wavelength. In [Fig. 13.17b](#), the lightning rod effect is dominant over the plasmon-mode resonance enhancement. Difference between [Fig. 13.17a, b](#) may originate from the difference in the resonance conditions of the nanorods or from microscopic structures created at the edges of the nanorod.

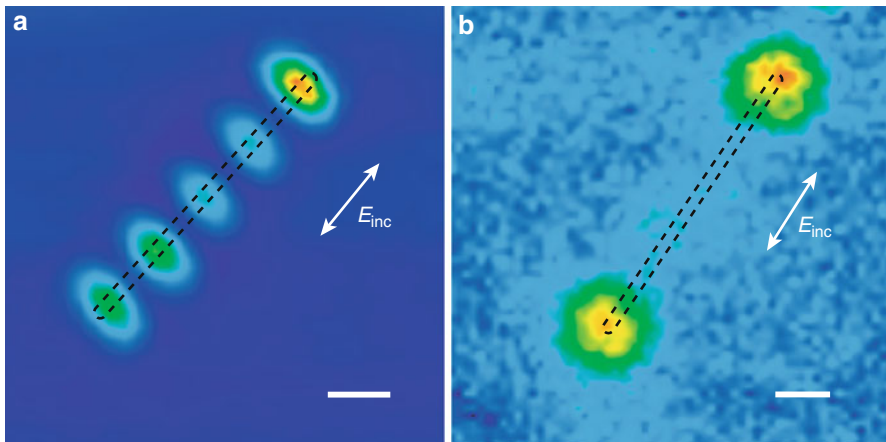


Fig. 13.17 Two-photon excitation images of single gold nanorods. (a) Diameter 20 nm, length 540 nm, (b) diameter 21 nm, length 565 nm (The images are taken at 780 nm excitation). *Dotted lines*: approximate shape of the nanorod. Scale bars: 100 nm

13.9.2 Gold Nanoplates [107]

Near-field TPI-PL excitation imaging is applicable to various shapes of nanoparticles. Two-dimensional structures such as nanoplates are of fundamental interest in optical-field imaging because the excited plasmons may extend over the nanoparticles as two-dimensional waves. The TPI-PL intensities of gold nanoplates are found to be, in general, more intense than those of gold nanorods. Single gold triangles show one or two orders of magnitude more intense PL compared to gold nanorods. The optical field enhancement in the nanotriangles is also interesting in relation to SERS. Figure 13.18a shows a near-field two-photon excitation image of a single nanotriangle. The dotted line in the figure shows the approximate shape of the particle estimated from the topography image. The two-photon excitation image shows that the excitation is probably highly localized near one of the apexes of the triangle. It is noted that the lightning rod effect was operative at the sharp corners or at the edges and was observed in the nanorod (Fig. 13.17b). In Fig. 13.18a, however, the enhanced field observed is located at the inner part of the triangle. In addition, it was found that the excitation probability (i.e., the PL intensity) is very sensitive to the excitation wavelength. As described before, the lightning rod effect shows little wavelength dependence, but the plasmon-mode resonance effect shows strong wavelength dependence. It is likely that in the triangle the plasmon resonance effect is dominant over the lightning rod effect. The calculated optical field image in Fig. 13.18b is in excellent agreement with the observation, and the spatial feature found in the image is assigned to the plasmon wave function resonantly excited with the incident wavelength. The location of the enhanced optical field can be controlled from one apex to the other by rotation of the incident-field polarization. This fact

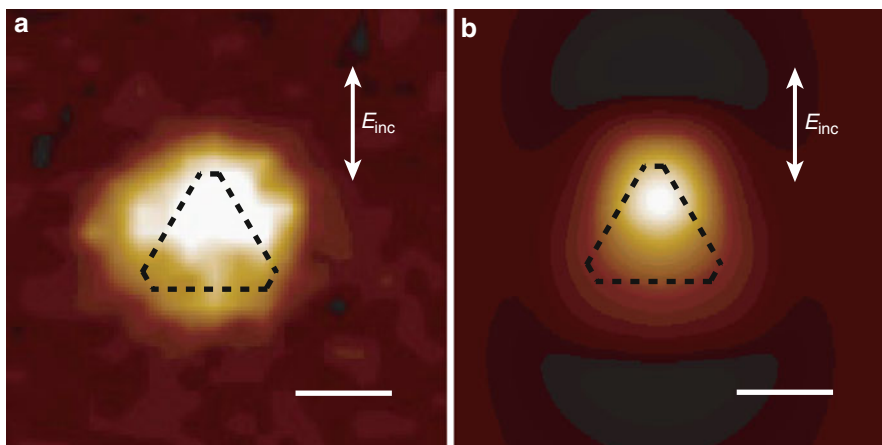


Fig. 13.18 (a) Two-photon excitation image of a *triangular* gold nanoplate (thickness 18 nm, base length 160 nm). (b) Calculated optical field distribution near the triangle. *Arrows* indicate the incident polarization. *Dotted lines*: approximate shape of the *triangle*. Scale bars: 100 nm

indicates that the plasmon mode is degenerated as a pair of two-dimensional waves with a degenerate resonance frequency, and one of the waves can be selectively visualized by the polarized incident light.

13.9.3 Dimeric Nanoparticles [108, 109]

Assemblies of nanoparticles exhibit very unique properties which are very different from those of single nanoparticles. The unique properties sometimes originate in near-field interactions between elemental excitations such as excitons and plasmons. Near-field interactions between optical fields and molecules also give rise to remarkable phenomena such as SERS [118]. Signal enhancement of SERS is 10^4 - to 10^6 -fold on roughened metal surfaces or on isolated metal particles [6, 12]. Noble metal nanoparticle dimers were predicted theoretically to exhibit extraordinarily enhanced optical fields at the junctions of the dimers [119–121]. In the late 1990s, SERS with single-molecule-level sensitivity was reported experimentally [10, 11], and since then, noble metal nanoparticle dimers have been studied extensively as prototypical systems to theoretically examine the mechanism of the enhancement. Figure 13.19a, b show typical examples of calculated optical field intensity maps for a gold nanosphere dimer. When the incident field is polarized across the interparticle axis of the dimer (Fig. 13.19a), the field is only slightly enhanced. This is because plasmons excited in the individual particles do not interact with each other through the gap. On the contrary, when the incident field is polarized along the interparticle axis of the dimer (Fig. 13.19b), the field is significantly enhanced at the junction. The enhancement mechanism can be explained by considering the near-field interaction of plasmons in the dimer. As the incident field is parallel to the dimer axis, particle plasmons excited in individual particles interact with each other through the space at the junction, and a new plasmon resonance (“dimer plasmon” mode) is formed. The dimer plasmon amplifies the optical field greatly up to four orders of magnitudes because of the Coulombic interaction at the junction. In SERS, signal enhancement is operative not only for the incident field but also for the scattering radiation, and thus signal enhancement is approximately proportional to the fourth power of the field enhancement. The enhancement of SERS thus reaches 10^{11} – 10^{13} in the highest case. If the optical field localized at the interstitial site is visualized in real space, it is highly advantageous in the detailed investigation of SERS mechanisms. Near-field TPI-PL imaging is promising for this purpose. Visualization of the enhanced fields is important not only for understanding the SERS mechanism but also for applications of the field enhancement to photochemical reactions. Recently, it has been reported for noble metal nanoparticle dimers that the multiphoton polymerization reaction is promoted predominantly at the junction of the dimer [18].

Figure 13.19c shows a typical topography image of dimeric and isolated gold nanoparticles prepared on a cover slip. From the SEM observation of the sample, particles in the aggregate do not directly contact each other but are separated by a few nm to 10 nm. A two-photon excitation image of the sample is shown in Fig. 13.19d.

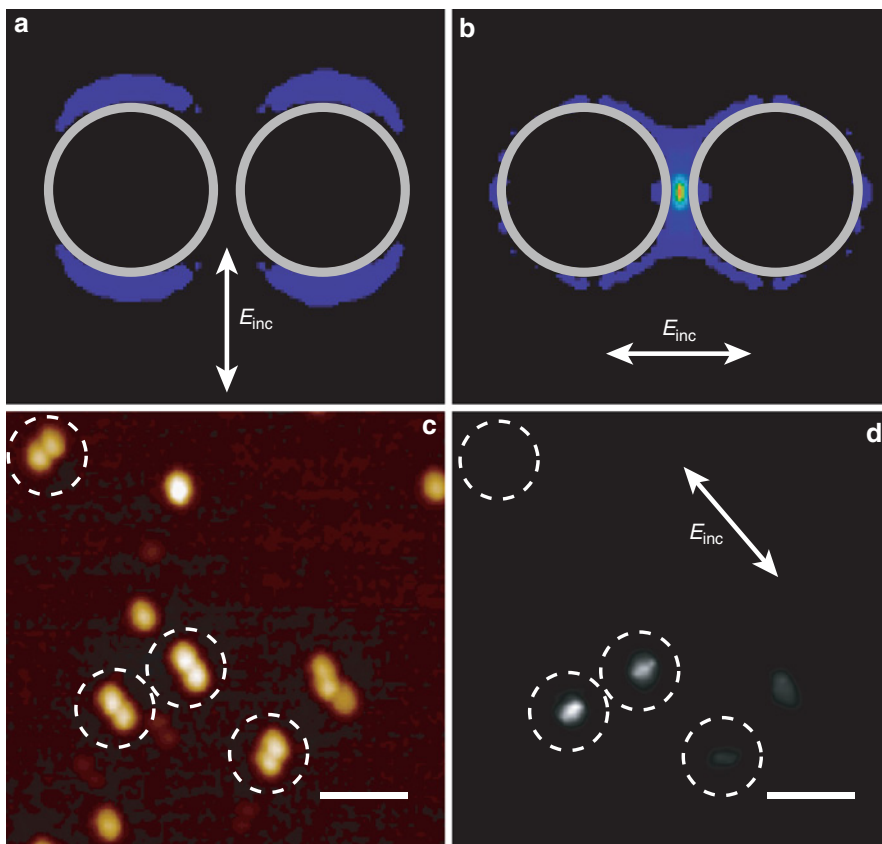


Fig. 13.19 (a) and (b) Calculated optical field distributions near a dimer of spherical gold nanoparticles (diameter 100 nm). *Arrows* indicate the incident polarization. (c) Topography of single and aggregated gold nanoparticles. (d) Two-photon excitation image of the sample (c) taken with incident polarization indicated by the *arrow*. Scale bars: 500 nm

The image obtained sensitively reflects the optical field distribution of the sample. The optical field of the sample was greatly enhanced at the dimers (and at the trimer) in comparison with the isolated nanoparticles. Among four dimers in the sample, two dimers whose axes were parallel to the polarization of the incident light exhibited huge enhancements at the interstitial sites of the dimers. The other two dimers, whose axes are perpendicular to the incident field, showed only little enhancement. These observations are in excellent agreement with the theoretical predictions illustrated in Fig. 13.19a, b.

To examine the influence of the localized optical field on Raman enhancement, dimeric gold nanospheres doped with Raman active dye molecules were investigated. Figure 13.20a shows the topography of the sample and Fig. 13.20b the near-field excited Raman spectrum for dimer A. Raman scattering excited at the

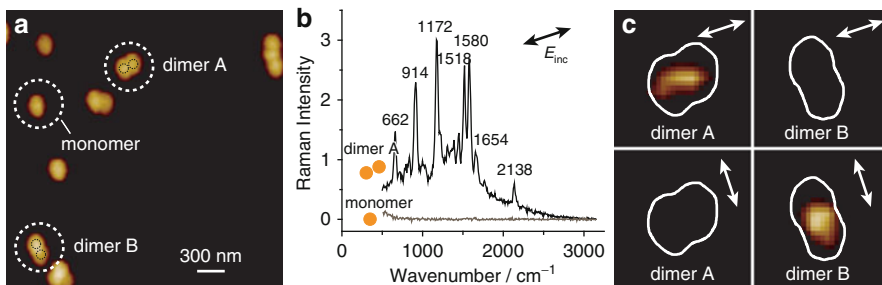


Fig. 13.20 (a) Topography of single and aggregated gold nanoparticles. (b) Near-field Raman spectra taken at dimer A and the isolated particle indicated in (a). Excitation wavelength is 785 nm. (c) Polarized near-field Raman excitation images of the dimer A and dimer B. Arrows indicate the incident polarization. Solid curves: approximate shape of the dimer

interstitial site of the dimer shows very high intensity in Fig. 13.20b. Most of the bands observed are assigned to vibrational modes of the dye molecule [122]. Raman active sites can be visualized by monitoring one of the vibrational bands while the sample position relative to the probe is scanned. Figure 13.20c shows the observed near-field Raman excitation image, and the Raman active site is localized at the junction. Raman signal is strongest as the incident field is polarized along the interparticle axis of the dimer. The location of the Raman active site spatially overlaps well with the alternatively visualized optical field in the near-field TPI-PL experiment [109]. These results are consistent with the proposed SERS mechanism described above. The average number density of dye molecules was about 100 molecules/ μm^2 , which means only several molecules were excited at the near-field probe tip. From this figure, the Raman enhancement factor is estimated to be even greater than 10^{10} at the most intense sites. Furthermore, Raman signals fluctuate at a time scale of a few seconds, which suggests that the Raman signal originates from a very small number of molecules. These observations indicate that single-molecule-level sensitivity has been achieved in this near-field SERS experiment, where optical field enhancement at the junction of the dimer is essential for the giant Raman signal.

13.9.4 Larger Assemblies of Nanoparticles [110, 111]

In many-body assemblies of nanoparticles, a number of interparticle near-field interactions are involved and may give further unique properties. Many-particle assemblies have been paid much attention in relation to the development of the SERS active substrates. Various protocols have been reported for the preparation of the assemblies with close-packed forms [123–125]. Most of them give moderate SERS enhancements on the order of 10^6 – 10^8 , which are much lower than those needed for single-molecule-level sensitivity. The results may indicate that a simple increase of the particle number in the assembly is not enough to attain the ultimate

field enhancement. To clarify the reason for this finding, visualization of the optical field is one of the most straightforward methods.

Figure 13.21a shows a near-field two-photon excitation image of an island-like assembly of gold nanospheres (diameter 100 nm). Because the topography image obtained simultaneously with the near-field image is not clear enough to discuss fine details of the nanostructures, such as the interparticle separation of the nearly touching nanoparticles, SEM observation of the sample is of great use to gain finer information of the nanostructure. From the SEM image in Fig. 13.21b, the interparticle distances were found to be less than 10 nm for the close-packed portion. The optical-field image in Fig. 13.21a reveals that the enhanced field is nonuniformly distributed over the island-like assembly. The enhancement is more significant at the rim of the assembly than at the inner part. The difference between the inner part and the rim may originate from the delocalization character of plasmon excitations in the assembly. At the inner part, particles are surrounded by many particles, and excited plasmons may propagate in all of the directions through the near-field interactions. On the other hand, at the rim part, particles are only partially surrounded by the other particles. Localization of the excited plasmon may be stronger in this case because the plasmon propagation into the surroundings is geometrically restricted compared with that at the inner part.

From close inspection of the image, it is found that the highest enhancement occurs at the isolated dimer A, and the enhancement observed at the rim or at the defect sites in the assembly is lower. This observation implies that the enhancement is the highest in the dimer and becomes lower with increasing size of the assembly. The finding may have some correlation with the relatively low SERS enhancement reported in close-packed assemblies. Plasmon localization at the rim of the assembly may have some similarities with photon localizations at the boundaries of photonic crystals [126]. The analysis based on FDTD approach as well as simple point dipole model that incorporates the interparticle interaction through dipole-dipole potential

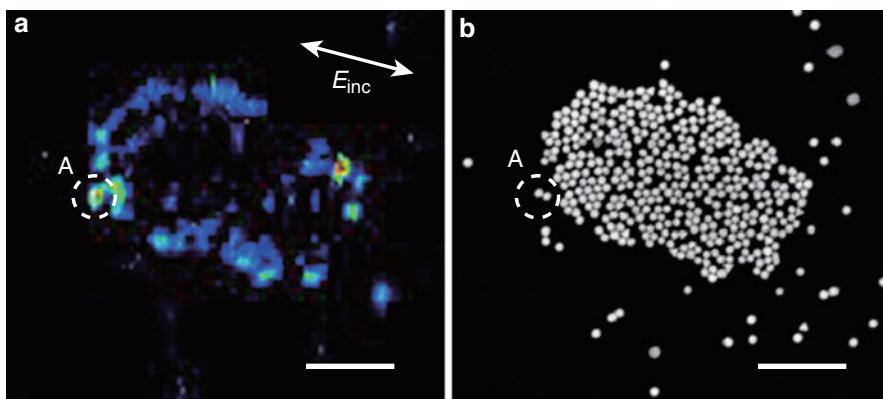


Fig. 13.21 (a) Near-field two-photon excitation image of an assembly of spherical gold nanoparticles (diameter 100 nm). (b) SEM image of the assembly. Scale bars: 1 μm

revealed that the interparticle interaction, that causes the propagation of the plasmon excitation in the assembly, are essential for the localization of the enhanced field at the rim [127].

Near-field observation of the optical field distribution in the nanostructures reveals a wealth of information about the enhancement mechanism of the optical field and will give useful guidelines to design a desirable SERS substrate. It is also practically important to consider the potential applications of the confined optical fields to nano-optical devices, bioimaging, and photochemical reactions.

13.10 Summary

In this review, the visualization of plasmon wave functions and optical fields using near-field methods was described. Longitudinal plasmon wave functions visualized for single gold nanorods showed periodic spatial oscillations along the long axis of the nanorod. The periods of the oscillations depended on the excitation wavelength and became longer with the increase of the excitation wavelength. Spatial features of the plasmon wave functions and their resonance energy dependencies were similar to those in the “particle in a box.” The number of nodes in the wave function increased with the increment of the eigen energy of the plasmon mode. Spatiotemporal behaviors of the plasmon wave function upon photoexcitation were also discussed. Visualized transient transmission images of the nanorod showed characteristic spatial features that were different from the static plasmon wave function images. The observed transient image was understood as a variation of plasmon wave functions due to the elevation of the electronic temperature in the nanorod.

The optical fields excited in various nanostructures were visualized with the nonlinear near-field imaging technique. The optical field strength in the nanorod was found to be larger than that in the spherical nanoparticle and was effectively enhanced either by the resonance excitation of a plasmon mode or by the lightning rod effect. In the case of the dimer of nanoparticles, the near-field interaction of plasmons excited in the individual nanoparticles induced extraordinarily large enhancements of the optical field with respect to that of the isolated nanoparticle. The optical field induced in the interstitial site of the dimer was found to enhance Raman scattering from molecules, and the sensitivity was close to the single-molecule level. For the larger assembly, the optical field was larger at the rim of the assembly than at the internal positions of the assembly. The distribution of the optical fields in the assembly was discussed in relation to the spatial localization character of the plasmons.

In the near future, dynamic visualization of plasmon wave functions will become more important. Experimentally, however, imaging with time resolutions shorter than the lifetime of a plasmon (<20 fs) is a challenge. On the other hand, electromagnetic field calculation has fewer barriers and is feasible. Calculation protocols with high precision, high reliability, and reasonable computational cost

are expected to be developed and applied to reveal the dynamic features of plasmon wave functions.

Basic studies on plasmons and their related materials will influence wider research areas in fundamental and applied fields. Among them, applications of plasmonic optical fields to photochemical reactions have a large impact in photo- and material-sciences. For instance, the interaction between localized optical (or plasmon) fields with molecular electronic wave functions may enhance photochemical reaction rates, which is sometimes forbidden under the far-field irradiation of light. It has a potential to open up new chemical reaction routes beyond the dipolar approximation. Such novel photochemical reactions shed new light on photo- and material-sciences.

Acknowledgements The authors thank Dr. T. Nagahara (Kyoto Inst. Tech.), Dr. J. K. Lim (Chosun Univ.), Dr. N. Horimoto (Tohoku Univ.), Dr. T. Shimada (Hiroasaki Univ.), Dr. M. K. Hossain (King Fahd Univ.), Prof. M. Kitajima (Natl. Def. Acad.), Profs. K. Ueno, and H. Misawa (Hokkaido Univ.) for their many essential contributions to this work. The authors also thank the Equipment Development Center of IMS for collaboration in construction of the SNOM apparatus. This work was supported by the Asahi Glass Foundation, the Sumitomo foundation, the Research Foundation for Opto-Science and Technology, Grants-in-Aid for Scientific Research (Grant Nos. 16350015, 16750017, 17655011, 17034062, 18205004, 18685003, 19049015, 22655007, and 22225002) from the Ministry of Education, Culture, Sports, Science and Technology, the Asian CORE program from the Japan Society for the Promotion of Science, and JST PRESTO.

References

1. M. Kerker, *The Scattering of Light and Other Electromagnetic Radiation* (Academic, New York, 1969)
2. U. Kreibig, M. Vollmer, *Optical Properties of Metal Clusters* (Springer, Berlin, 1995)
3. C.F. Bohren, D.R. Huffman, *Absorption and Scattering of Light by Small Particles* (Wiley, New York, 1998)
4. R.H. Ritchie, *Surf. Sci.* **34**, 1 (1973)
5. S. Kawata, *Near-Field Optics and Surface Plasmon Polaritons* (Springer, Berlin, 2001)
6. M. Moskovits, *Rev. Mod. Phys.* **57**, 783 (1985)
7. M. Fleishmann, P.J. Hendra, A.J. McQuillan, *Chem. Phys. Lett.* **26**, 163 (1974)
8. D.J. Jeanmaire, R.P. Van Duyne, *J. Electroanal. Chem.* **84**, 1 (1978)
9. M.G. Albrecht, J.A. Creighton, *J. Am. Chem. Soc.* **99**, 5215 (1977)
10. S. Nie, S.R. Emory, *Science* **275**, 1102 (1997)
11. K. Kneipp, Y. Wang, H. Kneipp, L.T. Perelman, I. Itzkan, R.R. Dasari, M. S. Feld, *Phys. Rev. Lett.* **78**, 1667 (1997)
12. G.C. Schatz, R.P. Van Duyne, *Handbook of Vibrational Spectroscopy*, ed. by J.M. Chalmers, P.R. Griffiths (Wiley, New York, 2002)
13. S.A. Maier, M.L. Brongersma, P.G. Kik, S. Meltzer, A.A.G. Requicha, H.A. Atwater, *Adv. Mater.* **13**, 1501 (2001)
14. N.F. van Hulst, *Nature* **448**, 141 (2007)
15. N. Engheta, *Science* **317**, 1698 (2007)
16. R.M. Stöckle, Y.D. Suh, V. Deckert, R. Zenobi, *Chem. Phys. Lett.* **318**, 131 (2000)
17. N. Hayazawa, Y. Inouye, Z. Sekkat, S. Kawata, *Chem. Phys. Lett.* **335**, 369 (2001)
18. K. Ueno, S. Juodkazis, T. Shibuya, Y. Yokota, V. Mizeikis, K. Sasaki, H. Misawa, *J. Am. Chem. Soc.* **130**, 6928 (2008)

19. Y. Tsuboi, R. Shimuzu, T. Shoji, N. Kitamura, *J. Am. Chem. Soc.* **131**, 12623 (2009)
20. A.N. Grigorenko, N.W. Roberts, M.R. Dickinson, Y. Zhang, *Nat. Photon.* **2**, 365 (2008)
21. M. Righini, P. Ghenuche, S. Cherukulappurath, V. Myroshnychenko, F.J. García de Abajo, R. Quidant, *Nano Lett.* **9**, 3387 (2009)
22. W. Zhang, L. Huang, C. Santschi, O.J.F. Martin, *Nano Lett.* **10**, 1006 (2010)
23. Y. Tsuboi, T. Shoji, N. Kitamura, M. Takase, K. Murakoshi, Y. Mizumoto, H. Ishihara, *J. Phys. Chem. Lett.* **1**, 2327 (2010)
24. E. Pordan, C. Radloff, N.J. Halas, P. Nordlander, *Science* **302**, 419 (2003)
25. W.L. Baner, A. Dereux, T.W. Ebbesen, *Nature* **424**, 824 (2003)
26. E. Ozbay, *Science* **311**, 189 (2006)
27. R. Zia, M.L. Bringersma, *Nat. Nanotechnol.* **2**, 426 (2007)
28. N. Fang, H. Lee, C. Sun, X. Ahang, *Science* **308**, 534 (2005)
29. M. Aeschlimann, M. Bauer, D. Bayer, T. Brixner, F.J. Garcia de Abajo, W. Pfeiffer, M. Rohmer, C. Spindler, F. Steeb, *Nature* **446**, 301 (2007)
30. A.V. Akimov, A. Mukherjee, C.L. Yu, D.E. Chang, A.S. Zibrov, P.R. Hemmer, H. Park, M.D. Lukin, *Nature* **450**, 402 (2007)
31. S. Kim, J. Jin, Y.-J. Kim, I.-Y. Park, Y. Kim, S.-W. Kim, *Nature* **453**, 757 (2008)
32. H.J. Lezec, J.A. Dionne, H.A. Atwater, *Science* **316**, 430 (2007)
33. R. Liu, C. Ji, J.J. Mock, J.Y. Chin, T.J. Cui, D.R. Smith, *Science* **323**, 366 (2009)
34. E. Abbe, *Ark. Mikrosk. Anat.* **9**, 413 (1873)
35. M. Born, E. Wolf, *Principles of Optics* (Cambridge University Press, Cambridge, 1999)
36. D.W. Pohl, W. Denk, M. Lanz, *Appl. Phys. Lett.* **44**, 651 (1984)
37. U. Durig, D.W. Pohl, F. Rohner, *J. Appl. Phys.* **59**, 3318 (1986)
38. E. Betzig, J.K. Trautman, T.D. Harris, J.S. Weiner, R.L. Kostelak, *Science* **251**, 1468 (1991)
39. L. Novotony, B. Hecht, *Principle of Nano-Optics* (Cambridge University Press, Cambridge, 2006)
40. N. Hosaka, T. Saiki, *Opt. Rev.* **13**, 262 (2006)
41. T. Taubner, R. Hillenbrand, K. Keilmann, *Appl. Phys. Lett.* **85**, 5064 (2004)
42. H. Okamoto, K. Imura, *Surf. Sci. Rep.* **84**, 199 (2009)
43. K. Imura, H. Okamoto, *Bull. Chem. Soc. Jpn.* **81**, 659 (2008)
44. H. Okamoto, K. Imura, *J. Mater. Chem.* **16**, 3920 (2006)
45. G. Mie, *Ann. Phys.* **25**, 377 (1908)
46. R. Ganz, *Ann. Phys.* **37**, 881 (1912)
47. S. Link, M.B. Mohamed, M.A. El-Sayed, *J. Phys. Chem. B* **103**, 3073 (1999); S. Link, M.A. El-Sayed, *J. Phys. Chem. B* **109**, 10531 (2005)
48. M. Meier, A. Wokaun, *Opt. Lett.* **8**, 581 (1983)
49. A. Taflov, S.C. Hagness, *Computational Electrodynamics: The Finite-Difference Time-Domain Method*, 3rd edn. (Aetech House, Norwood, 2005)
50. B.T. Drain, P.J. Flatau, *J. Opt. Soc. Am. A* **11**, 1491 (1994)
51. C. Girard, A. Dereux, *Rep. Prog. Phys.* **59**, 657 (1996)
52. J.-J. Greffet, R. Carminati, *Prog. Surf. Sci.* **56**, 133 (1997)
53. K. Imura, K. Ueno, H. Misawa, H. Okamoto, *Nano Lett.* **11**, 960 (2011)
54. M.F. Crommie, C.P. Lutz, D.M. Eigler, *Nature* **363**, 524 (1993)
55. A. Nilius, T.W. Wallis, W. Ho, *Science* **297**, 1853 (2002)
56. G. Colas des Francs, C. Girard, J.-C. Weeber, C. Chiane, T. David, A. Dereux, *Phys. Rev. Lett.* **86**, 4950 (2001)
57. R.Y. Chiao, P.G. Kwiat, A.M. Steinberg, *Physica B* **175**, 257 (1991)
58. E.N. Economou, *Green's Function in Quantum Physics* (Springer, Berlin, 1983)
59. K. Masuda, T. Saiki, S. Nomura, M. Mihara, Y. Aoyagi, S. Nair, T. Takagahara, *Phys. Rev. Lett.* **91**, 177401 (2003)
60. C. Chicanne, T. David, R. Quidant, J.C. Weeber, Y. Lacroute, E. Bourillot, A. Dereux, *Phys. Rev. Lett.* **88**, 097402 (2002)
61. E.H. Synge, *Philos. Mag.* **6**, 356 (1928)

62. M. Ohtsu, *Near-Field Nano/Atom Optics and Technology* (Springer, Tokyo Berlin Heidelberg New York, 1998)
63. S. Smith, N. Christian, R. Holme, B. Orr, R. Kopelman, T. Norris, *Ultramicroscopy* **71**, 213 (1998)
64. B.A. Nechay, U. Siegner, M. Achermann, H. Bielefeldt, U. Keller, *Rev. Sci. Instrum.* **70**, 2758 (1999)
65. T. Guenther, C. Lienau, T. Elsaesser, M. Glanemann, V. Martin Axt, T. Kuhn, *Phys. Rev. Lett.* **89**, 057401 (2002)
66. T. Nagahara, K. Imura, H. Okamoto, *Rev. Sci. Instrum.* **75**, 4528 (2004)
67. M. Labardi, M. Zavelani-Rossi, D. Polli, G. Cerullo, M. Allegrini, S. De Silvestri, O. Svelto, *Appl. Phys. Lett.* **86**, 031105 (2005)
68. K. Imura, T. Nagahara, H. Okamoto, *J. Phys. Chem. B* **108**, 16344 (2004)
69. B. Hecht, H. Bielefeldt, Y. Inouye, D.W. Pohl, L. Novotny, *J. Appl. Phys.* **81**, 2492 (1997)
70. P.M. Morse, H. Feshbach, *Methods of Theoretical Physics* (McGraw-Hill, New York, 1953)
71. K. Imura, H. Okamoto, *Opt. Lett.* **31**, 1474 (2006)
72. C.E. Jordan, S.J. Stranick, L.J. Richter, R.R. Cavanagh, *J. Appl. Phys.* **86**, 2785 (1999)
73. K. Imura, T. Nagahara, H. Okamoto, *Chem. Phys. Lett.* **400**, 500 (2004)
74. B.J. Messinger, K. Ulrich von Raben, R.K. Chang, P.W. Barber, *Phys. Rev. B* **24**, 649 (1981)
75. K. Imura, T. Nagahara, H. Okamoto, *J. Chem. Phys.* **122**, 154701 (2005)
76. G. Schider, J.R. Krenn, A. Hohenau, H. Ditlbacher, A. Leitner, F.R. Aussenegg, *Phys. Rev. B* **68**, 155427 (2003)
77. J.K. Lim, K. Imura, T. Nagahara, S.K. Kim, H. Okamoto, *Chem. Phys. Lett.* **41**, 412 (2005)
78. S. Link, M.A. El-Sayed, *J. Phys. Chem. B* **103**, 8410 (1999)
79. H. Petek, G. Ogawa, *Prog. Surf. Sci.* **56**, 239 (1997)
80. J.-Y. Bigot, V. Halté, J.-C. Merle, A. Daunois, *Chem. Phys.* **251**, 181 (2000)
81. C.-K. Sun, F. Vallée, L. Acioli, E.P. Ippen, J.G. Fujimoto, *Phys. Rev. B* **48**, 12365 (1993)
82. J.H. Hodak, A. Henglein, G.V. Hartland, *J. Phys. Chem. B* **104**, 9954 (2000)
83. C. Voisin, D. Christofilos, P.A. Loukakos, N. Del Fatti, F. Vallée, J. Lermé, M. Gaudry, E. Cottancin, M. Pellarin, B. Broeyer, *Phys. Rev. B* **69**, 195416 (2004)
84. M. Hu, G.V. Hartland, *J. Phys. Chem. B* **106**, 7029 (2002)
85. O.L. Muskens, N. Del Fatti, F. Vallée, *Nano Lett.* **6**, 552 (2006)
86. M. Pelton, M. Liu, S. Park, N.F. Scherer, P. Guyot-Sionnest, *Phys. Rev. B* **73**, 155419 (2006)
87. D. Brinks, F.D. Stefani, F. Kulzer, R. Hildner, T.M. Taminiu, Y. Avlasevich, K. Müllen, N.F. van Hulst, *Nature* **465**, 905 (2010)
88. A. Kubo, K. Onda, H. Petek, Z. Sun, Y.S. Jung, H.K. Kim, *Nano Lett.* **5**, 1123 (2005)
89. A. Kubo, N. Pontius, H. Petek, *Nano Lett.* **7**, 470 (2007)
90. A. Stella, M. Nisoli, S. De Silvestri, O. Svelto, G. Lanzani, P. Cheyssac, R. Kofman, *Phys. Rev. B* **53**, 15497 (1996)
91. T.V. Chahbazyan, I.E. Perakis, J.-Y. Bigot, *Phys. Rev. Lett.* **81**, 3120 (1998)
92. C. Voisin, D. Christofilos, N. Del Fatti, F. Vallée, B. Prével, E. Cottancin, J. Lermé, M. Pellarin, M. Broeyer, *Phys. Rev. Lett.* **85**, 2200 (2000)
93. K. Imura, H. Okamoto, *Phys. Rev. B* **77**, 041401 (R) (2008)
94. S.D. Brorson, J.G. Fujimoto, E.P. Ippen, *Phys. Rev. Lett.* **59**, 1962 (1987)
95. N. Bloembergen, *Nonlinear Optics* (World Scientific, Singapore, 1996)
96. A. Mooradian, *Phys. Rev. Lett.* **22**, 185 (1969)
97. K. Imura, T. Nagahara, H. Okamoto, *J. Am. Chem. Soc.* **126**, 12730 (2004)
98. P.J. Schuck, D.P. Fromm, A. Sundaramurthy, G.S. Kino, W.E. Moerner, *Phys. Rev. Lett.* **94**, 017402 (2005)
99. R.A. Farrer, F.L. Butterfield, V.W. Chen, J.T. Fourkas, *Nano Lett.* **5**, 1139 (2005)
100. A. Bouhelier, R. Bachelot, G. Lerondel, P. Royer, G.P. Wiederrecht, *Phys. Rev. Lett.* **95**, 267405 (2006)
101. A. Hohenau, J.R. Krenn, J. Beermann, S.I. Bozhevolnyi, S.G. Rodrigo, L. Martin-Moreno, F. Garcia-Vidal, *Phys. Rev. B* **73**, 155404 (2006)
102. M. Mühlischlegel, H.-J. Eisler, O.J.F. Martin, B. Hecht, D.W. Pohl, *Science* **308**, 1607 (2005)

103. H. Wang, T.B. Huff, D.A. Zweifel, W. He, P.S. Low, A. Wei, J.-X. Cheng, *Proc. Natl. Acad. Sci. USA* **102**, 15752 (2005)
104. N.J. Durr, T. Larson, D.K. Smith, B.A. Korgel, K. Sokolov, A. Ben-Yakar, *Nano Lett.* **7**, 945 (2007)
105. Y. Jiang, N.N. Horimoto, K. Imura, H. Okamoto, K. Matsui, R. Shigemoto, *Adv. Mater.* **21**, 2309 (2009)
106. K. Imura, T. Nagahara, H. Okamoto, *J. Phys. Chem. B* **109**, 13214 (2005)
107. K. Imura, T. Nagahara, H. Okamoto, *Appl. Phys. Lett.* **88**, 023104 (2006)
108. K. Imura, H. Okamoto, M.K. Hossain, M. Kitajima, *Chem. Lett.* **35**, 78 (2006)
109. K. Imura, H. Okamoto, M.K. Hossain, M. Kitajima, *Nano Lett.* **6**, 2173 (2006)
110. T. Shimada, K. Imura, M.K. Hossain, H. Okamoto, M. Kitajima, *J. Phys. Chem. C* **112**, 4033 (2008)
111. M.K. Hossain, T. Shimada, M. Kitajima, K. Imura, H. Okamoto, *Langmuir* **24**, 9241 (2008)
112. G.T. Boyd, Z.H. Yu, Y.R. Shen, *Phys. Rev. B* **33**, 7923 (1986)
113. P. Apell, R. Monreal, S. Lundqvist, *Phys. Scr.* **38**, 174 (1988)
114. R. Rosei, *Phys. Rev. B* **10**, 474 (1974); M. Guerrisi, R. Rosei, P. Winsemius, *Phys. Rev. B* **12**, 557 (1975)
115. J.I. Gersten, *J. Chem. Phys.* **72**, 5779 (1980)
116. J. Gersten, A. Nitzan, *J. Chem. Phys.* **73**, 3023 (1980)
117. P.F. Liao, A. Wokaun, *J. Chem. Phys.* **76**, 751 (1982)
118. A.M. Michaels, M. Nirmal, L.E. Brus, *J. Am. Chem. Soc.* **121**, 9932 (1999)
119. H. Xu, J. Aizpurua, M. Käll, P. Apell, *Phys. Rev. E* **62**, 4318 (2000)
120. E. Hao, G.C. Schatz, *J. Chem. Phys.* **120**, 357 (2004)
121. T.E. Talley, J.B. Jackson, C. Oubre, N.K. Grady, C.W. Hollars, S.M. Lane, T.R. Huser, P. Nordlander, N.J. Halas, *Nano Lett.* **5**, 1569 (2005)
122. H. Watanabe, N. Hayazawa, Y. Inouye, S. Kawata, *J. Phys. Chem. B* **109**, 5012 (2005)
123. H. Wang, C.J. Levin, N.J. Halas, *J. Am. Chem. Soc.* **127**, 14992 (2005)
124. J.A. Fan, C. Wu, K. Bao, J. Bao, R. Bardhan, N.J. Halas, V.N. Manoharan, P. Nordlander, G. Shvets, F. Capasso, *Science* **328**, 1135 (2010)
125. T. Kodo, F. Matsumoto, K. Nishio, H. Masuda, *Chem. Lett.* **37**, 466 (2008)
126. N. Nedyalkov, T. Sakai, T. Miyanishi, M. Obara, *Appl. Phys. Lett.* **90**, 123106 (2007)
127. H. Okamoto, K. Imura, T. Shimada, M. Kitajima, *J. Photochem. Photobiol. A* **221**, 154 (2011)

Andrei Vasilyevich Zvyagin, Zhen Song, Annemarie Nadort,
Varun Kumaraswamy Annayya Sreenivasan, and
Sergey Mikhailovich Deyev

Contents

14.1	Introduction.....	564
14.2	Luminescent Nanodiamonds (LND).....	566
14.2.1	Nanodiamond.....	566
14.2.2	Nitrogen-Vacancy Center.....	568
14.2.3	Luminescent Nanodiamonds for Cellular Imaging Applications.....	571
14.2.4	Ultrasmall LND.....	572
14.2.5	Surface Effects on the NV Emission.....	574
14.2.6	Limitations of LND for Optical Biomedical Imaging.....	575
14.3	Upconversion Nanoparticle (UCNP).....	577
14.3.1	Photophysics of Upconversion Nanomaterials.....	577
14.3.2	Production and Characterization of UCNP.....	579
14.3.3	Merits of the UCNP-Assisted Optical Biomedical Imaging.....	580
14.3.4	Optical Imaging of UCNP in Biological Samples.....	581
14.3.5	Shortcomings of the UCNP Technology.....	583
14.4	Luminescent Nanoparticle Bioconjugation.....	584
14.4.1	Colloidal Stability in Water and Buffer Solutions.....	585
14.4.2	A Universal Bioconjugation Platform Based on a High-Affinity Molecular Pair Barnase:Barstar.....	586
14.4.3	Bioconjugates of Upconversion Nanoparticle Coated with Amphiphilic Polymer.....	587
14.5	Communication of Nanoparticles and Cells.....	589
14.6	Conclusion.....	593
	References.....	594

A.V. Zvyagin (✉) · Z. Song · V.K.A. Sreenivasan
MQ Biofocus Research Centre and MQ Photonics Research Centre, Macquarie University,
Australia

A. Nadort
Department of Biomedical Engineering and Physics, Academic Medical Center, University of
Amsterdam, 1100 DE Amsterdam, The Netherlands

S.M. Deyev
Laboratory of Molecular Immunology, Shemyakin & Ovchinnikov Institute of Bioorganic
Chemistry of the Russian Academy of Sciences, Moscow, Russia

Abstract

Imaging of molecular trafficking in cells and biological tissue aided by molecular-specific fluorescent labeling is very attractive, since it affords capturing the key processes in comprehensive biological context. Several shortcomings of the existing organic dye labeling technology, however, call for development of alternative molecular reporters, with improved photostability, reduced cytotoxicity, and an increased number of controllable surface moieties. Such alternative molecular reporters are represented by inorganic luminescent nanoparticles (NP) whose optical, physical, and chemical properties are discussed on the examples of luminescent nanodiamonds (LND) and upconversion nanoparticles (UCNP). The emission origins of these nanomaterials differ markedly. LND emission results from individual nitrogen-vacancy color-centers in a biocompatible nanodiamond host whose properties can be controlled via size and surface groups. Photophysics of UCNP is governed by the collective, nonlinear excitation transfer processes, resulting in conversion of longer-wavelength excitation to the shorter-wavelength emission. The emission/excitation spectral properties of UCNP falling within the biological tissue transparency window open new opportunities of almost complete suppression of the cell/tissue autofluorescence background. The developed surface of these nanoparticles represents a flexible platform populated with biocompatible surface moieties onto which cargo and targeting biomolecules can be firmly docked through a process called bioconjugation. These bioconjugated modules, e.g., nanodiamond-antibody, (quantum dot)-somatostatin, or (upconversion nanoparticle)-(mini-antibody) can gain admission into the cells by initiating the cell-specific, cell-recognized communication protocol. In this chapter, we aim to demonstrate the whole bottom-up bio-nano-optics approach for optical biological imaging capturing luminescent nanoparticle design, surface activation, and bioconjugation and the resultant bioconjugate module deployment in specific internalization in the cell.

14.1 Introduction

Optical imaging assisted by molecular-specific luminescent labeling is a direct, minimally invasive approach to investigate cellular morphology and processes in living cells and/or tissues, in their comprehensive biological context. Enabled by the recent developments in biophotonics, single-molecule imaging unobscured by the ensemble averaging has become a powerful and common imaging modality suitable for complex biological systems. As an example, single-molecule imaging is instrumental in tracking molecular trafficking events in cell signaling via activation of membrane receptors, and investigating the fates of individual receptors and ligands [1]. Another example represents detection of a single virus tagged with fluorescent molecule that has allowed tracking the virus invasion of the cell and its diffusion toward the nucleus, providing an important insight in the area of virology [2]. These studies place stringent demands on the fluorophore performance,

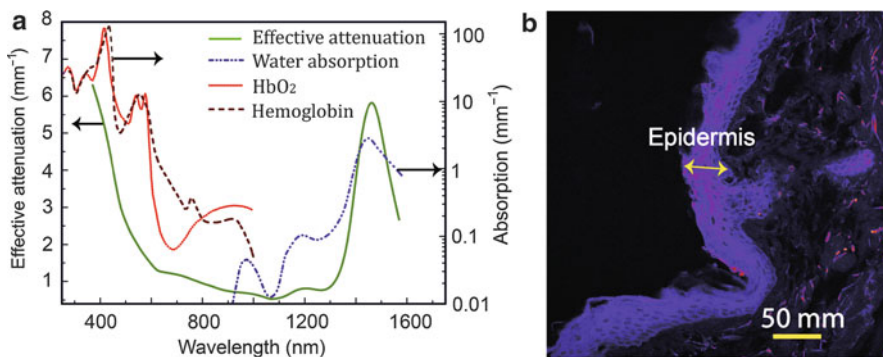


Fig. 14.1 (a) Optical effective attenuation spectrum of living skin tissue (*solid green line*) dominated by water (H_2O , *blue --- line*), hemoglobin (Hemoglobin, *brown - line*), oxy-hemoglobin (HbO_2 , *red solid line*), proteins (not shown), with the scattering effect also taken into account. Biological tissue transparency window ranges from 700 to 1,300 nm. (b) Autofluorescence image of human skin under the excitation at 405 nm. The viable epidermis layer is color-coded *purple* and marked by an *arrow*, with cell nuclei visible as *dark ovals*. Dermis, visualized primarily via collagen and elastin bundles, is situated right next to the epidermis extending to the right

which is frequently compromised by undesirable photophysical properties, such as fluorescence intermittency (blinking) and irreversible light-induced transitions to dark states (photobleaching) that hinder its photostability. The dark state transitions are particularly limiting in the single-molecule studies, which require high illumination intensities. Indeed, if an organic dye fluorophore survives only one million excitation/emission cycles before undergoing an irreversible transition to the dark state (photobleaching), the continuously emitting fluorophore lifetime spans only ≈ 3 ms (assuming the fluorescence lifetime $\tau = 3$ ns under saturation pumping condition). The longer-wavelength fluorophores, such as Cy5 and Cy7, Alexa Fluor 750, and CF dyes, whose excitation/emission fall into the so-called biological tissue transparency window (wavelength range, [The definition of the biological tissue transparency window is not settled varying from the given range to a range of 680–900 nm depending on the biological tissue constituents.] 700–1,300 nm) (Fig. 14.1a), are especially prone to photobleaching. These dyes are also widely used in applications where high signal-to-noise ratios are required, such as fluorescence resonance energy transfer (FRET). Photostability is also critical in applications, including stimulated emission depletion microscopy (STED), and despite progress in the design of organic fluorophores that are less prone to photobleaching, improved alternatives are in high demand. The other shortfalls of the fluorescence dyes include potential cytotoxicity, poor resilience to aggressive chemical and biological environment, and limited ability to carry cargo to cellular sites.

Nanotechnology has provided a powerful impetus to the new generation of molecular probes based on luminescent nanoparticles that are capable of addressing the major shortfalls of the existing molecular probes. In particular, a variety of nanoparticles, including luminescent nanodiamonds (LND) [3] and

upconversion NPs (UCNPs) [4], exhibit enviable photostability, i.e., unfading continuous emission. Besides, reduced cytotoxicity of these nanomaterials has been recently reported [5,6]. The upconversion NPs offer improved signal-to-noise ratio in the time-gated imaging and high-contrast detection employing time-gated schemes that have been reported using lanthanide-based UCNPs [7]. NP surface is amenable to modification to enable grafting a variety of surface moieties suitable for applications, such as molecular targeted drug delivery [8].

We review two types of luminescent nanoparticles in the context of optical cellular/tissue imaging: luminescent nanodiamond and upconversion nanoparticle. The choice of the NPs is underpinned by the diversity of their luminescence properties that capture important classes of nano-emitters. LND comprises several isolated color-centers in a nanodiamond host; UCNP luminescence is governed by nonlinear excitation transfer processes between strongly coupled ionic emitters. The underlying photophysics of these luminescent nanomaterials makes them useful for bioimaging, in particular, render NPs imaging contrast on the crowded cell morphology and autofluorescence background of the cells/tissues. The NP core chemical inertness is essential to preserve NP integrity in often aggressive biological environments and minimize its potential toxicological consequences (or cytotoxicity). Surface moieties are important for interfacing NPs with the biomolecular world. To this end, the basic principles of linking nanoparticles with biomolecules of programmable functionality, the process termed bioconjugation, is covered and several examples are presented. The bioconjugated NP-biomolecule complex is capable of performing programmable functions by, for example, activating a communication protocol with the cell that can result in gaining admission into the cell. We will present several examples of this specific cellular internalization visualized by means of optical luminescence imaging.

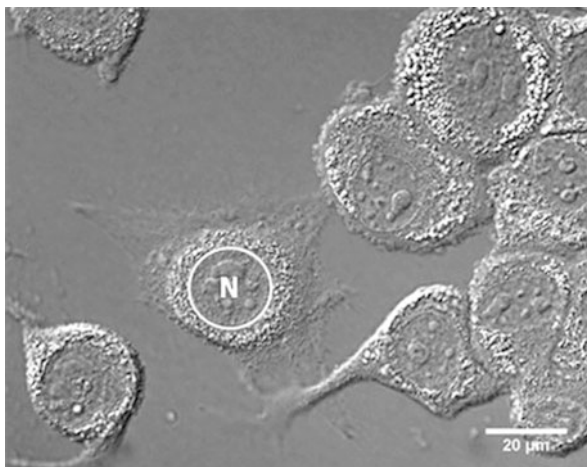
This book chapter is organized, as follows: The two types of luminescence nanoparticles are addressed in the first two sections, with particular focus on their photophysical properties in relation to optical biological imaging. Diverse surface properties of these nanomaterials enable adequate coverage of the existing surface functionalization strategies and lead to the following section (Sect. 14.4), where the key principles of the nanoparticles bioconjugation to biological molecules will be addressed and several examples given. Section 14.5 is devoted to reviewing specific interaction of the programmable nanoparticle-biomolecule conjugates with the cell. In Conclusions, the progress in the nanotechnology as applied to luminescent molecular probes is summarized.

14.2 Luminescent Nanodiamonds (LND)

14.2.1 Nanodiamond

Luminescent nanodiamond is usually referred to a diamond nanocrystal (ND) that hosts luminescent color centers. The diamond crystalline matrix is the most rigid material on the Earth, made of carbon atoms bonded together with the energy

Fig. 14.2 Differential interference contrast image of nanodiamond particle uptake into 3T3 cells. The nanodiamonds exhibit high contrast against the cell background due to strong elastic scattering and are observable as bright rims around the dim cell nuclei which are impermeable for the NDs (a nucleus is indicated with a circle) (Adapted from Ref. [17])



of ≈ 7.4 eV per atom. The diamond core is chemically inert, so that the centers are well secluded from environmental perturbations in such a crystal host. Even high-energy cosmic radiation inflicts little damage to this crystalline material. At the same time, the diamond surface is chemically reactive, especially when the surface is well developed, as in the case of surface-functionalized nanodiamonds. For example, the most popular acid-treatment [9–11] or high-temperature annealing in air [8, 12–14, 48] results in the formation of oxygen-containing surface moieties on the diamond surface that facilitate interfacing with photonic devices and macromolecules. NDs can be produced via two methods: (1) High-temperature high-pressure (HTHP) synthetic growth followed by ball-milling produces NDs of high crystal quality sized 4 nm and larger [15] (19). (2) Detonation of explosives in an inert atmosphere followed by disintegration yields remarkably monodisperse 5-nm NDs [16]. Subsequent acid treatment and/or annealing in air removes the surface layer of amorphous carbon, replacing it with a variety of oxygen-containing groups, such as carboxyl groups [8].

Very high refractive index of the nanodiamond core renders NDs conspicuous on the crowded environment of the cell. Figure 14.2 shows NDs internalized in the cells via a micelle transport vehicle [17]. The nanodiamond clusters encapsulated in endosomes on passing into the cytoplasm became dominant scatterers that overpowered intrinsic scattering signals coming from, e.g., mitochondria, and rendered the cytoplasm bright against the dim nuclei (circled and designated by “N” in Fig. 14.2). However, this scattering contrast is by far insufficient in achieving detection sensitivity at the single nanoparticle level due to the hefty cell scattering overhead that is indistinguishable from the scattering signals of the nanodiamond-based molecular probes. Spectral separation of the scattering background from the molecular probe signals of non-elastic-scattering nature is an efficient strategy to improve the imaging contrast and, hence, detection sensitivity. This is realized by utilizing the luminescence properties of nanodiamonds.

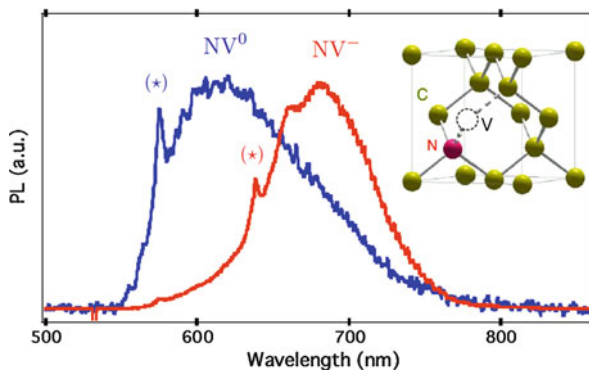


Fig. 14.3 Luminescence spectra normalized to their respective maximum value of single NV^- (red curve) and NV^0 (blue curve) color centers in diamonds. The zero-phonon lines (demarcated \star) of NV^- , NV^0 emissions are located at wavelengths 637 and 575 nm, respectively. The inset shows the atomic structure of the NV defect, consisting of a substitutional nitrogen atom (N_s , demarcated N) associated to a vacancy (V) in an adjacent lattice site of the diamond crystalline matrix (Reproduced from Ref. [22])

14.2.2 Nitrogen-Vacancy Center

The wide bandgap of diamond (5.5 eV) provides ample energy space to as many as ≈ 500 reported color-centers, where nitrogen-vacancy (NV), silicon-vacancy [18], and nickel-related [19] and chromium-related [20] centers are among the brightest, with the emission bands falling into the biological tissue transparency window (cf. Fig. 14.1a), making them promising candidates for optical biomedical applications. The NV center, however, exhibits several exceptional properties that attract considerable interest of the nano-optics community [21]. Therefore, only NV center in ND will be addressed hereafter, and referred to as “luminescent nanodiamond.” The NV center in diamond is formed by replacing one carbon atom with a nitrogen atom (termed “substitutional nitrogen,” N_s) and a vacancy at a location adjacent to the nitrogen atom, as schematically shown in Fig. 14.3, inset. The production process usually involves irradiation of diamond samples with high-energy electron or light-ion beams forming vacancy defects. In order to initiate migration of these vacancy defects in a diamond (nano)crystal, the sample is annealed at a high temperature ($\approx 800^\circ\text{C}$) in a high vacuum or oxygen-free atmosphere. This causes vacancy trapping at the substitutional nitrogen sites that are abundant in the majority of synthetic diamond samples. The NV center can remain neutral (NV^0) or acquire an additional electron from the neighboring donor defects, e.g., N_s , becoming negatively charged NV center (NV^-). Both centers are luminescent, with the spectra shown in Fig. 14.3. The acclaimed merits of the NV center are commonly associated with the negative-charge state of the NV center, and can be interpreted in terms of its physical, optical, and magneto-optical properties.

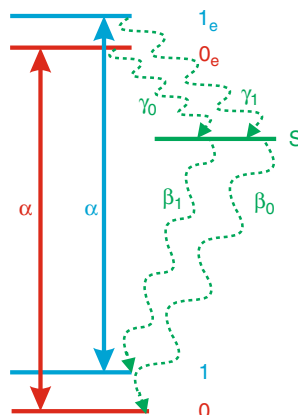


Fig. 14.4 Simplified five-level schematic diagram of the electronic levels of the NV⁻ color center appropriate for room temperature. The $m_S = 0$ levels are indicated in red, the $m_S = \pm 1$ in blue, and the singlets in green. The double-headed arrows indicate the radiative transitions. The solid blue and red arrows give the spin conserving transitions in the visible. The green wavy arrows indicate non-radiative decay that involves E-vibrations

The NV⁻ center action cross-section is large, $\eta\sigma_a = 3 \times 10^{-17} \text{ cm}^2$ (σ_a – absorption cross-section; η – quantum yield) [23], with the quantum yield reaching $\approx 80\%$ under favorable excitation conditions [24]. The energy diagram of the NV⁻ center (shown in Fig. 14.4) elucidates estimation of η , as stemming from the branching ratio of the radiative and non-radiative transitions, as well as the NV⁻ optical spin polarization property that is highly acclaimed in quantum science and spin magnetometry, and briefly touched below.

The ground state of NV⁻ is an orbital singlet and spin triplet. In trigonal symmetry the spin $m_S = +1$, and -1 states are exactly degenerate and, when modeling the optical cycle of the NV⁻ center, the $m_S = \pm 1$ can be described by one level (assuming no magnetic fields). The excited state is also a spin triplet, which is treated as an orbital singlet in the phenomenological model. The model, therefore, includes two spin levels, 0 and 1, in the ground electronic state and two electronic states in the excited state, 0_e and 1_e (Fig. 14.4). The optical transition (at a rate α) between the ground and excited state is independent of the spin projection giving rise to two transitions of identical strength between levels 0 and 0_e and between 1 and 1_e, where the spin projection is unchanged, despite the vibration coupling. Should these be the only energy levels and only transitions, the center would cycle between the ground and excited states, with constant spin projection. However, the situation is entirely changed by the presence of an intermediate state (denoted “S” in Fig. 14.4). The intermediate state is attributed to a spin singlet (or states) $S = 0$, with no spin projection. Inter-system crossing takes place from the excited state to the singlet and from the singlet to the ground state. These crossings are spin-dependent and give rise to spin polarization and optical spin readout.

The approximate rates of the crossing from the excited state spin levels to the singlet are $\gamma_1 = 0.55\alpha$ and $\gamma_0 = 0.15\alpha$, and from the singlet to the ground state spin levels are $\beta_0 = 0.035\alpha$ and $\beta_1 = 0.022\alpha$ (Fig. 14.4). The decay rate from the singlet to the ground state is low, with a combined rate of 0.056α . The decay out of the triplet to the singlet is comparable to the optical transition and the rate associate with $m_S = \pm$ states (from 1_e) is more rapid than for $m_S = 0$ states (from 0_e). These inter-system crossings underpin the NV^- center unique properties. They result in (a) population being transferred out of $m_S = \pm 1$ states, (b) the emission rates from $m_S = +1$ states being weaker than from $m_S = 0$ states, and (c) the associate luminescence lifetime (in diamond crystals) from $m_S = +1$ states being shorter at 7.8 ns than that from $m_S = +1$ states at 12 ns [25]. With continuous excitation, the relative populations in the excited state is given by P_{\pm}/P_0 by $\gamma_0/\gamma_1 \times \beta_1/\beta_0 = 0.15/0.55 \times 0.022/0.035 = 0.17$. This implies 14.5 % of the population is in the excited $m_S = \pm$ spins and 85.5 % in $m_S = 0$. The ground state polarization is less by the ratio of the lifetimes 7.8/12 and, hence, somewhat lower at 74 % in $m_S = 0$.

Depopulation of the spin-specific ($m_S = \pm 1$) ground state in favor of the $m_S = 0$ ground state in the course of optical excitation represents a venerable property of the NV^- center, which is realized by a possibility to read out thus-prepared spin-state by optical means. The coherence time of this spin state at room temperature is as short as several microseconds, but its extension to 1 ms has been demonstrated by the appropriate choice of an ultrapure diamond host in terms of the much reduced defects and impurities, especially N_s . This enables preparing and interrogating the entangled spin states. The quantum science applications rely on the preparation of an NV^- center spin-state (qubit), followed by its coupling to the neighbor spins associated with defects, such as NV center spins, substitutional nitrogen (N_s) or isotopic C^{13} nuclear spins, creating quantum entanglement of the qubits. Reading out the NV^- entangled spin state optically provides a measure of the entangled state of the ensemble. The magnetometry applications rely on the high sensitivity of the NV center polarized spin-state to (local) magnetic fields, as shown and briefly discussed in Fig. 14.7. The spin-state perturbation is read out optically by means of the optically detected magnetic resonance (ODMR) and reports on the local value and orientation of the perturbing magnetic field vector. The ultimate sensitivity is estimated at the level of a single spin at the nanoscale proximity [26]. The virtually unlimited photostability of the NV center is another important property manifested by uninterrupted continuous emission under continuous excitation, and it is important in biomedical imaging applications. This represents a radical solution to the problem of poor photostability of the widespread emitters, organic fluorescent dyes that undergo irreversible conversion to a low- or no-emission state (or photobleaching) after, approximately, one million excitation cycles. Luminescence intermittency, or blinking, represents another photostability impairment mechanism, and is reported in virtually all single emitters [27, 28] especially affecting semiconductor quantum dot emission [29–31]. Although the NV^- centers have also been reported to exhibit blinking behavior, this can be readily avoided under controllable conditions [32].

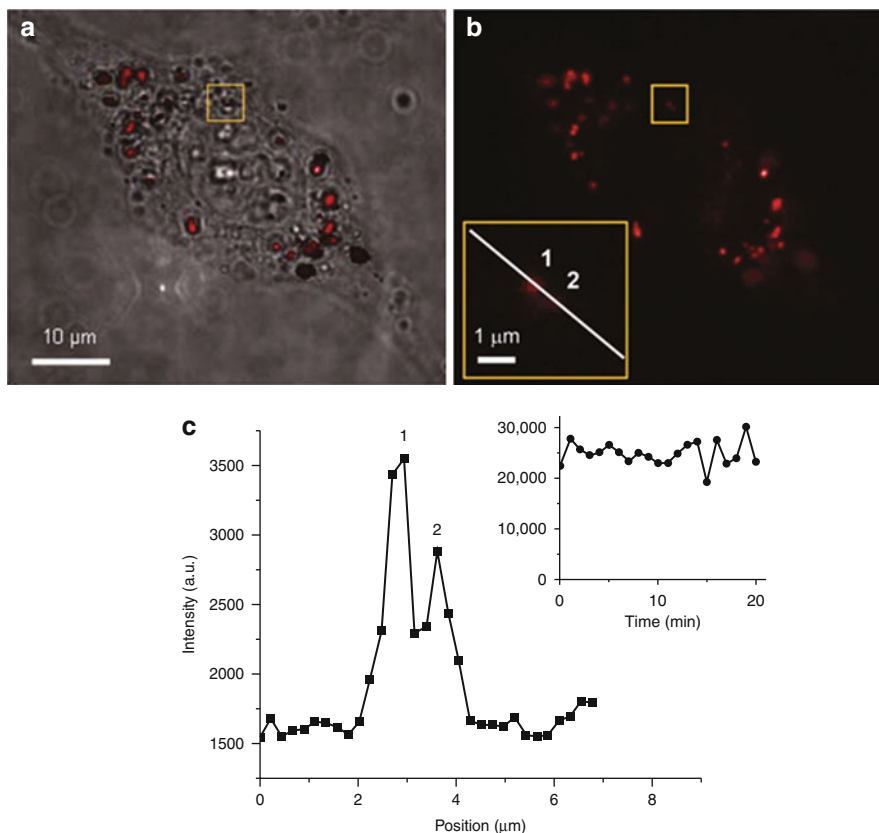


Fig. 14.5 Observation of single LNDs in a HeLa cell. (a) Bright-field and epi-luminescence images of a HeLa cell after uptake of 35-nm LNDs. Most of the up-taken LNDs are seen to distribute in the cytoplasm. (b) Epi-luminescence image of a single HeLa cell after the LND uptake. An enlarged view of the fluorescence spots (denoted by “1” and “2”) with diffraction-limited sizes (FWHM \approx 500 nm) is shown in *inset*. (c) Intensity profile of the fluorescence image along the line drawn in **b inset**. (c *inset*) Integrated fluorescence intensity (after subtraction of the signals from cell autofluorescence and background fluorescence from the microscope slides) as a function of time for particle “1.” The signal integration time was 0.1 s. No sign of photobleaching was detected after continuous excitation of the particle for 20 min (Reproduced from Ref. [3])

14.2.3 Luminescent Nanodiamonds for Cellular Imaging Applications

The first observation of NV-ND imaging in cells was reported by [3], where high-contrast imaging and virtually unlimited photostability of 35-nm LNDs were reported. The authors demonstrated nonspecific internalization of LNDs in the cells (see Fig. 14.5), followed, by the demonstration of several applications of single LND imaging and tracking in the cellular environment [33]. Nonspecific internalization

refers to poorly controlled process of the extraneous material uptake by the cell, and is discussed in [Sect. 14.4](#).

Our own observation of the nonspecific internalization of a single luminescent nanodiamond sized ≈ 100 nm in Chinese Hamster Ovary (CHO-K1) cells confirmed the feasibility of single luminescent nanoparticle imaging, with the scattering background largely suppressed [34]. Combined with the reported minute cytotoxicity of the nanodiamonds [35, 36], the single-particle imaging demonstration sparked considerable interest in the applications of LND, as a molecular probe in live systems. These high expectations were underpinned by the nanodiamond surface properties that made this material amenable to bioconjugation leading to targeted delivery in cells and specific tissue sites. And, indeed, a number of interesting demonstrations of the specific internalization in cells of the LND bioconjugated with targeting biomolecules have been demonstrated (see, e.g., comprehensive review by Schrand et al. [37]). It is worthwhile to note that the LND bioconjugates can serve not only as the molecular probes, but also as biomolecule delivery vehicles [38]. This aspect of luminescent nanotechnology will be detailed in [Sect. 14.5](#) of this chapter.

The optical spin-selective properties of NV-ND have also found new applications in cellular imaging applications. In particular, monitoring the decoherence rates in response to changes in the local environment may provide new information about intracellular processes [39]. The reported experiments demonstrate the viability of controlled single spin probes for nano-magnetometry in biological systems, opening up a host of new possibilities for quantum-based imaging in the life sciences. [Figure 14.7](#) shows optically detected magnetic resonance (ODMR) signals from the single NV centers in different ND crystals spatially localized in the cell cytoplasm. The ODMR signals appeared to be capable of reporting on the intracellular environment.

14.2.4 Ultrasmall LND

Considering imaging and sensing applications, the single-spin sensitive magnetometry [26] and Förster resonance energy transfer [40] require the nanodiamond layer to be thinned to exploit the strong dependence of the signal on the interaction radius r ($1/r^6$ and $1/r^3$, respectively). The single-spin-sensitive imaging at the nanoscale led to an estimation that the NV^- center had to be as close as 10 nm to an interrogated single spin for reliable detection [26]. In optical biological imaging applications, ultrasmall diamonds are crucial to minimize disruption to the molecular trafficking under observation [33]. It is desirable to reduce the size of NDs to match the size of an average protein, i.e., 5 nm, which is achievable due to the progress in the production of ultrasmall nanodiamonds, also referred to as ultra-dispersed nanodiamonds [41]. It has also been reported that NV-NDs of the size range less than 10 nm retain their luminescent properties characteristic of the NV centers.

At the same time, the NV center stability sets a size limit on the NV nanodiamond (NV-ND) matrix. A 2.5-nm ultra-small nanodiamond may be incapable

of hosting an NV center in the core, as predicted theoretically [42]. The environmental susceptibility of the NV-ND emission in small crystals, or NV centers in the nanoscale proximal surface layer, has been reported on several occasions [22, 32, 43]. The question of the NV center stability versus its distance to the diamond surface became essential two decades ago due to the progress toward production of the ultrasmall NDs of the detonation origin [9]. The problem of the existence of NV centers in such small nanocrystals became a hot research topic in view of the significant appeal of applications of low-cost detonation NDs. On the other hand, the experimental observations provided little support in favor of the existence of the NV-ND. For example, the theoretical calculations favored the location of nitrogen on the surface rather than in the core, which seemed to explain the limited observation of NV centers in chemical vapor deposition and high-pressure high-temperature (HPHT) grains less than 40 nm in size [44, 45], and favored the prediction that NDs smaller than 10 nm in size were deprived of NV centers [18, 42]. In particular, the spectroscopic studies revealed broadband luminescence [46] that was wavelength blue-shifted from the characteristic NV⁻ spectra, shown in Fig. 14.3. The origin of this luminescence was attributed to a graphitic layer that formed in the detonation process. The photoluminescence excitation spectra analysis of HPHT and CVD diamonds also corroborated the notion of NV center instability in ultrasmall NDs by showing broadband component attributed to the amorphous carbon phase [47].

The obscuring signal overhead of the graphite layer to the overall luminescence signal from NV-NDs was suppressed by employing a time-gated detection scheme making use of the difference in the luminescence lifetimes of graphite and NV⁻ (sub-ns versus ≈ 10 – 20 ns, respectively). As a result, the characteristic NV⁻ center spectral signature was observed, thus providing an unambiguous evidence of the existence of NV centers in the detonation nanodiamonds [43]. A direct obviation of the overshadowing luminescence signal background from the graphite layer was reported by [32]. Thoroughly acid-cleaned discrete detonation nanodiamonds were sparsely dispersed on a glass slide and interrogated individually, thus minimizing the graphite luminescent signal background, and so a signal originated from only one ND became observable. As a result, the characteristic NV⁻ spectral signatures from single centers were acquired.

An alternative top-down approach of production of the ultrasmall NDs has been reported by [15]. This approach was based on milling a millimeter-sized diamond crystal, following the NV center implantation using the conventional high-energy electron irradiation and high-temperature annealing procedure. The authors reported stable luminescence and high-contrast ODMR signal from the single NV centers in NDs sized less than 8 nm. Oxidative etching in air/oxygen at high temperature is another top-down approach of ultrasmall ND production. This method relies on the removal of carbon atoms from the ND surface at a controllable rate via oxidation reactions. Since an outer ND layer in the graphitized (sp^2) form is removed at a higher rate [48–50] than that of the diamond sp^3 phase, this method was originally employed to remove sp^2 carbon from ND, as a surface-cleaning procedure [8]. This method was later extended for in situ studies of ND size evolution, as the oxidative

etching in air provides a least disruptive method of graphite cleaning and ND core size reduction [51]. NV^- emission in the ND crystals sized less than 10 nm has been reported [52].

14.2.5 Surface Effects on the NV Emission

Diamond surface effects appear to play a considerable role in the emission behavior of the NV centers, if these are situated at the nanometer proximity. Three principal cases of the surfaces state are as follows: (1) Emission, absorption and quenching by the graphite sp^2 -layer. (2) Surface functional groups affect the NV center emission state – O- or H-containing groups promote or inhibit the NV emission. (3) NV centers luminescence intermittency (blinking) takes place, if the center center is proximal to a substrate, with abundant electron acceptors.

It has been demonstrated that a graphite (sp^2) shell surrounding the detonation nanodiamonds causes suppression of the NV luminescence [43], whereas oxygen-containing surface groups have little effect on the NV emission and, moreover, are capable of healing the surface defects that results in the NV emission activation [53]. The sp^2 shell is a low-density layer of graphite impregnated with noncarbon impurities that is loosely attached to the ND surface. This lax graphite layer is removable by acid cleaning or oxidative etching. As a result, the NV emission is converted from the latent non-emission state to active emission state. In addition, this sp^2 black carbon layer contributes to attenuation, of the excitation/emission light. Removal of this layer reduces the attenuation dramatically improving the NV excitation/emission optical properties. Besides, the sp^2 layer functions as an electron acceptor causing discharge of the NV^- center accompanied by its conversion to NV^0 or to “dark” non-emission state [22, 54].

The hydrogen termination of the ND surface resulted in a number of active NV emitters reduced almost tenfold in comparison with that of the original oxygenated NV-ND sample (Fig. 14.8). A subsequent oxidative treatment redressed the LND surface with oxygen groups and resulted in the recovery of the NV emission, as shown in Fig. 14.8c, where a number of the NV luminescent centers reappeared at their original sites (circled). Also, note that a number of blinking centers recovered their original blinking behavior after being in a latent dark state in the H-terminated LND (marked by a white downward arrowhead, Fig. 14.8).

The effect of the hydrogen surface group on the NV emission in ND on the charge state of the nitrogen-vacancy electron configuration has received much attention lately [53, 55]. In brief, the H-moieties cause an up-shift of the NV energy structure in the ND due to the modulation of the electron affinity. The valence band energy edge rises above the electrochemical potential of water, driving electrons from the nanometer-thick ND subsurface layer to water until the two-dimensional gas of holes in this ND subsurface layer compensates the gradient forces. It causes charge depletion of the NV^- center that enters either NV^0 charge state [53] or the dark state [53].

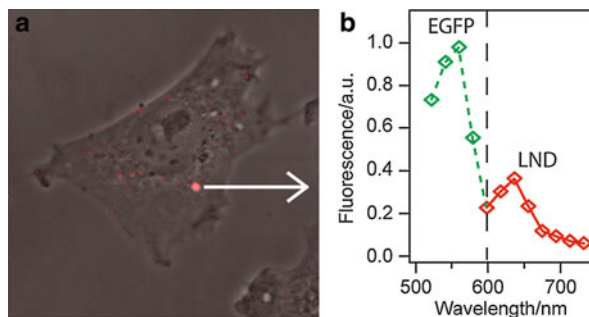


Fig. 14.6 Observation of a single LND bioconjugate in the CHO-K1 cell. (a) Laser scanning confocal microscopy of a ≈ 100 -nm luminescent nanodiamond (red spot). An arrow points from the LND to (b) Fluorescence spectra of LND and green fluorescence proteins (EGFP) conjugated to the nanodiamond surface (Reproduced from Ref. [34])

The surface effect on the NV emission state can be summarized, as follows: In general, the LND luminescence is immune to the surface effects, as long as the surface is deprived of e-acceptors, and the diamond crystal host is not distorted. This condition is realized in case of the surface-oxygenated ND, even if the centers are situated as close as 1 nm to the surface [22, 56].

14.2.6 Limitations of LND for Optical Biomedical Imaging

There are two major problems that limit the application scope of LNDs for cellular nano-photonics. Firstly, production of NV-ND remains expensive and cumbersome, since it relies on the high-energy electron or light-ion irradiation. These irradiation sources are costly, not readily available, and the production process is not easily scalable, despite some progress in this direction [33]. So, production of LND is limited to a relatively small amount of the nanomaterial. Annealing at relatively high temperatures in vacuum represents another complication in the LND production process that requires specialized equipment. Secondly, the LND excitation takes place in the visible spectral region, ranging from 488 nm (Ar-ion laser) to 545 nm (helium-neon laser), where an excitation at 532 nm (second harmonic, Nd:YAG laser) is often preferred. Biological systems respond to this excitation by emitting fluorescence, termed “autofluorescence,” which is spectrally broad extending to the near-infrared spectral range (tailing off at about 800 nm). This autofluorescence signal is spectrally overlapped with the broadband luminescence of LND (Fig. 14.2), thus making spectral filtering of the LND signal inefficient. Indeed, one can see non-negligible background in Figs. 14.5 and 14.6 due to the cell autofluorescence, which ultimately limits the detection sensitivity of LND precluding the use of ultrasmall

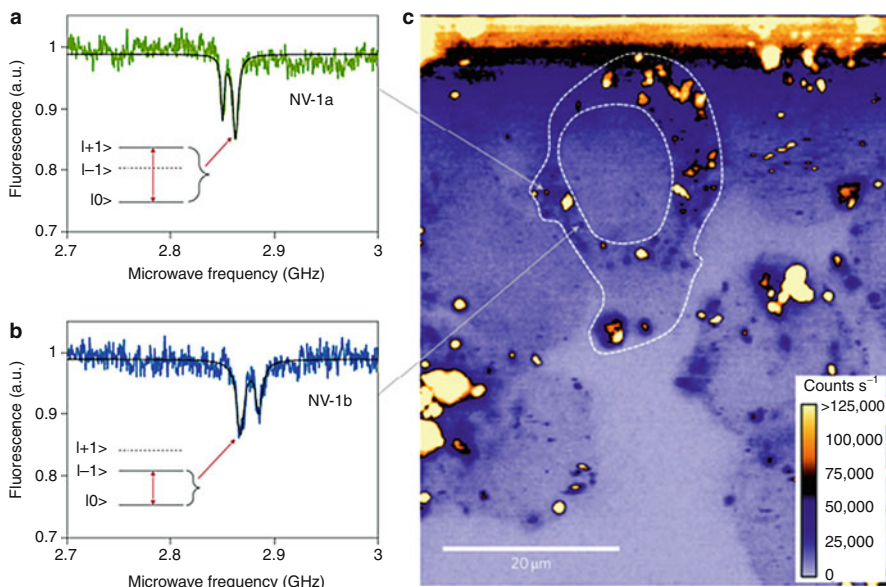


Fig. 14.7 (a–c) Confocal image of HeLa-1, with luminescence gated around the NV emission (650–800 nm). The nucleus and cell membrane are indicated with *dashed lines* for clarity. The optically detected magnetic resonance spectra of NV-1a (a) and NV-1b (b) show the different strain splitting between the two centers (Reproduced from Ref. [39])

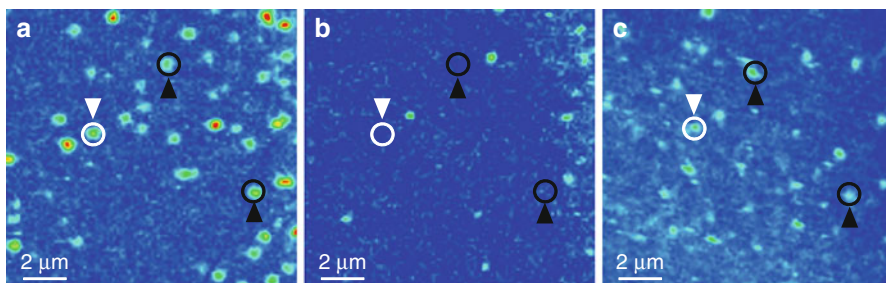


Fig. 14.8 The effect of the surface hydrogenation on the luminescent NDs. (a) NV luminescence after thermal oxidation. The *black* and *white arrowheads* point to stable and blinking NV emitters. (b) Hydrogenated NV centers exhibit diminished emission. (c) The sample redressing with oxygen groups led to the recovery of NV emission and blinking. Noticeable background fluorescence in (c) was activated by the H- and O-treatment (Reproduced from Ref. [52])

LND for imaging in live cells. More efficient mechanisms of suppression of the excitation light and biological system autofluorescence are required to realize the optical biomedical imaging at the single nanoparticle sensitivity. These mechanisms and their realizations are discussed in the following section.

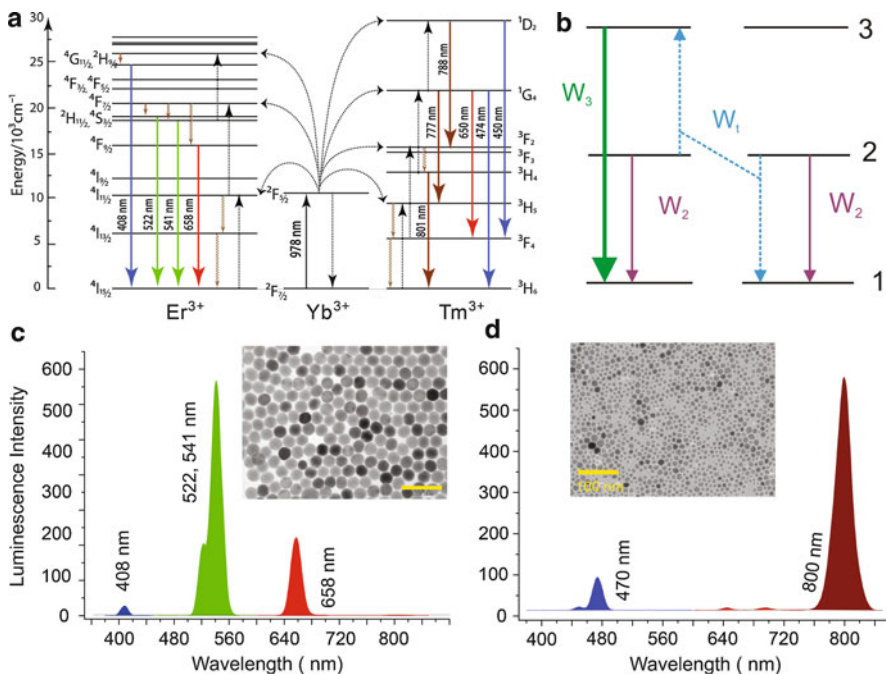


Fig. 14.9 Detailed and simplified schematic energy level diagram of Ytterbium Yb³⁺ ions with participating Erbium (Er³⁺) or Thulium (Tm³⁺) ions, respectively. Yb³⁺ and Er³⁺ (Tm³⁺) serve as the sensitizer and activator, respectively. Luminescent spectra of (c) NaYF₄:Yb:Er; and (d) NaYF₄:Yb:Tm nanomaterials, with their corresponding transmission electron microscopy images

14.3 Upconversion Nanoparticle (UCNP)

The unique photophysical properties of UCNP allow almost complete suppression of the biological tissue background that leads to the ultimate single nanoparticle photodetection sensitivity.

14.3.1 Photophysics of Upconversion Nanomaterials

Photon upconversion is a nonlinear process manifested by the conversion of the long-wavelength excitation to short-wavelength emission. The mechanism of upconversion is based on sequential absorption of two or more photons by the metastable long-lived energy states, as shown in Fig. 14.9a and briefly discussed later, which can be induced by relatively low-intensity ($1 \times 10^3 \text{ W cm}^{-2}$) continuous-wave excitation conveniently provided by an inexpensive 980-nm laser [4]. This process differs from a simultaneous two-photon absorption that occurs via a virtual intermediate level, stimulated by the excitation intensity as high as $1 \times 10^5 \text{ W cm}^{-2}$ usually realized by means of a complex and expensive femtosecond laser [57].

The majority of the upconversion processes involve absorption and non-radiative energy transfer steps. Theoretically, luminescent materials featuring $4f$ and $5d$ shell ions that have more than one metastable level are able to generate upconversion luminescence. Referring to Fig. 14.9a, a two-level Yb^{3+} ion serves as the donor (also known as the sensitizer) whose role is to absorb an IR excitation photon via ${}^2\text{F}_{7/2} \rightarrow {}^2\text{F}_{5/2}$ transition path, and non-radiatively transfer the excitation energy to a neighboring Yb-ion, or Er^{3+} (Tm^{3+}) ions, also known as activators. As a result, an ensemble of the excited dopant Yb-ions forms a non-localized exciton spread across the entire nanocrystal matrix maintained by the non-radiative energy exchange process. This excitation energy is continuously transferred to the network of the activators, Er^{3+} or Tm^{3+} , with the process rate order evaluated as $1,000\text{ s}^{-1}$ for the representative crystal matrix of $\text{Cs}_3\text{Lu}_2\text{Br}_9$ [58]. The activated ion, for example, Er^{3+} in the ${}^4\text{I}_{11/2}$ metastable state, can coalesce with the metastable Yb^{3+} (${}^2\text{F}_{5/2}$) via a collective pair-wise process of the energy transfer upconversion (Fig. 14.9b). As a result, the Er^{3+} (${}^4\text{I}_{11/2}$) makes a transition to the next-level excited state Er^{3+} (${}^4\text{F}_{7/2}$), followed by a rapid at the expense of the Yb^{3+} (${}^2\text{F}_{5/2}$) $\rightarrow \text{Yb}^{3+}$ (${}^2\text{F}_{7/2}$) non-radiative transition to Er^{3+} (${}^4\text{S}_{3/2}$) (refer to Fig. 14.9a, b). The Er^{3+} (${}^4\text{S}_{3/2}$) radiates in a multiplet green spectral band, and also in a multiplet red spectral band, following the non-radiative phonon-assisted transition Er^{3+} (${}^4\text{S}_{3/2}$) $\rightarrow \text{Er}^{3+}$ (${}^4\text{F}_{9/2}$), as one can see in Fig. 14.9c. The Er^{3+} (${}^4\text{F}_{9/2}$) population is also built up via an alternative excitation path: non-radiative transition Er^{3+} (${}^4\text{I}_{11/2}$) $\rightarrow \text{Er}^{3+}$ (${}^4\text{I}_{13/2}$), followed by the energy transfer upconversion [Er^{3+} (${}^4\text{I}_{13/2}$) $\rightarrow \text{Er}^{3+}$ (${}^4\text{F}_{9/2}$)] and [Yb^{3+} (${}^2\text{F}_{5/2}$) $\rightarrow \text{Yb}^{3+}$ (${}^2\text{F}_{7/2}$)].

This process is described by a set of kinetic equations of the Er^{3+} or Tm^{3+} energy level populations. Levels 1 (ground), 2, and 3 refer, respectively, to the energy states ${}^4\text{I}_{15/2}$, ${}^4\text{I}_{11/2}$, and ${}^4\text{F}_{9/2}$ (or ${}^4\text{S}_{3/2}$) – for Erbium ions, and ${}^3\text{H}_6$, ${}^3\text{H}_5$, and ${}^3\text{H}_4$ – for Thulium ions, as shown in Fig. 14.9a. A simplified energy level diagram is presented in Fig. 14.9b.

$$dN_3/dt = W_1 N_2^2 - (W_{31} + W_{32}) N_3 \quad (14.1)$$

$$dN_2/dt = -2W_1 N_2^2 - W_2 N_2 + W_{32} N_3 \quad (14.2)$$

$$dN_1/dt = W_1 N_2^2 + W_2 N_2 + W_{31} N_3 \quad (14.3)$$

where N_1 , N_2 , N_3 are populations of the levels 1, 2, 3, respectively; W_{31} , W_{32} transition probabilities $3 \rightarrow 1$ and $3 \rightarrow 2$, respectively; W_1 the upconversion probability, resulting in simultaneous transition of one ion to the level 3, and the other to the ground level 1. By analyzing the equation, one can conclude that at the low excitation intensity (I), the signal luminescence is proportional to I_2 in virtue of the N_2 [59]. Thus, it becomes clear that the power quantum yield (PQY) of the UCNP is a linear function of the pumping intensity, and its measurement versus the intensity is the key to optimal design of the synthesis of UCNP. It is also important to note that the level 3 decay rate is governed by the dependence of $\exp(-W_{31}t)$ in case of the pulsed excitation, with $t=0$ set to the excitation pulse falling edge. W_{31} contains both radiative ($\approx 5,000\text{ s}^{-1}$ [58]) and non-radiative

components that compete for the level 3 population decay. When the nanocrystal size becomes small (<30 nm), the non-radiative component ($\approx 20,000$ s $^{-1}$) prevails causing a dramatic reduction of PQY [60]. This poses a challenge on the production and surface passivation of UCNP in enhancing the upconversion energy transfer W_7 , preserving the crystal quality, and minimizing bulk and surface defects – to suppress the non-radiative component of W_{31} . The former is addressed by the breakthrough synthesis, and is described below.

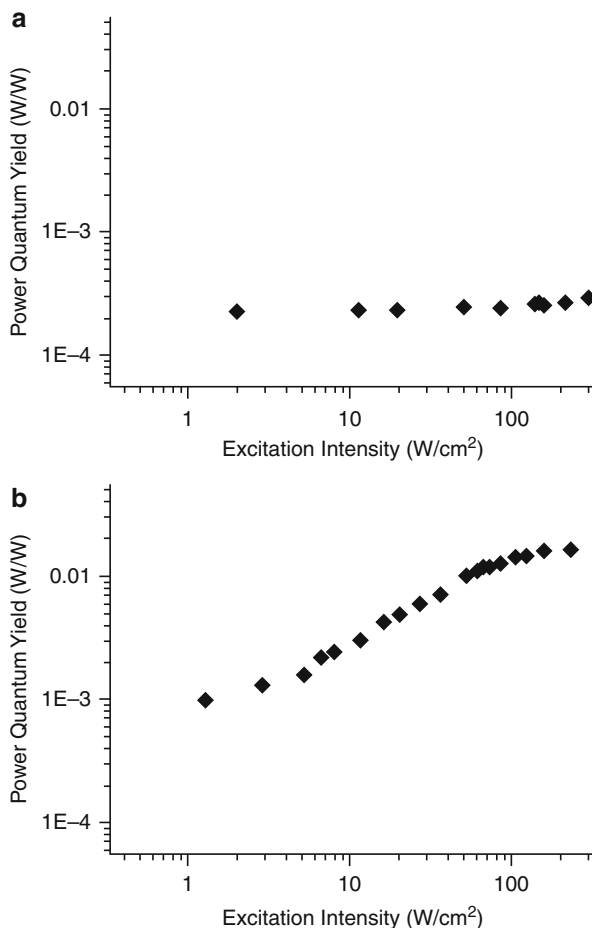
The most popular UCNP represents an inorganic nanocrystal matrix (NaYF₄) co-doped with sensitizer ytterbium (Yb³⁺) and activator erbium (Er³⁺) or thulium (Tm³⁺) lanthanide ions. In a particular case of NaYF₄:Yb:Tm, an ensemble of Yb-ions sensitizes infrared radiation at a wavelength of 980 nm and transfers it to Tm-ions characterized by multiple excited states with exceptionally long (sub-ms) lifetimes. As a result of the energy transfer upconversion, Tm³⁺ radiates at 474 nm (three sequential photons) and 800 nm (two sequential photons) spectral bands (Fig. 14.9d). Since the UCNP excitation/emission process is nonlinear, power quantum yield (η), i.e., the emission/excitation (Watts/Watts) power ratio, grows linearly versus the excitation intensity reaching saturation at a high intensity value of $I_{\text{sat}} \approx 10\text{--}1,000$ W cm $^{-2}$ [59], as shown in Fig. 14.10. Until recently, the dramatic reduction of η versus the crystal host size at the nanometer scale precluded practical applications of UCNPs. A breakthrough in the UCNP synthesis [61, 62] has resulted in much brighter nanoparticles, where “brightness” is measured in terms of the power quantum yield.

14.3.2 Production and Characterization of UCNP

An oxygen-free two-step protocol is used for the synthesis of the UCNPs [63]. The typical sample of NaYF₄:Yb:Er has molar concentrations of Yb and Er as 18 and 2 %, respectively. In step 1, aqueous solution of LnCl₃ (1.0 mM, Ln = Y, Yb, Er) is mixed with oleic acid and octadecane in a three-neck, round-bottom flask and heated first at 150 °C and at 110 °C on the addition of NH₄F and NaOH. This procedure yields small-size (<10 nm) NaYF₄:Yb:Er of cubic crystal phase (α -phase) characterized by low η . Step 2 is performed to convert these nanocrystallites in to the hexagonal phase (β -phase). The reaction mixture is sealed, quickly heated to 320 °C, while purged with argon, and nanocrystals are precipitated with acetone. As a result, one obtains nanocrystal powder of sizes ranging from <10 to 300 nm. This synthesis has been quickly adopted and modified to produce a great variety of UCNPs of different sizes (Fig. 14.9 insets) and spectral and temporal upconversion properties [64].

The power conversion coefficient has been greatly improved as a result of this new synthesis approach. Our measurements carried out using an integrating sphere showed a dramatic improvement of η of the α -UCNP from 0.03% (particle diameter, 10 nm) to 2 % of the β -UCNP (particle size, 60 nm) with a saturation intensity of ≈ 70 W cm $^{-2}$.

Fig. 14.10 Plots of the power quantum yield, η of (a) α - and (b) β -phases UCNPs. Particle mean diameters, (a) 10 nm and (b) 60 nm. The saturation intensity is (a) $>300 \text{ W cm}^{-2}$, (b) 70 W cm^{-2}



14.3.3 Merits of the UCNP-Assisted Optical Biomedical Imaging

There are several key advantages of UCNP in the context of biomedical optical imaging. Firstly, the $\text{NaYF}_4:\text{Yb:Tm}$ luminescence band (800 nm, see Fig. 14.9d) falls into the biological tissue transparency window. The excitation and emission radiation in biological tissue experiences reduced absorption and scattering in comparison with that in the ultraviolet (UV) and infrared (IR) spectral ranges. The biotissue absorption is dominated by oxygenated and deoxygenated hemoglobin constituents of blood, proteins (e.g., melanin) in the UV visible range of the spectrum, and by water in the IR spectral range. The biotissue scattering extinction represents a monotonic function slowly decreasing from the UV toward IR. The combined effect of the biotissue scattering/absorption is calculated and plotted in Fig. 14.1a using the following light transport equation, in the diffusion approxima-

tion, to describe the optical response of the tissue: $\mu_{\text{eff}} = (3\mu_a[\mu_a + \mu_s(1-g)])^{1/2}$, where absorption μ_a and scattering μ_s coefficients and anisotropy factor g for human skin epidermis and dermis layers (see Fig. 14.1b) were chosen for this calculation [65]. As one can see, absorption of the excitation light at 980 nm by water constituent and hemoglobin of the biological tissue, such as skin (Fig. 14.1a), is compensated by the reduced scattering of biotissue at this wavelength, and the UCNP-pertinent excitation/emission properties are advantageous for biomedical optical imaging.

Secondly, UCNP excitation at 980 nm elicits very little autofluorescence from biological tissue. Presuming a small autofluorescence signal, it has to be Stokes-shifted to the longer-wavelength, whereas the detection takes place in the shorter wavelength band ranging from UV to near-IR depending on the UCNP dopant structure. As we have demonstrated, UCNP topically applied both on freshly excised human skin and micro-needle-delivered in the dermis layer exhibited ultimately high imaging contrast, with the biotissue-induced laser light scattering and autofluorescence background totally suppressed (the background level was detected at the electronic noise level using a high-end cooled CCD camera). The acquired epi-luminescence images of skin autofluorescence and UCNP distribution excited, respectively, at 365 and 980 nm are shown in Fig. 14.11.

It turns out that the excitation light scattering bled through the interference filters contributes more to the imaging background than the autofluorescence signal, which is an unusual situation in optical biomedical imaging. In order to counter the excitation light bleeding into the detection path, the detection band can be spectrally offset by as much as 330 nm from the excitation band, by picking the NaYF₄:Yb:Er upconversion emission multiplet centered at 550 nm (Fig. 14.9c, green shaded band) [66]. The other major advantage of UCNP lies in a million-fold difference in the emission lifetimes of UCNP and endogenous fluorophores that make up the autofluorescence background ($\tau_{uc} \approx 1$ ms versus $\tau_{af} \approx 3$ ns) that allows complete suppression of the autofluorescence and excitation background by an optical time-gated approach alone, thus avoiding the use of expensive interference filters. This scheme is realized by setting a time delay (≈ 10 ms) between the excitation laser pulse and photodetection of the sample response. The long τ_{uc} of UCNP also lead to the enhanced efficiency of Förster resonance energy transfer (FRET) processes, used to investigate protein interactions [67].

14.3.4 Optical Imaging of UCNP in Biological Samples

The promise of upconversion nanoparticles has been recently demonstrated through the imaging of UCNP bioconjugates in cell cultures [4, 68] and whole animal models [6, 69], with the autofluorescence background suppressed. Figure 14.12 shows live-cell imaging of UCNPs in cells by using laser-scanning luminescence confocal microscopy [4]. The confocal imaging modality allows high-sensitivity detection since the high intensity at the sub-femtoliter focal excitation volume, such

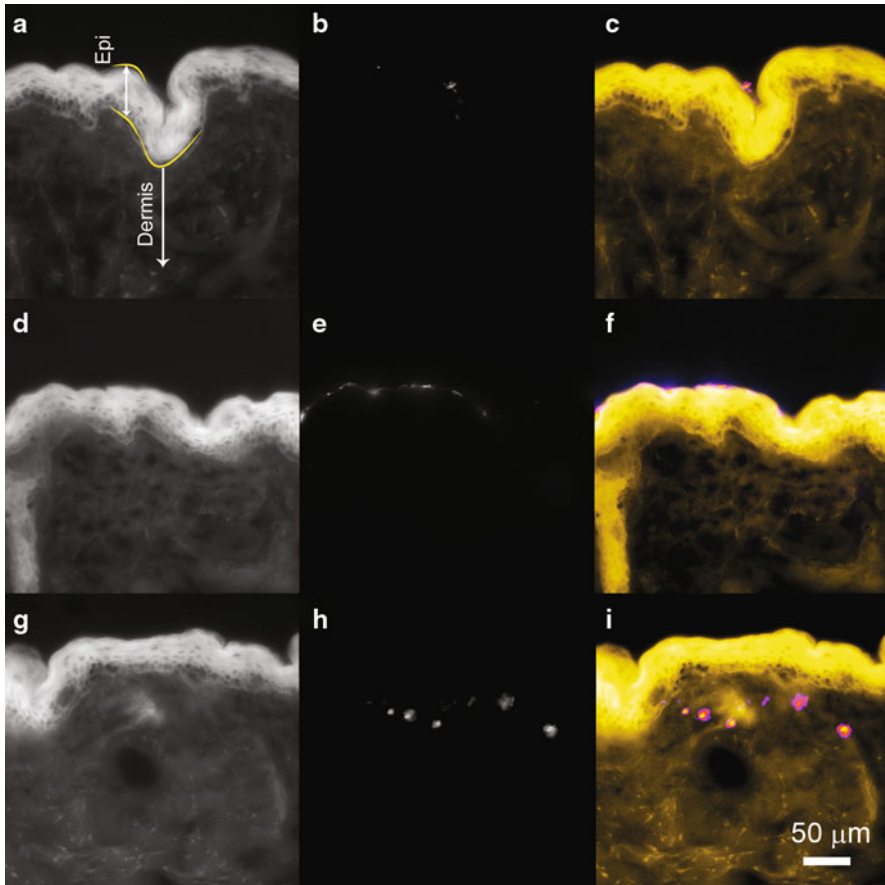


Fig. 14.11 NaYF₄:Yb:Tm nanoparticle distribution in human skin in case of (*top two rows*) the topical application, and (*bottom row*) micro-needle treatment. (**a**), (**d**), (**g**), UV (365 nm)-excited autofluorescence images of skin; (**b**), (**e**), (**h**), images of UCNP excited by 980-nm laser; (**c**), (**f**), (**i**), pseudo-color overlaid images of (**a**), (**d**), (**g**) showing UCNPs (*purple* color) in skin folds and dermis (*green* color), respectively

as $10 \times 10^5 \text{ W cm}^{-2}$ (used to obtain images in Fig. 14.11), is easily achievable. Evading the signal cross talks caused by the multiple scattering of the luminescence photons in the biological samples is important for single nanoparticle imaging, which would otherwise be obscured by intense signals from UCNP clusters. At the same time, the confocal imaging modality suffers from long image acquisition times arising from the necessity to dwell for several τ_{uc} -s on each acquisition pixel. As an example, consider $\tau_{uc} \approx 1 \text{ ms}$ that requires, at least, 5 ms per pixel and c.a. 1/2 h to capture a 512×512 pixel image – this is unaffordable for most practical applications.

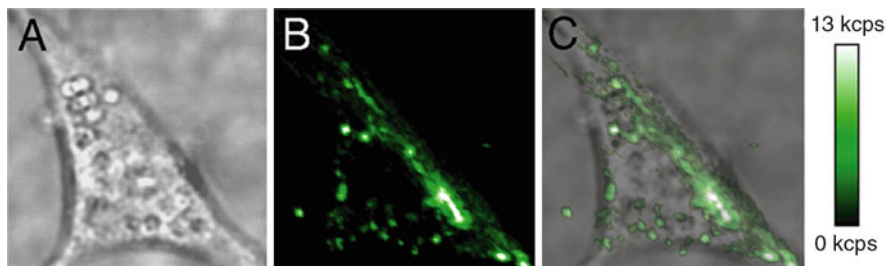


Fig. 14.12 Live-cell imaging of UCNPs in NIH 3T3 murine fibroblasts using laser-scanning luminescence confocal microscopy. (a) Bright field image of a cell with endocytosed UCNPs, (b) upconverted luminescence following 980-nm excitation, and (c) overlay. Scale bar, 10 μm

Intensive research activity has been streaming toward optical tomography of UCNP-tagged tissue sites, where upconversion nanoparticles are deployed as the molecular probes. In particular, the whole animal imaging has been reported on a number of occasions, where the UCNP-assisted target delivery and optical tomography imaging of cancer tumor sites demonstrated the imaging depth of up to 2 cm in transmission mode [70].

This raises the question on the ultimate sensitivity limit achievable for the UCNP imaging in biological tissue. In order to answer this question, we performed the single UCNP imaging through a layer of the hemolyzed blood using full-field optical microscopy configuration. It was realized that as long as the scattering of the biological sample was not overwhelming, such as in the case of the hemolyzed blood, sample absorption presented little problem for imaging, and no degradation of the imaging of a single (UCNP) nanoparticle was observed (see Fig. 14.13).

14.3.5 Shortcomings of the UCNP Technology

These studies have revealed shortcomings of the UCNP technology. These include limited penetration depth of the UCNP-assisted optical imaging in whole animals because of the requirement of high excitation intensity that is usually realized by focusing, and is not possible in turbid biological tissue [66]. This point is illustrated in Fig. 14.14, where a comparison between the optical tomography imaging deploying organic fluorescence dye and UCNP in an animal model is presented [66]. Although the UCNP-assisted optical tomography provided much more accurate localization of the luminescence probe (due to the background-free imaging and nonlinear dependency of the luminescence signal versus the excitation intensity), the sensitivity of the UCNP detection is inferior to that of the conventional infrared Cy5 fluorescence dye. It is important to note that, unlike in the case of Cy5, the UCNP signal intensity is quickly degraded versus the imaging depth. This sets an inherent limit on the applicability of the UCNP for deep tissue imaging, especially considering that the maximum intensity allowed at 980 nm

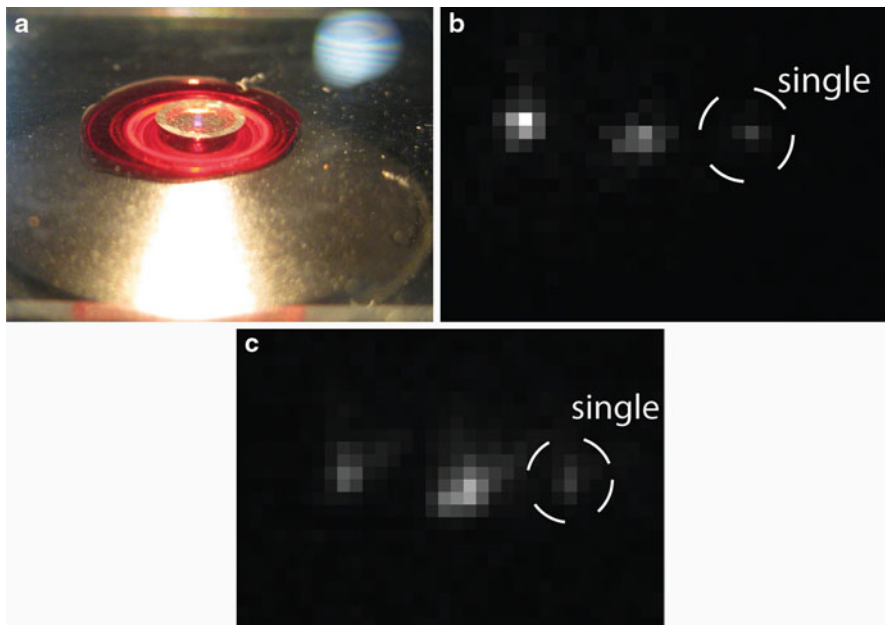


Fig. 14.13 Optical epi-luminescence microscopy of a single UCNP deposited on a glass slide using the “blood immersion” objective lens shown in (a). (b) and (c) Images of the constellation of UCNP particles acquired using correspondingly water- and blood-immersion objective lenses. The images were matched to those acquired by transmission electron microscopy. A single UCNP particle is circled. The epi-luminescence image acquisition time is 1 s

in humans is limited to 726 mW cm^{-2} . Besides, the spectral filtering efficiency of the UCNP luminescence is compromised by the broad angular distribution of unwanted background photons emerging from biological tissue (10×10^6 -fold versus 10×10^3 -fold [71]), although this can be mitigated by the time-gated imaging mode. These findings call for redefinition of the target applications, which will capitalize on the key UCNP merits, while minimizing their limitations. One such application is ultrasensitive imaging of UCNP particles in thin tissue slices, such as skin, aiming at demonstration of background-free imaging of nanoparticles paving a way toward ultrasensitive in vivo imaging of nanoparticle penetration in skin.

14.4 Luminescent Nanoparticle Bioconjugation

In most cases, living systems treat extraneous nanomaterial, as an unwelcome intruder, and engage disposal protocols. In order to usher in a more meaningful communication with cells, a nanoparticle needs to be decorated with biomolecule(s) whose role is to establish a communication interface between the nanoparticle and the cell. A luminescent nanoparticle participating in such communication events

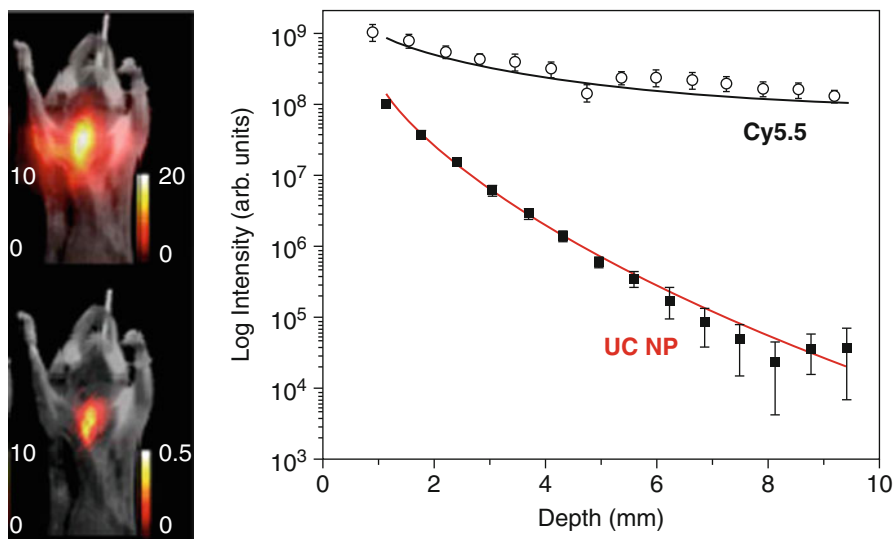


Fig. 14.14 *Left panel (top)*: Image of a mouse with a thin capillary tube inserted into the esophagus. The tube is filled with Cy5.5 dye (excitation at 680 nm and emission at 712 nm). *Left panel (bottom)*: The same mouse with UCNP instead of the dye (excitation at 980 nm and emission at 670 nm). The absence of autofluorescence in the bottom image is obvious. However, a much stronger excitation power is required in the case of UCNP probe. This is illustrated on the *right panel* where the decay of the signal is shown, as a function of the tissue imaging depth. The signal decays much faster for the UCNP, because it is proportional to the intensity in the power of 2.3 (Reproduced from Ref. [66])

furnished by biomolecular cascades can report on the molecular trafficking and serve diagnostic and therapeutic purposes. Therefore, grafting biomolecules onto the nanoparticle surface represents the key procedure underlying the convergence of Nanotechnology with Life Sciences.

14.4.1 Colloidal Stability in Water and Buffer Solutions

Deployment of luminescent nanoparticle in biomedical applications critically depends on NP bioconjugate stability in physiological solutions, currently an issue, as oftentimes synthesized NPs, such as upconversion NPs, are hydrophobic. Their dispersion in water results in rapid formation of aggregates that precipitate in the form of an insoluble residue. However, hydrophilicity of some NPs, such as the surface-oxygenated nanodiamonds, does not guarantee LND aqueous colloidal stability; unless the functional groups the NP surface acquire sufficient charge in water. This surface charge is measured in terms of the zeta-potential units, mV. Surface-oxygenated nanodiamonds are stable in water at the zeta-potential absolute value greater than 30 mV. However, when the nanodiamond aqueous

colloid is transferred to buffer, salt-induced surface charge screening leads to flocculation [72]. Existing NP surface functionalization methods to counter flocculation and to facilitate bioconjugation can be classified as covalent functionalization, e.g., amidation (utilizing surface carboxyl groups), silanization, adsorption, and lipid/polymer capping. While the reported covalent functionalization protocols showed stability of the resultant complexes, their realization was often complex and case dependent, whereas most of the other methods compromised functional stability. In the following two subsections, we address two surface functionalization and bioconjugation strategies using the examples of LND and UCNP to illustrate the main aspects of this side of bio-nanotechnology.

14.4.2 A Universal Bioconjugation Platform Based on a High-Affinity Molecular Pair Barnase:Barstar

Most of the nanodiamond surface cleaning procedures promotes formation of oxygen-containing surface functional groups, including carboxyls, hydroxyls, ketons, and aldehydes. Many of these groups are biologically compatible, thus forming a lucrative possibility for the direct covalent attachment of biomolecules using, e.g., a carboxyl group (COOH). COOH is universally employed in living systems to assemble proteins by fusing together a COOH terminal of one protein with an amino-terminal (NH₂) of the other protein, forming a strong covalent amide bond. Since COOH-abundance of the acid-cleaned nanodiamond surface is c.a. 7 %, it is conceivable to make use of this terminal to attach a biomolecule containing a NH₂-terminal. The implementation of this strategy is not straightforward due to the notorious colloidal instability of nanodiamonds in saline solutions, which are essential to maintain the structural conformation of biomolecules. Also, amide-bonding reactions can alter the functionality of biomolecules and, hence, need adjustments specific to each biomolecule. This is cumbersome, and calls for a universal straightforward bioconjugation approach. A novel nanoparticle-bioconjugation platform has been recently reported [73]. This approach is based on a high-affinity protein pair, barstar:barnase (Bs:Bn), a functional analogue of streptavidin:biotin, that provides a modular design toolkit by way of locking organic and inorganic modules together in a straightforward and robust manner. The LND biofunctionalization strategy based on Bs:Bn is as follows: A covalently assembled subunit LND-Bs (or LND-Bn) strongly attaches to a prefabricated counter subunit Bn-X (or Bs-X) by simply mixing the two colloidal substrates, where X is a terminal molecule/nanoparticle. The terminal molecule can be biologically significant, with a potential for targeted drug delivery and/or biolabeling applications (see Fig. 14.15).

Non-cytotoxic, biocompatible, and bright luminescent nanodiamonds (LNDs) represented a particularly attractive “docking station” due to their appeal for molecular probe and targeted delivery applications. The modified EDC/sNHS reaction yielded a covalently bonded 140- and 35-nm LND-Bs conjugate, which showed remarkable colloidal stability in buffer solutions. Using this platform, LND-Bs:Bn-(green fluorescent protein) and LND-Bs:Bn-nanogold were synthesized and

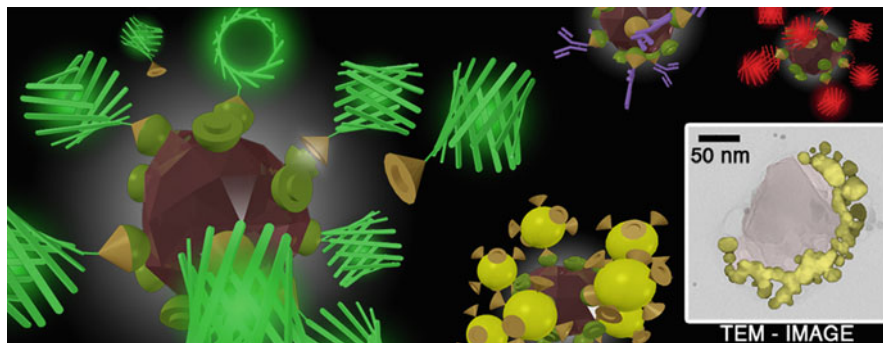


Fig. 14.15 Diagram of a universal platform for bioconjugation of macromolecules and nanoparticles to the nano-vehicle surface, in this example, nanodiamond. Covalently grafted to the diamond surface molecules, barstar (*green caps*) are able to selectively bind to molecules of barnase (*brown cones*), which, in turn, are pre-conjugated with such macromolecules as *green* fluorescent protein (fragment), antibodies (fragment at the top), or nanoparticles, e.g., nanogold (fragment). Transmission electron microscopy image shows the assembly of nanodiamond-nanogold, called “nano-diadem” (*inset*) [34]

tested in saline solutions and cellular environments. Assaying and optical/TEM imaging of these synthesized organic and inorganic complexes revealed their functional stability and structural integrity [34]. Most recently, the authors (AZ, SD, et al.) have demonstrated implementation of the same protocol to obtain antibody bioconjugates of upconversion nanoparticles UCNP-Bs:Bn-4D5, where 4D5 represents a recombinant mini-antibody to the HER2/neu receptor, a type of epithelial growth factor receptor.

14.4.3 Bioconjugates of Upconversion Nanoparticle Coated with Amphiphilic polymer

The bioconjugation strategy described for nanodiamonds represents an exceptional case of nanoparticles featuring biocompatible surface moieties, and often stable in aqueous colloids. In general, inorganic nanoparticles are non-mixable with water, and their surface provides no anchoring points for attachment of biomolecules. Considering a number of interesting luminescent nanoparticles emerging as a result of the rapid developments in Nanotechnology, a universal bioconjugation approach is highly demanded. Upconversion nanoparticles based on the popular nanocrystalline host NaYF_4 represent one of the most challenging cases. Firstly, as-synthesized UCNP are surface-coordinated with oleic groups that render this nanomaterial hydrophobic, i.e., not mixable with water and buffer solutions. Secondly, NaYF_4 does not seem to provide amiable surface anchoring points for firm docking of biomolecules or auxiliary moieties. Thirdly, the UCNP power quantum yield appeared to be highly susceptible to the surface functionalization, where high-energy

vibronic modes of some functional groups, such as COOH, provided non-radiative relaxation path to the upper excited states of Er or Tm in NaYF₄:Yb:Er(Tm) [64]. Early attempts to displace the weakly bonded oleic groups with more affine moieties, such as citric [4] and mercaptopropionic [74] groups, have demonstrated only marginal colloidal stability of UCNPs at the neutral pH (pH 7) values, precluding biomedical applications, where pH varies widely. This implies that the functional group attachment to the UCNP surface was governed by electrostatic and/or Van der Waals forces, i.e., attachment by adsorption. The absorption-based biofunctionalization protocol has been employed by Niedbala and coworkers to attach NeutrAvidin to the UCNP surface by a facile pot-mix reaction [75]. This approach is subject to desorption of the adsorbed molecules in biological solutions, and also depends on the pH of the medium. A common solution is to cover the surface of nanoparticles by polyethylene-glycol (PEG). These groups prevent nanoparticle merging and forming of aggregates, which adversely affect the colloidal stability, via the mechanism of steric hindrance [76]. Also, PEGylation represents the core of the so-called stealth technology preventing PEGylated nanoparticles intravenously injected into the blood stream from rapid immune-mediated removal. However, PEG groups have their disadvantages associated with poorly controlled polymer chains, and, most importantly, PEG chemistry is expensive.

A radical solution to avoid the dependency of bioconjugation reactions on the UCNP surface anchoring lies in coating nanoparticles with an additional layer that is amiable for subsequent bioconjugation. Coating the UCNP nanoparticle with a silica shell [77, 78] represents an attractive approach due to the shell stability in the range of pH, and maturity of the silica surface coating technology [77]. Another approach makes use of amphiphilic polymers that represent molecules with hydrophobic and hydrophilic terminals. This approach has been successfully demonstrated for surface activation of quantum dots [79], and partly accounted for the commercial success of quantum dots-based procedures. An amphiphilic polymer was wrapped around the particles, exploiting the nonspecific hydrophobic interactions between the alkyl chains of poly(maleic anhydride alt-1-tetradecene) and the nanocrystal surfactant molecules (oleic acids). This resulted in transferring hydrophobically capped nanocrystals from organic to aqueous solution. Addition of bis(6-aminoethyl)amine resulted in the cross-linking of polymer chains around each nanoparticle [79]. Our initial experiments using this protocol have resulted in UCNPs being stable in water and buffer solutions for a month. Nanocrystals coated with COOH-amphiphilic polymer [79] are readily processed using a universal bioconjugation protocol, i.e., EDC/sNHS reaction, which we have demonstrated by attaching streptavidin to UCNP, as presented in Fig. 14.16. A facile pot-mix reaction will lead to a strong attachment of a targeting biomolecule of choice, if this molecule is biotinylated. A range of commercially available biotinylated ligands and antibodies, including antibodies to epitope tags, permits versatile design of various bioconjugates that are linked together via a strong bond between streptavidin and biotin. An alternative approach, demonstrated by us, is based on a high-affinity protein pair barnase:barstar that makes use of the advantageous recombinant protein technology [34].

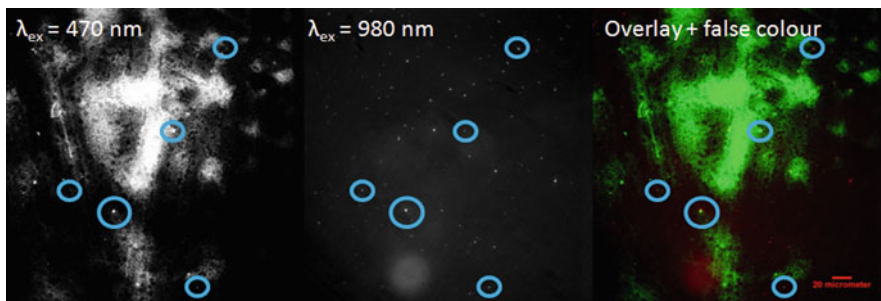


Fig. 14.16 Fluorescent microscopy images of UCNP bioconjugated with streptavidin-dylight (dylight – organic dye) obtained under excitations of 470 and 980 nm, and overlaid false-color image. Colocalization of several nanoparticles (*circled*) is clearly observed, demonstrating successful bioconjugation of streptavidin to UCNP

14.5 Communication of Nanoparticles and Cells

To sustain the lifecycle of living cells, extraneous material has to be absorbed from the extracellular medium. The absorption mechanisms fall into two categories: specific internalization, which requires the cell to actively recruit molecules into the cytoplasm, and nonspecific internalization, which is essentially a random process in which the cell exercises no active control; it can vary depending on the cell type and has poor material selectivity. Receptor-mediated endocytosis is an important example of the specific internalization mechanism that facilitates import of selected extracellular molecules and mediates intercellular signaling. This process is regulated by plasma membrane receptors that are predominantly activated by receptor-specific ligands. As a result, only biomolecular complexes grafted with these ligands can activate these receptors and gain access into the cell, and these represent a focus of this book chapter. In the process of endocytosis, the plasma membrane is invaginated inward from specialized membrane micro-domains forming either clathrin- or caveolin-coated pits. This specific cellular uptake mechanism has been a subject of intense research driven by the demand to elucidate cellular molecular trafficking and potential applications in targeted drug delivery.

Aiming at achievement of the highest possible target delivery specificity, we need to understand nonspecific (in contrast with the specific internalization via receptor-mediated endocytosis) internalization of nanoparticles that depends on many parameters of nanoparticles, such as size, surface charge, and surface functional groups, as we have presented in a separate publication on the example of quantum dots [80], and shown in Fig. 14.17. Charge affects the level of nanoparticle uptake in the cells considerably, and should be taken into account, especially when conducting experiments with cell cultures. Despite that, the mechanism of the cellular uptake is defined as nonspecific, it is mediated by the receptors, and realized either through direct interaction between charged particles and the receptor or through a preliminary attachment of free protein to the NP surface. Surface

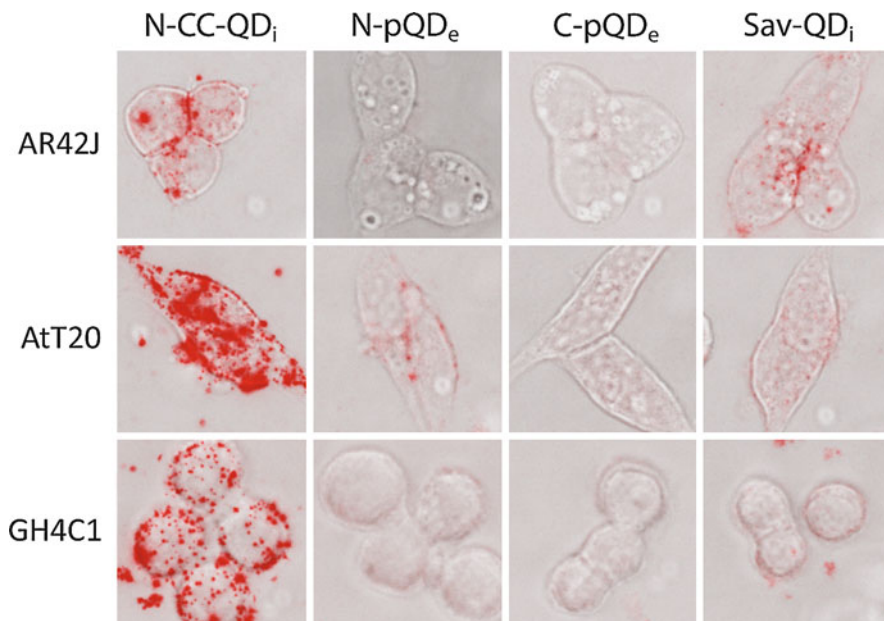


Fig. 14.17 Images showing the level of the quantum dot (QD) uptake in three immortalized cell cultures AR42J, AtT20, and GH4C1 depending on the surface of functional groups. Direct attachment of amino groups (far left column, N-CC-QD_i) shows the highest level of internalization, while a PEG-linker (amino-terminal, N-pQD_e and carboxyl-terminal, C-pQD_e) heavily suppresses internalization of nanoparticles (Reproduced from Ref. [80])

modification of nanoparticles with hydrophilic polymers, such as PEG, inhibits the nanoparticle uptake, making it ideally suitable for the negative controls to various cellular models, where the terminal amino group suppressed internalization significantly, as shown in Fig. 14.17 (columns, N-pQD_e, C-pQD_e). It is expected that amino or carboxyl surface functionalization of NP, deprived of PEG, will facilitate intensive uptake of particles in the cell, despite the positive and negative terminal charges. However, the positively charged nanoparticles are absorbed less effectively, and represent a good choice for the experiments on specific labeling and activation of the cells.

In order to investigate molecular trafficking using NP bioconjugates, the biomolecular part of the NP module must activate the biological process. In case of cell communication, it is often a ligand attached to the NP that activates the cell receptor, and thereby launches a cascade of biomolecular events that may be regarded as a process of communication of the cell and the nanoparticle. As a result, the particle is translocated to the cell cytoplasm, where it participates in the other sequence of the post-endocytosis events. As an example of the ligand that activates the communication protocol with the cell, we consider somatostatin (SST). Among the multitude of physiological functions that SST participates in, some are of high clinical relevance. The biological functions of SST are initiated upon its binding to trans-membrane G-protein-coupled receptors of six

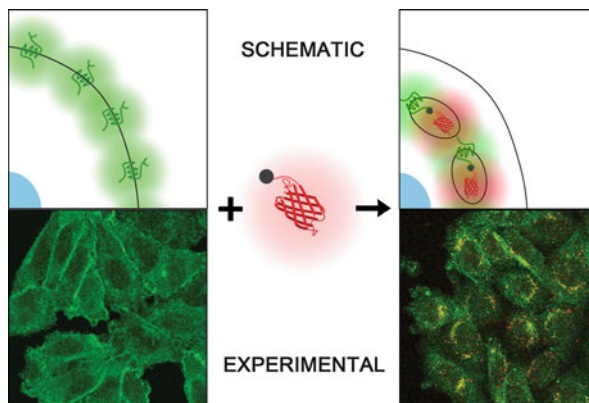


Fig. 14.18 (Top) A diagram of specific internalization of peptide somatostatin fused with a red fluorescent protein (RFP) (center) by binding and activating receptors sst_{2A} (green, upper left panel) in Chinese hamster ovary cells (CHO-K1). As a result of the endocytosis, SST and sst_{2A} are taken inside the cells (right top panel). (Bottom) Fluorescent confocal images of the CHO-K1 cells: (right) showing the colocalization of peptide somatostatin/red fluorescent protein (SST-mRFP) with the sst_{2A} receptor antibodies, labeled with fluorescent dye FITC, rendered in orange. The image on the left shows a negative control, obtained by the inhibition of SST-RFP (Reproduced from Ref. [82])

subtypes, including sst_{2A} , which are differentially distributed in organs such as brain, spinal cord, and pancreas, and over-expressed in neuroendocrine tumor cells. The physiological effects of SST, evoked after ligand binding and receptor activation, are mediated through intracellular signaling mechanisms including the adenylyl cyclase inhibition, K^+ channel opening, and, in some cases, the activation of phospholipase C leading to the opening of intracellular Ca^{2+} stores [81].

Somatostatin analogs, bearing a contrast agent, are useful for a variety of applications ranging from basic research into elucidating the post-endocytotic molecular pathways in cells to clinical scenarios, such as the targeting/diagnosis of neuroendocrine tumors. Prior to demonstration of the NP bioconjugate complex of NP-SST designed for specific target internalization in cells, the somatostatin activity and potency was tested using cell cultures that were activated by SST, together with the demonstration of the specific molecular processes that accompany receptor-mediated endocytosis.

For example, it is known that the specific receptor sst_{2A} activation triggers a cascade of processes, such as the opening of the calcium repositories in the cytoplasm, in genetically modified Chinese hamster ovary cells (CHO-K1). The design, production, and pharmacological characterization of a recombinant fluorescent SST analogue fused with a monomeric red fluorescent protein (SST-mRFP) has been reported [82], with the main result shown in Fig. 14.18. The SST moiety in the SST-mRFP complex was demonstrated to be active and potent for triggering signaling in both wild-type and transfected cells containing somatostatin receptors. The fluorescent complex of SST was internalized, as a result of the processes launched by the receptor activation, leading to the ligand translocation to the

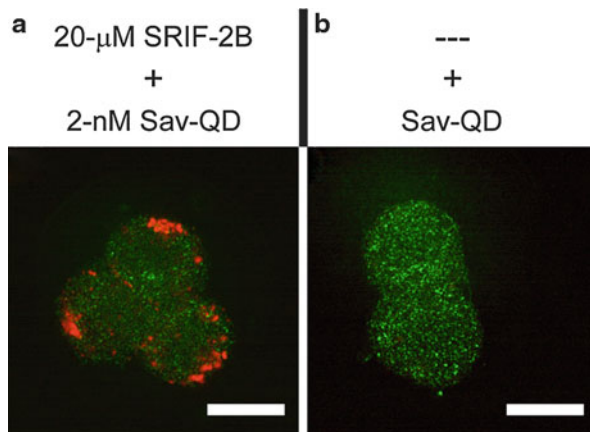


Fig. 14.19 Fluorescence confocal images of cells treated with (a) 20- μ M SST-2B, also known as SRIF-2B, and (b) blank negative control, followed by 2-nM Sav-QD at low temperature. The cells, when restored to 37 $^{\circ}$ C, internalized the pre-formed receptor:ligand complexes. The QD-luminescence is color-coded *red* and the cell-morphological contrast, originated from laser back-scattering, is color-coded *green*. The data is representative of at least three independent experiments. Scale-bar, 10 μ m

cellular cytoplasm in the process of endocytosis, and eventual accumulation in the perinuclear region (Fig. 14.18, bottom-right panel). It is interesting to note that SST and sst_{2A} remain colocalized even at the later stage of the endocytosis, being encapsulated either in the late endosomes or lysosomes, and visualized in a yellow-orange color in Fig. 14.18, bottom-right panel. This shows potential of fluorescent ligand complexes to elucidate the molecular fate of post-endocytotic events, which in this particular case demonstrate the receptor-ligand integrity.

The development of a somatostatin analogue that bears a luminescent nanoparticle contrast agent represented by a quantum dot has been recently reported. In virtue of exceptional luminescence properties and commercial availability of various surface functionalized types, QD was selected as the model nanoparticle. A biotinylated analogue of SST (SST-2B) was conjugated to a streptavidin-coated QD (Sav-QD), forming an SST-2B:Sav-QD complex. However, this preformed SST-2B:Sav-QD complex was incapable to bind/activate the somatostatin receptors. In order to mitigate this problem, an *in situ* two-step conjugation strategy was introduced to overcome the Sav-induced inhibitory effect, an approach that proved to be successful for specific targeting of the somatostatin receptors. Using this strategy, the receptor-mediated endocytosis of the nanoparticle-labeled SST was optically imaged. Despite the original inactivity, SST-2B and similar biotinylated SST-ligands are envisaged to be made functional again using a two-step approach. Their deployment for the targeted delivery into cells that express somatostatin receptors, e.g., in brain regions responsible for the regulation of blood pressure will be valuable (see Fig. 14.19).

14.6 Conclusion

We described a bottom-up strategy of luminescent nanoparticle-assisted imaging of cellular processes, such as the receptor-mediated endocytosis and associated molecular events. This strategy has three main building blocks: bright photostable luminescent nanomaterials conspicuous on the background of cell autofluorescence, surface modification to enable interfacing with the biological world, and modular engineering of the biomolecular complexes equipped with a ligand for programmable functions in the cell. Luminescent nanodiamonds (LND) and up-conversion nanoparticles (UCNP) were selected as representatives of different classes of luminescent emitters, and their photophysics was discussed in the context of optical biological imaging. The rapidly growing area of nanotechnology offers a number of lucrative possibilities of nanomaterial deployment in bio-nano-optics applications. The nanomaterial choice, however, needs to be carefully scrutinized based on the material's physical, chemical, and optical properties, where the core chemical inertness, amiable surface chemistry, and minimal cytotoxicity are essential. Optical properties remain the key factors determining the utility of these nanomaterials, where the nanoparticle brightness defined as the action cross section is a necessary, but not sufficient, prerequisite. It appears that the imaging contrast of luminescent nanoparticle against the crowded morphological and autofluorescence background of the cell needs to be taken into account. Despite the lower action cross-section of the UCNP, they offer excellent means for discrimination of the excitation and autofluorescence background paving a way toward ultimate detection sensitivity at the single-molecule level.

Interfacing of nanoparticles with biomolecules using bioconjugation procedures poses a challenge due to the poor dispersability of (often hydrophobic) nanoparticles in aqueous/buffer colloids exacerbated by the surface inability to anchor biomolecules or intermediate linkers. Luminescent nanodiamond represents a fortunate exception, whose surface is decorated with biologically amiable carbonyl groups that enable direct realization of a modular assembly of a LND bioconjugate in a facile pot-mix reaction. Hydrophobic UCNP require several extra-procedures to render these particles mixable with buffer solutions and graft COOH-groups on their surface. This is achieved by complete surface reshaping with a shell comprising, e.g., amphiphilic polymer prefabricated with COOH-groups that renders UCNP surface amenable to bioconjugation.

Biological properties of the nanoparticle bioconjugates are determined by a ligand firmly attached to the nanoparticle surface, and the choice of ligands and participating biological systems is substantial. We chose a peptide somatostatin, as the ligand, to demonstrate the potential of the luminescent nanoparticle tagging to elucidate its molecular pathway during the endocytotic and post-endocytotic events.

The development of luminescent nanoparticle bioconjugates capable of programmable interactions with the targeted cells opens new opportunities in several areas of life sciences, including new imaging modalities, enabling long time-lapse investigation of molecular trafficking in cells, cellular imaging at the unprecedented

single-molecule level, in vivo diagnosis based on ultrahigh-sensitivity optical tomography imaging, and, targeted drug delivery. This work sets first grounds for these exciting future prospects.

References

1. W.E. Moerner: Proc. Natl. Acad. Sci. **104**, 12596 (2007)
2. G. Seisenberger, M.U. Ried, T. Endre, H. Bning, M. Hallek, C. Bruchle: Science **294**, 1929 (2001)
3. C.-C. Fu, H.-Y. Lee, K. Chen, T.-S. Lim, H.-Y. Wu, P.-K. Lin, P.-K. Wei, P.-H. Tsao, H.-C. Chang, W. Fann: Proc. Natl. Acad. Sci. **104**, 727 (2007)
4. S.W. Wu, G. Han, D.J. Milliron, S. Aloni, V. Altoe, D.V. Talapin, B.E. Cohen, P.J. Schuck: Proc. Natl. Acad. Sci. U.S.A. **106**, 10917 (2009)
5. A.M. Schrand, H. Huang, C. Carlson, J.J. Schlager, E. sawa, S.M. Hussain, L. Dai: J. Phys. Chem. B **111**, 2 (2006)
6. T.Y. Cao, Y. Yang, Y.A. Gao, J. Zhou, Z.Q. Li, F.Y. Li: Biomaterials **32**, 2959 (2011)
7. J.L. Yuan, G.L. Wang: Trac-Trends in Analytical Chemistry, **25**, 490 (2006)
8. S. Osswald, G. Yushin, V. Mochalin, S.O. Kucheyev, Y. Gogotsi: J. Am. Chem. Soc. **128**, 11635 (2006)
9. V. Dolmatov, M. Veretennikova, V. Marchukov, V. Sushchev: Phys. Solid State **46**, 611 (2004)
10. E. Osawa: Pure Appl. Chem. **80**, 1365 (2008)
11. S. Turner, O.I. Lebedev, O. Shenderova, I.I. Vlasov, J. Verbeeck, G. Van Tendeloo: Adv. Funct. Mater. **19**, 2116 (2009)
12. F.K. de Theije, O. Roy, N.J. van der Laag, W.J.P. van Enckevort: Diam. Relat. Mater. **9**, 929 (2000)
13. F.K. de Theije, N.J. van der Laag, M. Plomp, W.J.P. van Enckevort: PhilosophicalMagazine A **80**, 725 (2000)
14. R.R. Nimmagadda, A. Joshi, W.L. Hsu: J. Mater. Res. **5**, 2445 (1990)
15. J. Tisler, G. Balasubramanian, B. Naydenov, R. Kolesov, B. Grotz, R. Reuter, J.-P. Boudou, P.A. Curmi, M. Sennour, A. Thorel, M. Borsch, K. Aulenbacher, R. Erdmann, P.R. Hemmer, F. Jelezko, J. Wrachtrup: ACS Nano **3**, 1959 (2009)
16. A. Krueger, M. Ozawa, G. Jarre, Y. Liang, J. Stegk, L. Lu: Phys. Status Solidi A **204**, 2881 (2007)
17. B.R. Smith, M. Niebert, T. Plakhotnik, A.V. Zvyagin: J. Lumin. **127**, 260 (2007)
18. I.I. Vlasov, A.S. Barnard, V.G. Ralchenko, O.I. Lebedev, M.V. Kanzyuba, A.V. Saveliev, V.I. Konov, E. Goovaerts: Adv. Mater. **21**, 808 (2009)
19. A. Smith, A. Mainwood, M. Watkins: Diam. Relat. Mater. **11**, 312 (2002)
20. I. Aharonovich, S. Castelletto, D.A. Simpson, A.D. Greentree, S. Praver: Phys. Rev. A **81**, 043813 (2010)
21. A. Gruber, A. Drabenstedt, C. Tietz, L. Fleury, J. Wrachtrup, C. von Borczyskowski: Science **276**, 2012 (1997)
22. L. Rondin, G. Dantelle, A. Slablab, F. Grosshans, F. Treussart, P. Bergonzo, S. Perruchas, T. Gacoin, M. Chaigneau, H.C. Chang, V. Jacques, J.F. Roch: Phys. Rev. B **82**, 115449 (2010)
23. T.-L. Wee, Y.-K. Tzeng, C.-C. Han, H.-C. Chang, W. Fann, J.-H. Hsu, K.-M. Chen, Y.-C. Yu: J. Phys. Chem. A **111**, 9379 (2007)
24. A.V. Zvyagin, N.B. Manson: Adv. Nanodiam. Sci. Technol. in press (2012)
25. A. Batalov, C. Zierl, T. Gaebel, P. Neumann, I.Y. Chan, G. Balasubramanian, P.R. Hemmer, F. Jelezko, J. Wrachtrup: Phys. Rev. Lett. **100**, 077401 (2008)
26. J.R. Maze, P.L. Stanwix, J.S. Hodges, S. Hong, J.M. Taylor, P. Cappellaro, L. Jiang, M.V.G. Dutt, E. Togan, A.S. Zibrov, A. Yacoby, R.L. Walsworth, M.D. Lukin: Nature **455**, 644 (2008)

27. F. Cichos, C. von Borczyskowski, M. Orrit: *Science* **12**, 272 (2007)
28. R.M. Dickson, A.B. Cubitt, R.Y. Tsien, W.E. Moerner: *Nature* **388**, 355 (1997)
29. M. Kuno, D.P. Fromm, H.F. Hamann, A. Gallagher, D.J. Nesbitt: *J. Chem. Phys.* **112**, 3117 (2000)
30. P.A. Frantsuzov, R.A. Marcus: *Phys. Rev. B* **72**, 155321 (2005)
31. T. Jau, R.A. Marcus: *J. Chem. Phys.* **123**, 054704 (2005)
32. C. Bradac, T. Gaebel, N. Naidoo, M.J. Sellars, Twamley J., L.J. Brown, A.S. Barnard, T. Plakhotnik, A.V. Zvyagin, J.R. Rabeau: *Nat. Nano* **5**, 345 (2010)
33. Y.-R. Chang, H.-Y. Lee, K. Chen, C.-C. Chang, D.-S. Tsai, C.-C. Fu, T.-S. Lim, Y.-K. Tzeng, C.-Y. Fang, C.-C. Han, H.-C. Chang, W. Fann: *Nat. Nano* **3**, 284 (2008)
34. V.K.A. Sreenivasan, E.A. Ivukina, W. Deng, T.A. Kelf, T.A. Zdobnova, S.V. Lukash, B.V. Veryugin, O.A. Stremovskiy, A.V. Zvyagin, S.M. Deyev: *J. Mater. Chem.* **21**, 65 (2011)
35. S.J. Yu, M.W. Kang, H.C. Chang, K.M. Chen, Y.C. Yu: *J. Am. Chem. Soc.* **127**, 17604 (2005)
36. A.M. Schrand, L. Dai, J.J. Schlager, S.M. Hussain, E. Osawa: *Diam. Relat. Mater.* **16**, 2118 (2007)
37. A.M. Schrand, S.A. Ciftan Hens, O.A. Shenderova: *Crit. Rev. Solid State Mater. Sci.* **34**, 18 (2009)
38. D. Ho: *Nanodiamonds: Applications in Biology and Nanoscale Medicine*. Technology and Engineering (Springer, New York, 2009)
39. L.P. McGuinness, Y. Yan, A. Stacey, D.A. Simpson, L.T. Hall, D. Maclaurin, S. Prawer, P. Mulvaney, J. Wrachtrup, F. Caruso, R.E. Scholten, L.C.L. Hollenberg: *Nat. Nano* **6**, 358 (2011)
40. Y.-Y. Chen, H. Shu, Y. Kuo, Y.-K. Tzeng, H.-C. Chang: *Diam. Relat. Mater.* **20**, 803 (2011)
41. A. Krger, F. Kataoka, M. Ozawa, T. Fujino, Y. Suzuki, A.E. Aleksenskii, A. Ya Vul, E. Osawa: *Carbon* **43**, 1722 (2005)
42. A.S. Barnard, M. Sternberg: *J. Phys. Chem. B* **109**, 17107 (2005)
43. B.R. Smith, D.W. Inglis, B. Sandnes, J.R. Rabeau, A.V. Zvyagin, D. Gruber, C.J. Noble, R. Vogel, E. Osawa, T. Plakhotnik: *Small* **5**, 1649 (2009)
44. C. Bradac, T. Gaebel, N. Naidoo, J.R. Rabeau, A.S. Barnard: *Nano Lett.* **9**, 3555 (2009)
45. J.R. Rabeau, A. Stacey, A. Rabeau, S. Prawer, F. Jelezko, I. Mirza, J. Wrachtrup: *Nano Lett.* **7**, 3433 (2007)
46. P.H. Chung, E. Perevedentseva, C.L. Cheng: *Surf. Sci.* **601**, 3866 (2007)
47. K. Iakoubovskii, G.J. Adriaenssens: *Philos. Mag. Lett.* **80**, 441 (2000)
48. R.R. Nimmagadda, A. Joshi, W.L. Hsu: *J. Mater. Res.* **5**, 2445 (1990)
49. Z. Du, A.F. Sarom, J.P. Longwell, C.A. Mims: *Energy Fuels* **5**, 214 (1991)
50. T. Ando, M. Ishii, M. Kamo, Y. Sato: *J. Chem. Soc. Faraday Trans.* **89**, 1783 (1993)
51. T. Gaebel, C. Bradac, J. Chen, J.M. Say, L. Brown, P. Hemmer, J.R. Rabeau: *Diam. Relat. Mater.* **21**, 28 (2011)
52. C. Bradac, T. Gaebel, C.I. Pakes, J.M. Say, A.V. Zvyagin, J.R. Rabeau: Effect of the Nanodiamond Host on a Nitrogen-Vacancy Color-Centre Emission State. *Small*, 9:132–139 (2013)
53. M.V. Hauf, B. Grotz, B. Naydenov, M. Dankerl, S. Pezzagna, J. Meijer, F. Jelezko, J. Wrachtrup, M. Stutzmann, F. Reinhard, J.A. Garrido: *Phys. Rev. B* **83**, 081304 (2011)
54. C. Santori, P.E. Barclay, K.-M.C. Fu, R.G. Beausoleil: *Phys. Rev. B* **79**, 125313 (2009)
55. M.T. Edmonds, C.I. Pakes, S. Mammadov, W. Zhang, A. Tadich, J. Ristein, L. Ley: *Appl. Phys. Lett.* **98**, 102101 (2011)
56. K.M.C. Fu, C. Santori, P.E. Barclay, R.G. Beausoleil: *Appl. Phys. Lett.* **96**, 121907 (2010)
57. M. Yu, F. Li, Z. Chen, H. Hu, C. Zhan, H. Yang, C. Huang: *Anal. Chem.* **81**, 930 (2009)
58. M.P. Hehlen, G. Frei, H.U. Gudel: *Phys. Rev. B* **50**, 16264 (1994)
59. R.H. Page, K.I. Schaffers, P.A. Waide, J.B. Tassano, S.A. Payne, W.F. Krupke, W.K. Bischel: *J. Opt. Soc. Am. B* **15**, 996 (1998)
60. J.C. Boyer, F. van Veggel: Absolute quantum yield measurements of colloidal NaYF₄: Er³⁺, Yb³⁺ upconverting nanoparticles. *Nanoscale*, 2:1417–1419 (2010)

61. F. Wang, R. Deng, J. Wang, Q. Wang, Y. Han, H. Zhu, X. Chen, X. Liu: *Nat. Mater.* **10**, 968 (2011)
62. H.-X. Mai, Y.-W. Zhang, R. Si, Z.-G. Yan, L.-d. Sun, L.-P. You, C.-H. Yan: *J. Am. Chem. Soc.* **128**, 6426 (2006)
63. H.-X. Mai, Y.-W. Zhang, L.-D. Sun, C.-H. Yan: *J. Phys. Chem. C* **111**, 13721 (2007)
64. F. Wang, J.A. Wang, X.G. Liu: *Angew. Chem. Int. Ed.* **49**, 7456 (2010)
65. V.V. Tuchin: *Tissue Optics: Light Scattering Methods and Instruments for Medical Diagnosis* (SPIE, Bellingham, 2007)
66. C. Vinegoni, D. Razansky, S.A. Hilderbrand, F.W. Shao, V. Ntziachristos, R. Weissleder: *Opt. Lett.* **34**, 2566 (2009)
67. P.R. Selvin: *Ann. Rev. Biophys. Biomol. Struct.* **31**, 275 (2002)
68. Q. Liu, Y. Sun, T.S. Yang, W. Feng, C.G. Li, F.Y. Li: *J. Am. Chem. Soc.* **133**, 17122
69. Q. Zhan, J. Qian, H. Liang, G. Somesfalean, D. Wang, S. He, Z. Zhang, S. Andersson-Engels: *ACS Nano* **5**, 3744 (2011)
70. A.D. Ostrowski, E.M. Chan, D.J. Gargas, E.M. Katz, G.Han, P. James Schuck, D.J. Milliron, B.E. Cohen: *ACS Nano* **6**, 2686 (2012)
71. F. Leblond, S.C. Davis, P.A. Valds, B.W. Pogue: *J. Photochem. Photobiol. B* **98**, 77 (2010)
72. F. Neugart, A. Zappe, F. Jelezko, C. Tietz, J.P. Boudou, A. Krueger, J. Wrachtrup: *Nano Lett.* **7**, 3588 (2007)
73. S.M. Deyev, R. Waibel, E.N. Lebedenko, A.P. Schubiger, A. Pluckthun: *Nat. Biotechnol.* **21**, 1486 (2003)
74. D. Li, B.A. Dong, X. Bai, Y. Wang, H.W. Song: *J. Phys. Chem. C* **114**, 8219 (2010)
75. H. Zijlmans, J. Bonnet, J. Burton, K. Kardos, T. Vail, R.S. Niedbala, H.J. Tanke: *Anal. Biochem.* **267**, 30 (1999)
76. J.C. Boyer, M.P. Manseau, J.I. Murray, F. van Veggel: *Langmuir* **26**, 1157 (2010)
77. S.A. Osseni, S. Lechevallier, M. Verelst, C. Dujardin, J. Dexpert-Ghys, D. Neumeyer, M. Leclercq, H. Baaziz, D. Cussac, V. Santran, R. Mauricot: *J. Mater. Chem.* **21**, 18365 (2011)
78. R.S. Niedbala, H. Feindt, K. Kardos, T. Vail, J. Burton, B. Bielska, S. Li, D. Milunic, P. Bourdelle, R. Vallejo: *Anal. Biochem.* **293**, 22 (2001)
79. T. Pellegrino, L. Manna, S. Kudera, T. Liedl, D. Koktysh, A.L. Rogach, S. Keller, J. Radler, G. Natile, W.J. Parak: *Nano Lett.* **4**, 703 (2004)
80. T.A. Kelf, V.K.A. Sreenivasan, J. Sun, E.J. Kim, E.M. Goldys, A.V. Zvyagin: *Nanotechnology* **21**, 285105 (2010)
81. M.Z. Strowski, A.D. Blake: *Mol. Cell. Endocrinol.* **286**, 169 (2008)
82. V.K.A. Sreenivasan, O.A. Stremovskiy, T.A. Kelf, M. Heblinski, A.K. Goodchild, M. Connor, S.M. Deyev, A.V. Zvyagin: *Bioconjug. Chem.* **22**, 1768 (2011)

Part IV

Devices, Fabricated Structures, and Relevant Materials

Integration and Evaluation of Nanophotonic Devices Using Optical Near Field

15

Takashi Yatsui, Wataru Nomura, Gyu-Chul Yi, and Motoichi Ohtsu

Contents

15.1	Introduction.....	600
15.2	Fabrication of Nanostructure Using Optical Near Field.....	601
15.2.1	Near-Field Optical Chemical Vapor Deposition.....	601
15.2.2	Regulating the Size and Position of Deposited Zn Nanoparticles by Optical Near-Field Desorption Using Size-Dependent Resonance.....	605
15.2.3	Observation of Size-Dependent Resonance of Near-Field Coupling Between Deposited Zn Dot and Probe Apex During NFO-CVD.....	611
15.2.4	Size-, Position-, and Separation-Controlled One-Dimensional Alignment of Nanoparticles Using an Optical Near Field.....	614
15.3	Near-Field Evaluation of Isolated ZnO Nanorod Single-Quantum-Well Structure for Nanophotonic Device.....	619
15.4	An Optical Far-/Near-Field Conversion Device.....	626
15.4.1	A Plasmon Waveguide with Metallic-Core Waveguide.....	627
15.4.2	A Nanodot Coupler with a Surface Plasmon-Polariton Condenser for Optical Far-/Near-Field Conversion.....	632
15.5	Conclusions.....	639
	References.....	640

T. Yatsui (✉) · W. Nomura · M. Ohtsu

School of Engineering, The University of Tokyo, Tokyo, Japan

Nanophotonics Research Center, The University of Tokyo, Tokyo, Japan

e-mail: yatsui@ee.t.u-tokyo.ac.jp; nomura@nanophotonics.t.u-tokyo.ac.jp; ohtsu@ee.t.u-tokyo.ac.jp

G.-C. Yi

Department of Physics and Astronomy, Seoul National University, Seoul, Korea

National Creative Research Institute, Center for Semiconductor Nanostructure, Seoul, Korea

e-mail: Gyuchul.yi@gmail.com

Abstract

In this chapter, we review the optical near-field phenomena and their applications to realize the nanophotonic device. To realize the nanometer-scale controllability in size and position, we demonstrate the feasibility of nanometer-scale chemical vapor deposition using optical near-field techniques (see Sect. 15.2). In which, the probe-less fabrication method for mass production is also demonstrated. To confirm the promising optical properties of individual ZnO for realizing nanophotonic devices, we performed the near-field evaluation of the ZnO quantum structure (see Sect. 15.3). To drive the nanophotonic device with external conventional diffraction-limited photonic device, the far-/near-field conversion device is required. Section 15.4 reviews nanometer-scale waveguide to be used as such a conversion device of the nanophotonic ICs.

15.1 Introduction

Progress in DRAM technology requires improved lithography. It is estimated that the technology nodes should be down to 16 nm by the year 2019 [1]. Recent improvement of the immersion lithography using excimer laser (wavelength of 193 and 157 nm) has realized the technology node as small as 90 nm. Further decrease in the node is expected using extreme ultraviolet (EUV) light source with a wavelength of 13.5 nm. However, their resolution of the linewidth is limited by the diffraction limit of light. Furthermore, continued innovation for transistor scaling is required to manage power density and heat dissipation.

To overcome these difficulties, we have proposed nanometer-scale photonic integrated circuits (i.e., nanophotonic ICs) [2]. These devices consist of nanometer-scale dots, and an optical near field is used as the signal carrier. Since an optical near field is free from the diffraction of light due to its size-dependent localization and size-dependent resonance features, nanophotonics enables the fabrication, operation, and integration of nanometric devices.

As a representative device, a nanophotonic switch can be realized by controlling the dipole-forbidden optical energy transfer among resonant energy states in nanometer-scale quantum dots via an optical near field [3]. To realize room-temperature operation of nanophotonic switch, ZnO nanocrystallites are promising material, owing to their large exciton binding energy [4–6]. By considering the amount of the energy shift of the ground state of the exciton in the ZnO nanocrystallites due to the quantum confinement effect at room temperature, it is estimated that the size accuracy in ZnO nanocrystallite deposition must be as low as $\pm 10\%$ in order to realize efficient near-field energy transfer among the resonant energy state in nanophotonic switch composed of 5-, 7-, and 10-nm dots [3].

15.2 Fabrication of Nanostructure Using Optical Near Field

15.2.1 Near-Field Optical Chemical Vapor Deposition

For realization of nanoscale photonic device required by the future system, electron beams [7] and scanning probe microscopes [8, 9] have been used to control the site on the substrate. However, these techniques have a fatal disadvantage because they cannot deal with insulators, limiting their application.

To overcome this difficulties, in this section, we demonstrated near-field optical chemical vapor deposition (NFO-CVD; Fig. 15.1), which enables the fabrication of nanometer-scale structures, while precisely controlling their size and position [10–15]. That is, the position can be controlled accurately by controlling the position of the fiber probe used to generate the optical near field. To guarantee that an optical near field is generated with sufficiently high efficiency, we used a sharpened UV fiber probe, which was fabricated using a pulling/etching technique [16]. In the uncoated condition, the diameter of the sharpened probe tip remained sufficiently small. This enabled high-resolution position control and in situ shear-force topographical imaging of the deposited nanometer-scale structures. Since the deposition time was sufficiently short, the deposition of metal on the fiber probe and the resultant decrease in the throughput of optical near-field generation were negligible. The separation between the fiber probe and the sapphire (0001) substrate was kept within a few nanometers by shear-force feedback control. Immediately

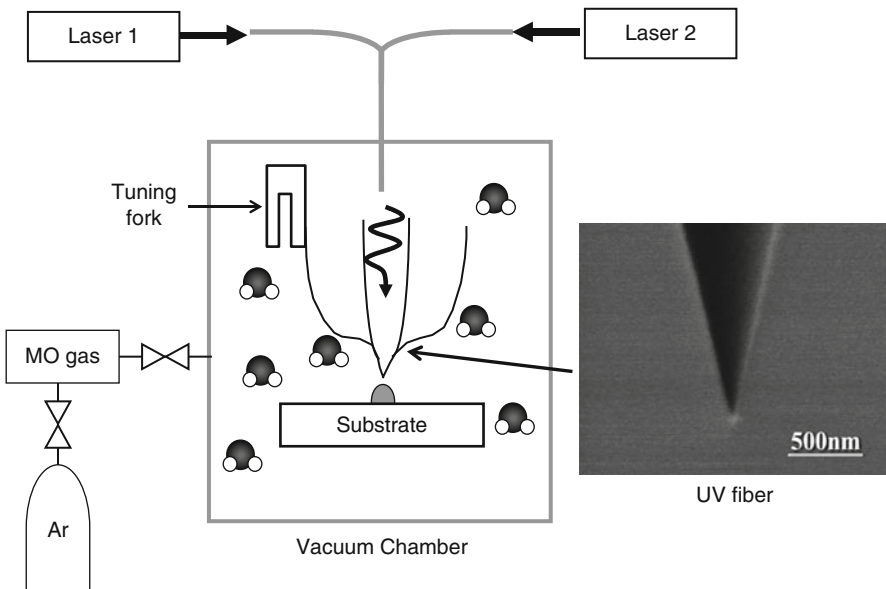


Fig. 15.1 Schematic of NFO-CVD

after the nano-dots were deposited, their sizes and shapes were measured by in situ vacuum shear-force microscopy [10], using the same probe as used for deposition. Due to the photochemical reaction between the reactant molecules and the optical near field generated at the tip of an optical fiber probe, NFO-CVD is applicable to various materials, including metals, semiconductors, and insulators.

Conventional optical CVD method uses a light source that resonates the absorption band of megalomaniac (MO) vapor and has a photon energy that exceeds the dissociation energy [17]. Thus, it utilizes a two-step process: gas-phase photodissociation and subsequent adsorption. In this process, resonant photons excite molecules from the ground state to the excited electronic state and the excited molecules relax to the dissociation channel, and then the dissociated metallic atoms adsorb to the substrate [18]. However, we found that the dissociated MO molecules migrate on the substrate before adsorption, which limits the minimum lateral size of deposited dots (Fig. 15.2a). A promising method for avoiding this migration is dissociation and deposition in the adsorption phase (Fig. 15.2b).

As an example of NFO-CVD, we introduce the deposition of Zn dot. Since the absorption band edge energy of the gas-phase diethylzinc (DEZn) was 4.6 eV ($\lambda = 270$ nm) [17], we used He–Cd laser light (3.81 eV, $\lambda = 325$ nm) as the light source (laser 1 in Fig. 15.1) for the deposition of Zn; it is nonresonant to gas-phase DEZn. However, due to the absorption spectrum in DEZn with respect to that in the gas-phase, that is, it resonates the adsorption-phase DEZn. The redshift may be attributed to perturbations of the free-molecule potential surface in the adsorbed phase [17, 19]. Using a sharpened UV fiber probe, we achieved selective dissociation of adsorbed DEZn; as a result, we successfully fabricated 20-nm Zn dots with 65-nm separation on sapphire (0001) substrate (see Fig. 15.3a) [12, 14]. Furthermore, since the nonresonant propagating light that leaked from the probe did not dissociate the gas-phase DEZn, the atomic-level sapphire steps around the deposited dots were clearly observed after the deposition. By changing the reactant molecules during deposition, nanometric Zn and Al dots were successively deposited on the same sapphire substrate with high precision (see Fig. 15.3b) [15].

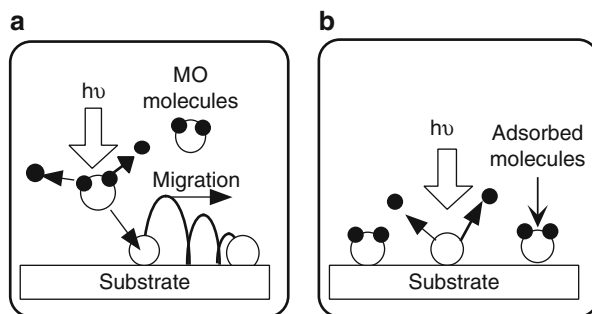


Fig. 15.2 Schematic diagrams of the photodissociation of the (a) gas-phase and (b) adsorption-phase MO molecules

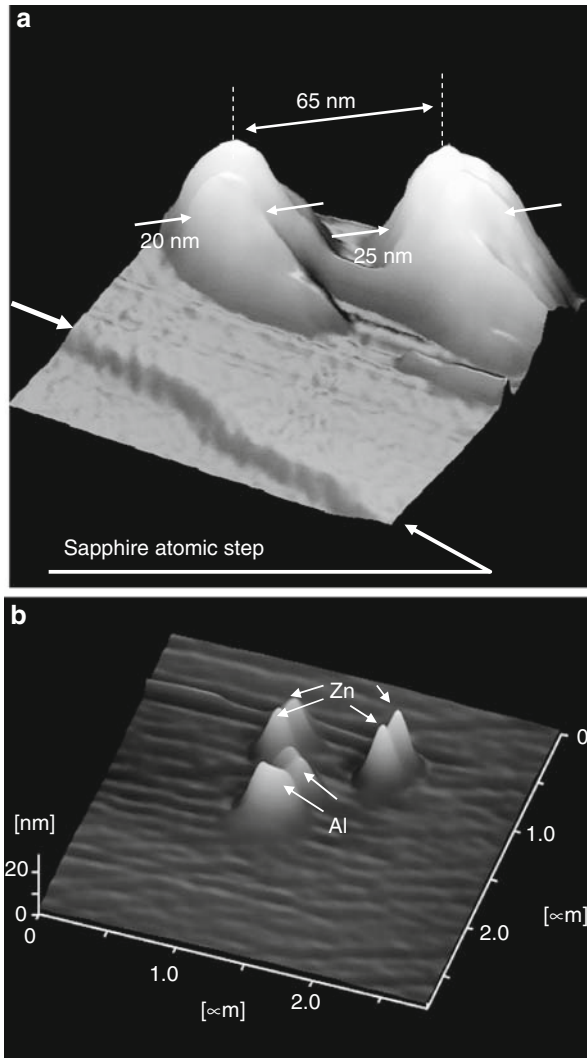


Fig. 15.3 Shear-force image of closely spaced (a) Zn dots and (b) Zn and Al dots

Since high-quality ZnO nanocrystallites can be obtained by oxidizing Zn nuclei [20, 21], NFO-CVD could be used to produce high-quality ZnO nanocrystallites, a promising material for use in nanometer-scale light emitters and switching devices in nanophotonic IC. Furthermore, to confirm that the deposited dots were Zn, we fabricated a UV-emitting ZnO dot by oxidizing the Zn dot immediately after deposition [12].

First, the Zn dot was deposited using selective dissociation of adsorbed DEZn (Fig. 15.4a). Next, laser annealing was employed for this oxidation [21]; that

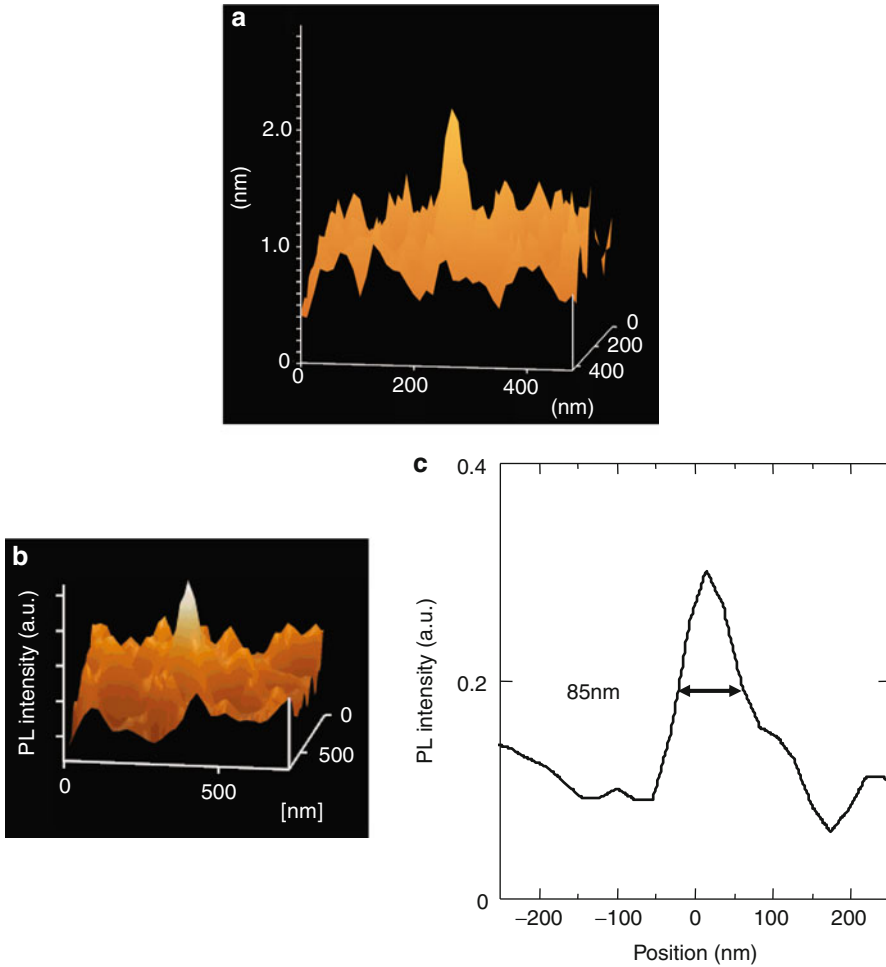


Fig. 15.4 (a) Shear-force image of Zn dot. (b) Spatial distribution of the optical near-field PL intensity ($\lambda > 360$ nm) of an oxidized Zn dot (a). The image is of a 750×750 -nm area. (c) Cross-sectional profile through the spot of (a)

is, the deposited Zn dot was irradiated with a pulse of an ArF excimer laser ($\lambda = 193$ nm; pulse width, 30 ns; fluence, 120 mJ/cm^2) in a high-pressure oxygen environment (5 Torr). Finally, to evaluate the optical properties of the oxidized dot, the photoluminescence (PL) intensity distribution was measured using an illumination and collection mode (IC-mode) near-field optical microscope. For this measurement, a He–Cd laser ($\lambda = 325$ nm) was used as the light source and the signal collected through a fiber probe and a long wave ($\lambda > 360$ nm) pass filter was focused on a photomultiplier tube (PMT) to count photons.

Figure 15.4b shows the PL intensity distribution ($\lambda > 360$ nm) of an oxidized dot. The low collection efficiency due to the IC-mode configuration did not establish the spectrum. Thus, a Zn thin film was deposited using the same CVD process, except the optical near field was replaced by far-field propagating light. After it was annealed with an excimer laser, we found that the PL intensity of the spontaneous emission from the free exciton was ten times greater than that of the deep-level green emission. Thus, we concluded that the PL in Fig. 15.4a originated from spontaneous emission from the free exciton. Figure 15.4c is the cross-sectional profile through the spot in Fig. 15.4b. Note that the full width at half maximum (FWHM) in Fig. 15.4c is smaller than the dot size (FWHM of 100 nm; see Fig. 15.4a), which was estimated using a shear-force microscope. This originates from the high spatial resolution capability of the IC-mode near-field microscope. The next stage of this study will be a more detailed evaluation of the optical properties of single ZnO nanocrystallites.

15.2.2 Regulating the Size and Position of Deposited Zn Nanoparticles by Optical Near-Field Desorption Using Size-Dependent Resonance

In order to realize further controllability of size, in this section, we utilize the dependence of plasmon resonance on the photon energy of optical near fields and control the growth of Zn nanoparticles during the process of Zn deposition. Using this dependence, we demonstrate the deposition of a nanometer-scale dot using NFO-CVD [13].

First, we studied nanoparticle formation on the cleaved facets of UV fibers (core diameter = 10 μm) using conventional optical CVD (see Fig. 15.5a).

Gas-phase DEZn at a partial pressure of 5 mTorr was used as the source gas. The total pressure, including that of the Ar buffer gas, was 3 Torr. As the light source for the photodissociation of DEZn, a 500- μW He–Cd laser (photon energy $E_p = 3.81$ eV [$\lambda = 325$ nm]) was coupled to the other end of the fiber. The irradiation time was 20 s. This irradiation covered the facet of the fiber core with a layer of Zn nanodots. Figure 15.6a shows a scanning electron microscopic (SEM) image of the deposited Zn nanodots, and their size distribution is shown in Fig. 15.6d. The peak diameter and FWHM of this curve are 110 and 50 nm, respectively.

In order to control the size distribution, we introduced 20 μW Ar⁺ ($E_p = 2.54$ eV [$\lambda = 488$ nm]) or He–Ne ($E_p = 1.96$ eV [$\lambda = 633$ nm]) lasers into the fiber, in addition to the He–Cd laser. Their photon energies are lower than the absorption band edge energy of DEZn; that is, they are nonresonant light sources for the dissociation of DEZn. The irradiation time was 20 s. Figure 15.6b, c shows SEM images of the Zn nanodots deposited with irradiation at $E_p = 3.81$ and 2.54 eV and at $E_p = 3.81$ and 1.96 eV, respectively. Figure 15.6e, f shows the respective size distributions. The peak diameters are 30 and 18 nm, respectively, which are smaller than those of the dots in Fig. 15.6d, and depend on the photon energy of the additional light. Furthermore, the FWHM (10 and 12 nm, respectively) was

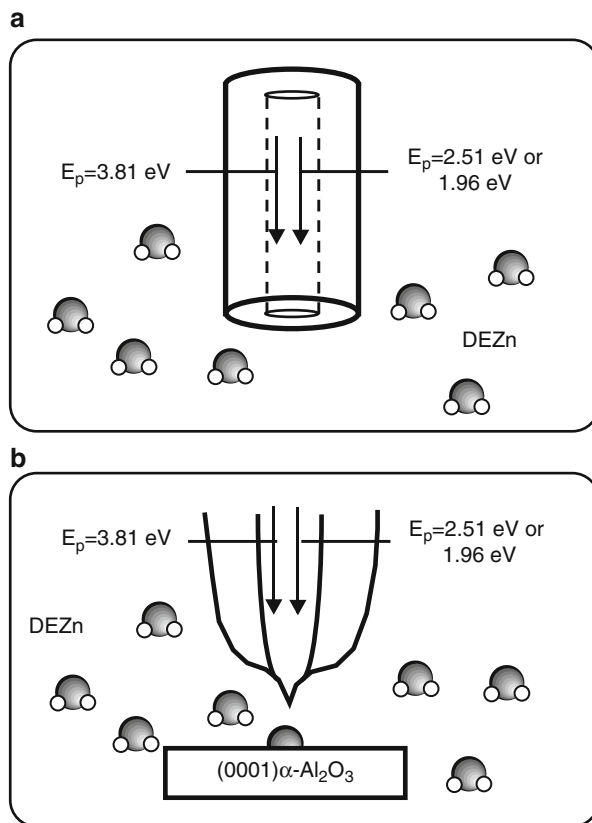


Fig. 15.5 Schematics of (a) conventional optical CVD on the cleaved facet of an optical fiber and (b) near-field optical CVD

definitely narrower than that of Fig. 15.6d. These results suggest that the additional light controls the size of the dots and reduces the size fluctuation; that is, size regulation is realized.

We now discuss the possible mechanisms by which the additional light regulates the size of the dots. A metal nanoparticle has strong optical absorption due to plasmon resonance [22, 23], which strongly depends on particle size. This can induce the desorption of the deposited metal nanoparticles [24, 25]. As the deposition of metal nanoparticles proceeds in the presence of light, the growth of the particles is affected by a trade-off between deposition and desorption, which determines their size, and depends on the photon energy. It has been reported that surface plasmon resonance in a metal nanoparticle is redshifted with increasing the particle size [24, 25]. However, our experimental results disagree with these reports (compare Fig. 15.6d–f). In order to find the origin of this disagreement, a series of calculations were performed and resonant sizes were evaluated.

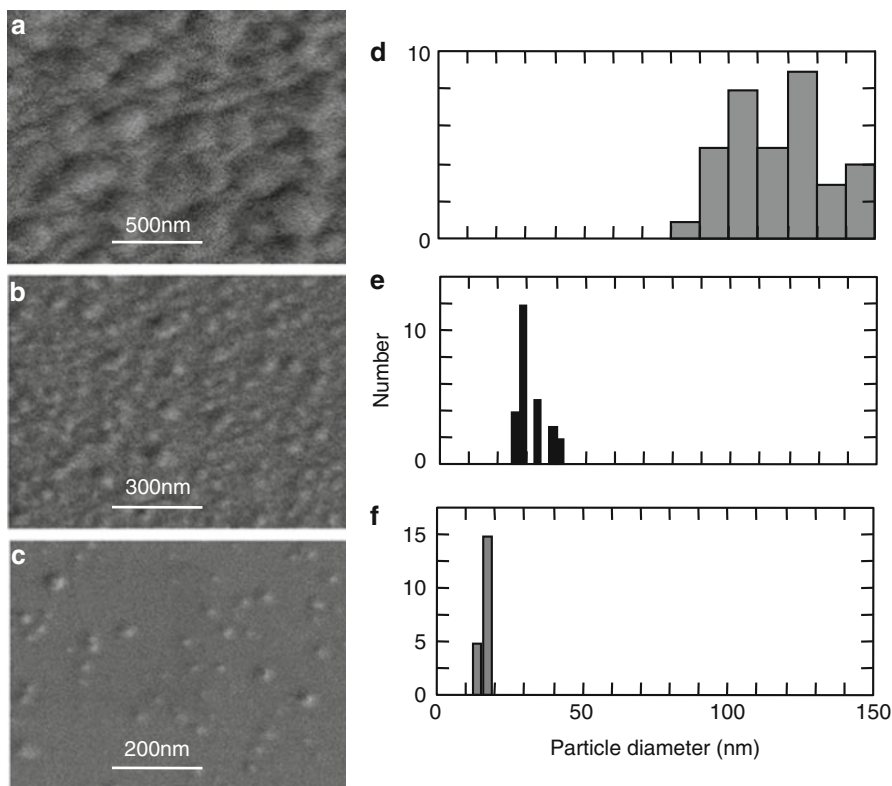


Fig. 15.6 SEM images of Zn nanoparticles deposited by optical CVD with (a) $E_p = 3.81$ eV, (b) $E_p = 3.81$ and 2.54 eV, and (c) $E_p = 3.81$ and 1.96 eV. (d) The diameter distributions of the Zn particles; (d), (e), and (f) are for (a), (b), and (c), respectively

Mie's theory of scattering by a Zn sphere was employed, and only the first mode was considered [26]. The curves in Fig. 15.7a represent the calculated polarizability α with respect to three photon energies. The vertical axis is the value of α normalized to the volume, V , of a Zn sphere in the air, which depends on its diameter and is maximal at a certain diameter, that is, at the resonant diameter. The solid curve in Fig. 15.7b represents the resonant diameter as a function of the photon energy, which is not a monotonous function and takes the minimum at $E_p = 2.0$ eV ($\lambda = 620$ nm). Since the imaginary part of the refractive index of the Zn also takes a maximum also at $E_p = 2.0$ eV ($\lambda = 620$ nm) (see the broken curve in Fig. 15.7b) [27], the minimum of the solid curve is due to the strong absorption in Zn.

Although Fig. 15.7a shows that the resonant diameter (95 nm) for $E_p = 2.54$ eV exceeds that (80 nm) for $E_p = 3.81$ eV, the calculated resonant diameter for $E_p = 3.81$ eV is in good agreement with the experimentally confirmed particle size (see curve A in Fig. 15.6d). Since the He–Cd laser light ($E_p = 3.81$ eV) is resonant for the dissociation of DEZn and is responsible for the deposition,

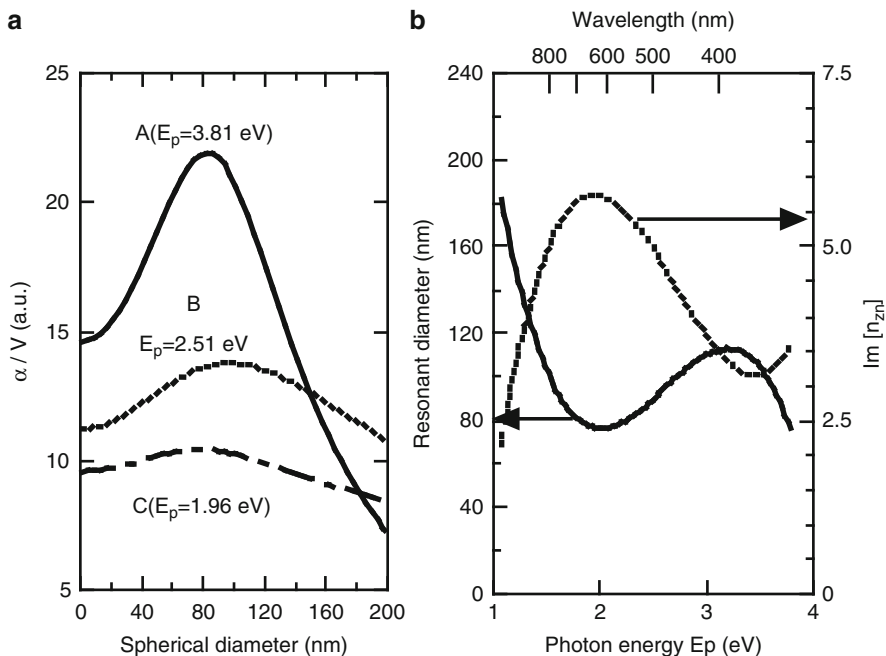


Fig. 15.7 (a) Curves A, B, and C show the calculated polarizability α normalized to the volume V for a Zn sphere surrounded by air for $E_p = 3.81$, 2.51, and 1.96 eV, respectively. (b) The resonant diameter of a Zn sphere (solid curve). The imaginary part of the refractive index of Zn, n_{Zn} , used for the calculation (broken curve) (see Ref. [27])

irradiation with a He–Cd laser during deposition causes the particles to grow, and this growth halts when the particles reach the resonant diameter, because the rate of desorption increases due to resonant plasmon excitation. This is further supported by the fact that the resonant diameter (75 nm) for $E_p = 1.96$ eV is smaller than that for $E_p = 3.81$ eV (see Fig. 15.7a) and illumination with the additional light causes the particles to shrink (see Fig. 15.6d).

Another possible mechanism involves the acceleration of dissociation by the additional light. The photodissociation of DEZn produces transient monoethylzinc; then, Zn results from the dissociation of monoethylzinc. Although the absorption band of monoethylzinc was not determined, the photon energy dependence of the size observed using the additional light might be due to the acceleration of the dissociation rate; that is, the additional light, which is nonresonant for DEZn, resonates the monoethylzinc [28], since the first metal-alkyl bond dissociation has a larger dissociation energy than the subsequent metal-alkyl bond dissociation [29, 30].

Finally, using this dependence, we used NFO-CVD (see Fig. 15.1) to control the position of the deposited particle. Figure 15.8a–c shows topographical images of Zn deposited by NFO-CVD with illumination with a 1- μ W He–Cd laser ($E_p = 3.81$ eV, laser 1 in Fig. 15.1) alone, or together with a 1- μ W Ar⁺ laser

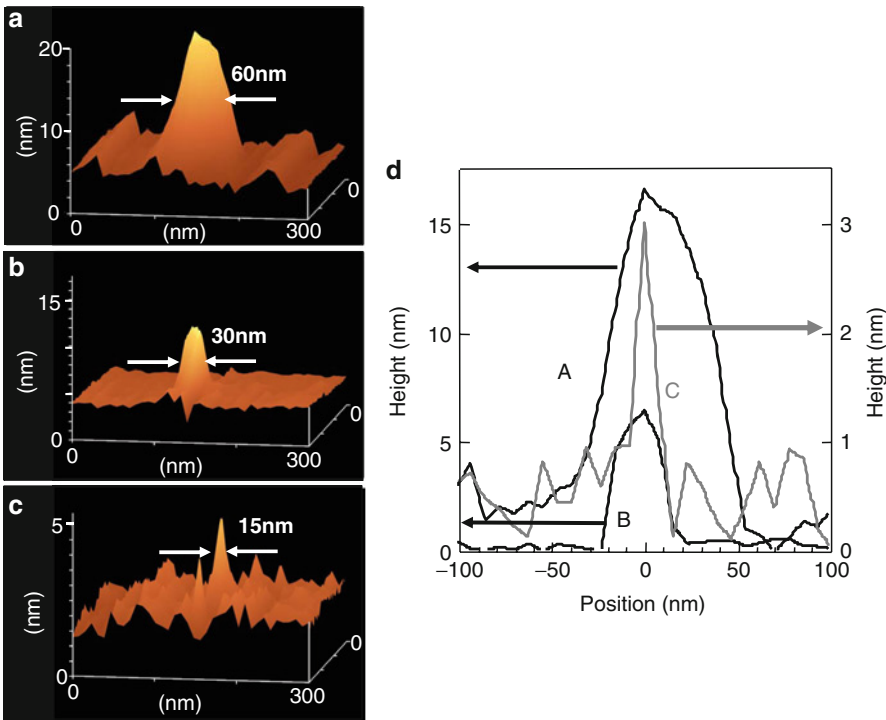


Fig. 15.8 Bird's-eye views of shear-force topographical images of Zn deposited by NFO-CVD with (a) $E_p = 3.81$ eV, (b) $E_p = 3.81$ and 2.54 eV, and (c) $E_p = 3.81$ and 1.96 eV, respectively. (d) Curves A, B, and C show the respective cross-sectional profiles through the Zn dots deposited in (a), (b), and (c)

($E_p = 2.54$ eV) or a 1- μ W He-Ne laser ($E_p = 1.96$ eV) (laser 2 in Fig. 15.1), respectively. The irradiation times were 60 s. During deposition, the partial pressure of DEZn and the total pressure including the Ar buffer gas were maintained to 100 mTorr and 3 Torr, respectively. In Fig. 15.8d, curves A, B, and C are the respective cross-sectional profiles through the Zn dots in Fig. 15.8a–c. The respective FWHM was 60, 30, and 15 nm; that is, a lower photon energy gave rise to smaller particles, which is consistent with the experimental results shown in Fig. 15.6.

These results suggest that the additional light controls the size of the dots and reduces the size fluctuation; that is, size regulation is realized. Furthermore, the position can be controlled accurately by controlling the position of the fiber probe used to generate the optical near field. The experimental results and the suggested mechanisms described above show the potential advantages of this technique in improving the regulation of size and position of deposited nanodots. Furthermore, since our deposition method is based on a photodissociation reaction, it could be widely used for nanofabrication of the other material, for example, GaN and GaAs.

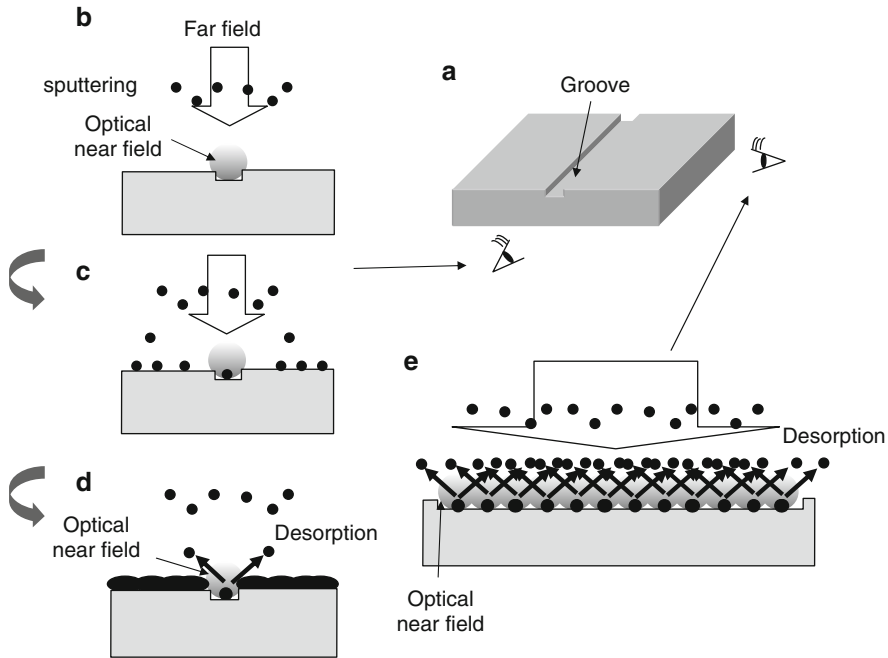


Fig. 15.9 Fabrication process of metal dot chain by the sputtering using near-field desorption technique

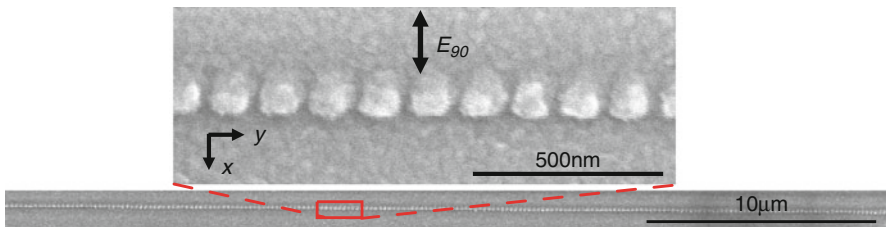


Fig. 15.10 Al dot chain with 2.33-eV light illumination

For realization of mass production of nanometric structures, we also demonstrated possibilities of applying such a near-field desorption to other deposition technique, which does not use fiber probe. We performed metal nanoparticle deposition over the preformed grooves on the glass substrate (Fig. 15.9a) by the sputtering under the illumination (Fig. 15.9b). Since the optical near field is enhanced at the edge of the groove, it can induce the desorption of the deposited metal nanoparticles when they reach at their resonant size for optical absorption (Fig. 15.9d, e).

By illuminating 1.96 eV (2.33 eV) light during the deposition of Al film, we successfully fabricated Al dot chain as long as 20 μ m (see Fig. 15.10) [31].

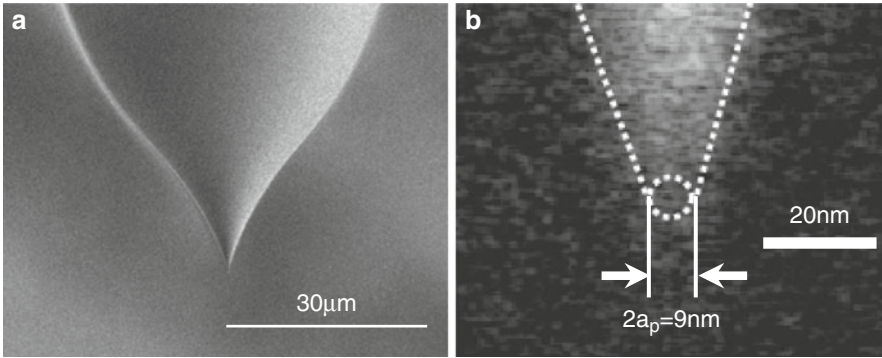


Fig. 15.11 A SEM image of (a) UV fiber probe and (b) its apex. $2a_p$: apex diameter

15.2.3 Observation of Size-Dependent Resonance of Near-Field Coupling Between Deposited Zn Dot and Probe Apex During NFO-CVD

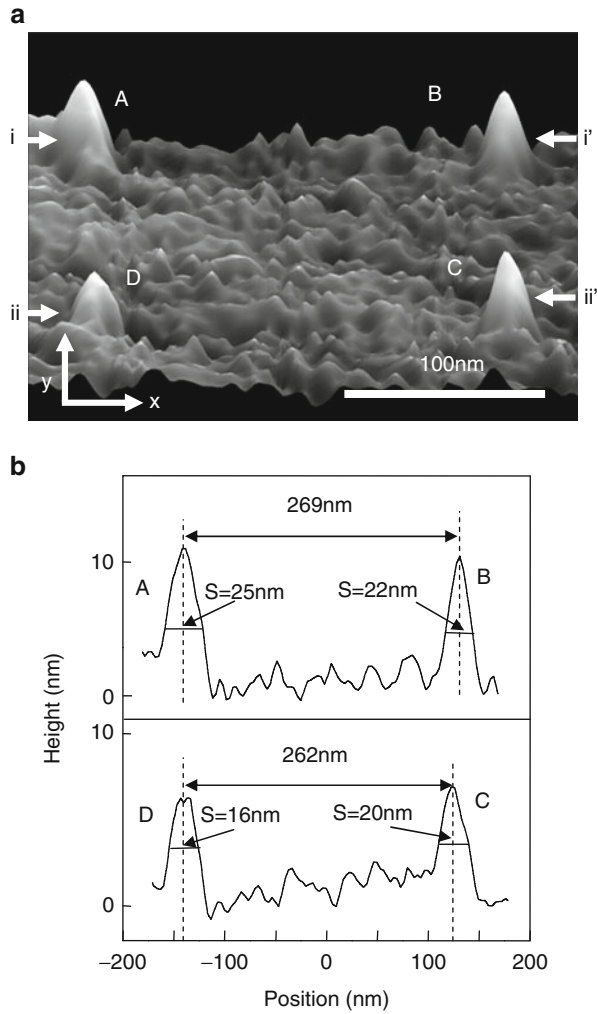
To realize sub-10-nm scale controllability in size, we report here the precise growth mechanism of Zn dots with NFO-CVD. We directly observe that the deposition rate is maximal when the dot grew to a size equivalent to the probe apex diameter. This dependence is well accounted for by the theoretically calculated dipole–dipole coupling with a Förster field. The theoretical support and experimental results indicate that potential advantages of this technique for improving regulation of the size and position of deposited nanometer-scale dots.

Figure 15.11b shows the SEM image of the fiber probe used in this study. The apex diameter $2a_p$ is estimated as 9 nm by referring to the fitted broken circle.

Figure 15.12a shows a shear-force image of four Zn dots deposited with the irradiation time of 60 (dot A), 30 (dot B), 10 (dot C), and 5 s (dot D) with the laser output power P of $5 \mu\text{W}$. We tried to deposit dots with 260-nm separations along the x -axis by servo-controlling the position of the fiber probe. As shown in the cross-sectional profiles in Fig. 15.12b, Zn dots as small as 20 nm in their size S (defined by the FWHM on this profile) were fabricated. Their separation are 269 and 262 nm, by which high accuracy in position (<10 nm) was confirmed. Major origin of this residual inaccuracy is the hysteresis of the PZT actuator used for scanning the fiber probe, which can be decreased by carefully selecting the actuator.

Figure 15.13a shows the normalized deposition rate R of Zn dots, as a function of the dot size S . Since the measured dot size S' was convolution of probe apex diameter $2a_p$ and the real size S , S was estimated as $S = S' - 2a_p$. It should be noted that R takes the maximum at $S = 2a_p$. This result indicates that the magnitude of the near-field optical interaction between the deposited Zn dot and the probe apex is enhanced resonantly with respect to S , resulting in the resonant increase in R . In other words, the near-field optical interaction exhibits the size-dependent resonance characteristics.

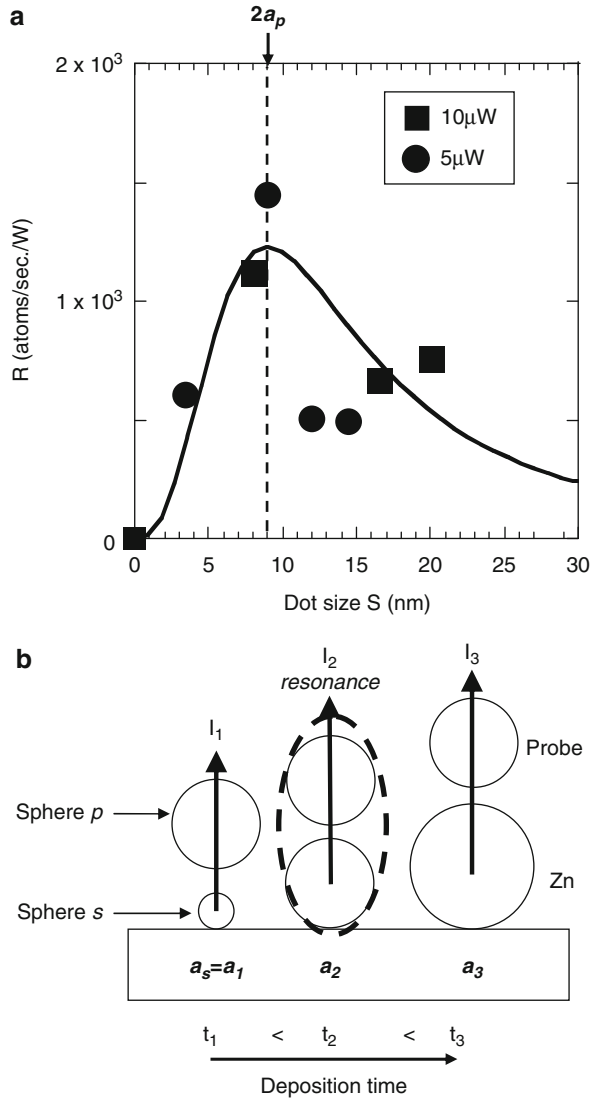
Fig. 15.12 (a) A shear-force image of deposited Zn dots. The laser irradiation time of dots A–D were 60, 30, 10, and 5 s, respectively. (b) Upper and lower curves show the cross-sectional profile along the line indicated by arrows i–i' and ii–ii', respectively



To find the origin of this size-dependent resonance, we calculated the magnitude of the near-field optical interaction between closely spaced nanoparticles (Fig. 15.13b). The spheres p and s represent the probe apex and the Zn dot, respectively. Since the separation between two particles is much narrower than the wavelength, the Förster field (proportional to R^{-3} , R is the distance from the dipole) is dominant in the oscillating dipole electric field. In this quasistatic model, the intensity I_s of the light scattered from the two closely spaced spheres p and s is given by Ohtsu and Kobayashi [32]

$$I_s = I_1 + I_2 = (\alpha_p + \alpha_s)^2 |E|^2 + 4\Delta\alpha (\alpha_p + \alpha_s) |E|^2, \quad (15.1)$$

Fig. 15.13 (a) The time-dependent deposition rate R . Solid squares and circles indicate the normalized deposition rate p with 10 and 5 μW , respectively. Solid curve indicates the calculated value of I_2/I_1 . (b) Schematic of growth process of Zn dot



where $\alpha_i = 4\pi\epsilon_0(\epsilon_i - \epsilon_0)/(\epsilon_i + 2\epsilon_0)a_i^3$ is a polarizability of the sphere i ($= p, s$) with diameter a_i . The first and second terms I_1 and I_2 represent the light intensity scattered from the spheres, and the light due to the dipole–dipole interaction induced by the Förster field. Thus, the light intensity under study, normalized to I_1 , is given by

$$I_2/I_1 = \frac{G_p A_p^3}{(A_p + 1)^3 (G_p A_p^3 + 1)}, \tag{15.2}$$

where $A_p = a_p/a_s$ and $G_p = (\varepsilon_p - 1)(\varepsilon_s + 2)/(\varepsilon_p + 2)(\varepsilon_s - 1)$. For the deposition by the fiber probe, dielectric constant of Zn and fiber probe are $\varepsilon_s = (0.6 + i4)^2$ [33] and $\varepsilon_p = 1.5^2$, respectively. The diameter $2a_p$ of the sphere p was 9 nm (see Fig. 15.12b). Solid curve in Fig. 15.13a shows the calculated value of I_2/I_1 as a function of the Zn dot size $S (= 2a_s)$, which agrees very well with the experimental results. This agreement indicates that the increase in R is originated from the dipole–dipole coupling with Förster field at the dot size equivalent to the probe apex diameter.

15.2.4 Size-, Position-, and Separation-Controlled One-Dimensional Alignment of Nanoparticles Using an Optical Near Field

Promising components for integrating the nanometer-sized photonic devices include chemically synthesized nanocrystals, such as metallic nanocrystals [34], semiconductor quantum dots [35], and nanorods [36], because they have uniform size, controlled shape, defined chemical composition, and tunable surface chemical functionality. However, position- and size-controlled deposition methods have not yet been developed. Since several methods have been developed to prepare nanometer-sized templates reproducibly [37], it is expected that the self-assembly of colloidal nanostructures into a lithographically patterned substrate will enable precise control at all scales [38]. Capillary forces play an important role, because colloidal nanostructures are synthesized in solution. Recently, successful integration of polymer or silica spheres [39, 40] and complex nanostructures such as nanotetrapods [40] into templates by controlling the capillary force using appropriate template structures has been reported, although their size and separation are typically uniform.

To fabricate nanophotonic devices, we propose a novel method of assembling nanoparticles by controlling the capillary force interaction and suspension flow. Further control of the positioning and separation of the nanoparticles is realized by controlling the particle–particle and particle–substrate interactions using an optical near field.

To control position and separation very accurately, preliminary experiment was performed on a patterned Si substrate, where an array of 10 μm holes in 100-nm-thick SiO_2 was fabricated using photolithography (Fig. 15.14a). Subsequently, a suspension containing latex beads with a mean diameter of 40 nm was dispersed on the substrate, and the latex beads were aligned after solvent evaporation. The deposited latex beads were not subjected to any surface treatment and were dispersed in pure water at 0.001 wt%. Although the 10- μm -sized template resulted in low selectivity in the position of the latex beads (Fig. 15.14b, c), the beads were deposited only on the SiO_2 surface owing to its higher capillarity.

For higher positional selectivity, the suspension containing latex beads was dropped onto a lithographically patterned Si substrate that was spinning at 3,000 revolutions per minute (rpm). As shown in Fig. 15.15a, the suspension flow split into two branches at the SiO_2 hole. SEM images (Fig. 15.15b–d) show that the chain of colloidal beads was aligned at the Si/ SiO_2 interface. Note that the number of rows of latex beads decreased (Fig. 15.15b, c) and only the smallest beads, which were

Fig. 15.14 (a) Schematic of lithographically patterned Si substrate. (b and c) SEM images of latex beads dispersed on the lithographically patterned Si substrate

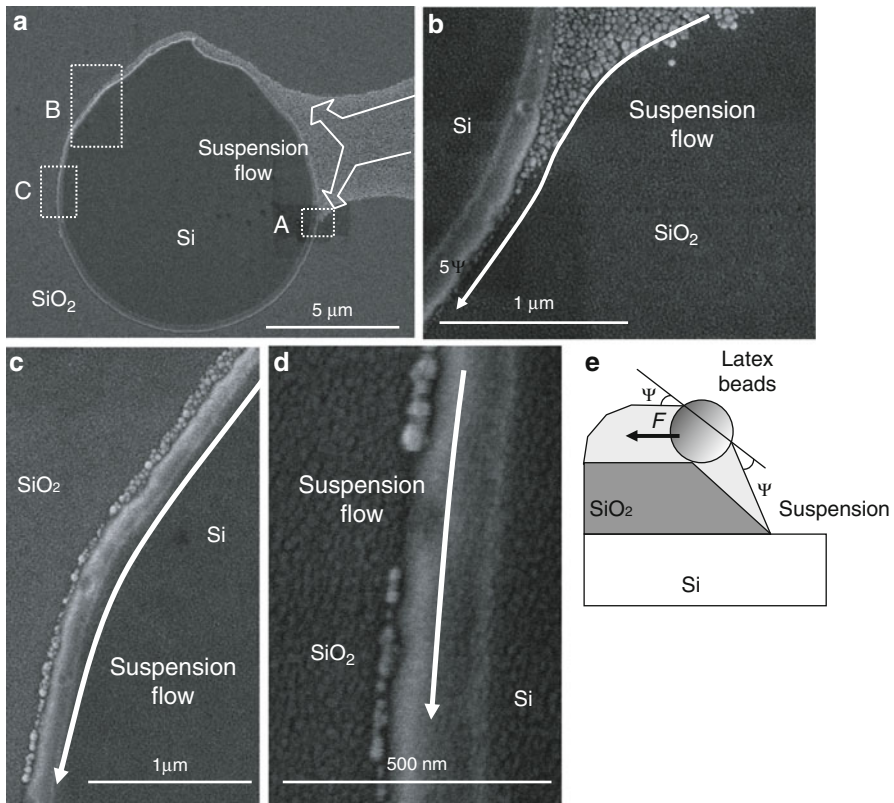
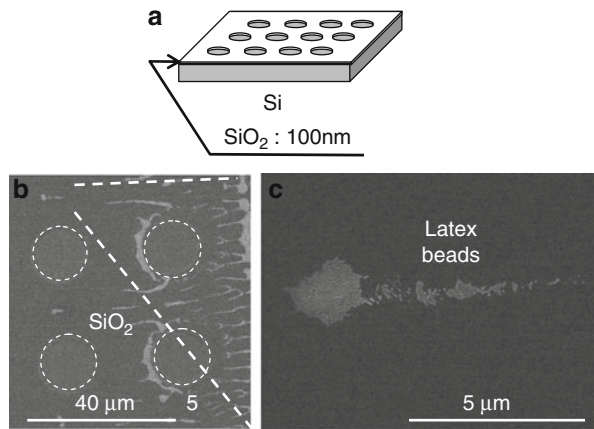


Fig. 15.15 (a) SEM image of latex beads dispersed on the lithographically patterned Si substrate rotated at 3,000 rpm. Higher magnification SEM images of white squares A (b), B (c), and C (d) in (a). (e) Schematic illustrating of the particle assembly process driven by the capillary force and suspension flow

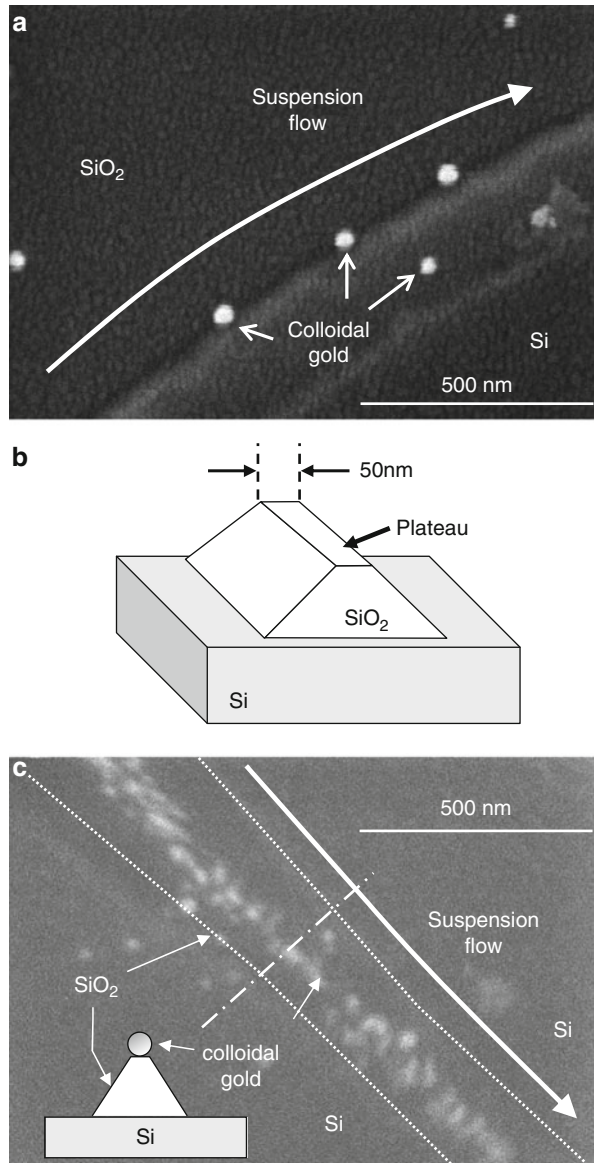
20 nm in diameter, reached the end of the suspension flow (Fig. 15.15d). Assuming the same particle–suspension contact angle (denoted ψ in Fig. 15.15e) for various particles diameters, the flow speed of the larger latex beads had greater deceleration since the magnitude of the force pushing the particles on the SiO₂ (denoted F in Fig. 15.15e) owing to evaporation of the solvent is proportional to the particle diameter [40]. In other words, the size selection was realized.

Based on the results of preliminary deposition, we tried assembling metallic nanoparticles because they are the material used to construct nanodot couplers [41]. In this trial, we investigated the assembly of colloidal gold nanoparticles with a mean diameter of 20 nm dispersed in citrate solution at 0.001 %. The nanoparticles were prepared by the citric acid reduction of gold ions and terminated by a carboxyl group (approximate length is 0.2 nm) with a negative charge [42]. However, they could not be aggregated using the same deposition process as for the latex beads (Fig. 15.16a). To aggregate these particles, we fabricated a SiO₂ line structure with a plateau width of 50 nm on the Si substrate using photolithography (Fig. 15.16b). The solvent containing the colloidal gold nanoparticles was dropped onto this substrate at 3,000 rpm. Then, the colloidal gold nanoparticles aggregated along the plateau of the SiO₂ line (Fig. 15.16b, c). This indicates that the capillary force induced by the lithographically patterned substrate, which is caused by the higher wettability of SiO₂ than that of the Si, was larger than the repulsive force owing to the negative charge of the carboxyl group on the colloidal gold nanoparticles, and this resulted in the aggregation and alignment of the colloidal gold nanoparticles at high density (Fig. 15.16c).

To further control size, separation, and positioning, we examined the aggregation of colloidal gold nanoparticles under illumination, because the colloidal gold nanoparticles have strong optical absorption. Strong absorption should desorb the carboxyl group from the colloidal gold nanoparticles and result in their aggregation. Such an aggregation of colloidal gold nanoparticles was confirmed by the illumination of light. Figure 15.17a, b shows the aggregated gold nanoparticles over the pyramidal Si substrate under the 690-nm-light illumination for 60 s. However, since the light was illuminated through the droplet of the colloidal gold nanoparticles, aggregated colloidal gold nanoparticles were spread outside the beam spot. In order to realize selective aggregation of the gold nanoparticles at the desired position, the suspension was illuminated from behind (Fig. 15.18a). Furthermore, we used a Si wedge, because this is a suitable structure for a far-/near-field conversion device [44]. The Si wedge structure (Fig. 15.18b) was fabricated by the photolithography and anisotropical etching of Si. Detailed fabrication process is described in Fig. 15.27.

For this structure, colloidal gold nanoparticles were deposited around the edge after evaporating the suspension without illumination (Fig. 15.19a, b). Such aggregation is owing to its wedge structure. This is because the suspension at the edge is thinner than that on the Si(111) plane owing to its low capillarity, and this causes the convective transport of particles toward the edge [43]. Further selective alignment along the edge of the Si wedge was realized using rear illumination. Figure 15.19c, d shows the deposited colloidal gold nanoparticles with illumination

Fig. 15.16 (a) SEM image of colloidal gold nanoparticles dispersed on the lithographically patterned Si substrate rotated at 3,000 rpm. (b) Schematic of the SiO₂ line structure fabricated on the Si substrate. (c) SEM images of colloidal gold nanoparticles dispersed on the SiO₂ line rotated at 3,000 rpm. *Inset*: cross-section of the substrate along the white line (*dashes and dots*)



under 690-nm light (25 mW/mm^2) for 60 s. Since the optical near-field energy is enhanced at the edge owing to the high refractive index of Si (see Fig. 15.18b) [82], selective aggregation along the edge with higher density is seen in these figures. This is due to the desorption of the carboxyl group by the absorption of light by the colloidal gold nanoparticles.

Fig. 15.17 (a) Frontal illumination. (b) Aggregated colloidal gold nanoparticles with frontal illumination under 690-nm light (25 mW/mm^2) for 60 s

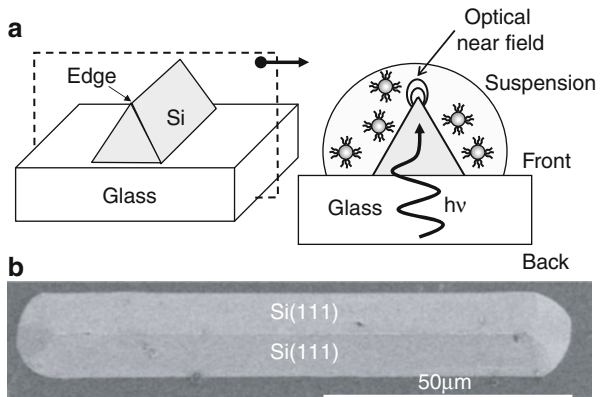
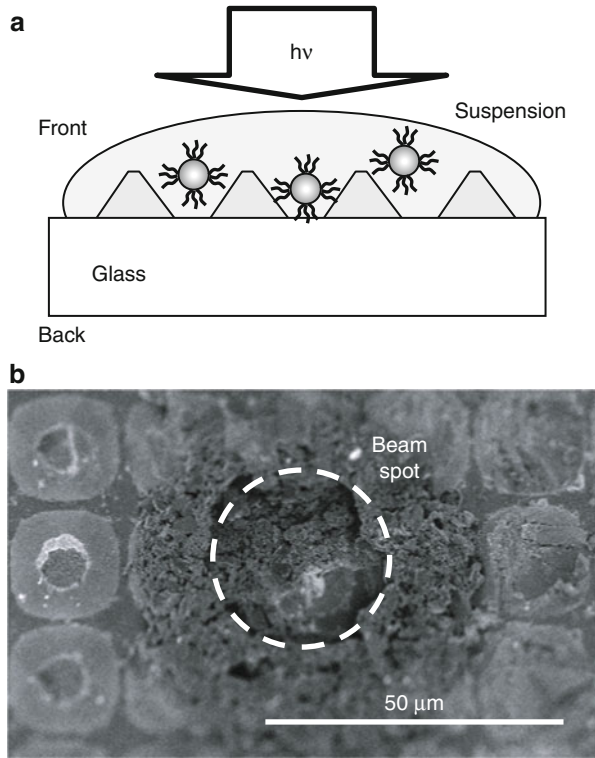
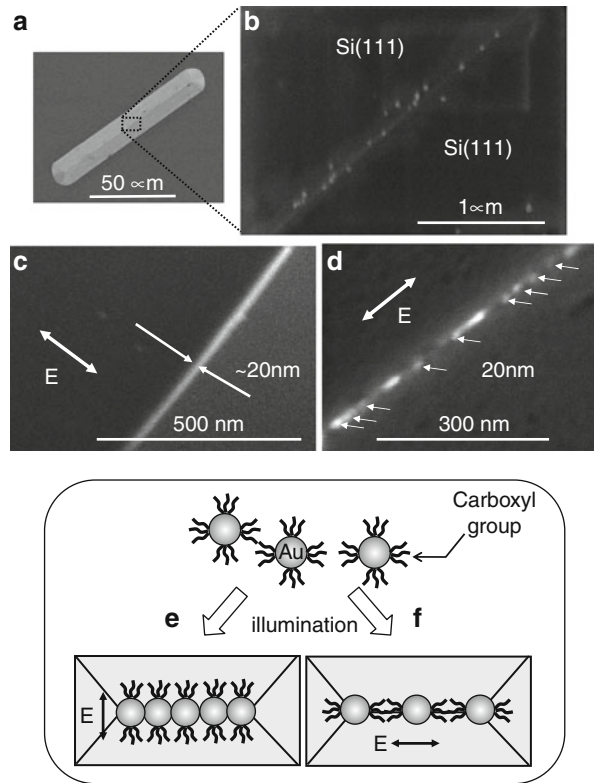


Fig. 15.18 (a) Schematic of the experimental setup. (b) SEM image of the fabricated Si wedge structure

Note that the colloidal gold nanoparticles were closely aggregated and aligned linearly to form a wire shape when the polarization was perpendicular to the edge axis (Fig. 15.19c), while they were aligned with separation of several tens of nanometers in the parallel polarization (Fig. 15.19d). As the optical near-field energy for parallel polarization is higher than that for perpendicular polarization [44], greater aggregation is expected for parallel polarization. Nevertheless, the parallel polarization resulted in less aggregation. The low resolution of SEM images does

Fig. 15.19 (a) Overview of the Si wedge structure. (b) SEM image of colloidal gold nanoparticles deposited on the edge of the Si wedge structure without illumination. SEM images of colloidal gold nanoparticles on the Si wedge structure under illumination with polarization perpendicular (c) and parallel (d) to the edge. Schematic diagrams of the aggregation of colloidal gold nanoparticles along the edge of the Si wedge with polarization perpendicular (e) and parallel (f) to the edge



not determine the distribution of the carboxyl molecules. However, such a repulsive force for disaggregation is caused by the carboxyl molecules which remained on the colloidal gold nanoparticles. Thus, we believe that the difference in the degree of aggregation originated from differences in the charge distribution induced inside the gold nanoparticles. Based on the polarization dependence of the aggregation, it is reasonable to consider that the aggregation along the edge with perpendicular polarization is owing to partially adsorbed carboxyl groups (Fig. 15.19e), while the disaggregation with the parallel polarization resulted from the repulsive force induced by the partially attached carboxyl group on the colloidal gold nanoparticles (Fig. 15.19f).

15.3 Near-Field Evaluation of Isolated ZnO Nanorod Single-Quantum-Well Structure for Nanophotonic Device

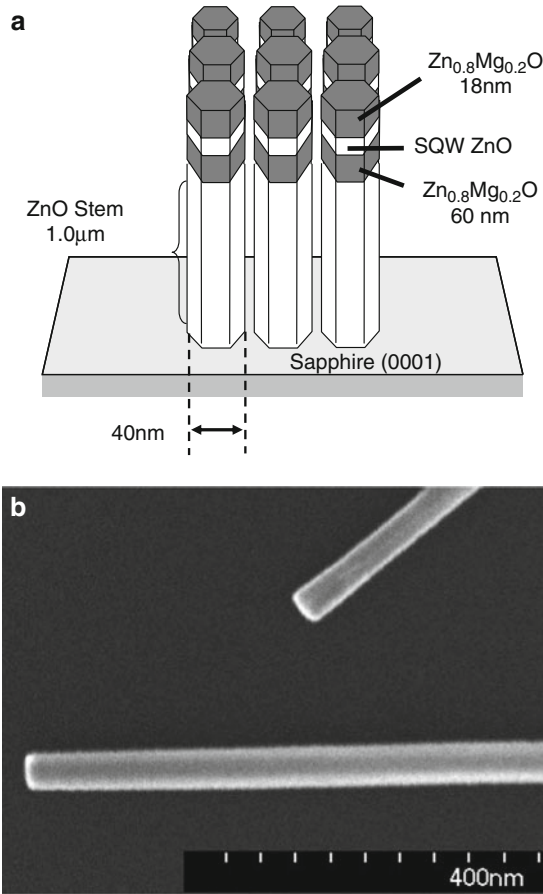
ZnO nanocrystallites are promising material for realizing nanophotonic devices [2] owing to their large exciton binding energy [4–6] and large oscillator strength [45]. Furthermore, the recent demonstration of semiconductor nanorod quantum-well structure enables us to fabricate nanometer-scale electronic and photonic devices

on single nanorods because of its extremely high quality of crystallinity [46–49]. Recently, ZnO/ZnMgO nanorod heterostructures were fabricated, and the quantum confinement effect even from the SQWs was successfully observed [50]. More recently, the realization of *p*-type ZnO opens up significant opportunities for the opto-electro device based on ZnO [51]. Near-field spectroscopy has made a remarkable contribution to investigations of the optical properties in nanocrystallite [52] and resulted in the observation of nanometer-scale optical image, such as the local density of exciton states [53]. However, reports on semiconductor quantum structure are limited to naturally formed quantum dot (QD) [53–55]. In this section, we report low-temperature near-field spectroscopy of artificially fabricated ZnO SQWs on the end of a ZnO nanorod.

ZnO/ZnMgO SQWs were fabricated on the ends of a ZnO stem with a mean diameter of 40 nm and a length of 1 μm . They were grown vertically from the sapphire (0001) substrate using catalyst-free metalorganic vapor phase epitaxy, in which the ZnO nanorod was grown in the *c* orientation [49, 50]. The Mg concentration in the ZnMgO layers averaged 20 atm.%. Two samples were prepared for this study, their ZnO well layer thickness, L_w , were 2.5 and 3.75 nm, while the thicknesses of the ZnMgO bottom and top barrier layers in the SQWs were fixed at 60 and 18 nm, respectively. After growing the ZnO/ZnMgO nanorod SQWs, they were dispersed so that they were laid down on a flat sapphire substrate to isolate them from each other (Fig. 15.20).

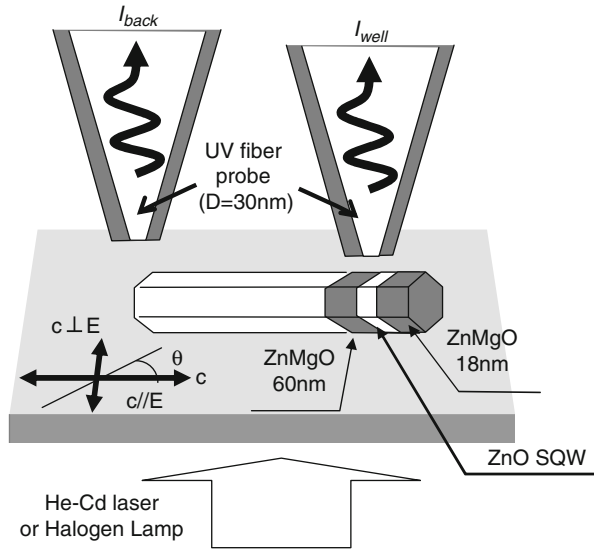
The far-field PL spectra were obtained using a He–Cd laser ($\lambda = 325 \text{ nm}$) before dispersion of the ZnO/ZnMgO nanorod SQWs. The emission signal was collected with the achromatic lens ($f = 50 \text{ mm}$). To confirm that the optical qualities of individual ZnO/ZnMgO SQWs were sufficiently high, we used a collection-mode near-field optical microscope (NOM) using a He–Cd laser ($\lambda = 325 \text{ nm}$) for excitation and a UV fiber probe with an aperture diameter of 30 nm. The excitation source was focused on a nanorod sample laid on the substrate with a spot size approximately 100 μm in diameter. The PL signal was collected with the fiber probe and detected using a cooled charge-coupled device through a monochromator. The fiber probe was kept in close proximity to the sample surface ($\sim 5 \text{ nm}$) using the shear-force feedback technique. The polarization of the incident light was controlled with a $\lambda/2$ waveplate. In contrast to the naturally formed QD structure (a high monolayer island formed in a narrow quantum well), the barrier and cap layers laid on the substrate allowed the probe tip access to PL source, which reduced carrier diffusion in the ZnO SQWs and the subsequent linewidth broadening, thereby achieving a high spatial and spectral resolution. In addition to the PL measurements, absorption spectra were obtained using a halogen lamp, where the absorption was defined by the ratio $I_{\text{well}}/I_{\text{back}}$ between the signal intensities transmitted through the well layer (I_{well}) and substrate (I_{back} , 50 nm apart from the well layer) (Fig. 15.21). The absorption signal was collected with the same fiber probe with an aperture diameter of 30 nm. Since the ZnMgO layers (bottom and top barrier layers are 60 and 18 nm, respectively) are much thicker than that of the well layer ($\sim 3 \text{ nm}$), any difference in the transmission signals between I_{well} and I_{back} was not detected, which resulted in no detection of the absorption peak originated from the ZnMgO layers.

Fig. 15.20 (a) Schematic of ZnO/ZnMgO SQWs on the ends of ZnO nanorods. (b) SEM image of the dispersed ZnO/ZnMgO SQWs



As a preliminary near-field spectroscopy experiment of the ZnO SQWs, we obtained near-field PL spectra of the ZnO SQWs with $L_w = 3.75$ nm (Fig. 15.22a) obtained with polarization perpendicular to the c -axis ($\theta = 90$ in Fig. 15.20b). Two typical spectra are shown, one with a single peak at 3.375 eV (NF₁) and the other with several sharp peaks around 3.375, 3.444, and 3.530 eV (NF₂), while NF_b is a background spectra (Fig. 15.22a). Several conclusions can be drawn from these spectral profiles. First, comparison with the far-field PL spectrum (FF, dashed curve in Fig. 15.22a) showed that the emission peak I_2^{ZnO} at 3.375 eV was suppressed and I_{QW} (3.444 eV) and I_{ZnMgO} (3.530 eV) were enhanced in NF₂, indicating that peaks I_2^{ZnO} and I_{ZnMgO} originated from the ZnO stem and ZnMgO layers, respectively. Second, since the peak position of I_{QW} was consistent with the theoretical prediction (3.430 eV) using the finite square-well potential of the quantum confinement effect in the ZnO well layer for $L_w = 3.75$ nm, we concluded that peak I_{QW} originated from the ZnO SQWs. The theoretical calculation used $0.28m_0$ and $1.8m_0$ as the effective masses of an electron and hole in ZnO, respectively, at a ratio of

Fig. 15.21 Schematic of experimental setup for near-field PL spectroscopy. c : c -axis of the ZnO stem. θ : angle between the ZnO stem and the direction of incident light polarization

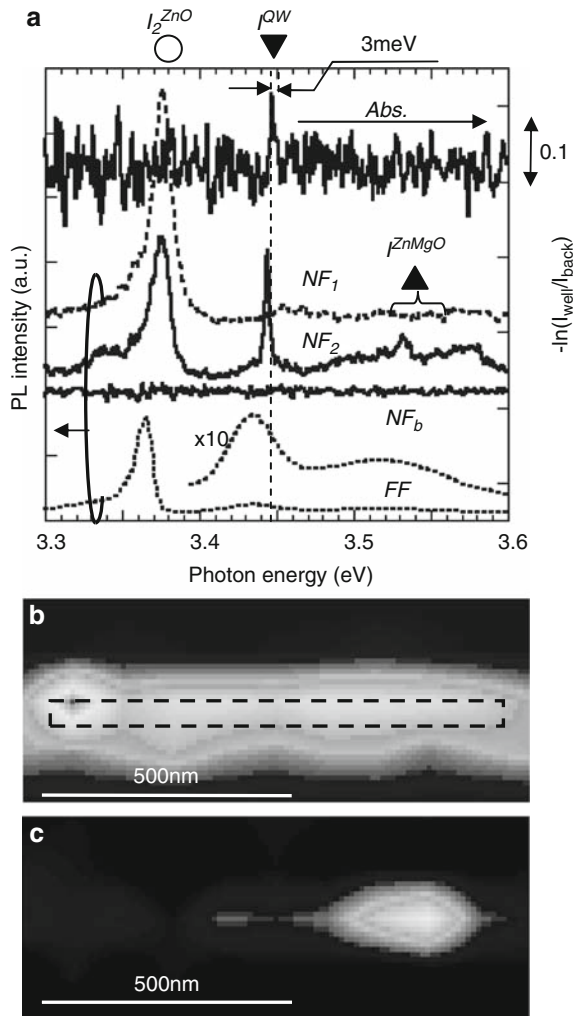


conduction and valance band offsets ($\Delta E_c/\Delta E_v$) of 9, and a band gap offset (ΔE_g) of 250 meV [50]. The spatial distributions of the near-field PL intensity of peaks I_2^{ZnO} and I_{QW} (Fig. 15.22b, c) supported the postulate that the blue-shifted emission was confined to the end of the ZnO stem. Third, the spectral width (3 meV) of peak I_{QW} was much narrower than those of the far-field PL spectra (40 meV).

To estimate the homogeneous linewidth of isolated ZnO SQWs, we observed the power dependence of the near-field PL spectra (Fig. 15.23a) by varying the excitation power densities from 0.6 to 4.8 W/cm². The shape of each spectrum was fitted using the Lorentzian function indicated by the solid curve. Figure 15.23b, c shows the integrated PL intensity (I_{PL}) and linewidth (Δ) of the fitted Lorentzian, which increased linearly and remained constant around 3 meV, respectively. These results indicate that emission peak I_{QW} represented the emission from a single-exciton state in ZnO SQWs and that the linewidth was governed by the homogeneous broadening. Fourth, the Stokes shift of 3 meV (Fig. 15.22a) was much smaller than the reported value (50 meV) in ZnO/ZnMgO superlattices [56, 57]. The small Stokes shift may result from the decreased piezoelectric polarization effect by the fully relaxed strain for the ZnO/ZnMgO nanorod quantum structures in contrast to the two-dimensional (2D) ZnO/ZnMgO heteroepitaxial multiple layers. This argument is supported by theoretical calculation of electronic structure of double barrier InAs/InP/InAs/InP/InAs nanorod heterostructures [58], concluding that any strain at heterointerfaces relaxes in nanorods within a few atomic layers in contrast to 2D pseudomorphic heteroepitaxy.

Based on these experiments, a major investigation of the optical properties of isolated ZnO SQWs was performed by analyzing the polarization-dependent PL spectrum of isolated ZnO SQWs ($L_w = 3.75$ nm). As shown in Fig. 15.24a,

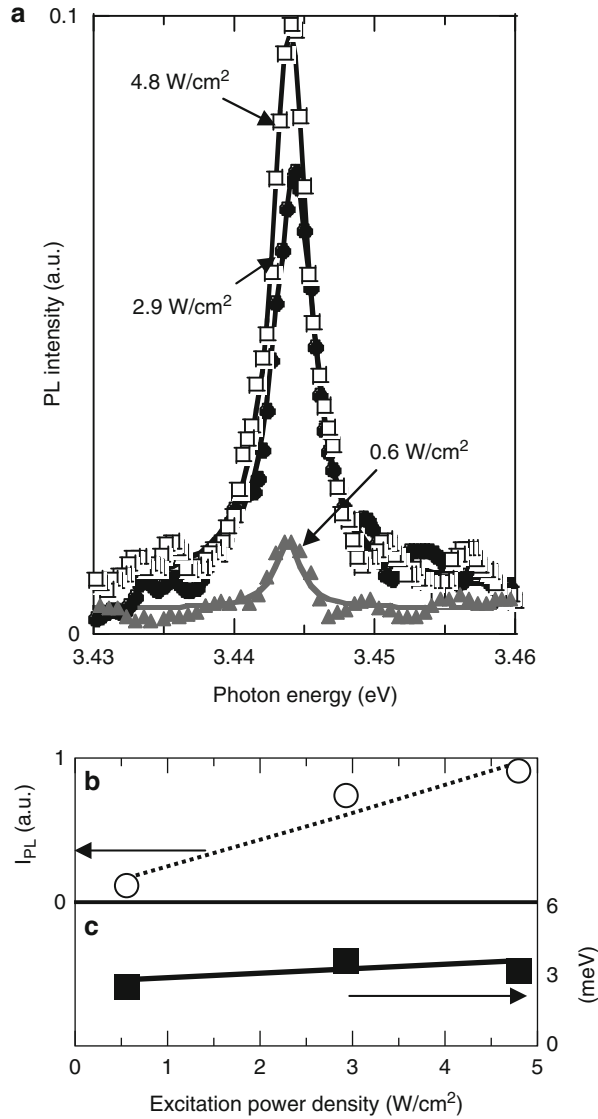
Fig. 15.22 Near-field PL and absorption spectroscopy of isolated ZnO SQWs ($L_w = 3.75$ nm) at 15 K. (a) NF_1, NF_2 : near-field PL spectra. NF_b : background noise. *Abs.*: near-field absorption spectrum, *FF*: far-field PL spectrum of vertically aligned ZnO SQWs ($L_w = 3.75$ nm). NOM images of isolated ZnO SQWs obtained at (b) 3.375 and (c) 3.444 eV. The rectangle shown in dashed white lines indicates the position of the ZnO stem



NF_0 is a near-field PL spectrum obtained with parallel polarization with respect to the c -axis, $\theta = 0^\circ$, and this exhibits a new peak I_{1b}^{QW} at 3.483 eV, which is out of peak in the far-field spectrum ($3.435 \text{ eV} \pm 20 \text{ meV}$). Peak I_{1a}^{QW} is the same as I_{QW} in Fig. 15.22a.

As the ZnO has valence-band anisotropy owing to the wurtzite crystal structure, the operator corresponds to the Γ_5 (Γ_1) representation when the electric vector \vec{E} of the incident light is perpendicular (parallel) to the crystalline c -axis, respectively. By considering the energy difference between Γ_5 and Γ_1 in the center of the zone around 40 meV for bulk material [45, 59, 60], and the direction of the incident light polarization with respect to the c -axis, emission peaks I_{1a}^{QW} and I_{1b}^{QW} in Fig. 15.24a are allowed for the exciton from Γ_5 and Γ_1 , respectively. Note that this

Fig. 15.23 Power-dependent near-field PL spectroscopy of isolated ZnO SQWs ($L_w = 3.75$ nm) at 15 K. (a) Near-field PL spectra of isolated ZnO SQWs at excitation densities ranging from 0.6 to 4.8 W/cm². The integrated PL intensity, I_{PL} , (b) and homogeneous linewidths, Δ , (c) as a function of the excitation power density



is the first observation of a Γ_1 exciton in a PL spectrum, while the observation of emission from Γ_1 has been realized only for bulk ZnO crystals using time-resolved reflection spectroscopy [59, 60]. Since the exciton binding energy of the emission from Γ_1 (50–56 meV) [60, 61] is comparable to that from Γ_5 (60 meV), this successful observation originates from the enhancement of the exciton binding energy owing to the quantum confinement effect [6]. Furthermore, in contrast to the bulk ZnO film, our sample configuration using laid ZnO nanorod SQWs has

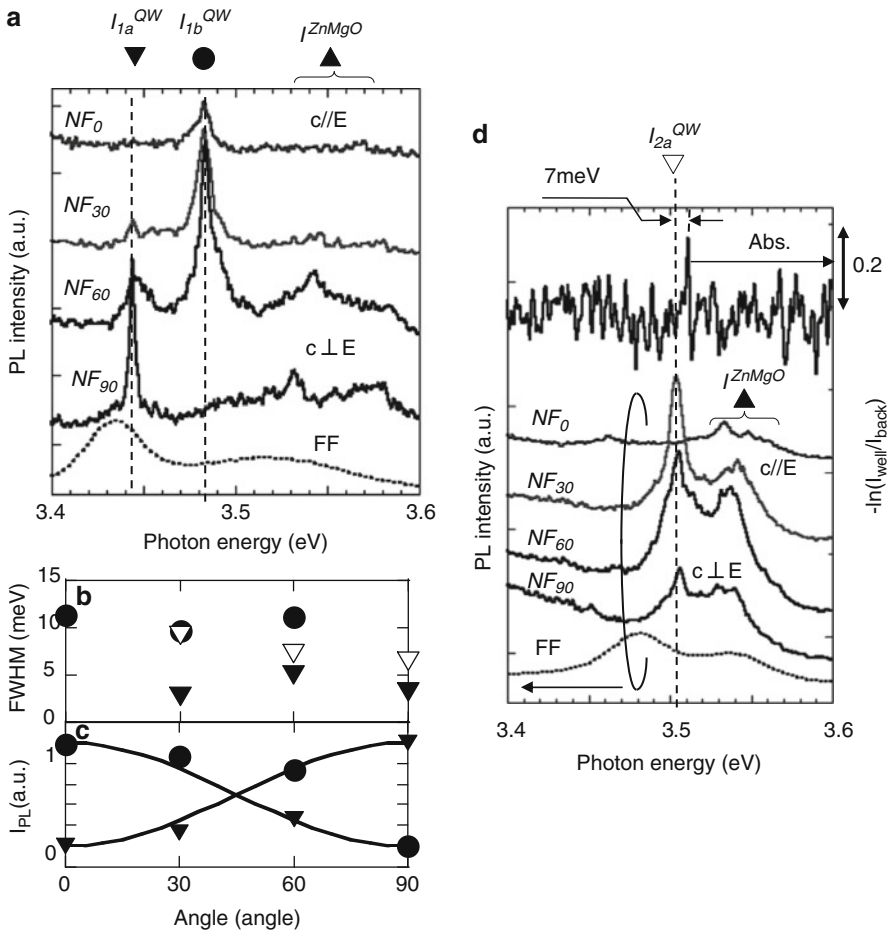


Fig. 15.24 Polarization dependence of near-field PL spectra of isolated ZnO SQWs obtained at 15 K. (a) NF_θ , FF near-field and far-field PL spectra of isolated ZnO SQWs ($L_w = 3.75$ nm) for $\theta = 0, 30, 60$, and 90° . (b) *Solid triangles* and *circles* are the polarization dependence of the linewidth of I_{1a}^{QW} and I_{1b}^{QW} , respectively, in (a). *Open triangles* are the polarization dependence of linewidth of I_{2a}^{QW} in (d). (c) *Solid triangles* and *circles* are the integrated PL intensities, I_{PL} , of I_{1a}^{QW} and I_{1b}^{QW} , respectively, normalized to the total PL intensities ($I_{1a}^{QW} + I_{1b}^{QW}$). (d) NF_θ , FF near-field and far-field PL spectra of isolated ZnO SQWs ($L_w = 2.5$ nm), *Abs.* absorption spectrum

realized π polarization ($\theta = 0^\circ$), allowing the detection of the emission from the Γ_1 exciton. The homogeneous linewidth of emission peak I_{1a}^{QW} (Γ_5) is in the range 3–5 meV, while that of I_{1b}^{QW} (Γ_1) is 9–11 meV (Fig. 15.24b). This difference is attributed to the degeneracy of the transition of the Γ_1 exciton with continuum and to the contribution of the residual strain field and results in sensitive dependence

of the Γ_1 exciton on the strain, as reported in the GaN [62]. The solid triangles and circles in Fig. 15.24c show the respective normalized integrated PL intensity at I_{1a}^{QW} and I_{1b}^{QW} , respectively, which are in good agreement with the sine-squared and cosine-squared functions represented by the solid curves. These results indicate that emission peaks I_{1a}^{QW} and I_{1b}^{QW} originate from unidirectional transition dipoles that are orthogonal each other.

To study the linewidth broadening mechanism, Fig. 15.24d shows the polarization-dependent near-field PL spectra (NF₀–NF₉₀) and absorption spectrum obtained for isolated ZnO SQWs with a thinner well layer ($L_w = 2.5$ nm). In NF₀–NF₉₀, the emission peaks I_{ZnMgO} around 3.535 eV originate from the ZnMgO layers. Emission peak I_{2a}^{QW} originates from the Γ_5 exciton in the SQWs, as was the case for I_{1a}^{QW} in Fig. 15.24a, since the position of peak I_{2a}^{QW} (3.503 eV) is consistent with the theoretical prediction (3.455 eV) using the finite square-well potential of the quantum confinement effect in the ZnO well layer. In comparison to ZnO SQWs with $L_w = 3.75$ nm, however, emission peak I_{2a}^{QW} had a broader linewidth (7–10 meV), which is attributed to the shorter exciton dephasing time. In the nanocrystallite where the excitons are quantized, the linewidth should be determined by the exciton dephasing time. Such dephasing arises from the collisions of the excitons at the irregular surface, so that the linewidth is d^{-2} (d is the effective size of the quantum structure) [63]. The observed well-width dependence of the spectral linewidth, $3.75^{-2}/2.5^{-2} \sim 3/7$, and the Stokes shift of 7 meV (see Fig. 15.24c) larger than that for $L_w = 3.75$ nm (3 meV) are supported by this dephasing mechanism quantitatively. Although emission peak I_{2a}^{QW} was suppressed for $\theta = 0^\circ$, no peaks corresponding to the Γ_1 exciton in SQWs were detected owing to the reduction of the exciton binding energy, since the peak energy of Γ_1 for the ZnO SQWs with $L_w = 2.5$ nm is comparable with that of ZnMgO.

15.4 An Optical Far-/Near-Field Conversion Device

For use in future photonic systems, the nanophotonic devices and ICs must be connected to conventional diffraction-limited photonic devices. This connection requires a far-/near-field conversion device, such as a nanometer-scale optical waveguide. The performance parameters required of this device include:

- (A) High conversion efficiency
- (B) A guided beam width of less than 100-nm for efficient coupling of the converted optical near-field to sub-100 nanometer-sized dots
- (C) A propagation length that is longer than the optical wavelength to avoid direct coupling of the propagating far-field light to the nanophotonic device consisted of nanometer-scale dots the propagation length l_t is defined as $I(z) = I(0) \exp(-z/l_t)$, where $I(z)$ is the optical intensity and z is the longitudinal position measured from the input terminal ($z = 0$)

15.4.1 A Plasmon Waveguide with Metallic-Core Waveguide

One candidate that meets these requirements is a tetrahedral tip, in which the one-dimensional (1D) mode has been excited efficiently by transverse magnetic (TM)-polarized incident light [64]. Setting the incoming beam at an oblique angle to the metal slit at the edge of a tetrahedral tip converts far-field light to the 1D internal edge mode. However, the guided mode profile in a tetrahedral tip has not been observed directly. Furthermore, since it consists of a dielectric core surrounded by metal, the smallest diameter of the optical beam is estimated to be 100 nm. This is the theoretical value of the HE plasmon mode in a cylindrical glass core (refractive index $n = 1.53$) surrounded by gold ($n = 0.17 + i5.2$) (Ref. [65]) at a wavelength of 830 nm (see Fig. 15.25c) [66].

This limitation does not meet requirement (B). In order to realize a narrower beam diameter, a more promising candidate is a cylindrical metal-core waveguide, through which the TM plasmon mode propagates [67].

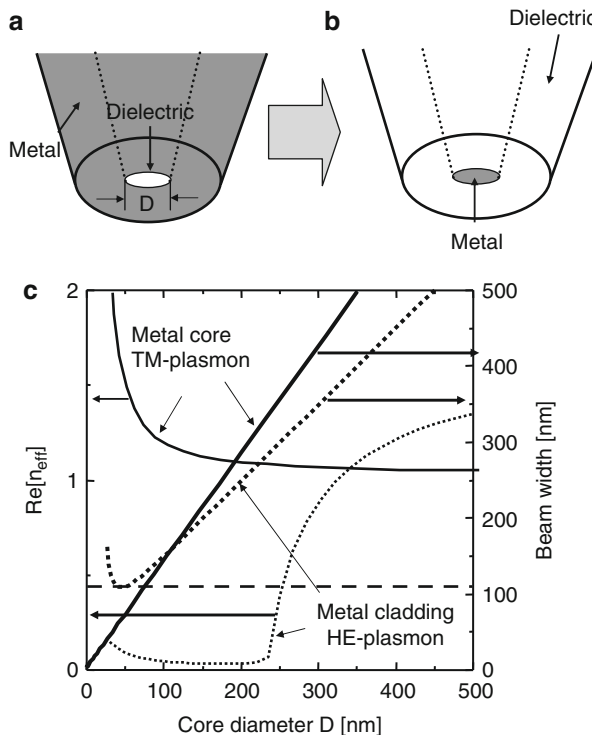


Fig. 15.25 Schematic of tapered (a) metallic-cladding and (b) metallic-core waveguide. (c) Real part of equivalent refractive index relevant guided through the waveguides and their respective beam width

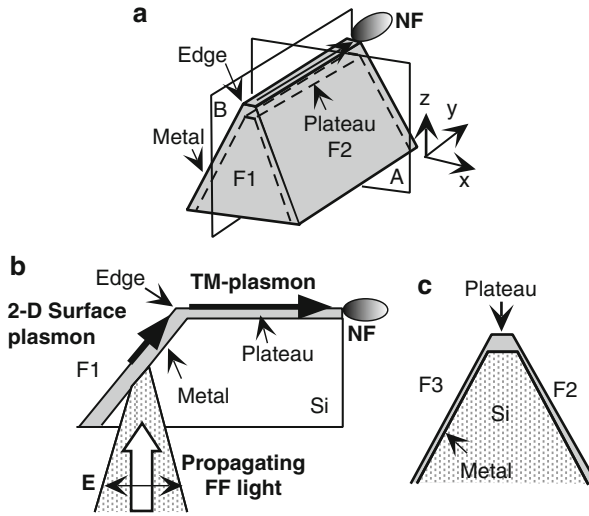


Fig. 15.26 (a) Bird's-eye view of a plasmon waveguide. The x and y axes are perpendicular and parallel to the plateau axis, respectively. (b) Cross section along plane B (yz) in (b). (c) Cross section along plane A (xz) in (b)

This is the basis for our proposed plasmon waveguide for optical far-/near-field conversion. However, the TM plasmon mode is not easily excited by far-field light, due to mode mismatching. To overcome this difficulty, we employed a metal-coated Si wedge structure. Using a near-field optical microscope, we were able to directly observe the TM plasmon mode propagating along the plateau of the Si wedge. Figure 15.26a shows our plasmon-waveguide scheme. The main part consists of a silicon dielectric wedge, coated with a thin metal film. Incoming far-field light, which is polarized parallel to the y -axis, is first transformed into the two-dimensional (2D) surface plasmon mode on the F_1 side (see Fig. 15.26b). Next, the 2D surface plasmon mode is converted into the 1D TM plasmon mode at the edge between F_1 and the plateau. This conversion occurs because of the scattering coupling at the edge [68]. Third, the TM plasmon mode propagates along the plateau in a manner similar to surface plasmon modes using metal stripes [69] or edge modes using metal wedges [70]. This propagation occurs because the metal film deposited on the plateau is thicker than on the other faces (F_1 , F_2 , and F_3) due to the normal evaporation process (see Fig. 15.26c) [71]. Consequently, the plateau acts as a metal-core waveguide. Finally, the TM plasmon mode at the waveguide outlet is converted to the optical near field so that it couples to the nanometer-scale dots, which are located in close proximity to the outlet.

However, the TM plasmon mode is not easily excited by far-field light, due to mode mismatching. To overcome this difficulty, we employed a metal-coated Si wedge structure (Fig. 15.26a) [64]. The main part consists of a Si wedge, coated with a thin metal film. Incoming far-field light, which is polarized parallel to the

y -axis, is first transformed into the two-dimensional (2D) surface plasmon mode on the F_1 side. Next, the 2D surface plasmon mode is converted into the 1D TM plasmon mode at the edge between F_1 and the plateau. This conversion occurs because of the scattering coupling at the edge [72]. Third, the TM plasmon mode propagates along the plateau in a manner similar to edge modes using tetrahedral tip [64]. Since the metal film deposited on the plateau is thicker than on the other faces (F_1 , F_2 , and F_3) due to the normal evaporation process, the plateau acts as a metal-core waveguide. Finally, the TM plasmon mode at the waveguide outlet is converted to the optical near field.

Advantages of our waveguide are:

- (a) High conversion efficiency from the 2D surface plasmon mode to the 1D TM plasmon mode, due to the scattering coupling [68, 72].
- (b) The beam width decreases (as narrow as 1 nm) with the core diameter, since this waveguide does not have a cutoff (see Fig. 15.25c) [66].
- (c) The propagation length of the TM plasmon mode is sufficiently long as to meet requirement (C). For example, the propagation length is $1.25\ \mu\text{m}$ (at $\lambda = 830\ \text{nm}$) for a TM plasmon with a gold core (diameter $D = 40\ \text{nm}$) insulated by air [66].

The plasmon waveguide was fabricated in four steps:

1. A (100)-oriented silicon wafer was bonded to the glass substrate by anodic bonding [81].
2. In order to avoid any deformation of the convex corners [73] (see Fig. 15.27b), the patterned rectangular mask was tilted 30° with respect to the $\langle 110 \rangle$ crystal orientation of silicon (see Fig. 15.27c).
3. The Si wedge was fabricated by anisotropic etching (40 g:KOH +60 g:H₂O +40 g: isopropyl alcohol, 80°C) (see Fig. 15.27d). Maintaining the Si wedge height at less than $10\ \mu\text{m}$ also kept its propagation loss sufficiently low.
4. After removing the SiO₂ layer, the Si wedge was coated with a 50-nm-thick gold layer (see Fig. 15.28a, b).

The spatial distribution of the electric-field energy throughout the plateau of metallized Si wedge was measured by scanning fiber probe with an aperture diameter D_a of 60 nm. In order to excite the plasmon mode, linearly polarized light ($\lambda = 830\ \text{nm}$) was focused onto the F_1 face. Figure 15.29a, b shows the observed electric-field energy distributions on the wedges with plateau width $W = 1\ \mu\text{m}$ and 150 nm for TM polarization (the incident light polarization is parallel to the y). Figure 15.29c, d is for TE polarization (parallel to the x). Comparing Fig. 15.29a, c (or 15.29b and d) shows that the propagating mode was excited efficiently only by TM-polarized incident light. The closed and open circles in Fig. 15.29c, d show the cross-sectional profiles along the lines in Fig. 15.29a (A–A' and a–a'), b (B–B' and b–b'). Here, transmission was defined as the ratio of the light power detected by the fiber probe to the input light power. From the dotted exponential curve in Fig. 15.29c fitted to the open circles, the propagation length was estimated as $1.25\ \mu\text{m}$ for the 150-nm wedge. This value is comparable to the theoretical value for TM plasmon mode in a cylindrical metal-core waveguide with $D = 40\ \text{nm}$ and consisting of a gold core and air cladding ($\lambda = 830\ \text{nm}$) [66]. From fitting the solid exponential

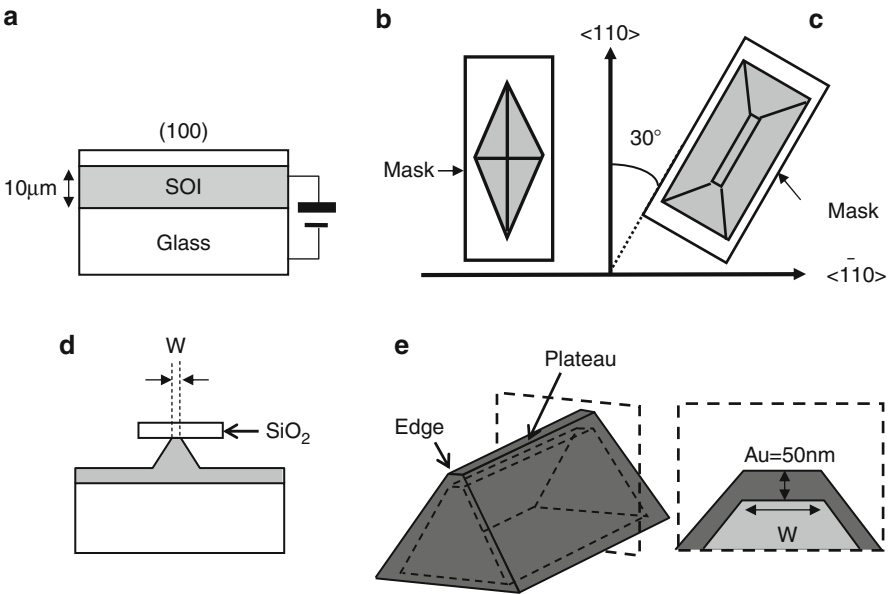


Fig. 15.27 Fabrication steps for a pyramidal Si probe: (a) anodic bonding; (b), (c), (d) anisotropic etching for fabrication of the Si wedge; (e) metal coating

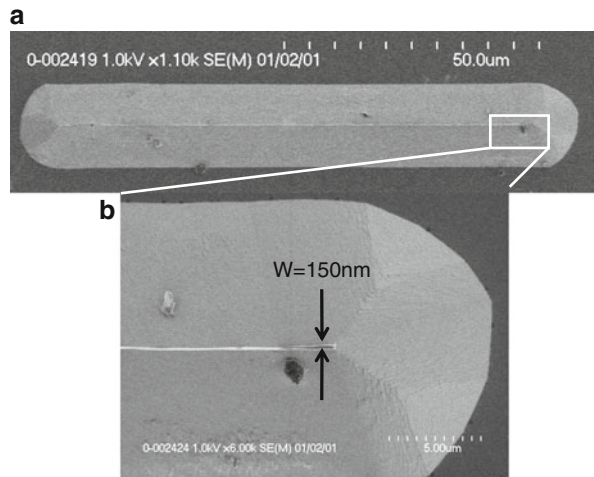


Fig. 15.28 SEM images of the fabricated pyramidal silicon probe: (a) overview; (b) magnified image of (a)

curve in Fig. 15.29c to the closed circles, the propagation length for $W = 1.0 \mu\text{m}$ was estimated as $2.0 \mu\text{m}$, which is longer than that for $W = 150 \text{nm}$. This is because, as W increases, the effective refractive index approaches that of surface plasmon at the planar boundary between gold and air [66]. These experimental results confirm that the observed excitation along the plateau was the TM plasmon mode. Figure 15.29d shows that FWHM of the cross-sectional profiles was 150nm

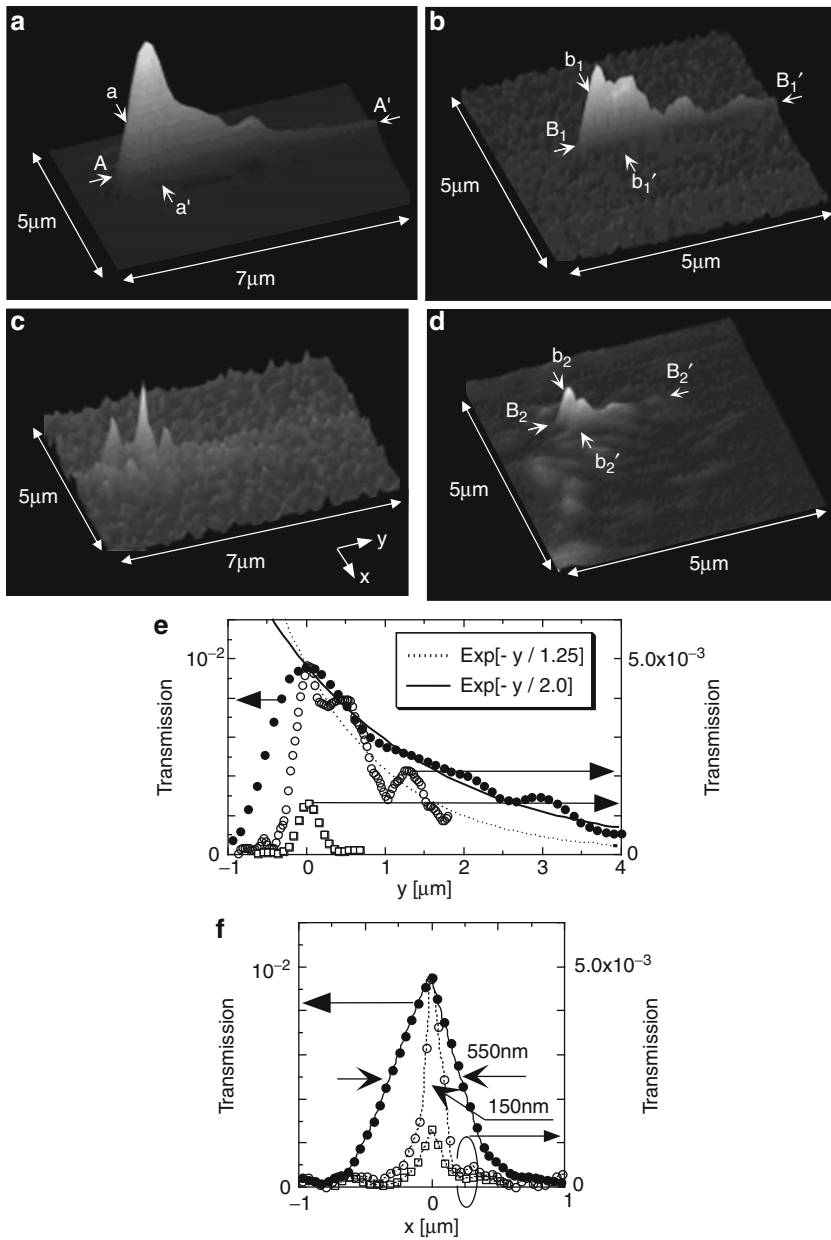


Fig. 15.29 Electric-field distribution ($\lambda = 830$ nm) on the silicon wedge plateau. (a) TM polarization: $W = 1 \mu\text{m}$. (b) TM polarization: $W = 150$ nm. (c) TE polarization: $W = 1 \mu\text{m}$. (d) TE polarization: $W = 150$ nm. (e) Cross-sectional profiles along A–A' (closed circles), B₁–B'₁ (open circles), and B₂–B'₂ (open squares) in (a), (b), and (d), respectively. Solid and dotted curves represent the exponential curves fitted to the experimental values. (f) Cross-sectional profiles along a–a' (closed circles), b₁–b'₁ (open circles), and b₂–b'₂ (open squares) in (a), (b), and (d), respectively

for $W = 150$ nm. With minor improvements to the waveguide, this FWHM value should meet requirement (B). Furthermore, note that the transmission was 5.0×10^{-3} for $W = 150$ nm, which is ten times higher than that of a fiber probe with $D_a = 150$ nm [74]. This efficient excitation of the TM plasmon mode can be attributed to the scattering coupling at the edge between F_1 and the plateau in Fig. 15.26a [68, 72]. This transmission efficiency meets requirement (A). Finally, the propagation length estimated above is longer than the incident light wavelength. This meets requirement (C).

15.4.2 A Nanodot Coupler with a Surface Plasmon-Polariton Condenser for Optical Far-/Near-Field Conversion

To increase propagation length, a more promising candidate is a nanodot coupler consisting of an array of closely spaced metallic nanoparticles, because higher transmission efficiency is expected owing to the plasmon resonance in the closely spaced metallic nanoparticles [75]. Energy transfer along the nanodot coupler relies on the near-field coupling between the plasmon-polariton mode of the neighboring nanoparticles.

To increase in the efficiency of exciting localized surface plasmon in the nanodot coupler than that excited by propagating far-field light, we equipped the nanodot coupler with a surface plasmon-polariton (SPP) condenser for efficient far-/near-field conversion. Figure 15.30 shows the proposed optical far-/near-field conversion device [76, 77].

Incoming far-field light is first transformed into the two-dimensional SPP mode on the gold film (see Fig. 15.31a). Then, the SPP mode is scattered and focused by the SPP condenser, which consists of several hemispherical metallic submicron particles that are arranged in an arc and work as a “phased array” (Fig. 15.31b) [78]. The input terminal of the nanodot coupler is fixed at the focal point of the SPP.

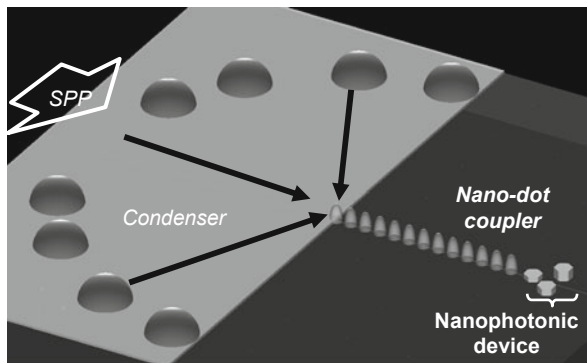


Fig. 15.30 Bird’s-eye view of a nanodot coupler with a surface plasmon-polariton (SPP) condenser

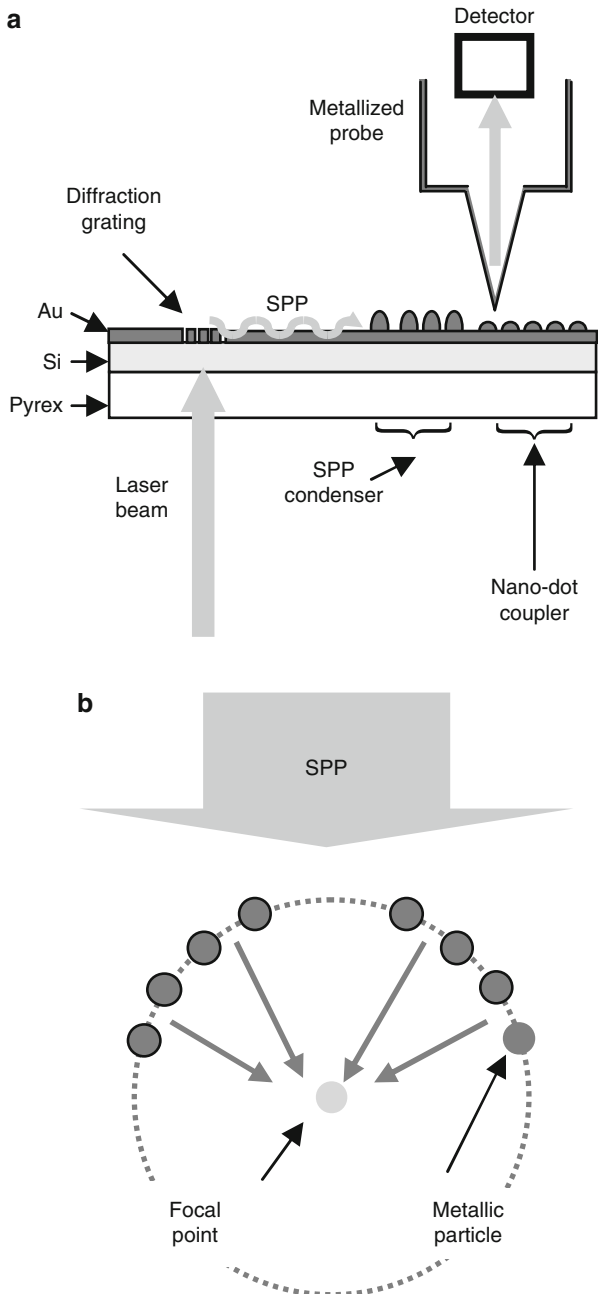


Fig. 15.31 (a) Experimental system of nanodot coupler with an SPP condenser. (b) Schematic illustration of the SPP condenser

Finally, after the localized surface plasmon transmits through the nanodot coupler, it is converted into an optical near-field so that it couples to the nanophotonic device.

The advantages of this device are that it has:

- (α) A high conversion efficiency, from the SPP mode to the localized surface plasmon in the nanodot coupler, owing to coupling the scattering at the inlet metallic nanoparticle [72].
- (β) No cutoff diameter of the metallic nanoparticle array, that is, the beam width decreases with the diameter because the electric-field vector, which is dominant in the nanodot coupler, involves only a Förster field [75].
- (γ) Longer-distance propagation than that of the metallic-core waveguide due to the reduction of metal content and plasmon resonance in the metallic nanoparticles. For example, the calculation using the finite-difference time domain (FDTD) method estimated a propagation length of $l_1 = 2 \mu\text{m}$ (at an optical wavelength $\lambda = 785 \text{ nm}$) for a plasmon-polariton mode with linearly aligned 50-nm dots with 10-nm separation [79, 80].

Advantages (α) to (γ) are compatible with meeting requirements (A) to (C), respectively.

To fabricate the nanodot coupler and SPP condenser using a focused ion beam (FIB), we used a silicon-on-insulator (SOI) wafer to avoid ion beam drift. The fabrication process was as follows:

- (i) A (100)-oriented SOI wafer was bonded to a glass substrate by anodic bonding (300 V, 350 °C, 10 min) (Fig. 15.32a) [81]. Maintaining the silicon wafer thickness at less than 10 μm kept the optical propagation loss sufficiently low.
- (ii) After removing the silicon substrate and SiO_2 layer from the SOI wafer by wet etching, carbon hemispheres were deposited using FIB (Fig. 15.32b).
- (iii) To excite SPP mode and enhance the optical near-field energy, a 120-nm-thick gold film was applied using sputtering (Fig. 15.32c). The number of hemispheres, their positions, and their sizes were optimized using the FDTD method in order to minimize the focused spot size [80].
- (iv) Finally, a diffraction grating was fabricated using a FIB milling technique 50 μm below the condenser in order to excite the SPP by the incident optical far field (a laser beam).

Figure 15.32d, e shows scanning electron microscopic (SEM) images of the SPP condenser and nanodot coupler.

Two banks were fabricated in order to avoid illumination of the nanodot coupler by the satellite spots (originating from higher-order diffraction) (Fig. 15.32d). The nanodot coupler consisted of a linear array of nanoparticles with diameters of 230 nm separated by 70 nm. The SPP condenser consisted of twelve scatterers 350 nm in diameter, aligned on an arc with a diameter of 10 μm .

The spatial distribution of the optical near-field energy was observed using a collection mode near-field optical microscope (see Fig. 15.31a). A light source with a wavelength of $\lambda = 785\text{-nm}$ light was used to transmit the far-field light through the 10- μm -thick Si substrate. A sharpened fiber probe with 20-nm-thick gold film was used to enhance the collection efficiency [82].

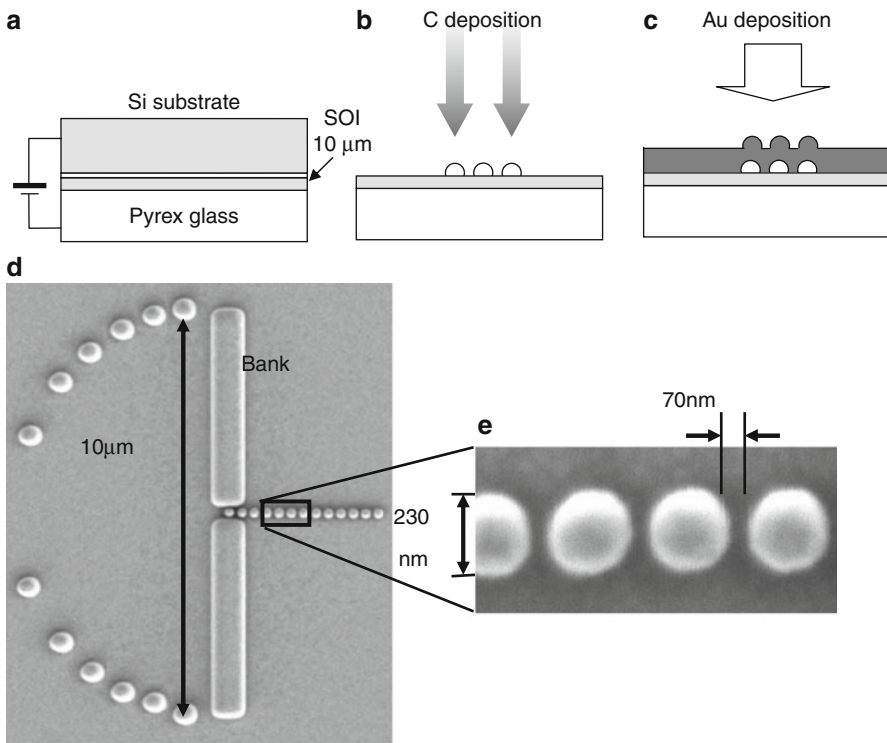


Fig. 15.32 Fabrication of the nanodot coupler and SPP condenser: (a) anodic bonding (step (i)), (b) carbon hemisphere deposition using FIB (step (ii)), (c) 120-nm gold film deposition using sputtering (step (iii)), (e) and (d) SEM images of the fabricated nanodot coupler and SPP condenser

First, we checked whether the SPP condenser led to efficient scattering and resultant focusing of the SPP by exciting the SPP mode through the grating coupler. Figure 15.33a, b shows a shear-force image of the SPP condenser and the spatial distribution of the optical near-field energy, respectively. As shown in the cross-sectional profile (dashed curve in Fig. 15.33d) through the focal point of the SPP (white dotted line in Fig. 15.33b), FWHM of the spatial distribution of the SPP was as narrow as 400 nm. Figure 15.33c shows the spatial distribution of the optical near-field energy in the SPP condenser calculated using the FDTD method, where each cell was $50 \times 50 \times 25$ nm and the model consisted of $240 \times 240 \times 80$ cells. Considering the tip diameter (50 nm) of the metallized fiber probe used for collection mode, the observed distribution (Fig. 15.33b and dashed curve in d) was in good agreement with the calculated results (FWHM = 380 nm, solid curve in Fig. 15.33d). These results imply that our device works as an efficient phased array.

Second, we measured the spatial distribution of the optical near-field energy on a linear nanodot coupler, the input terminal of which was fixed at the focal point

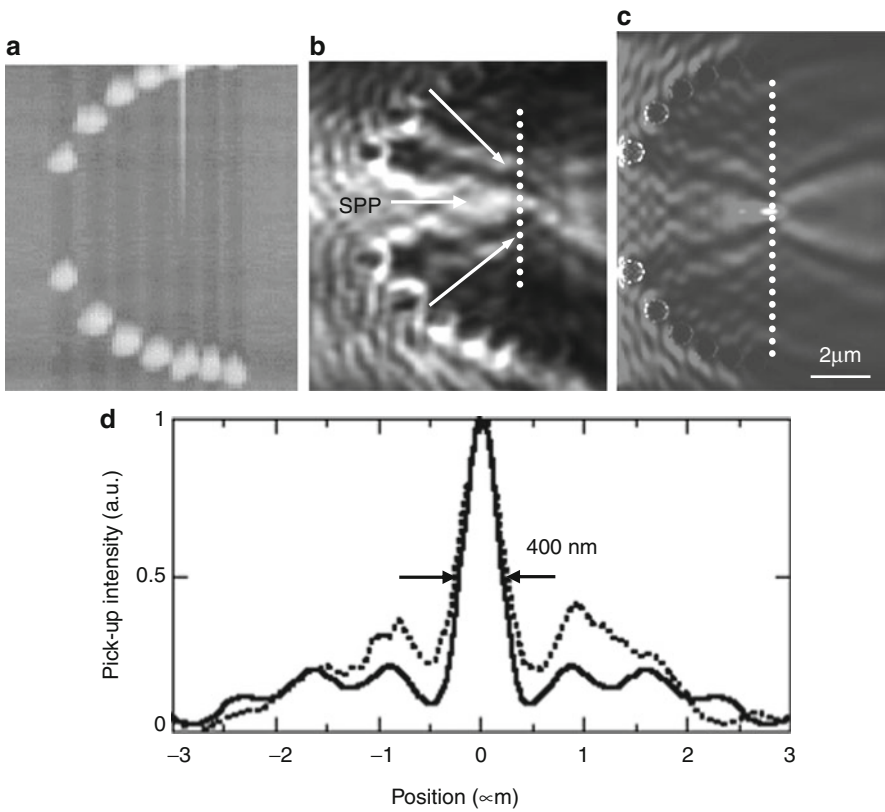
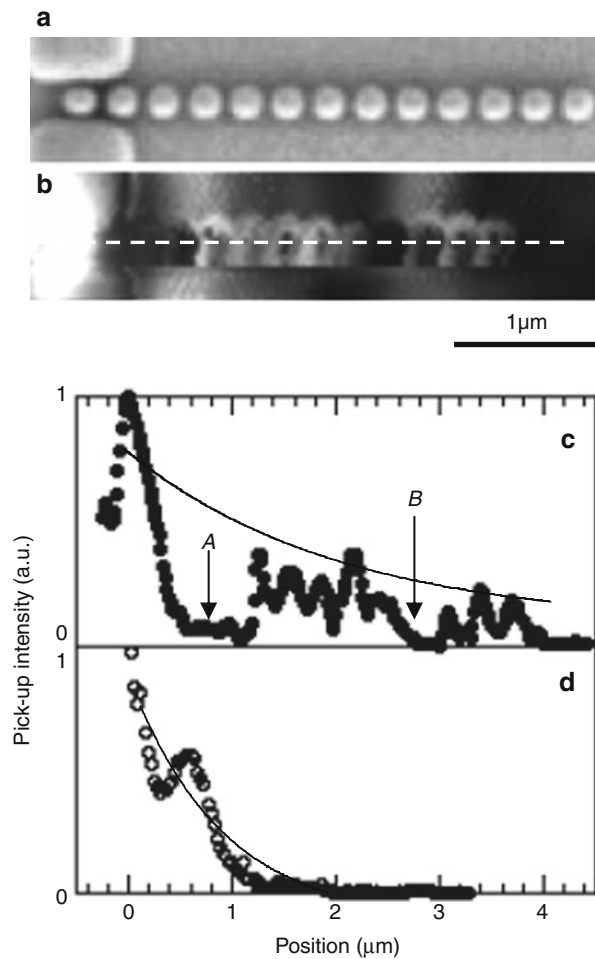


Fig. 15.33 (a) Shear-force image of the SPP condenser. (b) The near-field energy distribution of (a) taken at $\lambda = 785$ nm. (c) Calculated spatial distribution of the electric-field energy using the FDTD method. The *dashed* and *solid* curves in (d) are cross-sectional profiles along the *dashed* white lines in (b) and (c), respectively

of the SPP. Figure 15.34a, b shows an SEM image and the spatial distribution of the optical near-field energy on the nanodot coupler, respectively. The black dots in Fig. 15.34c show cross-sectional profiles along the white broken line in Fig. 15.34b. Position $x = 0$ corresponds to the focal point of the SPP condenser. Although not all of the energy couples to the nanodot coupler owing to mode mismatch, the optical near-field intensity has a maximum at each edge of the nanoparticles. This is due to artifact resulting from the fiber probe at constant height mode. The dips indicated by arrows A and B originate from interference of the localized surface plasmon in the nanodot coupler that arises from reflection at the output terminal. However, the exponential envelope (solid curve of Fig. 15.34c) fitted by neglecting these influences indicates that the propagation length l_t was $4.0 \mu\text{m}$. l_t was five times longer than the wavelength, which meets requirement (C). The beam width was 250 nm, which is comparable to the nanoparticle size. As the size of

Fig. 15.34 SEM image (a) and the near-field energy distribution (b) of a linearly chained nanodot coupler. (c) Solid circles show the cross-sectional profiles along the white dashed line in (b). The solid curve shows the fitted exponential envelope. A and B indicate dips resulting from the length of the nanodot coupler. (d) Open circles show the cross-sectional profiles along metallic-core waveguide, and the solid curve shows the fitted exponential envelope



the nanoparticles was determined by the resolution of FIB for carbon hemisphere deposition, the beam width can be decreased to sub-50 nm scale using electron beam lithography, which will meet requirement (B).

Third, we checked whether near-field coupling between the neighboring nanoparticles resulted in lower propagation loss by comparing our device with a metallic-core waveguide. For this purpose, we fabricated a gold-core waveguide the same width as the diameter of the nanoparticles in the nanodot coupler, with its input terminal also fixed at the focal point of the SPP. The open circles in Fig. 15.34d show the cross-sectional profile of the metallic-core waveguide, and the exponential envelope (solid curve in Fig. 15.34d) indicates that the propagation length l_t was 1.2 μm . To evaluate the observed propagation length, we calculated the theoretical value of our metallic-core waveguide. Since the Au-core waveguide is placed on a Si substrate, we calculated one-dimensional TM plasmon mode [66] in the cylindrical

Au-core waveguide with an diameter of 250 nm ($\epsilon_{\text{Au}} = (0.174 + i4.86)^2 = -23.59 + i1.69$) [65] surrounded by the medium with an average dielectric constant of Si and air [26], $\epsilon_{\text{cl}} = ((3.705 + i0.007)^2 + 1)/2 = 7.36 + i0.03$ [65]. Based on these assumptions, the calculated propagation length of our Au-core waveguide is 1.4 μm . Since this is in good agreement with the observed value (1.2 μm), the comparison confirmed that more efficient energy transfer was realized by the nanodot coupler.

Finally, we also observed the spatial distribution of the optical near-field energy for a zigzag-shaped nanodot coupler (see Fig. 15.35a, b). Corners A–D in Fig. 15.35c represent the profiles at locations A–D in Fig. 15.35d, respectively. Comparing adjacent curves, we found that the energy loss at corners A–D was negligible. This is attributed to efficient coupling of the TM and TE localized surface plasmon at the corners. As a result, the propagation length through this zigzag-shaped nanodot coupler was equivalent to that through a linear one. Although efficient coupling was predicted using the point-dipole approximation [75], this is the first experimental confirmation of it. Such high flexibility in the arrangement of nanoparticles is an outstanding advantage for optical far-/near-field conversion for driving nanophotonic devices.

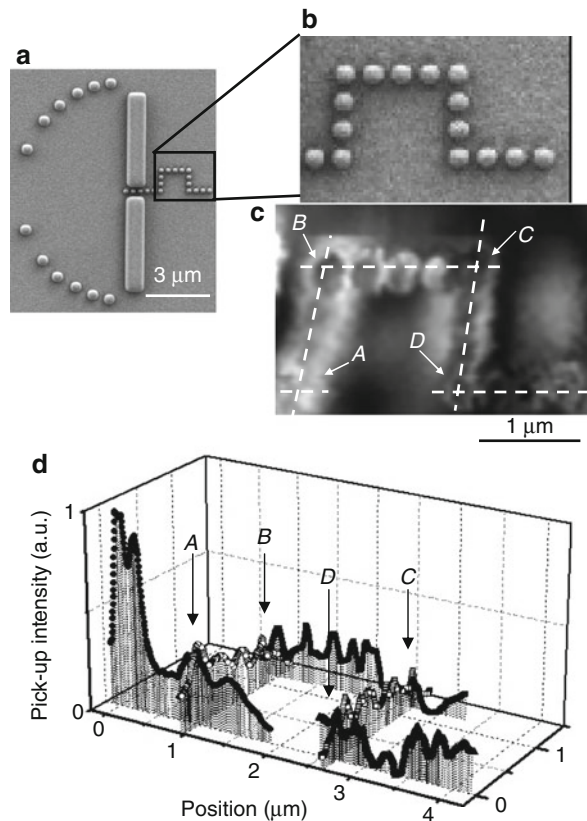


Fig. 15.35 SEM (a) (b) images and the near-field intensity distribution (c) of a zigzag-shaped nanodot coupler. (d) The cross-sectional profiles along the dashed white lines in (c). The arrows A to D indicate the corners

15.5 Conclusions

This chapter reviewed nanophotonics, a novel optical nanotechnology utilizing local electromagnetic interactions between a small number of nanometric elements and an optical near field. Its potential for high integration beyond the diffraction limit of light can solve the technical problems of the future optical industry.

To fabricate nanophotonic devices and ICs, we developed a new technique of chemical vapor deposition that uses an optical near field. We reported that optical near-field desorption can dramatically regulate the growth of Zn nanoparticles during optical chemical vapor deposition. The trade-off between the deposition due to 3.81-eV optical near-field light and desorption due to 2.54-eV optical near-field light allowed the fabrication of a single 15-nm Zn dot while regulating its size and position. Furthermore, we investigated the growth mechanism of Zn dots with NFO-CVD and found that the deposition rate was maximal when the dot grew to a size equivalent to the probe apex diameter, owing to resonant near-field coupling between the deposited Zn dot and the probe apex. The experimental results and suggested mechanisms show the potential advantages of this technique for realizing nanophotonic ICs.

As a self-assembling method for mass production of nanophotonic ICs, we presented experimental results that demonstrate the controlled assembly of 40-nm latex particles in desired positions using capillary force interaction. Further controllability in separation and positioning was demonstrated using colloidal gold nanoparticles by introducing the Si wedge structure and controlling the direction of polarization. The experimental results and suggested mechanisms described here show the potential advantages of this technique in improving the regulation of the separation and positioning of nanoparticles and possible application to realize a nanodot coupler for far-/near-field conversion.

In order to confirm the possibility of using a nanometric ZnO dot as a light emitter in a nanophotonic IC, we report on near-field optical spectroscopy of artificially fabricated ZnO/ZnMgO nanorod SQWs as a major breakthrough for realizing nanophotonic devices using a two-level system [83, 84]. We performed both polarization-dependent absorption and emission spectroscopy of isolated ZnO nanorod SQWs and observed valence-band anisotropy of ZnO SQWs in photoluminescence spectra directly for the first time. The success of near-field PL and absorption measurement of isolated SQWs described above is a promising step toward designing a nanophotonic switch and related devices.

To connect the nanophotonic IC with external photonic devices, we developed a nanometer-scale waveguide using a metal-coated silicon wedge structure. Propagation of the TM plasmon mode was observed using a near-field optical microscope. Illumination ($\lambda = 830$ nm) of the metal-coated silicon wedge ($W = 150$ nm) caused a TM plasmon mode with beam width of 150 nm and propagation length of 1.25 μ m. Further improvement of the performance was realized by a nanodot coupler with an SPP condenser. The FWHM of the spatial distribution of the optical near-field energy at the focal point of the SPP was as small as 400 nm at $\lambda = 785$ nm. Furthermore, installing a linear nanodot coupler at the focal

point of the SPP realized efficient excitation of plasmon-polariton mode with a transmission length of 4.0 μm . Equivalent energy transfer was observed in zigzag-shaped nanodot couplers. These results confirm that a nanodot coupler with an SPP condenser can be used as the optical far-/near-field conversion device required by future systems.

Acknowledgements We are grateful to Drs. Wataru Nomura and Tadashi Kawazoe (University of Tokyo) Itsuki Banno (Yamanashi University), Dr.Suguru Sangu (Ricoh Company, Ltd.), and Prof. Hirokazu Hori (University of Yamanashi) for many fruitful discussions. The authors thank Dr. Jinkyong Yoo and Sung Jin An (Los Alamos National Laboratory), and Dr. Won Il Park (Hanyang University) for sample preparation of ZnO nanorod and valuable discussions.

References

1. For example, see the International Technology Roadmap for Semiconductors. <http://public.itrs.net/>
2. M. Ohtsu, K. Kobayashi, T. Kawazoe, S. Sangu, T. Yatsui, IEEE J. Sel. Top. Quantum Electron **8**, 839 (2002)
3. T. Kawazoe, K. Kobayashi, S. Sangu, M. Ohtsu: Appl. Phys. Lett. **82**, 2957 (2003)
4. M.H. Huang, S. Mao, H. Feick, H. Yan, Y. Wu, H. Kind, E. Weber, R. Russo, P. Yang, Science **292**, 1897 (2001)
5. A. Ohtomo, K. Tamura, M. Kawasaki, T. Makino, Y. Segawa, Z.K. Tang, G.K.L. Wong, Y. Matsumoto, H. Koinuma, Appl. Phys. Lett. **77**, 2204 (2000)
6. H.D. Sun, T. Makino, Y. Segawa, M. Kawasaki, A. Ohtomo, K. Tamura, H. Koinuma, J. Appl. Phys. **91**, 1993 (2002)
7. T. Ishikawa, S. Kohmoto, K. Asakawa, Appl. Phys. Lett. **73**, 1712 (1998)
8. S. Kohmoto, H. Nakamura, T. Ishikawa, K. Asakawa, Appl. Phys. Lett. **75**, 3488 (1999)
9. M. Ara, H. Graaf, H. Tada, Appl. Phys. Lett. **80**, 2565 (2002)
10. V.V. Polonski, Y. Yamamoto, M. Kourogi, H. Fukuda, M. Ohtsu, J. Microsc. **194**, 545 (1999)
11. Y. Yamamoto, M. Kourogi, M. Ohtsu, V. Polonski, G.H. Lee, Appl. Phys. Lett. **76**, 2173 (2000)
12. T. Yatsui, T. Kawazoe, M. Ueda, Y. Yamamoto, M. Kourogi, M. Ohtsu, Appl. Phys. Lett. **81**, 3651 (2002)
13. T. Yatsui, S. Takubo, J. Lim, W. Nomura, M. Kourogi, M. Ohtsu, Appl. Phys. Lett. **83**, 1716 (2003)
14. J. Lim, T. Yatsui, M. Ohtsu, IEICE Trans. Electron (to be published)
15. Y. Yamamoto, M. Kourogi, M. Ohtsu, G.H. Lee, T. Kawazoe, IEICE Trans. Electron **E85-C**, 2081 (2002)
16. M. Ohtsu (ed.), *Near-Field Nano/Atom Optics and Technology* (Springer, Tokyo, 1999)
17. R.R. Krchnavek, H.H. Gilgen, J.C. Chen, P.S. Shaw, T.J. Licata, R.M. Osgood Jr., J. Vac. Sci. Technol. B **5**, 20 (1987)
18. R.L. Jackson, J. Chem. Phys. **96**, 5938 (1992)
19. C.J. Chen, R.M. Osgood, Jr., Chem. Phys. Lett. **98**, 363 (1983)
20. S. Cho, J. Ma, Y. Kim, Y. Sun, G. Wong, J.B. Ketterson, Appl. Phys. Lett. **75**, 2761 (1999)
21. T. Aoki, Y. Hatanaka, D.C. Look, Appl. Phys. Lett. **76**, 3275 (2000)
22. G.T. Boyd, Th. Rasing, J.R.R. Leite, Y.R. Shen, Phys. Rev. B **30**, 519 (1984)
23. A. Wokaum, J.P. Gordon, P.F. Liao, Phys. Rev. Lett. **48**, 957 (1982)
24. K.F. MacDonald, V.A. Fedotov, S. Pochon, K.J. Ross, G.C. Stevens, N.I. Zheludev, W.S. Brocklesby, V.I. Emel'yanov, Appl. Phys. Lett. **80**, 1643 (2002)
25. J. Bosbach, D. Martin, F. Stietz, T. Wenzel, F. Trager, Appl. Phys. Lett. **74**, 2605 (1999)
26. H. Kuwata, H. Tamaru, K. Miyano, Appl. Phys. Lett. **83**, 4625 (2003)
27. R.G. Yarovaia, I.N. Shklyarevsklii, A.F.A. El-Shazly, Sov. Phys.-JETP **38**, 331 (1974)

28. R.L. Jackson, Chem. Phys. Lett. **163**, 315 (1989)
29. A. Sato, Y. Tanaka, M. Tsunekawa, M. Kobayashi, H. Sato, J. Phys. Chem. **97**, 8458 (1993)
30. P.J. Young, R.K. Gosavi, J. Connor, O.P. Strausz, H.E. Gunning, J. Chem. Phys. **58**, 5280 (1973)
31. T. Yatsui, W. Nomura, and M. Ohtsu, Nano Lett. **5**, 2548 (2005)
32. M. Ohtsu, K. Kobayashi (eds.) *Optical Near Fields* (Springer, Berlin, 2003)
33. R.G. Yarovaya, I.N. Shklyarevskii, A.F.A. El-Shazly, Sov. Phys. JETP **38**, 331 (1974)
34. M. Brust, C.J. Kiely, Colloids Surf. A **202**, 175 (2002)
35. A.P. Alivisatos, Science **271**, 933 (1996)
36. P. Yang, Nature **425**, 243 (2003)
37. M.D. Austin, H. Ge, W. Wu, M. Li, Z. Yu, D. Wasserman, S.A. Lyon, S.Y. Chou, Appl. Phys. Lett. **84**, 5299 (2004)
38. G.M. Whitesides, B. Grzybowski, Science **295**, 2418 (2002)
39. Y. Yin, Y. Lu, Y. Xia, J. Mater. Chem. **11**, 987 (2001)
40. Y. Cui, M.T. Björk, J.A. Liddle, C. Sönnichsen, B. Boussert, A.P. Alivisatos, Nano Lett. **4**, 1093 (2004)
41. S.A. Maier, P.G. Kik, H.A. Atwater, S. Meltzer, E. Harel, B.E. Koel, A.G. Requicha, Nat. Mater. **2**, 229 (2003)
42. G. Frens, Nat. Phys. Sci. **241**, 20 (1973)
43. N.D. Denkov, O.D. Velev, P.A. Kralchevsky, I.B. Ivanov, H. Yoshimura, L. Nagayama, Nature **361**, 26 (1993)
44. T. Yatsui, M. Kurogi, M. Ohtsu, Appl. Phys. Lett. **79**, 4583 (2001)
45. D.C. Reynolds, D.C. Look, B. Jogai, C.W. Litton, G. Cantwell, W.C. Harsch, Phys. Rev. B **60**, 2340 (1999)
46. Y. Wu, R. Fan, P. Yang, Nano Lett. **2**, 83 (2002)
47. M.T. Björk, B.J. Ohlsson, C. Thelander, A.I. Persson, K. Deppert, L.R. Wallenberg, L. Samuelson, Appl. Phys. Lett. **81**, 4458 (2003)
48. M.S. Gudiksen, L.J. Lauhon, J. Wang, D.C. Smith, C.M. Lieber, Nature **415**, 617 (2002)
49. W.I. Park, G.-C. Yi, M.Y. Kim, S.J. Pennycook, Adv. Mater. **15**, 526 (2002)
50. W.I. Park, S.J. An, J. Long, G.-C. Yi, S. Hong, T. Joo, M.Y. Kim, J. Phys. Chem. B **108**, 15457 (2004)
51. A. Tsukazaki, A. Ohtomo, T. Onuma, M. Ohtani, T. Makino, M. Sumiya, K. Ohtani, S.F. Chichibu, S. Fuke, Y. Segawa, H. Ohno, H. Koinuma, M. Kawasaki, Nat. Mater. **4**, 42 (2005)
52. K. Matsuda, T. Saiki, S. Nomura, M. Mihara, Y. Aoyagi, Appl. Phys. Lett. **81**, 2291 (2002)
53. K. Matsuda, T. aiki, S. Nomura, M. Mihara, Y. Aoyagi, S. Nair, T. Takagahara, Phys. Rev. Lett. **91**, 177401 (2003)
54. J.R. Guest, T.H. Stievater, G. Chen, E.A. Tabak, B.G. Orr, D.G. Steel, D. Gammon, D.S. Katzer, Science **293**, 2224 (2001)
55. T. Guenther, C. Lienau, T. Elsaesser, M. Clanemann, V.M. Axt, T. Kuhn, S. Eshlaghi, D. Wiek, Phys. Rev. Lett. **89**, 057401 (2002)
56. A. Ohtomo, M. Kawasaki, I. Ohkubo, H. Koinuma, T. Yasuda, Y. Segawa, Appl. Phys. Lett. **75**, 980 (1999)
57. T. Makino, A. Ohtomo, C.H. Chia, Y. Segawa, H. Koinuma, K. Kawasaki, Phys. E **21**, 671 (2004)
58. M. Zerovos, L.-F. Feiner, J. Appl. Phys. **95**, 281 (2004)
59. M. Zamfirescu, A. Kavokin, B. Gil, G. Mapluech, M. Kaliteevski, Phys. Rev. B **65**, 161205 (2001)
60. S.F. Chichibu, T. Sota, G. Cantwell, D.B. Eason, C.W. Litton, J. Appl. Phys. **93**, 756 (2003)
61. D.C. Reynolds, C.W. Litton, D.C. Look, J.E. Hoelscher, C. Claffin, T.C. Collins, J. Nause, B. Nemeth, J. Appl. Phys. **95**, 4802 (2004)
62. M. Tchoukueu, O. Briot, B. Gil, J.P. Alexis, R.L. Aulombard, J. Appl. Phys. **80**, 5352 (1996)
63. T. Wamura, Y. Masumoto, T. Kawamura, Appl. Phys. Lett. **59**, 1758 (1991)
64. U.C. Fischer, J. Koglin, H. Fuchs, J. Microsc. **176**, 281 (1994)

65. E.D. Palik (ed.) *Handbook of Optical Constants of Solids* (Academic, New York, 1985)
66. L. Novotny, C. Hafner, Phys. Rev. E **50**, 4094 (1994)
67. J. Takahara, S. Yamagishi, H. Taki, A. Morimoto, T. Kobayashi, Opt. Lett. **22**, 475 (1997)
68. D. Marcuse (ed.) *Light Transmission Optics* (Van Nostrand Reinhold, New York 1972), Chap. IV
69. J.C. Weeber, J.R. Krenn, A. Dereux, B. Lamprecht, Y. Lacroute, J.P. Goudonnet, Phys. Rev. B **64**, 045411 (2001)
70. A. Eguiluz, A.A. Maradudin, Phys. Rev. B **14**, 5526 (1976)
71. K. Tachibana, T. Someya, S. Ishida, Y. Arakawa, Appl. Phys. Lett. **76**, 3212 (2000)
72. T. Yatsui, M. Kourogi, M. Ohtsu, Appl. Phys. Lett. **71**, 1756 (1997)
73. B. Puers, W. Sansen, Sens. Actuators **A21–A23**, 1036 (1990)
74. T. Yatsui, M. Kourogi, M. Ohtsu, Appl. Phys. Lett. **73**, 2090 (1998)
75. M.L. Brongersma, J.W. Hartmann, H.A. Atwater, Phys. Rev. B **62**, R16356 (2000)
76. W. Nomura, M. Ohtsu, T. Yatsui, Appl. Phys. Lett. **86**, 181108 (2005)
77. W. Nomura, M. Ohtsu, T. Yatsui, Appl. Phys. B **84**, 257 (2006)
78. I.I. Smolyaninov, D.L. Mazzoni, J. Mait, C.C. Davis, Phys. Rev. B **56**, 1601 (1997)
79. M. Quinten, A. Leitner, J.R. Krenn, F.R. Aussenegg, Opt. Lett. **23**, 1331 (1998)
80. The computer simulations in this paper are performed by a FDTD-based program, Poynting for Optics, a product of Fujitsu, Japan
81. T.R. Anthony, J. Appl. Phys. **58**, 1240 (1998)
82. T. Yatsui, K. Itsumi, M. Kourogi, M. Ohtsu, Appl. Phys. Lett. **80**, 2257 (2002)
83. A. Zenner, E. Beham, S. Stuffer, F. Findeis, M. Bichler, G. Abstreiter, Nature **418**, 612 (2002)
84. Z. Yuan, B.E. Kardynal, R.M. Stevenson, A.J. Shields, C.J. Lobo, K. Cooper, N.S. Beattie, D.A. Ritchie, M. Pepper, Science **295**, 102 (2002)
85. D. Leonard, M. Krishnamurthy, C.M. Reaves, S.P. Denbaars, P.M. Petroff, Appl. Phys. Lett. **63**, 3203 (1993)
86. S. Yamazaki, T. Yatsui, M. Ohtsu, T.W. Kim, H. Fujioka, Appl. Phys. Lett. **85**, 3059 (2004)
87. P.J. Young, R.K. Gosavi, J. Connor, O.P. Strausz, H.E. Gunning, J. Chem. Phys. **58**, 5280 (1973)
88. S. Cho, J. Ma, Y. Kim, Y. Sun, G. Wong, J.B. Ketterson, Appl. Phys. Lett. **75**, 2761 (1999)
89. T. Kawazoe, K. Kobayashi, S. Sangu, M. Ohtsu, Appl. Phys. Lett. **82**, 2957 (2003)

Properties of Optical Near-Field Excitation Transfers in Randomly Distributed Spherical Quantum Dots

16

Wataru Nomura, Takashi Yatsui, and Motoichi Ohtsu

Contents

16.1	Introduction.....	644
16.2	Optical Near-Field Energy Transfer Between Spherical Quantum Dots.....	644
16.2.1	Exciton Energy Levels in Spherical Quantum Dots.....	645
16.2.2	Resonant Energy Transfer Between CdSe QDs.....	646
16.2.3	Control of the Energy Transfer Between ZnO QDs.....	651
16.3	Structural Dependency of Energy Transfer Efficiency in Randomly Distributed Quantum Dots.....	654
16.3.1	Optical Excitation Transfer in Randomly Distributed Quantum Dots via Optical Near-Field Interactions.....	655
16.3.2	Theoretical Analyses.....	656
16.3.3	Experiment.....	660
16.4	Destination Selectivity of Optical Near-Field Signal Transfer System.....	662
16.4.1	Optical Near-Field Signal Transfer System.....	663
16.4.2	Experiments and Discussion.....	664
16.5	Conclusion.....	668
	References.....	669

Abstract

In this chapter, optical near-field interactions and energy transfer between spherical quantum dots are reviewed. The energy transfer was confirmed by time-resolved spectroscopy in both CdSe and ZnO quantum dots. Furthermore, structural dependency of quantum dots was theoretically and experimentally analyzed with respect to the basic properties of optical signal transfer using

W. Nomura (✉) · T. Yatsui · M. Ohtsu

School of Engineering, The University of Tokyo, Tokyo, Japan

Nanophotonics Research Center, The University of Tokyo, Tokyo, Japan

e-mail: nomura@nanophotonics.t.u-tokyo.ac.jp; yatsui@ee.t.u-tokyo.ac.jp; ohtsu@ee.t.u-tokyo.ac.jp

optical near-field interactions. The destination selectivity in the optical near-field signal transfer system was also evaluated.

16.1 Introduction

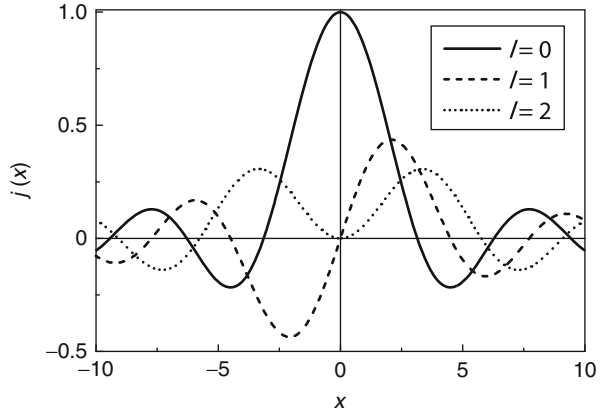
In this chapter, optical near-field interactions and energy transfer between spherical quantum dots (QDs) are reviewed. The optical near-field interaction is a short-range interaction mediated by optical electromagnetic fields that enable excitation energy transfer [1–3], which is advantageous in applications for biomolecular imaging, sensing, photonic devices, and nanofabrication. Many approaches have been used to explain the excitation energy transfer via the near-field interaction between nanoscale particles, including QDs, molecules, and metallic nanoparticles. Fluorescence resonance energy transfer based on the Förster mechanism is one of the popular treatments [4]. In this approach, the particle is approximated as an ideal single-point dipole or multipole; however, this is insufficient for examining the energy transfer between nano-sized particles because the distance between them is too short. Coherent excitation energy transfer in metallic nanoparticle chains has been analyzed using a polarization density distribution instead of a single electric dipole model. As long as the particles are large and the carriers are not quantized, the polarization density distribution is easily obtained. In the case of QDs, however, the polarization density distribution must be defined from the wave functions of photoexcited carriers because this distribution corresponds to the transition dipole distribution in two-level QDs. Therefore, we define the effective dipoles of the optical source and optical absorber for QDs (i.e., a donor and an acceptor). An additional problem is that the interaction between QDs in the host matrix is complicated because the polarization is induced simultaneously in the host matrix by a donor QD, making it difficult to obtain the polarization distribution in the host matrix. In our approach, we describe the optical near-field interaction between QDs as exciton-polariton tunneling to overcome these difficulties [5–8].

This chapter is organized as follows. The basic elements and experimental evaluation of optical near-field energy transfer in both CdSe/ZnS core-shell QDs and ZnO QDs are discussed in Sect. 16.2. In Sect. 16.3, the structural dependency of energy transfer efficiency is introduced with a numerical calculation and an experiment. The destination selectivity of energy transfer is also confirmed in Sect. 16.4.

16.2 Optical Near-Field Energy Transfer Between Spherical Quantum Dots

Systems of optically coupled quantum-size structures should be applicable to quantum information processing [9, 10]. Additional functional devices (i.e., nanophotonic devices [1, 11–13]) can be realized by controlling the excitonic excitation

Fig. 16.1 l th order of spherical Bessel function. (Solid curve) $l = 0$ ($j_0(x) = \frac{\sin x}{x}$), (dashed curve) $l = 1$ ($j_1(x) = \frac{1}{x}(\frac{\sin x}{x} - \cos x)$), and (dotted curve) $l = 2$ ($j_2(x) = \frac{1}{x}(\frac{3-x^2}{x^2})\sin x - \frac{3}{x}\cos x$)



in QDs and quantum wells. This section reviews the recent achievements with nanophotonic devices based on spherical QDs.

16.2.1 Exciton Energy Levels in Spherical Quantum Dots

The translational motion of the exciton center of mass is quantized in nanoscale semiconductors when the size is as small as an exciton Bohr radius. If the QDs are assumed to be spheres having radius R , with the following potential

$$V(x) = \begin{cases} 0 & \text{for } |x| \leq R \\ \infty & \text{for } |x| > R, \end{cases} \quad (16.1)$$

then the quantized energy levels are given by a spherical Bessel function as

$$R_{nl}(r) = A_{nl} j_l \left(\rho_{n,l} \frac{r}{R} \right). \quad (16.2)$$

Figure 16.1 shows the l th order of the spherical Bessel function. Note that an odd quantum number of l has an odd function, and it is a dipole-forbidden energy state. To satisfy the boundary conditions as

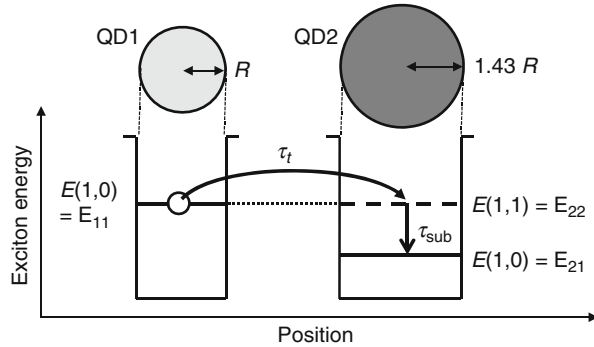
$$R_{nl}(R) = A_{nl} j_l(\rho_{n,l}), \quad (16.3)$$

the quantized energy levels are calculated using

$$E(n, l) = E_B + \frac{\hbar^2 \pi^2}{2mR^2} \xi_{n,l}^2, \quad (16.4)$$

Table 16.1 Calculated $\xi_{n,l}$ to satisfy the condition of $j_1(\pi\xi_{n,l})$

	$l = 0$	$l = 1$	$l = 2$	$l = 3$	$l = 4$	$l = 5$
$n = 1$	3.14	4.49	5.76	6.99	8.18	·
$n = 2$	6.26	7.73	9.10	10.42	·	·
$n = 3$	9.42	·	·	·	·	·
$n = 4$	·	·	·	·	·	·

Fig. 16.2 Schematic drawings of different-sized spherical QDs (QD1 and QD2) and the confined-exciton energy levels

where $\pi\xi_{n,l} = \rho_{n,l}$ is the n th root of the spherical Bessel function of the l th order. The principal quantum number, n , and the angular momentum quantum number, l , take values $n = 1, 2, 3 \dots$ and $l = 0, 1, 2 \dots$, while $\xi_{n,l}$ takes values $\xi_{1,0} = 1$, $\xi_{1,1} = 1.43$, and $\xi_{1,2} = 1.83$; $\xi_{2,0} = 2$; and so on (see Table 16.1) [14].

Figure 16.2 shows schematic drawings of different-sized spherical QDs (QD1 and QD2) and the confined exciton energy levels. Here, R and $1.43R$ are the radii of spherical QDs, QD1 and QD2, respectively. According to Eq. (16.3), the quantized exciton energy levels of $E(1,0)$ in QD1 (E_{11}) and $E(1,1)$ in QD2 (E_{22}) are in resonance.

Although the energy state $E(1,1)$ is a dipole-forbidden state, the optical near-field interaction is finite for such coupling to the forbidden energy state [15]. In addition, the inter-sublevel transition time τ_{sub} , from higher exciton energy levels to the lowest one, is generally less than a few picoseconds and is much shorter than the transition time due to optical near-field coupling (τ_t) [16]. Therefore, most of the energy of the exciton in a QD1 with radius R transfers to the lowest exciton energy level in the neighboring QD2 with a radius of $1.43R$ and recombines radiatively at the lowest level. In this manner, unidirectional energy flow is achieved.

16.2.2 Resonant Energy Transfer Between CdSe QDs

To evaluate the energy transfer and the energy dissipation, we used CdSe/ZnS core-shell QDs from *Evident Technologies*. As described in the adjacent subsection, assuming that the respective diameters of the QD1 and QD2 were $d_1 = 2.8$ and $d_2 = 4.1$ nm, the ground energy level in the QD1 and the excited energy level in

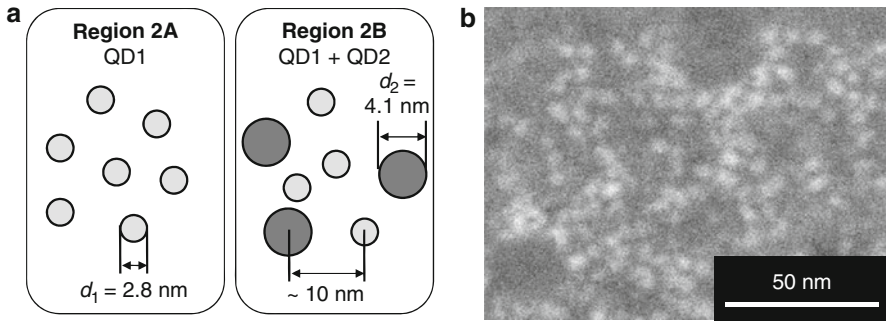


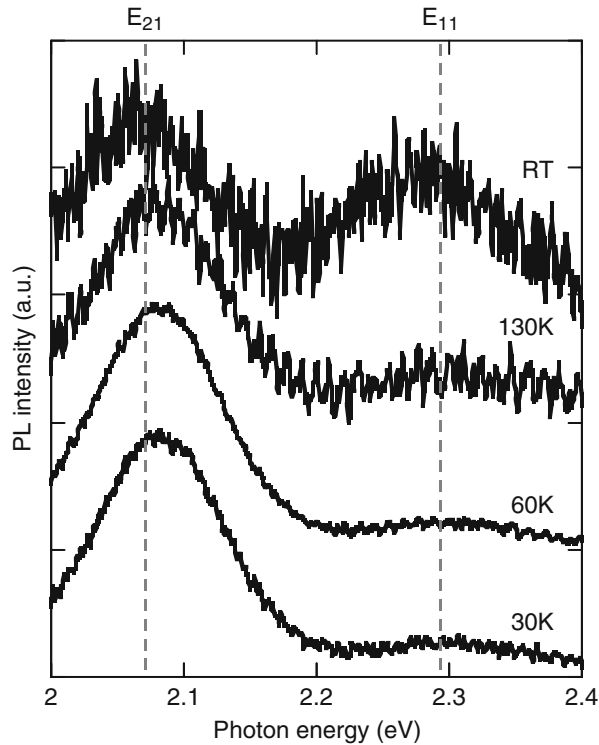
Fig. 16.3 (a) Schematic images of CdSe QDs dispersed substrate. Regions 2A and 2B are covered by QD1s and both QD1s and QD2s, respectively. (b) TEM image of dispersed CdSe/ZnS core-shell QDs in region 2B

the QD2 resonate [17]. A solution of QD1s and QD2s in 1-feniloctane at a density of 1.0 mg/mL was dropped onto a mica substrate (see Fig. 16.3a), such that regions 2A consisted of QD1s, while there were both QD1s and QD2s in region 2B. Using transmission electron microscopy (TEM), we confirmed that the average center-to-center distance of each QD was maintained at less than about 10 nm in all regions due to the 2-nm-thick ZnS shell and surrounding ligands (2-nm-length long-chain amine) of the QDs (Fig. 16.3b).

In the following experiments, the light source used was the third harmonic of a mode-locked Ti:sapphire laser (photon energy $h\nu = 4.05$ eV, frequency 80 MHz, and pulse duration 2 ps). The incident power of the laser was 0.6 mW, and the spot size was 1×10^{-3} cm². The density of QDs was less than 3.5×10^{12} cm⁻², and the quantum yield of CdSe/ZnS QD was 0.5. Under these conditions, the probability of exciton generation by one laser pulse in each QD was calculated to be 1.6×10^{-2} . Therefore, we assumed that single-exciton dynamics apply in the following experiments.

The energy transfer was confirmed using micro-photoluminescence (PL) spectroscopy. Temperature-dependent micro-PL spectra were obtained. In the spectral profile of the PL emitted from region 2A, we found a single peak that originated from E_{11} at a photon energy of 2.29 eV, between room temperature and 30 K. In contrast, region 2B had two peaks at room temperature, as shown in Fig. 16.4. This figure also shows that the PL intensity peak at $h\nu = 2.29$ eV decreased relative to that at $h\nu = 2.07$ eV on decreasing the temperature. This relative decrease in the PL intensity was due to the energy transfer from E_{11} to E_{22} and the subsequent rapid dissipation to E_{21} . This is because the coupling between the resonant energy levels becomes stronger due to the increase in the exciton decay time on decreasing the temperature [18]. Furthermore, although nanophotonic device operation using CuCl quantum cubes [11–13] and ZnO quantum wells [19] has been reported at 15 K, we observed a decrease in the PL intensity at $h\nu = 2.29$ eV at temperatures as high as

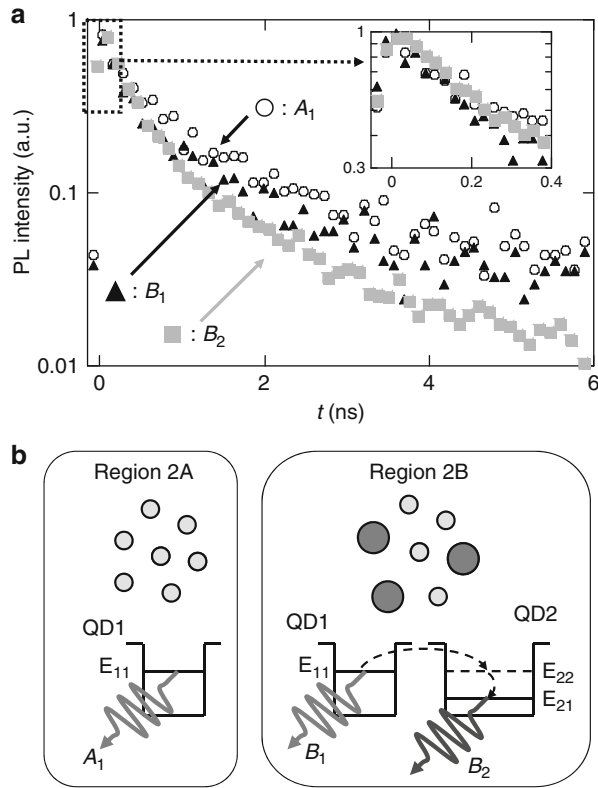
Fig. 16.4 Temperature dependence of the micro-PL spectra from region 2B. The dashed line shows the energy level of E_{11} and E_{21}



130 K, which is advantageous for the higher-temperature operation of nanophotonic devices.

To confirm this energy transfer from QD1 to QD2 at temperatures under 130 K, we evaluated the dynamic property of the energy transfer using time-resolved spectroscopy and applying a time-correlated single-photon counting method. Circles A_1 , triangles B_1 , and squares B_2 in Fig. 16.5a represent the respective time-resolved micro-PL intensities (at 60 K) from E_{11} in region 2A, E_{11} in region 2B, and E_{21} in region 2B. The peak intensities at $t = 0$ were normalized to unity. Note that B_1 decreased faster than A_1 , although these signals were generated from QDs of the same size. In addition, although the exciton lifetime decreases on increasing the QD size, owing to the increased oscillator strength, B_2 decreased more slowly than A_1 over the range $t < 0.2$ ns (see the inset of Fig. 16.5a). Furthermore, as we did not see any peak in the power spectra of A_1 , B_1 , and B_2 , we believe that the temporal signal changes originated from the optical near-field energy transfer and subsequent dissipation. Since the QD1s in region 2B were near QD2s whose excited energy level resonates with E_{11} (see Fig. 16.5b), near-field coupling between the resonant levels resulted in the energy transfer from the QD1 to the QD2 and the consequent faster decrease in the excitons of the QD1 in region 2B compared to region 2A.

Fig. 16.5 (a) Time-resolved PL intensity profiles from QD1s in region 2A (open circles $2A_1$), QD1s in region 2B (closed triangles $2B_1$), and QD2s in region 2B (gray squares $2B_2$). The peak intensities were normalized at $t = 0$. (b) Schematic of the respective system configurations in regions 2A and 2B

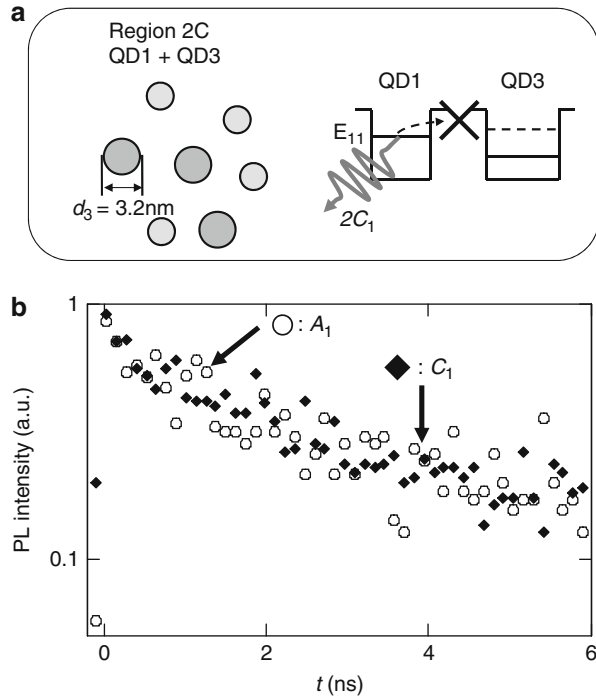


Furthermore, as a result of inflow of the carriers from the QD1 to the QD2, the PL intensity from the QD2 near the QD1 decayed more slowly than that of the QD1.

For comparison, we also obtained time-resolved PL profiles for different pairs of CdSe/ZnS QDs. Their diameters were $d_1 = 2.8$ nm (QD1) and $d_3 = 3.2$ nm (QD3), which means that their energy levels were not resonant with each other. Figure 16.6a shows a schematic of a sample named region 2C, where QD1s and QD3s are mixed with a mean center-to-center distance of less than 10 nm. Circles A_1 and cross marks C_1 in Fig. 16.6b show the time-resolved PL intensity (at 30 K) due to the ground energy level in QD1s from regions 2A and 2C, respectively. No difference was seen in the decay profiles, which indicates that the excited carriers in QD1s did not couple with QD3s due to being off-resonance, and consequently, no energy was transferred (Fig. 16.6c). This supports the idea that Figs. 16.4 and 16.5 demonstrate energy transfer and subsequent dissipation due to near-field coupling between the resonant energy levels of the QD1s and QD2s.

To evaluate the exciton energy transfer from QD1 to QD2 quantitatively, we investigated the exciton dynamics by fitting multiple exponential decay curve functions to curves A_1 , B_1 , and B_2 [20, 21]:

Fig. 16.6 (a) Schematic image of dispersed CdSe QDs and the system configuration in region 2C. (b) Time-resolved PL intensity profiles from QD1s in region 2A (*open circles* A_1) and QD1s in region 2C (*closed diamonds* C_1). The peak intensities were normalized at $t = 0$



$$A_1 = R_{11} \exp \frac{-t}{\tau_{11}} + R_{12} \exp \frac{-t}{\tau_{12}}, \quad (16.5)$$

$$B_1 = R_1 \cdot A_1 + R_t \exp \frac{-t}{\tau_t}, \quad (16.6)$$

and

$$B_2 = R_{21} \exp \frac{-t}{\tau_{21}} + R_{22} \exp \frac{-t}{\tau_{22}}. \quad (16.7)$$

We used a double-exponential decay for A_1 and B_2 (Eqs. (16.5) and (16.7)), which corresponds to the non-radiative lifetime (fast decay: τ_{11} and τ_{21}) and radiative lifetime of free-carrier recombinations (slow decay: τ_{12} and τ_{22}). Given the imperfect homogeneous distribution of the QD1s in region 2B, some QD1s lacked energy transfer routes to QD2s. However, we introduced the mean energy transfer time, τ_t , from QD1s and QD2s in Eq. (16.5). In these equations, we neglected the energy dissipation time τ_{sub} of about 1 ps [22] because that is much smaller than exciton lifetimes and energy transfer times. Figure 16.7 shows the best-fit numerical results and experimental data. Here, we used exciton lifetimes of $\tau_{12} = 2.10$ ns and $\tau_{22} = 1.79$ ns. The average energy transfer time was $\tau_t = 135$ ps, which is comparable to the observed energy transfer time (130 ps) in CuCl quantum cubes

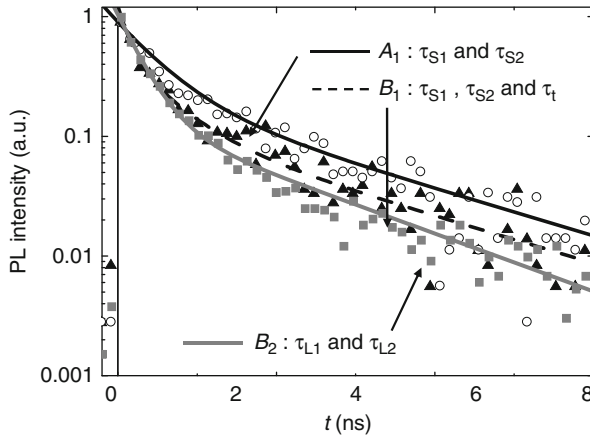


Fig. 16.7 Experimental results (open circles, closed triangles, and gray squares) and fitted curves (black solid, black broken, and gray solid curves) using Eqs. (16.5)–(16.7) for the PL intensity profiles. The fitting parameters were $R_{11} = 0.560$, $\tau_{11} = 2.95 \times 10^{-10}$, $R_{12} = 0.329$, $\tau_{12} = 2.10 \times 10^{-9}$, $R_1 = 0.740$, $R_t = 0.330$, $\tau_t = 1.35 \times 10^{-10}$, $R_{21} = 0.785$, $\tau_{21} = 2.94 \times 10^{-10}$, $R_{22} = 0.201$, and $\tau_{22} = 1.79 \times 10^{-9}$

[11] and ZnO QW structures [19]. Furthermore, the relation $\tau_t < \tau_{12}$ agrees with the assumption that most of the excited excitons in QD1s transfer to E_{22} in a QD2s before being emitted from the QD1.

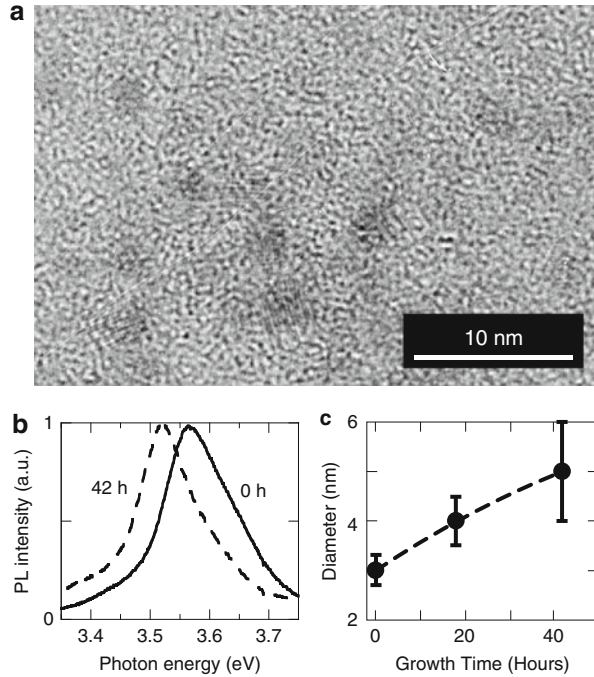
16.2.3 Control of the Energy Transfer Between ZnO QDs

ZnO is a promising material for room temperature operation of nanophotonic devices because of its large exciton-binding energy [23–25]. Here, we used chemically synthesized ZnO QDs to realize a highly integrated nanophotonic device. We observed the energy transfer from smaller ZnO QDs to larger QDs with mutually resonant energy levels. The energy transfer time and energy transfer ratio between the two QDs were also calculated from the experimental results [26].

ZnO QDs were prepared using the sol-gel method [27, 28] as follows:

- A sample of 1.10 g (5 mmol) of $\text{Zn}(\text{Ac})_2 \cdot 2\text{H}_2\text{O}$ was dissolved in 50 mL of boiling ethanol at atmospheric pressure, and the solution was then immediately cooled to 0°C . A sample of 0.29 g (7 mmol) of $\text{LiOH} \cdot \text{H}_2\text{O}$ was dissolved in 50 mL of ethanol at room temperature in an ultrasonic bath and cooled to 0°C . The hydroxide-containing solution was then added dropwise to the $\text{Zn}(\text{Ac})_2$ suspension with vigorous stirring at 0°C . The reaction mixture became transparent after approximately 0.1 g of LiOH had been added. The ZnO sol was stored at 0°C to prevent particle growth.
- A mixed solution of hexane and heptane, with a volume ratio of 3:2, was used to remove the reaction products (LiAc and H_2O) from the ZnO sol.

Fig. 16.8 (a) TEM image of the ZnO QD. (b) The PL spectra observed at 5 K. The solid and dashed curves indicate growth time $T_g = 0$ and 42 h, respectively. (c) The growth time dependence of the mean ZnO QD diameter



- To initiate particle growth, the ZnO solution was warmed to room temperature. The mean diameter of the ZnO QDs was determined from the growth time, T_g .

Figure 16.8a shows a TEM image of synthesized ZnO dots after the second step. The dark areas correspond to the ZnO QDs. This image suggests that monodispersed single crystalline particles were obtained.

To check the optical properties and diameters of our ZnO QD, we measured the PL spectra using He-Cd laser ($h\nu = 3.81$ eV) excitation at 5 K. We compared the PL spectra of ZnO QD with $T_g = 0$ and $T_g = 42$ h (solid and dashed curves in Fig. 16.8b, respectively). A redshifted PL spectrum was obtained, indicating an increase in the diameter of the QDs. Figure 16.8c shows the growth time dependence of the diameter of the QDs. This was determined from the effective mass model, with peak energy levels in the PL spectra, $E_g^{bulk} = 3.35$ eV, $m_e = 0.28$, $m_h = 1.8$, and $\epsilon = 3.7$ [29]. This result indicates that the growth rate at room temperature was 1.1 nm per day.

Assuming that the diameters of the QD1 and the QD2 were $d_1 = 3.0$ and $d_2 = 4.5$ nm, respectively, E_{11} in the QD1 and E_{22} in the QD2 resonated (Fig. 16.9a). An ethanol solution of QD1 and QD2 was dropped onto a sapphire substrate, and the mean surface-to-surface separation of the QD was found to be approximately 3 nm.

The black solid curve and dashed curve in Fig. 16.9b correspond to the PL spectra of QD1 and QD2, with spectral peaks of 3.60 and 3.44 eV, respectively. The gray

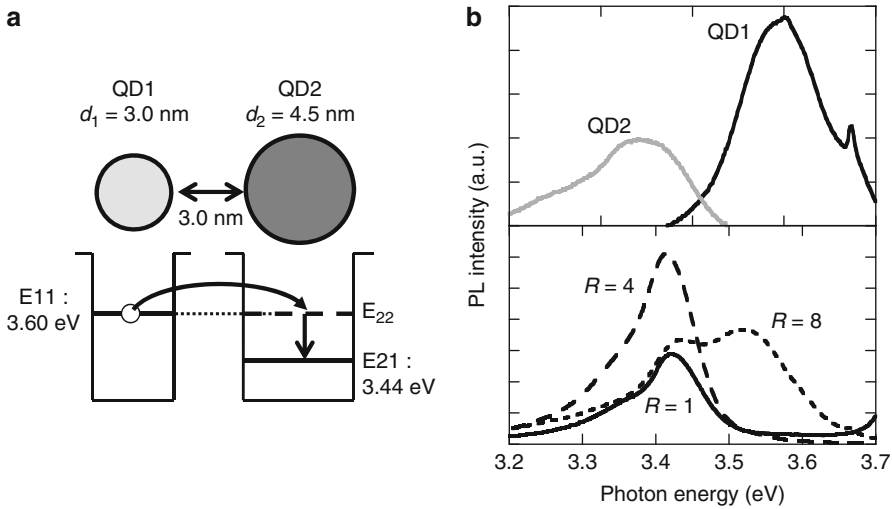


Fig. 16.9 (a) Schematic of the energy diagram between a QD1 and QD2. (b) The PL spectra of QD1 and QD2 observed at 5 K. In lower graph, solid curve, dashed curve, and dotted curve indicate mixes with R ratios of 1, 4, and 8, respectively

solid curve in Fig. 16.9b shows the spectrum from the QD1 and QD2 mixture with $R = 1$, where R is the ratio of (number of QD1s)/(number of QD2s). The spectral peak of 3.60 eV, which corresponded to the PL from the QD1, was absent from this curve. This peak was thought to have disappeared due to energy transfer from the QD1 to the QD2 because the first excited state of the QD2 resonated with the ground state of the QD1. Our hypothesis was supported by the observation that when R is increased by a factor of 8, the spectral peak from the QD1 reappeared (see the dotted curve in lower graph of Fig. 16.9b).

To confirm this energy transfer from the QD1 to the QD2 at 5 K, we evaluated dynamic effects with time-resolved spectroscopy using the time-correlated single-photon counting method. The light source used was the third harmonic of a mode-locked Ti:sapphire laser (photon energy 4.05 eV, frequency 80 MHz, and pulse duration 2 ps). We compared the signals from mixed samples with ratios $R = 2, 1$, and 0.5. The curves T_A ($R = 2$), T_B ($R = 1$), and T_C ($R = 0.5$) in Fig. 16.9 show the respective time-resolved PL intensities from the ground state of the QD1 (E_{11}) at 3.60 eV. We investigated the exciton dynamics quantitatively by fitting multiple exponential decay functions [20, 21]:

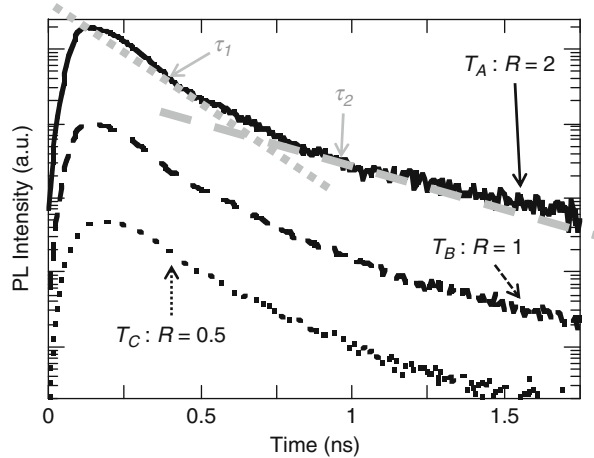
$$TRPL = A_1 \exp \frac{-t}{\tau_1} + A_2 \exp \frac{-t}{\tau_2}. \quad (16.8)$$

We obtained average τ_1 - and τ_2 -values of 144 and 443 ps, respectively (see Table 16.2). Given the disappearance of the spectral peak at 3.60 eV in the PL spectra, these values likely correspond to the energy transfer time from the QD1 to the QD2 and the radiative decay time from the QD1, respectively. This hypothesis

Table 16.2 Dependence of the time constants (τ_1 and τ_2) on R as derived from the two exponential fits of the time-resolved PL signals and the coefficient ratio A_1/A_2

$R = \text{QD1/QD2}$	τ_1 (ps)	τ_2 (ps)	A_1/A_2
2	133	490	12.4
1	140	430	13.7
0.5	160	410	14.4
Average	144	443	

Fig. 16.10 Time-resolved PL intensity observed at 5 K. The values of R were 2, 1, and 0.5 for curves T_A (solid curve), T_B (dashed curve), and T_C (dotted curve), respectively



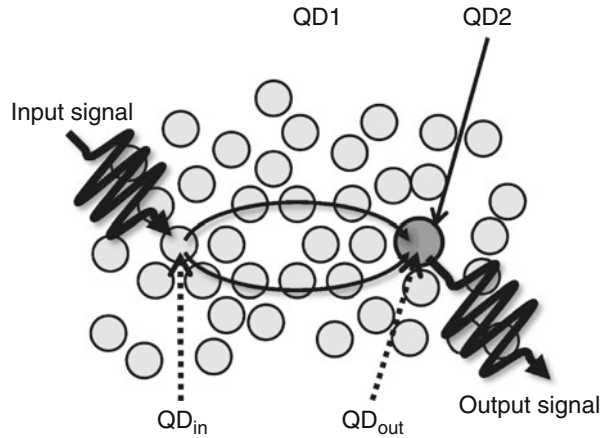
was supported by the observation that the average value of τ_1 (144 ps) was comparable to the observed energy transfer time in CuCl quantum cubes (130 ps) [11] (Fig. 16.10).

We also investigated the value of the coefficient ratio A_1/A_2 (see Table 16.2); this ratio was inversely proportional to R and, hence, proportional to the number of QD2s. This result indicated that an excess QD2 caused energy transfer from QD1 to QD2, instead of direct emission from the QD1.

16.3 Structural Dependency of Energy Transfer Efficiency in Randomly Distributed Quantum Dots

In this section, array dependency of QDs was theoretically and experimentally analyzed with respect to the basic properties of signal transfer using optical near-field interactions. More specifically, for signal transfer between QDs serving as signal input and output, the three-dimensional structure of the dot-array between the two ends was varied, and the resulting variation in the signal transfer performance was evaluated. The effects of dot-array control precision on the signal transfer performance were also evaluated by giving a certain randomness to the dot-array. In addition, signal transfer via stacked CdSe QDs was evaluated using a near-field optical probe that had a relatively large QD, to which optical excitation was transported, provided at its tip. Here, the dot-array dependency of the signal transfer

Fig. 16.11 Schematic representation of signal transfer system via optical near-field interactions



was experimentally evaluated by controlling the array structure of the QDs that acted as a transfer medium for signal. With these examinations, structural dependency of the signal transfer via optical near-field interactions was demonstrated, and basic insights were gained for achieving a nanostructure optimized for signal transfer.

16.3.1 Optical Excitation Transfer in Randomly Deistributed Quantum Dots via Optical Near-Field Interactions

If QD_{in} (QD1 at the signal input) and QD_{out} (QD2 at the signal output) are spatially arranged at a distance so that there is no optical near-field interaction between them, naturally, optical excitation transfer from QD_{in} to QD_{out} does not occur. However, by filling the space between QD_{in} and QD_{out} with the same-sized QD1s as QD_{in} , optical near-field interactions can occur between adjacent QDs, and an optical excitation occurring in QD_{in} can be consecutively transferred from one QD to the next. As described above, unidirectional optical excitation transfer occurs at the QD_{out} , due to the energy dissipation that occurs at QD_{out} . As a result, optical excitation transfers from QD_{in} to QD_{out} .

Therefore, even when QD_{in} and QD_{out} are arranged with a spatial separation, by appropriately arranging QD1s between the two, long-distance signal transfer becomes possible. In addition, the optical near-field interactions that are basis of the optical excitation transfer between QDs depend on the interdot distance; however, as shown in Fig. 16.11, as long as the interdot distance is maintained within a range allowing the optical near-field interactions to occur, the QDs need not be in an orderly array. Therefore, the proposed optical signal transfer system is expected to be highly resistant to positional displacement of the QDs. This characteristic will be described in more detail in the following subsection.

16.3.2 Theoretical Analyses

A three-dimensional distribution model of QDs, as shown in Fig. 16.11, was formulated in order to evaluate the structural dependency of the optical excitation transfer in the system formed of QD1 and QD2 described in the previous section. Here, the performance of the signal transfer between QD_{in} and QD_{out} was analyzed with respect to the effects of the distance between them, and the structure of the internal dot distribution.

The formulated model is based on a system composed of $(N - 1)$ smaller QDs QD1 and one larger QD QD2. Here, it is assumed that QD1 and QD2 are resonant with each other, and optical excitation transfer via optical near-field interactions can occur. QD1s are denoted as QD₁, QD₂, ..., and QD_{*N*-1}, and QD2 is denoted as QD_{*N*}, distinguishing individual QDs with subscripts 1 through *N*. The following rate equation is introduced, assuming optical near-field interactions between two arbitrary QDs QD_{*i*} and QD_{*j*}:

$$\frac{dn_i}{dt} = \sum_{j=1}^N \left(\frac{n_j}{\tau_{ji}} \right) - \sum_{i=1}^N \left(\frac{n_i}{\tau_{ij}} \right) - \frac{n_i}{\tau_i}. \quad (16.9)$$

Here, n_i is the probability of optical excitation occurring at the *i*th QD; τ_{ij} is the interaction time of the optical near-field interaction between QD_{*i*} and QD_{*j*}, satisfying the relation $\tau_{ij} = \tau_{ji}$; and τ_i is, for $i = 1$ to $N - 1$, the optical excitation relaxation lifetime of QD1 and, for $i = N$, the sublevel relaxation time from excitation level E_{22} of QD2 to the ground level E_{21} . Here, the interdot interaction time is defined as the reciprocal of the optical near-field interaction and is described by the following Yukawa function [1]:

$$\hbar U_{ij} = \frac{1}{\tau_{ij}} = A_{ij} \frac{\exp(-\mu r_{ij})}{r_{ij}}. \quad (16.10)$$

Here, \hbar is Planck's constant divided by 2π . U_{ij} is the optical near-field coupling strength between QD_{*i*} and QD_{*j*}; r_{ij} is the center-to-center distance between QD_{*i*} and QD_{*j*}; A_{ij} is a constant; and μ is the effective mass of the Yukawa function, which is given by

$$\mu = \frac{\sqrt{2E_p(E_m + E_p)}}{\hbar c}, \quad (16.11)$$

where E_p and E_m , when applying them to the experimental conditions described in following subsection, indicate the exciton energies of the CdSe QDs and the ZnS shell layer, respectively, and c is speed of light. Here, the output signal from the output QD, I_{out} , can be defined by

$$\frac{I_{\text{out}}}{dt} = \frac{n_N}{\tau_N}, \quad (16.12)$$

assuming that QD_N is the output QD QD_{out} and that the time integra of the optical excitation probability for QD_N at the ground state is I_{out} .

Parameters of the above theoretical model were set based on preliminary experimental results of CdSe/ZnS core-shell QDs used in the experiment described later. First, in our previous study (see Sect. 16.2), by evaluating time-resolved spectral properties of fluorescence lifetime from a mixed system with CdSe/ZnS core-shell QDs of $d_1 = 2.8$ and $d_2 = 4.1$ nm diameters, optical excitation transfer due to optical near-field interactions was indirectly confirmed in this system. Based on this insight, the optical excitation transfer time between QD1 and QD2 via optical near-field interactions at a center-to-center distance of 7.3 nm was set at 135 ps. In the CdSe/ZnS core-shell QDs of $d_1 = 2.8$ nm, E_p and E_m are 2.25 and 2.54 eV, respectively. Based on these, the coefficient A_{iN} ($= A_{Ni}$) in Eq. (16.11) was determined to be 65.3 s^{-1} . In addition, A_{ij} , which is a constant that defines the optical excitation transfer time between QD1s via optical near-field interactions, was defined as ($i, j \neq N$), based on the density of states ratio of excitons, estimated from the absorption coefficient of energy levels E_{22} and E_{21} . Also, the optical excitation lifetime of QD1 was experimentally determined as $\tau_i = 2.2 \text{ ns}$ ($i \neq N$), and the sublevel relaxation time τ_N for QD2 was set at 1 ps based on a previous study [22].

Furthermore, to evaluate the spatial array structure dependency of QDs between QD_{in} and QD_{out} , the three-dimensional structure shown in Fig. 16.12a was used. More specifically, QD1s were arrayed in the x , y , and z directions with the number of N_x , N_y , and N_z , respectively, and QD_{out} was placed adjacent to a QD1 that is a distance T away from QD_{in} in the x -direction. Distance dependency of the signal transfer was evaluated based on output signals from the output QD at varying positions. The effects of arrangement of the nanostructure composed of QD1s on the distance dependency was also evaluated.

Further details of the model are as follows: the center position of QD_{in} is set at the origin (0, 0, 0). QD1s are arrayed, 10 in $-x$ direction and 306 in $+x$ direction (i.e., $N_x = 317$). The center-to-center distance between adjacent dots is 7.3 nm. The number of QDs in y and z directions is given by N_y and N_z ; however, because they are arrayed in the most densely filled structure, QDs in adjacent rows are staggered by half of the interdot distance, as shown in Fig. 16.12a. Assuming the initial values at $t = 0$ for the probability of optical excitation for QD_{in} and output signal intensity to be $n_1 = 1$ and $I_{\text{out}} = 0$, respectively, the evolution of the optical excitation of individual QDs over time was numerically solved using Eqs. (16.9)–(16.12). The output signal of Eq. (16.12) was evaluated at $t = 12 \text{ ns}$, which is over 5 times the relaxation lifetime of optical excitation from QD1, namely, 2.2 ns.

Figure 16.12b shows the distance dependency of the output signal when the dot-array structures were $(N_y, N_z) = (1, 1)$, $(7, 1)$, $(7, 2)$, and $(15, 2)$. With respect to the varying x -positions T of QD2, the output signals showed nearly linear decays on a log scale, indicating that the output signals have decaying properties

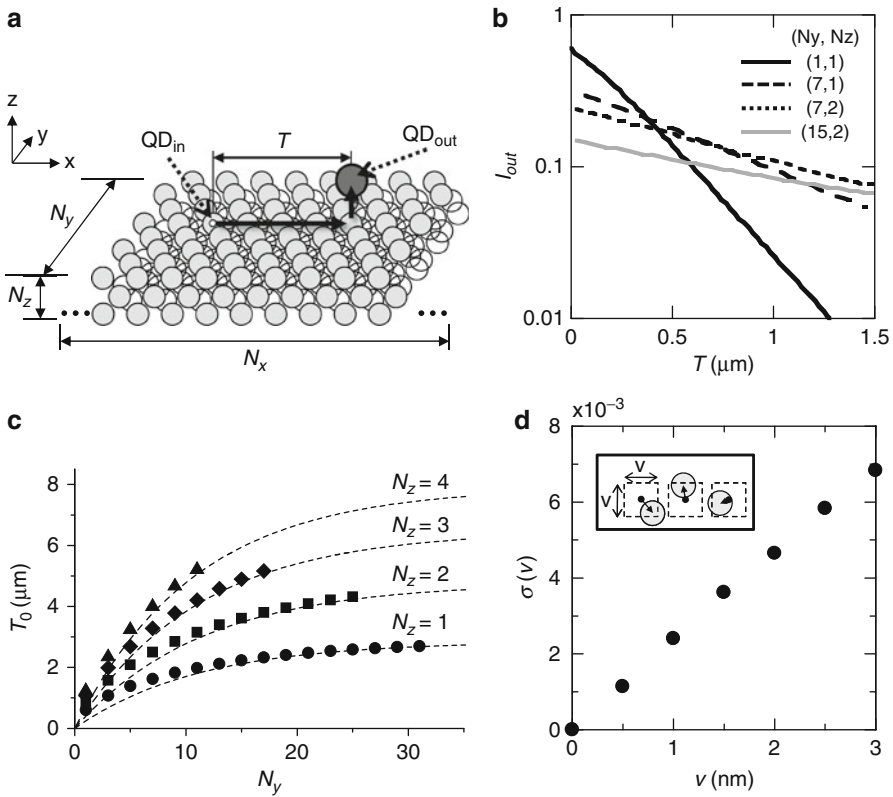


Fig. 16.12 (a) Schematic representation of the calculation model. (b) Calculation results of $I_{out}(N_y, N_z)$. Solid curve = $I_{out}(1, 1)$, dashed curve = $I_{out}(7, 1)$, dotted curve = $I_{out}(7, 2)$, and gray solid curve = $I_{out}(15, 2)$. (c) Calculation results of $T_0(N_y, N_z)$. Circles = $T_0(N_y, 1)$, squares = $T_0(N_y, 2)$, diamonds = $T_0(N_y, 3)$, triangles = $T_0(N_y, 4)$, and dashed lines are approximation curves, where $T_0(N_y, 1) = 2.85 - 2.85 \exp(-N_y/11.0)$, $T_0(N_y, 2) = 4.77 - 4.77 \exp(-N_y/11.5)$, $T_0(N_y, 3) = 6.48 - 6.48 \exp(-N_y/11.2)$, and $T_0(N_y, 4) = 7.91 - 7.91 \exp(-N_y/10.8)$. (d) Standard deviation $\sigma(v)$ of I_{out}^v/I_{out}^0 (change in output signal with respect to v , the displacement of QD1). Inset: schematic representation of QD1 position displacement model. Arrows indicate destinations of centers of QD1s. Side length of dashed squares is v , and the tips of the arrows always fall within these squares

of a monoexponential function with respect to the transfer distance. However, it is noteworthy that the decay trend greatly differs depending on the dot-array structures. That is, within a range of small transfer distance T , I_{out} is larger when the overall scale of the dot-array is smaller (i.e., when N_y and N_z are smaller); however, when the transfer distance T increases, the decay is moderate with larger N_y and N_z . Therefore, these results suggest that, strategically, it is better to keep the number of QDs small for a short-distance signal transfer and to increase it for a long-distance signal transfer.

Because I_{out} tends to show a decay described by a monoexponential function with respect to the transfer distance T , it has properties defined by

$$\frac{I_{\text{out}}}{dT} = \exp \frac{-2T}{T_0}. \quad (16.13)$$

Therefore, T_0 can be considered as the signal transfer distance, which is an index characterizing the signal transfer. Assuming this, how T_0 changes with respect to the dot-array dimensions N_y and N_z was analyzed. Figure 16.12c shows the N_y dependency of T_0 for $N_z = 1, 2, 3$, and 4, indicating monotonic increases of T_0 with increasing N_y and N_z , respectively. Furthermore, because T_0 shows a saturating trend with respect to N_y , the dependency of $T_0(N_y, N_z)$ on N_y is evaluated by

$$T_0(N_y, N_z) = B - B \exp(-N_y/C), \quad (16.14)$$

where the constant B is an index providing the maximum distance of the optical excitation transfer and the constant C is an index characterizing the saturation of the maximum distance. As a result, the constants B and C can be obtained, as shown in Table, for $N_z = 1, 2, 3$, and 4, respectively. Corresponding curves are shown in Fig. 16.12c. For example, when $N_z = 1$, the maximum transfer distance is $2.85 \mu\text{m}$, whereas when $N_z = 4$, it is $7.92 \mu\text{m}$, indicating also that a long-distance transfer is possible by increasing the number of QD1s involved in the transfer.

N_z	$B(\mu\text{m})$	C
1	2.85	11.0
2	4.77	11.5
3	6.48	11.2
4	7.91	10.8

In the above analyses, it is assumed that the dot-array is orderly with equal intervals, as in Fig. 16.12a. In reality, however, it is likely that the QDs are variously positioned, and therefore, it is important to evaluate the effects of position variability on the signal transfer performance. The evaluation was conducted as follows. A system of $(N_y, N_z) = (5, 1)$ was analyzed. The x - and y -coordinates of center positions of all QD1s except QD_{in} were randomly shifted by uniform random numbers between $-v/2$ and $+v/2$, as illustrated in the inset in Fig. 16.12d. Given this, QD_{out} is set at $T = 1,000 \text{ nm}$ to evaluate the output signal I_{out}^v . The rates of change, $I_{\text{out}}^v/I_{\text{out}}^0$, from the output signal with no displacement, I_{out}^0 , was examined with 500 iterations of position shifts by random numbers, the results of which were used to calculate the standard deviation $\sigma(v)$. Corresponding to the

increase in the maximum value of position displacement, $|\nu|$, $\sigma(\nu)$ increased nearly linearly; however, even when $|\nu| = 3$ nm, $\sigma(3)$ was merely 6.8×10^3 . As indicated by the Yukawa function of equation (16.10), the interdot interaction time between nearest neighbors is short with the optical excitation transfer via optical near-infrared interactions, and it is likely that the optical excitation transfer is occurring preferentially. Therefore, even when the overall distribution is random, the signal at QD_{in} is transferred to QD_{out} as long as there is a highly efficient transfer route in the system, which is likely reflected in the robustness of the signal transfer against positional displacements shown above.

16.3.3 Experiment

An experimental test of the above-described signal transfer performance was conducted as follows. CdSe/ZnS core-shell QDs (*Evidot* by *Evident Technologies*) of 2.8 and 4.1 nm diameters were used for the smaller QDs QD1s and the larger QD QD2, respectively.

The sample was prepared following the procedure below:

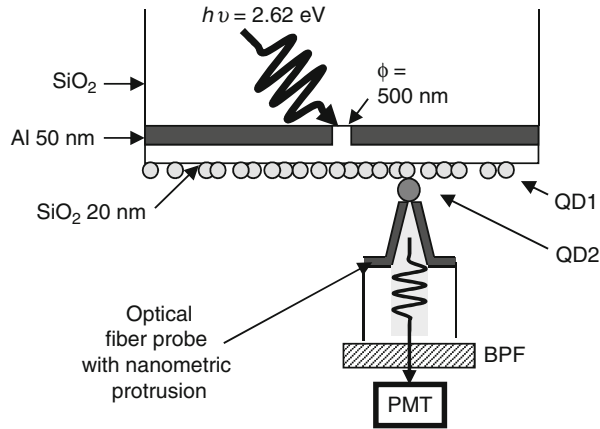
1. Al light-shielding film was applied to a SiO_2 substrate at 50 nm thickness by sputtering.
2. An aperture of 500 nm diameter was made in the Al light-shielding film using electron-beam (EB) lithography and reactive ion etching.
3. An SiO_2 film was formed on the Al light-shielding film at 20 nm thickness by sputtering.
4. QD1 solution in 1-phenyloctane was dropped on the substrate treated as above, and excess solution was blown off after leaving it for 10 min.

The SiO_2 film sputtered in Step 3 was formed for the purpose of preventing excitation energy loss due to optical near-field interactions between QDs and the Al light-shielding film. In Step 4, the concentration of the solution was varied at 0.5, 1.0, and 3.0 mg/mL to prepare samples 3A, 3B, and 3C, in which the heights of distributed QD1s were determined by atomic force microscopy to be $H = 10, 20,$ and 50 nm, respectively.

The following fiber probe was prepared for the measurement of the above samples. First, a fiber probe with nanometric protrusion [30], in which a sharpened core protrudes from an Au light-shielding film of a 800 nm thickness, was prepared, and then QD2s were attached to the tip of the probe by immersing the probe for 10 min in a QD2 solution (1-phenyloctane solution at 1 mg/mL).

By using this fiber probe, the fluorescence distribution was measured with the measuring system shown in Fig. 16.13b. CW laser light ($h\nu = 2.62$ eV) was radiated from the back of the substrate at a power density of 1.27 W/cm², thus exciting only QD1s at the aperture. At this time, by scanning near the aperture with the fiber probe at a controlled distance of 10 nm or less to the sample, QD2s adhered to the tip of the probe that served as the QD_{out} , and the excitation energy unidirectionally flowed toward the probe. The beam collected by the probe was passed through a bandpass filter with a center photon energy of $h\nu = 2.29$ eV and was detected by a

Fig. 16.13 Schematic representation of experimental system for near-field optical microscope measurements



photomultiplier tube, giving the measured value of emission intensity I_{QD1} of QD1. Because the output signal I_{out} at QD2 is proportional to the total level of the optical excitation of QD1s in the vicinity, it is possible to estimate the decay of I_{out} from the point of excitation beam introduction to the distance T by measuring I_{QD1} under the CW excitation.

Measurement results for samples 3A, 3B, and 3C are shown in Fig. 16.14a. Because the excitation intensity at the aperture on the substrates (dashed circles in the figure) was high enough for the signal to pass through the filter, the signal intensity at that point was high for all samples. Then, the signal intensity declined as the distance from the aperture increased. Setting $T = 0$ at the position with the maximum light intensity at the aperture, this maximum value was used to obtain normalized light intensity values I_{QD1} along the white dashed arrows in Fig. 16.14a, the profiles of which are shown in Fig. 16.14b. Profiles for samples 3A, 3B, and 3C are shown by dashed, dotted, and solid curves, respectively. In the region where $T \leq 500$ nm, it is assumed that the results reflect the distribution of the excitation intensity at the aperture, and for the range $T > 500$ nm, approximation with a monoexponential function was performed for each profile. Based on each approximation, a transfer distance T_0 , which is defined by $dI_{out}/dT = \exp(-2T/T_0)$, was calculated. As a result, approximated curves were obtained, and T_0 values were calculated to be 1.92, 4.40, and 11.8 μm for samples 3A, 3B, and 3C, respectively. As described above, I_{out} is proportional to I_{QD1} , and therefore, the calculated T_0 corresponds to the maximum transfer distance evaluated as the constant B in Eq. (16.14) in the previous subsection. The experimentally determined transfer distance and decay distance obtained from B in Table 3.2 are indicated in Fig. 16.14c with circles and squares, respectively. The increasing trend in the transfer distance with an increase in the height of the distributed QD1s, H , observed in the theoretical and experimental results shows good agreement with each other. It is speculated that the experimentally obtained transfer distance is generally low

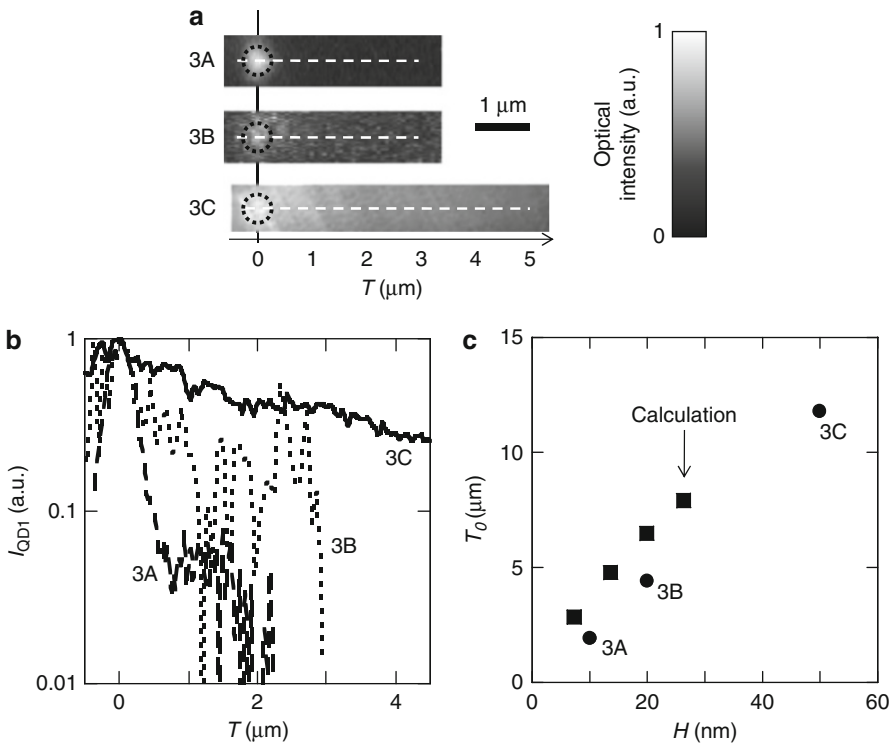


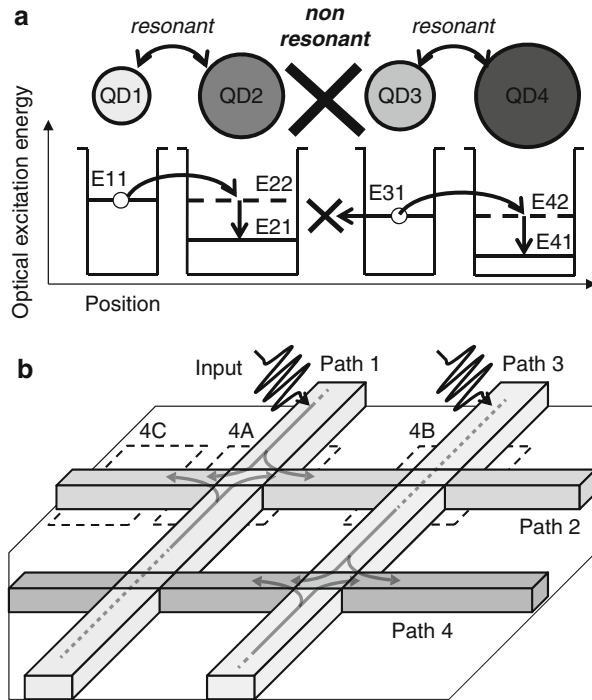
Fig. 16.14 (a) Distribution of I_{QD1} of samples 3A, 3B, and 3C obtained with the near-field optical microscope. (b) Profiles along white dashed lines in (a). Dashed curve = sample 3A, dotted curve = sample 3B, and solid curve = sample 3C. (c) Dependency of transfer distance T_0 on height H of distributed QD1s. Circles = experimental result and squares = theoretical results

because the relaxation time of optical excitation of QD1s is reduced by optical near-field interactions with metal, such as the Al light-shielding film on the substrate and the Au light-shielding film of the probe [31]. These results demonstrated the signal transfer performance between QDs via optical near-field interactions.

16.4 Destination Selectivity of Optical Near-Field Signal Transfer System

In this section, we designed and fabricated a structure for the purpose of a quantitative study of guided optical excitation transfer based on optical near-field interactions between QDs of different size randomly distributed in certain areas on a substrate. Measuring the intensity of emission from QD2 outside of the device, we succeeded in obtaining an output signal that had been transferred over a distance of several wavelengths, in the form of propagating light. Furthermore, we confirmed

Fig. 16.15 Schematic illustrations of (a) energy levels and (b) selective transfer at intersections of optical excitation transfer paths



the selectivity of the optical excitation transfer through a comparative experiment using a QD pair not having resonant energy levels.

16.4.1 Optical Near-Field Signal Transfer System

Since optical near-field interactions occur only between resonant levels, selectivity of optical excitation transfer is expected: Now, assume the presence of another resonant QD pair, QD3 and QD4, with diameters d_3 and d_4 (see Fig. 16.15a). If the diameters satisfy the condition $d_1 < d_3 < d_2 < d_4$, QD3 does not have an energy level that is resonant with QD1 or QD2. Therefore, optical near-field interactions are very weak, even if QD3 is placed in proximity to QD1 or QD2; thus, optical excitation transfer does not occur. Therefore, QD3 and QD4 can exchange optical excitation independently of QD1 and QD2. That is, optical excitation introduced into the QD1 is not transferred even if QD3 or QD4 is located in proximity, and the optical excitation is finally transferred only to QD2. Thus, an optical excitation transfer path through QDs with well-chosen parameters can exhibit selectivity of the signal transfer destination.

As an example, Fig. 16.15b shows a schematic illustration of optical excitation transfer paths consisting of two channels of QDs with intersections. Referring to the figure, QD1–QD4 are individually distributed at random in proximity to

each other in the areas of paths 1–4, so that two types of QDs coexist at the path intersections. In this device, when optical excitation is introduced to QD1 on path 1, as described earlier, an optical signal is transferred through path 1 by optical near-field interactions among the QD1s. At the intersection with path 2, unidirectional energy transfer from QD1 to QD2 occurs, so that the optical signal is transferred to path 2 (part 4A in Fig. 16.15b). At the intersection between paths 1 and 4, however, the signal does not transfer since QD1 and QD4 are nonresonant. Similarly, an optical signal introduced into path 3 is transferred to path 4 but is not transferred to path 2 (part 4B in Fig. 16.15b). Hence, each optical excitation in the different QDs autonomously selects its transfer destination. Optical excitations in nonresonant QDs do not interfere with each other, and it is therefore expected that wires can be crossed without any interactions.

The properties of the above-described optical excitation transfer paths are unique to optical near-field interactions and seem difficult to be realized with all-optical waveguides.

16.4.2 Experiments and Discussion

In order to evaluate the above-described optical excitation transfer properties of QDs, we conducted an experiment for actually confirming the difference in optical excitation transfer behavior in parts 4A and 4B shown in Fig. 16.15b. For the purpose of this experiment, we used CdSe/ZnS core-shell QDs (manufactured by *Quantum Design, Inc.*). As materials for QD1, QD3, and QD2 described above, those with central emission photon energies of $h\nu_1 = 2.31$ eV, $h\nu_3 = 2.26$ eV, and $h\nu_2 = 2.12$ eV were used. The outside of the shells was modified with an organic molecule carboxyl group. A sample in which QDs were placed in proximity to each other with gaps between them was obtained by drying drops of a solution. Using a transmission electron microscope, we estimated that the average distance between the centers of QDs closest to each other was about 10.4 nm. The distance is well within the effective field of optical near-field interactions calculated with Yukawa-function parameters appropriate for CdSe/ZnS core-shell QDs. Yet, it is far too large to expect significant tunnel coupling between adjacent QDs. We fabricated sample 4A, corresponding to part 4A in Fig. 16.15b, by the procedure described below and shown in Fig. 16.16a.

1. Electron-beam resist (ZEP-520A, a product of Zeon corporation) was spin-coated to a thickness of about 100 nm on a synthetic silica substrate and was baked at 180 °C for 240 s.
2. Path 2 with a width of 1,000 nm was drawn by an EB lithography system.
3. Path 2 was developed by immersing it in a developer.
4. By using the EB lithography system, path 1 with a width of 200 nm was drawn so as to perpendicularly intersect path 2 (Fig. 16.16a (i)).
5. Drops of QD2 solution were dropped onto the substrate and were left for 1 min, and then the remaining drops on the resist were blown away.
6. Path 1 was developed by immersing it in a developer.

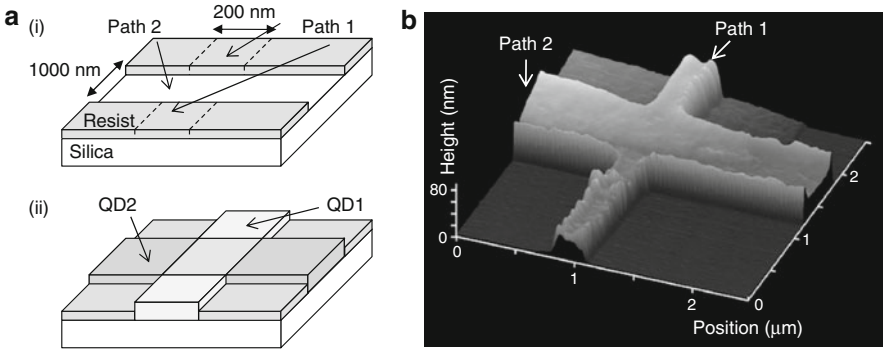


Fig. 16.16 (a) Schematic illustration of the procedure for fabricating samples. (b) AFM image of sample 4A

7. Drops of QD1 solution were dropped onto the substrate and were left for 1 min, and then the remaining drops on the resist were blown away (Fig. 16.16a (ii)).
8. The sample was immersed in resist cleaner (solvent ZEP-A) to remove the electron-beam resist.

Since the ZEP-520A film was hardly wetted with the QD solution, QDs were obtained almost exclusively on the paths in steps 5 and 7. Note that the QD1 which was distributed in path 2, where QD2 was already distributed in step 5, does not affect the optical excitation transfer properties since the optical excitation that reaches path 2 is all transferred to QD2, which is more stable.

Figure 16.16b shows an atomic force microscope (AFM) image of the intersection of the fabricated sample 4A. The result revealed that QDs were distributed in a region with a width of 300 nm and a height of 40 nm in the section of path 1. Furthermore, by using QD3 solution instead of QD1 solution in step 7 in a similar process, we fabricated sample 4B corresponding to part 4B in Fig. 16.15b. In addition, as a comparative example, we fabricated sample 4C in which only path 2 was present, corresponding to part 4C in Fig. 16.15b.

These samples were then used to experimentally study optically induced near-field energy transfer processes. The sample substrate was irradiated by CW He-Cd laser light (photon energy $h\nu = 3.81$ eV) from back side of the substrate at oblique incidence. The laser beam was beforehand shaped by a pinhole with a diameter of $10\ \mu\text{m}$ and excited QD1 by irradiating path 1 with an objective lens with $NA = 0.4$. The objective lens was scanned in a range of $-2 < T < 15\ \mu\text{m}$, where T denotes the distance between the irradiation spot and the intersection of paths 1 and 2. The laser power was 450 nW, and the diameter of the irradiation spot was $2\ \mu\text{m}$. The optical excitation generated by the excitation light was transferred along path 1 and was transferred to QD2 in part 4A, emitting light from the ground level E_{21} of QD2 ($h\nu_2 = 2.26$ eV). The light emission from E_{21} was observed with an electron multiplying CCD camera (Hamamatsu ImagEM C9100-13H, Hamamatsu Photonics K.K.) by using an objective lens with $NA = 0.55$ and a bandpass filter with

a center photon energy of $h\nu = 2.14$ eV, that is, near $h\nu_2$. The format of acquired images was 512×512 pixels, 16-bit grayscale, with a resolution of $0.37 \mu\text{m}/\text{pixel}$.

We evaluated the efficiency of the optical excitation transfer by studying the dependence of the intensity I of light emission from QD2 as function of its distance T from the excitation spot. More specifically, I is the peak value in CCD images which is observed at the path intersection. A difference in the density of QD2 among the samples was compensated for by normalization by the value at $T = 0 \mu\text{m}$. Finally, we define as a performance metric the distance T_0 at which the light emission intensity $I(T)$ has decreased to $1/e^2$ (see below).

As examples of the measurement results, Fig. 16.17a, b show CCD images of sample 4A (the intersection between paths 1 and 2, where QD1 and QD2 are

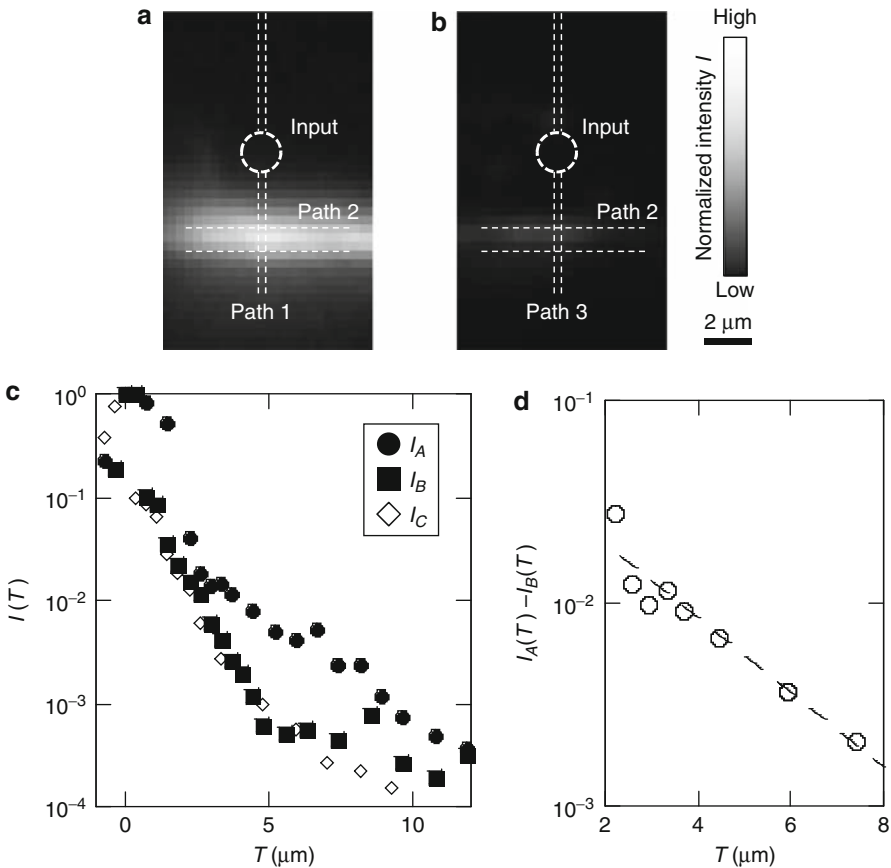


Fig. 16.17 (a) and (b) CCD images of samples 4A and 4B, respectively, observed at $T = 3.7 \mu\text{m}$. The white dotted lines mark the paths, and the dashed circles represent the irradiation positions of incident light. (c) $I(T)$ in samples 4A, 4B, and 4C, where the closed circles, closed squares, and open diamonds represent $I_A(T)$, $I_B(T)$, and $I_C(T)$, respectively. (d) Component $I_A(T) - I_B(T)$ of $I_A(T)$ associated with optical near-field interactions, where the dashed line represents a single-exponential attenuation curve

resonant) and sample 4B (the intersection between paths 3 and 2, where QD3 and QD2 are nonresonant) obtained at $T = 3.7 \mu\text{m}$. The color scale was normalized in previously discussed manner. Since a bandpass filter transparent at E_{21} was used, light emission is not observed in paths 1 and 3 and is observed mainly at the intersections.

Comparing samples 4A and 4B, we find generally much stronger light emission from sample 4A having a resonant level with, for example, $I_A(3.7) = 1.1 \times 10^{-2}$ and $I_B(3.7) = 2.6 \times 10^{-3}$, respectively. Furthermore, in a similar measurement performed on sample 4C, which did not have optical excitation transfer paths corresponding to paths 1 and 3, we obtained $I_C(3.7) = 2.3 \times 10^{-3}$, exhibiting essentially the same value as sample 4B. Since QD2 in sample 4C were directly excited by stray laser light, presumably, direct optical excitation of QD2 was also dominant in sample 4B, and the optical near-field excitation transfer from QD3 through path 3 was very small.

Figure 16.17c shows the results of plotting the measured values of $I_A(T)$, $I_B(T)$, and $I_C(T)$ evaluated and normalized as described, that is, $I_A(0) = I_B(0) = I_C(0) = 1$. No substantial differences were observed among $I_A(T)$, $I_B(T)$, and $I_C(T)$ for $T < 2 \mu\text{m}$. In this region, the emission profile matches the $2\text{-}\mu\text{m}$ -diameter Gaussian beam profile of the excitation laser rather well, and direct optical excitation of QD2 dominates over near-field excitation transfer. In sample 4C, no excitation transfer occurs, and the weak signal for $T > 2 \mu\text{m}$ in this sample thus represents a background signal reflecting limitations of our setup. The signal recorded in sample 4B in this region is very similar, and we therefore conclude that the effect of energy transfer from path 3 to path 2 in sample 4B can be disregarded. Thus, we confirmed that optical excitation transfer based on optical near-field interactions is strongly suppressed between QDs not having resonant energy levels, demonstrating selectivity of the optical excitation transfer destination with QDs.

In the range $T > 2 \mu\text{m}$, $I_A(T)$ clearly exceeds the other two. In order to quantify this effect, Fig. 16.17d shows the results of subtracting the background-dominated signal $I_C(T)$ from $I_A(T)$. As expected, $I_A(T) - I_C(T)$ decreases monotonically with increasing T . It can be approximated by a single-exponential attenuation curve indicated by a dashed straight line in the logarithmic plot Fig. 16.17d. From its slope, we obtain the optical excitation transfer distance T_0 at which the optical excitation energy was reduced to $1/e^2$ as $T_0 = 4.7 \mu\text{m}$. This value shows a good agreement with the transfer distance calculated according to Sect. 16.3.2 using a QD-center distance of 10.4 nm , a width of 300 nm and a height of 40 nm of path 1. This indicates that the optical energy transfer observed in sample 4A presumably occurred through optical excitation transfer based on optical near-field interactions. Our results demonstrate that sample 4A, in which QD1 and QD2 were distributed at random, operates as an optical excitation transfer path that can function at dimensions less than or equal to the diffraction limit, that is, with a width of 300 nm and a height of 40 nm . From these results, we believe that we succeeded in demonstrating that optical excitation transfer in randomly distributed QDs has properties unique to optical near-field interactions between resonant energy levels.

16.5 Conclusion

In Sect. 16.2, we observed the dynamic properties of excitonic energy transfer and dissipation between CdSe/ZnS core-shell QDs and ZnO QDs via an optical near-field interaction using time-resolved PL spectroscopy. We observed the dynamic properties of excitonic energy transfer and dissipation between CdSe/ZnS core-shell QDs and ZnO QDs via an optical near-field interaction using time-resolved PL spectroscopy. We experimentally confirmed that optical near-field coupling does not occur between nonresonant energy levels. Furthermore, we successfully increased the energy transfer ratio between the resonant energy states, instead of the radiative decay from the QD. Chemically synthesized spherical nanocrystals, both semiconductor QDs and metallic nanocrystals [32], are promising nanophotonic device candidates because they have uniform sizes, controlled shapes, defined chemical compositions, and tunable surface chemical functionalities.

In Sect. 16.3, The array dependency of QDs was theoretically and experimentally analyzed with respect to the basic properties of transfer via optical near-field interactions. Effects of the array structure of the QDs, which act as a medium, on the signal transfer performance were analyzed with a theoretical model using a rate equation. Increasing the number of QDs in the dot-array is detrimental to short-distance signal transfer (signal intensity decreases); however, it allows for long-distance transfer because decaying of the signal with respect to the transfer distance is alleviated. In addition, a high resistance against positional variations of QDs was shown. Using different-height, stacked CdSe/ZnS core-shell QDs and a near-field optical probe whose tip had QDs that serve as an output end, the dependency of signal transfer performance on the structure of distributed QDs was experimentally evaluated, and the obtained results were consistent with the theoretical calculations.

In Sect. 16.4, we fabricated a structure containing excitation paths formed by randomly distributed QDs and evaluated the optical excitation transfer properties. When two types of CdSe/ZnS core-shell QDs having resonant energy levels, namely, QD1 and QD2, were used, we succeeded in observing a directed optical excitation transferred by optical near-field interactions as propagating light emitted as an output signal from QD2. The transfer distance was estimated to be 4.7 μm . When using QDs with nonresonant energy levels, however, near-field optical excitation transfer was greatly reduced. These results demonstrate that optical excitation transfer in QDs occurs via excited levels of the QDs. Thus, it is possible to readily fabricate an optical excitation transfer path by randomly distributing QDs and to implement the functionality for selecting the signal transfer destination by utilizing nonresonant levels. These properties will be very effective in nanophotonic signal transfer devices, and randomly distributed QDs appear as a promising candidate technology for implementing these features.

Acknowledgements The works in Sect. 16.2 are supported in partial by the Global Center of Excellence (G-COE) “Secure-Life Electronics” sponsored by the Ministry of Education, Culture, Sports, Science and Technology (MEXT), Japan.

This work in Sect. 16.3 is partially supported by the Japan Science and Technology Agency (JST) and the German Research Foundation (DFG) under the Strategic International Cooperative Program, by the New Energy and Industrial Technology Development Organization (NEDO) under a program for comprehensive activity for personnel training and Industry-Academia Collaboration based on NEDO projects and by The University of Tokyo Global COE Program “Secure-Life Electronics.”

The work in Sect. 16.4 was financially supported by JST and DFG under the Strategic Japanese-German Cooperative Program, and by MEXT under the Special Coordination Funds for Promoting Science and Technology. T. Yatsui was financially supported by a Grant-in-Aid for Young Scientists (A) from MEXT and by a research grant (Basic Research) from the TEPCO Memorial Foundation.

References

1. M. Ohtsu, K. Kobayashi, T. Kawazoe, S. Sangu, T. Yatsui, *IEEE J. Sel. Top. Quantum Electron.* **14**, 1404 (2008)
2. K. Kobayashi, S. Sangu, H. Ito, M. Ohtsu, *Phys. Rev. A* **63**, 013806 (2001)
3. T. Kawazoe, K. Kobayashi, J. Lim, Y. Narita, M. Ohtsu, *Phys. Rev. Lett.* **88**, 067404 (2002)
4. B.W. van der Meer, G. Coker III, S.Y.S. Chen, *Resonant Energy Transfer: Theory and Data* (VCH, New York, 1994)
5. K. Kobayashi, S. Sangu, T. Kawazoe, M. Ohtsu, *J. Lumin.* **112**, 117 (2005)
6. D.P. Craig, T. Thirunamachandran, *Molecular Quantum Electrodynamics* (Academic, London, 1984)
7. E. Hanamura, *Phys. Rev. B* **37**, 1273 (1988)
8. S. Sangu, K. Kobayashi, A. Shojiguchi, M. Ohtsu, *Phys. Rev. B* **69**, 115334 (2004)
9. M. Bayer, P. Hawrylak, K. Hinzer, S. Fafard, M. Korkusinski, Z.R. Wasilewski, O. Stern, A. Forchel, *Science* **291**, 451 (2001)
10. E.A. Stinaff, M. Scheibner, A.S. Bracker, I.V. Ponomarev, V.L. Korenev, M.E. Ware, M.F. Doty, T.L. Reinecke, D. Gammon, *Science* **311**, 636 (2006)
11. T. Kawazoe, K. Kobayashi, S. Sangu, M. Ohtsu, *Appl. Phys. Lett.* **82**, 2957 (2003)
12. T. Kawazoe, K. Kobayashi, M. Ohtsu, *Appl. Phys. Lett.* **86**, 103102 (2005)
13. T. Kawazoe, K. Kobayashi, K. Akahane, M. Naruse, N. Yamamoto, M. Ohtsu, *Appl. Phys. B* **84**, 243 (2006)
14. N. Sakakura, Y. Masumoto, *Phys. Rev. B* **56**, 4051 (1997)
15. K. Kobayashi, S. Sangu, H. Itoh, M. Ohtsu, *Phys. Rev. A* **63**, 013806 (2000)
16. T. Suzuki, T. Mitsuyu, K. Nishi, H. Ohyama, T. Tomimasu, *Appl. Phys. Lett.* **69**, 4136 (1996)
17. C. Trallero-Giner, A. Debernardi, M. Cardona, M. Menendez-Proupin, A.I. Ekimov, *Phys. Rev. B* **57**, 4664 (1998)
18. T. Itoh, M. Furumiya, T. Ikehara, C. Gourdon, *Solid State Commun.* **73**, 271 (1980)
19. T. Yatsui, S. Sangu, T. Kawazoe, M. Ohtsu, S.J. An, J. Yoo, G.-C. Yi, *Appl. Phys. Lett.* **90**, 223110 (2007)
20. S.A. Crooker, T. Barrick, J.A. Hollingsworth, V.I. Klimov, *Appl. Phys. Lett.* **82**, 2793 (2003)
21. M.G. Bawendi, P.J. Carroll, L.W. William, L.E. Brus, *J. Chem. Phys.* **96**, 946 (1992)
22. P. Guyot-Sionnest, M. Shim, C. Matranga, M. Hines, *Phys. Rev. B* **60**, R2181 (1999)
23. A. Ohtomo, K. Tamura, M. Kawasaki, T. Makino, Y. Segawa, Z.K. Tang, G.K.L. Wong, *Appl. Phys. Lett.* **77**, 2204 (2000)
24. M.H. Huang, S. Mao, H. Feick, *Science* **292**, 1897 (2001)
25. H.D. Sun, T. Makino, Y. Segawa, M. Kawasaki, A. Ohtomo, K. Tamura, H. Koinuma, *J. Appl. Phys.* **91**, 1993 (2002)
26. T. Yatsui, H. Jeong, M. Ohtsu, *Appl. Phys. B* **93**, 199 (2008)
27. E.A. Meulenkaamp, *J. Phys. Chem. B* **102**, 5566 (1998)

28. L. Spanhel, M.A. Anderson, *J. Am. Chem. Soc.* **113**, 2826 (1991)
29. L.E. Brus, *J. Chem. Phys.* **80**, 4403 (1984)
30. S. Mononobe, M. Naya, T. Saiki, M. Ohtsu, *Appl. Opt.* **36**, 1496 (1997)
31. N. Hosaka, T. Saiki, *J. Microsc.* **202**, 362 (2001)
32. M. Brust, C.J. Kiely, *Colloids Surf. A* **202**, 175 (2002)

Hiroyuki Hieda, Katsuyuki Naito, Takashi Ishino, Kuniyoshi Tanaka,
Masatoshi Sakurai, Yoshiyuki Kamata, Seiji Morita, Akira Kikitsu,
and Koji Asakawa

Contents

17.1 Introduction.....	672
17.2 Magnetic Patterned Media.....	674
17.2.1 Preparation.....	674
17.2.2 Magnetic Properties.....	680
17.3 Organic Dye-Patterned Media.....	683
17.3.1 Preparation.....	683
17.3.2 Electrical and Optical Measurements.....	685
17.4 Conclusion.....	690
References.....	691

Abstract

Two types of recording media possessing nano-dot structures were investigated. The media were prepared by an artificially assisted (or aligned) self-assembling (AASA) method, which includes simple nano-patterning using a nano-imprint and fine nano-patterning using self-assembling organic molecules. The AASA method were successfully applied to fabricate magnetic patterned media for opto-magnetic hybrid recordings and fluorescent organic dye media for near-field optical recording.

H. Hieda (✉) · K. Naito · T. Ishino · K. Tanaka · M. Sakurai · Y. Kamata · S. Morita · A. Kikitsu
Storage Materials & Devices Laboratory, Corporate Research & Development Center, Toshiba
Corporation, Kawasaki, Japan
e-mail: hiroyuki.hieda@toshiba.co.jp; katsuyuki.naito@toshiba.co.jp; takashi.ishino@toshiba.co.jp;
kuniyoshi.tanaka@toshiba.co.jp; masatoshi.sakurai@toshiba.co.jp; yoshiyuki.kamata@toshiba.co.jp; sj.morita@toshiba.co.jp; akira.kikitsu@toshiba.co.jp

K. Asakawa
Organic Materials Laboratory, Corporate Research & Development Center, Toshiba Corporation,
Kawasaki, Japan
e-mail: koji.asakawa@toshiba.co.jp

17.1 Introduction

The data storage density is advancing because of the requirement of information data growth as shown in Fig. 17.1. 1 Tb/inch² density will be required around 2014. Physical limits, however, are predicted both for magnetic recording and for optical one. To overcome the optical limit (diffraction limit), near-field optics is required.

The magnetic recording density is currently increasing at rates of up to 30–40 % per year. To obtain the higher densities, grain sizes of the conventional continuous magnetic films should be reduced to maintain a necessary signal-to-noise ratio. The small grain sizes, however, reduce thermal stability of the magnetization of each bit. This, referred to as superparamagnetism, can be overcome by increasing KuV/kT , where Ku is an energy barrier to reversal per grain volume (anisotropic energy), V is a volume per grain, k is Boltzmann constant, and T is temperature. High Ku materials such as FePt are preferable to overcome the thermal fluctuation. Higher magnetic field is required to write the signals on the high Ku media. Magnetic fields generated by the thin-film magnetic head have almost reached to their limits. Hybrid recording ([1], shown in Fig. 17.2) consisting of near-field light and magnetic field is one of the good candidates to solve the paradox.

Magnetic patterned media, which consist of islands of magnetic material surrounded by a non-magnetic matrix, increase an effective V resulting in bit thermal

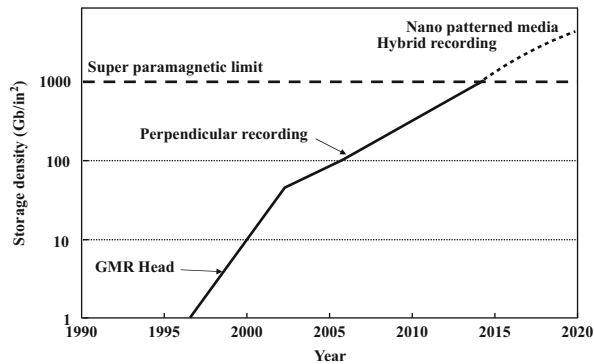


Fig. 17.1 Roadmap of hard drive technologies

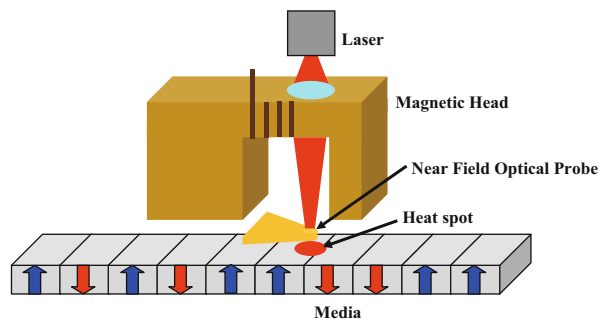
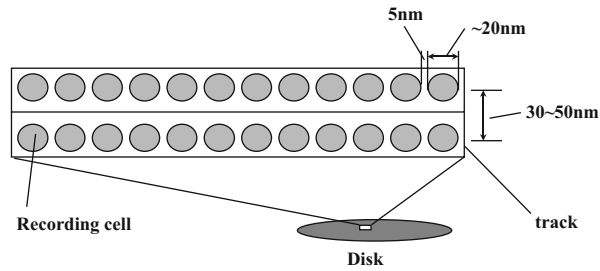


Fig. 17.2 Schematic explanation of hybrid recording

Fig. 17.3 Schematic explanation of patterned media



stability [2]. Magnetic patterned media (schematically shown in Fig. 17.3) can decrease in media transition noise, track edge noise, and nonlinear bit shift effects. Additionally, precise servo information can be embedded in the patterned media. This is very advantageous for narrower track widths of future HDDs [3]. Ultra-high density beyond 1 Tb/inch² should be obtained by the combination of the hybrid recording and the patterned media [4].

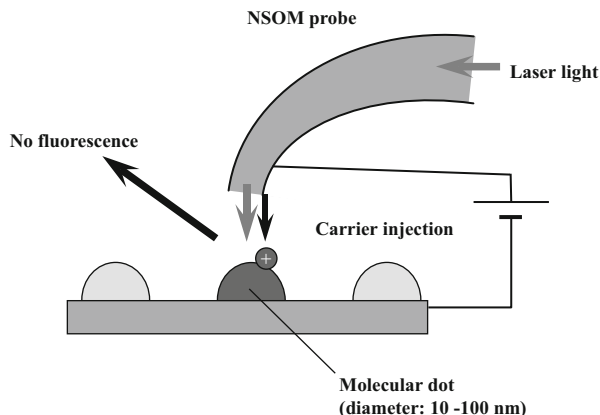
Some serious problems must be resolved such as a high cost of nano-patterning and write synchronization [5]. Magnetic patterned media have been prepared previously, for example, by electron beam or focused ion beam patterning [6], ion beam modification [7], interferometric lithography [8], nano-imprint lithography [9], self-assembling template lithography [10], and plating in anodized aluminum pores [11]. Recently, self-assembling template lithography [12–14] has attracted much attention, because of their possibility to fabricate nano-scale pattern on large area.

In this chapter, we show circumferential magnetic patterned media, prepared by an artificially assisted (or aligned) self-assembling (AASA) method [15], which includes simple nano-patterning using a nano-imprint and fine nano-patterning using self-assembling diblock polymers according to a graphoepitaxy method [16–18]. The fine nano-patterns created by the self-assembling method can be aligned in a large area by nano-imprinted guide patterns [19].

As another approach to ultrahigh-density recordings with near-field optics, we have aimed at a novel write/read principle media on the nm scale: organic dye-patterned media. In the previous near-field optical storage demonstrations, conventional recording media such as a magnetic-optical recording (MO) medium [20], a phase-change (PC) medium [21], or photochromic materials [22, 23] have been used. Using an MO medium and a PC MEDIUM, signal contrasts are 1 and 10 %, respectively. In future near-field storage devices, signal contrast will be insufficient to achieve practical readout speeds. As for photochromic materials, although better signal contrast is expected, readout without destroying the recorded information has been a major issue.

We showed that amorphous organic dye molecules formed droplet-like nm-scale structures and aligned by the AASA method [24]. It is possible to inject and confine charges into a single dot using AFM [25, 26]. Fluorescence changes in dye molecules associated with charge injection into their thin films was observed [27]. Fluorescence measurement has such a high signal-to-noise ratio that it can be observed even in a single molecule. Therefore, readout using fluorescence is

Fig. 17.4 Schematic explanation of charge injection writing and fluorescence reading



expected to achieve high accuracy even if recording marks are nm scale. Furthermore, electrical writing, namely, charge confinement, will prevent record rupture at readout as shown in Fig. 17.4.

17.2 Magnetic Patterned Media

17.2.1 Preparation

Self-assembly method has attracted much attention because of its ability to produce ordered fine nano-pattern with a large area. We adopted diblock copolymers as self-assembly system. Figure 17.5 shows the explanation of phase separation of diblock copolymers. There are several types of phase-separated states as shown in Fig. 17.6.

The diblock copolymer molecule used here consists of a hydrophobic polystyrene chain and a hydrophilic polymethylmethacrylate chain [28, 29]. These chains are not mixed resulting in a phase-separation state. The dot diameter and the dot pitch are determined by the molecular weights. For the diblock copolymer [polymethylmethacrylate (Mw 41500)-polystyrene (Mw 17200)], 40 nm diameter and 80 nm pitch were obtained. Figure 17.7 shows the dot patterns of the diblock copolymers on a flat surface. A polycrystalline structure was observed for phase-separation state where polymethylmethacrylate dots in polystyrene surrounding.

Figure 17.8 shows the concept of the artificially assisted (or aligned) self-assembly (AASA) method. Phase separation takes place in the grooves to produce aligned dot patterns. Figure 17.9 shows a schematic explanation of the preparation method for magnetic patterned media using AASA method. Nano-imprint process of guide groove patterns in AASA method are schematically shown in Fig. 17.10. A Ni master disk possessing spiral patterns with 60-, 100-, 150-, 200-, and 250-nm-width lands and a 400-nm-width groove (110 nm depth) was pressed to a resist film

Fig. 17.5 Schematic explanation of phase separation of diblock copolymers

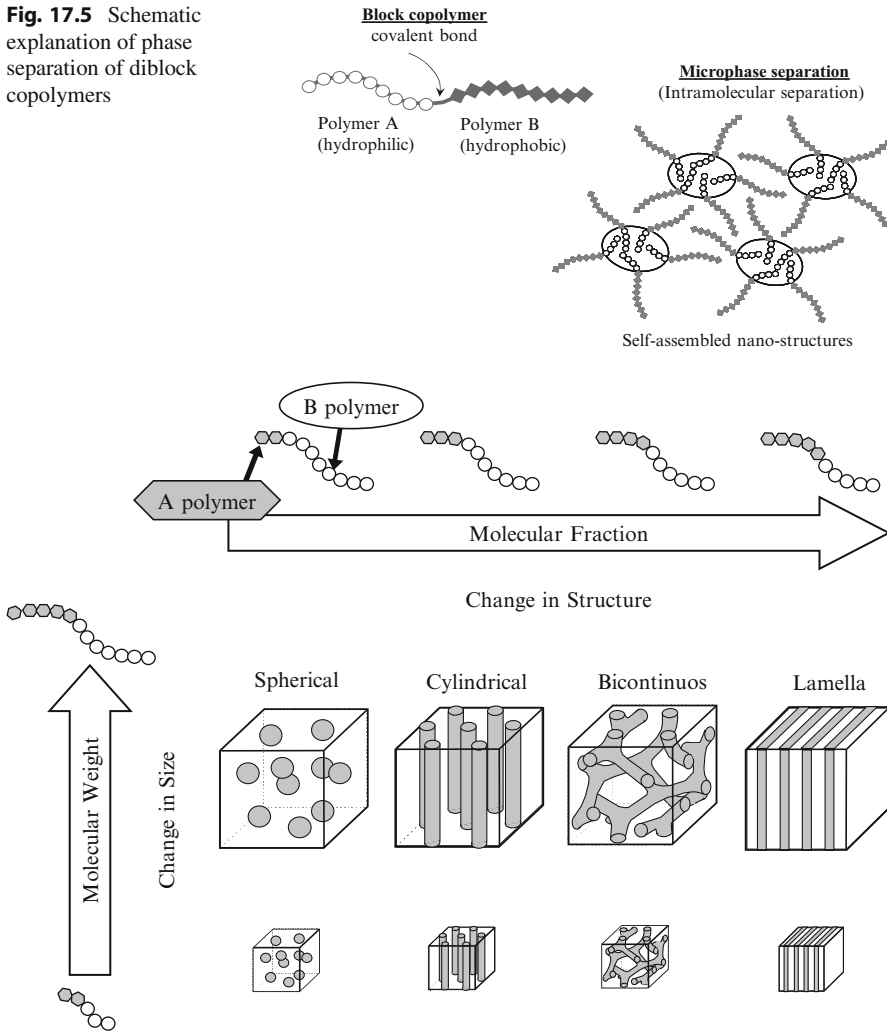


Fig. 17.6 Type of phase separation for diblock copolymer

on a CoCrPt film to transfer the spiral patterns at a room temperature at a pressure of 1,000 bar.

The AFM images of spiral patterns transferred to the resist film were shown in Fig. 17.11. The land-groove spiral patterns were precisely transferred.

A diblock copolymer solution was cast into the obtained grooves and then annealed to prepare self-assembling dot structures aligned along the grooves. Figure 17.12 indicates dot structures in grooves with different widths. One to four dot lines could be obtained by changing the groove width. The groove width should be controlled to obtain the regularly aligned dot lines along the

Fig. 17.7 Phase-separation dot patterns of the diblockpolymer on a flat Si substrate

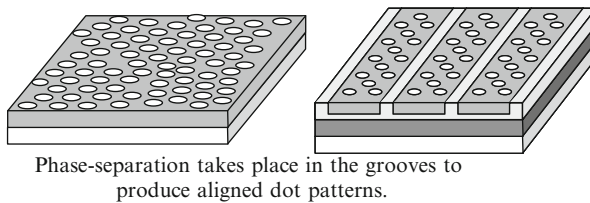
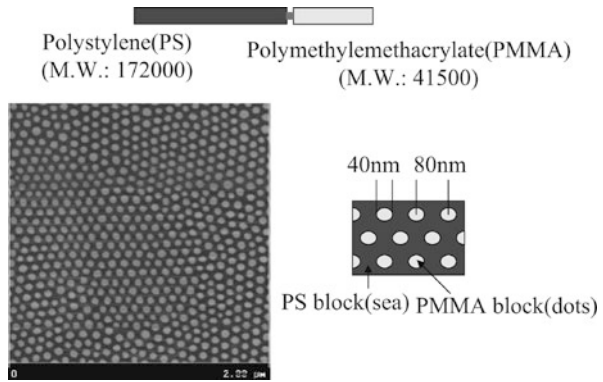


Fig. 17.8 Concept of AASA method

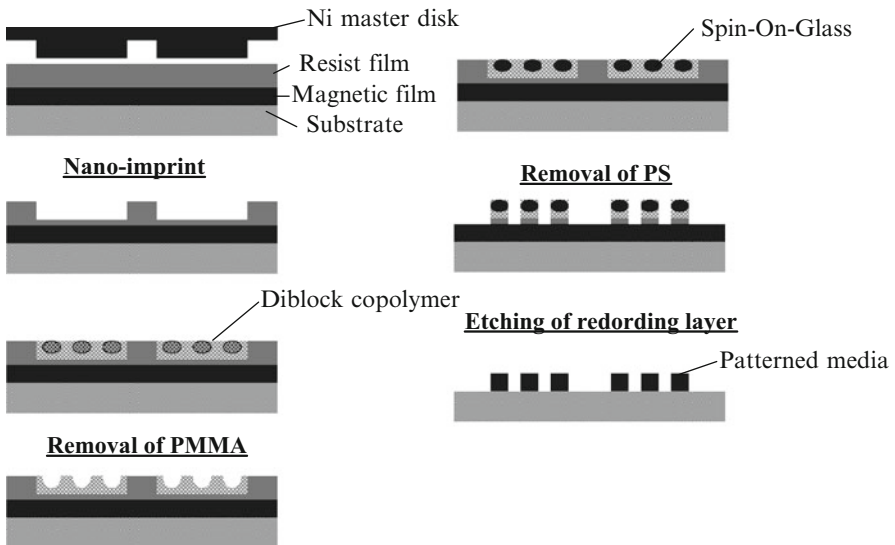
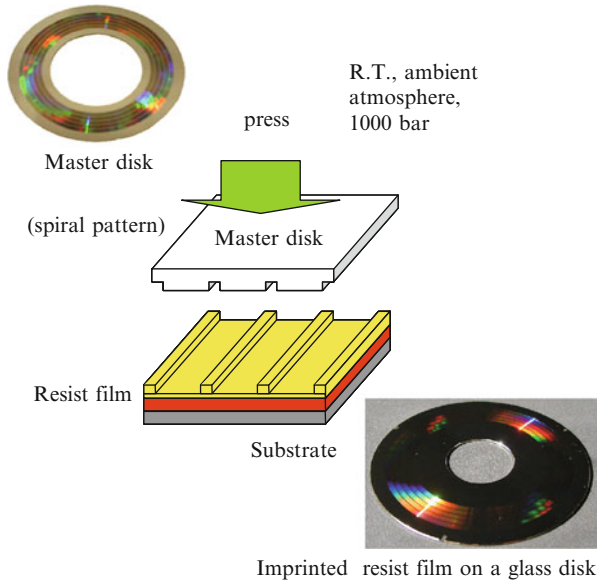
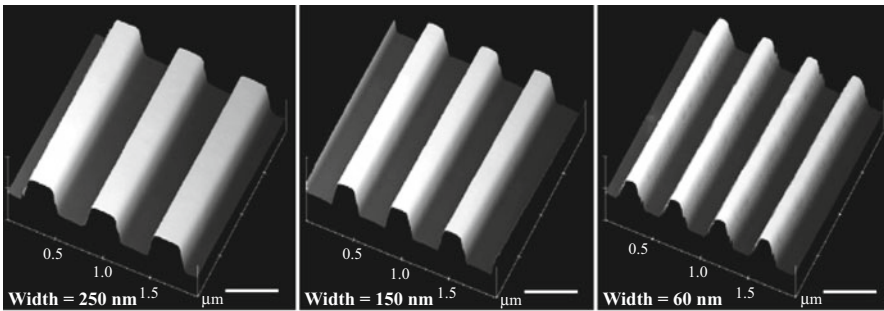


Fig. 17.9 Schematic explanation of nano-imprint process of guide groove patterns in AASA method

Fig. 17.10 Schematic explanation of nano-imprint process of guide groove patterns in AASA method



Ni master disk



Resist film after nano-imprint

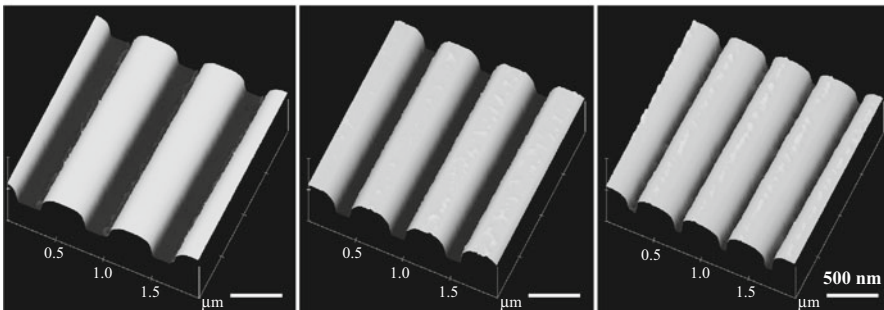
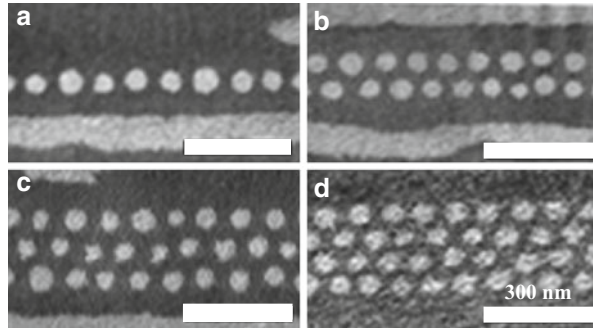


Fig. 17.11 AFM images of spiral patterns of the Ni master (*upper* images) and of the resist film (*under* images). The lengths mean the land widths of the master disk

Fig. 17.12 Phase-separation dot patterns of the diblock copolymers in grooves with different widths: (a) 60 nm, (b) 150 nm, (c) 200 nm, (d) 250 nm



dot size ~ 15 nm, dot pitch ~ 35 nm

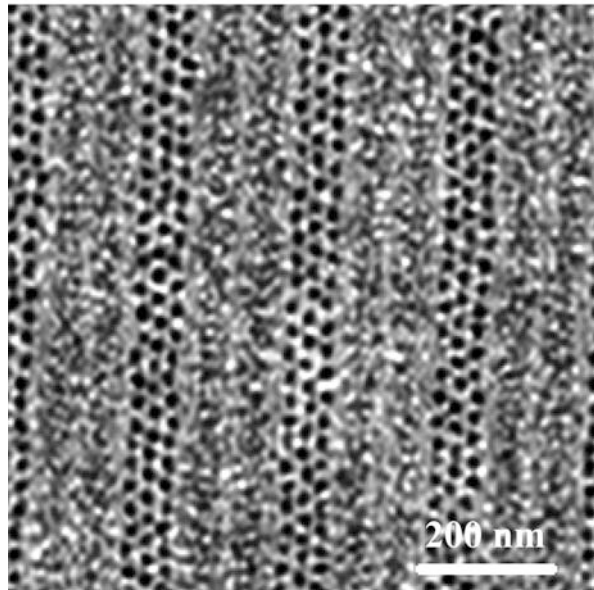


Fig. 17.13 Phase-separation dot patterns of another diblock copolymers in grooves

grooves. In the figure, the groove widths were considered rather suitable for the two and four dot lines. **Figure 17.13** shows the phase-separation dot patterns of another diblock copolymer in grooves. The dot size was 15 nm and the dot pitch was 35 nm. These small dots were obtained by using the diblock copolymer with low molecular weight [polymethylmethacrylate (Mw 13200)-polystyrene (Mw 65000)].

The PMMA dots were selectively removed by the oxygen plasma treatment [29]. The resulting holes were filled by spin on glass (SOG). The lower magnetic films were patterned by ion milling using the SOG dots as a mask.

Figure 17.14a shows the SEM image of the patterned magnetic media with 40 nm diameter. There are fluctuations in size and in position of the magnetic dots. The irregularities are probably caused by the diblock copolymer dot disorder and by the nano-patterning process fluctuation. The whole image of the patterned media

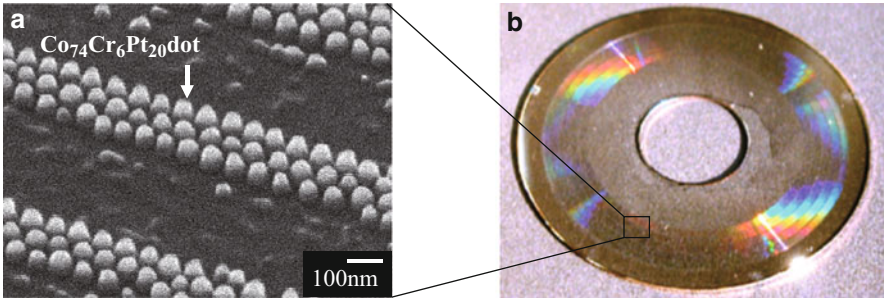


Fig. 17.14 (a) SEM image of the patterned magnetic media with a 40 nm diameter; (b) the whole image of the patterned media disk prepared on a 2.5-inch HDD glass plate

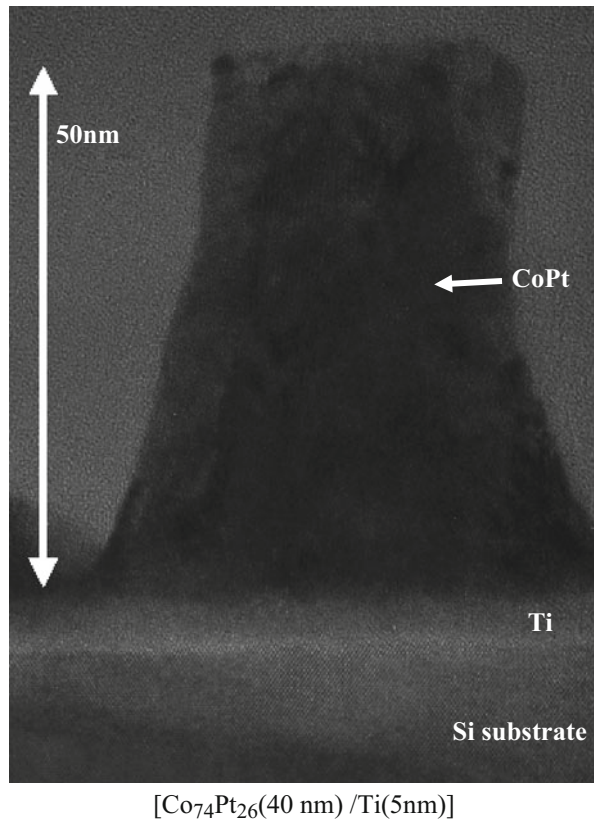


Fig. 17.15 TEM image of the patterned CoPt dot

disk prepared on a 2.5-inch-diameter HDD glass plate was shown in Fig. 17.14b. Interference colors based on the wide groove lines were observed. Figure 17.15 shows the TEM image of the patterned dot with about 40 nm diameter. This image indicates that the magnetic dot is completely separated.

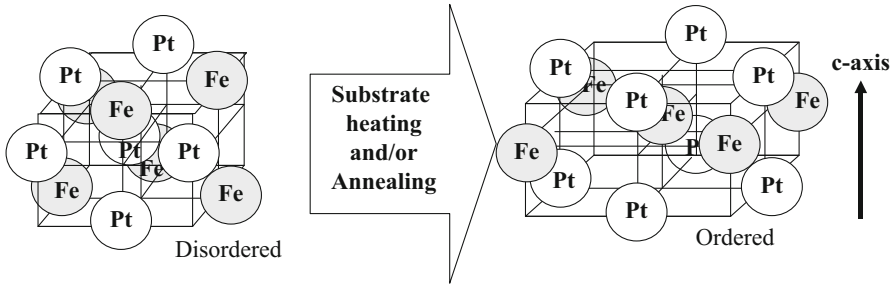


Fig. 17.16 Schematic explanation of ordering of FePt alloy

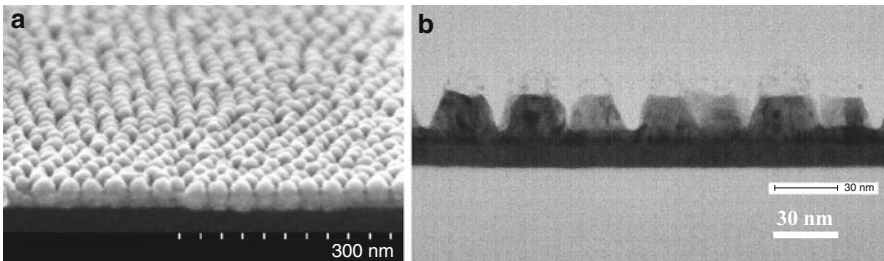


Fig. 17.17 (a) SEM image of the patterned FePt dots with 30-nm pitch, (b) TEM sectional image of the FePt dots

FePt-ordered alloys with extremely high magnetic anisotropy energy K_u have attracted increasing attention because of their possible application to magnetic-optical hybrid recording capable of extending the recording density of HDDs beyond the superparamagnetic limit in Co alloy materials which have been used in conventional magnetic recording media. High-temperature annealing process is required to obtain the ordered crystal structure as shown in Fig. 17.16. Figure 17.17 shows a demonstrations of fabrication of FePt patterned media with 35 nm dot pitch by the diblock copolymer method. As shown in Fig. 17.18, AASA method has been successfully applied to the high-density patterned media.

17.2.2 Magnetic Properties

Figure 17.19 shows the M - H loops of the raw continuous film (CoCrPt) and the patterned media. A coercive force H_c and squareness ratio of the patterned film increased compared to the continuous film. The magnetization of the patterned media decreased due to the decrement of the material volume. Squareness ratio was almost unity.

Figure 17.20 indicates the MFM images of the patterned magnetic media after AC erase and after DC erase. Three magnetic dot lines are observed corresponding to Figs. 17.12c and 17.14a. Bright and dark dots are randomly distributed after AC erase.

Fig. 17.18 AFM image of FePt patterned magnetic media with 30-nm pitch of dots

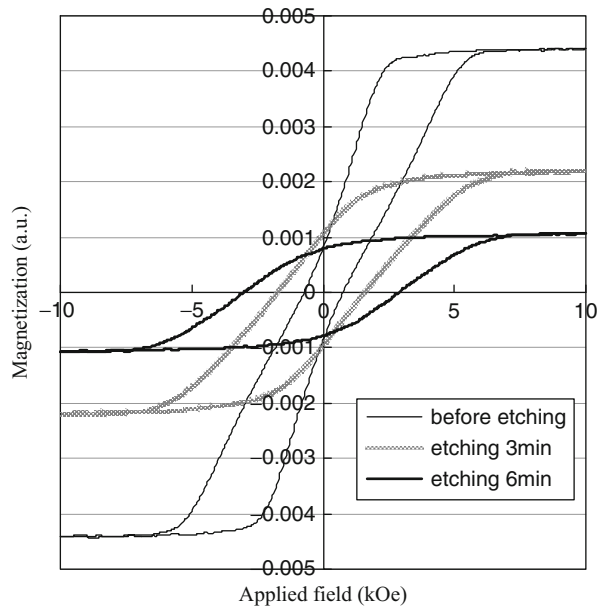
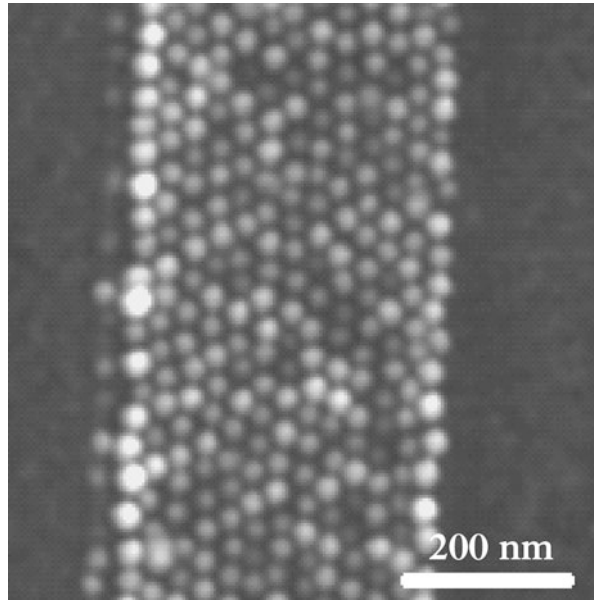


Fig. 17.19 M - H loops of the raw continuous film (CoCrPt) and the patterned media

The DC erased dots are observed magnetized in one direction in Fig. 17.20b. Single magnetic domains with an almost perpendicular orientation were confirmed in each magnetic dot.

Figure 17.21 shows M - H loops measured by VSM for a FePt film and dots. For the FePt film, the H_c was 4.5 kOe, and for the dots, the H_c increased to 13 kOe and

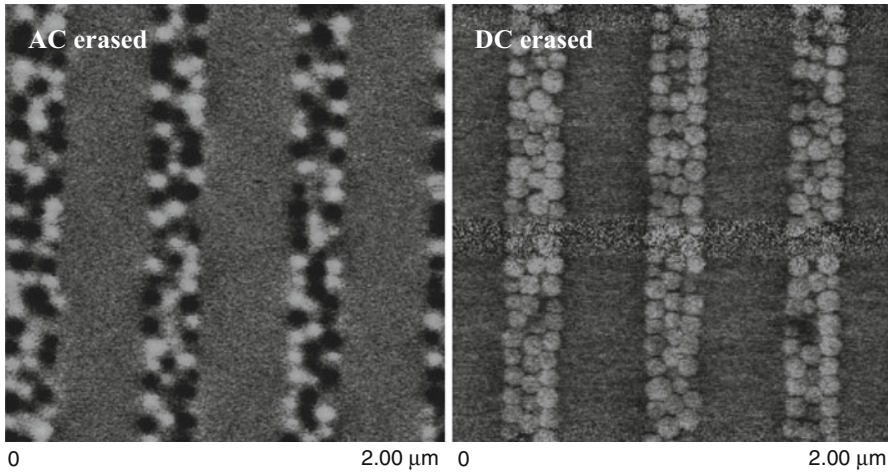


Fig. 17.20 MFM images of the patterned media

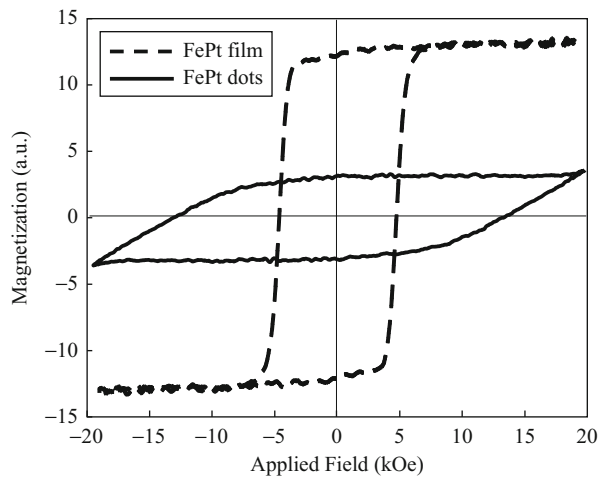


Fig. 17.21 M - H loops of the FePt film and the FePt patterned media

the squareness of the loops was 1.0. The magnetization of the dots was not saturated because the magnetic field our VSM could generate was limited to 20 kOe. The observed large increase of the H_c was thought to be attributable to enhancement of shape anisotropy by formation of isolated dots. Huge H_c exceeding 100 kOe has been reported, which was expected from the coherent magnetization rotation for highly ordered L10 FePt particles with diameter of about 20 nm [30]. The observed H_c in the present study was far smaller than the reported value. One possible explanation of the small H_c may be that a degradation of the degree of crystal order may cause lowering of H_c . To advance the further miniaturization of the dot size

in the magnetic patterned media, it is necessary to obtain a better understanding of effects of the etching process on magnetic materials.

17.3 Organic Dye-Patterned Media

17.3.1 Preparation

The organic molecule mainly used here was TTPAE or TPD, shown in Fig. 17.22. These molecules give amorphous films as a hole transport layer in organic EL devices [31]. The films were formed by vacuum evaporation onto thermally oxidized p-Si substrates with resistivity of 0.001–0.01 Ω -cm. The thickness of SiO₂ layer was 20 nm. The electrodes were fabricated on the back of the Si substrates by evaporating Cr and Au. Before the evaporation of molecules, the SiO₂/Si substrates were made hydrophobic by treatment in an atmosphere of hexamethyldisilazane.

Figure 17.23 shows the contact-mode topographic image of the TTPAE film observed using an AFM. It was clearly seen that the film was constructed of spatially isolated droplet-like domain structures. The size and the density of domain were varied according to the amount of deposition. The diameter, height, and density were varied from 20 to 300 nm, from 10 to 100 nm, and from 1,011 to 109 cm⁻², respectively. When the amount of deposition was increased to the film thickness of more than 40 nm, the film structure changed into a continuous layer with a flat surface. We verified that thin films of several amorphous molecules including TPD also showed similar domain structures.

The observed uniform droplet-like domain structures suggest that the film growth is based on the Volmer–Weber mechanism. In this mechanism, growth

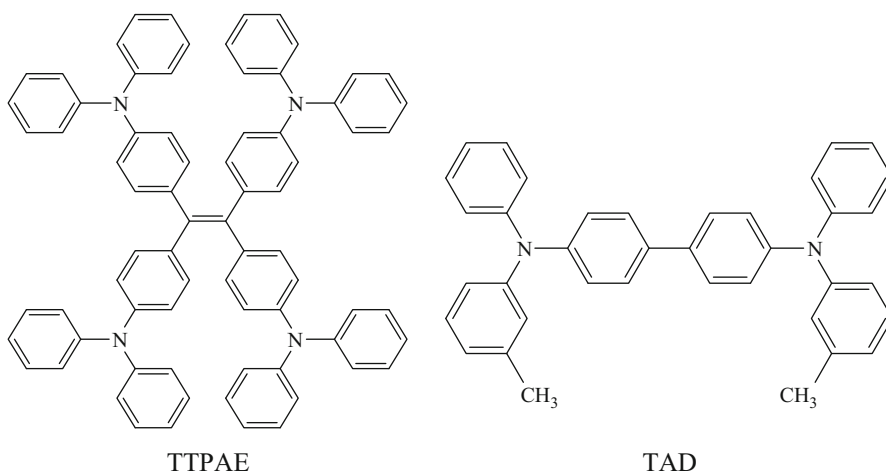


Fig. 17.22 Molecular structures of TTPAE and TPD

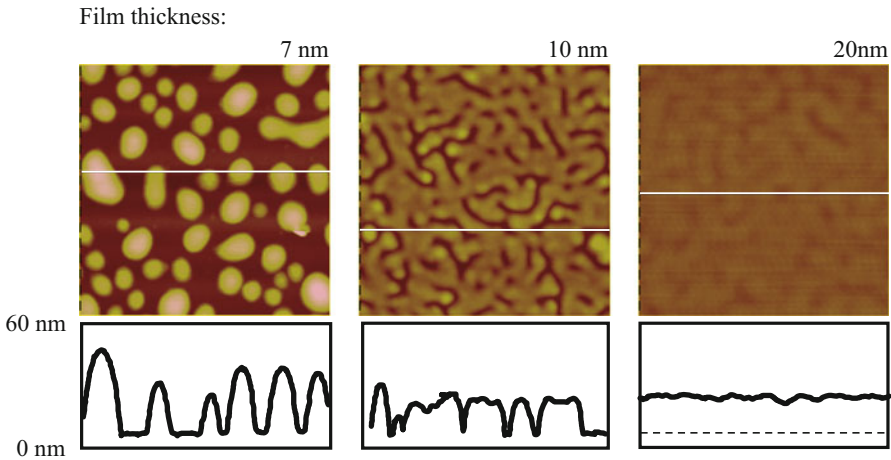


Fig. 17.23 AFM image of TTPAE films

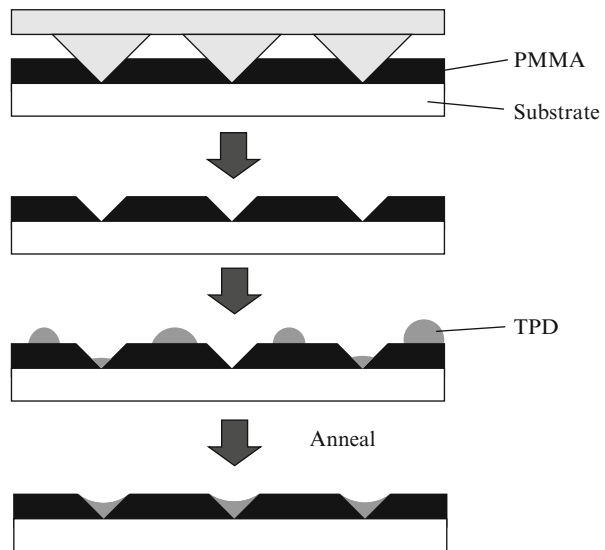


Fig. 17.24 Schematic explanation of the AASA method for TPD dot alignment

characteristics are known to depend strongly on the surface energies of the film and of the substrate. When the films were formed onto hydrophilic SiO_2/Si substrates, it was found that the domain size was much larger than films on the hydrophobic substrates.

The droplet size and alignment could be controlled by the AASA method. The hole arrays were prepared on polymethylmethacrylate film by using AFM. The pitch was 30 nm. TPD molecules were evaporated onto the arrays. TPD amorphous dots were selectively formed on the holes with the same size as shown in Fig. 17.24.

Fig. 17.25 AFM image of TPD dots prepared by AASA method

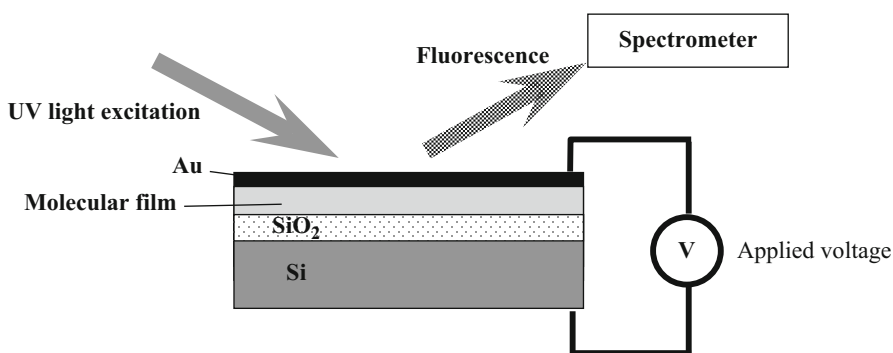
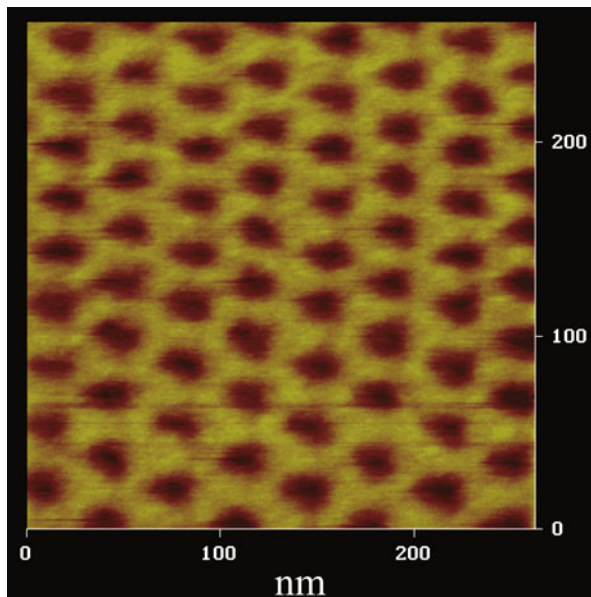


Fig. 17.26 Schematic diagram of device structure and fluorescence measurement

Using nano-imprint should produce the large area hole arrays to obtain the large area organic dye-patterned media (Fig. 17.25).

17.3.2 Electrical and Optical Measurements

Figure 17.26 shows a schematic diagram of the structure of the device used in this chapter. To apply voltage to the organic films, Au films of 10 nm thickness were fabricated on the substrates following the deposition of organic films. Au films of 10 nm were selected as thinnest providing good electrical contact and sufficient fluorescence intensity from the beneath organic films.

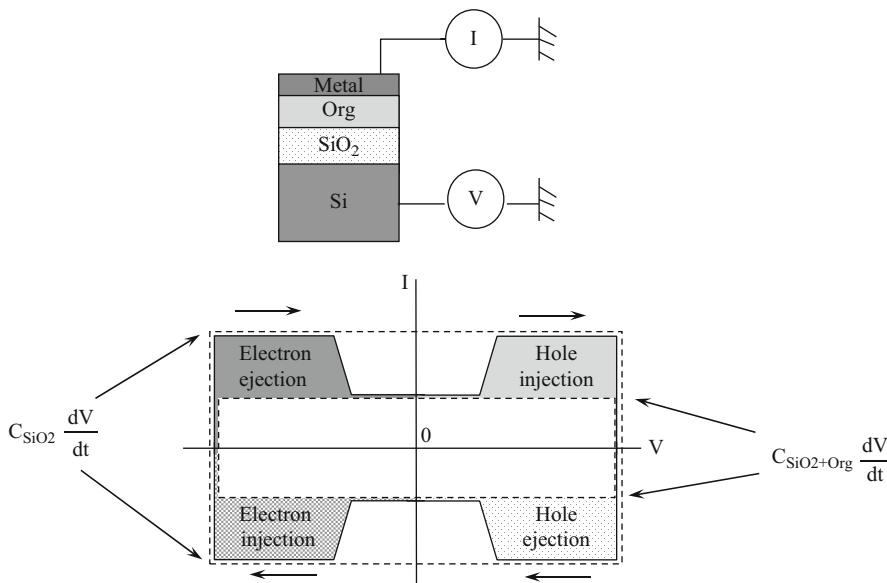


Fig. 17.27 Schematic diagram of displacement current measurement

Scanning of applied voltage started at 0 V. Fluorescence measurements were first obtained at positive-voltage regions and then at negative regions. The voltage scan speed was 0.02 Hz. All fluorescence measurements were carried out in air and at room temperature.

In order to investigate the electrical properties of TTPAE films, displacement current measurements were performed. Since details of displacement current measurements were described in a previous paper [32], only distinctive features are shown here. Figure 17.27 shows a schematic diagram of displacement current measurement. The measured current is expressed by the capacitance and scan speed of the applied voltage. In the simplest case, the organic film behaves as a dielectric and the measured current reflects the capacitance of entire dielectric film, that is, organic and SiO₂ (C_{SiO₂+Org}). As for the donor or acceptor molecules, carrier injection or ejection through Metal/Org interfaces occur. If carrier injection through the Metal/Org interface occurs, the measured current will reflect the capacitance of the SiO₂ (C_{SiO₂}) film. Therefore, the displacement current is sensitive to carrier injection into the organic film.

Figure 17.28 shows the applied voltage dependence of fluorescence in TTPAE film. These data were obtained in the first scan of voltage for positive and negative voltages, respectively. As shown later, large hysteresis was observed in fluorescence quenching. As shown in Fig. 17.28, fluorescence intensity decreases as applied voltage V increases at positive voltages. On the other hand, at negative voltages, no variations according to V are observed. Changes in the fluorescence spectrum

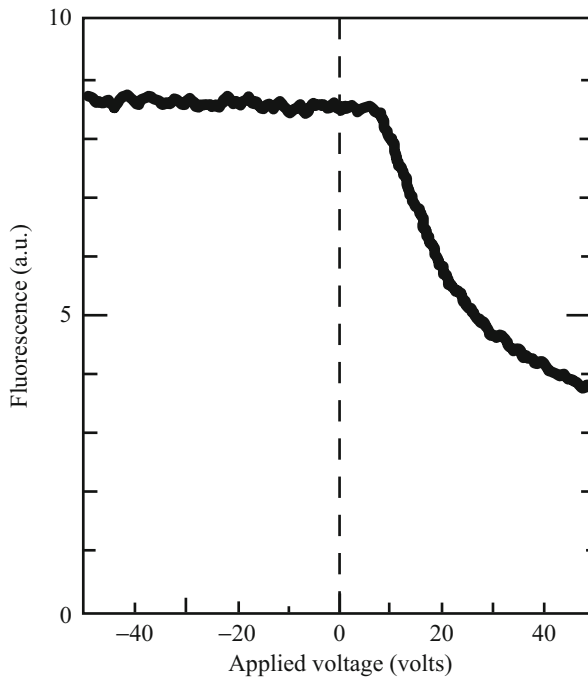


Fig. 17.28 Applied voltage dependence of fluorescence (PL) of Au/TTPAE/SiO₂/Si with TTPAE thickness of 15 nm and SiO₂ thickness of 100 nm. Excitation wavelength, 360 nm. Fluorescence wavelength, 540 nm

and excitation spectrum are shown in Fig. 17.29. It was found that the observed fluorescence quenching did not follow any shift of spectral peaks.

Figure 17.30 shows the displacement current characteristic of a TTPAE film under visible light irradiation. At positive bias voltages, hole injection and ejection were clearly observed, and at negative bias voltages, no carrier injection was observed. These findings are consistent with the fact that TTPAE is an electron donor material. Figure 17.31 shows a comparison between fluorescence measurements and displacement current measurements under UV irradiation. Since both fluorescence variations and displacement currents show large hysteresis especially at negative bias voltages, the results for the first cycle of voltage are shown separately from those for the second and third cycles. At positive bias voltages, fluorescence and current into TTPAE film were observed to vary in the same manner. Both fluorescence variations and displacement currents are reproducible at positive bias voltages. On the other hand, at negative bias voltages, large hysteretic variations were observed in both measurements. On the way to -25 V in the first cycle, no fluorescence change or negative current into the TTPAE film was observed. On the way back to 0 V, a positive current, which corresponded hole injection, and fluorescence quenching were observed at the same voltage. In the second or third

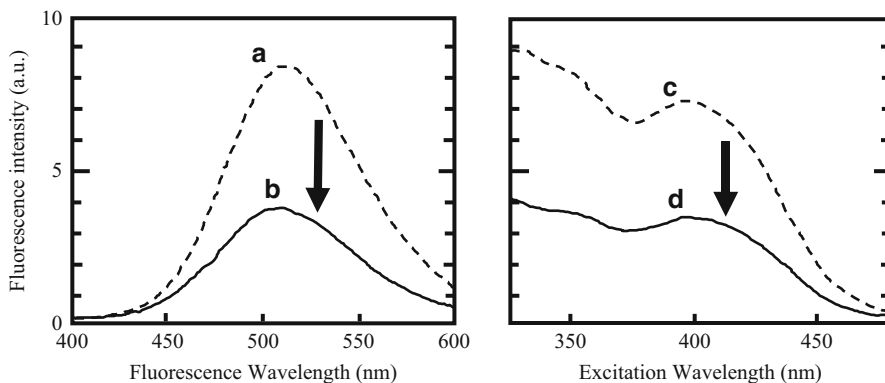


Fig. 17.29 Spectra of Au/TTPAE/SiO₂/Si with TTPAE thickness of 15 nm and SiO₂ thickness of 100 nm: (a) fluorescence spectra with bias voltage of 0 V (*dashed line*), excitation wavelength of 360 nm; (b) fluorescence spectra with bias voltage of +50 V (*solid line*), excitation wavelength of 360 nm; (c) excitation spectra with bias voltage of 0 V (*dashed line*), fluorescence wavelength of 540 nm; and (d) excitation spectra with bias voltage of +50 V (*solid line*), fluorescence wavelength of 540 nm

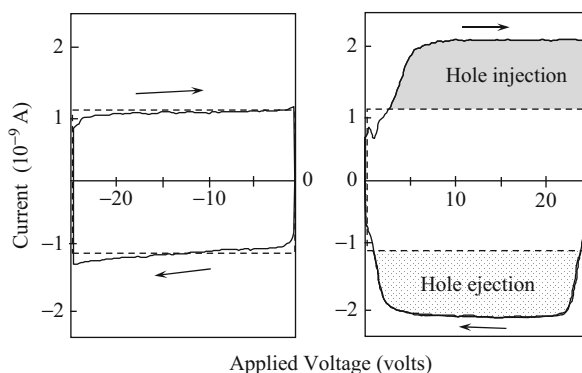


Fig. 17.30 Displacement current diagram of Au/TTPAE/SiO₂/Si with TTPAE thickness of 50 nm and SiO₂ thickness of 50 nm under *white light* irradiation

cycle, two current peaks were observed on the way to -25 V and one peak was observed on the way back to 0 V. The decrease of fluorescence quenching was observed at lower voltages where the first current peak, which corresponded to hole ejection, was observed on the way to -25 V, and no fluorescence quenching was observed at another current peak from -15 to -25 V, which corresponds to electron injection. On the way back to 0 V in the second and third cycle, fluorescence quenching was observed at the same voltage as the current, which corresponded to hole injection, was observed.

Figure 17.32 shows the fluorescence quenching efficiency for various thicknesses of TTPAE films. Fluorescence quenching efficiency increased as the film thickness decreased and had a peak value at a thickness of 15 nm. In the case of films thicker than 15 nm (c), uniform film structures were observed. On the other hand, in the case of thinner films, separated film structures (b) or isolated dot structures (a) were

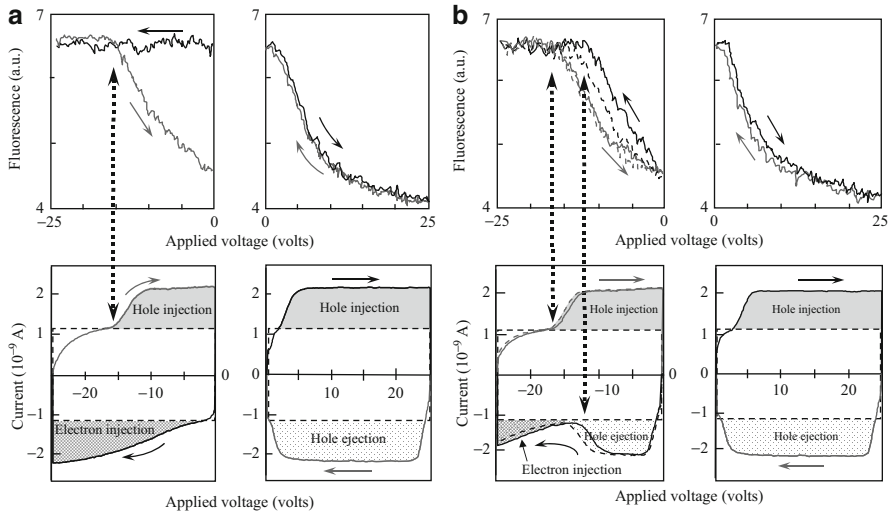
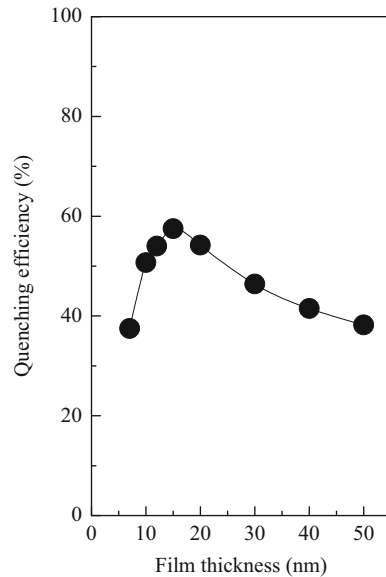


Fig. 17.31 Comparison between applied voltage dependence of fluorescence and displacement current diagram under UV irradiation (excitation wavelength, 360 nm). Sample was Au/TTPAE/SiO₂/Si with TTPAE thickness of 50 nm and SiO₂ thickness of 50 nm. (a) First scan of voltage. (b) Second (*solid line*) and third scans (*dashed line*) of voltage

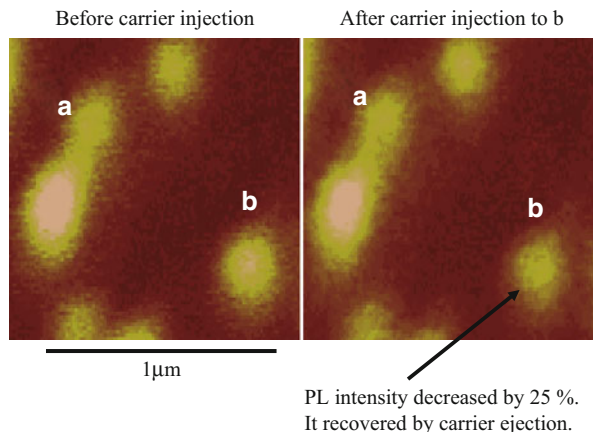
Fig. 17.32 TTPAE film thickness dependence of fluorescence quenching efficiency. Sample was Au/TTPAE/SiO₂/Si with SiO₂ thickness of 100 nm. Excitation wavelength, 360 nm. Fluorescence wavelength, 540 nm



observed. As for the separated structures or the dot structures, the effective thickness of the film was found to be thicker than the case for uniform films.

We directly observed fluorescence quenching for the TTPAE dots by a near-field optical microscope. Charge injection is carried out through contact electrification by

Fig. 17.33 NSOM images of fluorescence intensity reduction caused by charge injection



a gold-coated AFM tip with a positive bias. The charges were found to be very stable for a long time. This phenomenon will be the same as in a fresh silicon memory, where electrons are stored in a floating gate. Injected holes can be extracted by a negatively biased tip. Holes were injected to diamine dots at 3 V. These holes were extracted at -2 V. Therefore, the organic dot structure can be operated as a rewritable memory. However, it takes time to detect surface potential values. Optical readout procedures are required for high-speed scanning. Figure 17.33 shows that fluorescence intensity is reduced for the dot where the charge was injected.

We hypothesize that Coulomb interaction between photoexcited molecules and carriers (holes), as suggested by Deussen et al. in an earlier explanation of the effect of current flow on fluorescence quenching [33], plays an essential role in the fluorescence quenching described here.

17.4 Conclusion

We have shown the circumferential magnetic patterned media with a 40 nm diameter on a 2.5-inch-diameter glass plate. The media were prepared by an artificially assisted self-assembling (AASA) method, which includes simple nano-patterning of land-groove spirals using a nano-imprint and self-assembling of the diblock polymer aligned in the grooves. Magnetic films were etched by ion milling using the nano-dot structures of the diblock polymer as a mask. Fluctuations of size and position of the patterned cell, observed for the present media, should be reduced for the realization of patterned media.

We have also investigated organic dye-patterned media prepared by the AASA method. Fluorescence quenching of TTPAE dots with charge injection applying bias voltages. Displacement current measurements show that the quenching efficiencies depend strongly on the polarities of injected charges and that quenching cannot be explained by the external field-induced exciton dissociation. Charge injection

properties show that the hole injections play an essential role in fluorescence quenching. 60% fluorescence quenching efficiency is achieved. This will be a novel optical storage medium with high contrast and high signal-to-noise ratio.

These nm-scale dot structures should prove to be effective in the application of near-field optics to ultrahigh-density storage media.

Acknowledgements The authors are very grateful to T. Maeda for providing them with the samples of the magnetic films. They also acknowledge useful discussion with N. Kihara, H. Yoda, J. Akiyama, T. Hiraoka, and Y. Yanagita.

References

1. H. Sukeda, H. Saga, H. Nemoto, Y. Itoh, C. Haginoya, T. Matsumoto, *IEEE Trans. Magn.* **37**, 1234 (2001)
2. S.Y. Chou, M.S. Wei, P.R. Krauss, P.B. Fisher, *J. Appl. Phys.* **76**, 6673 (1994)
3. R.L. White, R.M.H. New, R.F.W. Pease, *IEEE Trans. Magn.* **33**, 990 (1997)
4. A. Kikitsu, *J. Magn. Magn. Mater.* **321**, 526 (2009)
5. R.L. White, *J. Magn. Magn. Mater.* **209**, 1 (2000)
6. C.T. Rettner, M.E. Best, B.D. Terris, *IEEE Trans. Magn.* **37**, 1649 (2001)
7. C. Chappert, H. Bernas, J. Ferre, V. Kottler, J.-P. Jamet, Y. Chen, E. Cambri, T. Devolder, F. Rousseaux, V. Mathet, H. Launois, *Science* **280**, 1919 (1998)
8. C.A. Ross, H.I. Smith, T. Savas, M. Schattenburg, M. Farhoud, M. Hwang, M. Walsh, M.C. Abraham, R.J. Ram, *J. Vac. Sci. Technol. B.* **17**, 3168 (1999)
9. B. Cui, W. Wu, L. Kong, X. Sun, S.Y. Chou, *L. Appl. Phys.* **85**, 5534 (1999)
10. S. Zhu, R.J. Gambino, M.H. Rafailovich, J. Sokolov, S.A. Schwarz, R.D. Gomez, *IEEE Trans. Magn.* **33**, 3022 (1997)
11. K. Nielsch, F. Muller, A.-P. Li, U. Gosele, *Adv. Mater.* **12**, 582 (2000)
12. P. Mansky, P. Chaikin, E.L. Thomas, *J. Mater. Sci.* **30**, 1987 (1995)
13. M. Park, C. Harrison, P.M. Chaikin, R.A. Register, D.H. Adamson, *Science* **276**, 1404 (1997)
14. T. Thurn-Albrecht, R. Steiner, J. deRouchey, C.M. Stafford, E. Huang, M. Bal, M.T. Tuominen, C.J. Hawker, T.P. Russell, *Adv. Mater.* **12**, 787 (2000)
15. K. Naito, H. Hieda, M. Sakurai, Y. Kamata, K. Asakawa, *IEEE Trans. Magn.* **38**, 1949 (2002)
16. R.A. Segalman, H. Yokoyama, E.J. Kramer, *Adv. Mater.* **13**, 1152 (2001)
17. M.J. Fasolka, D.J. Harris, A.M. Mayes, M. Yoon, S.G.J. Mochrie, *Phys. Rev. Lett.* **79**, 3018 (1997)
18. I. Bitá, J.K.W. Yang, Y.S. Jung, C.A. Ross, E.L. Thomas, K.K. Berggren, *Science* **321**, 939 (2008)
19. H. Hieda, Y. Yanagita, A. Kikitsu, T. Maeda, K. Naito, *J. Photopolym. Sci. Technol.* **19**, 425 (2006)
20. E. Betzig, J.K. Trautman, R. Wolfe, E.M. Gyorgy, P.L. Finn, M.H. Kryder, C.-H. Chang, *Appl. Phys. Lett.* **61**, 142 (1992)
21. S. Hosaka, T. Shintani, M. Miyamoto, A. Hirotsune, M. Terao, M. Yoshida, S. Honma, S. Kammer, *Thin Solid Films* **273**, 122 (1996)
22. S. Jiang, J. Ichihashi, H. Monobe, M. Fujihira, M. Ohtsu, *Opt. Commun.* **106**, 173 (1994)
23. M. Hamano, M. Irie, *Rev. Laser Eng.* **24**, 1045 (1996, in Japanese)
24. H. Hieda, K. Tanaka, N. Gemma, *J. Appl. Phys.* **40**, 1071 (2001)
25. N. Gemma, H. Hieda, K. Tanaka, S. Egusa, *Jpn. J. Appl. Phys.* **34**, L859 (1995)
26. H. Hieda, K. Tanaka, N. Gemma, *J. Vac. Sci. Technol. B* **14**, 1234 (1996)
27. H. Hieda, K. Tanaka, K. Naito, N. Gemma, *Thin Solid Films* **331**, 152 (1998)
28. A. Sakawa, T. Hiraoka, Annual APS Meeting, March 2000, I33-2
29. K. Asakawa, T. Hiraoka, *Jpn. J. Appl. Phys.* **41**, 6112 (2002)

-
30. W. Si, K. Williams, M. Campo, M. Mao, A. Devasahayam, C.-L. Lee, *J. Appl. Phys.* **97**, 10N901-1 (2005)
 31. K. Naito, M. Sakurai, S. Egusa, *J. Phys. Chem. A* **101**, 2350 (1997)
 32. S. Egusa, N. Gemma, A. Miura, K. Mizushima, M. Azuma, *J. Appl. Phys.* **71**, 2042 (1992)
 33. M. Deussen, M. Scheidler, H. Bassler, *Synth. Met.* **73**, 123 (1995)

Temperature-Induced and Photo-Induced Phase Transition in a Bistable Metal-Cyanide Polymer

18

Hiroko Tokoro and Shin-ichi Ohkoshi

Contents

18.1	Introduction.....	694
18.2	Synthesis of Rubidium Manganese Hexacyanoferrate.....	695
18.3	Crystal Structure of Rubidium Manganese Hexacyanoferrate.....	696
18.4	Temperature-Induced Phase Transition.....	698
18.4.1	Phase Transition Phenomenon in Magnetic Susceptibility.....	698
18.4.2	Change in Electronic State.....	698
18.4.3	Structural Change.....	700
18.4.4	Mechanism.....	701
18.5	Ferromagnetism of the Low-Temperature Phase.....	702
18.5.1	Magnetic Ordering and Heat Capacity.....	702
18.5.2	Entropy and Enthalpy of Magnetic Phase Transition.....	704
18.5.3	Long-Range Magnetic Ordering and Exchange Coupling.....	705
18.5.4	Mechanism of Magnetic Ordering.....	707
18.6	Control of Temperature-Induced Phase Transition.....	708
18.6.1	Huge Thermal Hysteresis Loop and a Hidden Stable Phase.....	708
18.6.2	Thermodynamical Analysis of Thermal Hysteresis Loop.....	710
18.7	Photo-Induced Phase Collapse.....	710
18.7.1	Non-phase Transition Material.....	710
18.7.2	Photo-Induced Structural Transition.....	712
18.7.3	Photo-Induced Phase Transition from a Metastable Phase to a Hidden Stable Phase.....	713
18.8	Photo-Induced Phase Transition at Room Temperature.....	714
18.9	Photomagnetism.....	717
18.9.1	Photo-Induced Demagnetization by One-Shot-Laser-Pulse.....	717
18.9.2	Reversible Photomagnetic Effect.....	719

H. Tokoro (✉) · S. Ohkoshi

Department of Chemistry, School of Science, The University of Tokyo, Tokyo, Japan
e-mail: tokoro@chem.s.u-tokyo.ac.jp; ohkoshi@chem.s.u-tokyo.ac.jp

18.9.3	Photo-Reversible Changes in the IR Spectra and SQUID Measurement.....	719
18.9.4	Magnetic Ordering of the Photo-Induced Phase.....	721
18.9.5	Mechanism of Visible-Light Reversible Photomagnetism.....	723
18.10	Summary.....	724
	References.....	725

Abstract

Studies that are related to thermal-induced phase transition and photo-induced phase transition are important issues in the field of solid state science. Rubidium manganese hexacyanoferrate $\text{RbMn}[\text{Fe}(\text{CN})_6]$, one of the Prussian blue analogs, is a suitable system for observing thermal-induced and photo-induced phase transitions since this compound is a mixed-valence compound that has a strong cooperativity due to the CN ligand bridges. Here, we describe the crystal structure, magnetic properties, thermal-induced phase transition, and photo-induced phase collapse and photomagnetic effect based on photo-induced phase transition of $\text{RbMn}[\text{Fe}(\text{CN})_6]$.

18.1 Introduction

Studies that are related to temperature-induced phase transitions and photo-induced phase transitions are extensively investigated in solid-state chemistry [1–4]. Temperature-induced phase transition phenomena are observed in spin crossover or intramolecular electron transfer. In a spin crossover complex, a transition metal ion can be in either the low-spin or the high-spin state depending on the strength of the ligand field. When the thermal energy is close to the exchange energy that corresponds to the crossover, a spin transition occurs between the two spin states. This phenomenon is observed in octahedral coordinate iron transition metal complexes [5–7]. Charge-transfer phase transitions have been observed in mixed-valence complexes [7–13], for example, $[\text{M}^{\text{III}}_2\text{M}^{\text{II}}\text{O}(\text{O}_2\text{C}_2\text{H}_3)_6\text{L}_3]$ ($\text{M} = \text{Fe}, \text{Mn}$; $\text{L} = \text{H}_2\text{O}, \text{pyridine}$) [12] and $\text{M}(\text{dta})_4\text{I}$ ($\text{M} = \text{Ni}, \text{Pt}$; $\text{dta} = \text{dithioacetato}$) [13]. Charge-transfer phase transitions that accompany spin crossovers have also been reported, for example, $\text{Co}(\text{py}_2\text{X})(3,6\text{-DBQ})_2$ ($\text{X} = \text{O}, \text{S}, \text{Se}$) [14] and $\text{Na}_{0.4}\text{Co}_{1.3}[\text{Fe}(\text{CN})_6] \cdot 4.9\text{H}_2\text{O}$ [15]. A temperature-induced phase transition often accompanies a thermal hysteresis loop, which is related to the cooperativity of the corresponding system. The cooperativity in a metal complex assembly is due to the interaction between a metal ion and lattice strain, for example, an electron-phonon coupling [16], a Jahn-Teller distortion [17], and an elastic interaction [18]. Cyano-bridged metal assemblies such as hexacyanometalate- [4, 19–39] and octacyanometalate-based magnets [40–45] are suitable for observing a thermal phase transition since they are mixed-valence compounds that have a strong cooperativity due to the CN ligand bridges.

To date, several types of photo-induced phase-transition phenomena have been reported, for example, a light-induced crystalline-amorphous transformation in

chalcogenide material [46–48], a light-induced spin-state change on the transition metal ion of a metal complex [3, 49–51], a light-induced charge transfer in donor-accepter stacked molecules [2, 52, 53], light-induced ferromagnetism bimetallic assemblies [36–45], light-induced reversible metal-semiconductor transition in a titanium oxide [54], or light-induced insulator-metal transition in perovskite manganite [55, 56]. Until now, we have demonstrated photomagnetic effects such as photo-induced magnetization and the photo-induced magnetic pole inversion with cyano-bridged bimetallic assemblies [4, 36, 39–45]. One possible method for achieving optical control of magnetization is to change the electron spin state of a magnetic material. For example, if photo-irradiation varies the oxidation numbers of transition metal ions within a magnetic material, its magnetization will be controlled. The bistability of the electronic states is also indispensable for observing photo-induced persistent magnetization since the energy barrier between these bistable states can maintain the photo-produced state even after photo-irradiation is ceased.

From this viewpoint, Prussian blue analogs are an attractive system due to their high T_c values [22]. In particular, Verdaguer et al. reported that $V^{II}[Cr^{III}(CN)]_{0.86} \cdot 2.8H_2O$ exhibits a T_c value of 315 K [24]. Successively, Girolami et al. and Miller et al. reported crystalline $K^IV[Cr^{III}(CN)_6]$ with $T_c = 103^\circ C$ and amorphous $K_{0.058}^I V^{II/III}[Cr^{III}(CN)_6]_{0.79}(SO_4)_{0.058} \cdot 0.93H_2O$ with $T_c = 99^\circ C$ powder, respectively [27, 28]. In multi-metal Prussian blue analogs, the rational design of magnets based on the molecular field theory is possible for the following reasons: (1) metal substitutions induce only small changes in the lattice constant and (2) superexchange interactions are only essentially effective between the nearest neighbor metal ions [25]. For example, we have designed a novel type of magnet that exhibits two compensation temperatures with the system of $(Ni^{II}_{0.22}Mn^{II}_{0.60}Fe^{II}_{0.18})_{1.5}[Cr^{III}(CN)_6] \cdot 7.5H_2O$, that is, the spontaneous magnetization changes sign twice as the temperature is varied [29]. In this study, we show the temperature-induced phase transition and photo-induced phase transition of ferromagnetic $Rb_xMn[Fe(CN)_6]_{(x+2)/3} \cdot zH_2O$ complex.

18.2 Synthesis of Rubidium Manganese Hexacyanoferrate

Preparing method of rubidium manganese hexacyanoferrate, $Rb_xMn[Fe(CN)_6]_{(x+2)/3} \cdot zH_2O$, is as follows: an aqueous solution (0.1 mol dm^{-3}) of $Mn^{II}Cl_2$ with a mixed aqueous solution of $Rb^I Cl$ (1 mol dm^{-3}) and $K_3[Fe^{III}(CN)_6]$ (0.1 mol dm^{-3}) was reacted to yield a precipitate. The precipitate was filtered, dried, and yielded a powdered sample. The prepared compound was a light brown and elemental analyses for Rb, Mn, and Fe indicated that the obtained precipitate had a formula of $RbMn[Fe(CN)_6]$ ($x = 1, z = 0$). The 1:1:1 ratio of Rb:Mn:Fe allowed the Mn ions to coordinate six cyanonitrogens. Consequently, the network does not contain water molecules. Scanning electron microscope (SEM) images

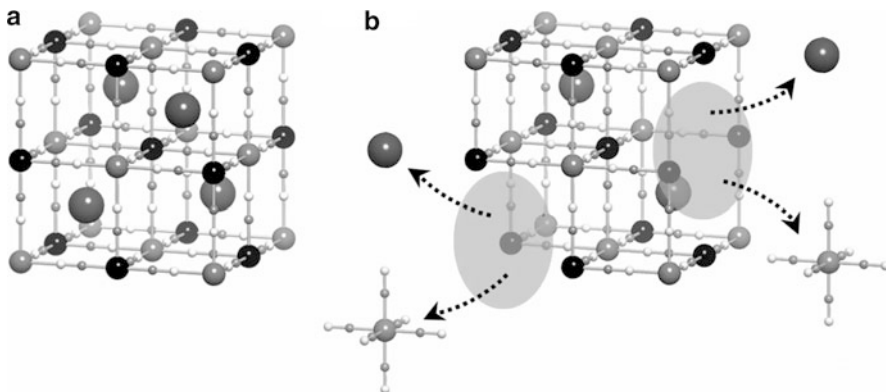


Fig. 18.1 Schematic structures of (a) $\text{Rb}^{\text{I}}\text{Mn}^{\text{II}}[\text{Fe}^{\text{III}}](\text{CN})_6$ and (b) $\text{Rb}_x^{\text{I}}\text{Mn}^{\text{II}}[\text{Fe}^{\text{III}}(\text{CN})_6]_{(x+2)/3} \cdot z\text{H}_2\text{O}$. Large gray circle is Rb^{I} ion, middle black circle is Mn^{II} ion, middle gray circle is Fe^{III} ion, small gray circle is C atom, and small white circle is N atom, respectively. Shadows indicate defects at the $\text{Fe}^{\text{III}}(\text{CN})_6$ sites. Water molecules are omitted for clarity

showed that the obtained powdered sample was composed of cubic microcrystals that were 2.1 ± 1.1 nm. For the sample of different x , the sample was prepared by reacting an aqueous solution (0.1 mol dm^{-3}) of $\text{Mn}^{\text{II}}\text{Cl}_2$ with a mixed aqueous solution of $\text{Rb}^{\text{I}}\text{C}$ ($0.05 - 1 \text{ mol dm}^{-3}$) and $\text{K}_3[\text{Fe}^{\text{III}}(\text{CN})_6]$ (0.1 mol dm^{-3}). The schematic structure of $\text{Rb}_x\text{Mn}[\text{Fe}(\text{CN})_6]_{(x+2)/3} \cdot z\text{H}_2\text{O}$ is shown in Fig. 18.1.

18.3 Crystal Structure of Rubidium Manganese Hexacyanoferrate

To study the crystal structure of rubidium manganese hexacyanoferrate, X-ray single crystal analysis was performed for $\text{Rb}_{0.61}\text{Mn}[\text{Fe}(\text{CN})_6]_{0.87} \cdot 1.7\text{H}_2\text{O}$ [57]. Crystal was obtained by the slow diffusion of MnCl_2 ($7 \times 10^{-3} \text{ mol dm}^{-3}$) dissolved in ethanol into $\text{K}_3[\text{Fe}(\text{CN})_6]$ ($3 \times 10^{-3} \text{ mol dm}^{-3}$) and RbCl ($1.4 \times 10^{-2} \text{ mol dm}^{-3}$) dissolved in water for 3 months. The obtained single crystals measured approximately $0.1 \times 0.1 \times 0.05 \text{ mm}^3$. Elemental analysis of Rb, Mn, and Fe of the single crystal was performed by microscopic fluorescent X-ray analysis (micro-FXA) with an X-ray spot size of $\varphi 10 \mu\text{m}$. The observed ratio of metal ions was $\text{Rb}:\text{Mn}:\text{Fe} = 0.58(\pm 0.04): 1.00(\pm 0.03): 0.86(\pm 0.03)$. The density (d) measured by the flotation method (tetrabromoethane and toluene) showed $d = 1.84(3) \text{ g cm}^{-3}$. These results of micro-FXA and density measurements showed that the formula of the crystal was $\text{Rb}_{0.61}\text{Mn}^{\text{II}}[\text{Fe}^{\text{III}}(\text{CN})_6]_{0.87} \cdot 1.7\text{H}_2\text{O}$. Crystal data was collected on a Rigaku RAXIS RAPID imaging plate area detector with graphite monochromated Mo-K α radiation.

The present single crystal, $\text{Rb}_{0.61}\text{Mn}[\text{Fe}(\text{CN})_6]_{0.87} \cdot 1.7\text{H}_2\text{O}$, contains an intermediate composition value of 0.61 for Rb^+ . This compound has vacancies of

Table 18.1 Crystallographic and refinement data

Formula	Rb _{0.61} Mn[Fe(CN) ₆] _{0.87} · 1.7H ₂ O
FW	322.1
Calculated density/g cm ⁻³	1.829
Temperature/K	93.1
Crystal system	Cubic
Space group	<i>Fm3m</i>
Lattice constants/Å	10.5354(4)
Unit cell volume/Å ³	1169.37(8)
Number of formula units Z	4
Absorption coefficient μ/cm ⁻¹	46.66
Number of measured reflections	20,363
Number of independent reflections	292
Number of refined parameters	15
GOF on F ²	1.270
R1[<i>I</i> > 2σ(<i>I</i>)]	0.0449
wR2	0.1081

0.13 × [Fe(CN)₆] in the cubic lattice to maintain charge neutrality. It is expected that the Mn ion around the vacancy is coordinated to a water molecule (so-called ligand water) and the interstitial sites are occupied by Rb ions or non-coordinated waters (so-called zeolitic water molecules).

X-ray crystallography shows that Rb^I_{0.61}Mn^{II}[Fe^{III}(CN)₆]_{0.87} · 1.7H₂O belongs to the face-centered cubic lattice *Fm3m* with lattice constants of $a = b = c = 10.5354(4)$ Å and $Z = 4$. The crystallographic agreement factors are $R1 = 0.0449$ [$I > 2\sigma(I)$] and $wR2 = 0.1081$ (further details are available from the Fachinformationszentrum Karlsruhe, D-76344 Eggenstein-Leopoldshafen: crysdata@fiz-karlsruhe.de by quoting the depository number CSD 417499). **Table 18.1** shows the crystal data and the refinement details. The asymmetric unit contained manganese atom [Mn(1)] at position 4a (0, 0, 0); iron atom [Fe(1)] at position 4b (1/2, 1/2, 1/2); rubidium atom [Rb(1)] at position 8c (1/4, 1/4, 1/4); cyanonitrogen [N(1)] and cyanocarbon [C(1)] at positions 24e (0.3174(4), 0, 0) and 24e (0.2068(4), 0, 0); respectively, oxygen atoms of the ligand water molecule [O(1)] at a vacancy; and oxygen atoms of zeolitic water molecule [O(2)] at position (0.369(4), 0.369(4), 0.369(4)) and [O(3)] at position (0.327(4), 0.327(4), 0.327(4)). **Figure 18.2** shows the *-plane* of unit cell for the cubic network. All the cyanide groups exist as bridges between Mn(1) and Fe(1) in the three-dimensional framework. Mn(1) is connected to N(1) and O(1) for an average composition of MnN_{0.87}O_{0.13} due to the vacancy of [Fe(CN)₆]³⁻. The interatomic distances of Fe(1)–C(1), C(1)–N(1), and Mn(1)–N(1) [or Mn(1)–O(1)] are 1.9238(1), 1.1652(1), and 2.1786(1) Å, respectively. Rb(1) occupies the center of the interstitial sites, and O(2) and O(3) are distributed in a disordered fashion inside the Mn(1)–N(1) [or Mn(1)–O(1)] interstitial sites of the cubic network as zeolitic waters.

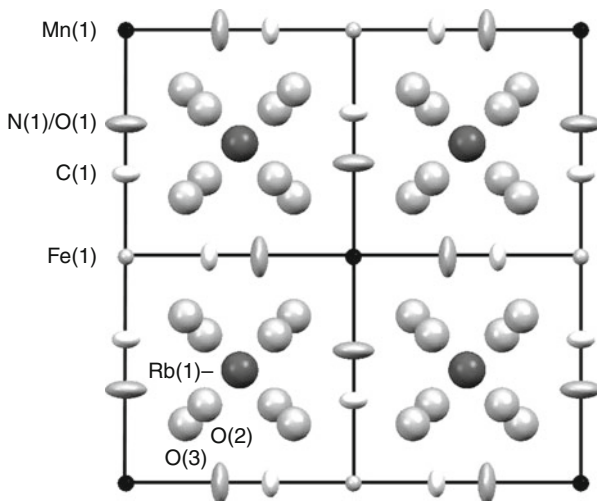


Fig. 18.2 Crystal structure for $\text{Rb}_{0.61}\text{Mn}[\text{Fe}(\text{CN})_6]_{0.87} \cdot 1.7\text{H}_2\text{O}$. The projection in the ab -plane (cubic, $\text{Fm}\bar{3}\text{m}$). Spheres and ellipsoids are drawn at a 50% probability level. All H atoms are omitted for clarity. Occupancies are 0.305 for Rb(1), 1.00 for Mn(1), 0.87 for Fe(1), 0.87 for C(1), 0.87 for N(1), 0.13 for O(1), 0.0528 for O(2), and 0.0624 for O(3), respectively

18.4 Temperature-Induced Phase Transition

18.4.1 Phase Transition Phenomenon in Magnetic Susceptibility

Figure 18.3 shows the product of the molar magnetic susceptibility (χ_M) and the temperature (T) vs. T plots of $\text{RbMn}[\text{Fe}(\text{CN})_6]$. The $\chi_M T$ value in the high-temperature (HT) phase is $4.67 \text{ cm}^3 \text{ K mol}^{-1}$ at 330 K, but cooling the sample at a cooling rate of 0.5 K min^{-1} decreases the $\chi_M T$ value around 235 K and at $T = 180 \text{ K}$ in the low-temperature (LT) phase reaches $3.19 \text{ cm}^3 \text{ K mol}^{-1}$. Conversely, as the sample in the LT phase is warmed at a heating rate of 0.5 K min^{-1} , the $\chi_M T$ value suddenly increases near 285 K and reaches the HT phase value at 325 K. The transition temperatures from HT to LT ($T_{1/2\downarrow}$) and from LT to HT ($T_{1/2\uparrow}$) are 225 and 300 K, respectively, and the width of the thermal hysteresis loop ($\Delta T = T_{1/2\uparrow} - T_{1/2\downarrow}$) is 75 K. This temperature-induced phase transition is repeatedly observed [58, 59].

18.4.2 Change in Electronic State

X-ray photoelectron spectroscopy (XPS) spectra of $\text{K}^1_3[\text{Fe}^{\text{III}}(\text{CN})_6]$, $\text{K}^1_4[\text{Fe}^{\text{II}}(\text{CN})_6]$, and the HT and LT phases were measured. In the HT phase, the Fe- $2\text{P}_{3/2}$ and Mn- $2\text{P}_{3/2}$ electron binding energies are 710.1 and 641.8 eV, respectively, and in

Fig. 18.3 The observed $\chi_M T - T$ plots under 5,000 Oe with the first measurement (black circles), second measurement (red circles), and third measurement (blue circles). The down and up arrows indicate cooling and warming processes, respectively

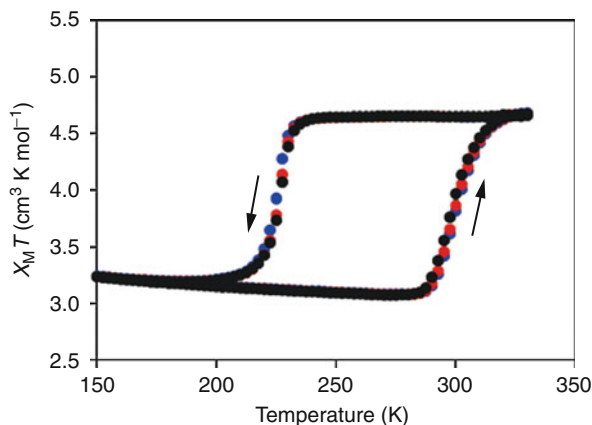
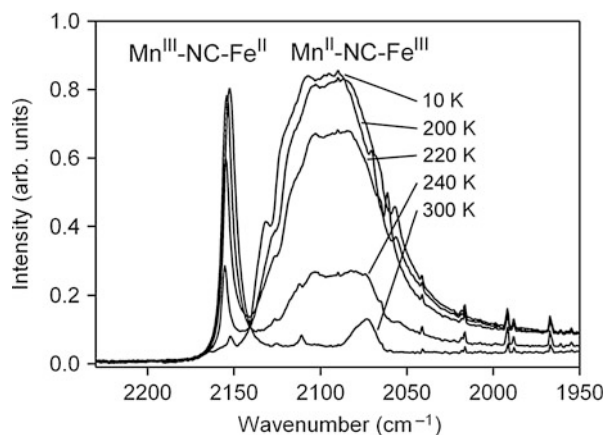


Fig. 18.4 Temperature dependence of the CN stretching frequencies in the IR spectra with cooling process



the LT phase, the Fe-2P_{3/2} and Mn-2P_{3/2} electron binding energies are 708.8 and 642.5 eV, respectively. The observed Fe-2P_{3/2} electron binding energy of 710.1 eV in the HT phase corresponds to that of 710.0 eV for Fe^{III} in K^I₃[Fe^{III}(CN)₆]. In contrast, Fe-2P_{3/2} binding energy of 708.8 eV in the LT phase is close to that of 709.1 eV for Fe^{II} in K^I₄[Fe^{II}(CN)₆]. The shift of the Mn-2P_{3/2} binding energy from the HT to the LT phases suggests that the oxidation number of the Mn ion increases from II to III.

Between 300 and 10 K, the infrared (IR) spectra are recorded. Figure 18.4 shows the CN⁻ stretching frequencies at 300, 240, 220, 200, and 10 K. At 300 K, a sharp CN⁻ peak is observed at 2,152 cm⁻¹ (linewidth=9 cm⁻¹), and as the temperature decreases, the intensity of this peak decreases. Near 220 K, a new broad peak appears at 2,095 cm⁻¹ (linewidth=65/cm⁻¹). These IR changes are in the same temperature range of the phase transition in the $\chi_M T - T$ plots. The CN stretching peak at 2,152 cm⁻¹ in the HT phase is due to the CN ligand bridged to Mn^{II} and Fe^{III}

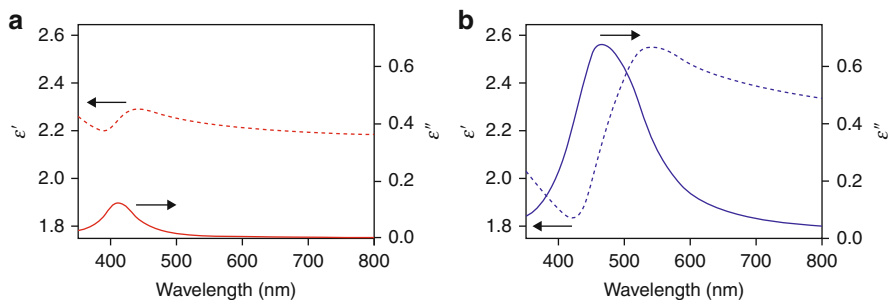


Fig. 18.5 Real (ϵ') and imaginary (ϵ'') parts of the dielectric constant (ϵ) spectra in the (a) HT phase and (b) LT phase. Dotted and solid lines represent the ϵ' and ϵ'' parts, respectively

ions ($\text{Mn}^{\text{II}}\text{-NC-Fe}^{\text{III}}$). In contrast, the broad CN stretching peak at $2,095\text{ cm}^{-1}$ in the LT phase is assigned to the CN ligand bridged to Mn^{III} and Fe^{II} ions ($\text{Mn}^{\text{III}}\text{-NC-Fe}^{\text{II}}$).

These XPS and IR spectra show that valence states for Mn and Fe ions in the HT phase are $\text{Mn}^{\text{II}}(d^5)$ and $\text{Fe}^{\text{III}}(d^5)$, respectively, and those in the LT phase are $\text{Mn}^{\text{III}}(d^4)$ and $\text{Fe}^{\text{II}}(d^6)$, respectively. The drop in the $\chi_{\text{M}}T$ value at $T_{1/2\downarrow}$ implies that the electronic states of the HT and LT phases are $\text{Mn}^{\text{II}}(d^5; S = 5/2) - \text{NC} - \text{Fe}^{\text{III}}(d^5; S = 1/2)$ and $\text{Mn}^{\text{III}}(d^4; S = 2) - \text{NC} - \text{Fe}^{\text{II}}(d^6; S = 0)$, respectively. These assignments are confirmed by Mn and Fe 3p-1s X-ray emission spectroscopy [60] and 1s X-ray absorption spectroscopy [61].

Figure 18.5a shows the real (ϵ') and imaginary (ϵ'') parts of the dielectric constant (ϵ) spectrum of the HT phase at 293 K, measured by spectroscopic ellipsometry [62]. A dispersive-shaped line, which was centered at 410 nm, was observed. In the corresponding position, an absorption-shaped peak was observed in the ϵ'' spectrum at 410 nm with $\epsilon'' = 0.13$. This peak is assigned to the ligand-to-metal charge transfer (LMCT) transition of $[\text{Fe}(\text{CN})_6]^{3-}$ (${}^2\text{T}_{2g} \rightarrow {}^2\text{T}_{1u}, \text{CN}^- \rightarrow \text{Fe}^{\text{III}}$). Figure 18.5b shows the ϵ' and ϵ'' parts of the ϵ spectrum in the LT phase. The LT phase was obtained by slowly cooling to 160 K using N_2 vapor and then measuring ϵ at 275 K. A large dispersive-shaped line, which was centered at 470 nm with a minimum value at 420 nm and a maximum at 540 nm, was observed in the ϵ' spectrum. The corresponding position in the ϵ'' spectrum showed a strong absorption-shaped peak of $\epsilon'' = 0.68$, which is assigned to the metal-to-metal charge transfer (MMCT) band of $\text{Fe}^{\text{II}} \rightarrow \text{Mn}^{\text{III}}$ (more accurately, $\text{CN}_{2px}, \text{CN}_{2py} \rightarrow \text{Mn}_{3dx^2-y^2}, \text{Mn}_{3dz^2}$).

18.4.3 Structural Change

Figure 18.6 shows the powder X-ray diffraction (XRD) patterns as the temperature decreased from 300, 240, and 220 to 160 K. The diffraction pattern of the HT phase is consistent with a face-centered cubic ($F\bar{4}3m$) structure with a lattice constant of 10.533 \AA (at 300 K). As the sample is cooled, the XRD peaks of the HT phase decrease and different peaks appear. The observed XRD pattern in

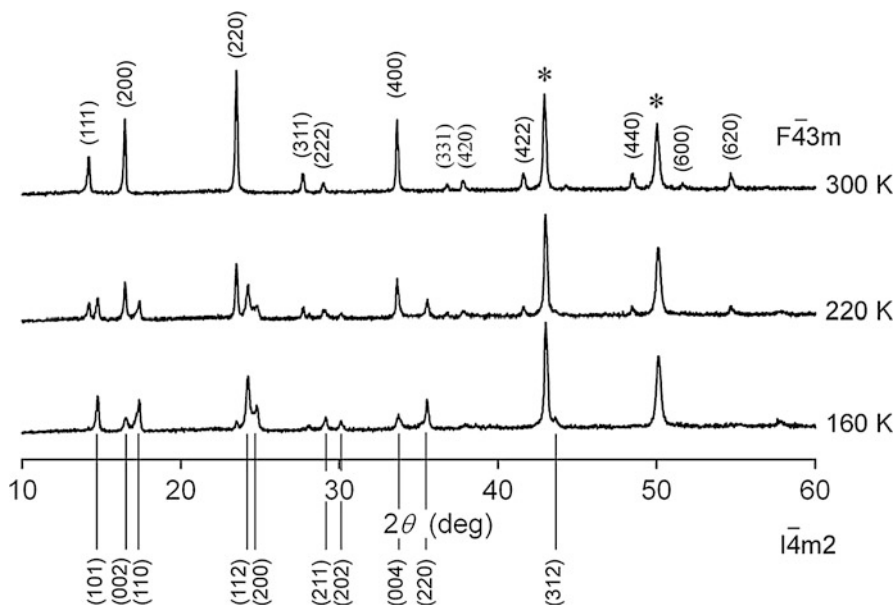


Fig. 18.6 Temperature dependences of XRD spectra (* indicates Cu from the sample holder)

the LT phase shows a tetragonal structure of $I\bar{4}m2$ with $a = b = 7.090 \text{ \AA}$ and $c = 10.520 \text{ \AA}$ (at 160 K), which corresponds to $a = b = 10.026 \text{ \AA}$ and $c = 10.520 \text{ \AA}$ in a cubic lattice. The unit cell volume of $1,169 \text{ \AA}^3$ in the HT phase is reduced about 10% to $11,057 \text{ \AA}^3$ in the LT phase, and warming caused the tetragonal structure to return to the cubic one. This structural change from cubic to tetragonal in the XRD measurement is understood by the Mn^{III} Jahn-Teller transformation of the tetragonally octahedral elongation type (B_{1g} oscillator mode). Synchrotron radiation X-ray powder structural analysis was used to determine the precise bond lengths of the LT phase, that is, two-long and four-short Mn–N bond distances are $2.26(2)$ and $1.89(3) \text{ \AA}$, respectively, and the two-short and four-long Fe–C bond distances are $1.89(2)$ and $2.00(3)$, respectively [63]. Thus, the d -orbital symmetry of both metal ions in the LT phase is D_{4th} (a_{1g} , b_{1g} , b_{2g} , and eg). Therefore, the precise electronic state of LT phase is $Mn^{III}(e_g^2 b_{2g}^1 a_{1g}^1; S = 2)$ -NC- $Fe^{II}(b_{2g}^2 e_g^4; S = 0)$ (Fig. 18.7).

18.4.4 Mechanism

Prussian blue analogs belong to class II mixed-valence compounds. This system is described by two parabolic potential-energy curves due to valence isomers in the nuclear coordinates of the coupled vibrational mode [8–11]. When these two vibronic states interact, the ground state surface has two minima in the vibrational

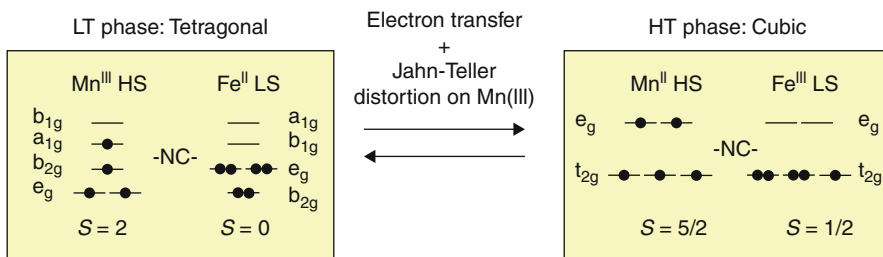


Fig. 18.7 Electronic states of the LT and HT phases

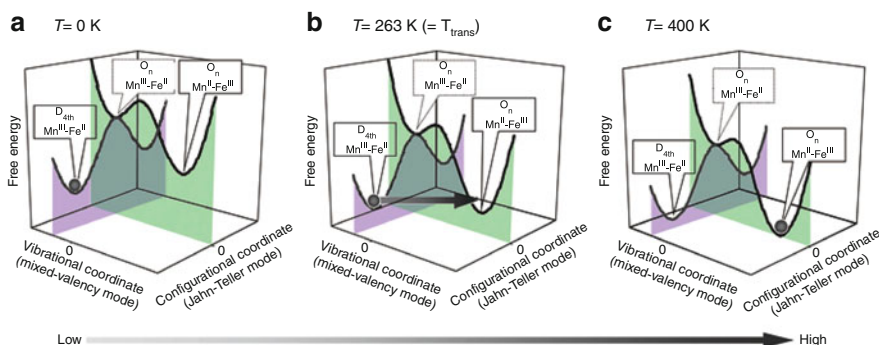


Fig. 18.8 The schematic free energy surfaces of this system in mixed-valence (*black curve*) and Jahn-Teller (*gray curve*) modes: (a) the ground state is $\text{Mn}^{\text{III}}\text{-Fe}^{\text{II}}$ and the metastable state is $\text{Mn}^{\text{II}}\text{-Fe}^{\text{III}}$ at $T = 0$ K, and (b) $T = 263$ K ($=T_{\text{trans}}$) and (c) the ground state is $\text{Mn}^{\text{II}}\text{-Fe}^{\text{III}}$ and meta-stable state is $\text{Mn}^{\text{III}}\text{-Fe}^{\text{II}}$ at $T = 400$ K. *Gray spheres* indicate population

coordinates (Fig. 18.8). In the present system, the $\text{Mn}^{\text{III}}\text{-Fe}^{\text{II}}$ vibronic state is a ground state at $T = 0$ K in the vibrational coordinates (mixed-valency mode) (black curve in Fig. 18.8a). Moreover, in this situation, Mn^{III} causes Jahn-Teller distortion, and then, the energy of the $\text{Mn}^{\text{III}}\text{-Fe}^{\text{II}}$ has two minima described in the configurational coordinates (Jahn-Teller mode) (gray curve in Fig. 18.8a). In the present system, Mn^{III} ion shows an elongation-type Jahn-Teller distortion. These potential surfaces change as the temperature increases, which cause a phase transition.

18.5 Ferromagnetism of the Low-Temperature Phase

18.5.1 Magnetic Ordering and Heat Capacity

When the LT phase is cooled to a very low temperature under an external magnetic field of 10 Oe, it exhibits spontaneous magnetization with a Curie temperature (T_c) of 11.3 K (Fig. 18.9a). The magnetization as a function of the external magnetic

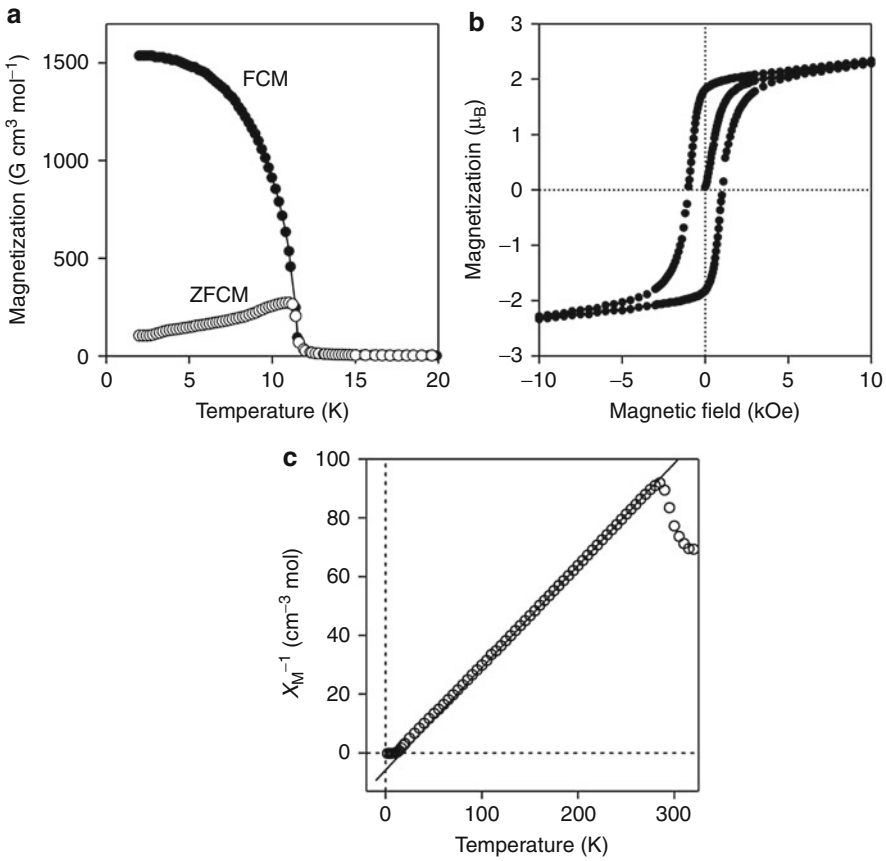


Fig. 18.9 (a) Magnetization vs. temperature plots of the LT phase by SQUID measurement: (●) field-cooled magnetization (FCM) at 10 Oe and (○) zero field-cooled magnetization (ZFCM) at 10 Oe. (b) Magnetic hysteresis loop of the LT phase at 3 K. (c) The observed $\chi_M^{-1} - T$ plots. The data between 150 and 270 K is fitted to Curie-Weiss plots (—)

field at 3 K indicates that the saturated magnetization (M_s) value is $3.6 \mu_B$ and the coercive field (H_c) value is 1,050 G (Fig. 18.9b). The $\chi_M^{-1} - T$ plots of the paramagnetic LT phase show positive Weiss temperatures (Θ) between 12 and 15 K, which are obtained by extrapolating the data in the temperature region of 150–270 K, respectively [64]. In low temperature region, the C_p value gradually increases with temperature and reaches a maximum, $27.1 \text{ J K}^{-1} \text{ mol}^{-1}$ at 11.0 K (denoted here as T_p), as shown in Fig. 18.10a. Then, it drops suddenly to $17.5 \text{ J K}^{-1} \text{ mol}^{-1}$, and increases gradually. The dependence of the C_p values on the external magnetic field is shown in Fig. 18.10b, c, where the T_p peaks shift to a higher temperature as the external magnetic field increases: $T_p = 11.0 \text{ K}$ (=0 T), 11.0 K (0.05 T), 11.2 K (0.10 T), 11.3 K (0.20 T), 11.4 K (0.30 T), 11.5 K (0.50 T), 11.9 K (1.00 T), 13.8 K (2.00 T), and 15.2 K (3.00 T).

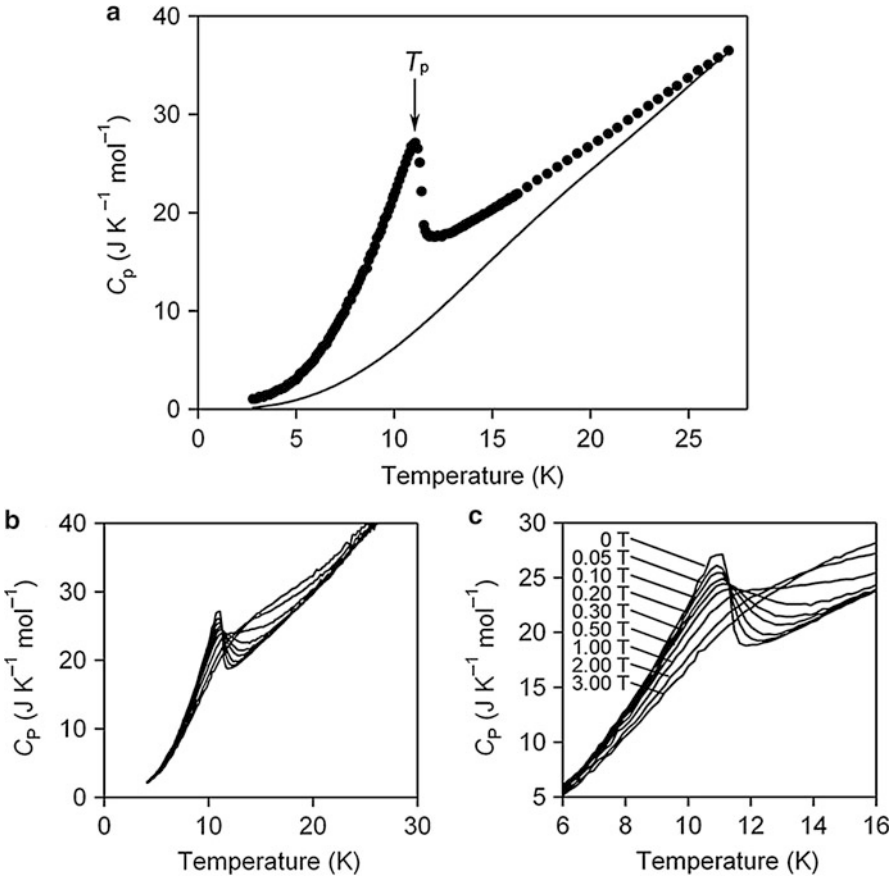


Fig. 18.10 (a) Plots of C_p vs. T in a zero external magnetic field: (●) experimental and (—) derived C_{lat} curve based on Eq. 18.3. (b) Plots of C_p vs. T in the presence of an external magnetic field. (c) Enlarged plots of (b)

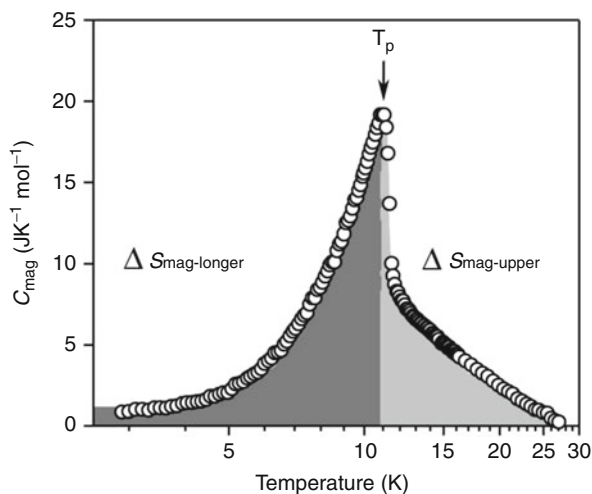
18.5.2 Entropy and Enthalpy of Magnetic Phase Transition

Because $\text{RbMn}[\text{Fe}(\text{CN})_6]$ is an insulating magnetic system, the C_p value is described as a sum of the contributions from lattice vibration, C_{lat} ; short-range magnetic ordering, C_{short} ; and long-range magnetic ordering, C_{long} :

$$C_p = C_{\text{lat}} + C_{\text{short}} + C_{\text{long}}. \quad (18.1)$$

C_{lat} is described by a polynomial function of temperature with odd powers [65]:

$$C_{\text{lat}} = aT^3 + bT^5 + cT^7 + dT^9 + eT^{11} + \dots, \quad (18.2)$$

Fig. 18.11 Plots of C_{mag} vs. $\log T$ 

and C_{short} is described by AT^{-2} [66]. We fitted the C_p data in the region between 15 K ($=1.4 \times T_c$) and 30 K ($=2.7 \times T_c$) by the contributions of $C_{\text{lat}} + C_{\text{short}}$, using analyses reported in other systems [67]. The derived coefficients, including the estimated uncertainties ($\pm 7.4\%$) from the experiment ($\pm 7.0\%$) and curve fitting ($\pm 2.3\%$), are as follows: $a = 8.08 \times 10^{-3} \text{ J K}^{-4} \text{ mol}^{-1}$, $b = -2.10 \times 10^{-5} \text{ J K}^{-6} \text{ mol}^{-1}$, $c = 2.56 \times 10^{-8} \text{ J K}^{-8} \text{ mol}^{-1}$, $d = -1.18 \times 10^{-11} \text{ J K}^{-10} \text{ mol}^{-1}$, and $A = 1,130 \text{ J K mol}^{-1}$. The solid line in Fig. 18.10a shows the C_{lat} curve. The magnetic heat capacity, $C_{\text{mag}} = C_{\text{short}} + C_{\text{long}}$, is obtained by subtracting C_{lat} from C_p , as shown in Fig. 18.11. The magnetic transition entropy, ΔS_{mag} , and enthalpy, ΔH_{mag} , can be obtained from

$$\Delta S_{\text{mag}} = \int_0^T C_{\text{mag}} d \ln T \quad (18.3)$$

and

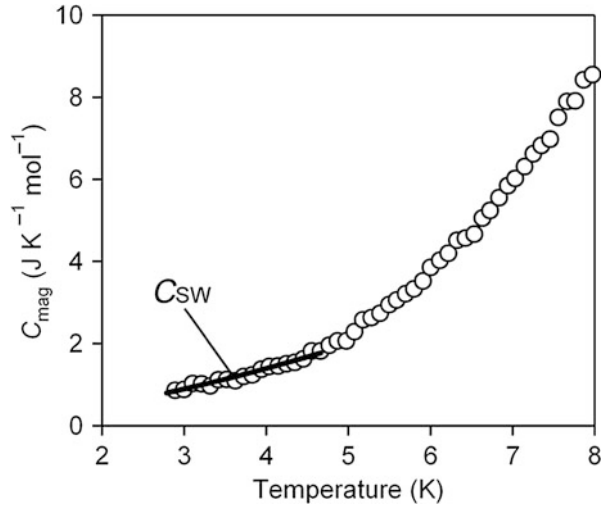
$$\Delta H_{\text{mag}} = \int_0^T C_{\text{mag}} dT. \quad (18.4)$$

The estimated values of ΔS_{mag} and ΔH_{mag} for $\text{Rb}^{\text{I}}\text{Mn}^{\text{III}}[\text{Fe}^{\text{II}}(\text{CN})_6]$ are $11.8 \pm 0.9 \text{ J K}^{-1} \text{ mol}^{-1}$ and $125 \pm 9 \text{ J mol}^{-1}$, respectively.

18.5.3 Long-Range Magnetic Ordering and Exchange Coupling

The T_p value of 11.0 K agrees with the T_c value of 11.3 K derived from a SQUID measurement; then, the anomalous peak at can be ascribed to a magnetic phase transition. The ΔS_{mag} value of $11.8 \pm 0.9 \text{ J K}^{-1} \text{ mol}^{-1}$ is close to the value calculated for the ordering of magnetic spins on the $\text{Mn}^{\text{III}}(\text{S} = 2)$ sites for $\text{Rb}^{\text{I}}\text{Mn}^{\text{III}}[\text{Fe}^{\text{II}}(\text{CN})_6]$

Fig. 18.12 Experimental plots of C_{mag} (\circ) and the C_{SW} curve ($-$) calculated from the spin-wave theory for a 3-D ferromagnet using Eq. 18.6 with $d/n = 1.51$ and $\alpha = 0.17 \text{ J K}^{-5/2} \text{ mol}^{-1}$



given by $R \ln(2S + 1) = 13.4 \text{ J K}^{-1} \text{ mol}^{-1}$, where R is the gas constant. Thus, the origin of this magnetic phase transition is attributed to the long-range magnetic ordering of the Mn^{III} sites.

The dimensionality of magnetic ordering, that is, two- or three-dimensional (2- or 3-D) magnetic lattice, can be determined by the temperature dispersion of ΔS_{mag} . When the value of ΔS_{mag} is divided into two terms, such as the magnetic entropy values below T_p ($\Delta S_{\text{mag-lower}}$) and above T_p ($\Delta S_{\text{mag-upper}}$), the ratio of $\Delta S_{\text{mag-lower}}/\Delta S_{\text{mag}}$ for the magnetic lattices of the 3-D Ising, 2-D Ising, and 3-D Heisenberg types are 81, 44, and 62 %, respectively [68]. The ratio of $\Delta S_{\text{mag-lower}}/\Delta S_{\text{mag}}$ in the present system is 65(3) % (Fig. 18.11). Therefore, in this framework, the magnetic ordering of the LT phase is most likely 3-D Heisenberg-type magnetic ordering.

Analyzing C_{mag} at very low temperatures using the spin-wave theory can determine if the long-range magnetic ordering of a target material is ferromagnetic or antiferromagnetic. The heat capacity due to the spin-wave excitation, C_{SW} , is expressed by Jongh and Miedema [69]

$$C_{\text{SW}} = \alpha T^{\frac{d}{n}}, \quad (18.5)$$

where d stands for the dimensionality of the magnetic lattice and n is the exponent in the dispersion relationship: $n = 1$ for antiferromagnets and $n = 2$ for ferromagnets. We fitted the C_{mag} values in the region between 2.8 and 4.7 K to Eq. 18.5 (Fig. 18.12), and the estimated parameter of d/n is 1.51(11). This d/n value is consistent with that predicted for the magnetic ordering of the LT phase, that is, the 3-D ferromagnet, where $d = 3$ and $d = 2$. The observed shifts in the T_p values of the in-field C_p data, 11.0 K (0 T) \rightarrow 15.2 K (3.00 T), are displayed in Fig. 18.10b, c, which also suggest ferromagnetic character. Since the shift in T_p to

higher temperatures is characteristic of ferromagnetic transitions [70], the trend of the infield C_p values observed in the present study gives direct evidence that the magnetic ordering of the LT phase is ferromagnetic.

This system shows a 3-D Heisenberg-type ferromagnetic ordering, although diamagnetic Fe^{II} is bridged to Mn^{III} in an alternating fashion. The exchange coupling constant, J , of this ferromagnet can be evaluated in the following manner. The α value derived from Eq. 18.5 is related to the J value. In C_{SW} for a 3-D ferromagnet, the coefficient α is described by Ohmae et al. [71]

$$\alpha = \frac{1}{\sqrt{2}} \frac{5R\zeta(5/2)\Gamma(5/2)}{16\pi^2 S^{3/2}} \left(\frac{k_B}{J} \right)^{3/2}, \quad (18.6)$$

where ζ is Riemann's zeta function, Γ is Euler's gamma function, and k_B is the Boltzmann constant. Since the α value obtained from Eq. 18.5 is $0.17(1) \text{ J K}^{-5/2} \text{ mol}^{-1}$, the estimated J value based on Eq. 18.6 is $+0.55(4) \text{ cm}^{-1}$. ΔH_{mag} is also related to the J value in an extension of the molecular-field theory. In this treatment, ΔH_{mag} due to long-range magnetic ordering is expressed by

$$\frac{\Delta H_{\text{mag}}}{R} = \frac{S^2 z J}{k_B}, \quad (18.7)$$

where the number of neighboring magnetic sites, z , is 6 in the present system. The estimated J value from Eq. 18.7, using $\Delta H_{\text{mag}} = 125 \pm 9 \text{ J mol}^{-1}$ is $+0.44(3) \text{ cm}^{-1}$.

18.5.4 Mechanism of Magnetic Ordering

Application of the superexchange interaction mechanism to the present ferromagnetic ordering is difficult since the diamagnetic Fe^{II} sites are connected by paramagnetic Mn^{III} sites. One plausible mechanism is the valence delocalization mechanism, in which ferromagnetic coupling arises from the charge-transfer configuration [72]. Day et al. explained the ferromagnetism of $\text{Fe}^{\text{III}}[\text{Fe}^{\text{II}}(\text{CN})_6]_{0.75} \cdot 3.5\text{H}_2\text{O}$ by the ferromagnetic exchange interaction based on a partial delocalization of the electrons that occupy the $\text{Fe}^{\text{II}}t_{2g}$ orbitals next to the neighboring high-spin Fe^{III} sites. Since Fe^{III} in Prussian blue is replaced with Mn^{III} , the same mechanism is feasible in our system. In fact, an intense intervalence transfer (IT) band of the LT phase has been observed at 540 nm and in the IT band of Prussian blue. In the valence delocalization mechanism, the T_c value is related to the valence delocalization coefficient of c as $T_c \propto c^4$. The c value is given by second-order perturbation theory as

$$c = \sum_{i=2,3} (\langle \psi_0 | H | \psi_i \rangle \langle \psi_1 | H | \psi_i \rangle / (E_1 - E_0)(E_i - E_0)), \quad (18.8)$$

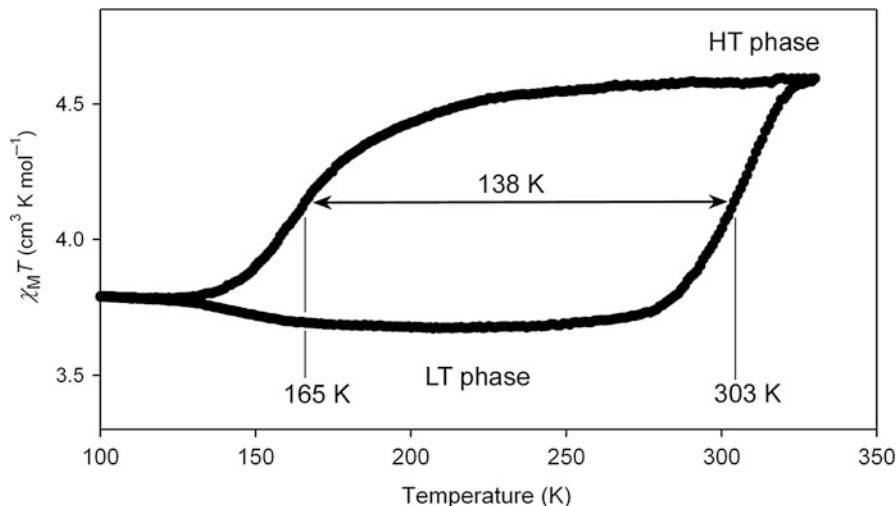


Fig. 18.13 The observed $\chi_M T$ vs. T plots for $\text{Rb}_{0.64}\text{Mn}[\text{Fe}(\text{CN})_6]_{0.88} \cdot 1.7\text{H}_2\text{O}$ under 5,000 Oe with cooling and warming by $\pm 0.5 \text{ K min}^{-1}$

where ψ_0 , ψ_1 , ψ_2 , and ψ_3 are the ground (pure $\text{Mn}^{\text{III}}\text{--Fe}^{\text{II}}$) state and the charge-transfer configurations of $\text{Fe}^{\text{II}} \rightarrow \text{Mn}^{\text{III}}$, $\text{Fe}^{\text{II}} \rightarrow \text{CN}$, and $\text{CN} \rightarrow \text{Mn}^{\text{III}}$, respectively, and $E_0 - E_3$ are their energies. Mixing these excited charge-transfer configurations with the ground state causes the ferromagnetic exchange coupling. The J value of $\approx +0.5 \text{ cm}^{-1}$ in the present system is three times larger than that of $+1.5 \text{ cm}^{-1}$ in Prussian blue. This large J value means that $\text{Rb}^{\text{I}}\text{Mn}^{\text{III}}[\text{Fe}^{\text{II}}(\text{CN})_6]$ has a large c value. Namely, the electrons on the Fe^{II} site are delocalized to the Mn^{III} site.

18.6 Control of Temperature-Induced Phase Transition

18.6.1 Huge Thermal Hysteresis Loop and a Hidden Stable Phase

$\text{Rb}_{0.64}\text{Mn}[\text{Fe}(\text{CN})_6]_{0.88} \cdot 1.7\text{H}_2\text{O}$ was prepared by reacting an aqueous solution (0.1 mol dm^{-3}) of MnCl_2 with a mixed aqueous solution of RbCl (1.0 mol dm^{-3}) and $\text{K}_3[\text{Fe}(\text{CN})_6]$ (0.1 mol dm^{-3}). The mixed solution was stirred for 5 min and the precipitate was filtered, yielding a light brown powder. The SEM image indicates that the precipitate is rectangular with the size of $0.3 \pm 0.1 \mu\text{m}$. The IR peak is observed at $2,153 \text{ cm}^{-1}$ at 300 K, which is assigned to the CN group of $\text{Fe}^{\text{III}}\text{--NC--Mn}^{\text{II}}$, that is, the electronic state of the prepared compound is $\text{Rb}^{\text{I}}_{0.64}\text{Mn}^{\text{II}}[\text{Fe}^{\text{II}}(\text{CN})_6]_{0.88} \cdot 1.7\text{H}_2\text{O}$.

The magnetic properties were measured using a SQUID magnetometer. Figure 18.13 shows the product of the $\chi_M T$ vs. T plots. The $\chi_M T$ value decreases

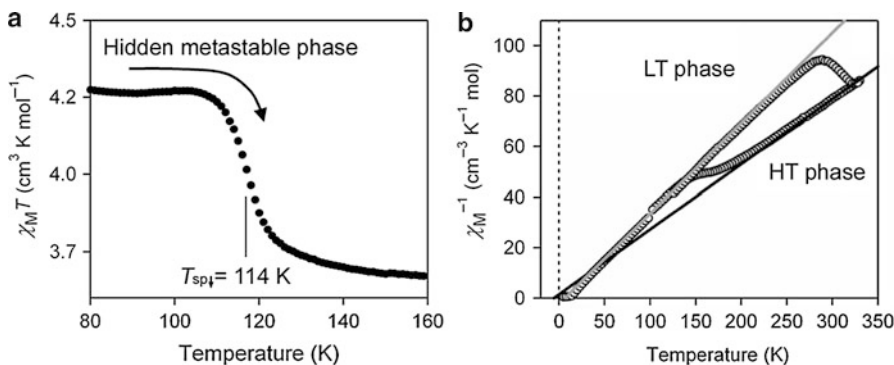


Fig. 18.14 (a) The observed $\chi_M T$ vs. T plots for $\text{Rb}_{0.64}\text{Mn}[\text{Fe}(\text{CN})_6]_{0.88} \cdot 1.7\text{H}_2\text{O}$ under 5,000 Oe with warming by $+0.1 \text{ K min}^{-1}$ after rapid cooling. (b) The observed χ_M^{-1} vs. T plots, and the χ_M^{-1} vs. T curves of the HT (black) and the LT (gray) phases, fitted by Curie-Weiss law

around 165 K ($=T_{1/2\downarrow}$) as the sample is cooled at a cooling rate of -0.5 K min^{-1} . Conversely, as the sample is warmed at a warming rate of $+0.5 \text{ K min}^{-1}$, the $\chi_M T$ value increases around 303 ($=T_{1/2\uparrow}$) and returns to the initial value. The thermal hysteresis value ($\Delta T \equiv T_{1/2\uparrow} - T_{1/2\downarrow}$) is surprisingly large, 138 K. In addition, the χ_M value of the rapidly cooled sample, that is, the sample placed directly into a sample chamber at 10 K, was measured. The rapidly cooled sample shows a high $\chi_M T$ value even at low temperature (hereafter called the hidden stable phase), which nearly corresponds to the value extrapolated from the HT phase, and then relaxes to the $\chi_M T$ value of low-temperature (LT) phase around 114 K ($=T_{\text{SP}\downarrow}$) (Fig. 18.14a). Since the χ_M^{-1} vs. T plots of the HT and LT phases are nearly linear as a function of T , these plots are fitted by the Curie-Weiss law and the Weiss temperatures of the HT and LT phases, which are estimated to be -6 and $+7$ K, respectively (Fig. 18.14b) [73].

To investigate the electronic state of the LT phase, the temperature dependence of the CN stretching frequencies in the IR spectrum was measured. As the temperature decreases, the intensity of the $\text{Mn}^{\text{II}}-\text{NC}-\text{Fe}^{\text{III}}$ peak at $2,153 \text{ cm}^{-1}$ decreases and a new broad peak appears between 2,080 and 2,140 (peak top: $2,108 \text{ cm}^{-1}$), which is assigned to the CN group of $\text{Mn}^{\text{II}}-\text{NC}-\text{Fe}^{\text{II}}$. From the analysis of the conversion in the IR spectra, the electronic state of the LT phase is determined to be $\text{Rb}^{\text{I}}_{0.64}\text{Mn}^{\text{II}}_{0.40}\text{Mn}^{\text{III}}_{0.60}[\text{Fe}^{\text{II}}(\text{CN})_6]_{0.60}[\text{Fe}^{\text{III}}(\text{CN})_6]_{0.28} \cdot 1.7\text{H}_2\text{O}$. The XRD pattern of the sample at 300 K shows a cubic crystal (Fm $\bar{3}$ m) with a lattice constant of $a = 10.535(6) \text{ \AA}$. As the temperature decreases, different XRD patterns due to the LT phase appear near $T_{1/2\downarrow}$. The observed XRD pattern in the LT phase is assigned to an orthorhombic crystal structure (F222) with lattice constants of $a = 10.261(16)$, $b = 10.044(10)$, and $c = 10.567(16) \text{ \AA}$. This distorted crystal structure is ascribed to the Jahn-Teller effect on the produced Mn^{III} sites.

18.6.2 Thermodynamical Analysis of Thermal Hysteresis Loop

The fractions (α) of the temperature-induced phase transition of $\Delta T = 138$ K are estimated as shown in Fig. 18.15a using the extrapolation curves of vs. χ_M^{-1} plots of the HT and LT phases. As a reference, χ_M^{-1} vs. T of $\text{RbMn}[\text{Fe}(\text{CN})_6]$ ($T_{1/2\downarrow} = 231$ K, $T_{1/2\uparrow} = 304$ K, and $\Delta T = 73$ K) from our previous work [58] is also shown in Fig. 18.15b. These thermal hysteresis loops are analyzed based on SD model [74]. The Gibbs free energy G of the system is described by $G = \alpha\Delta H + \gamma\alpha(1 - \alpha) + T\{R[\alpha\ln\alpha + (1 - \alpha)\ln(1 - \alpha)] - \alpha\Delta S\}$, taking G of the LT phase as the origin of the energies, where α is the fraction of the HT phase, ΔH is the transition enthalpy, ΔS is the transition entropy, R is the gas constant, and the γ is an interaction parameter as a function of temperature, $\gamma = \gamma_a + \gamma_b T$ [74, 75]. Experimental heat capacity measurements indicate that the ΔH and ΔS values of $\text{RbMn}[\text{Fe}(\text{CN})_6]$ are $\Delta H = 1.7$ kJ mol $^{-1}$ and $\Delta S = 6.0$ J K $^{-1}$, respectively [58, 59]. When these thermodynamic parameters are used, the thermal hysteresis loops of $\text{Rb}_{0.64}\text{Mn}[\text{Fe}(\text{CN})_6]_{0.88} \cdot 1.7\text{H}_2\text{O}$ and $\text{RbMn}[\text{Fe}(\text{CN})_6]$ are well reproduced with the parameters of $(\Delta H, \Delta S, \gamma_a, \gamma_b) = (1.24$ kJ mol $^{-1}$, 4.54 J K $^{-1}$ mol $^{-1}$, 20.1 kJ mol $^{-1}$, 12.0 J K $^{-1}$ mol $^{-1})$ and $(\Delta H, \Delta S, \gamma_a, \gamma_b) = (1.68$ kJ mol $^{-1}$, 6.0 J K $^{-1}$ mol $^{-1}$, 20.5 kJ mol $^{-1}$, 11.9 J K $^{-1}$ mol $^{-1})$, respectively (Fig. 18.15(a2), (a3), black lines). In addition, $\text{Rb}_{0.64}\text{Mn}[\text{Fe}(\text{CN})_6]_{0.88} \cdot 1.7\text{H}_2\text{O}$ shows that a hidden stable phase exists at low temperature under thermal equilibrium condition (Fig. 18.15(a2), gray line). In this low temperature region, a local energy minimum exists at $\alpha = 0.85$ – 0.9 and relaxes to LT phase at 111 K (Fig. 18.15(a3), gray circles), which well reproduces the experimental data (Fig. 18.15(a1), gray circles). In contrast, both the calculated and experimental data of $\text{RbMn}[\text{Fe}(\text{CN})_6]$ indicate that this hidden stable phase does not exist (Fig. 18.15b). These results suggest that the observed phase in $\text{Rb}_{0.64}\text{Mn}[\text{Fe}(\text{CN})_6]_{0.88} \cdot 1.7\text{H}_2\text{O}$ is a hidden stable state of HT phase under thermal equilibrium condition and is not a supercooled phase under nonequilibrium condition. Furthermore, we calculated the α vs. T plots with various parameters and thus concluded that only the system showing a large thermal hysteresis loop produces the hidden stable phase under thermal equilibrium condition.

18.7 Photo-Induced Phase Collapse

18.7.1 Non-phase Transition Material

$\text{Rb}_{0.43}\text{Mn}[\text{Fe}(\text{CN})_6]_{0.81} \cdot 3\text{H}_2\text{O}$ was prepared by reacting an aqueous solution (0.1 mol dm $^{-3}$) of MnCl_2 with a mixed aqueous solution of RbCl (0.05 mol dm $^{-3}$) and $\text{K}_3[\text{Fe}(\text{CN})_6]$ (0.1 mol dm $^{-3}$). The temperature dependence of the magnetic susceptibility of the initial $\text{Mn}^{\text{II}} - \text{Fe}^{\text{III}}$ phase was measured using a SQUID magnetometer, and Fig. 18.16 plots the product of the $\chi_M T$ vs. T at a very slow cooling rate of -0.05 K min $^{-1}$. In the $\chi_M T - T$ plots, $\chi_M T$ remained nearly constant, corresponding to the sum of Mn^{II} ($S = 5/2$) and Fe^{III} ($S = 1/2$).

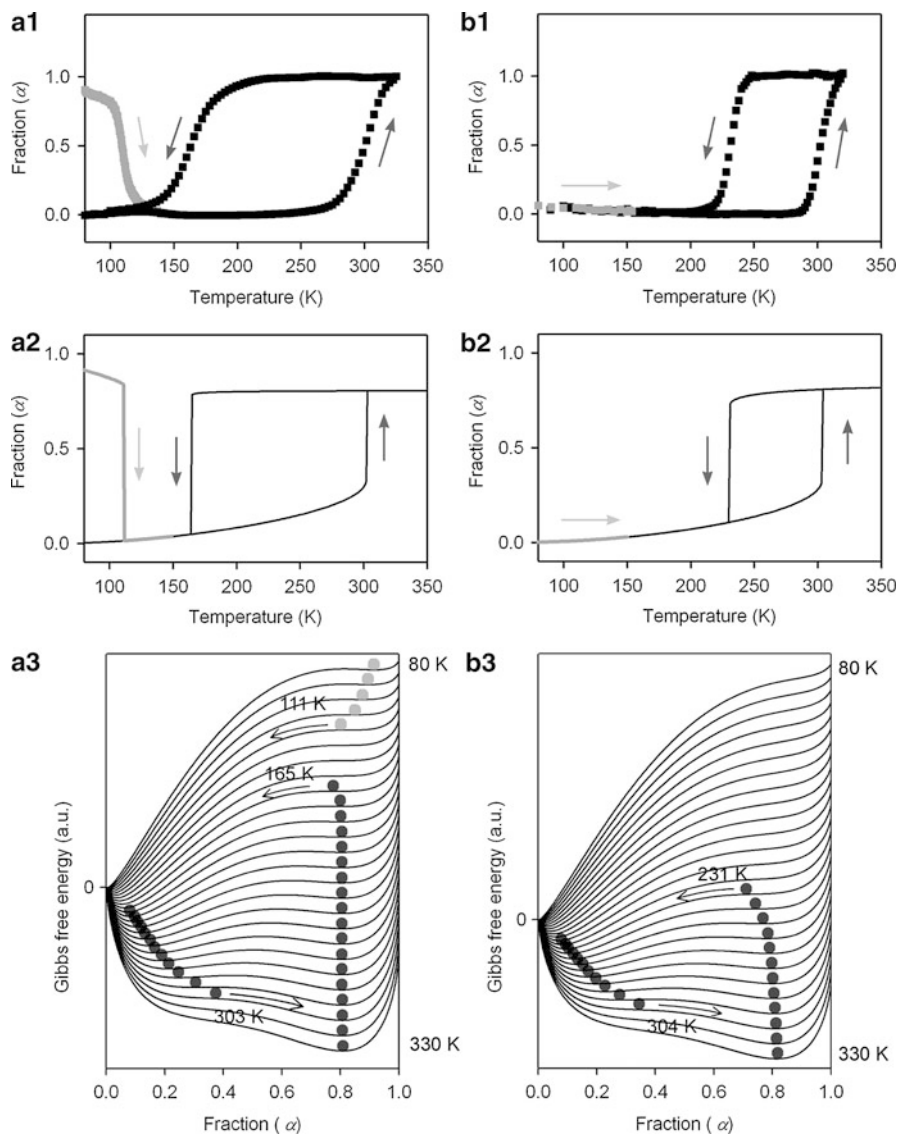
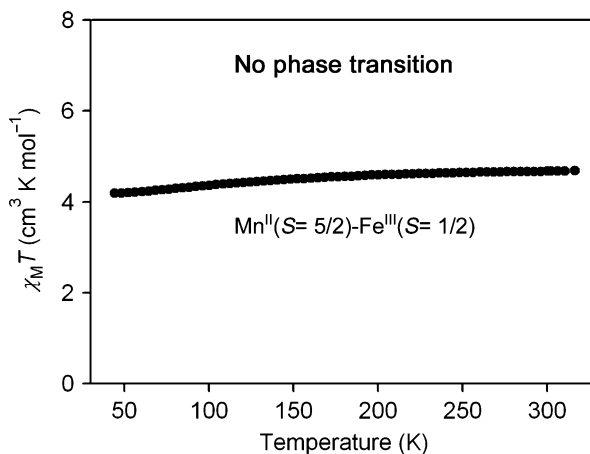


Fig. 18.15 The observed α vs. T plots of **(a1)** $\text{Rb}_{0.64}\text{Mn}[\text{Fe}(\text{CN})_6]_{0.88} \cdot 1.7\text{H}_2\text{O}$ and **(b1)** $\text{RbMn}[\text{Fe}(\text{CN})_6]$ from Ref. [58] where the *gray circles* show the rapidly cooled sample upon warming. Calculated thermal hysteresis loops of **(a2)** $\text{Rb}_{0.64}\text{Mn}[\text{Fe}(\text{CN})_6]_{0.88} \cdot 1.7\text{H}_2\text{O}$ and **(b2)** $\text{RbMn}[\text{Fe}(\text{CN})_6]$. Temperature dependence of calculated vs. curves between 80 and 330 K with 10 K interval for **(a3)** $\text{Rb}_{0.64}\text{Mn}[\text{Fe}(\text{CN})_6]_{0.88} \cdot 1.7\text{H}_2\text{O}$ and **(b3)** $\text{RbMn}[\text{Fe}(\text{CN})_6]$. The *circles* indicate the thermal populations. The *black* and *gray circles* indicate the temperature-induced phase transition and the relaxation, respectively

Fig. 18.16 The observed $\chi_M T$ vs. T plots for $\text{Rb}_{0.43}\text{Mn}[\text{Fe}(\text{CN})_6]_{0.81} \cdot 3\text{H}_2\text{O}$ under 5,000 Oe



Variable temperature IR spectra also showed that the CN stretching frequency peak due to $\text{Mn}^{\text{II}} - \text{NC} - \text{Fe}^{\text{III}}$ is maintained down to low temperature. The XRD pattern at 300 K confirmed that the crystal structure is face-centered cubic (space group: $\text{Fm}\bar{3}\text{m}$) with a lattice constant of $a = 10.473(9) \text{ \AA}$. In the temperature range between 300 and 20 K, the lattice constant was almost constant, that is, $a = 10.493(9) \text{ \AA}$ at 20 K. These results indicate that a temperature-induced charge-transfer phase transition does not occur in the present material [76]. In spectroscopic ellipsometry, an optical resonance due to the ligand-to-metal charge transfer (LMCT) transition on $[\text{Fe}(\text{CN})_6]^{3-}$ was observed at 410 nm.

18.7.2 Photo-Induced Structural Transition

Since $\text{Rb}_{0.43}\text{Mn}^{\text{II}}[\text{Fe}^{\text{III}}(\text{CN})_6]_{0.81} \cdot 3\text{H}_2\text{O}$ has absorption at 410 nm, we irradiated the sample in XRD equipment with blue light ($410 \pm 25 \text{ nm}$, 20 mW cm^{-2}) using a filtered Xe lamp. Upon blue-light irradiation, the XRD peaks of the $\text{Mn}^{\text{II}}-\text{Fe}^{\text{III}}$ phase decreased, and new XRD peaks appeared as shown in Fig. 18.17. The new XRD pattern of the PG phase was assigned to a face-centered cubic structure of $\text{Fm}\bar{3}\text{m}$ with $a = 10.099(3) \text{ \AA}$. When the XRD pattern due to the PG phase was cooled to 20 K and then warmed above room temperature, it was maintained over a wide temperature range, but at 310 K, the XRD pattern was perfectly restored to the original XRD pattern of the initial $\text{Mn}^{\text{II}}-\text{Fe}^{\text{III}}$ phase (Fig. 18.18a). The photoconversion efficiency depended on the irradiation temperature as shown in Fig. 18.18b, that is, 0% (20 K), 45% (100 K), 66% (140 K), 3% (180 K), 6% (220 K), and 0% (300 K) by blue light. To investigate the electronic state of the PG phase, the IR spectra after light irradiation were measured at 140 K. Upon irradiation, the $\text{Mn}^{\text{II}}-\text{NC}-\text{Fe}^{\text{III}}$ peak at $2,153 \text{ cm}^{-1}$ decreased and a broad peak appeared at $2,095 \text{ cm}^{-1}$, which corresponds to the CN stretching frequency of

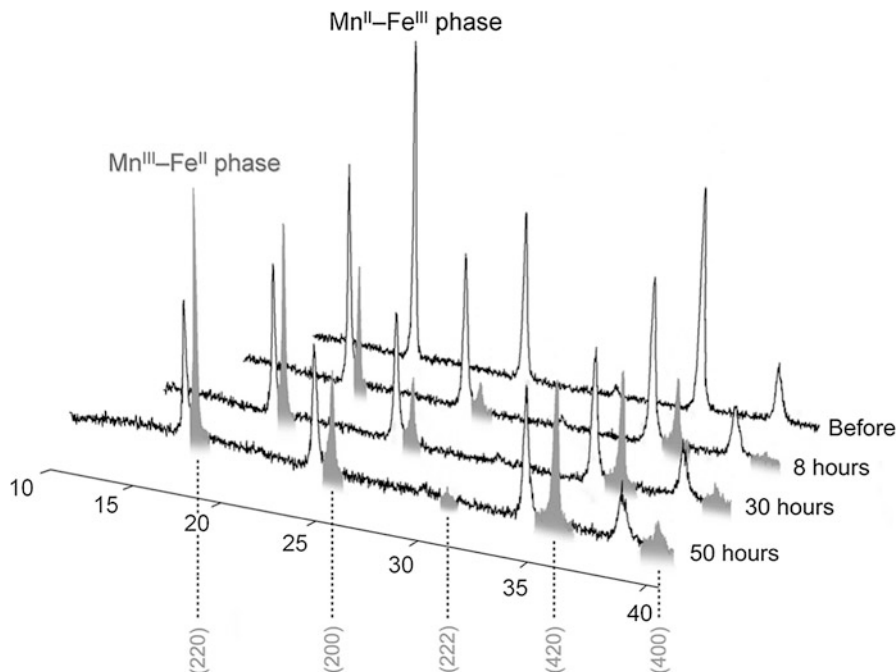


Fig. 18.17 Photo-induced phase collapse in $\text{Rb}_{0.43}\text{Mn}[\text{Fe}(\text{CN})_6]_{0.81} \cdot 3\text{H}_2\text{O}$ by blue-light irradiation. XRD patterns at 140 K before and after blue-light irradiation

$\text{Mn}^{\text{III}}\text{-NC-Fe}^{\text{II}}$. Hence, the observed photo-induced phase collapse is caused by the charge-transfer phase transition from the $\text{Mn}^{\text{II}}\text{-Fe}^{\text{III}}$ phase to the $\text{Mn}^{\text{III}}\text{-Fe}^{\text{II}}$ phase.

18.7.3 Photo-Induced Phase Transition from a Metastable Phase to a Hidden Stable Phase

To understand the mechanism of the observed photo-induced phase transition, we calculated the Gibbs free energy vs. the $\text{Mn}^{\text{II}}\text{-Fe}^{\text{III}}$ fraction for $\text{Rb}_{0.43}\text{Mn}[\text{Fe}(\text{CN})_6]_{0.81} \cdot 3\text{H}_2\text{O}$ using the Slichter and Drickamer mean-field model [74], described by $G = \alpha\Delta H + \gamma\alpha(1-\alpha) + T\{R[\alpha\ln\alpha + (1-\alpha)\ln(1-\alpha)] - \alpha\Delta S\}$, mentioned in Sect. 18.6.2. The thermodynamical parameters for the calculation were estimated by extrapolating our previous data. In the entire temperature range, a free-energy barrier existed between the mainly $\text{Mn}^{\text{II}}\text{-Fe}^{\text{III}}$ phase and the mainly $\text{Mn}^{\text{III}}\text{-Fe}^{\text{II}}$ phase, as shown in Fig. 18.19a. Since the material synthesis was carried out at room temperature and produced the $\text{Mn}^{\text{II}}\text{-Fe}^{\text{III}}$ phase, the $\text{Mn}^{\text{II}}\text{-Fe}^{\text{III}}$ phase is expected to be maintained in the entire temperature range as shown in Fig. 18.19a (dark gray circles). This calculation well explains the observed temperature dependence in $\text{Rb}_{0.43}\text{Mn}[\text{Fe}(\text{CN})_6]_{0.81} \cdot 3\text{H}_2\text{O}$, which does not exhibit a thermal phase transition.

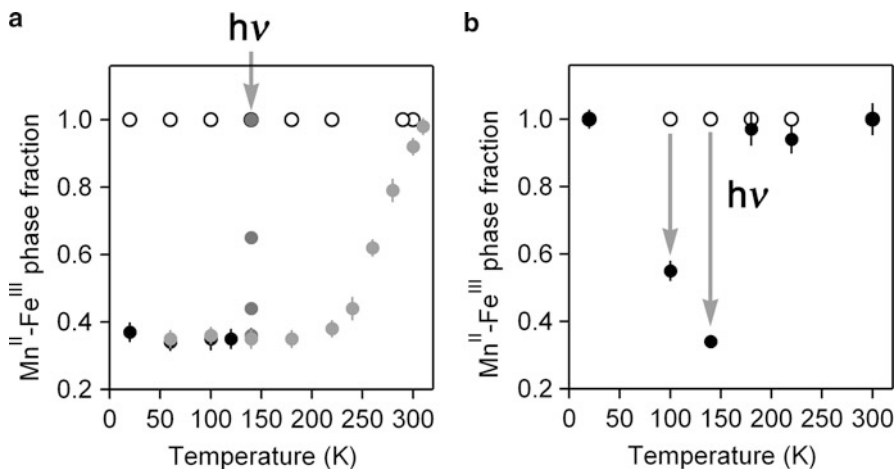


Fig. 18.18 (a) Temperature dependence of the Mn^{II}-Fe^{III} phase fraction before irradiation (*open circles*), during light irradiation at 140 K (*dark gray circles*), cooling process after irradiation (140 K → 20 K) (*black circles*), and warming process (20 K → 310 K) (*gray circles*). (b) Irradiation temperature dependence of the Mn^{II}-Fe^{III} phase fraction before (*open circles*) and after (*black circles*) light irradiation for 50 h (20 mW cm⁻²)

At the same time, this calculation predicts the existence of a hidden stable phase, the Mn^{III}-Fe^{II} phase (Fig. 18.19a, light gray circles). Its calculated temperature dependence (Fig. 18.19b, lower, light gray curve) corresponds well to the observed temperature dependence in Fig. 18.18a.

We thus conclude that the present photo-induced phase collapse is caused by a phase transition from a thermodynamically metastable Mn^{II}-Fe^{III} phase to a Mn^{III}-Fe^{II} true stable phase though the excited state of LMCT (CN⁻ → Fe^{III}), which is excited by blue-light irradiation (Fig. 18.19b, upper).

18.8 Photo-Induced Phase Transition at Room Temperature

The photo-induced effect in the paramagnetic region was investigated with Rb_{0.97}Mn[Fe(CN)₆]_{0.99} · 0.2H₂O using IR spectroscopy [77, 78]. A pulsed Nd³⁺; YAG laser ($\lambda = 532$ nm; pulse width: 6 ns) was used. The $\chi_M T - T$ plots showed that Rb_{0.97}Mn[Fe(CN)₆]_{0.99} · 0.2H₂O exhibited a temperature-induced phase transition (Fig. 18.20). The $T_{1/2\downarrow}$ and $T_{1/2\uparrow}$ were 220 and 314 K, respectively.

Figure 18.21 shows the changes in the IR spectra before and after a one-shot-laser-pulse irradiation at 295 K, which is a temperature inside the thermal hysteresis loop. A one-shot-laser-pulse irradiation changed the IR spectrum of the LT phase to that of the HT phase. The IR spectrum of the irradiated sample returned to that of the initial LT phase by cooling (295 K → 77 K → 295 K). Figure 18.22a shows the conversion fraction as a function of laser power density at 295, 280, 260,

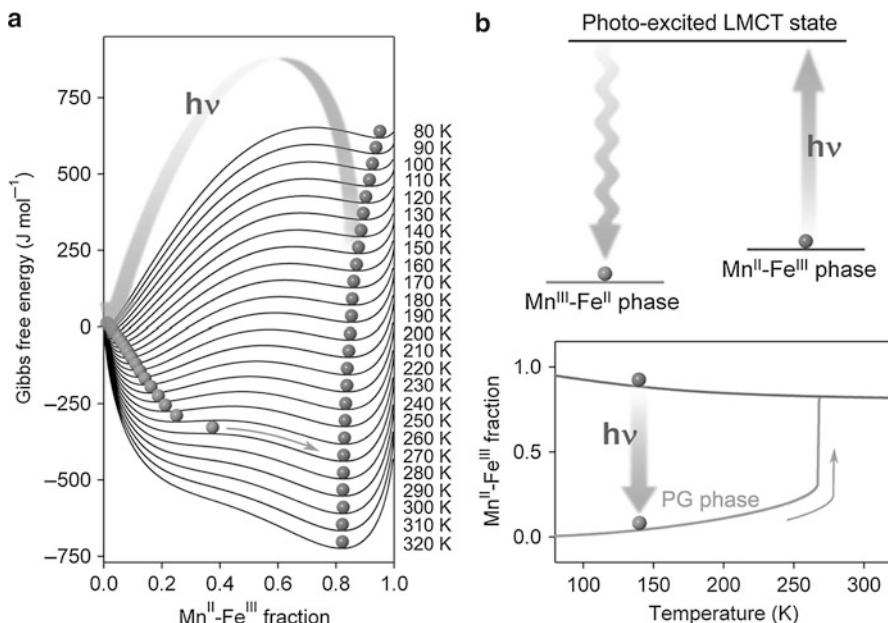


Fig. 18.19 Mechanism of the photo-induced phase collapse in $\text{Rb}_{0.43}\text{Mn}[\text{Fe}(\text{CN})_6]_{0.81} \cdot 3\text{H}_2\text{O}$. (a) Temperature dependence of calculated Gibbs free energy vs. the $\text{Mn}^{\text{II}}\text{-Fe}^{\text{III}}$ fraction for $\text{Rb}_{0.43}\text{Mn}[\text{Fe}(\text{CN})_6]_{0.81} \cdot 3\text{H}_2\text{O}$ based on the Slichter and Drickamer model. *Dark and light gray circles* indicate the existing populations of $\text{Mn}^{\text{II}}\text{-Fe}^{\text{III}}$ phase and $\text{Mn}^{\text{III}}\text{-Fe}^{\text{II}}$ phase, respectively. (b) Schematic picture of the pathway in the photo-induced phase collapse (*upper*). Temperature dependence of calculated fractions of $\text{Mn}^{\text{II}}\text{-Fe}^{\text{III}}$ mainly phase (*dark gray curve*) and $\text{Mn}^{\text{III}}\text{-Fe}^{\text{II}}$ mainly phase (*light gray curve*) (*lower*)

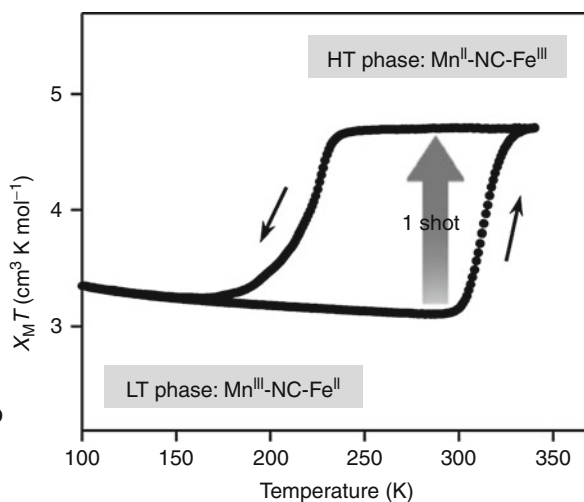


Fig. 18.20 The observed $\chi_M T - T$ plots for $\text{Rb}_{0.97}\text{Mn}[\text{Fe}(\text{CN})_6]_{0.99} \cdot 0.2\text{H}_2\text{O}$ in the cooling (\downarrow) and warming (\uparrow) processes under 5,000 Oe

Fig. 18.21 Change in the IR spectrum by a one-shot-laser-pulse irradiation of 532 nm with $80 \text{ mJ cm}^{-2} \text{ pulse}^{-1}$ at 295 K for $\text{Rb}_{0.97}\text{Mn}[\text{Fe}(\text{CN})_6]_{0.99} \cdot 0.2\text{H}_2\text{O}$. The spectra before and after irradiation are shown as *dotted* and *solid* lines, respectively

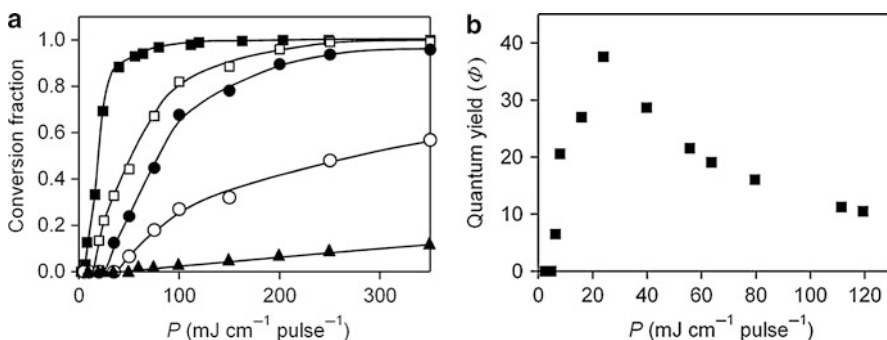
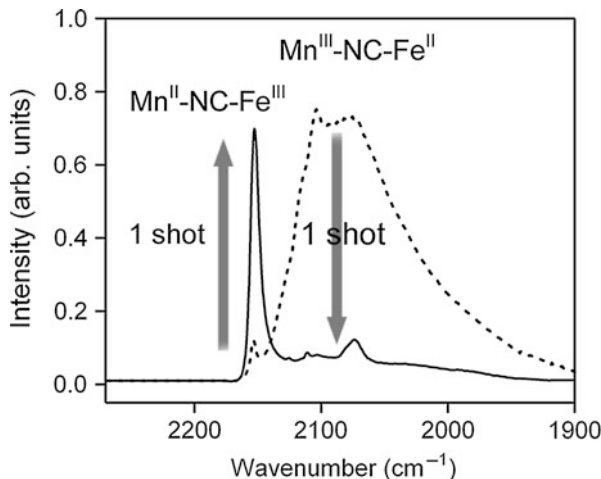


Fig. 18.22 (a) Laser power density (P) dependence of a one-shot-laser-pulse induced phase transition for $\text{Rb}_{0.97}\text{Mn}[\text{Fe}(\text{CN})_6]_{0.99} \cdot 0.2\text{H}_2\text{O}$ when irradiating with 532 nm at 295 (■), 280 (□), 260 (●), 240 (○), and 220 K (▲). *Solid line* is for the eye guide. (b) Laser power density (P) dependence of quantum yield Φ of a one-shot-laser-pulse induced phase transition at 295 K

240, and 220 K. The conversion fraction depended on the P value and temperature. A threshold in the laser power density (P_{th}) was observed. At 295 K, when the P value was greater than $6 \text{ mJ cm}^{-2} \text{ pulse}^{-1}$, the LT phase was converted to HT phase. In contrast, in the case of $P < P_{\text{th}}$, photoconversion did not occur even after irradiating more than 1,000 shots. The existence of a threshold suggests that cooperative effects exist in the present photo-induced phase transition and the maximum value of quantum yield was $\Phi = 38$ at $P = 24 \text{ mJ cm}^{-2} \text{ pulse}^{-1}$ (Fig. 18.22b).

In rubidium manganese hexacyanoferrate, temperature-induced phase transition is observed with large thermal hysteresis loops. The charge transfer from Mn^{II} to Fe^{III} accompanying the Jahn-Teller effect on the $\text{Mn}^{\text{III}}\text{N}_6$ moiety explains this phase

transition. In paramagnetic state of this system, the photo-induced phase transition inside the thermal hysteresis loop was observed at room temperature. Such a photo-induced phase transition phenomena are caused by (1) the change of valence states on transition metal ions due to a metal-to-metal charge transfer and (2) the bistability due to the Jahn-Teller distortion of Mn^{III} ion.

18.9 Photomagnetism

18.9.1 Photo-Induced Demagnetization by One-Shot-Laser-Pulse

In this section, the photomagnetic effect of the LT phase was investigated with $\text{Rb}_{0.88}\text{Mn}[\text{Fe}(\text{CN})_6]_{0.96} \cdot 0.6\text{H}_2\text{O}$ using SQUID magnetometer [39, 79]. A pulsed Nd^{3+} : YAG laser ($\lambda = 532$ nm; pulse width: 6 ns) was guided by optical fiber into the SQUID magnetometer. As $\text{Rb}_{0.88}\text{Mn}[\text{Fe}(\text{CN})_6]_{0.96} \cdot 0.6\text{H}_2\text{O}$ was cooled to a very low temperature under an external magnetic field of 10 Oe, the LT phase exhibited spontaneous magnetization with a T_c of 12 K. The M_s and H_c values at 2 K were $3.6 \mu_B$ and 1,800 G, respectively. This M_s value can be explained by the ferromagnetic spin ordering of Mn^{III} ($S = 2$) ions. From the χ_M^{-1} vs. T plots at temperature between 100 and 250 K, the positive Weiss temperature value of +15 K was obtained.

When the sample was irradiated by one-shot-laser-pulse with 532 nm-laser light at 3 K, the magnetization was decreased. Figure 18.23a shows the magnetization vs. temperature curve for the sample irradiated with $P = 130 \text{ mJ cm}^{-2} \text{ pulse}^{-1}$. The photoconversion increased with increasing the laser power density (P) as shown in Fig. 18.23b, c. A threshold in the laser power density (P'_{th}) was observed; when the P value was above $9.3 \text{ mJ cm}^{-2} \text{ pulse}^{-1}$, the magnetization value was decreased; however, in the case of $P < P'_{\text{th}}$, the magnetization value did not change. The quantum yields (Φ) for the present photodemagnetization were above one, for example, $\Phi = 4.5$ ($=43 \text{ mJ cm}^{-2} \text{ pulse}^{-1}$). The irradiated sample returned to the LT phase by an annealing treatment (3 K \rightarrow 150 K \rightarrow 3 K) with a relaxation at 120 K. The IR spectra before and after one-shot-laser-pulse irradiation (532 nm, $P = 14 \text{ mJ cm}^{-2} \text{ pulse}^{-1}$) at 8 K was obtained. After irradiation, the $\text{Mn}^{\text{III}}\text{-NC-Fe}^{\text{II}}$ peak at $2,095 \text{ cm}^{-1}$ disappears and a sharp peak due to the $\text{Mn}^{\text{II}}\text{-NC-Fe}^{\text{III}}$ peak at $2,152 \text{ cm}^{-1}$ appears. Note that, in the case of $P < P'_{\text{th}}$, the IR spectra were not changed by irradiation of several tens shots. An annealing treatment (8 K \rightarrow 150 K \rightarrow 8 K) returned the IR spectrum of the irradiated sample to the LT phase. From these results, we conclude that the present photo-demagnetization is caused by the photo-induced phase transition from the LT phase to the HT phase.

Temperature-induced phase transition between the LT and HT phases was observed in rubidium manganese hexacyanoferrate. In such a material with a bistability, a ground state can be converted to a hidden metastable state by the irradiation. Nasu et al. showed a simple scheme for a photo-induced phase transition using the adiabatic potential energy vs. order parameter (Fig. 18.24) [2]. In this

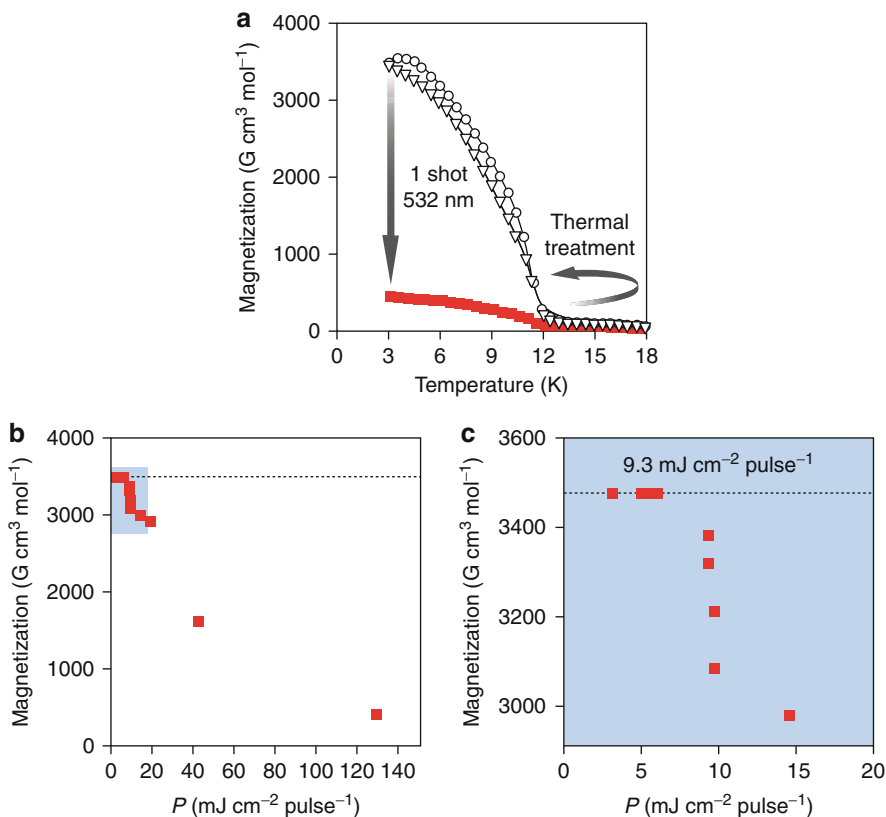
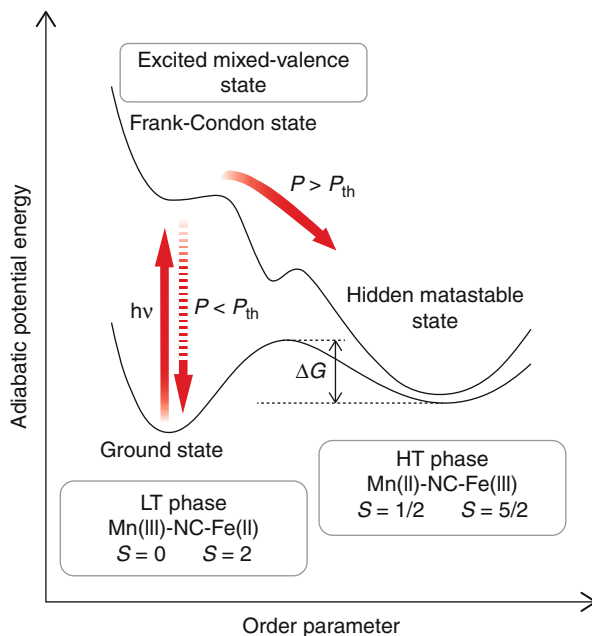


Fig. 18.23 (a) Magnetization vs. temperature plots for $\text{Rb}_{0.88}\text{Mn}[\text{Fe}(\text{CN})_6]_{0.96} \cdot 0.6\text{H}_2\text{O}$ at 200 Oe before (*white circles*) and after the one-shot-laser-pulse irradiation (*red squares*) and thermal treatment (*white triangles*). (b) Laser power density (P) dependences of the one-shot-laser-pulse-induced photodemagnetization phenomenon. (c) Enlarged plots of (b)

scheme, the ground state is excited to the Franck-Condon state by irradiation. This Franck-Condon state proceeds to a hidden substable state through a structural change state or relaxes to the ground state. In our case, irradiating with pulsed-laser light excites the LT phase to a mixed-valence state between the $\text{Mn}^{\text{III}}\text{-Fe}^{\text{II}}$ and the $\text{Mn}^{\text{II}}\text{-NC-Fe}^{\text{III}}$ states. This mixed-valence state proceeds to the HT phase or relaxes to the initial LT phase. The produced HT phase can be maintained in the low temperature range since it is sufficiently separated from the LT phase by the thermal energy (ΔG). In addition, when the P value is larger than P_{th}' , the excited state proceeds to the photo-produced HT phase as shown by the solid arrow in Fig. 18.24. In contrast, when $P < P_{\text{th}}'$, the excited state relaxes to the ground state as shown by the dotted arrow.

Fig. 18.24 Schematic illustration of the one-shot-laser-pulse-induced phase transition from the stable $\text{Mn}^{\text{III}}\text{-NC-Fe}^{\text{II}}$ phase to the hidden substable $\text{Mn}^{\text{II}}\text{-NC-Fe}^{\text{III}}$ phase



18.9.2 Reversible Photomagnetic Effect

In previous section, we have reported that irradiating with 532 nm light converts the LT phase to the photo-induced (PI) phase, which decreases its spontaneous magnetization. In this section, we have found that irradiating with a different wavelength of light recovers the PI phase in $\text{Rb}_{0.88}\text{Mn}[\text{Fe}(\text{CN})_6]_{0.96} \cdot 0.5\text{H}_2\text{O}$ to the LT phase. Furthermore, neutron powder diffraction using an analog complex, $\text{Rb}_{0.58}\text{Mn}[\text{Fe}(\text{CN})_6]_{0.86} \cdot 2.3\text{H}_2\text{O}$, has confirmed the magnetic ordering of the PI phase. Herein, we show the visible-light reversible changes in the electronic and magnetic properties of $\text{Rb}_{0.88}\text{Mn}[\text{Fe}(\text{CN})_6]_{0.96} \cdot 0.5\text{H}_2\text{O}$, the neutron powder diffraction pattern of $\text{Rb}_{0.58}\text{Mn}[\text{Fe}(\text{CN})_6]_{0.86} \cdot 2.3\text{H}_2\text{O}$, and the mechanism of the observed photo-reversible photomagnetism [80].

18.9.3 Photo-Reversible Changes in the IR Spectra and SQUID Measurement

Because a metal-to-metal charge transfer (MMCT) band was observed at 420–540 nm in the ϵ spectrum of the LT phase (Fig. 18.5), the LT phase was irradiated with a CW diode green laser ($h\nu$; $\lambda = 532$ nm). Figure 18.25 shows the IR spectra before and after the light irradiations at 3 K. Before irradiating (Fig. 18.25a, black line), the LT phase possessed a broad peak due to $\text{Mn}^{\text{III}}\text{-NC-Fe}^{\text{II}}$ around $2,100\text{ cm}^{-1}$. Irradiating with $h\nu$ reduced the $\text{Mn}^{\text{III}}\text{-NC-Fe}^{\text{II}}$ peak, and created a sharp peak

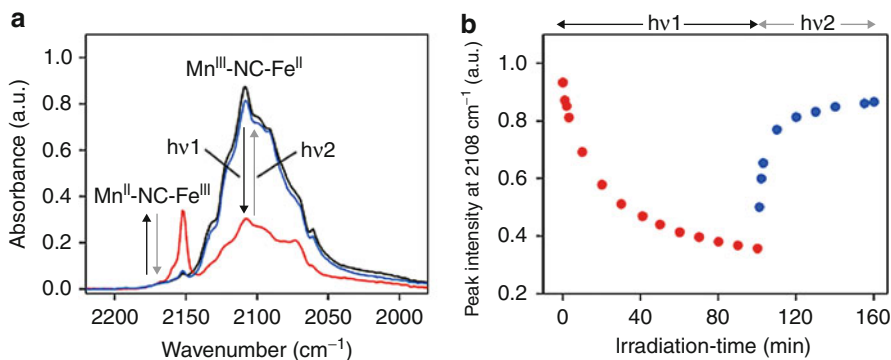


Fig. 18.25 Visible-light reversible change in the IR spectra of $\text{Rb}_{0.88}\text{Mn}[\text{Fe}(\text{CN})_6]_{0.96} \cdot 0.5\text{H}_2\text{O}$. (a) Changes in the IR spectrum at 3 K by irradiating with $h\nu_1$ ($\lambda = 532$ nm; *black arrows*) before irradiation (*black line*), after $h\nu_1$ irradiation (*red line*), and $h\nu_2$ ($\lambda = 410$ nm; *gray arrows*) irradiation (*blue line*). (b) Peak intensity at 2,108 vs. irradiation-time upon irradiating with $h\nu_1$ (*red circles*) and $h\nu_2$ (*blue circles*)

at $2,153\text{ cm}^{-1}$. The latter peak is assigned to the $\text{Mn}^{\text{II}}\text{-NC-Fe}^{\text{III}}$, which was also observed in the HT phase ($2,154\text{ cm}^{-1}$). It is concluded that the PI phase after $h\nu_1$ irradiation has a valence state similar to the HT phase. Based on the knowledge that resonance due to the LMCT band was observed at 410 nm in the spectrum of the HT phase, this PI phase was irradiated with blue light ($h\nu_2$; $\lambda = 410 \pm 30$ nm) from a filtered Xe lamp in order to investigate the photo-reversibility. Consequently, the $\text{Mn}^{\text{II}}\text{-NC-Fe}^{\text{III}}$ peak decreased and the $\text{Mn}^{\text{III}}\text{-NC-Fe}^{\text{II}}$ peak increased as shown in Fig. 18.25a. Figure 18.25b plots the peak intensities of $\text{Mn}^{\text{II}}\text{-NC-Fe}^{\text{III}}$ vs. irradiation time. This photo-reversibility was repeatedly observed.

Next, we measured the photo-reversible change in magnetization in situ using SQUID equipment. The field cooled magnetization curve under an external magnetic field of 200 Oe showed that the LT phase is a ferromagnet with a T_c of 12 K (Fig. 18.26a, closed squares). Upon irradiating with $h\nu_1$ at 3 K, the magnetization value decreased from $5,600$ to $700\text{ G cm}^3\text{ mol}^{-1}$ (Fig. 18.26a, open circles).

Successively irradiating the PI phase with $h\nu_2$ increased the magnetization, which reached $4,700\text{ G cm}^3\text{ mol}^{-1}$ (Fig. 18.26a, closed circles). The present photo-reversibility of the magnetization was repeatedly observed by alternately irradiating with $h\nu_1$ and $h\nu_2$ (Fig. 18.26b). The magnetization value after irradiating with $h\nu_2$, which is shown as the closed circles in Fig. 18.26a, was smaller than that of initial value, suggesting that a photo-equilibrium state persists. To confirm the photo-equilibrium behavior, we investigated the photo-effect of the reverse process, that is, from the PI phase to the LT phase, using a different light ($h\nu_3$; $= 425 \pm 45$ nm). Irradiating with $h\nu_3$ increased the magnetization, which reached plateau- $\text{Mag}_{h\nu_3}$ as shown in Fig. 18.27. Subsequent irradiation with $h\nu_2$ further increased the magnetization, which reached plateau- $\text{Mag}_{h\nu_2}$. This equilibrium behavior is due to a photo-stationary state between the photodemagnetization (LT \rightarrow PI phase) and the photo-induced magnetization (PI \rightarrow LT phase).

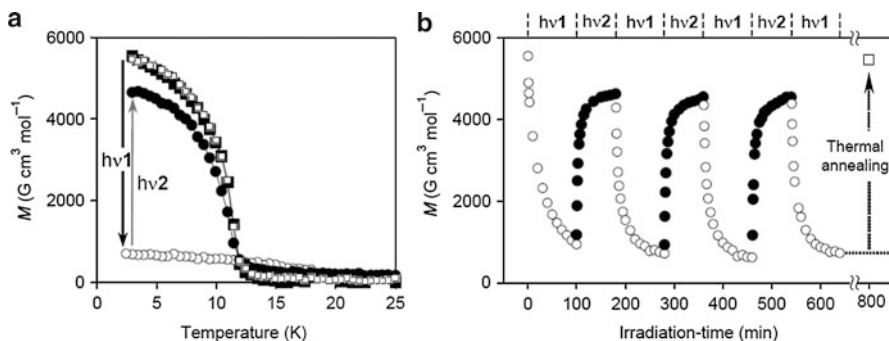
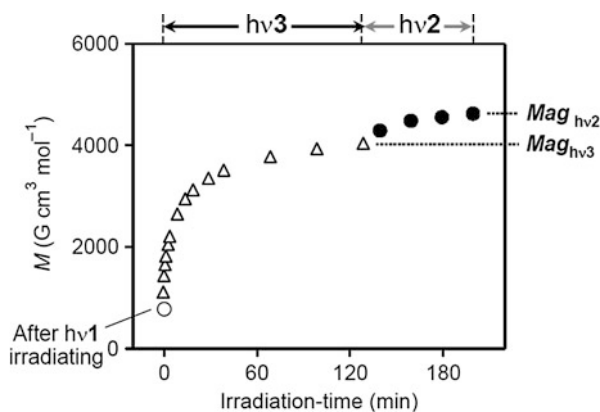


Fig. 18.26 Visible-light reversible photomagnetism in $\text{Rb}_{0.88}\text{Mn}[\text{Fe}(\text{CN})_6]_{0.96} \cdot 0.5\text{H}_2\text{O}$. (a) Magnetization vs. temperature curves at 200 Oe, before irradiating (■), after $h\nu_1$ ($\lambda = 532 \text{ nm}$, 30 mW cm^{-2}) irradiation for 100 min (○), after $h\nu_2$ ($\lambda = 410 \text{ nm}$, 13 mW cm^{-2}) irradiation for 80 min (●), and after the thermal annealing treatment of 180 K (□). (b) Magnetization vs. irradiation-time plot at 3 K by alternating with $h\nu_1$ (○) and $h\nu_2$ (●) light irradiation, and the magnetization value after a thermal treatment of 180 K (□)

Fig. 18.27 Photo-stationary state between photodemagnetization and photo-induced magnetization. Magnetization vs. irradiation-time plot at 3 K upon irradiating with $h\nu_3$ ($\lambda = 425 \pm 445 \text{ nm}$, 22 mW cm^{-2}) (open triangle) and then $h\nu_2$ ($\lambda = 410 \pm 30 \text{ nm}$, 13 mW cm^{-2}) (black circles)



18.9.4 Magnetic Ordering of the Photo-Induced Phase

To determine the magnetic ordering of the PI phase, we performed neutron powder diffraction using an analog complex, $\text{Rb}_{0.58}\text{Mn}[\text{Fe}(\text{CN})_6]_{0.86} \cdot 2.3\text{H}_2\text{O}$. A charge-transfer phase transition was not observed in the IR spectrum of $\text{Rb}_{0.58}\text{Mn}[\text{Fe}(\text{CN})_6]_{0.86} \cdot 2.3\text{H}_2\text{O}$ when the sample was cooled to 3 K at a rate of -0.5 K (Fig. 18.28a). The $\chi_M^{-1} - T$ plot showed a negative Weiss temperature of -16 K , which was obtained by the least-square fitting in the temperature region of 150–320 K. The magnetization vs. temperature curve under an external field of 10 Oe exhibited an antiferromagnetic behavior with a Neel temperature (T_N) of 11.5 K. The magnetization vs. external magnetic field plots at 2 K showed a linear change (Fig. 18.28b). These magnetic data suggest that in $\text{Rb}_{0.58}\text{Mn}[\text{Fe}(\text{CN})_6]_{0.86} \cdot 2.3\text{H}_2\text{O}$, the HT phase is maintained even

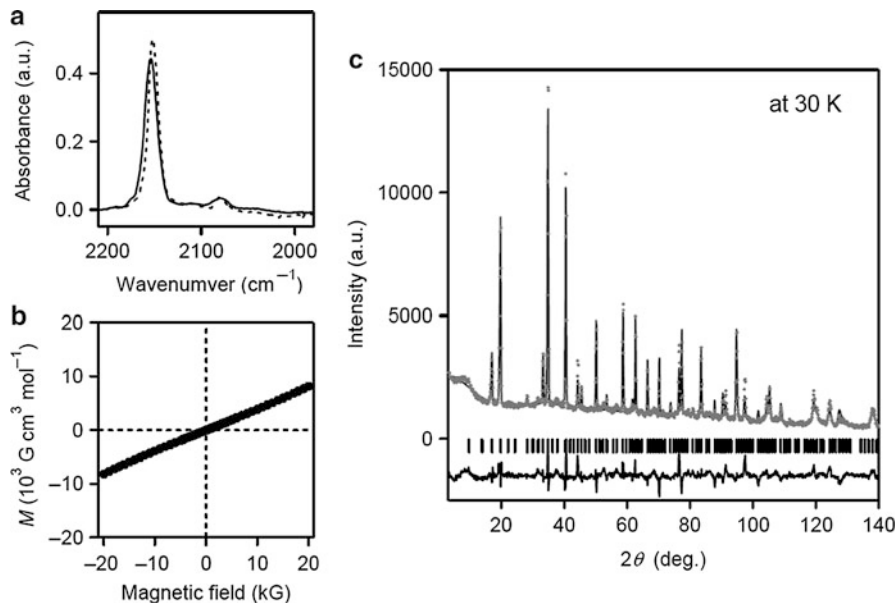


Fig. 18.28 Electronic state, magnetic property, and neutron powder diffraction pattern of $\text{Rb}_{0.58}\text{Mn}[\text{Fe}(\text{CN})_6]_{0.86} \cdot 2.3\text{H}_2\text{O}$. (a) IR spectra at 300 K (dotted line) and 3 K (solid line). (b) Magnetization as a function of the external magnetic field at 2 K. (c) Neutron powder diffraction pattern at 30 K. Gray dots, black pattern, and black line are the observed plots, calculated pattern, and their difference, respectively. Bars represent the calculated positions of the Bragg reflections

at low temperature and the HT phase shows antiferromagnetism. Figure 18.28c shows the neutron powder pattern for $\text{Rb}_{0.58}\text{Mn}[\text{Fe}(\text{CN})_6]_{0.86} \cdot 2.3\text{H}_2\text{O}$ at 30 K. Rietveld analysis showed that the crystal structure was tetragonal (P4/mmm) with lattice constants of $a = b = 7.424(6) \text{ \AA}$ and $c = 10.51(1) \text{ \AA}$, which correspond to $a' = b' = 10.499 \text{ \AA}$ and $c' = 10.51(1) \text{ \AA}$ in the frame of a cubic lattice. The interatomic distances of Fe and C in the ab plane ($\text{Fe} - \text{C}_{ab}$) and along the c axis ($\text{Fe} - \text{C}_c$) are 1.93(3) and 1.81(4) \AA , respectively. The distances of $\text{Mn} - \text{N}_{ab}$ and $\text{Mn} - \text{N}_c$ are 2.18(2) and 2.18(4) \AA , respectively.

Figure 18.29a, b show the neutron powder diffraction patterns at 2 and 30 K and the magnetic Bragg reflections as the difference in the patterns of 2 and 30 K, respectively. Analysis of the magnetic Bragg reflections suggests that this system is a layered antiferromagnet in which the magnetic coupling between the layers is antiferromagnetic. The spin arrangement as shown in Fig. 18.29d is a suitable configuration due to the following reason. The electronic state of Mn^{II} is a $3d^5$ high-spin state, and hence, all the $3d$ orbitals are magnetic orbitals. In contrast, Fe^{III} is a $3d^5$ low-spin state, and thus, only one of the t_{2g} orbitals becomes a magnetic orbital. Rietveld analysis showed elongation of $\text{Fe}(\text{CN})_6$ in the ab -plane, indicating that the d_{yz} and d_{zx} orbitals are more stabilized than the d_{xy} orbital due to backbonding of the cyanide ligand. Hence, the d_{xy} becomes the magnetic orbital of Fe^{III} . In this case, only the spin configuration shown in Fig. 18.29d is

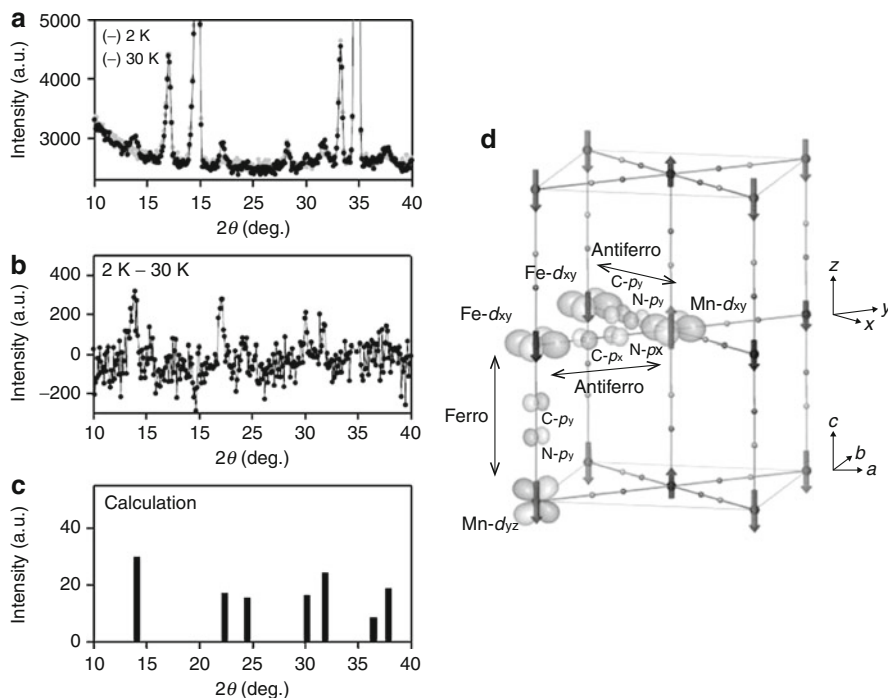


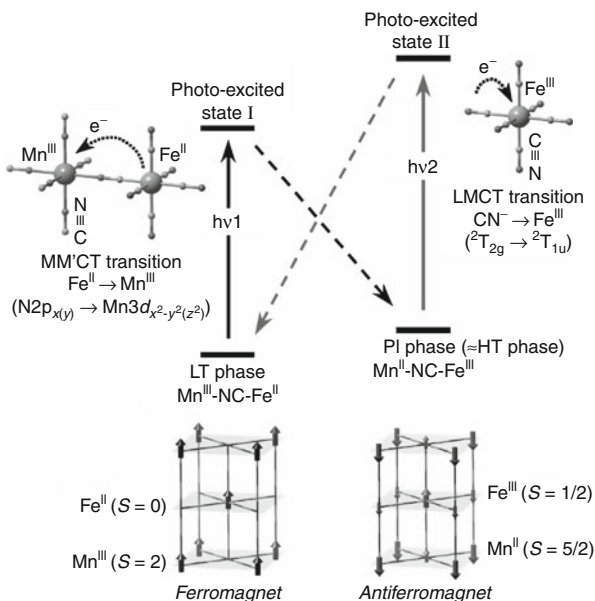
Fig. 18.29 (a) Neutron powder diffraction patterns at 2 K (*black line*) and 30 K (*gray line*). (b) Magnetic Bragg reflections as the difference in the neutron powder diffraction patterns at 2 and 30 K. (c) Calculated intensities of the magnetic Bragg reflections with an antiferromagnetic spin ordering. (d) Schematic illustration of the spin ordering. *Gray and dark gray arrows* indicate the spins on Mn^{II} and Fe^{III}, respectively. From the view of the superexchange pathway, an antiferromagnetic coupling operates between Fe- d_{xy} and Mn- d_{xy} magnetic orbitals in the xy (ab) plane. In contrast, a ferromagnetic coupling operates between Fe- d_{xy} and all the d orbitals of Mn (here, Mn- d_{yz} is depicted) along the z (c) axis

possible to be formed. The stick diagram of Fig. 18.29c, which was calculated by the layered antiferromagnet mentioned above, reproduced the observed data. Because the magnetic ordering of $\text{Rb}_{0.58}\text{Mn}[\text{Fe}(\text{CN})_6]_{0.86} \cdot 2.3\text{H}_2\text{O}$ is considered to be the same as that of the PI phase in $\text{Rb}_{0.88}\text{Mn}[\text{Fe}(\text{CN})_6]_{0.96} \cdot 0.5\text{H}_2\text{O}$, the PI phase should be a layered antiferromagnet.

18.9.5 Mechanism of Visible-Light Reversible Photomagnetism

The observed reversible photomagnetic effect can be explained by the scheme shown in Fig. 18.30. Irradiating with $h\nu$ excites the MM'CT ($\text{Fe}^{\text{II}} \rightarrow \text{Mn}^{\text{III}}$) band, which then excites the LT phase to photoexcited state I. Photoexcited state I proceeds to the PI phase, which has the same valence state as the HT phase. Thermal energy then suppresses the relaxation of the metastable PI phase to the stable LT

Fig. 18.30 Schematic illustration of the visible-light reversible photomagnetic effect in rubidium manganese hexacyanoferrate. Scheme for reversible charge-transfer (between and upper) and the spin ordering for the LT and PI phases (lower). LT phase is a ferromagnet due to ferromagnetic coupling between the Mn^{III} sites, whereas the PI phase is an antiferromagnet. Arrows on the LT phase represent the spins of Mn^{III} . Large and small arrows on the PI phase indicate the spins of Mn^{II} and Fe^{III} respectively



phase. In contrast, the excitation of the LMCT ($\text{CN}^- \rightarrow \text{Fe}^{\text{III}}$) band of $[\text{Fe}(\text{CN})_6]^{3-}$ by irradiating with $h\nu_2$ excites the PI phase to photoexcited state **III**, which then proceeds to the LT phase. The LT phase is a ferromagnet due to the ferromagnetic coupling between the Mn^{III} ($S = 2$) sites, but the PI phase is an antiferromagnet. Hence, the magnetization value changes by optical switching between the LT phase and the PI phase.

A visible light-induced reversible photomagnetism between the ferromagnetic and antiferromagnetic phases is observed in a rubidium manganese hexacyanoferrate, $\text{Rb}_{0.88}\text{Mn}[\text{Fe}(\text{CN})_6]_{0.96} \cdot 0.5\text{H}_2\text{O}$, by alternately irradiating with 532 and 410 nm lights. Optical switching from the LT phase to the PI phase occurs through a $\text{Fe}^{\text{II}} \rightarrow \text{Mn}^{\text{III}}$ MM'CT transition, causing photodemagnetization. In contrast, the reverse process is caused by an optical transition from the PI phase to the LT phase through a $\text{CN}^- \rightarrow \text{Fe}^{\text{III}}$ LMCT transition. The existence of a photo-stationary state between the LT \rightarrow PI phase and the PI \rightarrow LT phase is also confirmed by the light source changing experiment. Although photomagnetism has been observed in some compounds, this is the first example of optical switching between a ferromagnet and an antiferromagnet.

18.10 Summary

In conclusion, a temperature-induced phase transition between the high-temperature (HT) and low-temperature (LT) phases is observed with a thermal hysteresis

loop of 75 K in $\text{RbMn}[\text{Fe}(\text{CN})_6]$. The charge transfer from Mn^{II} to Fe^{III} that accompanies the Jahn-Teller effect on the $\text{Mn}^{\text{III}}\text{N}_6$ moiety explains this phase transition. By controlling the x of $\text{Rb}_x\text{Mn}[\text{Fe}(\text{CN})_6]_{(x+2)/3} \cdot z\text{H}_2\text{O}$, we found that $\text{Rb}_{0.64}\text{Mn}[\text{Fe}(\text{CN})_6]_{0.88} \cdot 1.7\text{H}_2\text{O}$ exhibits a surprisingly large thermal hysteresis loop of 138 K. A hidden stable phase of HT phase, which is experimentally observed in this system, is well explained by a SD model under thermal equilibrium condition. In addition, with non-phase transition material of $\text{Rb}_{0.43}\text{Mn}[\text{Fe}(\text{CN})_6]_{0.81} \cdot 3\text{H}_2\text{O}$, the *light-induced phase collapse* (LIPC) was realized. The LIPC is caused by blue-light irradiation inducing the transition from a *thermodynamically metastable phase* to a *hidden stable phase* in a material that does not undergo a thermal phase transition. Since the present phenomenon is driven only by the blue-light irradiation, it may provide a good strategy for the next generation of optical recording. As photo-induced phase transition at room temperature, the photoconversion from the LT to HT phases is observed inside the thermal hysteresis loop with a large Φ value of 38, by a one-shot-laser-pulse irradiation. This large yield and fast response will allow us to consider a new type of optical switching device. As photomagnetic effect at low temperature, the rapid photodemagnetization has been observed by a one-shot-pulsed-laser light irradiation. With cw lights, a visible light-induced reversible photomagnetism between the ferromagnetic and antiferromagnetic phases is observed, by alternately irradiating with 532 and 410 nm lights. These temperature- and photo-induced phase transition phenomena are caused by (1) the change in valence states on transition metal ions due to metal-to-metal charge transfer and (2) the bistability due to the Jahn-Teller distortion of Mn^{III} ion.

Acknowledgements The authors would like to thank Professor Yutaka Moritomo (University of Tsukuba) and Professor Kenji Ohoyama (Tohoku University) for the measurement of neutron powder diffraction. The present research was supported partly by the CREST program from the JST, a Grant-in-Aid for Young Scientists (S) from the JSPS, the Asahi Glass Foundation, the Next program from JSPS, a Grant for the Global COE Program "Chemistry Innovation through Cooperation of Science and Engineering," APSA from the MEXT, the Cryogenic Research Center, the University of Tokyo, and the Center for Nano Lithography & Analysis, the University of Tokyo, supported by the MEXT.

References

1. O. Kahn, *Molecular Magnetism* (VCH, New York, 1993)
2. K. Nasu, *Relaxations of Excited States and Photo-Induced Structural Phase Transitions* (Springer, Berlin, 1997)
3. P. Gutlich, A. Hauser, H. Spiering, *Angew. Chem. Int. Ed. Engl.* **33**, 2024 (1994)
4. S. Ohkoshi, K. Hashimoto, *J. Photochem. Photobiol. C* **2**, 71 (2001)
5. J.F. Letard, P. Guionneau, E. Codjovi, O. Lavastre, G. Bravic, D. Chasseau, O. Kahn, *J. Am. Chem. Soc.* **119**, 10861 (1997)
6. G.A. Renovitch, W.A. Baker, *J. Am. Chem. Soc.* **89**, 6377 (1967)
7. M. Sorai, *Bull. Chem. Soc. Jpn.* **74**, 2223 (2001)
8. K. Prassides, *Mixed Valency Systems, Applications in Chemistry, Physics and Biology*. NATO ASI series (Kluwer, Dordrecht, 1991)
9. M.B. Robin, P. Day, *Adv. Inorg. Chem. Radiochem.* **10**, 247 (1967)

10. N.S. Hush, *Prog. Inorg. Chem.* **8**, 391 (1967)
11. S.B. Piepho, E.R. Krausz, P.N. Schatz, *J. Am. Chem. Soc.* **10**, 2996 (1978)
12. R.D. Cannon, L. Montri, D.B. Brown, K.M. Marshall, C.M. Elliot, *J. Am. Chem. Soc.* **106**, 2591 (1984)
13. H. Kitagawa, T. Mitani, *Coord. Chem. Rev.* **190**, 1169 (1999)
14. O.S. Jung, D.H. Jo, Y.A. Lee, B.J. Conklin, C.G. Pierpont, *Inorg. Chem.* **36**, 19 (1997)
15. N. Shimamoto, S. Ohkoshi, O. Sato, K. Hashimoto, *Inorg. Chem.* **41**, 678 (2002)
16. R.J. Zimmermann, *Phys. Chem. Solids.* **44**, 151 (1983)
17. T.J. Kambara, *Phys. Soc. Jpn.* **49**, 1806 (1980)
18. S. Ohnishi, S. Sugano, *J. Phys. C* **14**, 39 (1981)
19. A. Ludi, H.U. Gudel, *Struct. Bonding (Berlin)* **14**, 1 (1973)
20. M. Verdaguer, T. Mallah, V. Gadet, I. Castro, C. Helary, S. Thiebaut, P. Veillet, *Conf. Coord. Chem.* **14**, 19 (1993)
21. S. Ohkoshi, K. Hashimoto, *Electrochem. Soc. Interface fall* **11**, 34 (2002)
22. T. Mallah, S. Thiebaut, M. Verdaguer, P. Veillet, *Science* **262**, 1554 (1993)
23. W.R. Entley, G.S. Girolami, *Science* **268**, 397 (1995)
24. S. Ferlay, T. Mallah, R. Ouahes, P. Veillet, M. Verdaguer, *Nature* **378**, 701 (1995)
25. S. Ohkoshi, T. Iyoda, A. Fujishima, K. Hashimoto, *Phys. Rev. B* **56**, 11642 (1997)
26. S. Ohkoshi, A. Fujishima, K. Hashimoto, *J. Am. Chem. Soc.* **120**, 5349 (1998)
27. O. Hatlevik, W.E. Bushmann, J. Zhang, J.L. Manson, J.S. Miller, *Adv. Mater.* **11**, 914 (1999)
28. S.M. Holmes, G.S. Girolami, *J. Am. Chem. Soc.* **121**, 5593 (1999)
29. S. Ohkoshi, Y. Abe, A. Fujishima, K. Hashimoto, *Phys. Rev. Lett.* **82**, 1285 (1999)
30. S. Ohkoshi, K. Arai, Y. Sato, K. Hashimoto, *Nat. Mater.* **3**, 857 (2004)
31. S. Margadonna, K. Prassides, A.N. Fitch, *J. Am. Chem. Soc.* **126**, 15390 (2004)
32. S.S. Kaye, J.R. Long, *J. Am. Chem. Soc.* **127**, 6506 (2005)
33. A.L. Goodwin, K.W. Chapman, C.J. Kepert, *J. Am. Chem. Soc.* **127**, 17980 (2005)
34. S. Ohkoshi, H. Tokoro, T. Matsuda, H. Takahashi, H. Irie, K. Hashimoto, *Angew. Chem. Int. Ed.* **3**, 857 (2007)
35. S. Ohkoshi, K. Nakagawa, K. Tomono, K. Imoto, Y. Tsunobuchi, H. Tokoro, *J. Am. Chem. Soc.* **132**, 6620 (2010)
36. S. Ohkoshi, S. Yorozu, O. Sato, T. Iyoda, A. Fujishima, K. Hashimoto, *Appl. Phys. Lett.* **70**, 1040 (1997)
37. A. Bleuzen, C. Lomenech, V. Escax, F. Villain, F. Varret, C.C.D. Moulin, M. Verdaguer, *J. Am. Chem. Soc.* **122**, 6648 (2000)
38. O. Sato, S. Hayami, Y. Einaga, Z.Z. Gu, *Bull. Chem. Soc. Jpn.* **76**, 443 (2003); H. Tokoro, S. Ohkoshi, K. Hashimoto, *Appl. Phys. Lett.* **82**, 1245 (2003)
39. H. Tokoro, S. Ohkoshi, K. Hashimoto, *Appl. Phys. Lett.* **82**, 1245 (2003)
40. S. Ohkoshi, N. Machida, Z.J. Zhong, K. Hashimoto, *Synth. Met.* **122**, 523 (2001)
41. G. Rombaut, M. Verelst, S. Golhen, L. Ouahab, C. Mathoniere, O. Kahn, *Inorg. Chem.* **40**, 1151 (2001)
42. J.M. Herrera, V. Marvaud, M. Verdaguer, J. Marrot, M. Kalisz, C. Mathoniere, *Angew. Chem. Int. Ed.* **43**, 5468 (2004)
43. S. Ohkoshi, H. Tokoro, T. Hozumi, Y. Zhang, K. Hashimoto, C. Mathoniere, I. Bord, G. Rombaut, M. Verelst, C.C.D. Moulin, F. Villain, *J. Am. Chem. Soc.* **128**, 270 (2006)
44. S. Ohkoshi, S. Ikeda, T. Hozumi, T. Kashiwagi, K. Hashimoto, *J. Am. Chem. Soc.* **128**, 5320 (2006)
45. S. Ohkoshi, Y. Hamada, T. Matsuda, Y. Tsunobuchi, H. Tokoro, *Chem. Mater.* **20**, 3048 (2008)
46. N. Yamada, E. Ohno, K. Nishiuchi, N. Akahira, M. Takao, *J. Appl. Phys.* **69**, 2849 (1991)
47. A.V. Kolobov, P. Fons, A.I. Frenkel, A.L. Ankudinov, J. Tominaga, T. Uruga, *Nat. Mater.* **3**, 703 (2004)
48. M. Wuttig, N. Yamada, *Nat. Mater.* **6**, 824 (2007)
49. S. Decurtins, P. Gutlich, C.P. Kohler, H. Spiering, A. Hauser, *Chem. Phys. Lett.* **105**, 1 (1984)
50. J.F. Letard, J.A. Real, N. Moliner, A.B. Gaspar, L. Capes, O. Cadpr, O. Kahn, *J. Am. Chem. Soc.* **121**, 10630 (1999)

51. S. Ohkoshi, K. Imoto, Y. Tsunobuchi, S. Takano, H. Tokoro, *Nat. Chem.* **3**, 564 (2011)
52. S. Koshihara, Y. Tokura, T. Mikami, G. Saito, T. Koda, *Phys. Rev. B* **42**, 6853 (1990)
53. E. Collet, M.H. Lemeec-Cailleau, M.B.L. Cointe, H. Cailleau, M. Wulff, T. Luty, S. Koshihara, M. Meyer, L. Toupet, P. Rabiller, S. Teichert, *Science* **300**, 612 (2003)
54. S. Ohkoshi, Y. Tsunobuchi, T. Matsuda, K. Hashimoto, A. Namai, F. Hakoe, H. Tokoro, *Nat. Chem.* **2**, 539 (2010)
55. M. Fiebig, K. Miyano, Y. Tomioka, Y. Tokura, *Science* **280**, 1925 (1998)
56. N. Takubo, I. Onishi, K. Takubo, T. Mizokawa, K. Miyano, *Phys. Rev. Lett.* **101**, 177403 (2008)
57. H. Tokoro, M. Shiro, K. Hashimoto, S. Ohkoshi, *Z. Anorg. Allg. Chem.* **633**, 1134 (2007)
58. S. Ohkoshi, H. Tokoro, M. Utsunomiya, M. Mizuno, M. Abe, K. Hashimoto, *J. Phys. Chem. B* **106**, 2423 (2002)
59. H. Tokoro, S. Ohkoshi, T. Matsuda, K. Hashimoto, *Inorg. Chem.* **43**, 5231 (2004)
60. H. Osawa, T. Iwazumi, H. Tokoro, S. Ohkoshi, K. Hashimoto, H. Shoji, E. Hirai, T. Nakamura, S. Nanao, Y. Isozumi, *Solid State Commun.* **125**, 237 (2003)
61. T. Yokoyama, H. Tokoro, S. Ohkoshi, K. Hashimoto, K. Okamoto, T. Ohta, *Phys. Rev. B* **66**, 184111 (2002)
62. S. Ohkoshi, T. Nuida, T. Matsuda, H. Tokoro, K. Hashimoto, *J. Mater. Chem.* **5**, 3291 (2005)
63. K. Kato, Y. Moritomo, M. Takata, M. Sakata, M. Umekawa, N. Hamada, S. Ohkoshi, H. Tokoro, K. Hashimoto, *Phys. Rev. Lett.* **91**, 255502 (2003)
64. H. Tokoro, S. Ohkoshi, T. Matsuda, T. Hozumi, K. Hashimoto, *Chem. Phys. Lett.* **388**, 379 (2004)
65. T. Nakamoto, Y. Miyazaki, M. Itoi, Y. Ono, N. Kojima, M. Sorai, *Angew. Chem. Int. Ed.* **40**, 4716 (2001)
66. H.M.J. Blote, *Phys. B* **79B**, 427 (1975)
67. T. Matsumoto, Y. Miyazaki, A.S. Albrecht, C.P. Landee, M.M. Turnbull, M. Sorai, *J. Phys. Chem. B* **104**, 9993 (2000)
68. R.L. Carlin, *Magnetochemistry* (Springer, New York, 1986)
69. L.J.D. Jongh, A.R. Miedema, *Adv. Phys.* **23**, 1 (1974)
70. M.A. Subramanian, A.P. Ramirez, W.J. Marshall, *Phys. Rev. Lett.* **82**, 1558 (1999)
71. N. Ohmae, A. Kajiwar, Y. Miyazaki, M. Kamachi, M. Sorai, *Thermochim. Acta* **267**, 435 (1995)
72. B. Mayoh, P. Day, *J. Chem. Soc. Dalton* **15**, 1483 (1976)
73. H. Tokoro, S. Miyashita, K. Kazuhito, S. Ohkoshi, *Phys. Rev. B* **73**, 172415 (2006)
74. C.P. Slichter, H.G. Drickamer, *J. Chem. Phys.* **56**, 2142 (1972)
75. K.P. Purcell, M.P. Edwards, *Inorg. Chem.* **23**, 2620 (1984)
76. H. Tokoro, S. Ohkoshi, *Appl. Phys. Lett.* **93**, 021906 (2008)
77. H. Tokoro, T. Matsuda, K. Hashimoto, S. Ohkoshi, *J. Appl. Phys.* **97**, 10M508 (2005)
78. H. Tokoro, K. Hashimoto, S. Ohkoshi, *J. Magn. Magn. Mater.* **310**, 1422 (2007)
79. S. Ohkoshi, H. Tokoro, K. Hashimoto, *Coord. Chem. Rev.* **249**, 1830 (2005)
80. H. Tokoro, T. Matsuda, T. Nuida, Y. Moritomo, K. Ohoyama, E.D.L. Dangui, K. Boukhedaden, S. Ohkoshi, *Chem. Mater.* **20**, 423 (2008)

Hiroshi Imahori and Tomokazu Umeyama

Contents

19.1	Introduction.....	730
19.2	Two-Dimensional Multiporphyrin Arrays.....	731
19.2.1	Self-Assembled Monolayers of Porphyrins on Gold Electrodes.....	731
19.2.2	Self-Assembled Monolayers of Porphyrins on ITO Electrodes.....	739
19.3	Three-Dimensional Porphyrin Arrays.....	740
19.3.1	Self-Assembled Monolayers of Porphyrins on Metal Nanoparticles.....	740
19.3.2	Self-Assembled Monolayers of Porphyrins on Semiconducting Nanoparticles.....	750
19.4	Molecular Nanostructures.....	752
19.4.1	Porphyrin J-Aggregates.....	752
19.4.2	Conjugated Polymer-Carbon Nanotube Composites.....	755
19.5	Conclusions and Outlook.....	759
	References.....	759

H. Imahori (✉)

Institute for Integrated Cell-Material Sciences (WPI-iCeMS), Kyoto University, Kyoto, Japan

Department of Molecular Engineering, Graduate School of Engineering, Kyoto University, Kyoto, Japan

e-mail: imahori@scl.kyoto-u.ac.jp

T. Umeyama

Department of Molecular Engineering, Graduate School of Engineering, Kyoto University, Kyoto, Japan

e-mail: umeyama@scl.kyoto-u.ac.jp

Abstract

Recent progress of photoinduced artificial photosynthetic energy transfer systems is highlighted. Self-assembled multiporphyrin arrays as well as related energy transfer systems are found to be highly promising for efficient photocatalysts, organic solar cells, and molecular optoelectronic devices.

19.1 Introduction

Artificial photosynthesis is a current topic of intensive investigations, both in order to understand the reactions that play a central role in natural photosynthesis and to develop highly efficient solar energy conversion systems and molecular optoelectronic devices [1–39]. Artificial photosynthesis is defined as a research field that attempts to mimic the natural process of photosynthesis. Therefore, the outline of natural photosynthesis is described briefly for the better understanding of artificial photosynthesis. Natural photosynthetic system is regarded as one of the most elaborate mesoscale biological machines [40, 41]. It converts solar energy into electrochemical potential or chemical energy, which is prerequisite for the living organisms on the earth. The core function of photosynthesis is a cascade of photoinduced energy and electron transfer between donors and acceptors in the antenna complexes and the reaction center. For instance, in purple photosynthetic bacteria (*Rhodospseudomonas acidophila* and *Rhodospseudomonas palustris*), there are two different types of antenna complexes: a core light-harvesting antenna (LH1) and peripheral light-harvesting antenna (LH2) [42–44]. LH1 surrounds the reaction center where charge separation takes place. The peripheral antenna LH2 forms two wheel-like structures: B800 with 9 bacteriochlorophyll *a* (Bchl *a*) molecules and B850 with 18 Bchl *a* molecules, which are noncovalently bound to two types of transmembrane helical α - and β -apoproteins. Carotenoids nearby the chlorophylls absorb sunlight in the spectral region where chlorophyll molecules absorb weakly and transfer the resultant excitation energy to the chlorophyll molecules via singlet-singlet energy transfer. The collected energy then moves from the LH2 to the LH1 in which the excitation energy migrates in the wheel-like arrays of chlorophylls of LH1 and LH2 and in turn is funneled into the chlorophyll dimer (special pair) in the reaction center [42–44]. Vectorial electron transfer event occurs along the array of chromophores embedded in the transmembrane protein, in a sequence of special pair, accessory chlorophyll, pheophytin, quinone A, and quinone B, yielding a long-lived, charge-separated state across the membrane with a quantum efficiency of $\sim 100\%$ [45, 46]. The final charge-separated state eventually results in the production of adenosine triphosphate (ATP) via the proton gradient generated across the membrane by the proton pump from the cytoplasm to the periplasm using the reduced quinone [40–46].

Light-harvesting systems also disclose a great variety in their structures. For instance, in purple bacteria, more than nine chlorophylls are arranged in symmetric ringlike structures (*vide supra*) [42–44], while in green bacteria a large number of chlorophylls are organized into rodlike aggregates without the help of proteins [47].

On the other hand, chlorophyll aggregate in photosystem (PS) I of cyanobacteria and higher plants exhibits a rather random array forming two-dimensional (2D) structures, which surround the reaction center [48–50]. Such complex structure and diversity in natural light-harvesting systems have made it difficult to uncover the close structure-function relationship in the light-harvesting systems. Meanwhile, the roles of quantum coherence and entanglement in photosynthetic light-harvesting complexes have been described [51–53]. In this context, various chromophore arrays, especially porphyrins, which are assembled covalently [54–107] or non-covalently [108–143], have been synthesized to shed light on the light-harvesting processes.

In this review we highlight our recent achievements relating to photoinduced energy transfer in artificial photosynthesis. In particular, the emphasis lies on self-assembled multiporphyrin arrays that are highly promising materials for photocatalysts, organic solar cells, and molecular optoelectronic devices throughout our studies.

19.2 Two-Dimensional Multiporphyrin Arrays

19.2.1 Self-Assembled Monolayers of Porphyrins on Gold Electrodes

Covalently linked multiporphyrin arrays bearing more than ~ 10 porphyrin units are superior to the corresponding porphyrin monomers and oligomers with respect to the structural control and light-harvesting properties, but the synthetic difficulty makes it difficult to employ such covalently linked multiporphyrin arrays in terms of future practical applications [54–107]. Another promising approach for achieving these goals is the self-assembly of porphyrin bearing molecular recognition units. These porphyrin self-assemblies are prepared easily but often afford less complete structural control and stability [108–143]. We have focused on self-assembled monolayers (SAMs) of porphyrins on flat gold substrates, because they can provide densely packed, highly ordered structures of porphyrins on 2D gold electrodes suitable for developing artificial photosynthetic systems [108–118].

Systematic studies on the structure and photoelectrochemical properties of the SAMs of porphyrin disulfide dimers **1** on gold electrodes (denoted as Au/**1**) were performed to examine the effects of the spacer length, as shown in Fig. 19.1 [108, 110, 114]. In the molecular design of porphyrin disulfide dimers **1**, six *t*-butyl groups were introduced into the *meso*-phenyl rings of the porphyrin moieties to increase the solubility in organic solvents and to suppress the quenching of the porphyrin excited states in the monolayers owing to the porphyrin aggregation (Fig. 19.1) [114]. The structure of the SAMs was investigated using ultraviolet-visible absorption spectroscopy in transmission mode, cyclic voltammetry, ultraviolet-visible ellipsometry, and fluorescence spectroscopy [114]. These measurements revealed that the SAMs tend to form highly ordered structures on the gold electrode with increasing the methylene spacer length, reaching to surface coverage of up to 1.5×10^{-10} mol cm⁻² (110 \AA^2 molecule⁻¹) [114]. The adjacent

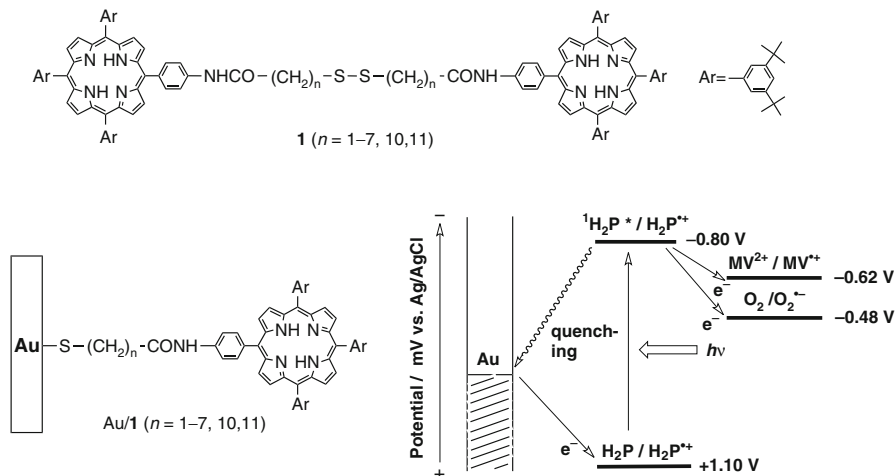


Fig. 19.1 Porphyrin disulfide dimers **1**, self-assembled monolayers of porphyrins on a gold electrode Au/**1**, and photocurrent generation diagram for Au/**1**/MV²⁺/Pt device

porphyrin rings are likely to adopt J-aggregate-like partially stacked structures in the monolayer [104]. The porphyrin ring plane in the monolayer with an even number ($n = 2, 4, 6, 10$) of the methylene spacer ($-(\text{CH}_2)_n-$) is tilted significantly to the gold surface, while the porphyrin with an odd number ($n = 1, 3, 5, 7, 11$) of the methylene spacer takes a nearly perpendicular orientation to the gold surface [114].

The photoelectrochemical experiments on the gold electrodes modified with **1** were carried out in an argon-saturated Na_2SO_4 aqueous solution containing methyl viologen (MV^{2+}) as an electron carrier using a platinum wire counter electrode and an Ag/AgCl reference electrode (denoted as Au/**1**/MV²⁺/Pt) [114]. An increase in the cathodic electron flow was observed with increasing the negative bias (0.7 V to -0.2 V) to the gold electrode [114]. This implies that vectorial electron transfer takes place from the gold electrode to the counter electrode through the SAM and the electrolyte. With increasing the spacer length, the absorbed photon-to-current efficiency (APCE) of the photocurrent generation in the Au/**1**/MV²⁺/Pt device was increased in a zigzag fashion to reach a maximum of 0.34% ($n=6$) and then decreased slightly. Such dependence of the APCE value on the spacer length can be rationalized by a trade-off between electron and energy transfer quenching of the porphyrin singlet excited state as illustrated in Fig. 19.1. Photoirradiation of the modified electrode results in electron transfer from the porphyrin singlet excited state ($E_{\text{ox}}^0 = -0.80$ V vs. Ag/AgCl) to MV²⁺ ($E_{\text{red}}^0 = -0.62$ V vs. Ag/AgCl) or O₂ ($E_{\text{red}}^0 = -0.48$ V vs. Ag/AgCl) [114]. The reduced electron carriers diffuse to release electrons to the platinum electrode, whereas the resultant porphyrin radical cation ($\text{H}_2\text{P}^{\bullet+}$; +1.10 V vs. Ag/AgCl) captures electrons from the gold electrode, generating the cathodic electron flow [114]. However, the energy transfer quenching of the porphyrin excited singlet state by the gold surface is competitive, judging from the extremely short fluorescence lifetimes (τ) of the porphyrins (10–40 ps) on

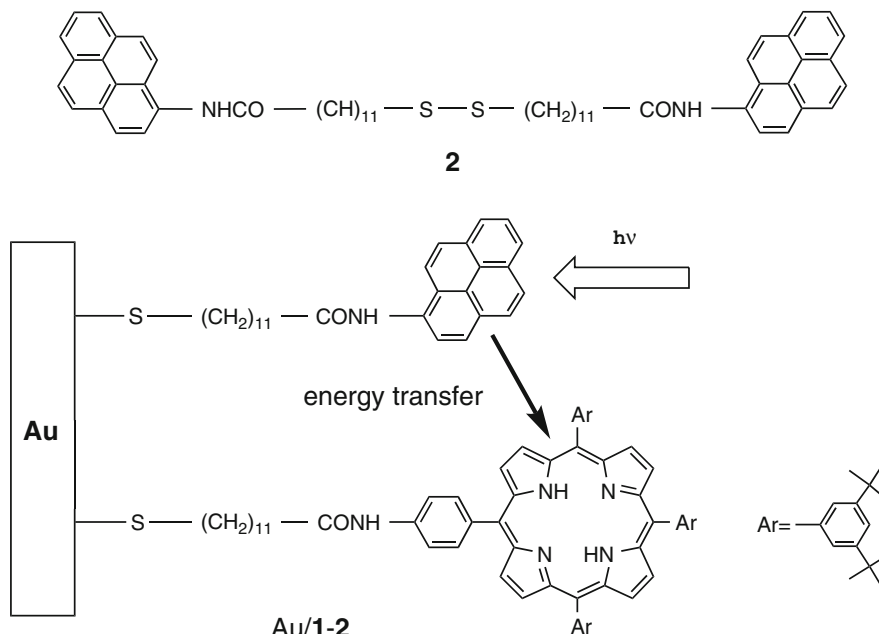


Fig. 19.2 Pyrene disulfide dimer **2** and mixed self-assembled monolayers of porphyrin and pyrene on a gold electrode Au/1-2

the gold surface compared with the values (1–10 ns) on quartz or semiconductor surfaces (*vide infra*) [114, 119, 121]. The electronic coupling between the porphyrin and the electrode is reduced with increasing the spacer length, leading to less energy transfer quenching of the porphyrin excited singlet state by the gold surface. On the other hand, an increase in the separation distance between the gold electrode and the $\text{H}_2\text{P}^{\bullet+}$ slows down the electron transfer from the gold electrode to the $\text{H}_2\text{P}^{\bullet+}$. Thus, the trade-off effect as a function of the spacer length may be responsible for a nonlinear dependence of the APCE value on the spacer length (*vide supra*). These results manifest that the optimization of each process is vital to achieve efficient photocurrent generation in the SAMs of photoactive chromophores on gold electrodes.

To realize efficient photoinduced energy transfer on a gold electrode, it is essential to integrate suitable energy donor and acceptor on the gold surface. As the first attempt, mixed SAMs of pyrene and porphyrin on gold electrodes were prepared to address the possibility of photoinduced energy transfer on the surface. Monolayers of a mixture of porphyrin disulfide dimer **1** ($n = 11$) and pyrene disulfide dimer **2** were formed by the coadsorption of **1** ($n = 11$) and **2** onto Au(111) mica substrates (denoted as Au/1-2), as depicted in Fig. 19.2 [112, 116].

The electrochemical measurements of Au/1 and Au/2 in CH_2Cl_2 containing 0.1 M $n\text{-Bu}_4\text{NPF}_6$ electrolyte suggested the formation of well-packed structures of **1** and **2** on the gold surfaces [112, 116]. In the mixed SAMs, however, the waves

arising from the first oxidations of the porphyrin and pyrene moieties were too broad to determine the adsorbed amounts of **1** and **2** in Au/**1-2** accurately. The ratio of **1:2** in Au/**1-2**, estimated from the absorption spectrum on the gold surface, is significantly lower than the value in CH₂Cl₂. The strong $\pi - \pi$ interaction of the pyrene moieties in comparison with the relatively weak interaction between the porphyrin moieties, because of the bulky *t*-butyl groups, may be attributed to the preference of the adsorption of **2** over **1** on the gold surface. In addition, the fact that the pyrene molecule occupies about half the surface area of the porphyrin would lead to a thermodynamic preference for pyrene adsorption, since displacement of a porphyrin for two pyrenes results in an extra S-Au interaction [112, 116].

To probe a singlet-singlet energy transfer from the pyrene excited singlet state to the porphyrin moiety in the mixed SAMs, time-resolved, single-photon counting fluorescence measurements were made for Au/**1-2** as well as **1** and **2** in CH₂Cl₂ with an excitation wavelength of 280 nm, where the light is mainly absorbed by the pyrene moiety [112, 116]. The decay of the fluorescence intensities at $\lambda_{\text{obs}} = 385$ and 720 nm, arising from the pyrene and the porphyrin singlet excited states, respectively, could be monitored. The decay curve could be fitted as a single exponential except for the case of **2** at 385 nm in CH₂Cl₂. The fluorescence lifetimes of Au/**2** at 385 nm (23 ps) and Au/**1** at 720 nm (40 ps) are much shorter than those of **2** (7.4 ns (30%), 3.2 ns (70%)) and **1** (8.1 ns) in CH₂Cl₂. This indicates that the excited singlet states of the pyrene and the porphyrin moieties in the SAMs are efficiently quenched by the gold surface via energy transfer. However, it should be noted here that the fluorescence lifetime of the pyrene moiety in Au/**1-2** at 385 nm decreases with increasing the ratio of the porphyrin to the pyrene. The fluorescence lifetime of the porphyrin moiety in Au/**1-2** at 720 nm is also decreased with increasing the ratio of the porphyrin to the pyrene. Thus, we can conclude that efficient energy transfer occurs from the pyrene excited singlet state to the porphyrin, followed by energy migration among the porphyrins, which can compete with the energy transfer quenching by the gold surface [112, 116].

Although efficient singlet-singlet energy transfer occurs from the pyrene excited singlet state to the porphyrin in the mixed SAMs of pyrene and porphyrin on the gold surface (*vide supra*), pyrene can absorb light in the ultraviolet region solely ($\lambda_{\text{max}} = 337$ nm), thereby making it impossible to collect light in the visible region (>400 nm). Boron-dipyrrin thiol **3** was then chosen as an improved light-harvesting molecule to achieve efficient energy transfer from the boron-dipyrrin excited singlet state (¹B*) in **3** to the porphyrin (H₂P) in **4** in the mixed SAMs that were prepared from **3** and porphyrin alkanethiol **4** (Fig. 19.3) [116]. The boron-dipyrrin dye exhibits a moderately strong absorption band in the visible region around 500 nm ($\sim 10^5$ M⁻¹ cm⁻¹) and a relatively long singlet excited-state lifetime (~ 5 ns) [116]. Taking into account the fact that the porphyrin moiety in **4** absorbs strongly in the blue (~ 420 nm) and weakly in the green region, an incorporation of the boron-dipyrrin pigments **3** into a SAM of **4** (denoted as Au/**4**) allows us to enhance the absorption properties in the green region as well as the blue region. More importantly, the fluorescent emission (~ 510 nm) from the boron dipyrin overlaps well with the absorption of Q bands (500–650 nm) of the porphyrin. Thus, an efficient Förster-type singlet-singlet energy transfer from the (¹B*) in **3** to the

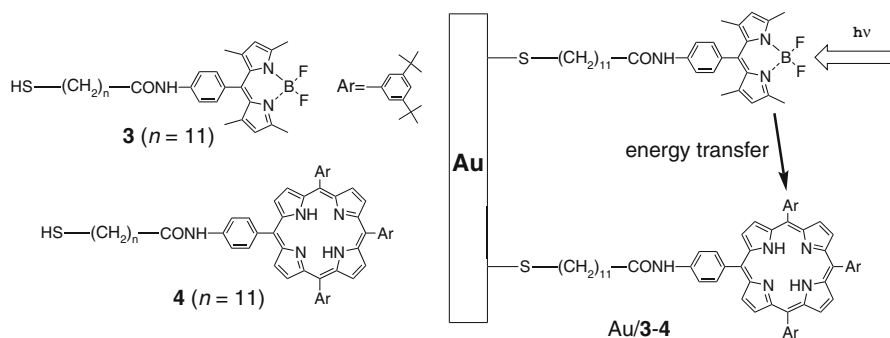


Fig. 19.3 Boron dipyrin **3** ($n = 11$) and porphyrin alkanethiol **4** ($n = 11$) and mixed self-assembled monolayers of boron dipyrin and porphyrin on a gold electrode Au/3-4

H₂P in **4** is anticipated to occur in the mixed SAMs of **3** and **4** on the gold surface (denoted as Au/3-4).

Actually, based on the energy diagram, energy transfer is expected to take place from ¹B* in **3** to H₂P in **4**, followed by intermolecular electron transfer from the resulting ¹H₂P* to diffusing electron carriers such as O₂ and MV²⁺ in the electrolyte, which eventually gives electrons to the counter electrode. On the other hand, the gold electrode gives electrons to the H₂P^{•+}, generating vectorial electron flow from the gold electrode to the counter electrode through the SAM and the electrolyte [116]. Thus, the present system can mimic both photosynthetic energy transfer and electron transfer in the mixed SAM.

Cyclic voltammogram measurements indicated the formation of densely packed monolayers of **3** and **4** on the gold surfaces, as in the cases of **1** and **2** [116]. The estimated ratio of **3**:**4** in the mixed SAMs is significantly higher than the value in the solution. The preference of the adsorption of **3** over **4** on the gold surface may also result from the strong $\pi - \pi$ interaction of the planar boron-dipyrin moieties against relatively weak interaction between the porphyrin moieties as a result of the bulky *t*-butyl groups and the thermodynamic preference for boron-dipyrin adsorption against the porphyrin that possesses the larger occupied area (*vide supra*) [116].

Efficient energy transfer from ¹B* in **3** to H₂P in **4** was confirmed by the fluorescence spectrum of Au/3-4 that reveals fluorescent emission from the porphyrin moiety solely ($\lambda_{\text{max}} = 650, 720 \text{ nm}$) irrespective of an excitation wavelength ($\lambda_{\text{ex}} = 510$ or 420 nm) [116]. The energy transfer efficiency from ¹B* in **3** to H₂P in **4** rises with rising the ratio of the porphyrin to the boron dipyrin, to reach a maximum value of 100% at a ratio of **3**:**4** = 69:31. Under the optimized conditions, the excitation spectrum of Au/3-4 with the fixed emission wavelength ($\lambda_{\text{em}} = 650 \text{ nm}$) matches the absorption spectrum of Au/3-4. This unambiguously corroborates that efficient energy transfer takes place from ¹B* in **3** to H₂P in **4** in the mixed SAMs on the gold surfaces.

The photoelectrochemical measurements were carried out using the SAMs of **3** and/or **4** on the gold electrodes in the standard three-electrode arrangement under the optimized conditions [electrolyte solution: O₂-saturated 0.1 M Na₂SO₄ solution

containing 30 mM MV^{2+}] (denoted as Au/**3-4**/ MV^{2+} /Pt) [116]. Unfortunately, the APCE values of the photocurrent generation in the Au/**3**/ MV^{2+} /Pt, Au/**4**/ MV^{2+} /Pt, and Au/**3-4**/ MV^{2+} /Pt devices are similar under the same conditions as a consequence of comparable performance of the Au/**3**/ MV^{2+} /Pt and Au/**4**/ MV^{2+} /Pt devices. Accordingly, we could not obtain unambiguous evidence for the photocurrent generation resulting from photoinduced energy transfer from $^1B^*$ in **3** to the H_2P in **4** in the mixed SAMs of **3** and **4** on the gold electrode.

To enhance the energy transfer-assisted photocurrent generation, it is crucial to incorporate efficient photocurrent generation molecules into a SAM of light-harvesting molecules. Thus, ferrocene (Fc)-porphyrin (H_2P)- C_{60} triad **5** [113, 115] was employed for the boron-dipyrrin SAM to improve the quantum yield of photocurrent generation (Fig. 19.4). The triad thiol **5** was designed to reveal photoinduced electron transfer from the $^1H_2P^*$ to the C_{60} , followed by the efficient electron transfer from the ferrocene to the resulting H_2P^{*+} , to yield the final charge-separated state, $Fc^+-H_2P-C_{60}^{\bullet-}$, as demonstrated in solutions [144, 145]. The $C_{60}^{\bullet-}$ moiety in the charge-separated state gives electrons to electron carriers such as MV^{2+} and O_2 in the electrolyte, whereas electrons are shifted from the gold electrode to the Fc^+ moiety, resulting in the efficient cathodic electron flow, as displayed in Fig. 19.4. In addition, the emission from the boron dipyrin in **3**, which exhibits better light-harvesting properties around 500 nm than **5**, matches well with the absorption of the porphyrin in **5**, as seen in the case of mixed SAMs of **3** and **4**. Thus, an efficient energy transfer from the $^1B^*$ in **3** to the H_2P in **5** would take place in the mixed SAMs of **3** and **5** on the gold surface (Fig. 19.4). Overall, it is anticipated that the mixed SAMs of **3** and **5** can lead to efficient photocurrent generation, which also mimics the light-harvesting and charge separation in photosynthesis.

The amounts of **3** and **5** on the gold surface were systematically altered by the competitive coadsorption onto the gold surface from CH_2Cl_2 solutions containing various molar ratios of **3** and **5** (molar ratio of **3**:**5** = 100:0; 75:25; 50:50; 25:75; 10:90; 0:100) [116]. From the cyclic voltammetric and absorption spectral measurements, the ratio of **3**:**5** in Au/**3-5** was found to be comparable to that in CH_2Cl_2 . In contrast to the cases of Au/**1-2** and Au/**3-4** (*vide supra*), no significant preference of the adsorption of **3** over **5** on the gold surface was observed, indicating that $\pi - \pi$ interaction of the boron-dipyrrin moieties is similar to that of **5** that contains both the porphyrin and fullerene moieties.

The photoelectrochemical measurements were conducted using the mixed SAMs of **3** and **5** on the gold electrodes in the three-electrode arrangement (denoted as Au/**3-5**/ MV^{2+} /Pt) [116]. The APCE values of the Au/**3-5**/ MV^{2+} /Pt device, determined based on the absorption of the porphyrin and the antenna molecules at 430 and 510 nm, increase with increasing the content of **5** in the SAMs. The energy transfer efficiency from $^1B^*$ in **3** to H_2P in **5** may also raise with raising the content of **5** in the SAMs to reach maximum APCE values of $21 \pm 3\%$ at 430 nm and $50 \pm 8\%$ at 510 nm with a ratio of **3**:**5** = 37:63. The incident photon-to-current efficiencies (IPCE) of the Au/**3-5**/ MV^{2+} /Pt device at 510 and 430 nm were also determined as 0.6 and 1.6 %, respectively [116]. Formation of the charge-separated

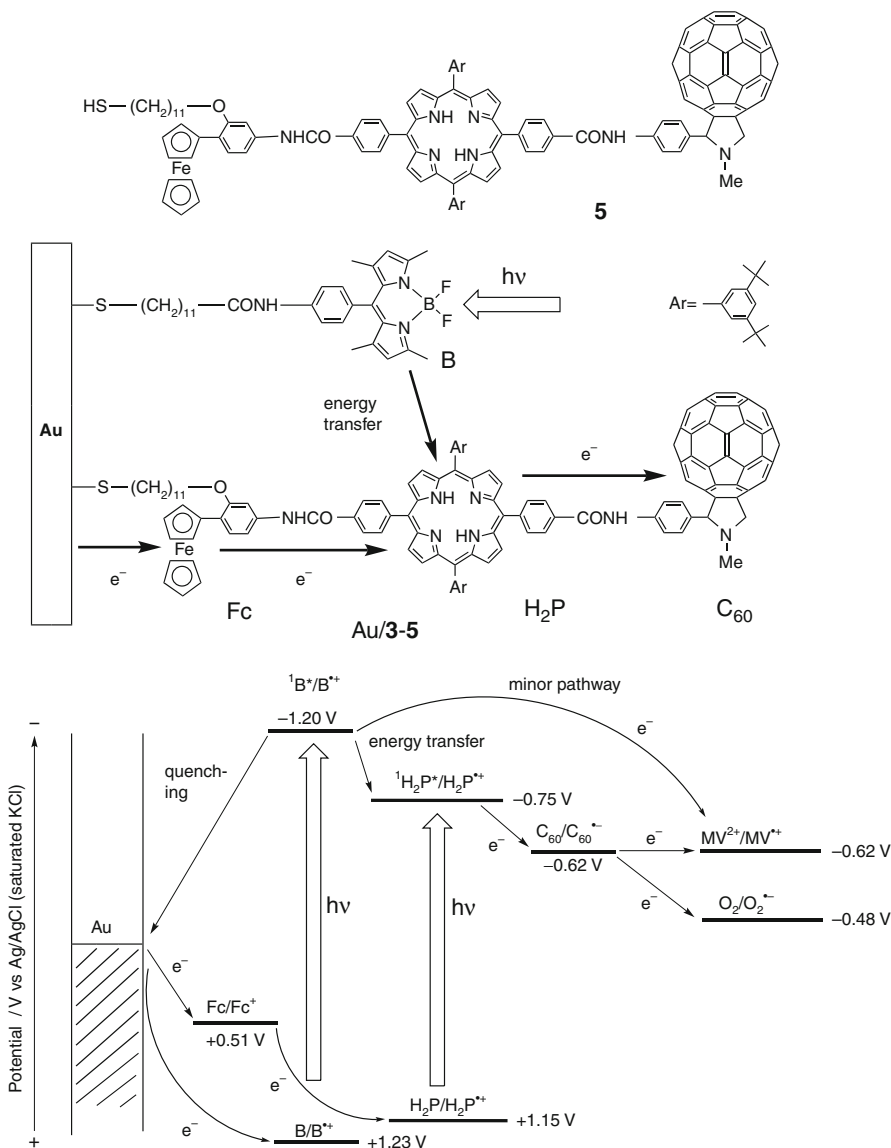


Fig. 19.4 Ferrocene-porphyrin-fullerene triad **5**, a self-assembled monolayer of boron dipyrin and ferrocene-porphyrin-fullerene triad on a gold electrode Au/3-5, and photocurrent generation diagram for the Au/3-5/MV²⁺/Pt device

state (i.e., Fc⁺-H₂P-C₆₀^{•-}) in **5** following the energy and electron transfer steps in Fig. 19.4 has been well established by the time-resolved transient absorption studies of the triad molecule together with the fluorescence lifetime measurements, although the small absorbance of the present system has precluded the direct

19.2.2 Self-Assembled Monolayers of Porphyrins on ITO Electrodes

As described in Sect. 19.2.1, we have successfully achieved photosynthetic electron and energy transfer on the gold electrode modified with SAMs of porphyrins and related photoactive chromophores. However, strong energy transfer quenching of the porphyrin excited singlet state by the flat gold electrode has precluded achievement of a high quantum yield for charge separation on the surface as attained in natural photosynthesis. To surmount such an energy transfer quenching problem, indium-tin oxide (ITO) with high optical transparency ($>90\%$) and electrical conductivity ($\sim 10^4 \Omega \text{ cm}$) seems to be highly attractive as an electrode. The quenching of the porphyrin excited singlet state on the surface may be suppressed because the conduction band (CB) of ITO is higher than the energy level of the porphyrin excited singlet state. Despite these advantages, development of SAMs on the ITO electrode has been rather limited in that their chemical modification requires carefully controlled conditions that have been difficult to achieve [121]. As such, the substituent effects of porphyrins in SAMs on ITO have not been fully addressed.

We examined the effects of bulkiness in porphyrin SAMs on the structure and photoelectrochemical properties [124]. 5,10,15,20-Tetraphenylporphyrin (TPP) and 5,10,15,20-tetraphenylporphyrin with bulky *tert*-butyl groups at the *meta* positions of the *meso*-phenyl groups (TBPP) were covalently linked to the ITO surface (denoted as ITO/6 and ITO/7), respectively, as illustrated in Fig. 19.5. The ultraviolet-visible absorption, steady-state fluorescence, and cyclic voltammetry measurements for the porphyrin SAMs revealed that the interaction between the porphyrins without bulky *tert*-butyl groups is much larger than that of the porphyrins with bulky *tert*-butyl groups. Photoelectrochemical measurements were carried out in a nitrogen-saturated Na_2SO_4 aqueous solution containing triethanolamine (TEA) as an electron sacrifier in the three-electrode arrangement using the ITO/6 and ITO/7 electrodes (denoted as ITO/6/TEA/Pt and ITO/7/TEA/Pt) [124]. Surprisingly, the APCE value of the ITO/6/TEA/Pt device ($2.2 \pm 0.9\%$) is virtually the same as that of ITO/7/TEA/Pt device ($3.4 \pm 0.6\%$), although there is a large difference in the interaction between porphyrins in ITO/6 and ITO/7 electrodes owing to the steric hindrance of the bulky *t*-butyl groups. The fluorescence lifetimes of ITO/6 [$\tau = 1.3 \text{ ns}$ (40%), 5.9 ns (60%)] and ITO/7 [$\tau = 1.9 \text{ ns}$ (29%), 8.2 ns (71%)] are moderately reduced relative to TPP ($\tau = 10 \text{ ns}$) and TBPP ($\tau = 10 \text{ ns}$) in THF. This means that the quenching of porphyrin excited singlet state on ITO is remarkably suppressed compared with the intensive quenching on flat gold electrodes ($\tau = 1\text{--}40 \text{ ps}$) [114, 119, 121]. It is noteworthy that the τ values of ITO/6 are largely similar to those of ITO/7. The results are in marked contrast with severe self-quenching of the porphyrin excited singlet state in conventional molecular assemblies such as Langmuir-Blodgett films [124]. The picosecond fluorescence anisotropy decay measurements for ITO/6 and ITO/7 suggested the occurrence of fast energy migration between porphyrin moieties in the SAMs [124]. The two-dimensional, densely packed structure of the porphyrins in SAMs is responsible for the long-lived excited singlet state, which resembles the antenna function of photosystem I

in cyanobacteria [48–50]. This conclusion is important for further development of porphyrin SAMs exhibiting antenna function, since we can densely pack porphyrin molecules on a 2D electrode surface where fast energy migration takes place between the porphyrins without losing the excitation energy.

19.3 Three-Dimensional Porphyrin Arrays

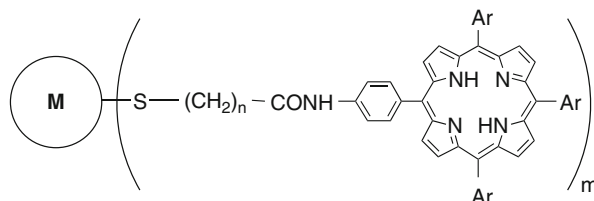
19.3.1 Self-Assembled Monolayers of Porphyrins on Metal Nanoparticles

To overcome the light-harvesting problem on a 2D surface, novel artificial light-harvesting systems, which remarkably enhance the light-harvesting properties, should be exploited to combine with charge separation system on an ITO electrode that also suppresses the undesirable energy transfer quenching. Metal nanoparticles, which can provide three-dimensional (3D) nanospace on the surface, are highly promising as nanoscaffolds for antenna molecules [148–156]. In particular, alkanethiolate-monolayer-protected gold nanoparticles are stable in air, soluble in common organic solvents, and therefore being capable of facile modification with other functional thiols through exchange reactions or by couplings and nucleophilic substitutions [150, 151]. Therefore, construction of the 3D architectures of porphyrin-modified gold nanoparticles, which have large surface area, on ITO electrode would improve the light-harvesting efficiency compared with the 2D porphyrin SAMs. Furthermore, the interaction of porphyrin excited singlet state with gold nanoparticles would be reduced significantly, relative to bulk gold surface, due to the “quantum effect” [152–156]. In this context, multiporphyrin monolayer-modified gold nanoparticles AuNP-**1** ($n = 3, 5, 7, 11$) were prepared as a new type of artificial photosynthetic materials (Fig. 19.6) [157–165]. The photophysical and electrochemical properties of AuNP-**1** ($n = 3, 5, 7, 11$) are compared to the corresponding 2D porphyrin SAM (Au/**1** ($n = 3, 5, 7, 11$)), as shown in Fig. 19.1 [157, 159]. For instance, AuNP-**1** ($n = 11$) was directly synthesized by reduction of AuCl_4^- with NaBH_4 in toluene containing the corresponding porphyrin disulfide dimer **1** or porphyrin alkanethiol **4** to avoid incomplete functionalization. AuNP-**1** ($n = 11$) was purified repeatedly by gel permeation chromatography and characterized by ^1H NMR, UV-visible and fluorescence spectroscopies, electrochemistry, elemental analysis, and transmission electron microscopy (TEM) [157, 159].

The mean diameter of the gold core determined by TEM was 2.1 nm (with a standard deviation $\sigma = 0.3$ nm) for AuNP-**1** ($n = 11$), which is comparable to the value obtained for alkanethiolate-protected gold nanoparticle under the same experimental conditions [157, 159]. Taking the gold core as a sphere, the model predicts that the core of AuNP-**1** ($n = 11$) contains 280 gold atoms, of which 143 lie on the gold surface. Given the values for elemental analysis of AuNP-**1** ($n = 11$), there are 57 porphyrin alkanethiolate chains on the gold surface for AuNP-**1** ($n = 11$). It should be emphasized here that the molecular weight of AuNP-**1** ($n = 11$) is estimated as 120,000, which is one of the highest values for multiporphyrin

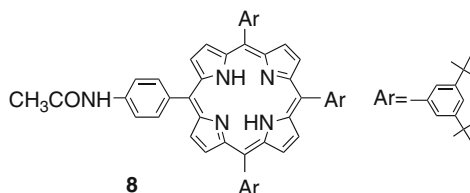
Fig. 19.6

Porphyrin-modified metal nanoparticles MNP-1 ($n = 3, 5, 7, 11$, $M = \text{Au, Ag, Pt, Pd, Ag-Au}$) and porphyrin reference **8**



AuNP-1 ($n = 3, 5, 7, 11$, $M = \text{Au}$)

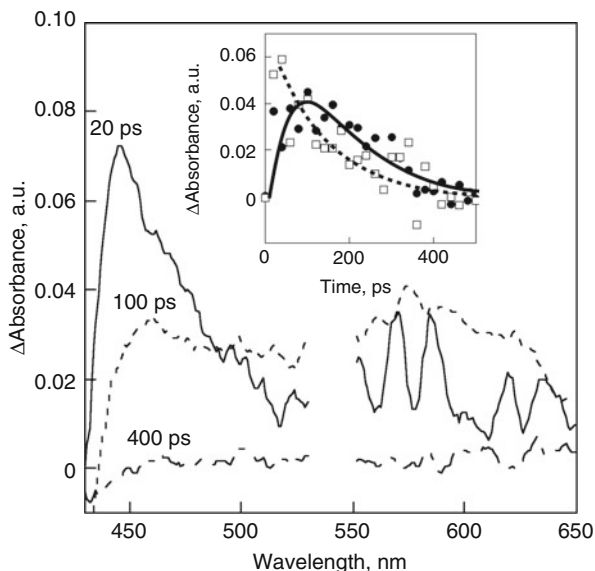
MNP-1 ($n = 11$, $M = \text{Ag, Pt, Pd, Ag-Au}$)



arrays with well-defined structure [21, 39, 86–89]. The coverage ratio of porphyrin alkanethiolate chains of AuNP-1 ($n = 11$) to surface gold atoms (γ) is determined as 40 %, which is remarkably increased relative to the coverage ratio ($\gamma = 6.5 \%$) of 2D porphyrin SAM Au/1 ($n = 11$). In other words, the light-harvesting properties of the 3D system are much improved compared with those of the 2D system. $^1\text{H-NMR}$, cyclic voltammetry, and absorption measurements of AuNP-1 ($n = 11$) revealed that the porphyrin environment of AuNP-1 ($n = 11$) is virtually the same as that of porphyrin reference **8** in solution and is less perturbed than that of Au/1 ($n = 11$) [157, 159].

To establish the excited-state deactivation pathways, nanosecond transient absorption spectra were recorded for AuNP-1 ($n = 11$) and **8** in benzonitrile [159]. AuNP-1 ($n = 11$) and **8** exhibit characteristic absorption arising from the porphyrin excited triplet state, but the intensity of transient absorption for AuNP-1 ($n = 11$) is much lower than that of **8** under the same experimental conditions. This implies that most of the porphyrin excited singlet state on the gold nanoparticles is quenched by the metal surface, whereas residual porphyrin excited triplet state is generated *via* the intersystem crossing from the unquenched porphyrin excited singlet state. Picosecond transient absorption spectra were also taken for AuNP-1 ($n = 11$) in benzonitrile (Fig. 19.7) [159]. Immediately after the excitation of AuNP-1 ($n = 11$), the transient absorption arising from the porphyrin excited singlet state appears. The decay rate constant of the band ($k_q = 7.7 \times 10^9 \text{ s}^{-1}$ at 460 nm) agrees well with the values for the rise of a hot band due to the surface plasmon around 600 nm [166] as well as for a short component of the fluorescence decay (Inset of Fig. 19.7). There is no evidence for the formation of the porphyrin radical cation. These results suggest that the porphyrin excited singlet state in the present systems is quenched by the metal surface via energy transfer rather than electron transfer [159]. The fluorescence of the 3D porphyrin AuNP-1 ($n = 11$) exhibited a double

Fig. 19.7 Picosecond transient absorption spectra of AuNP-1 ($n = 11$) in benzonitrile as a function of the time delay between the pump and probe laser beams (20, 100, 400 ps) at an excitation of 540 nm. The inset displays the time profiles at 460 nm (dotted curve with white squares) and 600 nm (solid curve with black circles)



exponential decay (0.13 ns (93%), 9.6 ns (7%)). The lifetime of the longer-lived, minor component of AuNP-1 ($n = 11$) in benzonitrile is close to that of **8** (~10 ns). This minor component may result from different ligation sites (vertex, edge, terrace, and defect) on the truncated octahedral Au core surface or **1** that does not bind covalently to the Au surface. The lifetime of the short-lived, major component (0.13 ns (93%)) is three times as long as that of Au/**1** ($n = 11$) (0.040 ns). These results unambiguously exemplify that the quenching of the porphyrin excited singlet state by the gold nanoparticle via energy transfer is much suppressed relative to the energy transfer quenching by the bulk Au(111) surface [157, 159].

We also prepared multiporphyrin-modified metal nanoparticles AuNP-1 with different chain lengths between the porphyrin and the gold nanoparticle to examine the spacer effects ($n = 3, 5, 7, 11$) on the structure and photophysical properties (Fig. 19.6) [159]. The TEM data revealed that the size of gold nanoparticle is not susceptible to the chain length of the spacer even in the case of the large porphyrin moiety. The TEM image of AuNP-1 ($n = 3$) exhibited hexagonal packing of AuNP-1 ($n = 11$) in which the edge-to-edge separation distance between the gold core (3.6 nm) is 2 times as large as the thickness of the porphyrin monolayer. Such hexagonal packing of AuNP-1 ($n = 3$) can be ascribed to the densely packed, rigid structure of the porphyrin moieties near the gold nanoparticle because of the short methylene spacer [159]. Although no similar hexagonal packing was seen for the other porphyrin-modified gold nanoparticles with a longer spacer ($n = 5, 7, 11$), the separation distances between the gold core in the TEM images are largely similar irrespective of the chain length of the spacer. Considering that the spacer is splayed outward from the highly curved outermost surface of gold nanoparticles, void space between the porphyrins increases with increasing the chain length of the spacer.

This allows the porphyrin moieties to be interdigitated with each other to leave the separation distance similar. The fluorescence lifetime was decreased slightly with decreasing the spacer length, which is in accordance with the energy transfer quenching trend in the 2D porphyrin SAMs [114]. Plots of $\ln k_q$ vs. d (edge-to-edge distance) yield the same β value (damping factor) of $0.1 \pm 0.01 \text{ \AA}^{-1}$ for AuNP-1 ($n = 3, 5, 7, 11$) and Au/1 ($n = 3, 5, 7, 11$) (Fig. 19.8) [159]. The slower energy transfer rate of the 3D surface than that of the 2D surface may originate from the less gold atoms ($\sim 10^2$) on the 3D surface of the nanoparticles involved in energy transfer in comparison with those on the 2D surface of the bulk flat electrode. The β value in this study is remarkably small relative to those for conventional energy transfer systems ($0.3 \sim 1.7 \text{ \AA}^{-1}$) [167–171]. The small β value suggests that the alky chain is not fully extended as the chain length increases or that surface plasmons play an important role in the fluorescence quenching, since energy transfer from the excited fluorophore to metal surface is known to be enhanced by surface plasmons and the energy transfer to surface plasmons is a slowly varying function of distance [159]. However, the exact mechanism of fluorescence quenching remains to be clarified.

A variety of porphyrin monolayer-protected metal nanoparticles MNP-1 ($n = 11$) were prepared to examine the effects of metal ($M = \text{Au}, \text{Ag}, \text{Au-Ag alloy}, \text{Pd}$, and Pt) and size (i.e., $1 \sim 3 \text{ nm}$ ($M = \text{Au}$)) on the structures and photophysical properties (Fig. 19.6) [158]. The quenching rate constants of the porphyrin excited singlet state by the surfaces of mono-metal nanoparticles and gold particles with a different diameter are virtually the same. In contrast, the quenching rate constant

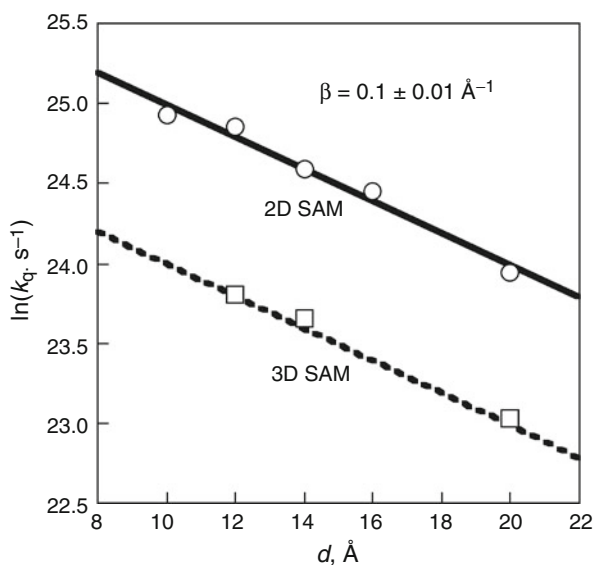


Fig. 19.8 Distance dependence of quenching rate constant for 3D porphyrin SAMs (dashed line with white squares) and 2-D porphyrin SAMs (solid line with white circles). The plots of $\ln(k_q)$ vs. d gave straight lines with the slope (-0.1 ± 0.01) according to $k_q = k_0 \exp(-\beta d)$

of the gold-silver alloy nanoparticles is smaller by a factor of 1/2 than that of the corresponding mono-metal particles (i.e., Au or Ag). This reveals that interaction between the surface of the gold-silver alloy and the porphyrin excited singlet state is reduced considerably in comparison with the mono-metal systems. Accordingly, porphyrin-modified metal nanoparticles are potential candidates as novel artificial photosynthetic materials and photocatalysts [158].

Given that the porphyrin-modified metal nanoparticles possess the high light-harvesting properties together with the suppression effect of energy transfer quenching by the metal surface, we envisaged that they would exhibit efficient energy transfer from the zinc porphyrin excited singlet state to the free base porphyrin when mixed SAMs of zinc porphyrins and free base porphyrins are formed on the gold nanoparticle. Preliminary experiments on the mixed system, however, did not show any clear evidence for the energy transfer process. No energy transfer behavior is rationalized by the relatively large separation distance and the unfavorable parallel orientation between the porphyrins.

However, such morphology is highly favorable to incorporate a guest molecule (i.e., acceptor) between the porphyrins, exhibiting photocatalytic and photovoltaic function. With these in mind, the photocatalytic properties of the porphyrin monolayer-protected gold nanoparticles with different chain lengths were investigated. The photocatalytic reduction of hexyl viologen (HV^{2+}) by 1-benzyl-1,4-dihydronicotinamide (BNAH) was compared with that of the reference porphyrin without the metal nanoparticle **8** (Fig. 19.9) [160]. Both porphyrin monolayer-protected gold nanoparticles and **8** act as efficient photocatalysts for the uphill reduction of HV^{2+} by BNAH to produce 1-benzylnicotinamidinium ion (BNA^+) and hexyl viologen radical cation ($HV^{\bullet+}$) in benzonitrile. In the case of the porphyrin monolayer-protected gold nanoparticle, the quantum yield reached a maximum value with an extremely low concentration of HV^{2+} , which is larger than the corresponding value of the reference system using **8**. The dependence of quantum yields on concentrations of BNAH and HV^{2+} as well as the time-resolved single-photon counting fluorescence and transient absorption spectroscopic results indicated that the photoinduced electron transfer from the triplet excited state of **8** to HV^{2+} initiates the photocatalytic reduction of HV^{2+} by BNAH but that the photoinduced electron transfer from the singlet excited state of porphyrin monolayer-protected gold nanoparticles to HV^{2+} , which forms supramolecular complex with them, is responsible for the photocatalytic reaction [160]. The intersystem crossing from the porphyrin singlet excited state to the triplet excited state is much suppressed by the quenching of the porphyrin excited singlet state via energy transfer to the gold surface of the 3D porphyrin-modified gold nanoparticles. However, the 3D architectures of porphyrin-modified gold nanoparticles with a suitable cleft between the porphyrin moieties allow us to interact HV^{2+} with them, resulting in fast electron transfer from the singlet excited state of porphyrin to HV^{2+} on porphyrin-modified gold nanoparticles [160]. Considering that $HV^{\bullet+}$ can generate H_2 in an acidic aqueous solution using Pt catalyst [172], the present system is fascinating as a photocatalyst for producing H_2 , which is expected to play an important role in hydrogen society.

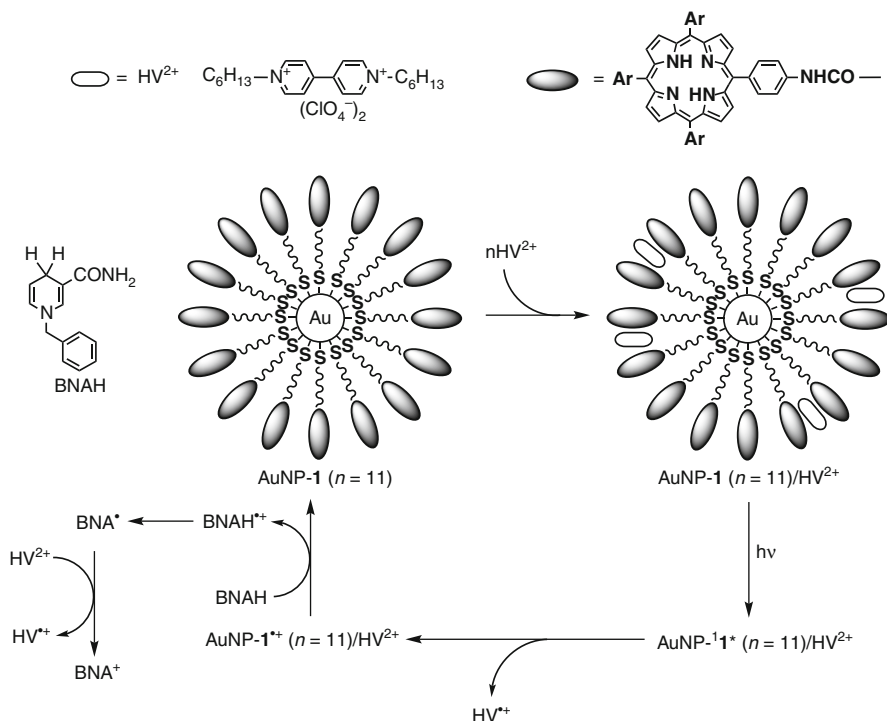


Fig. 19.9 Mechanism of AuNP-1 ($n = 11$)-photocatalyzed reduction of HV^{2+} by BNAH

Successful construction of the photocatalytic system using multiporphyrin-modified gold nanoparticles and hexyl viologen acceptor has encouraged us to design novel organic solar cells prepared by the bottom-up organization of porphyrin (donor) and fullerene (acceptor) with gold nanoparticles as nanoscaffolds on nanostructured semiconducting electrodes (Fig. 19.10) [161–165]. First, porphyrin disulfide dimers **1** or porphyrin alkanethiols **4** ($n = 5, 11, 15$) [114] were three-dimensionally organized onto a gold nanoparticle with a diameter of ~ 2 nm to give multiporphyrin-modified gold nanoparticles AuNP-**1** ($n = 5, 11, 15$) with well-defined size (~ 10 nm) and spherical shape (first organization) [157, 159]. These nanoparticles bear flexible host space between the porphyrins for guest molecules (i.e., C_{60}). Although there is equilibrium between the uncomplex and complex states in toluene (second organization), adding poor solvent (i.e., acetonitrile) into the toluene solution triggers the cluster formation in the mixed solvent by $\pi - \pi$ interaction between the porphyrin and C_{60} and the lyophobic interaction between the mixed solvent and the complex. Namely, the nanoparticles AuNP-**1** can be grown into larger clusters [denoted as $(AuNP-1+C_{60})_m$] with a size of ~ 100 nm in the mixed solvent by incorporating C_{60} molecules between the porphyrin moieties (third organization). Finally, electrophoretic deposition method is applied to the composite clusters in the mixed solvent to give a nanostructured SnO_2

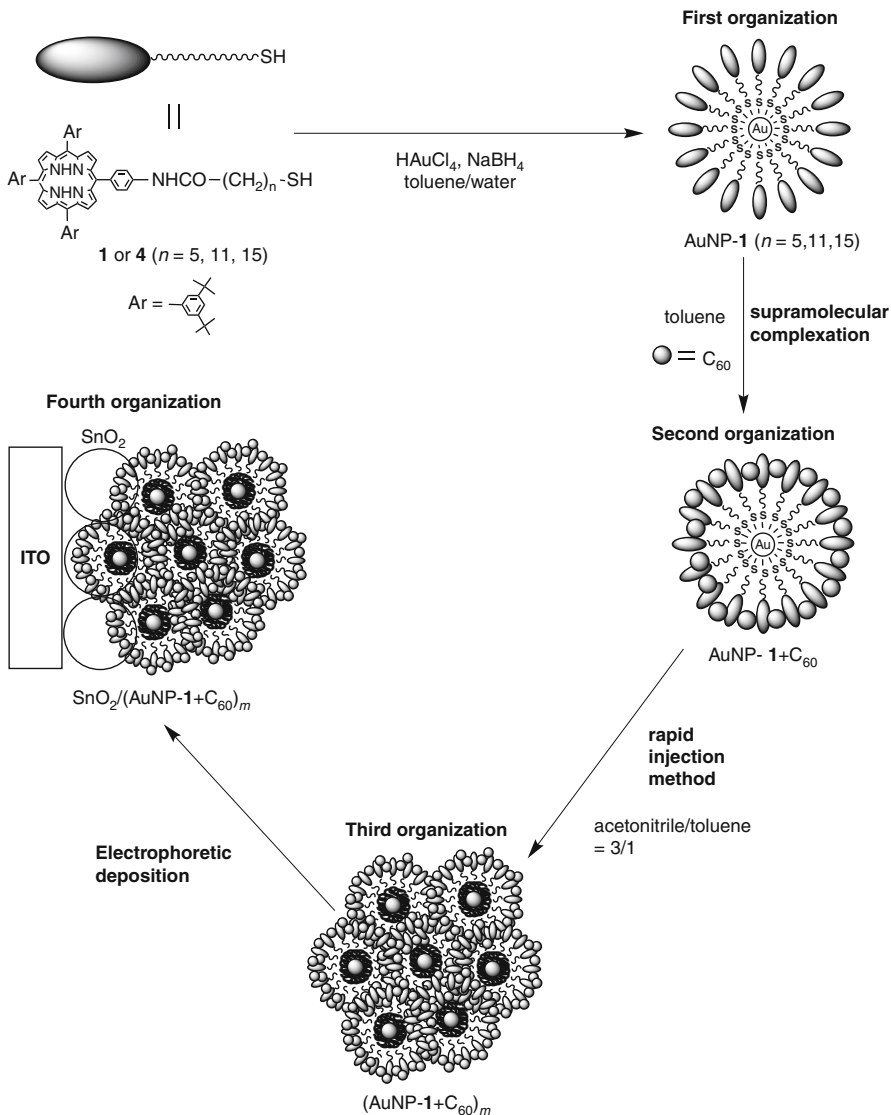


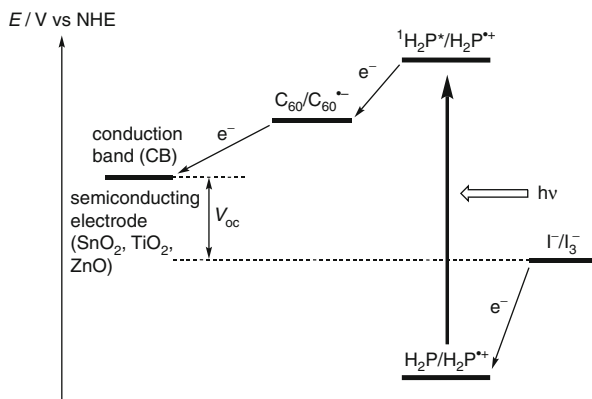
Fig. 19.10 Schematic view of *bottom-up* organization of porphyrin and fullerene by using gold nanoparticles as nanoscaffolds on a nanostructured SnO_2 electrode for dye-sensitized bulk heterojunction solar cells

electrode modified with the clusters (denoted as $\text{SnO}_2/(\text{AuNP-1+C}_{60})_m/\text{NaI+I}_2/\text{Pt}$), as shown in Fig. 19.10 (fourth organization). Under application of a dc electric field (100–500 V), the clusters in the mixed solvent become negatively charged and are deposited on the SnO_2 electrode as they are driven toward the positively charged electrode surface. The IPCE value of the $\text{SnO}_2/(\text{AuNP-1+C}_{60})_m/\text{NaI+I}_2/\text{Pt}$

device (up to 54% ($n = 15$)) was increased with increasing the chain length ($n = 5, 11, 15$) between the porphyrin and the gold nanoparticle [161, 162]. The long methylene spacer between the porphyrin and the gold nanoparticle allowed suitable space for C_{60} molecules to accommodate them between the neighboring porphyrin rings effectively compared to the nanoparticles with the short methylene spacer, leading to efficient photocurrent generation. On the other hand, further increase of the spacer length between the porphyrin and the gold nanoparticle resulted in a substantial decrease of the IPCE value [164]. Additionally, replacement of C_{60} with C_{70} or freebase porphyrin with zinc porphyrin led to a decrease of the photoelectrochemical response [162]. The preference may be explained by the difference in the complexation abilities between the porphyrin and fullerene molecules as well as in the electron or hole hopping efficiency in the composite clusters. The $\text{SnO}_2/(\text{AuNP-1 } (n = 15) + \text{C}_{60})_m/\text{NaI} + \text{I}_2/\text{Pt}$ device had a short circuit current (J_{SC}) of 1.0 mA cm^{-2} , an open circuit voltage (V_{OC}) of 0.38 V , a fill factor (ff) of 0.43 , and a power conversion efficiency (η) of 1.5% at a moderate input power (W_{IN}) of 11.2 mW cm^{-2} . The J - V characteristic of the $\text{SnO}_2/(\text{AuNP-1 } (n = 15) + \text{C}_{60})_m/\text{NaI} + \text{I}_2/\text{Pt}$ device was also remarkably enhanced by a factor of 45 in comparison with the $\text{SnO}_2/(\text{TBPP} + \text{C}_{60})_m$ device [162]. These results evidently illustrate that the large improvement of the photoelectrochemical properties arises from three-dimensional interdigitated structure of the porphyrin- C_{60} molecules on the SnO_2 electrode, which facilitates the injection of the separated electrons into the CB.

Photocurrent generation is initiated by photoinduced electron transfer from the porphyrin excited singlet state (${}^1\text{H}_2\text{P}^*/\text{H}_2\text{P}^{\bullet+} = -0.7 \text{ V}$ vs. NHE) to C_{60} ($\text{C}_{60}/\text{C}_{60}^{\bullet-} = -0.2 \text{ V}$ vs. NHE) in the porphyrin- C_{60} complex (Fig. 19.11). The reduced C_{60} transfers electrons to the CB of SnO_2 nanocrystallites ($E_{\text{CB}} = 0 \text{ V}$ vs. NHE) by electron hopping through the large excess of C_{60} molecules, to produce the current in the circuit. The regeneration of $\text{H}_2\text{P}^{\bullet+}$ ($\text{H}_2\text{P}/\text{H}_2\text{P}^{\bullet+} = 1.2 \text{ V}$ vs. NHE) is achieved by the iodide/triiodide couple ($\text{I}^-/\text{I}_3^- = 0.5 \text{ V}$ vs. NHE) present in the electrolyte system [162]. Our novel organic solar cells (i.e., dye-sensitized bulk heterojunction (DSBHJ) solar cell) possess both the dye-sensitized and bulk heterojunction characteristics [20–23, 25]. Namely, the device structure is similar to that of dye-sensitized solar cells, but donor-acceptor multilayers are deposited on the top surface of a nanostructured semiconducting electrode. Therefore, initial charge separation takes place at the blend interface of the donor-acceptor, which is typical characteristic of bulk heterojunction solar cells. Nevertheless, DSBHJ solar cells and dye-sensitized solar cells are alike in subsequent processes. It is noteworthy that the composite film reveals the donor-acceptor multilayer structure on a semiconducting electrode, which presents a striking contrast to the monolayer structure of adsorbed dyes on semiconducting electrodes of dye-sensitized solar cells. The sequential electron transfer from the donor excited state to the CB of the semiconducting electrode via the acceptor may inhibit charge recombination between electrons in the CB and donor radical cation or I_3^- in the electrolyte owing to the presence of the acceptor, resulting in improvement of the cell performance. Therefore, the photovoltaic properties of DSBHJ solar cells can be modulated by

Fig. 19.11 Schematic illustration of photocurrent generation in DSBHJ solar cells



altering device structure including the electrode (SnO_2 , TiO_2 , ZnO) as well as the donor-acceptor multilayers.

Bicontinuous donor-acceptor arrays at molecular level have attracted increasing scientific and technological interest due to their potential applications in organic photovoltaics [173]. Such donor-acceptor arrays would yield efficient charge separation and transportation of separated charges to respective electrodes leading to enhanced photocurrent generation provided ideally vertical arrangement of the donor-acceptor arrays on the electrodes. Although nanostructures with bicontinuous donor-acceptor arrays have been obtained by self-assembly of donor-acceptor molecules, it is still difficult to achieve desirable vertical arrangement of bicontinuous donor-acceptor arrays on an electrode [173]. A novel approach to construct vertical alignment of bicontinuous donor-acceptor arrays on a flat SnO_2 electrode was developed in DSBHJ photoelectrochemical device (Fig. 19.12) [174]. A palladium-mediated stepwise self-assembly of zinc porphyrins (ZnP) as a donor ensures the vertical growth of porphyrin chains on the flat SnO_2 electrode. Pyridylfullerenes (Py-C_{60}) as an acceptor are infiltrated into the porphyrin brush by using the coordination bonding of the pyridyl moiety to the zinc atom together with $\pi - \pi$ interaction between Py-C_{60} . Therefore, we can systematically investigate the relationship between the film structure and photoelectrochemical properties as a function of the number of porphyrin layer (n). With increasing n , the IPCE as well as APCE values increased to reach maxima ($n = 3$) and then decreased gradually. As described earlier, $^1\text{ZnP}^*$ injects electrons into the CB of SnO_2 , followed by electron transfer from I^- to the zinc porphyrin radical cation ($\text{ZnP}^{\bullet+}$), generating photocurrent. The trend is reasonable considering that the exciton diffusion length (~ 6 nm) of the porphyrin arrays, corresponding to the number of the porphyrins and the total length ($n = 3$), is comparable to that of copper phthalocyanine (8 ± 3 nm) in bulk heterojunction solar cells [175]. It is noteworthy that, for the $\text{SnO}_2/\text{C}_{60}\text{-acid}+(\text{ZnP})_n+\text{Py-C}_{60}$ electrodes, the trend on the IPCE and APCE values as a function of n is parallel to that on the infiltrated amount of Py-C_{60} as a function of n . Similar trend is noted for the $\text{SnO}_2/\text{C}_{60}\text{-acid}+(\text{ZnP})_n+\text{Ph-C}_{60}$ electrodes [174]. The photodynamics of the photoinduced charge separation processes was studied by femtosecond time-

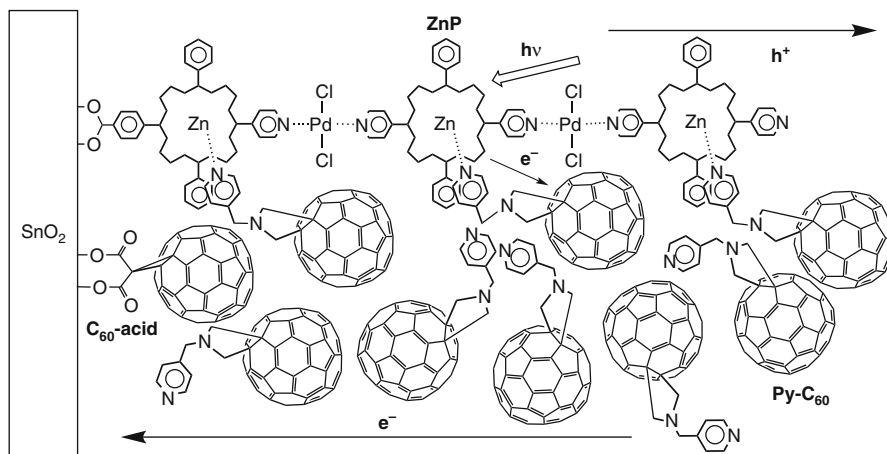


Fig. 19.12 Schematic illustration of vertical donor-acceptor bicontinuous arrays on a flat SnO_2 electrode in a DSBHJ photoelectrochemical device

resolved transient absorption measurements. The bleaching at 620 nm arises from $^1\text{ZnP}^*$, whereas the broad absorption around 660 nm originates from zinc porphyrin radical cation $\text{ZnP}^{\bullet+}$. Although both $^1\text{ZnP}^*$ and $\text{ZnP}^{\bullet+}$ appear simultaneously, large Δ absorbance of the $\text{SnO}_2/\text{C}_{60}\text{-acid}+(\text{ZnP})_7+\text{Py-C}_{60}$ relative to the $\text{SnO}_2/(\text{ZnP})_7$ around 660 nm exemplifies the additional contribution of the charge separation between ZnP and C_{60} to the enhancement in the photocurrent generation. This is consistent with the fact that the APCE value of the $\text{SnO}_2/\text{C}_{60}\text{-acid}+(\text{ZnP})_7+\text{Py-C}_{60}$ system (7.1% at 560 nm) is larger than that of the $\text{SnO}_2/(\text{ZnP})_7$ system (5.0% at 560 nm). That is, the exciton and carrier loss in the porphyrin arrays is suppressed due to the exciton capture and charge dissociation by C_{60} , which can rationalize the facts that the maximum IPCE and APCE values were attained at the higher number of the porphyrin layer for the $\text{SnO}_2/\text{C}_{60}\text{-acid}+(\text{ZnP})_n+\text{Py-C}_{60}$ systems ($n = 5$) than the $\text{SnO}_2/(\text{ZnP})_n$ systems ($n = 3$). The decreasing trend of the IPCE and APCE values in the $\text{SnO}_2/\text{C}_{60}\text{-acid}+(\text{ZnP})_7+\text{Py-C}_{60}$ system ($n = 6-8$) correlates with the decreasing amount of the incorporated C_{60} molecules between the porphyrin brushes, which arises from the porphyrin aggregation, as seen in the AFM measurements (vide supra). In that case the charge separation efficiency between the $^1\text{ZnP}^*$ and the C_{60} would be decreased with increasing the number of the porphyrin layers, leading to the decrease in the IPCE and APCE values. On the basis of the film structures and the photoelectrochemical properties of the $\text{SnO}_2/\text{C}_{60}\text{-acid}+(\text{ZnP})_n+\text{Py-C}_{60}$ systems together with the previously established photocurrent generation mechanism in similar porphyrin-fullerene composites on semiconducting electrodes, we can propose a photocurrent generation diagram. First, charge separation between $^1\text{ZnP}^*$ and C_{60} takes place in addition to direct electron injection from $^1\text{ZnP}^*$ to the CB of the SnO_2 . In the former case, the generated $\text{C}_{60}^{\bullet-}$ injects electrons into the CB of the SnO_2 via electron hopping through the C_{60} molecules infiltrated from top to bottom of the

porphyrin brushes. Thus, the bicontinuous donor-acceptor arrays for the $\text{SnO}_2/\text{C}_{60}$ -acid+(ZnP) $_n$ +Py- C_{60} ($n = 2-6$) electrodes are responsible for the enhancement of photocurrent generation [174].

19.3.2 Self-Assembled Monolayers of Porphyrins on Semiconducting Nanoparticles

Porphyrin alkanethiols have been successfully assembled on metal nanoparticles using sulfur-metal linkage. The multiporphyrin-modified metal nanoparticles MNP-1 have found to act as light-harvesting materials [157–159], photocatalysts [160] and organic solar cells [161–165]. In the case of metal nanoparticles, however, the relatively fast energy transfer quenching (40–260 ps) of the porphyrin excited singlet state by the metal nanoparticles has still precluded the further improvement of such systems [157–159]. Thus, replacement of the metal core by other nanoparticles is a challenge for exploring novel artificial photosynthetic materials. Along this line there are two promising candidates as nanoparticles: photochemically inactive nanoparticles and semiconducting nanoparticles exhibiting light-harvesting properties. In the former case, we have already reported silica nano- or microparticles covalently modified with multiporphyrins [176, 177]. The porphyrin excited singlet state is not quenched by the silica nanoparticle. Thus, the photocurrent generation efficiency of the silica nanoparticle-based photoelectrochemical device is significantly higher than that of metal nanoparticle-based corresponding device under the same conditions [177]. The drawback of the system is no light-harvesting properties of the silica nanoparticles that considerably reduce the total light-harvesting efficiency in the multiporphyrin-modified silica nanoparticles. Therefore, nanoparticles, which exhibit efficient light-harvesting, subsequent energy transfer to the immobilized porphyrins on the nanoparticles, and no quenching of the resulting porphyrin excited singlet state by the nanoparticles, are ideal as nanoscaffolds for the construction of efficient solar energy conversion system. Taking into account the requirement, luminescent semiconducting nanoparticles (i.e., CdS, CdSe, CdTe) [178] are potential nanoscaffolds owing to their broad absorption, narrow luminescence, and high photostability. Luminescent semiconducting nanoparticles have been employed as sensitizers in imaging analysis and for an increasing range of applications in biomedicine [179–181]. Such research often deals with energy transfer from luminescent semiconducting nanoparticles to dye molecules in imaging [182–186], photodynamic therapy [187–189], and drug delivery [190]. However, the detailed characterization of dye-luminescent semiconducting nanoparticle composites has been limited because of the complex structure arising from the weak interaction between dye and luminescent semiconducting nanoparticle. For instance, Zenkevich et al. have reported the formation of nanoassemblies consisting of CdSe/ZnS core/shell semiconducting nanoparticles and pyridyl-substituted porphyrin molecules, which were investigated by using UV-visible absorption and steady-state fluorescence spectroscopies and fluorescence lifetime measurements [191]. The weak complexation results from the coordination bonding of the pyridyl

nitrogen with the ZnS shell of the CdSe/ZnS nanoparticles. The emission quenching of the CdSe/ZnS nanoparticles by the pyridyl-substituted porphyrins was explained partially by energy transfer from the CdSe/ZnS nanoparticles to the porphyrins. In accordance with the fact, only a limited number of vacant binding sites and the weak complexation capability of the CdSe/ZnS nanoparticles for the porphyrins led to less than one porphyrin attached to the ZnS shell of the single CdSe/ZnS nanoparticle. As such, the photophysics of semiconducting nanoparticles covalently modified with chromophores (i.e., porphyrin) has not been fully understood [192–195].

We designed CdSe nanoparticles modified with multiporphyrins [196], as illustrated in Fig. 19.13. CdSe nanoparticles were chosen as a nanoscaffold for organizing porphyrins because of the light-absorbing capability in the UV-visible region, the large band gap (E_g) relative to that of freebase porphyrin (H₂P: 1.9 eV) [157–159], and the relatively facile modification by chromophore [197,198]. In such a case we can anticipate photoinduced energy transfer from the CdSe nanoparticle to the H₂P in CdSe-1 (Fig. 19.14). Thus, both porphyrin and CdSe nanoparticle are expected to absorb UV-visible light, leading to the eventual production of the porphyrin excited singlet state in CdSe-1. This is in sharp contrast with the multiporphyrin-modified metal or silica nanoparticles where only the porphyrins absorb the UV-visible light [157–159,177]. More importantly, the porphyrin excited singlet state would not be quenched by the CdSe semiconducting nanoparticle via energy transfer. However, there is possibility of the occurrence of photoinduced electron transfer between the porphyrin and CdSe nanoparticle. The photoinduced electron transfer process depends on the relationship between the CB and valence band (VB) of the CdSe nanoparticle vs. the first oxidation and reduction potentials of the porphyrin and the corresponding excited states of the porphyrin. Since it is difficult to anticipate the actual levels of the CB and VB of CdSe nanoparticles, such a study will provide basic and valuable information on the design of chromophore-modified luminescent semiconducting nanoparticles toward efficient solar energy conversion.

The multiporphyrin-modified CdSe nanoparticles CdSe-1 ($n = 11$) were obtained by place-exchange reactions of hexadecylamine-thiophenol-modified CdSe nanoparticles (CdSe-ref) with porphyrin disulfide dimer **1** ($n = 11$) or porphyrin alkanethiol **4** ($n = 11$) in toluene [196]. The number of porphyrin molecules (N) on the surface of single CdSe nanoparticle increased with increasing the reaction time to reach a saturated maximum of $N = 21$. The structures of CdSe-ref and CdSe-1 were characterized by various spectroscopic methods and surface and elemental analyses [196]. Both of the porphyrins and CdSe nanoparticle in the multiporphyrin-modified CdSe nanoparticle were found to absorb the UV-visible light. The steady-state emission and time-resolved emission lifetime measurements revealed energy transfer from the CdSe excited state to the porphyrins in the multiporphyrin-modified CdSe nanoparticles, as depicted in Fig. 19.15 [196]. The energy transfer efficiency of CdSe-1 ($N = 3.4$) is moderate (33%), whereas the value of CdSe-1 ($N = 21$) is estimated to be $\sim 100\%$, taking into account the correlation between the N value and the emission intensity from the porphyrins. The emission decay of the porphyrins in CdSe-4 exhibited a single exponential with

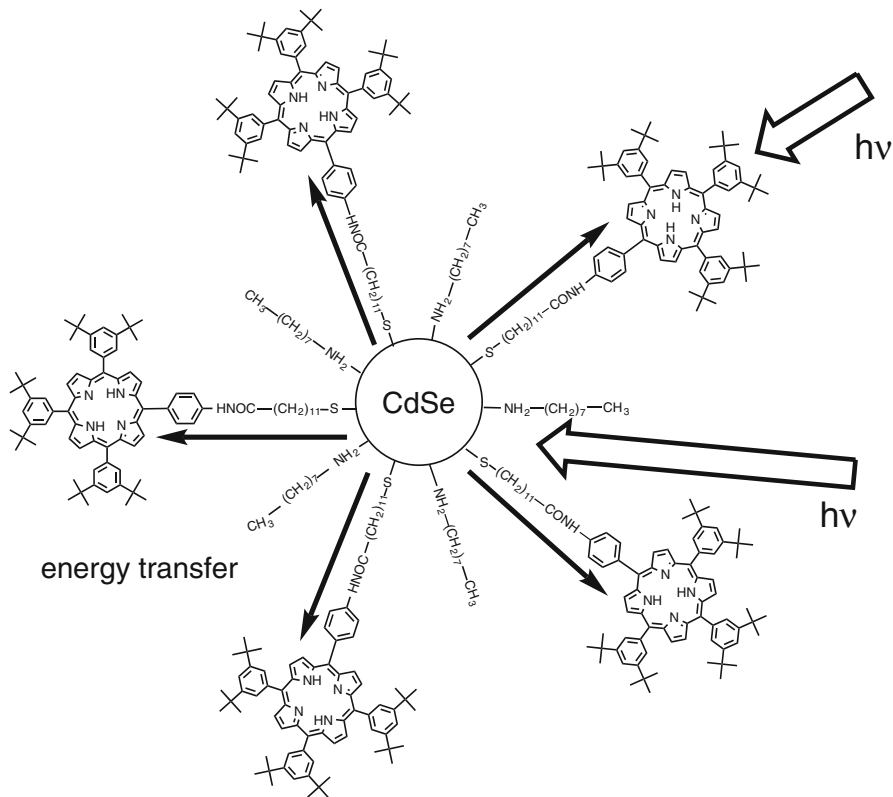


Fig. 19.13 Schematic view of light-harvesting and energy transfer in CdSe-1 ($n = 11$)

a lifetime of 12.3 ns, which is in good agreement with the value of the porphyrin reference **8** (12.3 ns). This exemplifies no quenching of the $^1\text{H}_2\text{P}^*$ by the CdSe core, as anticipated from the experimentally determined energy diagram (Fig. 19.14), together with no self-quenching of the $^1\text{H}_2\text{P}^*$. These unique properties are in sharp contrast with those in multiporphyrin-modified metal and silica nanoparticles [157–159, 177]. Multiporphyrin-semiconducting nanoparticle composites may be combined with suitable acceptors to develop organic solar cells and photocatalysts, thereby being highly promising as novel artificial photosynthetic materials.

19.4 Molecular Nanostructures

19.4.1 Porphyrin J-Aggregates

Natural chlorophyll aggregates in purple bacteria and chlorosomes have strong transition dipole moments stemming from the alignment of the head-to-tail direction [40–47]. Thus, J-aggregates of synthetic porphyrins are highly promising as

Fig. 19.14 Energy level diagram of CdSe-1 ($n = 11$). The experimental uncertainty to estimate the energy levels is ± 0.02 V

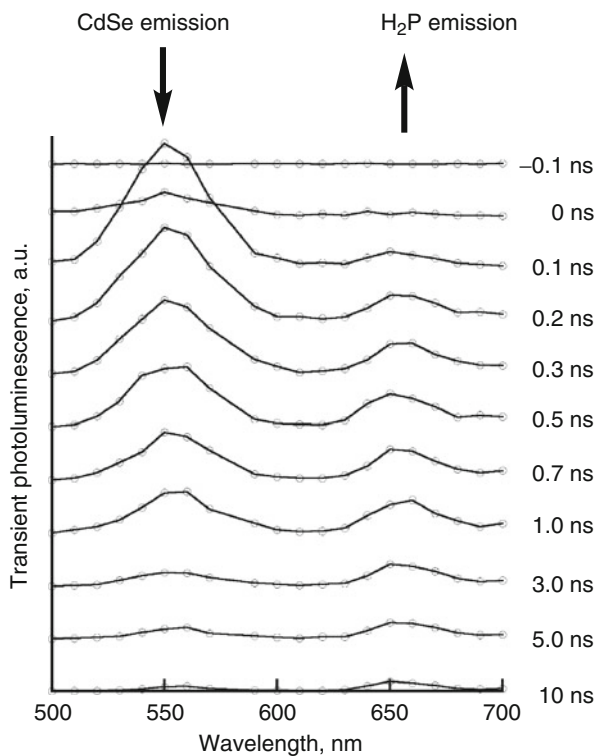
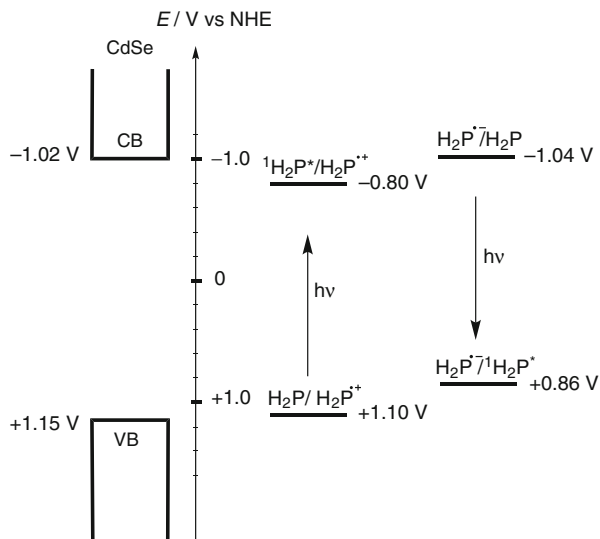


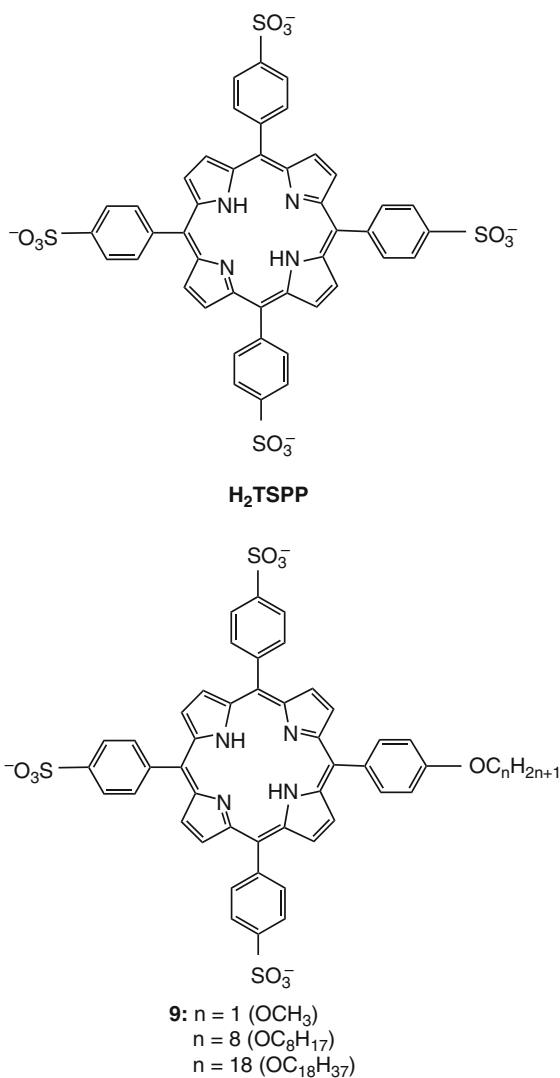
Fig. 19.15 Time-resolved emission spectra of CdSe-1 ($n = 11$, $N = 3.4$) in toluene at $\lambda_{\text{ex}} = 375$ nm

light-harvesting models to examine the structure-function relationship. However, the porphyrin J-aggregates have been rather limited to tetrakis(4-sulfonatophenyl) porphyrin (H_2TSPP) and its derivatives in acidic solutions [199–211], protonated tetraphenylporphyrins at the liquid-liquid [212, 213] or gas-liquid interface [213, 214], cationic tetraphenylporphyrins [215], dendritic porphyrins [216], and amphiphilic porphyrins [217]. As such, substituent effects of H_2TSPP on the structures and photophysical properties of J-aggregates have yet to be investigated in detail.

Substituent effects of porphyrin on the structures and optical and photophysical properties of the J-aggregates of protonated 5-(4-alkoxyphenyl)-10,15,20-tris(4-sulfonatophenyl)porphyrin **9** ($n = 1, 8, 18$) and their derivatives were examined systematically (Fig. 19.16) [218, 219]. The electrostatic interaction between the positively charged protonated core and negatively charged sulfonato groups is the driving force for the association of the protonated porphyrin monomers to J-aggregates under acidic conditions. Thus, the minimum requirement is the presence of two sulfonato groups at the *para*-positions of the *meso*-phenyl groups in 5,15 positions of the porphyrin ring to attain the slipped head-to-tail structure. To stabilize the J-aggregates, one sulfonato group is replaced by hydrophobic group (i.e., alkoxy group), whereas the three sulfonato groups remain intact. The length of alkyl moiety in the alkoxy group **9** ($n = 1, 8, 18$) would affect the interaction between the porphyrins under acidic conditions, making it possible to control the structures and photophysical properties of the porphyrin J-aggregates (Fig. 19.16).

Selective formation of the porphyrin J-aggregate was attained for protonated **9** ($n = 8$) [218]. The J-aggregate of the protonated **9** ($n = 8$) displayed the most red-shifted and intense bands, suggesting the highly ordered architecture. The atomic force microscopy (AFM) image of the J-aggregate from the protonated **9** ($n = 8$) exhibited striking contrast to those from protonated **9** ($n = 1, 18$). Regular leaflike structures (length = 260 nm, width = 60 nm, and height = 4.4 nm) are seen for the protonated **9** ($n = 8$), which largely matches the size (170 nm) determined by the dynamic light-scattering measurements. The cryo-transmission electron microscopy image revealed thin stringlike structure with a thickness of 4.9 nm, which is in good accordance with the height value (4.4 nm) determined from the AFM measurements. A bilayer structure was proposed to explain the unique porphyrin J-aggregate in which the hydrophobic alkoxy groups facing inside the bilayer are interdigitated with each other, whereas the hydrophilic porphyrin moieties are exposed outside, as schematically illustrated in Fig. 19.17 [218]. The lifetimes of the J-aggregates for the protonated **9** ($n = 1, 8, 18$) are much shorter than that for H_2TSPP ($\tau = 350$ ps). Furthermore, the lifetime becomes shorter with increasing the length of alkoxy group ($\tau = 2.3$ ps for $n = 1$, $\tau = 1.7$ ps for $n = 8$, $\tau = 1.4$ ps for $n = 18$). Fast energy migration and efficient quenching by defect site in the J-aggregates were suggested to rationalize the short lifetimes of the excited J-aggregates [218].

Fig. 19.16 Molecular structures of amphiphilic porphyrins H_2TSP and **9** ($n = 1, 8, 18$)



19.4.2 Conjugated Polymer-Carbon Nanotube Composites

Carbon nanotubes (CNTs) are current targets of general interest for their unique electronic, thermal, mechanical, and optical properties, particularly in connection with exploiting their properties into composites for molecular electronics [220–222]. However, the lack of their solubility in solvents results in a marked impediment toward harnessing their applications. Supramolecular functionalization

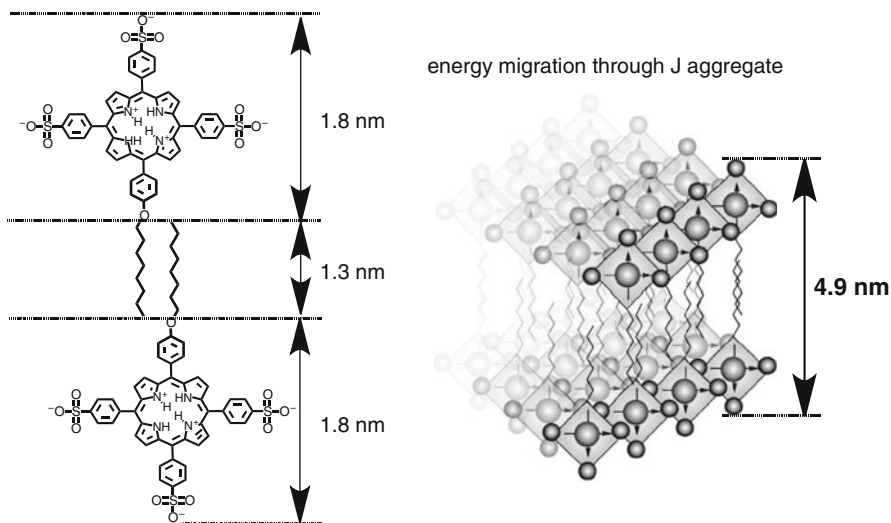


Fig. 19.17 Plausible bilayer structure for the porphyrin J-aggregate of protonated **9** ($n = 8$) in which the alkoxy chains are interdigitated with each other, exhibiting a layer thickness of 4.9 nm

of CNTs is a potential approach to overcome this problem, because supramolecular interaction does not disrupt unique properties of these composites [223–226]. Surfactants and hydrophilic polymers are known to exfoliate CNT bundles to disperse CNTs in aqueous solutions, but they are still insufficient for the solubilization of CNTs in organic solvents, which are more suitable for the fabrication of CNT composites into molecular devices.

Utilization of $\pi - \pi$ interaction is a promising methodology for dispersing CNTs in organic solvents [223–226]. Various π electron-rich compounds including pyrene, porphyrin, and π -conjugated polymers have been employed to interact with CNTs forming supramolecular composites. Specifically, conjugated polymers have been the subjects of extensive research as active materials for use in light-emitting diodes and photovoltaic devices [227]. Thus, the nanocomposites of highly exfoliated CNTs and conjugated polymers are appealing candidates exhibiting unique photophysical properties in molecular devices. There have been intensive researches on the composites of CNTs and poly(*m*-phenylenevinylene)-*co*-(2,5-dioctyloxy-*p*-phenylenevinylene) [224, 228, 229]. Furthermore, photophysics of the composites of poly(*p*-phenylenevinylene) (PPV) or polythiophene derivatives and CNTs have been studied in solutions and films [230–234]. Nevertheless, the photophysical properties including energy transfer or electron transfer process between conjugated polymers and CNTs have not been fully elucidated. For instance, only the emission quenching from the π -conjugated polymers in the composites but no emission from the CNTs due to the energy transfer have yet been observed.

To demonstrate energy transfer from π -conjugated polymers to CNTs unambiguously, it is essential to transform the bundle to isolated individual CNT in solvents

by wrapping it with novel π -conjugated polymers. A novel conjugated polymer, poly[(*p*-phenylene-1,2-vinylene)-*co*-(*p*-phenylene-1,1-vinylidene)] (*co*PPV), was prepared by the Heck coupling reaction to examine specific interactions between π -conjugated polymers and single-walled carbon nanotubes (SWNTs), as schematically illustrated in Fig. 19.18 [235]. The *co*PPV has the structural defect in the main chain of all-*trans* phenylene-1,2-vinylenes caused by 1,1-vinylidene moieties. It is expected that, as a result of the introduction of defect sites by 1,1-vinylidene units, the backbone structure of the copolymer can be fitted to the curvature of SWNTs more efficiently than the corresponding regular homopolymer, PPV, yielding individual SWNTs wrapped with the *co*PPV. The absorption and fluorescence properties of *co*PPV (vide infra) disclose that the band gap energy (2.5 eV) exceeds that of SWNTs. Accordingly, *co*PPV is anticipated to exfoliate CNTs more efficiently than the corresponding PPV to debundle SWNTs into individual SWNTs, allowing us

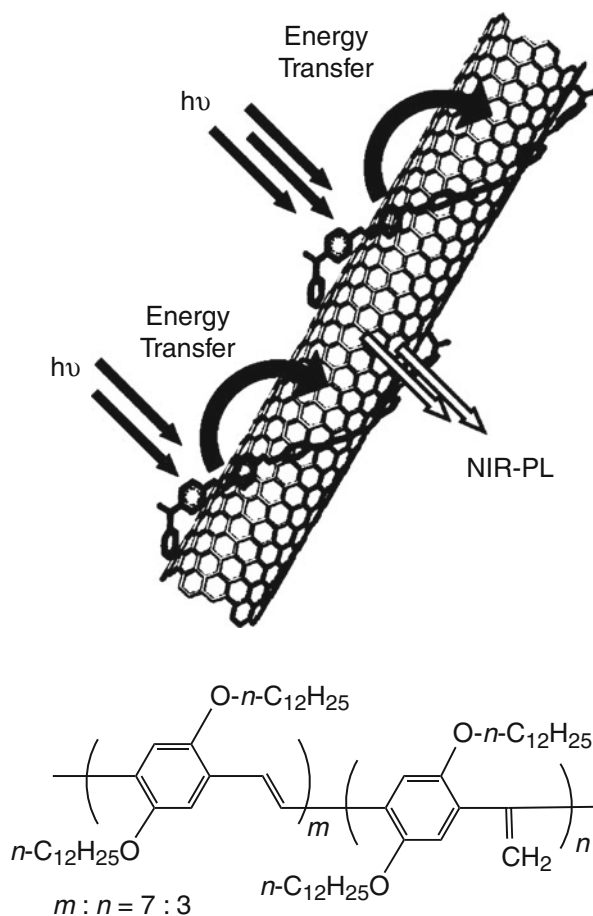
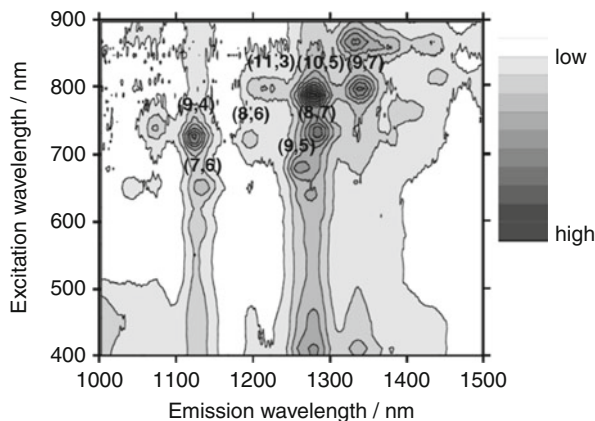


Fig. 19.18 Schematic view of energy transfer from *co*PPV to SWNT in the composite, followed by near-infrared photoluminescence from the SWNT

Fig. 19.19 Contour plot of photoluminescence spectra for *co*PPV-SWNTs in THF as a function of excitation and emission wavelengths



to detect the energy transfer process from the excited *co*PPV to the SWNTs in the composites (Fig. 19.18).

The absorption peaks associated with transitions between the symmetric van Hove singularities in the nanotube density of states are evident for the visible-near-infrared (vis-NIR) absorption spectrum of the redispersed *co*PPV-SWNT nanocomposites in THF [235]. The results demonstrate that *co*PPV acts as an efficient dispersing agent of SWNTs, since the sharpness of these peaks is widely considered to be a measure of the level of exfoliation of SWNT bundles. The AFM image of the composites revealed the SWNTs with a dramatic decrease in the size of bundles relative to SWNTs without dispersants, implying that the involvement of supramolecular interaction with *co*PPV for the debundling of SWNTs. The composite solution of *co*PPV-SWNTs exhibited a set of emissions in the contour plot (Fig. 19.19). The intensity of (10, 5) is much stronger than those of the other peaks, suggesting that (10, 5) SWNT is exfoliated to be isolated from bundles more efficiently than SWNTs with other chiral indices. It should be emphasized here that the contour plot of *co*PPV-SWNTs discloses enhancement of emission at an excitation wavelength (λ_{em}) of 400–500 nm. The excitation wavelength does not match the electronic absorption peaks of E_{22} (580–900 nm) and E_{33} (<410 nm) of SWNTs included in HiPco samples. Therefore, direct excitation of SWNTs is negligible under the experimental conditions. This emission can be accounted for by the initial excitation due to the $\pi - \pi^*$ transition of *co*PPV, followed by energy transfer from the excited *co*PPV to SWNTs in the composites. The energy transfer process was further substantiated by the excitation spectra of *co*PPV-SWNTs at $\lambda_{em} = 1,125$ nm, which are attributed mainly to (9, 4) and partially to (7, 6) and (8, 4) SWNTs [235]. Although there is a report on the enhancement of NIR emission intensity of SWNTs by the energy transfer from an organic molecule encapsulated in SWNTs [236], this is the first observation, to our best knowledge, of the enhancement of emission intensity by interaction with dispersing agents. Our strategy enables the polymer bound to the outside of SWNTs in organic solvents to act as a light-harvesting antenna for SWNTs. The observed characteristic features

will be utilized for further exploration of SWNTs as light-emitting and photovoltaic devices.

19.5 Conclusions and Outlook

Synthetic multiporphyrin arrays have been found to be artificial mimics of light-harvesting systems. We have successfully prepared 2D porphyrin arrays on gold and ITO electrodes as well as 3D porphyrin assemblies on metal and semiconducting nanoparticles. In particular, novel multiporphyrin-modified metal nanoparticles revealed improved light-harvesting properties as well as suppression of undesirable energy transfer quenching of the porphyrin excited singlet state by the metal surface. Since multiporphyrin-modified metal nanoparticles have flexible molecular recognition clefts between the porphyrins, they can be combined with acceptors (viologens or fullerenes) to exhibit photocatalytic and photovoltaic properties. Specifically, multiporphyrin-modified gold nanoparticles have been assembled with fullerenes in a bottom-up manner to make large and uniform composite clusters on nanostructured semiconductor electrodes, leading to a moderate power conversion efficiency of up to 1–2%. Molecular nanostructures including porphyrin J-aggregates and conjugated polymer-SWNT composites have disclosed unique energy transfer behavior based on the well-controlled nanostructures.

Well-defined molecule-based nanoarchitectures exhibiting energy transfer will open the door to nanoscience and nanotechnology, which stimulates a variety of fields including chemistry, biology, physics, and electronics to develop interdisciplinary novel principles and concepts.

Acknowledgements The authors are deeply indebted to the work of all collaborators and co-workers whose names are listed in the references (in particular, Prof. P. V. Kamat, Prof. S. Fukuzumi, Prof. H. Lemmetyinen, Prof. N. V. Tkachenko, Prof. S. Isoda, Prof. O. Ito, Prof. D. Kim). H. I. thanks Grand-in-Aids (No. 21350100 to H.I.), ALCA (JST), Strategic Japanese-Finnish Cooperative Program (JST), and WPI Initiative, MEXT, Japan, for financial support.

References

1. M.R. Wasielewski, *Chem. Rev.* **92**, 435 (1992)
2. D. Gust, T.A. Moore, A.L. Moore, *Acc. Chem. Res.* **26**, 198 (1993)
3. D. Gust, T.A. Moore, A.L. Moore, *Acc. Chem. Res.* **34**, 40 (2001)
4. A. Harriman, J.-P. Sauvage, *Chem. Soc. Rev.* **26**, 41 (1996)
5. M.-J. Blanco, M.C. Jimenez, J.-C. Chambron, V. Heitz, M. Linke, J.-P. Sauvage, *Chem. Soc. Rev.* **28**, 293 (1999)
6. V. Balzani, A. Juris, M. Venturi, S. Campagna, S. Serroni, *Chem. Rev.* **96**, 759 (1996)
7. V. Balzani (ed.), *Electron Transfer in Chemistry* (Wiley-VCH, Weinheim, 2001)
8. N. Armaroli, *Photochem. Photobiol. Sci.* **2**, 73 (2003)
9. J. Jortner, M. Ratner (ed.), *Molecular Electronics* (Blackwell, London, 1997)
10. M.N. Paddon-Row, *Acc. Chem. Res.* **27**, 18 (1994)
11. J.W. Verhoeven, *Adv. Chem. Phys.* **106**, 603 (1999)
12. K. Maruyama, A. Osuka, N. Mataga, *Pure Appl. Chem.* **66**, 867 (1994)

13. A. Osuka, N. Mataga, T. Okada, *Pure Appl. Chem.* **69**, 797 (1997)
14. L. Sun, L. Hammarstrom, B. Akermark, S. Styring, *Chem. Soc. Rev.* **30**, 36 (2001)
15. D. Holten, D.F. Bocian, J.S. Lindsey, *Acc. Chem. Res.* **35**, 57 (2002)
16. H. Imahori, Y. Sakata, *Adv. Mater.* **9**, 537 (1997)
17. H. Imahori, Y. Sakata, *Eur. J. Org. Chem.* **1999**, 2445 (1999)
18. H. Imahori, Y. Mori, Y. Matano, *J. Photochem. Photobiol. C* **4**, 51 (2003)
19. H. Imahori, *Org. Biomol. Chem.* **2**, 1425 (2004)
20. H. Imahori, S. Fukuzumi, *Adv. Funct. Mater.* **14**, 525 (2004)
21. H. Imahori, *J. Phys. Chem. B* **108**, 6130 (2004)
22. H. Imahori, *J. Mater. Chem.* **17**, 31 (2007)
23. H. Imahori, *Bull. Chem. Soc. Jpn.* **80**, 621 (2007)
24. T. Umeyama, H. Imahori, *Energy Environ. Sci.* **1**, 120 (2008)
25. H. Imahori, T. Umeyama, *J. Phys. Chem. C* **113**, 9029 (2009)
26. H. Imahori, T. Umeyama, S. Ito, *Acc. Chem. Res.* **42**, 1809 (2009)
27. D.M. Guldi, *Chem. Commun.* 321 (2000)
28. D.M. Guldi, M. Prato, *Acc. Chem. Res.* **33**, 695 (2000)
29. D.M. Guldi, *Chem. Soc. Rev.* **31**, 22 (2002)
30. M.E. El-Khouly, O. Ito, P.M. Smith, F. D'Souza, *J. Photochem. Photobiol. C* **5**, 79 (2004)
31. L. Sanchez, N. Martin, D.M. Guldi, *Chem. Soc. Rev.* **34**, 31 (2005)
32. J.H. Alstrum-Acevedo, M.K. Brennaman, T. Meyer, *J. Inorg. Chem.* **44**, 6802 (2005)
33. M.R. Wasielewski, *J. Org. Chem.* **71**, 5051 (2006)
34. S. Fukuzumi, *Phys. Chem. Chem. Phys.* **10**, 2283 (2008)
35. V. Balzani, A. Credi, M. Venturi, *ChemSusChem* **1**, 26 (2008)
36. D. Gust, T.A. Moore, A.L. Moore, *Acc. Chem. Res.* **42**, 1890 (2009)
37. M.R. Wasielewski, *Acc. Chem. Res.* **42**, 1910 (2009)
38. J.J. Concepcion, J.W. Jurss, M.K. Brennaman, P.G. Hoertz, A.O.T. Patrocínio, N.Y.M. Iha, J.L. Templeton, T.J. Meyer, *Acc. Chem. Res.* **42**, 1954 (2009)
39. N. Aratani, D. Kim, A. Osuka, *Acc. Chem. Res.* **42**, 1922 (2009)
40. J. Deisenhofer, J.R. Norris (eds.), *The Photosynthetic Reaction Center* (Academic, San Diego, 1993)
41. R.E. Blankenship, M.T. Madigan, C.E. Bauer (eds.), *Anoxygenic Photosynthetic Bacteria* (Kluwer Academic Publishing, Dordrecht, 1995)
42. G. McDermott, S.M. Prince, A.A. Freer, A.M. Hawthornthwaite-Lawless, M.Z. Papiz, R.J. Cogdell, N.W. Isaacs, *Nature* **374**, 517 (1995)
43. A.W. Roszak, T.D. Howard, J. Southall, A.T. Gardiner, C.J. Law, N.W. Isaacs, R.J. Cogdell, *Science* **302**, 1969 (2003)
44. C.J. Law, A.W. Roszak, J. Southall, A.T. Gardiner, N.W. Isaacs, N.W. Cogdell, *Mol. Membr. Biol.* **21**, 183 (2004)
45. J. Deisenhofer, O. Epp, K. Miki, R. Huber, H. Michel, *Nature* **318**, 618 (1985)
46. G. Fritzsche, J. Koepke, R. Diem, A. Kuglstatter, L. Baciou, *Acta Crystallogr.* **D58**, 1660 (2002)
47. J.M. Olson, *Photochem. Photobiol.* **67**, 61 (1998)
48. A. Zouni, H.-T. Witt, J. Kern, P. Fromme, N. Kraub, W. Saenger, P. Orth, *Nature* **409**, 739 (2001)
49. A. Zouni, H.-T. Witt, J. Kern, P. Fromme, N. Kraub, W. Saenger, P. Orth, *Nature* **411**, 909 (2001)
50. A. Ben-Shem, F. Frolow, N. Nelson, *Nature* **426**, 630 (2003)
51. G.S. Engel, T.R. Calhoun, E.L. Read, T.-K. Ahn, T. Mancal, Y.-C. Cheng, R.E. Blankenship, G.R. Fleming, *Nature* **446**, 782 (2007)
52. M. Sarovar, A. Ishizaki, G.R. Fleming, K.B. Whaley, *Nat. Phys.* **6**, 462 (2010)
53. G.D. Scholes, G.R. Fleming, A. Olaya-Castro, R. van Grondelle, *Nat. Chem.* **3**, 763 (2011)
54. S. Prathapan, T.E. Johnson, J.S. Lindsey, *J. Am. Chem. Soc.* **115**, 7519 (1993)
55. R.W. Wagner, T.E. Johnson, J.S. Lindsey, *J. Am. Chem. Soc.* **118**, 11166 (1996)

56. J. Li, A. Ambroise, S.I. Yang, J.R. Diers, J. Seth, C.R. Wack, D.F. Bocian, D. Holten, J.S. Lindsey, *J. Am. Chem. Soc.* **121**, 8927 (1999)
57. R.K. Lammi, A. Ambroise, T. Balasubramanian, R.W. Wagner, D.F. Bocian, D. Holten, J.S. Lindsey, *J. Am. Chem. Soc.* **122**, 7579 (2000)
58. D. Kuciauskas, P.A. Liddell, S. Lin, T.E. Johnson, S.J. Weghorn, J.S. Lindsey, A.L. Moore, T.A. Moore, D. Gust, *J. Am. Chem. Soc.* **121**, 8604 (1999)
59. K. Maruyama, A. Osuka, *Pure Appl. Chem.* **62**, 1511 (1999)
60. T. Nagata, A. Osuka, K. Maruyama, *J. Am. Chem. Soc.* **112**, 3054 (1990)
61. A. Osuka, N. Tanabe, S. Nakajima, K. Maruyama, *J. Chem. Soc. Perkin Trans.* **2**, 199 (1996)
62. O. Mongin, A. Schuwey, M.A. Vallot, A. Gossauer, *Tetrahedron Lett.* **121**, 8927 (1999)
63. N. Solladié, M. Gross, J.-P. Gisselbrecht, C. Sooambar, *Chem. Commun.* 2206 (2001)
64. R.V. Slone, J.T. Hupp, *Inorg. Chem.* **36**, 5422 (1997)
65. A. Prodi, M.T. Indelli, C.J. Kleverlaan, F. Scandola, E. Alessio, T. Gianferrara, L.G. Marzilli, *Chem. Eur. J.* **5**, 2668 (1999)
66. M.J. Crossley, P.L. Burn, *J. Chem. Soc. Chem. Commun.* 1569 (1999)
67. M.J. Crossley, L.J. Govenlock, J.K. Prashar, *J. Chem. Soc. Chem. Commun.* 2379 (1995)
68. D.L. Officer, A.K. Burrell, D.C.W. Reid, *Chem. Commun.* 1657 (1996)
69. M.G.H. Vicente, M.T. Cancilla, C.B. Lebrilla, K.M. Smith, *Chem. Commun.* 1261 (1998)
70. G.H. Vincente, L. Jaquinod, K.M. Smith, *Chem. Commun.* 1771 (1998)
71. A.K. Burrell, D.L. Officer, P.G. Plieger, D.C.W. Reid, *Chem. Rev.* **101**, 2751 (2001)
72. V.S.-Y. Lin, S.G. DiMugno, M.J. Therien, *Science* **264**, 1105 (1994)
73. V.S.-Y. Lin, M.J. Therien, *Chem. Eur. J.* **1**, 645 (1995)
74. J.T. Fletcher, M.J. Therien, *J. Am. Chem. Soc.* **122**, 12393 (2000)
75. K. Susumu, M.J. Therien, *J. Am. Chem. Soc.* **124**, 8550 (2002)
76. H.L. Anderson, S.J. Martin, D.D.C. Bradley, *Angew. Chem. Int. Ed. Engl.* **33**, 655 (1994)
77. H.L. Anderson, *Inorg. Chem.* **33**, 972 (1994)
78. H.L. Anderson, S. Anderson, J.K.M. Sanders, *J. Chem. Soc. Perkin Trans.* **1**, 2231 (1995)
79. T.E.O. Screen, J.R.G. Thorne, R.G. Denning, D.G. Bucknall, H.L. Anderson, *J. Am. Chem. Soc.* **124**, 9712 (2002)
80. C.C. Mak, N. Bampos, J.K.M. Sanders, *Angew. Chem. Int. Ed.* **37**, 3020 (1998)
81. S. Anderson, H.L. Anderson, J.K.M. Sanders, *Angew. Chem. Int. Ed. Engl.* **31**, 907 (1992)
82. S. Anderson, H.L. Anderson, A. Bashall, M. McPartlin, J.K.M. Sanders, *Angew. Chem. Int. Ed. Engl.* **31**, 907 (1992)
83. R.A. Hyacock, A. Yartsev, U. Michelson, V. Sundstrom, C.A. Hunter, *Angew. Chem. Int. Ed.* **39**, 3616 (2000)
84. Y. Kuroda, K. Sugou, K. Sasaki, *J. Am. Chem. Soc.* **122**, 7833 (2000)
85. K. Sugou, K. Sasaki, K. Kitayama, T. Iwaki, Y. Kuroda, *J. Am. Chem. Soc.* **124**, 1182 (2002)
86. N. Aratani, A. Osuka, *Bull. Chem. Soc. Jpn.* **74**, 1361 (2001)
87. N. Aratani, A. Osuka, H.S. Cho, D. Kim, *J. Photochem. Photobiol. C* **3**, 25 (2002)
88. D. Kim, A. Osuka, *J. Phys. Chem. A* **107**, 8791 (2003)
89. D. Kim, A. Osuka, *Acc. Chem. Res.* **37**, 735 (2004)
90. A. Osuka, H. Shimidzu, *Angew. Chem. Int. Ed.* **36**, 735 (1997)
91. N. Aratani, A. Osuka, Y.H. Kim, D.H. Jeong, D. Kim, *Angew. Chem. Int. Ed.* **39**, 1458 (2000)
92. Y.H. Kim, D.H. Jeong, D. Kim, S.C. Jeoung, H.S. Cho, S.K. Kim, N. Aratani, A. Osuka, *J. Am. Chem. Soc.* **123**, 76 (2001)
93. N. Aratani, H.S. Cho, T.K. Ahn, S. Cho, D. Kim, H. Sumi, A. Osuka, *J. Am. Chem. Soc.* **125**, 9668 (2003)
94. A. Nakano, A. Osuka, I. Yamazaki, T. Yamazaki, Y. Nishimura, *Angew. Chem. Int. Ed.* **38**, 1350 (1999)
95. A. Nakano, T. Yamazaki, Y. Nishimura, I. Yamazaki, A. Osuka, *Chem. Eur. J.* **6**, 3254 (2000)
96. A. Nakano, A. Osuka, T. Yamazaki, Y. Nishimura, S. Akimoto, I. Yamazaki, A. Itaya, M. Murakami, H. Miyasaka, *Chem. Eur. J.* **7**, 3134 (2001)
97. Y. Nakamura, N. Aratani, A. Osuka, *Chem. Soc. Rev.* **36**, 831 (2007)
98. K. Sugiura, H. Tanaka, T. Matsumoto, T. Kawai, Y. Sakata, *Chem. Lett.* **28** 1193 (1999)

99. M.R. Benites, T.E. Johnson, S. Weghorn, L. Yu, P.D. Rao, J.R. Diers, S.I. Yang, C. Kirmaier, D.F. Bocian, D. Holten, J.S. Lindsey, *J. Mater. Chem.* **12**, 65 (2002)
100. M.-S. Choi, T. Aida, T. Yamazaki, I. Yamazaki, *Angew. Chem. Int. Ed.* **40**, 3194 (2001)
101. M.-S. Choi, T. Aida, T. Yamazaki, I. Yamazaki, *Chem. Eur. J.* **8**, 2667 (2002)
102. M.-S. Choi, T. Aida, H. Luo, Y. Araki, O. Ito, *Angew. Chem. Int. Ed.* **42**, 4060 (2003)
103. M.-S. Choi, T. Yamazaki, I. Yamazaki, T. Aida, *Angew. Chem. Int. Ed.* **43**, 150 (2004)
104. T. Kato, N. Maruo, H. Akisada, T. Arai, N. Nishino, *Chem. Lett.* **96**, 890 (2000)
105. E.K.L. Yeow, K.P. Ghiggino, J.N.H. Reek, M.J. Crossley, A.W. Bosman, A.P.H.J. Schenning, E.W. Meijer, *J. Phys. Chem. B* **104**, 2596 (2000)
106. W.-S. Li, T. Aida, *Chem. Rev.* **109**, 6047 (2009)
107. T.M. Wilson, T. Hori, M.C. Yoo, N. Aratani, A. Osuka, D. Kim, M.R. Wasielewski, *J. Am. Chem. Soc.* **132**, 1383 (2010)
108. T. Akiyama, H. Imahori, Y. Sakata, *Chem. Lett.* **104**, 1447 (1994)
109. T. Akiyama, H. Imahori, A. Ajavakom, Y. Sakata, *Chem. Lett.* **25**, 907 (1996)
110. H. Imahori, H. Norieda, S. Ozawa, K. Ushida, H. Yamada, T. Azuma, K. Tamaki, Y. Sakata, *Langmuir* **14**, 5335 (1998)
111. H. Imahori, S. Ozawa, K. Ushida, M. Takahashi, T. Azuma, A. Ajavakom, T. Akiyama, M. Hasegawa, S. Taniguchi, T. Okada, Y. Sakata, *Bull. Chem. Soc. Jpn.* **72**, 485 (1999)
112. H. Imahori, Y. Nishimura, H. Norieda, H. Karita, I. Yamazaki, Y. Sakata, S. Fukuzumi, *Chem. Commun.* 661 (2000)
113. H. Imahori, S. Ozawa, S. Ozawa, K. Ushida, Y. Sakata, *Chem. Commun.* 1165 (1999)
114. H. Imahori, H. Norieda, Y. Nishimura, I. Yamazaki, K. Higuchi, N. Kato, T. Motohiro, H. Yamada, K. Tamaki, M. Arimura, Y. Sakata, *J. Phys. Chem. B* **104**, 1253 (2000)
115. H. Imahori, H. Yamada, Y. Nishimura, I. Yamazaki, Y. Sakata, *J. Phys. Chem. B* **104**, 2099 (2000)
116. H. Imahori, H. Norieda, H. Yamada, Y. Nishimura, I. Yamazaki, Y. Sakata, S. Fukuzumi, *J. Am. Chem. Soc.* **123**, 100 (2001)
117. H. Imahori, T. Hasobe, H. Yamada, Y. Nishimura, I. Yamazaki, S. Fukuzumi, *Langmuir* **17**, 4925 (2001)
118. H. Yamada, H. Imahori, S. Fukuzumi, *J. Mater. Chem.* **12**, 2034 (2002)
119. H. Yamada, H. Imahori, Y. Nishimura, I. Yamazaki, S. Fukuzumi, *Chem. Commun.* 1921 (2000)
120. H. Yamada, H. Imahori, Y. Nishimura, I. Yamazaki, S. Fukuzumi, *Adv. Mater.* **14**, 892 (2002)
121. H. Yamada, H. Imahori, Y. Nishimura, I. Yamazaki, T.K. Ahn, S.K. Kim, D. Kim, S. Fukuzumi, *J. Am. Chem. Soc.* **125**, 9129 (2003)
122. T. Hasobe, H. Imahori, H. Yamada, T. Sato, K. Ohkubo, S. Fukuzumi, *Nano Lett.* **3**, 409 (2003)
123. T. Hasobe, H. Imahori, K. Ohokubo, H. Yamada, T. Sato, Y. Nishimura, I. Yamazaki, S. Fukuzumi, *J. Porphyr. Phthalocyanines* **7**, 296 (2003)
124. H. Imahori, K. Hosomizu, Y. Mori, T. Sato, T.K. Ahn, S.K. Kim, D. Kim, Y. Nishimura, I. Yamazaki, H. Ishii, H. Hotta, Y. Matano, *J. Phys. Chem. B* **108**, 5018 (2004)
125. H. Imahori, M. Kimura, K. Hosomizu, S. Fukuzumi, *J. Photochem. Photobiol. A* **166**, 57 (2004)
126. H. Imahori, M. Kimura, K. Hosomizu, T. Sato, T.K. Ahn, S.K. Kim, D. Kim, Y. Nishimura, I. Yamazaki, Y. Araki, O. Ito, S. Fukuzumi, *Chem. Eur. J.* **10**, 5111 (2004)
127. K. Uosaki, T. Kondo, X.-Q. Zhang, M. Yanagida, *J. Am. Chem. Soc.* **119**, 8367 (1997)
128. T. Kondo, T. Kanai, K. Iso-o, K. Uosaki, *Z. Phys. Chem.* **212**, 23 (1999)
129. H. Imahori, M. Arimura, T. Hanada, Y. Nishimura, I. Yamazaki, Y. Sakata, S. Fukuzumi, *J. Am. Chem. Soc.* **123**, 335 (2001)
130. H. Imahori, S. Fukuzumi, *Adv. Mater.* **13**, 1197 (2001)
131. H. Tamiaki, T. Miyatake, R. Tanikaga, A.R. Holzwarth, K. Schaffner, *Angew. Chem. Int. Ed. Engl.* **35**, 772 (1996)
132. R.A. Haycock, C.A. Hunter, D.A. James, U. Michelsen, L.R. Sutton, *Org. Lett.* **2**, 2435 (2000)
133. K. Ogawa, Y. Kobuke, *Angew. Chem. Int. Ed.* **39**, 4070 (2000)

134. R. Takahashi, Y. Kobuke, *J. Am. Chem. Soc.* **125**, 2372 (2003)
135. A. Satake, Y. Kobuke, *Tetrahedron* **61**, 13 (2005)
136. I.W. Hwang, M. Park, T.K. Ahn, Z.S. Yoon, D.M. Ko, D. Kim, F. Ito, Y. Ishibashi, S.R. Khan, H. Miyasaka, C. Keda, R. Takahashi, K. Ogawa, A. Satake, Y. Kobuke, *Chem. Eur. J.* **11**, 3753 (2005)
137. A. Satake, Y. Kobuke, *Org. Biomol. Chem.* **5**, 1679 (2007)
138. P. Ballester, R.M. Gomila, C.A. Hunter, A.S.H. King, L.J. Twyman, *Chem. Commun.* **38** (2003)
139. C.M. Drain, J.-M. Lehn, *J. Chem. Soc. Chem. Commun.* 2313 (1994)
140. J. Fan, J.A. Whiteford, B. Olenyuk, M.D. Levin, P.J. Stang, E.B. Fleischer, *J. Am. Chem. Soc.* **121**, 2741 (1999)
141. R.K. Kumar, S. Balasubramanian, I. Goldberg, *Inorg. Chem.* **37**, 541 (1998)
142. T. Imamura, K. Fukushima, *Coord. Chem. Rev.* **198**, 133 (2000)
143. Y.S. Nam, T. Shin, H. Park, A.P. Magyar, K. Choi, G. Fantner, K.A. Nelson, A.M. Belcher, *J. Am. Chem. Soc.* **132**, 1462 (2010)
144. M. Fujitsuka, O. Ito, H. Imahori, K. Yamada, H. Yamada, Y. Sakata, *Chem. Lett.* **28**, 721 (1999)
145. H. Imahori, K. Tamaki, D.M. Guldi, C. Luo, M. Fujitsuka, O. Ito, Y. Sakata, S. Fukuzumi, *J. Am. Chem. Soc.* **123**, 2607 (2001)
146. D. Hirayama, K. Takimiya, Y. Aso, T. Otsubo, T. Hasobe, H. Yamada, H. Imahori, S. Fukuzumi, Y. Sakata, *J. Am. Chem. Soc.* **124**, 532 (2002)
147. K.-S. Kim, M.-S. Kang, H. Ma, A.K.-Y. Jen, *Chem. Mater.* **16**, 5058 (2004)
148. A.N. Shipway, E. Katz, I. Willner, *ChemPhysChem* **1**, 18 (2000)
149. P.V. Kamat, *J. Phys. Chem. B* **106**, 7729 (2002)
150. M. Brust, M. Walker, D. Bethell, D.J. Schiffrin, R. Whyman, *J. Chem. Soc. Chem. Commun.* 801 (1994)
151. A.C. Templeton, W.P. Wuelfing, R.W. Murray, *Acc. Chem. Res.* **33**, 27 (2000)
152. G. Schmid, *Clusters and Colloids: From Theory to Applications* (VCH, New York, 1994)
153. A.P. Alivisatos, *Science* **271**, 933 (1996)
154. A. Henglein, *Ber. Bunsenges. Phys. Chem.* **99**, 903 (1995)
155. M.P. Pileni, *New J. Chem.* **22**, 693 (1998)
156. S. Link, M.A. El-Sayed, *J. Phys. Chem. B* **103**, 4212 (1999)
157. H. Imahori, M. Arimura, T. Hanada, Y. Nishimura, I. Yamazaki, Y. Sakata, S. Fukuzumi, *J. Am. Chem. Soc.* **123**, 335 (2001)
158. H. Imahori, Y. Kashiwagi, T. Hanada, Y. Endo, Y. Nishimura, I. Yamazaki, S. Fukuzumi, *J. Mater. Chem.* **13**, 2890 (2003)
159. H. Imahori, Y. Kashiwagi, Y. Endo, T. Hanada, Y. Nishimura, I. Yamazaki, Y. Araki, O. Ito, S. Fukuzumi, *Langmuir* **20**, 73 (2004)
160. S. Fukuzumi, Y. Endo, Y. Kashiwagi, Y. Araki, O. Ito, H. Imahori, *J. Phys. Chem. B* **107**, 11979 (2003)
161. T. Hasobe, H. Imahori, S. Fukuzumi, P.V. Kamat, *J. Am. Chem. Soc.* **125**, 14962 (2003)
162. T. Hasobe, H. Imahori, P.V. Kamat, T.K. Ahn, S.K. Kim, D. Kim, A. Fujimoto, T. Hirakawa, S. Fukuzumi, *J. Am. Chem. Soc.* **127**, 1216 (2005)
163. H. Imahori, A. Fujimoto, S. Kang, H. Hotta, K. Yoshida, T. Umeyama, Y. Matano, S. Isoda, *Adv. Mater.* **17**, 1727 (2005)
164. H. Imahori, A. Fujimoto, S. Kang, H. Hotta, K. Yoshida, T. Umeyama, Y. Matano, S. Isoda, *Tetrahedron* **62**, 1955 (2006)
165. H. Imahori, A. Fujimoto, S. Kang, H. Hotta, K. Yoshida, T. Umeyama, Y. Matano, S. Isoda, M. Isosomppi, N.V. Tkachenko, H. Lemmetyinen, *Chem. Eur. J.* **11**, 7265 (2005)
166. T.S. Ahmadi, S.L. Logunov, M.A. El-Sayed, *J. Phys. Chem.* **100**, 8053 (1996)
167. A.M. Brun, A. Harriman, *J. Am. Chem. Soc.* **116**, 10383 (1994)
168. H. Oevering, J.W. Verhoeven, M.N. Paddon-Row, E. Cotsaris, N.S. Hush, *Chem. Phys. Lett.* **143**, 488 (1988)

169. B. Schlicke, P. Belsler, L. De Cola, E. Sabbioni, V. Balzani, *J. Am. Chem. Soc.* **121**, 4207 (1999)
170. F. Barigelletti, L. Flamigni, M. Guardigli, A. Juris, M. Beley, S. Chadorowsky-Kimmes, J.-P. Collin, J.-P. Sauvage, *Inorg. Chem.* **35**, 136 (1996)
171. G.L. Closs, P. Piotrowiak, J.M. MacInnis, G.R. Fleming, *J. Am. Chem. Soc.* **110**, 2652 (1988)
172. H. Kotani, K. Ohkubo, Y. Takai, S. Fukuzumi, *J. Phys. Chem. B* **110**, 24047 (2006)
173. T. Sagawa, S. Yoshikawa, H. Imahori, *J. Phys. Chem. Lett.* **1**, 1020 (2010)
174. A. Kira, T. Umeyama, Y. Matano, K. Yoshida, S. Isoda, J.K. Park, D. Kim, H. Imahori, *J. Am. Chem. Soc.* **131**, 3198 (2009)
175. P. Peumans, A. Yakimov, S.R. Forrest, *J. Appl. Phys.* **93**, 3693 (2003)
176. H. Imahori, K. Mitamura, T. Umeyama, K. Hosomizu, Y. Matano, K. Yoshida, S. Isoda, *Chem. Commun.* 406 (2006)
177. H. Imahori, K. Mitamura, Y. Shibano, T. Umeyama, Y. Matano, K. Yoshida, S. Isoda, Y. Araki, O. Ito, *J. Phys. Chem.* **110**, 11399 (2006)
178. G. Schmid (ed.), *Nanoparticles* (Wiley-VCH, Weinheim, 2004)
179. A.P. Alivisatos, *Science* **271**, 933 (1996)
180. E. Klarreich, *Nature* **413**, 450 (2001)
181. A.P. Alivisatos, *Nat. Biotechnol.* **22**, 47 (2004)
182. J.K. Jaiswall, H. Mattoussi, J.M. Mauro, S.M. Simon, *Nat. Biotechnol.* **21**, 47 (2003)
183. A.R. Clapp, I.L. Medintz, J.M. Mauro, B.R. Fisher, M.G. Bawendi, H. Mattoussi, *J. Am. Chem. Soc.* **126**, 301 (2004)
184. I. Medintz, H. Uyeda, E. Goldman, H. Mattoussi, *Nat. Mater.* **4**, 435 (2005)
185. X. Gao, Y. Cui, R.M. Levenson, L.W.K. Chung, S. Nie, *Nat. Biotechnol.* **22**, 969 (2004)
186. P.K. Chattopadhyay, D.A. Price, T.F. Harper, M.R. Betts, J. Yu. E. Gostick, S.P. Perfetto, P. Goepfert, R.A. Koup, S.C. De Rosa, M.P. Bruchez, M. Roederer, *Nat. Med.* **12**, 972 (2006)
187. A.C.S. Samia, X. Chen, C. Burda, *J. Am. Chem. Soc.* **125**, 15736 (2003)
188. R. Bakalova, Z. Ohba, Z. Zhelev, M. Ishikawa, Y. Baba, *Nat. Biotechnol.* **22**, 1360 (2004)
189. A.R. Clapp, I.L. Medintz, H. Mattoussi, *ChemPhysChem* **7**, 47 (2005)
190. I. Roy, T.Y. Ohulchanskyy, H.E. Pudavar, E.J. Bergey, A.R. Oseroff, J. Morgan, T.J. Dougherty, P.N. Prasad, *J. Am. Chem. Soc.* **125**, 7860 (2003)
191. E. Zenkevich, F. Cichos, A. Shulga, E.P. Petrov, T. Blaudeck, C. von Borczyskowski, *J. Phys. Chem. B* **109**, 8679 (2005)
192. O. Schmelz, A. Mews, T. Basche, A. Hermann, K. Mullen, *Langmuir* **17**, 2861 (2001)
193. I. Robel, V. Subramanian, M. Kuno, P.V. Kamat, *J. Am. Chem. Soc.* **128**, 2385 (2006)
194. L. Seeney-Haj-Ichia, B. Basnar, I. Willner, *Angew. Chem. Int. Ed.* **44**, 78 (2005)
195. S. Dayal, Y. Lou, A.C.S. Samia, J.C. Berlin, M.E. Kenney, C. Burda, *J. Am. Chem. Soc.* **128**, 13974 (2006)
196. S. Kang, M. Yasuda, H. Miyasaka, H. Hayashi, T. Umeyama, Y. Matano, K. Yoshida, S. Isoda, H. Imahori, *ChemSusChem* **1**, 254 (2008)
197. S.L. Cumberland, K.M. Hanif, A. Javier, G.A. Khitrov, G.F. Strouse, S.M. Woessner, C.S. Yun, *Chem. Mater.* **14**, 1576 (2002)
198. M.G. Berrettini, G. Braun, J.G. Hu, G.F. Strouse, *J. Am. Chem. Soc.* **126**, 7063 (2004)
199. D.L. Akins, H.-R. Zhu, C. Guo, *J. Phys. Chem.* **98**, 3612 (1994)
200. M.A. Castriciano, A. Romeo, V. Villari, N. Micali, L.M. Scolaro, *J. Phys. Chem. B* **107**, 8765 (2003)
201. R. Rubires, J.-A. Farrera, J.M. Ribo, *Chem. Eur. J.* **7**, 436 (2001)
202. C. Escudero, J. Crusats, I. Diez-Perez, Z. El-Hachemi, J.M. Ribo, *Angew. Chem. Int. Ed.* **45**, 8032 (2006)
203. R. Rubires, J. Crusats, Z. El-Hachemi, T. Jaramillo, M. Lopez, E. Valls, J.-A. Farrera, J.M. Ribo, *New J. Chem.* **23**, 189 (1999)
204. N. Micali, V. Villari, M.A. Castriciano, A. Romeo, L.M. Scolaro, *J. Phys. Chem. B* **110**, 8289 (2006)
205. N. Micali, F. Mallamace, A. Romeo, R. Purrello, L.M. Scolaro, *J. Phys. Chem. B* **104**, 5897 (2000)

206. A.D. Schwab, D.E. Smith, C.S. Rich, E.R. Young, W.F. Smith, J.C. de Paula, *J. Phys. Chem. B* **107**, 11339 (2003)
207. R. Rotomskis, R. Augulis, V. Snitka, R. Valiokas, B. Liedberg, *J. Phys. Chem. B* **108**, 2833 (2004)
208. Y. Kitahara, Y. Kimura, K. Takazawa, *Langmuir* **22**, 7600 (2006)
209. O. Ohno, Y. Kaizu, H. Kobayashi, *J. Chem. Phys.* **99**, 4128 (1993)
210. T. Nagahara, K. Imura, H. Okamoto, *Chem. Phys. Lett.* **381**, 368 (2003)
211. J.-J. Wu, N. Li, K.-A. Li, F. Liu, *J. Phys. Chem. B* **112**, 8134 (2008)
212. K. Fujiwara, S. Wada, H. Monjushiro, H. Watarai, *Langmuir* **22**, 2482 (2006)
213. S. Okada, H. Segawa, *J. Am. Chem. Soc.* **125**, 2792 (2003)
214. L. Zhang, Q. Lu, M. Liu, *J. Phys. Chem. B* **107**, 2565 (2003)
215. K. Kano, K. Fukuda, H. Wakami, R. Nishiyabu, R.F. Pasternack, *J. Am. Chem. Soc.* **122**, 7494 (2000)
216. T. Yamaguchi, T. Kimura, H. Matsuda, T. Aida, *Angew. Chem. Int. Ed.* **43**, 6350 (2004)
217. G. de Miguel, K. Hosomizu, T. Umeyama, Y. Matano, H. Imahori, M.T. Martin-Romero, L. Camacho, *ChemPhysChem* **9**, 1511 (2008)
218. K. Hosomizu, M. Oodoi, T. Umeyama, Y. Matano, K. Yoshida, S. Isoda, M. Isosomppi, N.V. Tkachenko, H. Lemmetyinen, H. Imahori, *J. Phys. Chem. B* **112**, 16517 (2008)
219. G. de Miguel, K. Hosomizu, T. Umeyama, Y. Matano, H. Imahori, M. Perez-Morales, M.T. Martin-Romero, L. Camacho, *J. Colloid Interface Sci.* **356**, 775 (2011)
220. R. Andrews, D. Jacques, D. Qian, T. Rantell, *Acc. Chem. Res.* **35**, 1008 (2002)
221. M. Ouyang, J.-L. Huang, C.M. Lieber, *Acc. Chem. Res.* **35**, 1018 (2002)
222. M. in het Panhuis, *J. Mater. Chem.* **16**, 3598 (2006)
223. E. Katz, I. Willner, *ChemPhysChem* **5**, 1084 (2004)
224. P. Liu, *Eur. Polym. J.* **41**, 2693 (2005)
225. Y. Lin, S. Taylor, H. Li, K.A.S. Fernando, L. Qu, W. Wang, L. Gu, B. Zhou, Y.-P. Sun, *J. Mater. Chem.* **14**, 527 (2004)
226. H. Murakami, N. Nakashima, *J. Nanosci. Nanotechnol.* **6**, 16 (2006)
227. T.A. Skotheim, R.L. Elsenbaumer, J.R. Reynolds, *Handbook of Conducting Polymers*, 2nd edn. (Marcel Dekker, New York, 1998)
228. S.A. Curran, P.M. Ajayan, W.J. Blau, D.L. Carroll, J.N. Coleman, A.B. Dalton, A.P. Davey, A. Drury, B. McCarthy, S. Maier, A. Strevens, *Adv. Mater.* **10**, 1091 (1998)
229. A. Star, J.F. Stoddart, D. Steuerman, M. Diehl, A. Boukai, E.W. Wong, X. Yang, S.-W. Chung, H. Choi, J.R. Heath, *Angew. Chem. Int. Ed.* **40**, 1721 (2001)
230. D.B. Romero, M. Carrard, W.D. Heer, L. Zuppiroli, *Adv. Mater.* **8**, 899 (1996)
231. J. Wery, H. Aarab, S. Lefrant, E. Faulques, *Phys. Rev. B* **67**, 115202 (2003)
232. S. Kazaoui, N. Minami, B. Nalini, Y. Kim, K. Hara, *J. Appl. Phys.* **98**, 084314 (2005)
233. S. Kazaoui, N. Minami, B. Nalini, Y. Kim, N. Takada, K. Hara, *Appl. Phys. Lett.* **87**, 211914 (2005)
234. H. Zhao, S. Mazumdar, C.-X. Sheng, M. Tong, Z.V. Vardeny, *Phys. Rev. B* **73**, 075403 (2006)
235. T. Umeyama, N. Kadota, N. Tezuka, Y. Matano, H. Imahori, *Chem. Phys. Lett.* **444**, 263 (2007)
236. K. Yanagi, K. Iakoubovskii, S. Kazaoui, N. Minami, Y. Maniwa, Y. Miyata, H. Kataura, *Phys. Rev. B* **74**, 155420 (2006)

Hiroaki Matsui and Hitoshi Tabata

Contents

20.1	Introduction.....	768
20.2	Zn-Polarity and Quantum Structures.....	770
20.2.1	Surface Character.....	770
20.2.2	Homoepitaxial Growth and Optical Properties.....	772
20.2.3	Mg _x Zn _{1-x} O/ZnO Heteroepitaxy.....	774
20.2.4	Stranski-Krastanov Mode and Lateral Composition Modulation.....	776
20.2.5	Multiple Quantum Wells and Excitonic Recombination.....	780
20.3	Nonpolarity and Quantum Structures.....	782
20.3.1	Nonpolar Growth of <i>M</i> -Face (10-10).....	782
20.3.2	Step-Edge Barrier and Self-Organized Nanowires.....	784
20.3.3	Linearly Polarized Light Emissions.....	788
20.3.4	Large Anisotropy of Electron Transport.....	791
20.4	Quantum Well Geometry Based on ZnCoO.....	793
20.4.1	Spin and Band Engineering.....	793
20.4.2	Ferromagnetism.....	798
20.4.3	Space Separation of Exciton and Localized Spin Systems.....	800
20.5	Conclusion.....	802
20.6	Prospects.....	804
	References.....	805

Abstract

This chapter represents growth of ZnO quantum nanostructures controlled at nano scale and its electro-magneto-optical characteristics. Multiple-quantum wells with isotropic and anisotropic structures are designed on the basis of

H. Matsui (✉)

School of Engineering, The University of Tokyo, Tokyo, Japan

e-mail: hiroaki@ee.t.u-tokyo.ac.jp

H. Tabata

School of Engineering, Department of Electronic Engineering, The University of Tokyo, Tokyo, Japan

e-mail: tabata@bioeng.t.u-tokyo.ac.jp

polarity character of ZnO, which provide interesting light emissions and low-temperature electron transport. Furthermore, Co-alloyed ZnO shows ferromagnetism and large magneto-optical response owing to coupling between charge carriers (excitons) and localized $3d$ spins. Electro-magneto-optics of quantum structures fabricated by various growth techniques are applied for practical applications based on ZnO-related materials.

20.1 Introduction

Studies have shown that zinc oxide (ZnO) is a practical candidate for the development of practical devices such as thin film transistors, transparent and electrodes [1, 2]. ZnO has a large exciton energy of 60 meV, which raises the interesting possibility of utilizing its excitonic effects at temperatures higher than 300 K [3]. Optically pumped UV-stimulated emissions from ZnO layers have been demonstrated [4, 5]. Furthermore, $\text{Mg}_x\text{Zn}_{1-x}\text{O}$ alloys are attracting a great deal of interest since they possess a larger band gap than ZnO [6] and have been utilized for $\text{Mg}_x\text{Zn}_{1-x}\text{O}/\text{ZnO}$ multiple and single quantum wells [7, 8]. These structures can form low-dimensional systems and produce interesting quantum phenomena, such as increased excitonic binding energy [9, 10] and two-dimensional (2D) electron transport [11] aspect that contribute to both basic science and practical applications.

Thus far, nanostructures on semiconductor materials have received much attention for fabrication techniques and have been investigated by many researchers. Especially, the number of papers concerning nanostructures based on ZnO is increasingly yearly. Self-organized techniques provide advantages for nanoscale engineering and have yielded many impressive results. Therefore, surface nanostructures in Si and GaAs have been fabricated using various growth mechanisms. Stranski-Krastanov (S-K) growth on lattice-mismatched systems induces three-dimensional (3D) nanodots on 2D wetting layers [12]. Lateral surface nanowires have been fabricated due to a step-faceting mode on vicinal surfaces [13, 14]. These surface nanostructures have been developed for zero-dimensional (0D) quantum dots and one-dimensional (1D) quantum wires [15, 16]. Low-dimensional properties are currently receiving attention as advantages for optoelectronics with ZnO.

In epitaxial growth, lattice mismatch between an epilayer and substrate plays a crucial role. Growth studies concerning ZnO epitaxy have been carried out using c - and a -sapphires [17, 18]. Heteroepitaxial layers have a high dislocation density of 10^9 – 10^{10} cm^{-2} due to large mismatches in the lattice structure and in thermal expansion [19]. The use of ZnO substrate not only allows the reduction of the number of lattice defects involved in the epilayers but also permits the selection of various growth directions without any lattice mismatch, which results in a direct understanding of growth dynamics. The growth polarity in ZnO is the primary factor. Zn (0001) and O (000-1) polarities have isotropic atom arrangements and possess spontaneous polarization along growth directions. On the other hand, the

M (10-10)-nonpolar surface has an anisotropic atom structure, and the spontaneous polarization occurs parallel to a surface plane [20]. For example, Zn-polar growth produces atomically flat surfaces due to a layer-by-layer mode [21–23]. Whereas M -nonpolar ZnO layers result in anisotropic morphologies with a nanowires structure based on the step-edge barrier effect [24]. Thus, the difference in growth directions influences the surface state, as well as optical and electrical properties of ZnO layers, which can be made more conspicuous through quantum structures. Quantum structures on various surface morphologies exhibit novel electronic and optical properties because quantized energy levels can be tailored by varying the geometric dimensions.

In the last 10 years, manipulating the spin of an electron rather than its charge has opened fascinating new fields for information processing on diluted magnetic semiconductors (DMS), which has emerged as “spintronics” [25]. II–V DMS is characterized by s , p - d exchange interactions between the localized $3d$ spins and the extended band states, opening new fields both in fundamental research and applications. $\text{Cd}_{1-x}\text{Mn}_x\text{Te}$ compounds have been made as practical as Faraday devices [26]. Recently, much interest has centered on magnetic functionality in ZnO DMS because of its magneto-optical effect and ferromagnetic properties [27, 28]. In particular, many researchers have focused on understanding the origin of ferromagnetism in $\text{Zn}_{1-x}\text{Co}_x\text{O}$ from experimental and theoretical viewpoints. Moreover, $\text{Zn}_{1-x}\text{Co}_x\text{O}$ has functionality as an alloy material and has a higher band gap than ZnO [29], which can be utilized in “band-gap engineering” and “spin engineering.” Therefore, one of the most exciting studies has dealt with advancements in DMS containing heterostructures. In DMS heterostructures, magnetism at the heterointerface can differ from the magnetism of the corresponding bulk materials [30]. A problem with $\text{Zn}_{1-x}\text{Co}_x\text{O}$ is that excitonic emissions are strongly suppressed when increasing doping content. This fact severely hinders the development of spin-dependent emitter devices that utilize excitonic technology characteristics of ZnO. However, a superlattice with quantum well geometry has the ability to spatially separate excitons from localized $3d$ spins and also retain excitonic emissions. Recently, we succeeded in fabricating a $\text{Zn}_{1-x}\text{Co}_x\text{O}/\text{ZnO}$ superlattice with sharp heterointerfaces using the homoepitaxial technique, based on precise understanding of the alloy parameters, growth modes, and magnetic properties of $\text{Zn}_{1-x}\text{Co}_x\text{O}$ [31]. This lays the foundations for quantum spin photonics with ZnO.

This chapter is organized as follows. In Sect. 20.2, we will first give a description of homoepitaxial growth of Zn-polar ZnO layers and $\text{Mg}_x\text{Zn}_{1-x}\text{O}/\text{ZnO}$ heteroepitaxy. Fabrication of multiple quantum wells and their low-dimensional optical properties are discussed. In Sect. 20.3, we focus on self-organized surface nanowires on M -nonpolar ZnO layers, wherein discussions concentrate on growth mechanism and developments for the low-dimensional structure, “quantum wires.” Section 20.4 is devoted to discussion of various properties of $\text{Zn}_{1-x}\text{Co}_x\text{O}$ DMS and to the fabrication of the quantum well geometry. Concluding remarks and future research directions in this field are given in Sect. 20.5.

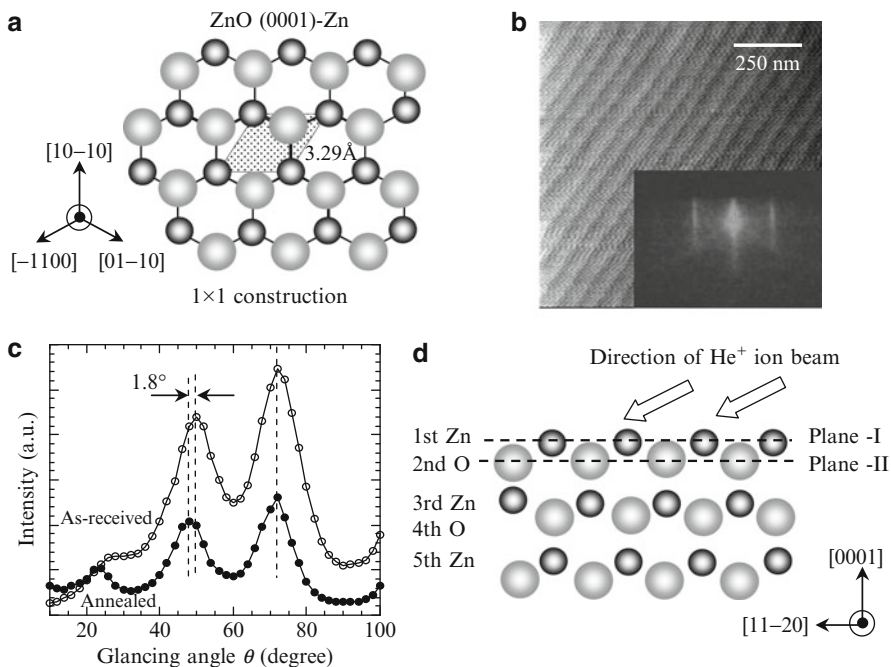


Fig. 20.1 (a) Structural models showing the bulk-terminated Zn-polar (0001) surfaces of ZnO. The surface unit cells are indicated. (b) AFM image of ZnO (0001) surface after annealing at high temperature. (c) Incident angle dependence of the Zn signal intensity when the sample was tilted along the $\langle 11\bar{2}0 \rangle$ azimuth. (○) and (●) show as-received and annealed Zn-polar surfaces, respectively. (d) Surface models of the Zn-terminated (0001) surface along the $[11\bar{2}0]$ direction. The *open arrows* indicate the direction of the He^+ ion beam

20.2 Zn-Polarity and Quantum Structures

20.2.1 Surface Character

ZnO has a hexagonal wurtzite structure ($a = 0.3250 \text{ nm}$, $c = 0.5201 \text{ nm}$), each Zn^{2+} ion bonded to four O^{2-} ions in a tetrahedral formation, representing a structure that can be described as alternating planes of Zn and O ions stacked along the c -axis. Various surface-sensitive methods have been used to investigate the polar surfaces of ZnO from fundamental and applied points of view. For example, the surface morphology was quite different for opposite polar surfaces when ZnO crystals were chemically etched [32]. Thus, epitaxy in ZnO with varying polarity should show different kinetics and material characteristics. Therefore, it is important to understand the uppermost surface structure and morphology in a Zn-polar surface.

Figure 20.1a shows a structural model of the bulk-terminated Zn-polar (0001) surfaces of ZnO. All O atoms on the borders have three nearest neighbors, i.e., only one bond is broken. The Zn-polar surface is unstable due to the existence of nonzero

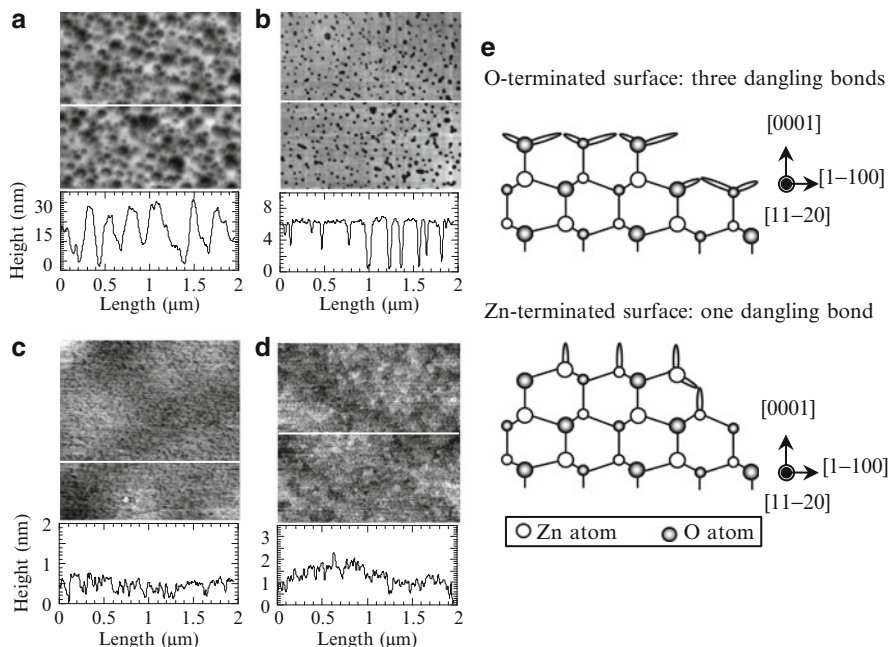


Fig. 20.2 AFM images of ZnO layers grown under an oxygen pressure “ $p(\text{O}_2)$ ” of (a) 1.4×10^{-4} , (b) 1.4×10^{-5} , (c) 1.4×10^{-4} , and (d) 6.0×10^{-4} mbar. Oxygen flux was supplied by O_2 gas flow (a) or O_2 plasma exposure (b)–(d). (e) Schematic surfaces along the Zn-polar direction in the ZnO lattice

dipole moment perpendicular to the surface, which raises a fundamental question regarding stabilization mechanisms [33]. Figure 20.2 shows the AFM image of the Zn-polar (0001) surface of a hydrothermal ZnO substrate annealed at 1,100°C in air. The annealed surface had a double-layer step structure whose step height was about 0.26 nm, which corresponds to the half lattice parameter of the unit cell of the c -axis. Analysis of the annealed surface using reflection high-energy electron diffraction (RHEED) revealed 2D streaks attributed to a (1×1) structure, as shown in the inset of Fig. 20.1b. This shows that no lattice reconstruction occurred in a direction parallel to the surface. However, there is lattice relaxation due to the polarity that occurs along the c -axis. Coaxial impact-collision ion scattering spectroscopy (CAICISS) is useful for surface analyses since this technique is sensitive to the atomic configuration of layer surfaces [34]. The sample was mounted on a two-axis goniometer with respect to the primary He^+ ion beam of ~ 2 keV at a repetition rate of 100 kHz. The time-averaged current of the incident ion beam was ~ 150 pA. The CAICISS time-of-flight spectrum taken by a microchannel plate is composed of peaks corresponding to head-on collisions between incident He^+ ions and target atoms on the surface. The Zn signal intensity measured in an ultrahigh vacuum of 10^{-10} Torr is shown in Fig. 20.1c and is consistent with results reported

previously [35]. Three peaks of the as-received surface were observed at $\theta = 23.5^\circ$, 49.9° , and 72.4° . The peaks of the annealed surface then appeared at $\theta = 23.5^\circ$, 48.1° , and 72.4° . Therefore, the peak angle of 49.9° of the as-received surface was 1.9° lower than that for the annealed surface. Here, we define two planes: one is along the [11-20] direction including Zn ions in the uppermost layer (plane I) as shown in Fig. 20.1d, and the other is parallel to plane I consisting of O ions in the second layer (plane II). The peaks at 23.5° and 72.4° are related to the focusing effect within plane II, being independent of the uppermost Zn ions, while the middle peaks of 49.9° and 48.1° are ascribed to the uppermost Zn ions (plane I). To be precise, the middle peak is due to the focusing effect of Zn ions on the first layers to Zn ions on the fifth layers. Thus, the uppermost Zn ions of the annealed surface relaxed toward the inside on the real surface, supported by the peak shift from 49.9° to 48.1° . However, the annealed surface distorts slightly compared to the surface without lattice relaxation ($\theta = 47.5^\circ$), indicating that lattice spacing (Zn-O bond length) is reduced between the uppermost Zn layer and the second O layer. Thus, the Zn-polar surface resulted in no lattice reconstruction in a direction parallel to the surface, while a slight distortion was induced along the c -axis.

20.2.2 Homoepitaxial Growth and Optical Properties

ZnO layers on sapphire usually have O-polarity [19]. Reports have appeared that deal with polarity conversion of ZnO layers on sapphire using buffer layers such as MgO and Cr_2O_3 [36, 37] since Zn-polarity shows a two-dimensional (2D) mode, speculated from the growth of GaN layers with Ga polarity. However, a large lattice mismatch and thermal expansion coefficient between a layer and substrate plays a crucial role in the performance of the Zn-polar layers. Polarity-controlled epilayers can easily be obtained using ZnO substrates and are necessary for the formation of precise device structures such as quantum wells.

Figure 20.2 shows AFM images of 300-nm-thick ZnO layers grown at 420°C . The top surface of the layer grown under an O_2 gas flow of 1.4×10^{-4} mbar was completely covered by highly faceted pit features (Fig. 20.2a). The layer grown under an O_2 plasma exposure of 1.4×10^{-5} mbar also exhibited a pitted surface, although the layer appeared to be quite smooth between the pits (Fig. 20.2b). An O_2 plasma exposure in the range of 1.4 to 6.0×10^{-4} mbar resulted in few pits with areas possessing a very flat surface (Fig. 20.2c, d). The surface roughness was about 0.5 nm, a value corresponding to the c -axis length. X-ray diffraction measurements showed line-widths of ω -rocking curves for the (002) and (100) planes were as narrow as 42 and 47 arcsec, respectively.

Figure 20.1e shows schematic images of O- and Zn-terminated surfaces along the c -axis. Negatively charged growth surfaces stabilized by oxygen-rich conditions are indispensable for 2D mode with Zn-polarity. Each surface atom on O- and Zn-terminated surfaces has one and three dangling bonds, respectively, suggesting that the O sticking coefficient on Zn-terminated surfaces is lower than the Zn sticking coefficient on O-terminated surfaces. The RF plasma source efficiently

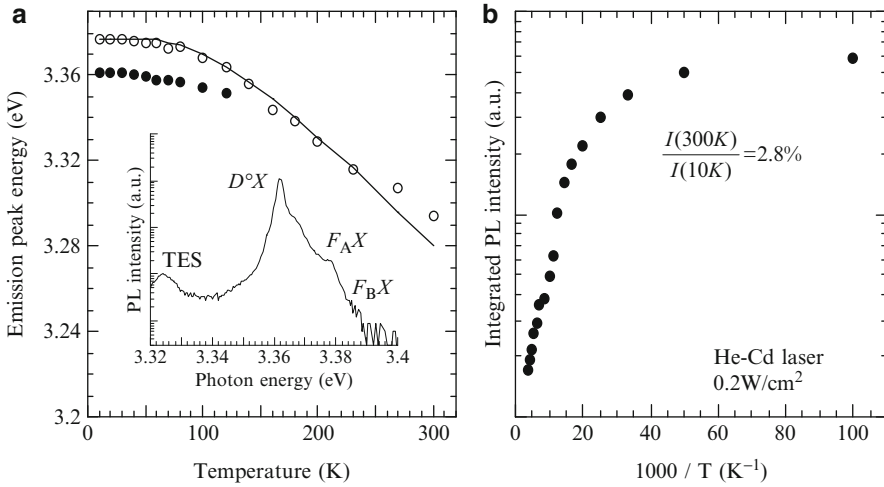


Fig. 20.3 (a) Excitonic transition energies of Zn-polar layers on ZnO substrates as a function of temperature. *Inset* shows PL spectrum at the band edge. (b) Spectrally integrated PL intensity as a function of T^{-1}

generates atomic oxygen (O^*), which enhances the O sticking coefficient on the growing surfaces. In contrast, O_2 molecule results in a low surface reaction due to a high binding energy (5.12 eV). The rough surface on the layer grown under O_2 gas flow is ascribed to incomplete O-terminated surfaces. In contrast, O_2 plasma exposure supplies excited O^* atoms to the growing surfaces. O sticking coefficient increased by the excited O^* atoms contributes to the smooth conversion from a Zn-terminated surface to an O-terminated surface. This facilitates formation of negatively charged surfaces and leads to stabilization of the 2D mode. The observed morphological transitions are associated with the variation in the coverage of the layer surface by O atoms.

The variation of exciton peak positions with temperature can be seen in Fig. 20.3a. The inset of Fig. 20.3a shows the photoluminescence (PL) spectrum at 10 K of the Zn-polar ZnO layer at 570 °C under O_2 plasma exposure. We identified the 3.377 and 3.384 eV peaks as the free A – ($F_A X$) and B – ($F_B X$) excitonic transitions, which were consistent with values reported in the literature for vapor-phase ZnO [38]. We also observed a narrow peak, with the strongest peak at 3.362 eV exhibiting a line-width of 2.3 meV, characteristic of a neutral donor-bound exciton ($D^0 X$) peak. Two electron satellites of the $D^0 X$ peak were seen at 3.325 eV. The $F_A X$ and $D^0 X$ peaks were observed for temperatures ranging from 10 to 120 K. The value of 3.295 eV at 300 K for the $F_A X$ peak was due to the widely accepted room temperature value for the band gap of ZnO (3.37 eV) minus the exciton binding energy of 64 meV [3]. The dependence of $F_A X$ peak intensity on temperature could be fitted using the Bose-Einstein relation with a characteristic temperature (Θ_E) of 335 K, being close to the energy (380 K) for phonon density

of state on ZnO. An equivalent internal quantum efficiency ($\eta_{\text{int}}^{\text{eq}}$) throughout this study of near band edge (NBE) emissions at 300 K, which is approximated as the integrated PL intensity divided by that at 10 K ($I_{(300\text{K})}/I_{(10\text{K})}$), directly correlates with τ_{PL} in the ZnO layer ($\eta_{\text{int}}^{\text{eq}} = 1/(1+\tau_{\text{R}}/\tau_{\text{NR}})$). τ_{R} and τ_{NR} are the radiative and nonradiative lifetimes, respectively. Integrated PL intensity for NBE emissions as a function of $1/T$ (Fig. 20.3b) shows that the value of $\eta_{\text{int}}^{\text{eq}}$ was 2.8 % at 300 K, which is ten times higher than that of ZnO layers grown on sapphires. In *n*-type ZnO, Zn vacancy (V_{Zn}) most probably represents defects. Since V_{Zn} produces nonradiative recombination centers in the form of V_{Zn} -defect complexes [39], the suppression of structural defects is enhanced $\eta_{\text{int}}^{\text{eq}}$. Thus, Zn-polar layers on ZnO substrates demonstrate a reduction of structural and point defects.

20.2.3 $\text{Mg}_x\text{Zn}_{1-x}\text{O}/\text{ZnO}$ Heteroepitaxy

The discovery of tunable ZnO band gap has made the alloy system a promising material for use in the development of optoelectronic devices. Characterization of alloys such as (Mg,Zn)O or (Cd,Zn)O is important from the viewpoint of band-gap engineering and *p-n* junction. It was found that a $\text{Mg}_x\text{Zn}_{1-x}\text{O}$ alloy is a suitable material for the barrier layers of ZnO/(Mg,Zn)O superlattices due to its wider band gap. Since the ionic radius of Mg (0.56 Å) is very close to that of Zn^{2+} (0.60 Å), Mg-rich (Mg,Zn)O alloys with a wurtzite phase have been stably conserved even when a rock salt-structured MgO is alloyed.

Mg contents doped into a ZnO layer usually depend on the surface polarity, growth technique, and type of substrate. It is known that Ga^{3+} and N^{3-} ions are relatively incorporated on O- and Zn-polarities of ZnO, respectively [40, 41]. Figure 20.4a shows the Mg content in $\text{Mg}_x\text{Zn}_{1-x}\text{O}$ layers as a function of the target Mg content. Under growth conditions in this work, the Mg content in Zn-polar layers was always 1.6 times the content of the ablation targets. This can be attributed to the low vapor pressure of Mg-related species compared to those of Zn. The incorporation efficiency of Mg atoms into the layers is more enhanced for O-polarity. Similar behavior was also observed in $\text{Cd}_x\text{Zn}_{1-x}\text{O}$ alloys (Fig. 20.4b). The amount of Cd atoms in the layers is much lower than that of targets, originating from a difference of vapor pressures between Cd- and Zn-related species. Reevaporation processes on the growing surfaces strongly dominate the doping efficiency of Mg and Cd atoms in the layers. On the other hand, the polarity dependence is related closely to a sticking coefficient of Zn atoms since this sticking coefficient is higher for Zn-polarity than O-polarity. This results from a number of dangling bonds on O-terminated surface structures of both polarities.

Micro (μ)-photoluminescence and μ -Raman scattering spectroscopy were carried out at room temperature (RT) to study luminescent properties. A fourth-harmonic generation of an yttrium aluminum garnet (YAG) laser at 266 nm was used as excitation source. A spectrum was detected using a 0.85-cm double monochromator. In this measurement, a reflective-type objective lens was used to

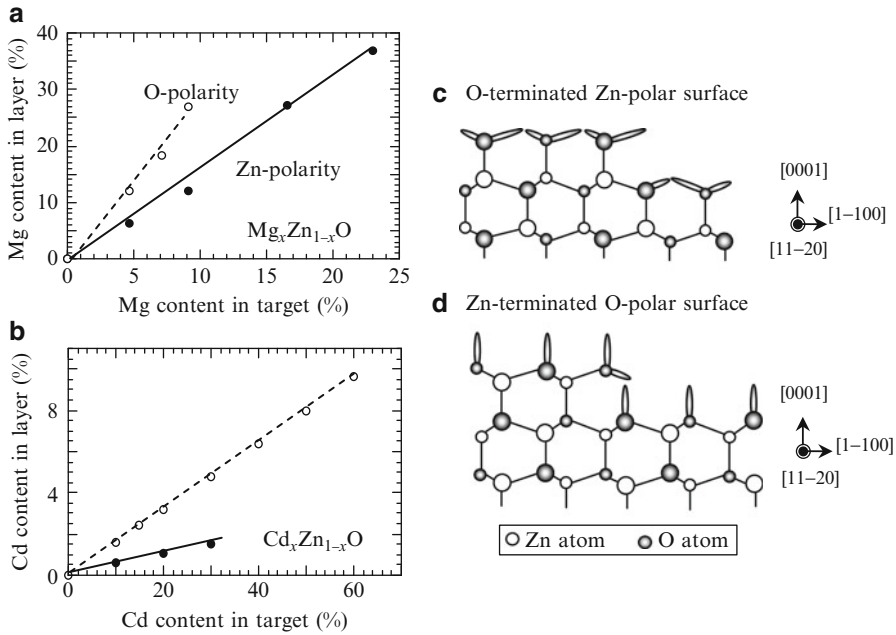


Fig. 20.4 (a) Mg and (b) Cd contents in $\text{Mg}_x\text{Zn}_{1-x}\text{O}$ and $\text{Cd}_x\text{Zn}_{1-x}\text{O}$ layers as a function of the target Mg and Cd contents, respectively. (b) and (c) show plane-view atomic arrangement of oxygen-terminated Zn-polar and O-polar ZnO surface structures, respectively

focus the laser to a diameter of 500 nm on the layer surface (Fig. 20.5). A microprobe system is an excellent complementary tool for the identification and characterization of the spatial resolution of a microscopic scale region [42].

Figure 20.6a shows the c - and a -axis lengths deduced from the (0004) and (11–24) diffraction peaks. When x increased from 0 to 0.37, the c -axis length decreased linearly from around 5.210 to 5.18 Å, while the a -axis length remained at 3.25 Å up to $x = 0.27$ and then suddenly increased to ~ 3.27 Å. As shown in Fig. 20.6b, the unit-cell volume shrinks toward the c -axis direction up to $x = 0.27$, storing the lattice strain and then suddenly expanding toward the a -axis direction by releasing the lattice strain at $x = 0.37$. Consequently, the cell volume comes to resemble that of ZnO substrates. Figure 20.6c shows the variation of μ -PL spectra at RT for $\text{Mg}_x\text{Zn}_{1-x}\text{O}$ ($x=0$ –0.37) with layer thicknesses ranging from 200 to 300 nm. Excitonic emissions of all layers systematically shifted from 3.3 to 4.0 eV in a linear manner with increasing x due to the band-gap widening. Careful inspection of Fig. 20.6c revealed that the layer with $x = 0.37$, which is lattice-strain relaxed (Fig. 20.6a, b), showed a secondary peak around 3.68 eV. Other layers showed only a single peak. The lattice relaxation promotes phase separation of alloy materials [43].

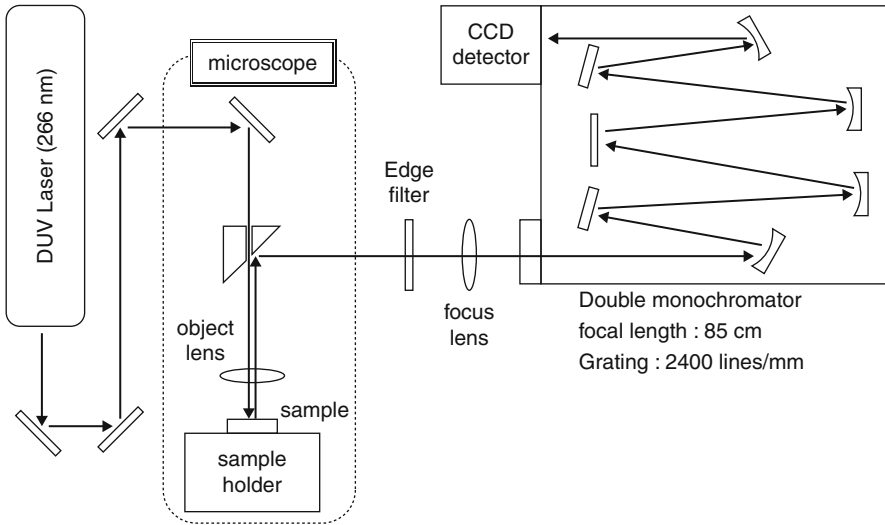


Fig. 20.5 Schematic picture of optical systems for μ -PL and μ -RRS measurements

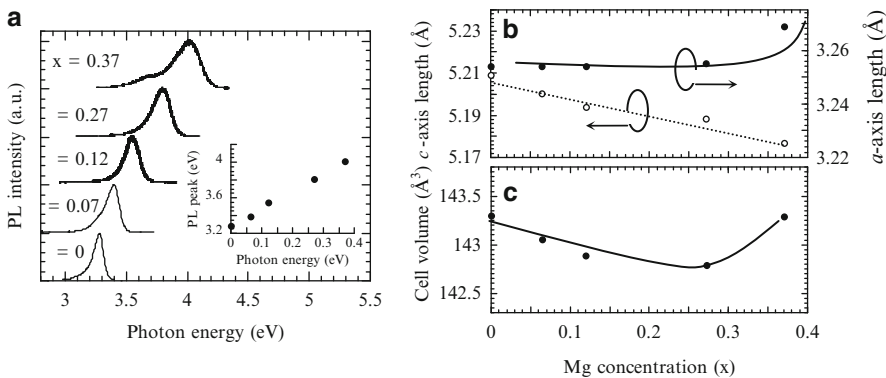


Fig. 20.6 (a) μ -PL spectra of $\text{Mg}_x\text{Zn}_{1-x}\text{O}$ layers ($x = 0-0.37$). *Inset* shows PL peak position as a function of Mg content. (b) Dependence of c - and a -axis lengths on Mg content. (c) Dependence of cell volume on Mg content

20.2.4 Stranski-Krastanov Mode and Lateral Composition Modulation

Self-assembled three-dimensional (3D) islands have received a great deal of attention due to the potential fabrication of nanoscale devices using epitaxial growth process. Lattice mismatch between a layer and substrate leads to Stranski-Krastanov (S-K) growth. Adatoms are initially deposited in the form of a 2D pseudomorphic layer, and elastic strain energy that increases with the layer thickness

is finally relieved by the formation of 3D dots [44]. S-K growth is of particular interest in strained alloy layers since this growth presents a promising bottom-up technique for the ordered assembly of quantum dots [45]. Due to atomic size differences between cations or anions, alloy layers have stored elastic stress that leads to accelerated growth instability. This hinders coherent growth of alloy layers and results in S-K growth. In particular, force field induced by local alloy fluctuation in strained layers leads to lateral or vertical composition modulation through S-K growth [46].

The surface morphologies of $\text{Mg}_{0.37}\text{Zn}_{0.63}\text{O}$ layers are shown in Fig. 20.7 [47]. The strained layer (thickness “ t ” = 38 nm) gives a flat (2D) surface, characteristic of Zn-polar growth (Fig. 20.7a). At a large thickness, nanodots appeared on the growing surface. When lattice relaxation began ($t = 65$ nm), nanodots formed spontaneously with a density of $1,010\text{ cm}^{-2}$ and a lateral distribution of 46 nm (Fig. 20.7b). The partially relaxed layer ($t = 100$ nm) was uniformly covered by nanodots in a hexagonal shape with an area density of 10^9 cm^{-2} , and the lateral size increased to 153 nm (Fig. 20.7c). Finally, the growth scheme in the fully relaxed layer ($t = 280$ nm) changes to a continuous 3D island growth through the coalescence of nanodots (Fig. 20.7d). The lattice parameters as a function of layer thickness are shown in Fig. 20.7e. When the layer thickness increases, the a -axis length remains at 3.250 \AA up to $t = 38$ nm; compressive stress at the heterointerfaces is estimated to be 0.52%. The a -axis length is then gradually expanded, releasing the strain energy up to 3.270 \AA in the layer with $t = 280$ nm, which was fully relaxed. The 2D to 3D transformation in the strained $\text{Mg}_{0.37}\text{Zn}_{0.63}\text{O}$ layer initiated dislocated S-K growth accompanying lattice relaxation at a critical thickness of 38–65 nm. A mechanical equilibrium model by Matthews and Blakeslee [48] gives the critical thickness h_c through the following formulation:

$$h_c = \frac{1}{1 + \nu} \frac{1}{4\pi} \left[\ln \left(\frac{h_c}{b} \right) + 1 \right], \quad (20.1)$$

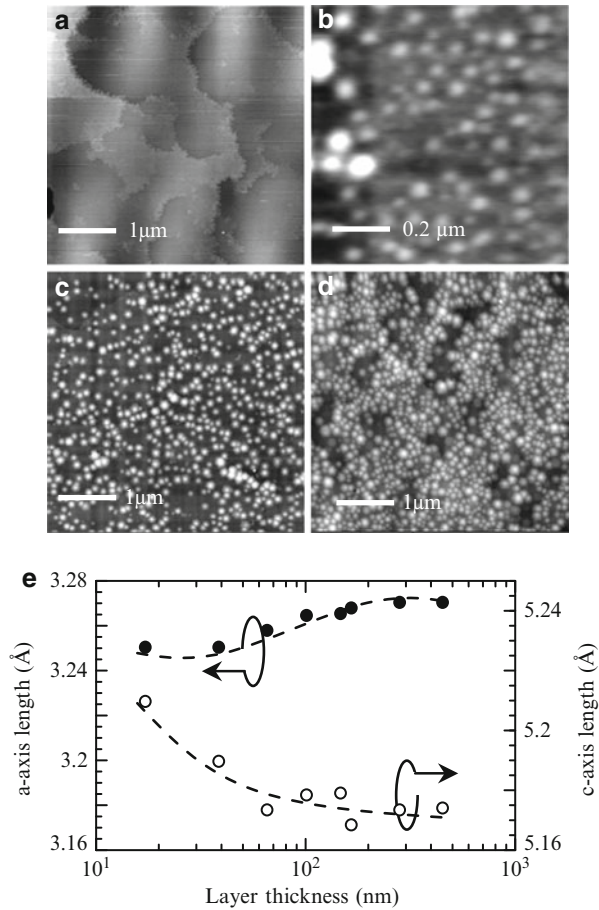
where b and ν are the Burgers vector and Poisson ratio, respectively, and f gives the lattice mismatch defined by

$$f = (a_{\text{MgZnO}} - a_{\text{ZnO}})/a_{\text{ZnO}}, \quad (20.2)$$

with a_{MgZnO} and a_{ZnO} being the a -axis length of $\text{Mg}_{0.37}\text{Zn}_{0.63}\text{O}$ and ZnO , respectively. For our calculations, values of $a_{\text{MgZnO}} = 3.268\text{ \AA}$, $a_{\text{ZnO}} = 3.251\text{ \AA}$, $f = 0.0052$, and $\nu = 0.271$ were used. Furthermore, we set $b = 6.137\text{ \AA}$, assuming a Burgers vector of the a/c type for a slip system $\{1-101\}\langle 11-23\rangle$ [49]. The deduced value of $h_c = 38$ nm was close to the lattice relaxation regions obtained from the experiment results.

Figure 20.8a shows the μ -resonant Raman scattering (μ -RRS) spectra of $\text{Mg}_{0.37}\text{Zn}_{0.63}\text{O}$ layers with different thicknesses. When the thickness increased from $t = 38$ to 280 nm, the $A_1(\text{LO})$ peak monotonically shifted to a higher frequency (from 620 to 631 cm^{-1}). The asymmetric Γ_a/Γ_b , defined by the ratio of full width

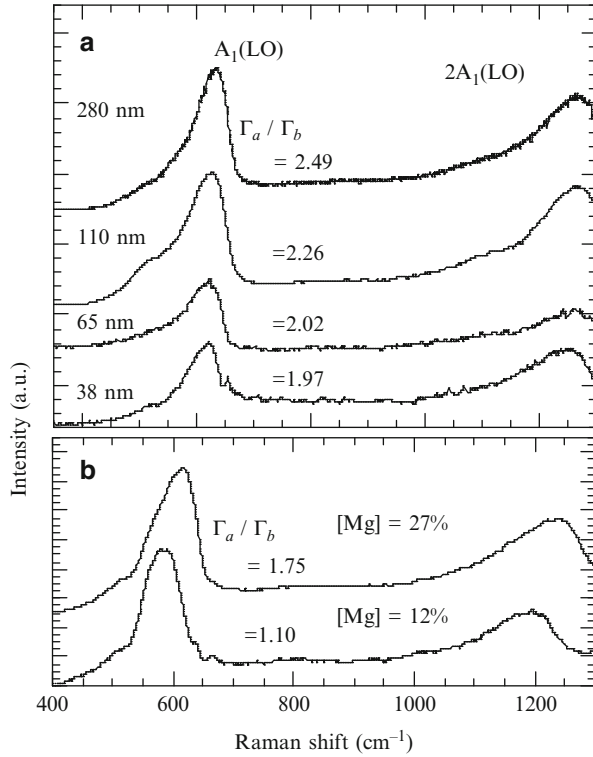
Fig. 20.7 AFM images of $\text{Mg}_{0.37}\text{Zn}_{0.63}\text{O}$ layers with $t = 38$ nm (a), 65 nm (b), 100 nm (c), and 280 nm (d). (e) Systematic variations of a - and c -axis length in $\text{Mg}_{0.37}\text{Zn}_{0.63}\text{O}$ layers in relation to the layer thickness



at half maximum (FWHM) of the lower-frequency side (Γ_a) to the higher-frequency side (Γ_b), also increased monotonically from 1.97 to 2.49. [Figure 20.8b](#) compares the spectrum of strained layers ($t = 38$ nm) with different Mg contents, $x = 0.12$ and 0.27. With increasing Mg content, the peak frequency shifted to a higher frequency, expected because of the reduction in reduced mass of the oscillating pairs. Furthermore, the peak broadened with increasing asymmetry Γ_a/Γ_b . These results may indicate that an increase in the Mg content leads to an increase in the randomness of the atomic arrangement and a relaxation of the Raman selection rule. Therefore, the 1st LO phonon of ZnO shows asymmetric broadening, reflecting its phonon DOS (density of states).

When lattice relaxation occurs in the thicker layers, the randomness in atomic arrangement will be more enhanced, resulting in lateral composition separation, as revealed clearly by the results of cathodoluminescence (CL) mapping. CL was

Fig. 20.8 (a) μ -RRS spectra at room temperature of $\text{Mg}_{0.37}\text{Zn}_{0.63}\text{O}$ layers with $t = 38, 65, 100,$ and 280 nm. (b) μ -RRS spectra of strained $\text{Mg}_{0.12}\text{Zn}_{0.88}\text{O}$ and $\text{Mg}_{0.27}\text{Zn}_{0.73}\text{O}$ layers



measured using a scanning electron microscope equipped with an Oxford mono-CL mirror and grating spectrometer system. Figure 20.9a, b show a $10 \times 10 \mu\text{m}^2$ topological surface image and the corresponding CL image, respectively, of the sample with $t = 280$ nm. The CL and topological surface images were observed simultaneously under measurement conditions of 10 kV and 150 nA. Use of these values made it possible to observe improved CL images. However, the topological surface image resulted in some degree of smearing since the focusing power of the electron beam slightly diffuses. Compositional fluctuation appears with local CL intensity variations. The CL image is mapped with emission intensity of 3.90 eV using the bright (intense) and dark (weak) scale. There are inhomogeneous regions in the micrometer scale in the CL image. Comparing Figs. 20.9a and 20.9b, the bright and dark regions of the topological image correlate to that of the CL image, as confirmed by the cross-section profiles of X and Y lines shown in Fig. 20.9c, d. This suggests a correlation between surface roughening and lateral segregation of Mg atoms. Local composition separation is characterized by a dislocated S-K growth of alloy layers. Thus, the origin of surface $\text{Mg}_{0.37}\text{Zn}_{0.63}\text{O}$ nanodots is clearly attributed to a dislocated S-K growth.

20.2.5 Multiple Quantum Wells and Excitonic Recombination

For advances concerning epitaxy of ZnO and related alloys, multiple quantum wells (MQWs) are of considerable practical interest. MQWs can provide larger oscillation strength, enhanced excitonic binding energy, and tenability of the operating wavelength due to a quantum confinement effect. The formation of abrupt interfaces between constituent layers is a key issue when fabricating MQWs. In the case of O-polar MQWs on sapphire substrates, the Mg content is strongly limited to 20 % because of inhomogeneous heterointerfaces between the well and barrier layers [50]. On the other hand, the use of lattice-matched ScMgAlO₄ imparted a high Mg content of 27 % which greatly improved structural quality in O-polar MQWs [8]. As mentioned in the preceding sections, homoepitaxial growth on the Zn-polar ZnO substrate was achieved, and preferential growth in the 2D mode was expected. Furthermore, the 2D growth of MgZnO alloy layers was fully maintained up to Mg content of 37 % [43]. The preservation of the 2D growth of MgZnO/ZnO heteroepitaxy is essential for the development of precise device structures, which can provide further enhancement of the degree of freedom in the fabrication of MQWs.

A fabrication scheme for MQWs is as follows. Thickness of barrier layers of Mg_{0.37}Zn_{0.63}O was set to below the critical thickness. After growing a 200-nm-thick ZnO buffer layer on a Zn-polar ZnO substrate, ten periods of a Mg_{0.37}Zn_{0.63}O (13 nm)/ZnO (3.3 nm) structure were grown at 500 °C under O₂ plasma exposure, followed by a 10-nm-thick ZnO capping layer (Fig. 20.10a). Here, the layer thickness was evaluated by comparing the high-resolution X-ray diffraction (HR-XRD) profile ($2\theta/\omega$ scan) of the (0002) plane, as shown at the top of Fig. 20.10b, with dynamic kinetic simulation [51] shown in the middle of Fig. 20.10b. The pronounced pendellosung fringes observed in the HR-XRD index HR-XRD profile suggests a high crystal quality for the MQWs since any imperfection or compositional inhomogeneity would decrease the phase coherence and eliminate the pendellosung fringes. The ω -rocking curves of SL-0, SL-1, and SL+1 peaks showed very narrow line-widths [40–50 arcsec]. This suggested small fluctuations in lattice axis orientation in the *c*-plane. The surface indicated a very flat morphology with a roughness of 0.41 nm. Sharp heterointerfaces between the well and barrier layers were observed by X-ray transmission electron microscopy (TEM) analysis as shown in the inset of Fig. 20.11c.

The optical properties of the MQWs were examined. Figure 20.11 shows the μ -PL spectra at RT observed from the cleaved edge of the (10-10) face [(a)–(d)] and top surface of the MQWs [(e)]. The surface spectrum (e) consisted of a strong broad peak at 3.46 eV and a weak signal around 3.90 eV. The 3.46 eV peak originated from carrier recombination in the ZnO well layers, while the 3.90 eV peak was ascribed to the Mg_{0.37}Zn_{0.63}O layers. This was supported by the PL spectra of the cleaved cross section. The spatial resolution of the apparatus ($\sim 0.5 \mu\text{m}$ as determined by the laser-beam waist at the sample surface) was smaller than the width of the MQWs constituent layers. Notwithstanding this fact, a systematic peak shift was observed from 3.28 to 3.46 eV (Fig. 20.11a–d) when moving the laser spot in the

Fig. 20.9 (a) Topological surface image. Note that the two bright spots do not indicate surface morphology, but dust used for a correction of focusing of the electron beam. (b) Monochromatic CL image taken at 3.90 eV. (c) and (d) Show cross-section profiles of X- and Y-lines, respectively, indicated by the white dotted lines of Fig. 20.9 (a) and (b)

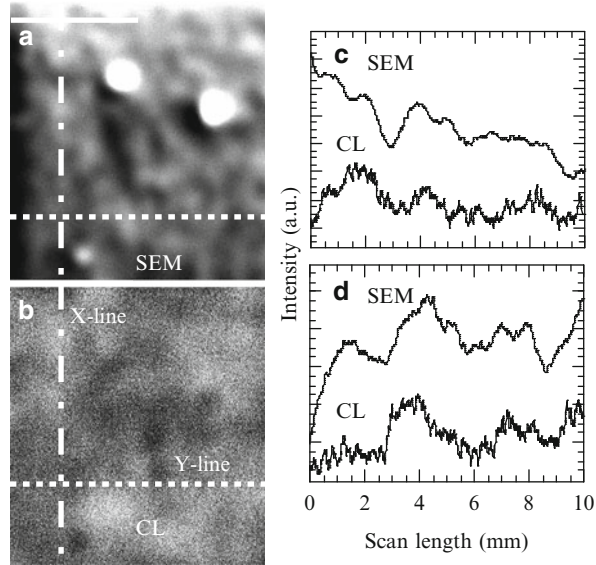
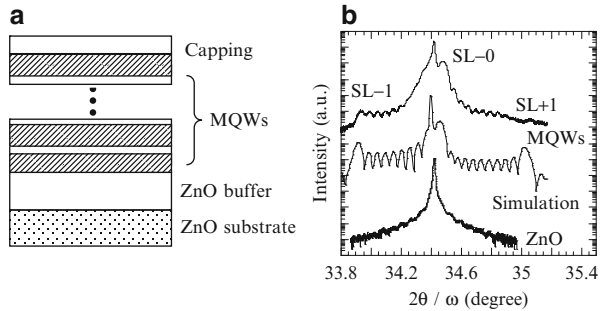


Fig. 20.10 (a) Schematic cross section of the MQWs. (b) High-resolution $2\theta/\omega$ profiles of the (0002) reflection for MQWs and the ZnO buffer including a theoretical simulation profile



cleaved edge cross section from the ZnO substrate to the MQWs' side (Fig. 20.11a). The 2D effect of the MQWs was confirmed by polarized μ -PL detection from the cleaved edge, as shown in Fig. 20.11c. The excitation laser with polarization perpendicular to the c -axis of the MQWs ($E \perp c$) yielded a stronger PL signal than that observed with parallel polarization ($E \parallel c$). Here, the polarization degree (P) was calculated as 0.43 by $(I_{\perp} - I_{\parallel}) / (I_{\perp} + I_{\parallel})$, showing a perfect polarization of the emission, where I_{\perp} and I_{\parallel} are MQWs emissions under $E \perp c$ and $E \parallel c$ configurations, respectively. The high P value at RT is related to a typical feature of 2D quantum confinement; the exciton can move freely within the MQWs plane but cannot move in a direction perpendicular to this plane [52, 56]. Therefore, the polarization-dependent PL spectra indicate that the excitons are sufficiently confined even at RT. In contrast, the polarized emission of barrier layers was weak due to the 3D nature of excitons. Such high-quality MQWs open up numerous possibilities for UV optoelectronic devices. These favorable properties cannot be attained for MQWs on sapphire substrates due to the lattice mismatch.

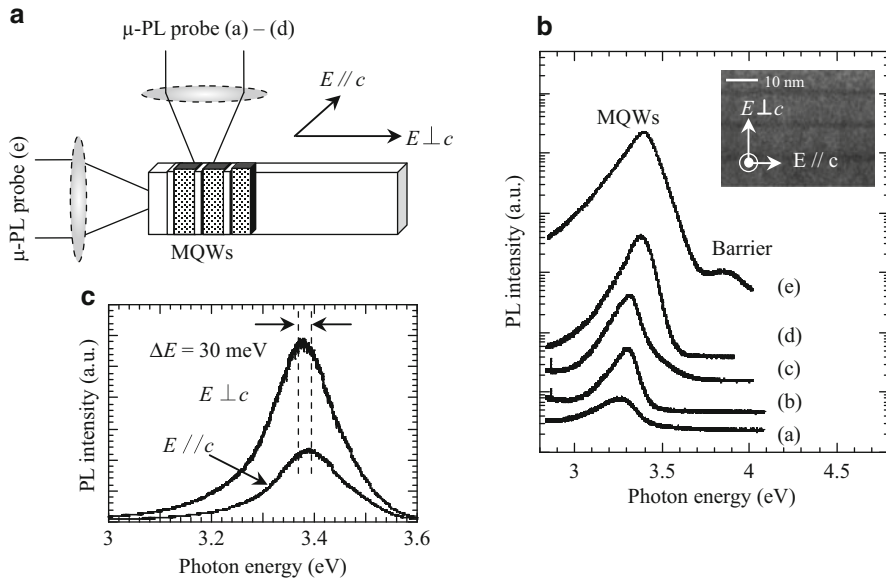


Fig. 20.11 (a) Schematic figure of an excitation method for the MQWs. (b) μ -PL spectra emitted from the surface layer (e) and from the cleaved edge (a)–(d). Inset shows an X-TEM image of the MQWs. (c) The μ -PL spectra measured with polarization oriented parallel ($E // c$) and perpendicular ($E \perp c$) to the c -axis of the MQWs

20.3 Nonpolarity and Quantum Structures

20.3.1 Nonpolar Growth of M -Face (10-10)

With homoepitaxial ZnO growth, one can select various growth directions without any lattice mismatch at the interface between the film and the substrate. This plays an important role in understanding the growth dynamics concerning epitaxial layers with different growth planes. ZnO layers on polar (0001) and (000-1) surfaces are dominated by 2D growth and spiral step-flow growth modes, respectively, which relate to specific atomic arrangement configurations and number of dangling bonds. In the nonpolar ZnO (10-10) plane, surface Zn and O atoms produce dimer rows running along the [1-210] direction [33]. This produces two types of step edges by polar and nonpolar faces toward the [1-210] and [0001] directions (Fig. 20.15b). This type of anisotropic surface morphology has been utilized in scientific studies of heterogeneous catalytic processes involving the absorption of molecular and metallic atoms on nonpolar surfaces [54]. We briefly describe the growth process and morphological evolution of surface nanowires in nonpolar ZnO on the basis of RHEED investigations [55].

In M -nonpolar layer growth up to 8 nm in thickness, a 2D streak pattern appeared to replace sharp patterns of ZnO substrates (Fig. 20.12a, b).

This is related to 2D nucleation at the initial growth stage, as evidenced by the smooth layer surface (Fig. 20.12f). Continued growth of ZnO changed to a mixed pattern, which relates to the onset of the transition from 2D to 3D modes. This results from the onset of a self-assembly of anisotropic 3D islands (Fig. 20.12c, g). Finally, the RHEED pattern showed 3D spots due to an island growth mode that originated from the formation of surface nanowires (Fig. 20.12d, h). Surface nanowires with high density (10^5 cm^{-1}) that formed on the ZnO layers were homogeneously elongated along the [0001] direction above $5 \mu\text{m}$ with a few branches (Fig. 20.12h).

Due to lattice strains at the heterointerface of layer/substrate, S-K growth naturally induces 3D islands that are surrounded by high-index facets on 2D wetting layers [12]. This has been observed in InGaAs/GaAs heteroepitaxy [56]. In an effort to examine the crystallinity in greater detail, plane-view and X-TEM observations were conducted to investigate the structural quality of the layer. Figure 20.13a shows a low-resolution X-TEM image with the [11-20] zone axis. Threading dislocations induced by lattice relaxation between the layer and substrate were not observed. The high-resolution X-TEM image of Fig. 20.13b reveals a lattice arrangement between a smoothly connected layer and substrate. A $3 \times 3 \text{ nm}^2$ space area selected from the layer region was utilized for fast Fourier transform (FFT) analysis to examine local lattice parameters and yielded a reciprocal space diffractogram (RSD) pattern (inset of Fig. 20.13b). From the RSD pattern, the estimated strains (ε_{yy} and ε_{zz}) at the interface were approximately 0.10 and 0.18 % with x , y , and z being parallel to the [0001], [10-10], and [11-20] directions, respectively. Figure 20.13c shows a bright field plane-view TEM image with $g=[11-20]$ excitation under two-beam conditions. Out-of-plane dislocations,

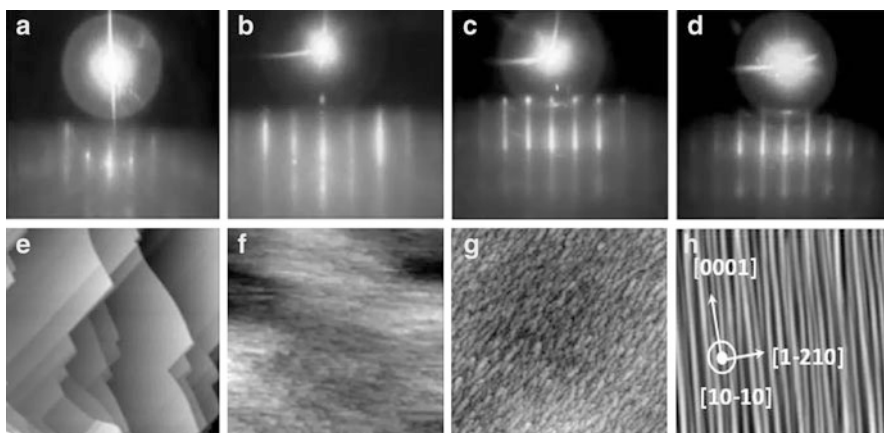


Fig. 20.12 RHEED patterns with the [0001] azimuth of the treated ZnO substrate (a) and ZnO layers with a thickness of (b) 8, (c) 20, and (d) 240 nm. AFM top view ($2 \times 2 \mu\text{m}^2$) of the treated ZnO substrate (e) and ZnO layers with different thicknesses (f)–(h). Layer thicknesses are (f) 8, (g) 20, and (h) 250 nm

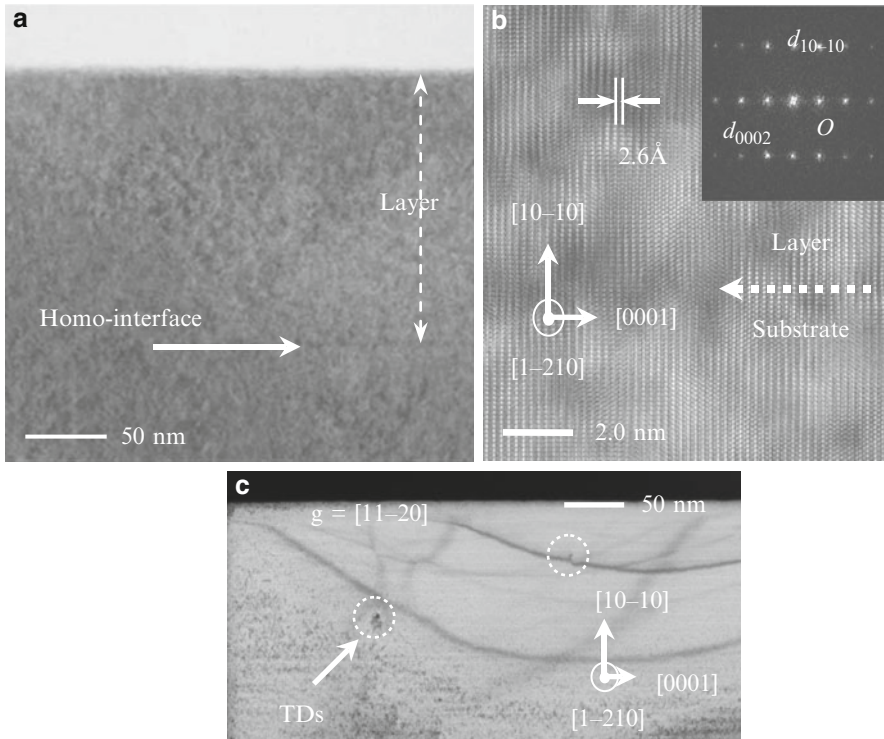


Fig. 20.13 (a) Low- and (b) high-resolution X-TEM images of the ZnO layer taken with the $[11\cdot20]$ zone axis. *Inset* shows the RSD obtained by FFT analysis. (c) A bright field plane-view TEM image of the ZnO layer with a $g = [11\cdot20]$ excitation under two-beam conditions

marked by a white open circle, were observed with a density of $3.2 \times 10^7 \text{ cm}^{-2}$, originating from threading dislocations running perpendicular to the layer surface. On the other hand, there were no in-plane dislocations propagating along the $[0002]$ and $[11\cdot20]$ directions from different g vector excitations. These results indicate that the homoepitaxial interface was almost strain-free. Thus, the elongated 3D islands that appeared on the 2D layers were formed under coherent homoepitaxy and had no correlation with the S-K growth.

20.3.2 Step-Edge Barrier and Self-Organized Nanowires

Similar surface nanowires have been formed by a step-faceting growth mode on vicinal GaAs (331) A and (553) B substrates [13, 14]. Mechanisms of the surface nanowires on non-vicinal ZnO (10-10) substrates differs clearly from that of vicinal GaAs substrates and the S-K mode based on lattice relaxation. On the other hand, it is known that morphological transformation from a 2D surface to

anisotropic 3D islands occurs during Si and GaAs (001) homoepitaxy [57, 58]. The Schwoebel barrier effect is considered as an important growth parameter. This barrier mechanism induces growth stability of nucleating anisotropic 3D islands on 2D growing surfaces above a critical thickness. Furthermore, the driving force of anisotropic surface morphology is associated with a difference in surface diffusion and sticking probability along the [110] and [-110] directions of GaAs (001) surfaces. The only research concerning the growth behavior on M-nonpolar ZnO (10-10) surfaces has been reported by Dulub et al. [59]. The anisotropic atomic arrangement of a ZnO (10-10) surface provides a corrugated surface that is related to the anisotropic diffusion coefficient for the growth of Cu on the surface since Cu diffusion was much faster along the [1-210] direction than along the [0001] direction. Cu grew two-dimensionally only up to a certain critical coverage, at which point it began to form 3D islands due to a Schwoebel barrier effect. The growth conversion from 2D to 3D modes of *M*-nonpolar ZnO layers may be associated with growth instability originating from a Schwoebel barrier effect and the atomic arrangement of surface Zn and O atoms leading to anisotropic surface diffusion.

Figure 20.14a, b show low- and high-resolution X-TEM images with the [0001] zone axis, respectively. A cross section of the surface nanowires displayed a triangular configuration with a periodicity of 84 nm. A high-resolution X-TEM image, marked by a white circle, revealed that the side facets did not consist of high-index facets but instead had a steplike structure with a height of 2.7 Å that corresponded to half a unit of the *m*-axis. Side facets of the surface nanowires possessed uniform step spacing ranging from 10 to 20 Å and were not surrounded by the high-index facets. A large number of surface nanowires showed flat tops with a (10-10) face and were separated laterally by deep grooves, as illustrated schematically in Fig. 20.14b. A similar structure was also seen in the anisotropic 3D islands on the 20-nm-thick layers, which indicated that the surface nanowires resulted from a coarsening of anisotropic 3D islands formed at the initial growth stage.

A multilayer morphology is determined not only by the transport of atoms within an atomic layer (*intralayer transport*) but also by the transport of atoms between different atomic layers (*interlayer transport*). Thus, evolution of mound shapes is understood in terms of activation of atomic processes along the step edge. Therefore, a sequence of multilayer growth is governed by activation of atomic processes which enable exchange and hopping of atoms between different atomic layers (Fig. 20.15a). Schwoebel and Shipsey introduced the schematic potential energy landscape near a step that has become the signature of what is often referred to as the *Ehrlich-Schwoebel barrier* (ESB) with a barrier energy of ΔE [60]. The mass transport of atoms between different atoms is inhibited by a strong ESB effect, resulting in mound formation. This induces a nucleation of islands on the original surface together with inhibited interlayer transport. Once the islands are formed, atoms arriving on top of the islands will form second-layer nuclei, and a third layer will nucleate on top of the second layer. This repetition leads to an increase of surface roughness with increasing layer thickness (\ominus), resulting in the formation of mound shapes. Mound formation is often observed on various systems such as semiconductors, metals, and organic materials. A mound structure possesses a

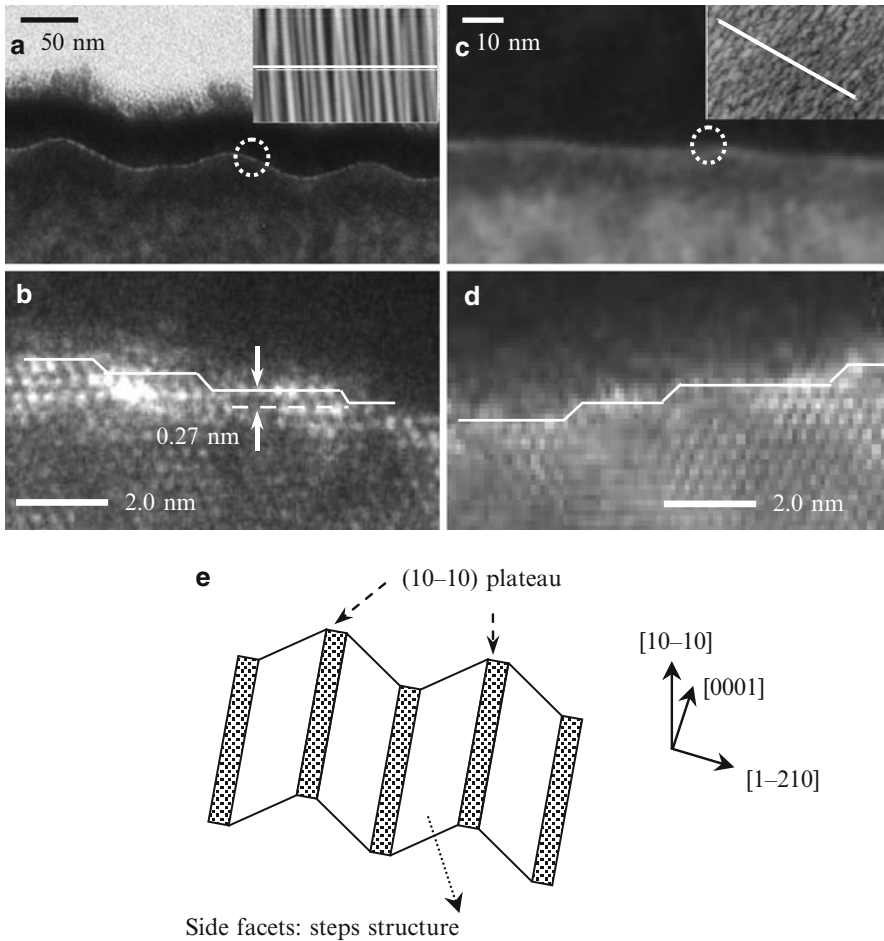


Fig. 20.14 (a) Low- and (b) high-resolution X-TEM images of the ZnO layer with a thickness of 240 nm. (c) Low- and (d) high-resolution X-TEM images of a 20-nm-thick ZnO layer. Insets (a) and (c) represent AFM images of the ZnO layers used for X-TEM observations. (e) Schematic representation of surface nanowires identified from X-TEM images

small flat plateau at the top and a side facet with constant step spacing and is separated from other mounds by deep grooves. This structure has been observed on dislocation-free metal homoepitaxial surfaces such as Pt/Pt (111) and Ag/Ag (100) systems and is often referred to as a *wedding cake* [61]. Here, emerging of mound formation under reduced interlayer transport is described by the coarsening $\lambda \sim \Theta^n$, and the surface width $w \sim \Theta^b$. λ and w values are the height-height correlation between the nanowires and the surface roughening, respectively. As seen in Fig. 20.16a, b, a coarsening exponent was indicated by $n = 0.23$, which was close to the n value of the mound formation seen after metal homoepitaxy [61].

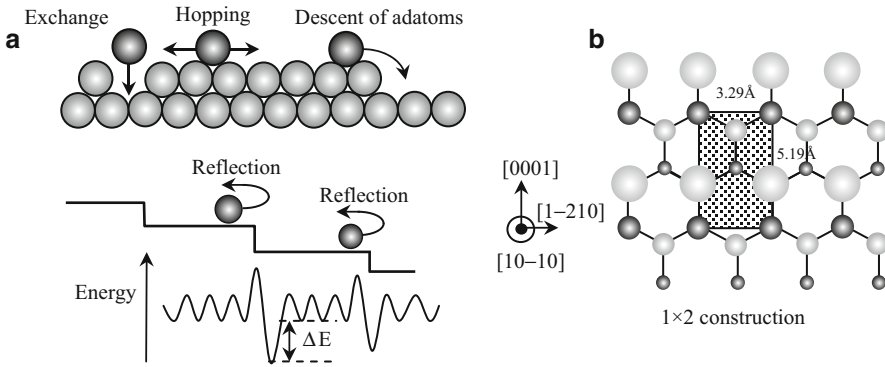


Fig. 20.15 (a) Upper part of the figure shows the descent of adatoms from an island by hopping and exchange. The lower part illustrates the energy landscape for hopping and the definition of ΔE_S . (b) Structural models showing the M -nonpolar (0001) surfaces of ZnO. The surface unit cells are indicated

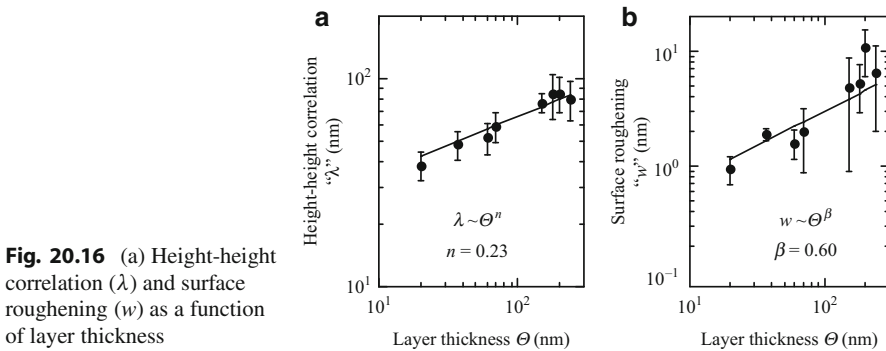


Fig. 20.16 (a) Height-height correlation (λ) and surface roughening (w) as a function of layer thickness

Furthermore, the high β value of 0.60 was suitable for mound growth based on the ESB. This indicates that the surface nanowires formed during M -nonpolar ZnO homoepitaxy are due to the growth process originating at the ESB. The ESB was also seen for layer growth of O-polar ZnO with a hexagonal island surface [62]. Furthermore, the appearance of an anisotropic morphology is related closely to a difference in surface diffusion and sticking probability as an important parameter. In M -nonpolar ZnO, the stoichiometric surface is auto-compensated since it contains an equal number of Zn and O ions per unit area. Surface Zn and O atoms form dimer rows running along the [1-210] direction, as shown in Fig. 20.15b. This produces two types of A and B step edges consisting of stable low-index (1-210) and (0001) planes, respectively. The [1-210] direction represents an auto-compensated nonpolar surface, while the [0001] direction consists of a polar surface with either Zn or O termination. Thus, the origin of the surface nanowires is based not only on an ESB barrier but a difference in the surface diffusion and sticking coefficient of atoms between the two types of step edges.

20.3.3 Linearly Polarized Light Emissions

ZnO has attracted great interest for new fields of optical applications. A characteristic of the wurtzite structure is the presence of the polarization-induced electric field along the c -axis. However, the optical quality of a quantum well structure grown along the c -axis suffers from undesirable spontaneous and piezoelectric polarizations in well layers, which lower quantum efficiency [1]. The use of nonpolar ZnO avoids this problem due to an equal number of cations and anions in the layer surface. Nonpolar ZnO surfaces have in-plane anisotropy of structural, optical, acoustic, and electric properties, which is useful for novel device applications. Recently, the number of investigations concerning nonpolar ZnO heteroepitaxial layers has grown considerably [63, 64], although heteroepitaxial growth involves introducing anisotropic lattice strains that modify the surface morphology and optical transitions. This hinders the elucidation of the intrinsic characteristics of the nonpolar layers and multiple quantum wells (MQWs). In this session, we discuss polarized PL of M -plane ZnO layers and $\text{Mg}_{0.12}\text{Zn}_{0.88}\text{O}/\text{ZnO}$ MQWs grown on M -plane ZnO substrates.

Figure 20.17 shows splitting of the valence band (VB) in ZnO under the influence of crystal-field splitting and spin-orbit coupling. The VB of ZnO is composed of p -like orbitals. Spin-orbit coupling leads to a partial lifting of the VB degeneracy, and the former six-fold degenerate VB is split into a fourfold ($j = 3/2$) and twofold ($j = 1/2$) band. The spin-orbit coupling is negative. The $j = 1/2$ band is at a higher energy than the $j = 3/2$ band. On the other hand, the crystal field in ZnO results in further lifting of VB degeneracy due to the lower symmetry of wurtzite compared to zinc blende. The crystal field causes a splitting of p states into Γ_5 and Γ_1 states. Crystal-field splitting Δ_{cf} and spin-orbit coupling Δ_{SO} together give rise to three twofold degenerate valence bands. These bands are denoted as A (Γ_9 symmetry), B (Γ_7), and C (Γ_7). These energies can be calculated as follows:

$$E_A(\Gamma_9) - E_B(\Gamma_7) = -\frac{\Delta_{\text{SO}} + \Delta_{\text{cf}}}{2} + \frac{\sqrt{(\Delta_{\text{SO}} + \Delta_{\text{cf}})^2 - \frac{8}{3}\Delta_{\text{SO}}\Delta_{\text{cf}}}}{2} \quad (20.3)$$

$$E_A(\Gamma_9) - E_C(\Gamma_7) = \sqrt{(\Delta_{\text{SO}} + \Delta_{\text{cf}})^2 - \frac{8}{3}\Delta_{\text{SO}}\Delta_{\text{cf}}} \quad (20.4)$$

For ZnO, the experimental results were $E_A - E_B = 0.0024$ eV and $E_C = 0.0404$ eV [67]. Solving the above two equations, we obtain Δ_{cf} (0.0391 eV) and Δ_{SO} (−0.0035 eV). A - and B -excitons are referred to as heavy (HH) and light hole (LH) bands, respectively, and the crystal-field split-off hole (CH) was related to the C -exciton. The detection of $E \perp c$ and $E // c$ points to A -exciton (X_A) and C -exciton (X_C), respectively, where E represents the electric field vector [68].

Figure 20.18a shows the $E \perp c$ and $E // c$ components of the normalized PL spectra of strain-free ZnO layers [69]. The peak energies of X_A and X_C were located at 3.377 and 3.419 eV, respectively. These energies coincided with

Fig. 20.17 Schematic energy level of band splitting by the crystal-field (Δ_{cf}) and spin-orbit (Δ_{so}) interactions in a wurtzite structure. $F_A(X)$ and $F_C(X)$ correspond to A- and C-excitons, respectively, which are indicated in the middle. In the electronic energy levels proposed by Park et al. (Ref. [9]) and Reynolds et al. (Ref. [10]), the uppermost Γ_9 and Γ_7 levels are interchanged

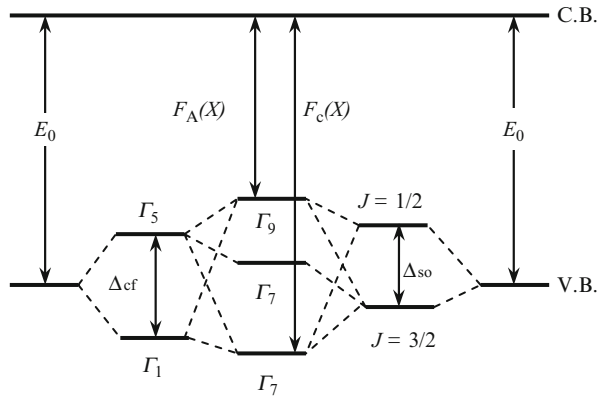
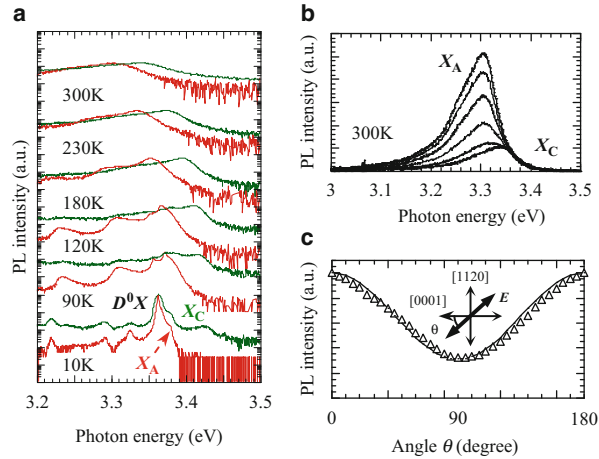


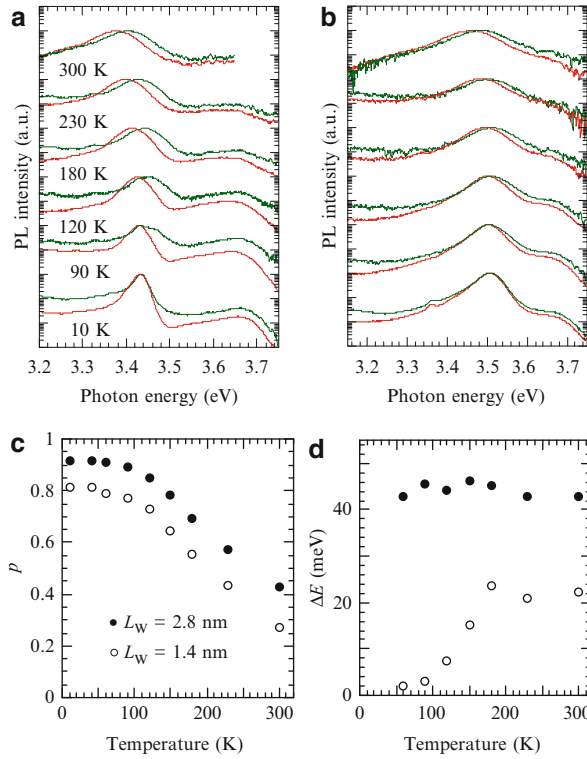
Fig. 20.18 (a) Temperature dependence of PL spectra on strain-free ZnO layers for $E \perp c$ (solid lines) and $E // c$ (dotted lines). (b) Polarization-dependent PL spectra at 300 K taken in steps of $\Delta\theta = 15^\circ$. (c) PL intensity as a function of polarization angle θ . Inset shows a schematic representation of the measurement geometry and sample orientation



the X_A (3.377 eV) and X_C (3.4215 eV) peaks in ZnO crystals, respectively. The dependence of peak intensities on temperature could be fitted using the Bose-Einstein relation with a characteristic temperature of 315 and 324 K for the X_A and X_C peaks, respectively. The bound exciton (D^0X) peak disappeared at 120 K due to the activation energy of 16 meV. The polarization degree (P) is defined as $(I_{\perp} - I_{\parallel}) / (I_{\perp} + I_{\parallel})$, where I_{\perp} and I_{\parallel} are the peak intensities for $E \perp c$ and $E // c$, respectively. Figure 20.18b shows the polarization-dependent PL spectra at 300 K. The layer strongly emitted polarized light. The P value was calculated as 0.49. Significant spectral shifts in PL were detected when altering the polarization angle. This is attributed to a difference in carrier distribution in the VB between the HH and CH levels at 300 K. Figure 20.18c shows the dependence of polarization angle on PL intensity. The experimental data (triangle dots) were in agreement with the $\cos(\theta)^2$ fit line (solid) obeyed by Malus' laws.

Polarized PL character in M -nonpolar MQWs will be discussed. ZnO wells are strain-free in the case of pseudomorphically grown MgZnO/ZnO MQWs.

Fig. 20.19 PL spectra under $E \perp c$ (solid lines) and $E//c$ (dotted lines) on MQWs with $L_W = 2.8$ nm (a) and 1.4 nm (b). (c) and (d) show the relationship of temperature with polarization degree (P) and energy separation (ΔE) on MQWs with different L_W



The PL spectra for $E \perp c$ and $E//c$ in MQWs with a well thickness (L_W) of 2.8 nm are shown in Fig. 20.19a. The emission peaks around 3.6 eV correspond to 7-nm-thick $\text{Mg}_{0.12}\text{Zn}_{0.88}\text{O}$ barriers. At 300 K, an energy separation (ΔE) of 37 meV was found between the MQWs emissions of 3.372 eV ($E \perp c$) and 3.409 eV ($E//c$). The emission peak for $E \perp c$ appeared under conditions of $E//c$ below 120 K since the thermal distribution of carriers in the high-energy level for $E//c$ is negligible at 10 K. A polarization degree close to unity was found with a high P of 0.92 at 10 K (Fig. 20.19c). In contrast, excited carriers at 300 K were sufficiently distributed in the high-energy level, resulting in a low P of 0.43. Furthermore ΔE between the emission peaks for $E \perp c$ and $E//c$ was retained at around 40 meV even at 60 K (Fig. 20.19d). This ΔE was close to the theoretical ΔE between the X_A and X_C states [70]. For unstrained bulk ZnO, a polarization magnitude of zero and unity in the C -exciton is detected along the normal direction and along the c -axis, respectively (Fig. 20.18a). However, the confinement of M -plane MQWs takes place perpendicular to the quantization of the [10-10] direction. This generates weak mutual mixing of the different p orbitals. Thus, a π polarization ($E//c$) component is expected for the A -excitonic state in these MQWs. In the case of M -plane MQWs, it is predicted that a 10% p_z orbital component is involved with the A -excitonic states [71], which is in agreement with the experimentally obtained

P value of 0.92. MQWs with a L_W of 1.4 nm showed that the polarized PL spectra of $E \perp c$ and $E // c$ were separated by a small ΔE of 27 meV at 300 K (Fig. 20.19b). ΔE decreased with temperature, and then completely disappeared at 60 K. The P value also dropped for all of the temperature regions. These behaviors are due to a large admixture of p_x to p_z orbitals for $E // c$, originating from an inhomogeneous roughening between the well and barrier layers. The interface roughness increased a potential fluctuation of quantized levels in the MQWs, being reflected by the broadened PL lines [72]. This was proven experimentally by the increase in line-width of PL spectra with a narrowing of L_W .

20.3.4 Large Anisotropy of Electron Transport

Self-organization of 1D nanostructures on growth surfaces has attracted much attention, as this phenomenon can form low-dimensional systems such as quantum wires and quantum dots. These low-dimensional superstructures produce interesting quantum phenomena in terms of both scientific and practical applications. Above all, understanding the formation of 1D surface morphology through a bottom-up process represents one of the challenges in crystal growth technology. However, the underlying origin of crystal growth of an anisotropic layer along one direction is still unclear. Recently, the ability to precisely control 2D growth for Zn-polarity in ZnO has blazed a new trail in the fields of quantum physics. Here, a surface roughening that occurs during layer growth provides a simple and efficient way to fabricate low-dimensional surface nanostructures, which can then spatially confine carriers. When spatial undulation occurs at a MgZnO/ZnO heterointerface, electron transport in MQWs shows anisotropic behavior. Previous studies have reported that 2D electron transport of AlGaAs/GaAs MQWs was anisotropically modulated using vicinal GaAs substrates with lateral surface corrugations [73].

A pronounced anisotropy of conductivity was observed in 7-period $\text{Mg}_{0.12}\text{Zn}_{0.88}\text{O}/\text{ZnO}$ MQWs grown on 200-nm-thick ZnO buffer layers. The barrier thickness was set to be 7 nm, and varying well widths were controlled between 1.4 and 4.0 nm. Surface nanowires elongated along the [0001] direction were retained even after growing the MQWs. Figure 20.20a shows an X-TEM image of MQWs with the [0001] zone axis. The layers with a bright contrast represent MgZnO barriers, while the darker layers indicate ZnO wells. The MgZnO layers repeat the surface structure of the underlying ZnO layers, indicating that $\text{Mg}_{0.12}\text{Zn}_{0.88}\text{O}/\text{ZnO}$ heterointerfaces are periodically modulated by the surface nanowires.

Figure 20.20c shows the temperature-dependent Hall mobility parallel ($\mu_{H[0001]}$) and perpendicular ($\mu_{H[1-210]}$) to the nanowires. The ex situ annealed ZnO substrates were treated as a semi-insulating substrate showing electrical resistivity in the order of 10^6 – $10^7 \Omega \cdot \text{cm}$. $\mu_{H[0001]}$ gradually increased with decreasing temperature and became constant just below 150 K due to a suppression of ionized impurity scattering. The electron concentration of MQWs also saturated below 100 K, suggesting that the entire electric current flows as 2D-like transport through the

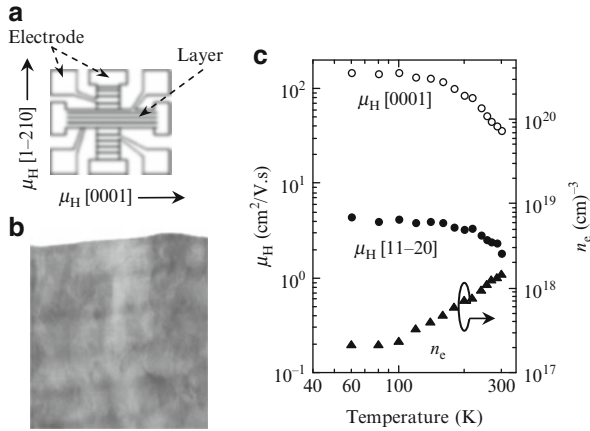


Fig. 20.20 (a) Hall bar pattern used to investigate anisotropic transport. (b) X-TEM image of $\text{Mg}_{0.12}\text{Zn}_{0.88}\text{O}/\text{ZnO}$ MQWs. (c) Temperature dependence of Hall mobility parallel ($\mu_{H[0001]}$) and perpendicular ($\mu_{H[11-20]}$) to the nanowire arrays and electron concentration (n_c) for MQWs with a $L_W = 3.2$ nm. Electrical properties parallel and perpendicular to the nanowires were measured using a Hall bar configuration with the perpendicular arms of the Hall bar aligned in the [0001] and [1-210] directions (Fig. 20.20 (b)). The Hall bars were fabricated by Ar ion milling of the samples through a photolithography-defined resist mask

ZnO wells. In contrast, $\mu_{H[1-210]}$ was much lower and resulted in large anisotropy of electron transport. Figure 20.21a shows the ratio of $\mu_{H[0001]}$ and $\mu_{H[1-210]}$ as a function of temperature. The curves correspond to different L_W of 2.2, 2.8, and 4 nm. For MQWs with a L_W of 4 nm, we observed almost no anisotropic behavior. However, the anisotropy of the Hall mobility increased to 52 for MQWs with a L_W of 2.8 nm at low temperature.

The transport properties indicate that electrons can move almost freely along the nanowires, but are blocked from moving perpendicular to the nanowires. We discuss a possible mechanism for this type of activation barrier. The large anisotropy of electron transport disappeared when a flat surface was realized using Zn-polar MQWs, as shown in Fig. 20.21b. Interface roughness scattering dominates low-temperature mobility in MQWs [74]. A slight roughness of the heterointerfaces induces a large fluctuation in quantization energy of confined electrons. This acts as a scattering potential barrier for electron motion and reduces mobility. Therefore, electrons may readily undergo frequent scattering in a direction perpendicular to the nanowires by potential barriers produced between nanowires and, consequently, may become extremely immobile.

In contrast, parallel conductance along the nanowires involves a lower scattering probability than perpendicular transport due to a weak heterointerface modulation. However, the P value for MQWs with a L_W of 2.2 nm decreased with a decrease in $\mu_{H[0001]}$. Inspection of polarized PL spectra showed that the energy fluctuations in the quantum well gradually increased with decreasing L_W (Fig. 20.18). A decreased

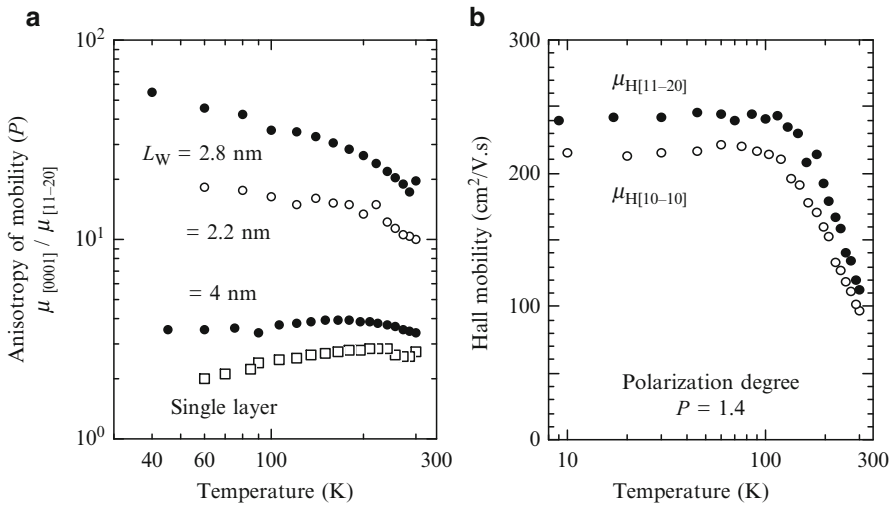


Fig. 20.21 (a) Temperature dependence of anisotropy of mobility (P) for M -nonpolar $\text{Mg}_{0.12}\text{Zn}_{0.88}\text{O}/\text{ZnO}$ MQWs with different well thicknesses (L_W) of 2.2, 2.8, and 4 nm. (b) Temperature dependence of Hall mobility ($\mu_{H[11-20]}$) and ($\mu_{H[10-10]}$) for Zn-polar $\text{Mg}_{0.27}\text{Zn}_{0.73}\text{O}/\text{ZnO}$ MQWs with a $L_W = 2.4$ nm

Hall mobility with a narrowing of L_W has been observed on very thin InAs/GaSb MQWs since energy fluctuations in a quantum well are caused by an increase in interface roughness [75]. It is concluded, therefore, that the large transport anisotropy was obtained through both a quantum size effect and small energy fluctuations in the quantum well, i.e., when L_W was in the vicinity of 3 nm.

20.4 Quantum Well Geometry Based on ZnCoO

20.4.1 Spin and Band Engineering

Diluted ZnCoO magnetic semiconductors (DMS) display $s, p-d$ exchange interactions between the localized magnetic moments of transition ions and the extended band states that yield a large Zeeman splitting. Although many investigations have been directed toward elucidating the origin of ferromagnetic ordering in ZnCoO [76,77], detailed studies concerning the modulation of band structure induced by the incorporation of Co ions remain unclear. For nonmagnetic $\text{Zn}_{1-x}\text{Mg}_x\text{O}$ alloy layers, excitonic-related optical properties at the band edge changed systematically with increasing band gap regardless of the synthetic methods employed, while the alloy parameters in ZnCoO tended to be strongly dependent on fabrication technique. CoO is a Mott-Hubbard insulator with a charge transfer gap of 5.0 eV [78] and differs largely from nonmagnetic MgO (band gap: 6.2 eV) with respect to electronic structure. It is expected to meet various fatal problems induced by utilizing doping

with Co atoms in comparison to Mg atoms. Therefore, a precise understanding of the properties of ZnCoO alloy is essential for the development of spin optics.

Figure 20.22a shows the absorption spectra at 10 K of $\text{Zn}_{1-x}\text{Co}_x\text{O}$ layers ($x=0-0.05$) grown on *C*-face sapphires. A free excitonic transition (*FX*) was clearly observed at 3.387 eV with phonon side bands of 72 meV for un-doped ZnO. The FX peak gradually shifted to a higher energy with increasing Co content, and then the excitonic structure diffused with an obvious band tail around 3.2 eV. Charge transfer (CT) levels from Co^{2+} to $\text{Co}^+ + h^+_{\text{VB}}$ in $\text{Zn}_{1-x}\text{Co}_x\text{O}$ seem to contribute to the sub-band gap since it holds a photon energy of 3.2 eV [79]. This is further illustrated in detail in the magnetic circular dichroism (MCD) spectra.

Figure 20.22b shows the MCD signals obtained at 10 K. An external magnetic field induces weak Zeeman splitting of the semiconductor band structure (Fig. 20.22c). In DMS, this splitting can be huge due to the *s*, *p-d* exchange interactions. Thus, the effective magnetic field on the *sp* band electrons is amplified by the magnetic moment of the transition metal ion through the *s*, *p-d* exchange interactions. Here, this splitting produces circularly polarized optical anisotropies that are widely known as the MCD effect, which allow a more precise evaluation of the magneto-optical properties of DMS. In general, MCD intensity is expressed by the following relation:

$$MCD = \frac{90}{\pi l} \frac{I^+ - I^-}{I^+ + I^-}, \quad (20.5)$$

where *l* is the thickness of the sample and I^+ and I^- are the intensities of transmitted light in σ^+ and σ^- polarizations, respectively. MCD depends on the photon energy, and it is usually very strong near a resonant line or band split by the Zeeman effect. The un-doped ZnO layer exhibits a very weak MCD signal at the Γ -point, which originates from excitonic transitions from the Γ_9 and Γ_7 levels of V.B. to C.B. The MCD response in $\text{Zn}_{1-x}\text{Co}_x\text{O}$ ($x \neq 0$) layers was strongly enhanced due to *p-d* electron coupling between the t_{2g} states of Co^{2+} and the $2p$ state of oxygen. In regions with Co contents above 2%, however, the MCD response is weakened and broadened due to alloy fluctuation. A broader shoulder with negative polarity then appeared at 3.2 eV corresponding to CT levels. The Co $3d$ (t_{2g}) levels occupied by up-spin are located at a neighbor of the V.B. Thus, the photoexcited CT states would appear in shallow levels near the C.B. As a result, excitonic recombination at the band edge is suppressed due to the appearance of the band tail. $\text{Zn}_{1-x}\text{Co}_x\text{S}$ and $\text{Zn}_{1-x}\text{Co}_x\text{Se}$ have also exhibited circularly polarized CT transitions [80].

The Γ -point in the MCD corresponds to the band-gap energy (E_0 edge). The shift in the E_0 edge to a higher energy with increasing Co content is shown in Fig. 20.23. A linear increase in the E_0 edge with increasing Co content (x) was obtained and is expressed by $E(x) = 3.387 \text{ eV} + 0.026x$, indicating a band-gap widening for $\text{Zn}_{1-x}\text{Co}_x\text{O}$. Here, the reason for the band-gap widening can be tentatively explained as follows. An electronic structure of CoO consists of double energy gaps: one represents a charge transfer gap of 5.0 eV from O($2p$) to the occupied $3d$ levels, while the other is a wide gap of 8 eV between the occupied $3d$ levels and Co($4s$)

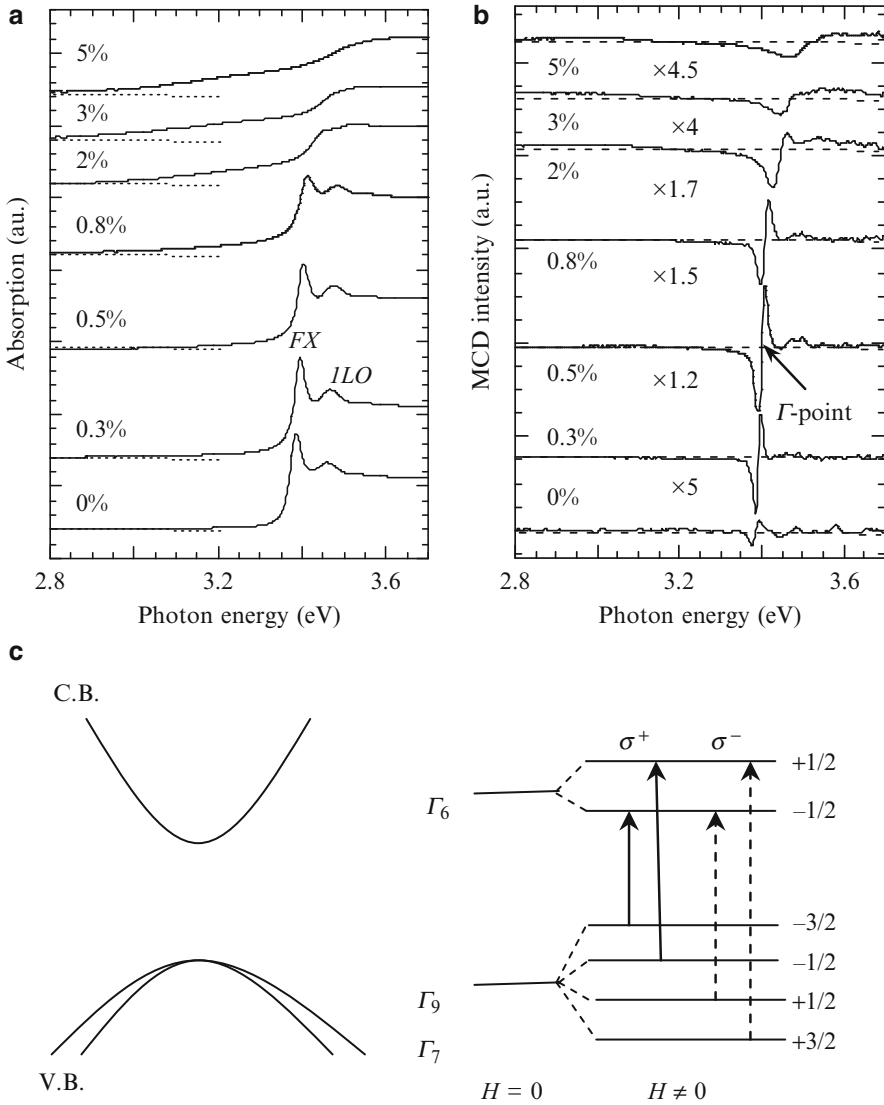
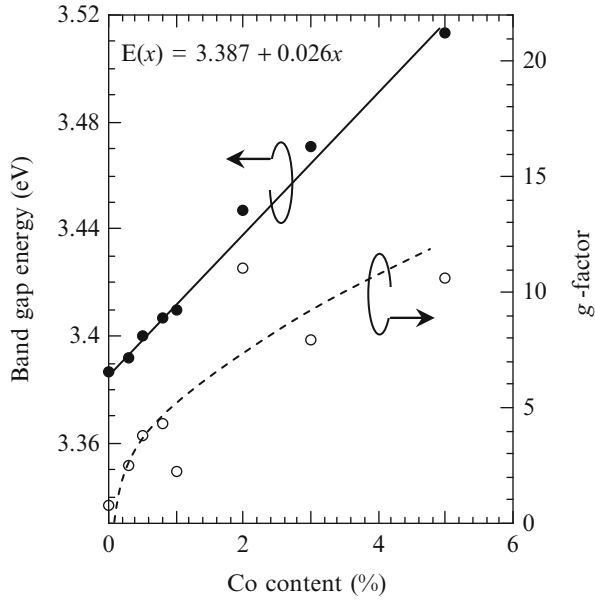


Fig. 20.22 (a) Optical absorption spectra and (b) MCD signals of Zn_{1-x}Co_xO ($x = 0-5\%$) layers measured at 10 K. (c) Zeeman splitting and σ^+ and σ^- optical transitions at Γ -points

levels, indicating that an optical gap between O(2p) and Co(4s) levels would be very wide [81]. Furdyna et al. stressed the close relationship of s and p electron bands in $A^{II}_{1-x}Mn_xB^{VI}$ systems to the bands of nonmagnetic $A^{II}B^{IV}$ [82]. The band-gap widening in Zn_{1-x}Co_xO can be ascribed to hybridization of the s , p band of ZnO with that of CoO. Furthermore, the g factor from the MCD spectra is qualitatively

Fig. 20.23 (●) Photon energy derived from the MCD E0 edge at 10 K, which essentially indicates the band gap of $\text{Zn}_{1-x}\text{Co}_x\text{O}$. (○) Dependence of g-factor on Co content in $\text{Zn}_{1-x}\text{Co}_x\text{O}$



estimated using the following equation:

$$MCD = -\frac{45}{\pi} \times \Delta E \times \frac{dK}{dE} (\Delta E = g\mu_B H), \quad (20.6)$$

where K is the absorption coefficient, E is the photon energy, μ_B is the Bohr magneton, and H is the magnetic field. From Fig. 20.23, the g factor linearly increases with increasing Co content and then gradually saturates over 2%. This correlates with an antiferromagnetic (AFM) exchange interaction between two nearest-neighbor Co^{2+} ions and is based on spin coupling viewed as an indirect exchange interaction mediated by the anion. This AFM coupling essentially produces a net zero magnetic moment for the pair, resulting in a decrease of total susceptibility. Thus, the probability of obtaining isolated Co^{2+} ions quickly decreases due to nearest-neighbor complexes with increasing Co content, resulting in a decrease of the effective number of isolated spins. Therefore, Co^{2+} ions are almost retained as an isolated ion with Co contents below 1%, while Co^{2+} -pair complexes gradually increased in the host with a Co content over 2%.

Excitonic luminescence in $\text{Zn}_{1-x}\text{Co}_x\text{O}$ layers is strongly suppressed (Fig. 20.24a). The PL intensity of the $\text{Zn}_{0.99}\text{Co}_{0.01}\text{O}$ layer decreased by an order of 1,000 compared to the ZnO layer. Although the origin of the remarkable suppression of excitonic luminescence is unclear at present, we provide a possible explanation. A neighbor of the C.B. in $\text{Zn}_{1-x}\text{Co}_x\text{O}$ can be constituted from complex levels such as excitonic states, internal $3d$ transitions, and photoexcited CT levels. Excited carriers may be transferred to intra $3d$ levels and/or the CT levels by nonradiative

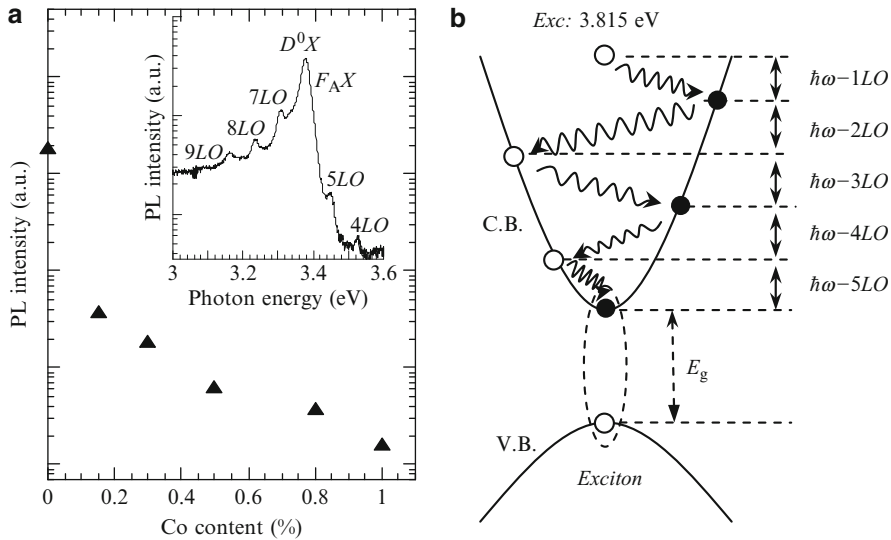
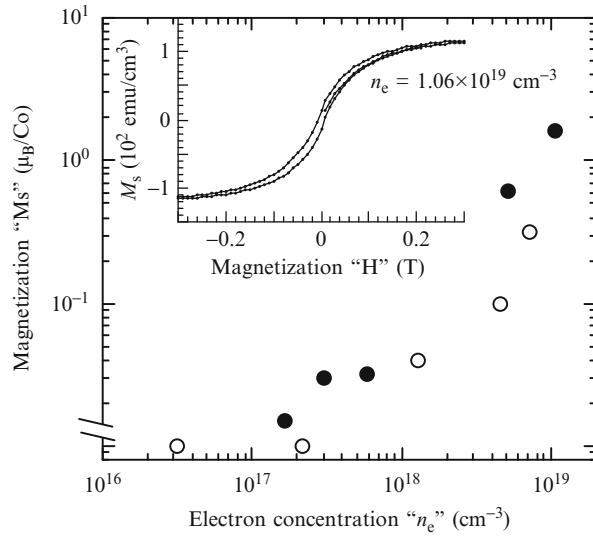


Fig. 20.24 (a) Dependence of integrated PL intensity at the band edge on Co content for Zn_{1-x}Co_xO layers. *Inset* shows PL spectrum of excitonic transitions at 10 K. (b) Schematic diagram of the cascade mode of OMRRS by a hot exciton-mediated process. The relaxation process is based on the hot exciton involving the quasi-LO phonon

processes. Nawrocki et al. observed energy transfer from excited carriers to Mn²⁺ ions in Cd_{1-x}Mn_xS due to “Auger recombination” [83]. It is important to note that weak PL emissions of Zn_{1-x}Co_xO layers are associated with nonradiative energy transfer to Co (3d) intra-levels. The inset figure shows the PL spectrum of a Zn_{1-x}Co_xO layer with $x = 0.15\%$. The F_AX emission shifted from 3.377 to 3.398 eV due to the wide band gap. The line shape of D⁰X is clearly broadened by Co doping because excited carriers experience spatial potentials that are dependent on local atomic fluctuations. The whole spectra were superimposed with n th ($n = 4-9$) resonant Raman scattering (RRS) [84]. Peak positions of the RRS are independent of temperature, correlating clearly with the Frohlich interaction that causes successive emissions of LO phonons, which can be explained by carrier-mediated cascade relaxation (Fig. 20.24b). Absorption of the incident photon energy (3.815 eV) is sufficient for the creation of hot electrons. The hot electrons relax to lower energy states with successive emission of LO phonons by cascade events. The RRS at the band edge of GaA_{1-x}N_x ($x = 0.001$) has been induced by impurity states consisting of excitons bound to isoelectronic nitrogen impurities. Isolated nitrogen centers, which are slightly perturbed by distant nitrogen, result in the RRS and a broadening of exciton bands [85]. This fact suggests that exciton states bound to isolated Co centers in ZnO induced the RRS. Investigations concerning excitonic recombination and nonradiative energy transfer will be enhanced through the use of magneto-PL measurements.

Fig. 20.25 (a) Logarithmic correlation between magnetization (M_s) at 10 K and electron density (n_e) at 300 K for Zn-polar (\circ) and O-polar (\bullet) $\text{Zn}_{0.94}\text{Co}_{0.06}\text{O}$ layers. Inset shows an M - H hysteresis curve for O-polar $\text{Zn}_{0.94}\text{Co}_{0.06}\text{O}$ layers with a n_e of $1.06 \times 10^{19} \text{ cm}^{-3}$



20.4.2 Ferromagnetism

Ferromagnetism (FM) based on Co-doped ZnO spawned a large number of experimental and theoretical studies. The reported experimental results show a broad distribution, indicating that this system is sensitive to preparation methods, measurement techniques, and types of substrate. For example, while some experiments report above room-temperature FM, others report a low FM-ordering temperature, or spin-glass or paramagnetic (PM) behavior. Therefore, many researchers have focused extensively on FM properties to elucidate its mechanism. Recent investigations in magneto-optics and magneto-transport in $\text{Zn}_{1-x}\text{Co}_x\text{O}$ layers have reported an interaction between carriers and localized 3d spins [86, 87]. For session Sect. 20.4.1, we explained magneto-optics due to the exchange interaction between excitons and localized 3d spins. In this session, we introduce a correlation between FM ordering and the concentration of free electrons.

Figure 20.25 shows the logarithmic correlation between magnetization (M_s) at 10 K and electron concentration (n_e) at 300 K for Zn-polar (\circ) and O-polar (\bullet) $\text{Zn}_{0.94}\text{Co}_{0.06}\text{O}$ layers on ZnO substrates. n_e was controlled by changing $p(\text{O}_2)$ from 10^{-4} to 10^{-7} mbar during layer growth. Detailed results of Ref. Ms at 10 K correlated closely with n_e at 300 K, indicating that FM ordering is associated with an increase in n_e and represents an essential phenomenon that is independent of the polarity. The inset figure shows M - H hysteresis at 10 K for the $\text{Zn}_{0.94}\text{Co}_{0.06}\text{O}$ layer with a n_e of $1.06 \times 10^{19} \text{ cm}^{-3}$. The saturation magnetization of 112 emu/cm^3 ($1.62 \mu_B/\text{Co}$ atom) was obtained in a tetrahedral crystal field. Furthermore, a correlation between M_s and n_e values was found for both polarities. From Fig. 20.25, the relationship shows a scaling behavior of the form $M_s \propto n_e^\alpha$, with values of 0.82 and 1.15 for data with Zn- and O-polarities, respectively.

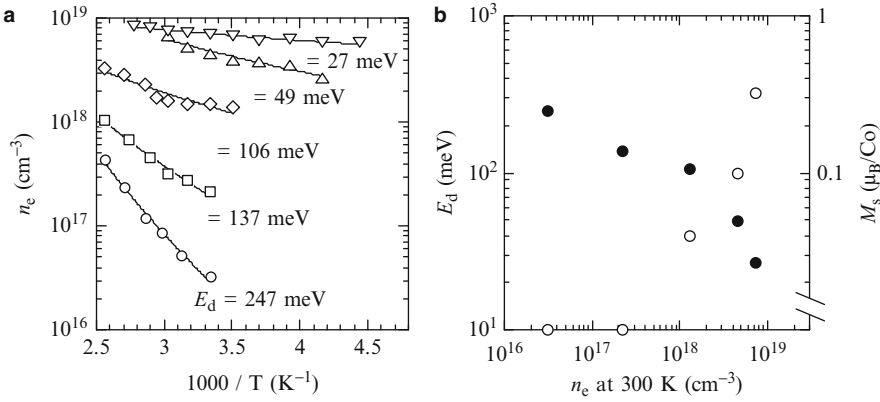


Fig. 20.26 (a) n_e as a function of reciprocal temperature for Zn-polar $\text{Zn}_{0.94}\text{Co}_{0.06}\text{O}$ layers grown under a $p(\text{O}_2)$ of 1.4×10^{-4} (\circ), 1.4×10^{-5} (\square), 1.4×10^{-6} (∇), 1.4×10^{-7} (\diamond), and 6.0×10^{-8} mbar (\triangle). The *solid line* represents the theoretical fit according to Eq. 20.7. (b) E_d and M_s at 10 K as a function of n_e at 300 K. (\bullet) and (\circ) indicate E_d and M_s values, respectively

Figure 20.26a shows n_e as a function of reciprocal temperature in Zn-polar $\text{Zn}_{0.94}\text{Co}_{0.06}\text{O}$ layers grown under different $p(\text{O}_2)$. By reducing $p(\text{O}_2)$, n_e at 300 K varied from 10^{16} to 10^{19} cm^{-3} . The carrier activation (E_d) behavior systematically evolves from a linear fitting of n_e near room temperature according to the following formula [88]:

$$n_e + N_A = \frac{N_D}{1 + g_d \left(\frac{n_e}{N_C} \right) \exp\left(\frac{E_d}{k_B T} \right)}, \quad (20.7)$$

where $g_d = g_1/g_0$ represents the factor with degeneracy of the unoccupied donor state $g_0 = 1$ and degeneracy of the occupied donor state $g_1 = 2$, assuming an s -like two-level system and E_d and N_D represent the donor activation and donor concentration, respectively. For clarity, the quantity N_A represents the total number of deep acceptors acting as electron trapping centers in the host. Furthermore, $N_C = 2(2\pi m^* k_B T / h^2)^{3/2}$ for ZnO denotes the effective density of states in the conduction band, where k_B and h are the Boltzmann and Planck constants, respectively, and m^* represents the electron effective mass in ZnO. E_d decreased from 247 to 49 meV with decreasing $p(\text{O}_2)$, and N_D and N_A values were in the order of 10^{19} to 10^{20} and 10^{17} cm^{-3} in all layers, respectively. The number of free electrons is only controlled by the activation energy of donor levels. Since Co ions in ZnO layers are in the divalent state, doped Co ions are considered a neutral dopant. Thus, n_e cannot be affected by doping with Co ions. One theoretical investigation proposed the formation of CoZn-native defects in ZnO under an oxygen-rich atmosphere [89]. The decrease in n_e with increasing $p(\text{O}_2)$ was due to an increase in E_d following the generation of deep donor levels. Figure 20.26b shows E_d and M_s at 10 K as a function of n_e at 300 K. A large M_s was observed in the high n_e regions supplied from shallow donor levels, while an increase in E_d was

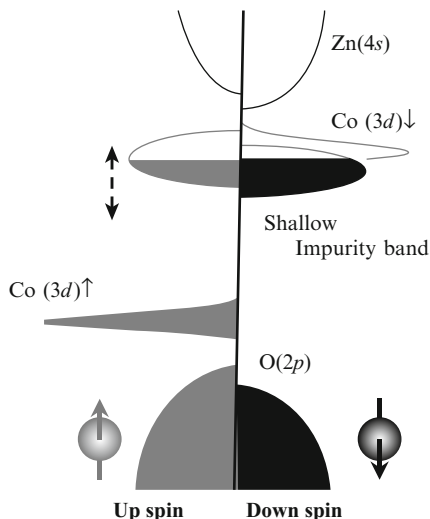
suppressed following FM ordering with a decrease in n_e . This suggests that the high n_e around the Mott transition supplied from shallow donor levels plays an important role in maintaining FM ordering.

Origin of FM ordering cannot be explained by super-exchange interactions with short-range order because FM ordering appears at a low concentration that is 6% below the percolation threshold (17%) associated with nearest-neighbor cation coupling in ZnO [90]. From theoretical aspects, ZnCoO possesses large exchange splitting. Up-spin states of the $3d$ orbital are fully occupied and were set on the top of the valence band. On the other hand, partially occupied down-spin states are located near the Fermi level. From theoretical aspects, ZnCoO possesses large exchange splitting. Up-spin states of the $3d$ orbital are fully occupied and were set on the top of the valence band. On the other hand, partially occupied down-spin states are located near the Fermi level. Until now, common models of FM ordering in ZnO DMS materials suggested a strong coupling between magnetic ions and charge carriers in the vicinity of the Fermi level. If donor impurity such as ZnO is introduced in the host lattice, shallow donor levels with low E_d are formed directly under the conduction band (C.B.) and are followed by the formation of an impurity band that causes a delocalization of carriers around the Mott transition. The Fermi level rises near the impurity band, resulting in strong hybridization and charge transfer from the impurity band to the empty $3d$ orbital of Co^{2+} ions near the Fermi level for FM ordering, as shown in Fig. 20.27. This physical origin is derived from the spin-split impurity band model [91] and is suitable for our data in explaining that the transition of magnetic ordering from PM to FM depends on n_e . In contrast, deep donor levels in the band gap are strongly localized charge carriers and suppress an itineration of electrons, resulting in low n_e and not FM ordering. Therefore, a hopping motion of free electrons in the impurity band is needed to mediate FM ordering in $\text{Zn}_{0.94}\text{Co}_{0.06}\text{O}$ layers.

20.4.3 Space Separation of Exciton and Localized Spin Systems

$\text{Zn}_{1-x}\text{Co}_x\text{O}$ is of particular interest in studies concerning quantum heterostructures derived from coupling of spins and carriers. However, growth control of a 2D mode has seldom been reported for $\text{Zn}_{1-x}\text{Co}_x\text{O}$ layers despite its practical use in applications such as spintronics. 2D growth for a sharp heterointerface is suitable for layer growth along the Zn-polarity. In session 2, we introduced homoepitaxial growth in ZnO and fabrications of $\text{Mg}_x\text{Zn}_{1-x}\text{O}/\text{ZnO}$ MQWs based on Zn-polarity. A detailed investigation of the growth mechanism should be performed for Zn-polar $\text{Zn}_{1-x}\text{Co}_x\text{O}$ layers. Quantum well (QW) geometry based on $\text{Zn}_{1-x}\text{Co}_x\text{O}/\text{ZnO}$ represents spatially separated excitons and localized $3d$ spins at the nanoscale. The quantum confinement systems of DMS enhance the exchange interaction and produce an interesting issue from both physics and applications point of view. In our case, electrons and holes were confined in the nonmagnetic ZnO layers because the $\text{Zn}_{1-x}\text{Co}_x\text{O}$ layer becomes a barrier layer. This QW geometry is subjected to the effect of the magnetic spins in the barriers

Fig. 20.27 The Fermi level lies in a spin-split impurity band. Schematic format (Adapted from Ref. [91])



only through wave function penetration. Therefore, this QW geometry becomes an effective investigation technique of spin-dependent luminescence showing a circular polarization reflecting the FM ordering in $\text{Zn}_{1-x}\text{Co}_x\text{O}$.

The FM ordering of $\text{Zn}_{1-x}\text{Co}_x\text{O}$ layers is due to the spin-split impurity band mechanism. Therefore, Zn-polar $\text{Zn}_{1-x}\text{Co}_x\text{O}$ layers should be grown in the lower $p(\text{O}_2)$ regions below 10^{-6} mbar. However, layer surfaces obtained with this strategy usually possess rough surfaces with many pit holes that are ascribed to threading dislocations in terms of V-pit holes [92]. The strain effect is the primary cause of the formation of the pits, and stacking faults generated by strain relaxation lead to the formation of pits. Thus, these pits cannot be formed to contain the strain energy in the layer below a critical thickness, at which point it is favorable to release the stress by forming pits. Figure 20.28a shows the dependence of pit density on layer thickness for Zn-polar $\text{Zn}_{0.94}\text{Co}_{0.06}\text{O}$ layers grown under a $p(\text{O}_2)$ of 10^{-6} and 10^{-7} mbar. Pit density decreased with a decrease in layer thickness and reduced to orders of 10^7 cm^{-2} at a layer thickness of 10 nm. The 2D growth in the $\text{Zn}_{0.94}\text{Co}_{0.06}\text{O}$ layer at the lower $p(\text{O}_2)$ regions was obtained while maintaining the high n_e required for FM ordering with a decrease in the layer thickness. These observations might suggest that a 2D mode in Zn-polarity is retained even at lower $p(\text{O}_2)$ within the initial stage of layer growth. An incomplete covering of O atoms on the growing surface due to an oxygen-poor atmosphere results in growth instability of the 2D mode and leads to pit formation. The density of pits rapidly increases as the layer thickness increases due to escalating strain relaxation.

$\text{Zn}_{0.94}\text{Co}_{0.06}\text{O}$ layers possess a high band offset of 156 meV compared with the one of ZnO. This band offset can sufficiently confine electrons and holes in the ZnO wells. We developed periodic oxygen-pressure modulated epitaxy to

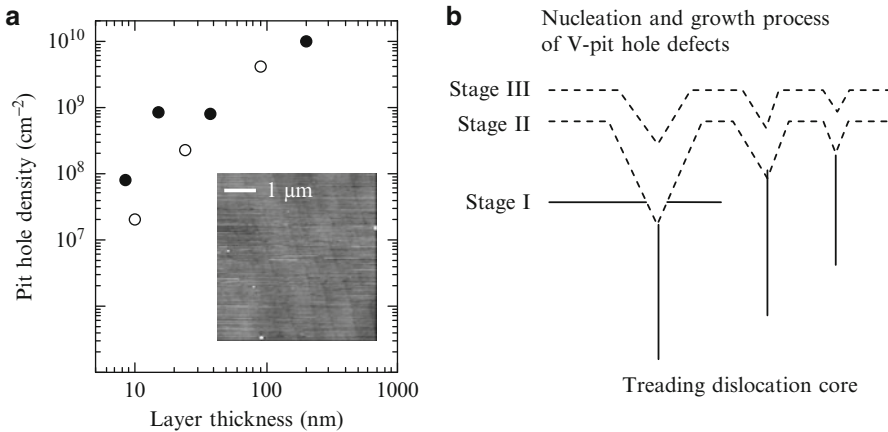


Fig. 20.28 (a) Dependence of pit hole density on layer thickness for Zn-polar $\text{Zn}_{0.94}\text{Co}_{0.06}\text{O}$ layers grown under a $p(\text{O}_2)$ of 10^{-6} (●) and 10^{-7} (○) mbar. Inset shows an AFM image of the layer with a thickness of 10 nm grown under a $p(\text{O}_2)$ of 10^{-6} mbar. (b) Schematic representation of the growth process concerning pit hole defects

fabricate a QW geometry. A superlattice (SL) sample with ten periods of ZnO (4.4 nm)/ $\text{Zn}_{0.94}\text{Co}_{0.06}\text{O}$ (8.2 nm) was grown at 400°C under a $p(\text{O}_2)$ alternating between 1.4×10^{-4} and 1.4×10^{-6} mbar, corresponding to the ZnO and $\text{Zn}_{0.94}\text{Co}_{0.06}\text{O}$ layers, respectively (Fig. 20.29a, b). SL period was evaluated using secondary ion mass spectroscopy (SIMS) analysis (Fig. 20.29c). Figure 20.30a shows the (0002) XRD pattern of the SL layer. The pronounced fringes and high-order satellite peaks suggest a high crystalline quality as a result of a decrease of imperfection or composition inhomogeneity. The ω -rocking curves of the satellite peaks had very narrow line-widths. Figure 20.30b shows the PL spectrum at the band edge of the SL layer. Excitonic emission originating from the ZnO wells was observed at 10 K. Furthermore, a clear hysteresis curve due to FM ordering of the sample was simultaneously obtained at 10 K from the $M-H$ curve (inset of Fig. 20.30b). Ferromagnetism and excitonic luminescence were simultaneously obtained by the repetition of the magnetic and non-magnetic layers based on a quantum well geometry. These results show quantum structures with an interesting coupling between spins and excitons.

20.5 Conclusion

Homoepitaxial growth and MQWs in ZnO along polar and nonpolar directions have been summarized on this chapter. The Zn-polar growth showed atomically flat surfaces, which led to the fabrication of high-quality MQWs with an efficient carrier confinement even at RT. Furthermore, it was found that the spatially separated 3D

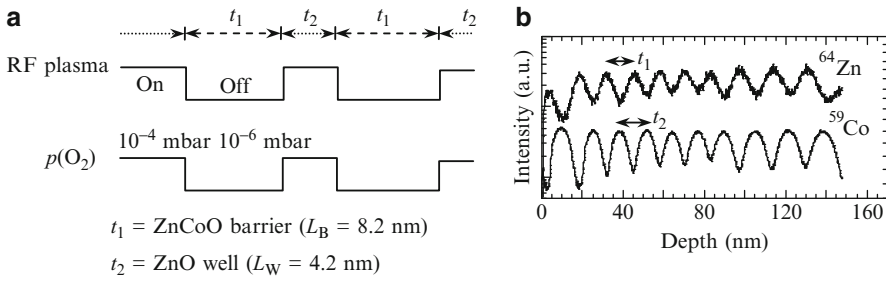


Fig. 20.29 (a) RF plasma power and $p(\text{O}_2)$ sequence used for the fabrication of a 10-period $\text{Zn}_{0.94}\text{Co}_{0.06}\text{O}/\text{ZnO}$ quantum well geometry. (b) In-depth profiles of ^{64}Zn and ^{59}Co atoms using SIMS analysis

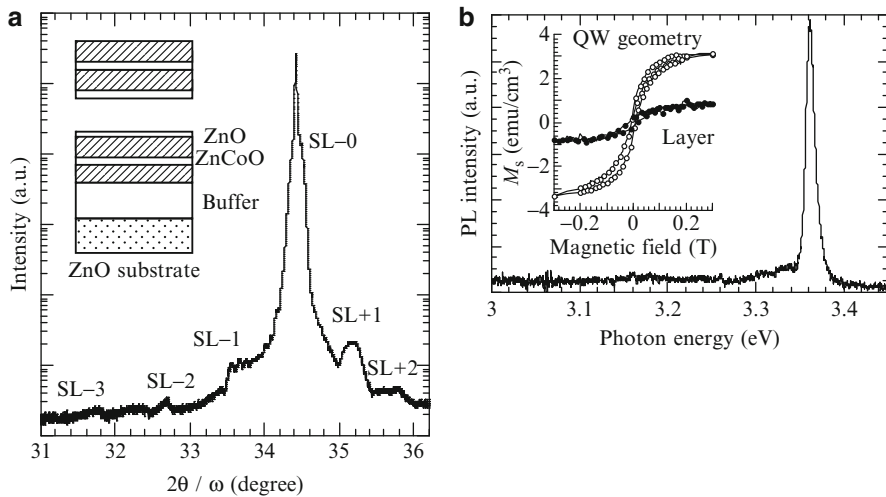


Fig. 20.30 (a) High-resolution $2\theta/\omega$ profile of the (0002) reflection for the SL layer with Zn-polarity. *Inset* shows a schematic cross-section structure of the sample. (b) PL spectrum at 10 K of the SL layer. *Inset* shows $M-H$ hysteresis loops at 10 K for SL alayer (○) and $\text{Zn}_{0.06}\text{Co}_{0.94}$ layers (●) grown under a $p(\text{O}_2)$ of 1.4×10^{-6} mbar

nanodots were naturally formed on the 2D wetting layers due to the elastic distortion induced by lattice misfit at the $\text{Mg}_{0.37}\text{Zn}_{0.63}\text{O}/\text{ZnO}$ heterointerface. This S-K forms the basic technology of quantum dots based on ZnO.

On the other hand, anisotropic surface nanowires were self-organized on M -nonpolar ZnO surfaces during homoepitaxial growth. The step-edge barrier effect was related closely to its growth mechanism. MQWs constructed on the nanowires structure allowed to observe highly anisotropic conductivity dependent on the surface morphology, which was similar to quantum wires. This origin was explained as follows. Quantization energy of confined electrons fluctuated due to

an interface roughness between the surface nanowires, which strongly restricted electron motion perpendicular to the nanowire arrays.

In Sect. 20.4, we discussed various properties of $\text{Zn}_{1-x}\text{Co}_x\text{O}$. An incorporation of Co atoms enlarged the band gap and caused huge magneto-optical response. The ferromagnetism in $\text{Zn}_{1-x}\text{Co}_x\text{O}$ layers only appeared when shallow donor levels were formed in the band gap and was explained by the spin-split impurity band model. Finally, we fabricated the $\text{Zn}_{1-x}\text{Co}_x\text{O}/\text{ZnO}$ superlattice with a quantum well geometry using a basic understanding of the growth mechanisms of Zn-polar growth in $\text{Zn}_{1-x}\text{Co}_x\text{O}$. This results in the possibility of spin-dependent photonics based on ZnO.

We believe our demonstrated homoepitaxial technique can be effective for electro-, magneto-, and optical applications based on ZnO. We hope that our technique and findings are applied widely with other oxide materials.

20.6 Prospects

ZnO is an old semiconductor that has attracted renewed interest as an electro-magneto-optical material. With a direct band gap of 3.4 eV at room temperature, ZnO is a wide gap semiconductor that emits light in the near-UV region of the spectrum. Accordingly, ZnO has many advantages for practical applications. Optical transparency makes it useful as transparent electrodes in flat-panel displays and solar cells. Charge carriers can be introduced by an external electric field, which are applied from thin-film transistors that are insensitive to visible light. By controlling the doping levels of donor and acceptor, the electrical properties can be tuned from n-type to p-type semiconductors.

Doping technology allows for the fabrication of light-emitting diodes and photo-diodes. ZnO is also a promising candidate for use in spintronics applications. For Co-doped ZnO, n-type doping in Co-alloyed ZnO was realized to stabilize the high Curie-temperature ferromagnetism. Recently, quantum Hall effects and linear polarization were observed in MgZnO/ZnO heterostructures. Nonvolatile memory effects appeared in highly resistive ZnO, a feature expected to be useful in applications pertaining to resistance-random access memory (Re-RAM).

Therefore, ZnO possesses a variety of potential use in new applications and fundamental science based on electro-magneto-optics. Various ZnO nanostructures have also been investigated. The number of papers published concerning ZnO nanostructures is increasing yearly. In particular, self-organized techniques provide advantages for nanoscale engineering and have yielded impressive results. The advantages of employing quantum dot fabrications based on Stranski-Krastanov growth and one-dimensional nanowires generated from vapor-liquid-solid (VLS) processes are currently receiving attention. We believe that a combination of electro-magneto-optics and nanostructure techniques opens new scientific fields which can produce novel future applications.

Cross-References

- ▶ Nano-Optical Imaging and Spectroscopy of Single Semiconductor Quantum Constituents
- ▶ Optical Interaction of Light with Semiconductor Quantum Confined States at the Nanoscale
- ▶ Recombination Dynamics in $\text{In}_x\text{Ga}_{1-x}\text{N}$ -Based Nanostructures
- ▶ Self-formation of Semiconductor Quantum Dots
- ▶ Simple Approaches for Constructing Metallic Nanoarrays on a Solid Surface

References

1. G.A. Hirata, J. Mckittrick, J. Siqueiros, O.A. Lopez, T. Cheeks, O. Contreras, J.Y. Yi, J. Vac. Sci. Technol. A **14**, 791 (1996)
2. S. Masuda, K. Kitamura, Y. Okumura, S. Miyatake, H. Tabata, T. Kawai, J. Appl. Phys. **93**, 1624 (2003)
3. D.G. Thomas, J. Phys. Chem. Solids **15**, 86 (1960)
4. P.Yu, Z.K. Tang, G.K.L. Wong, M. Kawasaki, A. Ohtomo, H. Koinuma, Y. Segawa, Solid State Commun. **103**, 459 (1997)
5. D.M. Bagnall, Y.F. Chen, Z. Zhu, T. Yao, S. Koyama, M.Y. Shen, T. Goto, Appl. Phys. Lett. **70**, 2230 (1997)
6. A.K. Sharma, J. Narayan, J.F. Muth, C.W. Teng, C. Jin, A. Kvit, R.M. Kolbas, O.W. Holland, Appl. Phys. Lett. **75**, 3327 (1999)
7. Y. Chen, H.-J. Ko, S.-K. Hong, T. Sekiuchi, T. Yao, Y. Segawa, J. Vac. Sci. Technol. B **18**, 1514 (2000)
8. T. Makino, C.H. Chia, N.T. Tuan, H.D. Sun, Y. Segawa, M. Kawasaki, A. Ohtomo, K. Tamura, H. Koinuma, Appl. Phys. Lett. **77**, 4250 (2000)
9. G. Coli, K.K. Bajaj, Appl. Phys. Lett. **78**, 2861 (2001)
10. H.D. Sun, T. Makino, Y. Segawa, M. Kawasaki, A. Ohtomo, K. Tamura, H. Koinuma, J. Appl. Phys. **91**, 1993 (2002)
11. A. Tsukazaki, A. Ohtomo, T. Kita, Y. Ohno, H. Ohno, M. Kawasaki, Science **315**, 1388 (2007)
12. J. Stangl, V.Holo, G. Bauer, Rev. Mod. Phys. **76**, 725 (2004)
13. H.P. Schonherr, J. Fricke, Z. Niu, K.J. Friedland, R. Notzel, K.H. Ploog, Appl. Phys. Lett. **72**, 566 (2001)
14. F.W. Yan, W.J. Zhang, R.G. Zhang, L.Q. Cui, C.G. Liang, S.Y. Liu, J. Appl. Phys. **90**, 1403 (2001)
15. V.A. Shchukin, D. Bimberg, Rev. Mod. Phys. **71**, 1125 (1999)
16. X.L. Wang, V. Voliotis, J. Appl. Phys. **99**, 121301 (2006)
17. R.D. Vispute, V. Talyansky, Z. Trajanovic, S. Choozum, M. Downes, R.P. Sharma, T. Venkatesan, M.C. Wood, R.T. Lareau, K.A. Jones, A.A. Ilidais, Appl. Phys. Lett. **70**, 2735 (1997)
18. P. Fons, K. Iwata, S. Niki, A. Yamada, K. Matsubara, M. Watanabe, J. Cryst. Growth **209**, 532 (2000)
19. F. Vigue, P. Vennegues, S. Vezian, M. Laugt, J.-P. Faurie, Appl. Phys. Lett. **79**, 194 (2001)
20. T.M. Parker, N.G. Condon, R. Lindsay, F.M. Leibsle, G. Thornton, Surf. Sci. **415**, L1046 (1998)
21. H. Kato, M. Sano, K. Miyamoto, T. Yao, Jpn. J. Appl. Phys. **42**, 2241 (2003)
22. H. Matsui, H. Saeki, T. Kawai, A. Sasaki, M. Yoshimoto, M. Tsubaki, H. Tabata, J. Vac. Sci. Technol. B **22**, 2454 (2004)
23. Z.X. Mei, X.L. Du, Y. Wang, M.J. Ying, Z.Q. Zeng, H. Zheng, J.F. Jia, Q.K. Xue, Z. Zhang, Appl. Phys. Lett. **86**, 112111 (2005)

24. H. Matsui, H. Tabata, Appl. Phys. Lett. **87**, 143109 (2005); J. Appl. Phys. **99**, 124307 (2006)
25. H. Ohono, Science **281**, 951 (1998)
26. A.E. Turner, R.L. Gunshor, S. Datta, Appl. Opt. **22**, 3152 (1983)
27. K. Ando, H. Saito, Z. Jin, T. Fukumura, M. Kawasaki, Y. Matsumoto, H. Koinuma, J. Appl. Phys. **89**, 7284 (2001)
28. K. Ueda, H. Tabata, T. Kawai, Appl. Phys. Lett. **79**, 988 (2001)
29. Z.Y. Xiao, H. Matsui, N. Hasuike, H. Harima, H. Tabata, J. Appl. Phys. **103**, 043504 (2008)
30. J.A. Gaj, W. Grieshaber, C. Bodin-Deshayes, J. Cibert, G. Feuillet, Y. Merle d'Aubigne, A. Wasiela, Phys. Rev. B **46**, 5266 (1992)
31. H. Matsui, H. Tabata, Phys. Rev. B **75**, 014438 (2007); Phys. Stat. Solid. (c) **3**, 4106 (2006)
32. A.M. Mariano, R.E. Hanneman, J. Appl. Phys. **34**, 384 (1963)
33. O. Dulub, L.A. Boatner, U. Diebold, Surf. Sci. **519**, 201 (2002)
34. M. Katayama, E. Nomura, N. Kanekama, H. Soejima, M. Aono, Nucl. Instrum. Methods Phys. Res. B **33**, 857 (1988)
35. T. Ohnishi, A. Ohtomo, I. Ohkubota, M. Kawasaki, M. Yoshimoto, H. Koinuma, Mater. Sci. Eng. B **56**, 256 (1998)
36. H. Kato, K. Miyamoto, M. Sano, T. Yao, Appl. Phys. Lett. **84**, 4562 (2004)
37. J.S. Park, S.K. Hong, T. Minegishi, S.H. Park, I.H. Im, T. Hanada, M.W. Cho, T. Yao, J.W. Lee, J.Y. Lee, Appl. Phys. Lett. **90**, 201907 (2007)
38. D.C. Reynolds, D.C. Look, B. Jogai, C.W. Litton, T.C. Collins, W. Harsch, G. Cantwell, Phys. Rev. B **57**, 12151 (1998)
39. S.F. Chichibu, T. Onuma, M. Kubota, A. Uedono, T. Sota, A. Tsukazaki, A. Ohtomo, M. Kawasaki, J. Appl. Phys. **99**, 093505 (2006)
40. S.-K. Hong, H.-J. Ko, Y. Chen, T. Yao, J. Vac. Sci. Technol. B **20**, 1656 (2002)
41. H. Maki, I. Sakaguchi, N. Ohashi, S. Sekiguchi, H. Haneda, J. Tanaka, N. Ichinose, Jpn. J. Appl. Phys. **75** (2003)
42. N. Hasuike, H. Fukumura, H. Harima, K. Kisoda, H. Matsui, H. Saeki, H. Tabata, J. Phys. Condens. Matter **16**, S5807 (2004)
43. H. Matsui, H. Tabata, N. Hasuike, H. Harima, J. Appl. Phys. **99**, 024902 (2006)
44. E. Bauer, Z. Kristallogr. **110**, 372 (1958)
45. D.J. Eaglesham, M. Cerullo, Phys. Rev. Lett. **64**, 1943 (1990)
46. T. Walter, C.J. Humphreys, A.G. Cullis, Appl. Phys. Lett. **71**, 809 (1997)
47. H. Matsui, N. Hasuike, H. Harima, T. Tanaka, H. Tabata, Appl. Phys. Lett. **89**, 091909 (2006)
48. J.W. Matthews, S. Mader, T.B. Light, J. Appl. Phys. **41**, 3800 (1970)
49. S.S. Srinivasan, L. Geng, R. Liu, F.A. Ponce, Y. Narukawa, S. Tanaka, Appl. Phys. Lett. **25**, 5187 (2003)
50. A. Ohtomo, M. Kawasaki, I. Ohkubo, H. Koinuma, T. Yasuda, Y. Segawa, Appl. Phys. Lett. **75**, 980 (1999)
51. P.F. Fewster, *X-ray Scattering from Semiconductors* (Imperial College Press, London, 2000)
52. B.P. Zhang, N.T. Binh, K. Wakatsuki, C.Y. Liu, Y. Segawa, N. Usami, Appl. Phys. Lett. **86**, 032105 (2005)
53. N.V. Lomasnov, V.V. Travnikov, S.O. Kognovitskii, S.A. Gurevich, S.I. Nesterov, V.I. Skopina, M. Rabe, F.Heneberger, Phys. Solid State **40**, 1413 (1998)
54. Beltran, J. Andres. M. Calatayud, J.B.L. Martins, Chem. Phys. Lett. **338**, 224 (2001)
55. H. Matsui, N. Hasuike, H. Harima, H. Tabata, J. Appl. Phys. **104**, 094309 (2008)
56. S. Guha, A. Madhukar, K.C. Rajkumar, Appl. Phys. Lett. **57**, 2110 (1990)
57. B. Rottger, M. Hanbucken, H. Neddermeyer, Appl. Surf. Sci. **162/163**, 595 (2000)
58. M.D. Johnson, C. Orme, A.W. Hunt, D. Graff, J. Sudijiono, L.M. Sander, B.G. Orr, Phys. Rev. Lett. **72**, 116 (1994)
59. O. Dulub, L.A. Boatner, U. Diebold, Surf. Sci. **504**, 271 (2002)
60. R.L. Schwoebel, J. Appl. Phys. **37**, 3682 (1966)
61. T. Michely, J. Krug, *Islands, Mounds, Atoms*, Springer Series in Surface Science, vol. 42 (Springer, New York, 2004)
62. Y.M. Yu, B.G. Liu, Phys. Rev. B **77**, 195327 (2008)

63. T. Moriyama, S. Fujita, *Jpn. J. Appl. Phys.* **44**, 7919 (2005)
64. J. Zuniga-Perez, V. Munoz-Sanjose, E. Palacios-Lidon, J. Colchero, *Appl. Phys. Lett.* **88**, 261912 (2006)
65. Y.C. Park, C.W. Litton, T.C. Collins, D.C. Reynolds, *Phys. Rev. B* **143**, 512 (1966)
66. D.C. Reynolds, D.C. Look, B. Jagai, C.W. Litton, T.C. Collins, T. Harris, M.J. Callahan, J.S. Bailey, *J. Appl. Phys.* **86**, 5598 (1999)
67. W.J. Fan, J.B. Xia, P.A. Agus, S.T. Tan, S.F. Yu, X.W. Sun, *J. Appl. Phys.* **99**, 013702 (2006)
68. D.C. Reynolds, D.C. Look, B. Jogai, C.W. Litton, G. Cantwell, W.C. Harsch, *Phys. Rev. B* **60**, 2340 (1999)
69. H. Matsui, H. Tabata, *Appl. Phys. Lett.* **94**, 161907 (2009)
70. A. Mang, K. Reimann, St. Rubenacke, *Solid State Commun.* **94**, 251 (1999)
71. A. Niwa, T. Ohtoshi, T. Kuroda, *Jpn. J. Appl. Phys.* **35**, L599 (1996)
72. A. Waag, S. Schmeusser, R.N. Bicknell-Tassius, D.R. Yakovlev, W. Ossau, G. Landwehr, I.N. Uraltsev, *Appl. Phys. Lett.* **59**, 2995 (1991)
73. R. Notzel, P.H. Ploog, *J. Vac. Sci. Technol. A* **10**, 617 (1992)
74. H. Sakai, T. Noda, K. Hirakawa, M. Tanaka, T. Matsusue, *Appl. Phys. Lett.* **51**, 1934 (1987)
75. F. Szmulowicz, S. Elhamri, H.J. Haugan, G.J. Brown, W.C. Mitchel, *J. Appl. Phys.* **101**, 043706 (2007)
76. K. Sato, H. Katayama-Yoshida, *Jpn. J. Appl. Phys.* **40**, L334 (2001)
77. M.H.F. Sluiter, Y. Kawazoe, P. Sharma, A. Inoue, A.R. Raju, C. Rout, U.V. Waghmare, *Phys. Rev. Lett.* **94**, 187204 (2005)
78. H. Zheng, *Phys. B* **212**, 125 (1995)
79. W.K. Liu, G.M. Salley, D.R. Gamelin, *J. Phys. Chem. B* **109**, 14486 (2005)
80. J. Dreyhsig, B.Litzenburger, *Phys. Rev. B* **54**, 10516 (1996)
81. R.J. Powell, W.E. Spicer, *Phys. Rev.* **2**, 2182 (1970)
82. J.K. Furdyna, *J. Appl. Phys.* **64**, R29 (1988)
83. M. Nawrocki, Y.G. Rubo, J.P. Lascaray, D. Coquillat, *Phys. Rev. B* **52**, R2241 (1995)
84. W.H. Sun, S.J. Chua, L.S. Wang, X.H. Zhang, *J. Appl. Phys.* **91**, 4917 (2002)
85. H.M. Cheong, Y. Zhang, A. Mascarenhas, J.F. Geisz, *Phys. Rev. B* **61**, 13687 (2000)
86. K.R. Kittilstved, D.A. Schwartz, A.C. Tuan, S.M. Heald, S.A. Chambers, D.R. Gamelin, *Phys. Rev. Lett.* **97**, 037203 (2006)
87. J.R. Neal, A.J. Behan, R.M. Ibranhim, H.J. Blythe, M. Ziese, A.M. Fox, G.A. Gehring, *Phys. Rev. Lett.* **96**, 197208 (2006)
88. R. Schaub, G. Pensl, M. Schulz, C. Holm, *Appl. Phys. A* **34**, 215 (1984)
89. F. Oba, T. Yamamoto, Y. Ikuhara, I. Tanaka, H. Adachi, *Mater. Trans.* **43**, 1439 (2002)
90. E.C. Lee, K.J. Chang, *Phys. Rev. B* **69**, 085205 (2004)
91. J. M. Coey, M. Venkatesan, C.B. Fitzgerald, *Nat. Mater.* **4**, 173 (2005)
92. T.L. Song, *J. Appl. Phys.* **98**, 084906 (2005)

Koichi Yamaguchi

Contents

21.1	Introduction.....	810
21.2	Stranski–Krastanov Growth of Quantum Dots.....	810
21.3	Uniform Formation of Quantum Dots.....	812
21.3.1	Self-Size-Limiting Growth of Uniform InAs/GaAs Quantum Dots.....	813
21.3.2	Capping Growth of Uniform InAs/GaAs Quantum Dots.....	817
21.3.3	Closely Stacked Growth of Uniform InAs/GaAs Quantum Dots.....	820
21.4	Control of Quantum Energy Level.....	823
21.5	Density Control of Quantum Dots.....	826
21.5.1	Sb-Mediated Growth of High-Density InAs/GaAs Quantum Dots.....	826
21.5.2	Intermittent Growth of Low-Density InAs/GaAs Quantum Dots.....	830
21.6	Quantum Dot Array.....	834
21.6.1	Vertical Array of InAs/GaAs Quantum Dots.....	835
21.6.2	In-Plane Arrays of InAs/GaAs Quantum Dots.....	837
21.7	Conclusion.....	841
	References.....	842

Abstract

We reviewed the self-formation control of InAs/GaAs quantum dots (QDs) by molecular beam epitaxy. Uniform InAs/GaAs QDs were demonstrated by self-size-limiting effect, the optimized capping growth, and the closely stacked growth using the nanoholes. High-density InAs QDs were achieved by Sb-mediated growth. In addition, an intermittent growth method was presented for ultralow density InAs QDs. Furthermore, the vertical and in-plane arrangements of InAs/GaAs QDs were attempted by using the strain-controlled underlying layers. One-dimensional QD chains were spontaneously formed

K. Yamaguchi (✉)

Department of Engineering Science, The University of Electro-Communications, Tokyo, Japan
e-mail: kyama@ee.uec.ac.jp

along the [1–10] direction on the GaAs/InGaAs/GaAs(001) buffer layers. Two-dimensional arrangement of InAs QDs was demonstrated by using GaAsSb/GaAs(001) buffer layers.

21.1 Introduction

Recent progress in epitaxial semiconductor growth techniques, such as molecular beam epitaxy (MBE) and metalorganic chemical vapor deposition (MOCVD), has enabled the fabrication of semiconductor nanostructures having low-dimensional electronic characteristics. Among their structures, semiconductor quantum dots (QDs) are expected to enable the development of high-performance next-generation optoelectronic devices based on zero-dimensional quantum confinement. Self-assembled QD growth using a Stranski-Krastanov (SK) growth mode has been actively studied since about 1990, and self-assembled QDs have attracted much attention in nanophotonics. In order to develop novel nanophononic QD devices, the QD structure must be precisely controlled. The well-controlled self-formation of QD structures remains an open challenge.

This chapter focuses on self-formation control of InAs/GaAs QDs by MBE. [Section 21.2](#) introduces the basics of the self-formation of QDs using the SK growth mode. [Section 21.3](#) introduces the uniform formation of QDs, based on a self-size-limiting effect, capping growth on QDs, and closely stacked growth using nanoholes. In [Sect. 21.4](#), the control of quantum energy levels is discussed, and adjustment of growth conditions and post-growth annealing are introduced. [Section 21.5](#) treats density control of QDs. Control of high density QDs can be realized in an Sb-mediated growth method, and low-density QDs can be controlled by an intermittent growth method. In [Sect. 21.6](#), vertical and in-plane arrays of QDs are introduced.

21.2 Stranski–Krastanov Growth of Quantum Dots

Thin film growth can be classified into three modes: Frank–van der Merwe (FM) mode, which results in 2-dimensional (2D) growth; Volmer–Weber (VM) mode, which forms 3D islands; and Stranski–Krastanov (SK) mode. The SK mode is a combination of the FM and VW modes, that is, 3D island growth occurs, followed by 2D growth. The SK mode frequently appears in the heteroepitaxial growth of lattice-mismatched materials, such as Ge/Si and InAs/GaAs. In 1985, self-assembled InAs QDs were first demonstrated using the SK growth mode [1]. During the initial growth in SK mode, the free energy of the 2D growth is always lower than that of the 3D growth. However, as the growth proceeds, this free-energy relationship inverts because of excess strain energy due to lattice mismatch

Fig. 21.1 In typical SK growth, free energy vs. growth amount for 2D and 3D growth. As the growth proceeds, the growth mode transits from 2D mode ① to 3D mode ②. Schematic diagrams show the change of the thin film structure. At ③, dislocations generate at the heterointerface

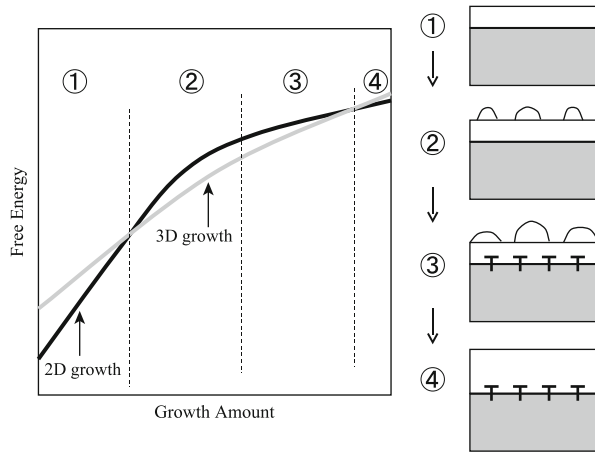
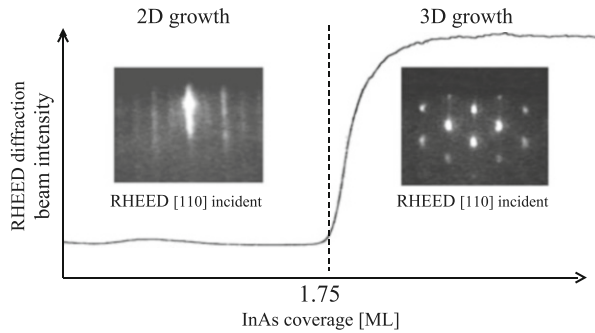


Fig. 21.2 InAs coverage dependence of RHEED diffraction-beam intensity in InAs/GaAs hetero-epitaxy. Critical thickness for growth mode transition was about 1.75 ML. RHEED pattern changed from streak to spot pattern at the critical thickness



between the materials. Therefore, a growth mode transition from 2D to 3D growth occurs spontaneously, as shown in Fig. 21.1.

After further growth, dislocations are formed because of excess strain energy. Hence, in order to fabricate coherent 3D islands with high crystal quality, the extent of growth must be controlled precisely [2]. The self-assembled QDs can be fabricated by sufficient control of the SK growth.

In MBE growth, reflection high-energy electron-beam diffraction (RHEED) is frequently used for real-time monitoring of the growth surface. In self-assembled QD growth using the SK mode, RHEED monitoring is a useful tool to control the growth. Figure 21.2 shows changes in the RHEED pattern and diffraction-beam intensity as a function of growth time for InAs growth on GaAs.

When the InAs coverage exceeds the critical thickness for the growth mode transition (about 1.75 monolayers (ML)), the RHEED pattern changes from a streak pattern to a spot pattern, and the diffraction-beam intensity increases rapidly [3]. By in situ RHEED observation, we can precisely control the extent of growth. However, since the 3D islanding proceeds quickly, control of the QD structure formation is

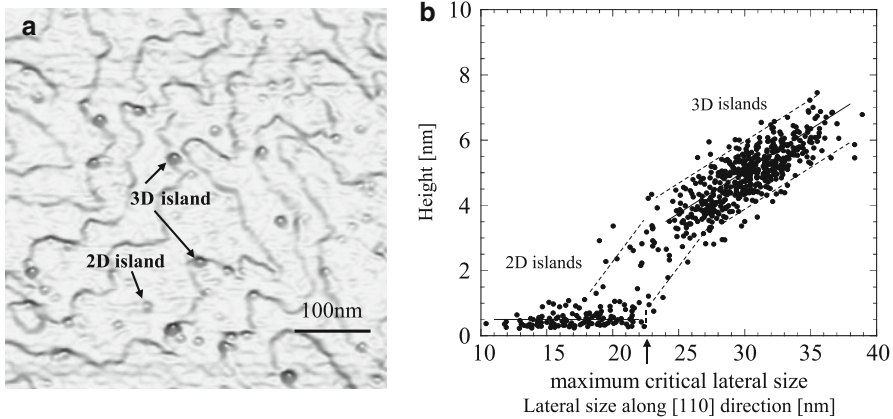


Fig. 21.3 AFM image of 2D and 3D InAs islands with 1.8-ML coverage (a). Relationship between height and [110] lateral size of InAs islands (b)

very difficult during the growth. Therefore, the SK growth conditions and the growth sequence should be modified to control the QD structures.

Figure 21.3a shows an atomic force microscopy (AFM) image of 2D and 3D InAs islands with 1.8 ML of coverage. InAs islands are often observed near step edges, which are preferential sites to reduce the strain energy. Figure 21.3b shows the relationship between the lateral size and height of InAs islands grown on GaAs with various InAs coverages ranging from 1.6 to 3.0 ML. During the initial growth, the 2D islands spread laterally, maintaining an island height of about 2 ML. As the growth proceeds, the island height increases rapidly, indicating a growth mode transition. 3D dots are spontaneously formed and fluctuate in size [4]. In the design of QD devices, well-controlled QD structures are highly desirable for the realization of high performance and new functionality. For example, uniform QDs with a narrow size distribution are required for some QD devices, such as QD lasers.

21.3 Uniform Formation of Quantum Dots

As described in Sect. 21.2, the SK growth technique is a powerful tool for the fabrication of self-assembled QDs. However, fluctuation of the QD structure causes inhomogeneous broadening of the QD energy levels and presents a critical problem in the development of certain device applications, such as QD lasers. In this section, three methods for improving the uniformity of the QD structure are described: self-size-limiting growth (Sect. 21.3.1), capping growth (Sect. 21.3.2), and closely stacked growth (Sect. 21.3.3).

21.3.1 Self-Size-Limiting Growth of Uniform InAs/GaAs Quantum Dots

QD structure strongly depends on the SK growth conditions, and there have been many reports concerning their growth condition dependences [5]. In order to reduce the size fluctuation of InAs/GaAs QDs, a low growth rate [6] and low arsenic pressure conditions [7] are effective because of the resulting enhanced surface migration. In particular, the above growth conditions induce a saturation of QD size, which is called a self-size-limiting effect. A typical result of the self-size-limiting phenomenon is shown in Fig. 21.4, which shows the lateral size and height of InAs QDs as a function of InAs coverage.

When the InAs coverage is larger than the critical thickness for the growth mode transition, the lateral size and height of the 3D dots immediately saturate [4]. Recently, such self-size-limiting of InAs/GaAs QDs has also been observed using in situ X-ray diffraction (XRD) analysis [8]. This limiting of lateral size may be attributed to a compressive strain at the island edges near the wetting layer [9]. The incorporation of In adatoms is suppressed at the strained island edges. However, since the top area of the 3D islands is relaxed, the height limiting cannot be due to the strain. In order to study the self limiting of the height, the RHEED pattern was monitored during InAs growth. Figure 21.5a shows RHEED chevron patterns obtained using a [100] incident electron beam. The chevron pattern provides some information regarding the formation of a micro-facet on the side walls of the QDs. For more than 2.1 ML of InAs coverage, a 45° chevron pattern clearly appeared, indicating {110} facet formation [10]. Therefore, the InAs QDs had a pyramidal shape with {110} facets, as shown in Fig. 21.6a, a typical AFM image of an InAs QD. The RHEED patterns for the [110] incident beam are shown in Fig. 21.5b. As the growth proceeds beyond 2.2 ML, a (4×) streak pattern appears, that is, the RHEED pattern changed from a (1×1) spot pattern to a (4×2) streak pattern with a

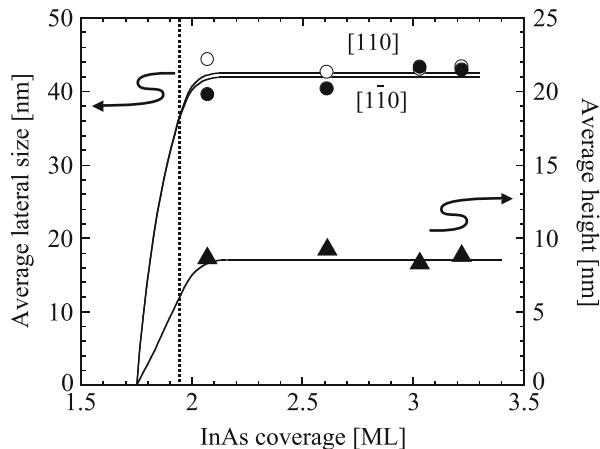


Fig. 21.4 Average lateral size and average height of the InAs 3D islands as a function of the InAs coverage

Fig. 21.5 RHEED patterns taken along the [100] azimuth (a) and the [110] azimuth (b) as a function of the InAs coverage

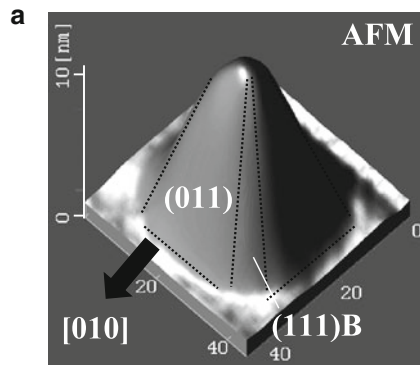
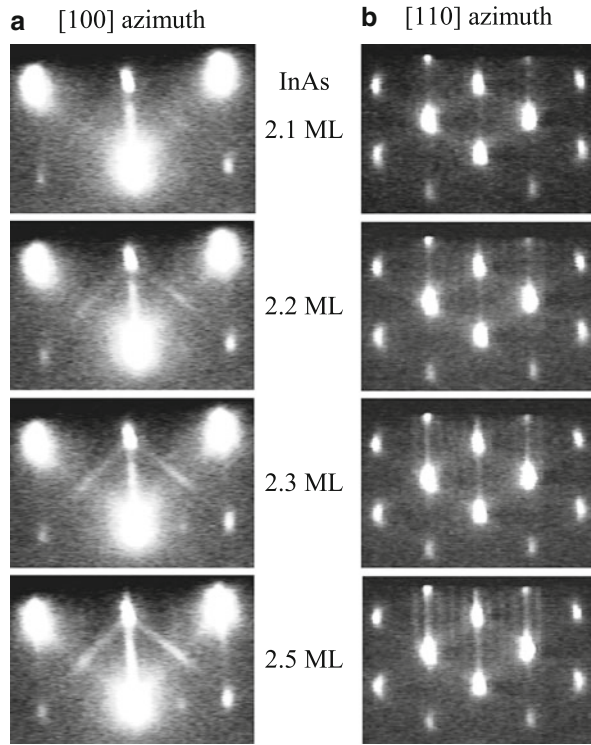
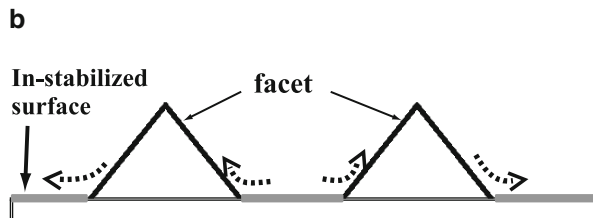


Fig. 21.6 AFM image of InAs QD with limited size and {110} facets (a). Schematic diagram of the size-limited QDs surrounded with stable facets (b). The wetting layer was covered with In-stabilized surface



(1×1) spot [10]. Once limited dots with $\{110\}$ facets are formed, In adatoms are no longer incorporated into the limited dots. Therefore, the dot height is spontaneously limited by the formation of stable facets. As a result, incoming In adatoms are accumulated on the wetting layer (Fig. 21.6b). Excess In adatoms cause the (4×2) streak pattern, which reveals the In-stabilized surface.

The self-size-limiting phenomenon, described above, plays an important role in the improvement of size uniformity. Figure 21.7 shows photoluminescence (PL) spectra of the InAs QDs as a function of InAs coverage. InAs QDs were embedded in the GaAs capping layers, as described in Sect. 21.3.2. At low coverage, the PL spectrum width is very large (a large size distribution). As the InAs coverage increased, a low-energy PL peak (1.05 eV) was enhanced and the high-energy components were suppressed. This coverage dependence of the PL spectrum can be explained by the self-size-limiting effect, and uniform QDs can be obtained.

Figure 21.8 shows in-plane distributions of InAs QDs (for 1.8 ML Fig. 21.8a and 2.5 ML Fig. 21.8b of coverage). In this experiment, the substrates were not rotated during the MBE growth, and the InAs coverage was evaluated at the center of the substrate using RHEED. The critical thickness for the 2D–3D transition was 1.75 ML, and the InAs growth at 1.8 ML was insufficient to trigger the size-limiting effect. Hence, a large distribution of InAs QDs was observed for 1.8 ML of coverage (Fig. 21.8a).

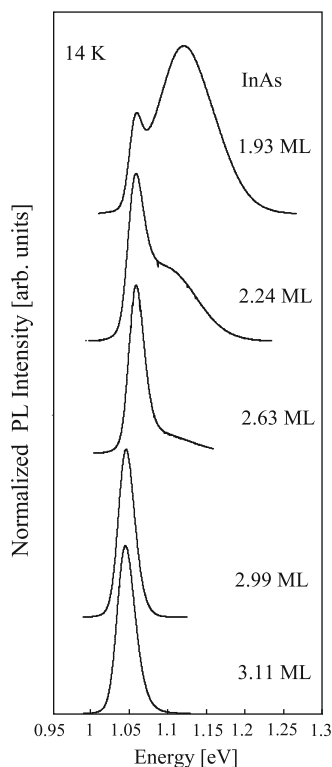


Fig. 21.7 PL spectra of InAs QDs with various InAs coverages (1.93, 2.24, 2.63, 2.99, and 3.11 ML). PL temperature was 14 K

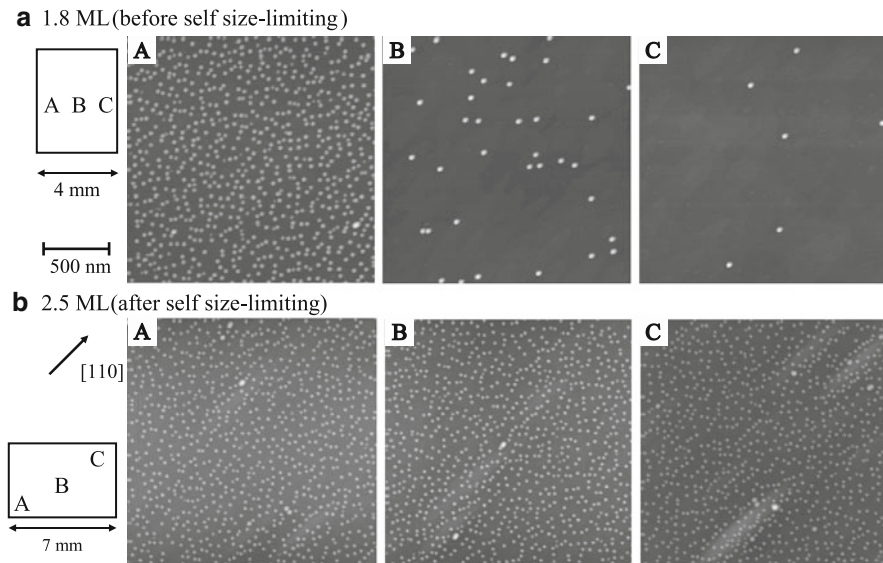
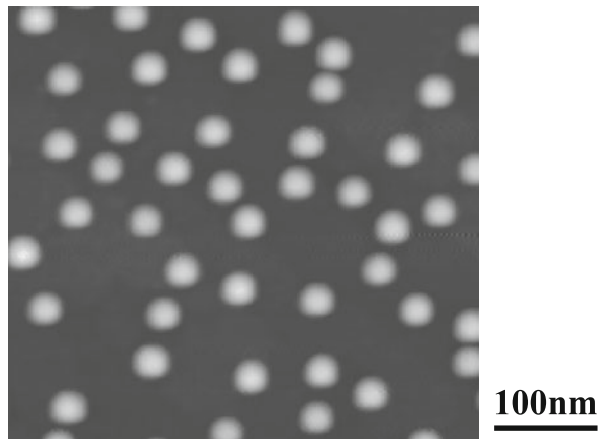


Fig. 21.8 AFM images of InAs QDs, measured at different positions (A, B, C) on the substrate. The InAs were grown, respectively, at 1.8-ML coverage (a) and 2.5-ML coverage (b). In this growth, the substrate was not rotated

Fig. 21.9 AFM image of uniform InAs QDs with limited size



On the other hand, for 2.5 ML of coverage (Fig. 21.8b), the in-plane uniformity of QD size and density improved because of the size-limiting effect.

Figure 21.9 shows an AFM image of uniform InAs QDs, grown at a low growth rate and low arsenic pressure, under the self-size-limiting effect. The standard deviations of the sizes of these QDs were 4% for the lateral size and 8% for the height. These values reveal narrower size distributions than growth under conventional SK growth conditions [7].

21.3.2 Capping Growth of Uniform InAs/GaAs Quantum Dots

For device applications, QDs are usually embedded within capping layers, which suppress undesirable electronic states near the QDs. It should be noted here that capping growth often modifies the QD structure [11]. Figure 21.10 shows InAs-QD structures with GaAs capping layers, which were calculated using a kinetic Monte Carlo method [12]. The surface segregation and surface desorption of InAs, depending on the strain, were included in this calculation. These effects modified the dot shape and induced the intermixing of GaAs and InAs during the GaAs capping growth [13]. When the growth temperature was increased, the growth rate decreased and the strain increased, enhancing the surface segregation and desorption effects. Therefore, the growth conditions and the growth structure of the capping layer are very important for the fabrication of a uniform QD structure of high crystal quality.

Figure 21.11 shows cross-sectional scanning transmission electron microscopy (STEM) images of InAs QDs with GaAs capping layers, grown at 400 °C (Fig. 21.11b), 450 °C (Fig. 21.11c), and 500 °C (Fig. 21.11d). As mentioned above, the dot height decreased with increasing growth temperature because of surface segregation and desorption of the InAs. This modification of the QD structure strongly affected the inhomogeneous broadening in the quantum energy level.

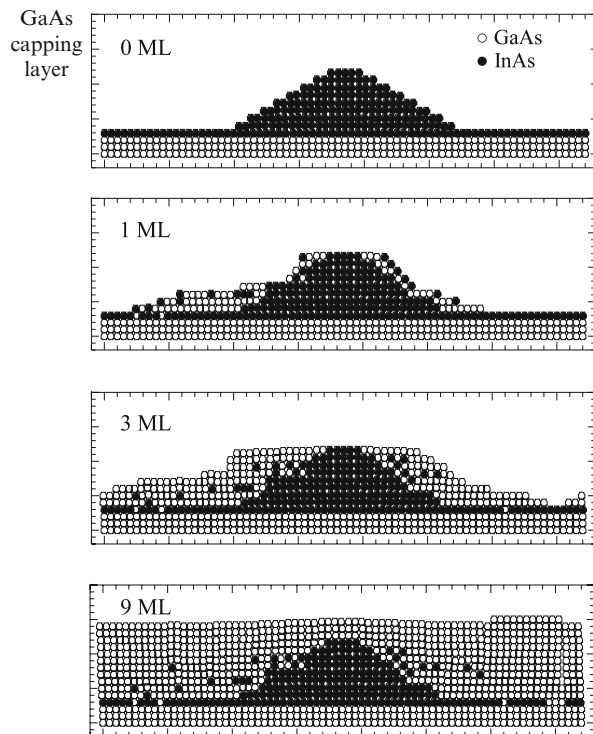


Fig. 21.10 Calculated cross-sectional images of InAs *dots*, embedded by GaAs capping layers with 0, 1, 3, and 9 ML coverages, respectively. The capping growth process was calculated by using kinetic Monte Carlo method. The base length and height of the *dots* were given, respectively, at 33 and 8 ML. The substrate temperature of the capping growth was 450 °C, and the growth rate was 0.56 ML/s

Fig. 21.11 ($\bar{1}\bar{1}0$)

cross-sectional STEM images of InAs QDs without capping layer (a) and with GaAs capping layers, which were grown at 400 °C (b), 450 °C (c), and 500 °C (d), respectively

- a InAs QDs
- b GaAs 400 °C
- c GaAs 450 °C
- d GaAs 500 °C

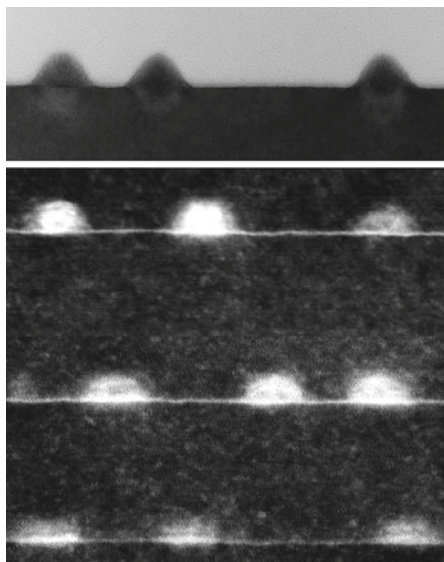


Figure 21.12 shows the relationships between the PL properties of InAs QDs and the growth temperature of the GaAs capping layer. For temperatures below 450 °C, the poor crystal quality of the GaAs layer drastically decreased the PL intensity. However, higher temperature growth induced a blue shift and broadening of the PL spectra. Therefore, at the intermediate temperature of 450 °C, the low growth rate and low arsenic pressure in the GaAs capping growth were optimized to obtain uniform QD structures of high crystal quality. As shown in Fig. 21.13, a narrow PL linewidth of 17.6 meV was achieved.

The extensive inhomogeneous broadening of the QDs, which causes overlapping of the second state of a QD with the ground state of other QDs, prevents accurate measurement. This problem can be overcome by adopting the above uniform QD samples. For instance, a phonon relaxation bottleneck [14], spin Pauli blocking [15], and spin relaxation dynamics [16] were clearly observed.

Next, InGaAs capping growth on InAs QDs is described. InAs QDs in a GaAs matrix have a large compressive strain. Hence, the excess strain often modifies the dot structure during the capping growth. In addition, the accumulated strain often induces dislocations near the heterointerface. InGaAs capping growth on InAs QDs reduces the strain, and as a result, the crystal quality improves and the decrease in dot height is suppressed [17]. Figure 21.14 shows PL spectra of InAs QDs (2.3 ML Fig. 21.14a and 2.7 ML Fig. 21.14b), covered by a GaAs capping layer and an InGaAs capping layer, respectively. For the InGaAs capping layers, the PL spectra shifted to a lower energy, and the inhomogeneous broadening became narrower, compared with GaAs capping layer spectra [18]. Strain-reduced InGaAs capping growth is a useful method for improvement of size uniformity and crystal quality.

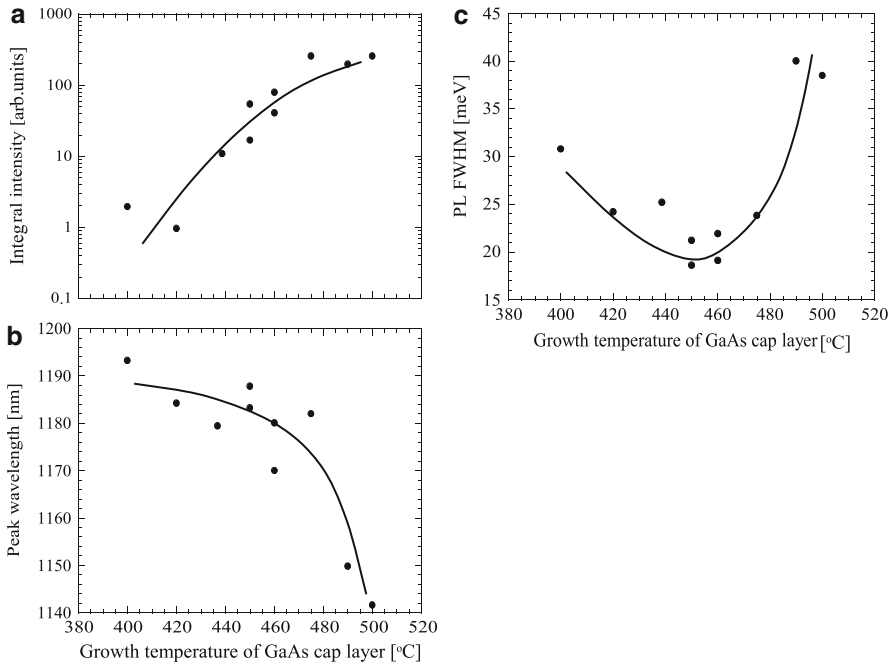


Fig. 21.12 PL properties (integral intensity (a), peak wavelength (b), and FWHM (c)) of InAs QDs as a function of growth temperature of GaAs capping layer. PL was measured at 12 K

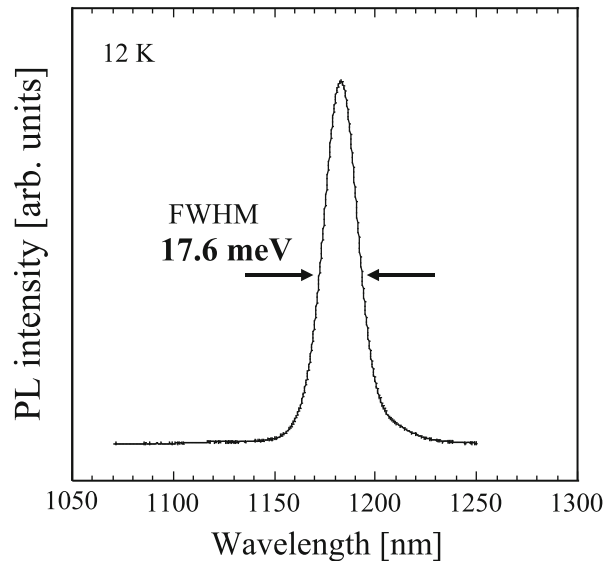
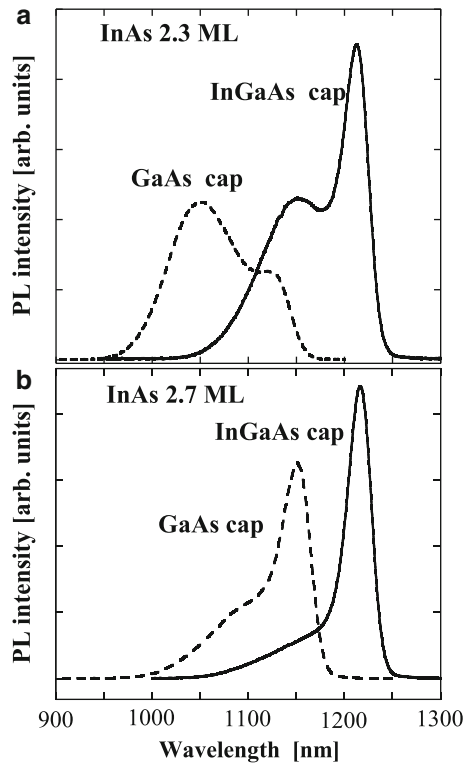


Fig. 21.13 PL spectrum of uniform InAs QDs. PL was measured at 12 K

Fig. 21.14 PL spectra of InAs QDs with GaAs and InGaAs capping layers. The InAs coverage was 2.3 ML (a) and 2.7 ML (b). PL temperature was 12 K

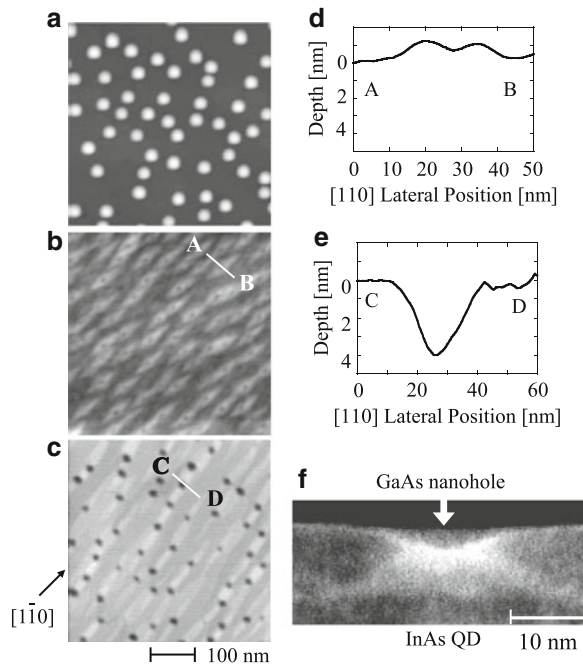


21.3.3 Closely Stacked Growth of Uniform InAs/GaAs Quantum Dots

A strong coupling between neighboring QDs forms QD molecules, which have many attractive properties arising from interaction between the QDs [19]. In order to fabricate QD molecules, closely stacked growth of the QDs has been actively investigated. In this growth technique, a spacing layer between two QD layers must be controlled precisely. In this section, the closely stacked growth of uniform InAs QDs is described. In particular, the upper InAs-QD layers were stacked through self-formed nanoholes in GaAs spacer layers onto underlying InAs-QD layers.

After the uniform growth of InAs QDs by the self-size-limiting effect (Fig. 21.15a), a 10-nm-thick GaAs capping layer was grown, as shown in Fig. 21.15b. On the GaAs surface, there were ridge structures and small dips, located above the embedded InAs QDs (Fig. 21.15d) [20]. By thermal annealing at 500 °C for 5 min, the ridges elongated along the $[1\bar{1}0]$ direction, and nanoholes were spontaneously formed (Fig. 21.15c) [21]. Figure 21.15e shows a line profile of a nanohole, which was approximately 4-nm deep. From the cross-sectional STEM image (Fig. 21.15f), it was determined that the nanohole was located just above an embedded InAs QD. In addition, the nanohole density was almost identical to the

Fig. 21.15 AFM images of InAs QDs without capping layer (a) and with 10-nm-thick GaAs capping layer (b) and (c). AFM image of (c) was obtained after thermal annealing at 500 °C for 5 min. Line profiles of (d) and (e) show the ridge structure (A–B in (b)) and nanohole structure (C–D, in (c)) just above the InAs QDs. (f) Indicates cross-sectional STEM image of the embedded InAs QDs with GaAs-nanohole capping layer



QD density. The self-formation of GaAs nanoholes and the change in the GaAs ridges can be explained as follows. Since the strained GaAs surface layer near InAs dots is energetically unstable, thermal annealing induces desorption of unstable GaAs molecules. During the annealing, desorbed GaAs molecules (or Ga atoms) migrate on the surface and are preferentially incorporated into $[1\bar{1}0]$ steps. As a result, nanoholes are formed just above dots, and the ridges flatten and lengthen along the $[1\bar{1}0]$ direction.

Next, InAs QDs were grown selectively on GaAs nanoholes to fabricate strongly coupled QD molecules [22]. Figure 21.16 shows AFM images of InAs islands grown on a GaAs-nanohole spacer layer. For 1.6 ML of InAs coverage (Fig. 21.16a), InAs was randomly incorporated into the nanoholes. Hence, the size fluctuation was very large, as shown in Fig. 21.16b. This random incorporation was caused by a longer surface migration distance of In adatoms, compared with the separation distance between the nanoholes. As the InAs coverage increased, the InAs islands formed more uniformly. Particularly, the self-size-limiting of the 2nd InAs QDs gave uniform InAs-QD molecules (Fig. 21.16c).

In Fig. 21.17, a cross-sectional STEM image of a uniform InAs-QD molecule is presented, and the 2nd InAs QDs are closely stacked on the 1st QDs through the GaAs nanoholes. Figure 21.18 shows low-temperature (12 K) PL spectra of uniform InAs-QD molecules, excited at 4 W/cm² (Fig. 21.18a) and 4 mW/cm² (Fig. 21.18b) of Ar⁺ laser power density. Not only ground states but also 1st excited states

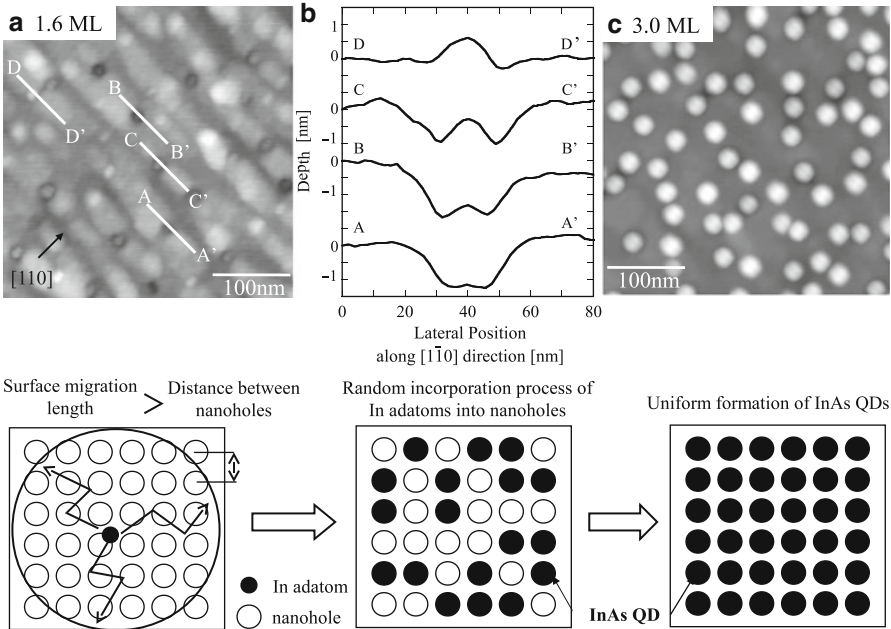


Fig. 21.16 AFM images of 2nd InAs islands with 1.6 ML (a) and (b) and 3.0 ML (c), which were grown on GaAs nanoholes. (b) Shows line profiles at various positions of the nanoholes in (a). Insert of schematic diagram indicates selective formation process of 2nd InAs QDs on nanoholes. Uniform 1st InAs QDs were embedded under nanoholes

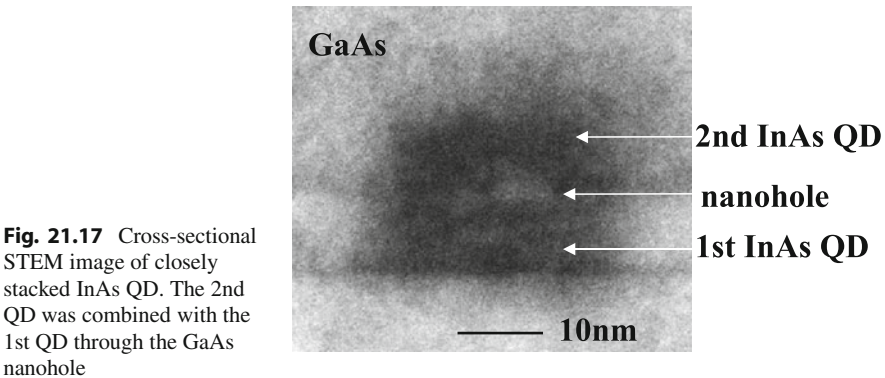


Fig. 21.17 Cross-sectional STEM image of closely stacked InAs QD. The 2nd QD was combined with the 1st QD through the GaAs nanohole

were observed at high excitation power density (4 W/cm^2). The energy separation between the quantum levels was about 64 meV, and the PL linewidth was 16.1 meV. At low excitation power density (4 mW/cm^2), a narrow PL linewidth of 13.2 meV was successfully obtained.

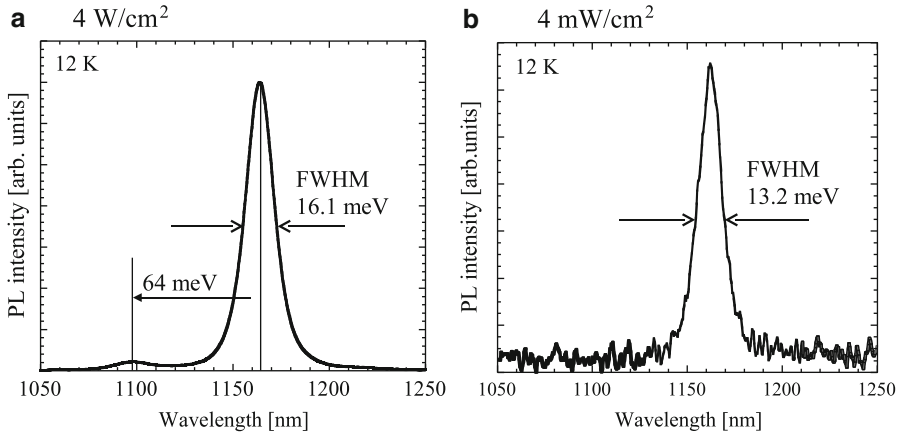


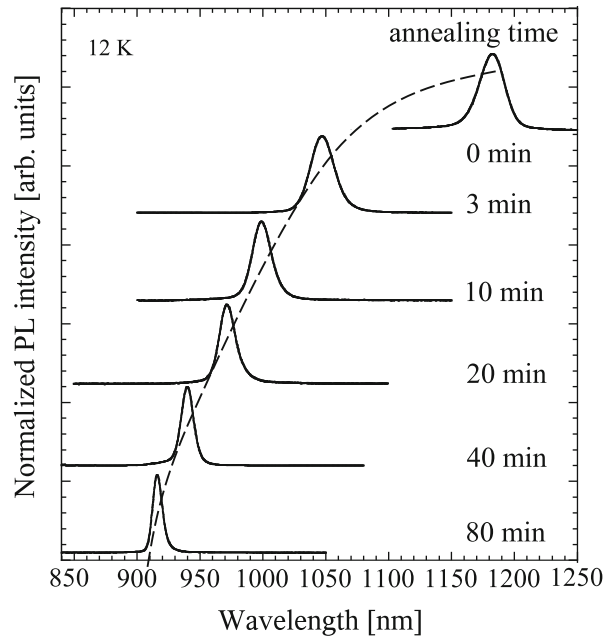
Fig. 21.18 Low-temperature (12 K) PL spectra of closely stacked InAs QDs. Excitation power density was 4 W/cm^2 (a) and 4 mW/cm^2 (b). PL sub-peak based on the 1st excited states was observed for high excitation power density (a)

21.4 Control of Quantum Energy Level

Control of QD energy levels is needed for various device applications. For example, for optical fiber communication systems, QD structures must be designed to have optical wavelengths of 1.3 and 1.55 μm . The quantum energy levels of the QDs can be adjusted by modification of the QD structures, material composition, and/or size. The QD size can be changed by adjusting the SK growth conditions. Generally, higher growth temperatures, lower growth rates, and lower arsenic pressures result in the formation of larger QDs with lower quantum energy levels. However, changing the SK growth conditions frequently provides a different QD density. On the other hand, the post-growth thermal annealing of QDs has been investigated as a means to modify QD structure [23–26], and it is possible to control the quantum energy levels using post-growth annealing. In this section, we present results from the post-growth annealing of uniform InAs QDs in a GaAs matrix and discuss the control of QD energy levels and an intermixing effect between In and Ga atoms.

In this experiment, as-grown InAs QDs revealed narrow PL spectra, about 20-meV wide. Following the MBE growth of a uniform InAs-QD sample, a 420-nm-thick SiO_2 film was deposited on the sample surface by rf sputtering at 250°C . Then, the SiO_2 -capped QD sample was annealed at 700°C in a nitrogen atmosphere. Figure 21.19 shows PL spectra of the uniform InAs QDs as a function of annealing time. As the annealing time increased, the PL spectra shrank and shifted toward a higher energy because of the changes in the QD structure. It is well known that modification of the dot structure due to annealing is mainly caused by interdiffusion of III-group materials [27–29]. The blue shift and narrowing of the PL spectra can be explained by broadening of the In-composition profile due to In–Ga

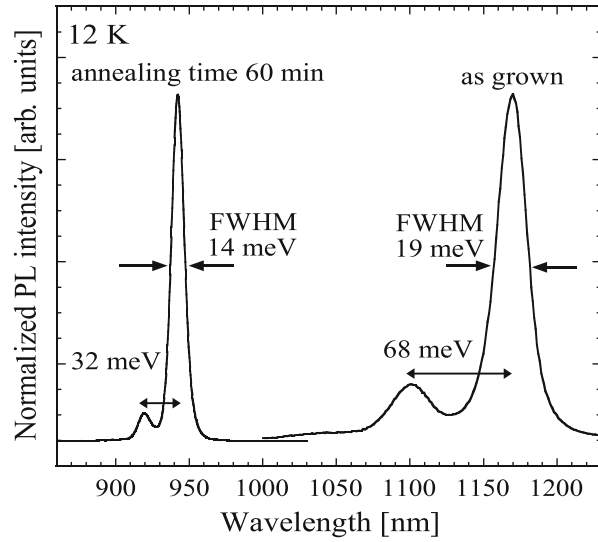
Fig. 21.19 PL spectra (12 K) of InAs QDs as a function of thermal annealing time. The annealing temperature was 700 °C



interdiffusion. In particular, III-group atomic vacancies enhanced the interdiffusion. In general, III-group vacancies existed near the SiO_2/GaAs interface because of the interface reaction and surface damage induced by sputtering of the SiO_2 capping film [27, 30]. As a result, the PL peak wavelength at 12 K shifted from 1180 nm (at 0 min) to 910 nm (at 80 min). This demonstrates the availability of wide control over the quantum energy level ($E = 312$ meV) by post-growth thermal annealing. In addition, an extremely narrow PL linewidth of 13 meV was obtained after 80 min of annealing. However, in the annealed QDs, the energy separation between the ground state and the first excited state became narrower, as shown in Fig. 21.20.

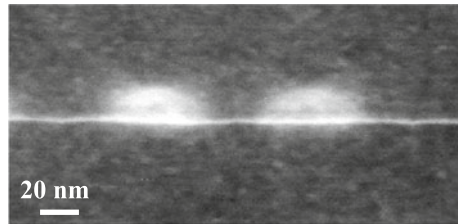
Figure 21.21 shows (110) cross-sectional STEM images of InAs QDs, annealed at 700 °C for 0 min (Fig. 21.21a), 40 min (Fig. 21.21b), and 80 min (Fig. 21.21c). From Fig. 21.21a–c, the lateral size (L) of the QDs, the thickness of the wetting layer (W), and the total height (D) were measured, and the results are plotted in Fig. 21.22 as a function of annealing time. Broadening of the InAs/GaAs heterointerface due to the annealing was clearly observed. However, the increment of the total height (D) was almost the same as the broadening width of the wetting layer in the vertical direction: the net height of the QD ($D - W$) did not depend on the annealing time. As the annealing time increased, the lateral size of the QD increased, and then saturated. It is probable that the In–Ga interdiffusion was enhanced by the strain. Since the compressive strain in the QD was relaxed by the broadening of the heterointerface, the interdiffusion effect weakened with increasing annealing time. However, as mentioned above, post-growth annealing is a useful tool for increasing QD energy levels.

Fig. 21.20 PL spectra (12 K) of as-grown InAs QDs and annealed InAs QDs. Low-energy and high-energy PL peaks were based on the transitions from ground states and 1st excited states of their QDs, respectively

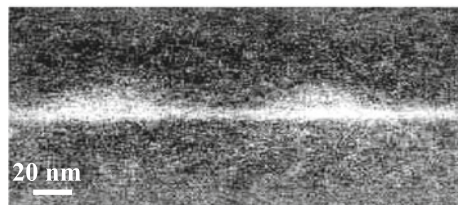


Annealing time

a 0 min



b 40 min



c 80 min

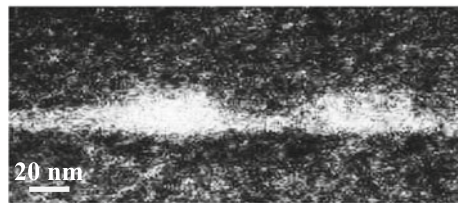


Fig. 21.21 (110) cross-sectional STEM images of as-grown InAs QDs (**a**) and annealed InAs QDs, which were annealed for 40 min (**b**) and 80 min (**c**), respectively

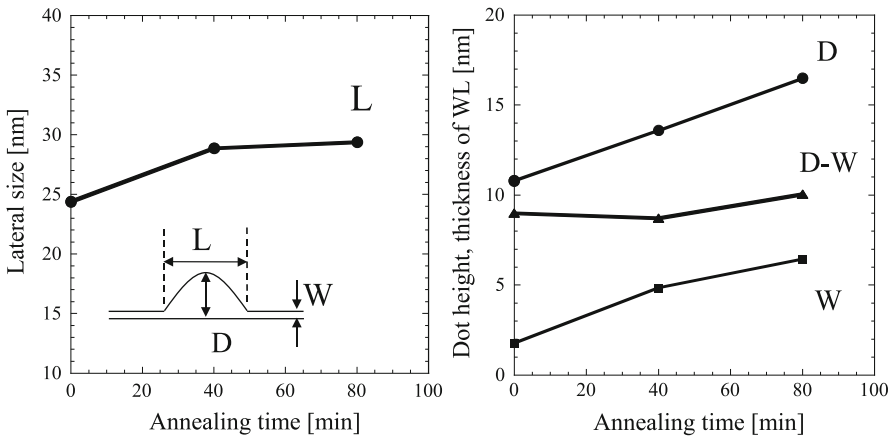


Fig. 21.22 (110) lateral size (L) and height (D) of InAs QDs and wetting layer thickness (W) as a function of the annealing time. Annealing temperature was 700 °C

21.5 Density Control of Quantum Dots

In the application of QDs to semiconductor lasers and solar cells, high-density QDs are expected to improve performance. In conventional SK growth of QDs, the QD density can be changed by adjusting the growth conditions. In general, low growth temperatures, high arsenic pressures, and high growth rates of InAs/GaAs QDs provide a high QD density. However, the crystal quality and uniformity of the high-density QDs are very important. In particular, the coalescence of neighboring QDs occurs easily for high-density QDs because of the short separation distance between the QDs. dislocations are usually observed in the giant dots that result from this coalescence. Therefore, coalescence should be suppressed to maintain a high crystal quality. In Sect. 21.5.1, Sb-mediated growth of high-density InAs/GaAs QDs is presented to resolve the trade-off relationship between high density, uniformity, and crystal quality.

On the other hand, low QD density is desirable for some devices that use individual QDs, such as single-photon sources. However, precise control of low-density QDs is difficult because the growth mode transition from 2D to 3D occurs rapidly. To realize low-density growth, the surface concentration of adatoms should be suppressed, and the supply amount of growth materials should be precisely controlled. In Sect. 21.5.2, an intermittent growth method is presented for the controlled formation of low-density InAs/GaAs QD.

21.5.1 Sb-Mediated Growth of High-Density InAs/GaAs Quantum Dots

As described in Sect. 21.3.1, a low growth rate and a low arsenic pressure can enhance surface migration and, as a result, produce highly uniform InAs/GaAs QDs

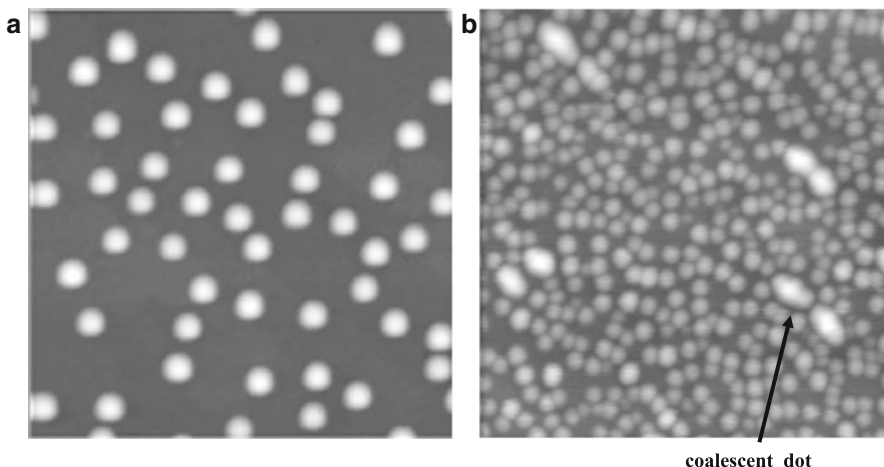


Fig. 21.23 AFM images of low-density InAs QDs (a) and high-density InAs QDs (b). (a): Growth temperature of 500 °C, growth rate of 0.035 ML/s, arsenic pressure of 3×10^{-6} Torr, (b): 480 °C, 0.070 ML/s, 6×10^{-6} Torr

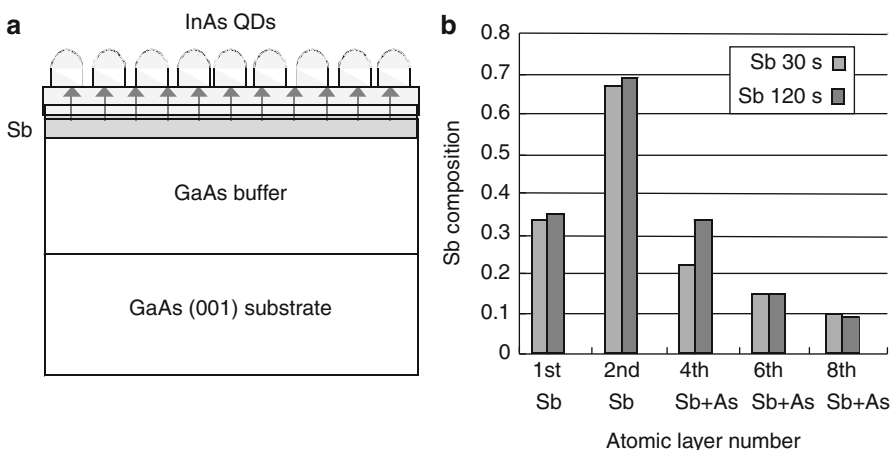


Fig. 21.24 Sample structure of high-density InAs QDs on Sb/GaAs(001) (a). Sb composition profiles of Sb-irradiated GaAs surface layers (b). Sb-irradiation time was 30 and 120 s

at a low density, as shown in Fig. 21.23a. Therefore, growth conditions opposite to those employed for high-density growth induce large size fluctuations (Fig. 21.23b). In addition, under high-density conditions (Fig. 21.23b), many giant dots appeared due to coalescence. In 2004, Yamaguchi et al. reported an Sb-mediated SK growth method using Sb-containing GaAs buffer layers of high-density InAs QDs [31, 32]. In this growth, the coalescence of the QDs was effectively suppressed. Figure 21.24a shows a schematic diagram of the growth structure in this Sb-mediated growth of InAs QDs. Prior to the InAs growth, an Sb flux was irradiated onto the GaAs

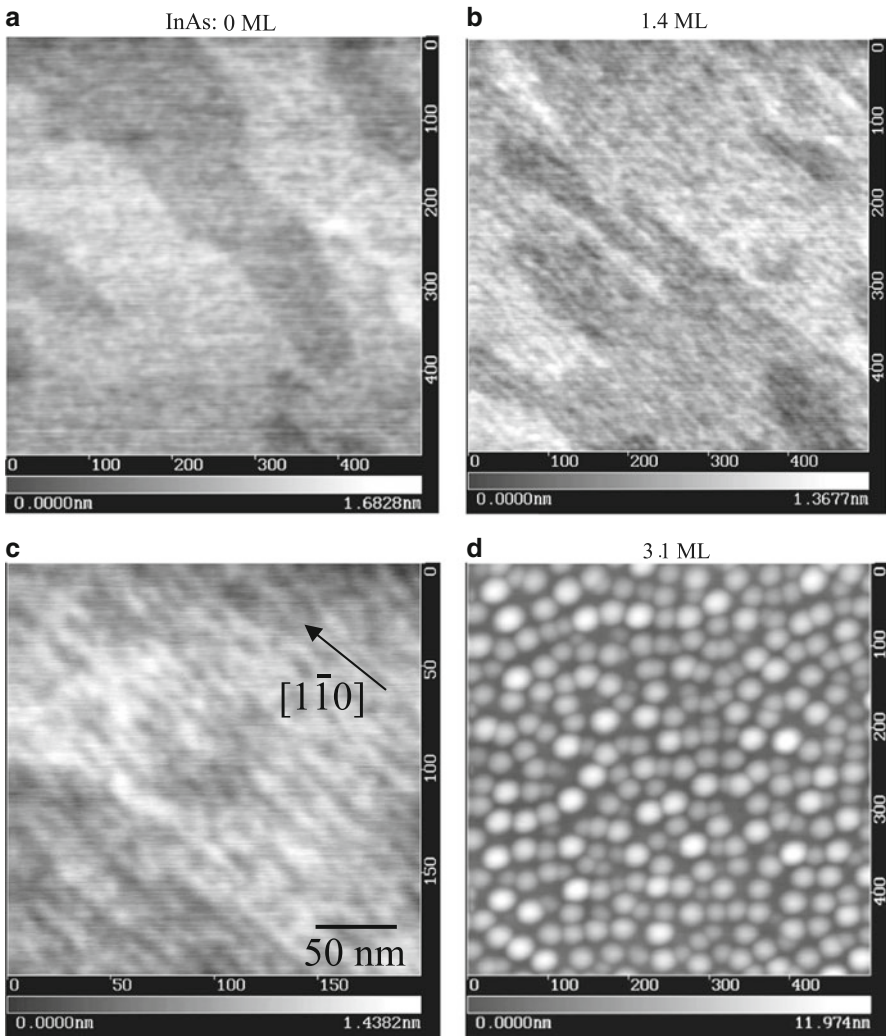


Fig. 21.25 AFM images of Sb-irradiated GaAs surface (a) and InAs islands with different coverage of 1.4 ML (b) and (c) and 3.1 ML (d)

buffer layer. The RHEED pattern changed from (2×4) to (1×3) or (2×3) , which indicated an Sb-stabilized surface. Figure 21.24b shows the Sb composition profiles of an Sb-irradiated GaAs surface, measured by X-ray crystal truncation rod (CTR) scattering. From the CTR scattering, it was found that the Sb-stabilized surface layer was composed from the Sb bilayer with 30% (1st) and 60% (2nd) in coverage [4]. Furthermore, 3-ML-thick GaAsSb alloy layers were formed beneath the surface.

After Sb irradiation of the GaAs buffer layer, InAs was grown on the surface. Figure 21.25 shows AFM images of the Sb-irradiated GaAs surface (Fig. 21.25a)

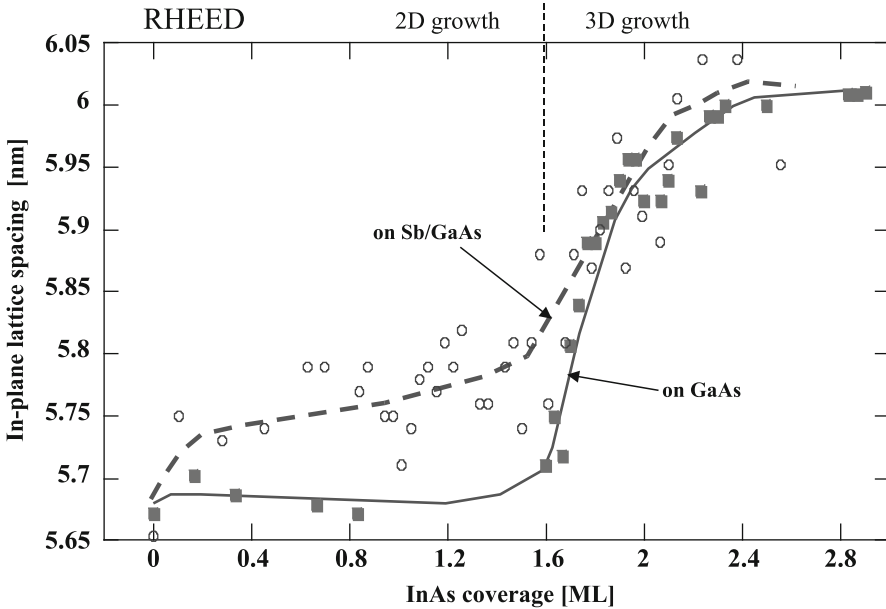


Fig. 21.26 InAs coverage dependence of in-plane lattice spacing of InAs layers, grown, respectively, on Sb/GaAs and on GaAs. In-plane lattice spacing was evaluated from RHEED pattern

and InAs islands with 1.4 ML (Fig. 21.25b, c) and 3.1 ML (Fig. 21.25d) of InAs coverage on the Sb-irradiated GaAs buffer layers. Although the Sb-irradiated GaAs layer (Fig. 21.25a) had an atomically flat surface, 2-dimensional wirelike structures appeared on the InAs wetting layer (Fig. 21.25b, c). These wirelike structures were about 2 ML in height and were aligned in the $[1\bar{1}0]$ direction.

Figure 21.26 shows the in-plane lattice spacing of InAs grown on GaAs and Sb/GaAs layers as a function of InAs coverage. The in-plane lattice spacings were measured using RHEED during the growth. During normal InAs/GaAs SK growth, the InAs has the same in-plane lattice spacing as the GaAs because of the coherent growth. However, the wirelike InAs structures on the Sb/GaAs layer revealed a large in-plane lattice spacing, which was caused by Sb incorporation. That is, surface segregation of Sb adatoms occurred during the InAs growth [33, 34], and the segregated Sb atoms were incorporated into the InAs wetting layer. According to Bennett's report, similar wirelike structures were observed in Sb-containing compound semiconductor (e.g., InSb, AlSb) growth on GaAs [35]. Therefore, InAsSb growth occurred during the InAs growth on Sb/GaAs, and the wirelike structures were spontaneously formed because of strain relaxation. In general, it is well known that in the SK growth of Ge/Si and InGaAs/GaAs, Sb surfactant suppresses 3D nucleation [36, 37]. However, such wirelike structures provide many step sites, which are preferential sites for 3D nucleation. As a result, high-density InAs QDs were formed, as shown in Fig. 21.25d [38].

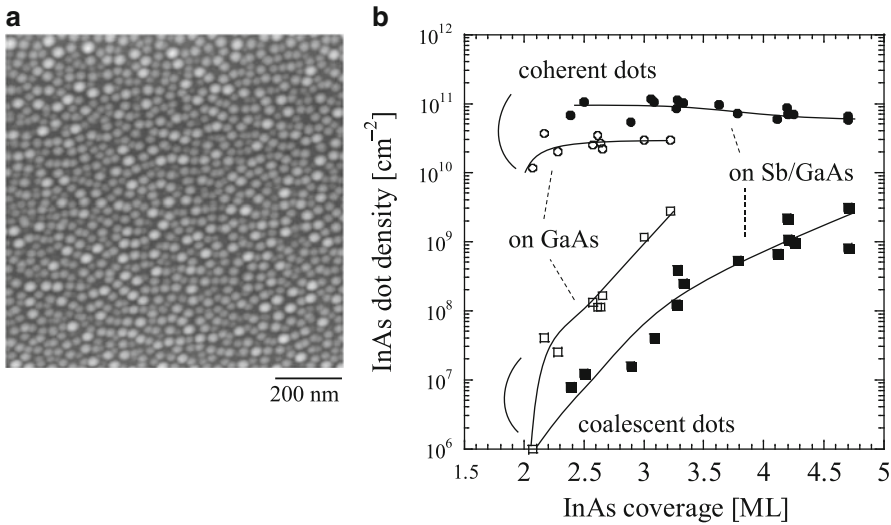


Fig. 21.27 AFM image of high-density InAs QDs on Sb/GaAs (a). Relationship between InAs dot density (*coherent dots*, *coalescent dots*) and InAs coverage (b). InAs dots were grown on GaAs and on Sb/GaAs, respectively

Figure 21.27a shows an AFM image of high-density InAs QDs on Sb/GaAs. The QD density was $1 \times 10^{11} \text{ cm}^{-2}$. There are no giant dots in this image, and it is possible that the segregated Sb surface atoms suppressed QD coalescence. Figure 21.27b shows the coherent QD density and the coalescent dot density for InAs on GaAs and InAs on Sb/GaAs as a function of InAs coverage. The InAs growth conditions were the same in both cases. In this experiment, the coherent QD density of the Sb/GaAs buffer layer was about three times higher than in a conventional GaAs buffer layer. However, the coalescent dot density on Sb/GaAs was one-tenth of that on GaAs. Figure 21.28 shows a narrow PL spectrum of high-density InAs QDs on Sb/GaAs. The QD density was $1 \times 10^{11} \text{ cm}^{-2}$, and the PL linewidth was about 28 meV. This Sb-mediated SK growth using Sb-containing GaAs buffer layers is a powerful method for obtaining high-density, high-uniformity InAs QDs with a high crystal quality.

21.5.2 Intermittent Growth of Low-Density InAs/GaAs Quantum Dots

In conventional SK growth, the QD density can be reduced by adjusting the growth conditions, such as by using a lesser extent of growth, a higher growth temperature, and/or a lower growth rate. However, reduction to below 10^8 cm^{-2} is very difficult because 3D islanding occurs rapidly and the density increases drastically. Figure 21.29 shows RHEED diffraction-beam intensity vs. growth time for InAs

Fig. 21.28 PL spectrum of high-density and high-uniformity InAs QDs, grown on Sb/GaAs

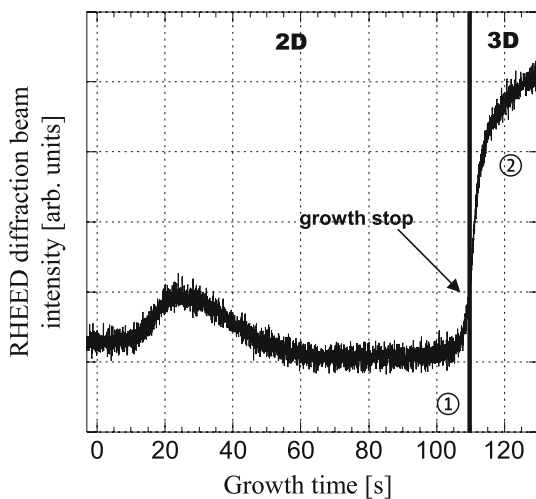
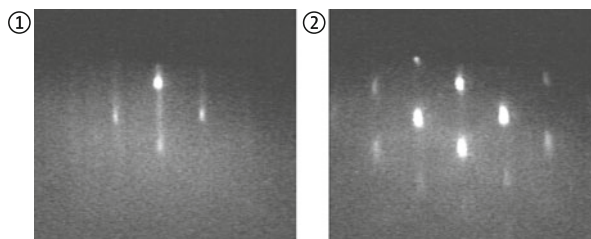
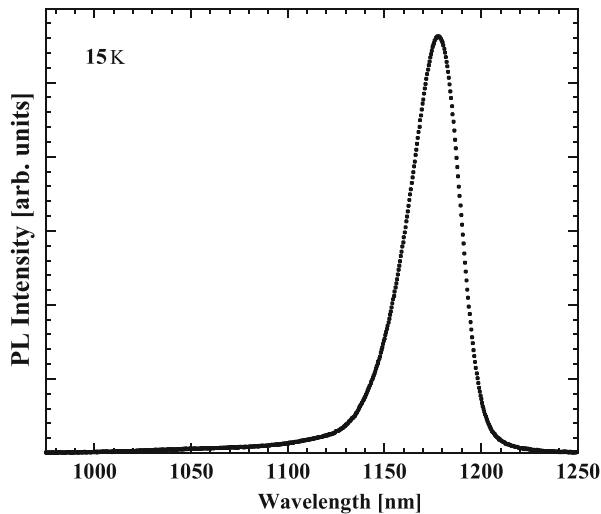


Fig. 21.29 RHEED diffraction-beam intensity as a function of growth time (including growth interruption time). The In flux was stopped at 110 s, and then the growth was interrupted. RHEED patterns were obtained at 105 s (①) and at 120 s (②)

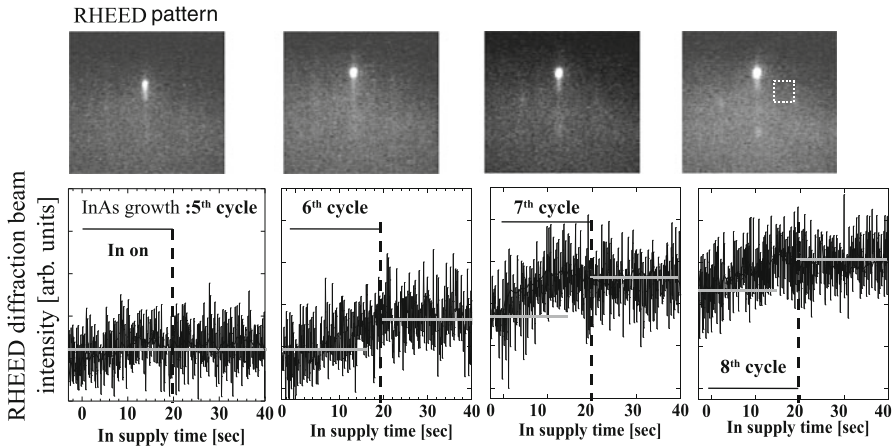


Fig. 21.30 RHEED patterns and RHEED diffraction-beam intensity as a function of intermittent growth cycle number. At each growth cycle, In flux was supplied for 16 s. For more than 6th cycle, diffraction-beam intensity slightly increased during the In supply, and then the intensity was almost kept constant during the growth interruption

growth on GaAs. In this experiment, the InAs growth was stopped just after the growth mode transition. However, the RHEED diffraction-beam intensity continued to increase despite the growth interruption, and the RHEED spot pattern developed, indicating that the initial 3D islanding was not controllable. In conventional SK growth, since the growth is easily limited by surface strain, the growth species often accumulates at the surface. Hence, even during the growth interruption, residual surface species formed 3D nuclei and/or were incorporated into 3D nuclei.

In order to precisely control low-density QD growth, an intermittent growth method was proposed [39]. In this growth method, 0.3-ML-thick InAs was grown intermittently after 1.5 ML of coverage (wetting layer). The growth was interrupted for 2 (or 3) min between each intermittent growth phase. Figure 21.30 shows RHEED patterns and diffraction-beam intensity as a function of the InAs growth cycle number. Until the 5th cycle, the diffraction-beam intensity did not change. At the 6th cycle, the diffraction-beam intensity increased slightly, and this increased intensity was maintained during the growth interruption. This indicates that the initial 3D islanding was maintained. In the 7th and 8th cycles, similar changes in the RHEED diffraction-beam intensity and a slight spot pattern were observed. Therefore, the QD density can be controlled by adjusting the number of growth cycles.

Figure 21.31 shows relationships between QD density and the number of growth cycles for two different conditions. As the cycle number increases, the QD density increases monotonically. At 0.018 ML/s (and G.I. for 3 min), the increase in the QD density per cycle was $1.0 \times 10^7 \text{ cm}^{-2}$. Therefore, InAs QDs with an ultralow density of 10^7 – 10^8 cm^{-2} can be controlled step by step using an intermittent growth technique. Figure 21.32 shows AFM images of ultralow density InAs QDs with a

Fig. 21.31 Relationship between InAs-QD density and supply cycle number after 2D–3D transition. (■: InAs growth rate of 0.027 ML/s, growth interruption time of 2 min. ●: 0.018 ML/s, 3 min.) The QD density for one supply cycle was $2.5 \times 10^7 \text{ cm}^{-2}$ for ■ and $1.0 \times 10^7 \text{ cm}^{-2}$ for ●

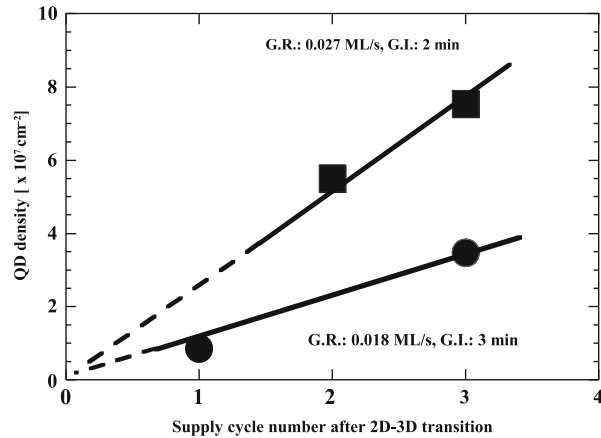
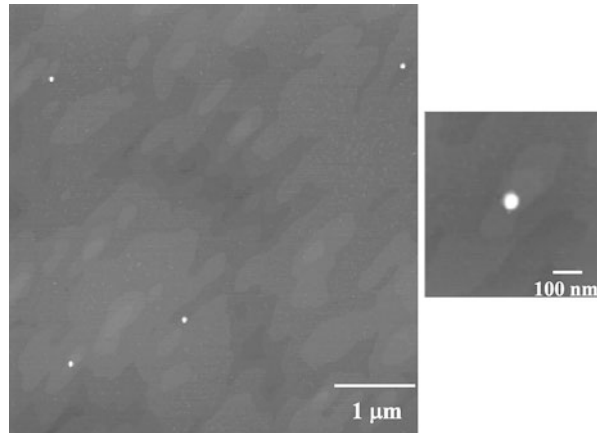


Fig. 21.32 AFM images of low-density InAs QDs with $5.5 \times 10^7 \text{ cm}^{-2}$, grown by the intermittent growth



density of $5.5 \times 10^7 \text{ cm}^{-2}$. From the RHEED chevron pattern, $\{110\}$ facets were confirmed on the side walls of the QDs.

Figure 21.33 shows a macroscopic PL spectrum of InAs QDs with an ultralow density of $5\text{--}8 \times 10^7 \text{ cm}^{-2}$. The substrate was rotated during the 2D growth and was fixed for observation of the RHEED diffraction-beam intensity during the intermittent growth. A PL peak appeared at about 1,195 nm, and the linewidth was 18 meV, which indicates uniform QD structures. Figure 21.34 shows a microscopic PL spectrum of ultralow density InAs QDs. There were probably several InAs QDs within the excitation laser spot, which was about 3 μm in diameter. The PL spectrum reveals two peaks due to exciton emissions from two individual QDs with different size. The PL linewidth indicates homogeneous broadening of about 0.9 meV, which was limited in this PL setup. Ultralow density QDs prepared by intermittent growth are useful to evaluate the characteristics of single QDs.

Fig. 21.33 A macroscopic PL spectrum of low-density InAs QDs with $5\text{--}8 \times 10^7 \text{ cm}^{-2}$, grown by the intermittent growth. PL was measured at 15 K

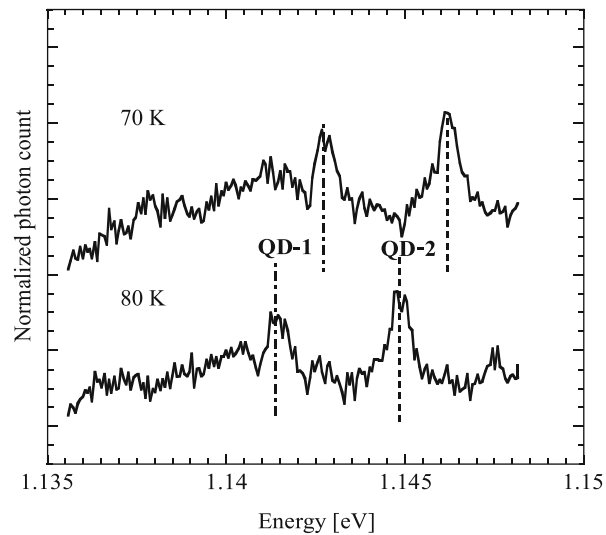
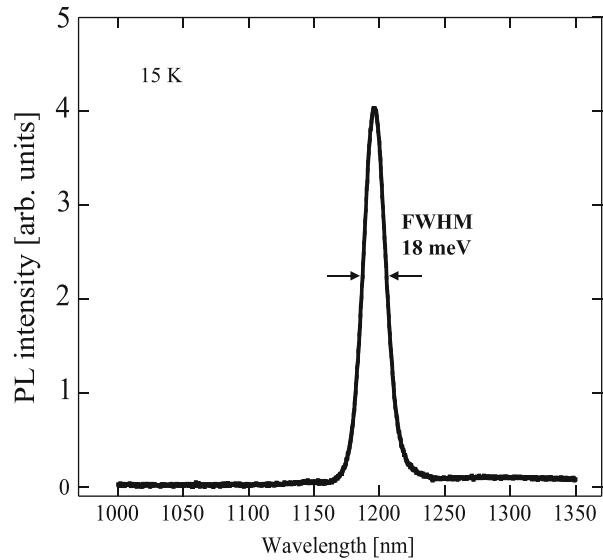


Fig. 21.34 Microscopic PL spectra of low-density InAs QDs, grown by the intermittent growth. PL was measured at 70 and 80 K

21.6 Quantum Dot Array

A QD array structure enables electronic and optical interaction between neighboring QDs. Recently, exciton interactions between QDs have become desirable for certain novel devices [40]. In normal SK growth, the 3D islands are randomly deposited on a surface. However, the self-formation of arranged QDs can be achieved by modification of the underlying layers. In this section, the self-arrangement of vertical and in-plane InAs/GaAs QDs is described.

21.6.1 Vertical Array of InAs/GaAs Quantum Dots

The vertical alignment of QDs has been already demonstrated via stacking growth of QDs with thin spacer layers [41]. For InAs/GaAs QDs, the GaAs capping layer just above the InAs QDs has a tensile strain. Therefore, stacked InAs QDs are preferentially grown above the embedded QDs. Figure 21.35 shows the relative growth rate of stacked InAs-QD layers (2nd and 3rd QDs) for that of the 1st QD layer as a function of the thickness of the GaAs spacer layers. In this experiment, the height of the 1st QD was about 10 nm. When the thickness of the spacer layer was increased above 30 nm, the growth rate of the stacked QD layer was almost the same as that of the 1st layer. This indicates that the strain interaction of the stacked QDs through the spacer layers becomes weak for spacer layers thicker than 30 nm [42]. When the spacer thickness was decreased below 30 nm, the stacking growth rate was enhanced. In this case, InAs was easily deposited just above the embedded QDs.

Figure 21.36 shows a cross-sectional STEM image of triple-stacked InAs QDs with a 15-nm-thick GaAs spacer layer. The stacked QDs are vertically aligned. For closely stacked QDs, it is possible to form an electronic coupling between the stacked QDs. Thus, vertical alignment of the QDs can be obtained by the stacking growth technique using thin spacer layers. It should be noted that the structure of the stacked QDs was different than that of the underlying QDs. Figure 21.37 shows cross-sectional STEM images of double-stacked InAs QDs with different coverage of the 2nd InAs layer (2.5 ML (Fig. 21.37a), 3.3 ML (Fig. 21.37b)). The coverage of the 1st QDs was 2.5 ML. Since the thickness of the GaAs spacer layer was 15 nm, the 2nd QDs were stacked just above the 1st QDs. Although the RHEED chevron pattern revealed (110) facets during the 1st QD growth, high-index planes of (136) or (137) were observed for 2.5-ML-thick 2nd InAs layer coverage (Fig. 21.37a).

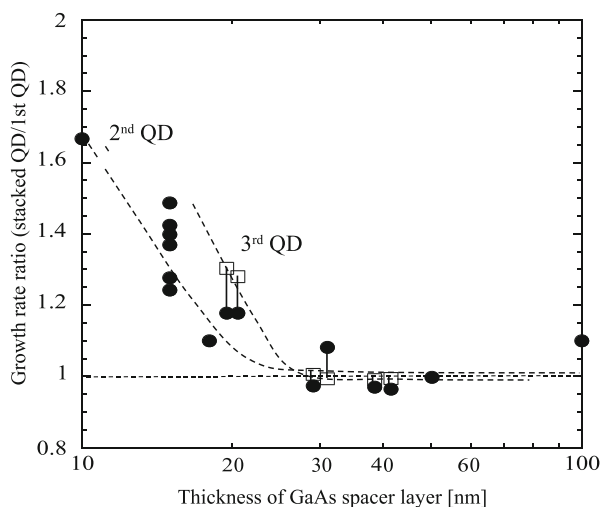


Fig. 21.35 Growth rate ratio of stacked InAs QDs for 1st QDs as a function of thickness of GaAs spacer layer

Fig. 21.36 A cross-sectional STEM image of three-stacked InAs QDs. Thickness of the GaAs spacer layer was 15 nm

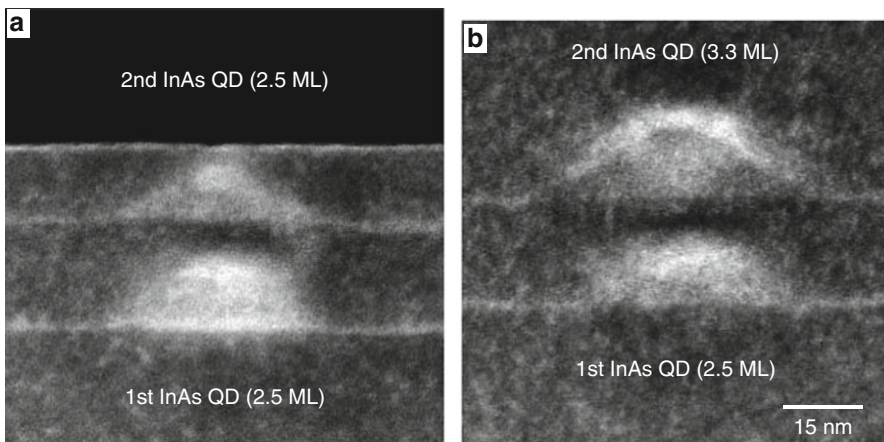
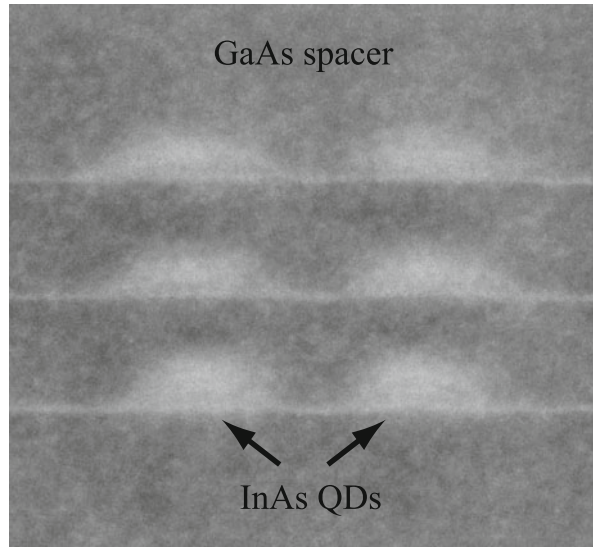


Fig. 21.37 Cross-sectional STEM images of double-stacked InAs QDs with different 2nd-InAs coverage of 2.5 ML (a) and 3.3 ML (b). The 1st-InAs coverage was 2.5 ML

In this stacking growth, a 2nd InAs layer coverage of more than 3 ML was needed to obtain the same QD shape with (110) facets. However, the volume of the 2nd QDs was larger than that of the 1st QDs, as shown in Fig. 21.37b. This modification of the stacked QDs can be attributed to strain interaction with the underlying QDs.

In order to achieve vertical alignment of the QDs without strain interaction, strain compensation layers were introduced as a spacer layer between the stacked QDs [43]. For example, an InGaAsP spacer layer was used in the stacking growth of InAs

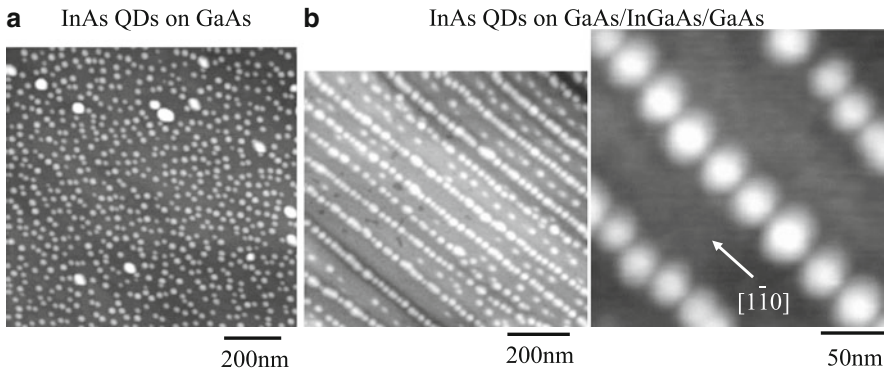


Fig. 21.38 AFM images of InAs QDs, grown, respectively, on GaAs buffer layer (**a**) and on GaAs/InGaAs/GaAs buffer layer (**b**). InAs-QD chains were aligned along $[1\bar{1}0]$ direction on the GaAs/InGaAs/GaAs (**b**)

QDs on InP substrates. In this growth system, 60 QD layers were vertically stacked [44]. For InAs QDs on a GaAs substrate, a GaNAs spacer layer was investigated to reduce the residual strain [45].

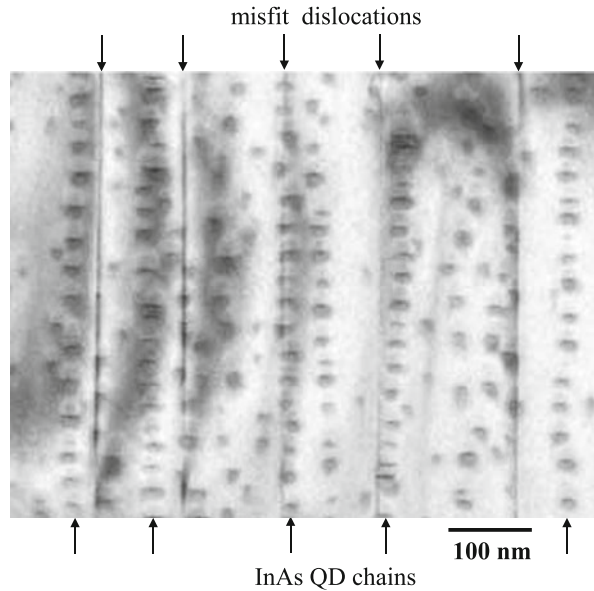
21.6.2 In-Plane Arrays of InAs/GaAs Quantum Dots

In-plane ordering of QDs has been demonstrated by the selective growth of QDs on patterned substrates [46]. In other studies, the self-formation of in-plane-arranged QDs has been attempted using a stacked growth technique [47, 48] or high-index plane substrates [49]. For site control and arrangement of QDs, strain control of the underlying buffer layers is important. 1D and 2D in-plane arrangements of InAs QDs on GaAs(001) substrates are described below.

The nucleation of 3D islands is related to the surface strain and surface undulation of the underlying buffer layers. Thereby, strained buffer layers have been used for the selective growth of QDs: InP QDs on an InGaP/GaAs buffer layer [50], Ge dots on a SiGe/Si buffer layer [51], and InAs QDs on an InGaAs/GaAs buffer layer [52]. Figure 21.38 shows AFM images of InAs QDs on a conventional GaAs buffer layer (Fig. 21.38a) and on a GaAs(70–80 nm)/In_{0.16}Ga_{0.84}As(175 nm)/GaAs buffer layer (Fig. 21.38b). In the conventional SK growth, 3D InAs islands were randomly deposited on the GaAs buffer layers (Fig. 21.38a). However, with a GaAs/InGaAs/GaAs buffer layer (Fig. 21.38b), the InAs QDs were periodically aligned in the $[1\bar{1}0]$ direction [53]. The periodic distance between the QD chains ranged from 100 to 150 nm. The self-formation of the QD chain structure can be attributed to misfit dislocations at the InGaAs/GaAs heterointerface.

Figure 21.39 shows a plan-TEM image of InAs-QD chains on a GaAs/InGaAs/GaAs buffer layer. The image reveals misfit dislocation lines at the upper

Fig. 21.39 A plan-TEM image of InAs QDs/GaAs/InGaAs/GaAs sample. In this image, QD chains and misfit dislocations were observed



GaAs/InGaAs heterointerface. No threading dislocations were observed in the buffer layer. Misfit dislocations were preferentially generated along the $[1\bar{1}0]$ direction, as opposed to the $[110]$ direction, because of the anisotropic residual strain in the buffer layer [54]. The $[110]$ misfit dislocations were arranged in an orderly manner and had a lateral spacing of about 100–150 nm. The lateral ordering of the misfit dislocations was mainly due to periodic corrugation of the InGaAs layer. As shown in Fig. 21.39, the periodic QD chains aligned near the misfit dislocation lines along the $[1\bar{1}0]$ direction. In addition, the line number of the QD chains was almost the same as that of the misfit dislocations. Therefore, the lateral ordering of the misfit dislocations probably induced the self-formation of periodic QD chains. By optimizing the growth conditions, uniform InAs-QD chains several micrometers in length were demonstrated on GaAs/InGaAs/GaAs buffer layers [55], as shown in Fig. 21.40. Figure 21.41 shows PL spectra of normal InAs QDs on a GaAs buffer layer (Fig. 21.41a) and those of InAs-QD chains on a GaAs/InGaAs/GaAs buffer layer (Fig. 21.41b). The InAs QDs and GaAs capping layers of both samples were grown under the same growth conditions. The PL peak of the InAs-QD chains was at 1,200 nm, which was longer than that of the normal InAs QDs. The PL linewidth of the QD chains (about 47 meV) was wider than that of the normal QDs (about 24 meV). The red shift and broadening in the PL spectra of the QD chains were mainly attributed not only to size fluctuation of the QDs but also to the lateral coupling of QDs along the chain.

The self-formation of a 2D QD array is more difficult in conventional SK growth without stacked layer structures and high-index plane substrates. In addition, high QD density and high uniformity of the QD structure are required for the fabrication of 2D-arranged QDs. In 2007, the 2D self-arrangement of high-density InAs QDs

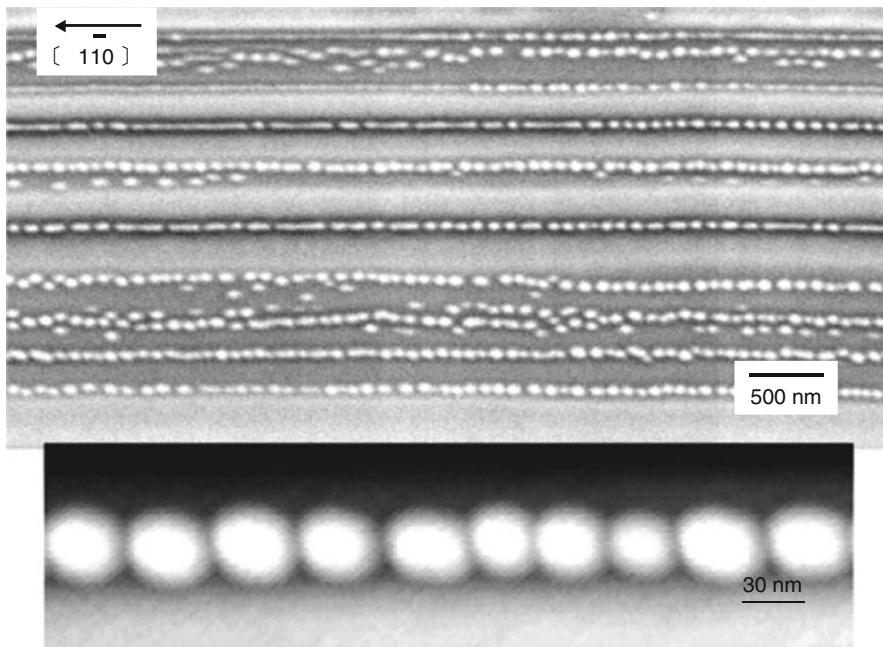


Fig. 21.40 SEM and AFM images of InAs-QD chains grown on GaAs/InGaAs/GaAs buffer layer. Length of the QD chains were several micrometers

was demonstrated using GaAsSb/GaAs(001) buffer layers [56]. Figure 21.42 shows AFM images of 2D and 3D InAs islands on GaAs(2 ML)/GaAsSb(10 ML, Sb flux ratio of 0.13)/GaAs(001) buffer layers. For 1.45 ML of InAs coverage (Fig. 21.42a), a number of small islands were formed, and several [010] steps appeared in addition to the $[1\bar{1}0]$ steps. When the InAs coverage was above 1.5 ML, the growth mode shifted from 2D to 3D growth. After the InAs growth at 1.6 ML (Fig. 21.42b), the initial dots were formed near the step edges. In addition, many holes and grooves of nanometer size were observed. The diameter of the nanoholes and the width of the nanogrooves were about 20–30 nm. The depths of these nanoholes and nanogrooves were less than about 3 nm, indicating that the nanoholes and the nanogrooves were formed in the strained GaAsSb buffer layer and did not reach the underlying GaAs layer. Therefore, the formation of the nanoholes and nanogrooves was caused by desorption of the unstable, highly strained GaAsSb during the InAs growth. In Fig. 21.42b, most of the nanoholes and nanogrooves are located next to the dots. In particular, 1D dot chains were formed along the [010] step edges. As the InAs growth proceeded, the dot density increased, and the density of nanoholes and nanogrooves also increased (Fig. 21.42c). The high dot density area coincided with the high nanohole density area. This suggests that the dot formation induced nanohole formation because the InAs dots stressed the GaAsSb layer; the dot essentially played the role of a stressor. In addition, the desorbed GaAsSb from

Fig. 21.41 PL spectra of InAs QDs on GaAs buffer layer (a) and InAs-QD chains on GaAs/InGaAs/GaAs buffer layer (b). Both InAs QDs were embedded by GaAs capping layers. PL was measured at 13 K

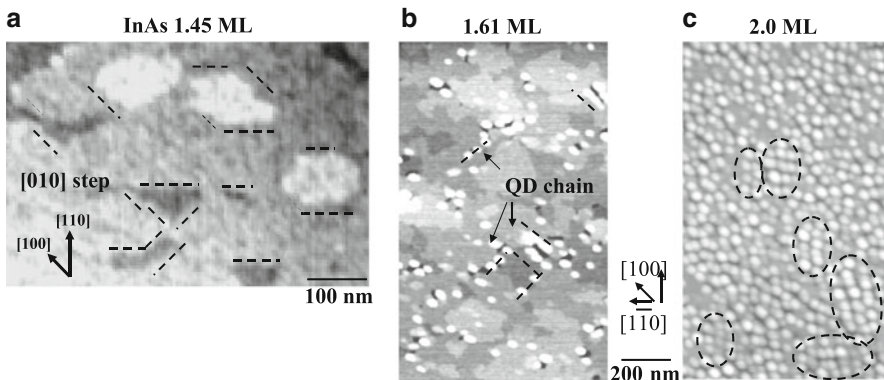
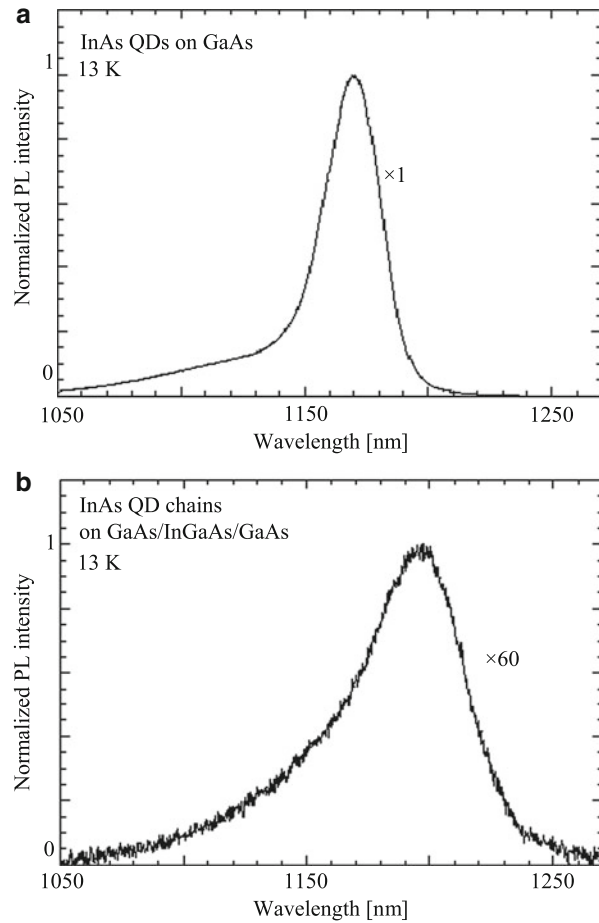


Fig. 21.42 AFM images of 2D and 3D InAs islands grown on GaAs/GaAsSb/GaAs buffer layer. InAs coverage were 1.45 ML (a), 1.61 ML (b), and 2.0 ML (c)

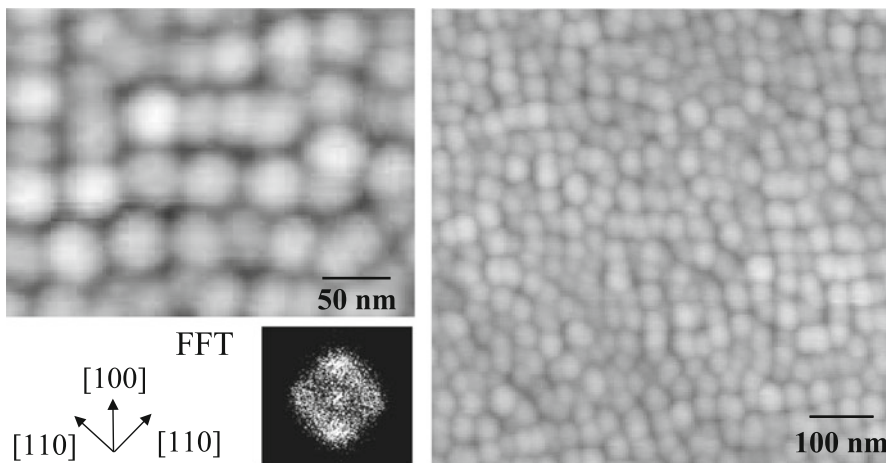


Fig. 21.43 AFM images of 2D array of InAs QDs, grown on GaAs/GaAsSb/GaAs buffer layer. InAs coverage was 2.6 ML. Inset is a fast Fourier transform (FFT) image, which indicates 2D periodic pattern of squared QD array for $\langle 010 \rangle$ direction

the nanoholes reformed small Sb-containing islands near the nanoholes. In fact, small 2D islands were observed beside the nanoholes (Fig. 21.42b, c). Such Sb-containing 2D islands would provide preferential sites for 3D nucleation. Therefore, it is also possible that the nanoholes induced nearby dot formation. Furthermore, for 2.0 ML of coverage (Fig. 21.42c), remarkably, a 2D arrangement of InAs dots was partially formed. In the in-plane-arranged area, the dots mainly aligned along the $[010]$ direction. Therefore, on the basis of these results and considerations, it can be concluded that the in-plane arrangement of the dots originated from the dot chains and nanogrooves, which were aligned along the $[010]$ edges. Figure 21.43 shows AFM images of in-plane InAs QDs with 2.6 ML of coverage, grown on a GaAs/GaAsSb/GaAs(001) buffer layer. The inset is a fast Fourier transform (FFT) image of the AFM image, which indicates 2D periodic pattern of squared QD array for the $\langle 010 \rangle$ direction. The QD density was about $1 \times 10^{11} \text{ cm}^{-2}$, and the QDs were partially arranged along the $\langle 010 \rangle$ direction. Control of the $[010]$ step structure is important for the wide-area 2D arrangement of QDs.

21.7 Conclusion

In this chapter, we reviewed the growth characteristics and optical properties of InAs/GaAs QDs grown by MBE. In order to develop novel nanophotonic QD devices, precise control of the QD structure is required. Based on SK mode growth of InAs/GaAs QDs (Sect. 21.2), the growth conditions, the growth structures, and post-growth annealing were extensively investigated for the achievement of narrow inhomogeneous broadening and wide control of the QD density and energy

levels (Sects. 21.3 and 21.4). Uniform InAs/GaAs QDs were achieved by the self-size-limiting effect, optimized capping growth, and closely stacked growth using nanoholes (Sect. 21.3). High-density InAs QDs with a narrow size distribution were formed by Sb-mediated growth, which is an attractive method for suppressing QD coalescence. For ultralow density InAs QDs, an intermittent growth method was presented, and the QD density was precisely controlled by real-time RHEED observation (Sect. 21.5). Furthermore, vertical and in-plane arrangements of InAs/GaAs QDs were attempted by using strain-controlled underlying layers. Stacked growth produced vertically aligned QDs. 1D InAs-QD chains were spontaneously formed along the $[1\bar{1}0]$ direction on GaAs/InGaAs/GaAs(001) buffer layers, and a 2D arrangement of InAs QDs was demonstrated using GaAsSb/GaAs(001) buffer layers (Sect. 21.6).

References

1. L. Goldstein, F. Glas, J.Y. Marzin, M.N. Charasse, G. Le Roux, *Appl. Phys. Lett.* **41**, 1099 (1985)
2. D.J. Eaglesham, M. Cerullo, *Phys. Rev. Lett.* **4**, 1943 (1990)
3. A. Marti Ceschin, J. Massies, *J. Cryst. Growth* **114**, 693 (1991)
4. K. Yamaguchi, T. Kaizu, K. Yujobo, Y. Saito, *J. Cryst. Growth* **237–239**, 1301 (2002)
5. For example, D. Bimberg, M. Grundmann, N.N. Ledentsov, *Growth and structural characterization of self-organized quantum dots*, in *Quantum Dot Heterostructures* (Wiley, New York, 1999)
6. R. Murray, D. Childs, S. Malik, P. Siverns, C. Roberts, J. Hartmann, P. Stavrinou, *Jpn. J. Appl. Phys.* **38**, 528 (1999)
7. K. Yamaguchi, K. Yujobo, T. Kaizu, *Jpn. J. Appl. Phys.* **39**, L1245 (2000)
8. M. Takahashi, T. Kaizu, J. Mizuki, *Appl. Phys. Lett.* **88**, 101917 (2006)
9. A.-L. Barabási, *Appl. Phys. Lett.* **70**, 2565 (1997)
10. T. Kaizu, K. Yamaguchi, *Jpn. J. Appl. Phys.* **42**, 4166 (2003)
11. J.M. García, G. Medeiros-Ribeiro, K. Schmidt, T. Ngo, J.L. Feng, A. Lorke, J. Kotthaus, P.M. Petroff, *Appl. Phys. Lett.* **71**, 2014 (1997)
12. Y. Saito, R. Ohtsubo, K. Yamaguchi, *Inst. Phys. Conf. Ser.* **170**, 531 (2002). Chap.7
13. P.B. Joyce, T.J. Krzyzewski, P.H. Steans, G.R. Bell, J.H. Neave, T.S. Jones, *Surf. Sci.* **492**, 345 (2001)
14. T. Kitamura, R. Ohtsubo, M. Murayama, T. Kuroda, K. Yamaguchi, A. Tackeuchi, *Phys. Status Solidi (c)* **0**, 1165 (2003)
15. M. Murayama, R. Ohtsubo, T. Kitamura, T. Kuroda, K. Yamaguchi, A. Tackeuchi, *Phys. Status Solidi (c)* **0**, 1145 (2003)
16. A. Tackeuchi, R. Ohtsubo, K. Yamaguchi, M. Murayama, T. Kitamura, T. Kuroda, T. Takagahara, *Appl. Phys. Lett.* **84**, 3576 (2004)
17. K. Mukai, M. Sugawara, *Appl. Phys. Lett.* **74**, 3963 (1999)
18. S. Tonomura, K. Yamaguchi, *J. Appl. Phys.* **104**, 054909 (2008)
19. M. Bayer, P. Hawrylak, K. Hinzer, S. Fafard, M. Korkusinski, Z.R. Wasilewski, O. Stern, A. Forchel, *Science* **291**, 451 (2001)
20. P.B. Joyce, T.J. Krzyzewski, G.P. Bell, T.S. Jones, *Appl. Phys. Lett.* **79**, 3615 (2001)
21. T. Satoh, K. Yamaguchi, *J. Appl. Phys.* **44**, 2672 (2005)
22. N. Tsukiji, K. Yamaguchi, *J. Cryst. Growth* **301–302**, 849 (2006)
23. A.O. Kosogov, P. Werner, U. Goesele, N.N. Ledentsov, D. Bimberg, V.M. Ustinov, A.Yu. Egorov, A.E. Zhukov, P.S. Kopev, N.A. Bert, *Appl. Phys. Lett.* **69**, 3072 (1996)

24. S.J. Xu, X.C. Wang, S.J. Chua, C.H. Wang, W.J. Fan, J. Jiang, X.G. Xie, *Appl. Phys. Lett.* **42**, 3335 (1998)
25. A. Babinski, J. Jasinski, R. Bozek, A. Szepielow, J.M. Baranowski, *Appl. Phys. Lett.* **79**, 2576 (2001)
26. Y. Kobayashi, K. Yamaguchi, *Appl. Surf. Sci.* **244**, 88 (2005)
27. D. Bhattacharyya, A. Saher Helmy, A.C. Bryce, E.A. Avrutin, J.H. Marsh, *J. Appl. Phys.* **88**, 4619 (2000)
28. R. Leon, Y. Kim, C. Jagadish, M. GaI, J. Zou, D.J.H. Cockayne, *Appl. Phys. Lett.* **69**, 1888 (1996)
29. S. Malik, C. Roberts, R. Murray, M. Pate, *Appl. Phys. Lett.* **71**, 1987 (1997)
30. O.P. Kowalski, C.J. Hamilton, S.D. McDougall, J.H. Marsh, A.C. Bryce, C.C. Button, J.S. Roberts, *Appl. Phys. Lett.* **72**, 581 (1998)
31. K. Yamaguchi, T. Kanto, Self-assembled InAs quantum dots on GaSb/GaAs(001) layers by molecular beam epitaxy, in *14th International Conference on Crystal Growth/12th International Conference on Vapor Growth and Epitaxy (ICCG-14/ICVGE-12)*, Grenoble, 9–13 Aug 2004, T03-3, p. 644
32. K. Yamaguchi, T. Kanto, *J. Cryst. Growth* **275**, e2269 (2005)
33. R. Magri, A. Zunger, *Phys. Rev. B* **65**, 165302 (2002)
34. T. Nakai, K. Yamaguchi, *Jpn. J. Appl. Phys.* **44**, 3803 (2005)
35. B.R. Bennett, B.V. Shanabrook, P.M. Thibado, L.J. Whitman, R. Magno, *J. Cryst. Growth* **175/176**, 888 (1997)
36. B. Voigtlander, A. Zinner, T. Weber, H.P. Bonzel, *Phys. Rev. B* **51**, 7583 (1995)
37. T. Matsuura, T. Miyamoto, T. Kageyama, M. Ohta, Y. Matsui, T. Furuhashi, F. Koyama, *Jpn. J. Appl. Phys.* **43**, L605 (2004)
38. T. Ohta, T. Kanto, K. Yamaguchi, *Jpn. J. Appl. Phys.* **45**, 3427 (2006)
39. P. Pachakapat, K. Yamaguchi, Self-formation control of low-density InAs quantum-dots, in *The 34th International Symposium on Compound Semiconductors (iscs2007)*, Kyoto, 15–18 Oct 2007, p. 172
40. M. Ohtsu, T. Kawazoe, T. Yatsui, M. Naruse, *IEEE J. Sel. Top. Quantum Electron.* **14**, 1404 (2008)
41. J. Tersoff, C. Teichert, M.G. Lagally, *Phys. Rev. Lett.* **76**, 1675 (1996)
42. Y. Suzuki, T. Kaizu, K. Yamaguchi, *Physica E* **21**, 555 (2004)
43. K. Akahane, N. Ohtania, Y. Okada, M. Kawabe, *J. Cryst. Growth* **245**, 31 (2002)
44. K. Akahane, N. Yamamoto, M. Tsuchiya, *Appl. Phys. Lett.* **93**, 041121 (2008)
45. R. Oshima, A. Takata, Y. Okada, *Appl. Phys. Lett.* **93**, 083111 (2008)
46. S. Kiravittaya, O.G. Schmidt, *Appl. Phys. Lett.* **86**, 206101 (2005)
47. G. Springholz, V. Holy, M. Pinczoltis, G. Bauer, *Science* **282**, 734 (1998)
48. G.S. Solomon, *Appl. Phys. Lett.* **84**, 2073 (2004)
49. K. Akahane, T. Kawamura, K. Okino, H. Koyama, S. Lan, Y. Okada, M. Kawabe, *Appl. Phys. Lett.* **73**, 3411 (1998)
50. K. Hausler, K. Eberl, F. Noll, A. Trampert, *Phys. Rev. B* **54**, 4913 (1996)
51. Y.H. Xie, S.B. Samavedam, M. Bulsara, T.A. Langdo, E.A. Fitzgerald, *Appl. Phys. Lett.* **71**, 3567 (1997)
52. K. Yamaguchi, E. Waki, H. Hasegawa, *Jpn. J. Appl. Phys.* **36**, L871 (1997)
53. K. Yamaguchi, K. Kawaguchi, T. Kanto, *Jpn. J. Appl. Phys.* **41**, L996 (2002)
54. K.L. Kavanagh, M.A. Capano, L.W. Hobbs, J.C. Barbour, P.M.J. Maree, W. Schaff, J.W. Mayer, D. Pettit, J.M. Woodall, J.A. Stroschio, R.M. Feenstra, *J. Appl. Phys.* **64**, 4843 (1988)
55. T. Kanto, K. Yamaguchi, *Jpn. J. Appl. Phys.* **44**, 7690 (2005)
56. T. Kanto, K. Yamaguchi, *J. Appl. Phys.* **101**, 094901 (2007)

Hidenobu Nakao

Contents

22.1	Introduction.....	846
22.2	Assembling MNPs in One Dimension.....	847
	22.2.1 Chemical Self-Assembly.....	847
	22.2.2 Physical Means.....	849
	22.2.3 Template-Assisted Assembly.....	849
22.3	Highly Aligned DNA as Templates for 1D Assembly of MNPs.....	850
	22.3.1 Stretching and Aligning DNA Molecules on Surfaces.....	851
	22.3.2 Assembling AuNPs onto Aligned DNA Molecules.....	854
22.4	Fabrication and Patterning of Metallic Nanoarrays with Long-Range Order.....	861
	22.4.1 Preparation of Longer Metallic Nanoarrays with DNA Nanofibers.....	861
	22.4.2 Transfer Printing of Metallic Nanoarray.....	866
22.5	Conclusions.....	867
	References.....	869

Abstract

This chapter concerns simple experimental approaches for constructing metallic nanoarrays on a solid surface for applications to miniaturized optical devices, sensors, and single-molecule detection. Simple interface (air-liquid) moving leads to the controlled formation of one-dimensional (1D) nanoarrays of DNA or its nanofiber without special equipment. The assembly of metallic nanoparticles onto DNA can be driven by electrostatic binding of gold nanoparticles with positive charges, leading the formation of 1D metallic nanoarrays. Specially, a method based on the process of evaporation-induced self-assembly with DNA

H. Nakao (✉)

Ion Beam Group, National Institute for Materials Science, Ibaraki, Japan

e-mail: NAKAO.hidenobu@nims.go.jp

and drying front movement leads to highly aligned 1D metallic nanoarrays with a longer scale. Higher anisotropic coupling of localized plasmon is observed in the arrays when the light is polarized parallel to the arrays, indicating a uniaxial alignment of Au nanoparticles along the arrays. Finally, the fabrication and patterning of metallic nanoarrays achieved with transfer-printing techniques are described.

22.1 Introduction

Metal nanoparticles (MNPs) such as Au or Ag can confine light (electromagnetic fields) to their dimensions on the order of or smaller than the wavelength. Such properties, called localized plasmon resonances (LPRs), are based on interactions between electromagnetic radiation and conduction electrons at metallic interfaces or in metallic nanostructures, leading to an enhanced optical near field of sub-wavelength dimension below the optical diffraction limit [1]. LPRs of MNPs are tunable throughout the visible and near-infrared region of the spectrum as a function of particle size, shape, aggregation state, and local environment [1]. When MNPs are organized in closely spaced arrays, their LPR peak is shifted toward lower energy, and the bandwidth increases because the dielectric constant of the surrounding MNPs is increased [1–3]. Since such a one-dimensional (1D) MNP array can exhibit coupled modes due to near-field interactions between adjacent MNPs, it is possible to propagate electromagnetic waves (light) with a transverse confinement below the diffraction limit (plasmon waveguides). Researchers have developed plasmon waveguides that operate well below the optical diffraction limit, $\lambda/2$, down to $\lambda/20$ [1–5]. Incident radiation on one particle gives rise to plasmon oscillation, which can induce plasmon oscillations in neighboring MNPs that are sufficiently close. The light coupled through nanoparticle plasmons can then propagate along the array, around corners, and through T junctions. Molecules absorbed by the surface of the array undergo a surface-enhanced Raman scattering (SERS) effect, enhancing its Raman signal [6–8]. This process has attracted much attention, due to its potential applications in miniaturized optical devices, sensors, and single-molecule detection via SERS [9–13]. Thus, constructing various architectures of ordered MNPs and investigating the light localized in such architectures should be of great interest.

In order to utilize these arrays for the above applications, we must know their precise assembly and patterning on solid surfaces. Here, we describe our own approach for fabricating 1D MNP arrays on surfaces. In our assembly, highly aligned DNA molecules or nanofibers on a surface are used as a 1D template and can be driven by simple interface (air-liquid) movement. Positively charged MNPs can be explored to produce MNPs that have strong binding properties with DNA strands, leading to highly aligned 1D metallic nanoarrays on surfaces. Furthermore, preparation and patterning of metallic nanoarrays with long-range order are presented using DNA nanofibers and transfer-printing (TP) techniques. Finally, optical applications that take advantage of light fields localized on prepared metallic nanoarrays are discussed.

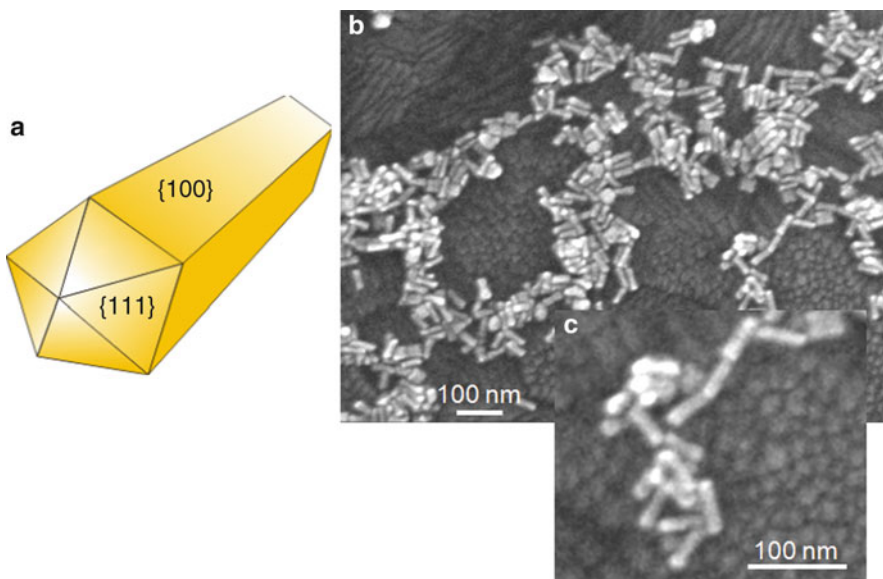


Fig. 22.1 (a) Schematic of three-dimensional (3D) morphology of a gold nanorod. (b) SEM image of the gold nanorod with the aspect ratio of 3.5. (c) Enlarged image of **b** (courtesy of Dr. K. Tsukamoto)

22.2 Assembling MNPs in One Dimension

Controlling assemblies of MNPs is useful for numerous sensing or electronic applications. 1D array of MNPs strongly absorbs light of specific wavelengths with polarizations parallel to the long axes oriented in the same direction, thus exhibiting useful properties for photonic applications. In general, MNPs can be organized using bottom-up approaches based on self-assembly. Simple self-assembly strategies introduce functional groups (ligands) onto MNPs, as specific physical and chemical affinities such as covalent or noncovalent (van der Waals, hydrophobic, or electrostatic) interactions can be exploited to achieve precise self-assembly of MNPs. With alkanethiol molecules, preferential binding of thiols to the {111} surface is obtained [14, 15].

22.2.1 Chemical Self-Assembly

Gold nanorods (AuNRs) with various aspect ratios have {111} at each end and {100} at their sides (Fig. 22.1). The most popular synthetic method for such AuNRs is that of seed-mediated nanoparticle growth in the presence of surfactant, as introduced by the Murphy group [9]. In the seed-mediated growth method, cetyltrimethyl ammonium bromide (CTAB) used as surfactant can form a bilayer around AuNR rather

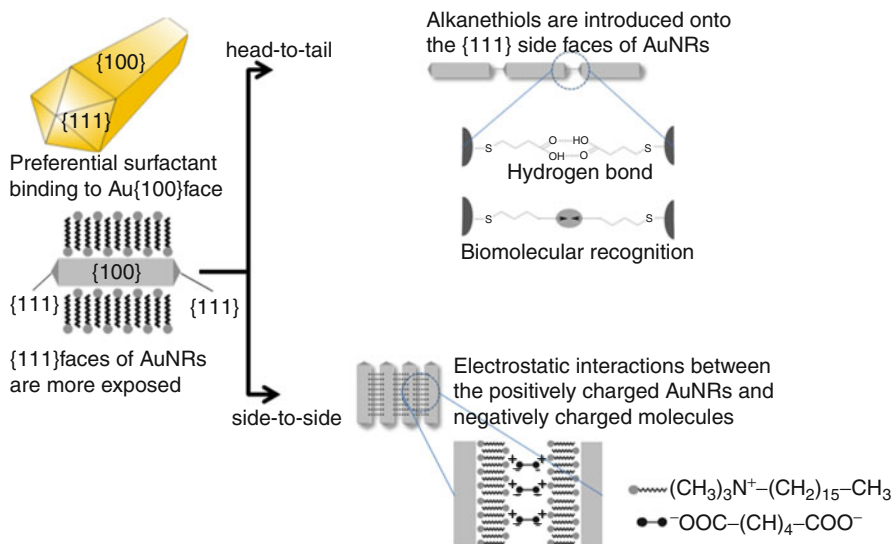


Fig. 22.2 Schematic of head-to-tail and side-to-side assemblies of gold nanorods

than a micellar form and prefers to bind with the {100} longitudinal side surface of the AuNR rather than the {111} end surface (Fig. 22.2). Thus, the {111} side faces of AuNRs are more exposed and accessible to the alkanethiols, preferentially binding to such faces. In several reports, alkanethiols were introduced onto the {111} side faces of AuNRs through hydrogen bonds [16] between alkanethiol molecules or through binding of biomolecules [17] to the alkanethiol layer, resulting in a head-to-tail chain-like formation of AuNR aggregates.

An alternative strategy for assembling AuNRs is to use side-to-side formation between {100} longitudinal side surfaces capped with the cationic CTAB bilayer. Simple concentration of AuNR solutions leads to preferential side-to-side assembly [18]. This process is entropically driven, in part by release of water and counter ions from the interface of adjacent AuNRs. Other side-to-side assemblies of AuNRs can also be prepared in a pH-dependent manner [19]. In this case, AuNRs capped with the cationic CTAB bilayer, are incubated with adipic acid ($\text{HOOC}(\text{CH}_2)_4\text{COOH}$). At pH values below the pKa of carboxylic acid, no particular assembly of nanorods is observed, but at pH 7–8, the deprotonated adipic acid acts as a short rigid bridge between AuNRs. As described above, 1D arrays of MNPs can behave as waveguides with high-field confinement. Recent work suggests that light propagation between adjacent particles can be increased by changing the geometry to the side-to-side formation of nanorods [2, 3].

Furthermore, De Vries et al. reported a simple method to place target molecules specifically at two diametrically opposed positions in the molecular coating of MNPs [20, 21]. This approach is based on functionalization of the polar singularities that must form when a curved surface is coated with ordered monolayers, such

as a phase-separated mixture of ligands. The molecules placed at these polar defects were used as chemical handles to form 1D AuNP chains.

22.2.2 Physical Means

Current lithography methods and microcontact printing can either directly produce arrays of MNP [2, 3, 22] or predefine a surface (geometrically, chemically, or electrostatically) to assist the assembly of MNPs on a surface [23–26]. Scanning probe nanolithography techniques with a local interaction between the probe and the substrate have been applied to patterning of self-assembly monolayers. One such technique is dip-pen nanolithography [27], where an atomic microscope tip is utilized as a pen to deposit general organic molecules directly onto solid substrates without any complicated processing steps (Fig. 22.3a). Barsotti et al. chemically directed mercaptopropionic acid-protected AuNPs onto the mercaptohexadecanoic acid lines, pre-patterned by dip-pen nanolithography [28].

In different MNP assembly approaches, interfaces such as gas-solid and liquid-liquid play important roles. The Langmuir-Blodgett technique is a typical interfacial assembly process [29–31]. Surface-protected MNPs are generally made to float over a water surface using hydrophobic interactions. At the water-air interface, MNPs form a monolayer, which is slowly compressed and transferred during compression, using horizontal or vertical lift-off, to substrates such as silicon (Fig. 22.3b). Using this technique, uniform 1D arrays of MNPs with sizes ranging from a few nanometers to a few micrometers can be readily produced with tunable particle density. Thus, 1D arrays or films of various well-ordered MNPs can be achieved [32].

Furthermore, an alternating electric field (dielectrophoresis) assembly of particles also gives composite wire-like structures, for example, if AuNPs are used [33–35]. AuNPs with a diameter of 10–20 nm are assembled via dielectrophoresis into long wires of micrometer thickness (Fig. 22.3c). Mertig's group reported 1D palladium nanowires grown from an aqueous palladium salt solution by dielectrophoresis, which have a thickness of 5–10 nm and a length of up to several micrometers [36].

22.2.3 Template-Assisted Assembly

Directional organization using suitable templates is the best approach for creating 1D assemblies. Various templates are available to achieve this purpose. Linear soft templates (e.g., organic polyelectrolytes [37–39] and biomolecules [40–44]) and hard templates (e.g., inorganic wires [45–48] and crystal step edges [49, 50]) are utilized for creating 1D MNP assemblies. For linear electrolytes acting as 1D scaffolds, Minko et al. reported Pd nanoparticles assembled onto cationic poly(2-polyvinyl pyridine) P2VP scaffolds, first by absorbing PdCl₄ anions onto the polyelectrolyte, via electrostatic interactions, followed by chemical reduction [51].

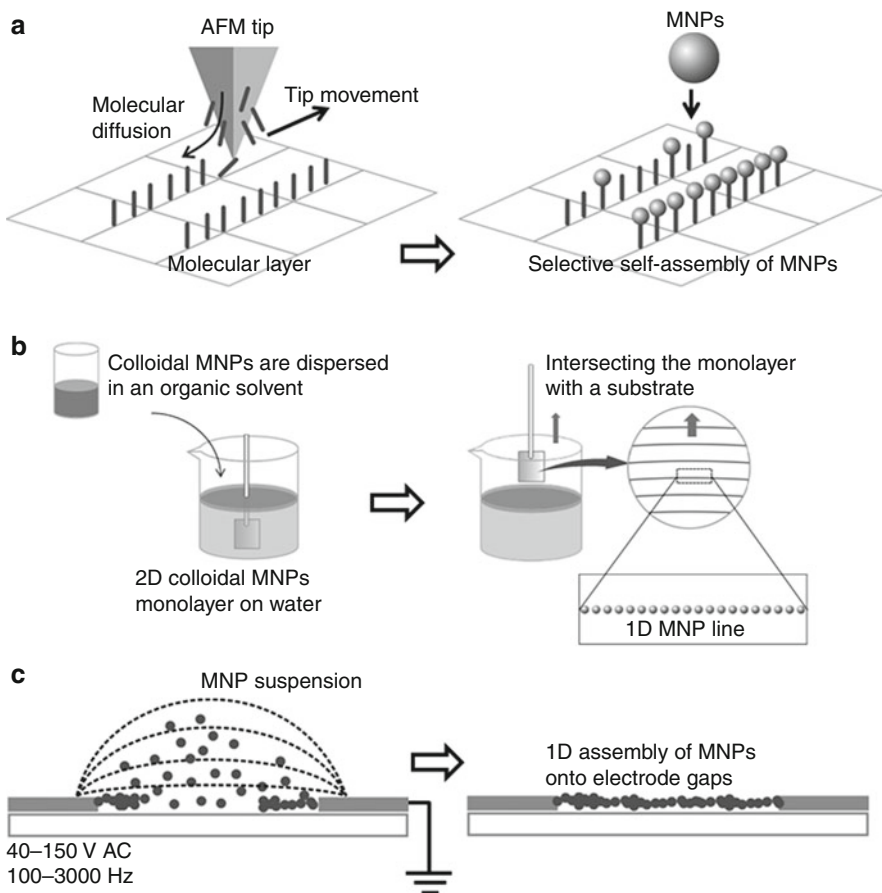


Fig. 22.3 Physical approaches for fabricating 1D MNP arrays on surfaces. (a) MNP are deposited or self-organized on the patterns fabricated with dip-pen nanolithography. (b) 1D MNP arrays of particles can be deposited on the substrate upon lifting through a stick-slip motion of the contact line. (c) Microwires of MNPs are assembled in an alternating electric field between two electrodes

Like polyelectrolytes, biomolecules such as DNA, or proteins, they are useful 1D templates. Their structures can be manipulated, and MNPs can be specifically located on their surfaces. For example, attaching AuNPs to linear or tile-like DNA structures creates fascinating nanoarchitectures [52–57].

22.3 Highly Aligned DNA as Templates for 1D Assembly of MNPs

DNA has a well-defined structure for the bottom-up construction of artificial nanostructures and networks in one, two, and three dimensions [58–64]. In particular,

the specificity of Watson-Crick base pairing enables the programming of its intramolecular and intermolecular associations then makes use of its unique molecular recognition and self-assembly capabilities to construct DNA-based architectures. Having a diameter of 2 nm and a virtually infinite length, providing a large variety of binding sites for different metal ions, and having remarkable mechanical properties, DNA constitutes an ideal template for organizing metallic and semiconductor nanoparticles into 1D assemblies. Metallic wires grown on DNA have been observed to possess peculiar transport properties both at room temperature and at low temperature and are thus good candidates for optoelectronic applications.

22.3.1 Stretching and Aligning DNA Molecules on Surfaces

Since DNA molecules in solution have the conformation of a random coil, they must be stretched and aligned on surfaces to create templates of 1D arrays. Generally, DNA molecules have been stretched and aligned at the macroscopic or single-molecule level by hydrodynamic flow [65–67], meniscus forces [68–72], electric field [73, 74], atomic force microscopy (AFM) [75, 76], optical trapping [77], or magnetic tweezers [78]. Surface modifications (e.g., silanization [68–71] and poly-L-lysine modification [79] of substrate surfaces) have also been utilized to facilitate the fixation and the stretching of DNA molecules using the above methods. Though controlling the interaction between DNA molecules and surfaces is very important for stretching and aligning DNA molecules, the interaction mechanism at the chemical structure level has not been sufficiently investigated.

We have reported a useful technique for reproducibly stretching and aligning DNA on surfaces. The point of this technique is controlling the interaction between surfaces and DNA using a polymer coating [80]. Chemical structures of the coating polymers selected in this study are presented in Fig. 22.4. A solution of 5 μL of DNA (4.5 ng/ μL) in TE buffer (10 mM Tris-HCl and 1 mM EDTA, $pH = 8$) was deposited on such polymer-coated glass surfaces, and its droplet was then sucked up using pipette. When a droplet of DNA solution on a surface is sucked up, the surface tension at the moving air-water interface is sufficient to stretch and align the molecules along the central direction of the droplet (Fig. 22.5).

The stretching of DNA on surfaces coated with various polymers was examined. We observed fluorescence microscopic images of DNA deposited on various polymer-coated coverslips (Fig. 22.6). On uncoated surfaces, the observed image revealed that only a few molecules were partially stretched and that many molecules were aggregated. Because the glass surface has strong polar groups, it seems that DNA interacts with the surface strongly and nonspecifically. However, DNA molecules were not sufficiently fixed on PVB-coated surfaces (Fig. 22.6a). PVB-coated glasses have hydrophobic surfaces, so that the interactions of DNA having negative charges or hydrophilic groups with these surfaces are very weak. In contrast, the observed DNA molecules on PVCz- and PPhenaz-coated coverslips were sufficiently fixed and stretched (Fig. 22.6b, c). In addition, these images demonstrate that DNA molecules are stretched and aligned in a central direction

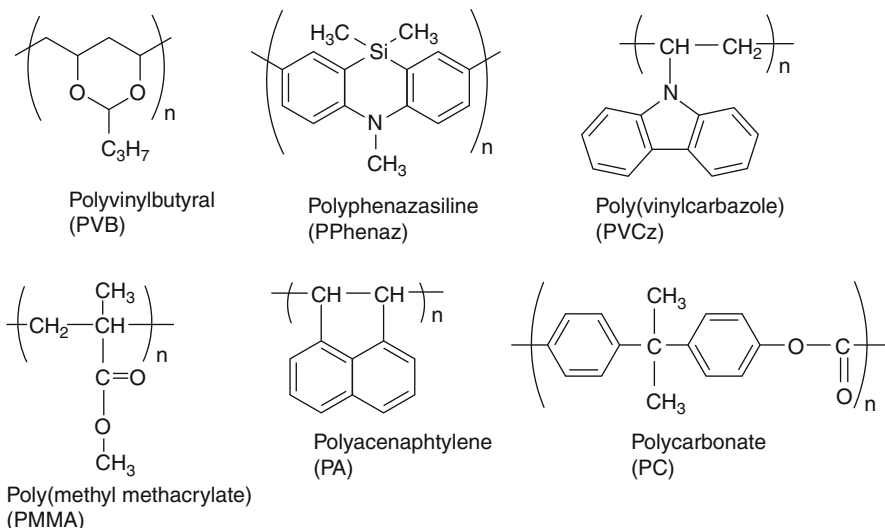


Fig. 22.4 Chemical structures of polymers in this study

The polymer solution (50 ml) was deposited on the coverslip and spin coated for 20 s at 5000 rpm

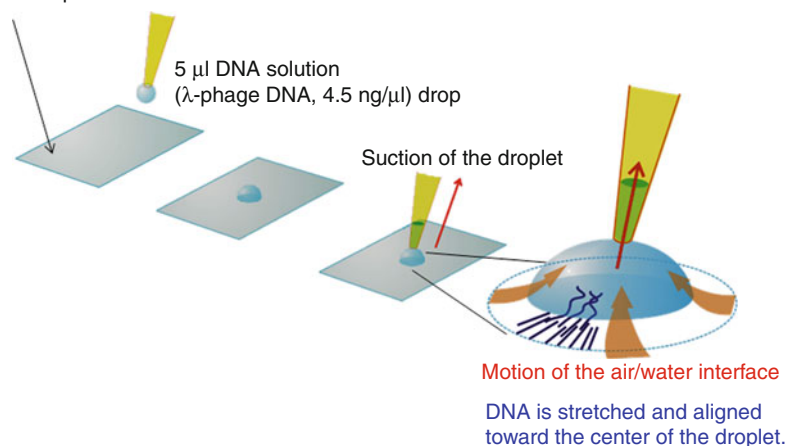


Fig. 22.5 Procedure of DNA stretching and alignment on surfaces (Reprinted with permission from Ref. [81]. Copyright (2012) by the Japan Society for Analytical Chemistry)

of the DNA droplet. Thus, it seems that PVCz- and PPhenaz-coated coverslips are useful for depositing and imaging well-stretched DNA. Fluorescence microscopy images reveal that the length of the well-stretched DNA on PPhenaz surface was $23.7 \pm 3.4 \mu\text{m}$ ($n = 35$) and that of the PVCz surface was $23.1 \pm 3.8 \mu\text{m}$ ($n = 30$).

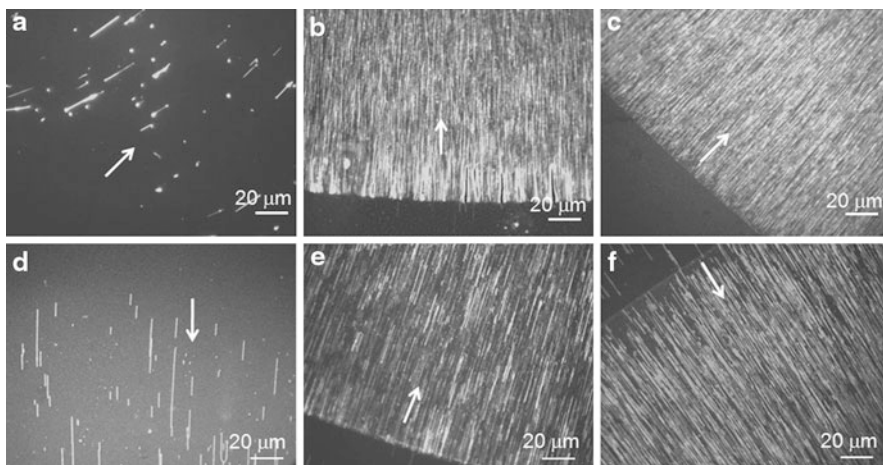


Fig. 22.6 Fluorescence microscopic images of DNA stretched on various polymer-coated surfaces. (a) PVB-coated glass. (b) PPhenaz-coated glass. (c) PVCz-coated glass. (d) PMMA-coated glass. (e) PA-coated glass. (f) PC-coated glass. The *arrow* indicates the central direction of the droplet (Reprinted with permission from Refs. [80] and [81]. Copyright (2012) by the American Chemical Society and the Japan Society for Analytical Chemistry)

The AFM image of well-stretched DNA on PPhenaz-coated coverslip is shown in Fig. 22.7. The AFM image of well-stretched DNA on PPhenaz-coated coverslip is presented in Fig. 22.7. The length of the DNA denoted segment A shown as A was $24.8 \mu\text{m}$, and its height was $\sim 1 \text{ nm}$. This length is similar to the average length of a single lambda DNA stretched on PPhenaz or PVCz surfaces, suggesting that the AFM image of segment A corresponds to a single lambda DNA. This idea is also supported by the fact that the observed height of the DNA is consistent with the height of a single double-stranded DNA imaged by AFM in a previous study [82,83]. Although the DNA stretched on PPhenaz or PVCz was longer than the crystallographic length of the 48.5 kb lambda DNA ($\sim 16.5 \mu\text{m}$), the length is close to that ($26.5 \mu\text{m}$) [70] on polystyrene obtained by Bension et al. Because the stretching force applied by the interface motion on hydrophobic surfaces is stronger than that on hydrophilic surfaces, the DNA is more stretched on PPhenaz and PVCz having hydrophobicity similar to that of polystyrene. DNA was almost the same on both polymers. Furthermore, the root mean square (RMS) roughness of the uncoated coverslip decreased from 5.013 to 0.319 nm after coating with PPhenaz and to 0.512 nm after coating with PVCz. It should be noted that these polymer coatings enabled the attainment of adequate AFM images of DNA on conventional coverslips.

Although PVCz and PPhenaz have hydrophobicity similar to that of PVB, DNA molecules sufficiently fixed and stretched on both surfaces. The results suggest that these polymers have a specific interaction with DNA. To understand the interactions between these polymers and DNA, we examined their absorption spectral properties. When we added DNA molecules to a solution (mixture of

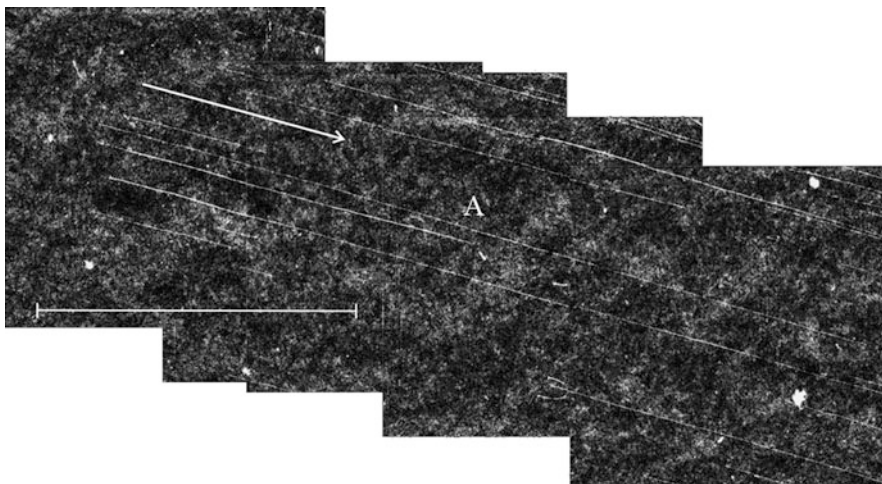


Fig. 22.7 AFM image of DNA stretched on PPhenaz-coated glass in a wide-range scan. DNA molecules are stretched and aligned in the direction of the *arrow* in the figure. The *white bar* denotes 10 μm . Height scale is 3 nm (Reprinted with permission from Ref. [80]. Copyright (2012) by the American Chemical Society)

TE-buffer (pH=8.0): THF = 1:1) containing PPhenaz, the absorption band at 390 nm, which is attributed to the π - π^* transition of PPhenaz, decreased gradually. Such a decrease in absorbance indicates strong interaction between the electronic state of the polymer and that of the DNA base. Consequently, it seems that these spectral changes are characteristic of an interaction, (e.g., π -stacking) between aromatic compounds and DNA [84–86]. We observed a similar phenomenon for PVCz. From the molecular viewpoint, their aromatic amine units are planar or almost planar, favoring the insertion of polymer units into the hydrophobic interior of the DNA base stack. We therefore assume that DNA attaches to surfaces through π -stacking between aromatic amines in polymers and base pairs in DNA. In addition, the λ -phage DNA used in this study was linear DNA with 12-base-long sticky ends, which expose the hydrophobic π -core (bases) on both ends of the helix. Since such positions have a strong affinity with surfaces, DNA molecules are preferentially anchored at either end [70]. Consequently, effective DNA stretching and fixations are achieved on surfaces. By using polymers containing π -units other than aromatic amines, we found that such polymers effectively stretch and fix DNA molecules on surfaces (Fig. 22.3e, f). Thus, the above results strongly indicate that π - π interaction is the important factor for DNA stretching and fixations in our system.

22.3.2 Assembling AuNPs onto Aligned DNA Molecules

The interaction of MNPs with DNA is a well-known phenomenon [87–90], and single- or double-strand DNA is decorated by MNPs, which can easily be imaged

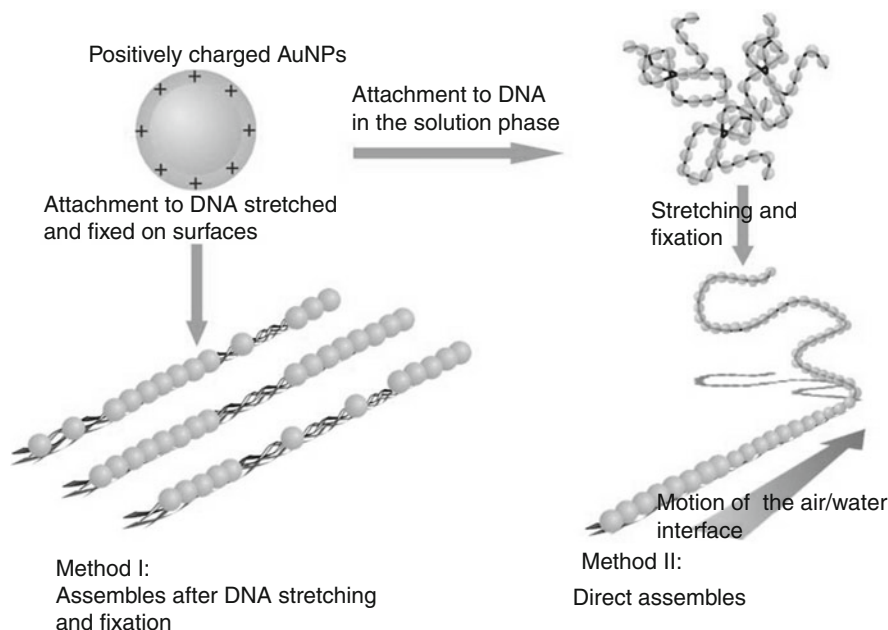


Fig. 22.8 Procedure of assembling AN-AuNPs onto DNA (Reprinted with permission from Ref. [96]. Copyright (2012) by the American Chemical Society)

by transmission electron microscopy (TEM) or AFM [91–93]. Various surface-functionalized AuNPs have been prepared to attach AuNPs securely to DNA molecules. In numerous studies, such AuNPs were prepared by surface modifications with cationic thiols [55, 56, 93] or intercalators [94, 95]. The 1D chains of AuNPs coated with cationic trimethyl(mercaptoundecyl) ammonium monolayers were electrostatically assembled along DNA molecules in solution by the relative molar quantities of AuNPs and DNA base pairs. Since psoralen acts as a specific intercalator for A-T base pairs, the functionalized AuNPs were assembled onto the pA-pT ds-DNA [94]. Furthermore, UV irradiations induced the reaction between the psoralen units and the thymine of DNA then covalently fixed AuNPs to the DNA.

Recently, we reported a one-step preparation of surface-functionalized AuNPs without ligand exchange [96]. Novel surface-functionalized AuNPs (AN-AuNPs) were prepared based on the conventional reduction of HAuCl_4 using aniline as a reducer, so that the AN-AuNPs had a positive charge and an aromatic ring on the surface (due to the formation of oxidized aniline during preparation), which resulted in their electrostatic binding to the negatively charged phosphate backbone of DNA. Characterization of prepared particles by electrophoresis analysis, zeta-potential measurements, and UV measurements revealed the presence of positive charges on their surfaces. We then experimented with assemblies of AN-AuNPs organized on DNA molecules. Two different procedures were used here (Fig. 22.8). In method I,

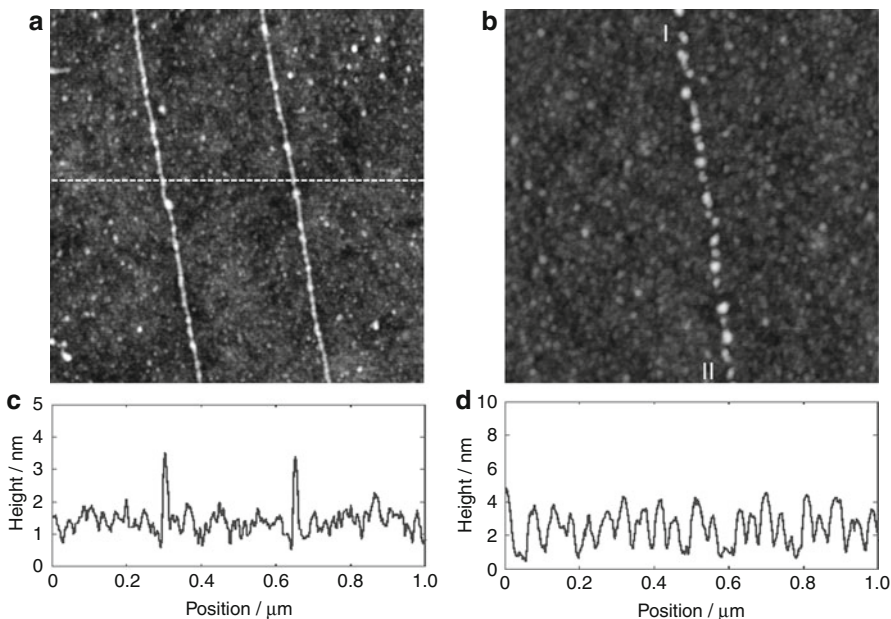


Fig. 22.9 AFM images of highly ordered assemblies of AN-AuNPs on DNA molecules using (a) method I and (b) method II. Image sizes are $1 \times 1 \mu\text{m}$. The height scale is 5 nm. (c) Scan profile along the *white line* of the image **b**. (d) Scan profile along particle line from I to II in image **b** (Reprinted with permission from Ref. [96]. Copyright (2012) by the American Chemical Society)

DNA was stretched and fixed on the surface according to the above method, which resulted in highly aligned DNA patterns formed on surfaces. Next, DNA molecules were treated with AN-AuNPs solution for 5 min then rinsed in water.

Before treatment with AN-AuNPs, the height (diameter) of DNA molecules imaged by AFM on the surface was ~ 1.0 nm, which agreed well with that of a single double-stranded DNA in the previous description. After treatment with AN-AuNPs, AFM observation revealed that many DNA molecules on the surfaces had contiguous particles with raised height, indicating that the observed heights of DNA molecules were 2.14 ± 0.35 nm. The majority of particles that can be distinguished from the background are 1.56 ± 0.21 nm. Consequently, it is reasonable that the increased DNA molecule heights after treatment were caused by particle deposition. In method II, we prepared a mixture of AN-AuNP solution and λ -DNA solution and incubated the mixture for 30 min. Next, samples were stretched and fixed on surfaces according to the above method. It was very interesting to note that AN-AuNPs with larger interparticle spacing were assembled along the DNA molecules in a necklace-like formation. Since the DNA molecules (to which AN-AuNPs were already attached) were stretched significantly by surface tension, interparticle spacing was greater. Figure 22.9 presents AFM images of AN-AuNPs-attached DNA molecules by two methods. By depositing different MNPs in interparticle spacing, it should be

Fig. 22.10 Chemical structures of PPhenaz-TMA and Phenaz-TMA

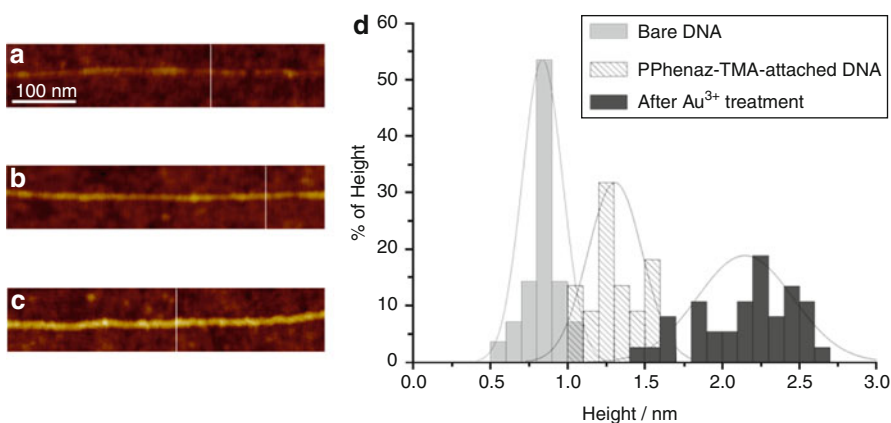
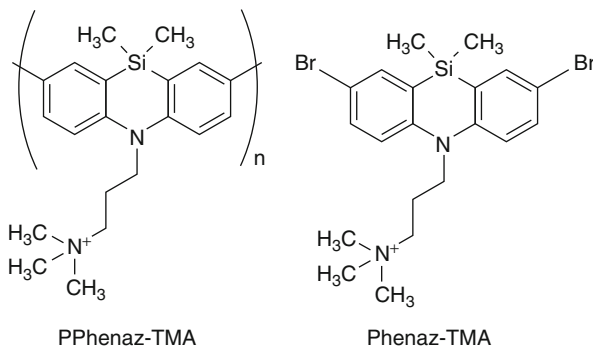


Fig. 22.11 Structural changes of DNA molecules induced by treatments. (a) AFM images of bare DNA. (b) AFM image of PPhenaz-TMA-attached DNA. (c) AFM image of PPhenaz-TMA-attached DNA after Au deposition. The height scale is 5 nm. (d) Histograms showing the height distributions of DNA induced by treatments

possible to tune the electrical or optical properties of linear arrays. Most recently, a one-step process achieved raspberry- [97] and mushroom-like aggregates [98] of AN-AuNPs that have 3D structures on a nano-order level. DNA templates should be also helpful in aligning such aggregates, which produce metallic nanoarrays having significant electrical and optical properties.

As described above, many DNA molecules were sufficiently stretched and fixed on PPhenaz-coated surfaces by the π - π interaction between π -conjugated units in polymer and base pairs in DNA. To enhance the solubility of PPhenaz in polar solvent such as water and interactions with DNA having negative charges, PPhenaz having alkylammonium salts on the N atom (PPhenaz-TMA) were synthesized (Fig. 22.10), directly forming π -conjugated polymer functionalized DNA (PPhenaz-TMA/DNA) nanowires [99]. AFM observations revealed structural changes of PPhenaz-TMA/DNA nanowires before and after treatments of AuCl_4^- (Fig. 22.11). Au depositions along PPhenaz-TMA/DNA nanowires could be also clarified by

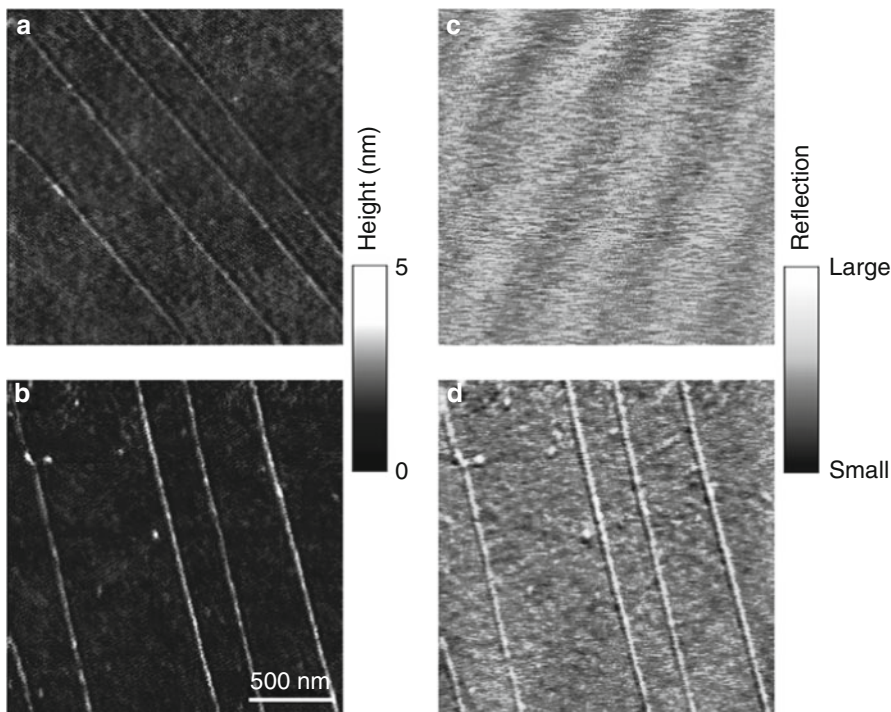


Fig. 22.12 AFM and SNOM images of PPhenaz-TMA/DNA nanowires before and after immersion in an Au^{3+} solution. (a) AFM topographic image and (b) SNOM image of PPhenaz-TMA/DNA nanowires before treatment. (c) AFM topographic image and (d) SNOM image of PPhenaz-TMA/DNA nanowires after treatment (Reprinted with permission from Ref. [99]. Copyright (2012) by the American Chemical Society)

using scanning near-field optical microscope (SNOM). Before treatment, the AFM topographic image of PPhenaz-TMA/DNA nanowires was observed, but the SNOM image of those was not observed (Fig. 22.12a, b). However, the SNOM image of PPhenaz-TMA/DNA nanowires after treatment was clearly observed, synchronizing exactly with its AFM topographic image (Fig. 22.12c, d). The observed SNOM image after treatment originates from near-field plasmon coupling between the probing tip and the AuNPs on PPhenaz-TMA/DNA nanowires, which leads to enhanced light scattering.

Phenaz-TMA-attached AuNPs (Phenaz-TMA/AuNPs) have also been prepared by photochemical reduction of AuCl_4^- with 365-nm UV light in the presence of Phenaz-TMA [81, 100]. Since Phenaz-TMA (Fig. 22.10), which is the monomer unit of PPhenaz-TMA, has an oxidation potential of +1.245 V (vs. SHE) [100], it cannot directly reduce AuCl_4^- , which has a reduction potential of +1.002 V (vs. SHE) [101]. However, Phenaz-TMA excited by photoreaction has greater

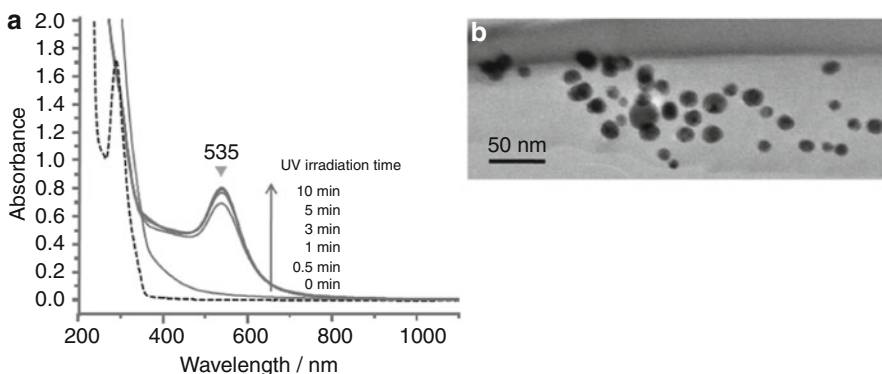


Fig. 22.13 (a) Absorption spectra corresponding to the growth of the Phenaz-TMA/AuNPs by photochemical reduction. A 3-mL aqueous solution containing Phenaz-TMA (150 nmol mL^{-1}) and AuCl_4^- (150 nmol mL^{-1}) was irradiated by 365-nm UV light with $6 \times 8 \text{ W}$. *Dashed line* is the spectrum of Phenaz-TMA without AuCl_4^- before UV irradiation. (b) TEM image of prepared Phenaz-TMA/AuNPs (Reprinted with permission from Ref. [81]. Copyright (2012) by the Japan Society for Analytical Chemistry)

reduction power, thus leading to a spontaneous electron transfer from excited Phenaz-TMA (oxidation) to AuCl_4^- (reduction). The photochemical formation of Phenaz-TMA/AuNPs was monitored by taking UV-vis absorption spectra as a function of irradiation time (Fig. 22.13a). As the HAuCl_4 solution was added, the absorption spectra of Phenaz-TMA resulted in a long tail on the long wavelength side (350–400 nm) of the peak. Au(III) gives stable complexes with C-, N-, P-, S-, or even O-donor ligands [102]. The resulting long tail on 350–400 nm suggests the formation of Au(III)-Phenaz-TMA complex. Thus, an effective electron transfer for reducing AuCl_4^- can be achieved with 365-nm UV light. Consequently, an absorption peak at 535 nm was clearly observed and increased with increasing irradiation time. This absorption peak is attributed to the surface plasmon resonance (SPR) absorbance band of AuNPs. After a certain irradiation time (10 min in this case), the UV absorption spectrum reached a state of stagnation because of the completion of photoreduction. The TEM micrograph indicated that the prepared Phenaz-TMA/AuNPs were 5–20 nm in diameter (Fig. 22.13b).

The interaction between Phenaz-TMA/AuNPs and DNA was subsequently examined. Figure 22.14a illustrates a typical DNA titration of Phenaz-TMA/AuNPs solution. As DNA was gradually added, the SPR band intensity gradually increased, and the peak maximum shifted toward lower energy. The binding of Phenaz-TMA/AuNPs to DNA brings them close together, modifying their local environment and changing SPR absorbance. Phenaz-TMA has alkylammonium salts on the N atom; additionally, it is oxidized during the preparation of AuNPs. Nanoparticles were electrostatically bound to the negatively charged phosphate backbone of DNA by using Phenaz-TMA/AuNPs with a positively charged protecting monolayer.

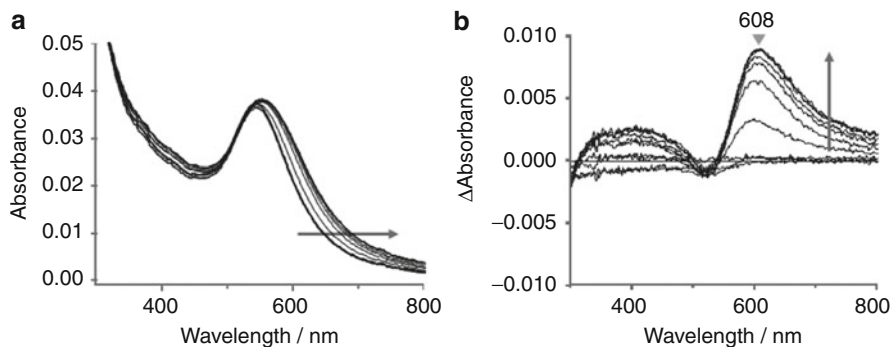


Fig. 22.14 (a) Absorption spectra taken during titration of Phenaz-TMA/AuNPs with λ -DNA and (b) their difference spectra. Here 0, 5, 10, 15, 20, 25, 30, 35, 40, 45, and 50 μL of DNA ($4.5 \text{ ng } \mu\text{L}^{-1}$) solution were added to 3 mL of Phenaz-TMA/AuNPs ($143 \text{ } \mu\text{g mL}^{-1}$) aqueous solution (Reprinted with permission from Ref. [81]. Copyright (2012) by the Japan Society for Analytical Chemistry)

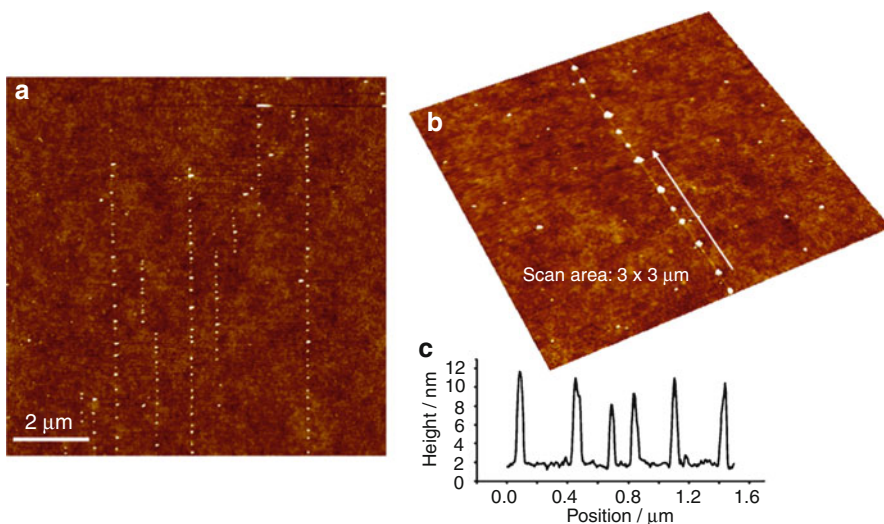


Fig. 22.15 AFM images of Phenaz-TMA/AuNPs assembled on DNA. (a) Image in a large scan range. (b) Image in a smaller scan range. (c) Scan profile along the *white arrow* in image **b**

Figure 22.14b also indicates differences in spectra changes. The absorption peak at 608 nm increases with an increase in DNA additions, suggesting the SPR of AuNPs assembled onto DNA molecules. Also, a mixture of Phenaz-TMA/AuNPs and DNA incubated for 1h was stretched and fixed on surfaces. AFM observations revealed that 1D arrays of particles with a diameter of 5–10 nm formed on surfaces (Fig. 22.15).

22.4 Fabrication and Patterning of Metallic Nanoarrays with Long-Range Order

Although DNA is an ideal 1D template to fabricate metallic nanoarrays, the length of prepared arrays essentially depends on that of the original DNA. For example, λ -DNA having a theoretical length of 16.5 μm is usually used as such a template. Since a 1D template with a greater geometrical aspect ratio leads to metallic nanoarrays with a larger scale, they can be easily manipulated during microscope observations, measuring their electrical and optical properties and sensing molecule interactions on them via SERS. Long DNA can be produced with some effort using a biochemical (enzymatic) technique such as polymerase chain reaction (PCR). In particular, rolling circle amplification (RCA) [103–105] can be used to produce a long single strand of DNA (>70 kb or more) [106], which has a repeating sequence with a designed repeat unit on the order of 100 bases, and these repeat units can be addressed by hybridization to their complementary DNA sequence. The applicability of RCA for preparing DNA with periodic binding motifs has been demonstrated for arranging MNPs and binding proteins [107, 108]. However, thus far, RCA and assembly reactions have been carried out solely in the liquid phase in a reaction tube. Such long DNA strands seem to be problematic for stretching and aligning on surfaces because of their intertwined state in solution.

22.4.1 Preparation of Longer Metallic Nanoarrays with DNA Nanofibers

Most recently, we have developed a simple method to create highly aligned DNA nanofibers on a surface [109]. This method is based on the processes of solvent vapor-induced buildup and controlled drying front movement and forms parallel aligned DNA nanofibers exceeding several hundred micrometers in length and 40 nm in diameter on a poly(dimethylsiloxane) (PDMS) sheet. Thus, this process leads to a DNA nanostrand that is much longer than the contour length of λ -DNA (16.5 μm) and facilitates manipulation of a single nanofiber under microscope observation, measuring its electrical and optical properties and connecting it to electrode pads. Various MNPs could also be attached to such nanofibers, forming metallic nanoarrays with a longer scale.

The formation process for long metallic nanoarrays with DNA nanofibers is illustrated in Fig. 22.16 [81, 110]. First, a mixture of Phenaz-TMA/AuNPs (or other positively charged AuNPs) and λ -DNA in a TE buffer ($pH = 8$) solution was added to 8 μL of ethanol. This solution was then deposited on a PDMS sheet, which was tilted at 15° during solvent evaporation to move the drying front downward. Solvent evaporation leads to a decrease in the volume of the solution, leaving behind line patterns. Line patterns of metallic nanoarrays were formed when DNA with AuNPs attached was continuously deposited at the highly concentrated finger positions. Metallic nanoarrays also exceed several hundred micrometers in length and can be made within 30 min.

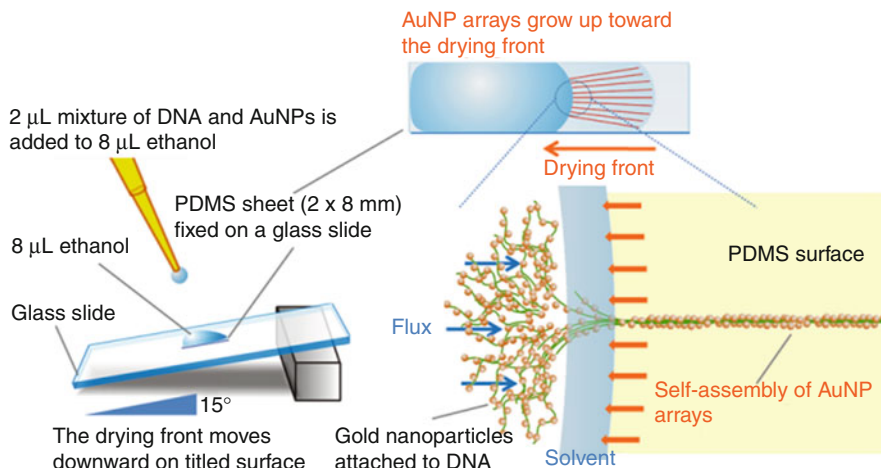
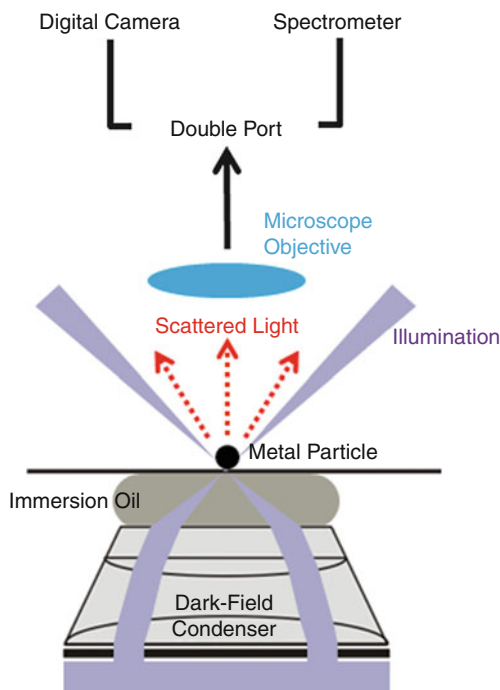


Fig. 22.16 Procedure of solvent vapor-induced assembly for generating metallic nanoarrays

Dark-field optical microscopy enables the observation of the LPR of single MNPs. In dark-field optical microscopy, only the light scattered by the structure under study is collected in the detection path, while directly transmitted light is blocked using a dark-field condenser. Dark-field light scattering images were acquired using a Nikon Eclipse 80i with a dark-field condenser and a Canon PowerShot A640 digital camera. The scattering spectra from the sample were collected by a miniature grating spectrometer (USB2000+, spectral resolution 3.67 nm), which was connected to the microscope using an optical fiber (core diameter 50 μm). Typical acquisition times were 5 s. Scattering spectra were corrected for spectral variations in system response and white-light intensity distribution through division by bright-field spectra recorded through the sample. The collection volume is nearly diffraction limited (cross-sectional area $\sim 1 \mu\text{m}^2$) for the 100 objective/fiber combination used here. [Figure 22.17](#) schematically illustrates the setup.

[Figure 22.18](#) is a dark-field optical microscope image depicting metallic nanoarrays on a PDMS sheet prepared by the above method. Many reddish lines originating from the plasmon resonance of AuNPs assembled on DNA nanofibers are clearly observed. Despite curvature of the lines at the edges of the surface due to the shape of the meniscus movement, they were aligned parallel to the moving drying front of the solvent. In general, individual spheres of AuNPs are observed as green particles originating from its LPR colors [111]. Before DNA attachment, many greenish spots were observed ([Fig. 22.19a](#)), and their scattering spectra exhibited a maximum peak at 570 nm (as indicated by spectra 1 and 2 in [Fig. 22.19c](#)). Thus, these spots denote isolated AuNPs. However, we observed a significant color change (reddish) in each of the spots along the DNA chains after DNA attachment ([Fig. 22.19b](#)). When two or more particles are brought into near-field interaction, the spectrum exhibits a clear red shift ([Fig. 22.19d](#)) [1, 112]. Each spot along the DNA cannot be resolved

Fig. 22.17 Schematic diagram of the experiment setup for dark-field imaging and spectroscopy



because of their diffraction-limited spots. However, the color clear is changed, as can also be seen from the corresponding scattering spectra exhibiting a maximum peak at 650 nm (as indicated by spectra 3 and 4 in Fig. 22.19c). Consequently, these results strongly indicate that many particles were assembled along the DNA. Figure 22.20 characterizes the morphology of the AuNP arrays by scanning electron microscopy (SEM), which indicated that dense packing of AuNPs 30 nm in diameter was realized. This may also be confirmed in enlarged SEM image (Fig. 22.20b), in which the width of the array with particles was about 100 nm, corresponding to approximately to 2–4 particles. As depicted in Fig. 22.20c, the particle alignments in microscopic areas vary indicating that AuNPs are nonuniformly attached over the entire nanofiber. Further optimizations of the pH or ion strength in solution would achieve more efficient formations of metallic nanoarrays.

As described above, when MNPs are organized in closely spaced arrays, their LPR peak shifts toward lower energy, and an increase in bandwidth is observed because the dielectric constant of the surrounding MNPs is increased. Such inter-particle spacing therefore serves as highly localized light fields for enhancing SERS. Termed “hot spots,” these highly confined fields also enable increasing fluorescent emission, albeit with more modest enhancement factors. Furthermore, since a 1D particle array can exhibit coupled modes due to near-field interactions between adjacent MNPs, it is possible to propagate electromagnetic waves (light) with a transverse confinement below the diffraction limit (plasmon waveguides). For our several-hundred-micrometer-long 1D metallic nanoarray, such optical properties

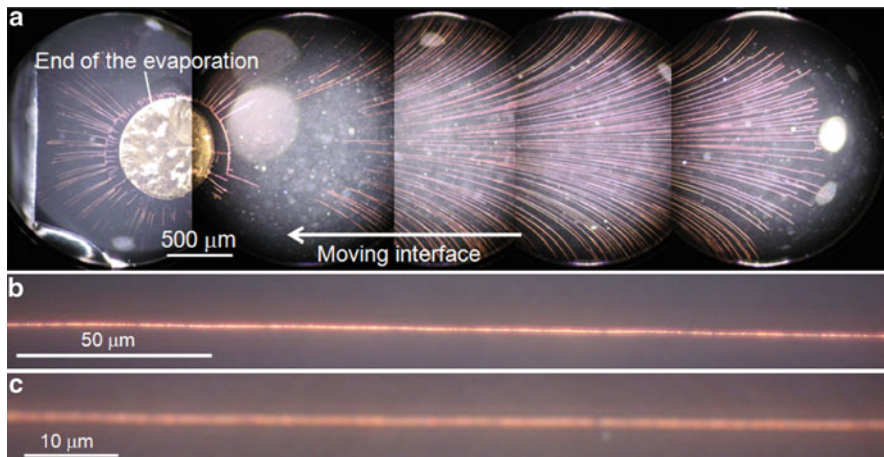


Fig. 22.18 Dark-field optical microscopy images of long metallic nanoarrays prepared with a DNA nanofibers as template. (a) Large-area image of metallic nanoarrays. (b) Enlarged image with 40 objective. (c) Enlarged image with 100 objective. The drying front moved from *right* to *left*

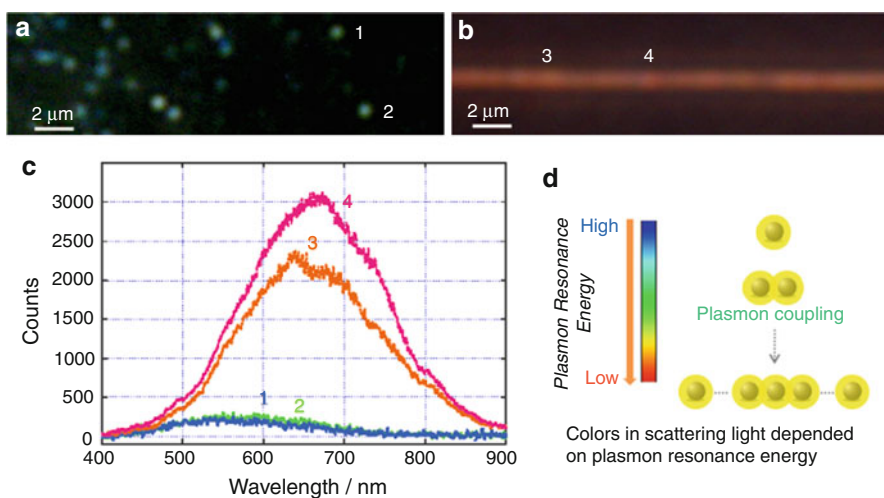


Fig. 22.19 Dark-field optical microscopy images of AuNPs (a) before attaching DNA and (b) after attaching DNA. (c) Scattering spectra of spots 1, 2, 3, and 4 in both images. (d) Schematic diagram of plasmon resonance energy induced by near-field coupling between MNPs

can be easily examined by microscopy. We observed dark-field optical images of our metallic nanoarrays under light polarization. The scattering light intensity of metallic nanoarrays is stronger when the light is polarized parallel to the arrays but weaker for vertical polarization (Fig. 22.21a, b). Furthermore, the scattering intensity exhibited a cosine-like dependence on the polarization angle (Fig. 22.21c).

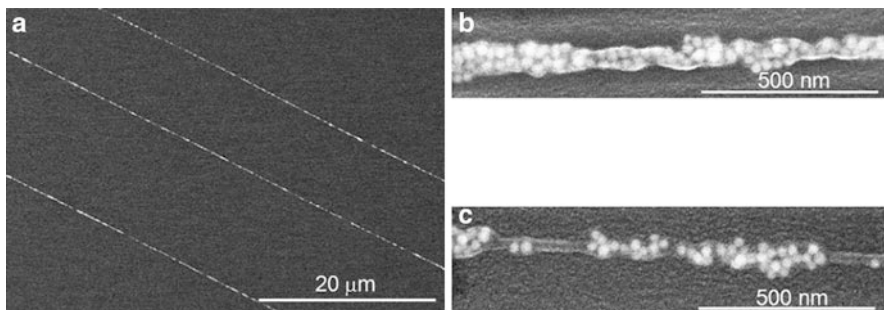


Fig. 22.20 SEM images depicting AuNP 30 nm in diameter arrays prepared on PDMS. (a) Large-area image of AuNP arrays. Enlarged images of arrays having (b) fully assembled and (c) partially assembled AuNPs

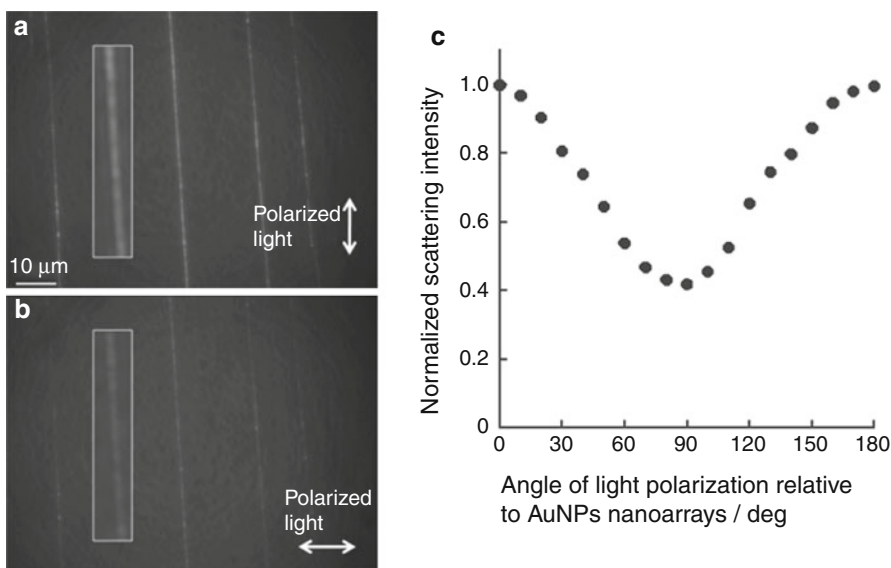


Fig. 22.21 (a, b) Polarized dark-field optical microscopy images of metallic nanoarrays. *Arrows* indicate the directions of polarized illumination. (c) Scattering light intensities from metallic nanoarrays as a function of the angle between the arrays and the polarization. The angle is 0° when the illumination polarization is parallel to the arrays (Reprinted with permission from Ref. [110]. Copyright (2012) by the Japan Society for Analytical Chemistry)

The enhancement of the light field localized in gaps between MNPs also strongly depends on incident light polarization [113]. We also obtained spectra for some microscopic areas along the AuNP array under polarized light (Fig. 22.22). In all areas, a stronger scattering intensity was obtained by polarizing the light parallel to the AuNP array than that obtained under perpendicular polarization. For an array of interacting point dipoles, the total point dipoles between adjacent particles coupled

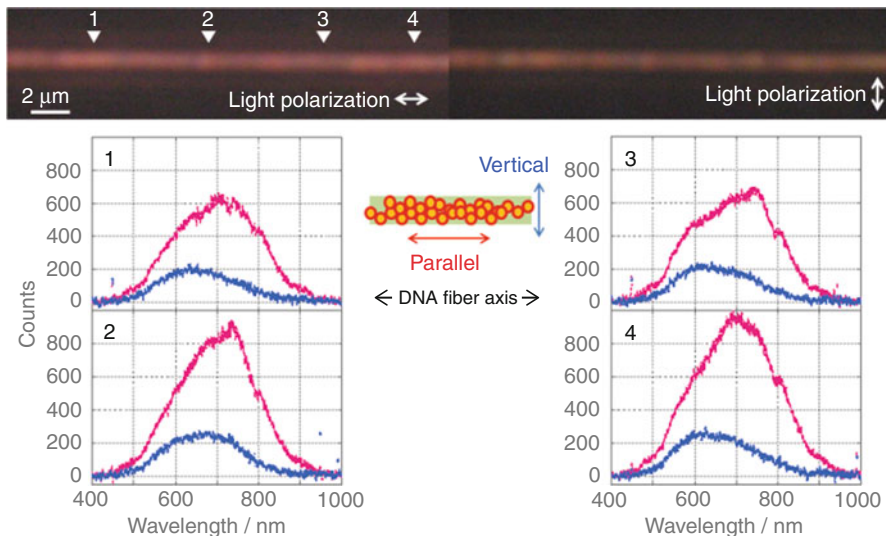


Fig. 22.22 Polarized dark-field optical microscopy images of the AuNP array and corresponding scattering spectra of microscopic areas (1, 2, 3, and 4) in the image. *Arrows* in the images indicate the directions of polarized illumination. *Red trace*: parallel polarization. *Blue trace*: perpendicular polarization

by optical near-field interaction have the greatest value when the polarization direction of the exiting light associates with the polarization of strongly interacting dipoles. Thus, the strong anisotropy of spectra obtained under polarized light indicates that the alignment of the AuNPs on the arrays was preferentially uniaxial to the array's axis. Furthermore, depending on the polarization direction of the exiting light, this leads to a blue shift in the LPR for excitation of transverse modes and a red shift for longitudinal modes. As indicated in Fig. 22.6, spectra obtained for the excitation parallel to the AuNP array exhibited a maximum peak at 700–750 nm, whereas those for perpendicular polarization exhibited a maximum peak at 600–650 nm. This additional result also supports the conclusion that prepared AuNP arrays have uniaxial anisotropy as described above. The intensity ratio was >3 , and this contrast could be further improved by increasing the uniformity of AuNPs attaching to DNA nanofibers.

22.4.2 Transfer-Printing of Metallic Nanoarray

We have reported that stretched DNA molecules and nanofibers initially present on the PDMS sheet were transferred onto another surface using transfer printing (TP) [109, 114]. Furthermore, by repeating TP onto the same surface, it was possible to realize a two-dimensional (2D) assembly of stretched DNA molecules and nanofibers. We also demonstrated the TP of 2D patterns of metallic nanoarrays onto

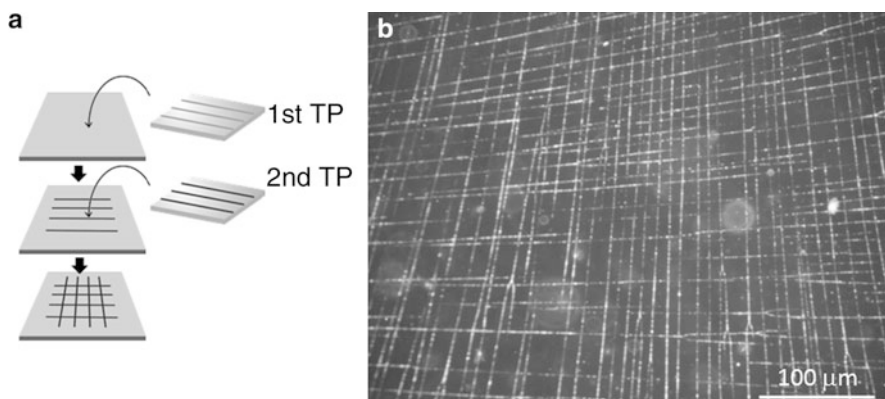


Fig. 22.23 (a) Procedure of TP for creating a 2D pattern of metallic nanoarrays. (b) Dark-field optical micrograph of 2D metallic nanoarrays (Reprinted with permission from Ref. [81]. Copyright (2012) by the Japan Society for Analytical Chemistry)

surfaces. To assemble the patterns, we first transferred metallic nanoarrays onto a coverslip and then overlapped the other PDMS sheet to which metallic nanoarrays were fixed onto the first one (Fig. 22.23a). Since the glass surface has polar groups stronger than those on the hydrophobic surface of PDMS, such arrays containing hydrophilic groups could be easily transferred from a PDMS surface to a glass surface. The dark-field micrograph of 2D metallic nanoarray patterns is depicted in Fig. 22.23b.

The main advantages of TP are that metallic nanoarrays can be printed in the desired position on the substrate and that they can be integrated on the same substrate by repeating the TP process. For example, metallic nanoarrays on the PDMS sheet can be printed onto electrode gaps (Fig. 22.24). Thus, the TP method allows the integration and more complex patterning of metallic nanoarrays and thus would facilitate fabrications for electronic/optical devices. By creating topological micropatterns on PDMS, it is also possible to achieve higher-ordered patterns of metallic nanoarrays.

22.5 Conclusions

In this chapter, we have presented our recent works on constructing metallic nanoarrays with a DNA template. Our methods first require DNA stretching and fixation on surfaces. We have demonstrated that surface coating with polymers containing π -conjugation units enhances DNA stretching and fixation on surfaces, due to the π - π interaction (π -stacking) between aromatic amines in polymers and base pairs in DNA molecules. Such polymer coating also enables adequate optical microscopy and AFM observation of well-stretched DNA on conventional coverslips. The next step is attaching MNPs to DNA. The AN-AuNPs prepared here

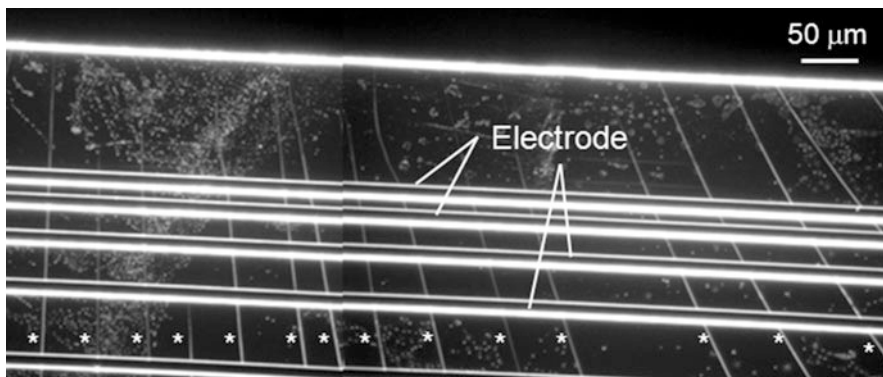


Fig. 22.24 Dark-field optical micrograph of metallic nanoarrays transferred onto micro electrode gaps. Transferred metallic nanoarrays are indicated by the asterisk (*) in image

strongly interacted with DNA. Two different assembly methods were employed. Consequently, continuous depositions and necklace-like depositions of AN-AuNPs along DNA molecules were achieved. The two approaches used in this study enabled different formations of metallic arrays of AN-AuNPs. Specifically, linear arrays of AN-AuNPs with interparticle spacing could be organized onto DNA molecules in a necklace-like formation. Furthermore, Phenaz-TMA/AuNPs were prepared by photochemical reduction of AuCl_4^- with 365-nm UV light in the presence of Phenaz-TMA. Phenaz-TMA/AuNPs also demonstrated strong interaction with DNA. DNA nanofibers were useful for constructing metallic nanoarrays with a long-range order. UV-vis spectroscopy and dark-field optical microscopic observations revealed assemblies of AuNPs on DNA and the LPR color changes involved. Furthermore, it was possible to create 2D patterns of metallic nanoarrays by the TP technique. Our methods summarized here do not require any special equipments and should provide a useful system for investigating the electromagnetic (light) field localized between MNPs.

Many applications of metallic nanoarrays enhance light fields localized between MNPs. A linear array of closely spaced MNPs can be viewed as a chain of interacting dipoles, which supports traveling polarization waves. This suggests applications of metallic nanoarrays as waveguides with high-field confinement, which would facilitate the realization of nano-optical devices. In the field of analytical chemistry, one promising application is optical sensors, and single-molecule detection via SERS has been reported. Gold nanospheres, immobilized on top of 1-mercaptopbenzoic acid monolayers, yielded an SERS enhancement factor of 10^7 , while other anisotropic shapes had enhancement factors of 10^8 – 10^9 [115]. Our highly anisotropic metallic nanoarrays therefore serve as highly localized light fields for enhancing SERS. In addition to SERS, surface-enhanced fluorescence has also been reported for molecules near the surfaces of MNPs [116–119]. While molecular fluorescence is quenched within 5 nm of the metal particle surface, at

distances of 10 nm or greater, fluorescence is enhanced up to 100-fold by the localized electric field and increased intrinsic decay of the fluorophore [116–119]. Our metallic nanoarrays can also be restructured by the TP technique and integrated into a desired position on various substrates, such as glass or silicon. Therefore, our method will advance the fabrication of nano-optical devices and optical sensor chips for single-molecule detection.

Acknowledgements The author is grateful for all the contributions from their collaborators, with special thanks to Dr. H. Hayashi (Nagoya Municipal Industrial Research Institute), Prof. H. Shiigi (Osaka Prefecture University), Mr. H. Karasawa, and Prof. F. Iwata (Shizuoka University). The author thanks Dr. H. T. Miyazaki (National Institute for Materials Science), Dr. S. Sugiyama, and Dr. T. Ohtani (National Agricultural and Food Research Organization) for the many most useful and inspiring scientific discussions. Financial support for these studies was provided by Iketani Science and Technology Foundation and Grants-in-Aid for Basic Sciences from the Ministry of Education, Science, Sports, and Culture, Japan (No. 18710106, No. 18310089 and No. 22550136).

References

1. S.A. Maier, *Plasmonics: Fundamentals and Application* (Springer, New York, 2007)
2. S.A. Maier, M.L. Brongersma, P.G. Kik, S. Meltzer, A.A.G. Requichia, H. Atwater, *Adv. Mater.* **13**, 1501 (2001)
3. S.A. Maier, P.G. Kik, H.A. Atwater, S. Meltzer, E. Harel, B.E. Koel, A.A. Requichia, *Nat. Mater.* **2**, 229 (2003)
4. W. Nomura, T. Yatsui, M. Ohtsu, *Appl. Phys. Lett.* **86**, 181108 (2005)
5. T. Yatsui, W. Nomura, M. Ohtsu, *Nano Lett.* **5**, 2548 (2008)
6. R. Garrell, *Anal. Chem.* **61**, 401A (1989)
7. A. Campion, P. Kambhampati, *Chem. Soc. Rev.* **27**, 241 (1998)
8. K. Kneipp, H. Kneipp, I. Itzkan, R.R. Dasari, M.S. Feld, *Chem. Rev.* **99**, 2987 (1999)
9. J. Murphy, T.K. Sau, A.M. Gole, C.J. Orendorff, J. Gao, L. Gou, S.E. Hunyadi, T. Li, *J. Phys. Chem. B* **109**, 13857 (2005)
10. B.P. Khanal, E.R. Zubarev, *Angew. Chem. Int. Ed.* **46**, 2195 (2007)
11. M.E. Stewart, C.R. Anderton, L.B. Thompson, J. Maria, S.K. Gray, J.A. Rogers, R.G. Nuzzo, *Chem. Rev.* **108**, 494 (2008)
12. P.K. Jain, X. Huang, I.H. El-Sayed, M.A. El-Sayed, *Acc. Chem. Res.* **41**, 1578 (2008)
13. S. Yamada, *Anal. Sci.* **25**, 1059 (2009)
14. C.X. Yu, J. Irudayaraj, *Anal. Chem.* **79**, 572 (2007)
15. J.Y. Chang, H.M. Wu, H. Chen, Y.C. Ling, W.H. Tan, *Chem. Commun.* 1092 (2005)
16. K.G. Thomas, S. Barazzouk, B.I. Ipe, S.T.S. Joseph, P.V.J. Kamat, *Phys. Chem. B* **108**, 13066 (2004)
17. K.K. Caswell, J.N. Wilson, U.H.F. Bunz, C.J. Murphy, *J. Am. Chem. Soc.* **125**, 13914 (2003)
18. N.R. Jana, L.A. Gearheart, S.O. Obare, C.J. Johnson, K.J. Edler, S. Mann, C.J. Murphy, *J. Mater. Chem.* **12**, 2909 (2002)
19. C.J. Orendorff, P. Hankins, C.J. Murphy, *Langmuir* **21**, 2022 (2005)
20. G.A. DeVries, M. Brunnbauer, Y. Hu, A.M. Jackson, B. Long, B.T. Neltner, O. Uzun, B.H. Wunsch, F. Stellacci, *Science* **315**, 358 (2007)
21. A.M. Jackson, J.W. Myerson, F. Stellacci, *Nat. Mater.* **3**, 330 (2004)
22. Q.H. Wei, K.H. Su, S. Durant, X. Zhang, *Nano Lett.* **4**, 1067 (2004)
23. C.R. Barry, N.Z. Lwin, W. Zheng, H.O. Jacobs, *Appl. Phys. Lett.* **83**, 5527 (2003)
24. L.M. Demers, D.S. Ginger, S.J. Park, Z. Li, S.W. Chung, C.A. Mirkin, *Science* **296**, 1836 (2002)

25. Y. Cui, M.T. Bjork, J.A. Liddle, C. Sonnichsen, B. Boussert, A.P. Alivisatos, *Nano Lett.* **4**, 1093 (2004)
26. Y. Yin, Y. Lu, Y. Xia, *J. Am. Chem. Soc.* **123**, 771 (2001)
27. S. Hong, R. Eby, S. Myung, B.Y. Lee, S.G. Rao, J. Jang, Dip-pen nanolithography, in *Scanning Probe Microscopies Beyond Imaging*, ed. by P. Samorí (WILEY-VCH Verlag GmbH & Co. KGaA, Weinheim, 2006), pp. 141–174
28. R.J. Barsotti Jr., F. Stellacci, *J. Mater. Chem.* **16**, 962 (2006)
29. S.W. Chung, G. Markovich, J.R. Heath, *J. Phys. Chem. B* **102**, 6685 (1998)
30. R.P. Sear, S.-W. Chung, G. Markovich, W.M. Gelbart, J.R. Heath, *Phys. Rev. E* **59**, R6255 (1999)
31. P. Yang, F. Kim, *Chem. Phys. Chem.* **3**, 503 (2002)
32. J. Huang, A.R. Tao, S. Connor, R. He, P. Yang, *Nano Lett.* **6**, 524 (2006)
33. K.D. Hermanson, S.O. Lumsdon, J.P. Williams, E.W. Kaler, O.D. Velev, *Science* **294**, 1082 (2001)
34. S.O. Lumsdon, D.M. Scott, *Langmuir* **21**, 4874 (2005)
35. K.H. Bhatt, O.D. Velev, *Langmuir* **20**, 467 (2004)
36. N. Ranjan, H. Vinzelberg, M. Mertig, *Small* **2**, 1490 (2002)
37. W.A. Lopes, H.M. Jaeger, *Nature* **414**, 735 (2001)
38. D. Wyrwa, N. Beyer, G. Schmid, *Nano Lett.* **2**, 419 (2002)
39. T. Reuter, O. Vidoni, V. Torma, G. Schmid, L. Nan, M. Oleiche, L. Chi, H. Fuchs, *Nano Lett.* **2**, 709 (2002)
40. J.D. Hartgerink, E. Beniash, S.I. Stupp, *Science* **294**, 1684 (2001)
41. J.D. Hartgerink, E. Beniash, S.I. Stupp, *Proc. Natl. Acad. Sci. USA* **99**, 5133 (2002)
42. M. Reches, E. Gazit, *Science* **300**, 625 (2003)
43. L. Li, S.I. Stuppe, *Angew. Chem. Int. Ed.* **44**, 1833 (2005)
44. W. Shenton, T. Douglas, M. Young, G. Stubbs, S. Mann, *Adv. Mater.* **11**, 253 (1999)
45. L.W. Yin, Y. Bando, Y.C. Zhu, D. Golberg, M.S. Li, *Adv. Mater.* **16**, 929 (2004)
46. W.Q. Han, A. Zettl, *Nano Lett.* **3**, 681 (2003)
47. Y. Wang, Z. Tang, X. Liang, L.M. Liz-Marzán, N.A. Kotov, *Nano Lett.* **4**, 225 (2004)
48. G. Ren, Y. Xing, *Nanotechnology* **17**, 5596 (2006)
49. F. Favier, E.C. Walter, M.P. Zach, T. Benter, R.M. Penner, *Science* **293**, 2227 (2001)
50. M.P. Zach, K.H. Ng, R.M. Penner, *Science* **290**, 2120 (2000)
51. S. Minko, A. Kiri, G. Gorodyska, M. Stamm, *J. Am. Chem. Soc.* **124**, 10192 (2002)
52. O. Harnack, W.E. Ford, A. Yasuda, J.M. Wessels, *Nano Lett.* **2**, 919 (2002)
53. K. Keren, M. Krueger, R. Gilad, G. Ben-Yoseph, U. Silvan, E. Braun, *Science* **72**, 297 (2002)
54. M. Mertig, L.C. Ciacchi, R. Seidel, W. Pompe, A.D. Vita, *Nano Lett.* **2**, 841 (2002)
55. M.G. Warner, J.E. Hutchison, *Nat. Mater.* **2**, 272 (2003)
56. T. Yonezawa, S. Onoue, S. Kimizuka, *Chem. Lett.* **31**, 1172 (2002)
57. J.D. Le, Y. Pinto, N.C. Seeman, K. Musier-Forsyth, T.A. Taton, R.A. Kiehl, *Nano Lett.* **4**, 2343 (2004)
58. P. Alivisatos, K.P. Johnson, X.G. Peng, T.E. Wilson, C.J. Loweth, M.P. Bruchez, P.G. Schultz, *Nature* **382**, 609 (1996)
59. R. Elghanian, R.C. Mucic, R.L. Letsinger, C.A. Mirkin, *Science* **277**, 1078 (1997)
60. N.C. Seeman, *Trends Biotechnol.* **17**, 437 (1999)
61. H. Yan, S.H. Park, G. Finkelstein, J.H. Park, T.H. LaBean, *Science* **301**, 1882 (2003)
62. Y. He, T. Ye, M. Su, C. Zhang, A.E. Ribbe, W. Jinag, C. Mao, *Nature* **452**, 198 (2008)
63. E.S. Andersen, M. Dong, M.M. Nielsen, K. Jahn, R. Subramani, W. Mamdouh, M.M. Golas, B. Sander, H. Stark, C.L.P. Oliveira, J.S. Pedersen, V. Birkedal, F. Besenbacher, K.V. Gothelf, J. Kjems, *Nature* **459**, 73 (2009)
64. S.M. Douglas, H. Dietz, T. Liedl, B. Hogberg, F. Graf, W.M. Shih, *Nature* **459**, 414 (2009)
65. C. Erler, M. Mertig, *J. Vac. Sci. Technol. B* **27**, 939 (2009)
66. K. Otobe, T. Ohtani, *Nucleic Acid Res.* **29**, e109 (2001)
67. H. Yokota, D.A. Nickerson, B.J. Trask, G. Van Den Engh, M. Hirst, I. Sadowski, R. Aebersold, *Anal. Biochem.* **264**, 158 (1998)

68. D. Bensimon, A.J. Simon, V. Croquette, A. Bension, *Phys. Rev. Lett.* **74**, 4754 (1995)
69. X. Michalet, R. Ekong, F. Fougerousse, S. Rousseaux, C. Schurra, N. Hornigold, M. Slegtenhorst, J. Wolfe, S. Povey, J.S. Beckmann, A. Bensimon, *Science* **277**, 1518 (1997)
70. J.F. Allemand, D. Bensimon, L. Jullien, A. Bensiom, V. Croquette, *Biophys. J.* **73**, 2064 (1997)
71. A. Bensimon, A. Simon, A. Chiffaudel, V. Croquette, V. Heslot, D. Bensimon, *Science* **265**, 2096 (1994)
72. Y. Okahata, T. Kobayashi, K. Tanaka, *Langmuir* **12**, 1326 (1996)
73. P.A. Smith, C.D. Nordquist, T.N. Jackson, T.S. Mayer, *Appl. Phys. Lett.* **77**, 1399 (2000)
74. X. Liang, K.J. Morton, R.H. Austin, S.Y. Chou, *Nano Lett.* **7**, 3774 (2007)
75. M. Rief, H. Clausen-Schaumann, H.E. Gaub, *Nat. Struct. Biol.* **6**, 346 (1999)
76. J. Hu, Y. Zhang, H. Gao, M. Li, U. Hartman, *Nano Lett.* **2**, 55 (2002)
77. Y. Arai, R. Yasuda, K. Akashi, Y. Harada, H. Miyata, K. Kinoshita Jr., H. Itoh, *Nature* **399**, 446 (1999)
78. S.B. Smith, L. Finzi, C. Bustamante, *Science* **258**, 1122 (1992)
79. A.T. Woolley, R.T. Kelly, *Nano Lett.* **1**, 345 (2001)
80. H. Nakao, H. Hayashi, T. Yoshino, S. Sugiyama, K. Otobe, T. Ohtani, *Nano Lett.* **2**, 475 (2002)
81. H. Nakao, *Anal. Sci.* **25**, 1387 (2009)
82. J.M. Kim, T. Ohtani, S. Sugiyama, T. Hirose, H. Muramatsu, *Amal. Chem.* **73**, 5984 (2001)
83. T. Thundat, D.P. Allison, R.J. Warmack, *Nucleic Acids Res.* **22**, 4224 (1994)
84. T. Yamamoto, T. Shimizu, E. Kurokawa, *React. Funct. Polym.* **43**, 79 (2000)
85. D. Yang, T. Strode, H.P. Spielmann, A.H.J. Wang, T.G. Burke, *J. Am. Chem. Soc.* **120**, 2979 (1998)
86. Y.-F. Song, P. Yang, *Polyhedron* **20**, 501 (2001)
87. A. Kumar, M. Pattarkine, M. Bhadhade, A.B. Mandale, K.N. Ganesh, S.S. Datar, C.V. Dharmadhikari, M. Sastry, *Adv. Mater.* **13**, 341 (2001)
88. J. Richter, R. Seidel, M. Kirsch, M. Mertig, W. Pompe, J. Plaschke, H.K. Schackert, *Adv. Mater.* **12**, 507 (2000)
89. W.E. Ford, O. Harnack, A. Yasuda, J.M. Wessels, *Adv. Mater.* **13**, 1793 (2001)
90. D. Zanchet, C.M. Micheel, W.J. Parak, D. Gerion, A.P. Alivisatos, *Nano Lett.* **1**, 32 (2001)
91. M. Mertig, L.C. Ciacchi, R. Seidel, W. Pompe, A. De Vita, *Nano Lett.* **2**, 841 (2002)
92. Y. Liu, W. Meyer-Zaika, S. Franzka, G. Schmid, M. Tsoli, H. Kuhn, *Angew. Chem. Int. Ed.* **4**, 95 (2003)
93. G. Wang, R.W. Murray, *Nano Lett.* **4**, 95 (2004)
94. F. Patolsky, Y. Weizmann, O. Lioubashevski, I. Willner, *Angew. Chem. Int. Ed.* **41**, 2323 (2002)
95. G. Wang, J. Zhang, R.W. Murray, *Anal. Chem.* **74**, 4320 (2002)
96. H. Nakao, H. Shiigi, Y. Yamamoto, T. Tokonami, T. Nagaoka, S. Sugiyama, T. Ohtani, *Nano Lett.* **3**, 1391 (2003)
97. H. Shiigi, Y. Yamamoto, N. Yoshi, H. Nakao, T. Nagaoka, *Chem. Commun.* 4288 (2006)
98. H. Shiigi, R. Morita, Y. Yamamoto, S. Tokonami, H. Nakao, T. Nagaoka, *Chem. Commun.* 3615 (2009)
99. H. Nakao, H. Hayashi, F. Iwata, H. Karasawa, S. Sugiyama, T. Ohtani, *Langmuir* **21**, 7945 (2005)
100. H. Nakao, H. Hayashi, K. Okita, *Anal. Sci.* **17**, 545 (2001)
101. A.J. Bard, R. Parsons, J. Jordan, *Standard Potentials in Aqueous Solution* (Dekker, New York, 1985)
102. M.C. Gimeno, The chemistry of gold, in *Modern Supramolecular Gold Chemistry*, ed. by A. Lagna (WILEY-VHC Verlag GmbH & Co. KGaA, Weinheim, 2008), pp. 41–48
103. G.T. Walker, M.C. Little, J.G. Nadeau, D.D. Shank, *Proc. Natl. Acad. Sci. USA* **89**, 392 (1992)
104. A. Fire, S.-Q. Xu, *Proc. Natl. Acad. Sci. USA* **92**, 4641 (1995)
105. H. Takahashi, K. Yamamoto, T. Ohtani, S. Sugiyama, *BioTechniques* **47**, 609 (2009)

106. L. Blanco, A. Bernad, J.M. Lázaro, G. Martin, C. Garmendia, M. Salas, *J. Biol. Chem.* **264**, 8935 (1989)
107. S. Beyer, P. Nickels, F.C. Simmel, *Nano Lett.* **5**, 719 (2005)
108. O.I. Wilner, S. Shimron, Y. Weizmann, Z.-G. Wang, I. Willner, *Nano Lett.* **9**, 2040 (2009)
109. H. Nakao, T. Taguchi, H. Shiigi, K. Miki, *Chem. Commun.* 1858 (2009)
110. H. Nakao, H. Hayashi, H. Shiigi, K. Miki, *Anal. Sci.* **25**, 1175 (2009)
111. C. Sonnichsen, T. Franzl, T. Wilk, G. von Plessen, J. Feldmann, O. Wilson, P. Mulvaney, *Phys. Rev. Lett.* **88**, 77402 (2002)
112. J. Prikulis, F. Svedberg, M. Käll, J. Enger, K. Ramser, M. Goksör, D. Hanstorp, *Nano Lett.* **4**, 115 (2004)
113. H. Xu, E.J. Bjerneld, M. Käll, L. Börjesson, *Phys. Rev. Lett.* **83**, 4357 (1999)
114. H. Nakao, M. Gad, S. Sugiyama, K. Otobe, T. Ohtani, *J. Am. Chem. Soc.* **125**, 7161 (2003)
115. C.J. Orendorff, A. Gole, T.K. Sau, C.J. Murphy, *Anal. Chem.* **77**, 3261 (2005)
116. K. Sokolov, G. Chumanov, T.M. Cotton, *Anal. Chem.* **70**, 3898 (1998)
117. J. Malicka, I. Gryczynski, J.R. Lakowicz, *Anal. Chem.* **75**, 4408 (2003)
118. A. Parfenov, I. Gryczynski, J. Malicka, C.D. Geddes, J.R. Lakowicz, *J. Phys. Chem. B* **107**, 8829 (2003)
119. J.R. Lakowicz, C.D. Geddes, I. Gryczynski, J. Malicka, Z. Gryczynski, K. Aslan, J. Lukomski, E. Matveera, J. Zhang, R. Badugn, J. J. Huang, *Fluorescence* **14**, 425 (2004)

Part V

Nanophotonic Systems

Nanophotonic Systems Based on Localized and Hierarchical Optical Near-Field Processes

23

Makoto Naruse

Contents

23.1	Introduction.....	876
23.2	System Architectures Based on Optical Excitation Transfer.....	877
23.2.1	Optical Excitation Transfer via Optical Near-Field Interactions and Its Functional Features.....	877
23.2.2	Parallel Architecture Using Optical Excitation Transfer.....	879
23.2.3	Secure Signal Transfer in Nanophotonics.....	883
23.3	Networks of Optical Near-Field Interactions.....	885
23.3.1	Optimal Network of Near-Field Interactions.....	885
23.3.2	Autonomy in Optical Excitation Transfer.....	888
23.4	Hierarchical Architectures in Nanophotonics.....	890
23.4.1	Physical Hierarchy in Nanophotonics and Functional Hierarchy.....	890
23.4.2	Hierarchical Memory Retrieval.....	891
23.4.3	Hierarchical Optical Elements.....	894
23.5	Shape-Engineered Nanostructures for Polarization Control for Nanophotonic Systems.....	897
23.5.1	Polarization and Geometry on the Nanometer Scale.....	898
23.5.2	Layout-Dependent Polarization Control.....	902
23.5.3	Application to Authentication Function.....	902
23.6	Summary.....	904
	References.....	906

Abstract

Nanophotonics offers ultrahigh-density system integration since it is based on local interactions between nanometer-scale matter via optical near-fields and is

M. Naruse (✉)

Photonic Network Research Institute, National Institute of Information and Communications Technology, Tokyo, Japan

Nanophotonics Research Center, The University of Tokyo, Tokyo, Japan

e-mail: naruse@nict.go.jp

not constrained by the diffraction limit. In addition, it also gives qualitatively novel benefits over conventional optics and electronics. From a system architectural perspective, nanophotonics drastically changes the fundamental design rules of functional optical systems, and suitable architectures may be built to exploit this. This chapter discusses system architectures for nanophotonics, taking into consideration the unique physical principles of optical near-field interactions, and also describes their experimental verification based on enabling technologies, such as quantum dots and engineered metal nanostructures. In particular, two unique physical processes in light–matter interactions on the nanometer scale are examined. One is optical excitation transfer via optical near-field interactions, and the other is the hierarchical property of optical near-fields. Also, shape-engineered nanostructures and their associated polarization properties are characterized from a system perspective, and some applications are shown. The architectural and physical insights gained enable realization of nanophotonic information systems that overcome the limitations of conventional light and provide unique functionalities that are only achievable using optical near-field processes.

23.1 Introduction

To accommodate the continuously growing amount of digital data and ubiquitous devices, as well as qualitatively new requirements demanded by industry and society, such as safety and security, optical technologies are expected to become more highly integrated and to play a wider role in enhancing system performance. However, many technological difficulties remain to be overcome in adopting optical technologies in critical information and communication systems; one problem is the poor integrability of optical hardware due to the diffraction limit of light [1, 2].

Nanophotonics, on the other hand, which is based on local interactions between nanometer-scale matter via optical near-fields, offers ultrahigh-density integration since it is not constrained by the diffraction limit. Fundamental nanophotonic processes, such as optical excitation transfer via optical near-fields between nanometer-scale matter, have been studied extensively [3–5]. This higher integration density is not the only benefit of optical near-fields over conventional optics and electronics. From a system architectural perspective, nanophotonics drastically changes the fundamental design rules of functional optical systems, and suitable architectures may be built to exploit this. As a result, nanophotonics will have a strong impact in terms of qualitative improvements to information and communication systems.

This chapter discusses system architectures for nanophotonics, taking into consideration the unique physical principles of optical near-field processes, and describes their experimental verification based on technological vehicles such as quantum dots and engineered metal nanostructures. In particular, two unique physical processes in light-matter interactions on the nanometer scale are exploited. One is optical excitation transfer via optical near-field interactions, and the other is the hierarchical property of optical near-field interactions.

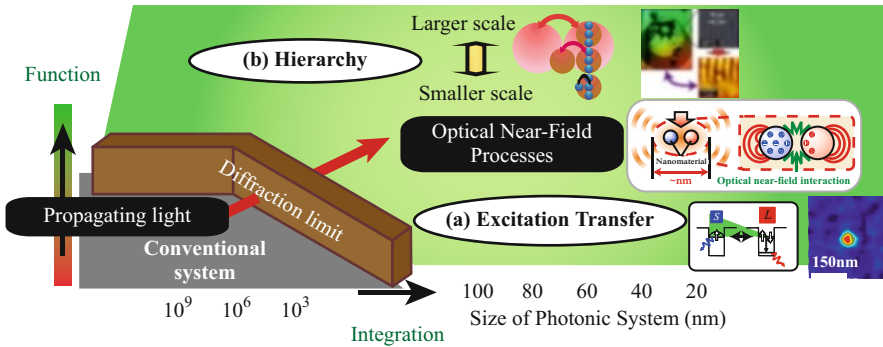


Fig. 23.1 Overview of the chapter: Nanophotonic systems based on optical excitation transfer mediated by optical near-field interactions and hierarchical properties in optical near-fields are examined

The overall concept of this chapter is outlined in Fig. 23.1. Section 23.2 discusses system architectures based on optical excitation transfer. Section 23.3 investigates networks of optical near-field interactions. Section 23.4 discusses hierarchical architectures based on optical near-field processes, followed by discussions on shape-engineered nanostructures in Sect. 23.5. The architectural and physical insights gained enable the realization of nanophotonic information and communications systems that can overcome the integration-density limit imposed by the diffraction of light while providing ultra low-power operation and unique functionalities that are only achievable using optical near-field interactions.

23.2 System Architectures Based on Optical Excitation Transfer

23.2.1 Optical Excitation Transfer via Optical Near-Field Interactions and Its Functional Features

In this section, optical excitation transfer processes involving optical near-field interactions are reviewed from a system perspective. First, their fundamental principles are briefly reviewed, and then their functional features are introduced for later discussion.

The interaction Hamiltonian between an electron and an electric field is given by

$$\hat{H}_{int} = - \int \hat{\psi}^\dagger(\mathbf{r}) \boldsymbol{\mu} \hat{\psi}(\mathbf{r}) \cdot \hat{\mathbf{D}}(\mathbf{r}) d\mathbf{r}, \quad (23.1)$$

where $\boldsymbol{\mu}$ is the dipole moment, $\hat{\psi}^\dagger(\mathbf{r})$ and $\hat{\psi}(\mathbf{r})$ are respectively creation and annihilation operators of an electron at \mathbf{r} , and $\hat{\mathbf{D}}(\mathbf{r})$ is the operator of electric flux density. In usual light–matter interactions, the operator $\hat{\mathbf{D}}(\mathbf{r})$ is a constant since the electric field of propagating light is considered to be constant on the

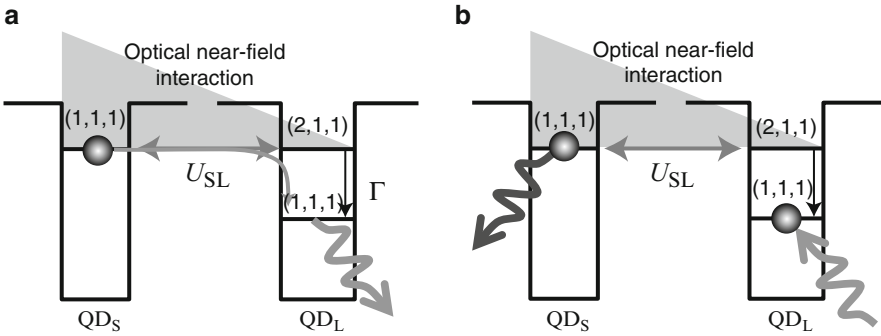


Fig. 23.2 (a) Optical excitation transfer from a smaller quantum dot to a larger one, mediated by optical near-field interactions. (b) State filling induced at the lower energy level in the larger dot results in different flows of optical excitation

nanometer scale. Therefore, as is well known, one can derive optical selection rules by calculating a transfer matrix of an electric dipole. As a consequence, in the case of cubic quantum dots, for instance, transitions to states described by quantum numbers containing an even number are prohibited. In the case of optical near-field interactions, on the other hand, due to the steep electric field of optical near-fields in the vicinity of nanoscale matter, an optical transition that violates conventional optical selection rules is allowed.

Optical excitations in nanostructures, such as quantum dots, can be transferred to neighboring ones via optical near-field interactions [3, 4]. For instance, assume two cubic quantum dots whose side lengths L are a and $\sqrt{2}a$, which are called QD_S and QD_L , respectively (see Fig. 23.2a). Suppose that the energy eigenvalues for the quantized exciton energy level specified by quantum numbers (n_x, n_y, n_z) in a QD with side length L are given by

$$E_{(n_x, n_y, n_z)} = E_B + \frac{\hbar^2 \pi^2}{2ML^2} (n_x^2 + n_y^2 + n_z^2), \quad (23.2)$$

where E_B is the energy of the bulk exciton and M is the effective mass of the exciton. According to Eq. (23.2), there exists a resonance between the level of quantum number (1,1,1) for QD_S and that of quantum number (2,1,1) for QD_L . There is an optical near-field interaction, which is denoted by U , due to the steep electric field in the vicinity of QD_S . Therefore, excitons in QD_S can move to the (2,1,1)-level in QD_L . Note that such a transfer is prohibited for propagating light since the (2,1,1)-level in QD_L contains an even number [6]. In QD_L , the exciton sees a sublevel energy relaxation, denoted by Γ , which is faster than the near-field interaction, and so the exciton goes to the (1,1,1)-level in QD_L . It should be emphasized that the sublevel relaxation determines the unidirectional exciton transfer from QD_S to QD_L .

Now, several unique functional aspects should be noted in the above excitation transfer processes. First, as already mentioned, the transition from the (1,1,1)-level in QD_S to the (2,1,1)-level in QD_L is usually a dipole-forbidden transition. In contrast, such a transition is allowed when intermediated by the optical near-field. Second, in the resonant energy levels of those quantum dots, optical excitations can go back and forth between QD_S and QD_L , which is called optical nutation. The direction of the excitations is determined by the energy dissipation processes. When another excitation sits in the (1,1,1)-level in QD_L , the excitation in the (1,1,1)-level in QD_S cannot be transferred to the (1,1,1)-level in QD_L , as schematically shown in Fig. 23.2b. Therefore, based on the above mechanisms, the flow of optical excitations can be controlled in quantum dot systems via optical near-field interactions.

From an architectural standpoint, such a flow of excitations directly leads to digital processing systems and computational architectures. First of all, two different physical states can be made to appear by controlling the dissipation processes in the larger dot; this is the principle of the nanophotonic switch [7]. Also, such flow control itself allows an architecture known as a binary decision diagram, where an arbitrary combinatorial logic operation is determined by the destination of a signal flowing from a root [8].

Such optical excitation transfer processes also lead to unique system architectures. In this regard, Sect. 23.2.2 discusses a massively parallel architecture and its nanophotonic implementations. Also, Sect. 23.2.3 demonstrates that optical excitation transfer provides higher tamper resistance against attacks than conventional electrically wired devices by focusing on environmental factors for signal transfer. It should also be noted that optical excitation transfer has been the subject of a wide range of research. For example, Pistol et al. demonstrated resonant energy transfer-based logic [9] using DNA-assisted self-assembly technologies [10] for sensing and other applications. Other system-related investigations using optical excitation transfer include interconnections [11], pulsation mechanisms [12], and skew dependence [13].

23.2.2 Parallel Architecture Using Optical Excitation Transfer

Memory-Based Architecture This section discusses a memory-based architecture where computations are regarded as a lookup table or database search problem, which is also called a content addressable memory (CAM) [14]. The inherent parallelism of this architecture is well matched with the physics of optical excitation transfer and provides performance benefits such as high-density, low-power operation [15].

In this architecture, an input signal (content) serves as a query to a lookup table, and the output is the address of data matching the input. This architecture plays a critical role in various systems, for example, in data routers where the output port for an incoming packet is determined based on lookup tables.

All-optical means for implementing such functions have been proposed, for instance, by using planar lightwave circuits [16]. However, since separate optical hardware for each table entry would be needed in implementations based on today's known methods, if the number of entries in the routing table is on the order of 10,000 or more, the overall physical size of the system would become impractically large. On the other hand, by using diffraction-limit-free nanophotonic principles, huge lookup tables can be realized with compact configurations.

It is important to note that the lookup table problem is equivalent to an inner product operation. Assume an N -bit input signal $\mathbf{S} = (s_1, \dots, s_N)$ and reference data $\mathbf{D} = (d_1, \dots, d_N)$. Here, the inner product $\mathbf{S} \bullet \mathbf{D} = \sum_{i=1}^N s_i \bullet d_i$ will provide a maximum value when the input perfectly matches the reference data with an appropriate modulation format [17]. Then, the function of a CAM is to derive j that maximizes $\mathbf{S} \bullet \mathbf{D}_j$.

Global Summation Using Near-Field Interactions As discussed above, the inner product operations are the key functionality of the memory-based architecture. The multiplication of 2 bits, namely, $x_i = s_i \bullet d_i$, has already been demonstrated by using a combination of three quantum dots [7]. Therefore, one of the key operations remaining is the summation, or data gathering scheme, denoted by $\sum x_i$, where all data bits should be taken into account, as schematically shown in Fig. 23.3.

In known optical methods, wave propagation in free space or in waveguides, using focusing lenses or fiber couplers, for example, is well-matched with such a data gathering scheme because the physical nature of propagating light is inherently suitable for collection or distribution of information, such as in global summation. However, the achievable level of integration of these methods is restricted due to the diffraction limit of light. In nanophotonics, on the other hand, the near-field interaction is inherently physically local, although functionally global behavior is required.

The global data gathering mechanism, or summation, is realized based on the unidirectional energy flow via an optical near-field, as schematically shown in Fig. 23.3, where surrounding excitations are transferred toward a quantum dot QD_C located at the center [18, 19]. This is based on the excitation transfer processes presented in Sect. 23.2.1 and in Fig. 23.2a, where an optical excitation is transferred from a smaller dot (QD_S) to a larger one (QD_L) through a resonant energy sublevel and a sublevel relaxation process occurring at the larger dot. In the system shown in Fig. 23.3, similar energy transfers may take place among the resonant energy levels in the dots surrounding QD_C so that excitation transfer can occur. The lowest energy level in each quantum dot is coupled to a free photon bath to sweep out the excitation radiatively. The output signal is proportional to the (1,1,1)-level population in QD_L .

A proof-of-principle experiment was performed to verify the nanoscale summation using CuCl quantum dots in a NaCl matrix, which has also been employed for demonstrating nanophotonic switches [7] and optical nano-fountains [19]. A quantum dot arrangement in which three small QDs (QD_1 to QD_3) surrounded a large QD at the center (QD_C) was chosen. Here, at most three light beams with different wavelengths, 325, 376, and 381.3 nm, are radiated to excite the respective quantum dots QD_1 to QD_3 , having sizes of 1, 3.1, and 4.1 nm. The excited excitons

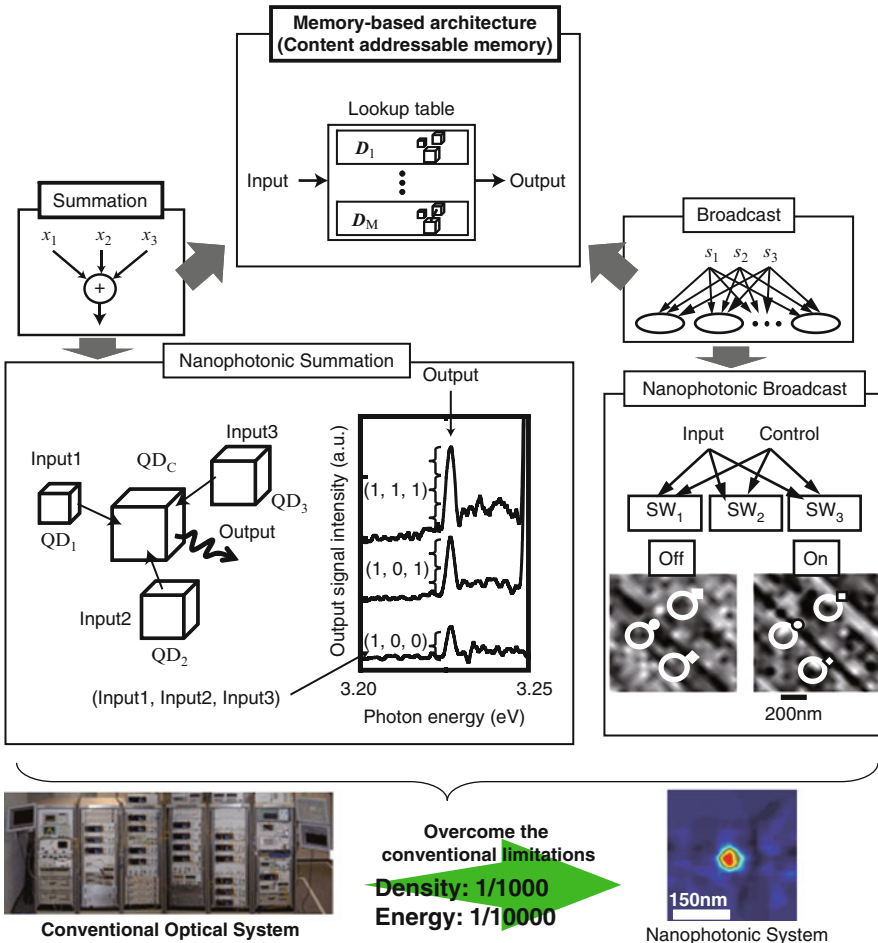


Fig. 23.3 Memory-based architecture of content addressable memory based on optical excitation transfer. Global summation and broadcast interconnects, which are both important subfunctions for the memory-based architecture, were demonstrated based on optical excitation transfer using different-sized QDs

are transferred to QD_C , and their radiation is observed by using a near-field fiber probe tip. Notice the output signal intensity at a photon energy level of 3.225 eV in Fig. 23.3, which corresponds to a wavelength of 384 nm, or a QD_C size of 5.9 nm. The intensity varies approximately as 1:2:3, depending on the number of excited QDs in the vicinity, as observed in Fig. 23.3. The spatial intensity distribution was measured by scanning the fiber probe, as shown in the bottom-right corner of Fig. 23.3, where the energy is converged at the center. Hence, this architecture works as a summation mechanism, counting the number of input channels, based on exciton energy transfer via optical near-field interactions.

Such a quantum-dot-based data gathering mechanism is also extremely energy efficient compared with other optical methods, such as focusing lenses or optical couplers. For example, the transmittance between two materials with refractive indexes n_1 and n_2 is given by $4n_1n_2/(n_1 + n_2)^2$; this gives a 4% loss if n_1 and n_2 are 1 and 1.5, respectively. The transmittance of an N-channel guided wave coupler is $1/N$ from the input to the output. In nanophotonic summation, the loss is attributed to the dissipation between energy sublevels, which is significantly smaller. Incidentally, it is energy and space efficient compared with electrical CAM VLSI chips [15, 20, 21].

Broadcast Interconnects For the parallel architecture shown above, it should also be noted that the input data should be commonly applied to all lookup table entries. In other words, a broadcast interconnect is another important requirement for parallel architectures. Broadcast is also important in applications such as matrix-vector products [22, 23] and switching operations, for example, broadcast-and-select architectures [24]. Optics is in fact well suited to such broadcast operations in the form of simple imaging optics [22, 23] or in optical waveguide couplers, thanks to the nature of wave propagation. However, the integration density of this approach is physically limited by the diffraction limit, which leads to bulky system configurations.

The overall physical operation principle of a broadcast using optical near-fields is as follows [25]. Suppose that arrays of nanophotonic circuit blocks are distributed within an area whose size is comparable to the wavelength. For broadcasting, multiple input QDs simultaneously accept identical input data carried by diffraction-limited far-field light by tuning their optical frequency so that the light is coupled to dipole-allowed energy sublevels.

The far- and near-field coupling mentioned above is explained based on a model assuming cubic quantum dots, which was introduced in Sect. 23.2.1. According to Eq. (23.2), there exists a resonance between the quantized exciton energy sublevel of quantum number (1,1,1) for the QD with effective side length a and that of quantum number (2,1,1) for the QD with effective side length $\sqrt{2}a$. Energy transfer from the smaller QD to the larger one occurs via optical near fields, which is forbidden for far-field light [7].

The input energy level for the QDs, that is, the (1,1,1)-level, can also couple to the far-field excitation. This fact can be utilized for data broadcasting. One of the design restrictions is that energy sublevels for input channels do not overlap with those for output channels. Also, if there are QDs internally used for near-field coupling, dipole-allowed energy sublevels for those QDs cannot be used for input channels since the inputs are provided by far-field light, which may lead to misbehavior of internal near-field interactions if resonant levels exist. Therefore, frequency partitioning among the input, internal, and output channels is important. The frequencies used for broadcasting, denoted by $\Omega_i = \{\omega_{i,1}, \omega_{i,2}, \dots, \omega_{i,A}\}$, should be distinct values and should not overlap with the output channel frequencies $\Omega_o = \{\omega_{o,1}, \omega_{o,2}, \dots, \omega_{o,B}\}$. A and B indicate the number of frequencies used for input and output channels, respectively. Also, there will be frequencies needed for internal device operations, which are not used for either input or output, denoted

by $\Omega_n = \{\omega_{n,1}, \omega_{n,2}, \dots, \omega_{n,C}\}$, where C is the number of those frequencies. Therefore, the design criteria for global data broadcasting are to exclusively assign input, output, and internal frequencies, Ω_i , Ω_o , and Ω_n , respectively.

In a frequency multiplexing sense, this interconnection method is similar to multi-wavelength chip-scale interconnects [26]. Known methods, however, require a physical space comparable to the number of diffraction-limited input channels due to wavelength demultiplexing, whereas in the nanophotonic scheme, the device arrays are integrated on the subwavelength scale, and multiple frequencies are multiplexed in the far-field light supplied to the device.

To verify the broadcasting method, the following experiments were performed using CuCl QDs inhomogeneously distributed in an NaCl matrix at a temperature of 22 K [25]. To operate a three-dot nanophotonic switch (two-input AND gate) in the device, at most two input light beams (IN1 and IN2) are radiated. When both inputs exist, an output signal is obtained from the positions where the switches exist, as described above. In the experiment, IN1 and IN2 were assigned to 325 and 384.7 nm, respectively. They were radiated over the entire sample (global irradiation) via far-field light. The spatial intensity distribution of the output, at 382.6 nm, was measured by scanning a near-field fiber probe within an area of approximately $1 \times 1 \mu\text{m}$. When only IN1 was applied to the sample, the output of the AND gate was ZERO (OFF state). When both inputs were radiated, the output was ONE (ON state). Note the regions marked by ■, ●, and ◆ in Fig. 23.3. In those regions, the output signal levels were respectively low and high, which indicates that multiple AND gates were integrated at densities beyond the scale of the globally irradiated input beam area. That is to say, broadcast interconnects to nanophotonic switch arrays are accomplished by diffraction-limited far-field light.

Combining this broadcasting mechanism with the summation mechanism will allow the development of nanoscale integration of massively parallel architectures, which have conventionally resulted in bulky configurations.

23.2.3 Secure Signal Transfer in Nanophotonics

In addition to breaking through the diffraction limit of light, such local interactions of optical near-fields also have important functional aspects, such as in security applications, particularly tamper resistance against attacks [27]. One of the most critical security issues in present electronic devices is so-called side-channel attacks, by which information is tampered with either invasively or noninvasively. This may be achieved, for instance, merely by monitoring their power consumption [28].

In this subsection, it is shown that devices based on optical excitation transfer via near-field interactions are physically more tamper resistant than their conventional electronic counterparts. The key is that the flow of information in nanoscale devices cannot be completed unless they are appropriately coupled with their environment [29], which could possibly be the weakest link in terms of their tamper resistance. A theoretical approach is presented to investigate the tamper resistance of optical excitation transfer, including a comparison with electrical devices.

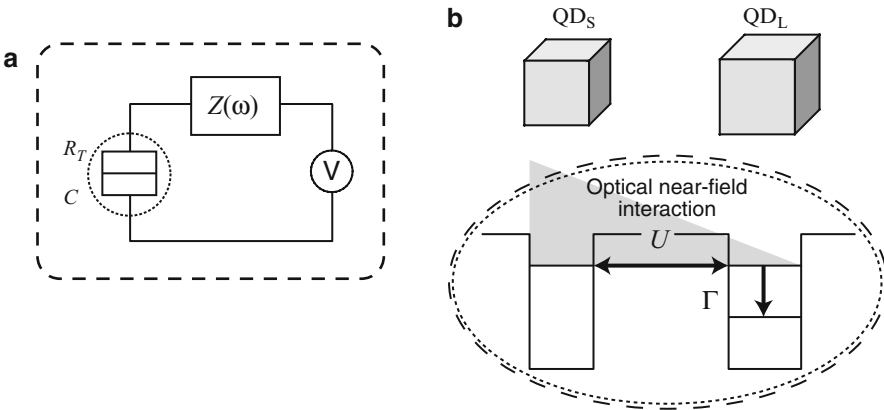


Fig. 23.4 Model of tamper resistance in devices based on (a) single charge tunneling and (b) optical excitation transfer. *Dotted curves* show the scale of a key device, and *dashed curves* show the scale of the environment required for the system to work

Here, tampering of information is defined as involving simple signal transfer processes, since the primary focus is on their fundamental physical properties.

In order to compare the tamper resistance, an electronic system based on single charge tunneling is introduced here, in which a tunnel junction with capacitance C and tunneling resistance R_T is coupled to a voltage source V via an external impedance $Z(\omega)$, as shown in Fig. 23.4a. In order to achieve single charge tunneling, besides the condition that the electrostatic energy $E_C = e^2/2C$ of a single excess electron be greater than the thermal energy $k_B T$, the environment must have appropriate conditions, as discussed in detail in Ref. [30]. For instance, with an inductance L in the external impedance, the fluctuation of the charge is given by

$$\langle \delta Q^2 \rangle = \frac{e^2}{4\rho} \coth\left(\frac{\beta \hbar \omega_S}{2}\right), \quad (23.3)$$

where $\rho = E_C/\hbar\omega_S$, $\omega_S = (LC)^{-1/2}$, and $\beta = 1/k_B T$. Therefore, charge fluctuations cannot be small even at zero temperature unless $\rho \gg 1$. This means that a high-impedance environment is necessary, which makes tampering technically easy, for instance by adding another impedance circuit.

Here, let us define two scales to illustrate tamper resistance: (I) the scale associated with the key device size and (II) the scale associated with the environment required for operating the system, which are respectively indicated by the dotted and dashed lines in Fig. 23.4. In the case of Fig. 23.4a, scale I is the scale of a tunneling device, whereas scale II covers all of the components. It turns out that the low tamper resistance of such wired devices is due to the fact that scale II is typically the macroscale, even though scale I is the nanometer scale.

In contrast, in the case of the optical excitation transfer shown in Fig. 23.3b, the two quantum dots and their surrounding environment are governed by scale I. It is also important to note that scale II is the same as scale I. More specifically, the transfer of an exciton from QD_S to QD_L is completed due to the non-radiative relaxation process occurring at QD_L , which is usually difficult to tamper with. Theoretically, the sublevel relaxation constant is given by

$$\Gamma = 2\pi |g(\omega)|^2 D(\omega), \quad (23.4)$$

where $\hbar g(\omega)$ is the exciton–phonon coupling energy at frequency ω , \hbar is Planck’s constant divided by 2π , and $D(\omega)$ is the phonon density of states [31]. Therefore, tampering with the relaxation process requires somehow “stealing” the exciton–phonon coupling, which would be extremely difficult technically.

It should also be noted that the energy dissipation occurring in the optical excitation transfer, derived theoretically as $E_{(2,1,1)} - E_{(1,1,1)}$ in QD_L based on Eq. (23.2), should be larger than the exciton–phonon coupling energy of $\hbar\Gamma$, otherwise the two levels in QD_L cannot be resolved. This is similar to the fact that the condition $\rho \gg 1$ is necessary in the electron tunneling example, which means that the mode energy $\hbar\omega_S$ is smaller than the required charging energy E_C . By regarding $\hbar\Gamma$ as a kind of mode energy in the optical excitation transfer, the difference between the optical excitation transfer and a conventional wired device is the physical scale at which this mode energy is realized: nanoscale for the optical excitation transfer and macroscale for electric circuits.

23.3 Networks of Optical Near-Field Interactions

23.3.1 Optimal Network of Near-Field Interactions

Consider the quantum dot system in Fig. 23.5a, where multiple smaller dots (denoted by S_i) can be coupled with one larger dot, denoted by L . We assume inter-dot interactions between adjacent smaller quantum dots; that is, (i) S_i interacts with S_{i+1} ($i = 1, \dots, N - 1$), and (ii) S_N interacts with S_1 , where N is the number of smaller quantum dots. For instance, the system shown in Fig. 23.5b(i) consists of two smaller quantum dots and one larger quantum dot, denoted by **S2–L1**. Similarly, **S3–L1**, **S4–L1**, and **S5–L1** systems, respectively, shown in Figs. 23.5b(ii–iv) are composed of three, four, and five smaller quantum dots in addition to one larger quantum dot.

Now, what is of interest is to calculate the flow of excitations from the smaller dots to the larger one. The theoretical and experimental details can be found in Ref. [32]; we introduce the information necessary for discussing the topology dependency and autonomy in optical excitation transfer in Sect. 23.3.2.

We deal with the problem theoretically based on a density matrix formalism. In the case of the **S2–L1** system, which is composed of two smaller quantum dots

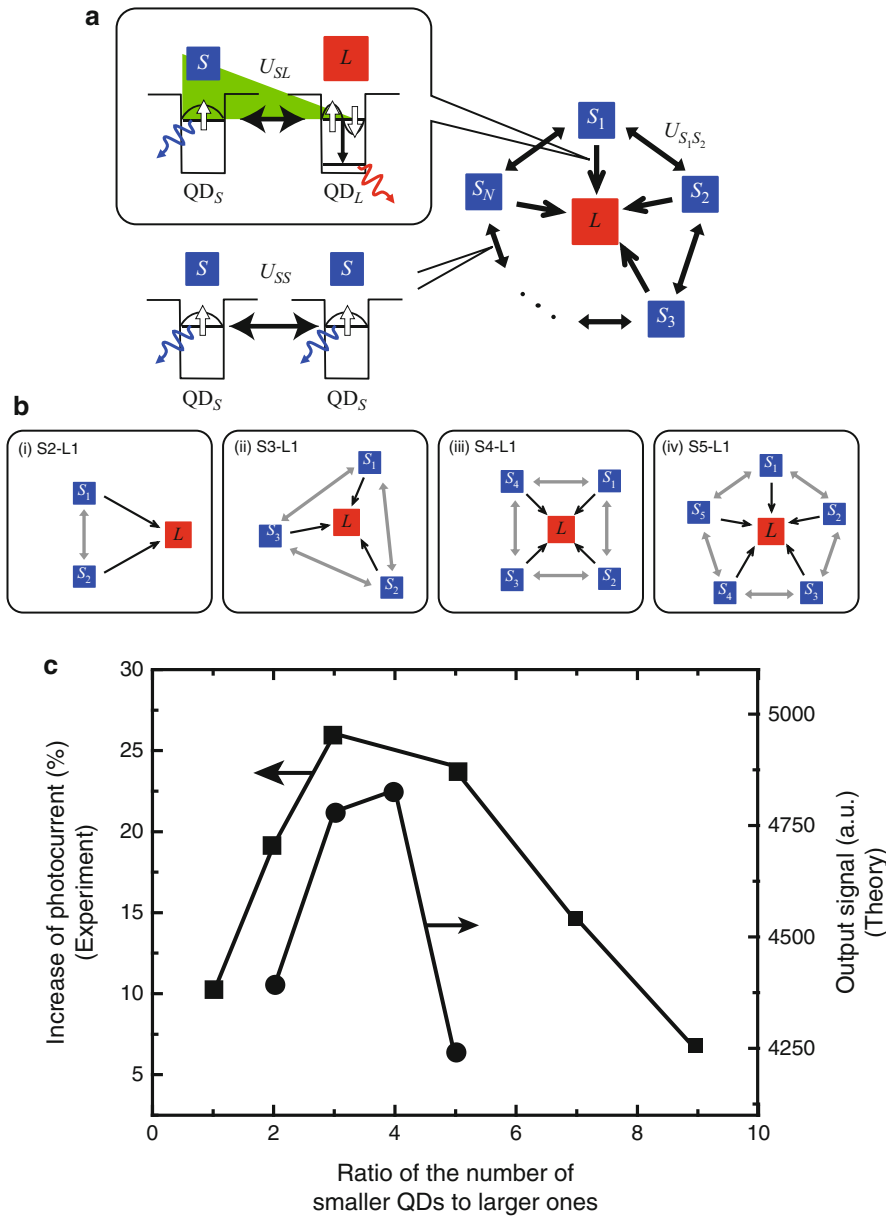


Fig. 23.5 (a) Network of optical near-field interactions in a system composed of multiple smaller quantum dots and one larger quantum dot networked via optical near-field interactions. (b) Example systems composed of multiple smaller quantum dots and one larger quantum dot. (c) Optimal ratio of the number of smaller quantum dots to larger quantum dots so that the optical excitation transfer is most efficiently induced

and one larger quantum dot, the inter-dot interactions between the smaller dots and the larger one are denoted by U_{S_iL} , and the interaction between the smaller dots is denoted by $U_{S_1S_2}$, as schematically shown in Fig. 23.5a. The radiations from S_1 , S_2 , and L are, respectively, represented by the relaxation constants γ_{S_1} , γ_{S_2} , and γ_L . We suppose that the system initially has two excitations in S_1 and S_2 . With such an initial state, we can prepare a total of eleven bases where zero, one, or two excitation(s) occupy the energy levels. In the numerical calculation, we assume $U_{S_iL}^{-1} = 200$ ps, $U_{S_1S_2}^{-1} = 100$ ps, $\gamma_L^{-1} = 1$ ns, $\gamma_{S_1}^{-1} = 2.92$ ns, and $\Gamma^{-1} = 10$ ps as parameter values. Following the same procedure, we also derive quantum master equations for the **S3-L1**, **S4-L1**, and **S5-L1** systems that have initial states in which all smaller quantum dots are excited. Finally, we calculate the population of the lower level of the larger quantum dot, whose time integral we regard as the output signal.

We compare the output signal as a function of the ratio of the number of smaller dots to the number of larger dots assuming that the total number of quantum dots in a given unit area is the same, regardless of their sizes (smaller or larger). As shown by the circles in Fig. 23.5c, the most efficient transfer is obtained when the ratio of the number of smaller dots to the number of larger dots is 4. In other words, increasing the number of smaller quantum dots beyond a certain level does not necessarily contribute to increased output signals. Because of the limited radiation lifetime of large quantum dots, not all of the initial excitations can be successfully transferred to the large quantum dots due to the states occupying the lower excitation levels of the large quantum dots. Therefore, part of the input populations of smaller quantum dots must decay, which results in a loss in the transfer from the smaller quantum dots to the large quantum dots when there are too many excitations in the smaller quantum dots surrounding one large quantum dot.

An optimal mixture of smaller and larger quantum dots was experimentally demonstrated by using two kinds of CdSe/ZnS core/shell quantum dots whose diameters were 2.0 and 2.8 nm [32, 33]. In the experiment detailed in Ref. [32], an increase of the photocurrent was measured for the output signal. As shown by the squares in Fig. 23.5c, the maximum increase was obtained when the ratio of the number of smaller quantum dots to larger dots was 3:1, which agrees well with the theoretical optimal ratio discussed above.

Efficient optical excitation transfer in layered quantum dot structures has also been experimentally demonstrated. The radiation from layered graded-size CdTe quantum dots exhibits a signal nearly four times larger than that from structures composed of uniform-size quantum dots, a phenomenon which has been called exciton recycling [34] or superefficient exciton funneling [35]. Adopting the theory of networks of optical excitation transfer mediated by optical near-field interactions, the theoretical approach allows systematic analysis of layered quantum dot systems, revealing dominant factors contributing to the efficient optical excitation transfer and demonstrating good agreement with previous experimental observations [36].

23.3.2 Autonomy in Optical Excitation Transfer

In the previous section, we observe that the amount of optical excitation transferred from smaller quantum dots to larger quantum dots depends on the ratio of their numbers. This suggests that we could increase the output by engineering the network structure of the quantum dots. This section takes the **S5–L1** system in Fig. 23.5b(iv) as an example and demonstrates that it is possible to increase the output signal by appropriately configuring the network of quantum dots. We set all of the inter-dot interaction times to 100 ps while keeping all other parameter values the same as those in Sect. 23.3.1.

In Fig. 23.6a, the original **S5–L1** system, denoted by **E0**, is the same as the system shown in Fig. 23.5b(iv). Assume that some of the interactions between the smaller quantum dots (denoted by S_1 to S_5) and the large quantum dot surrounded by them are degraded, or lost, due to, for instance, material disorders, such as a violation of the condition represented by Eq. (23.2). In total, there are eight such configurations when symmetries are taken into account. For instance, when one of the five links between the smaller quantum dots and the large quantum dot is degraded, we obtain the system **E1** in Fig. 23.6a. The mark “X” indicates a degraded interaction between S_1 and L . Similarly, when there are two degraded links, the system should be represented either by the system **E2** or the system **E2'** shown in Fig. 23.6a.

Figure 23.6b summarizes the integrated populations as a function of the network configurations in Fig. 23.6a. Interestingly, except for the system **E5**, which has no valid links between the smaller quantum dots and the large quantum dot, systems with degraded interactions exhibit a higher output signal than the system **E0** without the link defects. System **E2** exhibits an output signal that is about 1.64 times higher than system **E0**. This corresponds to the results described in Sect. 23.3.1, where the output is maximized when the ratio of the number of smaller dots to large dots is 4, meaning that the excessively high number of excitations in the smaller dots cannot be transferred to the large dot they surround. Due to the “limited” interactions between the smaller dots and the large dot, such as in the case of systems **E2** and **E2'**, the excitations located in the smaller dots have a higher probability to be transferred to the larger dot. Figure 23.6c demonstrates the evolution of populations associated with the total number of excitations contained in the system, ranging from 1 to 5. The solid and dashed curves in Fig. 23.6c respectively refer to systems **E0** and **E2**. The populations containing one excitation increase dramatically in **E2** as compared with **E0**, which is another indication that the excitations can be kept in the system until they are successfully transferred to the destination, exhibiting a topology-dependent efficiency increase [37].

The autonomous behavior traceable memory of optical excitation transfer is emphasized in Fig. 23.6d, which summarizes the evolutions of populations associated with S_1 to S_5 in system **E2**, where both the interaction between S_2 and L and the interaction between S_3 and L are negligible. Initially, all of the smaller dots contain excitations. Note that the populations associated with S_2 and S_3 remain at a higher level for a short initial time, indicating that the excitations in S_2 and S_3 are effectively “waiting” in the smaller dots until they have the opportunity to be transferred to a large dot.

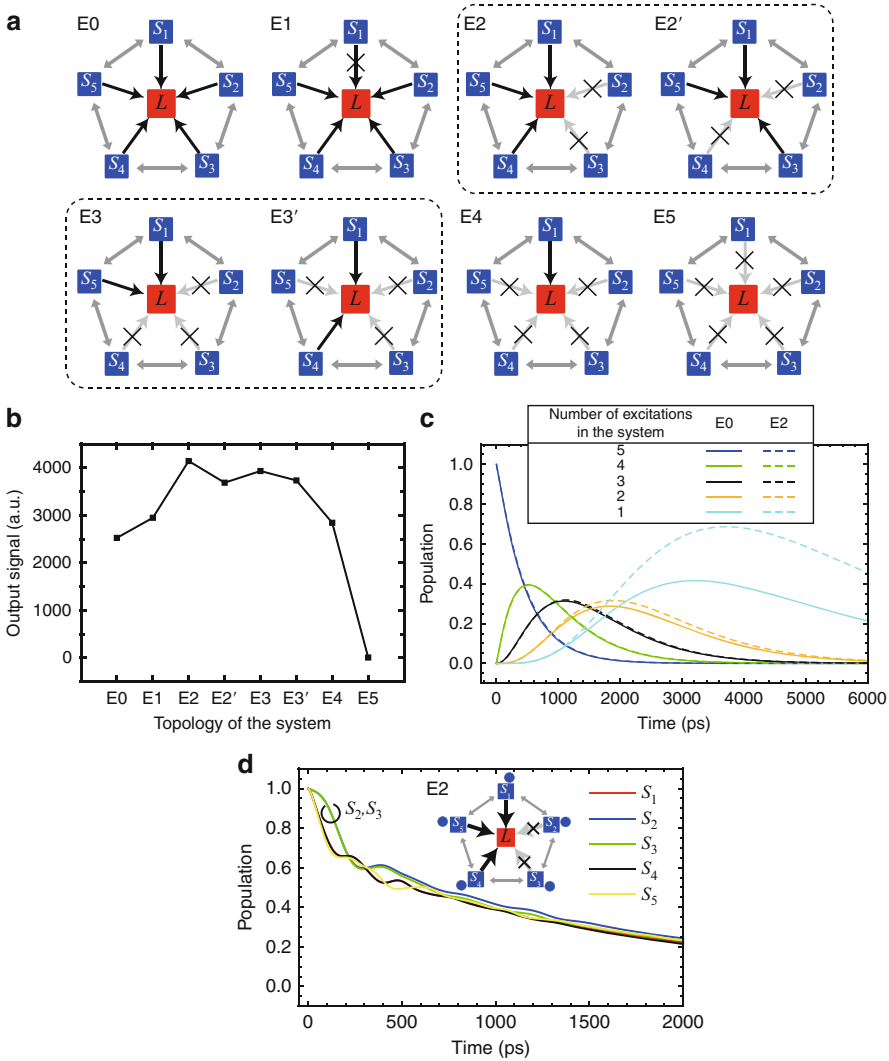
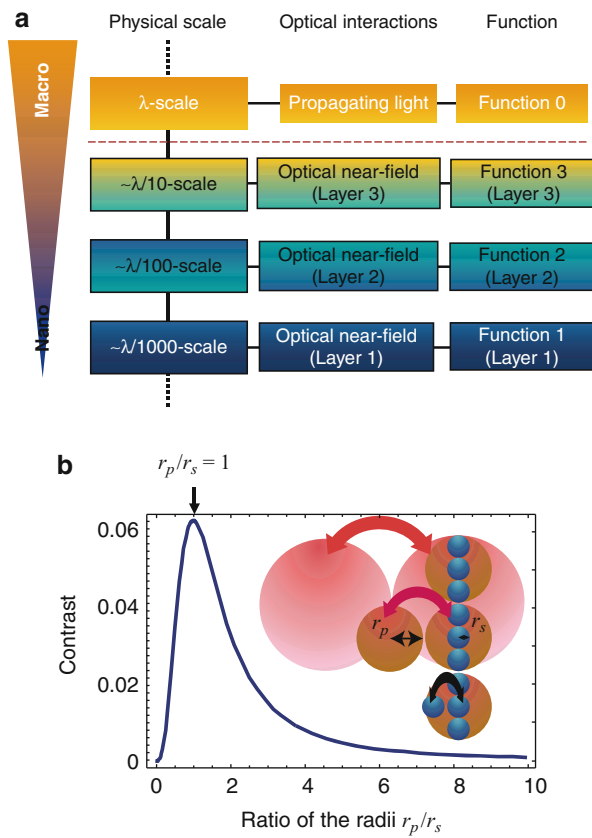


Fig. 23.6 (a) Eight different network topologies in the S_5-L_1 system, where some of the interactions between the smaller quantum dots QD_S and the large quantum dot QD_L are degraded, or lost. (Degraded interactions are indicated by "X.") The notation E_N indicates that the system contains N -degraded interactions. (b) Time-integrated populations for the systems in (a). (c) The evolution of the populations associated with the number of excitations (ranging from 1 to 5) in systems **E0** and **E2**. (d) Time evolutions of the populations associated with the smaller quantum dots (S_1 to S_5) in system **E2** in (a) while assuming that all smaller quantum dots contain excitations in the initial setup

Fig. 23.7 (a) Hierarchical system architecture based on the inherent hierarchical properties in optical near-field processes. (b) Signal contrast as a function of the ratio of the radii of the sample and the probe based on dipole–dipole interactions



23.4 Hierarchical Architectures in Nanophotonics

23.4.1 Physical Hierarchy in Nanophotonics and Functional Hierarchy

In this section, we describe another feature of nanophotonics that can be exploited, the inherent hierarchy in optical near-field interactions [38, 39]. As schematically shown in Fig. 23.7a, there are multiple layers associated with the physical scale between the macroscale world and the atomic-scale world, which are primarily governed by propagating light and electron interactions, respectively. Between those two extremes, typically in scales ranging from a few nanometers to wavelength size, optical near-field interactions play a crucial role. In this section, we describe how such hierarchical properties in this mesoscopic or subwavelength regime can be exploited.

This physical hierarchy in optical near-field interactions will be analyzed by using a simple dipole–dipole interaction model as demonstrated in Sect. 23.4.2.

Before going into details of the physical processes, functionalities required for system applications are first briefly reviewed in terms of hierarchy.

One of the problems for ultrahigh-density nanophotonic systems is interconnection bottlenecks, which were addressed in [Sect. 23.2.2](#) above with regard to broadcast interconnects [25]. In fact, a hierarchical structure can be found in these broadcast interconnects by relating far-field effects at a coarser scale and near-field effects at a finer scale.

In this regard, it should also be mentioned that such physical differences in optical near-field and far-field effects can be used for a wide range of applications. The behavior of usual optical elements, such as diffractive optical elements, holograms, or glass components, is associated with their optical responses in optical far-fields. In other words, nanostructures can exist in such optical elements as long as they do not affect the optical responses in the far-field. Designing nanostructures that are accessible only via optical near-fields allows additional, or hidden, information to be recorded in those optical elements while maintaining the original optical responses in the far-fields. In fact, a *hierarchical hologram* and *hierarchical diffraction grating* have been experimentally demonstrated, as described in [Sect. 23.4.3](#).

Since there is more hierarchy in the optical near-field regime, further applications should be possible; for example, it should be possible for nanometer-scale high-density systems to be hierarchically connected to coarse layer systems.

Hierarchical functionalities are also important for several aspects of memory systems. One is related to recent high-density, huge-capacity memory systems, in which data retrieval or searching from the entire memory archive has become even more difficult. One approach for solving such a problem is to employ a hierarchical system design, that is, by recording abstract data, metadata, or tag data in addition to the original raw data.

Hierarchy in nanophotonics provides a physical way of achieving such functional hierarchy. As will be introduced below, low-density, rough information is readout at a coarser scale, whereas high-density, detailed information is readout at a finer scale. [Section 23.4.2](#) will show physical mechanisms for such hierarchical information retrieval.

Another issue in hierarchical functionalities will be security. High-security information is recorded at a finer scale, whereas less-critical security information is associated with a coarse layer. Also, in addition to associating different types of information with different physical scales, another kind of information could also be associated with one or more layers of the physical hierarchy. For instance, a *traceable* memory has been demonstrated based on such hierarchical properties in optical near-fields [40,41].

23.4.2 Hierarchical Memory Retrieval

This section describes a physical model of optical near-field interactions based on dipole–dipole interactions [42] and their application to hierarchical memory retrieval [38]. Suppose that a probe, which is modeled by a sphere of radius r_P ,

is placed close to a sample to be observed, which is modeled as a sphere of radius r_S . The inset in Fig. 23.7b shows three different sizes for the probe and the sample. When they are illuminated by incident light whose electric field is \mathbf{E}_0 , electric dipole moments are induced in both the probe and the sample; these moments are, respectively, denoted by $\mathbf{p}_P = \alpha_P \mathbf{E}_0$ and $\mathbf{p}_S = \alpha_S \mathbf{E}_0$. The electric dipole moment induced in the sample, \mathbf{p}_S , then generates an electric field, which changes the electric dipole moment in the probe by an amount $\Delta \mathbf{p}_P = \Delta \alpha_P \mathbf{E}_0$. Similarly, \mathbf{p}_P changes the electric dipole moment in the sample by $\Delta \mathbf{p}_S = \Delta \alpha_S \mathbf{E}_0$. These electromagnetic interactions are called dipole–dipole interactions. The scattering intensity induced by these electric dipole moments is given by

$$\begin{aligned} I &= |\mathbf{p}_P + \Delta \mathbf{p}_P + \mathbf{p}_S + \Delta \mathbf{p}_S|^2 \\ &\approx (\alpha_P + \alpha_S)^2 |E_0|^2 + 4\Delta\alpha(\alpha_P + \alpha_S) |E_0|^2 \end{aligned} \quad (23.5)$$

where $\Delta\alpha = \Delta\alpha_S = \Delta\alpha_P$ [42]. The second term in Eq. (23.5) shows the intensity of the scattered light generated by the dipole–dipole interactions, containing the information of interest, which is the relative difference between the probe and the sample. The first term in Eq. (23.5) is the background signal for the measurement. Therefore, the ratio of the second term to the first term in Eq. (23.5) corresponds to a signal contrast, which will be maximized when the sizes of the probe and the sample are the same ($r_P = r_S$), as shown in Fig. 23.7b. Thus, one can see a scale-dependent physical hierarchy in this framework, where a small probe, say, $r_P = D/2$, can nicely resolve objects with a comparable resolution, whereas a large probe, say $r_P = 3D/2$, cannot resolve detailed structure but can resolve structure with a resolution comparable to the probe size. Therefore, although a large diameter probe cannot detect smaller-scale structure, it could detect certain features associated with its scale.

Based on the above simple hierarchical mechanism, a hierarchical memory system has been constructed. Consider, for example, a maximum of N nanoparticles distributed in a region of subwavelength scale. Those nanoparticles can be nicely resolved by a scanning near-field microscope if the size of its fiber probe tip is comparable to the size of individual nanoparticles; in this way, the *first-layer* information associated with each distribution of nanoparticles is retrievable, corresponding to 2^N -different codes. By using a larger-diameter fiber probe tip instead, the distribution of the particles cannot be resolved, but a mean-field feature with a resolution comparable to the size of the probe can be extracted, namely, the number of particles within an area comparable to the size of the fiber probe tip. Thus, the *second-layer* information associated with the number of particles, corresponding to $(N + 1)$ different signal levels, is retrievable. Therefore, one can access different sets of signals, 2^N or $N + 1$, depending on the scale of observation. This leads to hierarchical memory retrieval by associating this information hierarchy with the distribution and the number of nanoparticles using an appropriate coding strategy, as schematically shown in Fig. 23.8d.

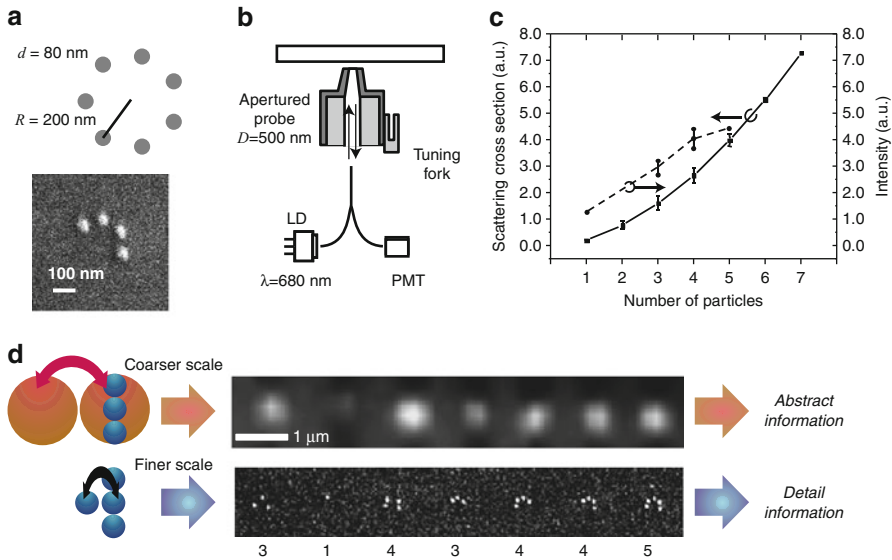


Fig. 23.8 Hierarchical information retrieval. (a) Each section consists of small particles. (b) Experimental setup. (c) Calculated scattering cross sections depending on the number of particles in each section (*squares*) and peak intensity of each section in the intensity pattern shown in (d). (d) SEM image of an Au particle array and intensity pattern captured by a NSOM with a fiber probe having a 500-nm-diameter aperture

For example, in encoding N -bit information, $(N - 1)$ -bit signals can be encoded by distributions of nanoparticles while associating the remaining 1-bit with the number of nanoparticles. Details of encoding/decoding strategies will be found in [38].

Simulations were performed assuming ideal isotropic metal particles to see how the second-layer signal varies depending on the number of particles by using a finite-difference time-domain simulator. Here, 80-nm-diameter particles are distributed over a 200-nm-radius circular grid at constant intervals. The solid circles in Fig. 23.8c show calculated scattering cross sections as a function of the number of particles. A linear correspondence to the number of particles was observed. This result supports the simple physical model described above.

In order to experimentally demonstrate such principles, an array of Au particles, each with a diameter around 80 nm, was distributed over a SiO_2 substrate in a 200-nm-radius circle. These particles were fabricated by a liftoff technique using electron beam (EB) lithography with a Cr buffer layer. Each group of Au particles was spaced by $2\ \mu\text{m}$. A scanning electron microscope (SEM) image is shown in Fig. 23.8d in which the values indicate the number of particles within each group. In order to illuminate all Au particles in each group and collect the scattered light from them, a near-field scanning optical microscope (NSOM) with a large-diameter-aperture (500-nm)-metalized fiber probe was used in an illumination–collection

setup. The light source used was a laser diode with an operating wavelength of 680 nm. The distance between the substrate and the probe was maintained at 750 nm. Figure 23.8d shows an intensity profile captured by the probe, from which the second-layer information is retrieved. The solid squares in Fig. 23.8c indicate the peak intensity of each section, which increased linearly. Those results show the validity of hierarchical memory retrieval from nanostructures.

23.4.3 Hierarchical Optical Elements

Holography, which generates natural three-dimensional images, is one of the most common anticounterfeiting techniques [43]. In the case of a volume hologram, the surface is ingeniously formed into microscopic periodic structures which diffract incident light in specific directions. A number of diffracted light beams can form an arbitrary three-dimensional image. Generally, these microscopic structures are recognized as being difficult to duplicate, and therefore, holograms have been widely used in the anticounterfeiting of bank notes, credit cards, etc. However, conventional anticounterfeiting methods based on the physical appearance of holograms are nowadays not completely secure [44]. Nanophotonic solutions, utilizing light–matter interactions on the nanoscale, would provide higher anticounterfeiting capability and would potentially enable other novel applications, such as artifact–metric systems [45].

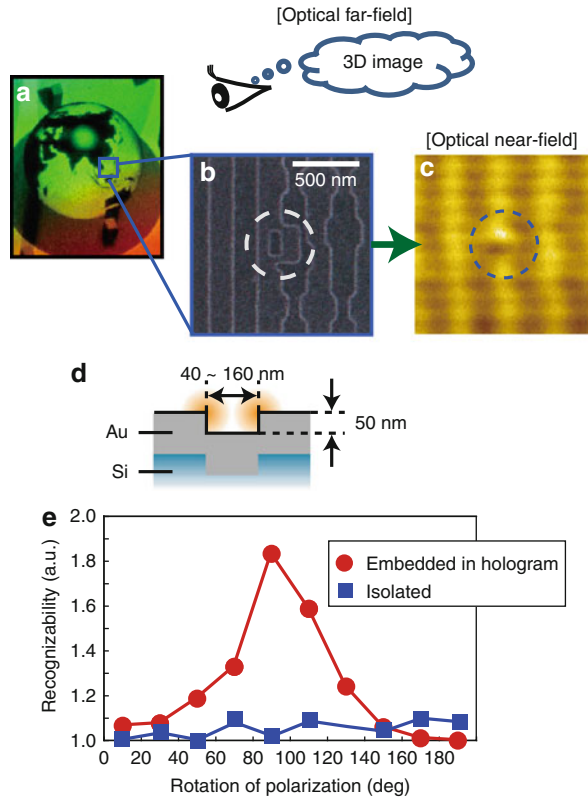
The hierarchical hologram works in both optical far-fields and near-fields, the former being associated with conventional holographic images (Fig. 23.9a) and the latter being associated with the optical intensity distribution based on a nanometric structure (Fig. 23.9b) that is accessible only via optical near-fields (Fig. 23.9c). In principle, a structural change occurring at the subwavelength scale does not affect the optical response function, which is dominated by propagating light. Therefore, the visual aspect of the hologram is not affected by such a small structural change on the surface. Additional data can thus be written by engineering structural changes in the subwavelength regime so that they are only accessible via optical near-field interactions without having any influence on the optical response obtained via the conventional far-field light. By applying this hierarchy, new functions can be added to conventional holograms.

There are at least two strategies for realizing a hierarchical hologram.

One strategy is to apply nanometric structural changes to the surface structure of a conventional hologram. In Ref. [46], a thin metal layer is coated on a conventional hologram and diffraction grating, followed by nanostructure patterning by a focused ion beam machine. Additional information corresponding to the fabricated nanostructures is successfully retrieved while preserving the macroscopic view of the original hologram or the diffraction efficiency of the diffraction grating.

The other strategy, employed in the case of embossed holograms composed of diffraction gratings, is to locally engineer the original hologram pattern from the beginning, that is, to embed nanostructures *within* the original pattern of the hologram [47]. In this case, since the original hologram is basically composed of

Fig. 23.9 Hierarchical optical elements, such as *hierarchical holograms*, based on the different optical responses obtained in (a) the optical far-field and (c) the optical near-field. (b) A nanostructure is embedded in the original grating structure of the hologram. (d) Evident polarization dependency in optical near-fields results based on the surrounding structures



one-dimensional grating structures, evident polarization dependence is obtained in retrieving the nanostructures via optical near-fields, as detailed below. There are some additional benefits with this approach: one is that we can fully utilize the existing industrial facilities and fabrication technologies that have been developed for conventional holograms, yet providing additional information in the hologram. Another is that the polarization dependence facilitates the readout of nanostructures via optical near-fields, as mentioned below.

As shown in Fig. 23.9, we created a sample device to experimentally demonstrate retrieval of the nanostructures embedded within an embossed hologram. The entire device structure, whose size was 15×20 mm, was fabricated by electron beam lithography on a Si substrate, followed by sputtering a 50-nm-thick Au layer. The cross-sectional profile is shown in Fig. 23.9d.

As indicated in Fig. 23.9a, we can observe a three-dimensional image of the earth reconstructed from the device. More specifically, the device was based on the design of *Virtuagram*®, developed by Dai Nippon Printing Co., Ltd., Japan, which is a high-definition computer-generated hologram composed of binary-level one-dimensional modulated gratings, as shown in the SEM image

in Fig. 23.9b. Within the device, we slightly modified the shape of the original structure of the hologram so that the nanostructural change was accessible only via optical near-field interactions. As shown in Fig. 23.9b, square- or rectangle-shaped structures, whose associated optical near-fields correspond to the additional or hidden information, were embedded in the original hologram structures. The unit size of the nanostructures ranged from 40 to 160 nm. Note that the original hologram was composed of arrays of one-dimensional grid structures, spanning along the vertical direction in Fig. 23.9b. To embed the nanophotonic codes, the grid structures were partially modified in order to implement the nanophotonic codes. Nevertheless, the grid structures remained topologically continuously connected along the vertical direction. On the other hand, the nanostructures were always isolated from the original grid structures. These geometrical characteristics provide interesting polarization dependence.

The input light induces oscillating surface charge distributions due to the coupling between the light and electrons in the metal. Note that the original one-dimensional grid structures span along the vertical direction. The y -polarized input light induces surface charges along the vertical grids. Since the grid structure continuously exists along the y -direction, there is no chance for the charges to be concentrated. However, in the area of the embedded nanophotonic code, we can find structural discontinuity in the grid; this results in higher charge concentrations at the edges of the embedded nanostructure. On the other hand, the x -polarized input light sees structural discontinuity along the horizontal direction due to the vertical grid structures, as well as in the areas of the embedded nanostructures. It turns out that charge concentration occurs not only in the edges of the embedded nanostructures but also at other horizontal edges of the environmental grid structures. When square-shaped nanophotonic codes are *isolated* in a uniform plane, both x - and y -polarized input light have equal effects on the nanostructures. These mechanisms indicate that the nanostructures embedded in holograms could exploit these polarization dependences.

In the experimental demonstration, optical responses in near-mode observation were detected using a NSOM operated in an illumination–collection mode with an optical fiber tip having a radius of curvature of 5 nm. The observation distance between the tip of the probe and the sample device was set at less than 50 nm. The light source used was a laser diode (LD) with an operating wavelength of 785 nm, and scattered light was detected by a photomultiplier tube (PMT).

We examined NSOM images in the vicinity of nanostructures that were embedded in the hologram and nanostructures that were not embedded in the hologram using light from a linearly polarized radiation source, with polarizations rotated by 0–180° at 20° intervals. In the case of nanostructures embedded in the hologram, clear polarization dependence was observed. To quantitatively evaluate the polarization dependency of the embedded nanophotonic code, we adopted a figure of merit that we call *recognizability* for the observed NSOM images [47], indicating the relative intensity compared with the surroundings.

The square and circular marks in Fig. 23.9e respectively show the recognizability of isolated nanostructures and those embedded in the hologram. Clear polarization

dependency is observed in the case of the nanostructures embedded in the holograms, facilitating near-field information retrieval.

23.5 Shape-Engineered Nanostructures for Polarization Control for Nanophotonic Systems

Shape engineering of nanostructures is one of the most useful and important means to implement nanometer-scale photonic systems, an example of which has already been demonstrated in the hierarchical hologram in described in Sect. 23.4.3. Electric field enhancement based on the resonance between light and free electron plasma in a metal nanostructure is one well-known feature [48] that has been used in many other applications, such as optical data storage [49], biosensors [50], and integrated optical circuits [51–53]. Such resonance effects are, however, only one of the possible light–matter interactions on the nanometer scale that can be exploited for practical applications. For example, it is possible to engineer the polarization of light in the optical near-field and far-field by controlling the geometries of metal nanostructures. Since there are a vast number of design parameters potentially available on the nanometer scale, an intuitive physical picture of the polarization associated with geometries of nanostructures can be useful in restricting the parameters to obtain the intended optical responses.

In this section, we consider polarization control in the optical near-field and far-field by designing the shape of a metal nanostructure, based on the concepts of *elemental shape* and *layout*, to analyze and synthesize optical responses brought about by the nanostructure [54]. In particular, we focus on the problem of rotating the plane of polarization. Polarization in the optical near-field is an important factor in the operation of nanophotonic devices [55]. Polarization in the far-field is, of course, also important for various applications. Devices including nanostructures have already been employed, for instance, in so-called wire-grid polarizers [56, 57].

The concepts of elemental shape and layout are physically related, respectively, to the electric current induced in the metal nanostructure and the electric fields, that is, the optical near-fields, induced between individual elements of the metal nanostructures, which helps in understanding the induced optical responses. For example, it will help to determine if a particular optical response originates from the shape of the nanostructure itself, that is to say, the elemental shape factor, or from the positional relations between individual elements, that is to say, the layout factor. Such analysis will also help in the design of more complex structures, such as multilayer systems. What should be noted, in particular in the case of multilayer systems, is that the optical near-fields appearing between individual elemental shapes, including their hierarchical properties, strongly affect the resultant optical response. This indicates that the properties of the system are not obtained by a superposition of the properties of individual elements, in contrast to optical antennas, whose behavior is explained by focusing on factors associated with individual elements [58].

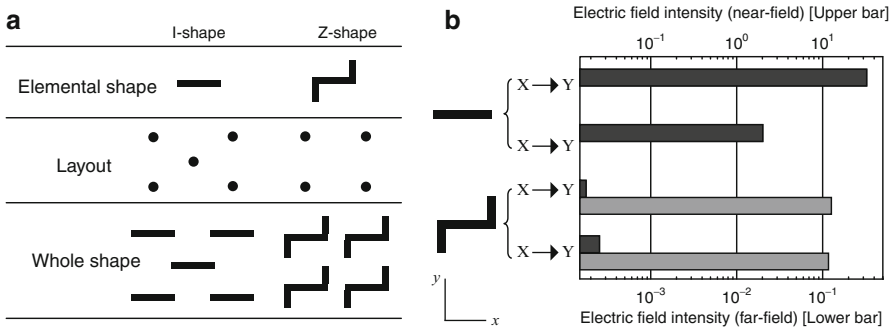


Fig. 23.10 (a) *Elemental shape* and *layout* factors used to describe the configuration of the entire structure. This chapter deals with two representative structures, what we call I- and Z-shapes. (b) Electric field intensity in near- and far-fields produced by I-shape and Z-shape structures

23.5.1 Polarization and Geometry on the Nanometer Scale

The nanostructure we consider is located on an xy -plane and is irradiated with linearly polarized light from the direction of the normal. We first assume that the nanostructure has a regular structure on the xy -plane; in other words, it has no fine structure along the z -axis. Here we consider the concepts of *elemental shape* and *layout*, introduced above, to represent the whole structure. Elemental shape refers to the shape of an individual structural unit, and the whole structure is composed of a number of such units having the same elemental shape. Layout refers to the relative positions of such structural units. Therefore, the whole structure is described as a kind of convolution of elemental shape and layout. This is schematically shown in Fig. 23.10a.

We begin with the following two example cases, which, as will shortly be presented in Fig. 23.10b, exhibit contrasting properties in their optical near-field and far-field responses. One is what we call an I-shape, which exhibits a strong electric field only in the optical near-field regime, while showing an extremely small far-field electric field. The other is what we call a Z-shape, which exhibits a weak near-field electric field, while showing a strong far-field electric field. They are schematically shown in the top row in Fig. 23.10a. In the case of the I-shape, the elemental shape is a rectangle. Such rectangular units are arranged as specified by the layout (second row in Fig. 23.10a); they are arranged with the same interval horizontally (along the x -axis) and vertically (along the y -axis), but every other row is horizontally displaced by half of the interval. In the case of the Z-shape, the element shape is like the letter “Z,” and they are arranged regularly in the xy -plane as specified by the layout shown in the second row in Fig. 23.10a.

We calculate the optical responses in both the near-field and far-field based on a finite-difference time-domain (FDTD) method [59, 60]. As the material, we assume gold, which has a refractive index of 0.16 and an extinction ratio of 3.8 at a wavelength of 688 nm [61]. Representative geometries of the I-shape and Z-shape structures in the xy -plane are shown in Fig. 23.11a, b, respectively. The width (line width)

of the structures is 60 nm, and the thickness is 200 nm. The light source is placed 500 nm away from one of the surfaces of the structures. We assume periodic boundary conditions at the edges in the x - and y -directions and perfectly matched layers in the z -direction.

The near-field intensity is calculated at a plane 5 nm away from the surface that is opposite to the light source, which we call the near-field output plane. With continuous-wave, linearly polarized 688-nm light parallel to the x -axis as the input light, we analyze the y -component of the electric field at the near-field output plane. From this, we evaluate the polarization conversion efficiency in the near-field regime, defined by

$$T_{x \rightarrow y}^{NEAR} = \frac{|E_y(\mathbf{p}_n)|^2}{|E_x(\mathbf{p}_i)|^2}, \quad (23.6)$$

where \mathbf{p}_n is the position on the near-field output plane, \mathbf{p}_i is the position of the light source, and $E_x(\mathbf{p})$ and $E_y(\mathbf{p})$, respectively, represent the x - and y -components of the electric field at position \mathbf{p} . Since $T_{x \rightarrow y}^{NEAR}$ varies depending on the position, we focus on the maximum value in the near-field output plane. The metric defined by Eq. (23.6) can be larger than 1 due to electric field enhancement. The energy conversion efficiency can be obtained by calculating Poynting vectors existing in the near-field output plane; however, the region of interest in the near-field regime is where the charge distributions give their local maximums and minimums, as discussed shortly in this section. Therefore, we adopted the metric in the near-field regime given by Eq. (23.6).

The far-field optical response is calculated at a plane 2 μm away from the surface of the structure opposite to the light source, which we call the far-field output plane. We assume an input optical pulse with a differential Gaussian form whose width is 0.9 fs, corresponding to a bandwidth of around 200–1,300 THz. The transmission efficiency is given by calculating the Fourier transform of the electric field at the far-field output plane divided by the Fourier transform of the electric field at the light source. Since we are interested in the conversion from x -polarized input light to y -polarized output light, the transmission is given by

$$T_{x \rightarrow y}^{FAR}(\lambda) = \left| \frac{F[E_y(t, \mathbf{p}_f)]}{F[E_x(t, \mathbf{p}_i)]} \right|^2, \quad (23.7)$$

where \mathbf{p}_f denotes the position on the far-field output plane and $F[E(t, \mathbf{p})]$ denotes the Fourier transform of $E(t, \mathbf{p})$. Here, $T_{x \rightarrow y}^{FAR}$ is also dependent on position, as well as wavelength, but it is not strongly dependent on \mathbf{p}_f . In this chapter, we represent $T_{x \rightarrow y}^{FAR}$ by a value given at a position on the far-field output plane with a wavelength $\lambda = 688$ nm.

Figure 23.10b summarizes the electric field intensity of y -polarized output light from x -polarized input light and that of x -polarized output light from y -polarized input light, in both the near- and far-fields at the wavelength of 688 nm. The horizontal scale in Fig. 23.10b is physically related to the polarization conversion efficiency.

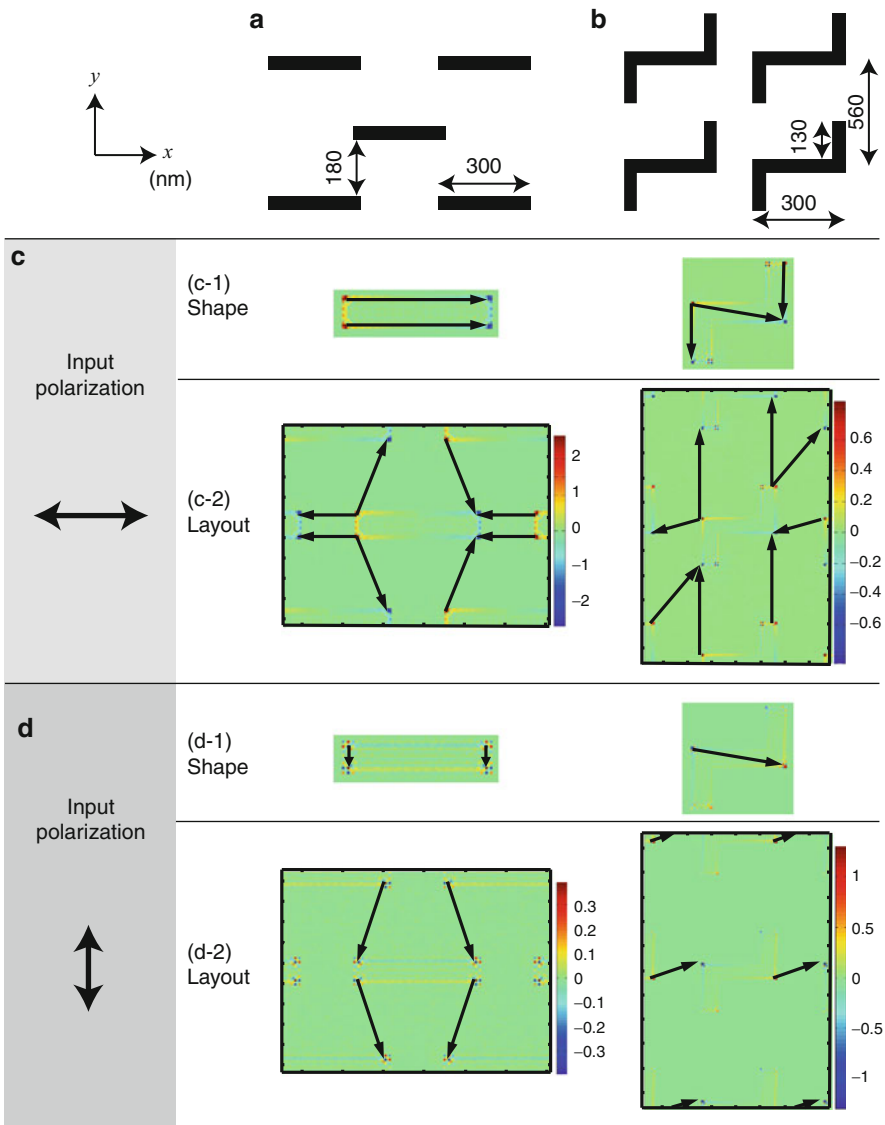


Fig. 23.11 Charge distributions induced in (a) I-shape and (b) Z-shape structures with (c) x -polarized and (d) y -polarized input light. The *arrows* in (c-1) and (d-1) are associated with the induced electric currents within the elemental shapes and those in (c-2) and (d-2) are associated with near-fields among elemental shapes

We first note the following two features. First, the near-field electric field intensity, represented by dark gray bars in Fig. 23.10b, is nearly 2,000 times higher with the I-shape than with the Z-shape. The far-field electric field intensity, shown by light gray bars, on the other hand, is around 200 times higher with the Z-shape

than with the I-shape. One of the primary goals of this chapter is to explain the physical mechanism of these contrasting optical responses in the near- and far-fields in an intuitive framework, which will be useful for analyzing and designing more complex systems.

Here we derive the distribution of induced electron charge density (simply referred to as charge hereafter) by calculating the divergence of the electric fields to analyze the relation between the shapes of the structures and their resultant optical responses. Figure 23.11 shows such charge distributions for I-shape and Z-shape structures.

First, we describe Fig. 23.11c, which relates to x -polarized input light. The images shown in Fig. 23.11(c-1), denoted by “Shape,” represent the distributions of charges at each unit, namely, charges associated with the elemental shape. The images in Fig. 23.11(c-2), denoted by “Layout,” show the distributions of charges at elemental shapes and their surroundings.

We can extract positions at which induced electron charge densities exhibit a local maximum and a local minimum. Then, we can derive two kinds of vectors connecting the local maximum and local minimum, which we call flow vectors. One is a vector existing inside an elemental shape, denoted by dashed arrows in Fig. 23.11(c-1), which is physically associated with an electric current induced in the metal. The other vector appears between individual elemental shapes, denoted by solid arrows in Fig. 23.11(c-2), which is physically associated with near-fields between elemental shapes. We call the latter ones inter-elemental-shape flow vectors.

From those flow vectors, first, in the case of the I-shape structure shown in Fig. 23.11a, we note that:

1. Within an elemental shape in Fig. 23.11(c-1), the flow vectors are parallel to the x -axis (There is no y -component in the vectors).
2. At the layout level in Fig. 23.11(c-2), flow vectors that have y -components appear. Also, flow vectors that have y -components are in opposite directions between neighboring elemental shapes.

From these facts, the y -components of the flow vectors are arranged in a quadrupole manner, which agrees with the very small radiation in the far-field demonstrated in Fig. 23.10b. Also, these suggest that the appearance of y -components in the flow vectors originates from the layout factor, not from the elemental shape factor. This indicates that the polarization conversion capability of the I-shape structure is layout sensitive, which will be explored in more detail in Sect. 23.5.2.

Second, in the case of the Z-shape structure, we note that:

1. In the elemental shape, y -components of the flow vectors appear.
2. In the layout, we can also find y -components in the flow vectors. Also, at the layout level, the y -components of all vectors are in the same direction.

In complete contrast to the I-shape structure, the Z-shape structure has y -components in the flow vectors arranged in a dipole-like manner, leading to strong y -polarized light in the far-field, as demonstrated in Fig. 23.10b. Also, the ability to convert x -polarized input light to y -polarized output light in the far-field, as quantified by $T_{x \rightarrow y}^{FAR}$, primarily originates from the elemental shape factor, not from the layout factor.

23.5.2 Layout-Dependent Polarization Control

As indicated in Sect. 23.5.1, the polarization conversion from x -polarized input light to y -polarized output light with the I-shape structure originates from the layout factor. Here, we modify the layout while keeping the same elemental shape, and we evaluate the resulting conversion efficiencies.

In Fig. 23.12, we examine such layout dependencies by changing the horizontal displacement of elemental shapes between two consecutive rows, indicated by the parameter D in the inset of Fig. 23.12c. The polarization conversion efficiency, $T_{x \rightarrow y}^{FAR}$, at the wavelength of 688 nm as a function of D is indicated by the circles in Fig. 23.12a. Although it exhibits very small values for the I-shape structure, it has a large variance depending on the layout: a maximum value of around 10^{-9} when D is 200 nm and a minimum value of around 10^{-12} when D is 80 nm, a difference of three orders of magnitude. On the other hand, the Z-shape structure exhibits an almost constant $T_{x \rightarrow y}^{FAR}$ with different horizontal positional differences, as indicated by the squares in Fig. 23.12a, meaning that the Z-shape structure is weakly dependent on the layout factor.

To account for such a tendency, we represent the I-shape structure by two inter-elemental-shape flow vectors denoted by \mathbf{p}_1 and \mathbf{p}_2 in Fig. 23.12b. Here, R_i and θ_i , respectively, denote the length of \mathbf{p}_i and its angle relative to the y -axis. All of the inter-elemental-shape flow vectors are identical to those two vectors and their mirror symmetry. Physically, a flow vector with a large length and a large inclination to the y -axis contributes weakly to y -components of the radiation. Therefore, the index $\cos \theta_i / R_i^2$ will affect the radiation. Together with the quadrupole-like layout, we define the following metric:

$$|\cos \theta_1 / R_1^2 - \cos \theta_2 / R_2^2|, \quad (23.8)$$

which is denoted by the triangles in Fig. 23.12a; it agrees well with the conversion efficiency $T_{x \rightarrow y}^{FAR}$ of the I-shape structure.

23.5.3 Application to Authentication Function

The structures that have been discussed so far contain a regular structure on a single plane, namely, they are single-layer structures. Now, we consider stacking another layer on top of the original layer. As an example, we consider adding another layer on top of the I-shape structure so that the y -component in the far-field radiation increases (recall that the original I-shape-only structure exhibits very small far-field radiation). We call the two nanostructures Shape A and Shape B hereafter.

Shape A and Shape B were designed as aligned rectangular units on an xy -plane at constant intervals horizontally (along the x -axis) and vertically (along the y -axis), as, respectively, shown in Fig. 23.13a, b. When we irradiate Shape A with x -polarized light, surface charges are concentrated at the horizontal edges

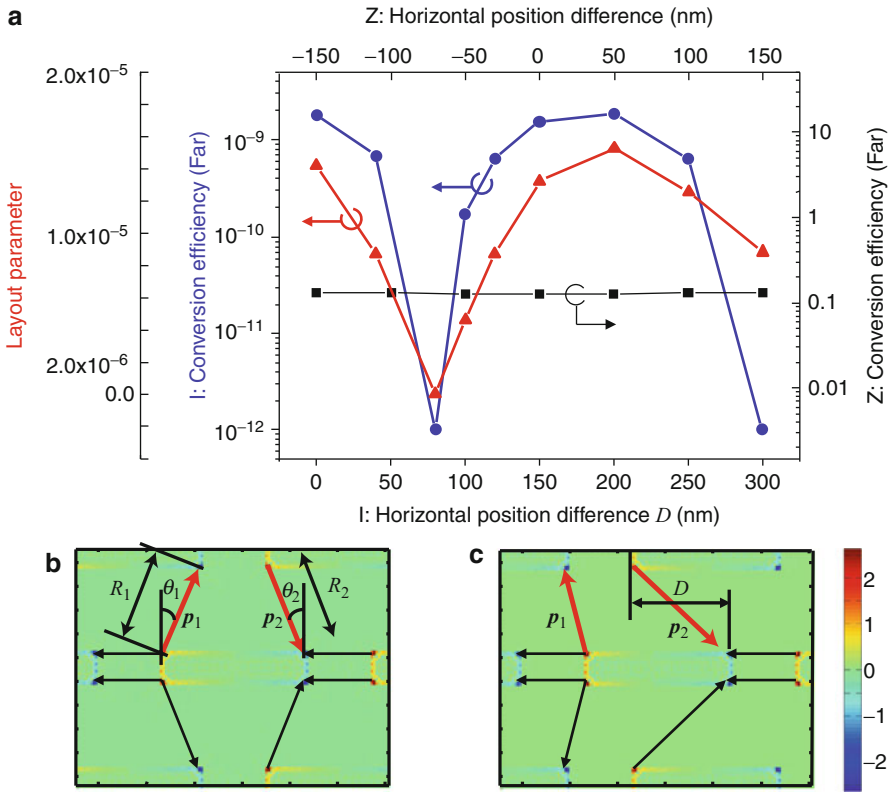


Fig. 23.12 (a) Conversion efficiency dependence on the layout factor. The I-shape structure exhibits stronger dependence on layout than the Z-shape structure. (b) and (c) Current distributions and inter-elemental-shape flow vectors for I-shape structure when (b) $D = 80$ nm and (c) $D = 200$ nm

of each of the rectangular units. The relative phase difference of the oscillating charges between the horizontal edges is π , which is schematically represented by + and - marks in Fig. 23.13a. Now, consider the y -component of the far-field radiation from Shape A, which is associated with the charge distributions induced in the rectangle. When we draw arrows from the + marks to the - marks along the y -axis, we find that adjacent arrows are always directed oppositely, indicating that the y -component of the far-field radiation is externally small. In other words, Shape A behaves as a quadrupole regarding the y -component of the far-field radiation. It should also be noted that near-field components exist in the vicinity of the units in Shape A. With this fact in mind, we put the other metal nanostructure, Shape B, on top of Shape A. Through the optical near-fields in the vicinity of Shape A, surface charges are induced on Shape B. What should be noted here is that the arrows connecting the + and - marks along the y -axis are now aligned in the same direction, and so the y -component of the far-field radiation appears; that is, the

stacked structure of Shape A and Shape B behaves as a dipole (Fig. 23.13c). Also, Shape A and Shape B need to be closely located to invoke such effects since the optical near-field interactions between Shape A and Shape B are critical. In other words, far-field radiation appears only when Shape A and Shape B are correctly stacked; that is to say, a *quadrupole–dipole transform* is achieved through shape-engineered nanostructures and their associated optical near-field interactions.

In Fig. 23.13d, we also consider the output signals when we place differently shaped structures on top of Shape A, instead of Shape B. With Shape B', Shape B'', and Shape B''', which are respectively represented in the insets of Fig. 23.13d, the output signals do not appear, as shown from the fourth to the sixth rows in Fig. 23.13d, since the condition necessary for far-field radiation is not satisfied with those shapes, namely, the correct *key* is necessary to unlock the *lock* [62].

We fabricated structures consisting of (i) Shape A only, (ii) Shape B only, and (iii) Shapes A and B stacked. Although the stacked structure should ideally be provided by combining the individual single-layer structures, in the following experiment, the stacked structure was integrated in a single sample as a solid two-layer structure to avoid the experimental difficulty in precisely aligning the individual structures mechanically. The fabrication process was detailed in Ref. [63]. The lower side in Fig. 23.13e also shows SEM images of fabricated samples of (i)–(iii). Because the stacked structure was fabricated as a single sample, the gap between Shapes A and B was fixed at 200 nm.

The performance was evaluated in terms of the polarization conversion efficiency by radiating x -polarized light on each of the areas (i), (ii), and (iii) and measuring the intensity of the y -component in the transmitted light. The light source was a laser diode with an operating wavelength of 690 nm. Two sets of polarizers (extinction ratio 10^{-6}) were used to extract the x -component for the input light and to extract the y -component in the transmitted light. The intensity was measured by a lock-in controlled photodiode. The position of the sample was controlled by a stepping motor with a step size of 20 μm . Figure 23.13e shows the polarization conversion efficiency as a function of the position on the sample, where it exhibited a larger value specifically in the areas where the stacked structure of Shapes A and B was located, which agrees well with the theoretically predicted and calculated results shown in Fig. 23.13d.

23.6 Summary

This chapter reviews nanophotonic systems based on localized and hierarchical optical near-field processes. In particular, optical excitation transfer involving optical near-field interactions and its hierarchical properties are highlighted while demonstrating their enabling functionalities. Networks of optical excitation transfers mediated by near-field interactions and shape-engineered nanostructures and their associated polarization properties have also been presented. It should be emphasized that those basic features enable versatile applications and functionalities besides the example demonstrations shown here. Also, there are many other degrees

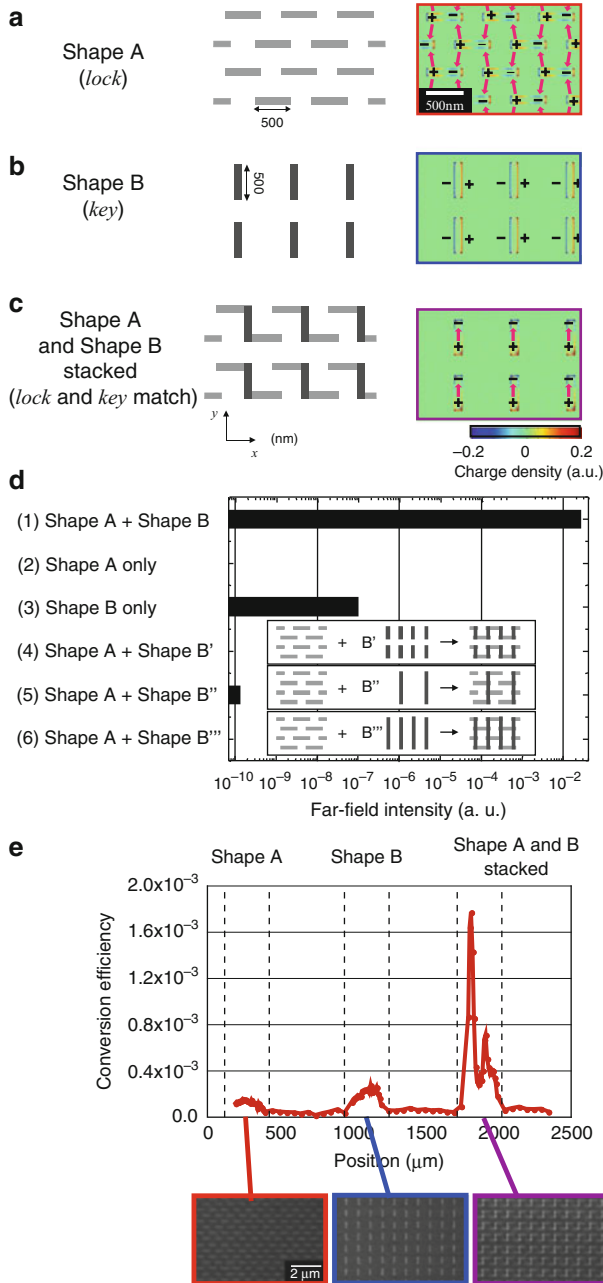


Fig. 23.13 (a)–(c) Shapes and the associated distributions of induced charge density. (a) Shape A, (b) Shape B, and (c) stacked structure of Shapes A and B. (d) Comparison of calculated far-field intensity for various combinations of shapes. Far-field intensity appears strongly only when Shape A matches the appropriate Shape B. (e) Measured polarization conversion efficiency for three areas of the fabricated device. Conversion efficiency exhibited a larger value specifically in the areas where the stacked structure of Shapes A and B was located. SEM images of each area are also shown

of freedom in the nanometer scale that need to be deeply understood in terms of their implications for systems. Further exploration and attempts to exploit nanophotonics for future devices and systems will certainly be exciting.

Acknowledgements Part of this work was supported by the Strategic Information and Communications R&D Promotion Programme (SCOPE) of the Ministry of Internal Affairs and Communications and Grants-in-Aid for Scientific Research from the Japan Society for the Promotion of Science. The author acknowledges Dai Nippon Printing Co., Ltd., for fabrication of the hierarchical hologram.

References

1. D.W. Pohl, D. Courjon (eds.), *Near Field Optics* (Kluwer, Dordrecht, 1993)
2. M. Ohtsu, H. Hori, *Near-Field Nano-Optics* (Kluwer/Plenum Publishers, New York, 1999)
3. M. Ohtsu, K. Kobayashi, T. Kawazoe, S. Sangu, T. Yatsui, *IEEE J. Sel. Top. Quantum Electron.* **8**, 839 (2002)
4. M. Ohtsu, K. Kobayashi, T. Kawazoe, T. Yatsui, M. Naruse, *Principles of Nanophotonics* (Taylor and Francis, Boca Raton, 2008)
5. S.A. Maier, P.G. Kik, H.A. Atwater, S. Meltzer, E. Harel, B.E. Koel, A.A.G. Requicha, *Nat. Mater.* **2**, 229 (2003)
6. Z.K. Tang, A. Yanase, T. Yasui, Y. Segawa, K. Cho, *Phys. Rev. Lett.* **71**, 1431 (1993)
7. T. Kawazoe, K. Kobayashi, S. Sangu, M. Ohtsu, *Appl. Phys. Lett.* **82**, 2957 (2003)
8. S.B. Akers, *IEEE Trans. Comput.* **C-27**, 509 (1978)
9. C. Pistol, C. Dwyer, A.R. Lebeck, *IEEE Micro* **28**, 7 (2008)
10. C. Dwyer, A. Lebeck, *Introduction to DNA Self-Assembled Computer Design* (Artech House, Norwood, 2007)
11. W. Nomura, T. Yatsui, T. Kawazoe, M. Naruse, M. Ohtsu, *Appl. Phys. B* **100**, 181 (2010)
12. M. Naruse, H. Hori, K. Kobayashi, T. Kawazoe, M. Ohtsu, *Appl. Phys. B* **102**, 717 (2011)
13. M. Naruse, F. Peper, K. Akahane, N. Yamamoto, T. Kawazoe, N. Tate, M. Ohtsu, *ACM J. Emerg. Technol. Comput. Syst.* **8**, 4 (2012)
14. H. Liu, *IEEE Micro* **22**, 58 (2002)
15. M. Naruse, T. Miyazaki, T. Kawazoe, S. Sangu, K. Kobayashi, F. Kubota, M. Ohtsu, *IEICE Trans. Electron.* **E88-C**, 1817 (2005)
16. A. Grunnet-Jepsen, A.E. Johnson, E.S. Maniloff, T.W. Mossberg, M.J. Munroe, J.N. Sweetser, *Electron. Lett.* **35**, 1096 (1999)
17. M. Naruse, H. Mitsu, M. Furuki, I. Iwasa, Y. Sato, S. Tatsuura, M. Tian, F. Kubota, *Opt. Lett.* **29**, 608 (2004)
18. M. Naruse, T. Miyazaki, F. Kubota, T. Kawazoe, S. Sangu, K. Kobayashi, M. Ohtsu, *Opt. Lett.* **30**, 201 (2005)
19. T. Kawazoe, K. Kobayashi, M. Ohtsu, *Appl. Phys. Lett.* **86**, 103102 (2005)
20. I. Arsovski, T. Chandler, A. Sheikholeslami, *IEEE J. Solid-State Circuits* **38**, 155 (2003)
21. P.-F. Lin, J.B. Kuo, *IEEE J. Solid-State Circuits* **36**, 666 (2001)
22. J.W. Goodman, A.R. Dias, L.M. Woody, *Opt. Lett.* **2**, 1 (1978)
23. P.S. Guilfoyle, D.S. McCallum, *Opt. Eng.* **35**, 436 (1996)
24. B. Li, Y. Qin, X. Cao, K.M. Sivalingam, *Opt. Netw. Mag.* **2**, 27 (2001)
25. M. Naruse, T. Kawazoe, S. Sangu, K. Kobayashi, M. Ohtsu, *Opt. Express* **14**, 306 (2006)
26. E.A. De Souza, M.C. Nuss, W.H. Knox, D.A.B. Miller, *Opt. Lett.* **20**, 1166 (1995)
27. M. Naruse, H. Hori, K. Kobayashi, M. Ohtsu, *Opt. Lett.* **32**, 1761 (2007)
28. P. Kocher, J. Jaffe, B. Jun, *Cryptography research* (1998), <http://www.cryptography.com/public/pdf/DPATechInfo.pdf>

29. H. Hori, Electronic and electromagnetic properties in nanometer scales, in *Optical and Electronic Process of Nano-Matters*, ed. by M. Ohtsu (Kluwer, Dordrecht, 2001), pp. 1–55
30. G.-L. Ingold, Y.V. Nazarov, Charge tunneling rates in ultrasmall junctions, in *Single Charge Tunneling*, ed. by H. Grabert, M.H. Devoret (Plenum, New York, 1992), pp. 21–107
31. H.J. Carmichael, *Statistical Methods in Quantum Optics I* (Springer, Berlin, 1999)
32. M. Naruse, T. Kawazoe, R. Ohta, W. Nomura, M. Ohtsu, Phys. Rev. B **80**, 125325 (2009)
33. W. Nomura, T. Yatsui, T. Kawazoe, M. Ohtsu, J. Nanophoton. **1**, 011591 (2007)
34. T. Franzl, T.A. Klar, S. Schietinger, A.L. Rogach, J. Feldmann, Nano Lett. **4**, 1599 (2004)
35. T.A. Klar, T. Franzl, A.L. Rogach, J. Feldmann, Adv. Matter. **17**, 769 (2005)
36. M. Naruse, E. Runge, K. Kobayashi, M. Ohtsu, Phys. Rev. B **82**, 125417 (2010)
37. M. Naruse, K. Leibnitz, F. Peper, N. Tate, W. Nomura, T. Kawazoe, M. Murata, M. Ohtsu, Nano Commun. Netw. **2**, 189 (2011)
38. M. Naruse, T. Yatsui, W. Nomura, N. Hirose, M. Ohtsu, Opt. Express **13**, 9265 (2005)
39. M. Naruse, T. Inoue, H. Hori, Jpn. J. Appl. Phys. **46**, 6095 (2007)
40. M. Naruse, T. Yatsui, T. Kawazoe, Y. Akao, M. Ohtsu, IEEE Trans. Nanotechnol. **7**, 14 (2008)
41. M. Naruse, T. Yatsui, J.H. Kim, M. Ohtsu, Appl. Phys. Express **1**, 062004 (2008)
42. M. Ohtsu, K. Kobayashi, *Optical Near Fields* (Springer, Berlin, 2004)
43. R.L. van Renesse, *Optical Document Security* (Artech House, Boston, 2005)
44. S.P. McGrew, Proc. SPIE **1210**, 66 (1990)
45. H. Matsumoto, T. Matsumoto, IPSJ J. **44**, 1991 (2003)
46. N. Tate, W. Nomura, T. Yatsui, M. Naruse, M. Ohtsu, Opt. Express **16**, 607 (2008)
47. N. Tate, M. Naruse, T. Yatsui, T. Kawazoe, M. Hoga, Y. Ohyagi, T. Fukuyama, M. Kitamura, M. Ohtsu, Opt. Express **18**, 7497 (2010)
48. P. Muhlschlegel, H.-J. Eisler, O.J.F. Martin, B. Hecht, D.W. Pohl, Science **308**, 1607 (2005)
49. T. Matsumoto, T. Shimano, H. Saga, H. Sukeda, M. Kiguchi, J. Appl. Phys. **95**, 3901 (2004)
50. A.J. Haes, S. Zou, G.C. Schatz, R.P.V. Duyne, J. Phys. Chem. B **108**, 109 (2004)
51. J. Takahara, S. Yamagishi, H. Taki, A. Morimoto, T. Kobayashi, Opt. Lett. **22**, 475 (1997)
52. M. Quinten, A. Leitner, J.R. Krenn, F.R. Aussenegg, Opt. Lett. **23**, 1331 (1998)
53. D.F.P. Pile, D.K. Gramotnev, M. Haraguchi, T. Okamoto, M. Fukui, J. Appl. Phys. **100**, 013101 (2006)
54. M. Naruse, T. Yatsui, H. Hori, M. Yasui, M. Ohtsu, Polarization in optical near- and far-field and its relation to shape and layout of nanostructures. J. Appl. Phys. **103**(11), 113525 (2008)
55. T. Yatsui, S. Sangu, T. Kawazoe, M. Ohtsu, S.J. An, J. Yoo, G.-C. Yi, Appl. Phys. Lett. **90**, 223110 (2007)
56. M. Xu, H. Urbach, D. de Boer, H. Cornelissen, Opt. Express **13**, 2303 (2005)
57. J.J. Wang, F. Walters, X. Liu, P. Sciortino, X. Deng, Appl. Phys. Lett. **90**, 061104 (2007)
58. K.B. Crozier, A. Sundaramurthy, G.S. Kino, C.F. Quate, J. Appl. Phys. **94**, 4632 (2003)
59. K. Yee, IEEE Trans. Antennas Propag. **14**, 302 (1966)
60. A. Taflove, S.C. Hagness, *Computational Electrodynamics: The Finite-Difference Time-Domain Method* (Artech House, Boston, 2005)
61. D.W. Lynch, W.R. Hunter, Comments on the optical constants of metals and an introduction to the data for several metals, in *Handbook of Optical Constants of Solids*, ed. by E.D. Palik (Academic, Orlando, 1985), pp. 275–367
62. M. Naruse, T. Yatsui, T. Kawazoe, N. Tate, H. Sugiyama, M. Ohtsu, Appl. Phys. Express **1**, 112101 (2008)
63. N. Tate, H. Sugiyama, M. Naruse, W. Nomura, T. Yatsui, T. Kawazoe, M. Ohtsu, Opt. Express **17**, 11113 (2009)

Probe-Free Nanophotonic Systems: Macroscale Applications Based on Nanophotonics

24

Naoya Tate, Makoto Naruse, and Motoichi Ohtsu

Contents

24.1	Introduction.....	910
24.2	Probe-Free Nanophotonic Systems.....	911
24.3	Nanophotonic Matching as Macroscale Observation.....	913
24.3.1	Macroscale Observation.....	913
24.3.2	Quadrupole–Dipole Transform.....	914
24.3.3	Nanophotonic Matching.....	915
24.3.4	Experimental Demonstration.....	918
24.3.5	Outlook.....	921
24.4	Nanophotonics-Induced Phase Transition as Magnified-Transcription.....	922
24.4.1	Magnified-Transcription of Optical Near-Fields.....	922
24.4.2	Photoinduced Phase Transition.....	923
24.4.3	Experimental Demonstrations.....	924
24.4.4	Outlook.....	927
24.5	Nanophotonic Hierarchical Hologram.....	927
24.5.1	Background.....	927
24.5.2	Basic Concept.....	928
24.5.3	Nanophotonic Code.....	930
24.5.4	Numerical Evaluations.....	931
24.5.5	Experimental Demonstration.....	934

N. Tate (✉) · M. Ohtsu

School of Engineering, The University of Tokyo, Tokyo, Japan

Nanophotonics Research Center, The University of Tokyo, Tokyo, Japan

e-mail: tate@nanophotonics.t.u-tokyo.ac.jp; ohtsu@ee.t.u-tokyo.ac.jp

M. Naruse

Photonic Network Research Institute, National Institute of Information and Communications
Technology, Tokyo, Japan

Nanophotonics Research Center, The University of Tokyo, Tokyo, Japan

e-mail: naruse@nict.go.jp

M. Ohtsu (ed.), *Handbook of Nano-Optics and Nanophotonics*,

DOI 10.1007/978-3-642-31066-9_25, © Springer-Verlag Berlin Heidelberg 2013

909

24.5.6 Hierarchical Security System.....	938
24.5.7 Outlook.....	938
24.6 Summary.....	940
References.....	940

Abstract

To implement innovative nanometric optical processing systems as probe-free nanophotonic systems, it is necessary to exploit the unique attributes of nanometer-scale optical near-field interactions in a completely parallel fashion. This chapter is devoted to describing basic concepts necessary for two-dimensional parallel processing of light–matter interactions on the nanometer scale in order to realize probe-free nanophotonic systems. Additionally, the concepts and some demonstrations of the hierarchy inherent in nanophotonics, based on the hierarchy between optical near- and far-fields, are described as practical applications of optical near-field interactions.

24.1 Introduction

Nanophotonics is a novel technology that utilizes the optical near-field, the electromagnetic field that mediates the interactions between closely spaced nanometric matter [1, 2]. By exploiting optical near-field interactions, nanophotonics has broken the integration density restrictions imposed on conventional optical devices by the diffraction limit of light. This higher integration density has enabled realization of *quantitative* innovations in photonic devices and optical fabrication technologies [3, 4]. Moreover, *qualitative* innovations have been accomplished by utilizing novel functions and phenomena made possible by optical near-field interactions that are otherwise unachievable with conventional propagating light [5, 6].

One of the most important technological vehicles that has contributed to the study of nanophotonics so far is high-quality optical near-field probing tips, such as those based on optical fiber probes [7]. They have achieved high spatial resolution and high energy efficiency—up to 10 % optical near-field generation efficiency in some cases. For instance, near-field optical microscope (NOM) has been widely used to obtain ultrahigh-resolution images [8]. However, methods of characterizing optical near-fields using probing tips normally require one-dimensional (1D) scanning processes, which severely limits the throughput in obtaining two-dimensional (2D) information on the nanometer scale. Additionally, precision technologies are indispensable in fabricating probe tips and also in controlling their position during processing. In particular, such technologies become large obstacles to implementing nanometric information processing and realizing further applications. Therefore, eliminating 1D scanning processes, or in other words achieving *probe-free nanophotonics*, is an important step toward further exploiting the possibilities of light–matter interactions on the nanometer scale.

In fact, utilization of optical near-field interactions without any scanning processes has been successfully demonstrated in nano-optical fabrication: For instance,

optical near-field lithography, utilizing the near-field interactions between photomasks and photoresists, has already been developed [9]. Furthermore, nonadiabatic processes, meaning that optical near-field interactions activate conventionally light-insensitive materials, are additional novelties that are available in fabricating nanostructures by nanophotonics [10]. Optical near-field etching is another example of probe-free nanophotonics; here, photochemical reactions are selectively excited in regions where optical near-fields are generated. This approach has been successfully demonstrated in flattening the rough surfaces of optical elements [11].

To implement innovative nanometric optical processing systems as probe-free nanophotonic systems, it is necessary to exploit the unique attributes of nanometer-scale optical near-field interactions in a completely parallel fashion. In this review, we highlight the basic concepts necessary for 2D parallel processing of light–matter interactions on the nanometer scale instead of the conventional 1D scanning method, based on our recent achievements. Those techniques allow us to observe optical far-field signals that originate from the effects occurring at the nanometer scale. The concepts and principles are numerically and experimentally verified within several frameworks of particular applications realized by precisely designing and fabricating nanostructures. Additionally, the concepts and some demonstrations of hierarchic applications of nanophotonics, based on the hierarchy between optical near- and far-fields, are described as one of the practical applications of the optical near-field interactions induced by such designed nanostructures.

24.2 Probe-Free Nanophotonic Systems

Nanometric optical processing systems, whose features include high integration density, low-energy operation, and innovative functions, are practical embodiments of the qualitative innovations offered by nanophotonics. Several fundamental proposals have been developed for their implementation; for instance, nanophotonic devices that consist of nanometric logic gates, switches, and wiring based on optical near-field interactions, as well as several related technologies, have been developed [12–15]. However, integration technologies are still required in order to implement actual processing systems based on existing nanophotonic devices. Moreover, regarding the interfaces between those nanometric systems and their associated surrounding systems, existing concepts that apply to conventional optical systems are not entirely applicable since the physical basis is completely different between conventional propagating light and optical near-fields. Hence, appropriate interfacing concepts and techniques that are well matched with the features of nanophotonics are strongly demanded. From such a viewpoint, optical near-field interactions and their characteristic behaviors *autonomy* and *robustness*, which are revealed only at the nanometric scale, ought to be focused on as key features for implementing nanometric information processing. For example, energy transfer in an optical near-field channel based on nanometric quantum dots that autonomously

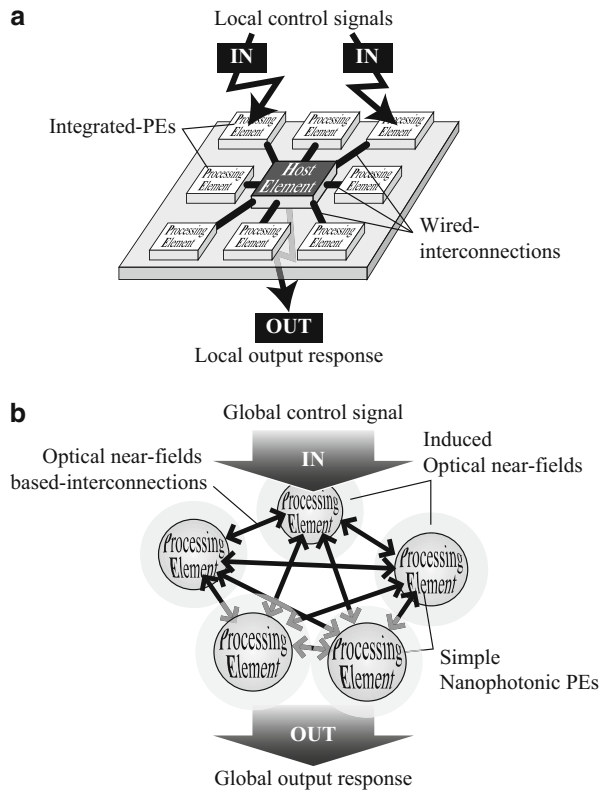
select an appropriate channel has been demonstrated to work with few problems, although the functions of some quantum dots have been lost [16]. In other types of applications, in the fabrication phase of a nanometric device, the most appropriate structure serving as the optical near-field source has been autonomously formed via induced optical near-field interactions with the assistance of suitable laser irradiation parameters, such as intensity, and polarization [17].

On the other hand, in order to realize more advanced computing systems, in terms of processing performance, development of parallel processing from both system architecture and algorithm aspects has been the general idea since the first prototype computing systems were invented. Parallel computing is defined as a processing system that utilizes multiple processors at the same time to rapidly execute a single program [18]. In general, in order to ideally implement such processing, it is necessary to realize spatially parallel operations in a two-dimensionally expanded information space, and this is one of the motivations that has been actively researched in *classical* optical computing, utilizing the parallelism and higher velocity of light [19]. Although the original meaning of optical computing has been lost in a certain sense, the basic concept can be usefully applied to the implementation of nanometric optical processing systems. In this case, the autonomy and the robustness of optical near-field interactions are quite appealing. Once the concepts and techniques of nanometric parallel processing have been successfully established, they can be directly expanded to macroscale applications, which is expected to dramatically expand the scope of application of nanophotonics.

Figure 24.1a, b show schematic diagrams that conceptually illustrate two kinds of representative *nanometric* parallel processing systems. The system shown in Fig. 24.1a is operated by the host element located at the center. All of the processing elements around the center are precisely controlled by the host element. In the case of such nanometric processing with existing techniques, however, this kind of centralized architecture is difficult to apply since it is technically difficult to precisely align a number of nanometric components and to precisely and flexibly interconnect each component. On the other hand, the system schematically shown in Fig. 24.1b is proposed for the implementation of nanometric optical processing systems. The processing elements are connected in an autonomous manner via optical near-field interactions, and the global control signals do not specify the detailed operations of each component. The local interactions between components in the system, involving optical near-field interactions, bring about certain behavior in the system as a whole.

In order to realize the parallel processing system shown in Fig. 24.1b, it is necessary to retrieve the information located at the nanometer scale and expose it at the sub-micrometer scale so that the outputs of the system are obtainable in the optical far-field. For this purpose, here we propose two fundamental techniques: One is the *macroscale observation* of optical near-field interactions, and the other is the *magnified-transcription* of the optical near-field [20]. These techniques eliminate 1D scanning processes; in other words, probe-free nanophotonics is accomplished.

Fig. 24.1 Basic concept of nanometric parallel processing systems (a) based on existing processing protocol and (b) utilizing nanophotonics as a probe-free nanophotonic system



24.3 Nanophotonic Matching as Macroscale Observation

24.3.1 Macroscale Observation

As we described in Sect. 24.2, in order to control and observe a spatially expanded nanometric field using existing optical techniques, it must be one-dimensionally scanned. Although it does not matter for measurement or fabrication, the loss of synchronism is a crucial disadvantage for use as an actual information processing system. In order to find a solution to this problem, in our idea, multiple nanometric processing components are aligned in a micrometer-scale unit, and the I/Os at each unit consist of parallel control with *broadcast* of the input signal and bundled retrieval with *narrowcast* of the output signals. The components are assigned individual functions and execute their functions based on holistic instructions from an external environment and interactions between neighboring components. An analogy of this concept can be seen in common biological systems, such as the human body, which is one of the most ideal and effectively constructed information processing systems.

This idea is one of the most effective solutions to utilize multiple nanometric components without impairing the spatial parallelism or the superior speed of optical signals. The key to this idea is how to determine the arrangement of nanometric components that generates the intended optical near-field interactions. This can be achieved by precisely designing and fabricating nanostructures, such as shapes, layouts, and compositions, that can induce arbitrary optical near-field interactions [21, 22]. Moreover, protocols for the broadcast control and the narrowcast retrieval must be appropriately defined.

24.3.2 Quadrupole–Dipole Transform

There are several physical implementation methods that can achieve such a transform using optical near-field interactions. One is based on optical excitation transfer between quantum dots via optical near-field interactions [23, 24]. For instance, assume two cubic quantum dots whose side lengths L are a and $\sqrt{2}a$, which we call QD_A and QD_B , respectively.

Suppose that the energy eigenvalues for the quantized exciton energy level specified by quantum numbers (n_x, n_y, n_z) in a QD with side length L are given by

$$E_{(n_x, n_y, n_z)} = E_B + \frac{\hbar^2 \pi^2}{2ML^2} (n_x^2 + n_y^2 + n_z^2), \quad (24.1)$$

where E_B is the energy of the exciton in a bulk crystal and M is the effective mass of the exciton. As shown in Fig. 24.2, there exists a resonance between the level of quantum number (1,1,1) for QD_A and that of quantum number (2,1,1) for QD_B . There is an optical near-field interaction, denoted by U , due to the steep gradient of the electric field in the vicinity of QD_A . Therefore, excitons in QD_A can transfer to the (2,1,1) level in QD_B . Note that such a transfer is prohibited if based on propagating light since the (2,1,1) level in QD_B contains an even number. In other words, near-field excitation can populate even the antisymmetric states of the coupled system, or the dark states, whereas far-field excitation can excite only

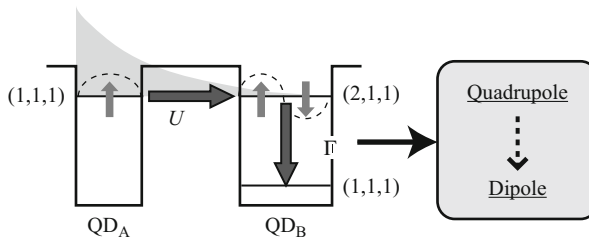


Fig. 24.2 A quadrupole–dipole transform in the transition from the (2,1,1) level to the (1,1,1) level in QD_B . Such a transform is unachievable without the optical near-field interactions between QD_A and QD_B , which allow the (2,1,1) level in QD_B to be populated with excitons

the symmetric states, that is, the bright states [23]. In QD_B , the exciton relaxes to the lower energy sublevel (1,1,1) with a time constant a , which is faster than the near-field interaction. Therefore, the exciton finally transfers to the (1,1,1) level of QD_B . Also, this sublevel relaxation, or energy dissipation, that occurs at QD_B guarantees unidirectional energy flow from QD_A to QD_B . Here, we can find a quadrupole–dipole transform in the transition from the (2,1,1) level to the (1,1,1) level in QD_B , and such a transform is unachievable without the optical near-field interactions between QD_A and QD_B , which allow the (2,1,1) level in QD_B to be populated with excitons [14, 25].

Another way of realizing a quadrupole–dipole transform is based on shape-engineered metal nanostructures, which are the principal concern of this chapter. In previous work, we have numerically shown that two metal nanostructures can be designed to exhibit far-field radiation only when their shapes are appropriately configured and when they are closely stacked [21, 26]. As discussed in detail below, here we can also find a quadrupole–dipole transform in the sense that individual single planes of the nanostructures work as quadrupoles, but they behave as a dipole when two planes of the nanostructures are appropriately configured. In the following, we discuss the shape design of the nanostructures and their experimental fabrication, and we describe optical characterization of the quadrupole–dipole transform.

24.3.3 Nanophotonic Matching

We demonstrate that two nanostructures can be designed to exhibit far-field radiation only under the condition that the shapes of the two structures are appropriately combined and closely stacked. This function of the two nanostructures can be regarded effectively as a *lock* and a *key*, because only an appropriate combination of a lock and a key yields an output signal, namely, far-field radiation [21, 27]. Figure 24.3 shows a schematic diagram of the nanophotonic matching system based on this function.

We design two nanostructural patterns, called *Shape A* and *Shape B* hereafter, to effectively induce a quadrupole–dipole transform via optical near-field interactions. Shape A and Shape B are designed as rectangular units on the xy -plane with constant intervals horizontally (along the x -axis) and vertically (along the y -axis), respectively. When Shape A is irradiated with x -polarized light, surface charges are concentrated at the horizontal edges of each of the rectangular units. The relative phase difference of the oscillating charges between the horizontal edges is π , which is schematically represented by $+$ and $-$ marks in Fig. 24.3. Now, note the y -component of the far-field radiation from Shape A, which is associated with the charge distributions induced in the rectangle. Drawing arrows from the $+$ marks to the $-$ marks along the y -axis, we find that adjacent arrows are always directed oppositely, indicating that the y -component of the far-field radiation is externally small. In other words, Shape A behaves as a quadrupole with regard to the y -component of the far-field radiation. It should also be noted that near-field

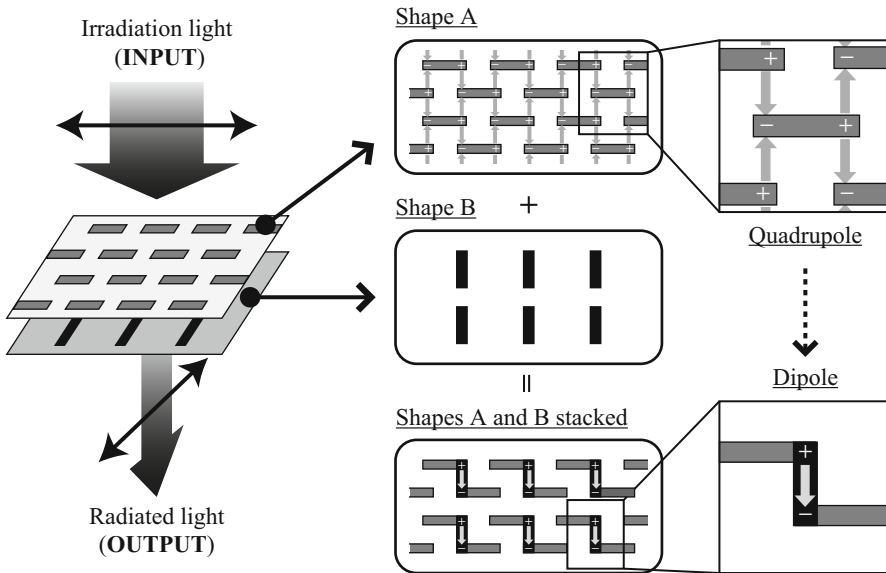


Fig. 24.3 Schematic diagram of nanophotonic matching system. The function is based on a quadrupole–dipole transform via optical near-field interactions, and it is achieved through shape-engineered nanostructure and their associated optical near-field interactions

components exist in the vicinity of the units in Shape A. With this fact in mind, we put the other metal nanostructure, Shape B, on top of Shape A. Through the optical near-fields in the vicinity of Shape A, surface charges are induced on Shape B. What should be noted here is that the arrows connecting the + and – marks along the y -axis are now aligned in the same direction, and so the y -component of the far-field radiation appears; that is, the stacked structure of Shape A and Shape B behaves as a dipole. Also, Shape A and Shape B need to be closely located to invoke this effect since the optical near-field interactions between Shape A and Shape B are critical. In other words, a quadrupole–dipole transform is achieved through shape-engineered nanostructure and their associated optical near-field interactions.

In order to verify this quadrupole–dipole transform mechanism brought about by shape-engineered nanostructure, we numerically calculated the surface charge distributions induced in the nanostructures and their associated far-field radiation based on a finite-difference time-domain (FDTD) electromagnetic simulator (*Poynting for Optics*, a product of Fujitsu, Japan). **Figure 24.4a** schematically represents the design of (i) Shape A only, (ii) Shape B only, and (iii) a stacked structure of Shape A and Shape B, which consist of arrays of gold rectangular units. The length of each of the rectangular units is 500 nm, and the width and height are 100 nm. As the material, we assumed a Drude model of gold with a refractive index of 0.16 and an extinction ratio of 3.8 at a wavelength of 688 nm [28].

When irradiating these three structures with continuous-wave x -polarized input light at a wavelength of 690 nm, the lower figures in **Fig. 24.4a** show the induced

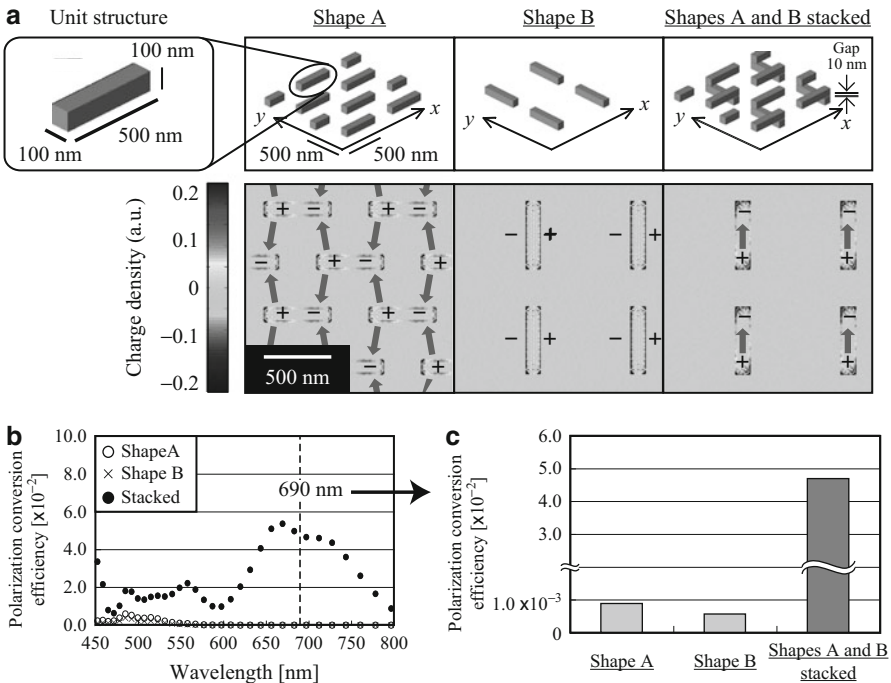


Fig. 24.4 (a) Specifications of the three types of nanostructures used in numerical evaluation of the conversion efficiency based on the FDTD method and corresponding surface charge density distributions induced in each nanostructure. (i) Shape A only, (ii) Shape B only, and (iii) a stacked structure of Shapes A and B. (b) Calculated performance figure of the quadrupole-dipole transform, namely, polarization conversion efficiency, with the three types of nanostructures. (c) Selective comparison at a wavelength of 690 nm

surface charge density distributions (simply called surface charge hereafter) obtained by calculating the divergence of the electric fields. For the Shape A-only structure (bottom left in Fig. 24.4a), we can find a local maximum and local minimum of the surface charges, denoted by the + and - marks. When we draw arrows from the + marks to the - marks between adjacent rectangular units, as shown in Fig. 24.3, we can see that the arrows are always directed oppositely between the adjacent units, meaning that the Shape A-only structure behaves as a quadrupole for the y -component of the far-field radiation. For the Shape B-only structure (bottom center in Fig. 24.4a), the charges are concentrated at the horizontal edges of each of the rectangular units, and there are no y -components that could contribute to the far-field radiation. The lower-right figure in Fig. 24.4a shows the surface charge distributions induced in Shape B when it is stacked on top of Shape A. We can clearly see that the charges are induced at the vertical edges of each of the rectangular units, and they are aligned in the same direction. In other words, a dipole arrangement is accomplished with respect to the y -component, leading to a drastic increase in the far-field radiation.

One of the performance figures of the quadrupole–dipole transform is

$$I_{\text{conv}} = I_{y\text{-OUT}}/I_{x\text{-IN}}, \quad (24.2)$$

where $I_{x\text{-IN}}$ and $I_{y\text{-OUT}}$ represent the intensities of the x -component of the incident light and the y -component of the radiated light, respectively. When we radiate a short optical pulse having a differential Gaussian form whose width is 0.9 fs, corresponding to a bandwidth of around 200–1,300 THz, Fig. 24.4b shows I_{conv} as a function of the input light wavelength, and Fig. 24.4c compares I_{conv} specifically at 690 nm. I_{conv} appears strongly with the stacked structure of Shapes A and B, whereas it exhibits a small value with Shape A only and Shape B only. We can clearly observe the quadrupole–dipole transform in the optical near-fields as the change of I_{conv} in the optical far-fields.

24.3.4 Experimental Demonstration

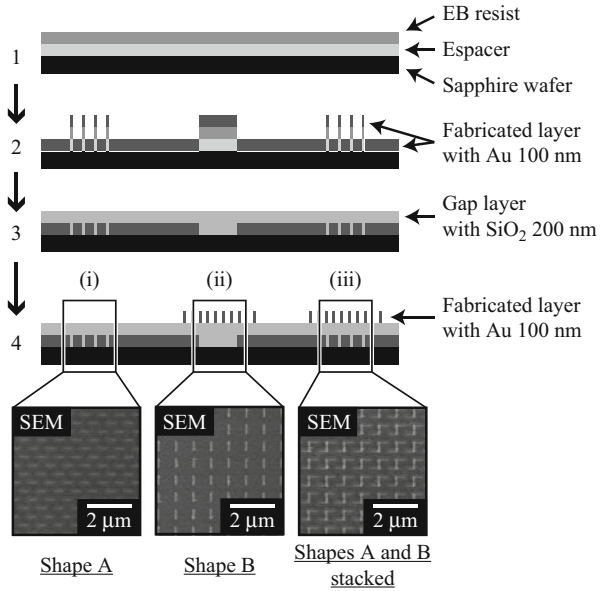
In the experiments, we fabricated structures consisting of Shape A only, Shape B only, and Shape A and Shape B stacked. Although the stacked structure should ideally be formed by combining the individual single-layer structures, in the following experiment, the stacked structure was integrated in a single sample as a solid two-layer structure to avoid experimental difficulty in precisely aligning the individual structures mechanically. The fabrication process was as follows.

1. Spacer 300Z and resist solution 2EP-520A were spin coated at a thickness of 350 nm on a sapphire substrate to be subjected to electron-beam lithography.
2. The first layer (Shape A) was fabricated by EB lithography, and an Au layer was vacuum evaporated to a thickness of 100 nm.
3. The Spacer layer and EB resist layer (2EP-520A) were removed by lift-off with 2EP-A and acetone. Then an SiO₂ layer was sputtered to a thickness 200 nm to form a gap layer between the first and second layers.
4. The second layer (Shape B) was fabricated in a similar manner to the above processes.

Figure 24.5 schematically represents cross-sectional profiles of these fabrication processes, where (i) Shape A-only structures are fabricated in the first layer, (ii) Shape B-only structures are fabricated in the second layer, and (iii) stacked structures have Shapes A and B in the first and second layers, respectively. The lower images in Fig. 24.5 also show scanning electron microscopy (SEM) images of fabricated samples of types (i), (ii), and (iii). Because the stacked structure was fabricated as a single sample, the gap between Shape A and Shape B was fixed at 200 nm.

The performance of the quadrupole–dipole transform, in terms of the polarization conversion efficiency I_{conv} given by Eq. 24.2, was experimentally evaluated by radiating x -polarized light on each of the areas (i), (ii), and (iii) and measuring the intensity of the y -component in the transmitted light. The light source was a laser diode with an operating wavelength of 690 nm. Two sets of Glan–Thompson prisms

Fig. 24.5 Schematic diagram of the fabrication process of the two-layer nanostructure. The stacked structure was integrated in a single sample as a solid two-layer structure to avoid experimental difficulty in precisely aligning the individual structures mechanically



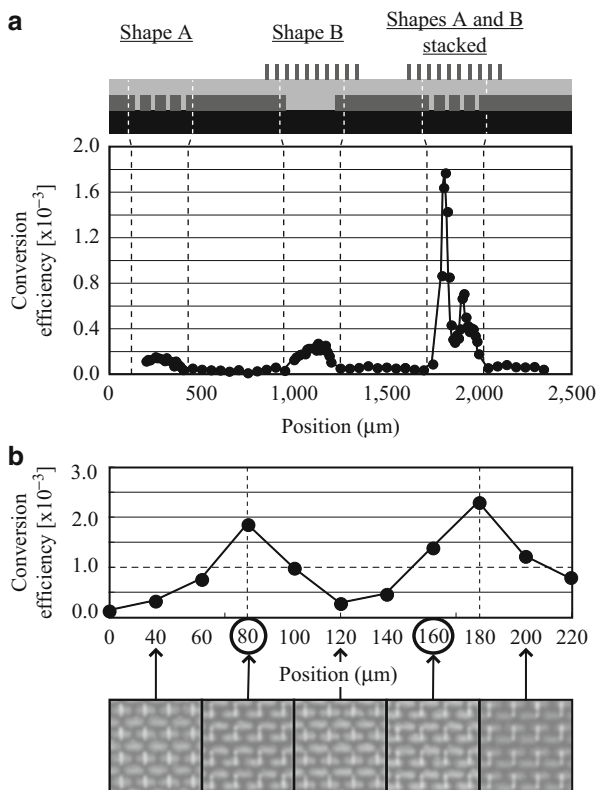
(extinction ratio 10^{-6}) were used to extract the x -component for the input light and to extract the y -component in the transmitted light. The intensity was measured by a lock-in controlled photodiode. The position of the sample was controlled by a stepping motor with a step size of 20 μm.

Figure 24.6a shows I_{conv} as a function of the position on the sample, where I_{conv} exhibited a larger value specifically in the areas where the stacked structure of Shapes A and B was located, which agrees well with the calculated result shown in Fig. 24.4c.

The conversion efficiency with the Shape B-only structure is slightly larger than that with the Shape A-only one, as shown in Fig. 24.6a, which exhibits opposite behavior from that obtained in the simulation shown in Fig. 24.4c. Also, the magnitude of the increase in conversion efficiency from the stacked structure of Shapes A and B is not so large compared with that predicted by the simulation in Fig. 24.4c. We attribute these effects mainly to the unintended inhomogeneity of the shapes and layout of the experimental devices, as indicated in the SEM images in Fig. 24.5. Slight rotational misalignment between the irradiated light and the device under study and other factors could also be involved.

Although I_{conv} was larger at the stacked structure, the signals fluctuated within the corresponding area. This was due to the variance of the misalignment between the first layer (Shape A) and the second layer (Shape B), as observed in the SEM images shown in Fig. 24.6b. From Fig. 24.6b, we can see that I_{conv} was larger when the misalignment between Shape A and Shape B was minimized. The variance of the misalignment was presumably due to drift effects in the lithography process during fabrication.

Fig. 24.6 (a) Measured conversion efficiency for the three types of nanostructures. Conversion efficiency was larger specifically in the areas where the stacked structure of Shapes A and B was located. (b) Conversion efficiency within the area of the stacked structure of Shapes A and B. SEM images are also shown corresponding to the evaluated position. Conversion efficiency was larger when the misalignment between Shape A and Shape B was minimized



The alignment tolerances were further analyzed as shown below. From the SEM images in Fig. 24.6b, horizontal and vertical misalignments were respectively evaluated as Δx and Δy shown in Fig. 24.7a. Figure 24.7b, c respectively show I_{conv} as a function of the horizontal and vertical misalignments. Solid lines represent calculated results, and the left-hand axis and right-hand axis represent the conversion efficiency of the experimental and calculated results, respectively. Although the absolute values of the efficiency were different between the experiments and simulations, they showed similar dependence on the misalignment. If we define the alignment tolerance as the maximum misalignment that yields 10% of the maximum efficiency, the horizontal and vertical alignment tolerances are respectively estimated to be about 150 and 200 nm.

In order to analyze the gap dependency of the conversion efficiency, other samples were also fabricated. As shown in Fig. 24.7d, the thicknesses of the SiO_2 gap layer between the first and second layers were 143, 216, and 363 nm. As shown in Fig. 24.7e, the conversion efficiency decreased as the gap between the layers increased, which also validates the principle of the quadrupole–dipole transform that requires optical near-field interactions between closely arranged nanostructures.

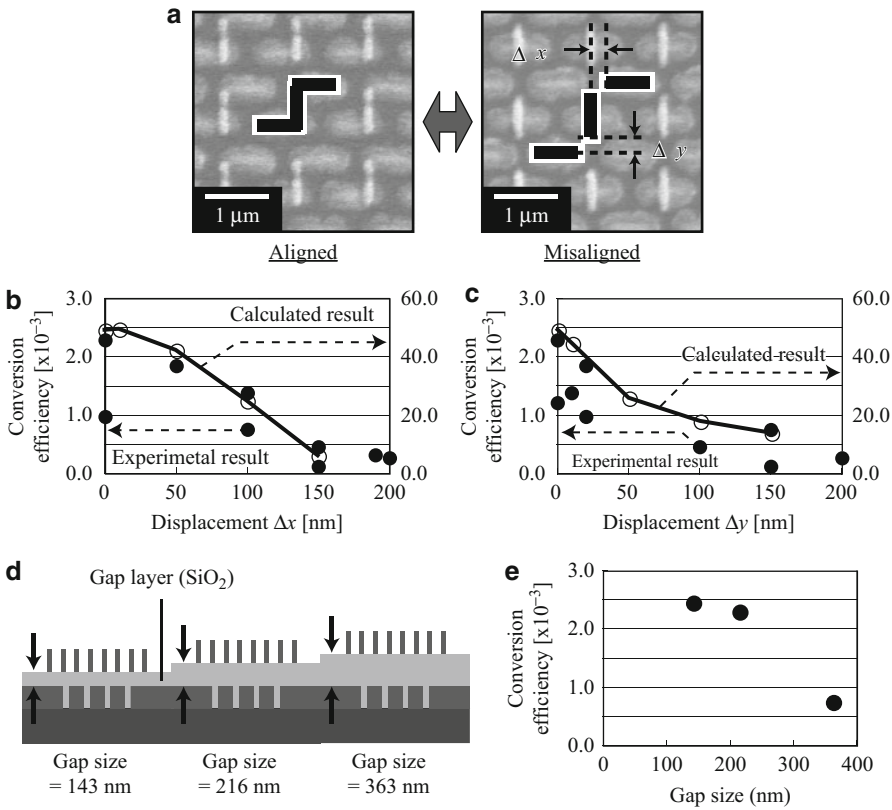


Fig. 24.7 (a) Horizontal and vertical misalignments between Shape A and Shape B denoted by Δx and Δy , and (b) and (c), their relations to conversion efficiency. (d) Schematic cross-sectional profiles of samples with different gaps. The thickness of the SiO_2 gap layer between the first and second layers was set in three steps. (e) The conversion efficiency decreased as the gap increased. The result validates the principle of the quadrupole–dipole transform that requires optical near-field interactions between closely arranged nanostructures

24.3.5 Outlook

Here, we make a few remarks regarding the quadrupole–dipole transform demonstrated in this study. We can engineer many more degrees of freedom on the nanometer scale while using far-field radiation for straightforward characterization. For practical use, on the other hand, more precise fabrication of nanostructures and more precise alignment between the two layers are necessary. Optical near-field lithography would be one solution for the mass production of large-area nanostructures [29, 30]. As for alignment, use of microelectro mechanical systems (MEMS) technologies [31] would be one option to resolve the alignment difficulties.

From a system perspective, the quadrupole–dipole transform can be regarded as a kind of mutual authentication or certification function of two devices, meaning that the authentication of Device A (with Shape A) and Device B (with Shape B) is achieved through the quadrupole–dipole transform. Because such fine nanostructures are difficult to falsify, the vulnerability of a security system based on this technology is expected to be extremely low.

Another relevant issue is to seek more general theories that account for the relationship between the shapes and layout of nanostructures and their associated hierarchical optical properties at the subwavelength scale [32]. Dependence on the internal structures of the materials could be exploited [22]. Also, the dependence on operating wavelength and other physical quantities [33] could be understood possibly in a unified manner. We will explore these issues in future work.

24.4 Nanophotonics-Induced Phase Transition as Magnified-Transcription

24.4.1 Magnified-Transcription of Optical Near-Fields

Here we describe *magnified-transcription* of optical near-fields, whereby their effects are spatially magnified so as to be detected in optical far-fields [34]. [Figure 24.8](#) shows a schematic diagram that represents the basic concept of parallel retrieval based on magnified-transcription. Generally, the 2D distribution of optical near-fields in the vicinity of the surface of a nanostructure in response to far-field light irradiation can be measured by one-dimensional scanning of an optical near-field probe tip, as shown in the upper half of [Fig. 24.8](#). The idea of the work presented here is to spatially magnify the distribution of optical near-fields so that their effects can be detected in optical far-fields, as schematically shown in the lower half of [Fig. 24.8](#). In other words, we transcribe the optical near-field distribution to another layer with a certain magnification factor.

The process of transcription is crucial for the implementation of this concept, and it should originate from the physical attributes associated with the material used. In our proposal, it is necessary to spatially magnify an optical near-field from the nanometric scale to the sub-micrometer scale in the resultant transcribed pattern so that it is observable in the optical far-field. It turns out that the magnification factor in the transcription should be 10–100. Once the spatial pattern is detectable in the far-field, various concepts and technologies common in parallel processing will be applicable, such as fully [35] parallel processing, so-called smart pixels, or parallel processing VLSI devices [36].

Several properties of optical near-field sources and transcription media can affect the transcription of spatial patterns. Therefore, it can be said that our proposal retrieves not only the existence or nonexistence of optical near-fields but also several of their characteristics, such as energy transfer [37] and hierarchy [38]. From this point of view, our proposal is fundamentally different from other recording and

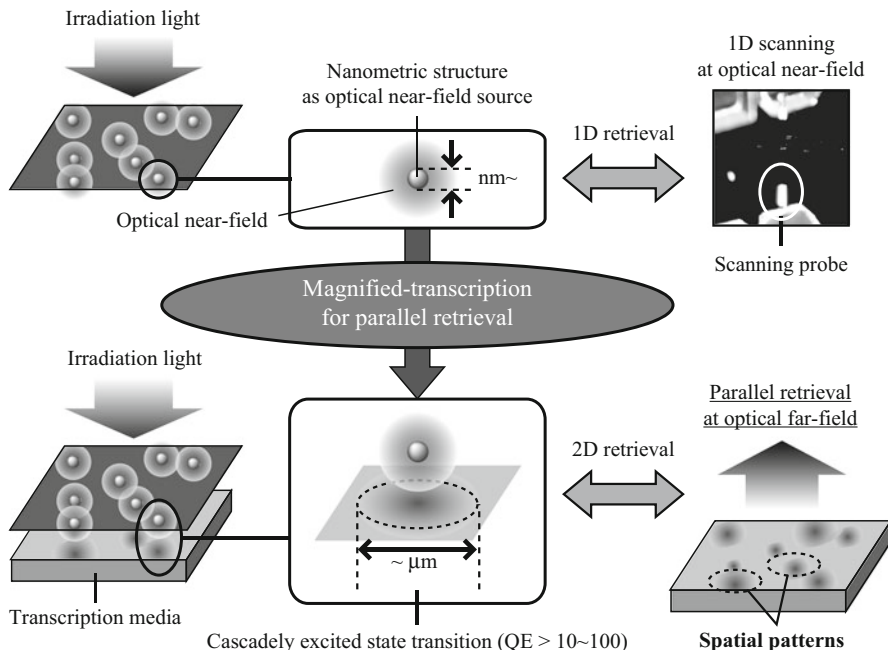


Fig. 24.8 Basic concept and fundamental process of optical parallel data retrieval based on the transcription of optical near-fields. Our fundamental idea is to spatially magnify the distribution of an optical near-field from the nanometric scale to the sub-micrometer scale in the resultant transcribed pattern so that it is observable in the optical far-field

retrieving methods, including near-field holography [39], which is concerned only with structural changes in the media.

24.4.2 Photoinduced Phase Transition

A photoinduced phase transition has been observed in several cyano-bridged metal complexes [40]. They exhibit bistable electronic states at room temperature. The energy barrier between these bistable states maintains a photoproduced state even after photo-irradiation is terminated. Also, the state can easily be reset either via optical irradiation or temperature control. Moreover, typical phase transitions are excited in a cascaded manner, meaning that they exhibit high quantum efficiencies.

Concerning the applicability of these features of cyano-bridged metal complexes to the transcription discussed previously, we chose rubidium manganese hexacyanoferrate [41] as a suitable material for the transcription medium. Compounds in this series show a charge-transfer phase transition from $\text{Mn}^{\text{II}} (S = 5/2)\text{-NC-Fe}^{\text{III}} (S = 1/2)$ as the high-temperature (HT) phase to $\text{Mn}^{\text{III}} (S = 2)\text{-NC-Fe}^{\text{II}} (S = 0)$ as the low-temperature (LT) phase [42, 43]. The LT phase is a ferromagnet because of

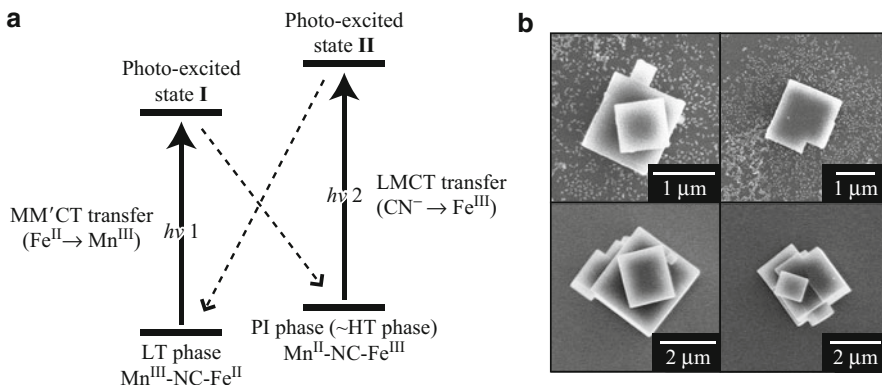


Fig. 24.9 (a) Schematic illustration of the visible-light-induced reversible photo-magnetic effect in rubidium manganese hexacyanoferrate. The charge-transfer phase transition is accompanied by a structural change from a cubic to a tetragonal structure due to Jahn–Teller distortion of Mn^{III} . (b) Observed SEM images of rubidium manganese hexacyanoferrate in the single-crystal state

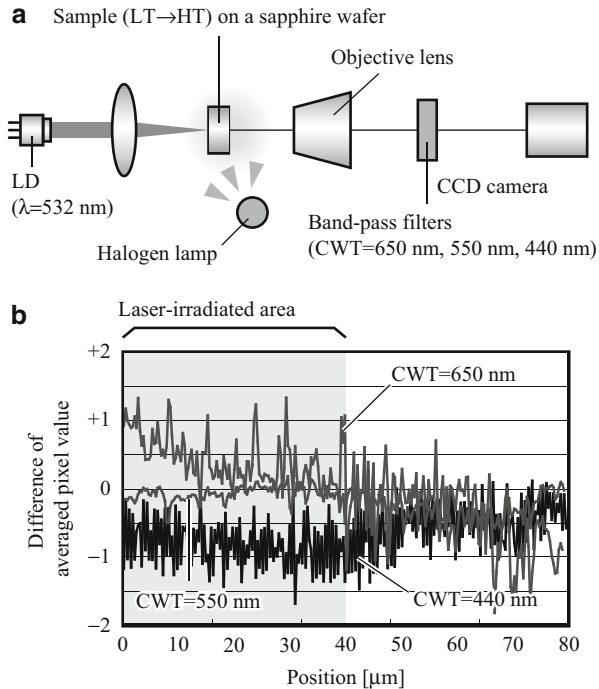
ferromagnetic coupling between the Mn^{III} sites ($S=2$ at the Mn^{III} sites), but the PI phase, which has a similar valence state to the HT phase, is an antiferromagnet ($S=5/2$ at the Mn^{II} sites and $S=1/2$ at the Fe^{III} sites). Figure 24.9a shows the scheme for reversible charge transfer between the $\text{Mn}^{\text{III}}\text{-NC-Fe}^{\text{II}}$ and $\text{Mn}^{\text{II}}\text{-NC-Fe}^{\text{III}}$ states and the spin ordering for the LT and HT phases. This charge-transfer phase transition is accompanied by a structural change from a cubic to a tetragonal structure due to Jahn–Teller distortion of Mn^{III} . The maximum value of the quantum efficiency of this type of material has been found to be more than 30 [44].

In their typical optical characterizations, these materials are prepared in bulk form. However, for our transcription purposes, especially for the proof-of-principle experiments shown earlier, it is important to spatially distribute these materials so that we can evaluate the optical responses individually from each material. Therefore, in this chapter, we mixed the materials with a dispersant based on an ester surfactant and dispersed the materials as single crystals in the solution. SEM images of single crystals are shown in Fig. 24.9b. The mean size of the single crystals was $1\ \mu\text{m}$ (horizontal) \times $1\ \mu\text{m}$ (vertical) \times $500\ \text{nm}$ (thick).

24.4.3 Experimental Demonstrations

For experimental confirmation of the photoinduced phase transition, we first measured microscopic optical responses of these single crystals on a sapphire substrate. Figure 24.10a shows the experimental setup. A green laser light source, emitting light at a wavelength of $532\ \text{nm}$ with a power density of $45\ \text{mW}/\text{cm}^2$, was employed for inducing the phase transition from the LT phase to the HT phase [41].

Fig. 24.10 (a) Schematic diagram of experimental setup for microspectroscopic detection of photoinduced phase transition. (b) Qualitative comparison of optical responses before and after irradiation. The change of the response at each wavelength, particularly at the wavelengths of 440 and 650 nm, in the irradiated area can be clearly observed, whereas the response remains unchanged in the unirradiated area



The optical responses of the materials were obtained by a CCD camera (Apogee, Alta U260) before and after 60 min of irradiation. In the characterization processes, the materials were irradiated with a halogen lamp. We alternately inserted three types of band-pass filters to evaluate the spectral responses before and after irradiation. The center wavelengths (CWTs) of the band-pass filters were 650, 550, and 440 nm, and the bandwidth of each filter was 20 nm.

To compare the differences in the images observed before and after irradiation, we calculated average pixel values in the horizontal direction and plotted each value along the vertical direction. Figure 24.10b shows the difference of the two results, before and after the irradiation. The shaded area in the profiles corresponds to the laser-irradiated area. We can clearly observe the change of the response at each wavelength, in particular at the wavelengths of 440 and 650 nm, in the irradiated area, whereas the responses remained unchanged in the unirradiated area. Such changes in the optical response correspond to changes of the dielectric constant found in previous research with bulk materials [41]. The results indicate that the phase transition of each single crystal could be successfully observed as a change of optical response at an appropriate wavelength.

To experimentally demonstrate the transcription of optical near-fields with the materials introduced previously, we employed an NOM setup, as shown in Fig. 24.11a. It was operated in an illumination–collection setup using an optical fiber probe with a tip radius of 50 nm. A change in the material was induced by laser

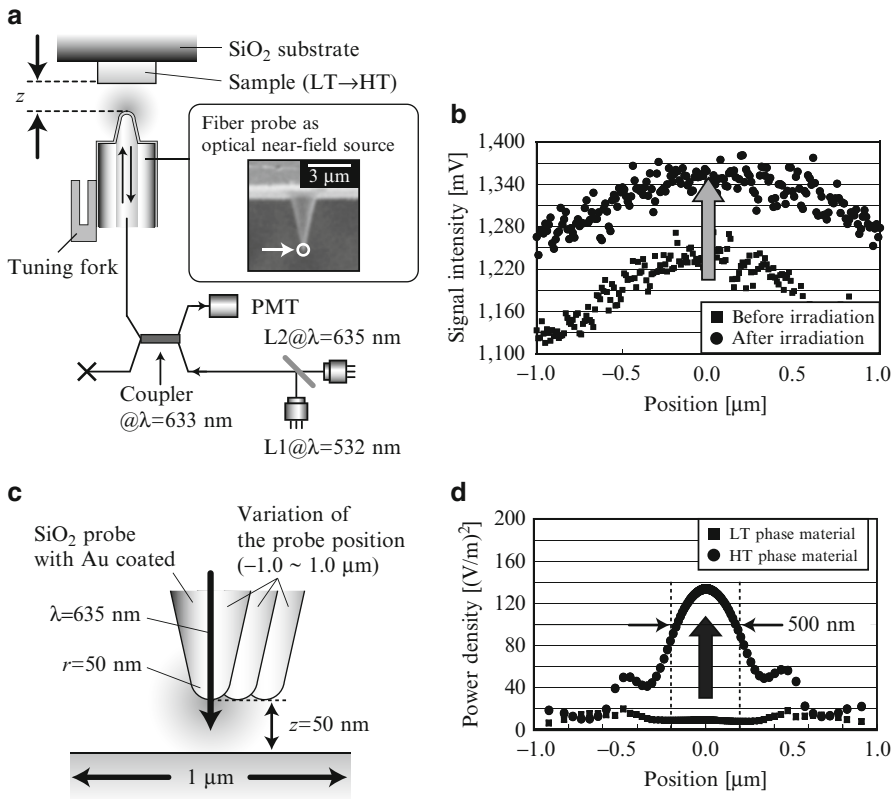


Fig. 24.11 (a) Schematic diagram of setup and (b) experimental results. (c) Schematic diagrams of calculation model for numerical validation of the transcription. (d) Numerical results. The signal intensity in the near-field is obviously increased by the irradiation

light with a wavelength of 532 nm (L1). The optical responses from the samples were evaluated microspectroscopically using laser illumination with a wavelength of 635 nm (L2). The power of L2 was kept as low as possible in order to avoid any unintended transitions during observation. The fiber probe tip was positioned close to the target crystal only when L1 was radiated for inducing a transition in the sample. Scattered light from the sample was detected with a photomultiplier tube (PMT) via a fiber probe, and an optical image was constructed from the detected signal. The spatial distributions evaluated with L2 illumination were obtained before and after 15-min irradiation with L1. From these distributions, we compared the differences; Fig. 24.11b shows the results. The detected signal intensity in the near-fields was obviously increased by the L1 irradiation.

Furthermore, for numerical proof, we simulated the difference of the optical response between the LT- and HT-phase materials using FDTD-based electromagnetic simulation. As shown in Fig. 24.11c, a nanometric scanning probe with a radius of

50 nm and an illumination light source with an operating wavelength of 635 nm were also included in the calculation model. The electric field intensity was evaluated at the surface of each material. The results are shown in Fig. 24.11d. The power density at the surface of the HT-phase material was much stronger than that of the LT-phase material. This change is similar to the NOM result in Fig. 24.11b. These results also indicate that the increase of scattered light intensity is attributed to the structural change in the rubidium manganese hexacyanoferrate material. From these results, we believe that we have successfully demonstrated the fundamental principle of the transcription of optical near-fields at the scale of a single crystal by using a nanometric fiber probe.

24.4.4 Outlook

We described the concept of transcription of optical near-field distributions for parallel nanophotonic processing, and we experimentally demonstrated its principle with nanometric light irradiation of a single crystal of a metal complex exhibiting a structural change that affects the change in its optical response. Specifically, rubidium manganese hexacyanoferrate was employed as the transcription medium, and we experimentally confirmed that the phenomenon could be induced on the scale of a single crystal. The transcription of optical near-fields that we demonstrated here will be one of the key techniques for implementing proposed parallel nanophotonic processing systems.

These processes are valuable system-level functions for implementing nanometric processing systems. Further advances, including the introduction of post-processing after the transcription and developing an original coding theorem that utilizes several features of nanophotonics, might yield highly integrated, real-time information processing at the scale of optical near-fields.

24.5 Nanophotonic Hierarchical Hologram

24.5.1 Background

Many anti-counterfeiting techniques have been proposed in the fields of security and product authenticity verification [45]. Optical techniques, which represent one kind of anti-counterfeiting, are well established; for instance, confidential information can be hidden in any of the physical attributes of light, such as phase, wavelength, spatial frequency, or polarization [46–48]. For example, holography, which generates natural three-dimensional images, is the most common anti-counterfeiting technique [49]. In the case of a volume hologram, the surface of the hologram is ingeniously designed into a complicated structure that diffracts incident light in a specific direction. A number of diffracted light beams can form an arbitrary three-dimensional image. Because these structures are generally recognized as being difficult to duplicate, holograms have been widely used in the anti-counterfeiting

of bills, credit cards, etc. However, conventional anti-counterfeiting methods based on the physical appearance of holograms are less than 100 % secure [50]. Although they provide ease of authentication, adding another security feature without causing any deterioration in the appearance is quite difficult.

Existing optical devices and systems operate based on several phenomena of *propagating* light. However, the performance is generally limited by the diffraction of light [51]. Reducing the physical scale beyond the scale of the optical wavelength is difficult. The critical dimension of a conventional hologram is also bounded by the diffraction limit, because the function of a conventional hologram is based on the diffraction of light.

However, with advances in nanophotonics, especially in systems utilizing optical near-field interactions, optical devices and systems can be designed at densities beyond those conventionally constrained by the diffraction limit of light [52]. Several nanophotonic device structures and operating principles based on optical near-field techniques have been proposed [1, 53]. Because several physical parameters of propagating light are not affected by nanometric structures, conventional optical responses in the far-field also are not affected by these structures. Essentially, this means that another functional hierarchical level in the optical near-field regime can be added to conventional optical devices and systems without any loss of the primary quality, such as reflectance, absorptance, refractive index, or diffraction efficiency. Here we focus on an embossed hologram as such a conventional optical device. We demonstrated our concept by utilizing a *nanophotonic hierarchical hologram* that works in both optical far- and near-fields [54].

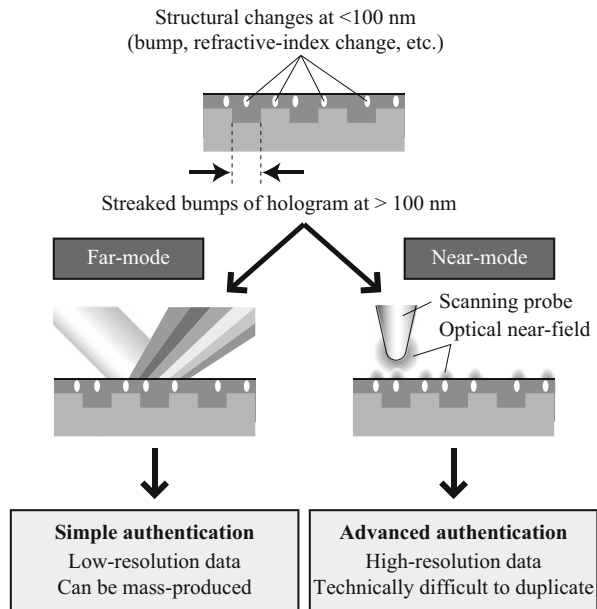
Moreover, we propose embedding a *nanophotonic code*, which is physically a subwavelength-scale shape-engineered metal nanostructure, in the hierarchical hologram to implement a near-mode function [55]. The basic concept of the nanophotonic code and fabrication of a sample device are described. In particular, since our proposed approach involves embedding a nanophotonic code *within* the patterns of the hologram, which is basically composed of one-dimensional grating structures, it yields clear polarization dependence compared with the case where it is not embedded within the hologram or arrayed structures. There are also other benefits with the proposed approach: A major benefit is that we can fully utilize the existing industrial facilities and fabrication technologies that have been developed for conventional holograms, yet adding novel new functionalities to the hologram.

24.5.2 Basic Concept

A nanophotonic hierarchical hologram can be created by adding a nanometric structural change to a conventional embossed hologram. Figure 24.12 shows the basic composition of the hierarchical hologram.

The physical scales of the nanometric structural changes and the elemental structures of the hologram are less than 100 nm and larger than 100 nm, respectively. In principle, a structural change occurring at the subwavelength scale does not affect the optical response functions, which are dominated by propagating light. Therefore, the visual aspect of the hologram is not affected by such a small structural change on

Fig. 24.12 Basic concept of functional hierarchy of hierarchical hologram. In principle, no interference occurs between the two layers, the far-mode and the near-mode



the surface. Additional data can thus be written by engineering structural changes in the subwavelength regime so that they are only accessible via optical near-field interactions (we call such information retrieval *near-mode* retrieval) without having any influence on the optical responses obtained via the conventional far-field light (what we call *far-mode* retrieval). By applying this hierarchy, new functions can be added to conventional holograms.

In actual use of the hierarchical hologram, we needed to demonstrate that a nanometric structural change does not affect the optical response in the far-mode retrieval. At the same time, an obvious change must be observed in the near-mode retrieval. To verify this, 500-nm-pitch Si diffraction gratings, in which nanometric depressions were embedded in the grid structures as near-mode data, were fabricated by using electron-beam(EB) lithography. A single isolated depression and multiple periodic depressions were embedded in each grating, as shown in Fig. 24.13a, b, respectively. The size of each depression was less than 50 nm. The fabricated diffraction gratings were illuminated by the light from a He-Ne laser ($\lambda = 633$ nm), and the intensity of each diffracted beam was measured. Figure 24.13c shows the diffracted light pattern from the grating with periodic depressions. Large regular diffraction spots due to the grid structure and a number of tiny spots due to the periodic depressions were observed in the diffraction pattern. The diffraction efficiencies of each order of diffraction spots for each grating, calculated from the measured optical intensity of each spot, are shown in Fig. 24.13d. The first-order diffraction efficiencies of a grating with no embedded depressions, the grating with the isolated depression, and the grating with the periodic depressions were 9.8, 9.7, and 10.3 %, respectively, showing a relative difference of less than 10 % between gratings with and without embedded depressions. No large differences

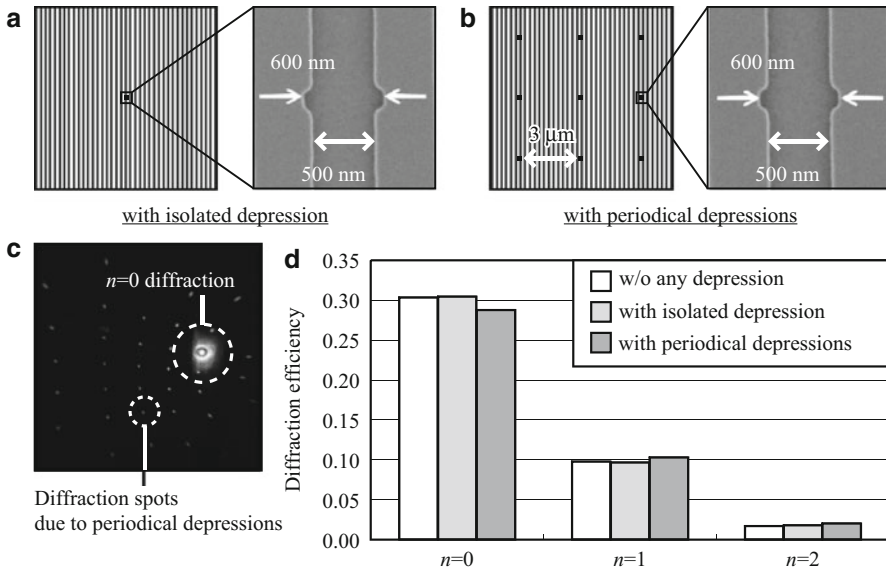


Fig. 24.13 SEM images of fabricated gratings with (a) single isolated depression and (b) multiple periodic depressions. (c) Diffraction pattern from the grating with periodic depressions. (d) Compared diffraction efficiencies of each grating, where n represents the diffraction order

were evident in the other diffraction orders either. This result shows that embedding the nanometric fabricated structures did not have a large effect on the function of conventional optical devices, that is, on their far-mode retrieval.

24.5.3 Nanophotonic Code

Our nanophotonic code is defined by induced optical near-fields, which are generated by irradiating a nanometric structure with light. An optical near-field is a non-propagating light field generated in a space extremely close to the surface of a nanometric structure [37]. Because the light distribution depends on several parameters of the structure and the retrieval setup, various types of coding can be considered. Moreover, several novel features of nanophotonics, such as energy transfer [23] and hierarchy [38], may be exploited.

As shown in Fig. 24.14, we created a sample device to experimentally demonstrate the retrieval of a nanophotonic code within an embossed hologram. As indicated, we could observe a three-dimensional image of the earth from the device as overt function of the hierarchical hologram. The entire device structure, whose size was 15×20 mm, was fabricated by electron-beam lithography on a Si substrate, followed by sputtering a 50-nm-thick Au layer. More specifically, our prototype device was essentially based on the design of *Virtuagram*[®], developed by Dai Nippon Printing Co., Ltd., Japan, which is a high-definition computer-generated hologram composed of binary-level one-dimensional modulated gratings. Within

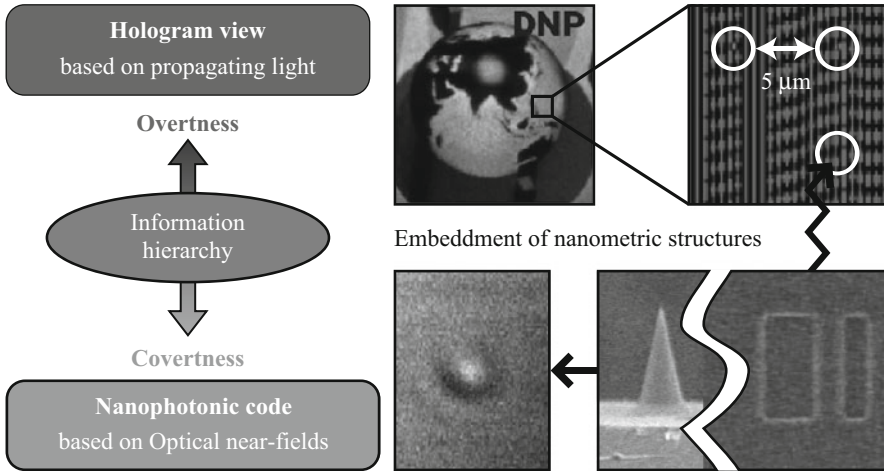


Fig. 24.14 Fabrication of a nanometric structure for a nanophotonic code within the embossed structure of Virtuagram[®] and SEM images of various designed patterns serving as nanophotonic codes. Signal of nanophotonic code can be induced by interactions between surface structures of hierarchical hologram and tip of scanning probe

the device, we slightly modified the shape of the nanostructure so that near-mode information was accessible only via optical near-field interactions between surface structures of hierarchical hologram and tip of scanning probe. We call such embedded information represented by distribution of optical near-fields as *nanophotonic codes*. The unit size of the nanophotonic codes ranged less than 200 nm.

Note that the original hologram was composed of arrays of one-dimensional grid structures, spanning along the vertical direction in Fig. 24.14. To embed the nanophotonic codes, the grid structures were partially modified in order to implement the nanophotonic codes. Nevertheless, the grid structures remained topologically continuously connected along the vertical direction. On the other hand, the nanophotonic codes were always isolated from the original grid structures. Those geometrical characteristics produce interesting polarization dependence, which is discussed in detail in Sect. 24.5.4.

24.5.4 Numerical Evaluations

First, electric fields at the surface of nanometric structures were numerically calculated by the FDTD method. As shown in Fig. 24.15a, d, two types of calculation models were created in order to examine polarization dependencies in retrieving the nanophotonic code. The nanophotonic code was represented by a square-shaped Au structure whose side length was 150 nm and whose depth was 100 nm, shown near the center in Fig. 24.15a, d.

As shown in Fig. 24.15a, the square-shaped structure was embedded in a periodic one-dimensional wire-grid structure, whose pitch was 150 nm, which models the

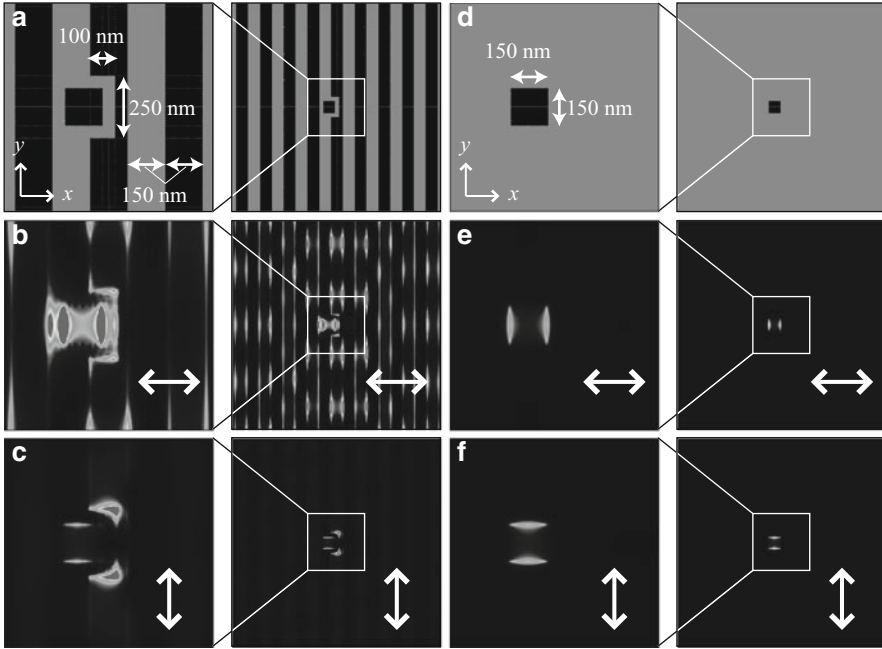


Fig. 24.15 (a) Calculation model of embedded nanophotonic code with environmental structures and calculated intensity distribution of electric field produced by (b) x -polarized input light and (c) y -polarized input light. (d) Calculation model of isolated nanophotonic code and calculated intensity distribution of electric field produced by (e) x -polarized input light and (f) y -polarized input light

typical structure of an embossed hologram. As shown in Fig. 24.15d, on the other hand, the square-shaped structure, whose size was the same as that in Fig. 24.15a, was not provided with any grid structure. By comparing those two cases, we can evaluate the effect of the environmental structures around the nanophotonic code. Also, we chose the square-shaped structure that is isotropic in both the x and y directions in order to clearly evaluate the effects of environmental structures and ignore the polarization dependency originating in the structure of the nanophotonic code itself. Periodic-conditioned computational boundaries were located $1.5\ \mu\text{m}$ away from the center of the square-shaped structure. The wavelength was set to $785\ \text{nm}$.

Figure 24.15b, e and c, f show the electric field intensity distribution on the surface of the structure assuming x -polarized and y -polarized input light irradiation, respectively. We then investigated how the environmental structures affected the electric fields in the vicinity of the nanophotonic code and the influence of input light polarization. For such purposes, we first evaluated the average electric field intensity in the area of the nanophotonic code, denoted by $\langle I \rangle_{\text{signal}}$, and that in the area including the surrounding areas, denoted by $\langle I \rangle_{\text{env}}$. More specifically, $\langle I \rangle_{\text{signal}}$

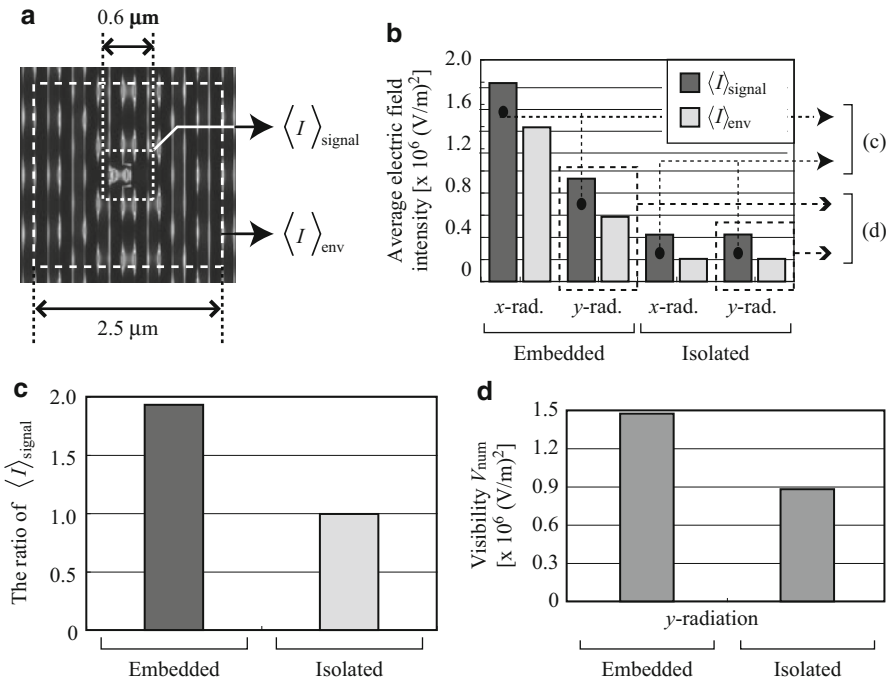


Fig. 24.16 (a) Schematic diagram explaining definition of average electric field intensity $\langle I \rangle_{\text{signal}}$ and $\langle I \rangle_{\text{env}}$ and (b) their graphical representations in each calculation model. Evident polarization dependency was exhibited in the case of the nanometric code embedded in environmental structures. (c) The ratio of $\langle I \rangle_{\text{signal}}$ with x -polarized input light to that with y -polarized input light for the embedded and isolated structures. (d) Numerical visibility V_{num} in two types of models with y -polarized input light. The result indicates that the visibility of the nanophotonic code was greatly enhanced by embedding it in the environmental structure

represents the average electric field intensity in the $0.6 \times 0.6 \mu\text{m}$ area covering the nanophotonic code, as shown by the dotted square in Fig. 24.16a, whereas $\langle I \rangle_{\text{env}}$ indicates that in the $2.5 \times 2.5 \mu\text{m}$ area marked by the dashed square in Fig. 24.16a. Figure 24.16b summarizes the calculated $\langle I \rangle_{\text{signal}}$ and $\langle I \rangle_{\text{env}}$, respectively shown by the left and right bars.

We first investigated the polarization dependencies. In the case of the nanophotonic code embedded in environmental periodic structures, evident polarization dependency was observed for both $\langle I \rangle_{\text{signal}}$ and $\langle I \rangle_{\text{env}}$. For example, $\langle I \rangle_{\text{signal}}$ with x -polarized input light was about two times larger than $\langle I \rangle_{\text{signal}}$ with y -polarized input light. On the other hand, the isolated nanophotonic code did not show any polarization dependency. Figure 24.16c compares the ratio of $\langle I \rangle_{\text{signal}}$ with x -polarized input light to that with y -polarized input light for the embedded and isolated structures.

Second, from the viewpoint of facilitating recognition of the nanophotonic code embedded in the hologram, it is important to obtain a kind of higher visibility for the

signals associated with the nanophotonic codes. In order to evaluate such visibility, here we define a figure-of-merit V_{num} as

$$V_{\text{num}} = \frac{\langle I \rangle_{\text{signal}}}{\langle I \rangle_{\text{env}}} \times \langle I \rangle_{\text{signal}} \quad (24.3)$$

which yields a higher value with higher contrast with respect to $\langle I \rangle_{\text{signal}}$ and $\langle I \rangle_{\text{env}}$ (indicated by the term $\langle I \rangle_{\text{signal}}/\langle I \rangle_{\text{env}}$) and with higher signal intensity (indicated by $\langle I \rangle_{\text{signal}}$). Figure 24.16d shows the calculated V_{num} in the case of y -polarized light input to the two types of models. The result indicates that the nanophotonic code embedded in the environmental structure is superior to that of the isolated code, in terms of the visibility defined by Eq. 24.3.

We consider that such a polarization dependency and the visibility of nanophotonic codes are based on the environmental grid structures that span along the vertical direction. The input light induces oscillating surface charge distributions due to coupling between the light and electrons in the metal. In the present case, the y -polarized input light induces surface charges along the vertical grids; since the grid structure continuously exists along the y -direction, there is no chance for the charges to be concentrated. However, in the area of the embedded nanophotonic code, we can find structural discontinuity in the grid; this results in higher charge concentrations at the edges of the embedded nanophotonic code.

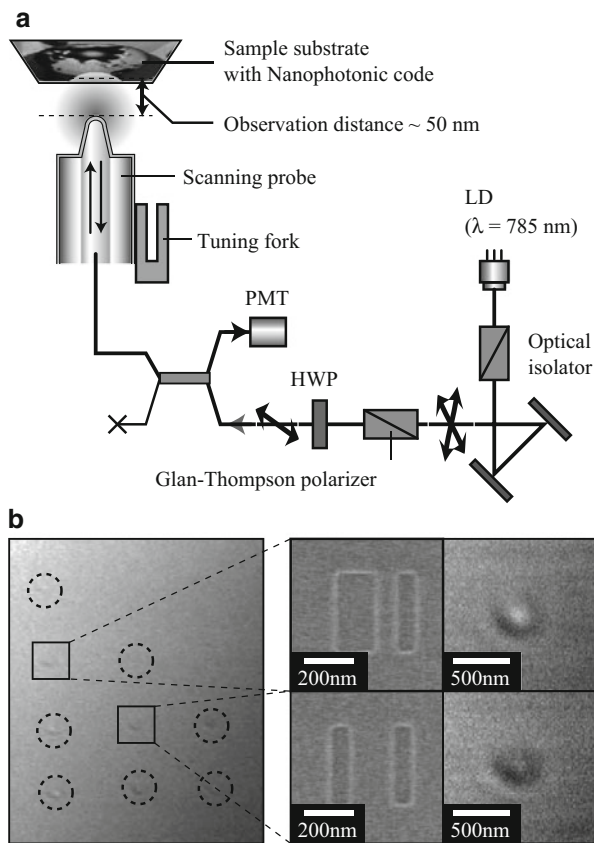
On the other hand, the x -polarized input light sees structural discontinuity along the horizontal direction due to the vertical grid structures, as well as in the areas of the nanophotonic codes. It turns out that charge concentrations occur not only in the edges of the nanophotonic codes but also at other horizontal edges of the environmental grid structures. In contrast to these nanophotonic codes embedded in holograms, for the isolated square-shaped nanophotonic codes, both x - and y -polarized input light have equal effects on the nanostructures.

These mechanisms indicate that such nanophotonic codes embedded in holograms could also exploit these polarization and structural dependences, not only for retrieving near-mode information via optical near-field interactions. For instance, we could facilitate near-mode information retrieval using suitable input light polarization and environmental structures.

24.5.5 Experimental Demonstration

In the experimental demonstration, optical responses during near-mode observation were detected using an NOM. A schematic diagram of the detecting setup is shown in Fig. 24.17a, in which the NOM was operated in an illumination–collection mode with a near-field probe having a tip with a radius of curvature of 5 nm. The fiber probe was connected to a tuning fork. Its position was finely regulated by sensing a shear force with the tuning fork, which was fed back to a piezoelectric actuator. The observation distance between the tip of the probe and the sample device was set at less than 50 nm. The light source used was an LD with an operating wavelength of

Fig. 24.17 (a) Schematic diagram of the experimental setup for retrieving a nanophotonic code and (b) basic retrieval results



785 nm, and scattered light was detected with a PMT. A Glan–Thompson polarizer (extinction ratio 10^{-6}) selected only linearly polarized light as the radiation source, and a half-wave plate (HWP) rotated the polarization.

Figure 24.17b summarizes the experimental results obtained in retrieving nanophotonic codes which were *not* embedded in the hologram. In this demonstration, different shapes of nanophotonic codes were formed at the positions marked by the dashed circles in Fig. 24.17b. For the first step of our demonstration, the device was irradiated with randomly polarized light by removing the polarizer from the experimental setup. Clear near-field optical distributions that depended on the structures of the nanophotonic codes were obtained.

Figures 24.18 and 24.19 show other retrieved results of nanophotonic codes that were embedded in the hologram and *not* embedded in the hologram, respectively, using a linearly polarized radiation source. Figure 24.18a, b respectively show observed NOM images of the nanophotonic code embedded in the hologram with a standard polarization (defined as 0-degree polarization) and 60-degree-rotated polarization. Figure 24.18c summarizes the NOM images obtained with

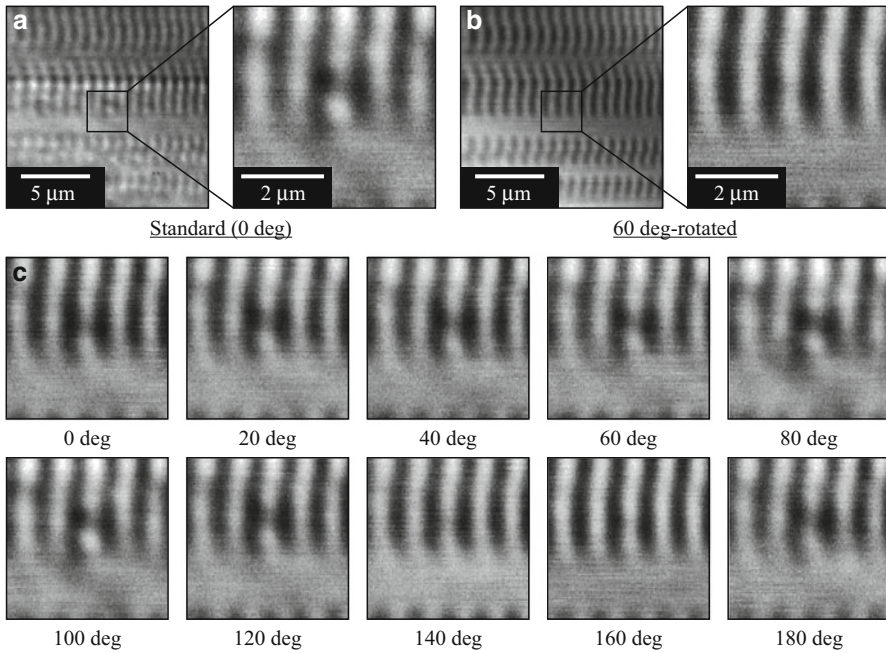


Fig. 24.18 Observed NOM images of optical intensity distributions of retrieved nanophotonic code embedded in environmental structures with (a) standard polarization and (b) polarization rotated by 60 degree, and (c) NOM images observed by radiating light with various polarizations

input polarizations rotated by 0 degree to 180 degree at 20-degree intervals. Also, Fig. 24.19a–c show the NOM images of the nanophotonic code which was not embedded in the hologram. As is evident, in the case of the nanophotonic code embedded in the hologram, clear polarization dependence was observed; for example, from the area of the nanophotonic code located in the center, a high-contrast signal intensity distribution was obtained with polarizations around 80°.

To quantitatively evaluate the polarization dependency of the embedded nanophotonic code, we investigated two kinds of intensity distribution profiles from the NOM images observed. One is a horizontal intensity profile along the dashed line in Fig. 24.20a, which crosses the area of the nanophotonic code, denoted by $I(x)$, where x represents the horizontal position. The other was also an intensity distribution as a function of horizontal position x ; however, at every position x , we evaluated the average intensity along the vertical direction within a range of 2.5 μm , denoted by $\langle I(x) \rangle_{\text{env}}$, which indicates the environmental signal distribution. When a higher intensity is obtained selectively from the area of the nanophotonic code, the difference between $I(x)$ and $\langle I(x) \rangle_{\text{env}}$ can be large. On the other hand, if the intensity distribution is uniform along the vertical direction, the difference between $I(x)$ and $\langle I(x) \rangle_{\text{env}}$ should be small. Thus, the difference

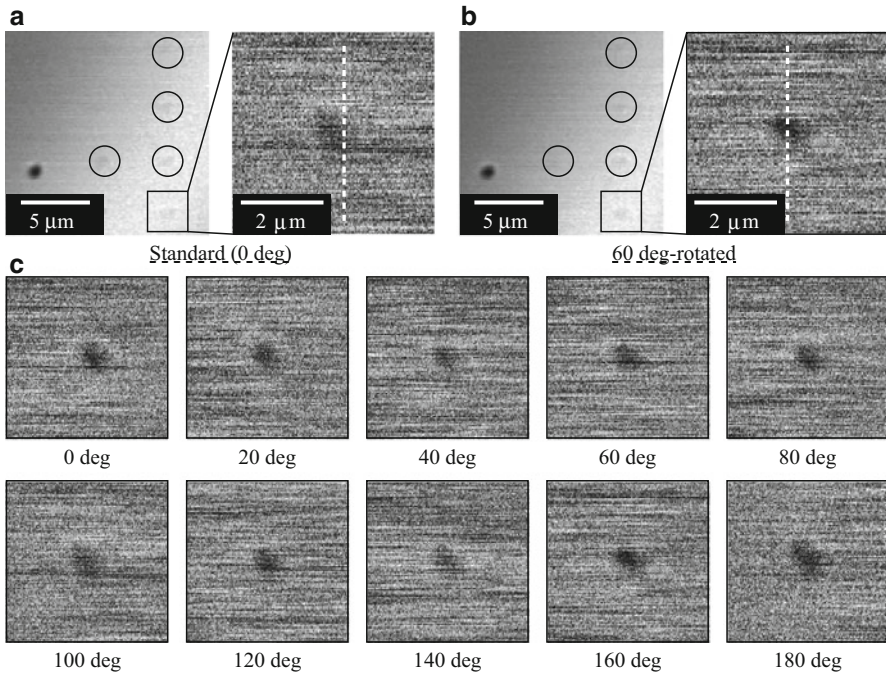


Fig. 24.19 Observed NOM images of optical intensity distributions of retrieved isolated nanophotonic code with (a) standard polarization and (b) polarization rotated by 60 degree, and (c) NOM images observed by radiating light with various polarizations

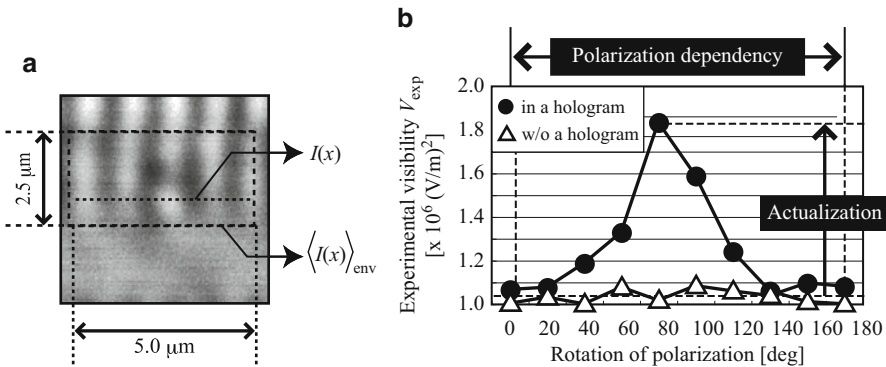


Fig. 24.20 (a) Schematic diagram explaining definition of $I(x)$ and $\langle I(x) \rangle_{env}$, and (b) calculated experimental visibility V_{exp} of embedded nanophotonic code and that of isolated nanophotonic code, showing actualization of optical response as evident visibility and its polarization dependency

between $I(x)$ and $\langle I(x) \rangle_{\text{env}}$ indicates the visibility of the nanophotonic code. We define an experimental visibility V_{exp} as

$$V_{\text{exp}} = \sum_x |I(x) - \langle I(x) \rangle_{\text{env}}|. \quad (24.4)$$

Figure 24.20b shows V_{exp} as a function of input light polarization based on the NOM results shown in Figs. 24.18c and 24.19c. The nanophotonic code embedded in the hologram exhibited much greater polarization dependency, as shown as “in a hologram” in Fig. 24.20b, where the maximum V_{exp} was obtained at 80° input polarization, whereas only slight polarization dependency was observed with the isolated nanophotonic code, as shown as “w/o a hologram” in Fig. 24.20b. Such polarization dependence in retrieving the nanophotonic code agrees well with the results of the simulations in Fig. 24.15.

24.5.6 Hierarchical Security System

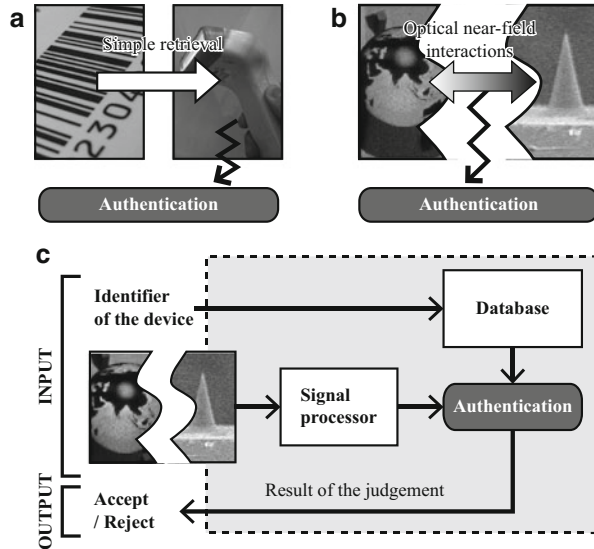
Presently, we are discussing an implementation of a *hierarchical security system* using *artifact-metrics* based on optical near-field interactions. *Artifact-metrics* is a coined term, generally defined as an automated method of authenticating artifacts based on a measurable intrinsic characteristic [56]. Unlike general authentication, in which a *device* holds secure data and a corresponding *reader* simply retrieves and decodes the data, as illustrated in Fig. 24.21a, the feature of our proposal is that the data observed from our *device* for authentication is physically dependent on optical near-field interactions between the *device* and a *reader*, which respectively serve as a nanophotonic code and a retrieval probe, as shown in Fig. 24.21b. This means that secure data is effectively divided between the device and the reader, physically guaranteeing their copy resistance and uniqueness.

Figure 24.21c shows a schematic model of our hierarchical security system based on this concept, in which the presence of specific attackers is assumed. For an attacker, it is quite difficult to duplicate an authentic device from the observed data or to estimate accurate observed data from the device, because the observed data will show drastic variations when using an only slightly different device or reader. Besides hierarchical holograms, many other experimental demonstrations of nanophotonics also confirm to this concept.

24.5.7 Outlook

In this section, we described the basic concept of a nanophotonic hierarchical hologram and a nanophotonic code embedded in a hologram as an implementation of a hierarchical hologram, and we demonstrated its features by numerical simulations, experimental fabrication of prototype devices, and optical characterization. Our concept can be applied not only to a hologram but also to any other media, such as lenses and jewelry. Adding extra functions creates value-added media with only

Fig. 24.21 Fundamental difference between (a) general authentication and (b) our hierarchical security approach. (c) Conceptual diagram of proposed hierarchical security system based on nanophotonic artifact-metrics



a slight impact on the primary functions. However, a trade-off occurs between the nanometric fabrication conditions (e.g., size and pitch) and the impact on the primary functions. We are currently investigating these trade-offs for several types of media in actual use. Moreover, the number of layers can be increased in the near-mode observation to further extend the hierarchical function. An optical near-field interaction between multiple nanometric structures produces a characteristic spatial distribution depending on the size, the alignment, etc. Therefore, various optical signal patterns can be observed depending on the size of the fiber probe, and another layer can be added in the near-mode observation [32, 38].

One of the most notable characteristics of our proposed approach is embedding a nanophotonic code within the patterns of a hologram composed of one-dimensional grating structures; it yields clear polarization dependence compared with an isolated nanophotonic code that is not embedded within a grid structure. These features were successfully demonstrated both numerically and experimentally. Also, because embedding and retrieval of a nanophotonic code requires highly advanced technical know-how, this approach can also improve the strength of anti-counterfeiting measures.

Our results indicated that the environmental structure provides interesting polarization dependency and, more interestingly, facilitates the retrieval of near-field information. In our future research, we may come to understand the relation between the retrieved optical intensity distributions and the design of the nanometric structures, including their environmental conditions. Such insights should allow us to propose, for instance, an optimized strategy for implementing nanophotonic codes, or a strategy robust to errors that possibly occur in the fabrication and/or retrieval processes [57]. Moreover, a simpler method for retrieving the nanophotonic code is required, without using optical fiber probe tips [22]. These aspects are currently being investigated by the authors.

24.6 Summary

In this review, we have described the basic concepts and experimental demonstrations of some proposals for probe-free nanophotonics and have demonstrated the potential of nanophotonics for application to far-field systems without using any probe-scanning method. Probe-free nanophotonics is an innovative proposal for sparking explosive expansion of the applications of nanophotonics. An important point is that, if the probe-scanning process can be eliminated, we could adopt nanophotonics as a fundamental technique for implementing, on the nanometric scale, several of the parallel processing tasks that have been the subject of fundamental research in the field of optical computing since the invention of laser technology.

Although the capabilities of classical optical computing have been restricted by the diffraction limit of light, in the scale from submicron to nanometer, the primacy of electrical processing over optical processing has not been clearly demonstrated. This scale is conventionally called the *mesoscopic* scale, and it is still interesting in several research fields, such as physics, biology, materials science, and information science. It is likely that some aspects of our ideas will also need to be discussed in view of this scale because the extraction of an output from the optical near-field scale to the optical far-field scale, one of the fundamental processes in our concept, occurs via an *optical mesoscopic scale*. In light of this, we strongly expect that our proposals will lead not only to progress in nanophotonics but also to the establishment and development of new research fields.

Acknowledgements The authors thank the members of the Ohtsu Research Group in the Department of Electrical Engineering and Information Systems, the University of Tokyo; and also thank Prof. S. Ohkoshi, Dr. H. Tokoro, and Dr. K. Takeda in the Department of Chemistry, the University of Tokyo, Prof. T. Matsumoto in Yokohama National University; and Dr. M. Hoga, Mr. Y. Ohyagi, Ms. Y. Sekine, Mr. T. Fukuyama, and Mr. M. Kitamura in Dai Nippon Printing Co. Ltd., for their valuable contributions to our collaborative research.

These works were supported in part by a comprehensive program for personnel training and industry-academia collaboration based on projects funded by the New Energy and Industrial Technology Development Organization (NEDO), Japan, the Global Center of Excellence (G-COE) Secure-Life Electronics project, Special Coordination Funds for Promoting Science and Technology sponsored by the Ministry of Education, Culture, Sports, Science and Technology (MEXT), Japan, and Strategic Information and Communications R&D Promotion Programme (SCOPE) sponsored by the Ministry of Internal Affairs and Communications (MIC).

References

1. M. Ohtsu, K. Kobayashi, T. Kawazoe, S. Sangu, T. Yatsui, *IEEE J. Sel. Top. Quantum Electron.* **8**(4), 839 (2002)
2. M. Naruse, T. Miyazaki, T. Kawazoe, K. Kobayashi, S. Sangu, F. Kubota, M. Ohtsu, *IEICE Trans. Electron.* **E88-C**, No. 9, 1817 (2005)
3. T. Nishida, T. Matsumoto, F. Akagi, H. Hieda, A. Kikitsu, K. Naito, *J. Nanophotonics* **B**, 011597 (2007)
4. E. Ozbay, *Science* **311**, 189 (2006)
5. M. Ohtsu, *J. Nanophotonics* **1**, 011590 (2007)

6. M. Naruse, T. Kawazoe, T. Yatsui, S. Sangu, K. Kobayashi, M. Ohtsu, *Progress in Nano-Electro-Optics V* (Springer, Berlin, 2006)
7. S. Mononobe, *Near-Field Nano/Atom Optics and Technology* (Springer, Berlin, 1998)
8. U. Maheswari Ra-jagopalan, S. Mononobe, K. Yoshida, M. Yoshimoto, M. Ohtsu, *Jpn. J. Appl. Phys.* **38(12A)**, 6713 (1999)
9. Y. Inao, S. Nakasato, R. Kuroda, M. Ohtsu, *Microelectron. Eng.* **84**, 705 (2007)
10. T. Kawazoe, M. Ohtsu, Y. Inao, R. Kuroda, *J. Nanophotonics* **1**, 011595 (2007)
11. T. Yatsui, K. Hirata, W. Nomura, Y. Tabata, M. Ohtsu, *Appl. Phys. B* **93**, 55 (2008)
12. K. Kobayashi, S. Sangu, T. Kawazoe, A. Shojiguchi, K. Kitahara, M. Ohtsu, *J. Microscopy* **210**, 247 (2003)
13. T. Kawazoe, K. Kobayashi, K. Akahane, M. Naruse, N. Yamamoto, M. Ohtsu, *Appl. Phys. B* **84**, 243 (2006)
14. T. Yatsui, S. Sangu, T. Kawazoe, M. Ohtsu, S.-J. An, J. Yoo, *Appl. Phys. Lett.* **90**, No. 22, 223110 (2007)
15. W. Nomura, T. Yatsui, T. Kawazoe, M. Ohtsu, *J. Nanophotonics* **1**, 011591 (2007)
16. W. Nomura, T. Yatsui, T. Kawazoe, M. Naruse, M. Ohtsu, *Appl. Phys. B* **100**, in press (2010)
17. T. Yatsui, Y. Ryu, T. Morishima, W. Nomura, T. Kawazoe, T. Yonezawa, M. Washizu, H. Fujita, M. Ohtsu, *Appl. Phys. Lett.* **96**(13), 133106 (2010)
18. U. Schendel, *Introduction to Numerical methods for parallel computers* (Ellis Horwood, New York, 1984)
19. H.H. Hopkins, *Proc. Roy. Soc.* **A217**, 408 (1953)
20. N. Tate, W. Nomura, T. Yatsui, T. Kawazoe, M. Naruse, M. Ohtsu, *Nat. Comput.* **2**, 298 (2010)
21. M. Naruse, T. Yatsui, T. Kawazoe, N. Tate, H. Sugiyama, M. Ohtsu, *Appl. Phys. Exp.* **1**, 112101 (2008)
22. N. Tate, W. Nomura, T. Yatsui, M. Naruse, M. Ohtsu, *Appl. Phys. B* **96**(1), 1 (2009)
23. M. Ohtsu, K. Kobayashi, T. Kawazoe, T. Yatsui, M. Naruse (eds.), *Principles of Nanophotonics* (Taylor and Francis, Boca Raton, 2008)
24. T. Kawazoe, K. Kobayashi, J. Lim, Y. Narita, M. Ohtsu, *Phys. Rev. Lett.* **88**, 067404 (2002)
25. T. Kawazoe, K. Kobayashi, M. Ohtsu, The optical nanofountain: a biomimetic device that concentrates optical energy in a nanometric region. *Appl. Phys. Lett.* **86**, 103102 (2005)
26. M. Naruse, T. Yatsui, H. Hori, M. Yasui, M. Ohtsu, *J. Appl. Phys.* **103**, 113525 (2008)
27. N. Tate, H. Sugiyama, M. Naruse, W. Nomura, T. Yatsui, T. Kawazoe, M. Ohtsu, *Opt. Exp.* **17**, 11113 (2009)
28. D.W. Lynch, W.R. Hunter, in *Handbook of Optical Constants of Solids* (Academic, Orlando, 1985)
29. M. Naya, I. Tsurusawa, T. Tani, A. Mukai, S. Sakaguchi, S. Yasutani, *Appl. Phys. Lett.* **86**, 201113 (2005)
30. H. Yonemitsu, T. Kawazoe, K. Kobayashi, M. Ohtsu, *J. Lumin.* **122–123**, 230 (2007)
31. P.-Y. Chiou, A.T. Ohta, A. Jamshidi, H.-Y. Hsu, M.C. Wu, *IEEE J. Microelectromech. Sys.* **17**, 525 (2008)
32. M. Naruse, T. Inoue, H. Hori, *Jpn. J. Appl. Phys.* **46**, 6095 (2007)
33. S. Zhang, D.A. Genov, Y. Wang, M. Liu, X. Zhang, *Phys. Rev. Lett.* **101**, 047401 (2008)
34. N. Tate, H. Tokoro, K. Takeda, W. Nomura, T. Yatsui, T. Kawazoe, M. Naruse, S. Ohkoshi, M. Ohtsu, *Appl. Phys. B* **98**(4), 685 (2010)
35. J. Tanida, Y. Ichioka, *Appl. Opt.* **27**, No.14, 2926 (1988)
36. M. Ishikawa, A. Morita, N. Takayanagi, *Proceedings of the IEEE International Conference on Intelligent Robots and Systems*, Raleigh, NC, p. 373 (1992)
37. M. Ohtsu, T. Kawazoe, T. Yatsui, M. Naruse, *IEEE J. Sel. Top. Quantum Electron.* **14**(6), 1404 (2008)
38. M. Naruse, T. Yatsui, W. Nomura, N. Hirose, M. Ohtsu, *Opt. Exp.* **13**(23), 9265 (2005)
39. B. Lee, J. Kang, K.-Y. Kim, *Proc. SPIE* **4803**, 220 (2002)
40. O. Sato, S. Hayami, Y. Einaga, Z.Z. Gu, *Bull. Chem. Soc. Jpn.* **76**(3), 443 (2003)
41. H. Tokoro, T. Matsuda, T. Nuida, Y. Morimoto, K. Ohoyama, E.D.L.D. Dangui, K. Boukheddaden, S. Ohkoshi, *Chem. Mater.* **20**, 423 (2008)

42. S. Ohkoshi, H. Tokoro, M. Utsunomiya, M. Mizuno, M. Abe, K. Hashimoto, *J. Phys. Chem. B* **106**, 2423 (2002)
43. H. Tokoro, S. Ohkoshi, T. Matsuda, K. Hashimoto, *Inorg. Chem.* **43**, 5231 (2004)
44. H. Tokoro, T. Matsuda, K. Hashimoto, S. Ohkoshi, *J. Appl. Phys.* **97**, 10M508 (2005)
45. W.F. Fagan (ed.), *Optical Security and Anti-counterfeiting systems* (Society of Photo Optical Instrumentation Engineers, Washington, D.C. 1990)
46. B. Javidi, J.L. Horner, *Opt. Eng.* **33**, 1752 (1994)
47. P. Refregier, B. Javidi, *Opt. Lett.* **20**, 767 (1995)
48. G.A. Rakuljic, V. Leyva, A. Yariv, *Opt. Lett.* **17**, 1471 (1992)
49. R.L. Van Renesse (ed.), *Optical Document Security* (Artech House Optoelectronics Library, Boston/London, 1998)
50. S.P. McGrew, *Proc. SPIE* **1210**, 66 (1990)
51. G.S. Zhdanov, M.N. Libenson, G.A. Martynovskii, *PHYS-USP* **41**, 719 (1998)
52. M. Ohtsu, *Tech. Dig. 18th Congr. Int. Commission for Optics, SPIE* **3749**, 478 (1999)
53. T. Yatsui, K. Itsumi, M. Kourogi, M. Ohtsu, *Appl. Phys. Lett.* **80**, 2257 (2002)
54. N. Tate, W. Nomura, T. Yatsui, M. Naruse, M. Ohtsu, *Opt. Exp.* **16**, 607 (2008)
55. N. Tate, M. Naruse, T. Yatsui, T. Kawazoe, M. Hoga, Y. Ohyagi, T. Fukuyama, M. Kitamura, M. Ohtsu, *Opt. Exp.* **18**, 7497 (2010)
56. H. Matsumoto, T. Matsumoto, Technical report of IEICE, ISEC 2000–59, 7 (2000)
57. M. Naruse, H. Hori, K. Kobayashi, M. Ishikawa, K. Leibnitz, M. Murata, N. Tate, M. Ohtsu, *J. Opt. Soc. Am. B* **26**, 1772 (2009)

Part VI

Related Basic Sciences

Jongsuck Bae, Ryo Ishikawa, and Koji Mizuno

Contents

25.1	Introduction.....	946
25.2	Review of Experiments.....	947
25.2.1	Smith–Purcell Effect.....	947
25.2.2	Schwarz–Hora Effect.....	948
25.3	Basic Principle.....	949
25.4	Microgap Interaction Circuits.....	952
25.4.1	Circuit Configuration.....	952
25.4.2	Transition Rates of Electrons.....	953
25.5	Theoretical Analyses of a Microslit.....	957
25.5.1	Near-Field Distributions.....	957
25.5.2	Wave-Number Spectrum.....	960
25.5.3	Numerical Simulations.....	961
25.6	Experiment.....	964
25.6.1	Experimental Setup.....	964
25.6.2	Electron-Energy Spectrum.....	965
25.6.3	Modulation with Laser Field.....	967
25.6.4	Wave-Number Spectrum.....	969
25.7	Multiple-Gap Circuit.....	969
25.7.1	Inverse Smith–Purcell Effect.....	970

J. Bae (✉)

Department of Engineering Physics, Electronics and Mechanics, Nagoya Institute of Technology,
Nagoya, Japan

e-mail: bae@nitech.ac.jp

R. Ishikawa

Department of Communication Engineering and Informatics, Graduate School of Informatics and
Engineering, The University of Electro-Communications, Chofu, Japan

e-mail: r.ishikawa@uec.ac.jp

K. Mizuno

Research Institute of Electrical Communication, Tohoku University, Sendai, Japan

e-mail: koji@riec.tohoku.ac.jp

25.7.2	Experimental Setup.....	971
25.7.3	Phase-Matching Condition.....	972
25.7.4	Field Distributions.....	973
25.8	Microslit for Visible Light.....	973
25.9	Conclusion.....	975
	References.....	976

Abstract

In free space, electrons cannot interact with light waves, because the energy and momentum conservations are not simultaneously preserved in the interaction. On the other hand, optical near-fields, that is, evanescent waves with wave number larger than that of light waves in free space can modulate the energy and momentum of electrons. Theoretical analyses and experimental results on the modulation of electrons in optical near-fields have been presented.

25.1 Introduction

Many kinds of electron-beam devices have been developed and utilized in various scientific areas since the early 1900s [1]. For instance, microwave amplifiers and oscillators, electron accelerators, and various types of electron microscopes have made major contributions to establish modern science and technology, such as high-speed communication, elementary particle physics, and solid-state physics. On the other hand, most of those for commercial use have been replaced by solid-state devices due to their power consumption and device size. Beam devices, however, have several advantages over solid-state devices, such as wider tuning frequency range and higher output power. Recent advances in vacuum microelectronics [2] and micromachining technology [3] provide a useful means for realizing small beam devices. In fact, electron emitters with dimensions of several microns have been fabricated through semiconductor processes [4].

The operating frequencies of conventional beam devices are usually less than 1 THz [5]. Though free-electron lasers can operate at optical frequencies, these utilize relativistic bunched electron beams with high density for laser action, and consequently, their device size is huge [6]. Development of lower-energy electron-beam devices operating at optical frequencies would thus be desirable.

In order to realize compact, convenient beam devices using nonrelativistic electrons, the interaction mechanism for energy and momentum exchange between electron and light, including quantum effects, must be carefully studied. Those studies are also required to develop new microscopic techniques that are able to investigate the surface state of nanoparticles. For instance, electron-energy-loss spectroscopy (EELS) [7] is one of those, in which electrons passing in the proximity of a nanoparticle excite near-fields on its surface and suffer specific energy loss resulting from the interaction with the fields. Analyses for the energy-loss spectrum of the electrons bring out useful information about the electronic and optical properties of the nanoparticle [8].

In this chapter, energy modulation of nonrelativistic electrons with light waves, especially with evanescent waves contained in optical near-fields, is discussed. We shall briefly review in the next section the electron–light interaction effects, called the Smith–Purcell effect and the Schwarz–Hora effect. In Sect. 25.3, a basic principle of electron–light interaction is explained in both classical and quantum terms. In Sect. 25.4, microgap circuits used for the interaction are presented. In Sect. 25.5, a metal microslit among those circuits is chosen as a potential circuit to realize the interaction with light waves. The energy modulation of low-energy electrons with optical evanescent waves in a microslit circuit has been demonstrated experimentally. The results are presented in Sect. 25.6. In Sect. 25.7, a multiple-slit circuit structure, that is, a diffraction grating, is treated as an interaction circuit. Based on the results, we discuss in Sect. 25.8 the possibility of experimental observation of electron-energy modulation with visible light. Section 25.9 concludes this chapter.

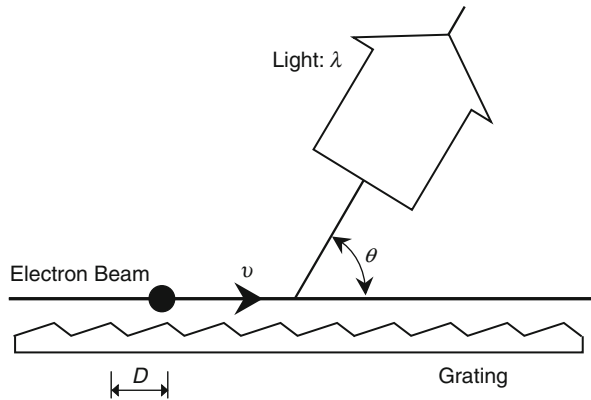
25.2 Review of Experiments

Low-energy electron-beam amplifiers and oscillators, klystrons, traveling wave tubes, and backward wave oscillators are mostly for the microwave region. For these devices, it has been thought that extending their operation to optical frequencies would be difficult. The reason for this is as follows. In order to obtain signal gain in the beam devices, the electron beam must be density modulated at a signal frequency. In the microwave region, density modulation (bunching) is easily achieved, because the energy of the electrons changes in proportion to the amplitude of the signal electric field. On the other hand, in the optical region, the electron energy changes by multiples of the energy of a signal photon. This effect would prevent a smooth change in beam density, diminishing the signal gain. In 1954, Senitzky concluded through his theoretical consideration that operation of klystron-type beam devices is limited to frequencies below submillimeter waves [9]. Contrary to his theoretical prediction, light emission effects with a nonrelativistic electron beam have been reported. In this section, two well-known effects, the Smith–Purcell effect and the Schwarz–Hora effect, are reviewed.

25.2.1 Smith–Purcell Effect

In 1953, Smith and Purcell demonstrated that light was emitted from an electron beam passing close to the surface of a metal diffraction grating [10]. Figure 25.1 shows the experimental configuration of the Smith–Purcell effect. They observed that the wavelength of the light could be changed from 450 to 550 nm by adjusting the initial energy of electrons from 340 to 309 keV. The relationship between the wavelength λ and the electron velocity v is given by

Fig. 25.1 Schematic drawing of the Smith–Purcell effect



$$\lambda = \frac{D}{n} \left(\frac{1}{\beta} - \cos \theta \right), \quad (25.1)$$

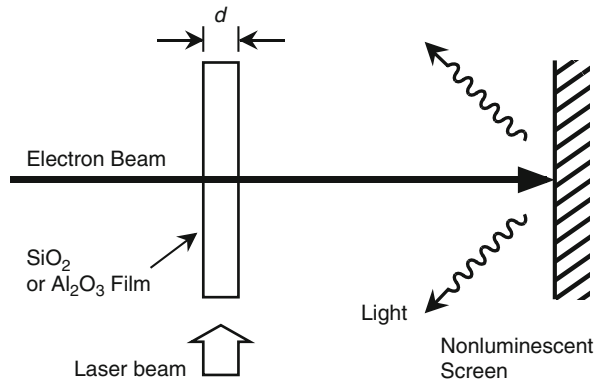
where D is the period of the grating, n is the spectral order, β is the electron velocity normalized to the light speed c , that is, v/c , and θ is the angle between the direction of motion of the electron and the light ray. This equation was derived by them through a simple Huygens analysis for radiation caused by the periodic motion of the charge induced on the surface of the grating. This emission of radiation from the electrons has been also explained in terms of the interaction between the electrons and evanescent surface waves induced on the grating [11].

Smith and Purcell used relatively high-energy electrons with $\beta \sim 0.8$ for their experiment. In 1997, Goldstein et al. successfully observed Smith–Purcell radiation using a lower-energy electron beam with an energy of 27–40 keV, though the radiation was in the far infrared [12]. After the report by Smith and Purcell, many researchers proposed various types of beam devices using the Smith–Purcell effect and its inverse [13], such as the laser-driven grating linac [14, 15] and free-electron lasers with a grating [16]. Most of those devices have not yet been demonstrated experimentally in the optical region.

25.2.2 Schwarz–Hora Effect

In 1969, Schwarz and Hora reported that quantum modulation of nonrelativistic electrons with light had been achieved using a thin dielectric film as an interaction circuit [17]. Figure 25.2 shows a schematic drawing of their experimental system. In the experiment, a 50-keV electron beam and an Ar laser (wavelength: $\lambda = 488$ nm) were used. The interaction circuit was a SiO_2 or Al_3O_2 film with a thickness of less than 200 nm. The electron beam passed through the film illuminated with the 10-W laser beam and then hit a nonluminescent screen. They reported that light of the same color as the laser was emitted from the screen. For the experimental

Fig. 25.2 Schematic drawing of the Schwarz–Hora effect



parameters used by Schwarz and Hora, the laser produces a maximum electric field of about 10^7 V/m in the dielectric film. This field only gives an energy of 2 eV or less to the electrons in the film. This energy is less than the photon energy, 2.54 eV of the Ar laser, so that quantum effects might come into play in this interaction. They claimed that the wave function of coherent electrons was modulated by the light, and consequently density modulation of the electron beam was achieved [18]. Though the Schwarz–Hora effect has not yet been reproduced by other experimental groups, their results have suggested the possibility of new electron-beam devices utilizing quantum effects.

25.3 Basic Principle

Though the Schwarz–Hora effect has not been confirmed experimentally yet, we believe that a thin dielectric film could be used as an interaction circuit between electrons and light. This is because energy and momentum conservation are satisfied by the interaction [19]. Let us consider the case in which an electron absorbs a photon. The dispersion relations for the electron and photon are represented by (Eq. 25.2) and (25.3), respectively, and are illustrated in Fig. 25.3:

$$W_e = \sqrt{m_0^2 c^4 + c^2 p_e^2}, \quad (25.2)$$

$$W_p = \hbar \omega = c p_p, \quad (25.3)$$

where W and p indicate the energy and the momentum, respectively, and the subscripts e and p stand for electron and photon, m_0 is the rest mass of the electron, c is the speed of light, $\hbar = h/2\pi$, h is Planck's constant, and ω is the angular frequency. In the thin dielectric film shown in Fig. 25.2, p_e is perpendicular to p_p . Therefore, the increase in electron momentum p_e when W_e increases by W_p is

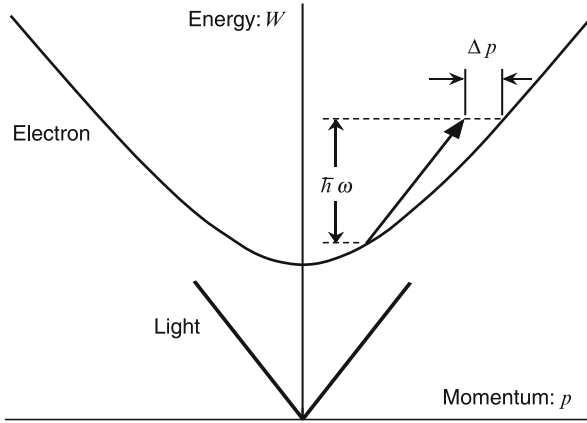


Fig. 25.3 Energy–momentum dispersions for a free electron and a photon

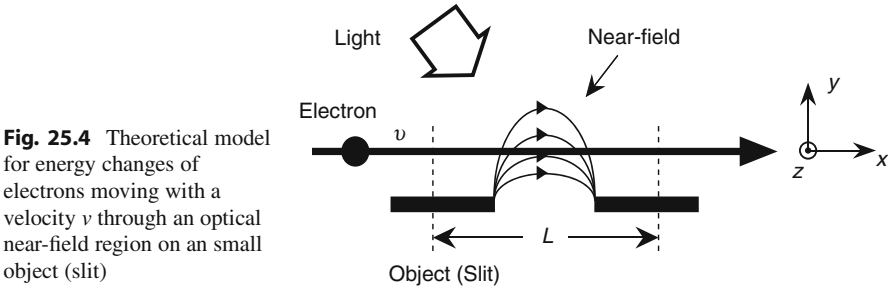


Fig. 25.4 Theoretical model for energy changes of electrons moving with a velocity v through an optical near-field region on a small object (slit)

$$\Delta p = \frac{\hbar\omega}{v}, \tag{25.4}$$

where v is the electron velocity. The interaction between an electron and a photon in free space does not occur due to this shortage of momentum.

From an evanescent wave theory [20], it is known that localized optical fields in an area small compared to the wavelength, such as optical near-fields, have wave components whose momentum is greater than that of free photons. Therefore, those fields could modulate an electron beam. This argument is supported by the experimental results in the Smith–Purcell effect described in Sect. 25.2.1, in which electrons interact with optical evanescent waves induced on the surface of a metal grating, and coupling to the field gives rise to radiation.

For ease of consideration, let us assume a simple object: a slit of infinite length in the z direction, as shown in Fig. 25.4. When the slit is illuminated by light with angular frequency ω , an optical near-field is induced on the surface of the slit. The electric field E_x on the slit can be expressed in terms of its spatial plane-wave spectrum A and is given by

$$E_x(x, t) = \frac{1}{2\pi} \int_{-\infty}^{+\infty} A(k_x) \exp j(k_x x - \omega t) dk_x, \quad (25.5)$$

where

$$A(k_x) = \int_{-\infty}^{+\infty} E_x(x, t) \exp[-j(k_x x - \omega t)] dx. \quad (25.6)$$

When an electron passes through the near-field region with velocity v in the x direction, the electron suffers an energy loss (or gain) W ,

$$W = \int_{-L/2}^{+L/2} q E_x(x, t) dx, \quad (25.7)$$

where L is the interaction length on the slit and q is the electron charge. Substituting (Eq. 25.5) for E_x into (Eq. 25.7), we obtain

$$W = \frac{q}{2\pi} \int_{-L/2}^{+L/2} \int_{-\infty}^{+\infty} A(k_x) \exp j(k_x x - \omega t) dk_x dx. \quad (25.8)$$

Using the relation $t = x/v$, it follows that

$$W = q \int_{-\infty}^{+\infty} A(k_x) \left\{ \frac{L}{2\pi} \frac{\sin(k_x - k_e) \frac{L}{2}}{(k_x - k_e) \frac{L}{2}} \right\} dk_x, \quad (25.9)$$

where

$$k_e = \omega/v. \quad (25.10)$$

The sampling function in (Eq. 25.9) becomes a delta function in the limit $L \rightarrow \infty$:

$$\lim_{L \rightarrow \infty} \left\{ \frac{L}{2\pi} \frac{\sin(k_x - k_e) \frac{L}{2}}{(k_x - k_e) \frac{L}{2}} \right\} = \delta(k_x - k_e).$$

Hence, we have

$$W = q \int_{-\infty}^{+\infty} A(k_x) \delta(k_x - k_e) dk_x = q A(k_e). \quad (25.11)$$

From this result, it is seen that an electron with velocity v interacts selectively with the wave component with wave number k_e in the near-field. Since k_e is greater than

the wave number $k_0 = \omega/c$ of light in free space, this wave is evanescent. Since the momentum of the evanescent wave, $\hbar k_e$, is greater than that of a wave propagating in free space, energy and momentum conservation are satisfied for the interaction with electrons. In fact, substituting $\hbar k_e$ for Δp in (Eq. 25.4), the same expression, that is, (Eq. 25.10) can be derived.

An analogous treatment of the interaction has been carried out using the uncertainty principle. When optical fields are localized on a slit with a small width d , the effective interaction length on the slit is limited, so that an uncertainty exists in momentum. This additional momentum p_c from the slit is approximately

$$p_c \sim \frac{h}{d}. \quad (25.12)$$

When $p_c > \Delta p$, momentum conservation for the interaction can be also satisfied. From (Eq. 25.4) and (Eq. 25.12), the condition for d is

$$d < \beta\lambda. \quad (25.13)$$

This equation indicates that the requirement for interaction between electrons and light is not the slit itself, but limitation of the interaction length. More detailed discussion on the limitation is given in [21]. From (Eq. 25.13), it is seen that for Schwarz and Hora's experiment, significant interaction can occur when the film thickness is less than 200 nm.

25.4 Microgap Interaction Circuits

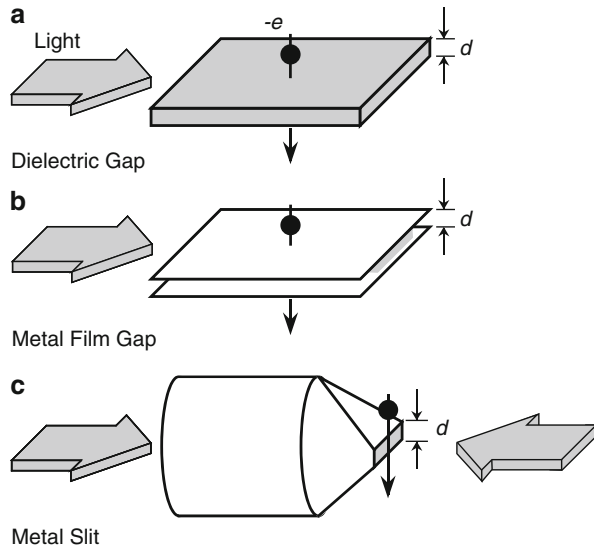
Three kinds of circuit structures for the interaction between free electrons and light are presented. The transition rates of electrons in the interaction circuits are theoretically estimated in quantum mechanical fashion. The results indicate that measurable signal electrons can be obtained under practical experimental conditions.

25.4.1 Circuit Configuration

As discussed in Sect. 25.3, localized field distributions are necessary for interaction with electrons. Figure 25.5 shows three kinds of circuits used in the optical region: (a) a dielectric film, (b) a metal film gap, and (c) a metal slit. These microgap circuits localize optical fields in a small gap of width d less than the wavelength.

In Fig. 25.5, the dielectric film is the interaction circuit used by Schwarz and Hora. The metal film gap is most similar to the conventional microwave circuits used in klystrons [5]. The metal microslit was proposed as an optical near-field generator used for the interaction with low-energy electrons [22]. This type of metal microslit is more suitable than the other gap circuits for measurement of energy exchange

Fig. 25.5 Schematic drawing of three different gap circuits. The gap width d is smaller than the wavelength of the incident laser



between free electrons and light and for investigating quantum effects, because there is not a disturbance such as electron scattering in metal films or dielectric medium. On the other hand, the near-fields only exist in proximity to the slit surface so that the interaction space for the electrons is small compared to the other circuits. The electron–light interaction in the metal microslit is discussed in detail in [Sect. 25.5](#).

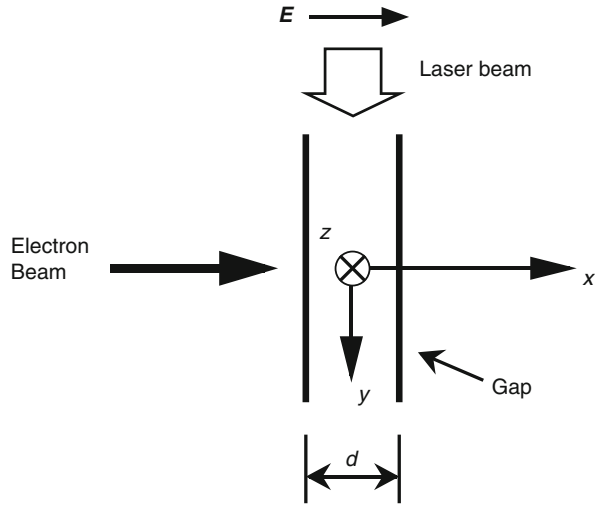
25.4.2 Transition Rates of Electrons

The transition rates of electrons in a metal film gap and a thin dielectric film were theoretically estimated in [22]. The calculation model is shown in [Fig. 25.6](#). The electron beam passes through the gap and travels in the $+x$ direction, and the laser wave propagates in the $+y$ direction. To simplify the calculation, the following assumptions were made: (i) the initial velocities of the electrons are identical; (ii) the propagation modes of the light wave in the metal film gap and the thin dielectric film are TEM_{00} and TM_{01} , respectively; (iii) the incident light wave is polarized in the x direction; (iv) the gap materials have no rf loss; and (v) the electrons interact only with the light. The transition rate for an electron in the metal film gap was calculated in accordance with the analyses by Marcuse [23]. The calculated rate w_m is

$$w_m = \frac{2qc\beta^2}{\varepsilon_0\hbar^2\omega^4} iP_i \sin^2\left(\frac{\omega d}{2v}\right), \quad (25.14)$$

where i is the electron current density, ε_0 is the dielectric constant of free space, and P_i is the power density of the incident light.

Fig. 25.6 The gap circuit configuration used for the theoretical analysis



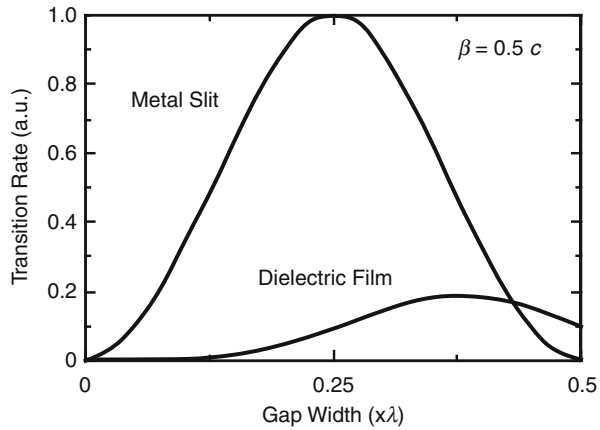
In (Eq. 25.14), the value of w_m represents the rate at which an electron absorbs one photon with energy $\hbar\omega$. The rate to emit the photon is almost the same as that in (Eq. 25.14). Similarly, it is possible to calculate a transition rate w_d for the dielectric film by quantizing the laser field of the fundamental TM_{01} propagation mode. The expression for w_d is

$$\begin{aligned}
 w_d = & \frac{qc}{\epsilon_0 \hbar^2 \omega^4} i P_i \left| \frac{k_0 k_y d^2}{2n_i^2 \cos(k_{ix} d/2)} \right|^2 \\
 & \times \left| \frac{4 k_{ix} d \sin(k_{ix} d/2) \cos(\omega d/2v) - (\omega d/2v) \cos(k_{ix} d/2) \sin(\omega d/2v)}{(k_{ix} d)^2 - (\omega d/v)^2} \right|^2 \\
 & \times \left\{ \frac{k_0 d}{2n_i \cos(k_{ix} d/2)} \right\}^2 + \left\{ \frac{(k_y^2 - k_{ix}^2)}{(n_i k_{ix})^2} - \frac{n_i^2 (k_y^2 - k_{ex}^2)}{(n_e k_{ex})^2} \right\} \\
 & \times \frac{1}{\frac{k_{ix} d}{2n_i^2} \tan(k_{ix} d/2)}, \tag{25.15}
 \end{aligned}$$

where

$$\begin{aligned}
 k_{ix}^2 + k_y^2 &= (n_i k_0)^2, \\
 k_{ex}^2 + k_y^2 &= (n_e k_0)^2, \\
 |k_{ex}| &= \left(\frac{n_e}{n_i} \right)^2 k_{ie} \tan k_{ix} d/2,
 \end{aligned}$$

Fig. 25.7 Calculated transition rates of an electron with a velocity of $\beta = 0.5$ as a function of the gap width of the metal film gap and the SiO₂ dielectric film. The gap width is normalized to the laser wavelength



n_i and n_e are the refractive indices inside and outside the dielectric film, respectively, k_y is the wave number in free space in the y direction, and k_{ix} and k_{ex} are the wave numbers inside and outside the film in the x direction. From (Eq. 25.14) and (Eq. 25.15), the transition rates can be estimated as a function of the gap width. Figure 25.7 shows the calculated results used to find the optimum gap width. The parameters used in the calculation are $\beta = 0.5$, $\lambda = 780$ nm, $n_i = 1.45$ (SiO₂), and $n_e = 1$. As seen from (Eq. 25.14), w_m varies sinusoidally and has the peak at the gap width satisfying the equation

$$d = \beta\lambda\left(m + \frac{1}{2}\right), \quad (25.16)$$

where m is an integer. Substituting $\beta = 0.5$ and $m = 0$ for the first peak, an optimum gap width of $\lambda/4$ is obtained. The variation of w_m in Fig. 25.7 is different from the klystron theory in which the maximum value of w_m is at $d \sim 0$ [5]. The difference between these comes from the different treatments of photon density in the gap. The klystron theory assumes that the total number of photons stored in the gap is constant, but in our treatment, it is assumed that the photon density in the gap is constant and is determined by the incident laser power.

From Fig. 25.7, it can be seen that for the SiO₂ film, the first peak value of w_d is 0.18 times that of w_m . The optimum film thickness of 0.38 is also longer than the optimum width of the metal film gap. In the dielectric film, the laser field is distributed outside the film as an evanescent wave so that the number of photons inside the gap is smaller than that for the metal gap. The longer gap width increases the number of photons inside the dielectric film.

Figure 25.8 shows the calculated transition rates as a function of the light intensity for the metal film gap and the SiO₂ film. These transition rates represent the probability per unit time of one electron absorbing a photon. In the calculation, the optimum gap widths of 0.25λ and 0.38λ were used for the metal film gap and the SiO₂ film, respectively. The other calculation parameters were described

Fig. 25.8 Calculated transition rates as a function of the power intensity of the incident light for the metal film gap and the SiO₂ dielectric film at a wavelength of 780 nm

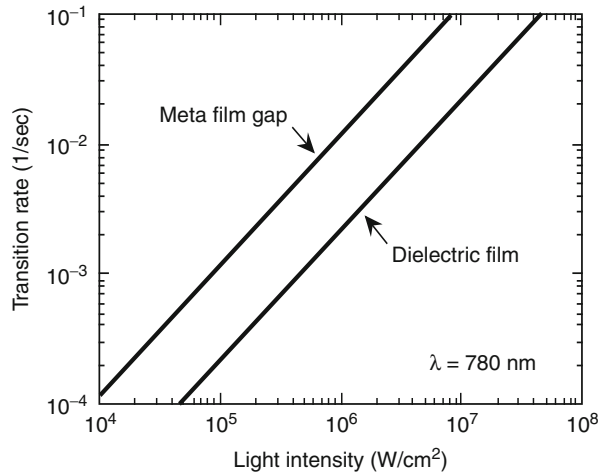
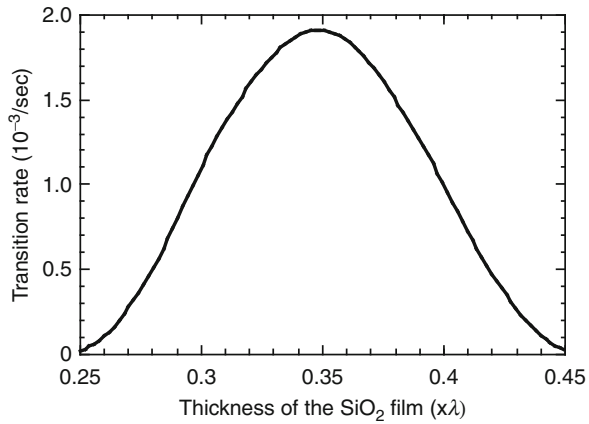


Fig. 25.9 Transition rate in the SiO₂ dielectric film versus the film thickness at $\lambda = 488 \text{ nm}$



previously. From Fig. 25.8, it can be seen that the transition rates are 1.1×10^{-2} and $2 \times 10^{-3}/s$ for a power intensity of 10^6 W/cm^2 in the metal film gap and the SiO₂ film, respectively. The power intensity of the laser corresponds to an output power of 790 mW focused onto a $10 \mu\text{m}$ diameter area.

The transition rate just in front of the metal slit is intended to be the same as that of the metal film gap because the field distribution at the surface of the metal slit is similar to that in the film gap. The detailed results for the metal slit are derived via classical theoretical analyses in the next section.

Figure 25.9 shows the evaluated electron transition rates using (Eq. 25.15) for the experimental conditions described by Schwarz and Hora, that is, an Ar laser with a power of 10 W and a beam diameter of $10 \mu\text{m}$ at $\lambda = 488 \text{ nm}$, and $v \sim 0.4c$. The optimum film thickness is about 170 nm, which agrees with the one used in the experiment, and is also consistent with the theoretical prediction

given in (Eq. 25.13). Since the electron transition rate is about $2 \times 10^{-3}/\text{s}$, they probably obtained signal electrons at more than 1,000 particles/s for the electron beam used. Though it is still not clear whether detection of signal electrons with a nonluminescent screen is possible or not, the number of signal electrons may be sufficient to detect the interaction when modern electron detection systems with high sensitivity are used.

25.5 Theoretical Analyses of a Microslit

Metal microslits can generate near-fields that modulate an electron beam at optical frequencies. The circuit configuration of microslits is suitable for investigating energy exchange of electrons with light, because the near-field distribution on the microslit is precisely determined. In this section, the electron-energy modulation in the microslits is analyzed theoretically in classical terms [24]. Firstly, optical near-field distributions on the slit are determined using the method of moments. The validity of the theory is confirmed by comparing with measured field distributions. The energy changes of electrons are evaluated numerically through computer simulation. From the results, the relationship among wavelength, slit width, and electron velocity is determined.

25.5.1 Near-Field Distributions

In accordance with Chou and Adams' analysis [25], near-field distributions on a metal microslit have been calculated using the method of moments. The calculation model is shown in Fig. 25.10. For ease of calculation, it has been assumed that (i) the metal slit consists of two semi-infinite plane screens with perfect conductance and zero thickness and (ii) a normally incident plane wave is polarized perpendicular to the slit in the x direction in which electrons move above the slit.

In order to verify the theory, near-field intensity distributions on a metal slit were measured using a scaled model of the slit at a microwave frequency of 9 GHz (wavelength $\lambda = 33$ mm). The experimental setup is shown in Fig. 25.11. The metal slit consists of two aluminum plates with a height of 400 mm, a width of 190 mm, and a thickness of 1 mm. A rectangular horn antenna with an aperture size of 116×157 mm was positioned 1,650 mm from the slit. This longer distance assures plane-wave incidence. A small antenna probe detects the electric field in the x direction, $|E_x|$, which is the dominant field for the interaction with electrons. The antenna probe, with a length of 1.6 mm, terminated a thin coaxial cable with a diameter of 0.8 mm connected to a spectrum analyzer.

Figure 25.12 compares (a) the calculated and (b) measured field intensity distributions of $|E_x|$ on the slit. The slit width d was 0.5λ . The field intensities were normalized to $|E_x^i|$ measured at $x = y = 0$ without the slit. In Fig. 25.12, the shapes of the field distributions for both the theory and the experiment are quite

Fig. 25.10 Calculation model for the near-field distribution in a metal microslit. $|E_x^i|$ denotes the electric field of the incident wave

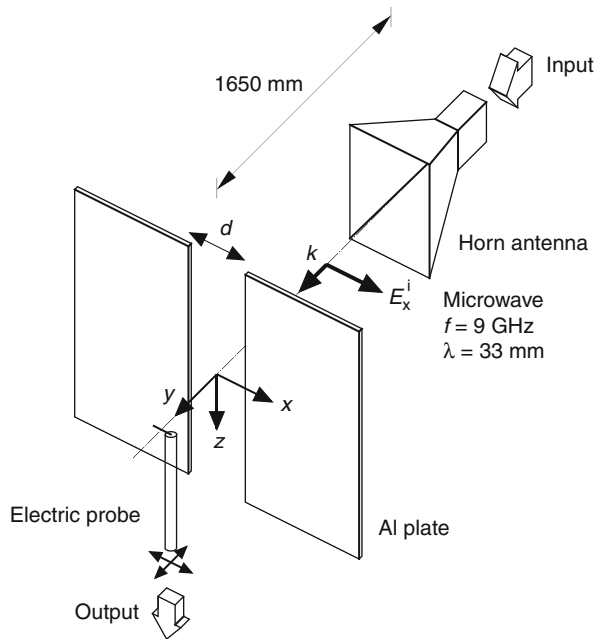
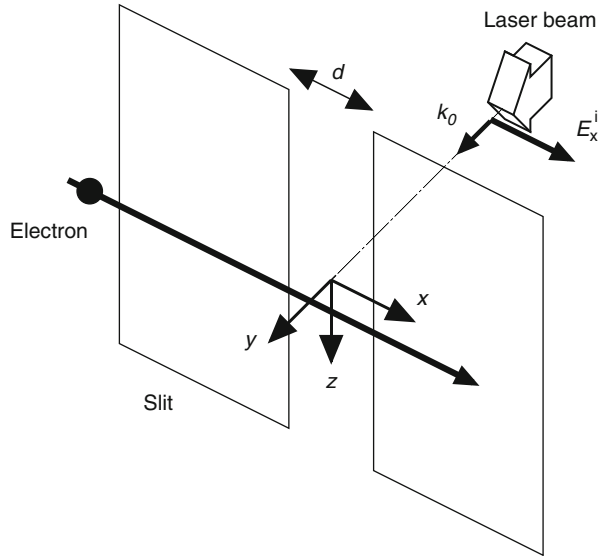


Fig. 25.11 Experimental setup for measuring the near-field distribution on the metal slit at 9 GHz

similar, though the measured near-field in Fig. 25.12b has small ripples. These would result from interference of waves scattered from the coaxial probe and the slit.

Figure 25.13 shows the calculated and measured field intensities for slits of different width as a function of the distance from the slit surface y at the center of

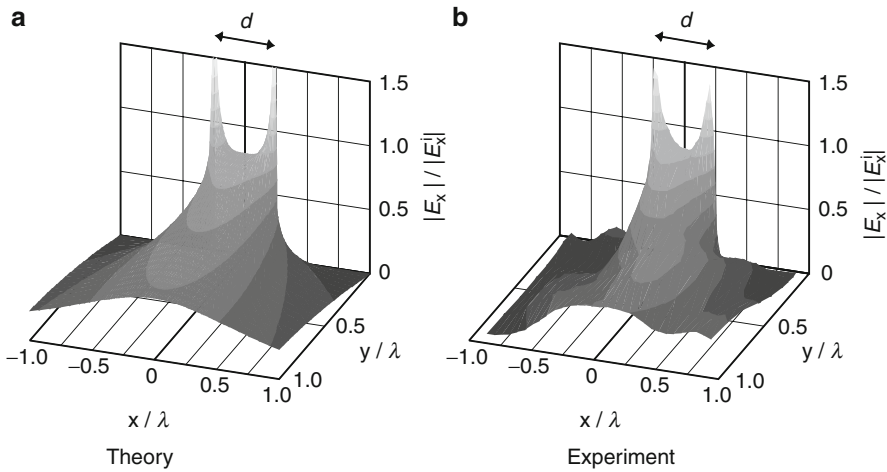


Fig. 25.12 (a) Calculated and (b) measured field distributions of the electric field component E_x in the x direction on a slit of width $d = \lambda/4$. E_x is normalized to the incident field intensity E_x^i , and the positions x and y are also normalized to the wavelength

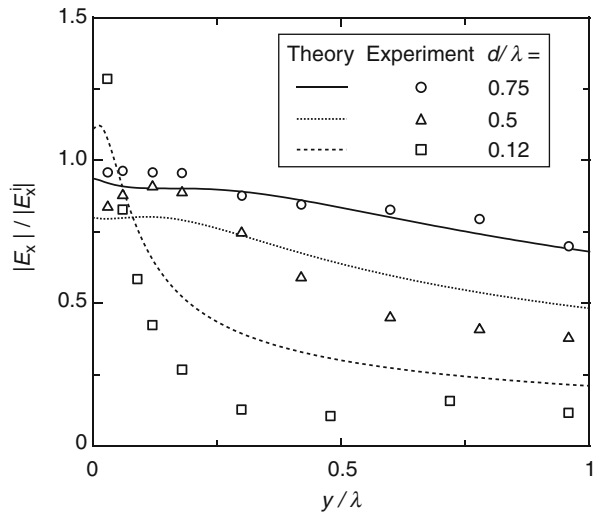
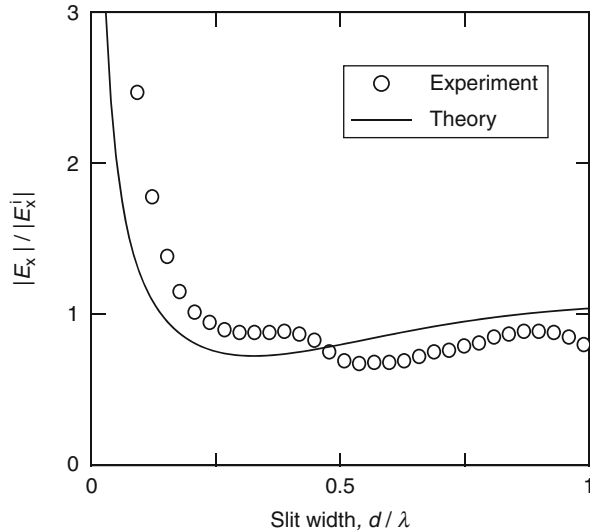


Fig. 25.13 Comparison between the calculated and measured field intensities for slit widths 0.75λ , 0.5λ , and 0.12λ , as a function of the distance from the slit surface y at $x = 0$

the slit, that is, $x = 0$. In the results for $d = 0.75\lambda$, the theory agrees well with the measurement. When d decreases from 0.75λ to 0.12λ , deviations of the measured intensities from the theoretical ones increase mainly due to the probe having a finite size of about 0.05λ . In Fig. 25.13, the smaller the slit width, the steeper the field decay. The near-fields are localized at a distance within $y \sim d$ from the surface. The near-field distributions on the slit are similar to those on small apertures used as optical near-field probes in scanning near-field optical microscopes [26].

Fig. 25.14 Comparison between calculated and measured field intensities as a function of normalized slit width d/λ at $x = y = 0$

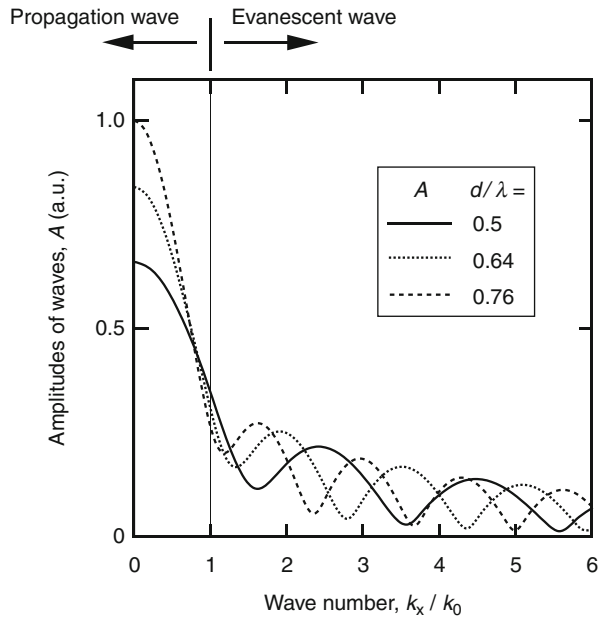


The variation with slit width of the field intensities at $x = y = 0$ has been measured and plotted in Fig. 25.14. When the slit width decreases from λ to zero, the field intensity is almost the same as that of the incident wave at widths up to about 0.2λ and then quickly increases. The small ripple in the measured curve might be caused by scattered waves from the coaxial probe as mentioned earlier. The theory predicts the measured variation of field intensities well. Those results indicate that the theory is valid, allowing for experimental errors.

25.5.2 Wave-Number Spectrum

As mentioned in Sect. 25.3, an optical near-field contains a number of wave components with different wave numbers. We now examine the spatial plane wave spectrum, that is, the wave-number (k) spectrum for the near-field on the slit. Using (Eq. 25.6), the near-fields in the spatial domain as shown in Fig. 25.12 have been transformed to those in the k domain. The transformed spectra for the near-fields E_x at $y = 0.01\lambda$ are shown in Fig. 25.15. The abscissa is the normalized wave number k_x/k_0 in the x direction. The amplitudes of the wave components, A , are normalized to the maximum value in the curve for $d/\lambda = 0.76$ at $k_x = 0$. The wave components with $k_x > k_0$ in Fig. 25.15 are evanescent waves that cannot propagate in free space because the wave number $k_y = (k_0^2 - k_x^2)^{1/2}$ in the y direction is imaginary. As seen from Fig. 25.15, the k spectra spread over large wave numbers above $6k_0$ and have several peaks at different wave numbers in the evanescent wave region. The wave number k_m where A has a peak shifts toward larger values as d

Fig. 25.15 Calculated amplitudes of the wave components in the near-fields for the slits with widths of 0.5λ , 0.64λ , and 0.76λ in the x -direction. The amplitudes A are normalized to the maximum value for the slit with $d/\lambda = 0.76$ at $k_x = 0$



decreases from 0.76λ to 0.5λ . For the first peaks of A in the three spectra, the wave numbers k_m/k_0 are 1.67, 1.92, and 2.38 for slits with $d/\lambda = 0.76$, 0.64 , and 0.5 , respectively. From the calculation results, it has been found that

$$k_m \cong \frac{2\pi}{d} \left(m + \frac{1}{4} \right), \tag{25.17}$$

where m is an integer. This relationship is utilized to design a microslit circuit with the optimum width.

25.5.3 Numerical Simulations

Using the theoretical near-field distributions, energy changes of electrons passing close to the slit surface were estimated through computer simulation. Referring to Fig. 25.16, electrons with velocity v move in the x direction at distance from the slit surface y_i . All field components in the near-field, that is, electric fields, E_x , E_y , and a magnetic field, H_z , were taken into account for calculation. The total energy variations of the electrons were determined by integrating small energy changes due to the Lorentz force over a small distance Δx along the electron trajectory. A total length L of ten times of the slit width was chosen to entirely cover the near-field region on the slit. In the calculation, a CO_2 laser with power density 10^8 W/cm^2 at $\lambda = 10.6 \mu\text{m}$ was assumed as the incident wave. This power density corresponds to a 10 kW output power focused onto a $100 \mu\text{m}$ diameter area.

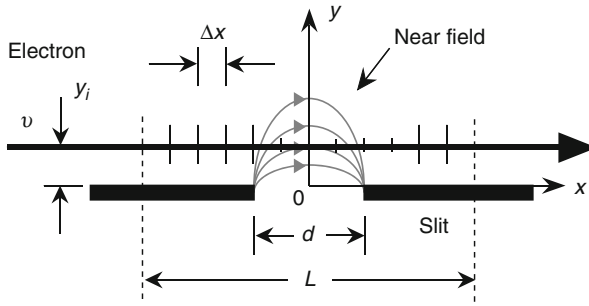


Fig. 25.16 Calculation model of electron-energy changes with a near-field on a slit of a width d . An electron, with an initial velocity v and its position y_i , is accelerated or decelerated by Lorentz force in the near-field region. The integration length L of ten times the slit width was chosen to fully cover the near-field region on the slit

Fig. 25.17 Calculated energy changes ΔW of electrons passing through the near-fields with the k spectra shown in Fig. 25.15 with various velocities β at $y_i = 0.01\lambda$. The electron velocities β were chosen to satisfy the relation $\beta = k_0/k_x$ for each of the k spectra. The amplitudes A are normalized to the maximum value in the curve for the slit with $d/\lambda = 0.5$ at $k_x/k_0 = 1$, and ΔW is also normalized to the maximum value of 34 eV for the slit with $d/\lambda = 0.76$ at $\beta = 0.6$

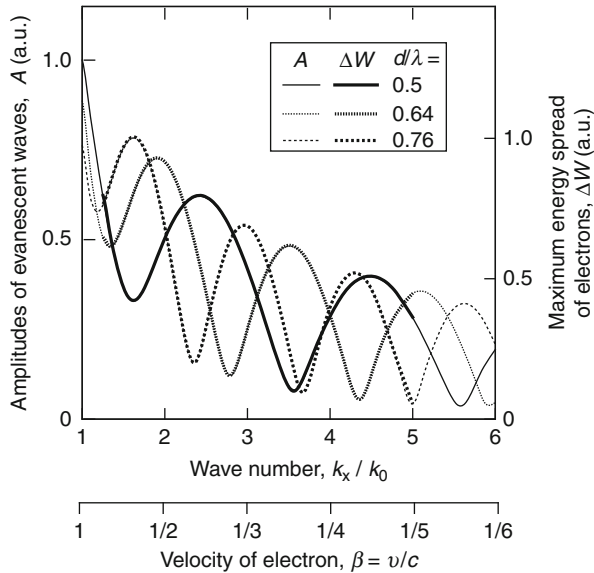
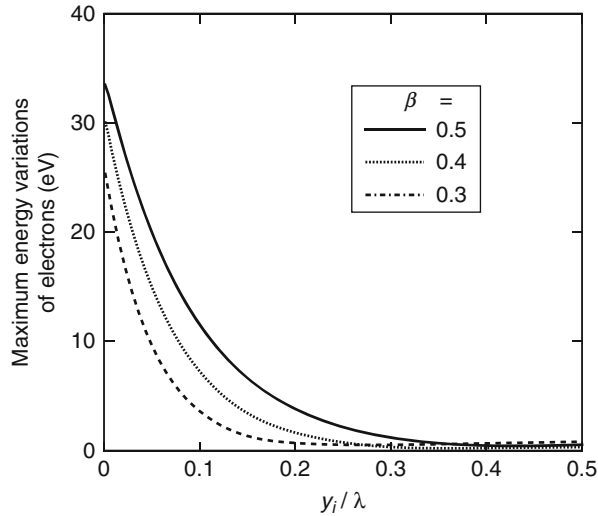


Figure 25.17 shows the calculated energy changes ΔW of electrons passing through the same slits shown in Fig. 25.15 with various velocities β between 0.8 and 0.2 at $y_i = 0.01\lambda$. The thick lines indicate ΔW and the thin lines are for the k spectra and are the same as those shown in Fig. 25.15. ΔW is normalized to the maximum value of the curve for $d = 0.76\lambda$ at $\beta = 0.6$. The two abscissas for k_x and β are related by $\beta = k_0/k_x$, that is, (Eq. 25.10).

As seen from the results in Fig. 25.17, ΔW is proportional to the amplitude A of the evanescent wave in the near-field on the slit. Those results indicate that electrons interact with a single evanescent wave among a number of wave components contained in the near-field. The computer simulation results thus

Fig. 25.18 Calculated maximum electron-energy spreads as a function of the distance y_i/λ from the slit surface for electron velocities $\beta = 0.3, 0.4$, and 0.5



support the theoretical predictions described in Sect. 25.3. In Fig. 25.17, when β decreases, ΔW changes periodically in accordance with the variation of A , and the peaks slowly decrease. In the curve for the slit with $d/\lambda = 0.64$, the peak values of ΔW are 0.93 at $\beta = 0.52$ and 0.61 at $\beta = 0.28$. Those electron velocities correspond to an initial energy of 88 and 21 keV, respectively. This fact indicates that the variation of the peaks in the ΔW curves is small compared to that of the initial electron energy.

Using (Eq. 25.10) and (25.17), the slit widths d_m for the peaks of ΔW are given by

$$d_m \cong \beta\lambda\left(m + \frac{1}{4}\right). \quad (25.18)$$

Equation (Eq. 25.18) gives the optimum slit width in the metal microslit. Comparing with (Eq. 25.16), it is seen that d_m in the microslit is narrower than in the metal film gap by $\beta\lambda/4$. In the metal film gap, electrons are modulated with a uniform field at the film gap. Therefore, the difference between the optimum widths would arise from the difference of the field distributions in the two circuits.

Figure 25.18 shows the calculated ΔW for various electron velocities as a function of y_i . Slits having the optimum widths $d_m/\lambda = (0.38, 0.5, 0.62)$ for $\beta = (0.3, 0.4, 0.5)$, respectively, were used for calculation. In Fig. 25.18, when y_i increases from zero to 0.5λ , ΔW falls off exponentially to near zero. Since ΔW is proportional to the field intensity, these curves represent spatial field distributions of the evanescent waves interacting with the electrons. From the evanescent wave theory, the decay constant α of the evanescent wave [27] is given by

$$\alpha = k_0 \sqrt{\left(\frac{k_x}{k_0}\right)^2 - 1}. \quad (25.19)$$

From (Eq. 25.10) and (Eq. 25.19), the decay constants are estimated to be $\alpha_0 = k_0 \times (3.2, 2.3, 1.7)$ for $\beta = (0.3, 0.4, 0.5)$, respectively, which agree with those estimated from the exponential curves shown in Fig. 25.18.

The effective interaction space of the slit can be defined as $y_e = 1/\alpha$, because the field intensity of the evanescent wave falls off by e^{-1} . Using (Eq. 25.10) and (Eq. 25.19), y_e is

$$y_e = \frac{\lambda}{2\pi} \frac{\beta}{\sqrt{1 - \beta^2}}. \quad (25.20)$$

This equation indicates that the interaction space in the slit circuit is highly restricted, particularly for a lower-energy electron beam. The electrons thus must pass very close to the slit surface in order to obtain significant energy exchange with the laser beam. From the ΔW curve for $\beta = 0.5$ in Fig. 25.18, it is seen that the interaction space for $\lambda = 10.6 \mu\text{m}$ is about $3 \mu\text{m}$, where measurable electron-energy changes of greater than 1 eV are obtained.

25.6 Experiment

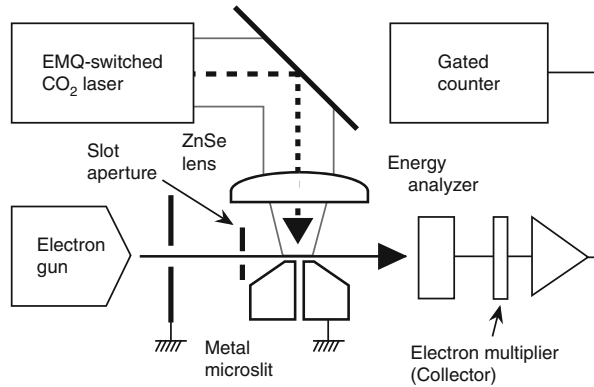
This section gives experimental verification to the theory. Experiments have been performed in the infrared region, where a wider space on a metal microslit is available for interaction. Electron-energy changes of more than $\pm 5 \text{ eV}$ with a 10-kW CO_2 laser pulse at wavelength $10.6 \mu\text{m}$ have been successfully observed for an electron beam with energy less than 80 keV [28]. The experimental results have been compared with theoretical predictions.

25.6.1 Experimental Setup

The experimental setup is shown in Fig. 25.19. An electromechanical Q -switched (EMQ) CO_2 laser [29] oscillates in the TEM_{00} mode and generates output pulses with maximum peak power 10 kW, width 140 ns, and repetition rate 1 kpps at $\lambda = 10.6 \mu\text{m}$. The laser beam was focused on the slit surface down to a diameter of about $200 \mu\text{m}$ using a ZnSe lens. The slit consisted of two polished copper blocks, and the width was $8.4 \mu\text{m}$. The initial energy W_i of the electron beam was adjusted between 40 and 90 keV. A slot aperture in front of the slit confines the beam area on the slit to $10 \mu\text{m}$ in height and $100 \mu\text{m}$ in width. The electron energy was measured using a retarding field analyzer [30]. This analyzer passes all the higher-energy electrons than the filter bias V_f , which is a variable retarding potential.

The pulsed laser output modulates the energy of the electron beam, so that the electron current through the analyzer varies during the pulse. Electrons passed the energy analyzer were detected by a secondary electron multiplier (collector) connected to a gated counter triggered by the laser pulse.

Fig. 25.19 Experimental setup for measurements of electron–light interaction in the infrared



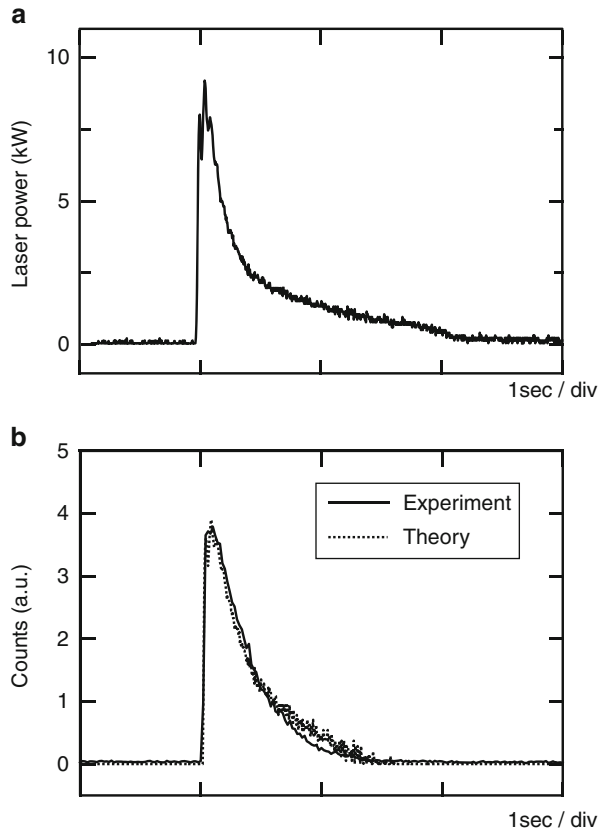
25.6.2 Electron-Energy Spectrum

Figure 25.20 shows the measured temporal variations of (a) the laser pulse and (b) the corresponding response from the gated counter for an electron beam with $W_i = 80$ keV. The collector current i was 2 pA. The output response was measured by the counter in box-car averager mode with temporal resolution 20 ns and integration time 0.5 s. In this experiment, V_f was set to -5.5 V so that the counts in Fig. 25.20 represent the number of electrons gaining energy more than $|qV_f|$ from the laser.

As seen from Fig. 25.20, the shape of the output response is considerably different from that of the laser pulse. The response time of 380 ns in Fig. 25.20b is much longer than the laser pulse width of 140 ns. This output response results from the fact that the number of signal electrons is proportional to the laser field, not to the power. In Fig. 25.20b, the dotted curve is the theoretical response calculated in a computer simulation described in Sect. 25.5. In the calculation, the spatial field distribution on the slit has been taken into account. The calculated counts were normalized to the measured peak value. It is seen that the theoretical curve agrees well with the measurement.

Figure 25.21 shows (a) the measured energy spectra of electrons **A** with and **B** without laser illumination, while (b) shows the difference between the two spectra **A**–**B**. The peak power of the laser was 10 kW and $W_i = 80$ keV. The ordinates are the output counts from the counter with a gate width of $1.5 \mu\text{s}$ and an integration time of 10 s. In Fig. 25.21a, the measured spectrum **B** without laser illumination shows that our energy analyzer has resolution better than 0.8 eV for an 80 keV electron beam. The output count decreases gradually as V_f increases from $+1$ eV, due to the dispersion of the energy analyzer. When the laser beam irradiates the electrons, spectrum **B** becomes spectrum **A**, with a wider energy spread. Spectrum **A** still contains a number of electrons that have not interacted with light. In order to remove these electrons and the dispersion effect from the measured spectrum **A**, the output counts in **B** were subtracted from those in **A**. Figure 25.21b thus indicates the energy spectrum only for electrons that interacted with light. From Fig. 25.21b,

Fig. 25.20 Measured temporal variation of (a) input laser pulse and (b) output response from a gated counter for electrons with $W_i = 80$ keV at $\lambda = 10.6 \mu\text{m}$

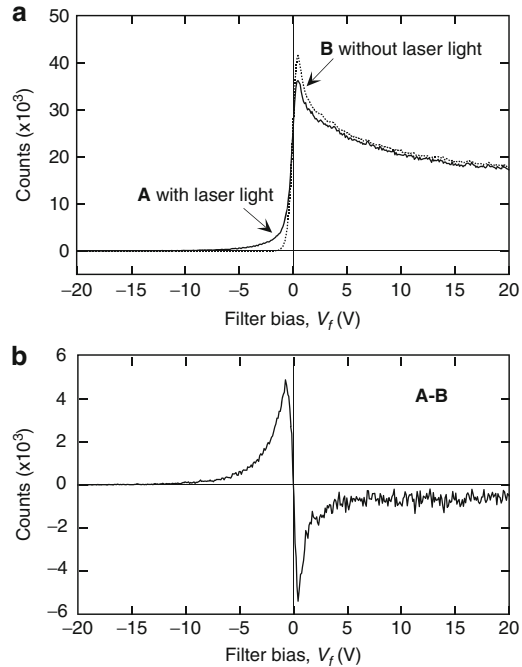


it is seen that the 10-kW laser beam can give an energy spread of more than ± 5 eV to the electrons. The experimental results clearly show that using the metal slit, the energy of the electrons can be modulated with a laser at $\lambda = 10.6 \mu\text{m}$.

Since the energy analyzer passes all higher-energy electrons, it is expected that for large bias voltages, the output counts with laser illumination should be same as without. However, as shown in Fig. 25.21b, the count with laser illumination is slightly less than without, even at $V_f > +10$ V. This might be due to deflection of the electron beam by the laser illumination. Consequently, a part of the electron beam has been clipped by the aperture before the collector.

In Fig. 25.21, about 70,000 electrons have passed on the slit, and about 13,000 electrons among them have interacted with the laser beam. Since the height of the electron beam on the slit is $10 \mu\text{m}$, this ratio of the signal electrons to the total ones implies that the interaction space of the slit is about $2 \mu\text{m}$ which agrees with the theoretical prediction as described in Sect. 25.5.3.

Fig. 25.21 (a) Measured electron-energy spectra **A** and **B**, with and without laser illumination, and (b) the difference between the two spectra **A–B** for an electron beam with initial energy 80 keV



25.6.3 Modulation with Laser Field

In order to accelerate or decelerate electrons with a laser, the laser field must be polarized in the direction of motion of the electrons. Figure 25.22 shows the measured electron-energy spread as a function of the angle θ between the direction of the electron velocity and the laser polarization. The inset defines θ . The electron-energy spreads ΔW are normalized to the maximum value at $\theta = 0$. The experimental parameters used are the same as the ones described in the previous section. The solid curve is the theoretical variation of ΔW given by $\Delta W \propto E_i \cos \theta$, where E_i is the field intensity of the laser beam.

The variation of the maximum energy spread of electrons with the incident laser power has been measured and is plotted in Fig. 25.23. In the experiment, the energy spreads were measured for electrons with $W_i = 80$ keV and a current of 0.5 nA at $V_f < -3$ eV. The solid curve indicates the theoretical variation of the electron energy, which is proportional to the field intensity of the incident wave, that is, the square root of the laser power, as mentioned for the results shown in Fig. 25.20. The theory agrees well with the measurements. The measured electron-energy spread is 13 eV at a laser power of 8.3 kW, which can be compared with the theoretical value of 22 eV predicted via computer simulation. Reduction of the energy spread would arise from differences between the actual slit and the theoretical slit. Since the actual

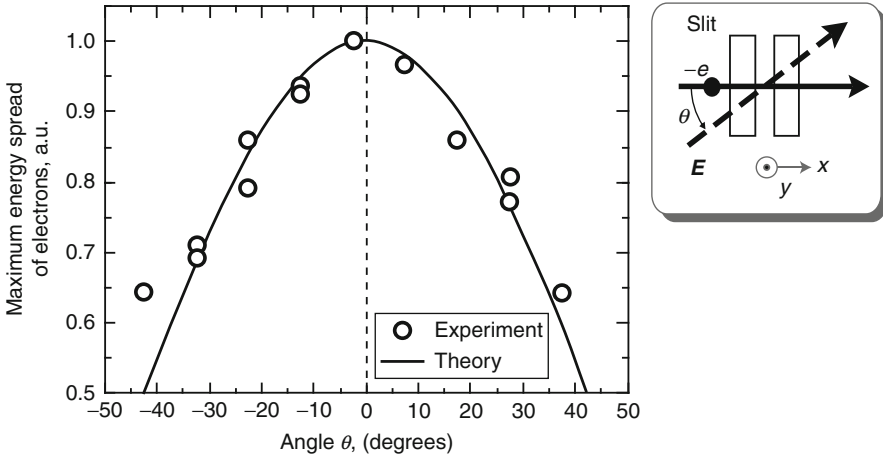


Fig. 25.22 Measured electron-energy spread versus the polarization angle θ of the incident laser beam. The *solid curve* is the theoretically predicted variation with θ . In the inset, E is the electric vector of the laser beam

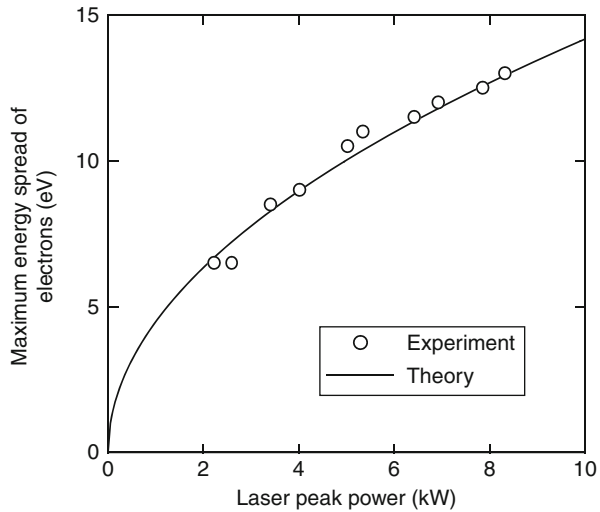
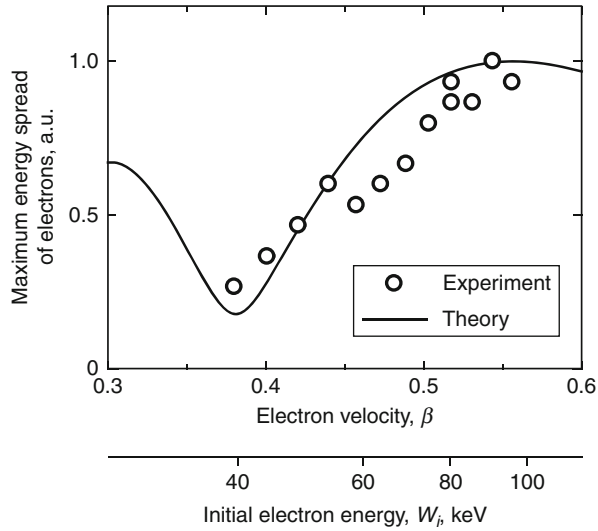


Fig. 25.23 Maximum energy spread of electrons as a function of laser peak power. The *solid curve* is a theoretical fit to the measurements

slit consisted of two thick copper blocks with finite conductance, the amplitude of the evanescent wave can be small compared to the theoretical value. Those experimental results confirm that the measured energy variations of the electrons result from interaction with the laser field.

Fig. 25.24 Maximum energy spread of electrons as a function of initial electron velocity. The *solid curve* indicates theoretical variations in electron energy in a slit of width $7.2 \mu\text{m}$



25.6.4 Wave-Number Spectrum

Figure 25.24 shows the measured electron-energy spread as a function of initial electron energy W_i . In the figure, the electron velocity corresponding to W_i is also indicated. The solid curve is the theoretical variation of the electron energy fitted to the measurements by adjusting the slit width d . The best fit was obtained for $d = 7.2 \mu\text{m}$. The measured and theoretical energy spreads of the electrons have been normalized to the maximum values, 15 eV for the measurements and 34 eV for the theory, respectively, at $W_i = 90 \text{ keV}$. These experimental results confirm the evanescent wave theory for a metal microslit allowing for experimental errors. In Fig. 25.24, the electron-energy spread is 4 eV at $W_i = 40 \text{ keV}$. The small modulation at low W_i can be increased by adjusting the slit width. The results indicate that a metal microslit can be used to modulate a nonrelativistic electron beam at optical frequencies. The results shown in Fig. 25.24 also imply that the k spectrum in an optical near-field on a small object might be measured using an electron beam.

25.7 Multiple-Gap Circuit

Efficient modulation of an electron beam with a laser can be achieved using an array of metal slits instead of a single microslit. In this section, we describe the interaction between electrons and electromagnetic waves in an interaction circuit with a periodic structure, that is, a metallic diffraction grating. Experiments performed in the far infrared have also verified the evanescent wave theory.

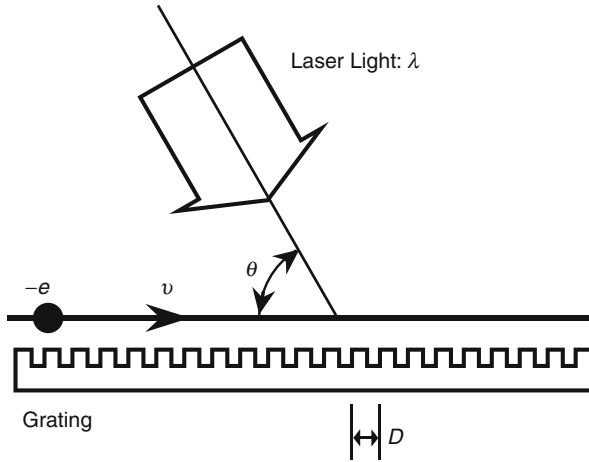


Fig. 25.25 Schematic drawing of the inverse Smith–Purcell effect. D is the period of the grating, d is the gap width, v is the electron velocity, and θ is the incident angle of the laser light

25.7.1 Inverse Smith–Purcell Effect

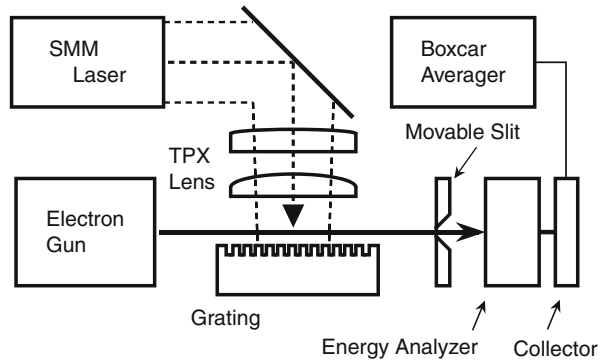
In Sect. 25.6, we described energy variations of electrons induced by an infrared laser in a metal microslit. The maximum energy change with a 10-kW laser beam was about 15 eV. This modulation degree could be raised by using an array of microslits, that is, a diffraction grating. Laser acceleration of electrons using a metal grating is called the inverse Smith–Purcell effect [13].

Figure 25.25 shows the configuration for the inverse Smith–Purcell effect. When a metal grating is illuminated by a laser with wavelength λ , a near-field is induced on the surface of the grating. Electrons passing through the grating with velocity v interact with an evanescent wave in the near-field region, and consequently their energy is modulated at the laser frequency. Similarly to the interaction in the microslit, the evanescent wave in the grating must satisfy the interaction condition, (Eq. 25.10), to interact with the electrons because of energy and momentum conservation. From Fourier optics theory, it is known that the near-field on the grating in the spatial domain transforms to a line spectrum in the k domain. When the incident angle θ of the laser beam is taken into account, the wave numbers k_n in the line spectrum are given by

$$k_n = k_0 \cos \theta + \frac{2n\pi}{D}, \quad (25.21)$$

where n is the number of space harmonics. Substituting k_n for k_e into (Eq. 25.10), we obtain

Fig. 25.26 Experimental setup for measuring the inverse Smith–Purcell effect. The SMM laser is a submillimeter wave laser, and TPX is poly 4 methylpenten-1 which is a low-loss material in the submillimeter wave region



$$\lambda = \frac{D}{n} \left(\frac{1}{\beta} - \cos \theta \right). \quad (25.22)$$

This equation is exactly the same as (Eq. 25.1) in the Smith–Purcell effect in which electrons emit light. This is the reason why the effect shown in Fig. 25.25 is called the inverse Smith–Purcell (ISP) effect.

The relation $k_e = \omega/v$ in (Eq. 25.10) can be written, $v = v_p$, where $v_p (= \omega/k_e)$ is the phase velocity of the evanescent wave. The interaction condition in (Eq. 25.10) and (Eq. 25.22) is thus also called the synchronous condition or the phase-matching condition. The above discussion shows that the basic principle of the interaction is the same for both a metal microslit and a grating. Therefore, the theoretical prediction for the field distributions of evanescent waves described in Sect. 25.5 has been confirmed by measuring the ISP effect in the far infrared [31] and in the infrared [32].

25.7.2 Experimental Setup

Experiments have been carried out using a far-infrared laser at $496 \mu\text{m}$ [33]. Figure 25.26 shows the experimental setup. A submillimeter wave (SMM) gas laser with a longer wavelength provides a wide enough interaction space on the grating to measure the field distribution of the evanescent waves precisely. In Fig. 25.26, the metal grating has gaps with a rectangular cross section, the pitch is $246 \mu\text{m}$, and the gap width and depth are 40 and $104 \mu\text{m}$, respectively. The laser was an optically pumped CH_3F laser [34] which oscillated in the fundamental (TEM_{00}) mode and had the pulsed output with peak power between 1 and 80 W. Two lenses focused the laser beam to the grating surface at $\theta = \pi/2$ (refer to Fig. 25.25). The spot sizes on the surface were calculated to be 1.2 mm for the CH_3F laser on the basis of Gaussian beam theory.

The electron-energy analyzer is the same as the one described in Sect. 25.6.1. The secondary electron multiplier and the gated counter were replaced by a metal

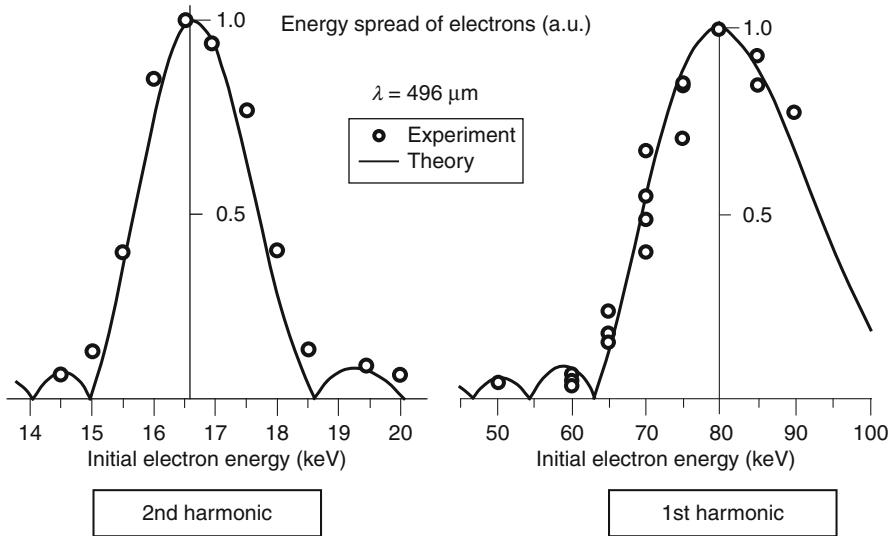


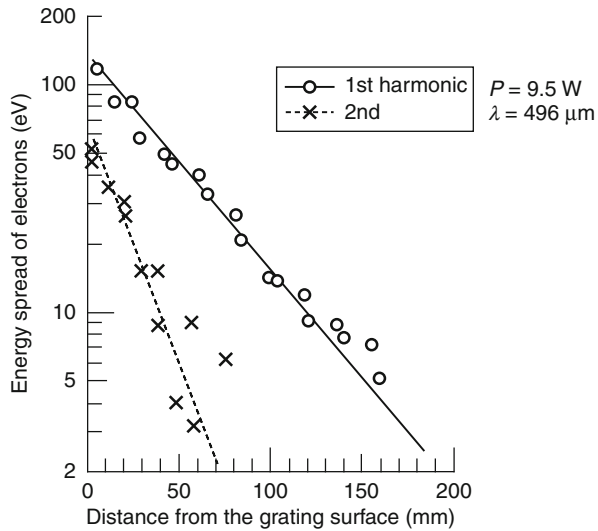
Fig. 25.27 Measured electron-energy spread for the first order and the second order of space harmonics as a function of the initial electron energy. The points represent the experimental values normalized to the maximum values, and the *solid lines* are the theoretically predicted variation in energy spread for an interaction length of 3 mm

plate collector and a boxcar averager because larger numbers of signal electrons were expected in the experiment. A movable slit with a gap of $10\ \mu\text{m}$ was placed at the end of the grating and was used to specify the position of the electron beam above the grating to an accuracy of $\pm 3\ \mu\text{m}$.

25.7.3 Phase-Matching Condition

Figure 25.27 shows the experimental results for the phase-matching condition between the electron velocity and the phase velocity of the evanescent waves in the first and second space harmonics, that is, $n = 1$ and 2 in (Eq. 25.22). The laser power was between 8.3 and 12 W. The ordinate is electron-energy spread normalized to its maximum value. The abscissa is the initial electron energy W_i . As the interaction length between electrons and evanescent waves on the grating is finite, an effective interaction can occur for electrons with a certain range. The largest energy spreads are produced at $W_i = 16.6\ \text{keV}$ for the second harmonic and $80\ \text{keV}$ for the first harmonic, respectively, which can be compared to 16.5 and $77.5\ \text{keV}$ estimated from (Eq. 25.22). By curve fitting, we can deduce that the effective interaction length is 3 mm. Theoretical plots for the length are given by the solid curves in Fig. 25.27 [35]. These experimental results show that the theoretical considerations for the electron–light interaction in the grating is valid, allowing for experimental errors.

Fig. 25.28 Measured energy spread of electrons interacting with the first order and second order of space harmonics as a function of distance from the grating surface. The *solid* and *dotted* lines are the theoretically predicted variations, and P is the incident laser power



25.7.4 Field Distributions

As described in Sect. 25.5.3, the field intensity of the evanescent wave in the microgap is proportional to $\exp(-\alpha y)$, where y is the distance from the grating surface. The decay constant α is given by (Eq. 25.19). Figure 25.28 shows experimental results that show the field decay characteristics of the evanescent waves of the first and second harmonics with the electron beam. In Fig. 25.28, the abscissa is the electron position, which is the position of the movable slit mentioned earlier. The ordinate is the energy spread of the electron beam passing through the slit. The initial electron energy is the center energy shown in Fig. 25.27, that is, 16.6 keV for the second harmonic and 80 keV for the first. The solid lines indicate the theoretically predicted changes, that is, $\exp(-0.022y)$ and $\exp(-0.049y)$ for the first and second harmonics, respectively. The experimental results are in good agreement with theory. The experimental results are a direct verification of the evanescent wave theory for the inverse Smith–Purcell effect and thus for the metal microslit interaction circuit.

25.8 Microslit for Visible Light

Figure 25.29 shows a conceptual drawing of the experimental system for the interaction of electrons with light at shorter wavelengths. A metal microslit is fabricated at the end of an optical fiber so that the laser beam is guided to the slit without requiring precise adjustment. When a laser beam with photon energy greater than 1 eV is used for the interaction, the quantum effects are detectable because the electron-energy analyzer can resolve energy changes in electrons due to photons.

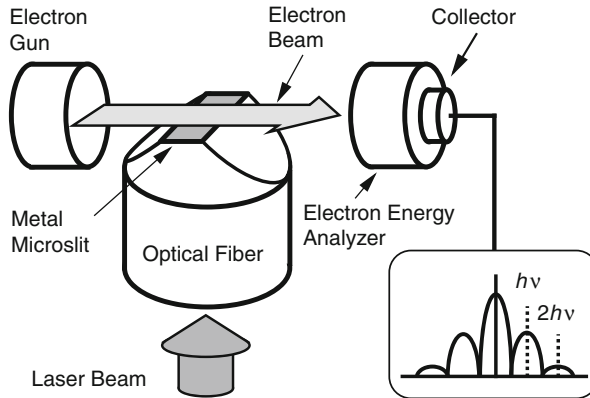


Fig. 25.29 Conceptual drawing of the experimental setup for measurements of the electron–light interaction in near-infrared and visible light regions

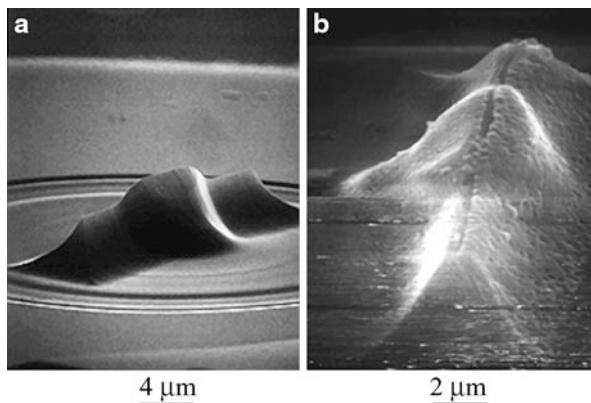
Based on the theoretical and experimental results, the number of signal electrons in the interaction was estimated in both classical and quantum treatments, assuming a laser output power of 30 mW at $\lambda = 780$ nm, and an electron beam with velocity $\beta = 0.5$ and density 1 mA/cm^2 . It was also assumed that the diameter of the laser beam in the fiber was $6 \mu\text{m}$.

Using the classical theory described in Sect. 25.5, the energy variation of the electrons was estimated to be less than 0.2 eV. This is too small to observe the interaction in practical experiments. In order to transfer a detectable energy of 1 eV to the electrons, a laser power of more than 1 W is required.

In contrast to the conclusion in the classical consideration, a different result is derived from a quantum mechanical treatment. Assuming the transition rates in the metal film gap and the microslit are same, a transition rate of about $1 \times 10^{-3}/\text{s}$ was obtained using (Eq. 25.14). From (Eq. 25.18) to (Eq. 25.20), the optimum slit width and interaction space are 490 and 72 nm, respectively. Then 2.7×10^7 electrons per second can pass through the space of $72 \text{ nm} \times 6 \mu\text{m}$ on the slit. The number of signal electrons is thus more than 20,000 particles per second. This number is enough to experimentally demonstrate electron–light interaction. Since the interaction behavior between electron and light in a transition region from classical to quantum regime is still vague, the final conclusion for the above discussions should be based on experimental evidence.

In the experiment in the visible light region, the key device is a metal microslit with submicron width. Figure 25.30 shows a prototype of the microslit fabricated at the center of the core of an optical fiber with $125 \mu\text{m}$ diameter utilizing a chemical etching technique [36]. In Fig. 25.30, (a) is a ridge structure and (b) is the same ridge with aluminum coating and a 270 nm gap at the top. The ridge structure is needed to avoid collision of the electrons with the slit due to the image force. The dimensions of the ridge structure are $5.5 \mu\text{m}$ in length and $7.2 \mu\text{m}$ in height. The

Fig. 25.30 Metal microslit fabricated at the center of the end of a single-mode optical fiber: (a) ridge structure with a taper angle of 80° and (b) metal slit with a width of 270 nm fabricated on the ridge structure



taper angle is 80° . Both the flatness along the length of ridge and the radius of curvature at the top of the ridge are less than 30 nm. Another probe with a 180-nm-width slit was fabricated using gold instead of aluminum as a coating metal. Those metal microslits can be used for measurements of the interaction in the visible light region. The metal microslits with a narrower width could be fabricated in a way similar to how conventional near-field probes with nanometric apertures have been fabricated [37].

25.9 Conclusion

Energy modulation of nonrelativistic electrons with optical near-fields has been discussed. A theory based on Fourier optics has shown that the electrons exchange energy with an evanescent wave contained in the near-field when the phase velocity of the wave is equal to the velocity of the electrons. This interaction condition derived from the evanescent wave theory is also consistent with conservation of energy and momentum in the interaction. A metal microslit has been adopted to generate optical near-fields with laser illumination. For the interaction in the microslit, the relationship among slit width, electron velocity, and wavelength has been found through theoretical analyses based on computer simulation. Those theoretical predictions have been verified experimentally in the infrared. Electron-energy changes of more than ± 5 eV with a 10 kW CO_2 laser pulse at a wavelength of $10.6 \mu\text{m}$ have been observed for an electron beam with an energy of less than 80 keV. From the experimental and theoretical results, it can be concluded that the microslit could be used to investigate physical processes involving in electron–light interaction including its quantum effects in the visible light region. The research results will contribute to developing new types of optical near-field microscopes which measure wave-number distributions in the near-field of a nano-object by using an electron beam.

References

1. S. Okamura, *History of Electron Tubes* (IOS, Washington DC, 1994)
2. C.A. Spindt, I. Brodie, L. Humphrey, E.R. Westerberg, *J. Appl. Phys.* **47**, 5248 (1976)
3. J. Mohr, C. Burbaum, P. Bley, W. Menz, U. Wallrabe, in *Micro System Technologies*, ed. by H. Reichl (Springer, Berlin/Heidelberg/New York, 1990)
4. K. Yokoo, M. Arai, M. Mori, J. Bae, S. Ono, *J. Vac. Sci. Technol. B* **13**, 491 (1995)
5. R.G.E. Hutter, *Beam and Wave Electronics in Microwave Tubes* (D. Van Nostrand, Toronto, 1960)
6. C.A. Brau, Free-electron lasers, in *Advances in Electronics and Electron Phys., Suppl. 22* (Academic, New York, 1990)
7. J. Lecante, Y. Ballu, D.M. Newns, *Phys. Rev. Lett.* **38**, 36 (1977)
8. H. Cohen, T. Maniv, R. Tenne, Y. Rosenfeld Hacoheh, O. Stephan, C. Colliex, *Phys. Rev. Lett.* **80**, 782 (1998)
9. I.R. Senitzky, *Phys. Rev.* **95**, 904 (1954)
10. S.J. Smith, E.M. Purcell, *Phys. Rev. Lett.* **92**, 1069 (1953)
11. P.M. van den Berg, *J. Opt. Soc. Am.* **63**, 1588 (1973)
12. M. Goldstein, J.E. Walsh, M.F. Kimmitt, J. Urata, C.L. Platt, *Appl. Phys. Lett.* **71**, 452 (1997)
13. K. Mizuno, S. Ono, O. Shimoe, *Nature* **253**, 184 (1975)
14. Y. Takeda, I. Matsui, *Nucl. Instrum. Methods* **62**, 306 (1968)
15. R.B. Palmer, *Part. Accel.* **11**, 81 (1980)
16. J.M. Wachtel, *J. Appl. Phys.* **50**, 49 (1979)
17. H. Schwarz, H. Hora, *Appl. Phys. Lett.* **15**, 349 (1969)
18. H. Hora, P.H. Handel, New experiments and theoretical development of the quantum modulation of electrons (Schwarz-Hora Effect), in *Advances in Electronics and Electron Physics*, ed. by P.W. Hawkes (Academic, New York, 1987), pp. 55–113
19. R.H. Pantell, Interaction between electromagnetic fields and electrons, in *AIP Conference Proceedings No. 87, Physics of High Energy Particle Accelerators*, ed. by R.A. Crrigan, F.R. Huson (American Institute of Physics, New York, 1981), pp. 863–918
20. G.A. Massey, *Appl. Opt.* **23**, 658 (1984)
21. K. Mizuno, S. Ono, *Proc. IEEE (Lett.)* **63**, 1075 (1975)
22. J. Bae, S. Okuyama, T. Akizuki, K. Mizuno, *Nucl. Instrum. Methods* **331**, 509 (1993)
23. D. Marcuse, *Engineering Quantum Electrodynamics* (Academic, New York, 1970), pp. 127–142
24. R. Ishikawa, J. Bae, K. Mizuno, *J. Appl. Phys.* **89**, 4065 (2001)
25. T.Y. Chou, A.T. Adams, *IEEE Trans. Electromagn. Compat.* **19** 65 (1977)
26. Y. Leviatan, *J. Appl. Phys.* **60**, 1577 (1986)
27. D.P. Tsai, H.E. Jackson, R.C. Reddick, S.H. Sharp, R.J. Warmack, *Appl. Phys. Lett.* **56**, 1515 (1990)
28. J. Bae, R. Ishikawa, S. Okuyama, T. Miyajima, T. Akizuki, K. Okamoto, K. Mizuno, *Appl. Phys. Lett.* **76**, 2292 (2000)
29. J. Bae, T. Nozokido, H. Shirai, H. Kondo, K. Mizuno, *IEEE J. Q. Electron.* **30**, 887 (1994)
30. J.F. Graczyk, S.C. Moss, *Rev. Sci. Instrum.* **40**, 424 (1969)
31. K. Mizuno, J. Bae, T. Nozokido, K. Furuya, *Nature* **328**, 45 (1987)
32. R. Ishikawa, J. Bae, K. Mizuno, *IEICE Trans. Electron.* **E85-C**, 2086 (2002)
33. J. Bae, H. Shirai, T. Nishida, T. Nozokido, K. Furuya, K. Mizuno, *Appl. Phys. Lett.* **61**, 870 (1992)
34. M.S. Tobin, *Proc. IEEE* **73**, 61 (1985)
35. J. Bae, K. Furuya, H. Shira, T. Nozokido, K. Mizuno, *Jpn. J. Appl. Phys.* **27**, 408 (1988)
36. J. Bae, T. Okamoto, T. Fujii, K. Mizuno, *Appl. Phys. Lett.* **71**, 3581 (1997)
37. M. Ohtsu, *J. Lightwave Tech.* **13**, 1200 (1995)

Haruhiko Ito

Contents

26.1	Introduction.....	978
26.2	Atom Deflection.....	980
26.2.1	Slit-Type Deflector.....	981
26.2.2	Fabrication.....	982
26.2.3	Intensity Distribution.....	984
26.2.4	Deflection Angle.....	985
26.2.5	Experiment.....	987
26.2.6	Cross Section.....	989
26.3	Atom Detection.....	992
26.3.1	Slit-Type Detector.....	993
26.3.2	Fabrication.....	994
26.3.3	Simulations.....	995
26.3.4	Suppression of Scattering Light.....	997
26.3.5	Ionization Efficiency.....	999
26.4	Nano-slit with Rounded Edges.....	1000
26.4.1	FDTD Simulations.....	1000
26.4.2	Intensity Profile.....	1002
26.4.3	Photoionization Efficiency.....	1004
26.4.4	Throughput.....	1005
26.5	Two-Step Photoionization with Two-Color Evanescent Lights.....	1006
26.5.1	Approach.....	1007
26.5.2	Experiment.....	1008
26.5.3	Ionization Cross Section.....	1010
26.6	Blue-Fluorescence Spectroscopy with Two-Color Evanescent Lights.....	1011
26.6.1	Approach.....	1011
26.6.2	Experiment.....	1012
26.6.3	Detection Efficiency.....	1013
	References.....	1014

H. Ito (✉)

Department of Electronics and Applied Physics, Interdisciplinary Graduate School of Science and Engineering, Tokyo Institute of Technology, Kanagawa, Japan
e-mail: Ito@ep.titech.ac.jp

Abstract

An atom deflector and detector operating with local selective interaction are illustrated from both experiments and computations, including their fabrication. The feature of a nano-slit is examined in detail by conducting finite-difference time-domain simulations. Two ways of detecting atoms with two-color evanescent lights are also demonstrated for Rb atoms.

26.1 Introduction

Manipulating atoms with freedom has been one of scientist's dreams for a long time. From a historical perspective, atoms have been utilized as a touchstone of whether quantum mechanics is correct or not. In metrology, 1 s was defined in relation to the frequency of transition between two hyperfine ground states of ^{133}Cs . Atomic clocks [1] with Sr and Yb are developed for accuracy enhancement these days. Meanwhile, researchers are trying to apply atoms to sub-nanoscale engineering and quantum information processing [2]. The advantage of using gaseous atoms is that they are interaction-free with each other and the treatment of the system is relatively easy. However, such atoms move about actively with high speed in vacuum. The thermal motion at random formed a barrier against high-resolution laser spectroscopy. For example, some important signals are hidden away in Doppler-broadened spectra. Consequently, it is a critical issue to control the atomic motion.

The only way of controlling neutral free atoms is to employ interaction with light. When laser light is tuned to an atomic transition, it exerts resonant mechanical forces on atoms [3]. It was demonstrated that the forces change the direction of atomic motion or take kinetic energy away from gaseous atoms [4–8]. To date, magneto-optical trap (MOT) [9, 10] is a standard technique to create cold atoms. In the mechanism, atoms are decelerated by mutually orthogonal three pairs of opposed $\sigma^+ - \sigma^-$ circularly polarized light beams and trapped at the center where the six light beams cross by modulating the atomic Zeeman sublevels with anti-Helmholtz coils. The mean temperature of the captured atoms drops to several μK when polarization gradient cooling (PGC) [11, 12] is performed.

The laser-cooling techniques have been applied to nonlinear spectroscopy [13], optical lattice [14], ultracold collisions [15–17], atomic fountain [18], atom interferometry [19, 20], atom holography [21, 22], quantum chaos [23], and so forth. The highlight was the realization of Bose-Einstein condensation (BEC) of alkali-metal atoms [24–26]. To this end, atoms were cooled further down to the order of 10 nK by evaporative cooling and put in a tricky magnetic trap. Then, many theoretical and experimental studies on the relevant topics have been promoted. A coherent output of atomic waves from BEC was also observed, which was called atom laser [25–27].

The mechanical forces of light on atoms are approximately divided into two parts. One is a spontaneous force induced by photon absorption followed by random

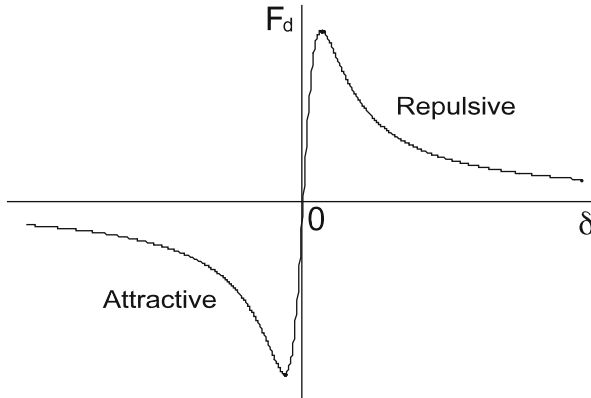


Fig. 26.1 Dipole force F_d plotted as a function of the frequency detuning δ . It is repulsive for $\delta > 0$ (blue detuning), while attractive for $\delta < 0$ (red detuning)

photon scattering in resonance. For a two-level atom with an electric dipole moment μ , the spontaneous force F_{sp} is given by [28]

$$F_{\text{sp}} = \hbar \gamma k \frac{\Omega^2}{4\delta^2 + \gamma^2 + 2\Omega^2}, \quad (26.1)$$

where \hbar is Planck constant, γ is the natural linewidth, k is the wave number vector, $\Omega = \mu E / \hbar$ with an electric field amplitude E is the Rabi frequency, and $\delta = \omega_L - \omega_0$ is the detuning of the light frequency ω_L from the atomic resonant frequency ω_0 . The spontaneous force acts in the direction of light propagation, namely, in the direction of the wave number vector k , and dissipates atomic kinetic energy. For an atom moving with a velocity v , the frequency detuning δ is replaced by $\Delta = \omega_L - \omega_0 - k \cdot v$ including a Doppler shift $k \cdot v$. The spontaneous force depending on the atomic velocity is used for Doppler cooling in MOT [12].

The other is a dipole force, which is also called a gradient force. For a two-level atom, the dipole force F_d is given by [28]

$$F_d = -\frac{\hbar \delta \nabla \Omega^2}{4\delta^2 + \gamma^2 + 2\Omega^2}. \quad (26.2)$$

As shown in Fig. 26.1, the dipole force has a dispersion character. When the light frequency is higher than an atomic resonant frequency, the dipole force acts in the direction where the light intensity decreases. In the contrary case, it acts in the direction where the light intensity increases. That is, the dipole force is repulsive when $\delta > 0$ (blue detuning), while attractive when $\delta < 0$ (red detuning). The dipole force is used as a mirror, a splitter, and a grating for atomic beams [29, 30]. Guiding of atoms with hollow optical fibers was proposed [31–34] and then demonstrated [35–37]. In the atom guiding, blue-detuned evanescent light

is generated around the inner-wall surface of the hollow core. Some different kinds of atom guiding are introduced in Ref. [38, 39].

The research field dealing with resonant interaction between light and atoms is called atom optics. Atom manipulation using laser light is discussed in Ref. [40]. One of the fascinating applications of atom optics is nanofabrication. Indeed, by focusing an atomic beam by means of atom-optical methods, minute lines and arrays with each individual width of 10-nm order were produced [41–48]. Atom lithography was also performed [49, 50]. However, the conventional methods using propagative light have limited spatial accuracy of atom control due to the diffraction limit, which is about half the wavelength of light used. The broadened light field cannot locate atoms well. It is generally difficult to make arbitrary shapes by propagative-light techniques. To our knowledge, dots have not been made using pure atom-optical methods.

The use of near-field light that is not affected by diffraction like propagative light allows us to overcome the diffraction limit. Such near-field light is generated, for example, at the nanometric aperture of a sharpened fiber probe [51]. It should be recalled that the dipole force is proportional to the spatial gradient of the light intensity as shown in Eq. (26.2). The near-field light that decays as a Yukawa-type function [52, 53], therefore, exerts a strong dipole force on atoms. Thus, it is expected to precisely control atomic motion by the dipole force from nanometric near-field light.

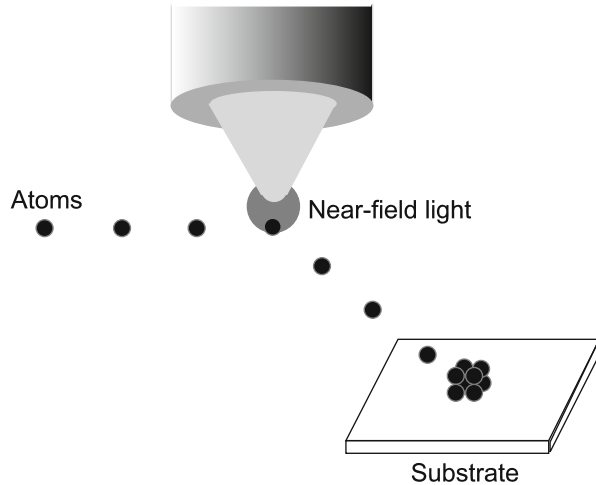
First, a slit-type atom deflector to control the direction of atomic motion is described in Sect. 26.2. After showing the fabrication process, experiments of measuring the light-intensity distribution at an edge of the slit with scanning near-field microscope are mentioned. The deflection angle for laser-cooled Rb atoms is numerically estimated as a function of the frequency detuning and the light intensity. Then, demonstration experiments of deflecting Rb atoms is presented, where the deflected atoms are detected by two-step photoionization. The influence of the finite extent of the cold atomic source viewed from the narrow slit is considered. Second, a slit-type atom detector with high spatial resolution is introduced in Sect. 26.3, where two-step photoionization with two-color near-field lights is employed. After showing the fabrication process, finite-difference time-domain (FDTD) simulations are performed by examining the intensity distribution as well as suppression of scattering light. The ionization efficiency for Rb atoms is numerically estimated as a function of the atomic velocity. In Sect. 26.4, the characteristics of rounded edges of the nano-slit is discussed in detail based on FDTD simulations. The last two sections deal with experiments of detecting atoms with two-color evanescent lights. Two-step photoionization and blue-fluorescence spectroscopy come up in Sects. 26.5 and 26.6, respectively.

26.2 Atom Deflection

The means of changing the direction of atomic motion by near-field light generated at the tip of a fiber probe is proposed [54, 55], and then the feasibility is theoretically examined [56, 57]. The deflection technique is expected to be used

Fig. 26.2

Optically-controlled atom-by-atom deposition with a fiber probe. Atoms are deflected by a repulsive dipole force from blue-detuned near-field light and sent to the aimed location on a substrate. The deflection angle is controlled by the frequency detuning and the light intensity



for nanofabrication including atom-by-atom deposition. Figure 26.2 schematically shows an optically controlled atom deposition on a substrate. The repulsive dipole force deflects atoms passing through blue-detuned near-field light. The deflection angle can be controlled by changing the blue detuning and the light intensity. Accordingly, atoms are sent to certain position on the substrate. By choosing the resonant frequency, a specific atomic species is selectively deposited [58]. The atom deflection can be also applied to nondemolition measurement of near-field light. This will deepen our understanding of microscopic and mesoscopic interactions between atoms and near-field light.

A small number of atoms are involved in the deflection using near-field light and it is a tough task to detect the deflected atoms. Therefore, in order to facilitate the detection, a slit-type deflector is introduced. This section presents the atom deflection with blue-detuned near-field light generated at a nano-slit. The fabrication process of the nano-slit is first shown followed by the experiment of measuring the intensity profile of the near-field light. The deflection angle is estimated based on the results. Then, the demonstration experiment with cold Rb atoms is described.

26.2.1 Slit-Type Deflector

A pyramidal silicon probe is developed for high-density and high-speed recording/reading by near-field light [59]. It has a small aperture at the apex and efficiently generates nanometric near-field light with high throughput, which is defined as the conversion ratio from far-field light to near-field light. So, the slit structure is designed as a deflector element by considering the advantage of the pyramidal probe.

Figure 26.3 illustrates the atom deflection with the slit-type deflector under blue-detuning conditions [60, 61]. A triangle-pole part to introduce a light beam is made on one side of the slit. Since near-field light generated along an edge of the nano-slit

Fig. 26.3 Sketch of a slit-type atom deflector fabricated from an SOI substrate. Only atoms entering the slit are deflected by the repulsive near-field light generated at an edge of the slit. Al-metal coating is made for suppression of scattering light

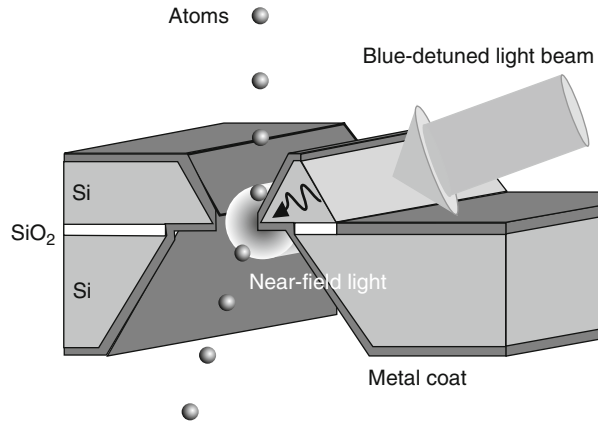
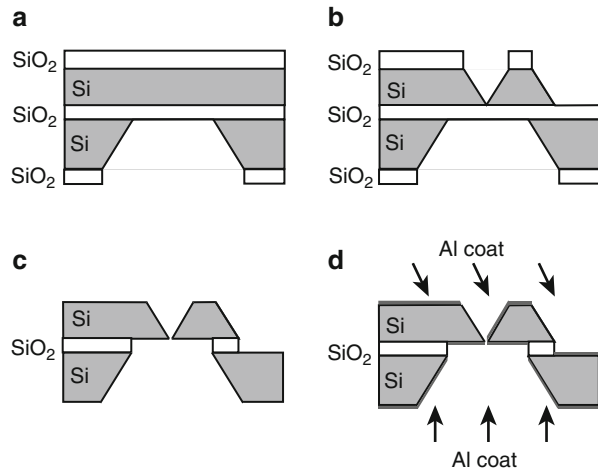


Fig. 26.4 Fabrication process of the slit-type deflector. (a) The midportion of the under surface is removed by photolithography and anisotropic etching. (b) A V-shaped groove is formed on the upper surface, and an incidence plane for excitation light is made to the right. (c) The bare SiO₂ layers are removed. (d) Al coating is conducted from the direction indicated by arrows

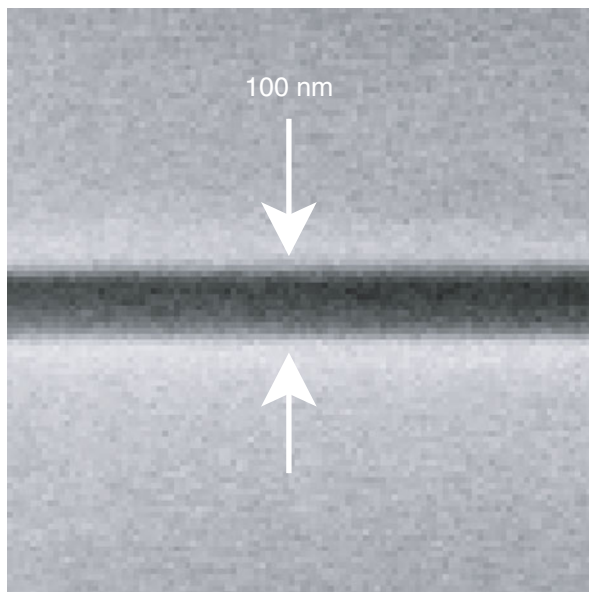


by irradiating the back side with a light beam deflects considerable atoms passing through the nano-slit at once, the number of deflected atoms is increased by making the slit longer. Atoms not entering the near-field light are blocked by the V-shaped groove in front of the slit, so that only deflected atoms leave the deflector. For suppression of scattering light, Al metal is coated. Thus, the slit-type deflector is suitable for the demonstration of precisely controlling the direction of atomic motion with near-field light.

26.2.2 Fabrication

A 100-nm-wide and 100- μm -long slit is made by fabricating a (100)-oriented silicon on insulator (SOI) substrate composed of two Si and three SiO₂ layers with photolithography and anisotropic chemical etching. Figure 26.4 shows the process.

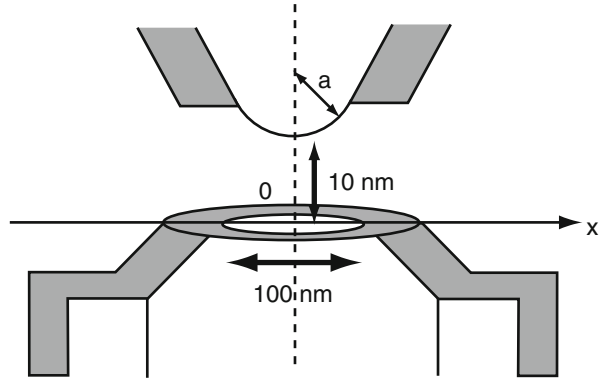
Fig. 26.5 SEM image of a 100-nm-wide slit. The total length is 100 μm



1. The central part of the underside where atoms go out is removed by photolithography and anisotropic chemical etching with a 34-wt% KOH solution at a temperature of 80 °C (Fig. 26.4a).
2. A V-shaped groove on the (111) face is formed on the upper side where atoms come into by photolithography and KOH etching. The groove is 10 μm deep, and the length and the apex angle of the slope are 14 μm and 54.8°, respectively. Then, a slant face exposed to light is made on the right-hand side by photolithography and KOH etching (Fig. 26.4b).
3. The surface SiO_2 is removed by etching with a buffered-hydrofluoric acid. The residual Si substructure on the underside provides support for the slit element (Fig. 26.4c).
4. Coating of Al is applied by vacuum deposition on both sides of the structure. The metal coating curbs the generation of far-field light. As shown by arrows, the directional deposition is adopted in such a way as to leave the light-entrance face and the fourchee tip uncoated. In order to generate near-field light with the localization length equal to the slit width, the radius of curvature of the slit edge and the thickness of Al coating are adjusted to 50 and 40 nm, respectively (Fig. 26.4d).

Figure 26.5 shows a SEM image of the fabricated slit. The width and length of the slit are 100 nm and 100 μm , respectively. In the case where a Rb atom enters, the displacement from the incident axis is estimated to exceed 10 μm under realistic conditions [62]. If a smaller or shorter slit is needed, the slit width and length are changed by controlling the etching time. On this occasion, the dimension of the slit is determined to correspond with that of a slit-type

Fig. 26.6 Measurement of the light-intensity distribution near the slit edge with a 100-nm-apertured fiber probe. The scanning is performed along the x -axis at 10 nm below the edge with the radius of curvature a



atom detector mentioned in Sect. 26.3. When used in combination, the deflected atoms can be detected with the spatial uncertainty of less than 1% and the efficiency of more than 10% [63]. The spatial resolution of detecting atoms is comparable to the slit width, while the detection efficiency is proportional to the slit length.

26.2.3 Intensity Distribution

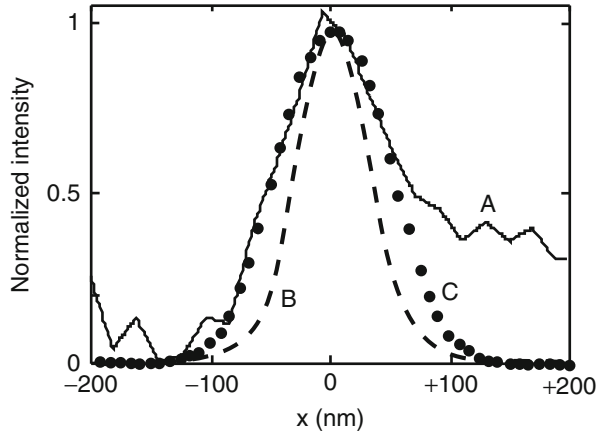
The spatial distribution of light generated at the edge of the slit is obtained from scanning near-field optical microscopy. Figure 26.6 shows the experimental setup with a 100-nm-apertured fiber probe. The origin of the x -axis denoting the scanning direction is taken at 10 nm below from the tip. Hereafter, for simplicity, the uncoated tip of the slit is assumed to be approximately hemicylindrical with the radius of curvature a .

The solid curve A in Fig. 26.7 shows the light-intensity profile produced by a light beam with the wavelength of 780 nm, which is the transition wavelength of the Rb D₂ line, a power of 1 mW, and a spot diameter of 10 μm. Here, the light beam is polarized perpendicularly to the longitudinal direction of the slit, since there is no cutoff and near-field light is efficiently generated [64]. In the measurement, the other side of the slit where near-field light is not generated is removed to facilitate scanning of the fiber probe. The decay length of the near-field light component is estimated to be 180 nm. It should be noted that the value convolutes the size of the aperture. Incidentally, a propagative-light component appears from a distance of at least 90 nm.

The numerical curves B and C representing the intensity profile $I_{\text{nf}}(\mathbf{R})$ are calculated with the phenomenological formula [52]:

$$I_{\text{nf}}(\mathbf{R}) = I_{\text{nf}}(\mathbf{0}) \frac{H(\mathbf{R})}{H(\mathbf{0})}, \quad (26.3)$$

Fig. 26.7 The solid curve *A* shows the light-intensity profile experimentally obtained by using a light beam with the wavelength of 780 nm. The broken curve *B* shows the numerical result obtained in the case where the aperture size is not convoluted, while the dotted curve *C* shows that obtained in the case where the aperture size is convoluted. In the curve *A*, a far-field component arises +90 nm away



where the Hamiltonian density $H(\mathbf{R})$ is written as

$$H(\mathbf{R}) = |\nabla\Psi(\mathbf{R})|^2 + \frac{1}{\Lambda^2}|\Psi(\mathbf{R})|^2, \quad (26.4)$$

and the Yukawa-type function $\Psi(\mathbf{R})$ is given by

$$\Psi(\mathbf{R}) = \iint \frac{\exp(-|\mathbf{R} - \mathbf{R}'|/\Lambda)}{|\mathbf{R} - \mathbf{R}'|} dS. \quad (26.5)$$

The coordinate vectors \mathbf{R} and \mathbf{R}' indicate the measurement point on the aperture of the probe and the source point on the slit edge, respectively. The origin is at the top. The surface integral is performed over the area $\pi a \times L$, where L is the spot diameter of the incident light beam. In the calculations, the decay length is taken as $\Lambda = a = 50$ nm. The effective distribution length that is defined as the full width at the e^{-2} maximum is estimated to be 126 nm from the broken curve *B*. Moreover, the dotted curve *C* comes out of the integral

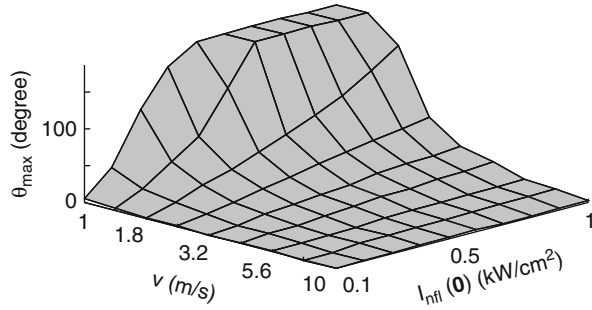
$$I_{\text{nf}} = \iint I_{\text{nf}}(\mathbf{R}) dS \quad (26.6)$$

over the aperture area of $\pi \times 50^2$ nm². It closely matches the experimental result *A* and the effective distribution length is estimated to be 180 nm as mentioned above.

26.2.4 Deflection Angle

The deflection angle θ of a ballistic atom is given by [65]

Fig. 26.8 Maximal deflection angle θ_{\max} of a Rb atom plotted as a function of the atomic velocity v and the near-field light intensity $I_{\text{nf}}(\mathbf{0})$ for the frequency detuning $\delta/2\pi = +1$ GHz. The atomic velocity is log-plotted



$$\theta = \pi - 2b \int_{r_t}^{\infty} \frac{dr}{r^2} \left(1 - \frac{b^2}{r^2} - \frac{U_{\text{tot}}(r)}{K_a} \right)^{-1/2}, \quad (26.7)$$

where b , r_t , and K_a are the impact parameter, the turning point, and the atomic kinetic energy, respectively. The distance r is measured from the center of the hemicylindrical slit edge. The total potential $U_{\text{tot}}(r)$ consists of the repulsive dipole-force potential $U_{\text{dip}}(r)$ written as [28, 38]

$$U_{\text{dip}}(r) = \frac{1}{2} \hbar \delta \ln \left(1 + \frac{I(r)}{I_s} \frac{\gamma^2}{4\delta^2 + \gamma^2} \right) \quad (26.8)$$

and the attractive van der Waals potential $U_{\text{vdw}}(r)$ written as [66–68]

$$U_{\text{vdw}}(r) = -\frac{1}{16(r-a)^3} \sum_j \frac{\hbar \gamma_j n_j^2 - 1}{k_j^3 n_j^2 + 1}. \quad (26.9)$$

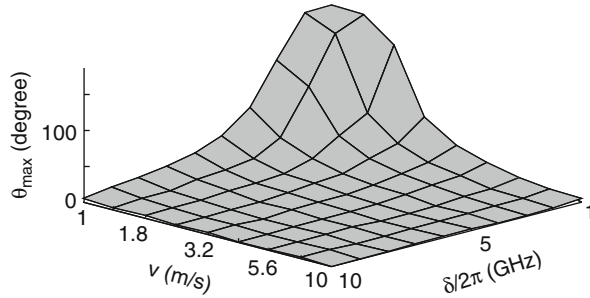
The natural linewidth γ and the saturation intensity I_s are $2\pi \times 6.1$ MHz and 1.6 mW/cm² for the Rb D₂ line, respectively. The van der Waals potential is summed over the allowed dipole transitions labeled with j . Each natural linewidth and wave number are γ_j and k_j , respectively. The refractive index n_j of the slit edge is 3.7 for the Rb D₂ line.

Figure 26.8 shows the maximal deflection angle θ_{\max} plotted as a function of the atomic velocity v and the near-field light intensity $I_{\text{nf}}(\mathbf{0})$, where the atomic velocity is log-plotted. For the sake of avoiding troublesome calculations, the approximate expression

$$I_{\text{nf}}(r) \simeq I_{\text{nf}}(\mathbf{0}) \exp \left[-\frac{(r-a)}{1.6 \times 10^{-8}} \right], \quad (26.10)$$

which is obtained from the curve B in Fig. 26.7, with $\delta = +2\pi \times 1$ GHz, is used in place of the exact Yukawa-type function. Since the throughput is about 0.01, the intensity of the near-field light changes from 0.1 to 1 kW/cm² as the power of the incident light changes from 1 to 10 mW. Slow atoms with a velocity of

Fig. 26.9 Maximal deflection angle θ_{\max} of a Rb atom plotted as a function of the atomic velocity v and the frequency detuning $\delta/2\pi$ for the near-field light intensity $I_{\text{nf}}(\mathbf{0}) = 10^3 \text{ W/cm}^2$. The atomic velocity is log-plotted



less than 10 m/s can be easily created by MOT. Such cold atoms are required for efficient interaction with nanometric near-field light. The maximal deflection angle θ_{\max} increases in proportion to the intensity $I_{\text{nf}}(\mathbf{0})$ but in inverse proportion to the atomic velocity v . When $I_{\text{nf}}(\mathbf{0}) = 0.5 \text{ kW/cm}^2$, a Rb atom with $v = 1 \text{ m/s}$ is retro-reflected.

Meanwhile, Fig. 26.9 shows the maximal deflection angle θ_{\max} plotted as a function of the atomic velocity v and the frequency detuning $\delta/2\pi$ for $I_{\text{nf}}(\mathbf{0}) = 1 \text{ kW/cm}^2$. When $v = 1 \text{ m/s}$, the maximal deflection angle θ_{\max} increases from 5.3° to 180° as the frequency detuning changes from +10 to +1 GHz.

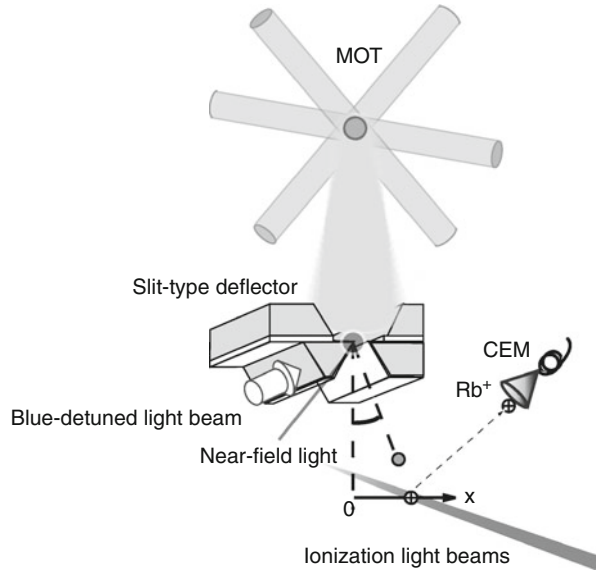
26.2.5 Experiment

The first demonstration is conducted with cold ^{87}Rb atoms. Figure 26.10 shows the experimental setup incorporated a slit-type deflector with the slit width of 200 nm and the slit length of $30 \mu\text{m}$. The radius of curvature of each edge is approximately 50 nm. The 50-nm-thick Au coating is also made by shadow evaporation in order to avoid the emission of far-field components.

Near-field light is generated along an edge of the slit by illuminating a $35\text{-}\mu\text{m}$ -wide incidence plane with a $7\text{-}\mu\text{m}$ -waist Ti-sapphire laser beam polarized perpendicularly to the longitudinal direction of the slit. The HWHM of the light-intensity profile is estimated to be $85 \pm 10 \text{ nm}$ by scanning with the fiber probe at 10 nm below the edge. Here, the error comes from the uncertainty of the aperture diameter of the fiber probe. The HWHM value is comparable to the decay length of the near-field light. Given the throughput of 1.0×10^{-3} , the intensity $I(a)$ of the near-field light on the surface of the edge is evaluated to be $2.9 \times 10^6 \text{ mW/cm}^2$ when the power of the incident light is 5.0 mW.

Double magneto-optical traps [69] are employed for manipulating a small number of atoms in ultrahigh vacuum. Cold ^{87}Rb atoms are created by the first MOT under a pressure of 10^{-7} Pa . Then, they are sent down to the second MOT 26 cm below and recaptured under a lower pressure of 10^{-8} Pa . Here, 1.0×10^9 ^{87}Rb atoms with 6 mm in diameter and a mean temperature $T = 16 \mu\text{K}$ are introduced

Fig. 26.10 Experimental configuration. Cold ^{87}Rb atoms created by MOT are introduced into the slit-type deflector 9 mm below, while near-field light is generated at an edge of the slit by irradiation of a blue-detuned light beam. The cold atoms passing through the slit are deflected by a repulsive dipole force and ionized by means of two-step photoionization with a 780.2-nm diode-laser beam and a 476.5-nm Ar-ion laser beam at 2 mm below, followed by detection with CEM



into the slit-type deflector $h = 9$ mm below by turning off the second MOT. The incident flux intensity of $8.7 \pm 1.1 \times 10^{10}$ atoms/cm²s is obtained from a time-of-flight measurement [70], and the number of atoms entering the slit is about 70 a trial run. The other atoms not entering the slit are blocked by the V-groove structure. The most probable speed v_{mp} of the incident atoms is 46 cm/s in front of the slit from the expression

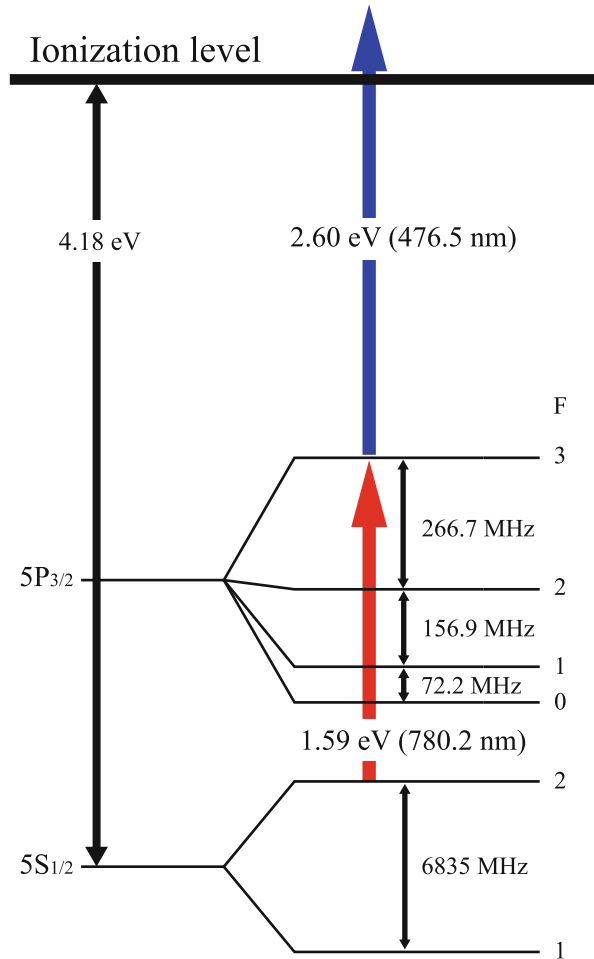
$$v_{\text{mp}} = \sqrt{\frac{2k_{\text{B}}T}{m} + 2gh} \quad (26.11)$$

with the atomic mass m , Boltzmann constant k_{B} , and gravitational acceleration g .

The displacement of the output ^{87}Rb atoms is measured by two-step photoionization with a 780.2-nm diode-laser beam and a 476.5-nm Ar-ion laser beam [61, 62]. Figure 26.11 shows the relevant energy levels of ^{87}Rb . The diode-laser beam with 10 μW first excites the ^{87}Rb atoms in the $5S_{1/2}$, $F = 2$ upper ground state of the hyperfine energy levels to the $5P_{3/2}$, $F = 3$ state, and then the Ar-ion laser beam with 3 W lifts up them to the ionization level at 4.18 eV above the $5S_{1/2}$ ground state [63]. The two laser beams are overlapped at 2 mm below the deflector and scanned along the horizontal x -axis. The waists of the diode-laser beam and the Ar-ion laser beam are 100 and 70 μm , respectively. In this case, the ionization efficiency is 34%. The ionized ^{87}Rb atoms are counted by a channel electron multiplier (CEM) negatively biased with the voltage of -3 kV. The effective detection efficiency is estimated to be 30% including the quantum efficiency of 0.9.

Figure 26.12 shows the spatial profile of the deflected ^{87}Rb atoms plotted as a function of the deflection angle θ . Here, the number of atoms is the integrated value after 500-times MOT loading. The circles indicate the results obtained for the blue

Fig. 26.11 Relevant energy levels of ^{87}Rb in two-step photoionization. A *red arrow* indicates resonance transition as the first step, and a *blue arrow* indicates ionization as the second step. The ionization level is at 4.18 eV above the $5S_{1/2}$ ground state

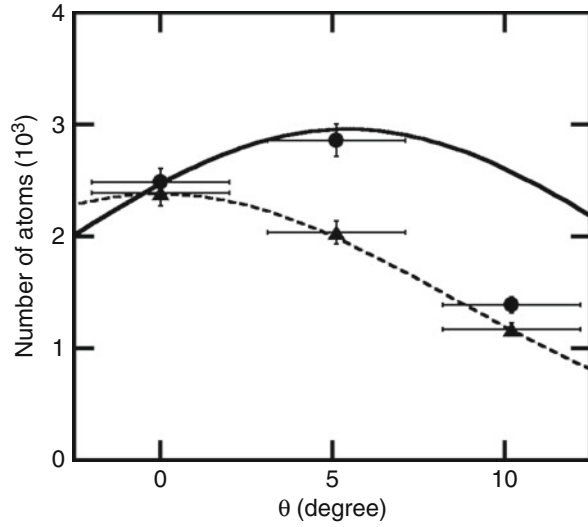


detuning of $\delta = 2\pi \times (+1)$ GHz. The uncertainty of number count comes from the error of incident atom flux in the time-of-flight measurement, which is $\pm 5\%$. Each horizontal error bar represents the spatial resolution of $140\ \mu\text{m}$, that is, the diameter of the Ar-ion-laser beam. It results in the uncertainty of $\pm 2.0^\circ$ in angle. Compared to the values in the case of not generating near-field light indicated by the triangles, the number of atoms increases by amount of $40 \pm 7.2\%$ at $\theta = 5.1 \pm 2.0^\circ$ due to deflection.

26.2.6 Cross Section

The spatial profile reflects the scattering cross section. Under the first Born approximation [65], the differential cross section $\sigma(\theta)$ is given by

Fig. 26.12 Number of ^{87}Rb atoms at 2 mm below the slit plotted as a function of the deflection angle θ . The circles indicate the case of $\delta = 2\pi \times (+1)$ GHz, while the triangles indicate the case without near-field light. The solid curve shows the theoretical profile, folded the effective angle 12° of the atomic source viewing from the slit. It is normalized to the number of atoms experimentally obtained at $\theta = 0$. The broken curve shows a Gaussian function $\exp(-l \tan^2 \theta / w^2)$ with $l = 2$ mm and $w = 0.43$ mm



$$\sigma(\theta) \simeq \frac{m^2}{4\pi^2 \hbar^4} \left| \iiint U_{\text{tot}}(r') \exp(i\mathbf{q} \cdot \mathbf{r}') d^3 r' \right|^2, \quad (26.12)$$

where the momentum transfer $|\mathbf{q}| = q = 2(mv/\hbar) \sin(\theta/2)$ with the atomic velocity v . In the cylindrical coordinate system (r', θ', z') , the cross section is expressed as

$$\sigma(\theta) \simeq \frac{m^2}{\hbar^4} \left| \int_0^\infty r' dr' \int_{-L/2}^{L/2} dz' U_{\text{tot}}(r', z') J_0(qr') \right|^2, \quad (26.13)$$

where $J_0(qr')$ is the 0-th order Bessel function of the first kind and L is the slit length. The z' -axis is taken in the direction of the longitudinal length of the slit. The total potential $U_{\text{tot}}(r', z')$ is the sum of the repulsive dipole-force potential $U_{\text{dip}}(r', z') = U_{\text{dip}}(r') \exp(-z'^2/W^2)$ and the attractive van-der-Waals-force potential $U_{\text{vdw}}(r')$ given by [66]

$$U_{\text{vdw}}(r') = -\frac{1}{16(r' - a)^3} \sum_j \frac{\hbar \gamma_j}{k_j^3} \frac{n_j^2 - 1}{n_j^2 + 1}, \quad (26.14)$$

where W is the waist of the incident light beam and n_j is the refractive index. The summation is made over the allowed dipole transitions with the natural linewidth γ_j and the wave number k_j .

The atomic cloud generated by the second MOT has a diameter $2d = 6$ mm. In this situation, the inclination angle of the atomic source viewed from the

200-nm-wide slit 9 mm below is approximately $(d/h) \times (360/2\pi) = 19^\circ$, neglecting gravitational acceleration. Consequently, the atomic distribution broadens out to $(d/h) \times l = 0.67$ mm at $l = 2$ mm below the slit.

The spatial profile in the case without near-field light directly reflects the broadening due to the source-size effect. Fitting of the experimental data with a Gaussian function $\exp(-y^2/w^2)$ results in $w = 0.43$ mm at the e^{-1} maximum. It is comparable to the above rough estimation. In fact, since atoms are accelerated by gravity, most of atoms coming from the rim of the atomic cloud do not enter the slit. From the experimental result, the effective broadening angle θ_b is estimated to be $(w/l) \times (360/2\pi) = 12^\circ$.

Given the broadening, the spatial profile of the deflected atoms is expressed as

$$N(\theta) \simeq \frac{N_0}{\sigma_0} \int_{-\theta_b}^{+\theta_b} \sigma(\Theta) \exp\left[-\frac{(\theta - \Theta)^2}{\theta_b^2}\right] d\Theta, \quad (26.15)$$

where N_0 is the number of atoms at $\theta = 0$ and

$$\sigma_0 = \int_{-\theta_b}^{+\theta_b} \sigma(\Theta) \exp\left(-\frac{\Theta^2}{\theta_b^2}\right) d\Theta. \quad (26.16)$$

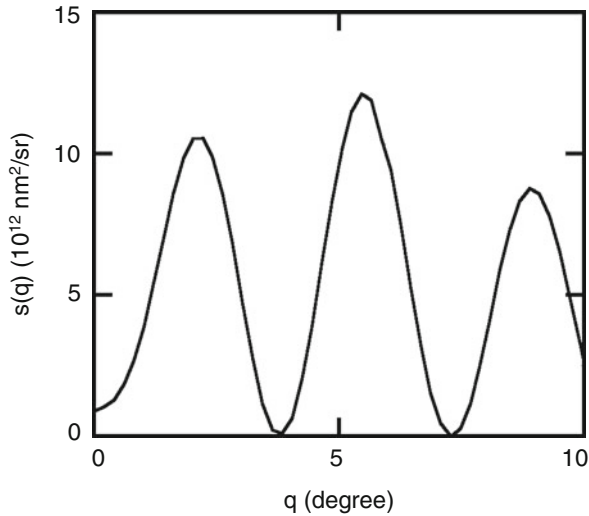
The solid curve in Fig. 26.12 shows the case where $\delta = 2\pi \times (+1)$ GHz with $a = 50$ nm, $\Lambda = 85$ nm, and $v = v_{\text{mp}} = 46$ cm/s. For the Rb D₂ line with 780.2 nm, γ , I_s , and n_j of Si are $2\pi \times 6.1$ MHz, 1.6 mW/cm², and 3.7, respectively. The number N_0 is equal to the experimental value. The theoretical profile is in good agreement with the experimental one.

The collimation of the incident atom bunch by hollow-light beam guiding may reduce the effective source size. Under blue-detuning conditions, the hollow-light beam decelerates the lateral atomic velocity due to Sisyphus cooling [71]. The use of an ideal point atomic source allows us to obtain the narrow spatial profile corresponding to the differential cross section shown in Fig. 26.13, where the first order diffraction appears at $\theta = 2.1^\circ$. In the current experiments, the spatial resolution of $140 \mu\text{m}$ of the two-step photoionization detection is too low to show the fine diffraction pattern. In order to greatly improve the spatial resolution, a slit-type detector using two-step photoionization with two-color near-field lights will be introduced in Sect. 26.3.

The spontaneous scattering force is dominant over the stimulated dipole force for smaller blue detuning, so that many atoms are lost without deflected. Indeed, the number of atoms appearing at $\theta = 0^\circ$ for $\delta = 2\pi \times (+0.5)$ GHz is 0.6 times as large as that for $\delta = 2\pi \times (+1)$ GHz. The 0th-order atoms are also lost by the attractive van der Waals force. Atoms deflected in the negative direction can be observed, although it is not shown in Fig. 26.12.

It is an interesting problem to inversely determine the optical potential from the scattering cross section experimentally obtained. In the case of using a fiber probe

Fig. 26.13 Differential cross section of ^{87}Rb atoms numerically obtained, where $a = 50 \text{ nm}$, $\Lambda = 85 \text{ nm}$, $I(a) = 2.9 \times 10^6 \text{ mW/cm}^2$, $\delta = 2\pi \times (+1) \text{ GHz}$, and $v = 46 \text{ cm/s}$



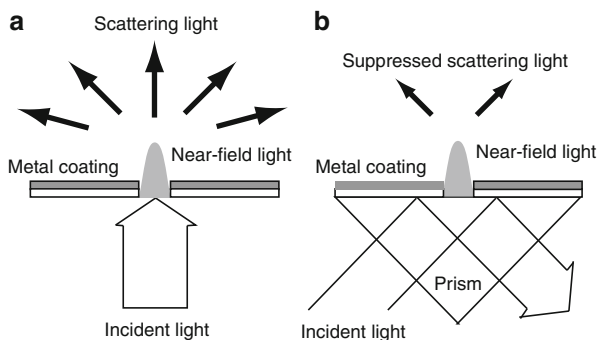
to examine the intensity profile, the optical near field is significantly disturbed. On the other hand, atoms have less influence on the light field. Therefore, the atom-deflection method will be very useful for nondemolition measurements of the net spatial distribution of near-field light.

26.3 Atom Detection

A popular method of detecting neutral atoms is to use a microchannel plate (MCP). However, the highest resolution of commercial MCP is only $5 \mu\text{m}$. Although an elaborate detection system including a secondary-electron multiplier with a resolution of $1 \mu\text{m}$ is reported [72], it is effective for metastable atoms but not for ground-state atoms. These detectors use surface ionization and the ionization efficiency for the ground-state atoms is estimated to be at most 10^{-4} per second at room temperature from the Saha-Langmuir equation and the adsorption time [73, 74]. Thus, the conventional atom detectors have low detection efficiency as well as low spatial resolution, so that they are insufficient for the experiments of demonstrating the precise control of atoms with nanometric near-field light.

This section covers in detail a slit-type detector of observing a small number of neutral atoms in the ground state with high spatial resolution exceeding 100 nm . The nano-slit is illuminated with two-wavelength laser beams for the generation of two-color near-field lights that species and state selectively ionize atoms. The slit width is comparable to the localization length of near-field lights determining the spatial resolution. A 50-nm -wide slit is made on a glass substrate through the lift-off process. The spatial profile of near-field lights at the slit is examined by conducting the finite-difference time-domain (FDTD) simulations. Then, the throughput from propagative light to near-field light is estimated. In addition, the decay behavior as

Fig. 26.14 Generation of near-field light at a narrow slit with metal coating. (a) Normal illumination configuration. Scattering light occurs in the *front side*. (b) Total-internal reflection (TIR) configuration. Incidence of scattering light is greatly suppressed



away from the slit surface is discussed. Finally, based on the results, the ionization efficiency of Rb atoms is given as a function of the incident velocity.

26.3.1 Slit-Type Detector

Since near-field light is localized in a region comparable to the slit width, the spatial resolution is almost equal to the slit width. However, far-field components appear in generating near-field light and the spatial resolution is decreased. Figure 26.14 shows the two ways of illuminating the narrow slit. In the first one, localized near-field light is generated by vertically irradiating the slit from the rear side as shown in Fig. 26.14a. In this case, scattering propagative light simultaneously occurs in the front side and ionizes atoms away from the slit. For the suppression of the perturbative light, it is advantageous to use total-internal reflection (TIR) as shown in Fig. 26.14b. In this case, near-field light appears at the narrow slit illuminated with evanescent light generated on a prism surface, and the occurrence of propagative light that decreases the spatial resolution is sufficiently suppressed. In the TIR configuration, there are four ways of illuminating the slit with a linearly polarized light beam, whether the incidence plane is parallel or perpendicular to the slit alignment and whether *s*-polarization or *p*-polarization.

Figure 26.15 shows a slit-type detector with two-color near-field lights for two-step photoionization with the high spatial resolution [63, 75]. Each near-field light is generated at the nano-slit fabricated by thinly evaporating metal on a glass prism via TIR of each light beam. One near-field light resonantly transfers atoms from the ground state to an excited state, and another near-field light ionizes them. Then, a channel electron multiplier (CEM) negatively biased drags the ions and outputs a current signal in proportion to the number of ions. Since two-color near-field lights are localized near the slit, the spatial resolution of atom detection is approximately equal to the slit width. The spatial distribution of atomic projectile can be obtained by moving the slit device with a nanoactuator.

Fig. 26.15 Detecting atoms with a nano-slit fabricated by thinly evaporating metal on a glass. Atoms entering two-color near-field lights generated via total-internal reflection of two-wavelength light beams incident along the slit are positive-ionized and counted with a CEM negatively biased

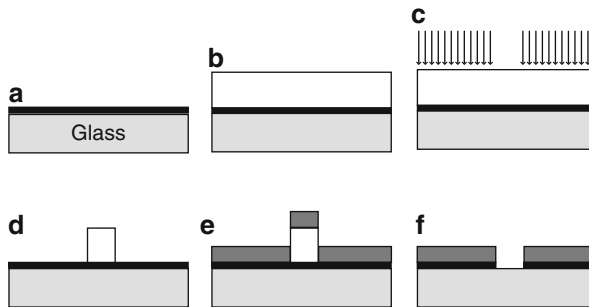
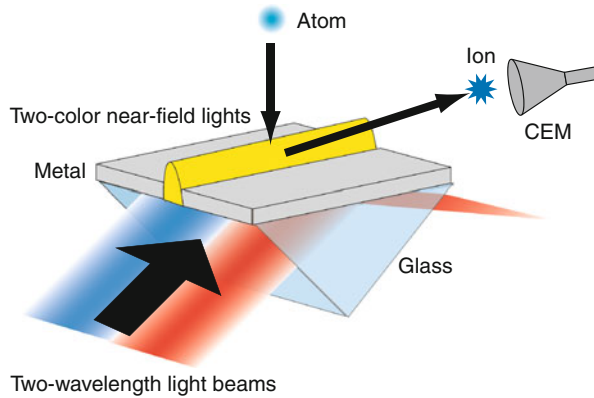


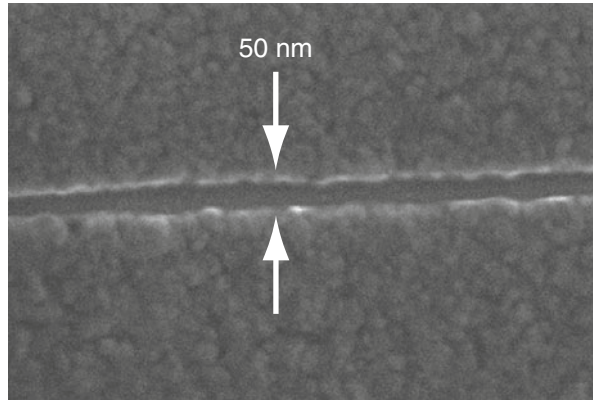
Fig. 26.16 Fabrication of a sub-100-nm-wide slit on a glass substrate through the lift-off process with bilayer resist: (a) deposition of Cr by sputtering, (b) spin-coating of a ZEP520A resist, (c) patterning by electron-beam exposure, (d) creating a line structure, (e) evaporation of Al, and (f) removing the center resist and Cr at the *bottom* of the slit

26.3.2 Fabrication

In order to conduct the TIR illumination, a narrow slit is built on a fused silica substrate by the lift-off method [76]. Figure 26.16 shows the fabrication process.

1. A 5-nm-thick Cr film is first coated on the front side of the glass substrate by sputtering (Fig. 26.16a). The Cr layer prevents electrification in electron-beam exposure.
2. A 50% diluted ZEP520A resist, spun for 5 s at 500 rpm and again for 90 s at 5,000 rpm, is spin-coated to cover the Cr layer (Fig. 26.16b).
3. After baking for 240 s at 180 °C on a hot plate, a 90-nm-thick resist film is formed. The ZEP520A resist is then exposed by an electron beam (Fig. 26.16c).

Fig. 26.17 SEM image of the slit. The width is estimated to be 50 nm



4. The exposed region is developed and removed by immersing in a ZED-N50 solvent for 4 min and then in a ZMD-B rinse for 5 s (Fig. 26.16d).
5. A 40-nm-thick Al coat is deposited by evaporation (Fig. 26.16e).
6. The residual ZEP520A resist covered by the Al film in the center is lifted off. It is washed in acetone after immersing in a 502A liquid for 10 min at 100 °C and again washed in acetone after immersing for 30 min, followed by aqua-pura washing. Finally, the Cr layer at the bottom of the slit is removed in etchant (Fig. 26.16f).

Figure 26.17 shows the SEM image of the slit produced on the glass substrate. The width and the depth are 50 and 40 nm, respectively, while the length is 100 μm . The width of the developed region basically depends on ability of the electron-beam system used. Narrower slits may be made by using a higher performance system.

26.3.3 Simulations

The light distribution at the slit is examined by FDTD simulations [77]. Figure 26.18 shows the coordinate system and the light incident ways used in the calculation. The x -axis is taken in the direction of the slit alignment. The center of the slit is at $y = 0$, while the Al surface is at $z = 0$. Let us compare the normal illumination (Fig. 26.18a) with the TIR illumination where the incidence plane is perpendicular (Fig. 26.18b) and parallel (Fig. 26.18c) to the slit.

Figure 26.19 shows the intensity profiles at $z = 0$ plotted as a function of y/a , where the slit width a is 50 nm. The throughput η is defined as the ratio of the near-field light intensity to the incident light intensity. Linearly polarized light with a wavelength of 780 nm is incident. The refractive indices of fused silica and Al are 1.54 and 2.63, respectively. The thin Cr layer is neglected for the sake of saving the computing time. Figure 26.19a, b indicates the two cases where the polarization in the normal illumination is parallel and perpendicular to the slit, respectively. The

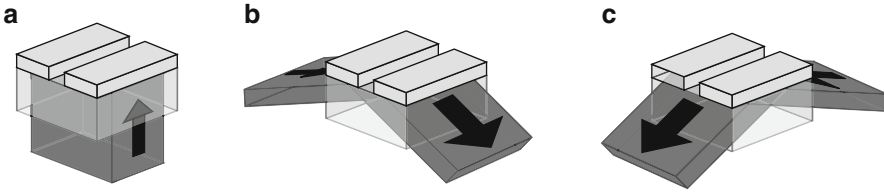


Fig. 26.18 Configuration in FDTD simulations: (a) light incidence in the normal configuration, (b) light incidence perpendicular to the slit in the TIR configuration, and (c) light incidence parallel to the slit in the TIR configuration. The x -axis equals the direction of the slit alignment, where the center of the slit is at $y = 0$. The z -axis is normal to the Al surface at $z = 0$

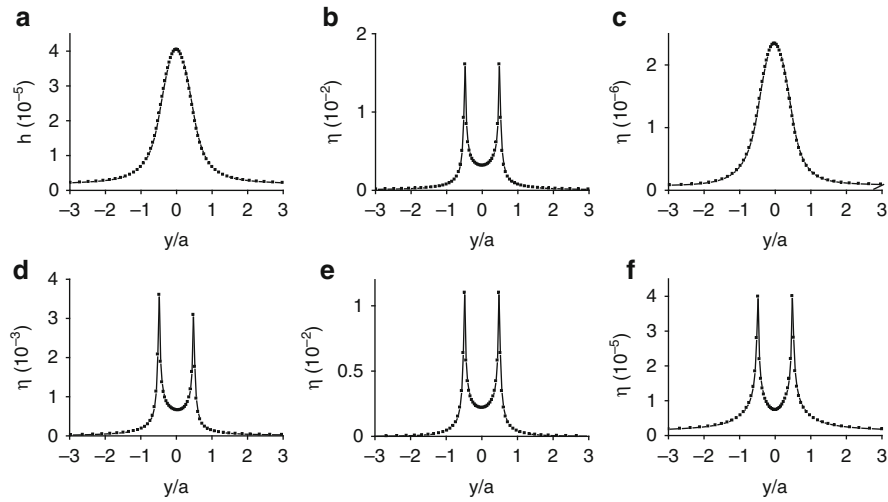


Fig. 26.19 Throughput η at $z = 0$ plotted as a function of y/a for a wavelength of 780 nm: (a) parallel polarization in the normal configuration, (b) perpendicular polarization in the normal configuration, (c) perpendicular incidence with s -polarization in the TIR configuration, (d) perpendicular incidence with p -polarization in the TIR configuration, (e) parallel incidence with s -polarization in the TIR configuration, and (f) parallel incidence with p -polarization in the TIR configuration. The incidence angle is 60° in the TIR configuration. The critical angle of TIR at the interface of fused silica and air is estimated to be 40.6°

intensity is maximum at $y = 0$ for the parallel polarization, while the distribution obtained in the perpendicular polarization shows twin peaks at both slit edges. These profiles reflect orientation of the electric polarization induced on the slit edges [78, 79]. Namely, the electric dipole moments aligned perpendicularly to the slit produce the double-peak profile. In this case, the light field concentrates near the slit edges, so that the intensity is very large compared to the wide single-peak profile. Indeed, the throughput of 10^{-2} in Fig. 26.19b is about 10^3 times as large as the throughput of 10^{-5} in Fig. 26.19a.

Meanwhile, there are four cases in the TIR illumination: the incidence plane is perpendicular to the slit (see Fig. 26.18b) with s -polarization (Fig. 26.19c) or p -polarization (Fig. 26.19d) and parallel to the slit (see Fig. 26.18c) with s -polarization (Fig. 26.19e) or p -polarization (Fig. 26.19f). As expected, Fig. 26.19d, e has twin peaks since electric dipole moments are induced perpendicularly to the slit. The electric dipole moments turning to the z -axis also produce the double-peak profile. Consequently, twin peaks appear in Fig. 26.19f. The throughputs obtained in the twin-peak cases are larger than the throughput obtained in the single-peak case, similarly to the normal illumination. At the incident angle of 60° , the value of 10^{-2} in Fig. 26.19e is about 10^4 times as large as the value of 10^{-6} in Fig. 26.19c.

Figure 26.20 shows the intensity decay profile at $y = 0$ plotted as a function of z/a , corresponding to each case of Fig. 26.19. The light field generated in the normal illumination slowly decays (Fig. 26.20a, b). This implies the occurrence of far-field components. It is similar in the perpendicular incidence case of the TIR illumination (Fig. 26.20c, d). In contrast, the light field appearing in the parallel incidence case rapidly decays (Fig. 26.20e, f). The light intensity shown in Fig. 26.20e decreases to 10^{-7} at $z = 500$ nm.

The same simulations is also conducted for the wavelength of 476.5 nm. Figure 26.21 shows the results obtained in the parallel-incident TIR configuration with s -polarization. In this case, the throughput is 3.3×10^{-2} and the decay length Λ defined as

$$\frac{I(z)}{I(0)} = \exp\left(-\frac{2z}{\Lambda}\right) \quad (26.17)$$

with the light intensity $I(z)$ is estimated to be about 50 nm.

26.3.4 Suppression of Scattering Light

Two-step photoionization is available for detecting a small number of ground-state atoms with high spatial accuracy that exceeds 100 nm. It is important to suppress scattering light since such stray light ionizes atoms far from the slit. Table 26.1 summarizes the FDTD simulations mentioned above. In the case where the s -polarized light is incident parallel to the slit, x -TIR with s -polarization in Table 26.1, scattering light is greatly decreased with high throughput.

The occurrence of far-field components in the TIR configuration strongly depends on the incident direction and the polarization since the slit width is much smaller than the slit length. From the direction of the wave vector of the propagative component along the surface of the evanescent field, many electric dipole moments aligned along the slit length will produce far-field photons in the perpendicular incidence case with s -polarization, while few dipole moments induced along the slit width scatter photons in the parallel case with s -polarization. Similarly, for p -polarization where far-field photons are also caused by dipole moments oriented

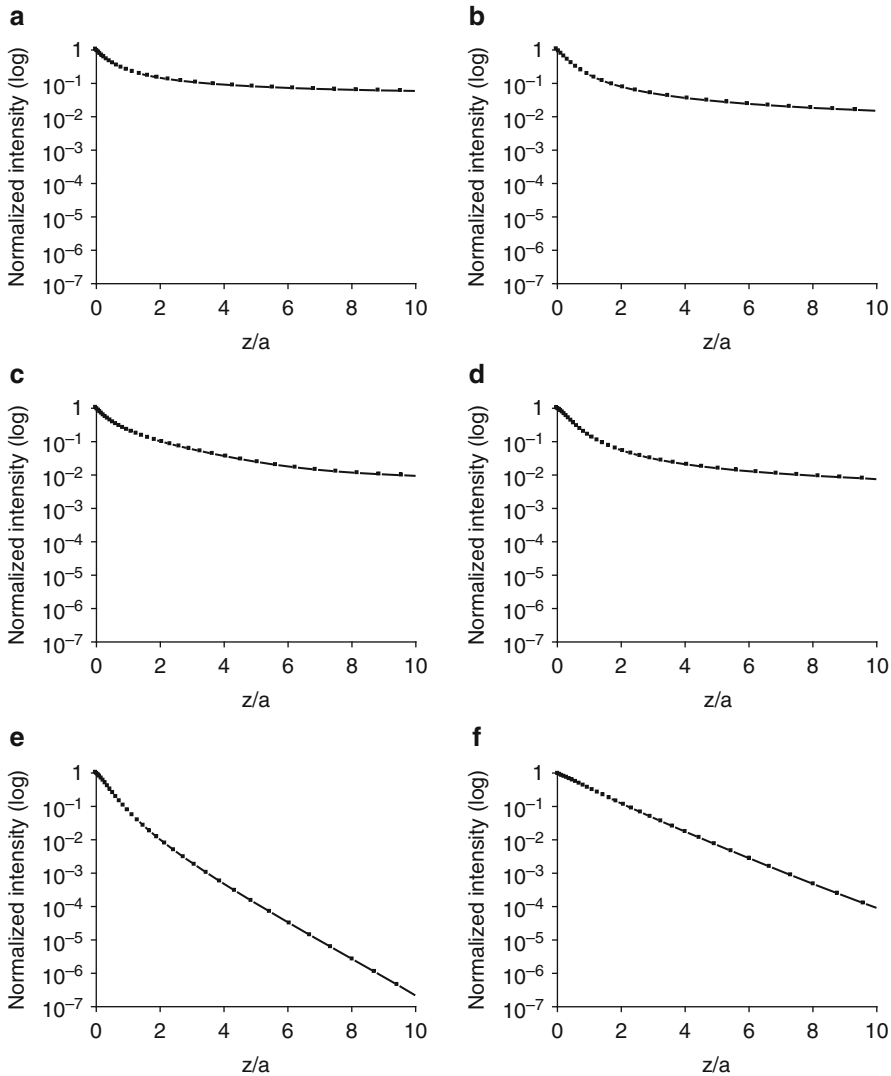


Fig. 26.20 Intensity decay profile at $y = 0$ plotted as a function of z/a for a wavelength of 780 nm: (a) parallel polarization in the normal configuration, (b) perpendicular polarization in the normal configuration, (c) perpendicular incidence with s -polarization in the TIR configuration, (d) perpendicular incidence with p -polarization in the TIR configuration, (e) parallel incidence with s -polarization in the TIR configuration, and (f) parallel incidence with p -polarization in the TIR configuration

toward the z -axis, more dipole moments contribute to light scattering in the perpendicular case, compared to the parallel case. Thus, the light field rapidly decays in the parallel incidence case. The slit structure is essential because it is possible to control the direction and the polarization of incident light.

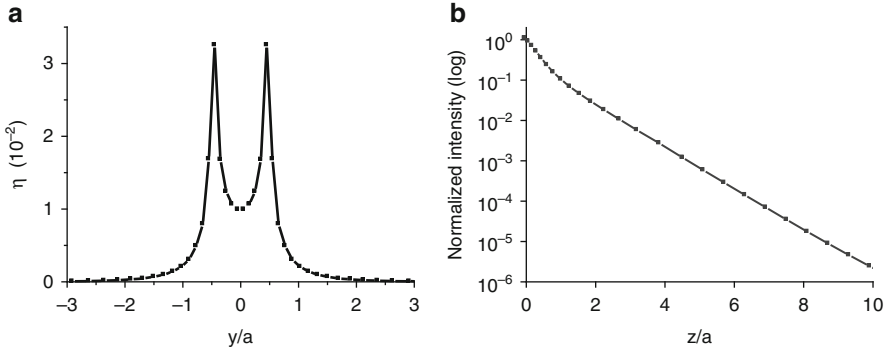


Fig. 26.21 (a) Throughput η at $z = 0$ plotted as a function of y/a and (b) intensity decay profile at $y = 0$ plotted as a function of z/a for the wavelength of 476.5 nm in the case of parallel incidence with s -polarization in the TIR configuration

Table 26.1 Throughput and attenuation for 780 nm. Normal, y -TIR, and x -TIR correspond to Fig. 26.18a–c, respectively. Attenuation is valued at $z/a = 10$

Configuration	Polarization	Throughput	Attenuation
Normal	x	4.0×10^{-5}	6.0×10^{-2}
Normal	y	1.6×10^{-2}	1.5×10^{-2}
y -TIR	s	2.3×10^{-6}	9.6×10^{-3}
y -TIR	p	3.6×10^{-3}	7.6×10^{-3}
x -TIR	s	1.1×10^{-2}	2.2×10^{-7}
x -TIR	p	4.0×10^{-5}	8.8×10^{-5}

26.3.5 Ionization Efficiency

The ionization efficiency of the ^{87}Rb atoms in the hyperfine upper ground state using two-step photoionization with two-color near-field lights is estimated in the case where the $5S_{1/2}$, $F = 2 \rightarrow 5P_{3/2}$, $F = 3$ transition by the 780-nm near-field light is saturated. The ionization efficiency $P(v)$ of the ^{87}Rb atom in the $5P_{3/2}$, $F = 3$ state by the 476.5-nm near-field light is given by

$$\begin{aligned}
 P(v) &= \frac{1}{2} \times \left[1 - \exp \left\{ -\sigma \int_{-\infty}^{\Lambda/v} \phi \exp \left[-\frac{2(\Lambda - vt)}{\Lambda} \right] dt \right\} \right] \\
 &= \frac{1}{2} \left[1 - \exp \left(-\sigma \phi \frac{\Lambda}{2v} \right) \right]
 \end{aligned} \tag{26.18}$$

as a function of the atomic velocity v with the cross section $\sigma = 2.0 \times 10^{-17} \text{ cm}^2$ [80]. The photon flux intensity ϕ is given by

$$\phi = I(0) \frac{\lambda}{hc} \tag{26.19}$$

with the Planck constant h , the light speed c , and $\lambda = 476.5 \text{ nm}$.

Fig. 26.22 Ionization efficiency plotted as a function of the incident velocity in the parallel-incident TIR configuration with *s*-polarization. Two-color near-field lights generated by a 780 nm diode-laser beam with the saturation intensity and a 476.5-nm Ar-ion laser beam with 240 kW/cm^2 ionize the ^{87}Rb atoms in the $5S_{1/2}$, $F = 2$ ground state

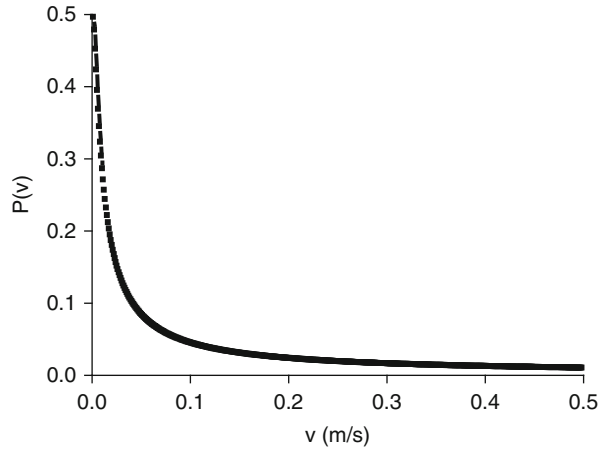


Figure 26.22 shows the ionization efficiency of ^{87}Rb atoms with the 50-nm-wide slit plotted as a function of the incident velocity in the case of *x*-TIR with *s*-polarization in Table 26.1. Here, the Ar-ion-laser intensity is 240 kW/cm^2 and the throughput is 3.3×10^{-2} , so that $I(0) = 240 \times 3.3 \times 10^{-2} = 7.9 \text{ kW/cm}^2$. The ionization efficiency exceeds 1% for the incident velocity of less than 50 cm/s. It will be improved by increasing the light intensity. The spatial position is measured by moving the slit element with a nanoactuator.

26.4 Nano-slit with Rounded Edges

The first step of photoionization only needs a low light intensity due to resonant transition, while the second step with a wavelength λ_2 needs a substantial high intensity since the reaction cross section is very small. Consequently, intense near-field light is required for the second step. Generation of near-field light depends strongly on the radius of curvature of the slit edge. When the edge gets dull, near-field light is drawn into the slit and extends transversally so that the peak intensity decreases. In this section, the influence of rounding the slit edges on the intensity profile of near-field light generated at a 50-nm-wide slit is examined by running FDTD simulations [81].

26.4.1 FDTD Simulations

In order to check whether the intensity of near-field light is high enough to photoionization, the actual microfabrication accuracy of the slit edge is considered in FDTD simulations. Figure 26.23 is the cutaway view presumed from scanning electron microscope images of a 50-nm-wide slit. The height of the slit is assumed to be 50 nm equal to the slit width.

Fig. 26.23 Cross-sectional view of the 50-nm-wide slit fabricated by evaporating Al metal on a silica glass surface. The height is assumed to be the same as the width. The radius of curvature R ranges from 0 to 50 nm in FDTD simulations

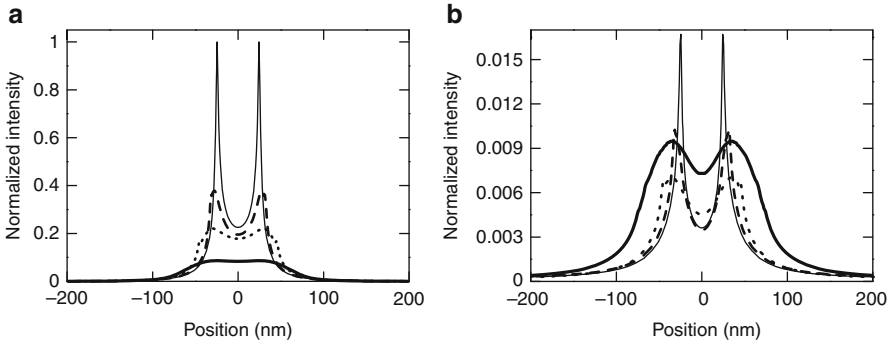
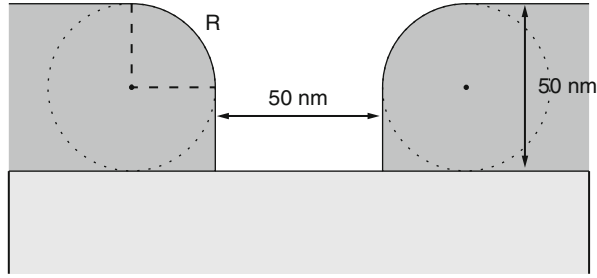


Fig. 26.24 Intensity profile of near-field light at the upper surface of the 50-nm-wide slit generated by (a) the s -polarized light beam and (b) the p -polarized light beam with $\lambda_2 = 476.5$ nm for Rb in the TIR configuration, where the intensity is normalized to the peak value in the case of $R = 0$ at a fixed intensity of incident light. The origin of the lateral axis indicates the center of the slit. The *thin solid line*, the *broken line*, the *dotted line*, and the *thick solid line* show the four cases of $R = 0, 10, 25,$ and 50 nm, respectively

Figure 26.24 shows the intensity profiles at the upper surface of the slit in the case where a linearly polarized light beam with $\lambda_2 = 476.5$ nm entering along the slit is total-internal-reflected at an incident angle of 60° . Here, the intensity of resultant light is normalized to the peak value for $R = 0$ at a fixed intensity of incident light. The center of the slit is located at the origin of the lateral axis. The refractive indices of silica glass and Al are 1.55 and 0.694, respectively. The extinction coefficient of Al is 5.795. The incident light beam is a Gaussian beam with the beam diameter of $2 \mu\text{m}$. Figure 26.24a, b shows the two cases of s -polarization and p -polarization, respectively. The thin solid line, the broken line, the dotted line, and the thick solid line indicate the four cases of $R = 0, 10, 25,$ and 50 nm, respectively.

Near-field light is generated by electric dipole moments induced near the surface. A lot of electric dipole moments are induced perpendicular to the inner wall of the slit by s -polarized light. Meanwhile, a few electric dipole moments are induced perpendicularly to the upper surface by the longitudinal component of p -polarized light. Since the intensity of near-field light is proportional to the density of electric dipole moments, intense near-field light is generated in the s -polarization. Indeed, the peak intensity in the s -polarization is 37 times as

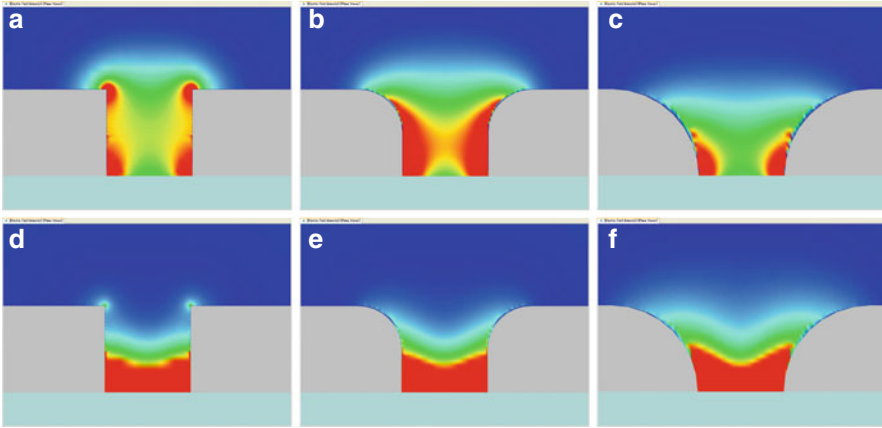


Fig. 26.25 Cross-sectional intensity distribution of near-field light in the 50-nm-wide slit when the wavelength is 476.5 nm in the six cases of (a) $R = 0$ in the s -polarization, (b) $R = 25$ nm in the s -polarization, (c) $R = 50$ nm in the s -polarization, (d) $R = 0$ in the p -polarization, (e) $R = 25$ nm in the p -polarization, and (f) $R = 50$ nm in the p -polarization. The color changes from red to blue as the intensity decreases

large as that in the p -polarization when $R = 10$ nm. It should be noted that the component of light electric field parallel to the slit contributes not at all to induced electric dipole moments. This is the reason why, in the case where an s -polarized light beam is incident perpendicularly to the slit, the peak intensity is 10^{-4} times compared to the case where an s -polarized light beam is incident parallel to the slit.

26.4.2 Intensity Profile

It is impossible to fabricate a nano-slit with $R = 0$ without special processing units. As shown in Fig. 26.24a, the peak intensity decreases with increasing the radius of curvature of the slit edge in the s -polarization, and the twin-peak character is lost. Figure 26.25 shows the spatial distribution of near-field light drawn based on FDTD simulations in the cases of (a) $R = 0$ in the s -polarization, (b) $R = 25$ nm in the s -polarization, (c) $R = 50$ nm in the s -polarization, (d) $R = 0$ in the p -polarization, (e) $R = 25$ nm in the p -polarization, and (f) $R = 50$ nm in the p -polarization. The place where the intensity is high is painted in red.

Let us consider the s -polarization case. When the shape of the edge is square, the electric field is greatly enhanced in the four corners of the slit as indicated in red in Fig. 26.25a. As a result, intense near-field light with twin narrow peaks is generated at the upper surface. The enhancement in the upper left and right corners is resolved as the edge gets dull as shown in Fig. 26.25b, c, and the twin peaks

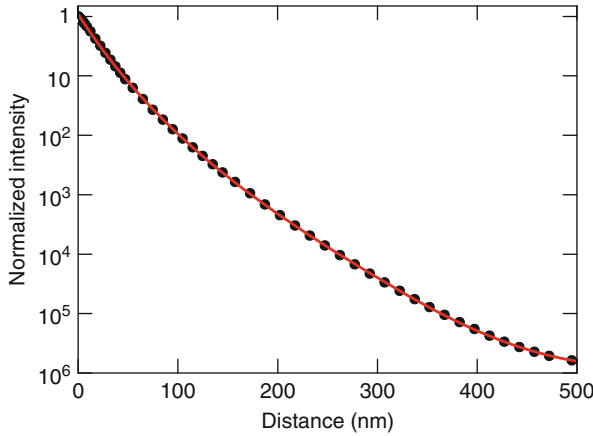


Fig. 26.26 Decay of light intensity with the distance from the upper surface of the 50-nm-wide slit with $R = 10$ nm when an s -polarized light beam with the wavelength of 476.5 nm is incident along the slit in the TIR configuration. The intensity is normalized to the value at the surface. The filled circles indicate the value obtained from an FDTD simulation, and the red line is the fitting obtained from a regression analysis calculation

disappear with decreasing the intensity as shown in Fig. 26.24a. It is similar in the p -polarization case as shown in Fig. 26.25d, e, although resultant near-field light is weak. However, when the edging down is further done, the distribution of electric dipole moments induced on the upper surface by the longitudinal component of p -polarized light spreads outward as shown in Fig. 26.25f. Accordingly, near-field light broadens and the intensity turns into increase at the upper surface as shown in Fig. 26.24b.

Scattering light is well suppressed when the s -polarized light beam is incident along the slit in the TIR configuration. An example is shown in Fig. 26.26, where the change of light intensity is plotted as the function of the distance from the upper surface of the 50-nm-wide slit with $R = 10$ nm for the wavelength of 476.5 nm. The filled circles indicate the value, which is normalized to the one at the surface, obtained from an FDTD simulation. In this case, the intensity ratio of scattering light to near-field light is approximately 10^{-6} at the distance of 500 nm.

In Fig. 26.26, the red line is the fitting obtained from a regression analysis calculation. The light intensity function $I(z)$ composed of three parts is given by

$$I(z) = I_1 \frac{\exp\{-2(z + a_1)/a_1\}}{(z + a_1)^2} + I_2 \exp\left(-2\frac{z}{a_2}\right) + \frac{I_3}{(z + a_3)^2}, \quad (26.20)$$

where the coordinate z is the distance from the upper surface. The Yukawa-function term is the near-field component, the exponential term is the evanescent component that contributes to the mid-distance intensity, and the third term is the far-field

Table 26.2 Six parameters of I_1 , I_2 , I_3 , a_1 , a_2 , and a_3 in Eq. (26.20) on the occasion of $I(0) = 1$ for $R = 0, 10, 20, 30, 40$, and 50 nm

R (nm)	I_1 (10^4 nm ²)	I_2	I_3 (nm ²)	a_1 (nm)	a_2 (nm)	a_3 (nm)
0	3.1341	0.02976	0.13930	63.043	86.725	6.4483
10	3.1422	0.03821	0.86383	63.449	85.914	334.58
20	2.8123	0.10306	2.1400	63.100	69.377	562.46
30	3.6609	0.04984	0.77933	70.744	78.543	24.604
40	3.4839	0.11686	4.6749	71.555	69.692	735.33
50	4.8917	0.01861	0.33842	81.342	100.46	16.415

component. Table 26.2 shows the value of the six parameters of I_1 , I_2 , I_3 , a_1 , a_2 , and a_3 when $I(0) = 1$ in the six cases of $R = 0, 10, 20, 30, 40$, and 50 nm.

26.4.3 Photoionization Efficiency

Under the assumption that the first resonant transition with λ_1 of two-step photoionization is saturated, the ionization efficiency is approximately expressed as [75]

$$P = \frac{1}{2} \left[1 - \exp \left\{ -\sigma \phi \int_{-\infty}^0 I(-vt) dt \right\} \right], \quad (26.21)$$

where v is the atomic incident speed and $I(-vt)$ is normalized to $I(0)$. The photon flux intensity ϕ is given by

$$\phi = I(0) \frac{\lambda_2}{hc}, \quad (26.22)$$

where h and c are Planck constant and the speed of light, respectively.

The ionization efficiency P is evaluated by assigning the value obtained from FDTD simulations to the intensity $I(0)$ at the upper surface of the slit and substituting Eqs. (26.20) and (26.22) into Eq. (26.21). Figure 26.27 shows the result for ^{87}Rb atoms with $v = 10$ cm/s when the radius of curvature of the slit edge changes from 0 to 50 nm with 10-nm increments in between. Here, the intensity of s -polarized incident light is taken to be 5×10^4 W/cm², which can be obtained by focusing a high-power Ar⁺ laser beam with $\lambda_2 = 476.5$ nm.

Figure 26.28 shows the correlation between the radius of curvature of the slit edge and the intensity of s -polarized incident light in the case of ionizing ^{87}Rb atoms with $v = 10$ cm/s with the efficiency of 10%. For example, if the upper limit of the available intensity of incident light is 5×10^4 W/cm², two-step photoionization with the efficiency exceeding 10% of slow Rb atoms requires the processing accuracy of more than 15 nm in fabrication of the slit.

Fig. 26.27 Ionization efficiency of ^{87}Rb atoms with $v = 10$ cm/s plotted as a function of the radius of curvature R of the slit edge in the case where the intensity of s -polarized incident light is 5×10^4 W/cm 2

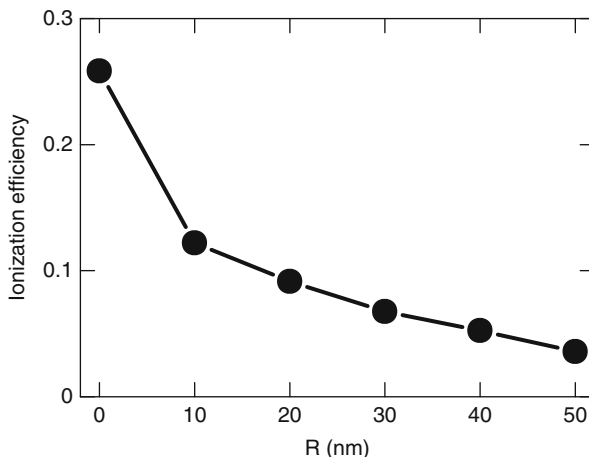
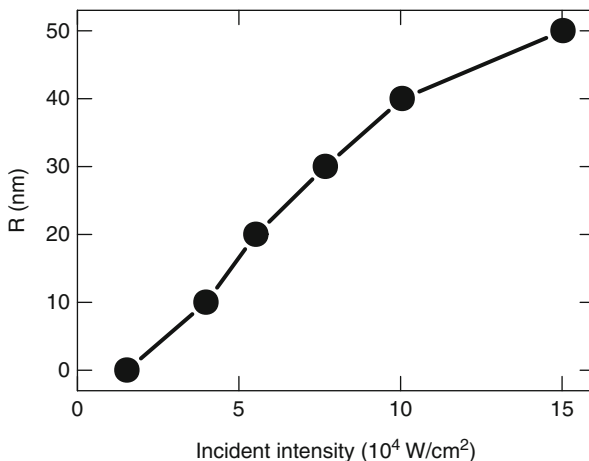


Fig. 26.28 Relation between radius of curvature R of the slit edge and the intensity of s -polarized incident light required for ionizing ^{87}Rb atoms with $v = 10$ cm/s with the efficiency of 10 %



26.4.4 Throughput

The nano-slit system with two-step photoionization can be applied to detecting every alkali-metal atoms listed in Table 26.3. Figure 26.29 shows the throughput, which is defined as the ratio $I(0)/I_0$ of the intensity $I(0)$ at the upper surface to the intensity I_0 of linearly polarized incident light, plotted as a function of the wavelength in the two cases of (a) the s -polarization and (b) the p -polarization. Here, the filled squares, the open circles, the filled triangles, the open inverse triangles, and the filled diamonds indicate the five cases of $R = 10, 20, 30, 40,$ and 50 nm, respectively.

In the s -polarization case shown in Fig. 26.29a, the throughput increases with the wavelength and the radius of curvature. Since the decay length of evanescent

Table 26.3 Several constants with respect to two-step photoionization of alkali-metal atoms, where Δ is the ionization energy measured from the $S_{1/2}$ level; λ_1 and I_s are the wavelength and the saturation intensity of the D_2 line, respectively, and λ_2 is an example of the laser wavelength available for the second step; and σ is the cross section of ionization from the $P_{3/2}$ level

	Δ (eV)	λ_1 (nm)	I_s (mW/cm ²)	λ_2 (nm)	σ (10 ⁻¹⁷ cm ²)
Li	5.39	670.97	2.56	349.8	1.48 [83]
Na	5.14	589.16	6.40	353.3	0.37 [84]
K	4.34	766.70	1.77	355	0.72 [85]
Rb	4.18	780.24	1.64	476.5	2.0 [80]
Cs	3.89	852.35	1.09	496.5	1.86 [86]

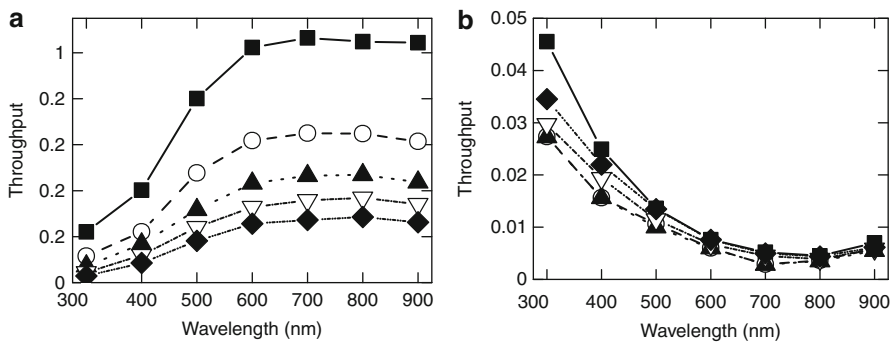


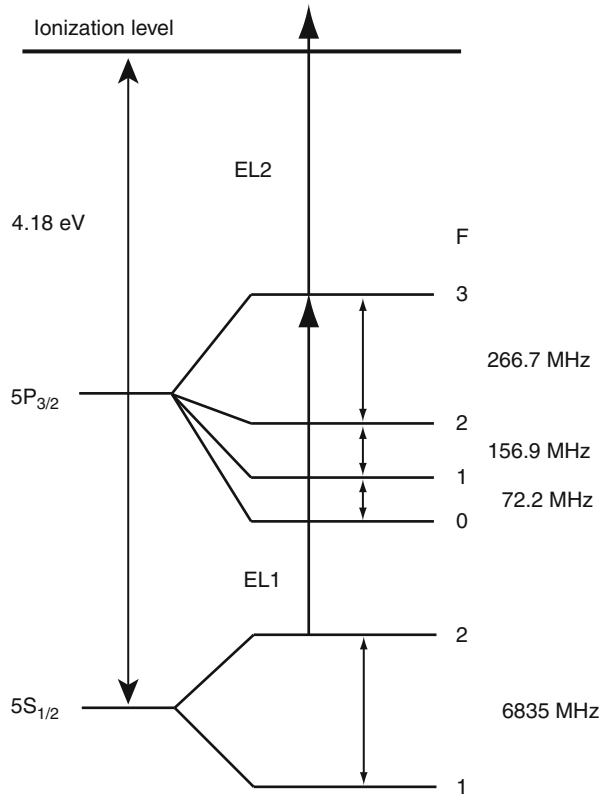
Fig. 26.29 Throughput plotted as a function of the wavelength: (a) s -polarization in the evanescent-light illumination and (b) p -polarization in the evanescent-light illumination

light illuminating the slit is longer with the wavelength of incident light at a fixed incident angle in the TIR configuration, more electric dipole moments are induced in the long-wavelength side and the intensity of near-field light is higher. On the other hand, in the p -polarization case shown in Fig. 26.29b, the throughput decreases as the wavelength is longer. It implies that less electric dipole moments are induced in the long-wavelength side.

26.5 Two-Step Photoionization with Two-Color Evanescent Lights

Two-step photoionization is suitable for detecting a small number of atoms with a high signal-to-noise ratio [82]. Table 26.3 shows several constant data on two-step photoionization of alkali-metal atoms, where Δ is the ionization energy of the ground-state atom, λ_1 is the resonant wavelength of the D_2 line, I_s is the saturation intensity of the resonant transition, λ_2 is a wavelength of a laser available for

Fig. 26.30 Relevant energy levels of ^{87}Rb . The first evanescent light (EL1) generated by TIR of an LD beam with 780.2 nm excites the ^{87}Rb atoms in the $5S_{1/2}$, $F = 2$ ground state to the $5P_{3/2}$, $F = 3$ state. The second evanescent light (EL2) generated by TIR of an Ar-ion laser beam with 476.5 nm excites the ^{87}Rb atoms in the $5P_{3/2}$, $F = 3$ state over the ionization level at 4.18 eV above the $5S_{1/2}$ state. The photon energies of EL1 and EL2 are 1.59 and 2.60 eV, respectively



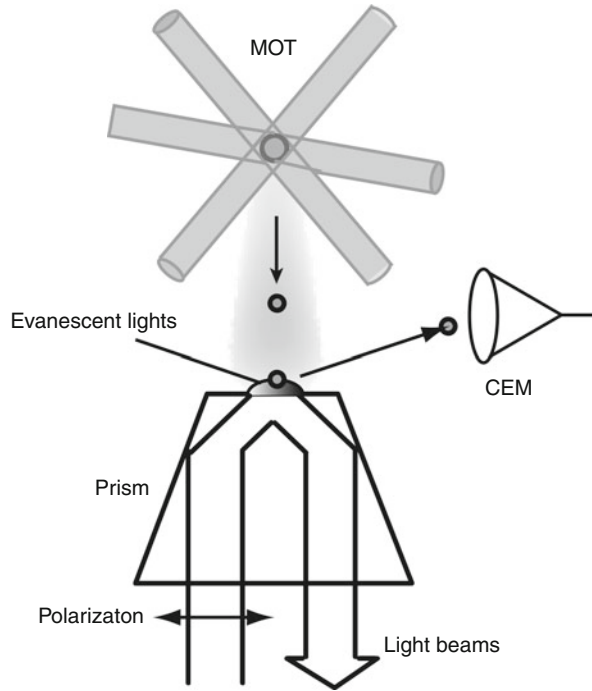
ionization from the $P_{3/2}$ state, and σ is the ionization cross section experimentally obtained. The photoionization cross section is usually very small.

This section deals with two-step photoionization of cold Rb atoms by two-color evanescent lights generated on a prism plane. The ionization cross section of the $5P$ state is evaluated from the experimental results.

26.5.1 Approach

Two-step photoionization with combination of evanescent light and propagative light is reported in Ref. [87]. Afterward, two-step photoionization with only evanescent lights is demonstrated for cold Rb atoms [80]. Figure 26.30 shows the relevant energy levels of ^{87}Rb . The first evanescent light (EL1) generated via TIR of a diode-laser (LD) beam with a wavelength $\lambda_1 = 780.2$ nm selectively excites ^{87}Rb atoms in the $5S_{1/2}$, $F = 2$ hyperfine upper ground state to the $5P_{3/2}$, $F = 3$ state. Then, the second evanescent light (EL2) generated via TIR of an Ar-ion laser beam with $\lambda_2 = 476.5$ nm lifts the ^{87}Rb atoms up to the ionization level at 4.18 eV above the $5S_{1/2}$ state.

Fig. 26.31 Experimental setup of two-step photoionization with two-color evanescent lights. An MOT with three pairs of $\sigma^+ - \sigma^-$ circularly polarized light beams creates a ^{87}Rb atom ensemble with a mean temperature of $16\ \mu\text{K}$. The released cold atoms fall on a BK7 prism $26\ \text{mm}$ below and then they are ionized by two-color evanescent lights generated on the prism surface via TIR of a 780.2-nm LD beam and a 476.5-nm Ar-ion laser beam. Each beam is p -polarized. The ionized atoms are counted with a CEM negatively biased



26.5.2 Experiment

Figure 26.31 shows the experimental setup with an uncoated BK7 prism. The double MOT system [69] is applied to detecting a small number of cold ^{87}Rb atoms. The cold ^{87}Rb atoms are generated by the first MOT under a pressure of 10^{-7} Pa. Next, they are sent down to the second MOT $26\ \text{cm}$ below and recaptured under a lower pressure of 10^{-8} Pa. As a result, a 5-mm -diameter cloud of 10^9 ^{87}Rb atoms is produced at $h = 26\ \text{mm}$ above the prism surface. The cold ^{87}Rb atoms in the $5S_{1/2}$, $F = 2$ ground state are released by turning off the second MOT. The time-of-flight (TOF) measurement indicates that the initial mean temperature T and the atom flux intensity are $16\ \mu\text{K}$ and 2.8×10^{11} atoms/ cm^2s , respectively. It follows that the atomic density d is 3.9×10^{15} atoms/ m^3 at the prism surface. The incident most probable speed v_m is $\sqrt{2k_B T/m + 2gh} = 0.71\ \text{m/s}$, where m , k_B , and g are the atomic mass, Boltzmann constant, and gravitational acceleration, respectively.

Two-color evanescent lights are generated on the prism surface via TIR of an LD beam and a high-power Ar-ion laser beam at the incident angle $\theta = 46^\circ$. Each light beam is p -polarized. The beam waists w_i ($i = 1, 2$) at the prism surface are 580 and $165\ \mu\text{m}$, respectively. The effective ionization area A_{ion} is $\pi \times w_2^2 / \cos \theta = 1.8 \times 10^5\ \mu\text{m}^2$. The amplitude of the electric field of evanescent light exponentially

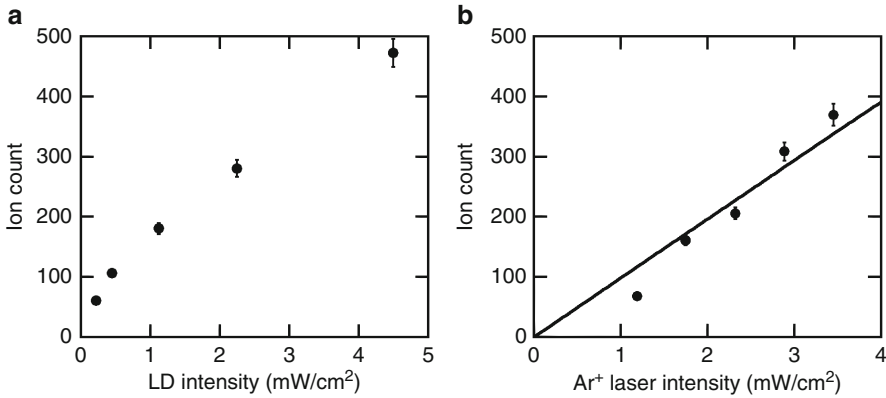


Fig. 26.32 Ion count plotted as a function of (a) the LD intensity and (b) the Ar-ion laser intensity. The Ar-ion laser intensity is fixed at 3.5 kW/cm^2 in (a), while the LD intensity is fixed at 4.5 mW/cm^2 in (b). The *filled circles* indicate experimental data. The *solid line* in (b) shows the least-square fitting for the estimation of the ionization cross section of the 5P-state ^{87}Rb atoms. There is a fluctuation of about 10% with respect to the number of cold Rb atoms created by MOT in each experimental event. Therefore, the ion count in (a) is not necessarily the same as the corresponding ion count in (b) even if the laser intensities are the same

decays as $E_0 \exp(-z/\Lambda_{\text{EL}i})$ [88], where the z -axis is taken upward perpendicularly to the prism surface and E_0 is the value at $z = 0$. The decay lengths $\Lambda_{\text{EL}i} = \lambda_i/2\pi \sqrt{n_i^2 \sin^2 \theta - 1}$ are 291 nm for EL1 with the refractive index $n_1 = 1.51$ and 177 nm for EL2 with $n_2 = 1.52$.

The cold ^{87}Rb atoms are repeatedly loaded from the second MOT to the prism surface every 5 s and ionized by the two-color evanescent lights. A channel electron multiplier (CEM) biased with -3 kV detects the ionized ^{87}Rb atoms with the quantum efficiency of 0.9. The number of ions is counted for 200 ms after the release from the second MOT and integrated over 300 times MOT loading. Figure 26.32a shows the ion count plotted as a function of the LD intensity I_1 . The filled circles indicate the results obtained in the case where the Ar-ion laser intensity I_2 is fixed at 3.5 kW/cm^2 . Meanwhile, Fig. 26.32b shows the ion count plotted as a function of I_2 . The filled circles indicate the results obtained in the case of $I_1 = 4.5 \text{ mW/cm}^2$. In both cases, the LD frequency is tuned to the $5S_{1/2}, F = 2 \rightarrow 5P_{3/2}, F = 3$ transition. The error bars indicate the uncertainty of 5% obtained from the TOF measurement with respect to the number of cold ^{87}Rb atoms. As shown in Fig. 26.32a, a saturation occurs similarly to the case of photoionization with propagative light. On the other hand, as shown in Fig. 26.32b, the ion count is proportional to the Ar-ion laser intensity. Consequently, the ionization efficiency is principally determined by the Ar-ion laser intensity.

26.5.3 Ionization Cross Section

Under the assumption that the light intensity in the horizontal direction is homogeneous, the position-dependent ionization efficiency $\eta(z)$ of ^{87}Rb atoms in the $5\text{P}_{3/2}$ state by EL2 is approximately written as

$$\eta(z) = 1 - \exp\left(-\sigma_{\text{ion}} \int_{\infty}^z \phi_{\text{EL2}}(z') \frac{1}{v_m} dz'\right), \quad (26.23)$$

where σ_{ion} is the ionization cross section of the $5\text{P}_{3/2}$ state. The photon flux intensity $\phi_{\text{EL2}}(z)$ of EL2 is given by

$$\phi_{\text{EL2}}(z) = \phi_{\text{EL2}}^0 \exp\left(-\frac{2z}{\Lambda_{\text{EL2}}}\right). \quad (26.24)$$

Using the Fresnel coefficient C_i for p -polarization [89],

$$C_i = \frac{4n_i^2 \cos^2 \theta}{(\cos^2 \theta + n_i^4 \sin^2 \theta - n_i^2)}, \quad (26.25)$$

the value ϕ_{EL2}^0 at the prism surface is $I_2 C_2 / \hbar \omega_2 = 1.98 \times 10^{22}$ photons/cm²s with $C_2 = 4.89$ and Dirac constant \hbar , where ω_2 is the frequency of the Ar-ion laser beam.

The effective interaction time of the photoionization is roughly $\Lambda_{\text{EL2}}/v_m = 249$ ns because of $\Lambda_{\text{EL1}} > \Lambda_{\text{EL2}}$. It is long enough compared to the lifetime 27 ns of the 5P state. For the steady state of the EL1 excitation on resonance, the population $\rho_e(z)$ of the ^{87}Rb atoms excited to the $5\text{P}_{3/2}$, $F = 3$ state by EL1 is written as [12]

$$\rho_e(z) = \frac{1}{2} \frac{s(z)}{1 + s(z)}. \quad (26.26)$$

Here, the Doppler shift due to the lateral velocity of cold atoms is also ignored. The saturation parameter $s(z)$ with $C_1 = 4.90$ is given by

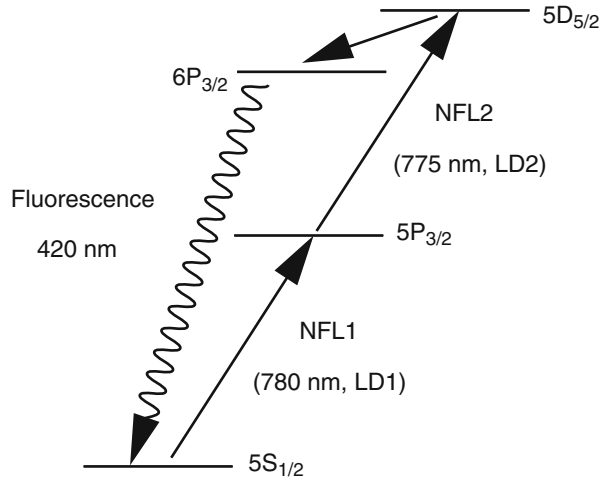
$$s(z) = C_1 \frac{I_1}{I_s} \exp\left(-\frac{2z}{\Lambda_{\text{EL1}}}\right), \quad (26.27)$$

where I_s is the saturation intensity of the Rb D_2 line.

The total number N of ^{87}Rb atoms ionized per MOT loading is obtained from Eqs. (26.23) and (26.26) as

$$N = dA_{\text{ion}} \int_0^{\infty} \rho_e(z) \eta(z) dz. \quad (26.28)$$

Fig. 26.33 Relevant energy levels of Rb. The first near-field light (NFL1) generated by a 780-nm diode laser (LD1) induces the $5S_{1/2} \rightarrow 5P_{3/2}$ transition. The second near-field light (NFL2) generated by a 775-nm diode laser (LD2) induces the $5P_{3/2} \rightarrow 5D_{5/2}$ transition. Some of the excited Rb atoms spontaneously decay to the $5S_{1/2}$ state via the $6P_{3/2}$ state and emit fluorescence with a wavelength of 420 nm



The ion count shown in Fig. 26.32 equals $N_{IC} = 0.9 \times 300 \times N$ with $\gamma = 2\pi \times 6.1$ MHz and $I_s = 1.6$ mW/cm². The ionization cross section $\sigma_{ion} = (2.0 \pm 0.1) \times 10^{-17}$ cm² is obtained from the least-square fitting (solid line) of the expression N_{IC} to the experimental data in Fig. 26.32b.

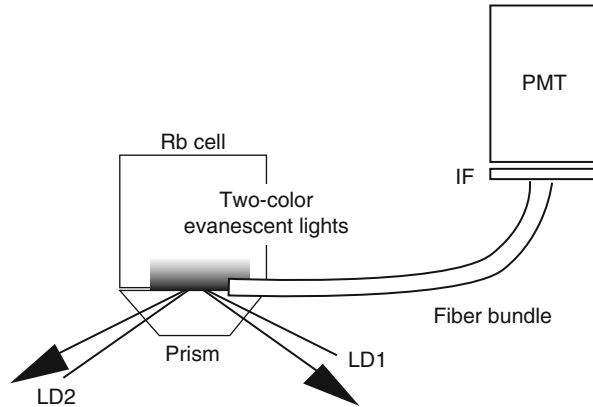
26.6 Blue-Fluorescence Spectroscopy with Two-Color Evanescent Lights

This section describes an alternative way of detecting a small number of atoms with the slit-type detector. In the case of Rb atoms, it uses the stepwise resonant excitation from the $5S_{1/2}$ ground state to the $5D_{5/2}$ state via the $5P_{3/2}$ state [90]. The Rb atoms in the $5D_{5/2}$ state can decay into the $5S_{1/2}$ ground state via the $6P_{3/2}$ state, emitting blue fluorescence with a wavelength of 420 nm. This method requires no intense laser beam contrary to two-step photoionization. Two-color near-field lights causing the transition are generated by two low-power diode lasers with different wavelengths. Consequently, the Rb atoms can be efficiently detected by monitoring the 2nd D₂ line different from the infrared excitation laser lights without being disturbed by scattered light.

26.6.1 Approach

Figure 26.33 shows the relevant energy levels of Rb for blue-fluorescence excitation. The first near-field light (NFL1) generated by a 780-nm diode-laser (LD1) beam stimulates the $5S_{1/2} \rightarrow 5P_{3/2}$ transition. Then, the second near-field light (NFL2) generated by a 775-nm diode-laser (LD2) beam stimulates the $5P_{3/2} \rightarrow 5D_{5/2}$

Fig. 26.34 Experimental setup with a Rb vapor cell. Two-color evanescent lights are generated on a surface of a prism attached to a cell window via TIR of two opposite diode-laser beams *LD1* and *LD2*. Fluorescence with a wavelength of 420 nm is collected by a fiber bundle and sent to a photomultiplier tube (*PMT*) through an interference filter (*IF*)



transition. The excited Rb atoms spontaneously decay to the $6P_{3/2}$ state or the $5P_{3/2}$ state with a branching ratio of 3 to 5 in a lifetime of $1.56 \mu\text{s}$. The Rb atoms in the $6P_{3/2}$ state decay again to one of the $5S_{1/2}$, $6S_{1/2}$, $4D_{5/2}$, and $4D_{3/2}$ states in a lifetime of $3.45 \mu\text{s}$. The ratio of the $5S_{1/2}$ decay channel to the other three channels is 1 to 4. When the Rb atoms decay to the $5S_{1/2}$ state, they emit fluorescence with a wavelength of 420 nm. Thus, emission of the blue fluorescence occurs at a rate of $2.9 \times 10^5 \text{ s}^{-1}$. Observation of the blue fluorescence allows us background-free detection of a small number of atoms.

26.6.2 Experiment

The stepwise resonant excitation is conducted by using two-color evanescent lights [90]. Figure 26.34 shows the experimental setup for fluorescence spectroscopy with a Rb vapor cell heated up to 140°C . Two-color evanescent lights are generated on a surface of a prism attached to a cell window via TIR of two opposite diode-laser beams *LD1* and *LD2*. The incident angles of *LD1* and *LD2* are 43° and 53° , respectively. Blue-fluorescence photons are collected by a fiber bundle with the efficiency of 0.02 and then guided to a photomultiplier tube (PMT) through a 420-nm interference filter (IF) with the bandwidth of 7 nm.

Figure 26.35 shows a fluorescence spectrum plotted as a function of the frequency detuning of *LD2*, where the frequency of *LD1* is fixed to the $5S_{1/2}$, $F = 3 \rightarrow 5P_{3/2}$, $F = 4$ transition. The linewidth of each diode laser is below 1 MHz and the beam diameter is 2 mm. The intensities of *LD1* and *LD2* are 2.9 and 112 mW/cm^2 , respectively. The FWHM of the spectrum is 80 MHz. Note that the FWHM is narrower than the Doppler width of about 500 MHz. It is due to the configuration with two opposite light beams. The sub-Doppler profile is determined by the natural linewidths of the relevant transitions and the transit-time broadening originating from those atoms traverses the evanescent light.

Fig. 26.35 Sub-Doppler spectrum of 420-nm fluorescence. The intensity is plotted as a function of the frequency detuning of LD2, where LD1 is fixed to the $5S_{1/2}, F = 3 \rightarrow 5P_{3/2}, F = 4$ transition. The FWHM of the spectrum is 80 MHz

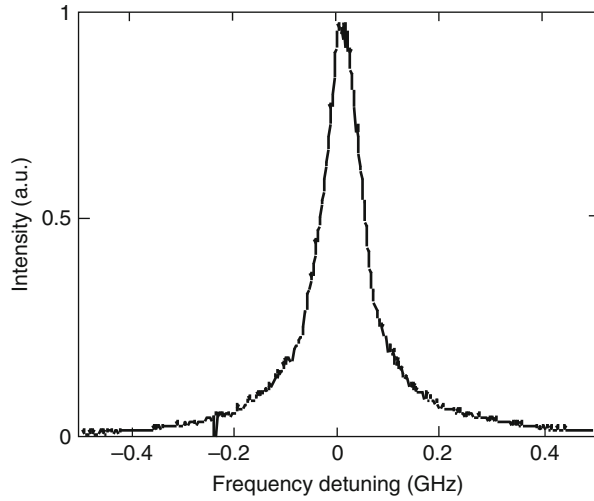
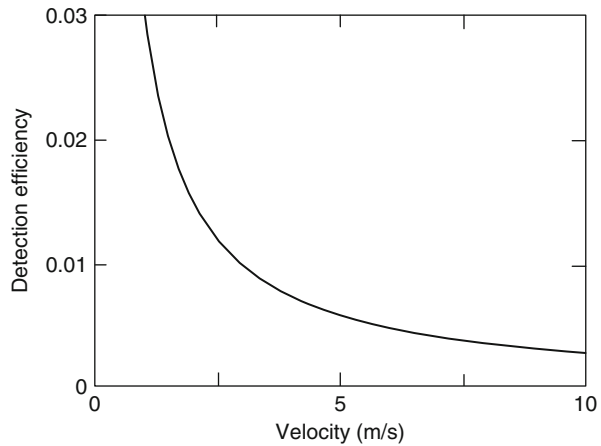


Fig. 26.36 Detection efficiency of Rb atoms plotted as a function of the atomic velocity



26.6.3 Detection Efficiency

If both the Rabi frequencies of the $5S_{1/2} \rightarrow 5P_{3/2}$ and $5P_{3/2} \rightarrow 5D_{5/2}$ transitions are the same and much larger than both the natural linewidths, the atomic decay from the $5P_{3/2}$ state does not occur, so that the occupation probability of the $5D_{5/2}$ state is a maximum of 0.5. Note that the $5P_{3/2}$ state is a so-called dark state. Since the density matrix elements with respect to the transitions from the $5S_{1/2}$ and $5D_{5/2}$ states are out of phase with each other, the $5P_{3/2}$ state is not occupied due to the destructive interference [91]. In this case, the blue-fluorescence emission occurs most frequently. From the fact that the rate of the $5D_{5/2} \rightarrow 6P_{3/2} \rightarrow 5S_{1/2}$ decay is $2.9 \times 10^5 \text{ s}^{-1}$, it follows that the blue fluorescence is emitted at a rate of $1.5 \times 10^5 \text{ s}^{-1}$. The collection efficiency of a lens with an NA exceeding 0.2 used here is 0.01,

and the quantum efficiency of the PMT is 0.2 for 420 nm. Then, the detection rate r_{bf} in the blue-fluorescence spectroscopy is estimated to be $3 \times 10^2 \text{ s}^{-1}$.

In the case where a Rb atom with a velocity of 1 m/s moves along a 100- μm -long slit, the interaction time t_{int} with near-field light is 1×10^{-4} s. Consequently, the detection efficiency is approximately $r_{\text{bf}} \times t_{\text{int}} = 0.03$. The detection efficiency is proportional to the interaction time. [Figure 26.36](#) shows the detection efficiency for slow Rb atoms. Although the detection efficiency is not necessarily high, it is sufficient for the deflection experiment using the slit-type deflector.

References

1. P. Gill, *Science* **294**, 1666 (2001)
2. I.A. Walmsley, M.G. Raymer, *Science* **307**, 1733 (2005)
3. C. Cohen-Tannoudji, J. Dupont-Roc, G. Grynberg, *Atom-Photon Interaction* (Wiley, New York, 1992)
4. P. Meystre, S. Stenholm (eds.), The mechanical effects of light. Special issue of *J. Opt. Soc. Am. B* **2**, 1707–1860 (1985)
5. S. Chu, C. Wieman (eds.), Laser cooling and trapping of atoms. Special issue of *J. Opt. Soc. Am. B* **6**, 2023–2278 (1989)
6. E. Arimondo, W.D. Phillips, F. Strumia (eds.), *Laser Manipulation of Atoms and Ions* (North-Holland, Amsterdam, 1992)
7. V.G. Minogin, V.S. Letokhov, *Laser Light Pressure on Atoms* (Gordon and Breach Science Publishers, New York, 1987)
8. A.P. Kazantsev, G.I. Surdutovich, V.P. Yakovlev, *Mechanical Action of Light on Atoms* (World Scientific, Singapore, 1990)
9. E.L. Raab, M. Prentiss, A. Cable, S. Chu, D.E. Pritchard, *Phys. Rev. Lett.* **59**, 2631 (1987)
10. C. Monroe, W. Swann, H. Robinson, C. Wieman, *Phys. Rev. Lett.* **65**, 1571 (1990)
11. C.N. Cohen-Tannoudji, W.D. Phillips, *Phys. Today* **43**(10), 33 (1990)
12. H.J. Metcalf, P. van der Straten, *Laser Cooling and Trapping* (Springer, New York, 1999)
13. J.W.R. Tabosa, G. Chen, Z. Hu, R.B. Lee, H.J. Kimble, *Phys. Rev. Lett.* **66**, 3245 (1991)
14. P.S. Jessen, I.H. deutsch, Optical lattices, in *Advances in Atomic, Molecular, and Optical Physics*, vol. 37, ed. by B. Bederson, H. Walther (Academic, San Diego, 1996), pp. 95–138
15. P.S. Julienne, A.M. Smith, K. Burnett, Theory of collisions between laser cooled atoms, in *Advances in Atomic, Molecular, and Optical Physics*, vol. 30, ed. by D.B. Bates, B. Bederson (Academic, San Diego, 1992), pp. 141–198
16. T. Walker, P. Feng, Measurements of collisions between laser-cooled atoms, in *Advances in Atomic, Molecular, and Optical Physics*, vol. 34, ed. by B. Bederson, H. Walther (Academic, San Diego, 1994), pp. 125–170
17. J. Weiner, Advances in ultracold collisions: experimentation and theory, in *Advances in Atomic, Molecular, and Optical Physics*, vol. 35, ed. by B. Bederson, H. Walther (Academic, San Diego, 1995), pp. 45–78
18. M.A. Kasevich, E. Riis, S. Chu, R.G. Devoe, *Phys. Rev. Lett.* **63**, 612 (1989)
19. C.S. Adams, O. Carnal, J. Mlynek, Atom interferometry, in *Advances in Atomic, Molecular, and Optical Physics*, vol. 34, ed. by B. Bederson, H. Walther (Academic, San Diego, 1994), pp. 1–34
20. P.R. Berman (ed.), *Atom Interferometry* (Academic, San Diego, 1997)
21. J. Fujita, M. Morinaga, T. Kishimoto, M. Yasuda, S. Matsui, F. Shimizu, *Nature* **380**, 691 (1996)
22. F. Shimizu, Atom holography, in *Advances in Atomic, Molecular, and Optical Physics*, vol. 42, ed. by B. Bederson, H. Walther (Academic, San Diego, 2000), pp. 182–260

23. M.Z. Raizen, Quantum chaos with cold atoms, in *Advances in Atomic, Molecular, and Optical Physics*, vol. 41, ed. by B. Bederson, H. Walther (Academic, San Diego, 1999), pp. 43–82
24. M.R. Anderson, J.R. Ensher, M.R. Matthews, C.E. Wieman, E.A. Cornell, *Science* **269**, 198 (1995)
25. M. Inguscio, S. Stringari, C.E. Wieman (eds.), *Bose-Einstein Condensation in Atomic Gases* (IOS, Amsterdam, 1999)
26. C.J. Pethick, H. Smith, *Bose-Einstein Condensation in Dilute Gases* (Cambridge University Press, Cambridge, 2002)
27. M.R. Andrews, C.G. Townsend, H.-J. Miesner, D.S. Durfee, D.M. Kurn, W. Ketterle, *Science* **275**, 637 (1997)
28. C. Cohen-Tannoudji, Atomic motion in laser light, in *Fundamental Systems in Quantum Optics*, ed. by J. Dalibard, J.M. Raimond, J. Zinn-Justin (Elsevier, Amsterdam, 1992), pp. 1–164
29. V.I. Balykin, V.S. Letokhov, *Atom Optics with Laser Light* (Harwood Academic, Chur, 1995). Chapter 4
30. P. Meystre, *Atom Optics* (Springer, New York, 2001)
31. C.M. Savage, S. Marksteiner, P. Zoller, Atomic waveguides and cavities from hollow optical fibers, in *Fundamentals of Quantum Optics III*, ed. by F. Ehlotzky (Springer, Berlin, 1993), pp. 60–74
32. S. Marksteiner, C.M. Savage, P. Zoller, S.L. Rolston, *Phys. Rev. A* **50**, 2680 (1994)
33. H. Ito, K. Sakaki, T. Nakata, W. Jhe, M. Ohtsu, *Opt. Commun.* **115**, 57 (1995)
34. H. Ito, K. Sakaki, T. Nakata, W. Jhe, M. Ohtsu, *Ultramicroscopy* **61**, 91 (1995)
35. M.J. Renn, E.A. Donley, E.A. Cornell, C.E. Wieman, D.Z. Anderson, *Phys. Rev. A* **53**, R648 (1996)
36. H. Ito, T. Nakata, K. Sakaki, W. Jhe, M. Ohtsu, *Phys. Rev. Lett.* **76**, 4500 (1996)
37. H. Ito, K. Sakaki, W. Jhe, M. Ohtsu, *Opt. Commun.* **141**, 43 (1997)
38. J.P. Dowling, J. Gee-Banaclouche, Evanescent light-wave atom mirrors, resonators, waveguides, and traps, in *Advances in Atomic, Molecular, and Optical Physics*, vol. 37, ed. by B. Bederson, H. Walther (Academic, San Diego, 1996), pp. 1–94
39. V.I. Balykin, Atom waveguide, in *Advances in Atomic, Molecular, and Optical Physics*, vol. 41, ed. by B. Bederson, H. Walther (Academic, San Diego, 1999), pp. 182–260
40. K. Sengstock, W. Ertmer, Laser manipulation of atoms, in *Advances in Atomic, Molecular, and Optical Physics*, vol. 35, ed. by B. Bederson, H. Walther (Academic, San Diego, 1995), pp. 1–34
41. G. Timp, R.E. Behringer, D.M. Tennant, J.E. Cunningham, M. Prentiss, K.K. Berggren, *Phys. Rev. Lett.* **69**, 1636 (1992)
42. M. Prentiss, G. Timp, N. Bigelow, R.E. Behringer, J.E. Cunningham, *Appl. Phys. Lett.* **60**, 1027 (1992)
43. J.J. McClelland, R.E. Scholten, E.C. Palm, R.J. Celotta, *Science* **262**, 877 (1993)
44. R. Gupta, J.J. McClelland, Z.J. Jabbour, R.J. Celotta, *Appl. Phys. Lett.* **67**, 1378 (1995)
45. R.W. McGowan, D.M. Giltner, S.A. Lee, *Opt. Lett.* **20**, 2535 (1995)
46. W.R. Anderson, C.C. Bradley, J.J. McClelland, R.J. Celotta, *Phys. Rev. A* **59**, 2476 (1999)
47. Th. Schulze, T. Mütter, D. Jürgens, B. Brezger, M.K. Oberthaler, T. Pfau, J. Mlynek, *Appl. Phys. Lett.* **78**, 1781 (2001)
48. E. Jurdik, J. Hohlfeld, H. van Kempen, Th. Rasing, J.J. McClelland, *Appl. Phys. Lett.* **80**, 4443 (2002)
49. K.K. Berggren, A. Bard, J.L. Wilbur, J.D. Gillaspay, A.G. Helg, J.J. McClelland, S.L. Rolston, W.D. Phillips, M. Prentiss, G.M. Whitesides, *Science* **269**, 1255 (1995)
50. K.S. Johnson, K.K. Berggren, A. Black, C.T. Black, A.P. Chu, N.H. Dekker, D.C. Raiph, J.H. Thywissen, R. Younkin, M. Tinkham, M. Prentiss, G.M. Whitesides, *Appl. Phys. Lett.* **69**, 2773 (1996)
51. M. Ohtsu, *J. Lightwave Technol.* **13**, 1200 (1995)
52. M. Ohtsu, H. Hori, *Near-Field Nano-Optics* (Kluwer/Plenum, New York, 1999). Chapter 8
53. K. Kobayashi, M. Ohtsu, *J. Microsc.* **194**, 249 (1999)

54. M. Ohtsu, K. Kobayashi, H. Ito, G.-H. Lee, Proc. IEEE **88**, 1499 (2000)
55. H. Ito, K. Totsuka, M. Ohtsu, Atom deflector and detector with near-field light, in *Progress in Nano-Electro Optics II*, ed. by M. Ohtsu (Springer, Berlin, 2003), pp. 149
56. K. Kobayashi, S. Sangu, H. Ito, M. Ohtsu, Effective probe-sample interaction: toward atom deflection and manipulation, in *Near-Field Optics: Principles and Applications, 2nd Asia-Pacific Workshop on Near Field Optics, 2000*, vol. 82 ed. by X. Zhu, M. Ohtsu (World Scientific, Singapore, 2000), pp. 82–88
57. K. Kobayashi, S. Sangu, H. Ito, M. Ohtsu, Phys. Rev. A **63**, 013806 (2001)
58. H. Ito, K. Sakaki, M. Ohtsu, W. Jhe, Appl. Phys. Lett. **70**, 2496 (1997)
59. T. Yatsui, M. Kourogi, K. Tsutsui, M. Ohtsu, J. Takahashi, Opt. Lett. **25**, 1279 (2000)
60. K. Totsuka, H. Ito, K. Suzuki, K. Yamamoto, M. Ohtsu, T. Yatsui, Appl. Phys. Lett. **82**, 1616 (2003)
61. H. Ito, K. Yamamoto, A. Takamizawa, H. Kashiwagi, T. Yatsui, J. Opt. A Pure Appl. Opt. **8**, S153 (2006)
62. H. Ito, M. Ohtsu, Near-field optical atom manipulation: toward atom photonics, in *Near-Field Nano/Atom Optics and Technology*, ed. by M. Ohtsu (Springer, Tokyo, 1998). Chapter 11
63. K. Totsuka, H. Ito, T. Kawamura, M. Ohtsu, Jpn. J. Appl. Phys. **41**, 1566 (2002)
64. H.U. Danzebrink, Th. Dziomba, T. Sulzbach, O. Ohlsson, C. Lehrer, L. Frey, J. Microsc. **194**, 335 (1999)
65. R.G. Newton, *Scattering Theory of Waves and Particles*, 2nd edn. (Springer, New York, 1982)
66. M. Chevrollier, M. Fichet, M. Oria, G. Rahmat, D. Bloch, M. Ducloy, J. Phys. II France **2**, 631 (1992)
67. W. Jhe, J.W. Kim, Phys. Rev. A **51**, 1150 (1995)
68. H. Nha, W. Jhe, Phys. Rev. A **54**, 3505 (1996)
69. A. Steane, P. Szriftgiser, P. Desbiolles, J. Dalibard, Phys. Rev. Lett. **74**, 4972 (1995)
70. P.A. Molenaar, P. van der Straten, H.G.M. Heideman, H. Metcalf, Phys. Rev. A **55**, 605 (1997)
71. J. Söding, R. Grimm, Yu.B. Ovchinnikov, Opt. Commun. **119**, 652 (1995)
72. Ch. Kurtsiefer, J. Mlynek, Appl. Phys. B **64**, 85 (1997)
73. S. Datz, E.H. Taylor, J. Chem. Phys. **25**, 389 (1956)
74. M.D. Scheer, J. Fine, J. Chem. Phys. **39**, 1752 (1963)
75. T. Sato, H. Ito, J. Nanophoton. **1**, 011560 (2007)
76. A.A. Tseng, K. Chen, C.D. Chen, K.J. Ma, IEEE Trans. Electron. Packag. Manuf. **26**, 141 (2003)
77. A. Taflove, S.C. Hagness, *Computational Electrodynamics: The Finite-Difference Time-Domain Method*, 2nd edn. (Artech House, Boston, 2000)
78. P.-K. Wei, H.-Li. Chou, W.-S Fann, Opt. Express **10**, 1418 (2002)
79. C.H. Wei, P.H. Tsao, W.-S Fann, P.-K. Wei, J.O. Tegenfeldt, R.H. Austin, J. Opt. Soc. Am. B **21**, 1005 (2004)
80. K. Yamamoto, H. Ito, K. Totsuka, T. Sato, Opt. Commun. **265**, 692 (2006)
81. T. Sato, H. Ito, J. Nanophoton. **5**, 053501 (2011)
82. V.S. Letokhov, *Laser Photoionization Spectroscopy* (Academic, San Diego, 1987)
83. N. Amin, S. Mahmood, M. Saleem, M.A. Kalyar, M.A. Baig, Eur. Phys. J. D **40**, 331 (2006)
84. C.E. Burkhardt, J.L. Libbert, J. Xu, J.J. Leventhal, Phys. Rev. A **38**, 5949 (1988)
85. N. Amin, S. Mahmood, S.U. Haq, M.A. Kalyar, M. Rafiq, M.A. Baig, J. Quant. Spectrosc. Radiat. Transf. **109**, 863 (2008)
86. B.M. Patterson, T. Takekoshi, R.J. Knize, Phys. Rev. A **59**, 2508 (1999)
87. Y. Ohdaira, K. Kijima, K. Terasawa, M. Kawai, H. Hori, K. Kitahara, J. Microsc. **202**, 255 (2001)
88. F.de Fornel, *Evanescent Waves* (Springer, Berlin, 2001), p. 9
89. W. Seifert, C.S. Adams, V.I. Balykin, C. Heine, Yu. Ovchinnikov, J Mlynek, Phys. Rev. A **49**, 3814 (1994)
90. K. Totsuka, H. Ito, M. Ohtsu, IEICE Trans. Electron. **E85-C**, 2093 (2002)
91. M.O. Scully, M.S. Zubairy, *Quantum Optics* (Cambridge University Press, Cambridge, 1997). Chapter 7

Lee Chuin Chen, Hirokazu Hori, and Kenzo Hiraoka

Contents

27.1	Introduction.....	1018
27.1.1	Matrix-Assisted Laser Desorption/Ionization Mass Spectrometry	1019
27.1.2	Laser Desorption/Ionization with Inorganic Matrix and Nanostructure.....	1021
27.1.3	Time-of-Flight Mass Spectrometry.....	1021
27.2	Surface Plasmon-Polariton.....	1022
27.2.1	Plasmon-Induced Desorption.....	1024
27.3	Fabrication of Gold Nanostructure Substrates.....	1025
27.3.1	Fabrication of Gold-Coated Porous Silicon.....	1026
27.3.2	Gold Nanorod Arrays.....	1029
27.4	Experimental Details.....	1032
27.4.1	Time-of-Flight Mass Spectrometer.....	1032
27.4.2	Sample Preparation.....	1034
27.5	Laser Desorption/Ionization (LDI) with Gold Nanostructure.....	1034
27.5.1	LDI with Gold-Coated Porous Silicon.....	1034
27.5.2	LDI with Gold Nanorods.....	1036
27.5.3	Gold Nanoparticle-Assisted Excitation of UV-Absorbing MALDI Matrix by Visible Laser.....	1041
27.6	Discussion and Future Prospect.....	1052
	References.....	1054

Abstract

This chapter describes the use of plasmonic substrates for the laser desorption/ionization in mass spectrometry. Interesting phenomenon such as polarization and wavelength dependence has been observed for the laser

L.C. Chen (✉) · H. Hori

Interdisciplinary Graduate School of Medicine and Engineering, University of Yamanashi, Yamanashi, Japan

e-mail: leechuin@yamanashi.ac.jp; hirohori@yamanashi.ac.jp

K. Hiraoka

Clean Energy Research Center, University of Yamanashi, Yamanashi, Japan

e-mail: hiraoka@yamanashi.ac.jp

M. Ohtsu (ed.), *Handbook of Nano-Optics and Nanophotonics*,

DOI 10.1007/978-3-642-31066-9_28, © Springer-Verlag Berlin Heidelberg 2013

1017

desorption/ionization of molecules from gold-coated porous silicon, gold nanorod arrays, and nanoparticles, and these results suggest the presence of near-field effects on the desorption/ionization process.

27.1 Introduction

Mass spectrometry is an indispensable tool for biochemistry and life science, and it offers the analytical information such as sample composition which is not available from other analytical techniques. The basic principle of mass spectrometry is to generate ions from the inorganic or organic compound and to separate these ions according to their mass-to-charge ratio (m/z). To mass analyze the sample, analyte molecules need to be electrically charged. Thus, ion source is one of the key parts in a mass spectrometer. The analyte may be ionized by a variety of methods, for example, electron ionization [1], field ionization [2], field desorption [3], chemical ionization [4], electrospray ionization [5], and laser-based desorption/ionization. At present, large biomolecules such as proteins and peptides are analyzed exclusively using electrospray ionization (ESI, developed by John Fenn in 1989) and matrix-assisted laser desorption/ionization (MALDI, developed by Koichi Tanaka and Franz Hillenkam [6, 7]).

When the nanostructured surface of metal of high conductivity, for example, gold, is irradiated with laser of certain wavelength at appropriate polarization, collective electron motion, known as localized surface plasmon-polariton oscillation, will be excited. The localized surface plasmon-polariton resonance leads to enhanced photon absorption and huge concentration of optical near-fields at a small volume, which contribute to the enhancement in the surface-enhanced spectroscopy. Although intensive research on the plasmonic electronics and plasmon biosensing is in progress [8, 9], there is little work on the exploitation of the plasmon effect in the desorption/ionization of biomolecule for mass spectrometry. In this chapter, we describe the visible laser desorption/ionization of biomolecules using nanostructured plasmonic substrates.

Three types of nanostructured substrates are described here: gold-coated porous silicon, gold nanorods, and gold nanoparticles. The porous silicon made by electrochemical etching was coated with gold using argon ion sputtering. The gold nano-rod arrays were fabricated by electrodepositing the gold into the porous alumina template and the subsequent partial removal of the alumina template. A frequency-doubled Nd:YAG laser was used to irradiate gold nanostructured substrate, and the desorbed molecular ions were mass analyzed by a time-of-flight mass spectrometer. The present technique offers a potential analytical method for the low molecular weight analytes which are rather difficult to handle in the conventional matrix-assisted laser desorption/ionization (MALDI) mass spectrometry. With the presence of Au nanoparticles, the UV-MALDI matrix was also found to be photoionized by the 532 nm laser even though the photon energy is insufficient for free molecules.

27.1.1 Matrix-Assisted Laser Desorption/Ionization Mass Spectrometry

For laser mass spectrometry, matrix-assisted laser desorption/ionization (MALDI) is a very effective and soft method in obtaining mass spectra for synthetic and biological samples, such as peptides and proteins with less molecular fragmentation [6, 7]. Depending on the matrices, laser wavelengths of ultraviolet (UV) and infrared have been employed. The established UV-MALDI method usually employs a nitrogen laser (337 nm), or a frequency-tripled Nd:YAG laser (355 nm) for desorption/ionization, while the Er:YAG lasers (2.94 μm) and CO₂ (10.6 μm) are used in the IR-MALDI.

In MALDI, biomolecular analytes are mixed with photo-absorbing chemical matrix of suitable functional groups to assist the energy transfer. Thus, the matrix molecules must possess suitable chromophores to absorb the laser photons efficiently. Besides having high optical absorption coefficients, matrix molecules must possess suitable chemical properties for efficient ionization. All of the matrices that act as protonating agents for analytes contain OH and/or NH₂ functional groups. Thus, protons are believed to be transferred from these groups during the ionization process.

Nicotinic acid (NA) was historically the first UV-MALDI matrix for successful detection of peptides and proteins. Ever since, many other better matrices, for example, 2,5-dihydroxybenzoic acid (DHB) and α -cyano-4-hydroxycinnamic acid (CHCA), had also been found. As for IR-MALDI, the laser wavelength of $\sim 3 \mu\text{m}$ effectively excites the O–H and N–H stretch vibration of the molecules, while the laser wavelength of $\sim 10 \mu\text{m}$ causes the excitation of C–O stretch and O–H bending vibration [10, 11]. Molecular structures of typical MALDI matrices are shown in Fig. 27.1.

Except for the light-absorbing analytes, direct photoionization of macromolecules rarely takes place, and the peptides and protein ions observed in laser

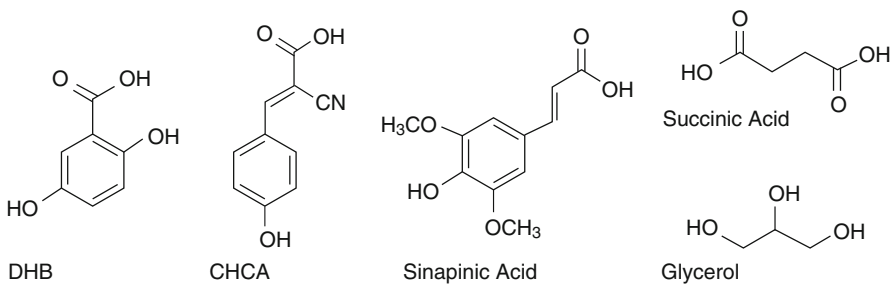


Fig. 27.1 Commonly used MALDI matrices. 2,5-Dihydroxybenzoic acid (DBD), α -cyano-4-hydroxycinnamic acid (CHCA), and sinapinic acid are for UV-MALDI. Succinic acid and glycerol are for IR-MALDI. Glycerol is also used as liquid matrix incorporation with UV-absorbing material (e.g., metallic nano powder, graphite) for UV-MALDI

Table 27.1 Ions produced by LDI/MALDI

Ion species	Positive ions	Negative ions
Radical	$M^{+\bullet}$	$M^{-\bullet}$
Protonated/deprotonated	$[M + H]^+$	$[M - H]^+$
Alkali adducts	$[M + Na]^+$, $[M + K]^+$, etc.	
Cluster	$n[M + H]^+$	$n[M - H]^-$
Multiple charged	$[M + 2H]^{2+}$, $[M + 2Na]^{2+}$, etc.	$[M - 2H]^{2-}$

desorption/ionization are mostly protonated (molecular ions generated by proton attachment, e.g., $[M + H]^+$). For the analytes such as underivatized carbohydrates, due to their poor proton affinity, the molecules are difficult to be protonated and instead are mostly ionized by alkali metal attachment, for example, $[M + Na]^+$ and $[M + K]^+$ [12]. Typical ion species produced by LDI/MALDI are listed in Table 27.1.

The typical laser fluences in UV-MALDI are in the range of 10–100 mJ cm⁻¹, which correspond to 10⁶–10⁷ W cm⁻² for a pulsed laser of 10 ns pulse width. For IR-MALDI, the required fluence is somewhat 10 times higher than that of UV-MALDI. At the laser threshold, a sharp onset of desorption/ionization takes place. The threshold laser fluence depends on the type of matrix as well as the matrix-to-analyte mixing ratio. The mixing ratio of 5,000 is usually used in MALDI. Although the detailed desorption/ionization mechanism of MALDI had not been thoroughly understood, it is generally believed that the radical ions of the matrix molecules produced by either two-photon ionization or the molecular exciton pooling played crucial roles in ionizing the desorbed analytes via gas-phase interaction [13, 14].

Common UV-MALDI matrices have a wider absorption band than that of IR-MALDI, and the desorption/ionization performance is less affected by photon energies over a certain range of UV wavelength [15, 16]. However, restricted by their optical absorption coefficients, the UV and IR-MALDI matrices do not work with visible or near-IR lasers.

Early investigations on visible-MALDI (VIS-MALDI) were conducted by Tang et al. using rhodamine dyes as matrices [17]. Cornett et al. introduced a binary matrix consisted of rhodamine 6G which was dissolved in a liquid matrix (3-nitro-benzylalcohol) for VIS-MALDI with 532 nm frequency-doubled Nd:YAG laser [18]. Since the liquid matrix is transparent to the visible laser, the optical absorption was due to the dye, and the method is similar to the two-phase matrix method of Tanaka et al. in which the laser energy was absorbed by metal nanoparticles suspended in the liquid glycerol. Other VIS-MALDI studies were performed using Neutral Red [19], 2-amino-3-nitrophenol [20], and rhodamine 575 [21].

Despite their high optical absorption at the visible wavelength, the ionization efficiency with these VIS-MALDI matrices is not as efficient as that with UV-MALDI matrices. Suitable chemical matrix for visible laser has not been found

thus far, and the existing UV-MALDI matrices are not accessible by the laser wavelength ranging from 400 nm to $\sim 2.7 \mu\text{m}$ [22].

27.1.2 Laser Desorption/Ionization with Inorganic Matrix and Nanostructure

Although MALDI is highly sensitive for large biomolecules ($>700\text{Da}$), the detection for analytes of low molecular weight is rather difficult due to the matrix interferences. Thus, in the low mass range, direct laser desorption/ionization (LDI) on surface modified substrates or the use of inorganic matrices becomes alternatives to chemical MALDI. The use of nanoparticles as efficient UV-absorbing matrices was first introduced by Tanaka et al. [6], of which 30 nm cobalt powders were suspended in glycerol solution. A variety of nanomaterials, for example, titanium nitride [22], zinc oxide and titanium oxide [23], and gold nanoparticles [24], had been proposed as inorganic matrices.

Direct LDI on various substrates, for example, graphite [25], silicon, titania sol-gel [26], and metal-coated porous alumina [27], has also been studied. In particular, porous silicon, which has high absorption in the ultraviolet region, has received considerable attention due to its reported high sensitivity [28, 29]. Such method is named as desorption/ionization on silicon (DIOS). Other silicon-based substrates include silicon nanowires [30], column/void silicon network [31], nano-grooves [27], and nano-cavities [32]. Matrix-less IR laser desorption/ionization was also reported on flat silicon surface [33].

27.1.3 Time-of-Flight Mass Spectrometry

Molecular ions can be analyzed by a number of different instruments, for example, time-of-flight mass spectrometer (TOF-MS), magnetic sector mass spectrometer, quadrupole ion trap mass spectrometer (QIT-MS), and Fourier transform ion cyclotron resonance mass spectrometer (FT-ICR-MS) [10, 11]. In particular, the TOF-MS is used almost exclusively for ions produced by laser desorption/ionization. The ions generated upon the irradiation of pulsed laser are separated during their flight along the field-free path and arrive at the detector at different time depending on their m/z . The flight time is given as

$$t = \frac{L}{\sqrt{2eU}} \sqrt{\frac{m}{z}} \quad (27.1)$$

where e is the electron charge, L is the flight tube length, and U is the accelerating voltage. Equation 27.1 can be converted to $m/z = 2eU(t/L)^2 = At^2$, where A is the calibration constant which is determined by least squares fitting of this equation to a series of known m/z peak and their measured arrival time. To account for

the other effects, say, electronic delay, a second calibration constant, B is usually introduced, and the calibration equation becomes [10]

$$m/z = At^2 + B \quad (27.2)$$

For TOF-MS, the initial ion velocity produced from the laser plume and the initial position of the generated ions can contribute to the measurement errors and reduce the resolution of the instrument. To certain extent, the initial velocities' effect can be reduced by using the delayed extraction, in which the accelerating voltage is applied only after certain time interval (typically tens to hundreds ns) after the laser pulse [10]. The initial velocity/energy distribution can also be compensated by using an ion reflector or reflectron. The TOF mass spectrometers used in our experiment are equipped with both reflectron and delayed ion extraction.

27.2 Surface Plasmon-Polariton

Surface plasmon-polariton is the collective oscillation of electron density on the metal surface [34]. At surface plasmon-polariton resonance, all the free electrons within the conduction band oscillate in phase and lead to a huge concentration of optical near-field at a small volume (Fig. 27.2). The localized electronic oscillation which is coupled with the optical near-field is usually referred as localized plasmon-polariton.

For the nanoparticles of noble metal, for example, silver and gold, the surface plasmon-polariton resonance takes place at the visible light, and their optical properties can be described by the Mie-extinction, σ_{ext} , and

$$\sigma_{ext} = \sigma_{abs} + \sigma_{sca} \quad (27.3)$$

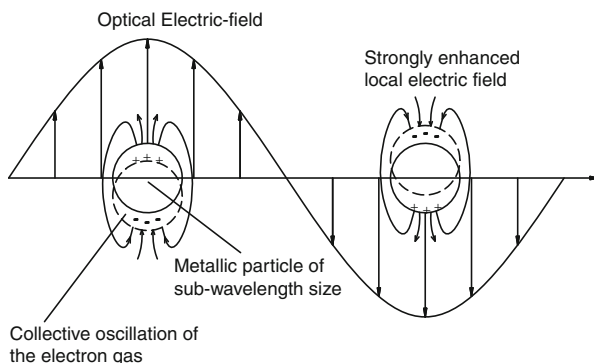
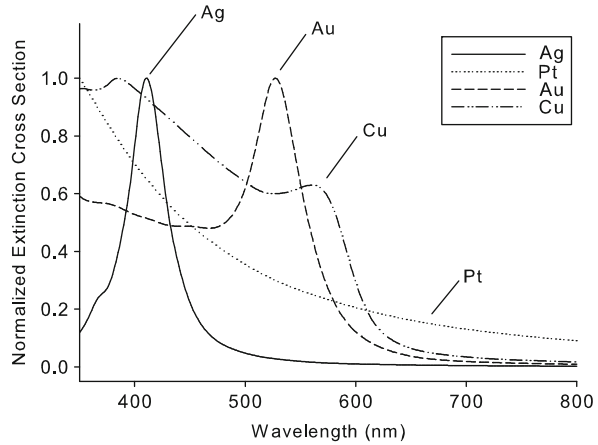


Fig. 27.2 The plasmon-polariton oscillation of metallic particles which have diameter much smaller than the wavelength under the illumination of polarized optical wave

Fig. 27.3 Normalized extinction cross section for various noble metals' nanoparticles: gold (*Au*), silver (*Ag*), copper (*Cu*), and platinum (*Pt*)



where σ_{abs} , and σ_{sca} are the absorption and scattering cross section, respectively. Figure 27.3 shows the calculated normalized extinction cross section of the nanoparticles for various noble metals. The particles diameter is assumed to be 40 nm, and the Mie-extinction [35, 36] is solved numerically. For gold, silver, and copper, the nanoparticles have unique absorption bands in the visible region (see Fig. 27.3), and they can be easily identified by the color of their scattered light. The intense red color of the aqueous dispersion of the colloidal gold nanoparticles is the manifestation of the localized surface plasmon-polariton resonance, which peaks at ~ 520 nm.

For the nanoparticles which are much smaller than the exciting optical wavelength ($r \ll \lambda$, where r is the radius of the nanoparticle and λ is the optical wavelength), the extinction cross section is primarily due to the dipole oscillation, and the Mie theory reduces to dipole approximation [37, 38]:

$$\sigma_{ext}(\omega) = 9 \frac{\omega}{c} \varepsilon_m^{3/2} V \frac{\varepsilon_2(\omega)}{[\varepsilon_1(\omega) + 2\varepsilon_m]^2 + \varepsilon_2(\omega)^2} \quad (27.4)$$

where $V = \frac{4}{3}\pi r^3$, ω is the angular frequency of the exciting light, c is the speed of light, $\varepsilon(\omega) = \varepsilon_1(\omega) + i\varepsilon_2(\omega)$ is the dielectric function of the nanoparticles, and ε_m is dielectric function of the surrounding medium. The resonance condition for surface plasmon-polariton is fulfilled when

$$\varepsilon_1(\omega) = -2\varepsilon_m \quad (27.5)$$

if $\varepsilon_2(\omega)$ is small or weakly dependent on ω [37].

The surface plasmon-induced electromagnetic field enhancement on the metallic nanoparticles had been known to be accountable for the surface-enhanced Raman spectroscopy (SERS) [39], and nonlinear optical response such as second harmonic

generation [40], and optical frequency mixing [41]. Besides electromagnetic enhancement, the metal-absorbates' electronic coupling had also been known to have contributed to the chemical enhancement for SERS [42, 43]. Upon absorption on the metal surface, the interaction between the absorbate molecules and the electron gas on the metal surface results in the broadening and shifting in energy of the free molecular states [42]. Thus, even though the states' transition of the free molecule may be too energetic to be excited by, say, a visible laser, a near resonance could be found for the laser once the molecule is adsorbed on the metal surface.

The exploitation of localized surface plasmon-polariton resonance using ordered nanoparticle arrays and aggregates includes optical near-field lithography [44] and plasmonic waveguides [45]. Functionalized or conjugated gold nanoparticles, which have high binding affinity to specific analytes, are used for biosensing [46] and DNA detection [47]. Selective laser photothermal therapy using nanoparticles had also been proposed for cancer treatment [48].

27.2.1 Plasmon-Induced Desorption

Desorption of Metallic Ions Because the surface plasmon resonance is strongly damped, the local heating which is due to the joule losses on the metal surface could take place. For the gold nanoparticles which have small heat capacity, the heat transfer was estimated to be in the picosecond time scale, and the high lattice temperature can be reached rapidly [38]. However, due to the strong electron oscillation, the plasmon-induced nonthermal desorption had been reported for several metals. By irradiating the roughened silver surface with visible or near-ultraviolet laser, two prominent peaks were observed in the kinetic-energy distribution of Ag^+ ions produced from the surface [49].

In another experiment where the surface plasmon was coupled using the attenuated total reflection method, similar results were also obtained for the metal atoms desorbed from the Au, Al, and Ag films [50]. While the lower energy peak was generally referred as thermal peak, they attributed the peak of the higher kinetic energy to the nonthermal electronic process. Nonthermal visible laser desorption of alkali atoms was also reported for sodium particles and sodium film [51, 52]. Theoretical model that involves energy coupling of surface plasmon via ion collision had also been put forward to support the plasmon hypothesis [53].

Desorption of Absorbates On the metal surface, the adsorbed molecules produce physical or chemical bonding via, at least by part, interaction with the electron gas on the metal substrate. At plasmon resonance, due to the collective motion of electron gas, the strong optical near-field enhancement and associated strong modulation of electronic energy levels take place (Fig. 27.4).

This plasmonic process near the metallic surface produces the highly excited plasmonic sideband states due to the nonlinear optical effect. Regardless of the nature of the bonding between molecules and metallic substrate, the plasmonic

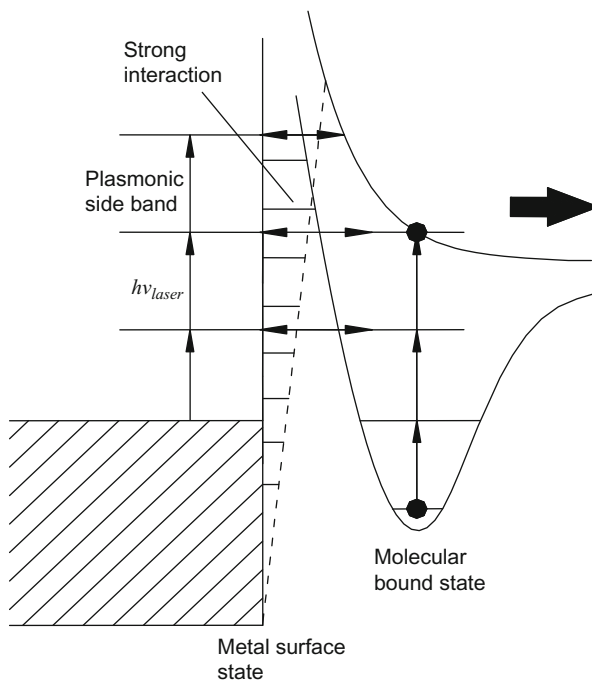


Fig. 27.4 Schematic diagram showing the possible process of plasmon-assisted desorption of adsorbates

sideband formation results in the optical near-field excitation of the bonding, and some of the highly excited bonding state can exert stochastic transition into the dissociation states of the absorbed molecules (see Fig. 27.4).

27.3 Fabrication of Gold Nanostructure Substrates

Although the gold nanoparticles, for example, gold colloids, have a strong optical extinction at ~ 520 nm due to the surface plasmon resonance, the colloids aggregate when mixed with certain analytes, and the plasmon frequency redshifts drastically to a longer wavelength. This poses a problem to a non-tunable laser for excitation. When used as the matrix, the chemical contents in the colloids' buffer solution can also contribute to the background noise. Instead of gold colloids, recently, we demonstrated the use of gold nanostructure for nonorganic matrix-based laser desorption/ionization [54, 55].

Two different substrates were tested in our experiments: gold-coated porous silicon and gold nanorod arrays. The porous silicon with random structure was used as the nanostructured template and was coated with gold using argon ion sputtering.

Depending on the type of the silicon, the nanostructure of the porous silicon can be tailored by the etching condition [56, 57].

The vertically aligned gold nanorod arrays, which had more regular surface morphology, were fabricated by electrodeposition of gold into the nanopores of the porous alumina template [58, 59]. The diameter of the gold nanorods follows the pores of the alumina template, and the aspect ratio can be controlled through the deposition time. The porous alumina template with ordered nanopore arrays can be easily fabricated using anodic oxidation. The pore diameter can be tuned from ~ 10 to 100 nm depending on the electrolyte and the anodization voltage [60, 61]. Compared to the colloids' aggregates and the electrochemically roughened surface, which are of random structure, the surface morphology of the gold nanorod arrays can be better controlled and fabricated reproducibly.

27.3.1 Fabrication of Gold-Coated Porous Silicon

Owing to their photoluminescence properties, the porous silicon has attracted considerable research interest since their first discovery by Canham [56]. Porous silicon can be fabricated easily using electrochemical etching. Depending on the type of silicon, etching parameters such as etching current, time, etchant concentration, and illumination are reported to affect the pore size and the porosity of the etched silicon [57].

Owing to their high UV absorption, porous silicon has also been used as substrate in direct UV-LDI (DIOS). Encouraged by the success of DIOS, the morphology of the porous silicon with random structure was used as the fabrication template and was coated with gold using argon ion sputtering. However, it is noted that in our experiment, the operating laser wavelength was different from that of DIOS.

Anodic Etching with Hydrofluoric Acid The porous silicon in our experiment was made by anodic etching of $0.02 \Omega \text{ cm}$ n-type silicon (Nilaco, Japan) using aqueous solution of $\sim 23 \text{ wt. \%}$ hydrofluoric acid (HF). The etching was conducted at $\sim 5 \text{ mA/cm}^2$ for 2 min under white light LED illumination. The etching was performed in a Teflon etching cell with platinum as the counter electrode. A super bright LED produced approximately 5 mW/cm^2 front illumination to the etching surface. Schematics in Fig. 27.5 show the electrochemical etching of the silicon using a Teflon etching cell. With illumination, macropores with diameter of 50–100 nm and pore depth of 100–200 nm were formed (microporous: dia. $< 2 \text{ nm}$, mesoporous: dia. = 2–50 nm, macroporous: dia. $> 50 \text{ nm}$).

Post-etching When the freshly etched porous silicon was coated with gold using argon ion sputtering coater, the pores appeared to be fully covered by the gold and lost its nanostructural identity. Such substrate produced no observable ion signal for most of the analytes for 532 nm laser irradiation. To increase the pore size, the freshly etched porous silicon was further treated with piranha ($\text{H}_2\text{SO}_4/\text{H}_2\text{O}_2 = 1/3$) for 4 min, followed by 10 % HF etching. The Piranha treatment oxidized the porous silicon lightly and formed a thin layer of silicon oxide. After stripped by 10 % HF, the pores were enlarged to 100–200 nm.

Fig. 27.5 Electrochemical etching of the silicon using Teflon etching cell

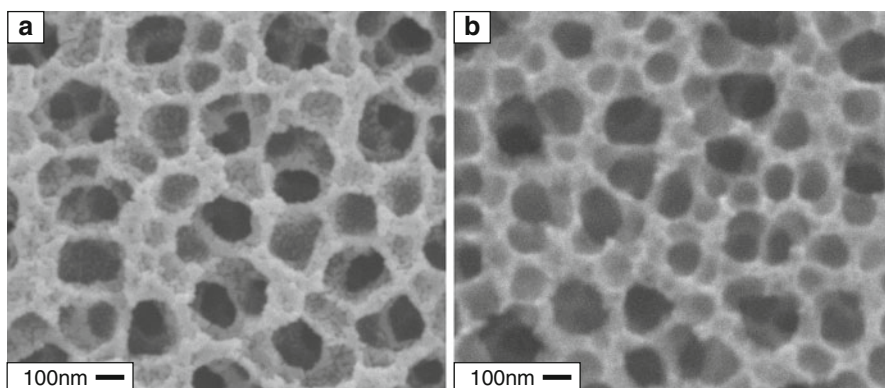
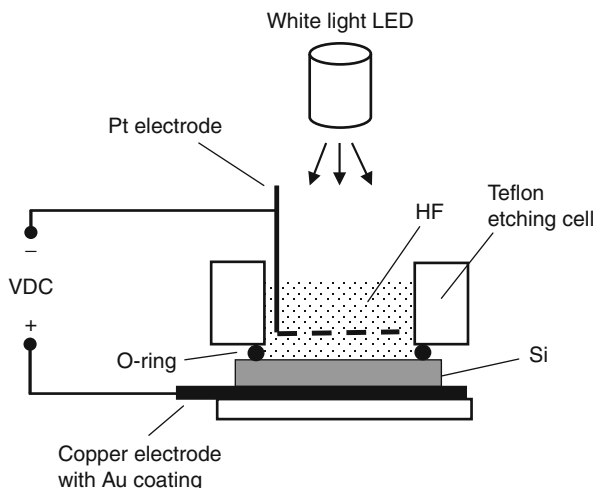


Fig. 27.6 Porous silicon (a) with ~ 15 nm gold coating and (b) without coating

Metallization of Porous Silicon The porous silicon was metallized with gold using argon ion sputtering coater with thickness control. The scanning electron microscopy inspection showed that the coating was not a continuous layer, and gold formed particles on the porous silicon structure with its size about the thickness of the coating. The porous silicon with and without gold coating is shown in Fig. 27.6. The cross-sectional view of the gold-coated porous silicon is depicted in Fig. 27.7. The depths of the irregular pore range are in the range of few hundreds of nm.

The coated surface had also been analyzed using Auger electron spectroscopy to confirm the complete coverage of gold on the porous silicon structure. The specular reflectivity of the gold-coated porous silicon is shown in Fig. 27.8. The measurement was made at normal incidence. The macroporous silicon is an efficient light trap, and it has high optical extinction extended to the visible region. After coated with

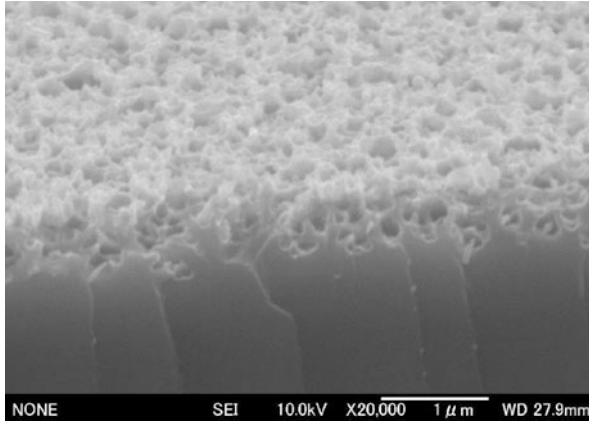


Fig. 27.7 SEM image showing the cross-sectional view of the gold-coated porous silicon. The depths of the irregular pore range are in the range of few hundreds of nm

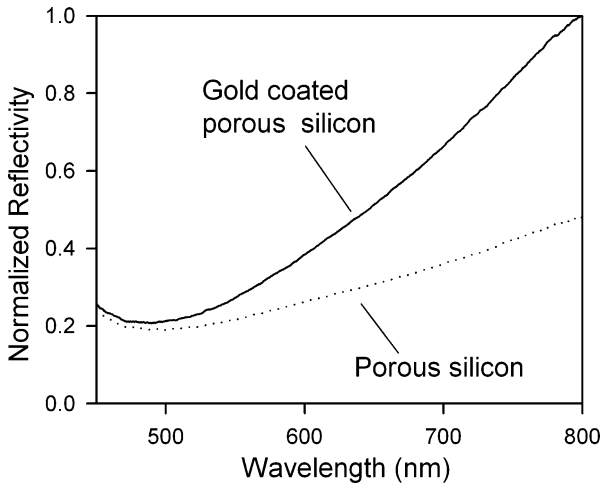


Fig. 27.8 Normalized reflectivity of porous silicon with and without gold coating

~10 nm gold, its reflectivity has increased significantly in the red and near-infrared region. However, the visible region of ~500 nm remained very much unchanged due to the surface plasmon-polariton resonance.

Throughout the experiment, the porous silicon was coated with 10 ~ 15 nm thick gold. The porous silicon of other different etching conditions had also been examined for their performance in desorption/ionization. Decreasing the etching current and the strength of light illumination reduced the pores' density, size, and depth, and the ion signals became weaker. Increasing the pore depth by longer etching time and current did not improve the ion yields.

27.3.2 Gold Nanorod Arrays

In order to have better understanding of the desorption/ionization from the metallic nanostructure, it is desirable to have substrates with more regular and better defined surface morphology. Lithography method offers the best control over the nanostructure size, shape, and spacing, but the techniques are expensive and with limited effective area. In comparison, template method is inexpensive and can be used to pattern a large area of surface.

Nanoporous anodic alumina has been a favorable template material or mask for fabricating nanoparticle arrays [62, 63]. With suitable electrolytes and appropriate anodization condition, a high density of ordered pores can be formed easily. The pore diameter can be tuned from ~ 10 to >100 nm by varying the anodization condition [60–62, 64]. Usually sulfuric acid is used for fabricating the alumina of pore size $10 \sim 20$ nm, whereas oxalic acid and phosphoric acid are used for bigger pore size. The pore size generally increases with the anodization voltage; however, the self-ordering takes place only under limited voltage condition.

Porous alumina membranes were first used by Martin et al. in the synthesis of gold nanorods [65, 66]. The Au was electrochemically deposited within the pores, and subsequently, the Au nanorods were released and re-dispersed into organic solvent, followed by polymer stabilization. Because the excessive use of organic chemicals and polymers (which are essential to stabilize the nanoparticles) would likely contribute to the background noise in the mass spectrum, a modified approach was adopted in this work.

Fabrication of Nanorod Arrays In our experiment, the embedded Au nanorods were partially released, and the nanorods were held by the template, preventing the aggregation of particle without using stabilizing agent. A schematic describing the fabrication processes is depicted in Fig. 27.9.

Aluminum sheet or the aluminum film coated on the glass or silicon substrate could be used as the starting material. Sulfuric acid (~ 20 wt.%) was used as the electrolyte for the anodic oxidation of aluminum. Platinum counter electrode was used in the anodic oxidation as well as in the electrodeposition of gold. The aluminum was oxidized at the anodization voltage of ~ 12 V for 5–10 min to form porous alumina. The pore diameter was in the range of ~ 15 nm. As shown in Fig. 27.9a, a thin barrier layer was also formed at the bottom of the pores. Although it was possible to remove the barrier layer using etching method, at ~ 12 V anodization voltage, the barrier was thin enough that the gold could be electrodeposited directly within the pores at moderate voltage. The aqueous solution of 40 mM chlorauric acid (HAuCl_4) was used as the working electrolyte. The pulsed electrodeposition was conducted at ~ 12 V with the duty cycle of 1/10 and pulse repetition rate of 1 s^{-1} . After several minutes, the deposited surface became ruby red in color, and the grown nanorods were embedded inside the porous alumina as illustrated in Fig. 27.9b.

It is noted that, the quality of the alumina template also depends on its initial surface roughness, and multiple anodizing steps are usually used to produce high-quality alumina template [63]. Occasionally, we oxidize the aluminum at

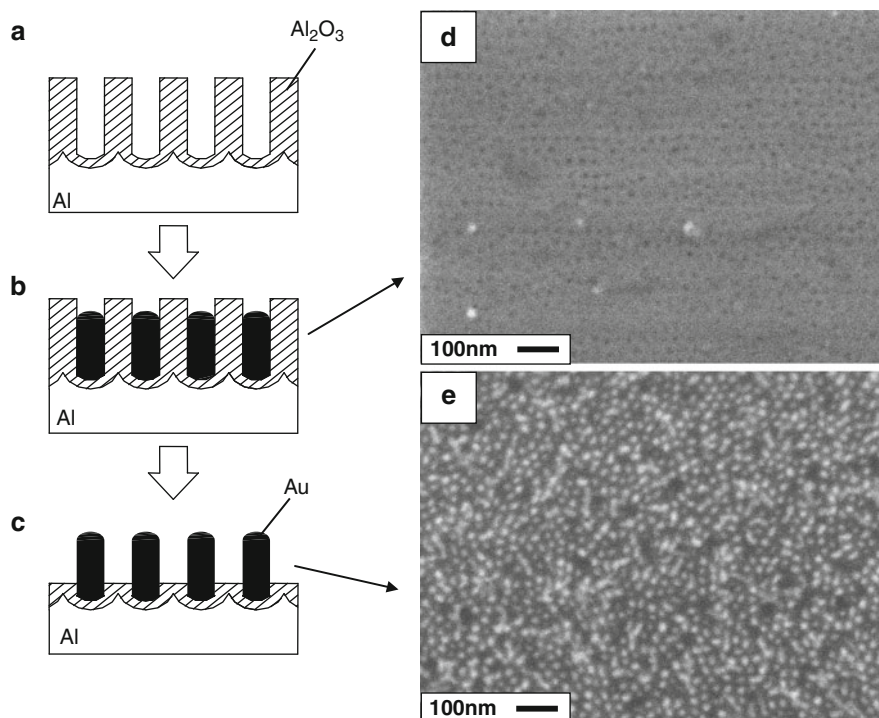


Fig. 27.9 Fabrication processes of the gold nanorods substrate. (a) Porous alumina (Al_2O_3) template fabricated by anodic oxidation using aqueous solution of ~ 20 wt.% sulfuric acid. (b) Pulsed electrodeposition of gold within the pores of the porous alumina. (c) Partial removal of the alumina template using aqueous solution of 8% v/v phosphoric acid. (d) The scanning electron micrograph of the porous alumina template embedded with gold nanorods. (e) The nanorods emerged after partial removal of the alumina template using aqueous solution of phosphoric acid

higher voltage (e.g., ~ 20 V) for a few minutes and gradually reduced anodization voltage to ~ 12 V. Higher anodization voltage had been known to produce more ordered and bigger nanopores [60, 61, 64]. Beginning the anodization with slightly higher voltage had been found to have more homogeneous deposition of gold onto the template.

Post-etching of the Alumina Template To trap the analyte molecules on the gold surface, the embedded nanorods were partially exposed to the surface (Fig. 27.9c) by chemical etching of the alumina template. The etching was done by using aqueous solution of ~ 8 % v/v phosphoric acid.

Figure 27.9d, e show the SEM micrographs of the porous alumina embedded with gold nanorods and the appearance of gold nanorods after partial removal of the alumina template, respectively. The diameter of the gold nanorods was ~ 15 nm, and the average lengths could be fabricated in the range of ~ 50 to ~ 200 nm depending

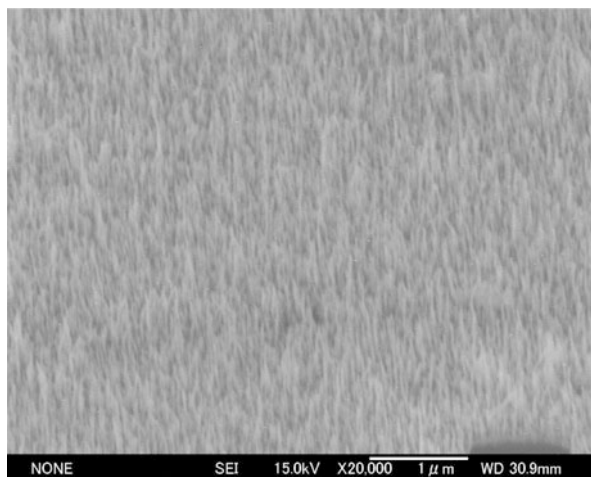


Fig. 27.10 SEM image of the gold nanorods viewed at 45° tilt angle

on the deposition condition. The SEM image of the fabricated gold nanorods viewed at 45° tilt angle is shown in Fig. 27.10.

All the rods were oriented at the same direction with their major (long) axis perpendicular to the surface. Thus, the oscillation direction of the localized plasmon resonance could be selectively excited by the TM- or TE-polarized light. The optical electric field was perpendicular to the substrate surface (i.e., along the major axis of the gold nanorods) when it was TM-polarized and vice versa when it was TE polarized. Unless otherwise stated, the standard substrate used in this study consisted of gold nanorods with length of ~ 100 nm and diameter of ~ 15 nm. **Reflectivity of Gold Nanorods** Figure 27.11 shows the normalized reflectivity of the gold nanorod substrate measured at normal incidence (light source not polarized). Compared to the porous silicon, the substrate consisted of vertically aligned gold nanorod arrays possesses a more regular surface morphology. Owing to its ordered structure, the reflectivity of the gold nanorod substrate shows a distinct optical absorption at ~ 520 nm, which coincides spectrally with the surface plasmon resonance of spherical nanoparticles. These visible absorption bands can be excited efficiently by a frequency-doubled Nd:YAG laser at 532 nm.

Figure 27.11b shows the specular reflectivity of the gold nanorod substrate measured using the 532 nm laser with different optical polarization. The length of the nanorods was ~ 100 nm, and the measurement was taken at 60° incidence angle, which was close to our LDI experimental condition. Normalized reflectivity of flat aluminum and gold film is included for comparison. The reflected optical intensity was normalized to that of TE-polarization. Unlike the flat metal in which the reflectivity is minimum for TM-polarized light [67], the ~ 100 nm gold nanorods have a higher optical absorption for the 532 nm laser at TE polarization due to the transverse plasmon resonance [38, 59].

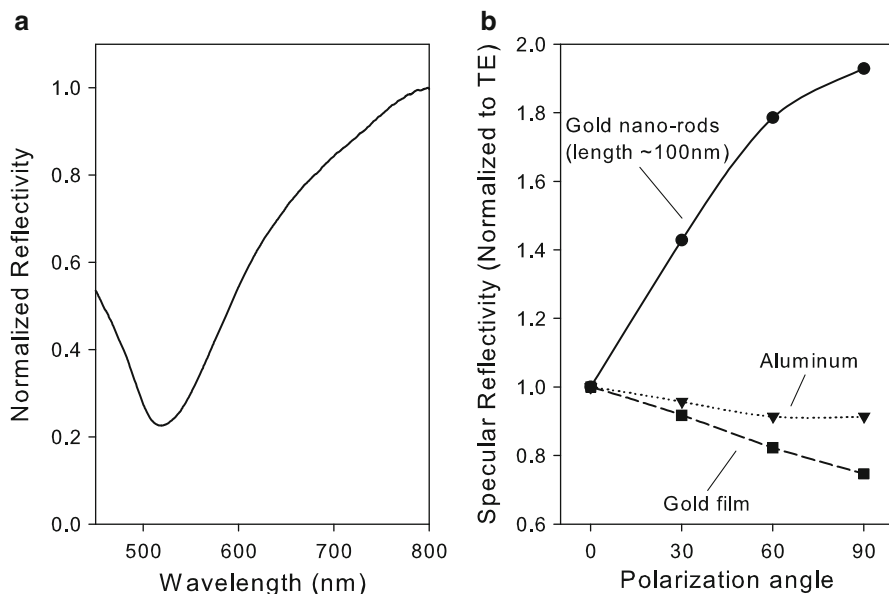


Fig. 27.11 (a) Normalized reflectivity of gold nanorods. (b) Specular reflectance of gold nanorods (●), aluminum (▼), and gold film (■) measured at 60° incidence angle using 532 nm laser with different polarization angle. The reflected intensity is normalized to that of TE polarization

27.4 Experimental Details

27.4.1 Time-of-Flight Mass Spectrometer

The laser desorption/ionization experiment was performed with a 2.5 m time-of-flight mass spectrometer (JEOL 2500) with delayed ion extraction. The instrument can be operated in linear or reflectron mode. A simplified schematic showing the mass spectrometer in reflectron mode is shown in Fig. 27.12. The acceleration voltage for ions was 20 kV. The vacuum pressures in the ion source and the detector were 7.5×10^{-5} and 5×10^{-7} torr, respectively. The primary laser source for the desorption/ionization experiment was a frequency-doubled Nd:YAG laser which was operated at 532 nm wavelength and pulse width of 4 ns. The gold nanostructured substrate was attached to a modified target plate and was irradiated by the laser at 60° to the surface normal. Pictures showing the time-of-flight spectrometer and the target plated are depicted in Figs. 27.13 and 27.14, respectively.

The output of the laser was originally at TE-polarization, and a calcite polarizer was added to increase the polarization extinction ratio. The laser polarization on the target was adjusted using a half-wave plate. The laser spot size on the target substrate was about $\sim 200 \mu\text{m}$ in diameter. Unless otherwise stated, the mass spectra were

Fig. 27.12 Simplified schematic of the time-of-flight mass spectrometer in reflectron mode

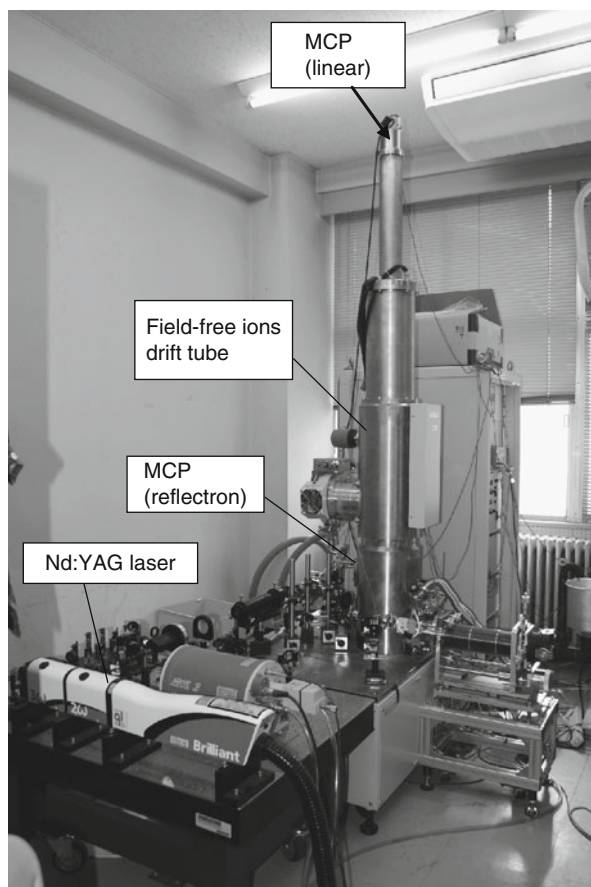
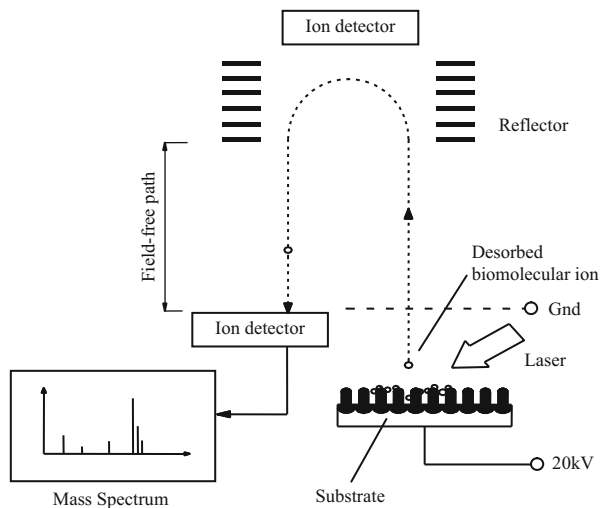
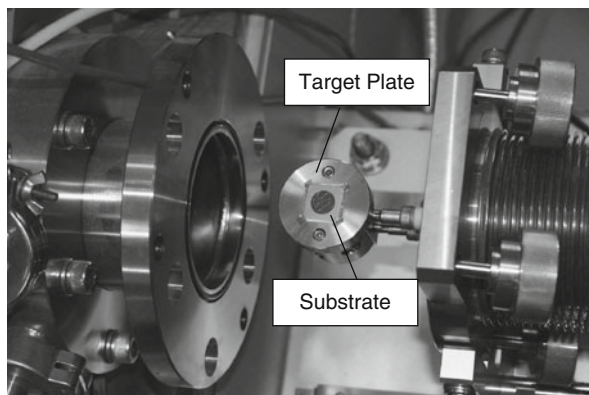


Fig. 27.13 Picture of the time-of-flight mass spectrometer, laser, and the optical arrangement employed in the experiment

Fig. 27.14 Modified target plate for the attachment of gold nanorod substrate



acquired at optimized laser fluence which was estimated to be in the range of few 10 to ~ 100 mJ/cm^2 . For comparison, the frequency-tripled Nd:YAG laser (355 nm wavelength, no further polarized) was also used to investigate the wavelength dependence. Throughout the experiment, the substrate was scanned, and 40–60 laser shots were used to acquire the mass spectra.

27.4.2 Sample Preparation

All chemicals and analytes were obtained commercially and used without further purification. Bovine insulin was prepared in the aqueous solution of 1% trifluoroacetic acid (TFA). Lys–Lys, Lys–Lys–Lys–Lys–Lys, bradykinin, and melittin were dissolved in water. Lactose was prepared in the aqueous solution of sodium chloride (~ 10 ppm) to promote cationization. The citric buffer was prepared by mixing the aqueous solution of citric acid 10 mM with the diammonium citrate (10 mM) at the ratio of 1/2. Working stocks containing the analyte were prepared in the concentration of 1 \sim 10 $\text{pmol}/\mu\text{l}$. About 0.2–1 μl of the working stock was pipetted onto the gold nanorod substrate, and the droplet was gently dried using warm air blower. When the droplet was dried, the gold nanorod substrate loaded with the analytes was transferred into the vacuum chamber of the time-of-flight mass spectrometer.

27.5 Laser Desorption/Ionization (LDI) with Gold Nanostructure

27.5.1 LDI with Gold-Coated Porous Silicon

Figure 27.15a shows the mass spectrum of 5 pmol bradykinin (1,060 Da) obtained by irradiating the 532 nm visible laser on the analytes deposited on the gold-coated porous silicon. Besides the protonated ions, $[\text{M} + \text{H}]^+$, the alkali metal ion adducts, $[\text{M} + \text{Na}]^+$ and $[\text{M} + \text{K}]^+$, are also observed in the mass spectrum.

On the bare porous silicon (no gold coating), no molecular ion signal was observed at the same or higher laser fluence (Fig. 27.15b). This clearly shows that the gold nanostructure rather than the porous silicon template contributes to the desorption/ionization of the analytes. In an attempt to desorb/ionize the bradykinin from the flat gold surface (~ 50 nm Au film coated on the flat silicon surface) using the 532 nm laser, only very weak signal was obtained at high laser power (Fig. 27.15c). This indicates that the gold nanostructure was essential in assisting the desorption/ionization of analytes.

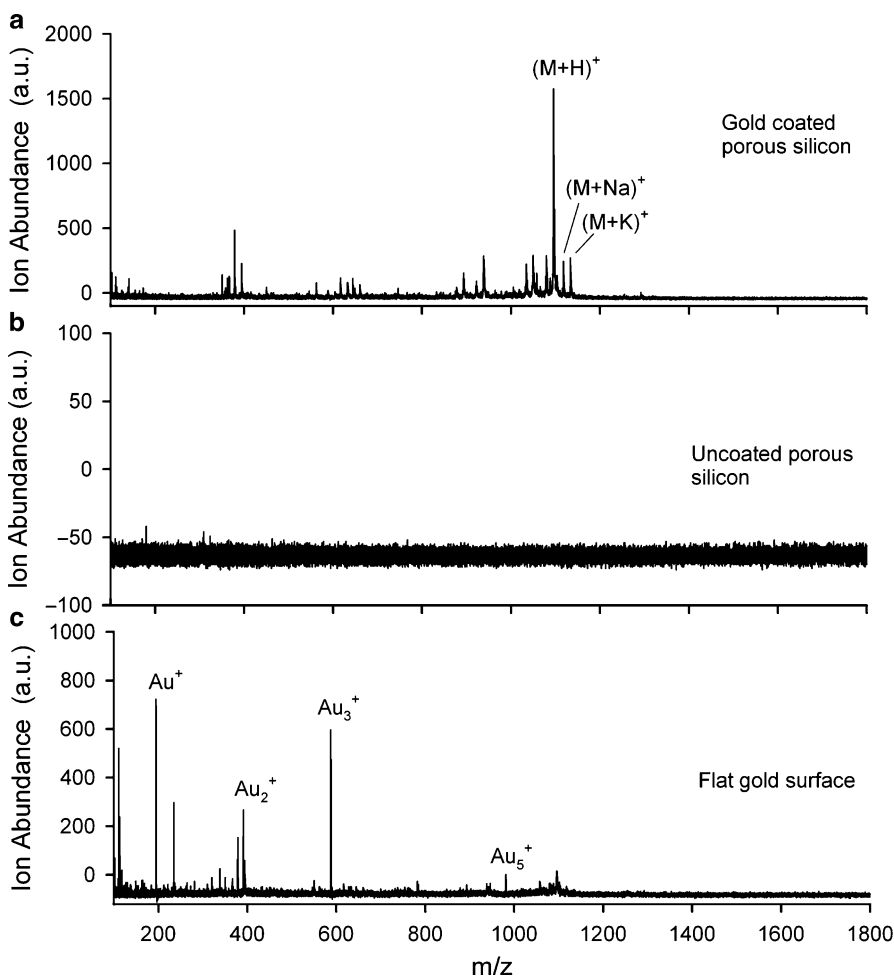


Fig. 27.15 Mass spectrum of bradykinin (1,060 Da) obtained by the irradiation of the visible 532 nm laser on (a) gold-coated porous silicon. (b) Uncoated porous silicon. (c) Flat gold surface (~ 50 nm gold film coated on the flat silicon surface) at higher laser intensity

27.5.2 LDI with Gold Nanorods

Polarization Dependence Due to the random structure of the porous silicon substrate, the optical polarization of the incidence light was not well defined. The optical polarization effect was studied using the gold nanorods. The mass spectra of angiotensin I (1,296 Da) obtained using the gold nanorod substrate with different laser polarization are shown in Fig. 27.16.

The laser polarization incidence on the substrate was adjusted using a half-wave plate, without significant change in the incidence laser fluence. The same laser fluence was applied to obtain mass spectra of different laser polarization.

For the shorter nanorods with length <50 nm, the molecular ion signal became maximum when the laser was TM-polarized and minimum when TE polarized (Fig. 27.16a, b). These short nanorods behave optically as particles on the flat surface, and the dependence of optical absorption on the laser polarization is similar to that of gold thin film. Such optical property could also be influenced by the dielectric alumina template.

As the length of the gold nanorods increases, (e.g., ~100 nm), the optimum polarization at the excitation wavelength of 532 nm was reversed to TE (Fig. 27.16c, d).

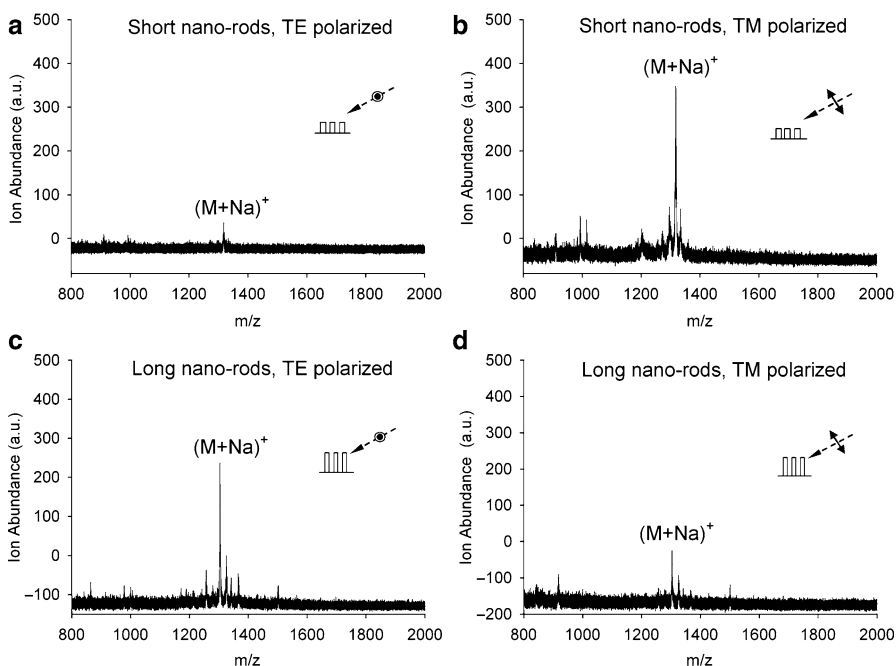


Fig. 27.16 Mass spectra of angiotensin I (1,296 Da) obtained from the gold nanorods excited by the laser of different optical polarization. (a) and (b): the optimum optical polarization for short nanorods (length ~50 nm) was TM. (c) and (d): the optimum polarization was reversed to TE for longer nanorods (length ~100 nm)

The reverse of the optimum polarization was due to the excitation of transverse surface plasmon resonance of the gold nanorods. In sum, the obtained mass spectra which are sensitive to the laser polarization agree reasonably with their optical properties. In the following experiments, the gold nanorods were of ~ 100 nm in length, and the optical polarization was optimized at TE. As for the gold-coated porous silicon, significant polarization dependence was not observed, but the polarization was arbitrarily maintained at TM.

Post-etching of Gold Nanorods Substrate The chemical etching of the alumina template was also a key process in obtaining good mass spectrum of the deposited analyte. The desorption/ionization efficiency was found to be quite dependent on the etching time. Figure 27.17 shows the mass spectra of 5 pmol melittin (2,847 Da) acquired from the gold nanorods prepared with different etching times. In Fig. 27.17, T_o denotes the time at which the chemical etching of the alumina template has just reached the gold nanorods. The SEM images of the gold nanorod substrate taken after the LDI experiment are shown in Fig. 27.18. The analyte ion signals increased as the gold nanorods started to emerge from the template. The optimum condition was achieved at about $T_o + 13$ min when ~ 100 nm nanorods were almost completely released from the template. Further etching of the alumina template caused the nanorods to topple (see Fig. 27.18c), and the ion signal started to diminish. Excessive etching detached some of the nanorods from the alumina template (Fig. 27.18d), and it became difficult to observe ion signals.

Wavelength Dependence The frequency-doubled (532 nm) and frequency-tripled (355 nm) output from the Nd:YAG laser were used to study the laser wavelength dependence. The mass spectra of 5 pmol pentyllysine (Lys–Lys–Lys–Lys–Lys, 659 Da) acquired from the gold-coated porous silicon and gold nanorods are shown in Fig. 27.19. The visible LDI using 532 nm laser is depicted in Fig. 27.19a, c, and the UV-LDI is shown in Fig. 27.19b, d. The UV laser fluence irradiated on the substrate was estimated to be slightly higher than the visible laser, but accurate comparison was difficult. Instead, the background ions, for example, Au⁺ ions (Fig. 27.19c, d), were used as the indirect references for comparison. For both substrates, the 532 nm laser gave better ion yields with less background noise (Fig. 27.19a, c). Although ions were also observed with the 355 nm laser, the desorption/ionization was not as efficient, and the background ions appeared to be stronger, probably due to the higher laser threshold fluence. The background ions might be due to the contaminants absorbed from the air or vacuum chamber.

Desorption/Ionization of Low-Molecular-Weight Analytes Because ions could be produced without the addition of chemical matrix, the present method may find application in the analysis of low-molecular-weight analytes, which are rather difficult to handle in the conventional MALDI. Figure 27.20a, b show, respectively, the mass spectra of 5 pmol lactose (342 Da) acquired from the gold nanorods and gold-coated porous silicon by using 532 nm laser. Both substrates produced similar mass spectra. Although gold atoms were consumed during the laser desorption/ionization, no obvious damage was observed on the substrate at the moderate laser fluence,

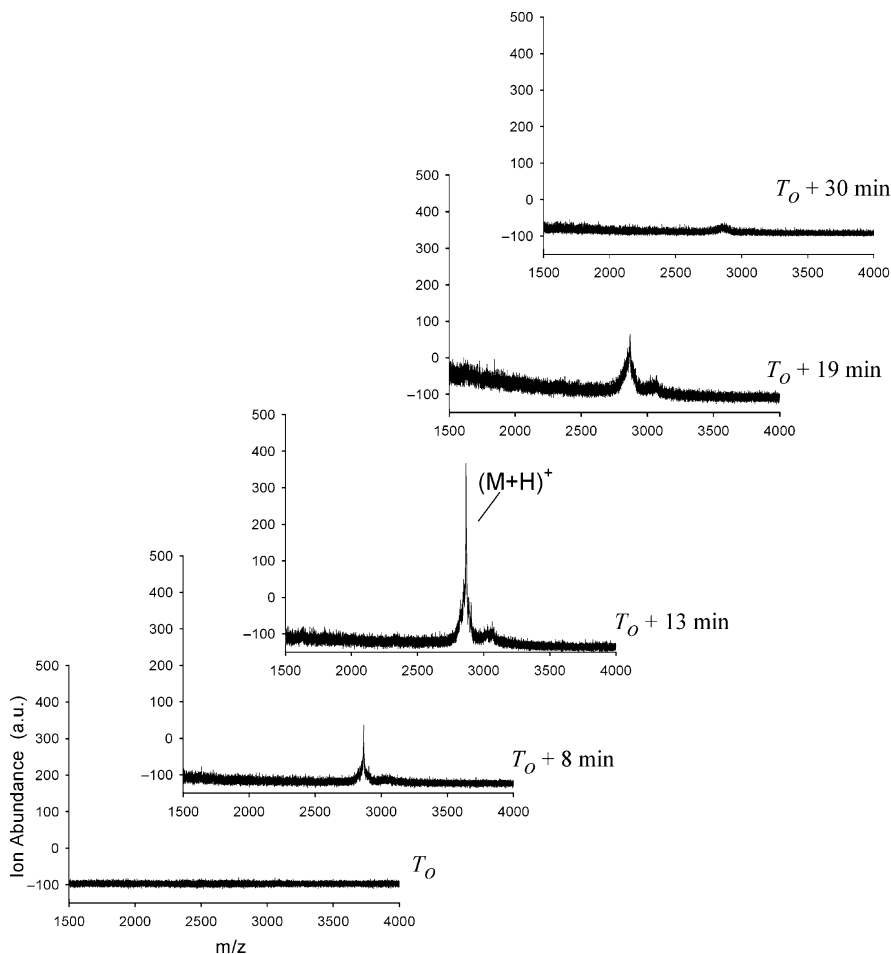


Fig. 27.17 The mass spectra of 5 pmol melittin (2,847 Da) acquired from the gold nanorods of different etching time. T_o denotes the time at which the chemical etching of the alumina template had just reached the gold nanorods, and no ion was detected before T_o . The nanorods started to protrude from the template after T_o , and for this substrate, ion signal reached maximum at $T_o + 13$ min. Nanorods started to topple after $T_o + 19$ min, and the ion signal decreased. After $T_o + 30$ min, some nanorods were detached from the substrate, and the melittin ions were difficult to be detected

which was the threshold for most of the peptides and small carbohydrates. The gold cluster ions, Au_n^+ , were easily identified and were used as the references for mass calibration.

The mass spectra for ~ 6 pmol Lys–Lys (274 Da) acquired from the gold nanorods and stainless steel target plate by using 532 nm are shown in Fig. 27.21. At high laser fluence, Lys–Lys ion signals were also observable from the stainless steel

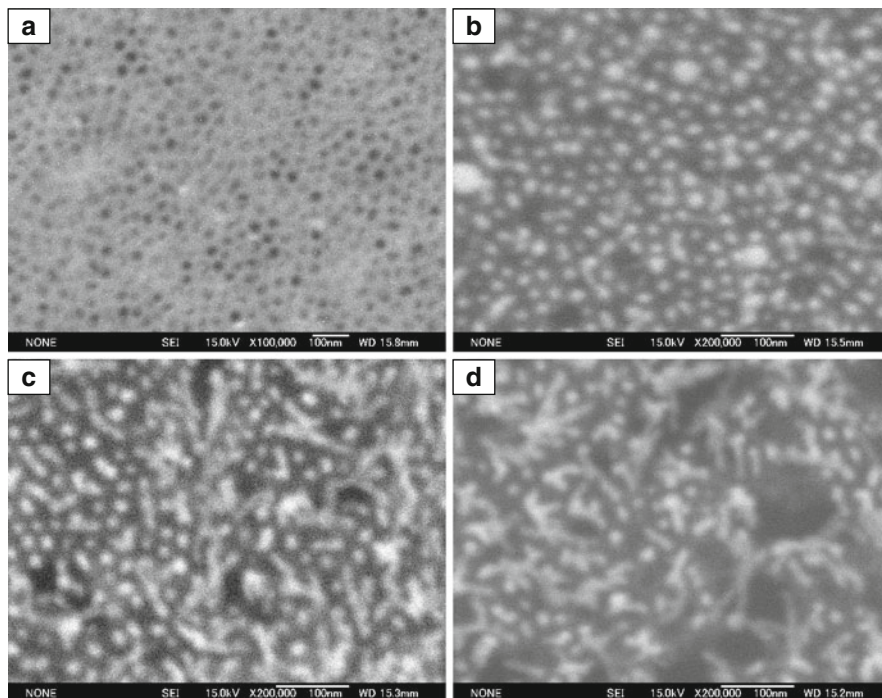


Fig. 27.18 The SEM images of the gold nanorods at different etching. (a): before T_0 , (b): $T_0 + 13$ min, (c): $T_0 + 19$ min, and (d): $T_0 + 30$ min

(Fig. 27.21b), but the most intense and homogeneous ion signals were produced from the gold nanorods (Fig. 27.21a). Besides Au^+ , some background ions ($<300 m/z$) were also present in the low mass region, which were probably due to contaminants and hydrocarbons which were absorbed by the nanorods from the air or vacuum.

Addition of Proton Source Probably due to the lack of acid or proton source on the gold nanostructured substrate, the protonation of peptide and protein was not as efficient as the MALDI method. Besides glycerol (which is the usually used liquid matrix), it had been reported recently that the citric buffer (mixture of citric acid and ammonium citrate) could also work efficiently as the proton donor [26].

The visible laser desorption/ionization of 650 fmol bradykinin and 2 pmol bovine insulin from the gold nanorods with the addition of citric buffer during the sample preparation is shown in Fig. 27.22a, b, respectively. The molar ratio of analyte to citric acid was $\sim 1/350$. The citric buffer significantly improved the analytes' ion yields and the resolution of the mass spectra. The ions contributed by the citric buffer were also observed in the mass spectra. The peaks at m/z 215 and 231 (in Fig. 27.22a) correspond to the sodium and potassium ion adducts of the citric acid

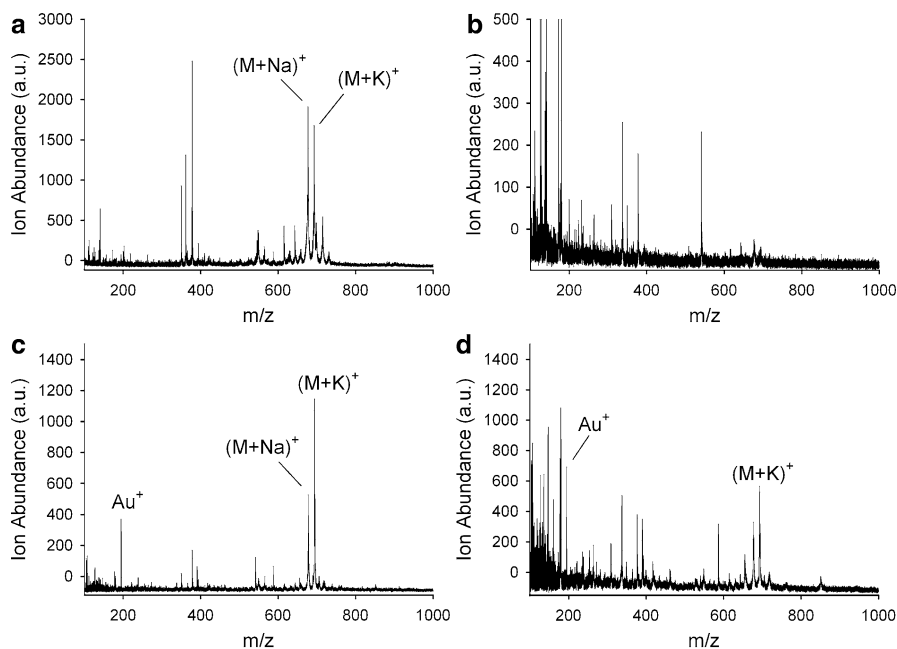


Fig. 27.19 Mass spectra of pentalyisine obtained from gold-coated porous silicon using (a) 532 nm and (b) 355 nm laser. Mass spectra from gold nanorods using (c) 532 nm and (d) 355 nm laser

([M + Na]⁺ and [M + K]⁺). The yet determined background peak at m/z 183 was probably due to the contaminant absorbed on the gold nanorods.

For the two-phase matrix, the nano-powders have to be suspended in the liquid glycerol to prevent agglomeration, and the ion signals deteriorate after complete evaporation of glycerol in the vacuum [22]. In contrast, the nanostructures allow the use of various solid proton sources. Besides citric acid, several compounds with suitable hydroxyl groups, for example, tartaric acid, xylitol, and mannitol, were also found to be useful in analytes ionization.

Surface-Enhanced Raman Spectroscopy (SERS) from Gold Nanorods In a separate experiment, we demonstrated that the gold nanorods used in our experiments were also SERS-active. The Raman experiment was conducted using Jasco NRS-2100 micro-Raman monochromator spectrometer. The analyte, rhodamine 6G, was dissolved in water, and a continuous-wave 488 nm argon laser was used for excitation. The operating laser power was about 0.35 mW, and the exposure time was 10 s. The Raman spectroscopy of 5 pmol rhodamine 6G (R6G) deposited on the gold nanorods is shown in Fig. 27.23a. For comparison, the signal obtained from the aluminum substrate under the same experimental condition is shown in Fig. 27.23b, and the respective mass spectra acquired by using 532 nm laser are shown in Fig. 27.23c, d.

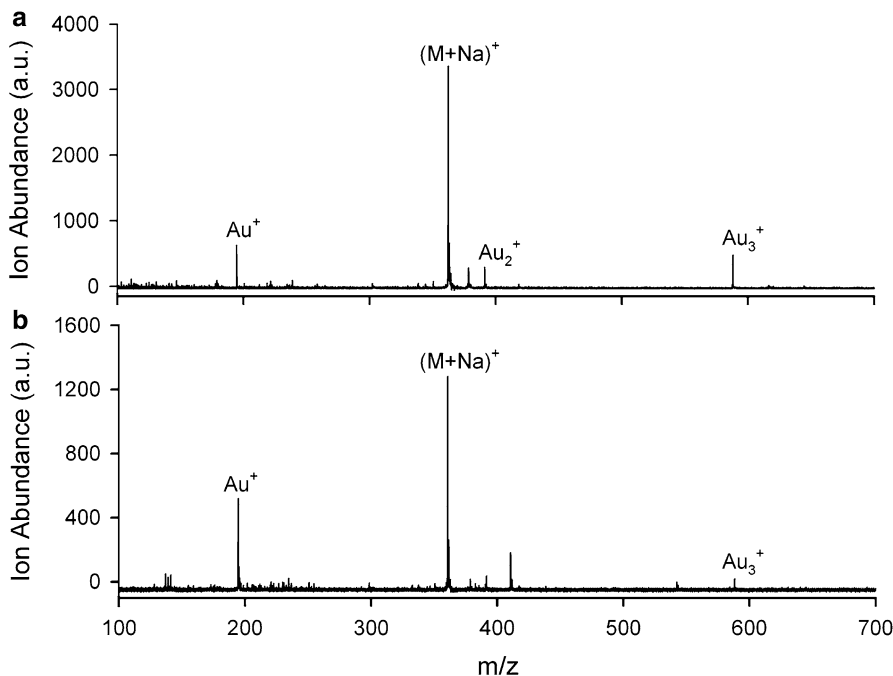


Fig. 27.20 Desorption/ionization of lactose (342 Da) (a) from the gold nanorods using 532 nm laser and (b) from the gold-coated porous silicon using 532 nm

27.5.3 Gold Nanoparticle-Assisted Excitation of UV-Absorbing MALDI Matrix by Visible Laser

In this section, we demonstrate the excitation of UV-absorbing MALDI matrix and the desorption/ionization of the doped biomolecular analytes by using a frequency-doubled Nd:YAG laser (532 nm), assisted by gold nanoparticles [68].

In UV-MALDI, the photoionization routes to produce radical ions include direct two-photon ionization [13] and exciton pooling of the excited matrix molecules [14]. The ionization potential (IP) for DHB is 8 eV, and the energy for first excited state is 3.466 eV [69]. Because the IP is still higher for the two-photon energy from the typical UV laser (e.g., nitrogen laser), the photo/thermal hypothesis was proposed [70], of which the energy deficit is made up by the thermal energy. For the exciton pooling, it is readily accessible by one UV photon, and two or more excited matrix molecules pool their energies to form radical ions or higher excited states of which the transfer of proton to the target analytes takes place.

In our experiment, Au thin film (~10 nm) was first coated on the matrix surface, and the Au nanoparticles were prepared and deposited directly on matrix surface by ablating the Au film in the vacuum. Coating the bio-sample with Au thin film is common in the secondary ion mass spectrometry (SIMS) [71], and recently,

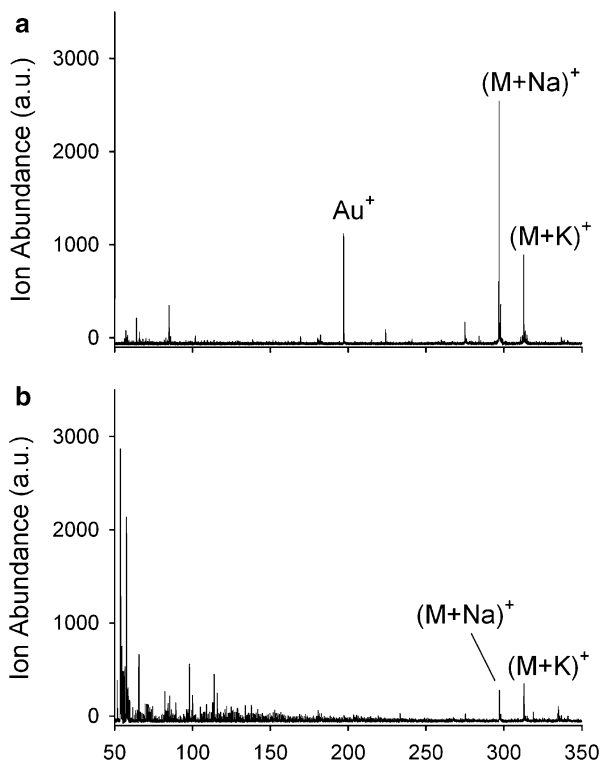


Fig. 27.21 Mass spectra of Lys–Lys (274 Da, ~6 pmol) acquired from (a) gold nanorods and (b) stainless steel using 532 nm laser

metallic coating has also been reported to improve the UV-MALDI imaging [72]. However, in our experiment, the bulk Au film on the laser spot will be ablated, and the remaining Au nanoparticles were used to excite the matrix molecule using visible laser, of which the photon energy is insufficient for the free molecules.

Laser Ablation of Au Film The experiment began by ablating the Au film which was pre-coated on the MALDI matrix to form nanoparticles (Fig. 27.24). The laser fluence was adjusted to the ablation threshold, and the Au cluster ions were monitored directly from the mass spectrum. As the Au thin film was of ~10 nm, the laser threshold fluence for ablation was much lower compared to that of bulk Au. The laser spot size on the target was about ~0.2 mm in diameter, and the operating laser fluence was estimated to be 50 ~ 100 mJ/cm².

After few laser shots, the Au ions were significantly reduced, and the mass spectra were acquired directly or with slight adjustment of the laser fluence. Unless otherwise stated, the mass spectra for matrix and analytes were usually acquired after 5 ~ 10 initial laser shots and from the accumulation of 30–100 single-shot mass spectra on the same laser spot. Each mass spectrum in the following section represents the ions produced from a fixed position, that is, from the same crater/hole formed by the laser ablation.

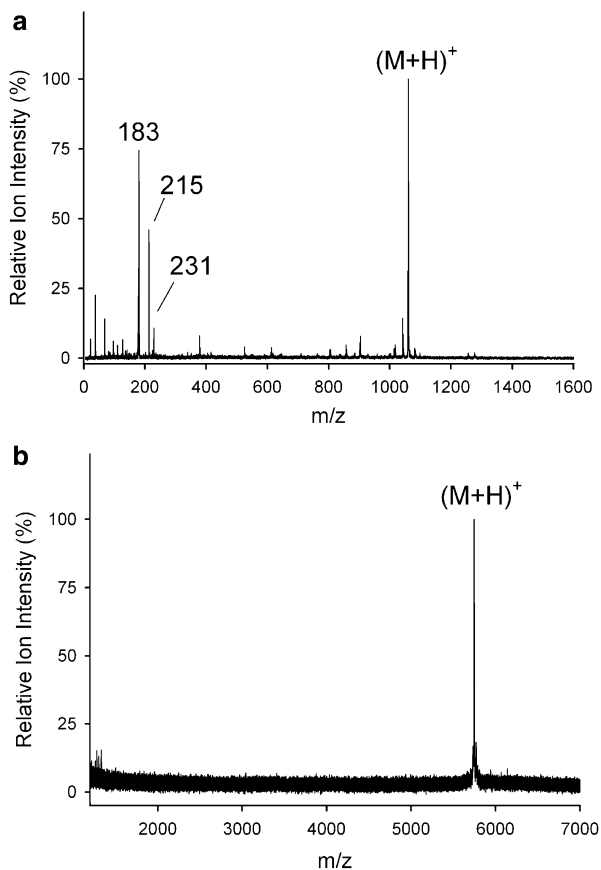


Fig. 27.22 Visible laser desorption/ionization of (a) 650 fmol bradykinin and (b) 2 pmol bovine insulin from the gold nanorods with addition of citric buffer

Figure 27.25a shows the scanning electron microscope (SEM) image of the Au thin film ablated by the Nd:YAG laser after several laser shots. The target was irradiated at $\sim 60^\circ$ incident angle, and the ablated crater was of an elliptical shape with a major axis of $\sim 200 \mu\text{m}$. A close-up inspection on the ablated region showed the formation of gold nanoparticles with size ranging from <10 to 50 nm (Fig. 27.25b).

Several processes could be conceivable for the formation of the gold nanoparticles on the sample surface, for example, the melting of the Au film, and the redeposition of the ablated Au clusters back onto the surface. Some nanoparticles could also be embedded into the matrix after ablation due to migration. Considerable heating was also expected in the initial ablation laser shots.

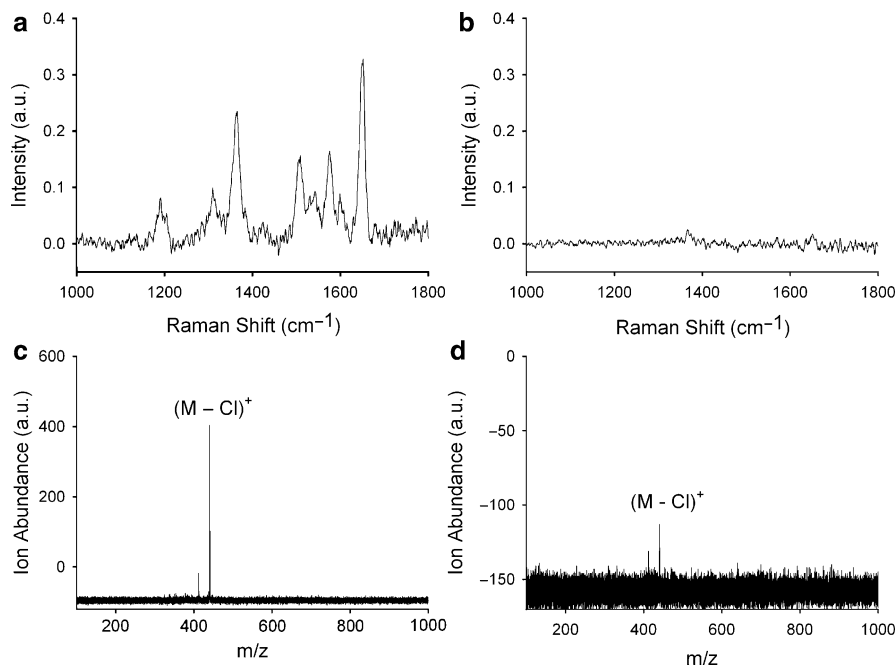


Fig. 27.23 Raman signals of 5 pmol rhodamine 6G (471 Da) obtained from (a) the gold nanorods and (b) aluminum substrate. The excitation wavelength was 488 nm. The prominent peaks are at 1,365, 1,510, 1,575, and 16,550 cm^{-1} . (c) and (d) are the respective mass spectra acquired by using 532 nm laser. The R6G ions appeared as $(M - \text{Cl})^+$

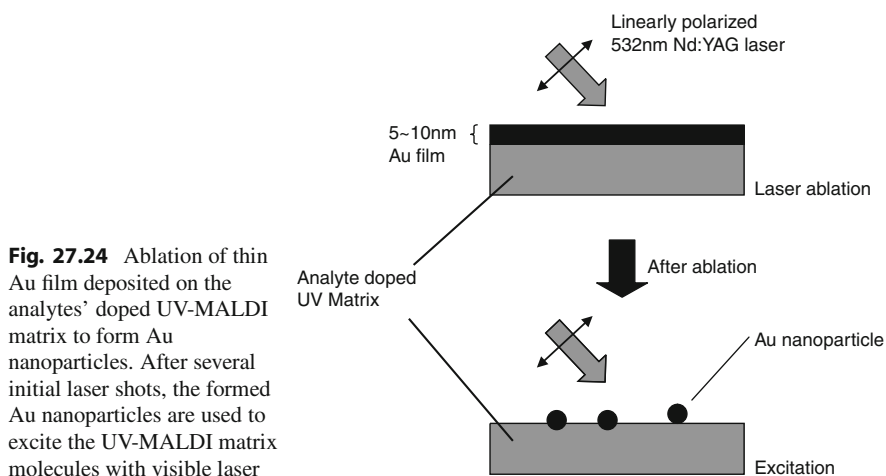


Fig. 27.24 Ablation of thin Au film deposited on the analytes' doped UV-MALDI matrix to form Au nanoparticles. After several initial laser shots, the formed Au nanoparticles are used to excite the UV-MALDI matrix molecules with visible laser

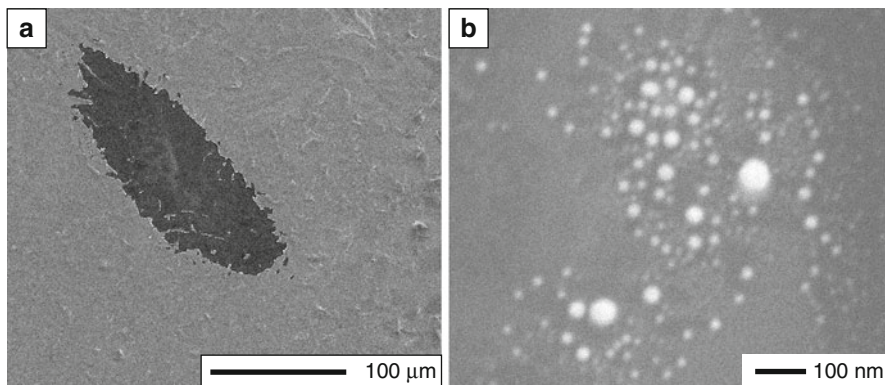


Fig. 27.25 SEM images showing the ablation of Au by the Nd:YAG laser. (a) The ablation of the bulk Au thin film. (b) A close-up on the ablated region showing the formation of Au nanoparticles by laser ablation

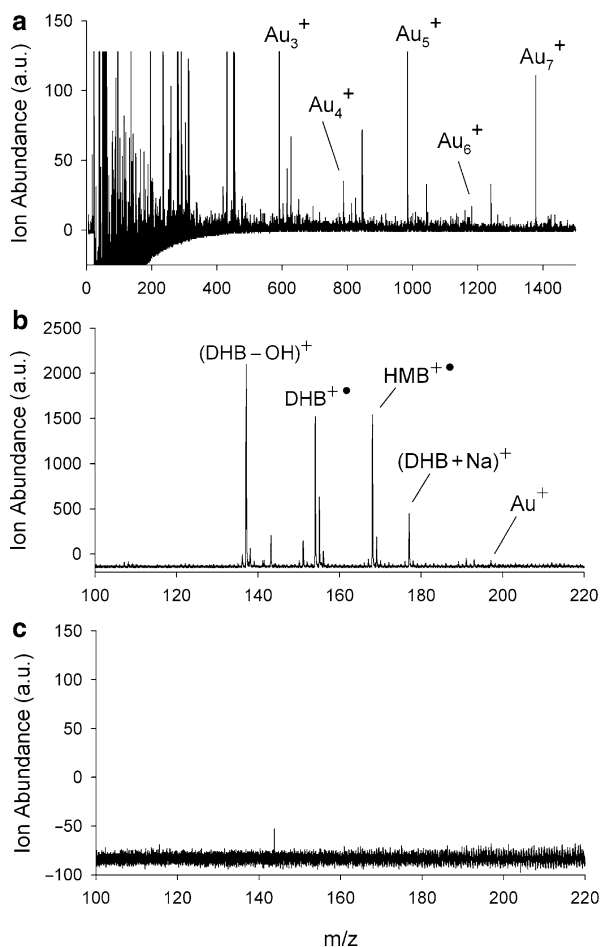
Radical Matrix Ions Produced by Visible Laser The typical first laser shot mass spectrum is shown in Fig. 27.26a. The first laser shot ablated most of the Au atoms, and the mass spectrum was dominated by intense Au cluster ions. Because the Au film was deposited on the matrix surface, the laser ablation Au film was less likely to assist the desorption of the underneath matrix. Only very weak or no matrix ion signal was observed at first few laser shots. Figure 27.26b shows the Au nanoparticles assisted visible-MALDI mass spectrum of the super-DHB (2,5-dihydroxybenzoic acid [DHB, 154 Da] and 2-hydroxy-5-methoxybenzoic acid [HMB, 168 Da]).

The desorbed ions consist of $\text{DHB}^{+\bullet}$, $[\text{DHB}+\text{H}]^+$, $[\text{DHB}+\text{Na}]^+$, $[\text{DHB}-\text{OH}]^+$, $\text{HMB}^{+\bullet}$, and $[\text{HMB}+\text{H}]^+$, which are the typical matrix-related ions observed in UV-MALDI. Gold ions Au^+ also appeared in the mass spectrum but with relatively lower abundance. Irradiating the matrix without Au coating produces no observable matrix ions (see Fig. 27.26c).

The mass spectra of analytes obtained by the visible laser-excited MALDI matrix are shown in Figs. 27.27 and 27.28. Figure 27.27a–d show the single-shot mass spectra that correspond to the successive laser shots. The mass spectra are dominated by the Au cluster ions during first few laser shots, and no analyte ion is observed (Fig. 27.27a, b). The m/z for $[\text{M}+\text{H}]^+$ is denoted as * in the mass spectra. The analyte and the matrix-related ions became apparent after the 5th laser shot and lasted for more than 50 laser shots from a single spot. Since the initial ablation laser shots did not produce any analyte ions except the huge abundance of Au clusters, “these initial ions” will be excluded during the analysis.

Materials and Film Thickness Dependence Figure 27.28a shows the mass spectrum of the bradykinin (1,060 Da) acquired by accumulation of 26 single-shot spectra from the same laser spot. Protonated bradykinin ion, $[\text{M}+\text{H}]^+$, was observed

Fig. 27.26 (a) The mass spectrum of the ablated Au clusters at the first laser shot. (b) Visible laser desorption/ionization of super-DHB assisted by gold nanoparticles. (c) No observable matrix signal was obtained without gold nanoparticles using visible laser



as the base peak with some contribution from metal ion adducts ($[M+Na]^+$ and $[M+Au]^+$). $[DHB+Au]^+$ was, however, not observed.

Comparison was also made with the platinum and silver nanoparticles prepared with the same laser ablation method. Visible-MALDI mass spectra of bradykinin assisted by platinum and silver nanoparticles are shown, respectively, in Fig. 27.28b, c. Although analyte ion signal was also observed from platinum nanoparticles, the ion intensity was not as strong as that of Au nanoparticles at the same laser fluence. In the case of silver, the mass spectrum was dominated by the silver ion adducts of the matrix, $[DHB+Ag]^+$, and the protonation of analyte was largely suppressed. The abundance of $[M+Ag]^+$ ion appeared to be higher than $[M+H]^+$.

The matrix-assisted visible laser desorption/ionization of angiotensin I from the Au coatings of different initial thickness is shown in Fig. 27.29. The initial Au film thickness was found to affect the optimization of laser fluence for the film ablation

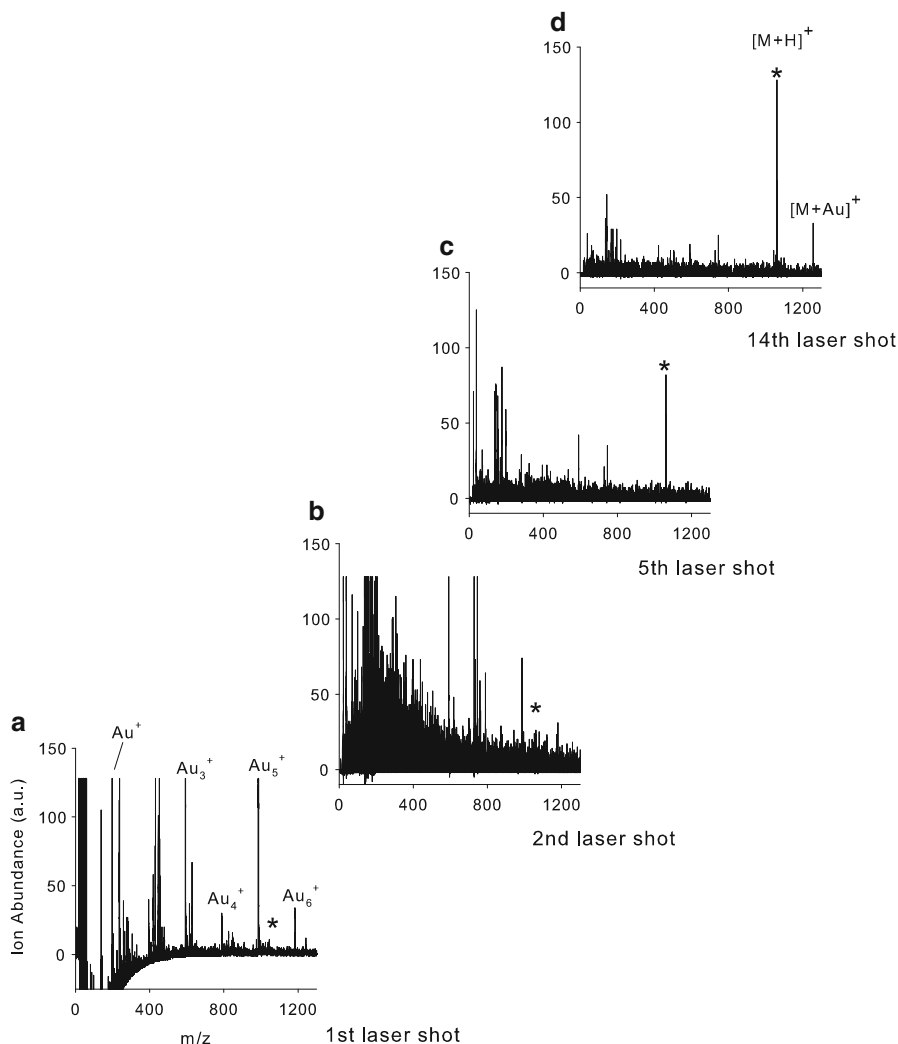
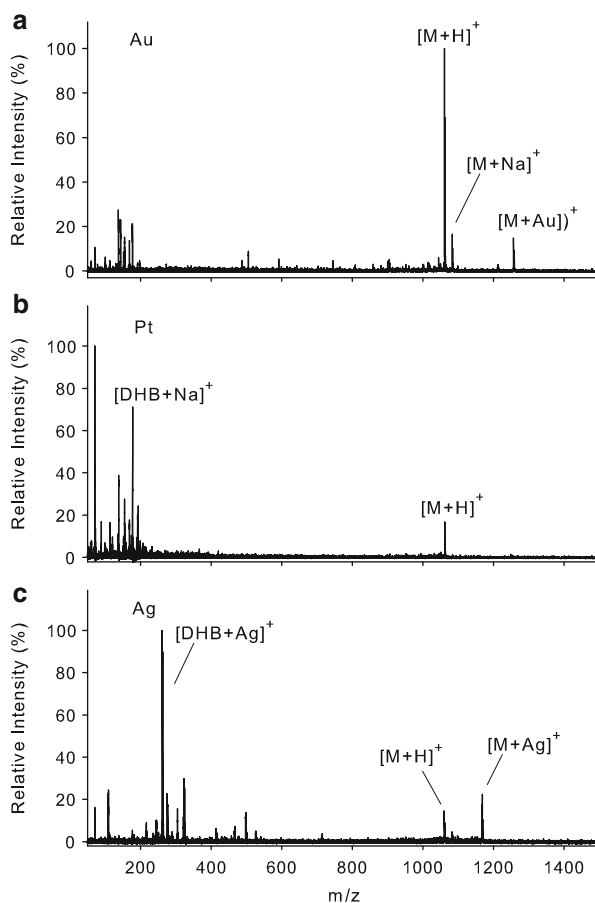


Fig. 27.27 Single-shot visible laser MALDI mass spectra of Au-coated bradykinin and matrix mixture obtained at (a) 1st, (b) 2nd, (c) 5th, and (d) 14th laser shot. * denotes the location of $[M+H]^+$

and the generation of analyte ions. The optimum initial thickness was in the range of 5 ~ 10 nm (see Fig. 27.29a, b), and for thicker coating (25 nm), higher laser fluence was needed to produce the equivalent ablation effect as well as for the desorption/ionization of analytes. As shown in Fig. 27.29c, the ion intensity was also reduced probably due to larger average size of the nanoparticles formed from the thicker Au film.

Fig. 27.28 Visible-MALDI mass spectra of bradykinin assisted by (a) gold, (b) platinum, and (c) silver nanoparticles formed by laser ablation on the metal films. Accumulation of 26 laser shots. The matrix was super-DHB (9:1 mixture of 2,5-dihydroxybenzoic acid and 2-hydroxy-5-methoxybenzoic acid)

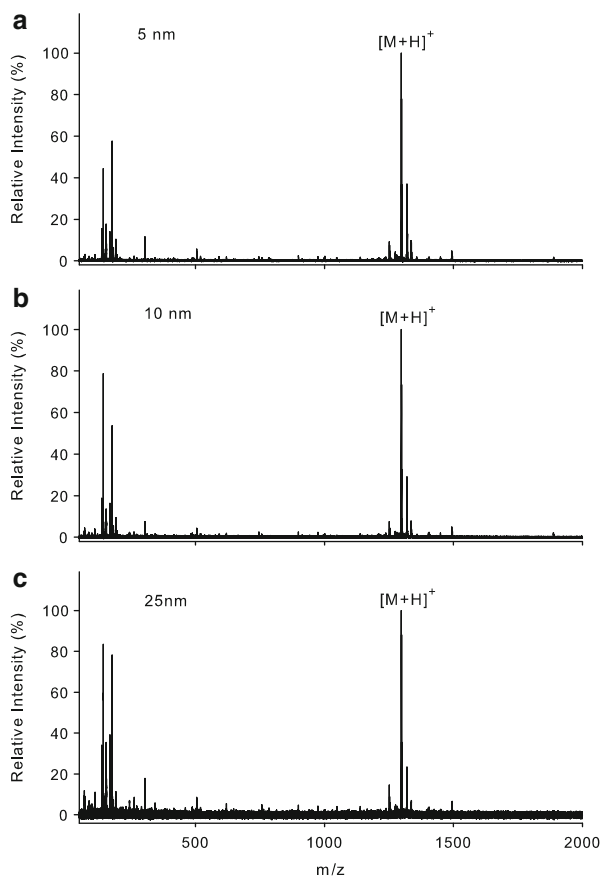


Thermometer Molecule and Wavelength Dependence The thermal property of the Au-assisted visible laser MALDI was examined using 4-chlorobenzyl pyridinium chloride (4CBP) as the thermometer molecule. This thermometer molecule was synthesized according to the literature [73]. The pyridine containing benzyl chloride was heated at 60°C for $5 \sim 6$ h, and the white solid salts were collected after the pyridine was evaporated. The pyridinium salts were used without further purification.

The survival yield of the thermometer molecule, S , reflects the internal energy gained from the neighboring matrix molecules either in the solid phase or gas phase [74] and is given as

$$S = \frac{I(M^+)}{I(M^+) + I(F^+)} \quad (27.6)$$

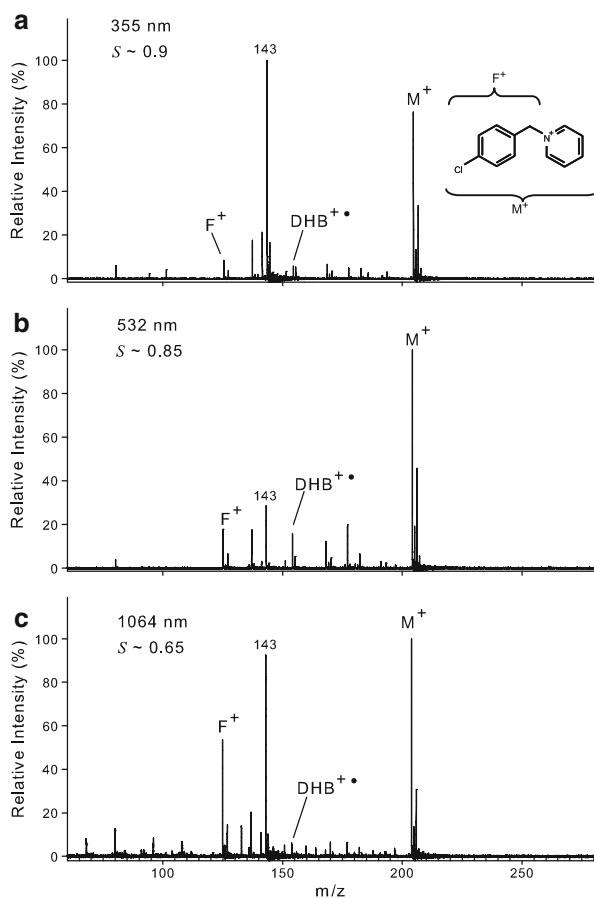
Fig. 27.29 Visible laser MALDI-MS of angiotensin I assisted by Au nanoparticles formed by laser ablation of (a) 5 nm, (b) 10 nm, and (c) 25 nm Au film. The matrix was super-DHB (9:1 mixture of 2,5-dihydroxybenzoic acid and 2-hydroxy-5-methoxybenzoic acid)



where $I(M^+)$ and $I(F^+)$ are the abundances of molecular ion, M^+ , and the fragment ion, F^+ of 4CBP, respectively. If comparison, the measurement was conducted with three different laser wavelengths (355, 532, and 1,064 nm), and the thermometer molecule was mixed with the matrix (super-DHB) at a molar ratio of ~ 500 . For the case of visible (532 nm) and IR (1,064 nm) lasers, the mixture was coated with ~ 10 nm Au, and after 5–10 laser ablation shots, the laser fluence was slightly reduced to acquire the mass spectra. For UV-MALDI, the same sample (with Au coating) was irradiated with the UV laser (355 nm) at optimum laser fluence, without laser ablation.

The mass spectra and the survival yield of 4CBP acquired using UV, visible, and IR lasers are shown in Fig. 27.30a–c, respectively. The highest survival yield for 4CBP was obtained with UV-MALDI as the UV laser excited the matrix electronically (Fig. 27.30a, survival yield ~ 0.9). For the Au nanoparticle-assisted MALDI using 532 nm visible laser (Fig. 27.30b), the survival yield of 4CBP exceeded 0.8 at the typical threshold laser fluence but is lower than that of the

Fig. 27.30 The MALDI mass spectra of thermometer molecule (4CBP) using (a) 355 nm UV laser, (b) 532 nm visible laser with the presence of Au nanoparticles, and (c) 1,064 nm IR laser with the presence of Au nanoparticles. F^+ denotes the fragment ion of 4CBP. S is survival yield of the thermometer molecule



UV irradiation, indicating some heating effect produced by the gold nanoparticles. In Fig. 27.30c, the mass spectrum was obtained with the IR laser of 1,064 nm wavelength which is away from the surface plasmon resonance and is less energetic to induce sufficient electronic excitation. Although the matrix radical ions were also observed, it was of much lower abundance and of poor shot-to-shot repeatability. The low survival yield (~ 0.65) of 4CBP also indicates considerable heating when the IR laser was used. In sum, the results suggest that the excitation of matrix molecules with the presence of gold nanoparticles is rather wavelength dependent, and the heating effect produced by the nanoparticles could not solely contribute to the observed ions.

SERS with Au Nanoparticles Formed by Laser Ablation In a separate experiment, we demonstrated that the Au nanoparticles prepared by the laser ablation method were also SERS-active by performing the Raman spectroscopy on rhodamine 6G. About $0.5 \mu\text{L}$ of rhodamine 6G ($\sim 1 \text{ mM}$) was deposited on the glass substrate, and after being dried, the sample was coated with 10 nm Au using

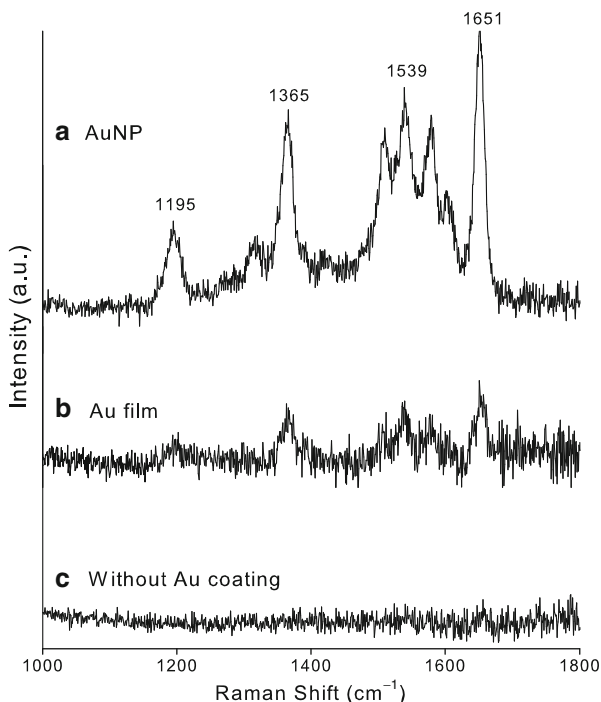


Fig. 27.31 The surface-enhanced Raman spectra of rhodamine 6G obtained from the samples (a) with Au nanoparticles formed by laser ablation, (b) with un-ablated Au coating, and (c) without Au coating

sputtering deposition. The Au-coated rhodamine 6G was irradiated by one ablation laser shot with 532 nm laser in vacuum. The Raman spectroscopy was conducted using micro-Raman monochromator spectrometer (NRS-2100, Jasco, Japan), and the excitation source was a continuous-wave 488 nm argon laser. The operating laser power was about 3 mW, and the exposure time was 10 s.

The Raman spectrum of Au-coated rhodamine 6G after laser ablation is shown in Fig. 27.31a. The prominent peaks are at 1,195, 1,365, 1,539, and 1,651 cm^{-1} . Raman spectra obtained from those without laser ablation and without Au coating are shown, respectively, in Fig. 27.31b, c. Although SERS signal was also observed from the un-ablated Au coating (Fig. 27.31b), as the Au film may form nanostructure on the surface rather than a homogeneous layer, the intensity is much weaker compared to that in Fig. 27.31a where Au nanoparticles were formed by the laser ablation.

Ionization Mechanism Regarding the ionization mechanism for DHB, it is generally believed that in the case of UV excitation (e.g., using nitrogen laser or frequency-tripled Nd:YAG laser), the main processes involve multiphotons photoionization, and/or the exciton pooling, in which two or more excited matrix molecules pool their energies to form radical ions [14]. For DHB, the ionization

potential (IP) is ~ 8 eV, and the energy for first excited state is 3.466 eV [69]. For the visible laser (532 nm wavelength, 2.33 eV) employed in our experiment, at least three or more photons are needed for multiphoton ionization and two photons for excitation. Although the presence of Au nanoparticles increases the thermal heating of the matrix molecules, which could lead to the phase evaporation and molecular desorption, it remains questionable if the thermal process is sufficient for the excitation and ionization of the matrix molecules.

As the gold nanoparticles were also SERS-active, the chemical and electromagnetic field enhancements, which are the two prominent mechanisms for SERS, may also play considerable roles in the excitation of the UV-absorbing DHB matrix by the visible laser. For example, as the gold nanoparticles couple the photon to surface plasmon efficiently, the induced electromagnetic field enhancement could promote the nonlinear optical processes for the multiple photon excitation and photoionization of the matrix molecules. The chemical enhancement, of which the optical absorption band was broadened or red-shifted due to the interaction between absorbate molecules and the conduction electrons on the metal surface, also allows the excitation of matrix molecules by the visible laser. Besides nanoparticles, the inhomogeneous Au film remnants, which were in the form of nanostructure left on the ablated crater, could also contribute to similar assistant effects.

27.6 Discussion and Future Prospect

For the silicon based-substrate, the macroporous structure or grooves of ~ 100 nm (but not smaller) are required to produce good ion signal [27, 29]. Since the nanorods, which is ~ 15 nm in diameter, work equally well with the gold-coated porous silicon, the macroporous feature is not essentially required in the case of gold. Due to the inert nature of gold, the nanorod substrate can be kept in the atmospheric environment and reused after proper cleaning, without significant deterioration in performance.

Regarding the desorption/ionization mechanism, because the gold porous silicon and nanorods essentially resemble the finely divided particles, it may function as the two-phase matrix (inorganic particles in liquid suspension), in which the rapid heating of the substrate and the resultant peak surface temperature leads to the desorption/ionization of the residual solvent molecules that may subsequently assist the formation of analyte ions [75, 76]. The observed alkali ion adducts in some of the spectra also suggest that the ions were formed by the gas-phase cationization which are likely thermal driven.

The sensitivity of the LDI was also found to be enhanced with the addition of proton source. Besides citric acid and glycerol (which have been frequently used in MALDI), we found that certain sugar alcohol (e.g., xylitol and mannitol) and tartaric acid are also useful as proton donors. In the case where proton source was added, they were excited by the nanostructure as their optical absorption is almost negligible in the near-UV and visible region, and the ionization of analytes took place probably in the gas phase. Regarding the desorption/ionization mechanism,

it is usually assumed that the heating is the only process induced by the nanoparticles or nanostructure upon photon absorption. However, photo heating and the peak temperature might not be the exclusive mechanism for ion desorption, and localized effect, such as enhanced electric field had also been proposed [76]. As seen from the laser wavelength and polarization dependence, the optimum condition of the desorption/ionization was achieved when the surface plasmon resonance is excited. Certain degree of optical-field enhancement is also expected at the plasmon resonance as we had obtained the surface-enhanced Raman spectrum of rhodamine 6G from the gold nanorods. However, it remains uncertain whether this is merely due to the plasmon-enhanced optical absorption.

In the visible-MALDI experiment, we showed that with the presence of Au nanoparticles, the UV-MALDI matrix could also be photoionized by the 532 nm laser even though the photon energy is insufficient for free molecules. Since the 532 nm laser (2.33 eV) was employed in our experiment, at least three or more photons are needed for direct photo/thermal multiphoton process and two photons for excitation. Although the presence of Au nanoparticles increases the thermal heating of the matrix molecules, which could lead to the phase evaporation and molecular desorption, it remains questionable if the thermal process is sufficient for the excitation and ionization of the matrix molecules. Thus, in addition to heating effect, a combination of several processes could contribute to the observed ions. As gold nanoparticles couple the photon to surface plasmon efficiently, the induced electromagnetic field enhancement, which promotes nonlinear optical processes, introduces the possibility of two or multiple photon excitation of the matrix molecules. The chemical enhancement in the SERS, of which the optical absorption band was broadened or red-shifted due to the interaction between absorbates and conduction electrons on the metal surface, also allows the excitation of matrix molecules by the visible laser.

Before ending this chapter, here are some updates on the works done by other researchers in this interesting field. By tuning the laser wavelength to close to the surface plasmon peak, the strong optical absorption has allowed Spencer and co-worker to detect as little as 50 attomole of peptide from one single aerosol that contains $\sim 2,000$ gold nanoparticles of 5 nm diameter [77]. Also with gold nanoparticles as laser absorbing matrix, Shibamoto et al. have detected ultra trace amount of sample molecules, which is less than several hundred zeptomoles with laser desorption/ionization [78]. Using gold nanorods, laser desorption/ionization has also been performed with near-infrared laser (wavelength=1,064 nm) that excites the longitudinal surface plasmon resonance (LSPR) mode of the gold nanorods [79, 80].

Finally, it is noted that the optical near-field enhancement is only active in the vicinity of the nanostructure and is characterized by the penetration depth corresponding to the size of the nanoparticles [81]; thus, a metallic tip sharpened to sub-wavelength radius may be used as a scanning nano-probe to desorb the biomolecules with nanometer resolution. The Au nanoparticles may also find application in selective ionization, of which only the specific sides of the bio-sample that are bound to the particles are ionized by the laser.

References

1. F.H. Field, J.L. Franklin, *Electron Impact Phenomena and the Properties of Gaseous Ions*, 1st edn. (Academic, New York, 1957)
2. R. Gomer, M.G. Inghram, *J. Am. Chem. Soc.* **77**, 500, (1955)
3. H.D. Beckey, *Int. J. Mass Spectrom.* **2**, 500, (1969)
4. M.S.B. Munson, F.H. Field, *J. Am. Chem. Soc.* **88**, 2621 (1966)
5. J.B. Fenn, M. Mann, C.K. Meng, S.F. Wong, C.M. Whitehouse, *Science* **246**, 64 (1989)
6. K. Tanaka, H. Waki, Y. Ido, S. Akita, Y. Yoshida, T. Yoshida, T. Matsuo, *Rapid Commun. Mass Spectrom.* **2**, 151 (1988)
7. M. Karas, F. Hillenkamp, *Anal. Chem.* **60**, 2299 (1988)
8. E. Hutter, J.H. Fendler, *Adv. Mater.* **16**, 1685 (2004)
9. P. Englebienne, A.V. Hoonacker, M. Verhas, *Spectroscopy* **17**, 255 (2003)
10. F. Hillenkamp, J. Peter-Katalinić, *MALDI MS* (Wiley-VCH, Weinheim, 2007)
11. J.H. Gross, *Mass Spectrometry* (Springer, Berlin, 2004)
12. T.J.P. Naven, D.J. Harvey, *Rapid Commun. Mass Spectrom.* **10**, 829 (1996)
13. H. Ehring, M. Karas, F. Hillenkamp, *Org. Mass Spectrom.* **27**, 472 (1992)
14. R. Zenobi, R. Knochenmuss, *Mass Spectrom. Rev.* **17**, 337 (1998)
15. X. Chen, James A. Carroll, R.C. Beavis, *J. Am. Chem. Soc.* **9**, 885 (1998)
16. K. Dreisewerd, *Chem. Rev.* **103**, 395 (2003)
17. K. Tang, S.L. Allman, R.B. Jones, C.H. Chen, *Org. Mass Spectrom.* **27**, 1389 (1992)
18. D.S. Cornett, M.A. Duncan, I.J. Amster, *Anal. Chem.* **65**, 2608 (1993)
19. C.J. Smith, S.Y. Chang, E.S. Yeung, *J. Mass Spectrom.* **30**, 1765 (1995)
20. L.C. Chen, D. Asakawa, H. Hori, K. Hiraoka, *Rapid Commun. Mass Spectrom.* **21**, 4129 (2007)
21. C. Yang, X. Hu, A.V. Loboda, R.H. Lipson, *J. Am. Soc. Mass Spectrom.* **21**, 294 (2010)
22. M. Schürenberg, K. Dreisewerd, F. Hillenkamp, *Anal. Chem.* **71**, 221 (1999)
23. T. Kinumi, T. Saisu, M. Takayama, H. Niwa, *J. Mass Spectrom.* **35**, 417 (2000)
24. J.A. McLean, K.A. Stumpo, D.H. Russell, *J. Am. Chem. Soc.* **127**, 5304 (2005)
25. J. Sunner, E. Dratz, Y.C. Chen, *Anal. Chem.* **67**, 4335 (1995)
26. C.-T. Chen, Y.-C. Chen, *Rapid Commun. Mass Spectrom.* **18**, 1956 (2004)
27. S. Okuno, R. Arakawa, K. Okamoto, Y. Matsui, S. Seki, T. Kozawa, S. Tagawa, Y. Wada, *Anal. Chem.* **77**, 5364 (2005)
28. J. Wei, J.M. Buriak, G. Siuzdak, *Nature* **399**, 243 (1999)
29. Z. Shen, J.J. Thomas, C. Averbuj, K.M. Broo, M. Engelhard, J.E. Crowell, M.G. Finn, G. Siuzdak, *Anal. Chem.* **73**, 612 (2001)
30. E.P. Go, J.V. Apon, G. Luo, A. Saghatelian, R.H. Daniels, V. Sahi, R. Dubrow, B.F. Cravatt, A. Vertes, G. Siuzdak, *Anal. Chem.* **77**, 1641 (2005)
31. J.D. Cuiffi, D.J. Hayes, S.J. Fonash, K.N. Brown, A.D. Jones, *Anal. Chem.* **73**, 1292 (2001)
32. N.H. Finkel, B.G. Prevo, O.D. Velev, L. He, *Anal. Chem.* **77**, 1088 (2005)
33. S.H. Bhattacharya, T.J. Raiford, K.K. Murray, *Anal. Chem.* **74**, 2228 (2002)
34. R.H. Ritchie, *Surf. Sci.* **34**, 1 (1973)
35. H.C. van de Hulst, *Light Scattering by Small Particles* (Dover, New York, 1981)
36. H. Du, *Appl. Opt.* **43**, 1951, (2004)
37. U. Kreibig, M. Vollmer, *Optical Properties of Metal Clusters* (Springer, Berlin, 1995)
38. S. Link, M.A. El-Sayed, *Int. Rev. Phys. Chem.* **19**, 409 (2000)
39. M. Moskovits, *Rev. Mod. Phys.* **57**, 783 (1985)
40. R. Antoine, M. Pellarin, B. Palpant, M. Broyer, B. Prével, P. Galletto, P.F. Brevet, H.H. Girault, *J. Appl. Phys.* **84**, 4532 (1998)
41. M. Danckwerts, L. Novotny, *Phys. Rev. Lett.* **98**, 026104 (2007)
42. K. Arya, R. Zeyher, *Phys. Rev. B* **24**, 1852 (1981)
43. A. Champion, J.E. Ivanecky III, C.M. Child, M. Foster, *J. Am. Chem. Soc.* **117**, 11807 (1995)
44. P.G. Kik, S.A. Maier, H.A. Atwater, *Mater. Res. Soc. Symp. Proc.* **705**, Y3.6 (2001)

45. S.A. Maier, P.G. Kik, H.A. Atwater, S. Meltzer, E. Harel, B.E. Koel, A.A.G. Requicha, *Nat. Mater.* **2**, 229 (2003)
46. D.J. Maxwell, J.R. Taylor, S. Nie, *J. Am. Chem. Soc.* **124**, 9606 (2002)
47. Y.C. Cao, R. Jin, C.A. Mirkin, *Science* **297**, 1536 (2002)
48. I. El-Sayed, X. Huang, M. El-Sayed, *Cancer Lett.* **239**, 129 (2006)
49. M.J. Shea, R.N. Compton, *Phys. Rev. B* **47**, 9967 (1993)
50. I. Lee, T.A. Callcott, E.T. Arakawa, *Phys. Rev. B* **47**, 6661 (1993)
51. W. Hoheisel, K. Jungmann, M. Vollmer, R. Weidenauer, F. Träger, *Phys. Rev. Lett.* **60**, 1649 (1988)
52. J. Brewer, H.G. Rubahn, *Chem. Phys.* **303**, 1 (2004)
53. R.H. Ritchie, J.R. Manson, P.M. Echenique, *Phys. Rev. B* **49**, 2963 (1994)
54. L.C. Chen, T. Ueda, M. Sagisaka, H. Hori, K. Hiraoka, *J. Phys. Chem. C* **111**, 2409 (2007)
55. L.C. Chen, J. Yonehama, T. Ueda, H. Hori, K. Hiraoka, *J. Mass Spectrom.* **42**, 346 (2007)
56. L.T. Canham, *Appl. Phys. Lett.* **57**, 1046 (1990)
57. O. Bisi, S. Ossicini, L. Pavesi, *Surf. Sci. Rep.* **38**, 1 (2000)
58. M.S. Sander, L.-S. Tan, *Adv. Funct. Mater.* **13**, 393 (2003)
59. J. Pérez-Juste, I. Pastoriza-Santos, L.M. Liz-Marzán, P. Mulvaney, *Coord. Chem. Rev.* **249**, 1870 (2005)
60. H. Masuda, K. Yada, A. Osaka, *Jpn. J. Appl. Phys.* **37**, L1340 (1998)
61. O. Jessensky, F. Müller, U. Gösele, *Appl. Phys. Lett.* **72**, 1173 (1998)
62. H. Masuda, K. Fukuda, *Science* **268**, 1466 (1995)
63. H. Masuda, M. Satoh, *Jpn. J. Appl. Phys.* **35**, L126 (1996)
64. S. Ono, N. Masuko, *Surf. Coat. Technol.* **169**, 139 (2003)
65. C.A. Foss Jr., G.L. Hornyak, J.A. Stockert, C.R. Martin, *J. Phys. Chem.* **96**, 7497 (1992)
66. C.R. Martin, *Science* **266**, 1961 (1994)
67. M. Born, E. Wolf, *Principles of Optics*, 2nd edn. (Pergamon, Oxford, 1964)
68. L.C. Chen, K. Mori, H. Hori, K. Hiraoka, *Int. J. Mass Spectrom.* **279**, 41 (2009)
69. V. Karbach, R. Knochenmuss, *Rapid Commun. Mass Spectrom.* **12**, 968 (1998)
70. D.A. Allwood, P.E. Dyer, R.W. Dreyfus, *Rapid Commun. Mass Spectrom.* **11**, 499 (1997)
71. A. Delcorte, N. Medard, P. Bertrand, *Anal. Chem.* **74**, 4955 (2002)
72. G. McCombie, R. Knochenmuss, *J. Am. Soc. Mass. Spectrom.* **17**, 737 (2006)
73. J. Naban-Maillet, D. Lesage, A. Bossée, Y. Gimbert, J. Sztáray, K. Vékey, J.-C. Tabet, *J. Mass. Spectrom.* **40**, 1 (2005)
74. G. Luo, I. Marginean, A. Vertes, *Anal. Chem.* **74**, 6185 (2002)
75. S. Zumbuhl, R. Knochenmuss, S. Wulfert, F. Dubois, M.J. Dale, R. Zenobi, *Anal. Chem.* **70**, 707 (1998)
76. S. Alimpiev, S. Nikoforov, V. Karavanskii, T. Minton, J. Sunner, *J. Chem. Phys.* **115**, 1891 (2001)
77. M.T. Spencer, H. Furutani, S.J. Oldenburg, T.K. Darlington, K.A. Prather, *J. Phys. Chem. C* **112**, 4083 (2008)
78. K. Shibamoto, K. Sakata, K. Nagoshi, T. Korenaga, *J. Phys. Chem. C* **113**, 17774 (2009)
79. E.T. Castellana, R.C. Gamez, M.E. Gómez, D.H. Russell, *Langmuir* **26**, 6066 (2010)
80. F. Gámez, P. Hurtado, P.M. Castillo, C. Caro, A.R. Hortal, P. Zaderenko, B. Martínez-Haya, *Plasmonics* **5**, 125 (2010)
81. M. Ohtsu, H. Hori, *Near-Field Nano-Optics* (Kluwer/Plenum Publishers, New York, 1999)

Index

A

- Adiabatic approximation, 253
- Adsorbed photon-to-current efficiency, 732
- Aerosol, 1053
- Aggregation, 616, 618
- Ag-MgF₂-Al-coated probe, 304, 305
- Alkali-metal atom, 1006
- Alkali metals attachment, 1020
- Alloy, 768, 769, 774, 775, 777, 779, 780, 793, 794
 - broadening, 485, 489, 522
 - nanoparticles, 744
- Al metal, 982
- Alternating electric field, 849, 850
- 2-amino-3-nitrophenol, 1020
- Amorphous, 673, 683, 684, 729
- AN-AuNP, 855–857, 867, 868
- AND-logic gate, 230–233, 239, 245–247
- Angiotensin I, 1036
- Angular momentum quantum number, 646
- Angular spectrum representation, 112
- Anisotropic chemical etching, 982
- Anisotropy, 788, 791–793
- Anodic bonding, 351, 361
- Anodic oxidation, 1029
- Anodization voltage, 1029
- Antenna effect, 540, 545
- Anti-counterfeiting techniques, 894, 927, 928, 939, 942, 943
- Anti-ferromagnetic system, 138, 167
- Anti-Helmholts coil, 978
- Anti-Hermitian operator, 265, 266
- Aperture, 369–373, 376, 378, 379, 382, 443
- Apertured-type double-tapered probe, 308
- Aperture formation, 412
- Apertureless NSOM, 405
- Aperture NSOM, 405
- Aperture-NSOM probe, 446
- Aperture probe, 282, 283, 292, 305, 306, 404, 406
- Application-oriented probe, 284, 326
- Architectures for nanophotonics, 876
- Argon ion sputtering, 1027
- Argon laser, 1040
- Array of microslits, 970
- Artifact-metric systems, 894
- Artificially assisted self-assembling method (AASA), 673, 674, 684, 690
- Artificial photosynthesis, 730, 731
- Aspect ratio, 531–533
- Assemblies of nanoparticles, 556
- Assembly, 846, 848–850, 861, 862, 866, 868
- Atom-by-atom deposition, 981
- Atom clock, 978
- Atom deflection, 93, 97, 981
- Atom guiding, 979
- Atom holography, 978
- Atomic force microscope/microscopy (AFM), 406, 505, 511, 754, 770, 812–814, 816, 821, 822, 827, 828, 830, 832, 833, 837, 839–841, 851, 853–858, 860, 867
- Atomic fountain, 978
- Atom interferometry, 978
- Atom laser, 978
- Atom lithography, 980
- Atom manipulation, 68, 93, 96, 99, 980
- Atom optics, 980
- Atom trapping, 93, 94, 96
- Auger scattering process, 429
- AuNP, 849, 850, 854, 855, 858–862, 866
- Authentication function, 902
- Au thin film, 1041
- Autonomous behavior, 888
- Autonomy, 885
- Autonomy and robustness, 911

B

- Background-free detection, 1012
 - Band filling, 494, 499
 - Bandgap energy, 485, 486, 522
 - Band structure, 550
 - Barnase, 586–588
 - Barstar, 586–588
 - Beam device, 946
 - Bell entangled state, 219
 - 1-benzyl-1,4-dihydronicotinamide, 744
 - Bessel function, 990
 - Biexciton, 431, 456, 459, 460, 464, 466–469
 - Biexciton PL image, 433
 - Biexciton state, 432, 433, 456, 464, 466
 - Binary decision diagram, 879
 - Bioconjugation, 564, 566, 572, 584, 586–589, 593
 - Bio-sensors, 897
 - Bit-patterned magnetic media, 394
 - Bleached absorption, 547, 548
 - Bloch function, 195
 - Bloch vector, 122, 129, 136, 144, 146, 153, 156, 160, 162
 - Blue detuning, 979
 - Blue-fluorescence spectroscopy, 1011, 1014
 - Blue-green emitter, 489
 - Bohr radius, 645
 - Born approximation, 207, 989
 - Born-Markov approximation, 155, 165, 212, 213, 222
 - Boron dipyrin, 734–737
 - Bose-Einstein condensation (BEC), 978
 - Bose-Einstein statistics, 207
 - Boson approximation, 116, 119, 123, 129
 - Bosonic exciton, 119, 122, 129
 - Boundary charge density, 13, 21, 23, 33, 35, 36
 - Boundary charge factor (BCF), 23
 - Boundary effect, 13, 37, 46, 49, 54
 - Boundary electro-optical effect, 29
 - Boundary magnetic current density, 43, 44, 46, 49
 - Boundary magneto-optical effect, 26, 29
 - Boundary scattering formulation/problem with
 - dual electromagnetic potential, 13
 - dual EM potential, 40, 44, 46, 52
 - scalar potential, 13, 34, 36, 38
 - Boundary source
 - boundary charge density, 22
 - boundary magnetic current density, 52
 - Boundary value formulation/problem with
 - dual EM potential, 46
 - scalar potential, 34, 37
 - Bowing parameter, 486
 - Bradykinin, 1034
 - Broadcast-and-select architectures, 882
 - Broadening angle, 991
 - Buffered HF solution (BHF), 287, 289–291, 301, 305, 309, 313, 316, 324, 325, 328, 331, 406, 412
 - Buffered-hydrofluoric acid, 983
 - Buffered hydrogen fluoride solution, 322, 324
 - Bulk effect, 13, 22, 46, 49
 - Bulk magnetic current density, 43, 49
 - Bulk magneto-optical effect, 27
 - Bulk source, 22
 - bulk magnetic current density, 52
 - Bunching, 947
- C**
- C_{60} , 736, 745–747
 - Canonical transformation, 80
 - C-aperture, 376
 - Capillary force, 614, 616, 639
 - Carbon nanotubes, 755
 - Carniglia–Mandel mode, 113
 - Carrier-carrier interaction, 426
 - Carrier/exciton recombination, 484
 - Carrier localization, 434, 475
 - Carrier recombination time, 495
 - Carrier-to-noise ratio, 362
 - Cathodic, 732, 736
 - Cathodoluminescence (CL), 485, 486, 516, 778
 - CdSe, 750–753
 - CdSe/ZnS core-shell QDs, 646, 647, 657, 660, 664, 668
 - Cetyltrimethyl ammonium bromide (CTAB), 847, 848
 - Channel electron multiplier (CEM), 988, 993, 1009
 - Chaotic system, 171, 178, 183
 - Charge injection, 673, 674, 689, 690, 729
 - Charge neutrality, 697
 - Charge-separated state, 730, 736–738
 - Charge separation, 730, 736, 739, 740, 747–749
 - Charge transfer (CT), 793, 794, 800
 - Chemical enhancement, 1052
 - Chemical-etching method, 406, 1030, 1037
 - Chevron pattern, 813, 833, 835
 - Chiral-PS, 319, 320
 - Chlorauric acid, 1029
 - 4-chloro-benzylpyridinium chloride (4CBP), 1048
 - Citric acid, 1039
 - Classical approach, 66
 - Classical theory of optics, 12
 - Cluster, 745–747, 759

- C-mode NSOM, 282–284, 292, 294, 296–298, 303, 305
Coalescence, 826, 827, 830, 842
Coarse-grained, 254, 259
Coaxial impact-collision ion scattering spectroscopy (CAICISS), 771
Coercive force, 680
Coherently-coupled state, 218, 219, 221, 225, 245
Coherent phonon, 4
Coherent state, 141, 172, 268, 273, 275, 276
Collection efficiency, 411, 415
Collection (C) mode, 282, 500
Colloidal gold nanoparticle, 616, 618, 639
Commutation relation, 261, 262, 265, 267
Compositional modulation, 484, 487
Conduction band, 739
Conductivity of metal, 26
Constant linear velocity, 361
Contact-mode topography, 683
Content addressable memory, 879, 881
Contour plot, 758
Controlled AND-logic gate, 237
Controlled-NOT logic gate, 219
Controlled XOR-logic gate, 237
Conversion efficiency, 917, 919–921
Corrugation, 791
Coulomb gauge, 76
Coulombic dipole-dipole interaction, 156
Coulomb potential, 77
Coulomb's law, 13, 21, 24, 33, 34, 50
Coupling constant, 259, 265, 269
Creation and annihilation operators, 83, 84, 89
Critical thickness, 801, 811, 813, 815
Cross-section, 999
Crystal-field splitting, 788
CTR, 828
Cut-off diameter, 372, 373
Cut-off wavelength, 504
CW-PL, 509
Cyanobacteria, 731, 740
Cyano-bridged metal complex, 923
 α -Cyano-4-hydroxycinnamic acid (CHCA), 1019
Cyclic voltammogram, 735
- D**
1D, 846–851, 855, 860, 861, 863
Damping factor, 743
Dark-field optical microscopy, 861, 862, 864, 865
Dark state, 220, 236, 1013
Database search, 879
Data storage density, 672
Davydov transformation, 264, 265, 268, 273, 276
Decay length, 371, 389, 984, 985, 997, 1009
Defect, 259, 262
Deflection angle, 985–987
Delayed extraction, 1022, 1032
2D electron gas, 473
Delocalization, 259, 276, 707
Delocalized, 259, 262, 263, 269, 271, 276
Delocalized phonon, 263
Demagnetization, 717
Density of state (DOS), 489, 490, 493, 499, 509
Depolarization field, 376, 378, 386
Design rules, 876
Desorption/ionization on silicon (DIOS), 1021, 1026
Detection efficiency, 988, 1014
Detection rate, 1014
Diblock copolymer, 674, 675, 678, 680, 729
Dicke master equation, 143, 146, 151, 161
Dicke model, 114, 115, 117, 134, 143, 144, 154, 164, 167–169, 181–183
Dicke state, 143, 145, 146, 152, 156, 157, 162
Dielectric constant, 700
Dielectric film, 949
Dielectrophoresis, 849
Diethylzinc (DEZn), 602, 603, 605, 607–609
Differential cross-section, 989, 991
Diffraction grating, 947, 969
Diffraction limit, 2, 12, 16, 19, 20, 50, 67, 93, 192, 214, 230, 370, 639, 672, 846, 863, 980
Diffraction pattern, 991
Diffusion length, 516
Digital processing systems, 879
2,5-dihydroxybenzoic acid (DHB), 1019, 1045
Diluted magnetic semiconductor (DMS), 769
Dilute limit, 114, 116
Dilute nitride semiconductors, 474
Dimer plasmon, 554
Dipolar approximation, 529, 530, 559
Dipole–dipole decoherence, 116
Dipole–dipole interactions, 116, 143, 154, 156–159, 181, 182, 890–892
Dipole distribution, 116, 129, 133, 135, 137, 138, 141, 162, 169, 181, 182
Dipole-forbidden, 252
 energy state, 645
 state, 131, 169
 transition, 113
Dipole force, 979
Dipole-force potential, 986

- Dipole inactive, 194, 195, 202, 203, 245, 246
 Dipole moment, 375
 Dipole-ordered state, 115, 130, 131, 138, 142, 162, 167, 169, 170, 181, 182
 Dipole transition, 990
 Dip-pen nanolithography, 849, 850, 870
 3D island, 810, 811, 813, 830, 832, 837
 Dislocation, 811, 818, 826, 838
 Disorder, 487, 489
 Dispersion-compensating fiber (DCF), 289, 291, 305, 313
 Dispersion curve, 544, 545
 Dispersion relation, 543, 544
 Displacement, 983, 988
 Displacement current, 686, 687
 D₂ line, 984
 2nd D₂ line, 1011
 DNA, 302, 304, 305
 DNA-assisted self-assembly, 879
 DNA stretching, 846, 850–857, 859–864, 866–868
 Donor-acceptor, 738, 747–750
 Doppler-broadened spectrum, 978
 Doppler shift, 979
 Doppler width, 1012
 Double antenna, 390–392
 Double clad fiber, 313, 327
 Double core fiber, 316, 321
 Double magneto-optical traps, 987
 Double-tapered probe, 284, 289, 306, 308, 310–312, 320, 321, 326, 409, 412
 Down-spin, 800
 Dressed photon, 2, 68, 92, 267, 268, 275, 276
 Dressed photon technologies, 188
 Dual Ampere law, 50
 Dual EM potential, 13, 40, 42
 Dual transformation, 41, 42
 2D WL, 429
 Dye, 671, 673, 685, 690, 729
 Dye-sensitized bulk heterojunction, 809
 solar cell, 746, 747
 Dynamic light-scattering, 754
 Dynamics, 546, 547, 549
- E**
- E-antenna, 376
 Edged probe, 346, 347
 Edging down, 1003
 Effective interaction, 75, 87, 88, 90, 92, 101, 104, 253, 254
 Effective mass, 68, 91, 92, 96, 99, 100
 Effective mass approximation, 195
 Effective optical near-field interaction, 67
 Efficiency, 372–374, 381, 384, 386, 389, 397, 443
 Elastic stiffness constant, 488
 Electric dipole-forbidden state, 4
 Electric dipole moment, 996, 997, 1001
 Electric-field, 851
 Electrochemical etching, 1026
 Electro-deposition, 1029
 Electroluminescence (EL) mapping, 485
 Electromagnetic field enhancement, 1023
 Electromagnetic field(s), 66, 67, 75, 103
 Electromagnetic waves, 846, 863
 Electron beam lithography, 918
 Electron beam patterning, 673
 Electron energy loss spectroscopy, 946
 Electron-energy modulation, 957
 Electron-energy spread, 967
 Electronic excitation, 253, 255, 256, 258, 264, 275, 276
 Electronic temperature, 548, 549, 558
 Electron–longitudinal acoustic (LA) phonon interaction, 421, 423
 Electron–longitudinal optical (LO) phonon interaction, 421, 423
 Electron-surface scattering, 546, 547
 Electron transfer, 730, 732, 733, 735–737, 741, 744, 747, 748, 751, 756
 Electron transport, 768, 791, 792
 Electro-optical-effect-related boundary charge factor, 30
 Electrophoretic deposition, 745
 Elementary excitation, 67, 68, 82, 83
 Energy-dispersive x-ray (EDX), 512
 Energy dissipation processes, 189, 546, 547
 Energy fluctuation, 437
 Energy transfer, 3, 7, 189, 190, 192–194, 199–205, 209, 210, 213, 214, 216–220, 225, 226, 229, 230, 232, 234, 237, 239, 240, 242, 243, 245–247, 419, 600, 638, 640, 644, 646–651, 653, 654, 664, 665, 667, 668, 730–736, 738–744, 750–752, 756–759
 Enhanced optical field, 527, 528, 550, 552–554, 563
 Enhancement factor, 556
 Epitaxial growth, 484, 810
 EPP model, 255, 257
 Etching time, 1038
 Evanescent field, 112, 113
 Evanescent light, 111, 979, 993
 Evanescent wave, 950
 Evaporative cooling, 978

- Excitation power-dependent broadening, 430
 Excitation probability, 268, 269
 Excitation transfer, 252
 Excited state, 821, 823–825
 Exciton, 83–85, 114, 116–120, 122, 126, 132, 136, 158, 162, 165, 166, 172, 177, 180–183, 190–193, 195, 197, 201, 203–205, 210, 213, 214, 216, 218, 219, 226, 227, 229–233, 238–240, 243, 245, 246, 422, 431, 484, 485, 487, 489, 490, 508, 509, 511, 514, 522, 523, 600, 605, 619, 622, 623, 626
 density, 513, 516
 diffusion, 522
 energy level, 645, 646
 excited state, 464, 469
 localization, 484, 489, 499, 510, 520
 operator, 122, 127, 166
 PL image, 432
 pooling, 1020, 1041, 1051
 population, 204–206, 210, 213–217, 221, 229–232, 234, 238, 242, 243, 245
 recycling, 887
 transition, 487, 490
 Exciton-binding energy, 651
 Exciton Bohr radius, 197, 487, 489, 500
 Exciton–exciton interaction, 136, 222
 Exciton–free photon interaction, 164
 Excitonic absorption, 498, 499
 Exciton-localized photon interaction, 136
 Exciton-phonon coupling, 204, 210, 217, 218, 222
 Exciton-polariton, 4, 68, 83–86, 88–92, 96, 99, 100, 196, 198–202, 206, 240, 245–247
 Exciton-polariton operator, 122
 Experimental visibility, 937, 938
 Extinction coefficient, 1001
- F**
 Facet, 813–815, 833, 835, 836
 Faraday and Kerr effects, 26
 Far-field, 20
 excitation, 462, 463
 intensity, 31
 observation, 19
 scattering, 541, 545
 Far-field amplitude
 due to boundary magneto-optical effect, 28
 of Rayleigh scattering, 24
 Far infrared, 948
 Fast Fourier transform (FFT), 783
 FDTD simulation, 309, 415, 416, 995, 1000
 Fermionic exciton, 119, 129, 181
 Ferrocene, 736, 737
 Ferromagnetic system, 138, 167
 Ferromagnetism (FM), 769, 798, 802, 804
 Feynman diagram, 3
 Fiber probe, 980
 Field intensity, 31
 Finite-difference time-domain (FDTD)
 method, 309, 378, 397, 408, 409, 418, 448, 449, 453, 916
 Fluorescence, 673, 674, 685–691, 729
 Fluorescence lifetime, 732, 734, 737–739, 743, 750
 Fluorine-doped clad, 290, 313, 324
 Fluorine-doped silica, 290, 316, 324, 327
 Flux intensity, 988
 Focused ion beam, 407
 Focused ion beam patterning, 673
 Förster field, 611–614, 634
 Förster-type, 734
 Fourier optics theory, 970
 Franck–Condon principle, 253
 Frank-van der Merwe (FM) mode, 810
 Frantz-Keldysh effect (FKE), 485, 493, 499
 Free-electron laser, 946, 948
 Free exciton, 794
 Free photon, 3, 4
 Frenkel exciton model, 182
 Frequency detuning, 979
 Frequency doubled Nd:YAG laser, 1032
 Frequency tripled Nd:YAG laser, 1019, 1034
 Fresnel coefficient, 1010
 Functional optical systems, 876
- G**
 GaAs, 810–813, 815, 817–824, 826–832, 834–842
 GaAs quantum dots, 300, 301
 GaAs quantum well, 301
 GaAsSb, 828, 839–842
 GaInNAs, 475
 GaNAs, 474, 475, 478
 Gas phase interaction, 1020
 Gauge invariance, 75
 Gaussian beam, 1001
 Gaussian function, 991
 GeO₂-doped core, 289, 301, 303, 316, 320
 GeO₂-doped fiber, 289, 301, 313
 GeO₂-doped silica core, 321, 327
 Geometrical factor, 530, 531
 Geometrical shadowing method, 407
 G-factor, 795, 796

Giant Raman signal, 556
 Glycerol, 1021, 1040
 Gold cluster ions, 1045
 Gold coated porous silicon, 1026
 Gold-coated probe, 418
 Gold electrode, 731–733, 735–739
 Gold nanodisk, 533, 545
 Gold nanoparticles, 740–742, 744–747, 759, 1023, 1041, 1043
 Gold nanorod, 532, 533, 542–544, 546–548, 550–553, 558, 847, 848, 1029
 Gold nanostructure, 1025
 Gold surface, 732–736, 738, 740, 744
 Gradient force, 979
 Greenberger-Horne-Zeilinger entangled state, 219
 Green dyadic, 531, 539
 Green's function for the Laplace equation, 38
 Greens function(s), 74
 Green's function for the vector Helmholtz' equation, 58
 Grid structure, 931, 932, 934, 939
 Ground state, 818, 821, 824, 825
 Group velocity dispersion, 538

H

Half-wave plate, 1036
 Hall mobility, 791–793
 Hamiltonian density, 985
 Hankel function, 112
 Hard disk drive, 368, 371
 Hard template, 849
 Head-to-tail, 848
 Heat capacity, 702, 705, 706, 710
 Heating-and-pulling, 283, 284, 301, 322, 406
 Heat transport, 548
 Heavy hole, 788
 Heisenberg equations of motion, 119, 181
 Heisenberg uncertainty relation, 3
 Helmholtz' equations, 57, 68, 113
 Helmholtz' theorem, 59
 HE-plasmon mode, 336, 337, 345–349, 627
 Heteroepitaxy, 769, 780, 783
 Heterointerface, 783, 791, 800
 Heterostructure, 484
 Hexyl viologen, 744
 Hidden stable, 708–710, 713, 714, 725
 Hidden substable, 718, 719
 Hierarchical architectures, 877
 Hierarchical hologram, 891, 894, 895, 897, 906, 927–929, 938
 Hierarchical memory retrieval, 891
 Hierarchical property of optical near-fields, 876

Higher plasmon mode, 533
 High spatial resolution, 534, 535, 538, 546
 High-temperature (HT) phase, 923
 High time resolution, 538, 546, 549
 HiPco, 758
 Hollow-light beam, 991
 Hollow optical fiber, 979
 Homoepitaxial growth, 769, 780, 800, 802, 803
 Homogeneous linewidth broadening, 421
 Hopping, 254, 265, 266, 268–276
 Hot electron, 797
 Hot spot, 863
 HR-XRD, 780
 Huygens' principle, 18
 HWHM, 987
 Hybrid recording, 673
 Hydrodynamic flow, 851
 Hydrofluoric acid solution, 406, 1026
 Hydrofluoric-buffered solution, 503
 Hydrophilic, 851, 853, 867
 Hydrophilic polymethylmethacrylate chain, 674
 Hydrophobic, 847, 849, 851, 853, 854, 867
 Hydrophobic polystyrene chain, 674
 Hydroxyl groups, 1040

I

I-c mode NSOM, 283, 284, 308, 311
 Identity tensor, 58
 Illumination and collection hybrid mode, 422
 Illumination-collection (I-C) mode, 283, 416, 501, 502, 505, 510, 512–514, 516, 518, 520, 522, 604, 605
 Illumination (I) mode, 282, 500, 501, 510, 513, 514, 516, 518, 521, 522
 Immersion lithography, 600
 i-mode near-field photoluminescence, 320
 i-mode NSOM, 282–284, 302, 305, 308, 312, 321
 i-mode UV-NSOM, 319
 Impact parameter, 986
 Impurity, 259, 262–264, 269, 272–275
 InAs, 810–842
 Incident light, 865
 Incident photon-to-current efficiency, 736
 Indium-tin oxide, 739
 Induced absorption, 548
 Induced polarization, 66, 68
 InGaAs, 818, 820, 829, 837–840, 842
 Inhomogeneous broadening, 487, 510
 Inhomogeneous linewidth broadening, 421
 Insulin, 1039
 Integrability, 876

- Intensity profile, 984, 995
Interaction length, 952
Interaction picture, 206
Interaction space, 964
Interaction time, 1010
Interconnections, 879
Interdiffusion, 823, 824
Interface fluctuation QD, 463
Interference characteristics of the guided modes, 340, 341, 351, 363
Interference filter, 1012
Interferometric lithography, 673
Intermittent chaos, 183
Intermittent growth, 810, 826, 830, 832–834, 842
Interparticle interaction, 557, 558
Inter-sublevel transition, 646
Intra-QD scattering process, 430
Intuitive picture/understandings of optical near field, 31, 39, 41, 50
Intuitive understandings of optical near field, 24
Inverse Smith–Purcell effect, 970
Ion beam modification, 673
Ionization cross-section, 1007, 1010
Ionization efficiency, 988, 999, 1004, 1010
Ionization energy, 1006
Ionization mechanism, 1051
- J**
J-aggregate, 752, 754, 756, 759
Jahn–Teller, 694, 701, 702, 709, 716, 717, 725
- K**
Kadanoff–Baym–Keldysh nonequilibrium Green’s function technique, 422
Klein–Gordon equation, 68
Klystron, 955
KOH solution, 983
K-spectra, 960
- L**
Langmuir–Blodgett, 849
LA phonon, 422
Laser ablation, 1042
Laser cooling, 978
Laser desorption/ionization (LDI), 021
Laser-driven grating linac, 948
Laser fluences, 1020
Lateral p-n junction, 311
Lateral resolution, 67, 102
Lattice mismatch, 810
Layered antiferromagnet, 722, 723
Le Chatelier’s principle, 13
Lift-off method, 994
Ligand-to-metal charge transfer, 700, 712
Ligand water, 697
Light-harvesting systems, 730, 731, 740, 759
Light hole, 788
Light-matter interaction, 77, 83
Lightning rod effect, 552, 553, 558
Lindblad’s master equation, 166
Linewidth, 1012
Linewidth broadening, 626
Local density-of-states, 444, 445, 454, 469, 472, 535, 544
Local interactions, 875, 876
Localization, 252, 258, 259, 264, 268–270, 272, 273, 275, 276
Localized, 262, 263, 269, 271
Localized exciton, 490
Localized light, 188
Localized phonon, 259, 263, 269, 271, 274
Localized photon, 113, 114, 116–118, 120, 123, 126–128, 131, 132, 135, 136, 139, 141, 142, 162, 164, 168, 171–173, 175, 177, 178, 182, 183, 253, 254, 275
Localized photon-exciton interaction, 118, 127, 132, 162, 170, 181
Localized plasmon resonances (LPRs), 846
Localized vibration mode, 259, 262, 276
Lollipop, 377
Longitudinal plasmon mode, 542
Longitudinal surface plasmon resonance, 1053
Longitudinal vector delta function, 61
Longitudinal vector field, 59
Longitudinal vector Green’s function for the Helmholtz’ equation, 62
Longitudinal vector Helmholtz’ equation, 59
Long-wavelength approximation, 4
LO-phonon, 422, 504, 507, 778, 797
Lorentz force, 962
Low-power operation, 877, 879
Low-temperature (LT) phase, 923
Luminescence, 485, 487, 522
Luminescent nanodiamonds, 564, 565, 586
Luminescent nanoparticles, 564–566, 587
Lyophobic interaction, 745
- M**
Macro-PL spectrum, 434
Macro-scale observation, 912, 913
Macroscopic Maxwell equations, 66
Magnetic circular dichroism (MCD), 794

- Magnetic-force-microscope, 396
Magnetic-optical recording medium, 673
Magnetic recording, 672
Magnetic susceptibility, 698, 710
Magnetic trap, 978
Magnetic tweezer, 851
Magnetization reversal, 397
Magneto-optical effect (MOE), 26
Magneto-optical-effect-related boundary charge factor, 27
Magneto-optical trap (MOT), 978
Magneto-optics, 798
Magnified-transcription, 912
Mark length, 362, 363
Markov approximation, 150
Massively parallel architecture, 883
Mass spectra, 1034
Mass spectrometry, 1018
Mass-to-charge ratio (m/z), 1018
Matrix, 1019
Matrix-assisted laser desorption/ionization (MALDI), 1019
Matrix-to-analyte mixing ratio, 1020
Matter fields, 252, 254, 268
Maxwell's boundary conditions (MBCs), 13, 22, 38, 43, 45, 52
Maxwell's equation, 41
Mean field approximation, 258, 270
Mean temperature, 978, 987
Mechanical impact, 407
Melittin, 1037
Meniscus etching, 283, 284, 286
Meniscus forces, 851
Mesa length, 362, 363
Metal-alkyl bond dissociation, 608
Metal coating, 412
Metal-dielectric-metal coat, 303, 305
Metal film, 953
Metallic-core waveguide, 627–629, 634, 637
Metallic disk, 378–382
Metallic nanoarray, 863, 866, 867
Metallic sphere, 373, 375, 376, 378, 379
Metallic waveguide, 372, 373
Metalized tapered probe, 283
Metal nanoparticles (MNPs), 846–850, 854, 856, 861–865, 867, 868
Metalorganic chemical vapor deposition (MOCVD), 504
Metalorganic vapor phase epitaxy (MOVPE), 486
Metal-to-metal charge transfer, 700, 719
Metastable, 713, 714, 717, 723, 725
Method of moments, 957
Methyl viologen, 732
M-face (10-10), 782
MgZnO, 777, 780, 789, 791
M-H hysteresis, 798
Microchannel plate (MCP), 992
Microcrystal, 696
Micro-photoluminescence (PL) spectroscopy, 647
Micropipette puller, 283, 284, 322, 323
Microscopic Maxwell equations, 66
Microslits, 957
Microtubules, 298, 306
Mie-extinction, 1022
Mie's theory, 529–532, 540, 541, 607
Minimal-coupling Hamiltonian, 75
Misfit dislocation, 837, 838
Mixed-valence, 694, 701, 702, 718
Molecular beam epitaxy (MBE), 810, 811, 815, 823, 841
Momentum conservation, 949
Momentum transfer, 990
Monte-Carlo method, 817
Most probable speed, 988, 1008
Mott transition, 800
Mound formation, 785, 786
Multimode-SNOM, 513, 522
Multi-photon ionization, 1052
Multiple quantum wells (MQWs), 494, 496, 498, 499, 780
Multipolar QED, 195
Multipole Hamiltonian, 75, 77, 82
Multi-step chemical etching, 408
Mur's boundary condition, 409
- N**
Nanobeak, 392–395, 397, 398
Nanodot coupler, 632, 634, 635, 637–639
Nano-fabrication, 252, 980
Nanohole, 810, 820–822, 839, 841, 842
Nano-imprint, 671, 673, 676, 677, 685, 690, 729
Nanomaterial, 253, 254
Nanometric aperture, 67
Nanometric protrusion, 67
Nanoparticles, 1021, 1022
Nano-patterning, 673, 678, 690
Nanophotonic code, 928, 930–939
Nanophotonic devices, 252, 253
Nanophotonic IC, 600, 603, 639
Nanophotonic matching, 913, 915, 916
Nanophotonics, 2
Nanophotonic switch, 193, 204, 213–215, 217, 218, 246, 247, 600, 639
Nanophotonic systems, 891, 904

- Nanorod, 614, 619, 620, 622, 624, 639
Nano-slit, 993, 1002
Nanostructure, 252, 253, 767, 768, 791, 804
Nanostructure fabrication, 252
Nanotriangle, 553
Nanowire, 768, 769, 782–787, 791, 792, 803, 804
Natural linewidth, 986
Naturally occurring QD, 477, 478
Natural photosynthesis, 730, 739
N-decyl-(s)-2-methylbutyl silane, 319
Near-field, 20
 amplitude due to boundary electro-optical effect, 30
 amplitude due to boundary magneto-optical effect, 28
 amplitude of Rayleigh scattering, 24
 intensity, 31, 33, 39, 55
 interaction, 554, 556–558
 observation, 20
 optical chemical vapor deposition, 601
 optical interaction, 253, 254
 optical nutation, 191
 optical recording, 367, 368, 370, 372, 373, 397
 photoluminescence, 308, 311, 325
 PL spectrum, 432, 435, 437
 scattering, 540
 transmission image, 542, 546–548
 transmission measurement, 540, 543, 545
Near-field condition (NFC), 20, 21, 29, 33, 34, 38, 43, 48–50
 for metallic material, 25
Near-field optical microscope/microscopy (NOM), 12, 335, 535, 536, 538, 604, 620, 628, 634, 639, 689, 910
Near field optics (NFO), 12, 672, 673, 691
Near-field Raman spectroscopy, 312, 321
Near-field scanning optical microscope/microscopy (NSOM), 282, 284, 297, 300, 303, 308, 311, 313, 326, 404, 445
Near-mode observation, 934, 939
Networks of optical near-field interactions, 877
Neuron, 306
Neutron powder diffraction, 719, 721–723, 725
NFO-CVD, 601–603, 605, 608, 611, 639
Nicotinic acid (NA), 1019
Nitrogen laser, 1019
0-nm aperture, 416
Noble metal nanoparticles, 528
Nonadiabatic, 253, 257
Noncontact-mode atomic force microscope, 304
Non-demolition measurement, 981, 992
Nonlinear spectroscopy, 978
Nonpolarity, 782
Non-radiative field, 21
Nonradiative recombination, 490, 505, 513, 522
Nonradiative recombination center, 484, 501, 516, 521, 522
Nonradiative recombination process, 427
Nonradiative recombination time, 518
Nonrelativistic electron, 946
Non-thermal desorption, 1024
Normal illumination, 995
NSOM fluorescence measurement, 416
Numerical visibility, 933
- O**
Occupation probability, 231, 1013
One-dimensional (1D), 846–851, 855, 860, 861, 863
One-dimensional (1D) scanning, 910
One-exciton state, 191, 193, 206, 214, 221–223, 226, 227, 229, 230, 233, 234, 237–240
One-shot-laser-pulse, 714, 716–719, 725
Open circuit voltage, 747
O polarity, 772, 774
Optical computing, 912
Optical data storage, 897
Optical density, 493, 495
Optical excitation transfer, 876, 877, 879, 881, 883–888
Optical far/near-field conversion, 628, 632, 638, 640
Optical-field enhancement, 1053
Optical field strength, 552, 558
Optical lattice, 978
Optical microscopy, 528, 529, 534, 535, 537, 541, 549
Optical near-field, 2, 12, 115, 188, 252, 253, 255, 257, 258, 264, 268, 275, 276, 368, 370–373, 376–385, 387, 389–394, 397, 537, 950, 1022
Optical near-field chemical vapor deposition (NFO-CVD), 255
Optical near-field interaction, 66
Optical near-field microscopy, 99
Optical near-field problems, 66, 93
Optical parametric amplifier (OPA), 495
Optical polarization, 1036
Optical properties, 528–531, 535, 541
Optical recording, 368–370, 397
Optical Stark effect, 495

- Optical trapping, 851
Organic films, 685
Organic solar cell, 731, 745, 747, 750, 752
Oxygen plasma, 772, 773, 780
- P**
Parallel processing, 911–913, 922, 940
Parallel writing, 372
Paramagnetic (PM), 798
Patterned media, 671–674, 678–683, 685, 690, 729
PDMS, 861, 862, 866, 867
Pencil-shaped probe, 303, 327, 329, 331
Phase-change media/medium, 394, 673
Phase collapse, 710, 713–715, 725
Phase evaporation, 1052, 1053
Phase matching condition, 972
Phase separation, 674, 678
Phenaz-TMA, 857
Phenaz-TMA/AuNPs, 858–861, 868
Phonon, 82, 83, 253, 257–260, 262–265, 267–271, 273–276
Phonon reservoir, 204–210, 212, 213, 216
Phosphoric acid, 1030
Photo-bleaching, 522
Photocatalytic, 744, 745, 759
Photochemical, 253, 255
Photochemical reduction, 858, 859, 868
Photocurrent, 732, 733, 736–738, 747–750
Photodarkening, 358
Photodissociation, 252, 253, 255, 275, 276, 602, 605, 608, 609
Photoelectrochemical, 731, 732, 735, 736, 739, 747–750
Photoenhanced chemical vapor deposition, 326
Photo-equilibrium, 720
Photoinduced phase transition, 923–925
Photolithography, 2, 982
Photoluminescence (PL), 486, 487, 490, 492, 497, 502–505, 507, 509, 511, 513, 514, 516, 518, 521, 522, 773, 815, 818–825, 830, 831, 833, 834, 838, 840
 PL band, 507
 PL decay time, 490
 PL imaging, 413, 415
 PL intensity, 505, 604, 605, 622, 626
 PL lifetime, 492, 496, 507, 516, 518
 PL linewidth, 510
 PL mapping, 485, 500, 502, 505, 522
Photon, 252–259, 264, 265, 267–276
Photon buffer memory, 240, 242, 247
Photon energy, 949
Photon flux intensity, 999, 1004, 1010
Photon ionization, 1020
Photon-phonon coupling, 268, 272, 273, 275, 276
Photon-phonon interaction, 253, 264, 265, 270, 271
Photostability, 564–566, 570, 571
Photo-stationary, 720, 721, 724
 π -conjugated polymers, 756, 757
 π -core, 854
Piezoelectric constant, 488, 499, 522
Piezoelectric field, 485, 488, 491, 499, 500, 522
Piezoelectric polarization, 488, 499
 π – π interaction, 854, 857, 867
 π -polarization, 790
 π -stacking, 854, 867
Planar near-field optical head, 371, 372
Plane wave basis, 114
Plasmonic optical fields, applications of, 559
Plasmon(s), 528, 534, 535, 544, 546, 549, 553, 554, 557–559
Plasmon induced desorption, 1024
Plasmon resonance, 529, 531, 605, 606, 632, 634
Plasmon wave function, 528, 529, 533, 534, 543, 546, 549, 552, 553, 558, 559
Plasmon waveguides, 628, 629, 846, 863
Platinum electrode, 1026, 1029
Platinum nanoparticles, 1046
Poisson's equation, 34, 54
Polar and nonpolar, 782, 802
Polariton, 83, 92, 257–259, 264, 271
Polarization, 847, 864, 865, 868
Polarization control, 897
Polarization conversion, 917, 918
Polarization dependence/dependency, 932–934, 936–939, 1031, 1036
Polarization fields, 252
Polarization gradient cooling (PGC), 978
Polarized light, 789
Polarized PL, 788, 789, 791, 792
Poly(2-polyvinyl pyridine), 849
Poly(AuNRs), 847, 848
Polydiacetylene, 312
Polydihexylsilane (PDHS), 319, 325
Poly-L-lysine, 851
Polymerase chain reaction (PCR), 861
Polysilanes, 318
Population, 1010
Porous alumina, 1029, 1030
Porous silicon, 1021, 1026

- Porphyrin, 731–736, 738–747, 750–752, 754–756, 759
- Porphyrin excited singlet state, 732, 733, 739–744, 747, 750, 751, 759
- Porphyrin excited triplet state, 741
- Porphyrin radical cation, 748, 749
- Post-etching, 1026
- Post-growth annealing, 810, 824, 841
- Potential fluctuation, 484, 489, 493, 510, 522
- Power conversion efficiency, 747, 759
- Power–Zienau–Woolley transformation, 78, 195
- PPhenaz, 852–854, 857
- PPhenaz-TMA, 857
- PPhenaz-TMA/DNA, 857, 858
- p*-polarization, 997, 1001, 1005
- Principal quantum number, 646
- Probe, 67, 68, 87, 88, 90, 93–104
- Probe-free nanophotonics, 910–912, 940
- Probe-sample system, 99, 100
- Probe-scanning, 940
- Probe tip, 254, 257–260, 275
- Probe-to-probe method, 341, 346, 348
- Projection operator, 4, 67–70, 87, 253
- Propagating light, 256, 257
- Protonated, 754, 756
- Protonated ions, 1020
- Protonation, 1039
- Proton source, 1039, 1052
- Protruded(ing) probe, 348
- Protrusion-type double-tapered probe, 308
- Protrusion-type probe, 284, 289, 292, 294, 296–298, 300–302, 305
- Pseudo one-dimensional, 259, 260, 264, 269, 276
- P-space, 199, 200
- Pulsation, 879
- Pulsed laser, 1020, 1021
- Pump-probe measurements, 538
- Pure silica fiber (PSF), 290, 313, 316, 322, 323, 325
- Pure silica fiber probe, 284, 313, 326
- Pure silica tapered probe, 325
- Purple photosynthetic bacteria, 730
- PVB, 851, 853
- PVCz, 851–854
- Pyramidal silicon probe, 350–352, 360–363, 981
- Pyrene, 733, 734, 756
- Q**
- Q-space, 199, 200
- Quadrupole-dipole transform, 904
- Qualitative innovations, 1
- Quantization, 253, 261
- Quantum chaos, 978
- Quantum chaotic system, 183
- Quantum coherence, 123, 157, 181
- Quantum confined Stark effect (QCSE), 485, 491, 493, 499
- Quantum confinement effect, 600, 620, 621, 624, 626, 780
- Quantum correlation, 134, 143, 154, 168, 170, 182
- Quantum disk, 484
- Quantum dots (QD), 404, 444, 454, 455, 469, 484, 489, 512, 810–814, 816–818, 820–824, 826, 830, 832–842
- Quantum efficiency, 788, 988, 1009
- Quantum entangled state, 220, 236, 243, 245
- Quantum fluctuation, 115, 168
- Quantum information processing, 978
- Quantum modulation of nonrelativistic electrons, 948
- Quantum structure, 768–770, 782, 802
- Quantum well, 485, 489
- Quantum wires, 318
- Quasiparticle, 82, 83, 257, 258, 264, 267, 268, 270, 273
- Quasi-particle representation, 113
- Quasi-static picture, 12, 20, 21, 24, 34, 38, 50, 54
- Quasi-steady state, 116, 135, 137, 138, 141, 142, 162, 181, 182
- Quenching, 686–690
- R**
- Rabi frequency, 979
- Radiation damping, 386
- Radiation gauge, 42
- Radiative recombination, 490, 501, 512, 521, 522
- Radiative recombination center, 516
- Radiative recombination lifetime, 490
- Radical ions, 1020, 1041, 1045
- Radius of curvature, 1004
- Radius of the apex, 378, 382–384
- Raman active site, 556
- Raman scattering, 774, 777, 797
- Raman spectroscopy, 1050
- Random alloy state, 478
- Rayleigh's far-field condition, 48–50
- Rayleigh's scattering, 20, 21, 23, 24
- Real photon, 3
- Reciprocal space diffractogram (RSD), 783

- Recombination, 485, 491, 522
Recombination lifetime, 519
Recombination probability, 491
Recording density, 367, 368, 370, 371, 389, 390, 396
Recording medium, 368–372, 386–390, 394, 397, 398
Red detuning, 979
Reflection, 1022
Reflection high-energy electron diffraction (RHEED), 771
Reflectivity, 1031
Regenerative amplifier (RGA), 495
Resonance enhancement, 552
Resonance wavelength, 380, 384–388, 391
Resonant diameter, 607
Resonant energy level, 647, 649, 651, 663, 667, 668
Resonant wavelength, 1006
Retardation effect, 18, 24, 26, 52, 54
Reversible, 719–721, 723–725
RF-molecular beam epitaxy (RF-MBE), 486
Rhodamine dyes, 1020
Rhodamine 6G, 307, 1040, 1050
Rietveld analysis, 722
Rolling circle amplification (RCA), 861
Rotating wave approximation, 118, 148
RRS, 777
- S**
- Salmonella* flagellar filaments, 294, 296, 297
Saturation, 1009
Saturation intensity, 986, 1006
Saturation parameter, 1010
Sb, 827–830, 839
Sb-mediated growth, 810, 826, 827, 842
Scalar potential, 13, 34
Scanning electron microscopy (SEM), 918
Scanning nano-probe, 1053
Scanning near-field optical microscopy (SNOM), 12, 14, 16, 29, 31, 33, 111, 282, 485, 501, 502, 505, 511, 513, 522, 858, 984
apertureless, 15, 32
Scattering light, 993, 997, 1003
Schäfer-Hubert effect, 29
Schrödinger equation, 66, 69, 75, 76
Schrödinger picture, 208
Schwarz-Hora effect, 949
Schwoebel barrier, 785
Screening, 485, 487, 493, 494, 498–500, 509, 522
Secondary ion mass spectroscopy (SIMS), 802, 803
Second-quantized representation, 196
Security, 876, 883, 891
Selection rules, 454, 462
Selective chemical etching technique, 342, 344, 347
Selective etching, 283, 284, 287, 289, 290, 294, 302, 303, 309, 316, 321, 325, 327
Selective resin coating (SRC), 292, 294, 311
Selective resin etching, 292
Self-assembled, 810
Self-assembled monolayer, 731–733, 735, 737–740, 750
Self-assembled QD, 810–812
Self-assembling diblockpolymer, 673
Self-assembling template lithography, 673
Self-assembly, 674, 847, 849, 851
Self-consistency, 252, 259
Self-formation, 809–811, 813, 815, 817, 819, 821, 823, 825, 827, 829, 831, 833–835, 837–839, 841, 843
Self-organization, 791
Self-quenching, 739, 752
Self size-limiting, 813, 815, 816, 820, 821
Semiclassical approach, 66, 67
Semi-classical approximation, 115, 132–134, 143, 153, 154, 160, 168, 170, 171, 181
Semiconducting nanoparticles, 750–752, 759
Semiconductor quantum dot, 404
Shadow evaporation, 987
Shape-engineered nanostructures, 876, 877, 904, 916
Sharpened UV fiber probe, 601, 602
Shear-force feedback, 282, 290, 298, 300, 305, 306, 311, 406
Shear-force feedback control, 601
Shear-force microscope, 605
Shear-force topographic image, 300, 301, 311, 325
Short circuit current, 747
Side-channel attacks, 883
Side-to-side, 848
Signal intensity in scanning near-field optical microscopy, 32
Silanization, 851
Silica nanoparticle, 750–752
Silicon-on insulator (SOI) substrate, 982
Silver nanoparticles, 1046
Silver nanorod, 544
Single crystal, 696
Single dot, 396, 398
Single-exciton state, 432

- Single-molecule imaging, 448
Single-molecule level sensitivity, 554, 556
Single QD, 415
Single-QD PL spectroscopy, 421, 427
Single quantum dot (QD) spectroscopy, 420, 461
Single quantum well (SQW), 485, 504, 522
Single-tapered probe, 309, 313, 327, 409
Sisyphus cooling, 991
Size-dependent electron-phonon interaction, 426
Size-dependent resonance, 611, 612
Size regulation, 606, 609
Skew, 879
Skin depth, 25
Slider, 371, 386, 387, 393, 394, 396, 397
Slit-shaped pyramidal Si probe, 352
Slit-type deflector, 981
Slit-type detector, 993
Smith-Purcell effect, 947
SnO₂ electrode, 746–749
SNOM-luminescence mapping, 485
SNOM-PL, 500, 504, 508, 510, 511
SNOM-PL mapping, 512
Soft template, 849
Sol-gel method, 651
Solid immersion lens, 369
Solvent evaporation, 861
Somatostatin, 564, 590–593
Source-size effect, 991
Spatial distribution, 264, 269, 270, 273, 984
Spatial Fourier transformation, 119
Spatial profile, 991
Spatial resolution, 415, 993
Spatio-temporal behavior, 548
s, *p* – *d* exchange interactions, 793
Spectral energy shift, 429
Spectroscopic ellipsometry, 700, 712
Spherical Bessel function, 645, 646
Spherical gold nanoparticle, 527, 529, 531, 532, 540, 541, 555, 557, 563
Spherical Hankel function, 112
Spheroid, 530, 531
Spin and band engineering, 793
Spin on glass (SOG), 678
Spin-orbit coupling, 788
Spin-split impurity band, 801
Spiral pattern, 674, 675
s-polarization, 997, 1001, 1005
Spontaneous emission, 213, 216, 217, 230, 240, 245, 246, 498
Spontaneous force, 979
Spot size, 368–370, 382–384, 389, 392, 393, 397
SPP condenser, 632, 634–636, 639
Sputtering coating method, 412
Sputtering deposition, 1051
Squareness ratio, 680
Stacking growth, 835, 836
Staircase concatenation method, 337, 338, 340
Steep interface, 35
STEM, 817, 818, 820–822, 824, 825, 835, 836
Step, 812, 821, 829, 832, 839, 841
Stimulated absorption and emission, 216, 217, 246
Stimulated emission, 497
Stokes-like shift, 484, 485
Stokes shift, 622, 626
Strain, 810–813, 817, 818, 821, 824, 829, 832, 835–839, 842
Stranski-Krastanov (SK) growth mode, 776, 810
Sub-Doppler profile, 1012
Submillimeter wave, 947
Sub-nanoscale engineering, 978
Substable, 718, 719
Sulfuric acid, 1029
Summation, 880–883
Super-efficient exciton funneling, 887
Super-exchange interaction, 800
Superradiance, 115, 116, 142, 143, 146, 157–159, 161–163, 167, 169, 174, 181–183
Superradiant state, 115, 143, 146, 158, 162
Super-resolution, 12, 14, 16
Surface-enhanced Raman scattering/spectroscopy (SERS), 846, 861, 863, 868, 1023, 1040
Surface ionization, 992
Surface migration, 813, 821, 826
Surface plasmon, 372, 373, 376, 377, 743
Surface plasmon polariton condenser, 632
Surface plasmon-polariton resonance, 1018, 1022
Surface segregation, 817, 829
Surfactant, 829
Survival yield, 1048, 1049
Susceptibility, 66, 67
- T**
Table lookup, 879, 880
Tamper resistance, 883, 884
Taper angle, 102–104
Tapered and metal-coated optical fiber, 404
Tapered probe, 282–284, 290–292, 294, 302, 304, 306, 322, 327
Teflon etching cell, 1026

- Temporal evolution, 269, 272
Ternary alloy, 484, 485
Tert-butyl groups, 739
Tetrahedral tip, 627, 629
Tetrakis(4-sulfonatophenyl) porphyrin, 754
Tetraphenylporphyrin, 739
Thermal heating, 1053
Thermally assisted magnetic recording, 370, 376, 377
Thermometer molecule, 1048
Threading-dislocation density, 484
Three-exciton state, 237–239
Threshold, 716, 717
Throughput, 284, 289, 301, 302, 306, 308, 326, 327, 331, 335–337, 341, 343–346, 349–352, 356, 357, 359, 360, 362–364, 407, 986, 995, 997, 1005
Time-convolution-less (TCL) formulation, 183
Time-correlated single-photon counting method, 648, 653
Time-of-flight mass spectrometer (TOF-MS), 1021, 1032
Time of flight (TOF) measurement, 988, 1008
Time-resolved method, 546
Time-resolved PL, 490
Tiny aperture, 535
TIPL, 492, 498–500, 507, 509, 518, 519
TM plasmon mode, 627–629, 637, 639
Topographic artifact, 538, 540
Topographic image, 435
Total internal reflection (TIR), 111
Total-internal reflection (TIR) illumination, 993, 995
Traceable memory, 888
Tracking, 564, 571
Transfer-printing (TP), 846, 866–869
Transient image, 549, 558
Transient transmission change, 547–549
Transition dipole moment, 198
Transition wavelength, 984
Transit-time broadening, 1012
Transmission efficiency, 413, 447
Transmission electron microscopy (TEM), 740, 754, 780, 837, 838, 855, 859
Transversal vector delta function, 61
Transversal vector field, 59
Transversal vector Green's function for the vector Helmholtz' equation, 46, 62
Transversal vector Helmholtz' equation, 59
Transverse photon, 77, 78
Transverse plasmon mode, 532, 542
Transverse plasmon resonance, 1031
Triethanolamine, 739
Triple-tapered probe, 303, 314, 316, 317, 319, 321, 327, 329, 331, 344–346, 349
TRPL, 490, 491, 497, 503–505, 507, 509, 513, 515, 516, 519, 522
True stable, 714
Tunnel photons, 535
Turning point, 986
Twin peaks, 996, 997
Two-dimensional (2D) mode, 772
Two-exciton state, 193, 213, 214, 221, 222, 224, 226–230, 234, 237, 238, 240, 456, 459
Two-level system, 113–117, 122, 123, 143–146, 153, 154, 156, 157, 159, 180, 181
Two-phase matrix, 1052
Two-step chemical etching, 412
Two-step photoionization, 988, 999, 1006
Type II quantum dot, 455
- U**
Ubiquitous devices, 876
Ultra-cold collisions, 978
Ultrahigh-density system integration, 875, 876
Ultrashort pulsed laser, 538
Uncertainty principle, 952
Unidirectionality, 189
Upconversion, 564, 566, 577–579, 581, 583, 585, 587, 593
Up-spin, 794
UV nanofabrication, 326
UV near-field optical microscopy, 313
UV near-field photoluminescence, 314, 318, 320, 321, 325
UV-NSOM, 313, 320
UV single-tapered probe, 314
UV triple-tapered probe, 313, 316, 318, 321
- V**
Vacuum evaporation, 283, 287, 292, 301, 303, 305, 318, 325
Vacuum microelectronics, 946
Van der Waals potential, 986
Vapor-phase axial deposition (VAD), 287, 289, 303, 316, 321, 330
Vector Helmholtz' equation, 41, 43, 46, 57
Vector Laplace's equation, 59
Vector potential, 77, 88
Virtual cloud, 3
Virtual photons, 3, 67, 68, 91, 92, 104
Visible laser desorption/ionization, 1025
Visualization of wave functions, 534, 535

- Volmer-Weber (VM) mechanism, 683
Volmer-Weber (VM) mode, 810
Volume damping effect, 533
V-pit hole, 801
V-shaped groove, 982
- W**
Wannier function, 197, 198
Wannier representation, 197
Wave equations, 529, 530, 539
Wave function, 444, 445, 454, 455, 461, 463–465, 468, 469, 480
Wavelength dependence, 1037
Wave vector of the plasmon, 543
Wedge-shaped antenna, 368, 377, 378, 380, 382, 385, 390, 392, 397
Wetting layer, 814, 815, 824, 826, 829, 832
Wide-bandgap ternary alloy, 491
Wurtzite, 788, 789
Wurtzite crystal phase, 484
- X**
XOR-logic gate, 230–232, 234, 239, 245, 247
X-ray crystal truncation rod (CTR) scattering, 828
- X-ray photoelectron spectroscopy, 698
XRD, 813
- Y**
Yukawa function, 4, 201, 246
Yukawa potential, 67, 86, 91, 92, 96
Yukawa-type function, 980, 985, 1003
- Z**
ZED-N50 solvent, 995
Zeeman effect, 794
Zeeman splitting, 794, 795
Zeeman sublevel, 978
Zeolitic water, 697
ZEP520A resist, 994
Zeptomoles, 1053
Zinc oxide, 768
Zincporphyrins, 748
ZMD-B rinse, 995
ZnCoO, 793, 794, 800
ZnO nanocrystallite, 600, 603, 605, 619
ZnO QDs, 651, 652, 668
Zn-polarity, 770, 772, 774, 791, 800, 801, 803